

# **Third Microgravity Fluid Physics Conference**

*Proceedings of a conference hosted  
by NASA Lewis Research Center,  
Cleveland, Ohio  
July 13–15, 1996*





*NASA Conference Publication 3338*

# **Third Microgravity Fluid Physics Conference**

*Proceedings of a conference sponsored by  
NASA Headquarters,  
Microgravity Science and Applications Division;  
organized by the Microgravity Fluid Dynamics Discipline Working Group;  
and hosted by Lewis Research Center,  
Space Experiments Division;  
held at the Cleveland Sheraton City Centre Hotel  
July 13–15, 1996*



National Aeronautics and  
Space Administration

Office of Management

**Scientific and Technical  
Information Program**

1996



# Table of Contents

<u>SESSION</u>	<u>Page</u>
<i>Preface</i> . . . . .	xiii
 <i>Keynote</i>	
<b>Multiphase flow: the gravity of the situation</b> Geoffrey Hewitt, Imperial College, London . . . . .	3
<b>Complex fluids: Science, technology and microgravity</b> D. A. Weitz, University of Pennsylvania . . . . .	25
 <i>Critical Phenomena</i>	
<b>Internal waves in CVX</b> Robert F. Berg, National Institute of Standards and Technology . . . . .	29
<b>Growth and morphology of phase separating supercritical fluids</b> John Hegseth, University of New Orleans; Daniel Beysens, CEN–Grenoble; Francoise Perrot and Vadim Nikolayev, Centre d’Etudes de Saclay; Yves Garrabos, CNRS–Universite de Bordeaux I. . . . .	35
<b>Isopycnic phases and structures in H<sub>2</sub>O/CO<sub>2</sub>/ethoxylated alcohol surfactant mixtures</b> Michael E. Paulaitis, Johns Hopkins University; Richard G. Zielinski and Eric W. Kaler, University of Delaware . . . . .	41
<b>Electric field induced interfacial instabilities</b> Robert E. Kusner and Kyung Yang Min, NASA–Lewis; Xiao-lun Wu, University of Pittsburgh; Akira Onuki, Kyoto University . . . . .	47
<b>A brief survey of the equilibrium and transport properties of critical fluids and the     degree to which microgravity is required for their experimental investigation</b> Richard A. Ferrell, University of Maryland . . . . .	53
<b>*Electrostriction of critical fluids in <math>\mu\text{g}</math></b> Greg Zimmerli . . . . .	59
<b>Solute nucleation and growth in supercritical fluid mixtures</b> Gregory T. Smedley, California Institute of Technology; Gerald Wilemski, Lawrence Livermore National Lab; W. Terry Rawlins, David B. Oakes, and Prakash Joshi, Physical Sciences, Inc.; William W. Durgin, Worcester Polytechnic Institute . . . . .	61
<b>Zeno: critical fluid light scattering experiment</b> Robert Gammon, J. N. Shaumeyer, Matthew E. Briggs, Hacène Boukari, and David A. Gent, University of Maryland; R. Allen Wilkinson, NASA–Lewis . . . . .	67
<b>*Critical fluid thermal equilibrium dynamics</b> R. Allen Wilkinson, NASA–Lewis . . . . .	73
<b>Turbidity of a binary fluid mixture: determining <math>\eta</math></b> Donald Jacobs, College of Wooster . . . . .	75
<b>Nonlinear dynamics and nucleation kinetics in near-critical liquids</b> Alexander Z. Patashinski and Mark A. Ratner, Northwestern University; Vladimir Pines, Case Western Reserve University. . . . .	81

# ***Multiphase Flow, Heat Transfer, and Phase Change***

<b>Fundamental processes of atomization in fluid-fluid flows</b>	
Christopher Gallagher, David T. Leighton, Hsueh-Chia Chang, and Mark J. McCready, University of Notre Dame . . . . .	89
<b>Observations of gas-liquid flows through contractions in microgravity</b>	
John McQuillen, NASA-Lewis . . . . .	95
<b>Stability of wavy films in gas-liquid two-phase flows at normal and microgravity conditions</b>	
V. Balakotaiah, University of Houston; S. S. Jayawardena, NASA-Lewis . . . . .	103
<b>Experimental and analytical study of two-phase flow parameters in microgravity</b>	
D. Abdollahian and J. Quintel, S. Levy, Inc.; J. Zahm, San Jose State University; J. McQuillen, NASA-Lewis . . . . .	109
<b>Two-phase annular flow in helical coil flow channels in a reduced gravity environment</b>	
Edward G. Keshock, Cleveland State University; Chin S. Lin, Analex Corporation . . . . .	115
<b>Bubble generation in a flowing liquid medium and resulting two-phase flow in microgravity</b>	
Yasuhiro Kamotani, Case Western Reserve University . . . . .	121
<b>Production of gas bubbles in reduced gravity environments</b>	
Hasan Oğuz, Johns Hopkins University; Shu Takagi, University of Tokyo; Masaki Misawa, Mechanical Engineering Laboratory, Japan . . . . .	127
<b>Phase distribution phenomena for simulated microgravity conditions: experimental work</b>	
Maneesh Singhal, Fabian J. Bonetto, and R. T. Lahey, Jr., Rensselaer Polytechnic Institute . . . . .	133
<b>Bubble dynamics, two-phase flow, and boiling heat transfer in microgravity</b>	
Jacob N. Chung, Washington State University . . . . .	141
<b>Non-isothermal experimental study of the constrained vapor bubble thermosyphon</b>	
Muthu Karthikeyan, Jianming Huang, Joel Plawsky, and Peter Wayner, Jr., Rensselaer Polytechnic Institute . . . . .	147
<b>Investigation of mechanisms associated with nucleate boiling under microgravity conditions</b>	
V. K. Dhir, University of California-Los Angeles . . . . .	153
<b>Acoustic behavior of vapor bubbles</b>	
A. Prosperetti and H. N. Oğuz, Johns Hopkins University . . . . .	159
<b>Design of an improved heater array to measure microscale wall heat transfer</b>	
Jungho Kim and Choon Ping Ch'ng, University of Denver; T. S. Kalkur, University of Colorado . . . . .	165
<b>The development of novel, high-flux, heat transfer cells for thermal control in microgravity</b>	
Marc K. Smith and Ari Glezer, Georgia Institute of Technology . . . . .	171
<b>The development of a full field three-dimensional microscale flow measurement technique for application to near contact line flows</b>	
Qun He and Kevin Hallinan, University of Dayton . . . . .	177
<b>A study of nucleate boiling with forced convection in microgravity</b>	
Herman Merte, Jr., University of Michigan . . . . .	183

<b>Evaporation on/in capillary structures of high heat flux two-phase devices</b> Amir Faghri and Dmitry Khrustalev, University of Connecticut . . . . .	189
<b>Experimental investigation of pool boiling heat transfer enhancement in microgravity in the presence of electric fields</b> Cila Herman, Johns Hopkins University . . . . .	195
<b>Marangoni effects in the boiling of binary fluid mixtures</b> Sayeed Ahmed and Van P. Carey, University of California–Berkeley; Brian Motil, NASA–Lewis . . . . .	201
<b>Rewetting of monogroove heat pipe in space station radiators</b> S. H. Chan, Ting Rong Shen, and John Blake, University of Wisconsin–Milwaukee . . . . .	207
<b>Electrohydrodynamic pool boiling in reduced gravity</b> B. D. Shaw and S. L. Stahl, University of California–Davis . . . . .	213
<b>Analysis of the hydrodynamics and heat transfer aspects of microgravity two-phase flows</b> Kamiel S. Rezkallah, University of Saskatchewan . . . . .	219
<b>Microgravity particle dynamics</b> Ivan O. Clark, NASA–Langley; Edward J. Johnson, Lockheed Martin . . . . .	227

## ***Mechanics of Granular Media***

<b>Microgravity segregation in binary mixtures of inelastic spheres driven by velocity fluctuation gradients</b> James T. Jenkins and Michel Y. Louge, Cornell University . . . . .	235
<b>Migrational instabilities in particle suspensions</b> J. D. Goddard, University of California–San Diego . . . . .	241
<b>Dynamics of granular materials</b> R. P. Behringer, Duke University . . . . .	245
<b>NMRI measurements of flow of granular mixtures</b> Masami Nakagawa, Sandia National Laboratories; R. Allen Waggoner and Eiichi Fukushima, The Lovelace Institutes . . . . .	251

## ***Pattern Formation, Flow Instability, and Thermocapillary Flows***

<b>Experimental study of buoyant-thermocapillary convection in a rectangular cavity</b> Manfred G. Braunsfurth and George M. Homsy, Stanford University . . . . .	259
<b>Long-wavelength instability in Marangoni convection</b> Stephen J. Van Hook, Michael F. Schatz, Jack B. Swift, W. D. McCormick, and Harry L. Swinney, University of Texas–Austin . . . . .	265
<b>An experimental study of Richtmyer-Meshkov instability</b> Jeffrey W. Jacobs and Charles E. Niederhaus, University of Arizona . . . . .	271
<b>Absolute and convective instability of a liquid jet in microgravity</b> S. P. Lin, I. Vihinen, A. Honohan, and M. Hudman, Clarkson University . . . . .	277
<b>Non-coalescence effects in microgravity</b> G. Paul Neitzel, Georgia Institute of Technology . . . . .	283
<b>Time-dependent thermally-driven interfacial flows in multilayered fluid structures</b> H. Haj-Hariri, University of Virginia; A. Borhan, Pennsylvania State University . . . . .	289
<b>Studies in thermocapillary convection of the Marangoni-Benard type</b> R. E. Kelly and A. C. Or, University of California–Los Angeles . . . . .	295
<b>Thermocapillary convection in a low Pr material under simulated reduced- gravity conditions</b> Y. Tao and S. Kou, University of Wisconsin . . . . .	301

<b>Oscillatory thermocapillary convection</b>	
Jieyong Xu and Abdelfattah Zebib, Rutgers University . . . . .	307
<b>Observations of time-dependent behavior in the two-layer Rayleigh-Bénard system</b>	
C. David Andereck, Peter W. Colovas, and Michael M. Degen, Ohio State University . . . . .	313
<b>Salt-finger convection in a stratified fluid layer induced by thermal and solutal capillary motion</b>	
C. F. Chen and Cho Lik Chan, University of Arizona . . . . .	319
<b>Low-dimensional dynamical models of thermal convection</b>	
A. Liakopoulos, Lehigh University . . . . .	325
<b>Surface tension driven convection experiment-2 (STDCE-2)</b>	
Simon Ostrach and Yasuhiro Kamotani, Case Western Reserve University . . . . .	331
<b>Thermocapillary motion in an emulsion</b>	
Vladislav V. Pukhnachov, Lavrentyev Institute of Hydrodynamics; Oleg V. Voinov, Institute for Mechanics of Multiphase Systems . . . . .	337

## *Solidification*

<b>Interface morphology during crystal growth: effects of anisotropy and fluid flow</b>	
S. R. Coriell, B. T. Murray, and G. B. McFadden, National Institute of Standards and Technology; A. A. Chernov, Universities Space Research Association and NASA-Marshall . . . . .	345
<b>Shear stabilization of a solidifying front</b>	
Stephen H. Davis, Northwestern University; Timothy P. Shulze, University of Cambridge . . . . .	351
<b>Fluid dynamics and solidification of molten solder droplets impacting on a substrate in microgravity</b>	
Dimos Poulikakos and Constantine M. Megaridis, University of Illinois-Chicago; M. Vedha-Nayagam, Analex Corporation . . . . .	357
<b>Crystal growth and fluid mechanics problems in directional solidification</b>	
S. Tanveer, G. R. Baker, and M. R. Foster, Ohio State University . . . . .	363
<b>Nonlinear convection in mushy layers</b>	
M. Grae Worster and T. P. Schulze, Cambridge University; D. M. Anderson, National Institute of Standards and Technology . . . . .	369

## *Complex Fluids*

<b>The extensional rheology of non-Newtonian materials</b>	
Stephen H. Spiegelberg and Gareth H. McKinley, Harvard University . . . . .	377
<b>The melting of aqueous foams</b>	
Douglas J. Durian, Anthony D. Gopal, and Moin U. Vera, University of California-Los Angeles; Stephen A. Langer, National Institute of Standards and Technology . . . . .	383
<b>Chain dynamics in a dilute magnetorheological fluid</b>	
Jing Liu and Martin Hagenbuehle, California State University-Long Beach . . . . .	389
<b>*Growth and morphology of crystals made in hard spheres</b>	
Bruce Ackerson, Oklahoma State University . . . . .	395

<b>Dynamics of disorder-order transitions in hard sphere colloidal dispersions in <math>\mu\text{g}</math></b>	
J. X. Zhu, M. Li, S. E. Phan, W. B. Russel, and P. M. Chaikin, Princeton University; R. Rogers and W. Meyer, NASA–Lewis . . . . .	397
<b>Dynamic light scattering from colloidal gels</b>	
A. H. Krall and D. A. Weitz, University of Pennsylvania . . . . .	403
<b>*Structure, hydrodynamics, and phase transition of freely suspended liquid crystals</b>	
Noel Clark, University of Colorado . . . . .	409
<b>*Behavior of rapidly sheared bubbly suspensions</b>	
Ashok Sangani, Syracuse University . . . . .	411
<b>Polymer-induced depletion interaction and its effect on colloidal sedimentation in colloid-polymer mixtures</b>	
Penger Tong, Oklahoma State University . . . . .	413
<b>Chiral symmetry breaking in crystal growth is hydrodynamic convection relevant?</b>	
B. Martin, A. Tharrington, and X-l. Wu, University of Pittsburgh . . . . .	419
<b>*Plasma dust crystallization</b>	
John Goree, University of Iowa . . . . .	425

## ***G-jitter Induced and Stochastic Flows***

<b>Fluid physics in a fluctuating acceleration environment</b>	
J. Ross Thomson, François Drolet, and Jorge Viñals, Florida State University . . . . .	429
<b>Resolving high amplitude surface motion with diffusing light</b>	
W. Wright, R. Budakian, and S. J. Putterman, University of California– Los Angeles . . . . .	435
<b>Effects of gravity on sheared turbulence laden with bubbles or droplets</b>	
Said Elghobashi, University of California–Irvine; Juan Lasheras, University of California–San Diego . . . . .	443
<b>Transport phenomena in stratified multi-fluid flow in the presence and absence of gravity</b>	
Norman Chigier and William Humphrey, Carnegie Mellon University . . . . .	449
<b>Decoupling the role of inertia and gravity on particle dispersion</b>	
Chris Rogers, Tufts University; Kyle Squires, University of Vermont . . . . .	455
<b>Analysis of residual acceleration effects on transport and segregation during directional solidification of tin-bismuth in the MEPHISTO furnace facility</b>	
J. Iwan D. Alexander and Arnaud Lizée, University of Alabama–Huntsville; J.-J. Favier and J.-P. Garandet, CEA-Grenoble . . . . .	461
<b>*Reliability of numerical solutions and two-dimensional turbulence in the problem of Rayleigh-Bénard convection</b>	
Olga Rodicheva and Evgeny Rodichev, Moscow State University . . . . .	465

## ***Dynamics and Stability of Liquid Bridges***

<b>Dynamics and statics of nonaxisymmetric liquid bridges</b>	
J. Iwan D. Alexander, Andrew H. Resnick, and L. A. Slobozhanin, University of Alabama–Huntsville . . . . .	469
<b>Stabilization and low-frequency oscillation of capillary bridges with modulated acoustic radiation pressure</b>	
P. L. Marston, M. J. Marr-Lyon, S. F. Morse, and D. B. Thiessen, Washington State University . . . . .	475

<b>Influence of thermocapillary flow on capillary stability: long float-zones in low gravity</b>	
Yi-Ju Chen and Paul H. Steen, Cornell University . . . . .	481
<b>Experimental control of thermocapillary convection in a liquid bridge</b>	
Valery Petrov, Michael F. Schatz, Kurt A. Muehlner, Stephen J. Van Hook, W. D. McCormick, Jack B. Swift, and Harry L. Swinney, University of Texas–Austin . . . . .	487
<b>Deformation of fluid column by action of axial vibration and some aspects of high-rate thermocapillary convection</b>	
Alexander I. Feonychev, Moscow Aviation Institute; Irina S. Kalachinskaya, Moscow State University; Victor I. Pokhilko, Russian Academy of Sciences . . . . .	493

## *Dynamics and Interaction of Bubbles and Drops*

<b>Investigation of drop formation by a vortex ring in microgravity</b>	
Luis P. Bernal and Pepi Maksimovic, University of Michigan . . . . .	501
<b>Droplet deformation in an extensional flow: the role of surfactant physical chemistry</b>	
Kathleen J. Stebe, Johns Hopkins University . . . . .	509
<b>Ground based studies of thermocapillary flows in levitated drops</b>	
Satwindar Singh Sadhal, University of Southern California; Eugene H. Trinh, Jet Propulsion Laboratory . . . . .	515
<b>Marangoni–Bénard convection in an evaporating liquid thin layer</b>	
An-Ti Chai, NASA–Lewis; Nengli Zhang, National Research Council . . . . .	521
<b>Bubble dynamics on a heated surface</b>	
M. Kassemi, Ohio Aerospace Institute; N. Rashidnia, NYMA, Inc. . . . .	527
<b>Computations of drop collision and coalescence</b>	
Grétar Tryggvason, Damir Juric, Selman Nas, and Saeed Mortazavi, University of Michigan . . . . .	535
<b>Marangoni effects on the bubble dynamics in a pressure driven flow</b>	
Chang-Won Park and S. R. K. Maruvada, University of Florida . . . . .	541
<b>Forced oscillations of supported drops</b>	
Edward D. Wilkes and Osman A. Basaran, Purdue University . . . . .	547
<b>Thermocapillary migration and interactions of bubbles and drops</b>	
R. Balasubramaniam, NASA–Lewis; Claud E. Lacy and R. Shankar Subramanian, Clarkson University; Günter Wozniak, University of Freiberg . . . . .	553
<b>Studies of the stability and dynamics of levitated drops</b>	
A. V. Anilkumar, C. P. Lee, and T. G. Wang, Vanderbilt University . . . . .	559
<b>Nonlinear bubble interactions in acoustic pressure fields</b>	
Tiberiu Barbat, Nasser Ashgriz, and Ching-Shi Liu, State University of New York–Buffalo . . . . .	565
<b>A theoretical study of remobilizing surfactant retarded fluid particle interfaces</b>	
Yanping Wang, New Jersey Institute of Technology; Charles Maldarelli, City College of New York . . . . .	571
<b>Self-diffusion of drops in a dilute sheared emulsion</b>	
M. Loewenberg, Yale University; E. J. Hinch, University of Cambridge . . . . .	579



<b>Drops in space: super oscillations and surfactant studies</b>	
Robert E. Apfel, Yuren Tian, Joseph Jankovsky, and X. Chen, Yale University; Tao Shi, Emory University; R. Glynn Holt, Jet Propulsion Laboratory and NASA-Johnson; Eugene Trinh and Arvid Croonquist, Jet Propulsion Laboratory; Kathryn C. Thornton, Albert Sacco, Jr., Catherine Coleman, Fred W. Leslie, and David H. Matthiesen, NASA-Johnson . . . . .	585
<b>The onset of resonance-controlled instability in spherical bubble oscillations</b>	
R. Glynn Holt and D. Felipe Gaitan, Jet Propulsion Laboratory . . . . .	591
<b>Shape oscillations of gas bubbles with Newtonian interfacial rheological properties</b>	
Ali Nadim, Boston University . . . . .	599

## ***Interfacial Phenomena***

<b>*Microscale hydrodynamics in near moving contact line</b>	
Stephen Garoff, Carnegie Mellon University . . . . .	607
<b>Free-surface and contact line motion of liquids in a microgravity</b>	
Leonard W. Schwartz, University of Delaware . . . . .	609
<b>On the boundary conditions at an oscillating contact line: a physical/numerical experimental program</b>	
Marc Perlin and William W. Schultz, University of Michigan . . . . .	615
<b>The micromechanics of the moving contact line</b>	
Minsub Han, Seth Lichter, Chih-Yu Lin, and Yeong-Yan Perng, Northwestern University . . . . .	621
<b>Dynamics of the molten contact line</b>	
Ain A. Sonin and Stefano Schiaffino, Massachusetts Institute of Technology . . . . .	627
<b>Wetting hysteresis at the molecular scale</b>	
Wei Jin and Joel Koplik, City College of the City University of New York; Jayanth R. Banavar, Pennsylvania State University . . . . .	635
<b>Fluid creep effects on near-wall solute transport for non-isothermal ampoules</b>	
Dimitrios Papadopoulos and Daniel E. Rosner, Yale University . . . . .	641
<b>*The dissolution of interface between miscible liquids</b>	
James Maher, University of Pittsburgh . . . . .	647
<b>Equilibrium fluid interface behavior under low- and zero-gravity conditions .II</b>	
Paul Concus, University of California-Berkeley; Robert Finn, Stanford University . . . . .	649
<b>Critical velocities in open capillary flow</b>	
Michael Dreyer, Dieter Langbein, and Hans J. Rath, University of Bremen . . . . .	655
<b>Thermoacoustic effects at a solid-fluid boundary: the role of a second-order thermal expansion coefficient</b>	
Ashok Gopinath, Naval Postgraduate School . . . . .	661
<b>A fluorescence recovery after photobleaching (FRAP) technique for the measurement of solute transport across surfactant-laden interfaces</b>	
Edward P. Browne and T. Alan Hatton, Massachusetts Institute of Technology . . . . .	667
<b>Investigation of thermal stress convection in nonisothermal gases under microgravity conditions</b>	
Daniel W. Mackowski and Roy W. Knight, Auburn University . . . . .	673
<b>Phoretic and radiometric force measurements on microparticles in microgravity conditions</b>	
E. James Davis, University of Washington . . . . .	679

<b>Cross-effects in microgravity flows</b>	
S. K. Loyalka, R. V. Tompson, I. N. Ivchenko, T. K. Ghosh, S. A. Hamoodi, K. A. Hickey, C. M. Huang, P. A. Tebbe, D. H. Gabis, P. Tekasakul, and J. A. Bentz, University of Missouri–Columbia . . . . .	685
<b>Dynamical modeling of surface tension</b>	
J. U. Brackbill and D. B. Kothe, Los Alamos National Laboratory. . . . .	693

## ***Electric and Magnetic Effects***

<b>Control of flowing liquid films by electrostatic fields in space</b>	
S. George Bankoff and Michael J. Miksis, Northwestern University; Hyo Kim, Korea Gas Company. . . . .	701
<b>Magnetothermal convection in nonconducting diamagnetic and paramagnetic fluids</b>	
Boyd F. Edwards, Donald D. Gray, and Jie Huang, West Virginia University . . . . .	711
<b>Waves in radial gravity using magnetic fluid</b>	
Daniel R. Ohlsen, John E. Hart, and Patrick D. Weidman, University of Colorado . . . . .	717
<b>Binary oscillatory crossflow electrophoresis</b>	
Richard F. Molloy, Christopher T. Gallagher, and David T. Leighton, Jr., University of Notre Dame . . . . .	723
<b>*Electrokinetic transport of heterogeneous particles in suspensions</b>	
John Anderson, Carnegie Mellon University. . . . .	729
<b>Electrohydrodynamic interaction of a pair of spherical drops</b>	
J. A. Erker and J. C. Baygents, University of Arizona . . . . .	731
<b>Cell and particle interactions and aggregation during electrophoretic motion</b>	
Shulin Zeng, Paul Todd, and Robert H. Davis, University of Colorado; Hua Wang, General Electric Company; Michael Loewenberg, Yale University . . . . .	737

## ***Biofluids***

<b>Microgravity effects on transendothelial transport</b>	
John M. Tarbell, Pennsylvania State University . . . . .	745
<b>The propagation of a liquid bolus through an elastic tube and airway reopening</b>	
Peter D. Howell and James B. Grotberg, Northwestern University . . . . .	751

## ***Convective Flows***

<b>Gravity-dependent transport in industrial processes</b>	
Simon Ostrach and Yasuhiro Kamotani, Case Western Reserve University. . . . .	759
<b>Experiments on thermal convection in rotating spherical shells with radial gravity: the geophysical fluid flow cell</b>	
John E. Hart, University of Colorado . . . . .	767
<b>A geophysical flow experiment in a compressible critical fluid</b>	
John Hegseth and Laudelino Garcia, University of New Orleans. . . . .	773
<b>Experimental study of liquid jet impingement in microgravity: the hydraulic jump</b>	
C. T. Avedisian and Z. Zhao, Cornell University. . . . .	779
<b>Studies of radiation-driven and buoyancy-driven fluid flows and transport</b>	
Paul D. Ronney and Justin M. Fortmeyer, University of Southern California . . . . .	785

<b>Acoustic streaming and heat and mass transfer enhancement</b>	
E. H. Trinh, Jet Propulsion Laboratory; A. Gopinath, Naval Post-Graduate School . . .	791
<b>Current results and proposed activities in microgravity fluid dynamics</b>	
V. I. Polezhaev, Russian Academy of Sciences . . . . .	797
<b>Effect of spacecraft rotation on fluid convection under microgravity</b>	
Valentin S. Yuferev, Elvira N. Kolesnikova, Yuri A. Polovko, and Alexander I. Zhmakin, Ioffe Physical-Technical Institute . . . . .	807
<b>System for measurement of convection aboard Space Station</b>	
Gennady P. Bogatyrev, Aleksei V. Gorbunov, and Gennady F. Putin, Perm State University; Alexander I. Ivanov, RSC Energia; Sergei A. Nikitin and Vadim I. Polezhaev, Russian Academy of Sciences . . . . .	813

## ***Experimental Techniques***

<b>A new generation fiber optic probe: characterization of biological fluids, protein crystals, and ophthalmic diseases</b>	
Rafat R. Ansari and Kwang I. Suh, NASA–Lewis . . . . .	821
<b>Applications of phase shifted, laser feedback interferometry to fluid physics</b>	
Ben Ovryn, NYMA, Inc.; Steven J. Eppell, Case Western Reserve University; James H. Andrews and John Khaydarov, Ohio Aerospace Institute . . . . .	829
<b>*Laser light scattering—expanding the boundaries</b>	
William Meyer, Ohio Aerospace Institute/NASA–Lewis . . . . .	835

<b><i>Schedule Overview</i></b> . . . . .	837
---	-----

<b><i>Attendance List</i></b> . . . . .	849
---	-----

<b><i>Author List</i></b> . . . . .	881
-------------------------------------	-----



## PREFACE AND ACKNOWLEDGEMENTS

The Third Microgravity Fluid Physics Conference was held in Cleveland, Ohio, on June 13 to 15, 1996. It was attended by 385 people from academia, industry, and government, representing seven countries. The conference's purpose was to inform the fluid physics community of research opportunities in reduced-gravity fluid physics, present the status of the existing and planned reduced-gravity fluid physics research programs, and inform participants of the upcoming NASA Research Announcement in this area.

The plenary sessions provided an overview of the Microgravity Fluid Physics Program, present and future areas of emphasis, information on NASA's plans to use the *International Space Station* for conducting fluid physics research, and the process by which investigators enter the program. A technical session dedicated to invited Russian scientists offered participants an opportunity to hear from speakers about the microgravity research programs in that country. Keynote speakers provided broad technical overviews on multiphase flow, complex fluids research, and research opportunities in exploration of space. NASA Headquarters personnel provided information on the upcoming NRAs and answered questions from the audience.

One hundred and thirty-two technical papers were presented in 28 sessions. Presenters briefed their peers on the scientific results of their ground-based and flight research. One hundred and twenty-two of the papers are included here. Titles and authors on papers that were not available are listed for completeness. Papers are grouped by subdisciplines rather than sessions in which they were presented. The conference agenda and an author index are included to facilitate the reader in locating papers.

Sincere appreciation is offered to the authors for providing the papers in a timely manner and to the members of the Microgravity Fluids Physics Branch of NASA Lewis Research Center for their many contributions. Assistance from the Logistics and Technical Information Division personnel at NASA Lewis Research Center in publishing this proceedings volume is gratefully acknowledged.

Dr. Bhim S. Singh, Conference Organizer  
Mail Stop 500-102  
NASA Research Center  
21000 Brookpark Road  
Cleveland, OH 44135  
Phone (216) 433-5396 or fax (216) 433-8660  
E-mail: [bhim.s.singh@Lerc.nasa.gov](mailto:bhim.s.singh@Lerc.nasa.gov)

This conference was made possible by the effort of many people. We acknowledge the contributions of the following individuals:

***Fluid Dynamics Discipline Working Group***

Stephen Davis (chair), Northwestern University  
Bhim Singh (vice-chair), NASA-Lewis  
Sanjoy Banerjee, University of California—Santa Barbara  
S. George Bankoff, Northwestern University  
Bradley Carpenter, NASA Headquarters  
Joe Goddard, University of California—San Diego  
Joel Koplik, City College of the City of New York  
Michael Moldover, NIST  
G. Paul Neitzel, Georgia Institute of Technology  
Harry Swinney, University of Texas at Austin  
Matthew Tirrell, University of Minnesota

***Session Chairs***

***Plenary Sessions***

S. George Bankoff  
Bradley Carpenter  
Paul Chaikin  
Jack Salzman

***Parallel Sessions***

David Andereck	David Leighton
Bruce Ackerson	Sung Lin
Paul Concus	Mark McCready
Robert Davis	Herman Merte
Richard Ferrell	Hasan Oguz
Robert Gammon	Daniel Rosner
Stephen Garoff	Ashok Sangani
Hossein Haj-Hariri	Ain Sonin
Cila Herman	Shankar Subramanian
George Homsy	Grétar Tryggvason
Jungo Kim	Peter Wayner, Jr.
Joel Koplik	Abdelfattah Zebib

***NYMA Conference Team***

Wilma Graham  
Debra Lawhun  
Linda Oliver  
Scharlene Schmidt  
John Toma  
Richard Ziegfeld

# Keynote





Cleveland, Ohio, June 1996

## MULTIPHASE FLOW: THE GRAVITY OF THE SITUATION

By

G.F. Hewitt  
Department of Chemical Engineering  
& Chemical Technology  
Imperial College of Science, Technology  
& Medicine,  
London, England

### ABSTRACT

A brief survey is presented of flow patterns in two-phase, gas-liquid flows at normal and microgravity, the differences between them being explored. It seems that the flow patterns in zero gravity are in general much simpler than those in normal gravity with only three main regimes (namely bubbly, slug and annular flows) being observed. Each of these three regimes is then reviewed, with particular reference to identification of areas of study where investigation of flows at microgravity might not only be interesting in themselves, but also throw light on mechanisms at normal earth gravity. In bubbly flow, the main area of interest seems to be that of bubble coalescence. In slug flow, the extension of simple displacement experiments to the zero gravity case would appear to be a useful option, supplemented by computational fluid dynamics (CFD) studies. For annular flow, the most interesting area appears to be the study of the mechanisms of disturbance waves; it should be possible to extend the region of investigation of the onset and behaviour of these waves to much low gas velocities where measurements are clearly much easier.

### 1. INTRODUCTION

Two-phase gas-liquid flow is important in a whole range of applications under earth gravity conditions; these include pipeline transport of oil/natural gas mixtures, flows in nuclear reactor systems under accident conditions, evaporation and condensation systems in power and process plant, geothermal energy systems etc. Such flows are also important in space applications where, of course, microgravity conditions apply. These space applications include transfer line flows of cryogenic fluids, heat transfer associated with space power systems, design and operation of the thermal bus which operates as a heat-sink etc. At normal gravity conditions, the existence of a gravitation force has a profound effect on the nature of the flows, due to the large density differences which normally exist between gas and liquid phases. Thus, in vertical flows, gravitation forces give rise to local slip between phase elements (drops or bubbles) and can cause periodic flow reversals (for instance in slug or churn flows). In horizontal flows, the effect of gravity is to cause asymmetry of the flow, the extreme case being that of a fully stratified flow with the liquid flowing at the bottom of the channel and the gas at the top. Thus, in micro gravity situations, one would expect major differences in flow behaviour and such differences are indeed observed. However, as we shall see, gravity is a *complicating factor* and flows at microgravity are essentially much simpler.

In what follows, Section 2 discusses flow regimes and the specific regimes of bubbly flow, slug flow and annular flow are discussed in Sections 3, 4 and 5 respectively.

## 2. FLOW REGIMES

A wide variety of descriptors has been given to flow regimes in gas-liquid flow; sketches of the more commonly accepted regimes for vertical and horizontal flows are given in Figures 1 and 2 respectively.

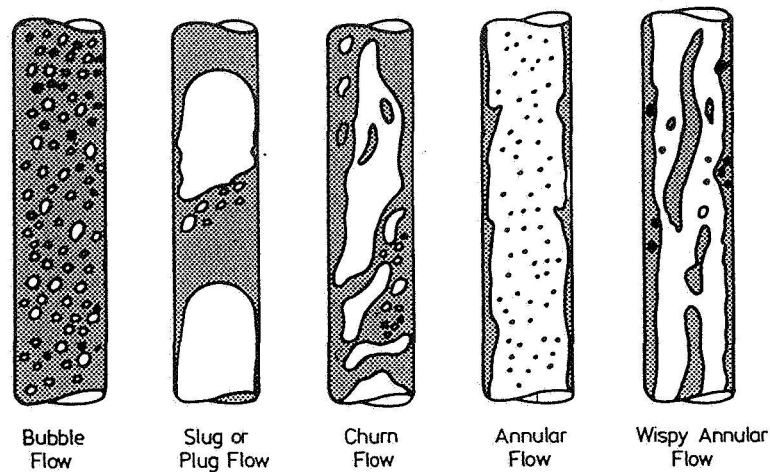


**Figure 1: Flow regimes in gas-liquid flow in a vertical tube at normal gravity**

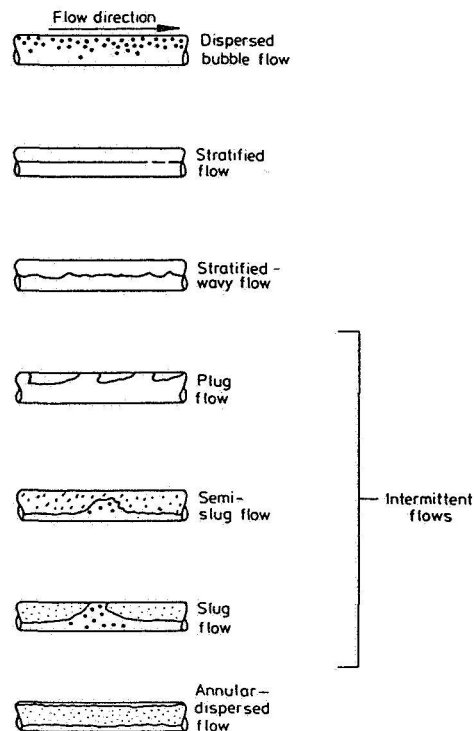


**Figure 2: Flow regimes in gas-liquid flow in a horizontal tube at normal gravity**

For flows at zero gravity, the regimes observed are bubbly flow, slug flow and annular flow and sketches of these regimes, taken from the paper of Dukler et al (1988) are shown in Figure 3.

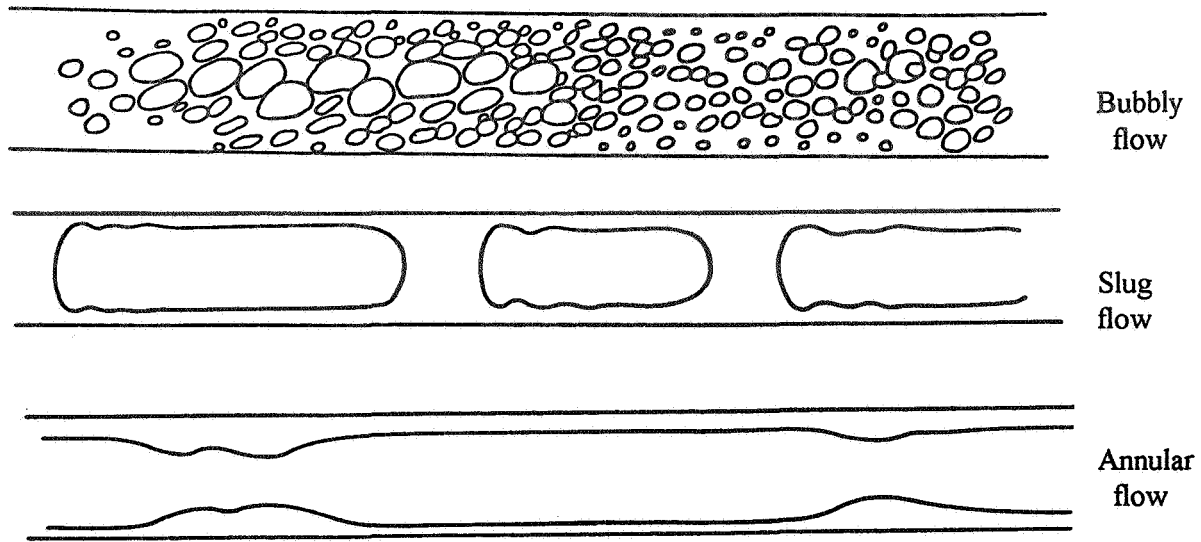
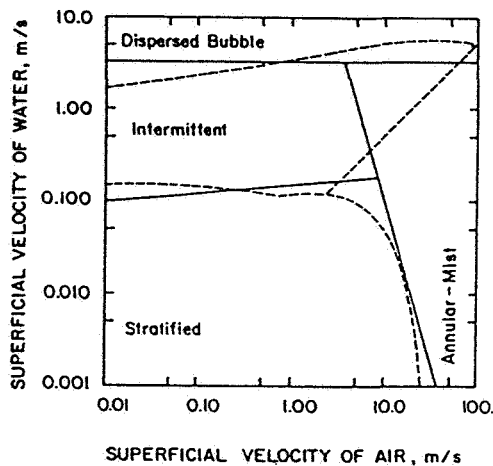
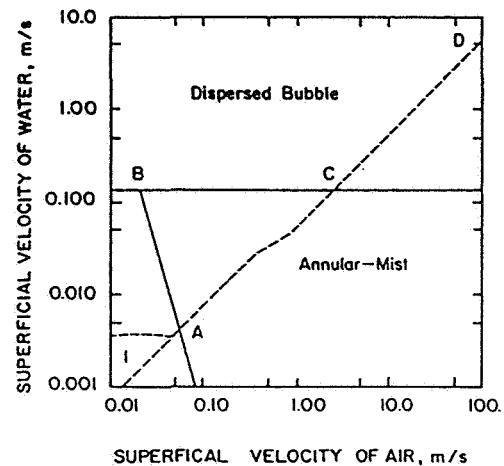


**Figure 3: Sketches of flow regimes in gas-liquid (air-water) flow under microgravity conditions (Dukler et al, 1988)**

A very large number of methods (ranging from purely empirical to semi-theoretical) have been developed for the prediction of flow pattern in normal gravity flows. The mechanistic models often take account of gravity as a parameter and a natural question is whether such models can be applied to the microgravity case. This approach was followed by Reddy Karri and Mathur (1988) who made predictions for a 2.54 cm internal diameter pipe using the mechanistic models of Taitel and Dukler (1976) and Weisman et al (1979) models. The results are shown in Figure 4 for the case of the horizontal flow models; though the two approaches give reasonable agreement at normal gravity (Figure 4a) they differ greatly at microgravity (Figure 4b).



(a)  $g = g_n$



(b)  $g = 0.000001 g_n$

**Figure 4: Predictions of flow patterns in normal and microgravity using mechanistic models proposed for normal gravity conditions (Reddy Kari and Mathur, 1988)**  
 - - - Taitel Dukler model — Weisman et al model

It is an unfortunate fact that most models for two-phase flow patterns are developed using air-water data at near atmospheric pressure. It is not necessary to go to microgravity conditions to show the deficiencies of these models. To illustrate this point, two examples may be cited:

- (1) Reiman et al (1982) compared a variety of models for the transition from slug to annular flow in horizontal pipes. Their results are shown in Figure 5. The predictions vary by an order of magnitude and, more worryingly, the trends of variation of the position of the transition with fluid velocities can be in opposite directions depending on the model.
- (2) System pressure is a very important variable in multiphase flow but most experiments (and their associated models) are carried out at near atmospheric pressure. Recent work at Imperial College on the stratified-slug transition in horizontal flows (Manolis, 1995) shows that the transition moves to higher liquid superficial velocities as the pressure increases (Figure 6) whereas the trends predicted from the Taitel-Dukler (1976) model are in entirely the opposite direction (Figure 7).

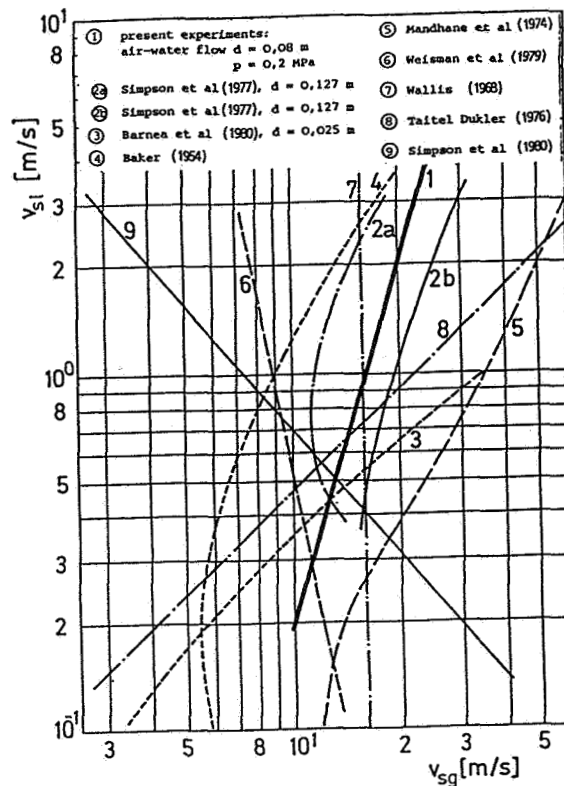


**Figure 5: Slug-annular transition in horizontal flow at normal gravity: Comparison of models (Reiman et al, 1982)**

The inadequacies of flow pattern prediction methods provide a serious barrier to the development of improved modeling methods for multiphase flows at normal gravity. A particularly difficult area is that of the transition from slug to churn flow and from churn flow to annular flow in vertical tubes. Some authors consider the churn flow regime to be merely a manifestation of a developing form of slug flow (see for instance Mao and Dukler, 1993) whereas an alternative view is to draw an analogy with flooding in counter-current flow of a falling liquid film and a rising gas stream; flooding appears to occur as a result of the formation of large waves ("flooding waves") which are swept up the channel by the gas stream, leading to transport of liquid above the injection point. It has been hypothesized that the transition from slug flow to churn flow occurs when such flooding waves are

formed in the large Taylor bubble (where there exists a falling liquid film around the periphery with upward gas flow in the centre of the pipe).

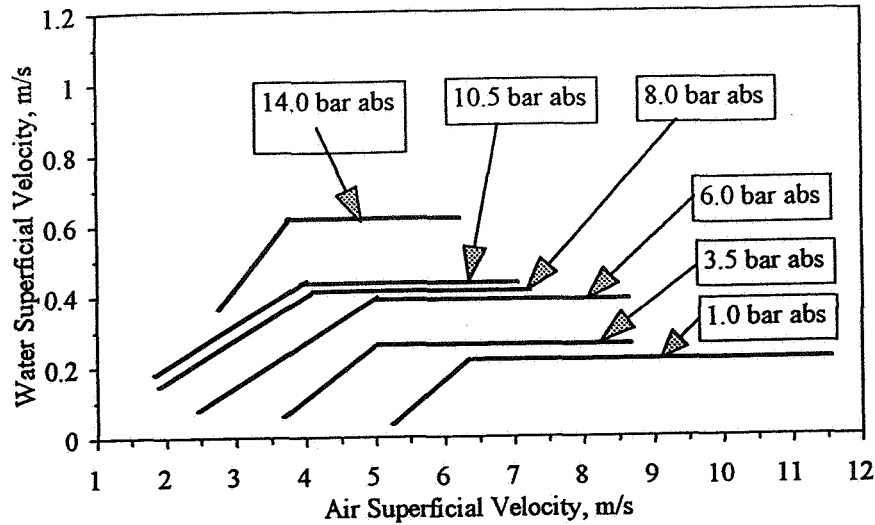


**Figure 6: Effect of pressure on stratified-slug transition in horizontal flow (Manolis, 1995)**

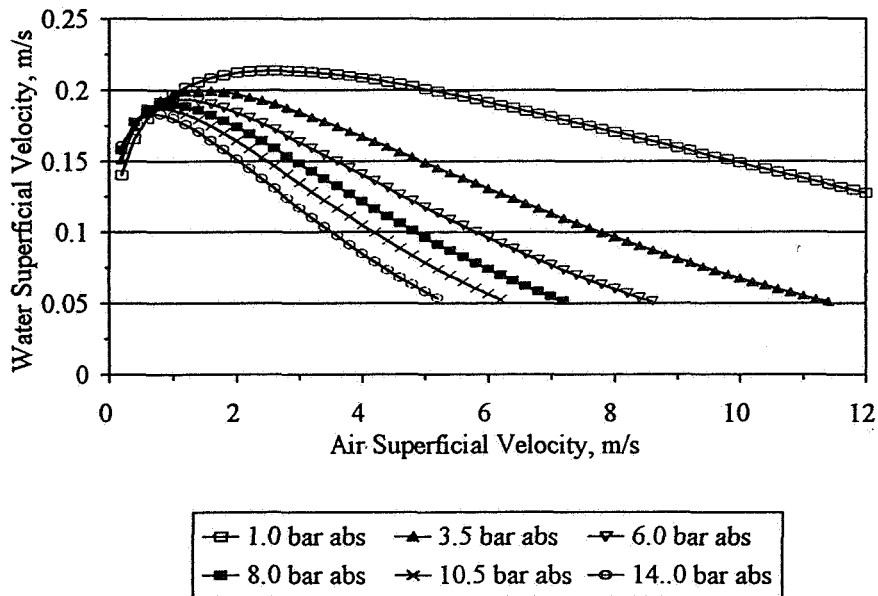


**Figure 7: Effect of pressure on transition from stratified to slug flow as predicted from the Taitel-Dukler (1976) model (Manolis, 1995)**

This explanation is consistent with experimental data, as is shown by Jayanti and Hewitt (1992). Hewitt and Jayanti (1993) show the observations by Mao and Dukler (1993) are also not inconsistent with the flooding hypothesis, though there is clearly a great deal of work to be done in the area since tube diameter has a crucial effect on flooding transitions (Jayanti et al, 1996).

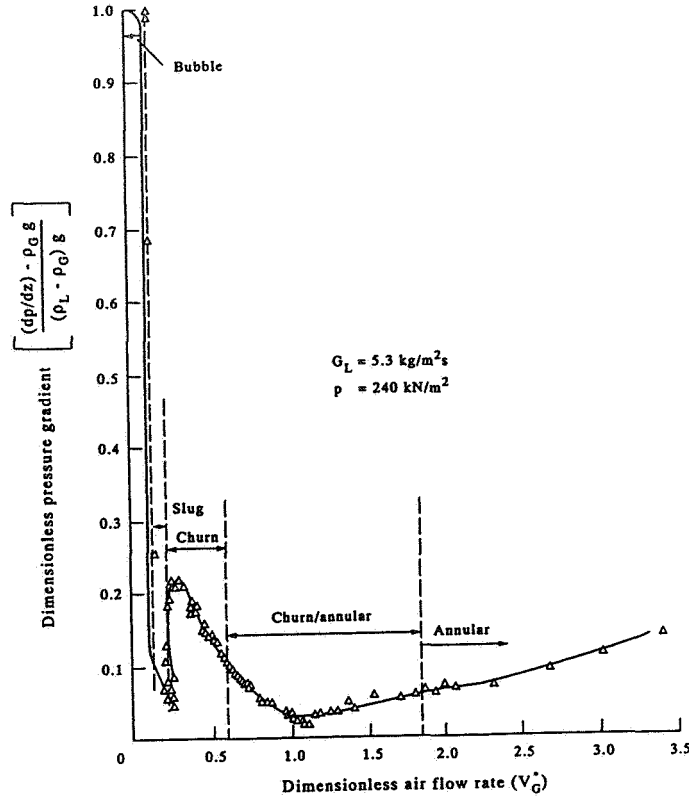


**Figure 8: Data for pressure gradient as a function of dimensionless gas velocity (Owen, 1986).  
Liquid flow rate constant.**

Figure 8 shows how the pressure gradient varies in vertical flow as a function of dimensionless gas flow rate,  $V_G^*$  which is defined as follows:

$$V_G^* = U_G \rho_G^{1/2} [gD(\rho_L - \rho_G)]^{-1/2} \quad (1)$$

where  $U_G$  is the superficial velocity of the gas phase,  $\rho_G$  and  $\rho_L$  are the gas and liquid phase densities,  $g$  is the acceleration due to gravity and  $D$  is the tube diameter. As will be seen, the pressure gradient at a fixed liquid flow rate decreases very rapidly with increasing gas flow rate in the bubbly flow and slug flow regions due to the decrease in the gravitational component of the pressure gradient as the void fraction increases. However, when the slug flow region breaks down due to the onset of flooding within the Taylor bubbles, a very rapid increase in pressure gradient occurs as the churn flow regime is entered. In churn flow, large flooding waves are formed periodically and traverse up the channel. As can be seen from observations using photochromic dye-tracing (Hewitt et al, 1985), the flow reverses between the large waves, with the liquid film on the tube wall beginning to descend and to fall into the subsequent wave. Eventually, the shear stress between the gas phase and the intervening film is sufficient to carry the film upwards and the flooding waves disappear since there is no replenishment mechanism for them. The region in which flow reversals occur is that to the left of the minimum in pressure gradient in the churn-annular region as is illustrated in Figure 9.

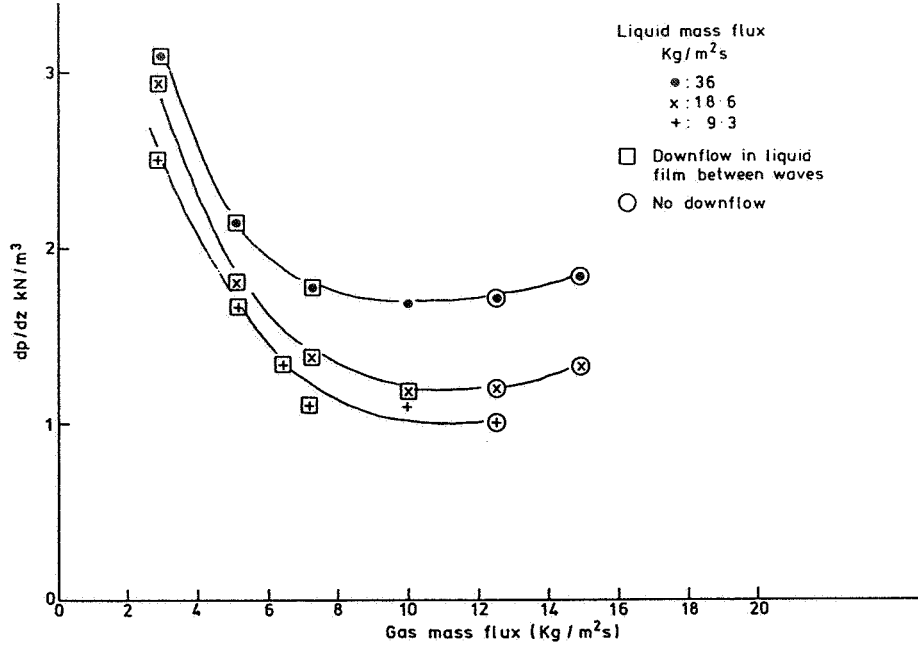


**Figure 9: Existence of regions of periodic downflow in the churn-annular transition region (Hewitt et al, 1985)**

The interesting features of microgravity flows which make them substantially different to those at normal gravity are, therefore:

- (1) The flows are essentially axisymmetric.
- (2) Though local variations in void fraction do occur, the flow velocity in a channel of constant cross section does not show the characteristic periodic reversals which occur in some regions of flow at normal gravity.

Feature (1) is, of course, shared with vertical flows though vertical flows are demonstrably subject to periodic flow reversals (feature (2)) which would not occur at zero gravity. One must conclude, therefore, that *flow patterns at zero gravity are much simpler than those found at normal gravity*. There is little point in attempting to use normal gravity methodologies to predict microgravity flows. Rather, a new approach to flow pattern transition needs to be adopted. Two interesting approaches have been followed in the literature on microgravity flows:

- (1) Zhao and Rezkallah (1993) argue that the interaction forces governing flow patterns are different under microgravity conditions and that the Weber numbers for the respective phases are the important determinants. The Weber numbers are defined as:

$$We_{SG} = \frac{U_G^2 \rho_G D}{\sigma} \quad (2)$$

$$We_{SL} = \frac{U_L^2 \rho_L D}{\sigma} \quad (3)$$

where  $U_L$  is the liquid superficial velocity and  $\sigma$  is the surface tension. A plot of Zhao and Rezkallah's own and literature data in terms of these two Weber numbers is shown in Figure 10.

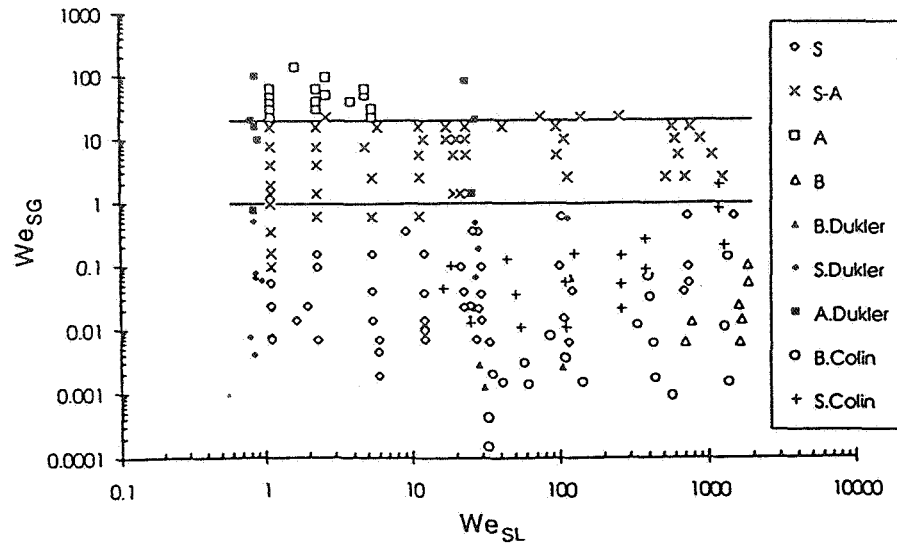


**Figure 10: Microgravity of flow patterns plotted in term of  $We_{SG}$  and  $We_{SL}$  (Zhao and Rezkallah, 1993) (B = bubbly flow, A = annular flow, S = slug flow, S-A = frothy slug annular flow)**

Zhao and Rezkallah suggest that, at high values of  $We_{SG}$ , the system is inertial controlled and annular flow would occur. At low values of  $We_{SG}$ , they suggest that the system is surface tension controlled, giving rise to bubble or slug flow. There is also an intermediate region in which frothy slug-annular flow occurs.

- (2) Dukler et al (1988) predicted the bubble-slug and slug-annular transitions on the basis of void fractions. The bubble-slug transition was hypothesized to occur at a void fraction ( $\epsilon_G$ ) of 0.45 and the slug-annular transition was hypothesized to occur when the void fraction predicted for annular flow equaled that predicted for slug flow. This predicts the transitions quite well as is illustrated in Figure 11.

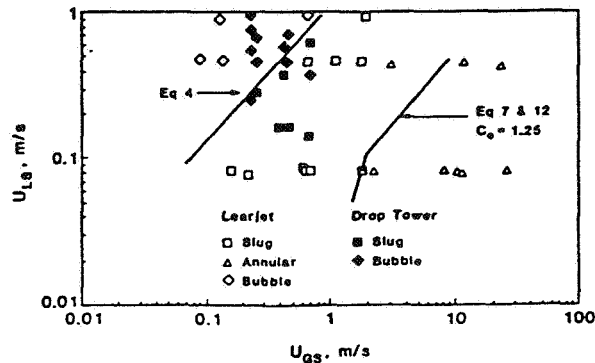


**Figure 11: Predictions of microgravity flow patterns by the method of Dukler et al (1988) compared with experimental data**

On the whole, a more phenomenological approach to flow pattern prediction is clearly preferable and the approach suggested by Dukler et al is a promising one. However, topics for further study might include:



- (1) The development of more mechanistic models for the bubble-slug transition. There is a growing consensus that this transition at normal gravity follows from the formation of void waves and not, as had once been believed, from progressive coalescence of the bubbles. However, in microgravity, the coalescence behaviour is very different (see Section 3 below) and this may have a significant effect on the regime transition behaviour.
- (2) The model used by Dukler et al (1988) for calculating void fraction in an annular flow included the calculation of interfacial friction factor based on normal gravity measurements. It is not clear whether it is appropriate to extrapolate such measurements into the microgravity transition region bearing in mind the non-existence of flow reversals and churn flow as discussed above.
- (3) In the absence of gravitational forces, surface tension must assume a more significant role, particularly in small diameter tubes. This aspect needs to be further investigated.

Although there is much work still to be done it is, however, clear that the transitions are fundamentally simpler than those in normal gravity and one might expect a better chance of success in prediction methodologies.

### 3. BUBBLY FLOW

A study of gas-liquid bubbly flow at microgravity conditions is reported by Colin et al (1991). Measurements of void fraction were made for both vertical normal gravity flows and microgravity flows and the results were plotted in terms of gas velocity  $u_G (= U_G/\epsilon_G)$  against  $U$ , the total superficial velocity. The results are illustrated in Figure 12.

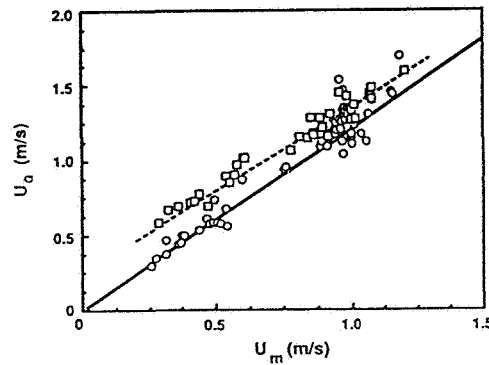


**Figure 12: Actual gas velocity as a function of total superficial velocity for normal gravity vertical bubbly flows (□) and microgravity bubbly flows (○). - - Zuber & Findlay (1965) relationship with  $u_\infty$  from Equation 5,  $C_0 = 1.1$ . — Zuber & Findlay relationship with  $C_0 = 12.$ ,  $u_\infty = 0$  (Colin et al, 1991)**

Colin et al followed the “drift-flux” approach of Zuber and Findlay (1965) fitting their data with an equation of the form:

$$u_G = C_o U + u_\infty \quad (4)$$

where  $u_{\infty}$  is the average local drift velocity and  $C_o$  is a constant which takes account of the differences between the profiles of velocity and void fraction. For normal-gravity vertical flows, the data were quite well fitted by setting  $C_o = 1.1$  and calculating  $u_{\infty}$  from the expression:

$$u_{\infty} = 1.53 \left[ \frac{(\rho_L - \rho_G) g \sigma}{\rho_L^2} \right]^{0.25} \quad (5)$$

The zero gravity flow was fitted best by setting  $C_o = 1.2$  and  $u_{\infty} = 0$ .

Perhaps the most interesting finding with respect to microgravity bubbly flows relates to bubble coalescence. Colin et al (1991) measured bubble size distributions at the inlet and outlet of a channel in normal and zero gravity respectively. The results are shown in Figure 13; as will be seen, the normal gravity vertical flow case shows little change of bubble size indicating minimal coalescence from the inlet to the outlet of the channel. This is in agreement with many other observations in normal gravity flow. However, at microgravity, the bubble size distribution changes dramatically, indicating extensive coalescence.

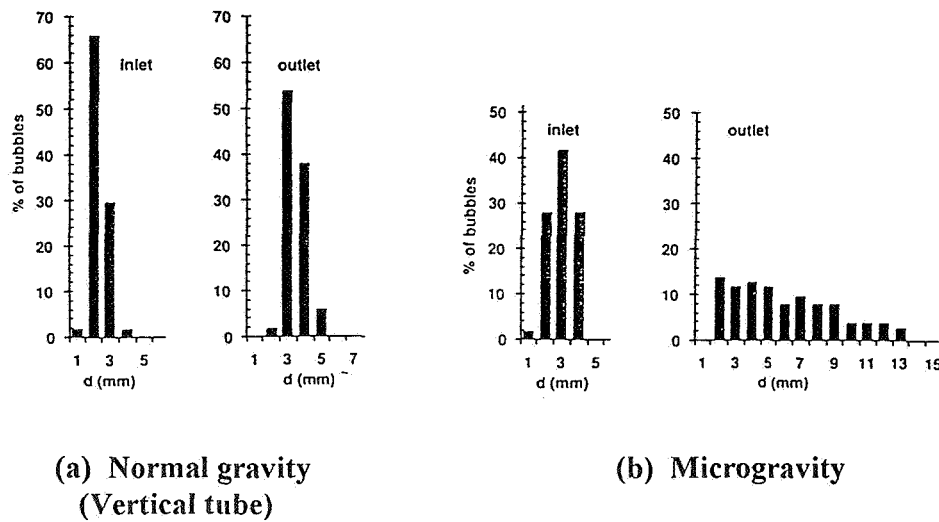


**Figure 13: Bubble-size distribution in air-water bubbly flow in a 3 m long 4 cm diameter tube (Colin et al, 1991)**

It is interesting to speculate on the causes of the differences between bubble coalescence behaviour at micro and normal gravity. The time required for coalescence is a strong function of the velocity of approach of the bubble to the interface at which it coalesces. This was demonstrated by some experiments by Kirkpatrick and Lockett (1974); they released bubbles below a flat interface and determined the coalescence time as a function of the distance (x) at which they were released relative to the interface. Clearly, the bubble accelerates as it moves towards the interface and the effect is one of velocity. Their results are illustrated in Figure 14. When the bubbles are released close to the interface, the velocity of approach is small and the coalescence time is of the order of a few milliseconds. However, when the initial separation distance reaches about 0.6 cm, the coalescence time rises dramatically to around 140 milliseconds, thereafter increasing only slightly with separation distance. If we consider a bubbly flow, the velocity of approach of bubble will depend on the turbulence and on the interactions with bubble wakes. A bubble trapped in the wake of a bubble ahead of it will rise more rapidly towards the preceding bubble and its coalescence time will be extended. Turbulent fluctuations within the flow would lead to separation before coalescence could take place. In a further set of experiments, Lockett and Kirkpatrick (1975) trapped a bed of bubble

in a counter-current flow of liquid through a diverging duct (in fact, a rotameter tube) as illustrated in Figure 15. They observed that, over very extended periods, no discernible coalescence occurred in the bubble bed. This is consistent with the observations of Colin et al (1991) as illustrated in Figure 13a. One may hypothesize that the approach velocities for bubbles in microgravity (where there would be no wake formation due to local relative velocity of the bubble in the surrounding liquid) are much lower and that the probability of success of coalescence is much higher.

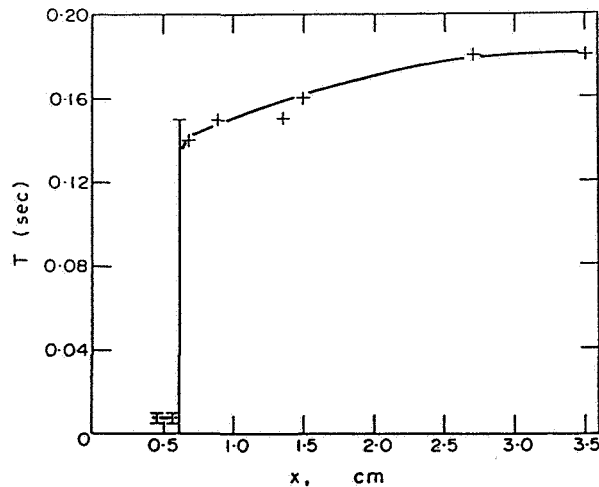


**Figure 14: Coalescence time as a function of release distance for a bubble approaching a flat interface (Kirkpatrick and Lockett, 1974)**

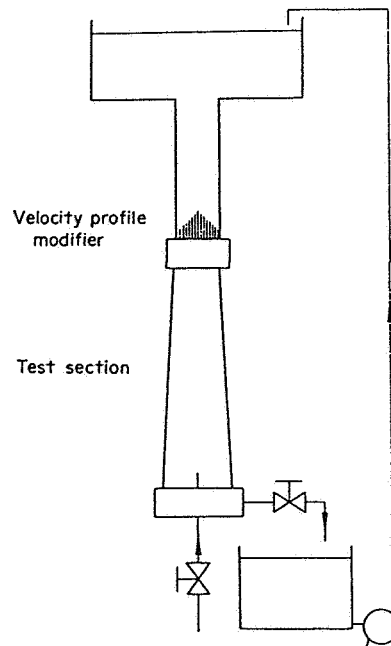


**Figure 15: Diverging duct apparatus used for the study of bubble beds (Kirkpatrick and Lockett, 1974, Lockett and Kirkpatrick, 1975)**

For bubbly flow, therefore, the coalescence phenomenon appears to represent a very interesting challenge. Possible areas for further work might include:

- (1) Simple experiments on bubble-bubble coalescence using two bubbles. These could include studies of the interaction of two bubbles growing from fixed locations at a controlled rate or experiments on controlled arrays of bubbles.
- (2) The role of system turbulence is crucial and one might suggest a whole range of experiments with controlled (grid generated) turbulence to investigate the turbulence of the continuous (liquid) phase in the absence of wake effects.

#### 4. SLUG FLOW

Colin et al (1991) report measurements of void fraction in slug flow for both normal gravity (vertical tube) and microgravity; the results were again plotted in terms of  $u_G$  as function of mixture velocity  $U$  and the data are shown in Figure 16.

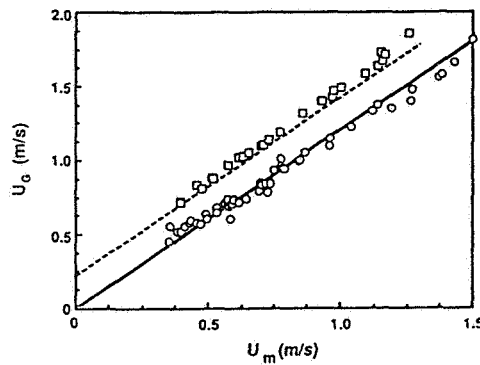


**Figure 16: Actual gas velocity as a function of total superficial velocity for normal gravity vertical slug flows (□) and microgravity slug flows (○). Zuber & Findlay (1965) relationship with  $u_\infty$  from Equation 6,  $C_o = 1.2$ . Zuber & Findlay relationship with  $C_o = 1.2$ ,  $u_\infty = 0$**

The normal gravity data well fitted by Equation 4 with  $C_o = 1.2$  and  $u_\infty$  given by the classical expression for the rise of a single Taylor bubble:

$$u_\infty = 0.35 \sqrt{\frac{(\rho_L - \rho_G) g D}{\rho_L}} \quad (6)$$

The microgravity data was fitted with  $C_o = 1.2$  and  $u_\infty = 0$ .

The experiments by Colin et al (1991) were for air-water mixtures in a relatively large bore tube (4 cms). It would be advantageous to have a methodology for predicting the effects of parameters such as viscosity and surface tension on gas velocity (i.e., slug propagation velocity). The prediction of slug propagation at normal gravity is a matter of some interest and controversy. Specifically, there is a question about whether, in horizontal tubes, the term  $u_\infty$  is significant. Clearly, if a horizontal tube full of a stationary liquid is emptied from one end, then the gas would penetrate into the tube, with the liquid falling out of the end. The gas bubble penetrates at the classical Benjamin bubble velocity given by:

$$u_\infty = 0.54 \sqrt{gD} \quad (7)$$

and this clearly represents a limiting case for slug propagation at the lowest velocities. However, at higher velocities, the bubble is known to become more symmetric (the nose moving down towards the centre of the tube) and Equation 7 may not apply. In order to investigate this question in more detail, two approaches have been followed in work at Imperial College:

- (1) The rate of bubble front propagation has been measured in experiments in which the liquid in a liquid-filled tube is pushed out by a known volumetric flowrate ( $\dot{V}_G$ ) of gas (the gas being fed through a critical flow valve to ensure constancy of mass flow, corrections being made to allow for compressibility in the inlet system). The gas velocity in the system is equal to the bubble propagation velocity  $u_b$  (which is measured using a series of conductance probes along the channel) and we may write:

$$u_G / U = Au_b / \dot{V}_G = 1 + C = C_o + u_\infty / U \quad (8)$$

where  $A$  is the cross sectional area of the channel and  $C$  is a parameter defined by Hubbard and Dukler (1966) according to Equation 8. Thus, the “push-out” experiment can allow precise measurements of  $u_G/U$  which can be compared with various analytical predictions. Data generated by this methodology are reported by Davies (1992) and Manolis (1995).

- (2) CFD calculations were carried out using the CFDS-CFX 4 code. The position of the interface was determined using the “homogeneous” (VOF) method and the methodology is illustrated in Figure 17.

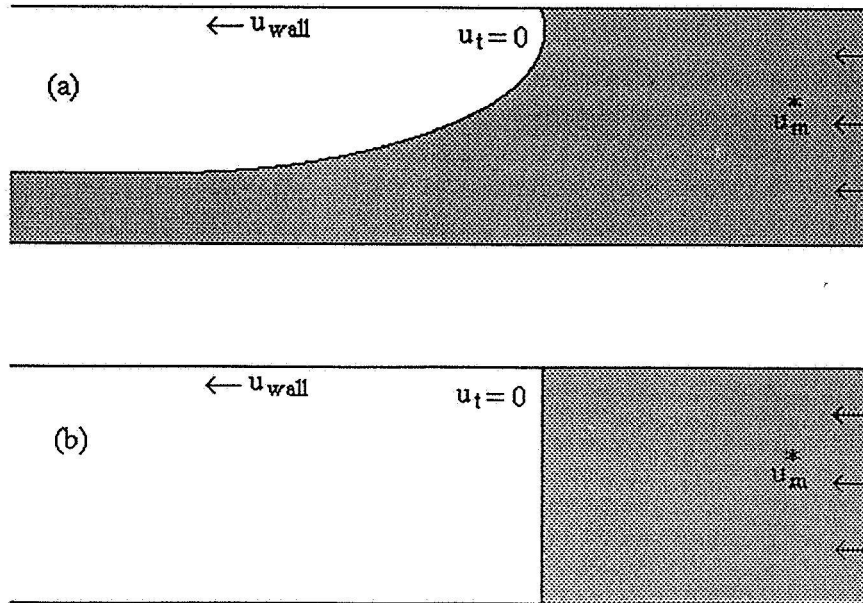


**Figure 17: Calculation of slug tail propagation using CFDS-CFX4 (Pan, 1996)**

In the steady-state, the interface remains stationary within the computational domain, with the wall of the channel moving and liquid being fed into the domain from the right hand side to maintain the interface in a constant position (Figure 17(a)). The computation is stated at zero time with the liquid in the (circular) tube being separated from the gas by a vertical plane (Figure 17(b)). Further details of the calculation method are given by Pan (1996). Figure 18 shows results for the steady-state condition at a variety of mixture velocities, illustrating how the nose of the bubble moves towards the centre of the tube at higher velocities.

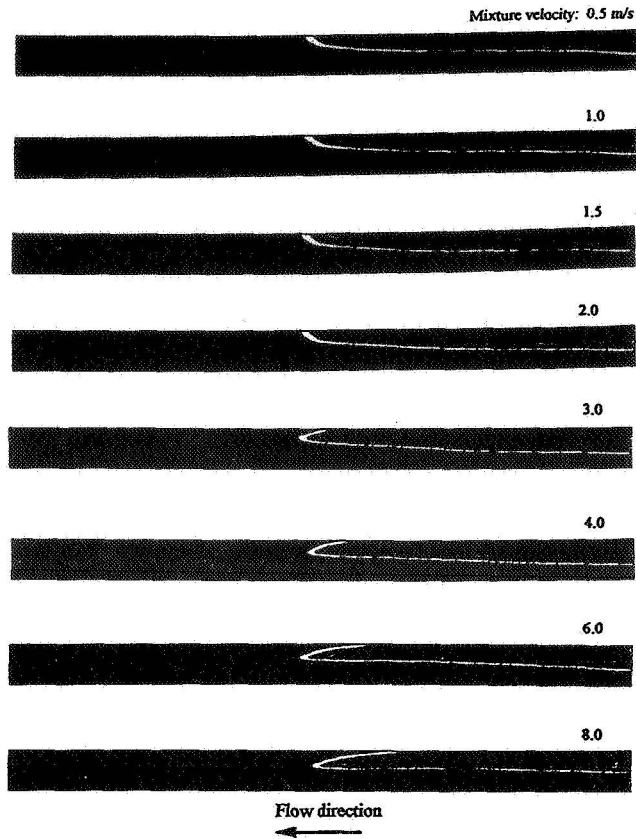


Figure 18: Prediction of slug tail propagation in a horizontal tube: interface shape as a function of mixture velocity (Pan, 1996)

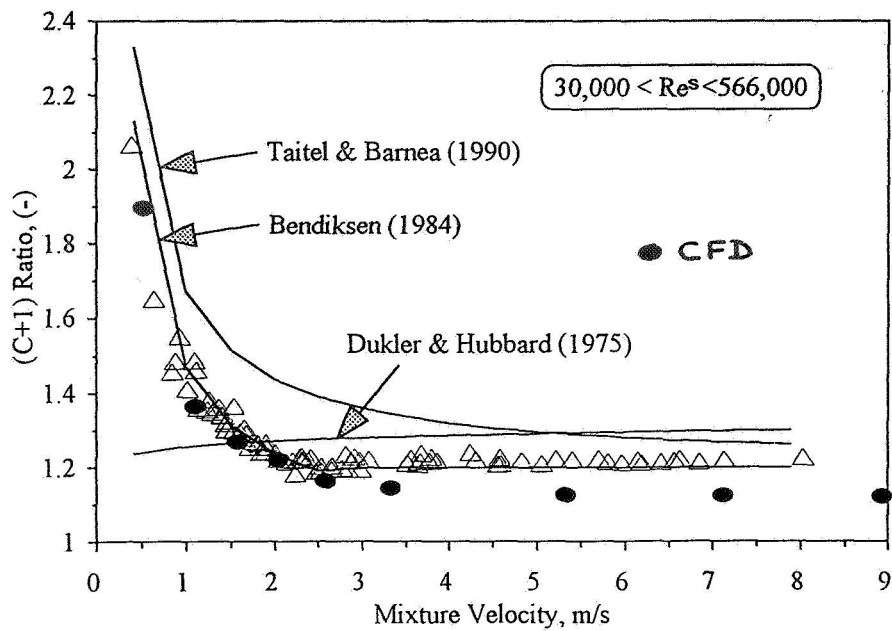
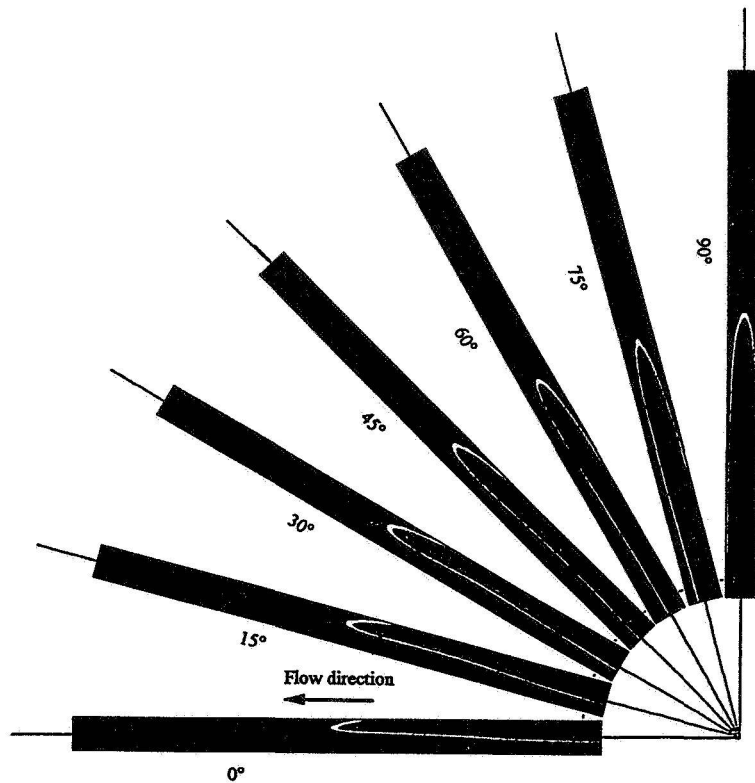


Figure 19: Comparisons of CFD calculation and data from the “push-out” experiments with various models for slug tail propagation

Figure 19 shows a comparison of the results from the push-out experiments (triangular symbols) and the CFD calculations with various models for slug propagation. The CFD calculations and the push-out experiments are in reasonable agreement and the data are consistent with the idea that the drift flux ( $u_{\infty}$ ) term disappears at higher mixture velocities giving a constant value of  $(1+C) = C_o$  of around 1.2; this is consistent with the analysis of Bendicksen (1984).



**Figure 20: Effect of angles on interface shape in slug tail propagation (Mixture velocity 4 m/s) (Pan, 1996)**

The CFD methodology can be applied to non-horizontal systems; Figure 20 shows predictions for a series of tube inclinations ranging from horizontal to vertical. Obviously, the axial symmetry of the flow increases progressively as the angle goes from 0 to 90°. The CFD methodology can also be applied to the zero gravity case and Figure 21 shows calculations of slug tail propagation at zero gravity. These calculations can be compared with calculations for vertical upwards flow and horizontal flow, and with the various models, and these comparisons are presented in Figure 22. As will be seen,  $C$  is constant independent of mixture velocity for zero gravity flows, the value being close to that for horizontal pipes at a higher velocities. For a given mixture velocity, it is possible also to calculate the translation velocity as a function of the fraction of normal gravity for horizontal and vertical flows respectively and calculations of this type are shown Figure 23. The vertical and horizontal flow cases converge at zero gravity, as expected.

Slug propagation under zero gravity conditions is thus an interesting limiting case for study and possible areas of work might include the following:

- (1) "Push-out" experiments at zero gravity. This experiment is a very simple method of investigating slug tail velocities and, by using parallel tubes, a whole range of tube diameters and fluids could be investigated simultaneously. The effects of viscosity and surface tension are particularly important.

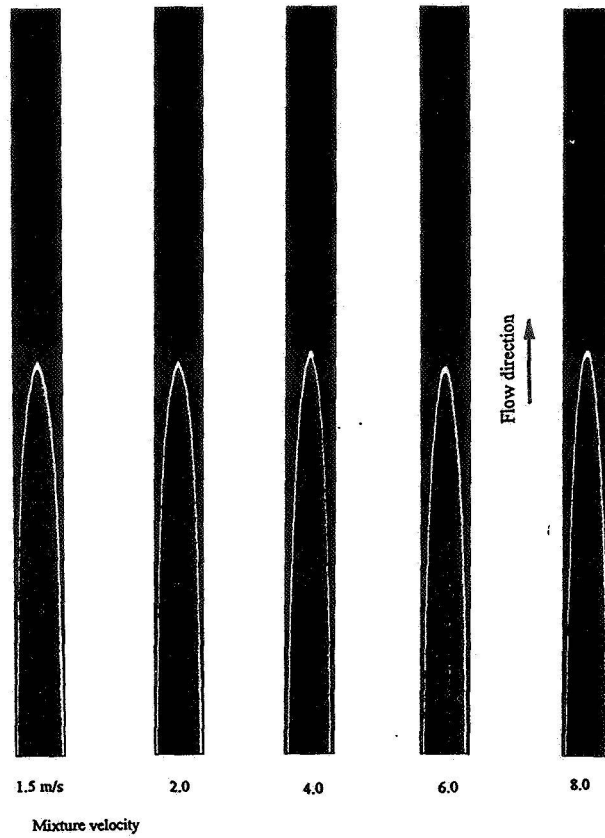


Figure 21: Interface shape of slug tail for zero gravity case (Tube diameter 77.92 mm, air water flows)

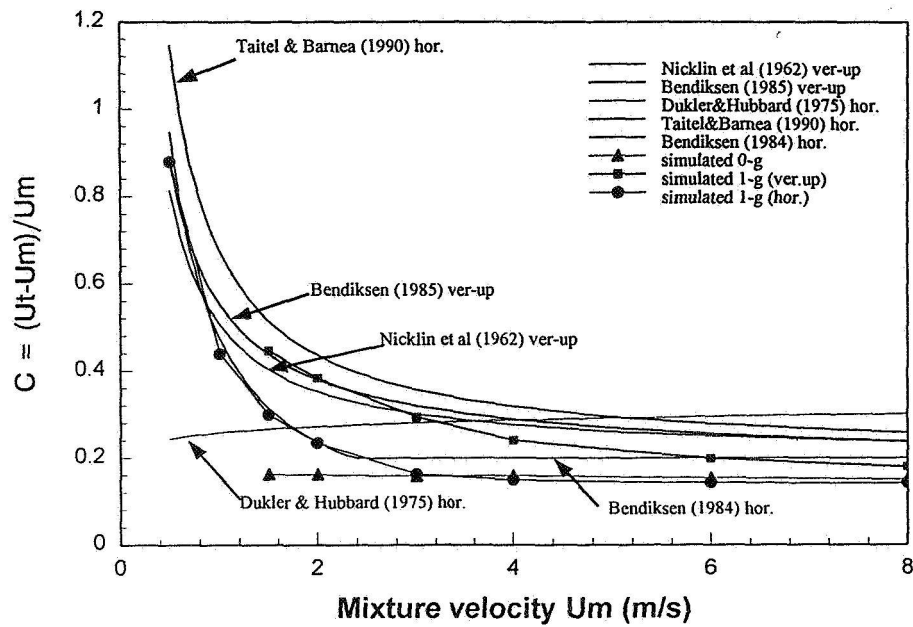
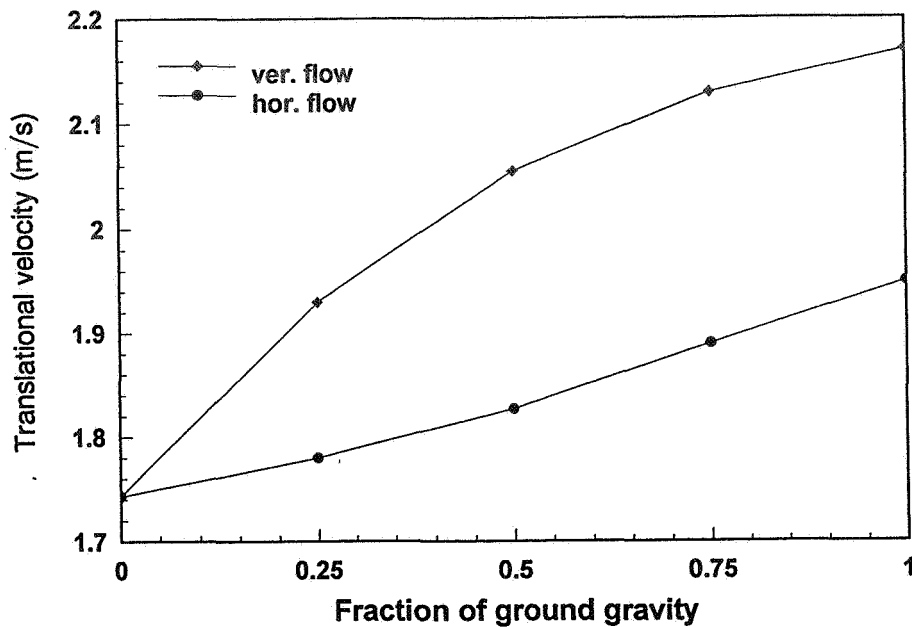


Figure 22: Comparison of  $C$  values obtained from models and from CFD calculations





**Figure 23: Slug tail translational velocity as a function of fractional gravity (Tube diameter 77.92 mm, mixture velocity, 1.5 m/s)**

- (2) The preliminary work on CFD prediction of slug tail propagation at zero gravity could be extended to cover a much wider range of tube diameter, fluid viscosity and surface tension. The results can also be evaluated in more detail with respect to velocity profiles, wall shear stresses (related to pressure gradient) etc.
- (3) It should in principle be possible to extend the CFD studies to include studies of the motion of bubble within the liquid slugs. There is evidence that these bubbles are traveling at the same velocity as the Taylor bubbles which implies that they are not in the wall region where there is a difference in velocity.

## 5. ANNULAR FLOW

In high velocity vertical annular flows, the most important characteristic feature is the existence of *disturbance waves*. The main features of these waves are as follows:

- (1) They do not occur at very low liquid rates, the transition being at film Reynolds numbers of around 250.
- (2) The waves are formed near the channel entrance at a frequency which may be related to turbulent burst frequencies. The frequency then falls with distance due to wave coalescence, reaching an asymptotic value at large distance. The spacing between the waves is random.
- (3) The waves have velocities typically in the range 3-10 m/s, namely much higher than the average velocity in the liquid film but much lower than the gas velocity in the core.
- (4) The waves are seen as “squally” regions in the flow which are typically 1-2 diameters in extent.

- (5) The wall shear stress in the wave region rises rapidly to a peak which is several times that in the intervening substrate film.
- (6) Disturbance waves are a necessary condition for droplet entrainment, the entrainment arising due to breakup of the wave tip. Such droplet entrainment is therefore the rule rather than the exception in annular flow.

Recent work at Harwell and Imperial College on annular flow is summarised, for instance, by Hewitt and Govan (1990) and by Wolf (1995). Recently, attempts have been made to model the flows in disturbance waves using CFD techniques. In order to achieve this, it is necessary to have a prescription for the interfacial shear stress. This is calculated assuming that the interfacial roughness is equal to five times the local film thickness in the wave region (this is consistent with experimental data) and using the expression of Shearer and Nedderman (1965) (who correlated interfacial friction for sub-critical films without disturbance waves) for the substrate region. Details of the calculations are given by Jayanti and Hewitt (1994) and some sample results are given in Figures 24 and 25; in these Figures, the vertical scale is exaggerated by a factor of 10 in the interests of clarity

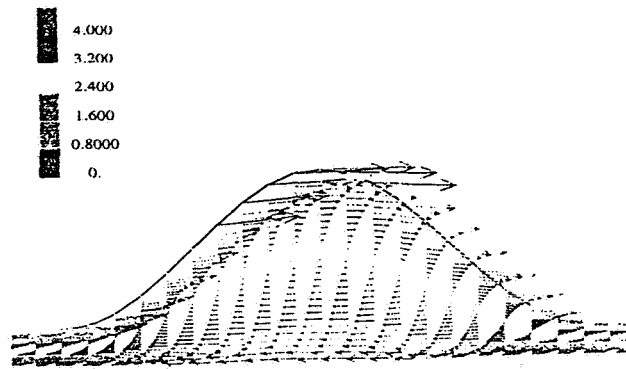


**Figure 24: Velocity vectors in a disturbance wave in annular flow (Jayanti and Hewitt, 1994)**

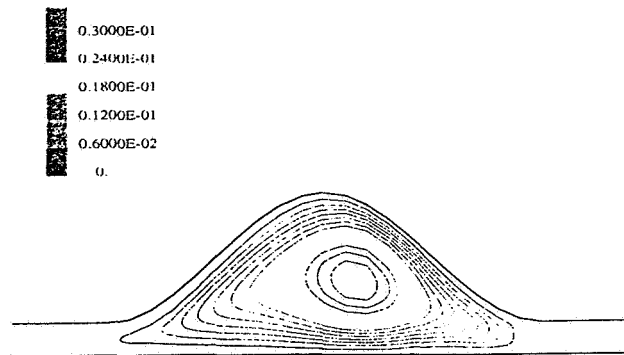


**Figure 25: Turbulent viscosity distribution in disturbance wave (Jayanti and Hewitt, 1994)**

The calculations shown in Figures 24 and 25 were carried out using the low Reynolds number  $k-\epsilon$  model.

Figure 24 shows velocity vectors within the wave indicating intense recirculation and Figure 25 shows the distribution of turbulent viscosity. Using the low Reynolds number  $k-\varepsilon$  model, the turbulent viscosity in the substrate region is predicted to be zero. Clearly, there is a sensitivity to prediction models and it is extremely difficult to establish the local nature of the flows within these flows experimentally. In normal gravity vertical flows, slug flow breaks down into churn flow in which, in addition to normal disturbance waves, there are large waves of the flooding type (see discussion above) and it is not until large gas velocities are reached that the characteristic disturbance wave region is firmly identified without the ambiguities associated with the occurrence of churn flow. In the zero gravity case, however, there is a direct transition from slug flow to annular flow and, thus, the flows can be studied without the complications of flow reversals and flooding waves. At the high gas velocities necessary to have an ambiguous disturbance wave under normal gravity, the liquid films are very thin and details of the flow within them cannot easily be measured. However, with zero gravity flows, the disturbance wave region could be investigated at much lower gas velocities and much more intensive measurements made.

Work on annular flow under zero gravity conditions might include the following:

- (1) The establishment of the regions of interface behaviour at zero gravity. Would the transition to disturbance waves at a constant liquid film Reynolds number extend through to the transition to slug flow?
- (2) Studies of the onset and behaviour of disturbance waves over the full range of flow from the transition from slug flow, and in particular measurements of flow characteristics within the liquid film (here, techniques such as photochromic dye-tracing may be used).
- (3) Studies of droplet generation and behaviour at zero gravity. Of particular interest here is the formation of holdup waves within the gas core which is believed to lead to the occurrence of wispy annular flow.

## 6. CONCLUSION

To conclude, it may be said that zero gravity two-phase flows are not only interesting in themselves (in the context of their many applications in space technology) but also in the context of investigating mechanisms of gas-liquid flows without the complicating effect of the gravitational field. Many possibilities exist for further work in this area, ranging from studies of bubble coalescence and slug tail propagation to studies of disturbance wave behaviour and droplet formation and deposition phenomena in annular flow.

## REFERENCES

- Bendicksen, K.H. (1984) An experimental investigation of the motion of long bubbles in vertical tubes. *Int. J. Multiphase Flow*, Vol. 11, 797-812.
- Colin, C., Fabre, J. and Dukler, A.E. (1991) Gas-liquid flow at micro-gravity conditions. I: dispersed bubble and slug flow. *Int. J. Multiphase Flow*, Vol. 17, 533-544.
- Davies, S.R. (1992) Studies of two-phase intermittent flow in pipelines. Ph.D. Thesis, Imperial College, University of London, UK.
- Dukler, A.E., Fabre, J.A., McQuillen, J.B. and Vernon, R. (1988) Gas-liquid flow at micro-gravity conditions: flow patterns and their transitions. *Int. J. Multiphase Flow*, Vol. 14, 389-400.

Hewitt, G.F. and Govan, A.H. (1990) Phenomena and prediction in annular two-phase flow. Proc. Symposium on Advances in Gas-Liquid Flows, Dallas, Texas, November 25th-30th, 1990 (ASME FED-Vol. 99, HTD-Vol. 155) pp 41-56.

Hewitt, G.F. and Jayanti, S. (1993) To churn or not to churn. *Int. J. Multiphase Flow*, Vol. 19, 527-529.

Hewitt, G.F., Martin, C.J. and Wilkes, M.S. (1985) Experimental and modeling studies of annular flow in the region between flow reversal and the pressure drop minimum. *Physico-Chemical Hydrodynamics*, Vol. 6, 69-86.

Hubbard, N.G. and Dukler, A.E. (1975) A model for gas-liquid slug flow in horizontal and near horizontal tubes. *Ind. Eng. Chem. Fundam.*, Vol. 14, 337-347.

Jayanti, S. and Hewitt, G.F. (1992) Prediction of the slug-to-churn flow transition in vertical two-phase flow. *Int. J. Multiphase Flow*, Vol. 18, 847-860.

Jayanti, S. and Hewitt, G.F. (1994) Hydrodynamics and heat transfer in wavy annular gas-liquid flow: a CFD study. Department of Chemical Engineering, Imperial College, London, UK, Report MPS/59 (September 1994).

Jayanti, S., Tokarz, A. and Hewitt, G.F. (1996) Theoretical investigation of the diameter effect on flooding in counter-current flow. *Int. J. Multiphase Flow*, Vol. 22, 307-324.

Kirkpatrick, R.D. and Lockett, M.J. (1974) The influence of approach velocity on bubble coalescence. *Chem. Eng. Sci.*, Vol. 29, 2363-2373.

Lockett, M.J. and Kirkpatrick, R.D. (1975) Ideal bubbly flow and actual flow in bubble columns. *Trans. Inst. Chem. Eng.*, Vol. 53, 267-273.

Manolis, I.G. (1995) High pressure gas-liquid slug flow. Ph.D. Thesis, University of London.

Mao, Z.S. and Dukler, A.E. (1993) The myth of churn flow? *Int. J. Multiphase Flow*, Vol. 19, 377-383.

Owen, D.G. (1986) An experimental and theoretical analysis of equilibrium annular flow. Ph.D. Thesis, University of Birmingham, UK.

Pan, L. (1996) High pressure three-phase (gas/liquid/liquid) flow. Ph.D. Thesis, Imperial College, University of London.

Reddy Karri, S.B. and Mathur, V.K. (1988) Two-phase flow regime map predictions under micro-gravity. *AIChE Journal*, Vol. 34, 137-139.

Shearer, C.J. and Nedderman, R.M. (1965) Pressure gradient and liquid film thickness in co-current upwards flow of gas-liquid mixtures: application to film cooler design. *Chem. Eng. Sci.*, Vol. 20, 671-683.

Taitel, Y. and Dukler, A.E. (1976) A model for predicting flow regime transitions in horizontal and near-horizontal gas-liquid flow. *AIChE Journal*, Vol. 22, 47.

Weisman, J., Duncan, D., Gibson, J. and Crawford, T. (1979) Effects of fluid properties and pipe diameter on two-phase flow patterns in horizontal lines. *Int. J. Multiphase Flow*, Vol. 5, 437.

Wolf, A. (1995) Film structure of vertical annular flow. Ph.D. Thesis, Imperial College, University of London, UK.

Zhao, L. and Rezkallah, L.S. (1993) Gas-liquid flow patterns at microgravity conditions. *Int. J. Multiphase Flow*, Vol. 19, 751-763.

Zuber, N. and Findlay, J.A. (1965) Average volumetric concentration in two-phase flow systems. *Trans. ASME J. Heat Transfer*, Vol. 87, 453-468.



# COMPLEX FLUIDS: SCIENCE, TECHNOLOGY AND MICROGRAVITY

D.A. Weitz

*Department of Physics and Astronomy  
University of Pennsylvania  
209 S33 rd St.  
Philadelphia, PA 19104-6396*

Complex fluids are materials which contain structures whose length scales are larger than those of the molecules of the fluid itself. Examples of complex fluids include surfactant systems that form lamellae, micellar or other structures, colloidal suspensions, microemulsion, emulsions, foams and polymer suspensions. Even granular materials often exhibit properties that are remarkably similar to those of other complex fluids. The properties of these systems are often determined to a large extent by the properties of these larger length scale structures, giving a complex fluid unique and interesting properties.

The key to the study of complex fluids is often the nature of the larger length scale structures within the material, and their relationship to the properties and dynamics of the material. As such, a major tool in their study is the use of scattering probes to investigate the structure within the fluid. Both X-ray and neutron scattering are used extensively; in addition, light scattering is often an ideal probe, both because the length scale of the wavelength of light is so often a good match to the important length scales of the complex fluid, and because dynamic properties can also be studied using laser light sources, through the use of dynamic light scattering. In addition to the study of the structures within the complex fluids, their macroscopic properties are also of great interest. They often exhibit strong viscoelastic behavior, and thus rheological methods are often used successfully.

Complex fluids also find a very wide range of technological uses. These are typically in the form of bulk chemicals, and can range from paints and coatings to foods, cosmetics and drugs. However, complex fluids are also finding increasing use as specialty materials. For example, some colloidal and emulsion materials can be strongly polarized through the application of an external electric or magnetic field. This causes the colloidal particles to align into chains, and can dramatically modify their viscoelastic properties, changing them from a viscous fluid to a highly elastic solid. These electro- or magneto-rheological fluids may find extensive uses in controlled viscoelastic devices such as active shock absorbers. In addition, colloidal particles can now be synthesized as highly monodisperse particles, enabling them to be used as model systems for the study of many

different phenomena. For example, they are used to study the order-disorder transition, nucleation and growth of both crystals and alloys, and the glass transition. Furthermore, the high degree of order that can be achieved with these materials may allow them to be used as superstructures for the manufacture of highly controlled materials that have long-range order with periodicity on the micron length scales. This "colloid engineering" offers the possibility of making novel materials that may be of use in electro-optics where the coupling of the structure to light is critical.

For many studies of complex fluids, the use of microgravity is highly beneficial. Very often, many of the critical properties of the complex fluids are determined by their equilibrium behavior, and, because of the size of the structures in the material, thermal or entropic effects are important. However, the effects of entropy can often be obscured by gravitational effects. There are two key effects by which gravity can be detrimental. The first is the relative sedimentation of the larger structures in the fluid. Although they are small, and although buoyancy greatly reduces sedimentation, delicate entropic effects can often be completely obscured by even a small amount of sedimentation. It is frequently impossible to eliminate these problems; buoyancy matching is not effective, either because of a large density mismatch, or because of the need to also index match the different materials within the complex fluid to eliminate any van der Waals interactions and to allow light scattering to be used to probe their properties. The second inevitable and deleterious effect of gravity is convection which results from small temperature gradients in the fluid. Although these gradients can be minimized by careful stabilization of the temperature, they can never be eliminated, and even very small amounts of convection can obscure some important entropically controlled properties. Thus, for both these reasons, microgravity offers great advantage for the study of the properties of complex fluids.

The potential importance of microgravity for the study of complex fluids is well recognized by the contributions to this meeting. There are a wide variety of contributions involving many different aspects of the study of complex fluids. These range from early work seeking to identify potentially important experiments to be performed in space, to several projects already in the flight definition stage, all the way to projects that have already been flown successfully. These latter have clearly established that the properties of complex fluids can be dramatically different under gravity, and that some of the most fundamental issues will only be resolved through the study of complex fluids in microgravity.



# **Critical Phenomena**



## INTERNAL WAVES IN CVX

Robert F. Berg

Physical and Chemical Properties Division  
National Institute of Standards and Technology  
Gaithersburg, MD 20899

### ABSTRACT

Near the liquid-vapor critical point, density stratification supports internal gravity waves which affect 1-g viscosity measurements in the CVX (Critical Viscosity of Xenon) experiment. Two internal-wave modes were seen in the horizontal viscometer. The frequencies of the two modes had different temperature dependences: with decreasing temperature, the higher frequency increased monotonically from 0.7 to 2.8 Hz, but the lower frequency varied nonmonotonically, with a maximum of 1.0 Hz at 20 mK above the critical temperature. The measured frequencies agree with independently calculated frequencies to within 15%.

### PURPOSE OF CVX

CVX will measure shear viscosity very close to the liquid-vapor critical point of xenon in microgravity. At critical density and close to the critical temperature  $T_c$ , the viscosity  $\eta$  is predicted to diverge according to

$$\eta \sim (T - T_c)^{-y} ,$$

where the exponent  $y$  has the same value for all fluids. Microgravity will allow this divergence to be observed directly in a pure fluid for the first time. This divergence is similar to those which have been seen in 1-g for static properties such as compressibility or heat capacity. However, two limitations have suppressed 1-g measurements of viscosity to a blunted increase of only 20% above the background viscosity.

### LIMITATIONS ON THE VISCOSITY MEASUREMENT

The first limitation is the fluid itself. The characteristic exponent is small:  $y \simeq 0.04$ . In addition, the amplitude of the viscosity increase is also small: no effect is noticable above  $T_c + 3$  K (for a fluid with  $T_c \approx 300$  K).

The second limitation is gravity, which has two manifestations in this experiment. The first, well-known, manifestation is the density stratification caused by the enormous compressibility near the critical point. The interesting region

having densities near the critical density  $\rho_c$  narrows to a thin layer near the sample's midplane. Thus, the precision of the measurement of the critical point enhancement of viscosity is limited in Earth's gravity.

The second manifestation, the excitation of internal waves, is the subject of this paper. In 1-g measurements, the stratification supported internal wave modes within the viscometer's bandwidth of operation. Because these internal-wave modes were not included in the model of the viscometer, they limited the measurement's accuracy. The viscometer has been demonstrated to have the required accuracy both in carbon dioxide below the critical density [1] and in xenon at the critical density far above the critical temperature. However, when both the temperature and the density were close to the critical point of xenon, the presence of internal waves prevented such a demonstration.

## INTERNAL WAVES

Internal waves are always possible in the presence of a stratified density profile. See, for example, Lighthill's book [3]. In a closed container, the stratification typical near the critical point can support internal gravity waves whose modes are reminiscent of the "sloshing" modes of a cup of water. Experimentalists have previously remarked on the existence of internal-wave modes near the critical point [4]. Only a few papers have been published on this subject, mostly in Soviet journals [5, 6, 7]. These papers were concerned with exploratory questions such as the existence of gravitational waves or the dispersion relation at the critical temperature  $T_c$ . Thus they could not help in identifying the observed internal-wave modes or in measuring and calculating their frequencies.

## THE CHARACTERISTIC FREQUENCY

The characteristic frequency for internal waves is the Brunt-Väisälä or buoyancy frequency, defined by

$$\omega_{BV} \equiv \left[ \frac{g (d\rho/dz)}{\rho} \right]^{1/2},$$

where  $g$  is the gravitational acceleration, and  $\rho$  and  $d\rho/dz$  are the fluid density and its derivative with respect to height  $z$ . In general,  $\omega_{BV}$  is a local quantity depending on the height  $z$  of the fluid element. A closed container of stratified fluid will have a spectrum of modes, none at a frequency higher than the maximum value of  $\omega_{BV}$  within the container.

Gravity-induced stratification just above the critical point of a pure fluid is a special case of a continuous density profile. Far above the critical point,

$\omega_{BV}$  is much less than 1 Hz and is nearly uniform with height. As the critical point is approached,  $\omega_{BV}$  increases, so that for xenon the frequency  $\omega_{BV}/2\pi$  is approximately 1 Hz at  $T_c + 60$  mK. Closer to  $T_c$ , the height dependence of  $d\rho/dz$  causes  $\omega_{BV}$  also to depend on height. Thus, in the thin region where  $\rho \simeq \rho_c$ ,  $\omega_{BV}$  diverges as  $T_c$  is approached. The resulting distribution of  $\omega_{BV}$  leads to a spectrum of internal-wave modes whose eigenfrequencies do not diverge.

## THE DISPERSION RELATION

The equation of motion for the internal waves in the stratified xenon comes from the inviscid Navier-Stokes equation and the conditions of continuity and incompressibility. (At frequencies of order 1 Hz, the fluid oscillations are adiabatic, and incompressibility is a good approximation.)

The simplest example of internal-wave modes is a small, periodic disturbance of an exponentially stratified fluid, namely one whose unperturbed density profile  $\rho_0(z)$  is

$$\rho_0(z) = \rho_{00}e^{-\alpha z} ,$$

where  $\alpha$  and  $\rho_{00}$  are independent of height  $z$ . The fluid is contained in a rectangular box whose dimensions are given by

$$\begin{aligned} -a/2 &< x < +a/2 \\ -b/2 &< y < +b/2 \\ -L &< z < +L ; \end{aligned}$$

where  $z$  is the vertical direction.

For the exponential density profile, the associated eigenvalue problem can be analytically solved (e.g. see [3]), yielding the eigenfrequencies  $\omega$  given by the dispersion relation

$$\omega^2 = \frac{\alpha g [(j\pi/a)^2 + (k\pi/b)^2]}{(\alpha/2)^2 + [(j\pi/a)^2 + (k\pi/b)^2 + (l\pi/L)^2]} .$$

This dispersion relation has the unusual feature that  $\omega$  decreases upon increasing the vertical index  $l$ .

Xenon's density profile is not exponential near the critical point. However, above  $T_c + 60$  mK, the nearly-linear profile could be approximated by an exponential profile. Thus this model was useful for revealing the symmetry of the internal-wave modes, which was important in deciding which modes coupled to the oscillating screen.

Close to  $T_c$ , the density profile is significantly nonlinear, and numerical solution of the equation of motion is necessary to obtain the dispersion relation from the eigenvalue problem consisting of the fluid's equation of motion and its boundary conditions. In collaboration with applied mathematicians at NIST, this problem was solved for density profiles both above and below  $T_c$ .

## APPARATUS

The viscometer consisted of an overdamped, oscillating screen immersed in the xenon. Changes in viscosity are inferred from changes of the oscillator's transfer function, the frequency-dependent ratio of the oscillator's displacement to its applied torque.

The oscillator was constructed by cutting an  $8 \times 19$  mm rectangle out of a larger piece of delicate nickel screen while leaving attached two wire extensions that formed the torsion fiber. The torsion fibers were attached to a stiff yoke with Pb-Sn solder. The yoke was centered between four electrodes parallel to the screen and separated by a 7.6 mm gap. The complete assembly was sealed into a cylindrical copper cell.

After characterization of the oscillator in vacuum, xenon was loaded into the viscometer cell to within 0.2% of the critical density  $\rho_c$ . After loading, the cell was placed into a thermostat consisting of three independently-controlled, concentric aluminum shells.

The measurements were made with prototype electronics at NIST. A commercial spectrum analyzer generated oscillating source voltages which, after modification, were used to apply torques to the oscillator. The oscillating screen and the fixed electrodes also formed a capacitance bridge that was operated at 10 kHz to detect the screen's displacement. The bridge's signal was detected by a lock-in amplifier, whose output was continuously measured by the spectrum analyzer.

Further details may be found in Reference [2].

## MEASUREMENT TECHNIQUE

The viscometer was designed for ultimate use in the Space Shuttle's microgravity, where the effect of internal waves will be negligible. To verify that internal waves were responsible for the deviations in 1-g, the frequencies of the modes were measured as a function of temperature. The measurements were made with the cell's axis horizontal and the oscillator's torsion axis vertical.

Our measurement technique assumed the internal-wave mode was a massive, high-Q oscillator coupled weakly to the low-mass oscillating screen. To bring the fluid into steady oscillations, the screen was driven at a frequency  $f_{drive}$  for at

least 10 cycles. Then the drive was turned off, and the screen's residual motion was recorded. If  $f_{drive}$  was near an internal-wave frequency, subsequent transient oscillations were visible, and the frequency of the internal wave was assigned after examination of the transient waveform's spectrum.

## COMPARISON

The xenon was contained within a simple cylinder; however, the internal geometry was complicated by the electrodes and the oscillator itself. The calculation of the frequencies of the internal wave modes relied on the approximation of the container's internal geometry as a rectangular box.

The viscometer's internal symmetry restricted the oscillator from coupling to most of the internal-wave modes. This restriction was useful due to the small spacing between modes. For example, even with the three modal indices restricted to only 0, 1 or 2, the frequencies calculated for 9 of the 16 possible modes can fall within a range of only 6%. Without the coupling restriction, the overlap of many modes would have complicated the interpretation of the measurements.

The frequencies computed for the modes with  $(jkl)$  equal to (111) and (112) are plotted in Figure 1. In these computations the density profiles, calculated using the parameters given in T[8], were the actual profiles expected from xenon's equation of state. The calculated and measured frequencies agree to within 15%.

## ACKNOWLEDGEMENTS

M.R. Moldover is co-Principal Investigator on CVX. The calculations were done by M.J. Lyell and G.B. McFadden with assistance from R.G. Rehm. This work was funded in part by NASA under Contract No. C-32-32014-C.

## REFERENCES

- [1] "Hydrodynamic similarity in an oscillating-body viscometer", R.F. Berg, Int. J. Thermophys. **16**, 1257 (1995).
- [2] "CVX Science Requirements Document", R.F. Berg and M.R. Moldover, report to NASA, 60009-DOC-006 (1993).
- [3] J. Lighthill, *Waves in Fluids* (Cambridge University Press, Cambridge, 1978).
- [4] H. Boukari, private communication (1994).

- [5] M.Sh. Gitterman, Sov. Phys. Doklady **12**, 1141 (1968).
- [6] V.D. Khait, Sov. Phys. JETP **30**, 177 (1970).
- [7] M.Sh. Gitterman and V.A. Shteinberg, Mekhanika Zhidkosti i Gosta **7**, 55 (1972). English translation in Fluid Dynamics **7**, 238 (1972).
- [8] "Gravity effects in fluids near the gas-liquid critical point", M.R. Moldover, J.V. Sengers, R.W. Gammon, and R.J. Hocken, Rev. Mod. Phys. **51**, 79 (1979).

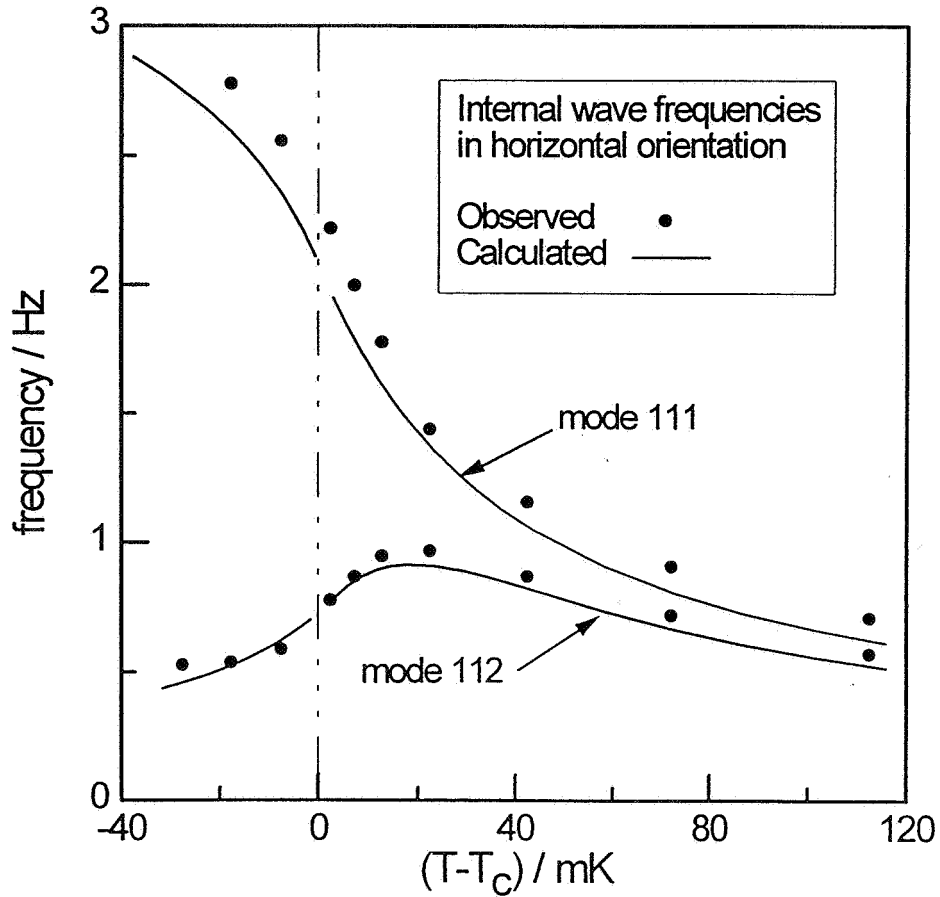


Figure 1. Internal-wave frequencies, measured (circles) and calculated (lines). The cell's axis was horizontal and the screen's torsion axis was vertical, so that the screen's motion was horizontal. The numerical calculations used the actual profiles derived from xenon's equation of state.



## **GROWTH AND MORPHOLOGY OF PHASE SEPARATING SUPERCRITICAL FLUIDS**

**John Hegseth**  
Department of Physics  
University of New Orleans, New Orleans, Louisiana 70148

**Daniel Beysens**  
Commissariat à l'Energie Atomique  
Departement de Recherche Fondamentale sur la Matiere Condensée  
CEN-Grenoble  
17, Avenue des Martyrs  
38054 Grenoble Cedex 9, France

**Françoise Perrot and Vadim Nikolayev**  
Commissariat à l'Energie Atomique  
Service de Physique de l'État Condensé  
Centre d'Etudes de Saclay  
F 91191 Gif sur Yvette Cedex, France

**Yves Garrabos**  
Laboratoire de Chimie du Solide du Centre National de Recherches Scientifiques  
CNRS-Universite de Bordeaux I  
351, Cours de la Liberation  
33405 Talence Cedex, France

### **SCIENCE OBJECTIVES**

The scientific objective is to study the relation between the morphology and the growth kinetics of domains during phase separation. We know from previous experiments performed near the critical point of pure fluids and binary liquids that there are two simple growth laws at late times. The "fast" growth appears when the volumes of the phases are nearly equal and the droplet pattern is interconnected. In this case the size of the droplets grows linearly in time. The "slow" growth appears when the pattern of droplets embedded in the majority phase is disconnected. In this case the size of the droplets increases in proportion to time to the power  $1/3$ . The volume fraction of the minority phase is a good candidate to determine this change of behavior. All previous attempts to vary the volume fraction in a single experimental cell have failed because of the extreme experimental difficulties.

### **RELEVANCE OF THE SCIENCE AND POTENTIAL APPLICATIONS**

Phase separation in liquid mixtures and pure fluids is a common process that occurs in many areas of natural science, engineering, and industry. Engineering applications are especially important in heat and mass transfer processes that occur in many industries. Phase separation is also ubiquitous in materials processing, e.g., metallic alloys, polymer alloys<sup>1</sup>, and flat panel displays. A clearer understanding of the exact physics of phase separation is desirable for improving industrial efficiency and in developing new products. Phase

separation is also an important fundamental scientific problem in which low gravity facilities are needed to improve understanding. A particularly important feature in the phase separation process, especially in applications, is the growth and morphology of domains (e.g., liquid droplets) after the process has been started. The connection between the morphology of the domains and the growth laws is still unclear. Only a few experimental results are available where density or concentration has been systematically varied<sup>2,3</sup>. In the region of the critical point, it has been found very easy to continuously vary the physical parameters that control phase separation (c.f., Figure 1). In addition, the critical slowing down of dynamics processes that occurs near the critical point enables a detailed investigation of the mechanisms involved in the separation process. Results from phase separation experiments done near the critical point can be described by scaled master curves<sup>1</sup> that are universal, i.e., curves that are *valid for all fluids* within two scale factors.

Binary liquids near a critical point of miscibility belong to the same universality class as pure fluids for static properties (c.f., the three dimensional Ising Model<sup>4</sup>). However, their dynamic behavior can be markedly different, especially in a gravitational field. This difference can be seen from the order parameter  $M$  ( $M$  is a generic variable that describes or controls a phase transition).  $M$  is the concentration difference  $M = c - c_c$  for liquid mixtures where  $c$  is the concentration and  $c_c$  is the critical concentration where phase separation occurs. At  $c_c$  the osmotic compressibility diverges and the mutual diffusion coefficient goes to zero. When  $M$  is changed to induce phase separation, sedimentation usually occurs because one phase is more dense than the other. In pure fluids,  $M$  is the density difference  $\rho - \rho_c$  ( $\rho$  is the density,  $\rho_c$  is the critical density). At the critical point in pure fluids the isothermal compressibility diverges and the thermal diffusivity goes to zero. Because pure fluids have a very large isothermal compressibility, they are very sensitive to the earth's gravitational field (acceleration  $g_0$ )<sup>3</sup>. Experiments are complicated by the very high compressibility of the fluid that induces density gradients even in the one-phase region. Convective flows, often turbulent, are also observed.

During phase separation, pure fluids and binary liquids are always sensitive to gravitational fields, through convection and/or sedimentation. Attempts have been made to avoid convection by preparing density-matched liquid mixtures, e.g., by adding a small amount of deuterated cyclohexane in a cyclohexane-methanol mixture<sup>6</sup>. These attempts show that it is impossible to avoid long-term sedimentation because density-matching can never be perfect. In a pure fluid near the critical point the thermal diffusivity becomes very small and the compressibility become very large. These two properties leads to a heat transport mechanism that becomes very fast, the so-called "piston effect." This effect allows thermalization of a fluid to be limited only by the thermal response of the thermostat<sup>7</sup>. Previous experiments with density-matched binary liquids and pure fluid  $\text{CO}_2$  under reduced gravity have shown<sup>8</sup> that when  $M=0$  (at  $M=0$  the volume fraction of the minority phase is  $\phi=1/2$  where  $\phi$ =ratio of the minority phase volume/total volume), an interconnected pattern of domains that coalesces continuously is formed. The characteristic wavelength  $L_m$ , at late times, grows linearly with time  $t$ . When expressed in the scaled units the corresponding wave number is  $K_m^* = 2\pi\xi/L_m$  ( $\xi$  is the correlation length for fluctuations of  $M$  that, at temperature  $T_f$ , is given by  $\xi = \xi_0(1 - T_f/T_c)^{-\nu}$ , where  $\xi_0$  is the correlation length amplitude,  $T_c$  is the critical temperature, and  $\nu = 0.63$  is a universal exponent). The corresponding time is  $t^* = t/t_\xi$  ( $t_\xi$  is the relaxation time for fluctuations of  $M$  given by  $t_\xi = 6\pi\eta\xi^3/k_B T_f$ , where  $k_B$  is the Boltzmann constant and  $\eta$  is the shear viscosity). Using these scaled variables the results obtained in all liquid mixtures and in  $\text{CO}_2$  during the gravity-free experiment can be placed on the same master curve<sup>8</sup> strongly supporting universality.

When the volume fraction is very small ( $\phi < 0.03$ ), and the gravity effects are negligible, the droplets do not coalesce. In this region they grow slowly by a diffusion mechanism. Experiments<sup>9</sup> show that the initial growth follows a power law in time with exponent  $1/2$  or  $1/3$ , depending on the initial supersaturation. Experiments also show that the late stages of growth are always characterized by a  $1/3$  power law exponent ("slow" growth) as described by Lifshitz and Slyosov<sup>10</sup>. Off-critical systems at a large volume fraction have been studied in a liquid mixture by Wong and Knobler<sup>2</sup>. For  $\phi > 0.10$  a "slow" growth characterized by a  $1/3$  growth law exponent is reported at early times and a faster growth at late times. The growth exponent varies from  $1/3$  to  $1$  as a function of  $\phi$  ("fast" growth).

If densities of liquid mixture components are close together, gravity effects are expected to be weak in

phase separation experiments. Density matching in a binary fluid mixture has been used in recent work<sup>3</sup>. In this experiment the temperature quenches were done in the presence of a controlled concentration gradient. This made it possible, in a single experiment, to determine both the coexistence curve and the boundary between the "fast" growth zone and the "slow" growth zone. Due to intrinsic experimental difficulties, however, the errors of the experimental results were large and difficult to estimate. The experiment was also performed using a gradient whose influence is also difficult to estimate. Based on these results it was only possible to state that the threshold between "fast" and "slow" growth has a value of  $\phi$  that is between 0.3 and 0.4.

## RESEARCH APPROACH

In order for this experiment to succeed it is necessary to perform very shallow quenches in a pure fluid very slightly off-critical and in a microgravity environment. Although in principle density-matched liquid mixtures on earth or under microgravity could be used for this experiment, they suffer from extremely slow evolution for such shallow quenches. This is not so with pure fluids whose viscosity is nearly 30 times smaller than liquid mixtures. In addition, a precise determination of the concentration of density-matched liquid mixtures is extremely difficult. This is not so with pure fluids whose volume fraction dependence can be accurately determined on earth (temperature variation of the meniscus height). In this experiment we will use two or more off-critical samples ( $(\rho - \rho_c)/\rho_c$  less than 1%) of  $SE_8$  to determine the critical threshold of the volume fraction where morphology and growth change. This will be done during a flight experiment using the ESA's Critical Point Facility (CPF).

A typical phase separation experiment consists of quenching a sample from an initial state (density  $\rho_0$ , initial temperature  $T_i$ ) where it is homogeneous to another state ( $\rho_0, T_f$ ). In this later state the homogeneous fluid is not stable and the process of phase separation starts. The main part of this experiment consists of a systematic variation of the quench depth,  $\delta T = T_{cx} - T_f$ , where  $T_{cx}$  is the liquid-gas phase transition temperature as shown in Figure 1. The starting point ( $\rho_0, T_i$ ) of each quench will be the same. To know the quench depth accurately, it is necessary to first determine  $T_{cx}$  with a precision of better than 50  $\mu K$ . After each quench, the system has to be heated 1K above  $T_{cx}$  to be homogenized again. The equilibrium volume fraction  $\phi$  of the minority phase is a key parameter for this experiment.  $\phi$  is controlled by controlling the quench depth,  $\delta T$ . This is possible because of the relation  $\phi = 1/2\{1 - (1 + \delta T/\Delta T)^{-\beta}\}$  where  $\beta = 0.325$  is a universal exponent and  $\Delta T = T_c - T_{cx}$  is calculated from the coexistence curve expression  $\rho - \rho_c = \pm B(-T/T_c)^\beta$  where B is a system dependent<sup>4</sup> constant.

The phase separation experiments require a very precise temperature control (temperature stability better than 50  $\mu K$  per hour) with negligible temperature gradients in the cell. Temperature quenches of step size 0.1 mK will be typical with an overshoot of less than 10% of the quench depth. This experiment will also require direct real time visualization of the sample with ground-based control. These are needed for the determination of the transition temperature and for adjusting the experimental protocol.

The experiment will also require the following optical diagnostics:

- small angle light scattering for determining the coexistence point temperature,  $T_{cx}$ , and the early stages of phase separation
- direct observation of the cell for the determination of  $T_{cx}$ , the study of the pattern morphology, and for the determination of the growth laws
- interferometry for estimating the temperature gradient in the cell unit.

## SCIENCE RESULTS

Although this project has just begun, there are previous results from other experiments that are relevant. In the IML1 mission using the CPF a sample of density matched binary fluid and a sample of pure fluid were flown. The density matched binary fluid was an off-critical sample of methanol and partially deuterated

cyclohexane at concentration  $c \approx c_c - 0.01$ . The pure fluid was an off-critical sample of sulfur hexafluoride at  $(\rho - \rho_c)/\rho_c = 0.036$ . In these experiments the samples were subjected to various quench depths. All the data obtained in liquid mixtures and in pure  $\text{SF}_6$  during the gravity-free experiments, when expressed in the scaled units  $K_m^* = 2\pi\xi/L_m$  and  $t^* = t/t_\xi$  fit remarkably well to the same master curve ( $K_m^* \approx 1t^{*1/3}$ ) giving clear evidence for the universality of phase separation in fluids and liquid mixtures<sup>11</sup>. Moreover, the crossover between slow and fast growth at  $\phi = 0.1$  reported by Wong and Knobler could not be observed when gravity effects were suppressed. It is likely that this discrepancy can be attributed to gravity effects that are difficult to see directly.

We have found that density-matched liquid mixtures could not be used on earth to study the crossover in morphology. This is because the range of interest is 0.01 in concentration around  $c_c$ . The determination of such a small concentration difference is extremely difficult to achieve. It is also necessary to perform shallow quenches to produce small volume fractions. These experimental conditions lead to very slow evolution. Typically, in partially deuterated cyclohexane-methanol at  $c - c_c = 0.005$ , for a quench depth of 100  $\mu\text{K}$ , the time to obtain droplets of  $\approx 30 \mu\text{m}$  is of order 3 hours. This time is much too long in comparison to the stability of the experiment conditions that can be obtained.

To avoid these difficulties an experiment with an off-critical fluid ( $\text{SF}_6$ ) was carried out in the IML2 mission. The density difference  $(\rho - \rho_c)$  was measured on earth by studying the temperature dependence of the meniscus between the liquid and gas phases. This precise method gave  $(\rho - \rho_c)/\rho_c = 0.0050$ . Under microgravity, a determination of the transition temperature  $T_{cx}$  with a precision of 50  $\mu\text{K}$  was first done. Fast growth, with interconnected patterns, occurred for quench depths of 300  $\mu\text{K}$  and 1000  $\mu\text{K}$ . This contrasts with the slow growth observed for quench depths of 50  $\mu\text{K}$  and 100  $\mu\text{K}$ . This shows that the volume fraction (related to quench depth as shown above) is the correct parameter for studying the connection between morphology and growth. The presence of a density gradient in the cell, however, (related to the very large compressibility of the fluid near its critical point) complicated the interpretation of the data. This was especially true for estimating the crossover volume fraction. To avoid density gradients during the determination of  $T_{cx}$ , it is necessary to use considerable time during the approach. These experiments were hampered by the short time allowed. The  $T_{cx}$  determination can only be done on earth to within a few mK because of the gravity-induced gradients present (the fluid is compressed under its own weight).

Another attempt to suppress gravity effects has been considered by Tanaka<sup>12</sup> who studied phase separation with oligomer mixtures between closely spaced plates. During the late stages of growth, when the sizes of the domains were of the order of the thickness of the liquid mixture layer, he also observed two different kinetics of growth. However, in this case the phase separation is controlled by the wetting phenomena from the plates and cannot reveal many interesting bulk effects.

Although the experimental results are few, phase separation has been the object of great theoretical interest over the last several decades. The work by Siggia<sup>13</sup> has initiated many attempts to explain the two growth laws by considering hydrodynamic arguments. Recently, several groups<sup>14-18</sup> have done large scale direct numerical simulations by using different approaches to solve coupled equations involving diffusion and hydrodynamics. Some of these simulations have recovered a  $t^1$  growth law<sup>14,15</sup>. Others were unable to reach the late stages of separation but did calculate the transient values of the growth exponent (between 1/3 and 1). In spite of these efforts, the physical mechanism for the linear growth has not been clarified. To our knowledge, the simulations have never shown the two asymptotic growth laws: the exponents are either larger than 1/3 when accounting for hydrodynamics or 1/3 for pure diffusion. Thus the simulations still do not explain the transition from one regime to the other. Recently, a new theoretical approach has been suggested by some of us that explains the existence of the two different regimes and their relation to the pattern morphology. One purpose of the present project is to check the predictions of this model.

## RESEARCH PLANS

From two space shuttle missions in the ESA's Critical Point Facility several important results have already

been obtained. In the IML1 experiment the universality of phase separation in fluids and liquid mixtures has been shown. The IML2 experiment yielded preliminary results in a 0.5% off-critical sulfur hexafluoride cell where a transition between disconnected-slow growth and the interconnected fast growth was observed. This has been obtained in a single cell, showing that the volume fraction is a crucial parameter. Nevertheless, the presence of a density gradient in the cell, related to the very large compressibility of the fluid near its critical point, complicated the interpretation of the data and prevented any precise determination of the volume fraction threshold, estimated to be within 30-40%.

To understand why morphology and growth undergo such a dramatic change at this "critical" value of the volume fraction, it is necessary to reproduce and refine the experiments. Systematic variations of the temperature quench depths must be made and significant reductions in density gradients in the cell must be achieved. Because these experiments are done extremely close to the critical point, a microgravity environment is essential.

The specific plan will be to operate two or more cells of sulfur hexafluoride in the Critical Point Facility (CPF) under microgravity. The ground-based program consists of preparation and testing of the sample cells, improvement of the sample cell to minimize temperature gradients in the fluid, and numerical simulation of the phenomena including hydrodynamics.

## REFERENCES

1. J. D. Gunton, M. San Miguel and P. S. Sahni, in *Phase Transitions and Critical Phenomena*, vol 8, edited by C. Domb and J. L. Lebowitz (Academic Press, 1983), p.269 and references therein.
2. N. C. Wong and C. M. Knobler, *Phys. Rev. A* **24**, 3205 (1981).
3. Y. Jayalakshmi, B. Khalil and D. Beysens, *Phys. Rev. Lett.* **69**, 3088 (1992).
4. H. E. Stanley, *Introduction to Phase Transitions and Critical Phenomena* (Clarendon Press, 1971).
5. M. R. Moldover, J. V. Sengers, R. W. Gammon and R. J. Hocken, *Rev. Mod. Phys.* **51**, 79 (1979).
6. D. Beysens, P. Guenoun and F. Perrot, *Phys. Rev. A* **38**, 4173 (1988).
7. see e.g. A. Onuki and R. A. Ferrel, *Physica A* **164**, 245 (1990); P. Guenoun, D. Beysens, Y. Garrabos, F. Kammoun, B. Le Neindre and B. Zappoli, *Phys. Rev. E* **47**, 1531 (1993).
8. Y. Garrabos, B. Le Neindre, P. Guenoun, B. Khalil and D. Beysens, *Europhys. Lett.* **19**, 491 (1992) and refs. therein.
9. A. Cumming, P. Wiltzius, F. S. Bates and J. H. Rosedale, *Phys. Rev. A* **45**, 885 (1992); T. Baumberger, F. Perrot and D. Beysens, *Phys. Rev. A* **45**, 7636 (1992).
10. I. M. Lifschitz and V. V. Sloyosov, *J. Phys. Chem. Solids* **19**, 35 (1961).
11. F. Perrot, P. Guenoun, T. Baumberger, D. Beysens, Y. Garrabos and B. Le Neindre, *Phys. Rev. Lett.* **73**, 688 (1994).
12. H. Tanaka, *Phys. Rev. Lett.* **72**, 1702 (1994).
13. E. D. Siggia, *Phys. Rev. A* **20**, 595 (1979).
14. S. Puri and B. Dünweg, *Phys. Rev. A* **45**, R6977 (1992).
15. F. J. Alexander, S. Chen, and D. W. Grunau, *Phys. Rev. B* **48**, 634 (1993).
16. A. Shinozaki and Y. Oono, *Phys. Rev. E* **48**, 2622 (1993).
17. O. T. Valls and J. E. Farrel, *Phys. Rev. E* **47**, R36 (1993).
18. K. Kawasaki, T. Ohta, *Physica A* **118**, 175 (1983); T. Koga, K. Kawasaki, M. Takenaka and T. Hashimoto, *Physica A* **198**, 473 (1993).

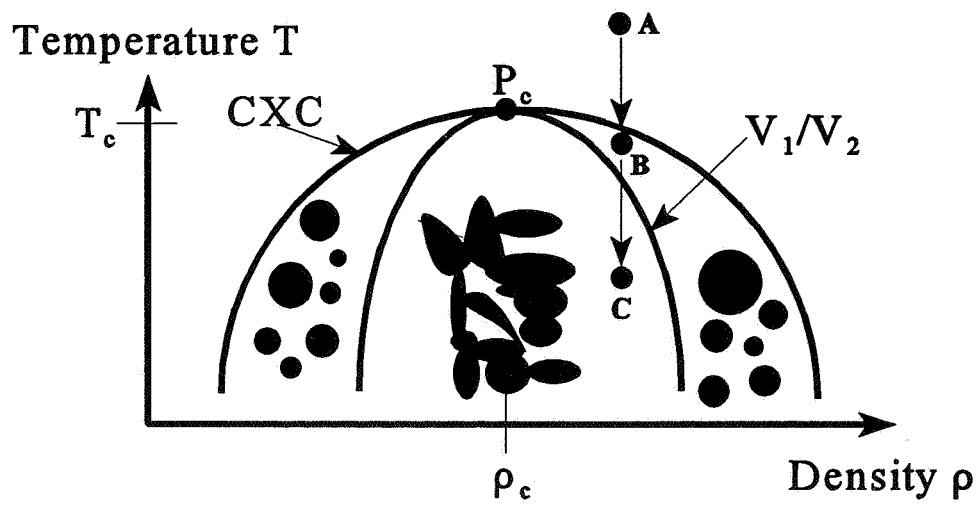


Figure 1.—Morphology and growth. A phase diagram (schematic) of  $\text{SF}_6$  that shows the critical point  $P_c$ , the critical temperature  $T_c$  ( $45.55^\circ\text{C}$ ), the critical density  $\rho_c$  ( $0.737\text{ g/cm}^3$ ), and the coexistence curve CXC. When the supercritical fluid (point A, density off-critical by  $+0.5\%$ ) is quenched below CXC, droplets of vapor (volume  $V_1$ ) and liquid (volume  $V_2$ ) nucleate and grow. The experiments in IML2 show that the curve  $V_1/V_2 \approx 50\%$  separates a region of “slow” growth (A  $\rightarrow$  B quench  $50\text{ }\mu\text{K}$  below CXC) where the droplets are disconnected and grow as  $(\text{time})^{1/3}$ , from a region of “fast” growth (A  $\rightarrow$  C quench  $3\text{ mK}$  below CXC), where the droplets are interconnected and grow as  $(\text{time})^1$ .

# ISOPYCNIC PHASES AND STRUCTURES IN H<sub>2</sub>O/CO<sub>2</sub>/ETHOXYLATED ALCOHOL SURFACTANT MIXTURES

Michael E. Paulaitis  
Department of Chemical Engineering  
Johns Hopkins University  
Baltimore, MD 21218

Richard G. Zielinski and Eric W. Kaler  
Center for Molecular and Engineering Thermodynamics  
Department of Chemical Engineering  
University of Delaware  
Newark, Delaware 19716

## ABSTRACT

Ternary mixtures of H<sub>2</sub>O and CO<sub>2</sub> with ethoxylated alcohol (C<sub>i</sub>E<sub>j</sub>) surfactants can form three coexisting liquid phases at conditions where two of the phases have the same density (isopycnic phases). Isopycnic phase behavior has been observed for mixtures containing the surfactants C<sub>8</sub>E<sub>5</sub>, C<sub>10</sub>E<sub>6</sub>, and C<sub>12</sub>E<sub>6</sub>, but not for those mixtures containing either C<sub>4</sub>E<sub>1</sub> or C<sub>8</sub>E<sub>3</sub>. Pressure-temperature (PT) projections for this isopycnic three-phase equilibrium were determined for H<sub>2</sub>O/CO<sub>2</sub>/C<sub>8</sub>E<sub>5</sub> and H<sub>2</sub>O/CO<sub>2</sub>/C<sub>10</sub>E<sub>6</sub> mixtures at temperatures from approximately 25 to 33°C and pressures between 90 and 350 bar. As a preliminary to measuring the microstructure in isopycnic three component mixtures, phase behavior and small angle neutron scattering (SANS) experiments were performed on mixtures of D<sub>2</sub>O/CO<sub>2</sub>/ n-hexaethyleneglycol monododecyl ether (C<sub>12</sub>E<sub>6</sub>) as a function of temperature (25-31°C), pressure (63.1-90.7 bar), and CO<sub>2</sub> composition (0-3.9 wt%). Parameters extracted from model fits of the SANS spectra indicate that, while micellar structure remains essentially unchanged, critical concentration fluctuations increase as the phase boundary and plait point are approached.

## INTRODUCTION

Surfactant solutions containing near-critical or supercritical fluids that form equilibrium phases of equal density (isopycnic phases) are uniquely suited for simulating phase separation in microgravity environments where density differences between the separating phases are irrelevant. For compressible supercritical-fluid mixtures, pressure becomes an additional field variable with which to adjust and control phase boundaries.<sup>1-3</sup> As a consequence, rapid pressure quenches can be made to access metastable or unstable regions of the phase diagram, thereby permitting the convenient study of phase separation dynamics and mechanisms. In addition, low interfacial tensions and the presence of colloidal microstructure in surfactant-containing mixtures<sup>1, 3-5</sup> retard phase separation. In this work, isopycnic phase behavior for three-phase, liquid-liquid-liquid (L1-L2-L3) equilibrium was investigated for ternary mixtures of H<sub>2</sub>O and CO<sub>2</sub> with the ethoxylated alcohol (C<sub>i</sub>E<sub>j</sub>) surfactants: C<sub>4</sub>E<sub>1</sub>, C<sub>8</sub>E<sub>3</sub>, C<sub>8</sub>E<sub>5</sub>, C<sub>10</sub>E<sub>6</sub>, and C<sub>12</sub>E<sub>6</sub>. CO<sub>2</sub> was chosen for study because it has a readily accessible critical point (31.06°C and 73.825 bar) and a reasonably high critical density (0.4660 g/cm<sup>3</sup>).<sup>6</sup>

Surfactant self-assembly in near-critical or supercritical fluids opens the possibility that pressure or fluid density could also be used to alter surfactant microstructure.<sup>7, 8</sup> Most prior studies of surfactant microstructure in solutions containing supercritical or near-critical fluids have focused on the supercritical fluid-rich corner of the phase diagram, where the effects of pressure on microstructure and phase behavior are expected to be large. Here we use small angle neutron scattering experiments to examine the effect of carbon dioxide on the interactions, critical fluctuations, and structure of C<sub>12</sub>E<sub>6</sub>/D<sub>2</sub>O micellar mixtures in the water-rich corner of the phase diagram. The scattering spectra are successfully modeled using a polydisperse hard sphere form factor to determine particle shape and size, together with an Ornstein-Zernike structure factor to quantify the critical phenomena. Using the model parameters, the micellar composition was calculated to determine the

partitioning of carbon dioxide between the water and the micelles.<sup>9</sup>

## EXPERIMENTAL SECTION

Observations of isopycnic phase behavior were made using a variable-volume view cell. The cell design and experimental technique are described in detail elsewhere.<sup>1</sup> The view cell is a sapphire tube (Insaco) 17.78 cm long with an inner diameter of  $1.113 \pm 0.001$  cm and an outer diameter of 1.67 cm. It is sealed internally on each end with Viton O-rings and Polymite backing rings mounted on stainless steel endcaps. The endcaps are held in place against the internal cell pressure by a C-bracket that also provides support for the sapphire tube. The cell in this configuration was hydrostatically tested to 551 bar. The view cell is also equipped with a movable piston to allow pressure to be varied independently of sample composition and temperature. Pressure in the cell is generated using a water-filled syringe pump (High Pressure Equipment) to move the piston and compress the sample. Two spring-loaded seals (Bal-Seal Engineering) near each end of the piston insure proper alignment of the piston in the sapphire tube and separate the pressurizing fluid from the surfactant solution. Sample pressure is determined indirectly by measuring the pressure of the pressurizing fluid to within  $\pm 0.5$  bar with a Bourdon tube gauge (Heise). The pressure drop across the piston was determined to be less than 1-2 bar at 300 bar. The entire assembly is immersed in a high precision water bath (Hart Scientific), which controlled temperature to  $\pm 0.001^\circ\text{C}$ . The temperature of the bath is measured with an NBS mercury thermometer ( $\pm 0.005^\circ\text{C}$ ). The custom-designed temperature bath has a window for phase behavior observations.

The L1 and L2 phase densities were measured to a maximum accuracy of  $\pm 10^{-5}$  g/cm<sup>3</sup> using a vibrating tube densimeter and the method of Kratky *et al.*<sup>10</sup> The densimeter (Anton-Paar DMA-512 rated to 400 bar) was calibrated at each temperature and pressure with nitrogen and water. Sample was transferred from the view cell to the densimeter using the movable piston as a syringe to displace the fluid. Sampling of a particular phase was facilitated by loading the view cell such that this phase was present in excess. Constant pressure ( $\pm 3$  bar) was maintained during sampling by filling the densimeter and all transfer lines with nitrogen to the pressure of the view cell. The densimeter temperature was controlled to  $\pm 0.05^\circ\text{C}$  by recirculating water from the temperature bath for the view cell. The pressure in the densimeter was measured directly to within  $\pm 0.3$  bar with a Bourdon tube gauge (Heise).

Densities of the surfactant/water solutions at ambient pressure were measured using a second vibrating tube densimeter (Anton-Paar DMA 602) with a maximum accuracy of  $\pm 10^{-6}$  g/cm<sup>3</sup>. The densimeter temperature in these experiments was controlled to  $\pm 0.1^\circ\text{C}$  by an external temperature bath (Neslab RTE 111) and was measured to  $\pm 0.02^\circ\text{C}$  using a quartz thermometer (Hereaus Sensor) immersed in the bath. Solutions were injected manually into the densimeter.

The non-ionic surfactants C8E3, C8E5 (Bachem and Biosciences, >98% pure C8E5), C12E6, C10E6 (Nikko, >99% pure), and C4E1 (Aldrich, >99% pure) were used as received. Water was distilled, deionized, and degassed of oxygen to minimize surfactant degradation over the course of the experiment. Carbon dioxide (Matheson, Coleman Grade, >99.99% pure) and nitrogen (Airco, high pressure, 99.998% pure) were used as received.

Small-angle neutron scattering was performed using the 30 meter spectrometer at the National Institute of Standards and Technology (NIST), in Gaithersburg, MD. Neutrons with a 5 Å wavelength ( $\Delta\lambda/\lambda = 0.15$ ) gave  $q$ -values from 0.007 to  $0.22 \text{ \AA}^{-1}$  where  $q$ , the magnitude of the scattering vector, is defined as  $q = (4\pi/\lambda)\sin(\theta/2)$  and  $\theta$  is the scattering angle. Data were put on absolute scale using a silica standard and data handling software supplied by NIST, and corrected for scattering from the empty cell and the D<sub>2</sub>O solvent. The high pressure SANS cell is made entirely of machined sapphire (Insaco Inc.) to facilitate measuring at large (30 degree) scattering angles. The scattering cell has a path length of 2mm and a total volume of 1.6 ml, and is thermostated by an aluminum heat transfer jacket. Temperature was measured with a platinum RTD (Newport Electronics,  $\pm 0.1^\circ\text{C}$ ) placed inside the scattering cell. Liquid-tight sealing at the ends of the SANS cell was accomplished with viton O-Rings (Parker size 2-013) and backing rings (Parker size 8-013) mounted on stainless steel endcaps.



## RESULTS

Three equilibrium phases were observed for mixtures of H<sub>2</sub>O, CO<sub>2</sub>, and C<sub>8</sub>E<sub>5</sub> at 25.5 to 30.0°C and 91 to 360 bar. The water-rich L1 phase and the surfactant-rich L2 phase were identified from the known overall composition of the mixture and the observed relative volumes of the two phases. The CO<sub>2</sub>-rich L3 phase was found to have the lowest density at all conditions studied. The measured L1 and L2 phase densities at 30.0°C are shown in Figure 1 as a function of pressure. At low pressures, the L1 phase has a higher density than the L2 phase, and at higher pressures, the L2 phase density is higher. The pressure at which the two densities are equal (the isopycnic pressure) is  $308 \pm 3$  bar, which is given by the intersection of the two linear fits to the densities near the isopycnic pressure. An experimental uncertainty of  $\pm 3$  bar is estimated from uncertainties in the pressure ( $\pm 2$  bar) and the density ( $\pm 10^{-4}$  g/cm<sup>3</sup>) measurements. The observed inversion of the L1 and L2 phases at this temperature was found to be within  $\pm 7$  bar of this value.

Isopycnic pressures at other temperatures and for ternary mixtures of H<sub>2</sub>O, CO<sub>2</sub>, and C<sub>10</sub>E<sub>6</sub> were determined only from observations of the L1-L2 phase inversion. The pressure-temperature (PT) projections for this isopycnic three-phase, L1-L2-L3 equilibrium are shown in Figure 2. These two projections are similar with the one for C<sub>10</sub>E<sub>6</sub>-containing mixtures shifted to higher temperatures by approximately 2°C. In both cases, the isopycnic pressure increases dramatically with increasing temperature. The L1-L2 phase inversion was also observed for H<sub>2</sub>O/CO<sub>2</sub>/C<sub>12</sub>E<sub>6</sub> mixtures in L1-L2-L3 equilibrium at 18.6°C and approximately 394 bar. However, the ternary mixtures containing either C<sub>4</sub>E<sub>1</sub> or C<sub>8</sub>E<sub>3</sub> did not exhibit an inversion at a temperature of 26.9°C and pressures between 90 to 310 bar.

Phase boundaries between one- and two-phase regions for mixtures of D<sub>2</sub>O/ CO<sub>2</sub>/ C<sub>12</sub>E<sub>6</sub> were determined at constant pressure and composition by measuring the temperature where the mixture became turbid.<sup>9</sup> Figure 3 shows the temperature-CO<sub>2</sub> concentration phase diagrams at 63.1 and 90.7 bar for a constant D<sub>2</sub>O to C<sub>12</sub>E<sub>6</sub> weight ratio of 12.8 to 1. Carbon dioxide at small concentrations depresses the coexistence curve in C<sub>12</sub>E<sub>6</sub>/D<sub>2</sub>O mixtures by more than 20 °C at 4.3 wt% CO<sub>2</sub>. The phase boundary changes little from 63.1 to 90.7 bar, increasing a maximum of 0.52°C at 4.3 wt% CO<sub>2</sub>.

SANS measurements were made on mixtures of C<sub>12</sub>E<sub>6</sub>, CO<sub>2</sub>, and D<sub>2</sub>O in the one- phase region in the water-rich corner of the phase diagram (7.5 wt% C<sub>12</sub>E<sub>6</sub> on a CO<sub>2</sub>-free basis) containing varying amounts of carbon dioxide. The compositions of the samples examined by SANS are represented by the crosses in Figure 3. SANS experiments are reported in detail elsewhere<sup>9</sup> were performed at 63.1, 76.9, and 90.7 bar and temperatures of 25, 28, and 31°C in order to span the carbon dioxide critical pressure near its critical temperature. As an example of the results, scattering spectra and model descriptions (solid lines) for the samples at 31°C and 63.1 bar are shown on log-log scales in Figure 4 as plots of neutron scattered intensity on an absolute scale as a function of the magnitude of the scattering vector,  $q$ . For clarity of presentation, some of the spectra are multiplied by 2 or 4 (shown as (x2) or (x4) in the figure caption) to be offset from the other spectra. These spectra are distinguished by different degrees of upturn at low  $q$ . This feature usually arises from the presence of either attractive interactions between micelles or critical scattering. The high  $q$  portions of the spectra change little in shape with changes in temperature, pressure, or CO<sub>2</sub> composition. This indicates that the micelle structure does not change under these conditions.

## DISCUSSION

Mixtures of H<sub>2</sub>O and CO<sub>2</sub> with either C<sub>8</sub>E<sub>5</sub> or C<sub>10</sub>E<sub>6</sub> form isopycnic L1 and L2 phases in three-phase, liquid-liquid-liquid equilibrium at elevated pressures and temperatures in the range of 25 - 35°C (Figure 2). The effect of pressure is to increase the density of the L2 phase to a greater extent than that of the L1 phase (Figure 1), which leads to the observed isopycnic phase behavior. The higher compressibility of the L2 phase can be attributed at least in part to the higher pure-component compressibilities of both the surfactant and CO<sub>2</sub>. However, the L1 phase densities are always greater

than the densities of each of the three pure components for the temperatures and pressures studied. Thus, the L2 phase density will always be less than that for the water-rich L1 phase if these components formed ideal mixtures at the conditions studied. It follows, therefore, that non-ideal mixing must account for the existence of isopycnic phases.

Non-ideal mixing in the form of negative excess molar volumes has been determined experimentally for binary mixtures of C<sub>8</sub>E<sub>5</sub> with CO<sub>2</sub> and with H<sub>2</sub>O. Excess molar volumes for binary mixtures of CO<sub>2</sub> and H<sub>2</sub>O, calculated from measured liquid densities at 26°C, are likewise negative.<sup>11, 12</sup> For example, Francis<sup>11</sup> reports a partial molar volume of 32.4 cc/mole for CO<sub>2</sub> in water at 26°C and 66.0 bar, which is much less than the liquid molar volume of pure CO<sub>2</sub> at these conditions (65.8 cm<sup>3</sup>/mol). The measured pressure dependence of CO<sub>2</sub> solubilities in water<sup>13</sup> gives similar values for the partial molar volume of CO<sub>2</sub> in water, indicating negative excess molar volumes for this binary mixture.

Liquid densities for ternary H<sub>2</sub>O/ CO<sub>2</sub>/ C<sub>8</sub>E<sub>5</sub> mixtures can be predicted from measured densities for the binary mixtures using a recent modification of the Peng-Robinson equation of state (PR EOS).<sup>14</sup> In this modification, the original form of the equation for mixtures and the conventional quadratic mixing rules have been retained, but the combining rule for the  $a_{ij}$  parameters when  $i \neq j$  is modified to incorporate an additional adjustable parameter for each pair of constituents. This PR EOS provides an accurate description of highly non-ideal thermodynamic behavior over the entire range of mixture compositions.

Turning now to microstructure studies, the scattering spectra of D<sub>2</sub>O/ C<sub>12</sub>E<sub>6</sub> mixtures show an upturn at low  $q$  as a function of CO<sub>2</sub> concentration (Figure 4). To model the spectra, we assume there is no correlation between particle size and interactions. For this case, the effects of particle shape (form factor) and interactions (structure factor) on the measured intensity can be determined independently. The model intensity as a function of  $q$  can be written as:

$$\frac{d\Sigma}{d\Omega} = (\Delta\rho)^2 \phi V \langle P(q) \rangle S(q) + B \quad (1)$$

where  $(\Delta\rho)^2\phi$  is the product of contrast and volume fraction of particles,  $V$  is the volume of a micelle,  $\langle P(q) \rangle$  is the form factor normalized by  $1/V^2$ ,  $S(q)$  is the structure factor, which depends on the correlation length  $\xi$ , and  $B$  represents the incoherent scattering background.

Because of the shape of the scattering curves and the proximity of the sample composition, pressure, and temperature to the phase boundary, a modified Ornstein-Zernike structure factor together with a form factor for polydisperse spheres were chosen to model the data. The form factor assumes a Schultz distribution for the particle radii and includes particle radius and the Schultz width parameter (a measure of the degree of polydispersity) as parameters.<sup>15</sup> The use of a form factor that accounts for polydispersity together with a structure factor that assumes a monodisperse population of aggregates is a good approximation for polydisperse hard spheres when the ratio of polydispersity to radius is less than 0.3.<sup>16</sup> The modified Ornstein-Zernike structure factor is  $S(q) = 1 + S(0) / [1 + (q\xi)^2]$ .

The values for the five fitted parameters: radius ( $r$ ), polydispersity, correlation length ( $\xi$ ),  $S(0)$ , and  $(\Delta\rho)^2\phi$  were determined by minimizing the  $\chi^2$  value between the model fit and the experimental data. The fits of the five parameter model to the data are excellent except at the highest values of  $q$ , which reflects the assumption that the incoherent background remains constant through all of the fitting. The fitting shows that the micelle size remains constant at about 50 Å diameter, while the correlation length increases from 70 to 110 Å as CO<sub>2</sub> concentration increases from 0 to 3.9 wt% (Figure 4). Analysis of  $(\Delta\rho)^2\phi$  shows that, for the 3.9 wt% CO<sub>2</sub> samples no more than 7% of the added carbon dioxide enters the micelles.

## CONCLUSIONS

Phase behavior observations show that isopycnic liquid phases form in ternary mixtures of  $\text{H}_2\text{O}/\text{CO}_2/\text{C}_8\text{E}_5$ ,  $\text{C}_{10}\text{E}_6$ , or  $\text{C}_{12}\text{E}_6$ , but not in mixtures of  $\text{H}_2\text{O}/\text{CO}_2/\text{C}_4\text{E}_1$  or  $\text{C}_8\text{E}_3$ . Isopycnic phase formation is favored by raising the pressure or decreasing the temperature. At elevated pressures, this phase behavior is due in large part to favorable changes in the L2 phase composition for three-phase, liquid-liquid-liquid equilibrium. Non-ideal mixing effects that lead to a density maximum for the  $\text{H}_2\text{O}/\text{CO}_2$  binary mixture are necessary for the formation of isopycnic phases in these ternary mixtures.

SANS measurements on the system  $\text{D}_2\text{O}/\text{CO}_2/\text{C}_{12}\text{E}_6$  in the water-rich corner of the phase diagram indicate the presence of spherical micelles ca. 50 Å in diameter. This dimension is similar to that of micelles formed in mixtures of  $\text{D}_2\text{O}$  and  $\text{C}_{12}\text{E}_6$  alone. Micelle structure does not change over the range of pressures, temperatures, and compositions studied. The increase in  $S(0)$  and  $\xi$  are consistent with increasing critical concentration fluctuations caused by the approach of a plait point and the phase boundary. Analysis of the product  $(\Delta\rho)^2\phi$  as a function of carbon dioxide density and concentration indicates that little or no carbon dioxide added to the solution partitions into the micelles.

## ACKNOWLEDGMENTS

This work was supported by the National Aeronautics and Space Administration (NAG3-1424) and a NASA graduate student researcher program fellowship for R. G. Z. We acknowledge the support of the National Institute of Standards and Technology, U.S. Department of Commerce, in providing the facilities used in this experiment. The assistance of John Barker and Charlie Glinka during the SANS experiments is gratefully acknowledged, as are helpful discussions with Steve Kline, Y. Jayalakshmi, K.-V. Schubert, and C.-P. Chai Kao.

## REFERENCES

1. J. M. Ritter and M. E. Paulaitis, *Langmuir* 6, 934-941 (1990).
2. G. J. McFann and K. P. Johnston, *Langmuir* 9, 2942-2948 (1993).
3. G. J. McFann, K. P. Johnston and S. M. Howdle, *AIChE J.* 40, 543-555 (1994).
4. E. W. Kaler, J. F. Billman, J. L. Fulton and R. D. Smith, *Journal of Physical Chemistry* 95, 458-462 (1991).
5. J. M. Tingey, J. L. Fulton, D. W. Matson and R. D. Smith, *Journal of Physical Chemistry* 95, 1443-1448 (1991).
6. "Carbon Dioxide International Thermodynamic Properties of the Fluid State -3"; S. Angus, B. Armstrong and K. M. d. Reuk, Eds.; Pergamon Press: Oxford, 1976.
7. J. L. Fulton and R. D. Smith, *Journal of Physical Chemistry* 92, 2903-2907 (1988).
8. R. W. Gale, J. L. Fulton and R. D. Smith, *Journal of the American Chemical Society* 109, 920-921 (1987).
9. R. G. Zielinski, E. W. Kaler and M. E. Paulaitis, *Journal of Physical Chemistry* 99, 10354-10358 (1995).
10. O. Kratky, H. Leopold and H. Stabinger, *Z. Angew. Phys.* 27, 273 (1969).
11. A. W. Francis, *Journal of Physical Chemistry* 58, 1099-1114 (1954).
12. T. Ohsumi, N. Nakashiki, K. Shitashima and K. Hirama, *Energy Conserv. Mgmt.* 33, 685-690 (1992).
13. W. J. Parkinson and N. DeNevers, *I&EC Fundamentals* 8, 709-713 (1969).
14. C.-P. C. Kao, M. E. Paulaitis, G. A. Sweany and M. Yokozeki, *Fluid Phase Equilibria* 108, 27-46 (1995).
15. M. Kotlarchyck and S. H. Chen, *Journal of Chemical Physics* 79, 2461-2469 (1983).
16. W. L. Griffith, R. Triolo and A. L. Compere, *Physical Review A* 35, 2200-2206 (1987).

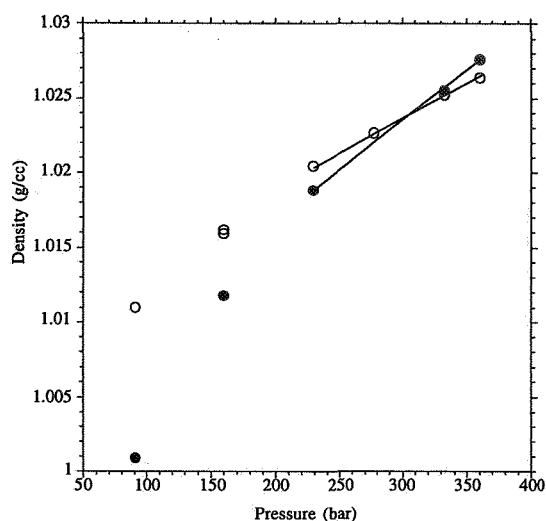


Figure 1. Measured densities of the L1 phase (open circles) and the L2 phase (closed circles) in three-phase, liquid-liquid-liquid equilibrium as a function of pressure at 30.0°C for  $\text{H}_2\text{O}/\text{CO}_2/\text{C}_8\text{E}_5$  ternary mixtures. The linear interpolations of the data define the isopycnic pressure at 308 bar.

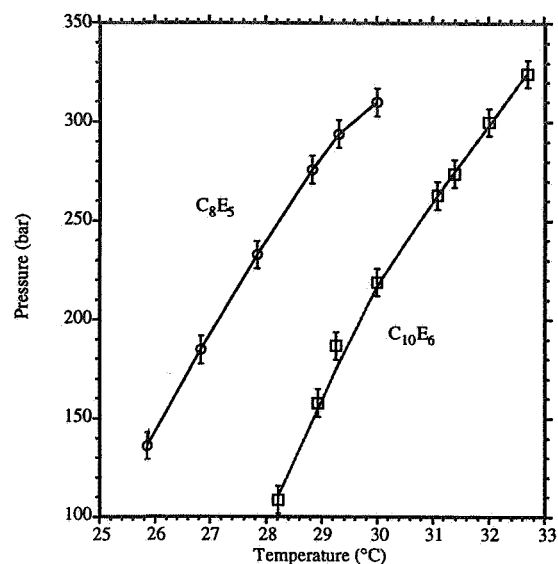


Figure 2. Measured pressure-temperature projections for isopycnic L1 and L2 phases in three-phase equilibrium for  $\text{H}_2\text{O}/\text{CO}_2/\text{C}_8\text{E}_5$  (circles) and  $\text{H}_2\text{O}/\text{CO}_2/\text{C}_{10}\text{E}_6$  (squares) ternary mixtures.

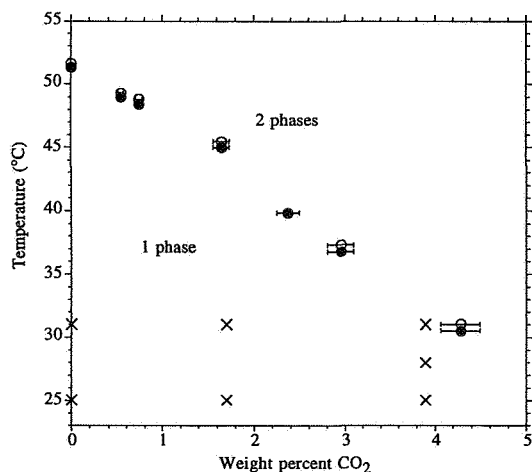


Figure 3. Temperature-composition phase diagrams for  $\text{D}_2\text{O}/\text{CO}_2/\text{C}_{12}\text{E}_6$  mixtures at a constant  $\text{D}_2\text{O}/\text{C}_{12}\text{E}_6$  weight ratio of 12.8 to 1. Open circles are data at 90.7 bar and the filled circles represent data at 63.1 bar. Crosses show the SANS operating conditions.

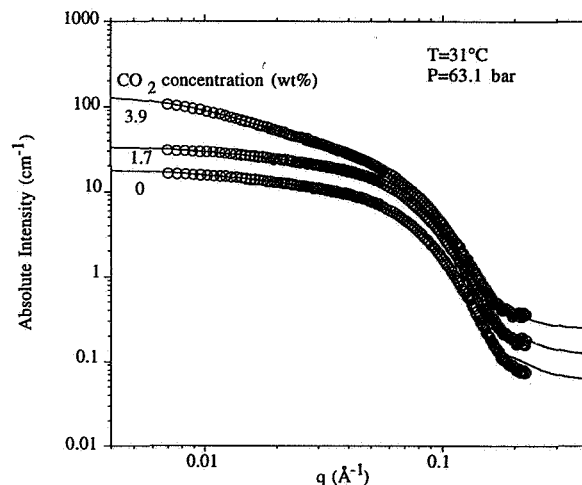


Figure 4. SANS spectra of solutions at 31°C and 63.1 bar for solutions at a constant  $\text{CO}_2$  concentrations of 0, 1.7 (x2), 3.9 (x4) wt%  $\text{CO}_2$  and constant  $\text{D}_2\text{O}/\text{C}_{12}\text{E}_6$  weight ratio of 12.8 to 1. There is a large intensity increase at low  $q$  at the highest  $\text{CO}_2$  concentration. Lines represent model fits to the data.

# ELECTRIC FIELD INDUCED INTERFACIAL INSTABILITIES

Robert E. Kusner, Kyung Yang Min, *NASA Lewis Research Center*  
Xiao-lun Wu, *University of Pittsburgh*  
Akira Onuki, *Kyoto University*

## ABSTRACT

The study of the interface in a charge-free, nonpolar, critical and near-critical binary fluid in the presence of an externally applied electric field is presented. At sufficiently large fields, the interface between the two phases of the binary fluid should become unstable and exhibit an undulation with a predefined wavelength on the order of the capillary length. As the critical point is approached, this wavelength is reduced, potentially approaching length-scales such as the correlation length or critical nucleation radius. At this point the critical properties of the system may be affected. In zero gravity, the interface is unstable at all long wavelengths in the presence of a field applied across it. It is conjectured that this will cause the binary fluid to break up into domains small enough to be outside the instability condition. The resulting pattern formation, and the effects on the critical properties as the domains approach the correlation length are of acute interest. With direct observation, laser light scattering, and interferometry, the phenomena can be probed to gain further understanding of interfacial instabilities and the pattern formation which results, and dimensional crossover in critical systems as the critical fluctuations in a particular direction are suppressed by external forces.

## INTRODUCTION

Several systems exhibit an interfacial instability in response to a stress resulting from the application of an external field. Two such systems closely related to the proposed system of study are a ferrofluid/air interface in the presence of a magnetic field [1, 2], and the interface between two fluids when charged with ions [3, 4, 5, 6]. Both systems lead to the formation of a hexagonal dimple pattern. One of our collaborators, Prof. A. Onuki, has recently proposed that such an effect could be observed at the neutral two-phase interface of a critical system, such as a binary fluid near its consolute point, or a simple fluid near the critical point of its liquid/vapor transition, in the presence of an externally applied electric field [7]. Although the physics for the instability, as presented below, is very similar to that for the ferrofluid, the large surface tension in ordinary liquid/vapor systems requires prohibitively large electric fields. However, in a two-phase critical system, the surface tension vanishes as the critical temperature is approached, so the instability may be observed within experimentally accessible electric fields near the critical point. An added benefit of the critical system is that as the surface tension is reduced, the length scale of the instability is also reduced, leading to interesting physics as this length scale approaches that of the critical fluctuations or nucleation droplets. In the absence of gravity, the entire nature of the instability changes, leading to an instability at all long wavelengths. These items will be discussed below.

## EFFECT OF ELECTRIC FIELD ON THE MACROSCOPIC INTERFACE

Through rigorous derivation, Onuki [7] has found the free energy of a surface wave with wave number  $k$  to be

$$G_k = \sigma k^2 + g(\Delta\rho) - C_E k, \quad (1)$$

where  $\sigma$  is the surface tension,  $g$  is the gravitational acceleration, and  $\Delta\rho$  is the mass density difference between the two phases, taken to be positive. The parameter  $C_E$  represents the effect of electric field, here

taken to be normal to the interface,

$$C_E = \frac{1}{4\pi} \frac{(\varepsilon_2 - \varepsilon_1)^2}{\varepsilon_1 \varepsilon_2 (\varepsilon_1 + \varepsilon_2)} D_0^2, \quad (2)$$

where  $D_0$  is the electric induction in the unperturbed state.

The first two terms in Equation (1) are the standard expressions used to describe a capillary wave on a liquid surface. The third term is the effect of the electric field and the source of the instability. Due to this term, the free energy exhibits a minimum at wave number

$$k^* = C_E/2\sigma. \quad (3)$$

The relevance of this experiment to microgravity investigation arises due to the stabilizing effect of gravity on the interface. In the absence of gravity ( $g = 0$ ), this minimum, due to the presence of an electric field oriented normally to the interface, will always correspond to a negative free energy. Hence, thermal excitations with wavevectors near and less than  $k^*$  will have diverging amplitudes, resulting in a distortion or breakup of the interface on a length scale of the reciprocal critical wavevector, Equation (3). In a gravitational field, the second term of Equation (1) will force the free energy minimum to be positive except for the case of large electric field, for which the surface fluctuation at  $k = k^*$  becomes unstable for

$$C_E > 2\sqrt{\sigma g \Delta\rho} \quad \text{and} \quad k^* > [g(\Delta\rho)/\sigma]^{1/2} = 1/a_g, \quad (4)$$

$a_g$  being the so-called capillary length. The difference between the two cases is clear: In a gravitational field, only wavevectors in the vicinity of  $k^*$ , Equation (3), are unstable and only at a sufficiently large field; in the absence of gravity, all wavelengths larger than  $1/k^*$  are unstable, for an arbitrarily small field.

An estimate of this effect with  $g = 980 \text{ cm/s}^2$  in the perfluorohexane/hexane critical binary mixture follows: At 1 K below  $T_c$  the capillary wavelength is approximately  $400 \text{ }\mu\text{m}$  requiring a  $16 \text{ kV/cm}$  field to produce the instability. As the critical point is approached, both the capillary wavelength and the critical field decrease with a critical exponent of 0.46 and 0.07 respectively. The critical properties will become affected when  $k^*\xi \approx 1$ , which occurs at  $T_c - T \approx 0.1 \text{ mK}$  at the onset of the instability. However by application of a field about ten fold greater than the critical field, this should occur at  $T_c - T \approx 10 \text{ mK}$ .

It has also been demonstrated [7] that an electric field oriented parallel to a fluid interface will serve to stabilize that interface. Considering the presence of an electric field with arbitrary orientation with respect to the interface, the coefficient of the third term in Equation (1),  $C_E$ , is replaced by

$$C_E = \frac{1}{4\pi} \frac{(\varepsilon_1 - \varepsilon_2)^2}{\varepsilon_1 + \varepsilon_2} \left( \frac{1}{\varepsilon_1 \varepsilon_2} D_0^2 - E_{0\perp}^2 \right), \quad (5)$$

where  $E_{0\perp}$  is the component of the electric field perpendicular to the surface normal, and  $D_0$  is the component of the displacement field parallel to the surface normal. In the case  $E_{0\perp} \geq D_0/(\varepsilon_1 \varepsilon_2)^{1/2}$ , the coefficient  $C_E$  becomes negative and the applied field serves to stabilize the interface. Besides the technological interest of stabilizing a two-phase boundary in zero gravity, this effect raises scientific interest in pattern formation and the suppression of critical fluctuations. This latter effect should manifest itself in the modification of the dimensionally dependent critical exponents for the system.

Hydrodynamic equations provide an alternative way of looking at this interfacial instability. Ignoring the effect of viscosity, Onuki [7] has found the dispersion relationship for capillary waves in the presence of an electric field,

$$\omega_k^2 = (\rho_1 + \rho_2)^{-1} k [\sigma k^2 - C_E k + g(\Delta\rho)], \quad (6)$$

where  $\rho_1$  and  $\rho_2$  are the mass densities in the two phases, and  $C_E$  is given by Equation (5). The instability occurs when  $\omega_k^2 < 0$ . Also of interest is the presence of negative wavepacket velocities ( $d\omega/dk < 0$ ). It should be noted that near the critical point, these capillary waves may become overdamped due to viscosity.

## EFFECT OF ELECTRIC FIELD ON NUCLEATION

The interaction between an electric field and the phase separation process through nucleation is complex. Physically it involves the competition of two opposing forces. While the electric field favors a homogeneous phase by rupturing droplets, thermodynamic forces favor the separation of the mixture into two phases. The analogous problem is the phase separation in the presence of a shear flow, where the mixing and shearing action of the flow induces the fragmentation of the minority phase [8, 9, 10].

In a traditional nucleation experiment, nucleation is usually viewed as a transient phenomenon [11]; one typically quenches or supersaturates a system and records the growth of droplets of the minority phase. But in this proposal, nucleation under the steady-state conditions will be studied.

We illustrate in the simplified way how a steady state can be achieved with an electric field and probed by light scattering. Initially, the system is driven into the two-phase state, where droplets are formed and grow. The electric field  $E$  is then abruptly turned on, rupturing those droplets which have grown to a sufficient size [7, 12]. Through the repeated mechanism of the growth and the destruction of droplets, the fluid mixture tends to a stationary state under the influence of the electric field. As the electric field is increased, droplets of an increasingly smaller size are fragmented. Eventually, a value of  $E = E_c$  is reached, at which point, the droplets as small as the critical radius are ruptured. At this value of  $E = E_c$ , nucleation is therefore inhibited and the light scattered from the mixture abruptly decreases by orders of magnitude.

### Simple Model

Nucleation can be induced by suddenly quenching an off-critical one-phase system through its coexistence temperature  $T_{cx}$  into the metastable state. The system then evolves toward a two-phase equilibrium by the formation and growth of droplets of the minority phase. For a small droplet, the surface free energy cost of creating the surface of the droplet outweighs the bulk free energy benefit of creating the state which represents the true minimum of the free energy. As a result, the homogeneous state is stable to such small fluctuations. On the other hand, if the droplet is sufficiently large, the bulk free energy overwhelms the surface energy, and the free energy of the system is reduced by the presence of big enough droplets. Hence the homogeneous state is unstable to such sufficiently large fluctuations. If the surface free energy is  $\sigma$ , and the bulk free energy per unit volume is  $e_f$ , then the difference in free energy between the system with one droplet of radius  $R$  and the system with no droplets is

$$\Delta\Phi(R) = -\frac{4}{3}\pi e_f R^3 + 4\pi\sigma R^2. \quad (7)$$

Note that  $\Delta\Phi(R)$  has a maximum for the critical radius  $R = R_c$ , where  $R_c = 2\sigma/e_f$ . The droplets with  $R < R_c$  shrink after they have been created, whereas droplets with  $R > R_c$  grow. In summary, the mechanism of nucleation is the instability of the homogeneous fluid to the creation of droplets of critical size,  $R = R_c$ . Local thermal fluctuations initiate this instability and enable the system to surmount an activation energy barrier,  $\Delta\Phi(R)$ , which blocks the formation of droplets [13]

The parameters  $\sigma$  and  $e_f$  depend on the state of the system. The surface tension  $\sigma$  is a function of temperature  $T$  near the critical temperature  $T_c$  and roughly equal to  $\sigma = 0.1k_B T/\xi^2$ , where  $k_B$  is the Boltzmann constant and  $\xi$  is the correlation length [14]. In the so-called “ $\phi^4$ ” model [15],  $e_f$  is roughly equal to  $\sigma x/\xi$ . The volume fraction of the minority phase  $x$  is related to the quench depth  $\delta T = T_{cx} - T$  and  $\Delta T = T_c - T_{cx}$  through the equation

$$x = \frac{1}{2} - \frac{1}{2} \left[ \frac{1}{1 + \delta T/\Delta T} \right]^\beta \approx \frac{\beta \delta T}{2\Delta T}, \quad (8)$$

with the latter approximation holding when  $\delta T/\Delta T$  is small. The coexistence-curve exponent  $\beta$  has the value 0.31 [16].

The situation is very different when a binary liquid mixture, quenched to a temperature  $T$ , is exposed to an electric field  $E$ . The electric field creates a dynamic equilibrium by constantly rupturing droplets of the minority phase, which have grown to a sufficient size. The maximum droplet size  $R = R_{max}$  that can exist in the presence of the electric field is given by the relation

$$C_E = \sigma/R_{max}, \quad (9)$$

where  $C_E$  is given by Equation 2 [7]. The result is a steady-state droplet distribution in which the size and the number density are determined by  $E$  and the degree of the supercooling,  $\delta T$ . That is, the steady state is completely characterized by two variables,  $\delta T$  and  $E$ , when droplets are present. These parameters are equivalent in the sense that both can change supersaturation.

The strength of the electric field necessary to suppress nucleation for a given value of the supercooling  $\delta T$ , is determined by whether the droplets are fragmented down to a radius  $R < R_c$ , where  $R_c$  is a function of  $\delta T$ . If this condition is satisfied, the droplets will disappear altogether, and the system will consist of one homogeneous phase. In mathematical terms, the value of the critical electric field  $E = E_c$  solves the following equation

$$C_E(E_c) = \sigma/R_c. \quad (10)$$

It is this equation with which the measurements are compared.

An estimate for this effect in the perfluorohexane/hexane mixture follows: We assume the Becker-Döring limit, which states that nucleation rate falls in a conveniently measurable range (i.e., 1 droplet/cm<sup>3</sup>) when  $\delta T/\Delta T \approx 0.15$ . If use is made of the scaling law  $\Delta\phi \equiv \phi_1 - \phi_2 = B(1 - T/T_c)^\beta$ , then

$$C_E \cong (8\pi\epsilon_{av})^{-1} B^2 \epsilon'^2 E_0^2 (1 - T/T_c)^{2\beta}, \quad (11)$$

where  $\epsilon_{av}$  is the average dielectric constant,  $\epsilon' \equiv d\epsilon/d\phi \approx 0.32$ , and the miscibility gap constant  $B$  is of the order three [17]. Since  $\sigma/R_c \approx 0.44$  for an off-critical sample at  $\Delta T = 15$  (mK), an electric field stronger than 25 kV/cm is required to rupture all the droplets of the critical radius.

## CONCLUSION

A static instability in the interface between two dielectrically mismatched fluids can be generated by the application of an electric field oriented perpendicularly to the interface. In a gravitational field, the onset of this instability will occur at the capillary wavelength when a sufficiently large field is applied. In the absence of gravity, the length scale of the instability, and hence the minimum required field are determined by the size of the system. In a phase separating, off-critical system, this instability should effect the nucleation process by rupturing minority phase droplets larger than the instability wavelength. By application of a sufficiently large field, it is conjectured that the instability wavelength can be made small enough to prevent all nucleation.

These phenomena can all be probed through laser light scattering and interferometry. Diffraction of light off and interference of light through a two phase interface can lead to a measure of the length scale and topography of the instability. Dynamic light scattering from the interface can be used to measure the effect of the applied field on the capillary wave dispersion relationship. Finally, dynamic light scattering and turbidity measurements can be used to probe a phase separating binary fluid in the presence of an electric field to determine the nucleation droplet distribution.

## ACKNOWLEDGEMENTS

Support to study the effect of electric field instabilities in a two phase fluid interface has been provided to General Vacuum, Inc by the National Aeronautics and Space Administration under contract # NAS3-2789.



## REFERENCES

- [1] M. D. Cowley and R. E. Rosensweig, J. Fluid Mech. **30**, 671 (1967).
- [2] A. Gailitis, J. Fluid Mech. **82**, 401 (1977).
- [3] L. P. Gorkov and D. M. Chernikova, Pis'ma Zh. Eksp. Teor. Fiz. **18**, 119 (1973) [JETP Lett. **18**, 68 (1973)].
- [4] K. Mima, H. Ikezi and A. Hasegawa, Phys. Rev. **B14**, 3953 (1976).
- [5] A. P. Volodin, M. S. Khaikin and V. S. Edel'man, Pis'ma Zh. Eksp. Teor. Fiz. **26**, 707 (1977) [JETP Lett. **26**, 543, (1977)].
- [6] M. Wanner and P. Leiderer, Phys. Rev. Lett. **42**, 315 (1979).
- [7] A. Onuki, Physica A **217**, 38 (1995).
- [8] A. Onuki and K. Kawasaki, Ann. Phys. (N.Y.) **121**, 456 (1979).
- [9] D. Beysens, M. Gbdamassi, and B. Moncef-Bouvenz, Phys. Rev. A **28**, 2491 (1983).
- [10] K. Y. Min and W. I. Goldberg, Phys. Rev. Lett. **70**, 469 (1993).
- [11] K. Binder and D. Stauffer, Adv. Phys. **25**, 343 (1976).
- [12] L. Tonks, Phys. Rev. **48**, 562 (1935). They give the bursting condition as  $E^2 > 16\pi\sigma/R$ ; C. G. Garton and Z. Krasuchi, Proc. R. Soc. London A, **280A**, 211 (1964). They observed the behavior of only conducting incompressible bubbles in an electric field.
- [13] F. F. Abraham, Homogeneous Nucleation Theory, Academic Press (1974).
- [14] M. Moldover, Phys. Rev. A **31**, 1022 (1985).
- [15] J. S. Langer and A. J. Schwartz, Phys. Rev. A **21**, 948 (1980).
- [16] W. I. Goldberg, in Light Scattering Near Phase Transitions, edited by H. Z. Cummins and L. P. Levanyuk (North-Holland, New York, 1983).
- [17] D. T. Jacobs, J. Phys. Chem. **86**, 1995-1998 (1982).



# A BRIEF SURVEY OF THE EQUILIBRIUM AND TRANSPORT PROPERTIES OF CRITICAL FLUIDS AND THE DEGREE TO WHICH MICROGRAVITY IS REQUIRED FOR THEIR EXPERIMENTAL INVESTIGATION

Richard A. Ferrell  
Center for Theoretical Physics of the Department of Physics,  
University of Maryland,  
College Park, Maryland 20742

## ABSTRACT

The modern theory of second order phase transitions is very successful in calculating the critical exponents as an asymptotic expansion in powers of  $\varepsilon = 4 - D$ , the deviation of  $D = 3$ , the spatial dimension of the actual physical system from that of the abstract four-dimensional reference model. This remarkable mathematical *tour de force* leaves unanswered, however, many fundamental questions concerning the exact nature of how the fluctuations interact. I discuss here some experiments which would help to further our understanding of the equilibrium critical properties. Especially promising would be a measurement of the temperature dependence of the turbidity very close to the critical point. This has the promise of determining the small and elusive but fundamentally important anomalous dimension exponent  $\eta$ . I also review various ways of measuring the critical transport coefficients and point out some cases where ground based experiments may usefully supplement flight experiments.

## INTRODUCTION

Consistent with the brevity of the oral presentation of this paper, I am presenting it in an outline, and almost telegraphic style. Those who find this too cryptic and desire more details are invited to write to me. (I hesitate to violate the decorum of these conference proceedings by listing here my telephone number.)

## I. EQUILIBRIUM PROPERTIES

The Fisher-Wilson  $\varepsilon$ -expansion is an effective technique for computing numerically the critical exponents, but a full fundamental understanding of second order phase transitions calls for a more thorough and probing investigation of how the fluctuations interact. To arrive at a more complete picture of what is happening in a fluid at thermal equilibrium when the temperature  $T$  is lowered toward the critical temperature  $T_c$ , we need to study, both theoretically and experimentally, the evolution of  $P(\Psi)$ , the probability distribution of the fluctuations in the variable

$$\Psi = \int_{\Omega=\ell^3} \psi(x) d^3x.$$

This integral of the order parameter  $\psi(x)$  is carried out over a small volume of linear dimensions  $\ell$ .

Far above the critical point, the correlation length,  $\xi$ , is much smaller than  $\ell$ . As  $T$  is lowered,  $P(\Psi)$  remains Gaussian but broadens. Upon further approach of  $T$  to  $T_c$ ,  $\xi$  will grow and become comparable to  $\ell$ . At this stage the broadening will cease, but the shape of  $P(\Psi)$  will change and become flatter. For  $T < T_c$ , the distribution becomes bimodal and splits into two peaks, at positive and negative values of  $\Psi$ .

#### A. Direct Observation of the Fluctuations

Beysens has reported<sup>1</sup> on a straightforward approach, by means of microscopy, to the determination of  $P(\Psi)$ . A microscope is focused on a thin layer of fluid. A spot, of dimensions determined by the wavelength of the light and the resolving power of the microscope, is observed at many successive instants over a period that is much longer than the longest equilibration time of the fluid. For this type of experiment, a special fluid containing small polymer spheres is prepared so as to obtain a correlation length that is large enough to be comparable to the spot size, thereby making possible the observation of critical behavior.

#### B. Light Scattering

##### 1. Turbidity

The suppression of the wings and the resulting flattening of the shape of  $P(\Psi)$  is a consequence of the repulsive interaction of the order parameter fluctuations. This effect also shows up in the mean square of the fluctuation of wave number  $k$ , proportional to  $k^{-2} \left( k / k_0 \right)^\eta$ , where  $k_0$  is a crossover parameter and  $\eta$  is the small anomalous dimension critical exponent. This formula, valid for  $\xi^{-1} \ll k \ll k_0$ , describes a shrinkage, or decrease, in the amplitude of the fluctuations, by the factor  $\left( k / k_0 \right)^{\eta/2}$ , and is an essential feature of critical phenomena. Both the  $\epsilon$ -expansion computations and an independent approach based on a sum rule<sup>2</sup> predict  $\eta \cong 0.04$ . Light scattering measurements<sup>3</sup> have yielded  $\eta = 0.03 \pm 0.03$ . I have argued<sup>4</sup> that a preferred method of determining this important exponent is the measurement of the temperature dependence of the turbidity. This corresponds to integrating over all of the scattering angles and is largely free of the complication of double scattering. Some studies

have been carried out on the experimental feasibility of measuring  $\eta$  for a binary liquid in this way<sup>5</sup>. For the one-component fluid, the Zeno cell also suggests itself.

## 2. Cross Correlations

As noted by Korenman<sup>6</sup> the cross correlation of the signals in two separate photo-detectors, placed in two different directions relative to the incident laser beam, yields information on the interaction of the fluctuations. An advantage of this experimental method is that, by introducing a time delay between the two detectors, information can also be obtained regarding the critical dynamics of the fluid.

## II. CRITICAL DYNAMICS

Dynamic scaling theory was first enunciated<sup>7</sup> for the divergence of the thermal conductivity at the lambda point of liquid <sup>4</sup>He, but was soon thereafter extended to the classical fluid.<sup>8,9</sup> Dynamic scaling has, furthermore, been extended to the critical behavior of the viscosity,<sup>10,11,12,13</sup> which can be regarded also as a transport coefficient—the transport of momentum through a fluid subjected to shear.

### A. Thermal Conductivity by Electrostriction

Electrically charging a wire in a fluid causes an adiabatic temperature rise in the vicinity of the wire. Observing the thermal equilibration and the resulting density change, in a microgravity environment, might make possible a measurement of the thermal conductivity that is free of the usual boundary effects.

### B. Critical Viscosity

A manifested flight experiment, CVX, promises<sup>14</sup> to yield a value for the critical exponent that is free of the complication of gravitational stratification. Nevertheless, it is useful to consider the possibility of a ground-based experiment in which stratification is minimized by using a very thin horizontal layer. Electrostriction, an effect demonstrated during the July, 1994 Columbia flight, could be used to drive the fluid against the opposing viscous force.<sup>15</sup>

### C. Critical Ultrasonic Attenuation

Of all the critical fluid properties, ultrasonic attenuation exhibits the strongest, and perhaps the most dramatic dependence on the reduced temperature—roughly as the inverse square (along the critical isochore). Unfortunately, there are strong deviations from pure dynamic scaling<sup>16</sup> that result from the

large non-critical background contribution to the thermal conductivity (which determines the relaxation rate of the fluctuations). For this reason, a microgravity environment will be required to explore experimentally the true asymptotic scaling region.

### III. ADIABATIC FAST EQUILIBRATION

#### A. Supercritical Fluid

The diverging thermal expansion coefficient endows a one-component fluid with some remarkable critical properties, such as adiabatic fast equilibration, the theory<sup>17</sup> of which predicts an inverse square root time dependence for the approach to equilibrium in the intermediate time regime. This adiabatic effect is important for CVX and also plays a dominant role in some of the density changes observed in Zeno.

#### B. Two-Phase Relaxation

The density changes in the coexisting liquid and vapor that have been observed in the liquid <sup>3</sup>He Duke experiments can be understood by means of a straightforward extension of the adiabatic theory. The temperature at the interface plays a dominant role in the analysis.

### SUMMARY

Many good experiments that would clarify our picture of what is happening at the critical point are calling out to be performed. Especially important would be the measurement of  $\eta$  by turbidity. In the dynamics, much work also remains to be done. Dynamic scaling for the ultrasonic attenuation, for example, remains to be explored and would require microgravity. The theory of two-phase equilibration has only recently been completed and requires experimental testing. Throughout all of this work, there is basically no difference between the second order phase transitions at ambient temperature and at low temperature. A unified approach would, thus, seem to be highly desirable.

## REFERENCES

1. D. Beysens, private communication.
2. R.A. Ferrell and J.K. Bhattacharjee, Phys. Rev. Letts. 42, 1505 (1979).
3. R.F. Chang, H. Burstyn, and J.V. Sengers, Phys. Rev. A 19, 866 (1979).
4. R.A. Ferrell, Physics A 177, 201 (1991).
5. D. Jacobs, these proceedings.
6. V. Korenman, Physical Review A2, 449 (1970).
7. R.A. Ferrell, N. Menyhard, H. Schmidt, F. Schwabl, and P. Szepefalusy, Phys. Rev. Letts. 18, 891 (1967); Ann. Phys. 47, 565 (1968).
8. K. Kawaski, Physics Lett. A 30, 325 (1969); Ann. Phys. (NY) 61, 1 (1970).
9. R.A. Ferrell, Phys. Rev. Letts. 24, 1169 (1970).
10. R. Perl and R.A. Ferrell, Phys. Rev. Letts. 29, 51 (1972); Phys. Rev 6A, 2358 (1972).
11. E. Siggia, B.I. Halperin, and P.C. Hohenberg, Phys. Rev. B 13, 2110 (1976).
12. J.K. Bhattacharjee and R.A. Ferrell, Physics Lett. 76A, 290 (1980).
13. H. Hong, Doctoral Thesis, Univ. of Maryland (1991), unpublished.
14. R. Berg, these proceedings.
15. R.A. Ferrell and M.R. Moldover, Ann. der Physik 3, 3 (1994).
16. R.A. Ferrell and J.K. Bhattacharjee, Phys. Rev. Letts. 44, 403 (1980); Physics Letts. 86A, 109 (1981).
17. A. Onuki and R.A. Ferrell, Physica A 164, 245 (1990); A. Onuki, R.A. Ferrell, and H. Hao, Phys. Rev. A 41, 2256 (1990); R.A. Ferrell and H. Hao, Physica A 197, 23 (1993).





**Electrostriction of a critical fluid in microgravity**

Greg Zimmerli, NYMA, Inc.

**Paper not available**



# SOLUTE NUCLEATION AND GROWTH IN SUPERCRITICAL FLUID MIXTURES

Gregory T. Smedley<sup>1</sup>, Gerald Wilemski<sup>2</sup>, W. Terry Rawlins<sup>3</sup>, David B. Oakes<sup>3</sup>,  
Prakash Joshi<sup>3</sup>, and William W. Durgin<sup>4</sup>

<sup>1</sup>*California Institute of Technology, Pasadena, CA 91125*

<sup>2</sup>*Lawrence Livermore National Lab, Livermore, CA 94551*

<sup>3</sup>*Physical Sciences Inc., Andover, MA 01810*

<sup>4</sup>*Worcester Polytechnic Institute, Worcester, MA 01609*

## ABSTRACT

This research effort is directed toward two primary scientific objectives: (1) to determine the gravitational effect on the measurement of nucleation and growth rates near a critical point and (2) to investigate the nucleation process in supercritical fluids to aid in the evaluation and development of existing theoretical models and practical applications. A nucleation pulse method will be employed for this investigation using a rapid expansion to a supersaturated state that is maintained for  $\approx 1$  ms followed by a rapid recompression to a less supersaturated state that effectively terminates nucleation while permitting growth to continue. Nucleation, which occurs during the initial supersaturated state, is decoupled from growth by producing rapid pressure changes. Thermodynamic analysis, condensation modeling, apparatus design, and optical diagnostic design necessary for the initiation of a theoretical and experimental investigation of naphthalene nucleation from supercritical CO<sub>2</sub> have been completed.

## INTRODUCTION

Supercritical fluids are of considerable scientific and technological interest in the fields of chromatography, solids extraction, and particle formation due to the greatly enhanced solubility of solutes. Supercritical fluids have liquid-like densities and gas-like compressibility; therefore, the density of the fluid and the solubility of solutes within them are a strong function of the pressure. It is precisely due to this latter behavior that particle formation in rapidly expanded supercritical solutions (RESS) is a promising application for supercritical fluid technology. Careful measurements of nucleation rates are essential for understanding the fundamental aspects underlying particle formation processes and for testing nucleation rate predictions.

In this research effort, the strong dependence of the solubility on the pressure will be exploited to produce tailored nucleation pulses in an apparatus that is capable of executing rapid pressure changes on the contained mixture. The apparatus is patterned after those used in the prior research efforts of Wagner and Strey [1] and Sieber and Woermann [2]. The nucleation pulse involves a rapid expansion to a supersaturated state that is maintained for  $\approx 1$  ms followed by a rapid recompression to a lower supersaturation that permits growth to continue. The purpose of the short supersaturated state is to eliminate significant growth so that nucleation and growth are effectively decoupled. However, under some conditions the rapidity of the expected pressure changes in this apparatus is not sufficient to decouple nucleation and growth. The nucleation rates and the growth rates will be determined experimentally using a combination of Mie scattering and extinction measurements [3]. The supercritical mixture chosen for this research is naphthalene-CO<sub>2</sub> due to the fact that physical properties of this system have been well studied in the past, the substances are relatively benign in the quantities used here, and the critical point of CO<sub>2</sub> (72.9 atm and 31°C) is readily accessible in the laboratory.

The research approach employed in this study is to: (1) utilize calculated results of thermodynamic expansions and compressions to determine the volume changes that the apparatus must be capable of in

order to cover the desired (P,T) envelope and to provide thermodynamic path input for the nucleation and growth models, (2) employ nucleation and growth models to determine operating conditions that should provide particle concentrations within the detectable limits of the optical instrumentation, (3) employ Mie calculations to determine requirements and limits for the optical diagnostics, (4) conduct experiments, (5) use the experimental results and Mie calculations to determine the refractive index, the number density, the size, and the growth rates of naphthalene particles, and (6) feed this information to the nucleation and growth models to evaluate and modify the existing models.

## THERMODYNAMIC ANALYSIS

Evaluation of thermodynamic paths for the apparatus has been achieved using an equation of state for CO<sub>2</sub> from Ref. [4]. Isentropic expansions were calculated for supercritical CO<sub>2</sub> starting from initial temperatures (T) of 307(7)335 K at 200 bar and initial pressures (P) of 80(20)200 bar at 335 K. These initial conditions were selected to lie on the edges of the expected (P, T) operating envelope for the apparatus. The results are shown in Figure 1, the thick curve represents the pure gas-liquid CO<sub>2</sub> phase boundary, the cross-hairs demark the critical point, and the thin curves (numbered 1 through 11) represent the calculated isentropic expansion paths. Note that a volume expansion factor of 1.30 was used for each curve except curves 1 and 2, which required only a factor of 1.12 and 1.20 respectively to penetrate deeply beyond the saturation curve. Up to the phase boundary, the trajectories followed by the isentropic paths lie on thermodynamically stable states for pure CO<sub>2</sub>. Beyond the phase boundary, the expansions produce metastable states that decay via CO<sub>2</sub> bubble or droplet nucleation or spinodal decomposition.

This plot reveals two issues that are worth noting. First, a strong decrease in temperature is observed during the isentropic expansions that leads to an enhanced decrease in pressure. Therefore, a volume change of 30% is sufficient to span the supercritical envelope. Second, an isentropic expansion path could be chosen such that the nucleation induction occurs very near the critical point as for example, on curve 7 which starts at 160 bar and 335 K. It may be very interesting to observe the effects of near-critical point phenomena, such as large density fluctuations, on the measured nucleation rates. In more refined consideration of the thermodynamic paths, the gas-liquid phase boundary for the CO<sub>2</sub>/naphthalene system must be considered. Since it is the intention in this research to study the nucleation of solute particles we must avoid crossing phase boundaries that will cause nucleation of CO<sub>2</sub> rich droplets or bubbles.

## EXPANSION CHAMBER CONDENSATION MODEL

A model that simulates the nucleation and growth of solute particles in the experimental expansion chamber has been developed. This model is being used to understand how different operating conditions affect the quality of the particle size distribution. This will aid in the selection of conditions that are more favorable for the light scattering measurements needed to determine the particle concentration.

The model uses the thermodynamic equation of state for CO<sub>2</sub> discussed above, a nucleation rate model based on classical homogeneous nucleation with the reversible work of critical nucleus formation modified to account for the extreme nonideality of the naphthalene-CO<sub>2</sub> fluid mixture [5], and a particle growth model that also handles the statistical characterization of the particle size distribution. The equilibrium concentration of dissolved naphthalene is calculated using a Peng–Robinson equation of state for the mixture [6]. The isentropic expansion calculation was modified to allow the volume change of the test chamber to be parametrically specified as a function of time. At each point in the process, the nucleation rate is computed, and once a sufficiently high value is achieved, the particle growth model is used to track the sizes of all the particles formed. The particle growth rates are computed using a growth law developed by Young [7] as simplified by Peters and Paikert [8]. This growth law is quite general, covering the entire range from

free molecular to continuum behavior. Given the relatively high density of the CO<sub>2</sub> solvent in the region of interest, the diffusion-controlled continuum regime will be most important.

Two simulations of potential experiments are presented here to illustrate the very different types of behavior that are possible. In both cases, initially saturated mixtures are at equilibrium at the upper right end of the paths, path 6 and path 10, indicated by •'s in Figure 1. The mixtures were expanded in 3 ms to the (P,T) indicated by o's where a nucleation period was maintained for 1 ms. Finally the mixtures were compressed in 0.3 ms to the (P,T) indicated by Δ's. Both mixtures were expanded to produce similar nucleation rates ( $\approx 2 \times 10^7 \text{ s}^{-1} \text{ cm}^{-3}$ ) and therefore similar particle number concentrations ( $\approx 2 \times 10^4 \text{ cm}^{-3}$ ). The behavior of the simulated particle size distributions is shown in Figure 2 at four successive times starting at the end of the nucleation period (0 ms) and ending at 10 ms. The most obvious feature of these distributions is the difference in their breadth and their height; however, the integrated particle number under each distribution is approximately constant. Due to the rapidity of particle growth under the conditions used on path 6, particles of 1 μm radius are already present at the end of the nucleation period whereas the particles created along path 10 do not grow that large in 10 ms. In both cases, the size distributions narrow at later times because growth rates are higher for smaller particles than for larger ones, but the presence of large particles during the nucleation period for path 6 eliminates the possibility of using the first Mie resonance to accurately determine the concentration of nucleated particles. The results along path 10 exhibit a much slower rate of growth and a significantly narrower size distribution. These conditions would be suitable for making measurements of the first Mie resonance to determine the particle concentration. The significant difference in growth rates is due to the reduced amount of solute present in the mixture on path 10 compared to the mixture on path 6.

## APPARATUS DESIGN CONCEPT

A membrane cell, in which the lower wall is a flexible diaphragm, is the focus of the current design effort. The cell is compact, measuring 3.25" OD × 2.0" Tall with an internal volume of 9.3 cm<sup>3</sup> (1.2" ID × 0.5" Tall). The radius of curvature of the membrane and the ratio of the height to the diameter of the cell have been chosen to theoretically provide a maximum volume change of 50%. The actual volume change will be limited by the various sources of dead volume and by the ability to operate the membrane over its entire design range without bursting it. The pressure of the contained mixture is varied by changing the pressure on the lower side of the diaphragm using fast valves and external reservoirs. The cell should be capable of generating rapid pressure changes, with a maximum pressure of 170 atm and initial temperatures of 293 K to 358 K with the current instrumentation.

The cell is designed to allow the top part to be replaced. For example, a top that is quite tall would enable measurement of the nucleation rate at well separated points to determine gravitational effects. By maintaining the same internal volume as the original top, it would be possible to use the same membrane, valves, and reservoirs to impose the desired pressure changes.

A cross-section of the cell is shown in Figure 3 to indicate the location of the instrumentation for pressure and temperature measurement, the windows for optical access, and the inflow/outflow ports/valves for the sample mixture. A piezo-resistive pressure transducer is used to measure both the static and dynamic pressure. A thermocouple is positioned near the inner wall of the cell to measure the temperature. Multiple optical access ports are provided to enable measurements at a variety of angles. This provides some options which might be useful as cross checks or to aid in the pinpointing of the refractive index of naphthalene.

## OPTICAL DIAGNOSTICS

The optical diagnostics will include simultaneous observation of the extinction at 0° and the forward scattering at 15°. These measurements permit the determination of scattering/extinction ratios as a function

of time during the growth phase of the experiment. These ratios are used to determine the particle size as a function of time, independent of the particle number density. Figure 4 shows plots of this ratio vs particle size for  $15^\circ$  scattering using two likely values for the refractive index of naphthalene. Once the size-vs-time dependence is known, the scattering and/or extinction signals can then be used to determine the particle number densities.

A sensitive measurement of the extinction is made by ratioing the transmitted and reference beams that result from splitting the original laser beam. The ratio removes fluctuations in the laser output, so that the measurement is affected only by slow thermal drifts in the optical train. The best sensitivity is achieved when the reference and transmitted beams have comparable intensities so the same shot noise limit can be attained in both detectors. For this condition, the measurement sensitivity is limited primarily by the dynamic range of the data acquisition system. With considerable care and a high-precision data acquisition system, extinction ratios down to perhaps  $10^{-4}$  should be achievable. Based on Mie calculations, the ability to determine extinction ratios as low as  $10^{-4}$  should make it possible to measure particle number densities above  $3 \times 10^4 \text{ cm}^{-3}$  over the entire size range of interest ( $0.2 \text{ }\mu\text{m}$  to  $2 \text{ }\mu\text{m}$ ).

The scattered power viewed by the detector is determined by the Mie scattering calculations, the particle number density, and the geometry of the cell. To experimentally measure this scattered light over the range of particle sizes ( $0.2 \text{ }\mu\text{m}$  to  $2 \text{ }\mu\text{m}$ ) and number densities ( $300 \text{ cm}^{-3}$  to  $3 \times 10^6 \text{ cm}^{-3}$ ), the detector must have high sensitivity to discern the lower range and must have a wide dynamic range to be able to capture the upper range. Some types of photomultiplier tubes have greater sensitivity than avalanche photodiode detectors (APD), but the APD has a greater dynamic range which makes it the detector of choice for this experiment. The expected range of the scattering signal, determined from Mie calculations of the scattered light intensity and the vendor specifications of the APD is plotted in Figure 5 for the two extremes of particle number density. Signal-to-noise estimates based on APD performance specifications and the cell geometry indicate that particle number densities of  $300 \text{ cm}^{-3}$  (4 particles/scattering volume) should be detectable over the size range of interest. Indeed, it should be possible to observe single-particle scattering over much of this range. However, to ensure favorable particle counting statistics, it is desirable to operate the experiment with particle number densities above  $3 \times 10^4 \text{ cm}^{-3}$  where extinction measurements can be made as well (see previous paragraph).

A major concern in these measurements is the uncertainty in the refractive index of naphthalene particles at the experimental temperatures, wavelength, and pressure. A source for the refractive index of  $\text{CO}_2$  has been located in Ref. [9]. Knowing the refractive index of  $\text{CO}_2$  with some confidence, the refractive index  $n$  of the naphthalene particles can be determined from the scattering/extinction data through comparisons of observed and computed relative peak intensities. This is illustrated in Figure 4 where two scattering/extinction ratios are plotted, one for  $n = 1.4$  and the other for  $n = 1.6$ ; therefore, the combination of experimental measurements and Mie calculations should yield the refractive index for naphthalene under the experimental conditions.

## CONCLUDING REMARKS

The chamber model enables us to explore potential experimental conditions to identify those that may result in narrow distributions of small particles at the end of the nucleation period. This model has already demonstrated the importance of avoiding particle growth rates so large that nucleation and growth cannot be decoupled even during induction times as short as 1 ms. Although the growth model should be reasonably accurate, it is worth noting that the predicted nucleation rates are notoriously inaccurate and could be off by many orders of magnitude. With inaccuracies in the prediction of nucleation rates, the resulting particle concentrations may be above or below the measurement range of the optical diagnostics. In the end, accurate empirical data from the apparatus will provide the means necessary to test and refine these models.

## ACKNOWLEDGEMENTS

Support for this work is provided by NASA contract NAS-27263. Part of this work was also performed under the auspices of the U.S. Department of Energy by the Lawrence Livermore National Laboratory under Contract No. W-7405-ENG-48. G. Smedley acknowledges productive discussions with Prof. R. Flagan of the California Institute of Technology.

## REFERENCES

- [1] P.E. Wagner and R. Strey, "Homogeneous nucleation rates of water vapor measured in a two-piston expansion chamber", *J. Phys. Chem.* **85**(18), pp. 2694-2698, (1981).
- [2] M. Sieber, and D. Woermann, "Study of non-equilibrium states of a homogeneous 2-butoxyethanol/water mixture of critical composition in the vicinity of its lower critical point using fast pressure jumps", *Ber. Bunsenges. Phys. Chem.* **95**(1), pp. 15-23, (1991).
- [3] P.E. Wagner, "A constant-angle Mie scattering method (CAMS) for investigation of particle formation processes", *J. Coll. Inter. Science* **105**(2), pp. 456-467, (1985).
- [4] W.C. Reynolds, *Thermodynamic Properties in SI*, (Dept. of Mechanical Engineering, Stanford, 1979).
- [5] P.G. Debenedetti, "Homogeneous nucleation in supercritical fluids", *AIChE J.*, **36**, pp. 1289-1298, (1990).
- [6] S.I. Sandler, *Chemical and Engineering Thermodynamics*, 2nd Ed., (Wiley, New York, 1989).
- [7] J.B. Young, "The condensation and evaporation of liquid droplets at arbitrary Knudsen number in the presence of an inert gas", *Int. J. Heat Mass Transfer*, **36**, pp. 2941-2956, (1993).
- [8] F. Peters and B. Paikert, "Measurement and interpretation of growth and evaporation of monodispersed droplets in a shock tube", *Int. J. Heat Mass Transfer*, **37**, pp. 293-302, (1994).
- [9] J. Obriot, J. Ge, T.K. Bose and J.M. St-Arnaud, "Determination of the density from simultaneous measurements of the refractive index and the dielectric constant of gaseous CH<sub>4</sub>, SF<sub>6</sub> and CO<sub>2</sub>", *Fluid Phase Equilibria*, **86**, pp. 315-350, (1993).

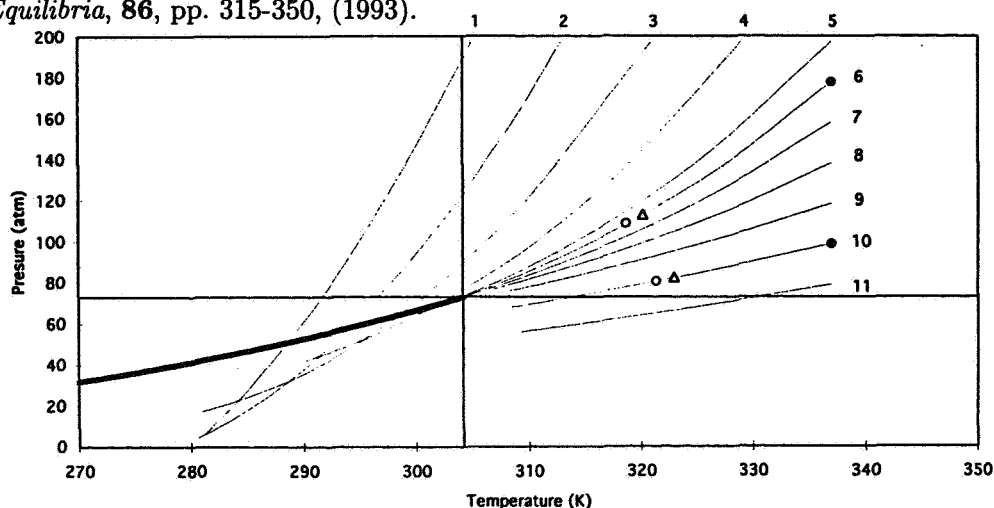


Figure 1: Isentropic Expansions for pure CO<sub>2</sub> that span the expected experimental envelope.

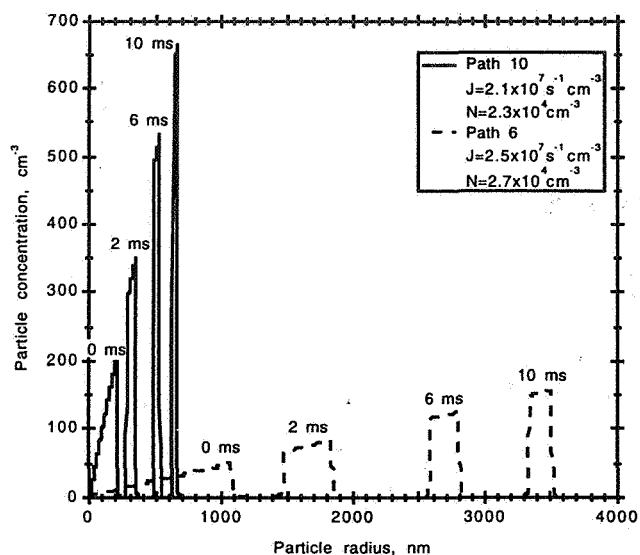


Figure 2: Size distributions for the total particle density  $N$  at the indicated times measured from the end of a 1 ms nucleation period at rate  $J$

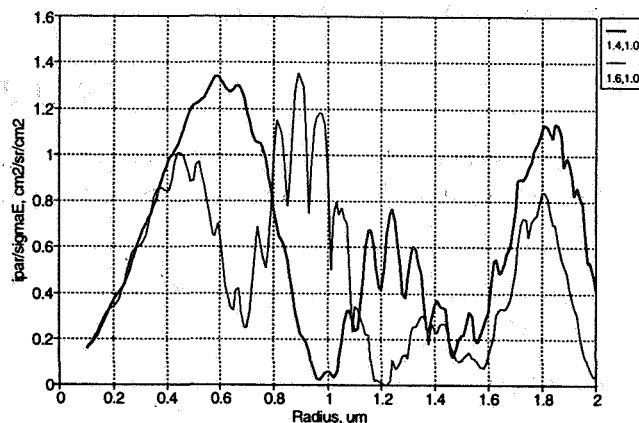


Figure 4: Scattering/Extinction ratios for two likely values of the refractive index of naphthalene  $n = 1.4$  and  $1.6$ , at  $15^\circ$  forward angle,  $\text{CO}_2$  refractive index  $n_m = 1.0$ , and laser wavelength  $\lambda = 670$  nm.

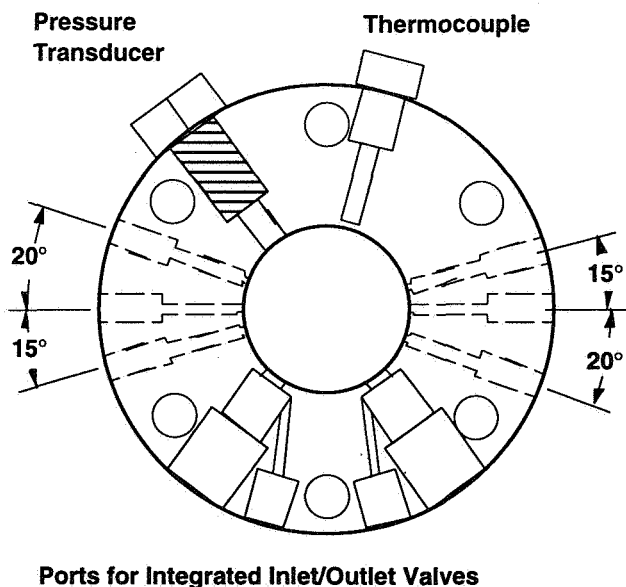


Figure 3: Top view of the general layout of instrumentation and ports for the expansion chamber.

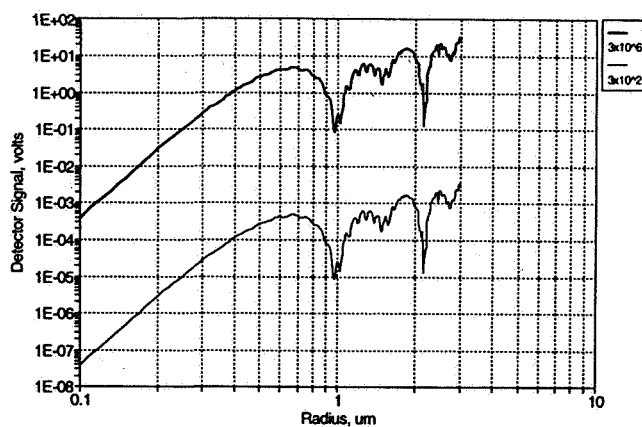


Figure 5: Calculated scattering detector signals for two extremes of the particle density ( $300$  and  $3 \times 10^6$ ) at  $15^\circ$  forward angle,  $n = 1.4$ ,  $n_m = 1.0$ , and  $\lambda = 670$  nm.



## ZENO: CRITICAL FLUID LIGHT SCATTERING EXPERIMENT

Robert W. Gammon, J.N. Shaumeyer, Matthew E. Briggs, Hacène Boukari, and David A. Gent  
Institute for Physical Science and Technology  
University of Maryland  
College Park, MD 20742

R. Allen Wilkinson  
Lewis Research Center  
Cleveland, Ohio 44135

### ABSTRACT

The Zeno (Critical Fluid Light Scattering) experiment is the culmination of a long history of critical fluid light scattering in liquid-vapor systems. The major limitation to making accurate measurements closer to the critical point was the density stratification which occurs in these extremely compressible fluids. Zeno was to determine the critical density fluctuation decay rates at a pair of supplementary angles in the temperature range 100 mK to 100  $\mu$ K from  $T_c$  in a sample of xenon accurately loaded to the critical density. This paper gives some highlights from operating the instrument on two flights March, 1994 on STS-62 and February, 1996 on STS-75. More detail of the experiment Science Requirements, the personnel, apparatus, and results are displayed on the Web homepage at <http://www.zeno.umd.edu>.

### INTRODUCTION

At a liquid-vapor critical point the equilibrium density fluctuations which are present in all materials become visible and the clear, dense fluid becomes milky and opalescent in appearance. For some years this has been studied with photon correlation light scattering spectroscopy. The Zeno experiment was to make such measurements in microgravity to overcome the density stratification which limits their accuracy when approaching the critical point closer than 10 mK on earth.<sup>1,2</sup> This report will describe the light scattering layout, and present some highlights from two flights.<sup>3</sup>

### APPARATUS

The availability of an ALV 5000 correlator adapted for our instrument meant that we could make simultaneous measurements at two angles during the flight. It was desirable to make measurements over as broad a range of scattering vectors (angles) as possible, limited only by the necessity of avoiding the forward scattering from the sample cell optics. Thus we came to the two phototube scattering layout shown in Fig. 1. The shutters SH gave a choice of split laser beams to use and thus which phototube saw forward or backward scattered light. Late in the development it was necessary to add filters (F1 and F2) on the shutters to limit the laser intensity into the sample to either 17 mW or 1.7 mW. These powers were chosen to avoid laser induced density gradients at the sample. The scattering angles inside the sample were 10.448 ° and 169.564 °. The thermostat TH had three controlled shells around the sample cell. The sample cell was at the center of these shells and had stepped windows whose center sections were adjusted to give a uniform 100 mm section of sample for the laser beam to pass through. This illuminated fluid is the scattering source for the experiment. The inner window surfaces are not coated to prevent reflections so there is a 10% interference modulation of the transmission due to reflections. This provided an essential monitor of the local sample density during the course of the experiment, as is discussed below.

## PERFORMANCE

The Shuttle communications systems provided 83% real-time communication for data downlink and commanding uplink during the flights. The data gaps were routinely played back to us within the next orbit (90 minutes). This level of communication meant that most of the time we operated as if the apparatus was in our lab on earth. Every second we received the next packet of measurements from the instrument and could command and see the measurement response in a few seconds. Thus the instrument computer and telemetry software performed as planned.

One of the most satisfying performance items was the excellent temperature control which we achieved in orbit. With the aluminum experiment enclosure controlled by side and bottom heaters and radiation losses occurring through the top, we routinely achieved  $< \pm 3\mu\text{K}$  (rms, 300 sec averaging) during flight. An example is shown from the first flight in Fig. 2. This four hour period is representative of the time necessary to accumulate 15 to 20 correlograms for a temperature data point.

The principal measurements were of intensity correlation functions. A set of forward scattering correlograms is shown in Fig. 3 covering a span of temperature of 100 mK to 400  $\mu\text{K}$  from  $T_c$  from the second flight.

## RESULTS

Overall we find convincing evidence that we reached the limiting decay rates for  $12^\circ$  and  $168^\circ$  angle scattering as the critical point was approached. In the forward direction the limit found is a factor of two lower than seen in the measurements on earth, as shown in Fig. 4. This reveals the very large errors in decay rates which occur from density stratification on earth. This data together with the back scattering correlograms is being analyzed in terms of the scaled wavevector, the scattering vector times the correlation range, to test the universal predictions for the approach to the limits.<sup>4</sup> These experiments reached scaled wavevectors of almost 100 for the forward scattering with no density stratification across the beam.

The greatest difficulty, and the reason for the second flight, was the extreme sensitivity of the local density to the way the temperature was changed in the experiment: it was possible to generate 1% density errors by moving the sample temperature too quickly while in low gravity. This was not noticed in earlier microgravity studies of critical fluids in the ESA Critical Point Facility. In Zeno these effects were very easy to detect because all the optical signals came from a thin section of sample where the wall induced density changes dominated the behavior. We saw both adiabatic effects<sup>5</sup> and longer term density responses using the cell window interferometer. These effects are largely hidden by surface flows on earth but are easily detected in microgravity. Our strategy for the second flight was to limit these effects by lowering the temperature towards  $T_c$  with ramps whose calculated rate at each stage was low enough not to cause more than 0.1% density change. Following this plan in flight gave excellent stability of the local density as seen by the laser interferometer and scattering signals until we changed the laser path and filter at 1 mK. Then we found the surprise that the 17  $\mu\text{W}$  beam had actually been heating the local region and causing a significant density error. This effect is also well masked on earth.

The excellent temperature resolution was exploited at the end of the second flight in which we recorded the scattering intensity while crossing the phase boundary while scanning at 100  $\mu\text{K/hr}$ . A segment of the forward scattering data is shown in Fig. 5. The least-squares fitting lines for the temperature of the slope break ( $T_0$ ) gave estimated precision of  $\pm 10\mu\text{K}$  ( $\pm 3 \times 10^{-9}$  in reduced temperature). The forward and backward scattered intensity provided two fitted  $T_0$  values which agreed within  $\pm 20\mu\text{K}$ . On earth such a crossing is ten times broader because of sedimentation dynamics giving widths of 200  $\mu\text{K}$ .

The case shown is known to be about 1% below the critical density so this region of the sample is not going through the critical point but is some 1 mK below the critical temperature.

#### ACKNOWLEDGMENTS

This work was supported by NASA through Lerc under contract number NAS3-25370. We gratefully acknowledge the continuing support of the Lerc project manager, Dr. Richard Lauver. We also want to commend the excellent work of the Ball Electronics and Cryogenics Division in producing the instrument with the direction of Dr. Richard Reinker and craftsmanship of Robert Stack.

#### REFERENCES

<sup>1</sup>Harry L. Swinney and Donald L. Henry, Phys. Rev. **A8**, 2586 (1973).

<sup>2</sup>Hannes Güttinger and David S. Cannell, Phys. Rev. **A22**, 285 (1980).

<sup>3</sup>The Zeno flights were: USMP-2 payload on STS-62, March, 1994 and USMP-3 payload on STS-75, February, 1996.

<sup>4</sup>H. C. Burstyn, J. V. Sengers, J. K. Bhattacharjee, and R. A. Ferrell, Phys. Rev. **A28**, 1567 (1983).

<sup>5</sup>Hacenè Boukari, Matthew E. Briggs, J.N. Shaumeyer, and Robert W. Gammon, Phys. Rev. **A41**, 22260 (1990).

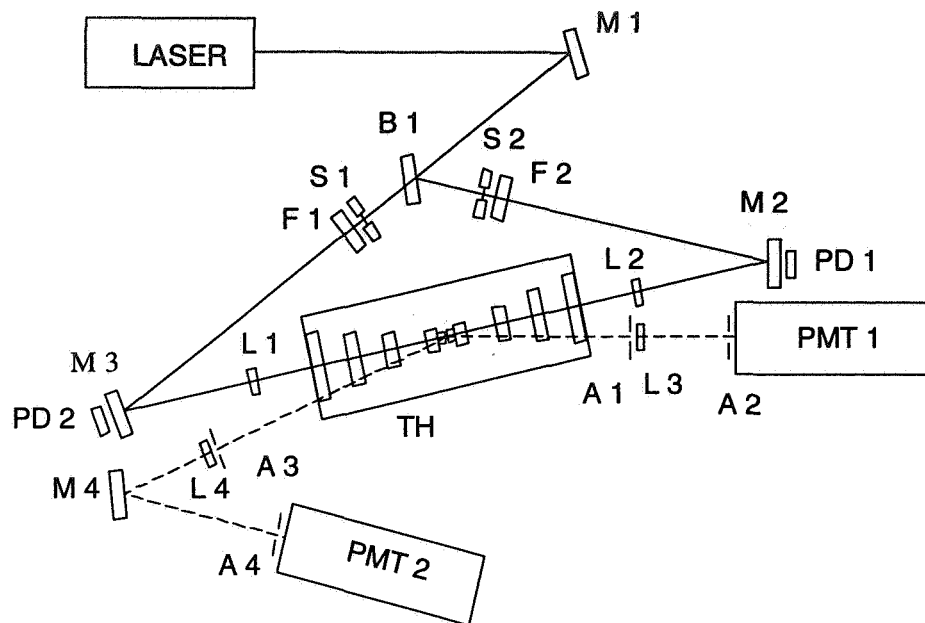


Figure 1. Zeno optical layout. M(i) are mirrors, L(i) are lenses, A(i) are apertures, B1 is a beam splitter, TH is the thermostat containing the sample cell, PMT(i) are photomultipliers, F(i) are filters, and SH(i) are shutters.

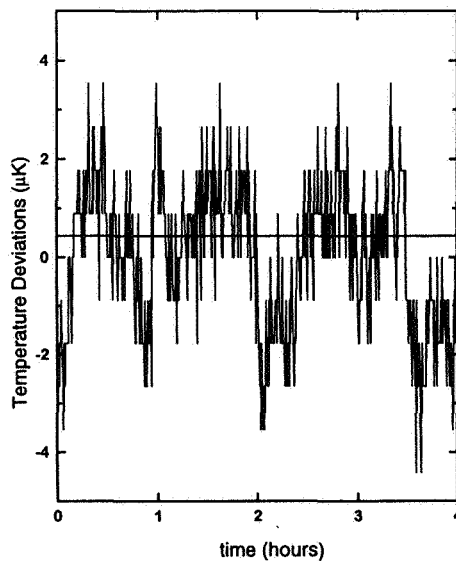


Figure 2. Zeno temperature control during the first flight. Temperature was 1 mK, duration was four hours, sampling averaging was 5 sec. Temperature deviation was  $1.5 \mu\text{K}$  rms during this period.

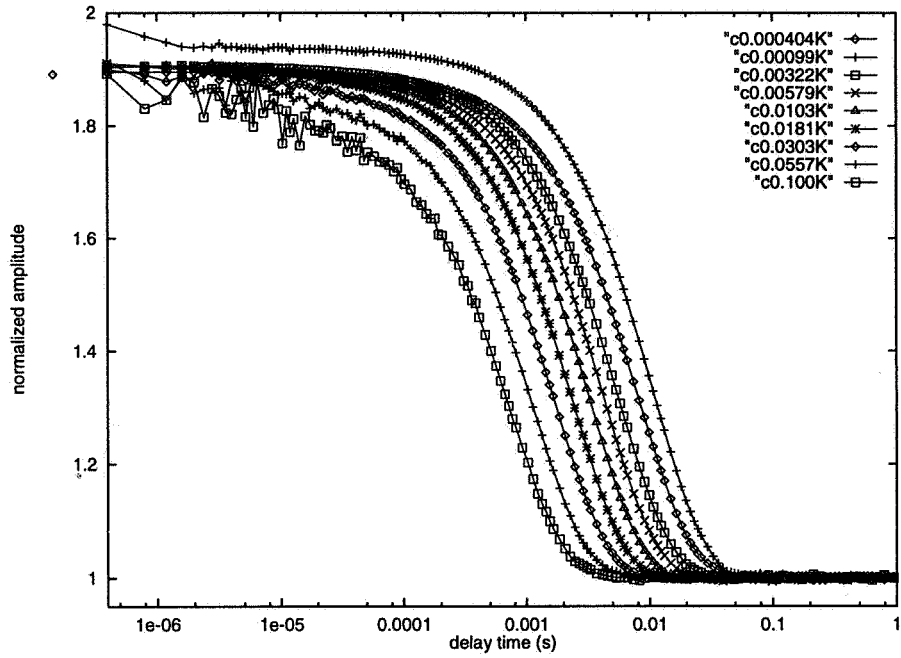


Figure 3. Correlograms for forward scattering, 12°, from Zeno flight 2. For  $(T-T_c) = 100, 56, 30, 18, 10, 5.8, 3.2, 0.99$  and  $0.40$  mK from left to right showing critical slowing down as  $T_c$  is approached.

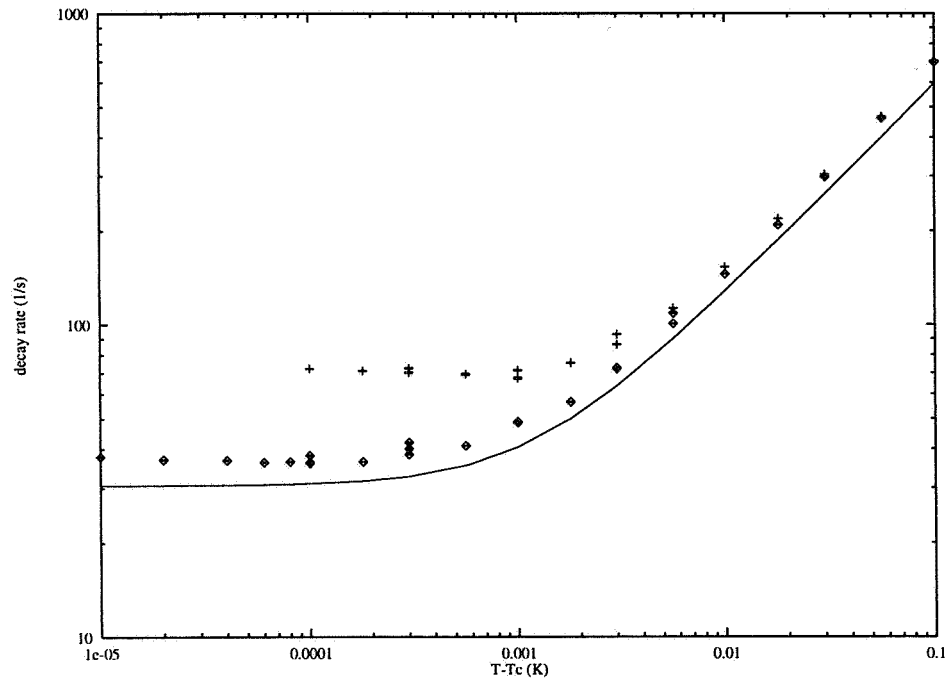


Figure 4. Comparison of ground and flight measured fluctuation decay rates from the first Zeno flight. Curve is an estimated theory line, not fitted. The crosses are ground data and the diamonds are flight data.

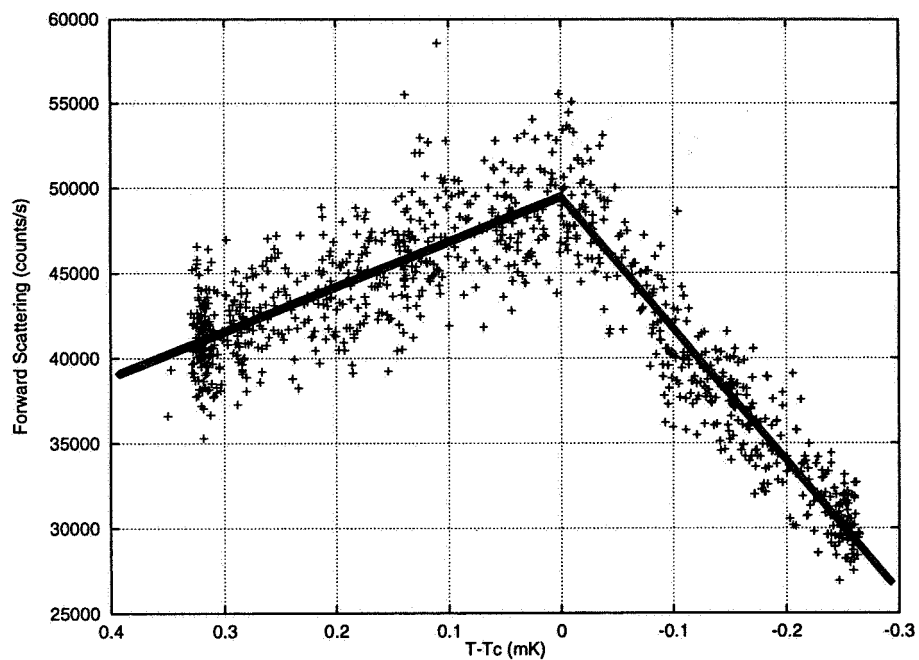


Figure 5. Search for  $T_c$  in micro-gravity. Forward scattering intensity vs. the temperature. The + symbols are unsmoothed, 5 sec. average samples. Scan rate was 100  $\mu$ K/hr. Plot shows the phase separation by the break in slope of the intensity data.

**Critical fluid thermal equilibrium dynamics**

R. Allen Wilkinson, NASA Lewis

**Paper not available**





## TURBIDITY OF A BINARY FLUID MIXTURE: DETERMINING $\eta$

Donald T. Jacobs  
Physics Department  
The College of Wooster  
Wooster, Ohio 44691

### ABSTRACT

A ground based (1-g) experiment is in progress that will measure the turbidity of a density-matched, binary fluid mixture extremely close to its liquid-liquid critical point. By covering the range of reduced temperatures  $t \equiv (T - T_c) / T_c$  from  $10^{-8}$  to  $10^{-2}$ , the turbidity measurements will allow the critical exponent  $\eta$  to be determined. No experiment has precisely determined a value of the critical exponent  $\eta$ , yet its value is significant to theorists in critical phenomena. Relatively simple critical phenomena, as in the liquid-liquid system studied here, serve as model systems for more complex systems near a critical point.

### INTRODUCTION

Comprehensive, quantitative models of critical phenomena have been developed<sup>1,2</sup> that provide a framework for the observations made on a multitude of physical systems which have similar behavior near a critical point. The numerous theoretical extensions and experimental verifications have provided a wealth of information but by no means has the understanding of critical points become complete. Numerous predictions remain untested or inadequately confirmed. One significant exponent prediction has still eluded precise experimental verification: the value of Fisher's "elusive exponent  $\eta$ ", which was predicted in order to explain light scattering measurements at small angles. An enhanced experimental technique is described that determines a value for  $\eta$  by measuring the total light being scattered (called the turbidity), in a density matched, binary fluid mixture of methanol and cyclohexane. In addition, the experiment will provide an important ground-based control for one aspect of an experiment on a recent shuttle mission: the Zeno project.

Since the correlation length is very large near the critical point compared to the molecular size, the behavior of a system is not determined by the type of molecule but by its critical properties. It is these critical properties that have universal descriptors. For example, the correlation length  $\xi$  diverges close to the critical point as a power law  $\xi = \xi_0 t^{-\nu}$  where  $t \equiv (T - T_c) / T_c$ ,  $\xi_0$  is the amplitude describing the correlation length far from the critical temperature  $T_c$ , and  $\nu$  is a universal critical exponent ( $\nu \approx 0.63$ ). Not only will the critical exponents be the same for all gases near their critical point but also for many other thermodynamic systems that have a critical point (second-order phase

transition). One example is a binary fluid mixture—two liquid components which are partially miscible below a certain temperature and completely miscible above.

The development of renormalization group theory from earlier concepts of scaling and universality provided a theoretical framework for distinguishing systems, predicting critical exponent relations, approximating values for critical exponents, and obtaining amplitude relations. The current consensus is that liquid–gas systems, uniaxial ferromagnets, and binary liquid mixtures all belong to the same universality class— $n=1$  (spin dimension),  $d=3$  (spatial dimension) which corresponds to the three-dimensional Ising model. Despite this dramatic success, there are still fundamental gaps in our knowledge of these systems. One of these is the critical exponent  $\eta$ , which has a small predicted value ( $\eta \approx 0.038$ ) that has made its measurement extremely difficult. It is one of the last exponents to lack direct experimental verification.

## PREVIOUS WORK

The critical exponent  $\eta$  describes<sup>3</sup> how the correlation function behaves at  $T_c$ . Recent field theoretic analysis and partial differential approximants predict the following values for the critical exponents  $\gamma$ ,  $\nu$  and  $\eta$ :

$\gamma$	$\nu$	$\eta$	Source
$1.237 \pm 0.002$	$0.630 \pm 0.0015$	$0.0359 \pm 0.0007$	Nickel and Rehr <sup>4</sup>
$1.2390 \pm 0.0025$	$0.630 \pm 0.0015$	$0.033 \pm 0.006$	LeGuillou and Zinn-Justin <sup>5</sup>
$1.2395 \pm 0.0004$	$0.632 \pm 0.001$	$0.039 \pm 0.003$	Fisher and Chen <sup>6</sup>

While the theoretical predictions may just agree within their quoted uncertainty, the experimental situation is less well-known. Three principal techniques have been used to look for  $\eta$  and they all involve scattering phenomena using either x-rays, neutrons, or light. Tracy and McCoy examined the experimental results before 1975 and concluded<sup>7</sup> that "no experiment to date unambiguously and directly establishes that the critical exponent  $\eta$  is greater than zero." At the same time, Cannell<sup>8</sup> published a measurement of  $\text{SF}_6$  which found  $\eta = 0.03 \pm 0.03$ . A high precision, angular light scattering experiment by Chang, Burstyn and Sengers<sup>9</sup> on the liquid-liquid mixture 3-methylpentane and nitroethane found  $\eta = 0.017 \pm 0.015$ ; the authors conclude "we cannot prove on the basis of the experimental data alone that  $\eta$  must be finite." A recent x-ray scattering measurement,<sup>10</sup> done on the liquid mixture perfluoromethylcyclohexane and n-heptane finds  $\eta = 0.03 \pm 0.03$ . The most recent light scattering measurement was done by Bailey<sup>11</sup>, a Ph.D. student of Cannell, on 3-methylpentane and nitroethane, which is a popular system because the close refractive index match of the components greatly reduces (but not eliminates) multiple scattering corrections.

Bailey determined the exponents  $\gamma$  and  $\nu$ , which if the scaling relation  $\gamma = \nu (2 - \eta)$  is assumed, gives values of  $\eta$  from 0.027 to 0.046. Angular scattering of photons or neutrons can determine the exponents  $\gamma$  and  $\nu$ , but only after careful consideration of multiple scattering effects which limits the precision and hence the ability to accurately calculate  $\eta$  from the scaling relation.

In 1991, Ferrell<sup>12</sup> developed the theory that would allow turbidity measurements to be used to determine  $\eta$ , a parameter which appears explicitly in his formulation. The turbidity measures the total amount of light scattered over all solid angle. A binary fluid mixture exhibiting an upper consolute point will be one phase, homogeneous, and essentially clear when the mixture is well above its critical consolute temperature  $T_c$ . The constant transmitted light intensity at these temperatures is referred to as  $I_0$ . As the temperature of the fluids approaches  $T_c$ , concentration fluctuations, "droplets," begin to form and cause the transmitted light intensity  $I$  to be reduced. The turbidity  $\tau$  is dependent upon the transmitted light intensities  $I$  and  $I_0$  by

$$\tau = L^{-1} \ln(I_0 / I)$$

where  $L$  is the optical path length. The turbidity is related to critical phenomena by assuming Ornstein-Zernike scattering<sup>12,13</sup> and has different forms if  $\eta$  is or is not zero. The effect of  $\eta$  can best be illustrated by a plot of turbidity  $\tau$  versus reduced temperature  $t$  (see Figure 1). Having  $\eta \neq 0$  is expected to result in lower turbidity values at small reduced temperatures (close to the critical point), but identical turbidity values as when  $\eta = 0$  when at large reduced temperatures. Previous turbidity experiments<sup>14</sup> have without exception assumed  $\eta = 0$  because data could not be taken sufficiently close to the critical point to warrant inclusion. An advantage of measuring the turbidity is that multiple scattering is not important because once the light is scattered out of the beam, it does not matter how many times it is scattered after that. A precise measurement of the turbidity very close to the critical point can provide a good determination of the exponent  $\eta$ .

## EXPERIMENT

The binary fluid mixture to be measured in this experiment is methanol and cyclohexane. These fluids combine similar densities ( $\Delta\rho/\bar{\rho} = 0.016$ ) which minimizes the effect of gravity, with quite different refractive indices which allows significant light scattering near the critical point. This system has also been studied extensively with published measurements of the turbidity, viscosity, surface wetting, dynamic light scattering, coexistence curve, and excess molar volume. The critical composition is 29.0% by weight methanol with a critical temperature of about 45°C, depending on the amount of water present.

A cylindrical cell with quartz optical windows encloses the fluid mixture, which is sealed with Kalrez o-rings. The optical path length is about 2.0 mm. This length allows adequate resolution at  $t \sim 10^{-3}$  yet also gives good resolution at small reduced temperatures ( $t \sim 10^{-8}$ ). The cell is temperature controlled by placing it within an onion-layer thermostat with low thermal mass stages for (relatively) fast changes in temperature. When properly controlled, such an enclosure can maintain the cell temperature to within  $\pm 10 \mu\text{K}$  at room temperatures ( $t \approx 3 \times 10^{-8}$ ). The temperature is sensed by stable, calibrated Thermometrics thermistors. The stage holding the cell is controlled using an AC bridge with a lock-in amplifier as a null-detector coupled to a PID controller in order to achieve the desired precision in temperature control. The outer stages use a digital control network where the resistance of each thermistor is measured by a precision digital voltmeter and reported to a computer which determines the correct voltage to be applied to that stage's heater.

The turbidity is determined from the transmitted light intensity  $I$  when the fluids are close to  $T_c$  compared to the transmitted intensity  $I_0$  when the fluids are well into the one-phase region. To obtain  $\eta$ , we use an optical system capable of measuring the turbidity with a resolution that can distinguish between the various theoretical predictions. With the small path length cell, the most stringent measurements will be at temperatures far from the critical temperature where the light scattering is weak. The ( $\pm 2\%$ ) fluctuations in a 3mW, polarized HeNe laser is reduced by passing the beam through a laser power amplitude stabilizer before passing through a beam expander, spatial filter. The central portion of this beam is split with one part passing through the fluids and the other part traveling around the thermostat to provide a reference intensity. A light chopper is used to sample the two beams at different frequencies. The light not scattered from the fluids in the cell passes through a pinhole before the beams are directed through a diffuser and a 632.8nm bandpass filter before striking photodiode detectors. The intensities are measured using lock-in amplifiers tuned to the chopper frequencies. The thermostat, laser, power controller, and photodetectors are placed on an optical table to minimize vibration and noise. Fig. 2 illustrates the optical system.

The interfacing software (written in LabVIEW) accesses the instruments via a GPIB and allows the computer to set and control the temperatures of the stages and then measure the light intensities in a sequential process. Stability of the light intensity ratio of the two beams is less than 0.1%, and the cell temperature can be controlled to  $30 \mu\text{K}$ . This stability and resolution are quite adequate for the turbidity. The process of collecting preliminary data and preparing a sample sufficiently close to the critical composition has begun.

## CONCLUSION

This turbidity experiment should provide the best determination of the exponents  $\nu$ ,  $\gamma$  and  $\eta$ , and amplitudes  $\xi_0$  and  $\chi_0$ . This research will be the investigation of the critical exponent  $\eta$ , on whose value the theorists disagree, and whose effect the experimentalists have been unable to definitively detect. The experiment outlined should provide the first evidence of a non-zero  $\eta$  and perhaps resolve which theoretical value is correct. This experiment also provides a good proving ground for the acquisition and analysis of turbidity data similar to that obtained in the shuttle experiment Zeno. Finally, a rigorous understanding of the turbidity very close to the critical point may allow its use as a temperature probe in future shuttle experiments on near-critical fluids, or at the very least, as a definitive indicator of the critical point.

## REFERENCES

1. S. C. Greer, *Acc. Chem. Res.* **11**, 427 (1978); G. Ahlers, *Rev. Mod. Phys.* **52**, 489 (1981).
2. S.C. Greer and M.R. Moldover, *Ann. Rev. Phys. Chem.* **32**, 233 (1981); A. Kumar, H.R. Krishnamur, and E.S.R. Gopal, *Phys. Rep. (Netherlands)* **98**, 57 (1983).
3. M.E. Fisher, *J. Math. Phys.* **5**, 944 (1964); M.S. Green, *J. Chem. Phys.* **33**, 1403 (1960).
4. B.G. Nickel and J.J. Rehr, *J. Stat. Phys.* **61**, 1 (1990).
5. J.C. LeGuillou and J. Zinn-Justin, *J. Physique* **50**, 1365 (1989).
6. M.E. Fisher and J.-H. Chen, *J. Physique* **46**, 1645 (1985).
7. C.A. Tracy and B.M. McCoy, *Phys. Rev. B* **12**, 368 (1975).
8. D.S. Cannell, *Phys. Rev. A* **12**, 225 (1975).
9. R.F. Chang, H. Burstyn, and J.V. Sengers, *Phys. Rev. A* **19**, 866 (1979).
10. Y. Izumi, *Phys. Rev. A* **39**, 5826 (1989)
11. A. Bailey, Ph. D. thesis (UCSB, 1993).
12. R.A. Ferrell, *Physica A* **177**, 201 (1991).
13. V.G. Puglielli and N.C. Ford, Jr., *Phys. Rev. Lett.* **25**, 243 (1970).
14. D.T. Jacobs, *Phys. Rev. A* **33**, 2605 (1986); R.B. Kopelman, R.W. Gammon, and M.R. Moldover, *Phys. Rev. A* **29**, 2048 (1984); C. Houessou *et al.*, *Phys. Rev. A* **32**, 1818 (1985).

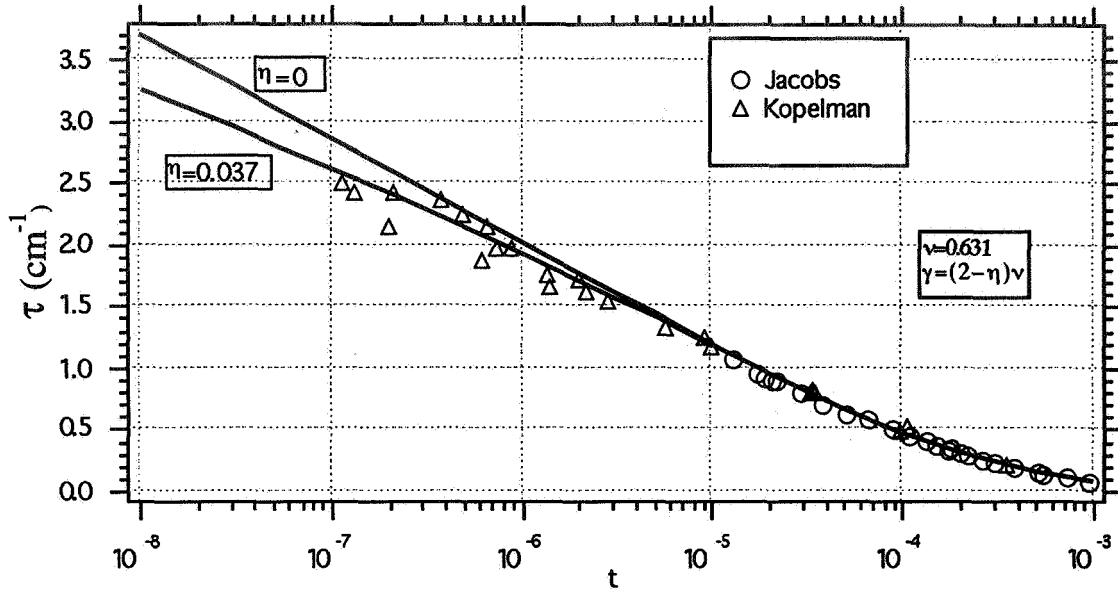


Figure 1: Theory and published data for the turbidity  $\tau$  of Methanol-Cyclohexane. The upper line is from Ref. 13 when the critical exponent  $\eta=0$ ; the bottom line is from Ref. 12 when  $\eta=0.037$ . Both curves use the same parameters and constants with the constraint that the scaling relation  $\gamma=\nu(2-\eta)$  holds. An effect due to  $\eta$  can only be detected close to the critical point (small reduced temperature,  $t$ ).

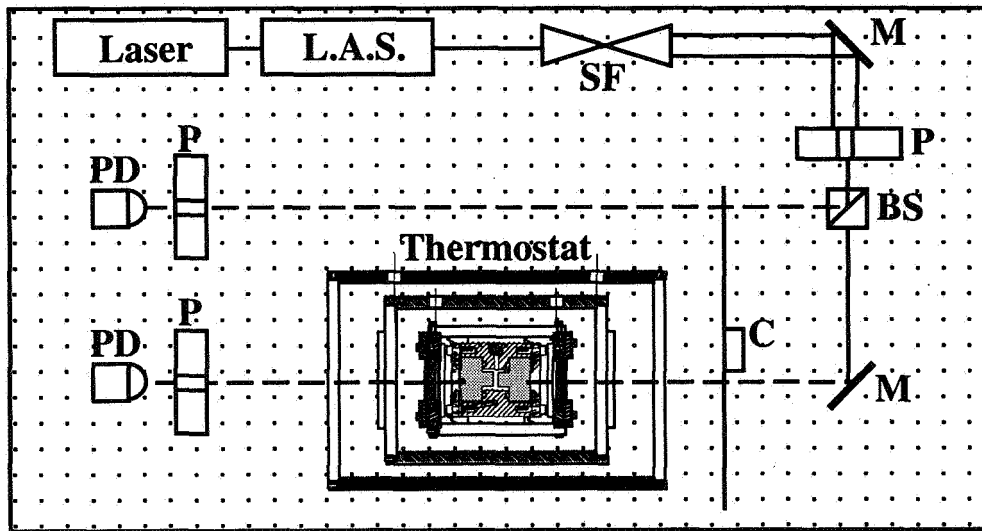


Figure 2: Optical Schematic. The laser beam passes through a laser amplitude stabilizer (L.A.S.) and a beam expander/spatial filter (SF) before the central portion is divided by the beam splitter (BS). Part of the beam goes through the outer ring of slots of an optical chopper (C) and around the fluids to provide a reference. The rest goes through the inner ring of slots on the chopper before passing through the fluids in the center of the thermostat. The beams are detected by photodiodes (PD) connected to lock-in amplifiers. Mirrors (M) and pinholes (P) are also shown.

## Nonlinear Dynamics and Nucleation Kinetics in Near-Critical Liquids

Principal Investigator: Prof. Alexander Z. Patashinski

Northwestern University

Co-Investigator: Prof. Mark A. Ratner

Northwestern University

Co-Investigator: Dr. Vladimir Pines

Case Western Reserve University

The objective of our study is to model the non-linear behavior of a near-critical liquid following a rapid change of the temperature and/or other thermodynamic parameters (pressure, external electric or gravitational field). The thermodynamic critical point is manifested by large, strongly correlated fluctuations of the order parameter (particle density in liquid-gas systems, concentration in binary solutions<sup>1-3</sup>) in the critical range of scales. The largest critical length scale is the correlation radius  $r_c$ . According to the scaling theory,  $r_c$  increases as  $r_c = r_0 \epsilon^{-\alpha}$  when the non-dimensional distance  $\epsilon = (T - T_c)/T_c$  to the critical point decreases. Here,  $T_c$  is the critical temperature, and the critical exponent  $\alpha$  is  $\approx 2/3$ . The relaxation time  $\tau(r_c)$  of fluctuations on the correlation radius length scale may be estimated near  $T_c$  as  $\tau(r_c) = \tau_0 \epsilon^{-(3\nu+z)}$ , where the microscopic time  $\tau_0$  is about  $10^{-13}$  sec, and the numerical value of the related critical exponent is approximately  $3\nu+z \approx 2$ .

The normal gravity alters the nature of correlated long-range fluctuations when one reaches  $\epsilon \sim 10^{-5}$ , and correspondingly  $\tau(r_c) \sim 10^{-3}$  seconds; this time is short when compared to the typical experimental time. In microgravity conditions, one may study a statistically homogeneous critical liquid which is orders of magnitude closer to  $T_c$  than that in a ground-based experiment. Recently, the ZENO experiment<sup>1</sup> has set a benchmark  $\epsilon \sim 10^{-7}$ - $10^{-8}$ ,  $r_c \sim 1$ - $10 \mu\text{m}$ , and  $\tau(r_c) \sim 10^1$ - $10^3$  s. This achievement manifests a qualitative change of the physical situation: that close to the critical point, the life-time of long-range fluctuations exceeds the typical experimental time-scale of seconds and minutes, and one is able to experimentally study the nonequilibrium, transient and steady, states of the material. On the other hand, in microgravity experiments conducted very close to the critical point a speeded-up equilibration may result in a long-living non-equilibrium state in some parts of the liquid. A theoretical model for the kinetics of those states is then needed to interpret the experimental data.

Close to the critical point, a rapid, relatively small temperature change  $\delta T \ll T_c$  may perturb the thermodynamic equilibrium on many length scales. The critical fluctuations have a hierarchical structure, and the relaxation involves many length and time scales. Due to fragility of the near-critical equilibrium, the response of the system to such a perturbation is nonlinear one, and non-linearity plays the main role in the relaxation kinetics.

Above the critical point, in the one-phase region, we consider the relaxation of the liquid following a sudden temperature change that simultaneously violates the equilibrium on many scales. Below  $T_c$ , a non-equilibrium state may include a distribution of small scale phase droplets (clusters of one phase in the matrix of the other one); we consider the relaxation of such a droplet following a temperature change that has made the phase of the matrix stable.

The transient near-critical states created by a rapid temperature change differ in important details from those studied in the equilibrium scaling theory and the dynamic renormalization group (DRG). The application of the DRG to the new situation assumes an extension of scaling hypothesis. We give physical arguments in favor of the proposed scenario of the hierarchical relaxation. The theory predicts new scaling laws for the large-time dependence of the temperature and for statistical characteristics of long-range fluctuations. These predictions may be tested by light

scattering experiments and by direct visualization techniques. An experimental test of the predictions will check the suggested scenario and the enhanced scaling hypothesis.

The following physical situations are considered.

1. A step away from the critical point where a large range of critical fluctuations disappears.
2. A step towards the critical point where a new range of strongly interacting fluctuations appear.
3. A phase droplet (nucleus) in a matrix of the other phase under varying conditions of the matrix stability.
4. The nucleation of FCC (face centered cubic) clusters following a deep quench of a computer-generated "liquid".

We start with a Langevin-type description of the system. The atomic scale fluctuations are assumed to play the role of a "thermal bath" for the larger scale degrees of freedom. At times  $t > \tau_0$  one characterizes this "thermal bath" by a time-dependent temperature  $T(t)$ . The time  $\tau_{ch}$  of the rapid temperature change  $\delta T$  is large when compared to  $\tau_0$ , but small when compared to the relaxation time on large scales  $r \gg r_0$ :  $\tau(r) > \tau_{ch} > \tau_0$ . On the macroscopic time-scales, one considers a sharp temperature step at  $t=0$ . The mathematical model is as follows. To study the fluctuations of the order parameter (particle density in the liquid-gas system), one represents the order parameter field  $\phi(r,t)$  in the form<sup>1,3</sup>

$$\phi(r,t) = \sum_{k=0}^{k_\lambda} \phi_k e^{-ikr}; \quad (1)$$

the variable cut-off length  $\lambda=1/k_\lambda$  is introduced in (1) following the Wilson-Kadanoff renormalization group (RG) method<sup>2,3</sup>. The probability  $W_{eq,\lambda}(\phi)D\phi(r)$  to find the equilibrium system in an element  $D\phi$  of the configuration space defines the effective Hamiltonian  $H_\lambda$ <sup>1,2</sup>:

$$\begin{aligned} W_{eq,\lambda}(\phi)D\phi &= \exp\left(\frac{F_\lambda - H_\lambda(\phi)}{k_b T_c}\right) D\phi, \quad F_\lambda = -k_b T_c \ln \int \exp\left(-\frac{H_\lambda}{k_b T_c}\right) D\phi, \\ H_\lambda &= -F_{reg} - k_b T_c \ln \sum_{(\phi(r))} \exp\left(-\frac{H^{(mic)}}{k_b T_c}\right), \quad F_{reg} = F - F_\lambda. \end{aligned} \quad (2)$$

In the definition (2),  $H^{(mic)}$  is the microscopic Hamiltonian of the system,  $k_b$  is the Boltzmann constant,  $F$  is the equilibrium free energy of the system,  $F_\lambda$  and  $F_{reg}$  are the singular and the regular parts of the free energy respectively<sup>2</sup>. The sum in (2) is over all states of the system with  $\phi(r)$  a given function. The field  $\phi(r)$  defined by (1) represents only a small fraction of the degrees of freedom of the system, most of which belong to small length scales  $r < \lambda$ . The effective Hamiltonian  $H_\lambda(\phi, \epsilon)$  is defined as an average over these small scale degrees of freedom. Up to a regular function of  $\epsilon$ ,  $H_\lambda(\phi, \epsilon)$  is the free energy of the system in the equilibrium state with a given configuration of the large scale field  $\phi(r)$ .

The fluctuations of the conserved order parameter  $\phi(r,t)$  are described by the Langevin equation of the form

$$\frac{\partial \phi}{\partial t} = -\Delta \Gamma_\lambda \left( -\frac{\delta H_\lambda}{\delta \phi} + f_{\lambda, ext} \right). \quad (3)$$

Here,  $\Gamma$  is the (conserving) kinetic coefficient. The extraneous random force  $f_{ext}(r,t)$  models the



interaction of the order parameter with small-scale degrees of freedom of the system. The kinetic coefficient  $\Gamma_\lambda$  and the effective Hamiltonian  $H_\lambda$  are dependent on the cut-off length  $\lambda$  as described by the dynamic renormalization group (DRG). An essential condition of applicability of the method is the thermal equilibrium at length-scales  $R < \lambda$ ; the thermodynamic equilibrium at scales larger than  $\lambda$  is not required by the renormalization group method, the relaxation on these scales is described by the equations of the theory. In the course of relaxation, the fluctuations on scales  $R > \lambda$  are non-equilibrium and exchange energy with smaller scales. One has to study separately a step towards the critical point ( $r_{c,fin} > r_{c,in}$ ) in which a new range of strongly interacting fluctuations appear, and a step away from the critical point ( $r_{c,fin} < r_{c,in}$ ) where a large range of critical fluctuations disappears. Here and below, the subscripts  $fin$  and  $in$  label the characteristics of the final and the initial ( $t < 0$ ) states of the system.

For a large temperature change away from the critical point,  $r_{c,fin} < r_{c,in}$ . Most important changes in the fluctuation picture are expected in the range of scales  $r_{c,fin} < r < r_{c,in}$ . In systems characterized by a conserved order parameter, the relaxation on small length-scales takes less time than on the large ones. At a given time  $t$ , the fluctuations on length-scales  $r < \lambda_{eq}(t)$  have approached the new equilibrium state while the larger scale fluctuations are still non-equilibrium. Here,  $\lambda_{eq}(t)$  is the equilibration length increasing with increasing time. At large  $t > \tau(r_{c,fin})$ ,  $\lambda_{eq}(t)$  exceeds the correlation radius  $r_{c,fin}$  of the final equilibrium state. We apply the DRG to find the effective Hamiltonian on large scales  $r > r_{c,fin}$ ,  $t > \tau(r_{c,fin})$  in the form

$$H_\lambda = \sum_{k < k_\lambda} H_k, \quad H_k = \frac{1}{2\chi_{fin}} |\phi_k|^2. \quad (4)$$

Here,  $\chi_{fin} \equiv \chi(\epsilon_{fin}) \sim \epsilon_{fin}^{-\nu(2-\eta)}$  is the susceptibility of the system in the final state (the isothermal compressibility for the liquid-gas system). The free field form of the resulting Hamiltonian means that at  $t > \tau(r_{c,fin})$  the temperature shift switches off the interaction in the range of scales  $r > r_{c,fin}$ . The relaxation of the long-range configuration to the final equilibrium state follows the laws of the free field kinetics. For the time-dependent average  $M_k(t) = \langle |\phi_k(t)|^2 \rangle$  one obtains

$$M_k(t) = (M_{k,in} - M_{k,fin}) e^{-\frac{2t}{\tau_k}} + M_{k,fin}, \quad (5)$$

$$M_{k,in} = \langle |\phi_k|^2 \rangle_{in}, \quad M_{k,fin} = 2k_b T_c \chi_{fin}; \quad \tau_k = \frac{1}{D_{fin} k^2}.$$

The diffusion coefficient  $D_{fin}$  is scale-independent at the length scales  $\lambda \gg r_{c,fin}$ . We have also studied the shape relaxation of probability distribution function of long-range fluctuations.

A rapid temperature increase requires more energy than a gradual heating. At large times, the excess energy is gradually released; in a system adiabatically insulated at  $t > \tau(r_{fin})$ , the energy release raises the temperature of the system. The scaling law for the large-time temperature "tail" has the form

$$\epsilon(t) - \epsilon_{fin} \sim \epsilon_{fin} [\tau(r_{c,fin})/t]^\zeta, \quad \zeta = (1+\eta)/2. \quad (6)$$

Here,  $\eta \approx 0.033$  is the critical exponent of the order parameter.

Let us now consider a step toward the critical point:  $\epsilon_{in} \gg \epsilon_{fin}$ . In contrast to the above case,

the harmonics  $\phi_k$  in the range  $r_{c,in} < 1/k < r_{c,fin}$  strongly correlate in the final state, and the problem cannot be reduced to that of a single harmonic. The suggested scenario is sequential equilibration: at a given time  $t$ , the fluctuations on small scales up to a time-dependent equilibration length scale  $\lambda_{eq}(t)$  will equilibrate while the harmonics  $\phi_k$  with  $k < 1/\lambda_{eq}$  will retain the initial magnitudes. These magnitudes are small compared to the final ones, and may be neglected. The statistics and the kinetics of the fluctuations on scales  $r < \lambda_{eq}(t)$  yield then the equilibrium scaling relations<sup>2,3,4</sup>: on a scale  $\lambda < \lambda_{eq}(t)$  the relaxation time is  $\tau(\lambda) \sim \lambda^2/D(\lambda) \sim \lambda^{3+z/v}$ , where  $z$  is the critical exponent for the viscosity<sup>2,4</sup>. The time dependence of  $\lambda_{eq}$  is controlled by the condition that  $\tau(r) < t$  for  $r < \lambda_{eq}(t)$ , and  $\tau(r) > t$  for  $r > \lambda_{eq}(t)$ . The scale  $\lambda_{eq}(t)$  has then the equilibration time  $\tau(\lambda_{eq}(t)) \sim t$ ; this relation gives the scaling law for  $\lambda_{eq}(t)$ .

$$\lambda_{eq}(t) = r_{in} [t/\tau(r_{in})]^p, \quad p = \frac{v}{3v+z}. \quad (7)$$

The theoretical values (see ref.<sup>5</sup>)  $v \approx 0.630$  and  $z \approx 0.063$  give  $p \approx 0.32$ .

The sequential "cooling" of large scale fluctuations is accompanied by release of heat  $Q(t)$ . The heat released on the scale  $\lambda_{eq}$  is transferred to smaller scales and through the small scale "heat bath" to the thermostat that maintains the temperature  $T(t)$ . In a system that is adiabatically insulated during relaxation, the heat transferred from the large scales to the smaller ones will result in an increase in the temperature  $T(t)$ . A rapid cooling results then in a temperature minimum. The scaling law for the large time "tail" in reduced temperature is

$$\epsilon(t) \propto \epsilon_1 [\tau(r_{c,in})/t]^{\zeta_-}, \quad \zeta_- = 1/(3v+z). \quad (8)$$

The critical exponent  $\zeta_- = 1/(3v+z)$  differs from  $\zeta_+$  given by (6). Using the approximate theoretical values for the critical exponents (see ref.<sup>5</sup>), one obtains for the liquid-gas and for the binary mixtures critical points  $\zeta_+ \approx 0.517$  and  $\zeta_- \approx 0.512$ . Both exponents are surprisingly close to each other and to the mean-field value  $1/2$ .

Below the critical temperature, there are two phases of the material, one of which is metastable except for the phase transition line. A non-equilibrium state may include droplets of one phase in the matrix of the other one. In the literature, this was studied for the case of a metastable matrix state, when the droplet is a nucleus of the new, stable, phase. We have considered a more general case when the embedding matrix may be metastable or stable. In the vicinity of a phase equilibrium line limited by the spinodals, the non-linearity of the equations for the two-phase system results in a finite width of the interface separating the droplet from the matrix. On both sides of the binodal, the droplet may be characterized by a critical radius; when the matrix is in the stable phase, the critical radius becomes negative. The nucleus then is always subcritical and decays with time. By changing the thermodynamic stability of the matrix, one is able to control the growth and decay of the nucleus. Outside the part of the thermodynamic plane separated by the spinodals of both phases, the relaxation of the droplet leads to the broadening of the boundary. Asymptotically, the profile of the order parameter tends to a Gaussian one, with the width  $R(t)$  growing according to the diffusion law  $R^2 \sim t$ .

The growth of small nuclei of the cubic central faced crystalline phase following a deep temperature quench to the liquid state spinodal was observed in a computer-generated "liquid". To discriminate clusters having the FCC local order, the statistical theory of pattern recognition was

applied. The method proposed allows one to compare nucleation kinetics in real and in simulated systems.

This study was supported by NASA grant (GRANT NAG3-1617).

The results of this study were published in the following papers:

1. A. Z. Patashinski, "Rapid temperature changes in near-critical systems", to appear in Physics Letters.
2. A. Z. Patashinski, "A temperature step away from a critical point", submitted to Phys.Rev.E.
3. A. Z. Patashinski, "A phase droplet near the phase transition line", submitted to J.of Chem. Phys.
4. A. C. Mitus, F. Smolej, H. Hahn, and A. Z. Patashinski, "Theory and practice of shape spectroscopy of local FCC structures in computer simulations of nucleation and crystallization", to appear in J.of Physics.
5. A. C. Mitus, F. Smollay, H. Hahn, and A. Z. Patashinski, "Q<sub>455</sub>-spectroscopy of shapes and FCC-nucleation in a Lennard-Johnes system", Europhysics Letters, **32**(9), 777 (1995).

#### REFERENCES

1. ZENO experiment (Critical Fluid Light Scattering Experiment) In the USMP-2 payload on the Space Shuttle flight STS-62, March 1995, private communication with R.W.Gammon.
2. A. Z. Patashinskii and V. L. Pokrovskii, *Fluctuation Theory of Phase Transitions*, Pergamon Press, Oxford (1979).
3. *Phase Transition and Critical Phenomena* (Ed. by C. Domb and M. S. Green), Academic Press, New York, Vol.3-5 (1974-1982).
4. P. C. Hohenberg, B. I. Halperin, Rev. Mod. Phys. **49**, (1977) 423
5. Jan V. Sengers, Effects of Critical Fluctuations on the thermodynamic and transport properties of supercritical fluids, In: *Supercritical Fluids: Fundamentals for Application*, E. Kiran and J. M. H. Levelt Sengers, eds., Kluwer, Dordrecht (1994).



# **Multiphase Flow, Heat Transfer, and Phase Change**



# FUNDAMENTAL PROCESSES OF ATOMIZATION IN FLUID-FLUID FLOWS

Christopher Gallagher, David T. Leighton, Hsueh-Chia Chang and Mark J. McCreedy

University of Notre Dame  
Department of Chemical Engineering  
Notre Dame, IN 46556

## ABSTRACT

This paper discusses our proposed experimental and theoretical study of atomization in gas-liquid and liquid-liquid flows. While atomization is a very important process in these flows, the fundamental mechanism is not understood and there is no predictive theory. Previous photographic studies in (turbulent) gas-liquid flows have shown that liquid is atomized when it is removed by the gas flow from the crest of large solitary or roll waves. Our preliminary studies in liquid-liquid laminar flows exhibit the same mechanism. The two-liquid system is easier to study than gas-liquid systems because the time scales are much slower, the length scales much larger, and there is no turbulence. The proposed work is intended to obtain information about the mechanism of formation, rate of occurrence and the evolving shape of solitary waves; and quantitative aspects of the detailed events of the liquid removal process that can be used to verify a general predictive theory.

## INTRODUCTION

Atomization of liquids in gas-liquid or liquid-liquid flows is one of the basic processes that determines the configuration of the phases and the overall behavior of the flows. Here we are defining atomization as the removal of liquid droplets from a flowing layer of a more viscous phase by shearing action of the (necessarily) faster-moving, less-viscous phase. For the air-water system, photographic experiments by Woodmansee and Hanratty [1] and Whalley et al. [2] have directly linked atomization to large waves -- liquid is removed by some mechanism from the crest of large solitary or roll waves. Preliminary work shown below for a mineral oil - water system exhibits the same mechanism. The primary questions about atomization to be addressed in our research are: how quantitative aspects of atomization (e.g. drop size and rate) change as viscosity, density and flow ratios, orientation and the presence of gravity are varied and which fundamental theory is needed to accurately describe atomization and allow prediction for situations outside the available range of data. Because atomization occurs at the crests of solitary waves, the behavior of such waves is of fundamental importance.

Atomization rates are an important issue in the design and operation of many industrial devices. Fore and Dukler [3] state that up to 20% of the pressure drop is from the atomization and deposition process. A stable oil film is needed on the walls of hydrocarbon transportation pipelines to protect the pipe from corrosion caused by CO<sub>2</sub> combined with condensed water. For pipelines with large gas-liquid flow ratios oriented close to horizontal sufficient atomization is needed. Numerous chemical processing operations rely on emulsification or atomization to create the interfacial area necessary for efficient reaction or contacting. Phase mixing is typically effected by agitation or pumping through nozzles. However, both of these processes are relatively inefficient. A fundamental study of the atomization mechanism can hence allow us to optimize these existing processes or suggest a more efficient new process, such as shearing a two layer configuration.

Figure 1 shows a comparison of solitary waves for air-water in a 1.27 cm tube taken during  $\mu$ -g aircraft flights by Dukler and coworkers. If these are compared to waves in vertical annular flow on earth by Schadel and Hanratty

[4] (figure 2) or in our horizontal channel (figure 3) by Peng et al [5], it is seen that the wave amplitude to substrate ratio is much larger for  $\mu$ -g. This is evidently because of the lack of uniform gravity that acts to drain liquid from waves in any flow geometry. Consequently based on the Woodmansee and Hanratty [1] mechanism, it is expected that atomization will occur more readily under microgravity conditions. As such, it becomes a fundamental consideration for the design of two-phase flow devices in spacecraft, space stations and lunar bases.

The importance of knowing the fraction of liquid entrained in gas-liquid flows has been recognized for many years. Studies originally focused on measuring the entrained fraction and developing empirical correlations (e.g. Dallman et al., [6] ; Asali et al., [7];). However as explained by Schadel and Hanratty [4], a better approach is to measure and correlate the atomization and deposition rates separately. Unfortunately, this still has not produced a general predictive relationship valid for all flows. This is perhaps because their correlations do not reflect the fundamental mechanism.

This paper describes some preliminary results that are intended to lead to verification of the mechanisms of liquid atomization by a gas stream or an immiscible liquid flow and to provide predictive capabilities for the widest possible parameter range. Experiments have been done for a two-liquid system in our rotating two-liquid Couette device and in an oil-water channel flow.

## EXPERIMENTAL RESULTS

Figure 4 shows our density-matched, two-liquid rotating concentric cylinder device that can provide wave behavior that is not limited by the length of contact of the two phases. Some experimental details are given in Sangalli et al. [8] and an extensive description will be available in a forthcoming publication. The two fluids used for the experiments are Dow 710, which is a phenylmethyl polysiloxane fluid and a mixture of ethylene glycol, water, and Pink Bismuth – an Osco® brand upset stomach remedy. The Pink Bismuth is used as a source of refractive particles. The viscosity and density of Dow 710 are  $0.555 \text{ Ns/m}^2$  and  $1110 \text{ kg/m}^3$  respectively. The viscosity and density of the ethylene glycol solution are  $0.0151 \text{ Ns/m}^2$  and  $1108 \text{ kg/m}^3$  respectively. Dow 710 is loaded on the outer cylinder after the ethylene glycol mixture has been added to the channel.

We use several lighting techniques to probe the experiment -- white light, a vertical plane of laser light, and a horizontal laser sheet. The two laser methods provide useful quantitative data that direct visualization with white light does not allow.

Figure 5 shows a map of wave behavior for conditions where the depth ratio is such that the positive growth region for wave modes always extends from zero wavenumber up to a cutoff determined by the rotation rate. It is seen that periodic waves occur at low rotation rates for all depth ratios and that waves become more irregular as the rotation rate is increased. The occurrence of short wavelength, steady periodic waves for a range of conditions where long waves are unstable is quite surprising and important. In both the falling film problem that we studied earlier (Chang, [9]), where the shape of the growth curve is always similar the ones for figure 5, and gas-liquid channel flow (McCready and Chang, [10]) which also has the same growth curve at high gas flow, the long distance dominant disturbance is always a solitary wave or roll wave. Apparently, at low shear rates there is enough nonlinear stabilization in these two-liquid flows to prevent the long wave modes from growing. This may be caused by direct interaction between long and short waves similar to what is observed at low shear in gas-liquid channel flow (Jurman et al., [11]). At higher rotation rates, solitary waves seem to evolve from periodic waves. Because the number of solitary waves in the device is always less than the original number of small amplitude periodic waves, solitary wave formation must also involve some type of energy transfer mechanism between short and long waves. These



examples underline the importance of understanding interactions between long and short waves. In the context of the current interest of two-phase flow in space, they suggest that even without gravity stabilization, a stratified state that does not suffer from atomization could exist. Thus, although previous studies have not reported stratified flow, it could occur -- perhaps in a small passage heat exchange device at a very inopportune time.

Figure 5 indicates that atomization occurs at sufficiently high rotation rates. The waves that occur in this range are irregularly-spaced large-amplitude waves. Our preliminary work has not allowed us to clearly discern the mechanism behind the formation of these waves and the subsequent atomization phenomenon because we need more light intensity to get sufficient video resolution. However there is no doubt that atomization occurs from the large solitary waves whose amplitude and separation can be precisely controlled by the experiment.

Figure 4 shows the cross-section another geometry that we have constructed specifically to demonstrate the mechanism of atomization. The channel is 1 cm high by 14 cm wide by 2.3 m long. The concurrent oil-water channel flow is operated so that the oil-water interface is imaged directly from the top. The oil and water have a curved interface and the oil is confined to a portion of the top wall. We have been able to get some dramatic video of oil droplets being formed by shearing water. When the water shear is significant, large semi-periodic waves form and travel along the interface. Figure 7a shows that if the shear is still higher, the crest becomes elongated. Figure 7b shows the later stage of the snap-off process. In this experiment, the oil waves are completely surrounded by water, they are not touching the top wall. For this geometry a shear instability must initiate the waves, growth is probably caused by a Bernoulli effect, and the actual pinch off by a combined capillary and shear instability. The size of the drop is determined by the size of the streamer from the crest. Note that even if the geometry of the base flow is parallel, such as in Woodmansee's experiment, drops will still be sheared from fingers of liquid because the waves that occur at very high shear have significant transverse variation; there will never be wide sheets of liquid sheared from the crests of waves. Thus our demonstration experiment is close to the general system that will be studied.

A final preliminary experiment is intended to directly probe the behavior of waves that are the precursors of solitary waves. The ultimate intention of our work is to actively control these waves. In the two-layer Couette cell, the initial transition from a flat film is supercritical and in agreement with linear and weakly nonlinear theory (Sangalli et al., [8]). Figure 8 shows a sample experiment where a weak oscillatory component is added to the steady rotation. The oscillation amplitude is 0.25 cm and the frequency is 6 Hz. It is seen that either with or without oscillation a supercritical transition occurs. The oscillation in this experiments and others that we have tried destabilizes the waves. This is consistent with the argument that the oscillation is adding energy to the flow which causes more wave growth.

## DISCUSSION

Figure 5 shows that atomization is a likely consequence for a flow at sufficient shear. However the non monotonic behavior indicates that onset of atomization is not a simple function of shear rate. Further, no attempt was made to quantify the extent of atomization. Figure 7 shows that it will be crucial to incorporate the mechanism into procedures for predicting atomization rates. The atomization process involves instability and growth of waves on the base state and then a further instability of the large wave structure. The formation of solitary or roll waves, commonly associated with atomization, and the waves of figure 7 are certainly governed by nonlinear process that are presently understood only for very simple model equations (e.g., see [9]).

Development of a complete understanding of the atomization process will take advances on a number of fronts. Figure 8 shows an example of our efforts in the weakly- nonlinear region where we are using oscillations to better

understand the wave growth and saturation mechanism. Although we have not yet found a region where waves are stabilized, theories suggest that certain ranges of oscillations should depress wave formation. We hope this will ultimately lead to wave control that could alter pressure drop or atomization.

## ACKNOWLEDGMENTS

This work has been supported by the NASA Microgravity Science and Applications Division under grant number NAG3-1398.

## REFERENCES

1. D. E. Woodmansee and T. J. Hanratty, Chem. Eng.Sci., 24 (1969) 299-307.
2. P. B. Whalley, G. F. Hewitt and J. Terry, UKAEA Report, AERE-R9389 (1969).
3. L. B. Fore and A. E Dukler, submitted AIChE J. (1994).
4. S. A. Schadel and T. J. Hanratty, Int. J. Mult. Flow, 15 (1989) 893-900.
5. C. -A. Peng, L. A. Jurman, and M. J. McCready, Int. J. Mult. Flow, 17, (1991) 767-782.
6. J. C. Dallman, J. E. Laurinat and T. J. Hanratty, Int. J. Mult. Flow, 10 (1984) 677-690.
7. J. C. Asali, G. W. Leman and T. J. Hanratty, Physicochemical Hydro. 6, (1985) 207-221.
8. M. Sangalli, C. T. Gallagher, D. T. Leighton, H. -C. Chang and M. J. McCready, Phys. Rev. Let. 75, (1995) 77-80.
9. H. -C Chang, Annual Review of Fluid Mech., 26 (1994) 103-136.
10. M. J. McCready and H. -C. Chang, Chem. Eng. Comm., 141-142, (1996) 347-358.
11. L. A. Jurman, S. E. Deutsch and M. J. McCready, J. Fluid Mech., 238 (1992) 187-219.

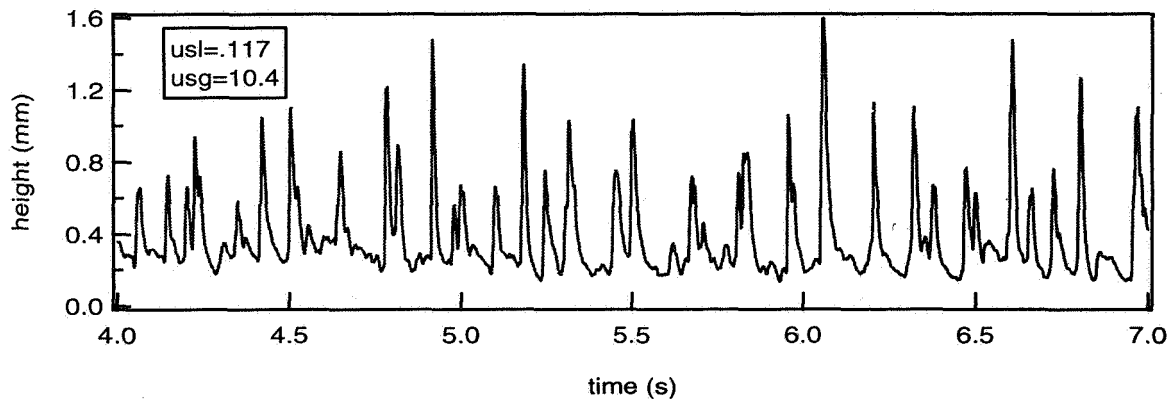


Figure 1. Wave tracings for air-water in a 1.27 cm pipe under  $\mu$ -g. Data from NASA Lewis Lear jet flights supervised by A. E. Dukler.

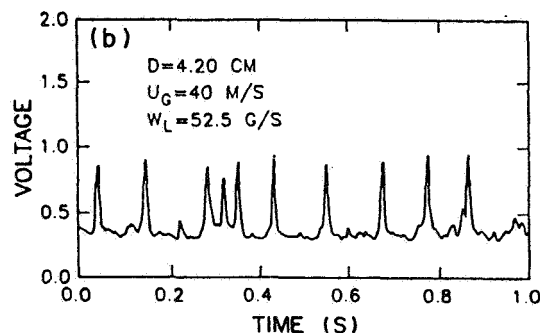


Figure 2. Wave tracings in vertical annular flow by Schadel and Hanratty (1989)

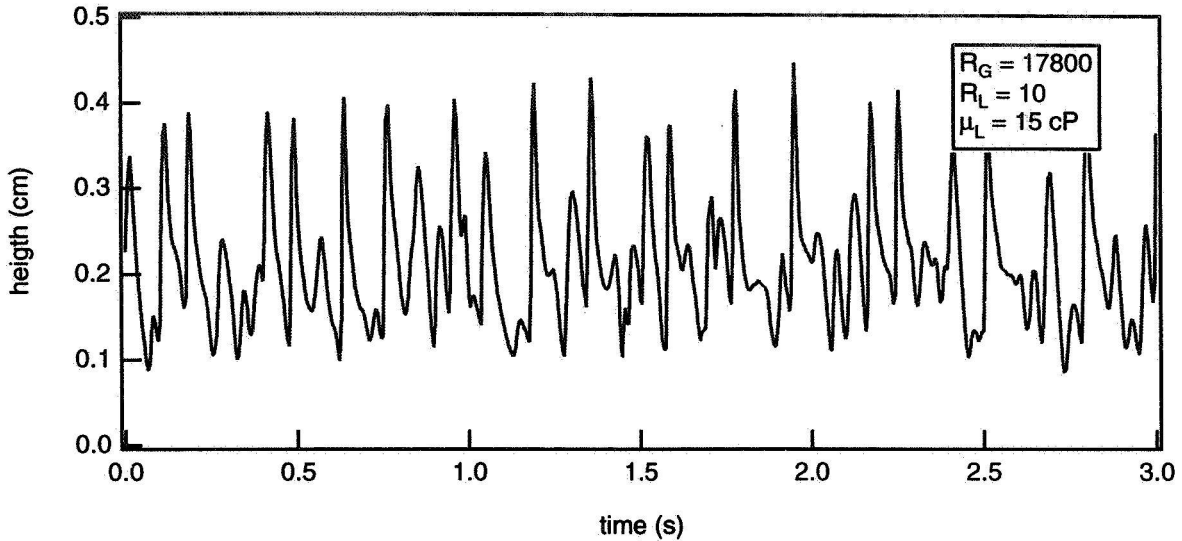


Figure 3. Solitary waves in a horizontal gas-liquid flow in earth gravity

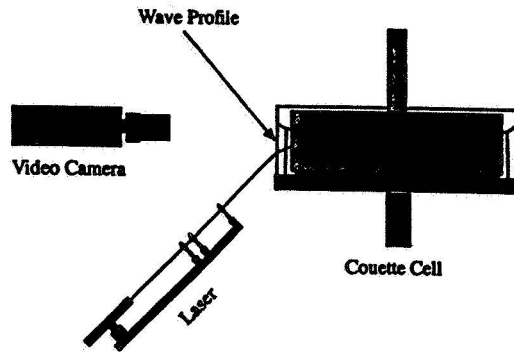


Figure 4. Two-layer Couette experiment with horizontal laser shown.

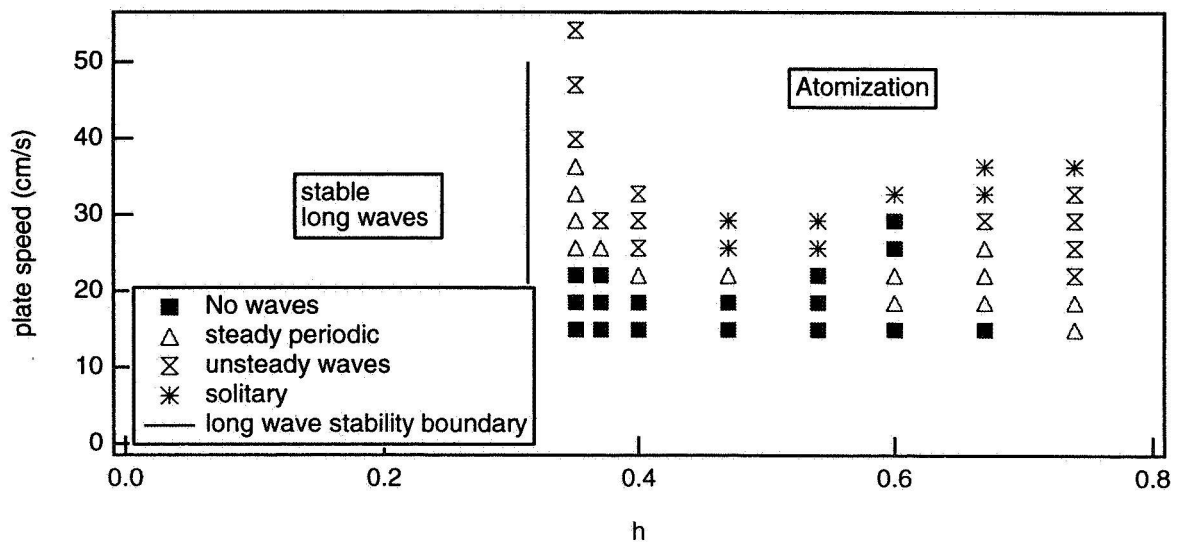


Figure 5. Wave regime map for the two-layer Couette experiment. Atomization occurs at high rotation rates.

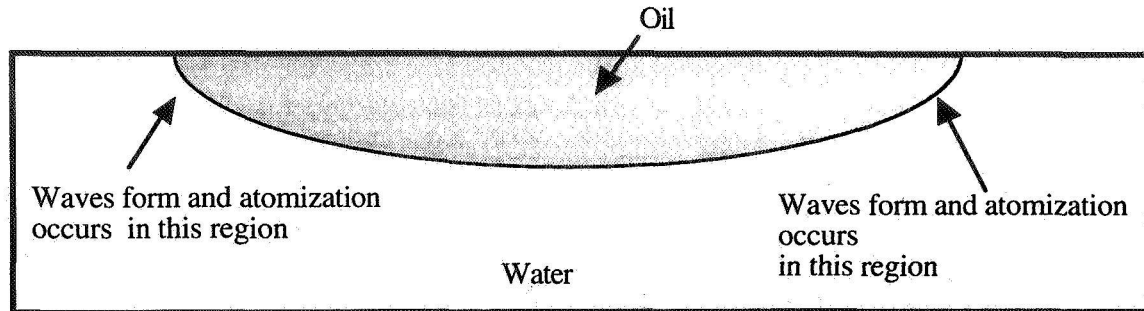


Figure 6. Cross section of cocurrent oil-water flow that demonstrates the mechanism of atomization.

Figure 7a.  
Large wave in  
oil water flow

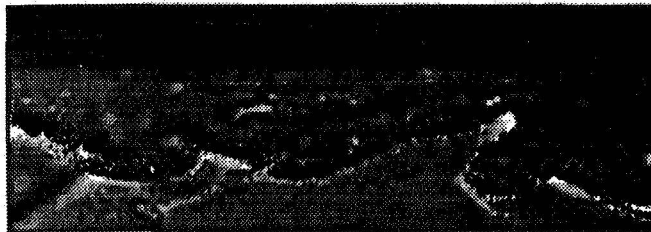


Figure 7b.  
Late stages of  
liquid removal  
from wave crest

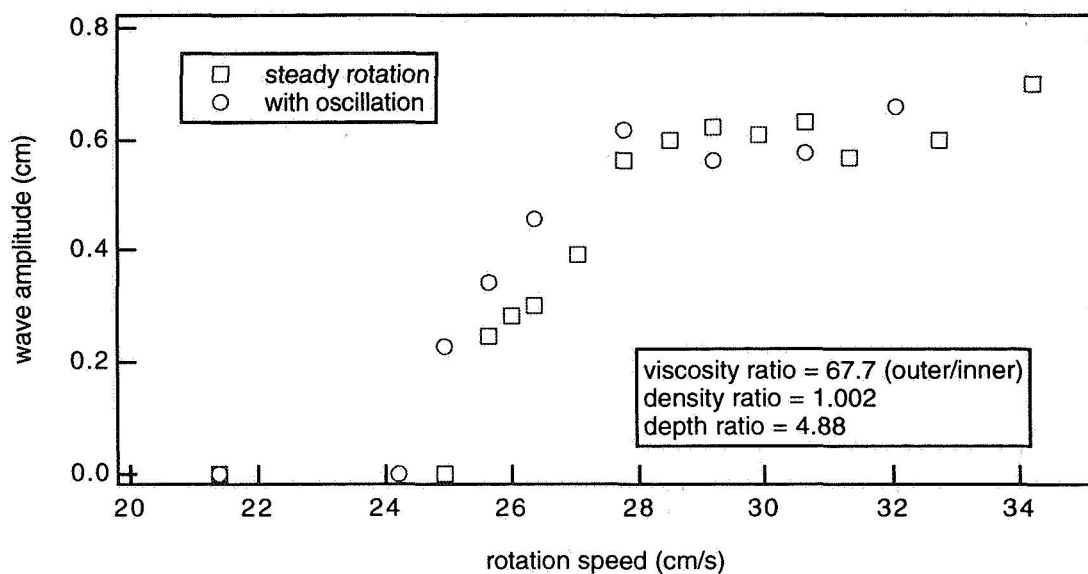
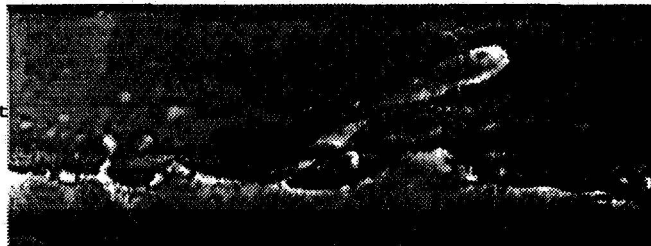


Figure 8. Wave amplitude as a function of rotation rate. Weak oscillation slightly destabilizes the waves.

# OBSERVATIONS OF GAS-LIQUID FLOWS THROUGH CONTRACTIONS IN MICROGRAVITY

John McQuillen  
NASA Lewis Research Center  
21000 Brookpark Road  
Cleveland, OH 44135

## ABSTRACT:

Tests were conducted for an air-water flow through two sudden contractions aboard the NASA DC-9 low gravity aircraft. Flow rate, residual accelerations, void fraction, film thickness, and pressure drop data were recorded and flow visualization at 250 images per second were recorded. Some preliminary results based on the flow visualization data are presented for bubbly, slug and annular flow.

## INTRODUCTION:

Studies of gas-liquid flows have been conducted by the nuclear and petroleum industries for many years. The influence of gravity on gas-liquid flows has been demonstrated many times by simply changing the orientation of the flow direction with respect to gravity. Changes in the flow regime, as well as the liquid film thickness and void fraction, have been documented for changing the angle between the gravity vector and the flow direction for as little as  $0.25^\circ$ .

Gas-liquid flows in reduced gravity have many space-based applications<sup>2</sup>, and also have been studied for many years with the earliest studies by Evans<sup>3</sup>. More recent studies by Dukler, et. al.<sup>4</sup>, Colin et. al.<sup>5</sup>, Huckerby and Rezkallah<sup>6</sup>, Kamp et al.<sup>7</sup>, Bousman and Dukler<sup>8</sup>, Bousman and McQuillen<sup>9</sup>, Hill and Best<sup>10</sup>, Colin and Fabre<sup>11</sup>, Colin et al.<sup>12</sup>, have focused on flow within straight cylindrical conduit. These studies have been conducted on aircraft flying low gravity trajectories and have revealed that the flow patterns, or flow regimes, are axi-symmetric because of the greater impact of surface tension forces in the slower flows and the lack of stratification caused by the reduced influence of buoyancy forces.

These studies have found that for gas-liquid flows in a reduced gravity environment, there are three flow regimes: Bubbly, slug, and annular. Bubbly flow consists of small gas bubbles suspended within a continuous liquid phase. Slug flow consists of cylindrical-shaped bubbles with a spherical nose surrounded peripherally by a thin liquid film and separated by liquid slugs. The liquid slugs and thin liquid film may or may not contain smaller gas bubbles. The annular flow regime consists of a thin liquid film on the wall that surrounds a gas core. Waves of liquid are transported across the thin liquid film and may generate liquid droplets which are suspended within the gas core and eventually deposited back into the liquid film.

Similar flow regimes exist for vertical upflow and downflow in a normal gravity, and these flow regimes are also axi-symmetric. However, the presence of gravity induces density-driven shear forces that affects the behavior of the flow and the phenomena being observed. This is apparent when comparing the bubbly to slug flow transition for vertical flow in normal gravity with microgravity conditions because the lack of density driven shear permits bubble coalescence to occur much easier. It should also be noted that for the slug and annular flow regimes, the liquid film in normal gravity vertical upflow will reverse its direction, rising with passage of a liquid slug or roll wave and then slowing, stopping and falling between slugs or waves. For vertical downflow, the liquid film may slow, but never stops. For slug and annular flow in microgravity, the liquid film will slow and sometimes completely stop between slugs and roll waves depending on the frequency of the slugs and roll waves.

Most studies have focused on flow through straight conduit; however, there have been several normal gravity studies of flow through fittings that result in changes in the conduit geometry. Usually, these studies of flow through fittings have centered on determining the pressure drop through the fitting. Techniques to predict the pressure drop are usually compared against either a homogenous model or empirical models based on experimental data. To determine the pressure drop, the homogenous model uses the single phase correlations with an averaged gas and liquid density and a liquid viscosity. Tests were conducted aboard the NASA Lewis Research Center's DC-9 Microgravity Aircraft using the DC-9/KC-135 Two Phase Flow Rig to examine the behavior of gas-liquid flows through a sudden contraction.

## EXPERIMENTAL HARDWARE AND TESTING:

An instrumented Plexiglas test section was installed in the DC-9/KC-135 rig described by McQuillen, et. al<sup>13</sup>. A Plexiglas test section, illustrated in Figure 1, consisting of four measurement locations was integrated into the rig. Two of these locations consisted of only pressure taps, while the other two locations consisted of pressure taps and conductivity probes. The conductivity probes were used as liquid film thickness probes and void fraction probes, similar to those described by Bousman (1995).

From the mixer to the contraction, the test section diameter was 2.54 cm. Two different size test sections and contractions were fabricated and test: 1.27 and 1.90 cm. The contraction consisted of three Plexiglas blocks that were fabricated. The first block was the inlet piece which into which a 2.54 cm diameter hole was drilled for the flow. At one end of the block, a hole was drilled and tapped to accommodate a straight thread fitting. The inlet Plexiglas tubing was fed through the fitting into the block. The remaining two blocks were similar in construction except that each of the blocks accommodated an o-ring for sealing against the block with the 2.54 cm diameter hole and that the hole diameters were either 1.27 or 1.90 cm.

The NAC HSV-500 high speed video system was used to record images of the contraction, both upstream and downstream at the contraction. The dual camera option for the video system was utilized, with the second camera focusing on the internals of the gas-liquid system.

Tests were conducted aboard the NASA DC-9 Reduced Gravity Aircraft. Air was used as the gas phase, and either water or a water-surfactant mixture was used as the liquid phase. Flow was initiated during the low gravity portion of the trajectory and the test duration was from 15 to 20 seconds.

## RESULTS:

Currently, only the flow rate and video data have been reviewed. From the video data, observations were made about the behavior of the flow as it passed through the contraction.

As bubbly flow entered the contraction, there was no significant amount of coalescence among finely dispersed bubbles. Larger spherical bubbles would become Taylor bubbles as their diameters were confined by the contraction. If one considers the critical void fraction transition criteria first proposed by Dukler (1988) and assumes no slip,

$$\frac{U_{LS}}{U_{GS}} = \frac{1 - \alpha}{\alpha}$$

or that proposed by Colin (1991) which was based on a drift-flux approach,

$$\frac{U_{LS}}{U_{GS}} = \frac{1 - C_o \alpha}{C_o \alpha}$$

Where  $U_{LS}$  and  $U_{GS}$  are the superficial liquid and gas velocities,  $C_o$  is the slip ratio and  $\alpha$  is the critical void fraction. Even though the superficial velocities are increasing as the flow progresses from the larger to the smaller diameter tubes, the ratio does not change. If there are large bubbles in the inlet, the transition occurs not because of coalescence in the contraction, but because of squeezing these large spherical bubbles, see Figure 2, that had probably coalesced from finer bubbles significantly upstream of the contraction.

For slug flow conditions, there were several interesting observations. First, at higher liquid flow rates, there was the generation of waves in the Taylor bubble as it passed through the contraction. For the 1.27 cm. diameter contraction, a significant amount of liquid bridging occurred. This liquid bridging, or snapoff as defined by Roof<sup>14</sup>, is unstable and would collapse downstream. At lower liquid flow rates, the bridging would not occur. Apparently, this bridging may be a mechanism for the thin liquid films around the Taylor bubbles to reach some suitable thickness as the Taylor bubble moves through the contraction.

The axisymmetric shape of the Taylor bubble tails as they passed through the contraction would typically become non-axisymmetric as it would slosh from side to side. The wobbling was responsible for axial bubble coalescence if there was a bubble, either spherical or Taylor, that was very closely trailing the wobbling tail. This coalescence would only occur if the trailing bubble was separated by a very thin fluid layer from the leading bubble prior to entering the contraction. It is questionable about whether it is the wobbling tail itself that is responsible for the axial coalescence, or if it is that the trailing bubble is actually traveling faster through the contraction than the leading bubble.

Within the field of view of the camera, long liquid slugs would not totally breakdown into the roll waves as the slugs passed through the contraction. As the liquid slugs become thinner at higher gas flow rates, there was some penetration of the gas bubble into the liquid slug, however, the field of view was very limited. Zhao and Rezkallah<sup>15</sup> proposed a flow regime transition criteria based upon critical gas phase Weber Numbers which are defined as

$$We_{GS} = \frac{\rho_G U_{GS}^2 D}{\sigma}$$

Where  $\rho_G$  is the gas phase density and  $\sigma$  is the surface tension. A critical Weber Number of 1 was used for the transition between either bubbly or slug flow regime and frothy slug-annular, and a critical Weber Number of 20 was used for the transition between frothy slug-annular and annular flow. By substituting mass flow rate for the superficial velocity, the Weber Number can be redefined as

$$We_{GS} = \frac{16 \dot{m}_{GS}^2}{\rho D^3 \sigma}$$

As can be seen, there is a significant diameter effect on the necessary flow rate to attain a critical Weber Number.

Slug-annular and annular flow through the contraction resulted in significant roll wave generation in the contraction, particularly when slugs, or large liquid waves, entered the contraction. The roll wave generation in the contraction would continue until the time that there was either no or very little liquid motion in the annular film upstream of the contraction. Preliminary estimates of the liquid film motion, which were made by measuring entrained bubble velocities within the liquid film were less than 40 cm/s. Typical roll wave velocities range from 2 to 5 m/s.

While it is not uncommon to observe liquid film rupture and drainage in microgravity both in straight conduit and the contractions, occasionally a gas phase vena contracta was observed. In the first instance, this dryout actually occurred in a finely-dispersed bubbly flow. Gas bubbles would become entrained in the vena contracta increasing the size of the dryout. Periodically the dryout would "shed" a gas bubble and thus decrease the size. In the second case, as Taylor bubbles passed through the contraction, a gas pocket would be trapped within the vena contracta, see Figure 3. Large spherical bubbles or Taylor bubbles would dislodge the dryout.

#### **FUTURE PLANS:**

Analysis of the void fraction and liquid film thickness data both upstream and downstream of the contraction needs to be completed. It is hoped that by examining this data with respect to previously collected straight tube data for 1.27 and 1.90 cm tube diameters, that a model can be developed with regards to the flow development as it flows down the test section. In addition, the evolution of liquid slugs and roll waves as they pass through the contraction needs further analysis.

It appears that the transition from bubble to slug flow does not occur because of coalescence but by squeezing the bubbles. Additional tests in the bubbly flow regime, particularly near the transition to the slug flow regime will verify this.

Additional studies are planned for flow through sudden expansions. Some preliminary work was conducted in the NASA LeRC 2.2 second Drop Tower with slug flow entering an expansion of a 0.95 to 1.27 cm tube (3:4 Diameter Ratio) and a 0.95 to 2.54 cm tube (3:8 Diameter Ratio). Significantly different behaviors were observed. For the 0.95 to 1.27 cm. tube expansion, as slug flow entered the expansion, the cylindrical bubbles would shrink in the axial direction and expand radially. For the most part, the mechanism for transitioning from slug to bubbly flow was that cylindrical bubbles would shrink enough axially not to be considered a cylindrical bubble. Because of the relatively low flow rates, these cylindrical bubbles that became large spherical bubbles were not sheared into smaller bubbles. Figure 4 is an illustration of slug flow entering an expansion with this diameter ratio.

For the initial tests conducted with the 0.95 to 2.54 cm tube expansion, the two phase flow was initiated in normal gravity. The test section on this drop test rig was aligned horizontally. Most of the wall of the expanded area was dry. In normal gravity, as the two phase flow entered the expanded area, the liquid would project out into the area and fall onto the bottom of the test section and flow out. There were not much, if any, gas bubbles entrained in the liquid film flowing along the bottom of the test section. The flow regime in the expanded region during the normal gravity startup was stratified.

Upon the release of the test rig and the start of the free-fall or microgravity period, the flow resembled that depicted in Figure 5 and was of a two phase jet. The flow did not expanded radially to fill the available flow area as it had done for the 3:4 diameter ratio expansion. Similar to the small diameter expansion ratio, the cylindrical bubbles would shrink axially and expand radially as they entered the expanded region. However, the liquid for the most part did not wet the walls of the expansion. The gas in the large bubbles were separated from the gas in the expanded area by a thin liquid film.

For both the contractions and the expansions, tests in vertical upflow and downflow in normal gravity are planned.



Title: (BUBB1.TIF)  
Creator: HiJaak for Windows 1.0  
CreationDate: 06/07/96 12:24:17

Title: (BUBB2.TIF)  
Creator: HiJaak for Windows 1.0  
CreationDate: 06/07/96 12:16:19

Title: (BUBB3.TIF)  
Creator: HiJaak for Windows 1.0  
CreationDate: 06/07/96 12:25:07

Title: (BUBB4.TIF)  
Creator: HiJaak for Windows 1.0  
CreationDate: 06/07/96 12:25:24

Title: (BUBB5.TIF)  
Creator: HiJaak for Windows 1.0  
CreationDate: 06/07/96 12:25:37

**Figure 2: Bubble to Slug Flow**

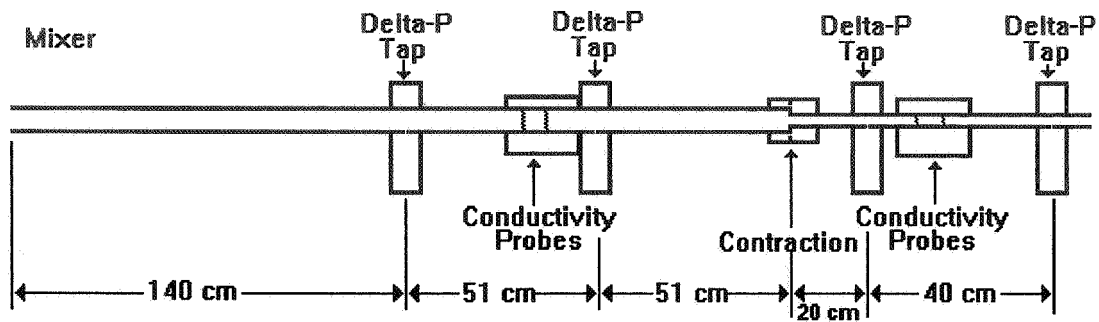


**Figure 1: Schematic of test section**

Title: (SLUGDRY.TIF)  
 Creator: HiJaak for Windows 1.0  
 CreationDate: 06/10/96 08:01:19

Title: (SLUGDRY3.TIF)  
 Creator: HiJaak for Windows 1.0  
 CreationDate: 06/10/96 08:01:43

Title: (SLUGDRY5.TIF)  
 Creator: HiJaak for Windows 1.0  
 CreationDate: 06/10/96 08:02:08

**Figure 3: Wall Dryout Downstream at Contraction After Taylor Bubble Passage**

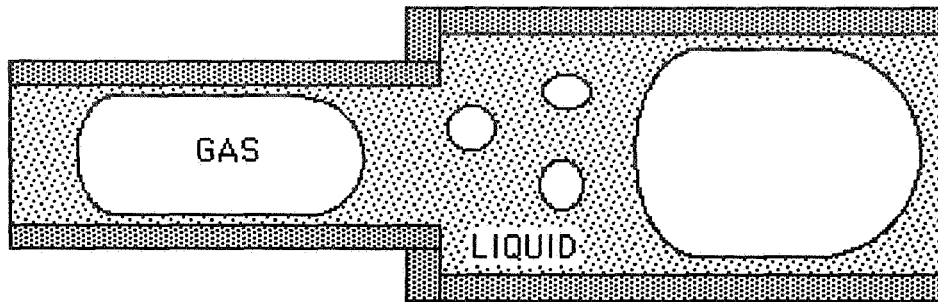


**Figure 4: Microgravity Slug Flow through a 3:4 Diameter Ratio Expansion**

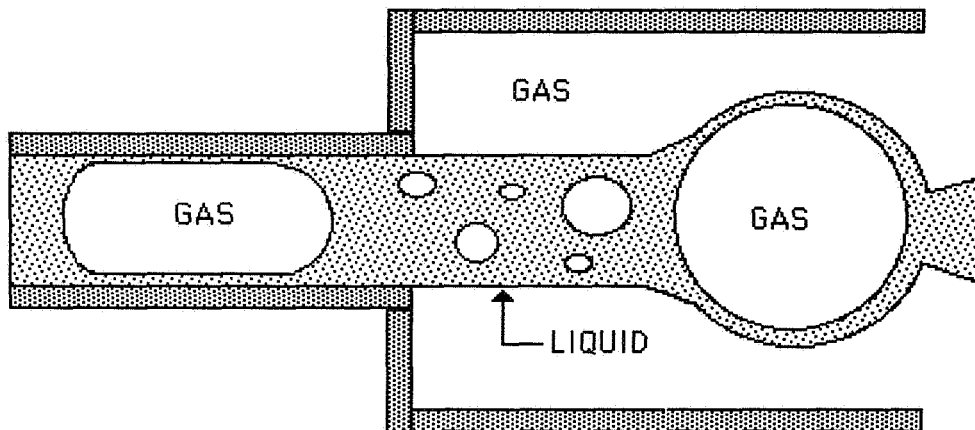


**Figure 5: Microgravity Slug Flow through a 3:8 Diameter Ratio Expansion**

## REFERENCES:

- <sup>1</sup> Barnea, D. "A Unified Model for Predicting Flow-Pattern Transitions for the Whole Range of Pipe Inclinations," *International Journal of Multiphase Flow*, Vol. 13, No. 1, pp. 1-12, 1987.
- <sup>2</sup> Swanson, Theodore D., Juhasz, Al, Long, W. Russ, and Ottenstein, Laura, "Workshop on Two-Phase Fluid Behavior in a Space Environment," *NASA Conference Publication 3043*, 1989.
- <sup>3</sup> Evans, David G., "Visual Study of Swirling and Nonswirling Two-Phase Two Component Flow at 1 and 0 Gravity," *NASA Technical Memorandum X-725*, August 1963.
- <sup>4</sup> Dukler, A. E., Fabre, J. A., McQuillen, J. B., and Vernon, R. W., "Gas-Liquid Flow at Microgravity Conditions: Flow Patterns and Their Transitions," *International Journal of Multiphase Flow*, Vol. 14, No. 4, pp. 389-400, 1988.
- <sup>5</sup> Colin, C., Fabre, J., and Dukler, A. E., "Gas Liquid Flow at Microgravity Conditions I. Dispersed Bubble and Slug Flow," *International Journal of Multiphase Flow*, Vol. 17, No. 4, pp. 533-544, 1991.
- <sup>6</sup> Huckerby, C.S. and Rezkallah, K.S. "Flow Pattern Observations in Two-phase Gas Liquid Flow in a Straight Tube under Normal and Microgravity Conditions," *Proceedings of the National Heat Transfer Conference*, San Diego, CA July 1992, American Institute of Chemical Engineers (1992)
- <sup>7</sup> Kamp, A., Colin, C., Fabre, J., "Bubbly flow in a pipe: influence of gravity upon void and velocity distributions", *Proceeding of the 3rd World Conference on Experimental Heat Transfer, Fluid Mechanics and Thermodynamics*, Honolulu, USA, 1418-1424, October 1993.
- <sup>8</sup> Bousman, W. S. and A. E. Dukler, "Studies of Gas-Liquid Flow in Microgravity: Void Fraction, Pressure Drop and Flow Patterns," *Proceeding of the 1993 ASME Winter Meeting, New Orleans, LA., Fluid Mechanics in Microgravity Session*, AMD-Vol. 174/FED-Vol. 175, December 1993.
- <sup>9</sup> Bousman, W. S. and McQuillen, J. B., "Characterization of Annular Two-Phase Gas-Liquid Flows in Microgravity," *Second Microgravity Fluid Physics Conference*, Cleveland, Ohio, *NASA CP 3276*, June 21-23, 1994.
- <sup>10</sup> Hill, Wayne S. and Best, Frederick R., "Microgravity Two-Phase Flow Experiment and Test Results," *SAE Technical Paper Series 911556*, presented at the 21st International Conference on Environmental System in San Francisco, California, July 15-18, 1991.
- <sup>11</sup> Colin, C., Fabre, J. "Gas-liquid pipe flow under microgravity conditions: influence of tube diameter on flow patterns and pressure drops," *Adv. Space Res.*, 1995.
- <sup>12</sup> Colin, C. Fabre, J., McQuillen, J. "Bubble and Slug Flow at Microgravity Conditions," *Chem. Engng. Comm.*, Vols. 141-142, pp 155-173, 1996.
- <sup>13</sup> McQuillen, J. B., Neumann, E. S, and Shoemaker, J. M., "Two-Phase Flow Research Using The Dc-9/Kc-135 Apparatus" *NASA Technical Memorandum 107175*, May 1996.
- <sup>14</sup> Roof, J. G. "Snapoff of Oil Droplets in Water-Wet Pores," *Society of Petroleum Engineers Journal*, Vol. 10, No. 1, pg 85, March 1970.
- <sup>15</sup> Zhao, L. and Rezkallah, K. S., "Gas-Liquid Flow Patterns at Microgravity Conditions," *International Journal of Multiphase Flow*, Vol. 19, pp. 751-763, 1993.

# Stability of Wavy Films in Gas-Liquid Two-Phase Flows at Normal and Microgravity Conditions

V. Balakotaiah

Department of Chemical Engineering, University of Houston, Houston, Texas 77204-4792

S. S. Jayawardena

NASA Lewis Research Center, Cleveland, OH 44135

## Abstract:

For flow rates of technological interest, most gas-liquid flows in pipes are in the annular flow regime, in which, the liquid moves along the pipe wall in a thin, wavy film and the gas flows in the core region. The waves appearing on the liquid film have a profound influence on the transfer rates, and hence on the design of these systems. We have recently proposed and analyzed two boundary layer models that describe the characteristics of laminar wavy films at high Reynolds numbers (300-1200). Comparison of model predictions to 1-g experimental data showed good agreement. The goal of our present work is to understand through a combined program of experimental and modeling studies the characteristics of wavy films in annular two-phase gas-liquid flows under normal as well as microgravity conditions in the developed and entry regions.

## 1. Introduction

It is well known that for conditions of technological interest, there are three major types of flow regimes observed for gas-liquid flows in pipes at microgravity. At low gas flow rates, a 'bubbly flow' pattern, in which, small gas bubbles are uniformly distributed in the liquid, is obtained. Increasing the gas flow rate leads to 'slug flow'. This flow pattern is characterized by large bullet shaped gas bubbles separated by liquid slugs. Increasing the gas flow rate further leads to the 'annular flow' regime in which, the liquid moves along the pipe wall in a thin, wavy film and the gas flows in the core region. A large fraction of gas-liquid flows of practical interest under normal as well as microgravity conditions fall in the annular flow regime.

Experiments have shown that in the annular flow regime, the waves appearing on the liquid film have a profound influence on the transfer of heat, mass and momentum in these systems. Neglecting the wavy nature of the film can seriously underestimate the transfer rates. For example, the heat and mass transfer rates into the liquid may be enhanced by 100 to 300% in the presence of the waves as compared to the flat film case.

Our recent work focussed on the simplest form of the annular flow regime in which the liquid film falls under gravity through either a stagnant or an upward moving gas stream (causing interfacial shear). Fig.1 shows the experimentally measured film thickness profile for a freely falling film at a liquid flow rate of practical interest.

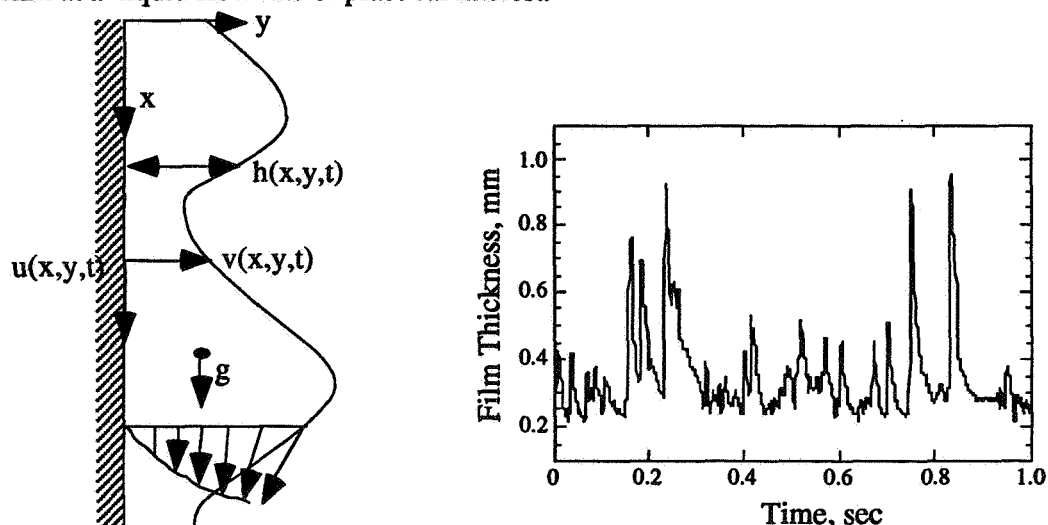


Fig.1: Schematic of a free falling film and experimentally measured film profile at  $Re = 600$

The liquid film surface consists of a series of large waves accompanied by an array of wavelets of smaller amplitude and length which exist between these large waves. The large waves are steeper in the front and slope more gradually in the back with slopes not exceeding ten degrees. The amplitude of these large waves can be two to three times the mean film thickness and they carry a large fraction of the total mass flow. As shown above, the wave amplitude and spacing display a chaotic behavior similar to that observed in many lower dimensional deterministic models. It is speculated that the large waves contain stagnation points and recirculating regions which enhance the transport rates.

A major goal of our work is to develop predictive models for wavy films occurring in gas-liquid annular two-phase flows (as well as other applications) at normal and microgravity conditions and validate them with experimental data. We summarize here our recent results and outline the work in progress.

## 2. Boundary Layer Models for Wavy Films:

We have formulated two boundary layer models that are suitable for the description of laminar wavy films under normal gravity conditions [1]. The first model is the Kapitza's boundary layer model [2], which, for a two-dimensional film is given by the equations

$$\frac{Du}{Dt} = -\frac{1}{\rho} \frac{\partial p}{\partial x} + g + v \frac{\partial^2 u}{\partial y^2}; -\infty < x < \infty, 0 < y < h, t > 0 \quad (1)$$

$$\frac{\partial p}{\partial y} = 0 \quad (2)$$

$$\frac{\partial u}{\partial x} + \frac{\partial v}{\partial y} = 0 \quad (3)$$

$$u = v = 0 \quad @ \ y = 0 \quad (4)$$

$$\frac{\partial u}{\partial y} = 0; \ v = h_t + u h_x; \ p - p_0 = -\sigma h_{xx} \quad @ \ y = h \quad (5)$$

This model is based on the assumptions that the pressure in the film is independent of  $y$ , the tangential stress condition is the same as that for the Nusselt film and the normal stress condition includes only surface tension effect. This model is analyzed in some detail and it is shown that it is adequate for describing the statistics of large amplitude waves at high Reynolds numbers (in the range 300-1200). However, it is found that the model has one serious deficiency, i.e. it predicts negative wall shear stress at the front of a large wave on a free falling film. In addition, it cannot predict large waves with peak to substrate ratio exceeding 3 (observed in experiments).

We extended the Kapitza's model to include pressure variations across the film as well as higher order viscous terms in the  $x$ -momentum equation and tangential and normal stress boundary conditions. This *new second order boundary layer model* for a free falling film is described by the equations

$$\frac{\partial u}{\partial t} + u \frac{\partial u}{\partial x} + v \frac{\partial u}{\partial y} = -\frac{1}{\rho} \frac{\partial p}{\partial x} + g + v \left( \frac{\partial^2 u}{\partial y^2} + \frac{\partial^2 u}{\partial x^2} \right); -\infty < x < \infty, 0 < y < h, t > 0 \quad (6)$$

$$\frac{\partial p}{\partial y} = \rho h_{xx} u^2 \quad (7)$$

$$\frac{\partial u}{\partial x} + \frac{\partial v}{\partial y} = 0 \quad (8)$$

$$v = h_t + u h_x \quad \text{at } y = h(x, t) \quad (9)$$

$$\frac{\partial u}{\partial y} + \frac{\partial v}{\partial x} - h_x^2 \frac{\partial u}{\partial y} + 4 h_x \frac{\partial v}{\partial y} = 0 \quad \text{at } y = h(x, t) \quad (10)$$

$$p - p_0 - 2\mu \left( \frac{\partial v}{\partial y} - h_x \frac{\partial u}{\partial y} \right) + \sigma h_{xx} = 0 \quad \text{at } y = h(x, t) \quad (11)$$

$$u = v = 0 \quad \text{at } y = 0 \quad (12)$$

It should be noted that this model is much easier to solve than the full two-dimensional Navier-Stokes equations because of the highly simplified y-momentum balance equation. To assess the accuracy of the models, we compared the linear stability results for the three models, i.e. the boundary layer model (hereafter referred to as BL model), the second order boundary layer model (SBL model) and the complete set of two-dimensional Navier-Stokes equations.

We note that the Nusselt solution

$$p - p_0 = 0; v_0 = 0; h_0 = 1; u_0(y) = \frac{3}{2} (2y - y^2), 0 < y < 1$$

satisfies all three models (after transforming to dimensionless form using the Nusselt velocity  $u_N$  and film thickness  $h_N$  to scale the variables). Linearization of the model equations around this solution and simplification gives the Orr-Sommerfeld equation [3].

$$F'''' - 2\alpha^2 F'' + \alpha^4 F - \frac{i\alpha Re}{4} (u_0 - Ce)(F'' - \alpha^2 F) + \frac{i\alpha Re}{4} u_0'' F = 0 \quad (13)$$

$$F(0) = 0; F'(0) = 0; F(1) = Ce - \frac{3}{2}; F''(1) + \alpha^2 F(1) = 3$$

$$F'''(1) - 3\alpha^2 F'(1) - \frac{i\alpha^3 Re We}{4} + \frac{i\alpha Re}{4} F'(1)(Ce - \frac{3}{2}) = 0, \quad (13a)$$

where

$$\alpha = \pi \frac{h_N}{\lambda}, \quad Ce = Ce_r + iCe_i, \quad Ce = \frac{V_w}{u_N}, \quad (13b)$$

and  $V_w$  is the (dimensional) velocity of waves of infinitesimal amplitude. The function  $F(y)$  represents the perturbation of the dimensionless streamfunction,  $We$  and  $Re$  are the Weber and Reynolds numbers defined by

$$We = \frac{\sigma}{\rho u_N^2 h_N} = 3^{1/3} 4^{5/3} Ka Re^{-5/3}; \quad Re = \frac{4\Gamma}{v} = \frac{4u_N h_N}{v},$$

$$u_N = \frac{gh_N^2}{3\nu}, \text{ (Nusselt average velocity)}; \quad Ka = \frac{\sigma}{\rho g^{1/3} \nu^{4/3}}.$$

(The Kapitza number,  $Ka$ , has a value of 3371 for pure water at 25°C). The corresponding eigenvalue problem for the boundary layer model may be shown to be

$$F''' - \frac{i\alpha Re}{4} (u_0 - Ce) F' + \frac{i\alpha Re}{4} u_0' F - \frac{i\alpha^3 Re We}{4} = 0 \quad (14a)$$

$$F(0) = 0; F'(0) = 0; F(1) = Ce - \frac{3}{2}; F''(1) = 3, \quad (14b)$$

while the second order boundary layer model gives

$$F''' - \alpha^2 F' - \frac{i\alpha Re}{4} [(u_0 - Ce)F' - u_0' F] - \frac{i\alpha^3 Re}{4} [1.2 + We - 0.45y^5 + 2.25y^4 - 3y^3] - 2\alpha^2 F'(1) = 0 \quad (15a)$$

$$F(0) = 0; F'(0) = 0; F(1) = Ce - \frac{3}{2}; F''(1) + \alpha^2 F(1) = 3. \quad (15b)$$

We compare in Fig. 2a the linear growth rate curves of the two boundary layer models with that of the Navier-Stokes equations (Orr-Sommerfeld analysis) for  $Re = 600$  and  $Ka = 3371$  (water). As can be expected intuitively, the curves nearly coincide for small wave numbers ( $0 < \alpha < 0.4$ ) but the boundary layer model deviates significantly from other two for  $\alpha$  values exceeding 0.5. Fig. 2b compares the critical wave numbers (on the neutral stability curves) for Reynolds numbers in the range zero to 1200 and  $Ka = 3371$ . From these comparisons, it may be concluded that the second order boundary layer model which includes pressure variations across the film and higher order viscous effects approximates the linear growth rate characteristics much better than the standard boundary layer model in the entire range of the wave numbers.

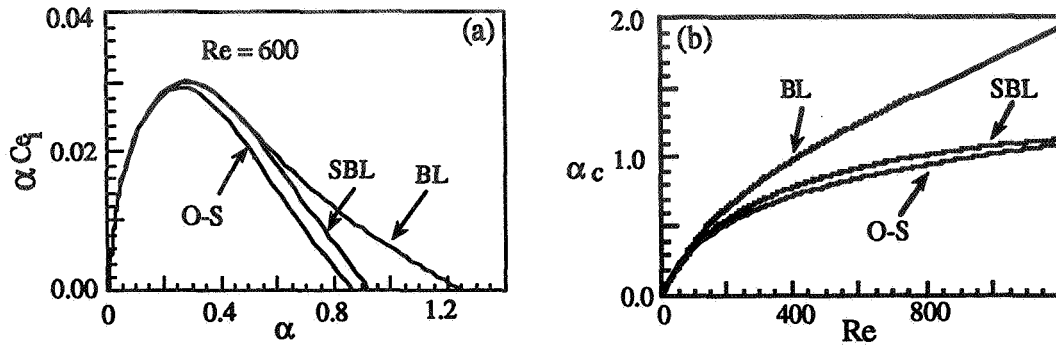


Fig. 2: Comparison of the linear growth rate and the neutral stability curves of the boundary layer models to the full Orr-Sommerfeld equation ( $Ka = 3371$ ).

### 3. Numerical Solution Method and Comparison with Experimental Data:

In order to solve the boundary layer models, we developed a numerical scheme based on the boundary collocation method. We expand the streamfunction in the normal coordinate  $y$ ,

$$\Psi(x, y, t) = a_0(x, t) + a_1(x, t)y + \sum_{i=2}^n a_i(x, t)b_i(y) \quad (16)$$

where  $y$  is measured from the wall,  $x$  is the streamwise coordinate and  $t$  is time. The coefficients in the series,  $a_i(x, t)$ , are determined from both boundary and integral conditions as described elsewhere [3,4].

The polynomial expansion for  $\Psi(x, y, t)$  is truncated at six terms to insure resolution of effects due to steep gradients, inertial forces, etc. The novel form of polynomial functions

$$b_i(y) = \left( y^i - \frac{(2i-3)y^{i+1}}{(2i-1)h} \right); \quad i = 2, 3, 4, 5 \quad (17)$$

is used. Here,  $b_2(y)$  corresponds to parabolic flat film solution while  $b_3$ ,  $b_4$  and  $b_5$  account for deviation from parabolic profile and non-zero values for  $\frac{\partial u}{\partial y}$  at the interface and the normal stress at the free surface. Determination of the coefficients  $a_i(x, t)$  follows from substituting the assumed form of the streamfunction into various boundary and integral conditions. This procedure reduces (discretizes) the model equations into a set of coupled equations in  $x$  and  $t$ . These discretized evolution equations describe the film profile from wave inception to an asymptotic state, but their solution requires heavy computational efforts, because they are a set of highly nonlinear partial differential equations (of parabolic type) in  $t$  and  $x$  ( $-\infty < x < \infty$ ). Results analogous to the linear stability are not available to describe the asymptotic form of the fully developed state. A systematic study of the fully developed steady film can be performed by transforming the equations to a traveling wave coordinate and reducing them to a finite dimensional set of ODEs whose behavior is parameterized by the wave celerity  $C_e$ . The computational procedure now requires only an initial condition (a perturbation upon a flat film) and yields the asymptotic behavior of the traveling waves.

A traveling coordinate system moving at a steady, nondimensional wave celerity  $C_e$  with respect to a stationary reference frame is defined by

$$z = x - C_e t \quad (18)$$

where  $z$ ,  $x$  and  $t$  are physical coordinates normalized by  $h_N$  and  $h_N/u_N$ , respectively. We use this transformation and assume that motion with respect to the  $z$  coordinate is steady to reduce the partial differential equations into a set of six nonlinear ordinary differential equations.

We now present results of our simulations for the second order model and compare them with experimental data. We show in Fig.3 the computed film profiles at  $C_e = 1.7457$  (below this



Ce value, no bounded solutions exist). Large waves with ripples in the front are interspersed between a random array of smaller waves. The streamlines for two large waves having peak to substrate ratio of 2.8 and 3.6, respectively are shown in Fig. 4. These streamlines clearly show the region of recirculation and how it increases with increasing peak to substrate ratio. This recirculation explains the experimentally observed heat and mass transfer enhancement in the presence of large waves. A comparison of the numerical results for the two models shows that both models predict the same qualitative behavior, but the second order model gives larger peak/substrate ratio and overcomes the main deficiency of the boundary layer model, i.e. negative wall shear stress at the front of large waves. We have calculated the flow fields in the film using the second order model and found that both  $\frac{\partial p}{\partial y}$  and  $\frac{\partial u}{\partial y}$  are not zero at the front of the large waves.

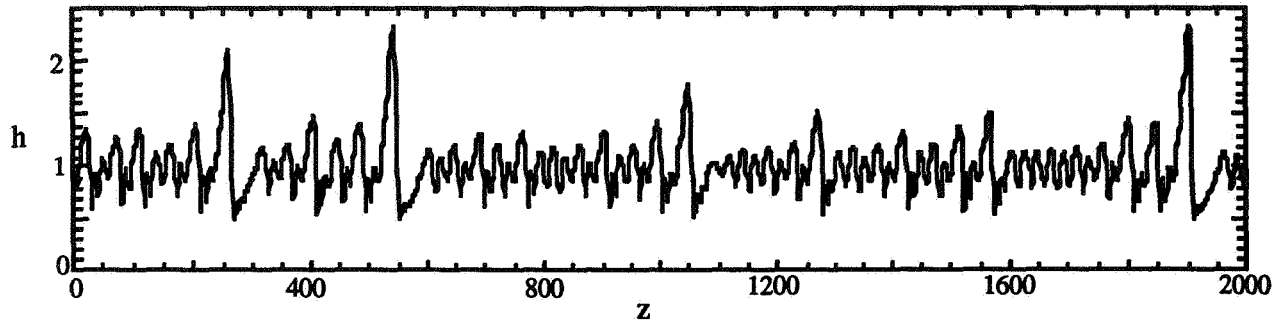


Fig. 3: Computed film profile for the second order boundary layer model and  $Re = 600$ ,  $Ce = 1.7357$  and  $Ka = 3371$ .

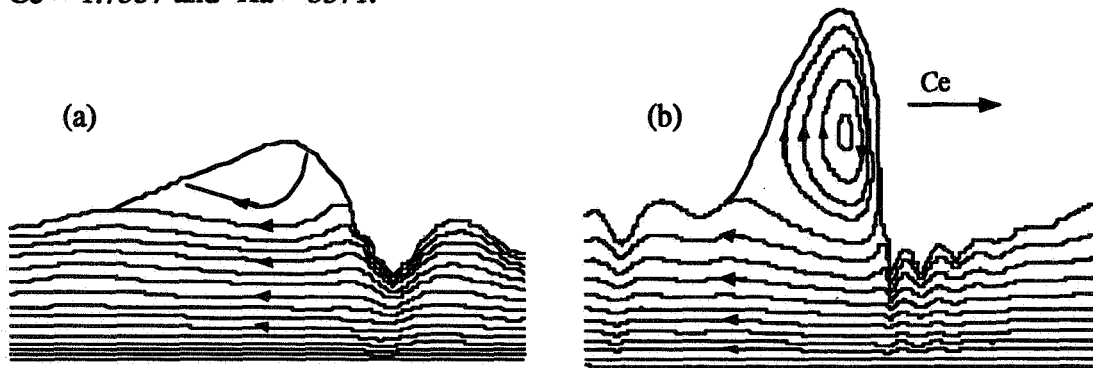


Fig.4: Computed streamlines under the large waves (in moving coordinate system) for peak thickness to substrate thickness ratio of 2.8 (a) and 3.6 (b).

We have compared the noise insensitive statistical properties of experimentally measured stationary wavy film profiles with the numerical results generated by integrating the model equations. The simulated waveforms are those obtained for the second order boundary layer model for a limiting wave celerity below which no bounded wave profiles exist. It was found that these chaotic waveforms have a structure similar to the naturally occurring (experimentally measured) traveling waves. Using the model equations, we have computed the wave celerity at inception (Hopf bifurcation), the celerity below which no bounded solutions exist, the rms film thickness, probability density function, power spectral density function and the mean and rms wave amplitudes using standard techniques. Fig. 5 shows good agreement between the computed and experimental values for celerity and rms film thickness. Similar agreement was also found for other statistical measures now shown here. The model equations show strong evidence that the wavy film is an example of a deterministic system displaying lower dimensional chaos.

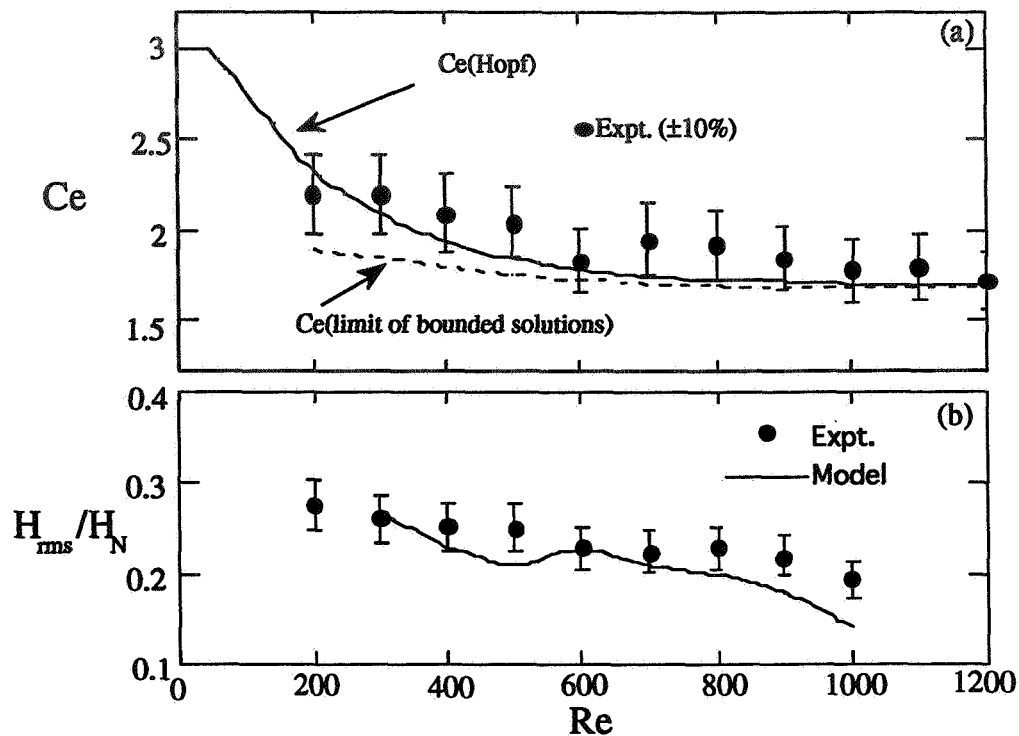


Fig. 5: Comparisons of computed wave statistics of chaotic film profiles ( $Ka=3371$ ) with measured waveforms ( $Ka=3350$ ). (a) Wave Celerity; (b) Wave rms film thickness.

#### 4. Conclusions:

The second order boundary layer model presented here is the only model presently available in the literature to predict the behavior of wavy films at high Reynolds numbers. The initial results on the comparison of the model predictions to experimental data are very encouraging. However, the model needs further testing and refinement.

The major goals of our current work are (i) extension of the boundary layer models to predict the wavy film behavior in the presence of gas flow under normal and microgravity conditions (ii) experimental and modeling studies on two-phase developing flows to determine the evolution of the wavy structure on the gas-liquid interface and the length of the entry region of annular flows (iii) measurement and analysis of experimental data on pressure drop in fully developed two-phase annular flows in microgravity and (iv) to study the transition between annular and slug flow regimes, especially in microgravity.

#### 5. References

- [1]. L.-Q. Yu, F. K. Wasden, A. E. Dukler and V. Balakotaiah, " Nonlinear Evolution of Waves on Falling Films at High Reynolds Numbers", *Physics of Fluids*, 7, 1866-1902 (1995).
- [2]. Kapitza, P. L. & Kapitza, S. P., "Wave flow in thin layers of a viscous fluid". *Zh. Exper. Teor Fiz.* 19,105(1949); also in *Collected Papers of P. L. Kapitza Vol. II*, Macmillan, NY (1964).
- [3]. Brauner, N., Moalem-Maron, D., "Modeling of Wavy flow in inclined thin films". *Chem. Eng. Sci.*, 38, 775 (1983).
- [4]. L.-Q. Yu, " Studies of Wavy Films in Vertical Gas-Liquid Annular Flows", Ph.D Thesis, University of Houston, Houston, Texas (1995).

**Acknowledgements:** This work described here was supported by the National Aeronautics and Space Administration under grants NAG9-854 and NAG3-1840.

## **Experimental and Analytical Study of Two-Phase Flow in Microgravity**

D. Abdollahian and J. Quintal  
S. Levy, Inc.  
Campbell, California

J. Zahm  
San Jose State University  
San Jose, California

J. McQuillen  
NASA Lewis Research Center  
Cleveland, Ohio

### **ABSTRACT**

Design of the two-phase flow systems which are anticipated to be utilized in future spacecraft thermal management systems requires a knowledge of two-phase flow and heat transfer parameters in reduced gravities. A program has been initiated by NASA to design a two-phase test loop and to perform a series of experiments to study the effect of gravity on the Critical Heat Flux (CHF) and onset of instability. The test loop is also instrumented to generate data for two-phase pressure drop. In addition to low gravity airplane trajectory testing, the experimental program consisted of a set of laboratory tests which were intended to generate data under the bounding conditions (+1g and -1g) in order to plan the test matrix. One set of airplane trajectory tests has been performed and several modifications to the test set-up have been identified. Preliminary test results have been used to demonstrate the applicability of the earth gravity models for prediction of the two-phase friction pressure drop.

### **INTRODUCTION**

Two-phase systems are generally designed for operation under the nucleate boiling regime in order to utilize the high heat transfer characteristics of two-phase flow. Operation of these systems beyond the critical heat flux may lead to a sudden jump in the surface temperature due to reduction in the heat transfer coefficient (film boiling regime). This temperature is usually above the melting point of many materials; the maximum surface heat flux is also called the limit of stable burnout. In many practical situations, two-phase components fail at heat fluxes well below the limit of stable burnout. This is due to hydrodynamic instabilities which result in sudden reductions in flow and burnout at smaller heat fluxes. Knowledge of stable burnout limit and the onset of hydrodynamic instability is crucial for operation of any two-phase loop. At this stage, it is generally concluded that considerably more data, preferably under long duration steady-state conditions, is needed to complete and confirm the design approaches for application to reduced gravities.

Operation of the boiling systems under CHF is an important design limitation. Most industrial systems are designed based on empirical CHF correlations which are valid under narrow range of operating conditions. Unlike the early attempts in developing generalized CHF correlations based on the pool boiling mechanisms, it is now believed that critical heat flux depends on the flow pattern at CHF. In Ref. (1) the existing CHF models and correlations are divided into three categories based on the underlying assumption for the flow regime at CHF. Due to the effect of gravity on the flow pattern and void distribution, applicability of the existing CHF models at reduced gravities should be evaluated.

There are a number of static and dynamic instability mechanisms which should be considered for the design of two-phase systems operating in reduced gravities. Instabilities resulting from the interaction of the system components and the characteristic of two-phase flow are particularly important for systems operating under a forced convective mode of heat transfer.

Excursive or Ledinegg instability can be analyzed by static equations and it occurs under operating conditions which result in an increase in two-phase pressure drop with decreasing flow rate. For an imposed external pressure drop under such conditions, operation at more than one flow rate is possible. Small disturbances may lead to a shift from one flow rate to another (usually lower) in a non-recurring manner and burnout may occur. Using a force balance on a boiling channel, it can be shown that the system will be stable if the slope of the pressure drop-flow rate characteristic is less negative than the imposed external supply.

When several two-phase channels are used in parallel, the variations in the flow rate through one channel do not affect the overall pressure drop. This situation is similar to imposing a constant pressure drop across a single channel which is prone to excursive instability. In such cases, severe maldistribution of flow could occur which would lead to burnout.

The most common form of dynamic instability encountered in industrial systems at earth gravity is density wave oscillation. This mechanism is due to multiple feedback between the flow rate, vapor generation rate, and pressure drop within the boiling channel. This form of instability is usually analyzed with linear system methods and frequency domain stability methods. However, due to availability and the speed of present day computers, time domain analysis of the non-linear conservation equations is being used more frequently.

It is known that the pressure drop-flow characteristic and the void distribution, which are affected by the gravity level, strongly influence the stability limits. Although the stability criteria are system dependent, it is expected that for a given flow rate and power input to a boiling channel, the instability limits will be different under reduced gravities.

The main objective of this research activity was to design a test loop and perform a series of airplane trajectory experiments in order to generate data for the critical heat flux under reduced gravity conditions and to investigate the effect of gravity on hydrodynamic instabilities. The data will be used to evaluate the existing CHF models and, if necessary, develop applicable physically based models.

## **EXPERIMENTAL APPARATUS**

The schematic of the test loop is shown in Figure 1. It is a closed loop consisting of a magnetically coupled gear pump, a bladder type accumulator, a preheater section, a heated and an adiabatic test section, and a tube-in-tube condenser. The test system was packaged on two Learjet racks and used to perform a series of normal gravity laboratory tests, as well as one set of airplane trajectory tests aboard the NASA DC9 airplane, (2). The measurements included the fluid temperature and pressure, surface temperature of the test section, flow rate, and pressure drop across the adiabatic section. Turbine flow meters were used to measure the total flow rate and the flow rate in the test section leg. Flush mounted flow through thermocouples were used to monitor the fluid temperature.

The heated section consisted of a 5/16-inch OD stainless steel tube with nickel-chromium heater wire wrapped over a 14-inch length of its mid-section. Measured test section surface temperatures were used to sense sudden rise in the wall temperature which indicates CHF or drop in flow rate due to instabilities. Ribbon type thermocouples were used to monitor the wall temperature in gaps between the wires and at the end of the heated section. Upon sensing a large temperature rise, the heater power was shut down and the test section path was flooded. The adiabatic section is 22 inches long and is intended for two-phase pressure drop measurements over a region where the vapor phase content is known. Differential pressures across two sections of the adiabatic tube were measured and recorded. A purge

system was used to flow subcooled liquid through the differential pressure transducer sense lines prior to recording.

Modularity of the test loop was one of the criteria in design and selection of the components. This loop can serve as a test bed for generating data for other two-phase flow parameters as well as evaluating the performance of loop components.

Freon 114 was used as the working fluid due to its low heat of vaporization and lower saturation pressure at ambient temperatures. The test variables were power level which ranged between 300 and 1000 watts, and flow rate which varied from 0.05 to 0.8 GPM. Due to phase-out of chlorofluorocarbons, a new working fluid is being evaluated which will be used in the future flights.

The earth gravity tests were intended for system checkout and to establish the test matrix and operational procedure of the reduced gravity tests. These tests were performed with vertical up (+1g) and vertical down (-1g) configurations in order to bound the reduced gravity conditions. The first set of airplane trajectory tests provided preliminary results on the two-phase pressure drop characteristics and indicated the need for modifications in design and operating procedures.

## RESULTS AND DISCUSSION

As mentioned earlier, only one set of airplane tests has been completed so far. These tests indicated the need for several design and operational changes and it was decided to modify the loop to implement the changes and accommodate the replacement of the working fluid before the next series of flights. Several observations were made which are briefly discussed below.

1. Comparison of the tests with downflow and upflow configurations shows that CHF occurs at nearly the same power at low flow rates. As the flow rate is increased, CHF occurs at higher powers for upflow configuration. This could be due to the differences in void distribution for upflow and downflow. At low flow rates the exit quality is so high that there is probably no difference between the upflow and downflow conditions. Measured critical heat flux vs. the test section mass flux for the laboratory tests is shown in Figure 2.
2. Imposing a fixed pressure drop across the test section by opening a bypass valve resulted in a lower critical heat flux for vertical upflow. These tests were performed at fixed powers and by gradually lowering the flow rate. There were significant flow oscillations close to CHF which resulted in sudden surface temperature rise. However, the existence of a parallel channel seemed to make the downflow configuration more stable and the test section flow rate had to be substantially reduced to show any surface temperature rise.
3. The packaging of the loop and the procedure for the low gravity testing were developed based on the idea that the 2g acceleration at the start of the low gravity trajectory was directed towards the tail of the aircraft. Therefore, the test section was placed in a horizontal position with flow direction towards the front of the plane (opposite to the assumed gravity vector). This was intended to avoid flow stratification during the 2g portion of the flight which would result in temperature rise along the portion of the test section covered by vapor, and subsequent system shutdown. Actually, most of the gravity vector during the 2g acceleration was towards the floor of the plane which resulted in system shutdown prior to reduced gravity dive. However, a few CHF points at reduced gravities were obtained which will be compared to earth gravity conditions. The test loop is going to be modified and the next series of tests performed with a vertical up configuration to avoid this problem.

Although the preliminary tests provided only a few CHF data points at zero g, there is sufficient data for the two-phase pressure drop which can be used to evaluate the applicability of the earth gravity models. The two-phase friction multiplier is defined by the ratio of two-phase to single-phase liquid pressure drop at the total flow rate. The two-phase multiplier obtained from the measured pressure drop across the adiabatic section was compared to the predicted values by several models including Homogeneous Equilibrium Model (HEM), Friedel correlation (Ref. 3), Chisholm B (4), and Chisholm's fit to Lockhart Martinelli correlation (4). The comparisons given in Figures 3 and 4 show that most of the reduced gravity data can be satisfactorily predicted by HEM or the Friedel correlation. It should be noted that due to existence of stratified flow, the pressure drop at earth gravity with the horizontal test section would have been considerably smaller. Figure 5 shows that HEM and the Friedel correlation predict the vertical upflow data fairly well, except at high qualities where HEM seems to overpredict the two-phase friction multiplier. As shown in Figure 6, the two-phase pressure drop for vertical downflow configuration is underpredicted by HEM. Although the Friedel correlation has been developed from a large data base with vertical upflow configuration, and HEM is appropriate for homogeneous mixture of the phases (bubbly flow), they both seem to predict the reduced gravity pressure drop over a wide range of equilibrium qualities.

Theoretically based CHF models can be categorized based on the underlying mechanism which depends on the type of flow pattern at CHF. One class of models assumes annular flow regime when CHF occurs due to dryout of a liquid film at the wall. Another class of models assumes bubbly or dispersed flow pattern where a vapor film forms at the wall and prevents the liquid from contacting the surface. Models based on both of the above mechanisms should be considered for evaluating the reduced gravity data, as it becomes available. In the meantime, applicability of a correlation which is based on dimensional analysis and has been successfully applied to several fluids is evaluated here. The correlation developed by Katto and Ohno (5) is used to predict the data for vertical up and downflow configurations as shown in Figure 7. Two points which are believed to be CHF at zero g are also shown in this figure. These points were obtained due to reduction in the flow rate which was resulted from system pressure rise at reduced gravities. Generally, CHF is underpredicted by the Katto and Ohno correlation. The reduced gravity data points are close to CHF obtained under vertical upflow configuration, possibly indicating the same type of flow pattern. The model developed in Ref. (6) for annular flow CHF and the Weisman and Pei model for bubble coalescence at CHF will be used as basis for developing a CHF model applicable to reduced gravities.

## REFERENCES

1. Yaniec, J. S., Users Guide for NASA Lewis Research Center DC-9 Reduced-Gravity Aircraft Program, NASA Technical Memorandum 106755, January 1995.
2. Weisman, J., "The Current Status of Theoretically Based Approaches to the Prediction of the Critical Heat Flux in Flow Boiling," Nuclear Tech. Vol. 99, July 1992.
3. Hewitt, G. F. and Hall-Taylor, N., Annular Two-Phase Flow, Pergamon Press, 1970.
4. Chisholm, D., Two-Phase Flow in Pipelines and Heat Exchangers, George Godwin, 1983.
5. Katto, Y. and Ohno, H., "An Improved Version of the Generalized Correlation of Critical heat Flux for the Forced Convection Boiling in Uniformly Heated Vertical Tubes," Int. J. Heat Mass Trans., Vol. 27, 1983.
6. Levy, S., Healzer, J. M., and Abdollahian, D., Prediction of Critical Heat Flux for Annular Flow in Vertical Pipes, EPRI Report NP-1619, 1980.

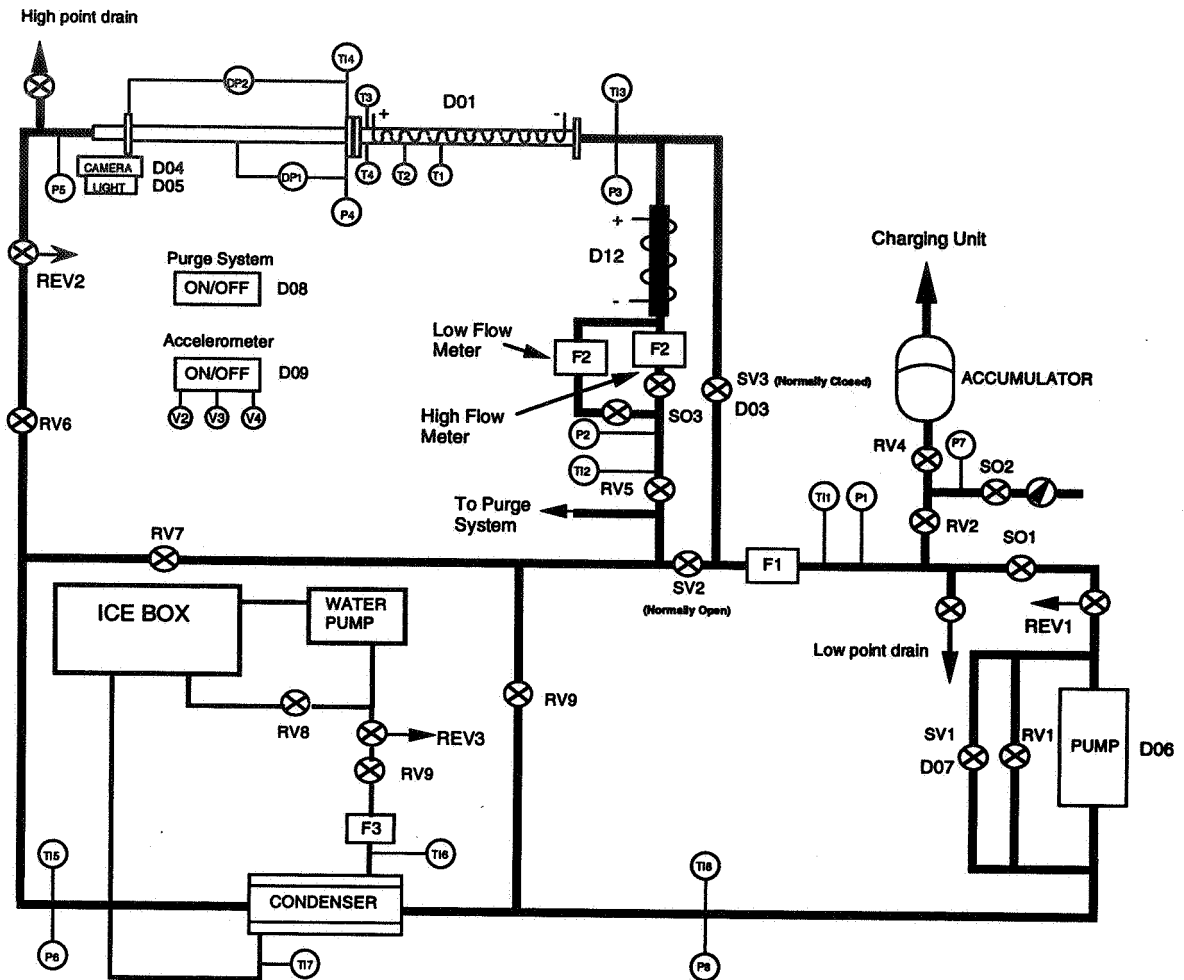


Figure 1 - Test Loop Schematic

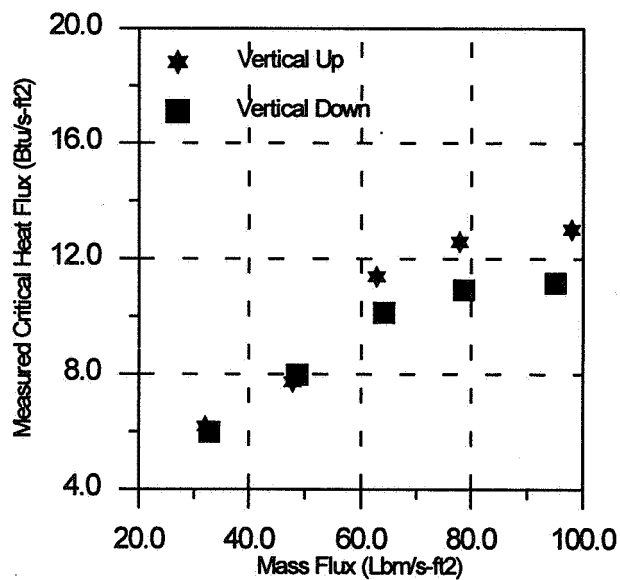


Figure 2. Experimental Critical Heat Flux vs. Mass Flux for Vertical Up and Down Flow Configurations.

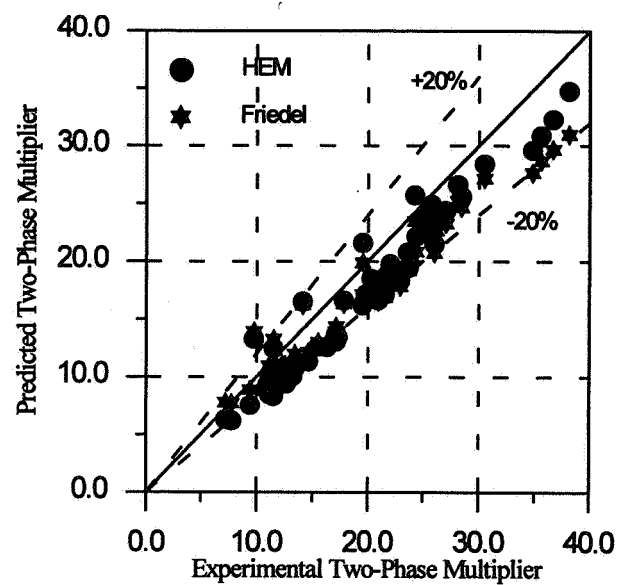


Figure 3. Comparison of the Predicted and Experimental Two-Phase Friction Multiplier Using HEM and Friedel for Reduced Gravity.

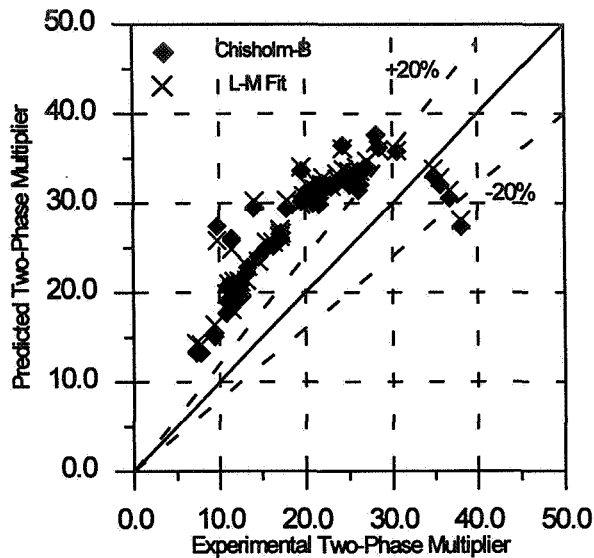


Figure 4. Comparison of the Predicted and Experimental Two-Phase Friction Multipliers Using Chisholm B and Fit to Lockhart-Martinelli for Reduced Gravity.

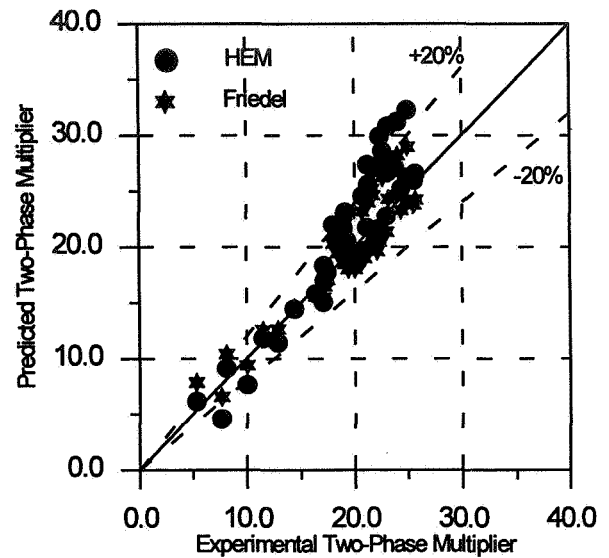


Figure 5. Comparison of the Predicted and Experimental Two-Phase Friction Multiplier Using HEM and Friedel for Vertical Upflow.

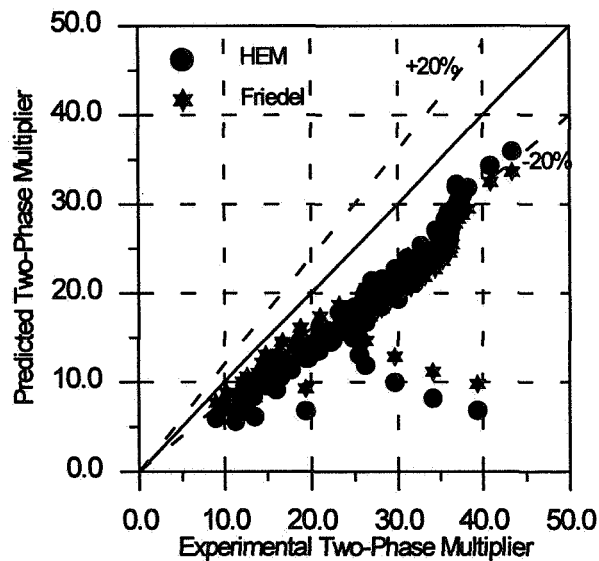


Figure 6. Comparison of the Predicted and Experimental Two-Phase Friction Multiplier Using HEM and Friedel for Vertical Downflow.

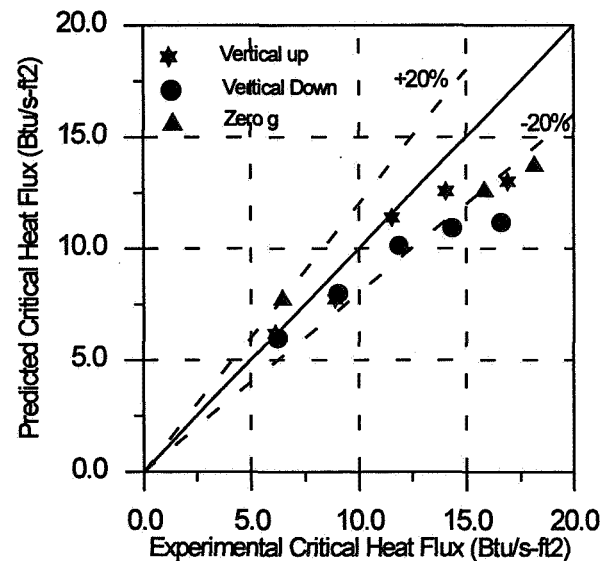


Figure 7. Comparison of predicted and Measured Critical Heat Flux Using Katto & Ohno Model for Vertical Up and Downflow.



# TWO-PHASE ANNULAR FLOW IN HELICAL COIL FLOW CHANNELS IN A REDUCED GRAVITY ENVIRONMENT

by

Edward G. Keshock\*

Chin S. Lin\*\*

## ABSTRACT

A brief review of both single- and two-phase flow studies in curved and coiled flow geometries is first presented. Some of the complexities of two-phase liquid-vapor flow in curved and coiled geometries are discussed, and serve as an introduction to the advantages of observing such flows under a low-gravity environment. The studies proposed -- annular two-phase air-water flow in helical coil flow channels are described. Objectives of the studies are summarized.

## INTRODUCTION

Two-phase liquid/vapor flow occurs in a wide variety of earth applications ranging across the petrochemical, power generation, refrigeration, and aerospace industries. A greater understanding of multiphase systems and flows would be of great practical benefit in terms of the improved design methodology that could be applied to such systems. Even though two-phase flows have been studied extensively under earth gravity conditions, the accuracy of the multiphase predictive and design tools is poor compared to those available for single-phase systems.

The presence of an earth gravitational environment can enormously complicate a two-phase liquid/vapor flow, resulting in a variety of perturbations, instabilities and generally undesirable unsteady features.

The orientation of the flow channel (e.g. horizontal versus vertical) can dramatically change the behavior and characteristics of a two-phase flow in a 1-g environment, contributing further to the difficulty of obtaining an fundamental understanding of two-phase liquid/vapor flow dynamics. Studying two-phase flow systems a low-gravity, or microgravity environment can remove such undesirable, masking flow complications which occur under earth gravity conditions.

Additionally, however, two-phase flow in microgravity conditions occurs in a variety of space system applications. Examples include the transfer of cryogenic fluids, cooling of electronic components, and heat pipe applications. Future applications include the design of the space station components and systems. Consequently, an understanding of two-phase flow under microgravity conditions is necessary to insure accurate design and reliable operation of future space systems.

## LITERATURE REVIEW

### Single Phase Flow

As early as 1927 Dean [1] made a theoretical study of fully developed laminar flow in a curved pipe. He pointed out the existence of a secondary flow set up by the centrifugal forces in the curved geometry (see Fig. 1-(a)). His considerations of dynamic similarity resulted in a parameter  $K = \text{Re}(r/R)^{1/2}$  (which is now called the Dean number), where  $r$  and  $R$  are the tube and coil radii, respectively.

In 1965 and 1967 Mori and Nakayama [2,3] performed an analysis of both fully developed laminar and turbulent flow in curved pipes. Using an approach analogous to that resulting in the Reynolds stress in turbulent flow analyses, they developed a relation between the secondary flow velocities and the stresses caused by the secondary flow. Their analytically obtained formulas for  $f_0/f_s$  for both laminar and turbulent flow agreed well with their experimental results, lending credence to the idea that additional flow resistance in curved geometries is caused by stresses due to secondary flow. Further, the secondary flows caused by centrifugal forces have a stabilizing effect on laminar fluid flow, and delay the transition to turbulence.

---

\* Mechanical Engineering Department, Cleveland State University, Cleveland, OH

\*\* Analox Corporation, 3001 Aerospace Parkway, Brookpark, OH

Ito [4] developed an empirical equation to describe the influence of the ratio of the tube and coil diameters upon the (delayed) transition to turbulent flow. Srinivasan [5] presented an improved empirical equation for the critical Reynolds number, which agrees well with experimental results.

Hart et al [6] proposed an expression for the friction factor of a coiled flow channel as a multiple of that in a straight tube, in terms of the Dean number, for laminar flow, as follows:

$$f_c = f_s \{ 1 + [ 0.090 \text{ De}^{1.5} / (70 + \text{De}) ] \}$$

where  $f_s = 16/\text{Re}$ , and valid for  $\text{Re} < \text{Re}_{\text{crit}}$ , and where  $\text{Re}_{\text{crit}} = 2100[1 + 12(d/D)^{1/2}]$ .

For turbulent flow, White [7], Ito [4], Srinivasan [5] and Mishra [8] have proposed expressions for friction factors for flow in coiled geometries that yield similarly good agreement with experimental results in their applicable ranges. By combining equations proposed for the laminar and turbulent domains, Hart et al [6] introduced a friction factor chart for single-phase fluid flow through curved tubes or helical coils, as presented in Figure 2.

### Two-Phase Flow

Relatively fewer studies of two-phase flows in curved or coiled geometries have occurred. Some of the earliest studies of such flows were by Owahdi, Bell & Crain [9-10], and Banerjee et al [11]. Initially, it was hypothesized that for annular two-phase flow in helically coiled tubes, the induced centrifugal forces should force the liquid onto the outside wall (see Fig. 1-(b)). However, Owahdi et al [9] indicated that his hypothesis was inaccurate since they obtained higher dryout qualities with the coiled tubes than those normally found in straight tubes. Based on these findings, Owahdi et al [9], Banerjee et al [11], and Crain et al [10] hypothesized that secondary flow similar to that shown in Fig. 1-(c) should exist in the gas core of an annular two-phase flow in a helically coiled tube.

For some high quality flows in helical coils, Banerjee [11] reported that at low liquid flow rates, but high gas flow rates, the liquid phase travels along the inside of the tube wall (nearest the coil axis), rather than on the outside wall as might be expected due to centrifugal forces. In other words, a film inversion was observed to occur under some flow conditions, typically of high vapor phase velocity and low liquid phase flow rates.

A more recent study is that of Uddin [12], who developed a model to predict two-phase flow patterns in helically coiled tubes. More recent studies by Yan [13] showed an apparent inadequacy of this map, based upon her studies of air-water and R-12 flow pattern and pressure drop characteristics in upward flows in vertically oriented helical coils of square, rectangular and circular cross-sections. Yan developed a frictional pressure drop correlation for the R-12 flows.

In another relatively recent study Saxena et al [14] studied flow patterns, holdup and pressure drop for air-water flows in vertically oriented helical coils, for upward and downward flows. A model was proposed to predict pressure drop for both upward and downward flows. Most recently, Awwad et al [15] studied flow patterns and pressure drop in air-water flows in horizontally oriented helical coils. They proposed frictional pressure drop multipliers based upon both the Lockhart-Martinelli parameter and the flow rates.

### Microgravity Two-Phase Flow

A rather limited number of studies of two-phase flows have been conducted under low- or micro-gravity conditions. Among the earliest studies were those of Williams et al [16], Keshock et al [17], and Hepner et al [18]. In [16] and [17] flow pattern observations were made of the flow condensation of R-12 in a 2.62 mm dia. x 1.83 m long tube. Hepner et al [18] observed flow patterns and made pressure drop

measurements for air/water flow in a 2.54 cm dia. tube with a length to diameter ratio of only 20. All of these studies were conducted using KC-135 flights to obtain the low-gravity condition.

Dukler et al [19] made flow pattern observations and limited pressure drop measurements of air/water two-phase flow in a 1.27 cm dia. x 1.06 m test section ( $L/D = 83$ ), using a Learjet aircraft. Their principal result was the development of a flow pattern map based upon modeling of the observed flow patterns and their transitions.

Chen et al [20-21] also made flow pattern observations and obtained the most extensive pressure drop data obtained to that time for two-phase R-114 flow in a 1.58 cm dia. x 1.83 m straight tube ( $L/D = 116$ ). A KC-135 aircraft was used to create the low-gravity condition. The measurements were compared with several existing correlations for predicting two-phase pressure drop. The principal result was the development of a new correlation for the prediction of pressure drops in a reduced gravity environment, based upon an annular flow model and using an interfacial friction factor developed from the data [21]. Also, their flow pattern observations were used to modify the Dukler map [20]. (The foregoing studies are representative of the studies of two-phase flow that have been conducted under microgravity conditions. They are not intended to be a totally comprehensive review of such studies, due to restrictions on article length.)

### PROPOSED MICROGRAVITY STUDIES

In the study of two-phase flows, one of the most important measurements and characteristics of interest is that of the pressure drop, whether under 1-g or reduced gravity conditions. However, the length of straight channel required to make accurate pressure drop measurements is relatively large. These length requirements are prohibitive, considering the spatial and geometric restrictions associated with facilities designed for the attainment of low-g environments, e.g. drop towers and aircraft. Consequently, a need exists for accurate and plentiful measurements of two-phase pressure drop for microgravity conditions. The use of a coil geometry in combination with a low-gravity environment offers an opportunity to obtain such accurate measurements, since the physical impediment of inadequate length can be eliminated.

The second major characteristic of interest in two-phase flows is that of the details of the distribution of the phases (i.e. flow patterns), and the transitions from one type of flow pattern to another. In the proposed study, the slug-annular transition will be focused upon, though with the long channel lengths possible in a coiled geometry, the "development" of bubble and slug flows can also be observed.

In the near absence of gravity, the enormous complications in a two-phase flow field created by our normal 1-g earth environment disappear. Instead, the only force akin to a gravitational force would be the centrifugal forces acting on the fluids owing to their centripetal acceleration through the curved flow passage. In effect, the two-phase flow in the extended length of coiled flow channel would be occurring in a fractional gravitational field, directed toward the outer radius of the coil.

It should be observed that the coiled flow path would induce secondary flows within the fluid(s) that are not present in a straight-channel geometry. However, the magnitude of such secondary flows diminishes with larger coil radii, and with smaller fluid velocities; Accordingly, their magnitude can be controlled to some extent by the experimental design. Furthermore, their influence could be established and quantified in comparative tests of straight and coiled channel geometries in ground-based laboratory tests, and perhaps also in aircraft flight tests.

With such comparative tests, a coiled geometry makes it possible to make fundamental measurements and observations of annular two-phase flows in a flow channel of considerable length, such as pressure drop, related interfacial characteristics, and conditions relating to the slug-annular flow regime transition.

## EXPERIMENTAL APPROACH

Only the adiabatic flow of air/water will be studied. Tests will initially be conducted under earth-gravity conditions, i.e. in a conventional test cell. Tests will then be conducted using the low-g environment possible using a DC-9 aircraft, which is capable of providing low-g test intervals of 22 second duration.

It is planned to study flow in both transparent flexible plastic tubing and lengths of stainless steel tubing, all of 3/4" diameter, wound into a helical coil shape of 20" diameter. One 20-ft stainless steel coil will be employed in ground tests to compare with pressure drop measurements in a straight length of 20-ft tubing of the same diameter. Aircraft tests will employ a stainless steel coil of 40-ft length ( $L/D = 640$ ) to insure the most accurate measurement of pressure drop.

Both ground and aircraft tests will utilize a 40' length of 3/4" I.D. flexible transparent tubing wound in a 20" diameter coil to provide accompanying flow visualization information. The test sections will be adapted for installation on an existing two-phase test rig developed specifically for aircraft flight testing.

## PROJECT OBJECTIVES

The primary experimental objectives of the proposed study will be to make (1) accurate measurements of pressure drop and (2) video/photographic observations of details of the two-phase flow dynamics, while operating in a microgravity environment.

In addition to the measurement of two-phase pressure drops, desired measurements to be sought are those of (1) Taylor bubble length, (2) liquid slug length, (3) slugging frequency, (4) bubble size and distribution. Measurements of liquid film thickness and void fraction are not feasible within the coil length, but only in the straight lengths preceding and following the coil.

The primary technical objectives are to:

- (1) Make a comparison/validation study of coil measurements and observations with respect to straight channel flows under 1-g and reduced gravity conditions.
- (2) Use the quantitative and observational data to evaluate the accuracy and validity of two-phase flow maps in predicting two-phase flow regimes and their transitions, especially generalized maps such as developed in [22], where the slug-annular transition is predicted over the entire range of accelerations vectors and magnitudes from earth gravity to microgravity conditions.
- (3) Use the data and observations to evaluate and improve upon the accuracy of two-phase pressure drop correlations in predicting pressure drops for the modified flow patterns associated with low-gravity and microgravity environments.
- (4) Provide data to be used as a basis of understanding for the definition of future flight experiments, ultimately leading to a sound fundamental understanding of two-phase fluid physics.

## REFERENCES

1. "Note on the Motion of Fluid in a Curved Pipe," W. R. Dean, Phil. Mag. 4, pp. 208-212, 1927, Phil. Mag. 5, pp. 637-695, 1928.
2. "Study on Forced Convective Heat Transfer in Curved Pipes (Laminar Region)," Y. Mori and W. Nakayama, Int. J. Heat Mass Transfer, V. 8, pp. 67-82, 1965.
3. "Study on Forced Convective Heat Transfer in Curved Pipes (Theoretical Analysis Under the Condition of Uniform Wall Temperature and Practical Formulae)," Y. Mori and W. Nakayama, Int. J. Heat Mass Transfer, V. 10, pp. 681, 695, 1967.
4. "Friction Factors for Turbulent Flow in Curved Pipes," H. Ito, J. Basic Engineering, Trans. ASME, D81, pp. 123-134, 1959.
5. "Friction Factors for Coils," P. Srinivasan, Trans. Inst. Chem. Engrs., 48, T156-T161, 1970.
6. "Single- and Two-Phase Flow Through Helically Coiled Tubes," J. Hart et al, Chem. Eng. Sci., V. 43, No. 4, pp. 775-783, 1988.
7. "Fluid Friction and Its Relation to Heat Transfer," C. White, Proc. R. Soc., A123, pp. 645-663, 1929.
8. "Momentum Transfer in Curved Pipes," P. Mishra and S. Gupta, Ind. Eng. Chem. Process Des. Dev., V. 18, No. 1, 1979.
9. "Forced Convective Boiling Inside Helically Coiled Tubes," A. Owhadi, K. Bell and B. Crain, Jr., Int. J. Heat Mass Transfer, V. 11, pp. 1779-1793, 1968.
10. "Forced Convection Heat Transfer to a Two-Phase Mixture of Water and Steam in a Helical Coil," B. Crain, Jr. and K. Bell, A.I.Ch.E. Symp. Series, V. 69, No. 131, pp. 30-36, 1973.
11. "Film Inversion of Cocurrent Two-Phase Flow in Helical Coils," S. Banerjee, E. Rhodes and D. Scott, A.I.Ch.E. Jnl., V. 13, No. 1, pp. 189-191, 1967.
12. "A Model to Predict Two-Phase Flow Patterns in Helically Coiled Tubes," A. Uddin, Particulate Phenomena and Multiphase Transport, V. 1, Hemisphere Publ. Co., 1988.
13. "Study of Two-Phase Flow Patterns and Frictional Pressure Drop in Helical and Spiral Coils," A. Yan, M.S. Thesis, Mech. & Aero. Eng. Dept., Univ. of Tenn., Knoxville, TN, 1992.
14. "Flow Regimes, Holdup and Pressure Drop for Two-Phase Flow in Helical Coils," A. Saxena et al, Canadian Jnl. of Chem. Eng., V. 68, No. 4, Aug., 1990.
15. "Flow Patterns and Pressure Drop in Air/Water Two-Phase Flow in Horizontal Helicoidal Pipes," A. Awwad et al, Trans. of ASME, V. 117, pp. 720-726, Dec., 1995.
16. "Development of a Direct Condensing Radiator for Use in a Spacecraft Vapor Compression Refrigeration System," J. Williams, E. Keshock and C. Wiggins, ASME Jnl. of Eng. for Industry, V. 96, pp. 1053-1063, 1973.
17. "An Experimental Study of Flow Condensation Phenomena Under Zero-Gravity Conditions in a Space Radiator System," E. Keshock et al, Proc. Fifth Int. Ht. Tr. Conf., V. 4, pp. 236-240, 1974.
18. "Zero-G Experiments in Two-Phase Flow Regimes," D. Hepner, C. King and J. Littles, ASME Paper 75-ENAS-24, 1975.
19. "Gas-Liquid Flow at Microgravity Conditions: Flow Patterns and Their Transitions," A. Dukler, J. McQuillen and R. Vernon, Int. Jnl. Multiphase Flow, V. 14, No. 4, 1988, pp. 389-400.
20. "Observed Flow Regimes and Pressure Drops of Vapor and Liquid Flow in Adiabatic Piping," I. Chen, R. Downing, R. Parish, E. Keshock, A.I.Ch.E. Sympos. Ser., V. 84, No. 263, pp. 203-216.
21. "Measurements and Correlation of Two-Phase Pressure Drop Under Microgravity Conditions," I. Chen, R. Downing, E. Keshock, M. Alsharif, AIAA Jnl. Thermophysics, V. 5, No. 4, Oct., 1991.
22. "Unified Flow Regime Predictions at Earth Gravity and Microgravity," C. J. Crowley, TN-483, Creare Inc., Hanover, NH, 1993.

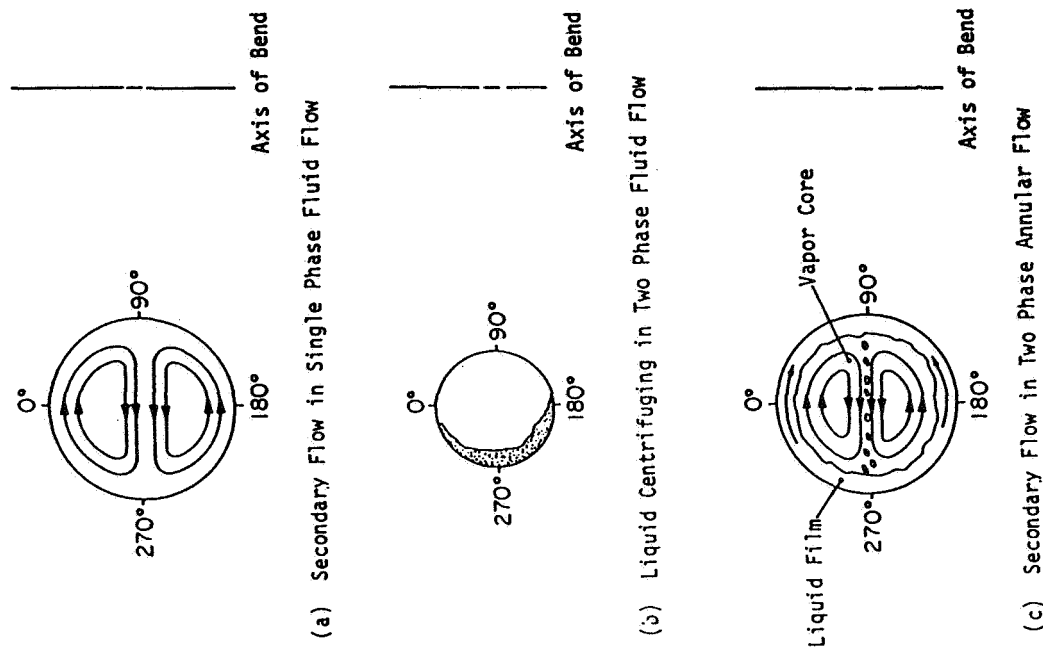


Figure 1. Secondary Flow in Coiled Tubes

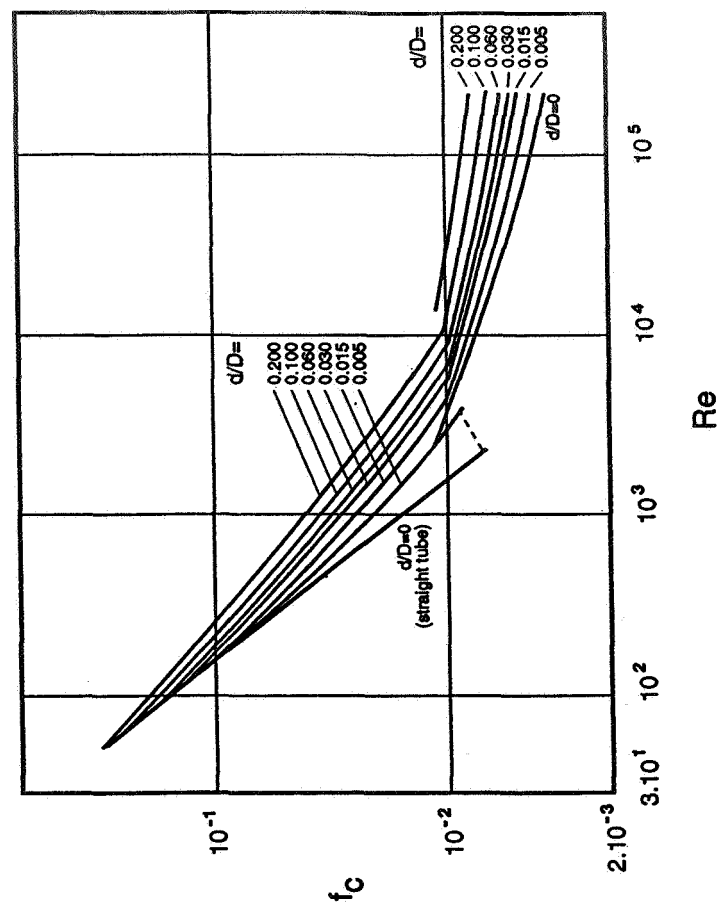


Figure 2. Friction factors for straight tubes and curved or helically coiled tubes (after Hart et al [6]).

# **BUBBLE GENERATION IN A FLOWING LIQUID MEDIUM AND RESULTING TWO-PHASE FLOW IN MICROGRAVITY**

Yasuhiro Kamotani  
Department of Mechanical and Aerospace Engineering  
Case Western Reserve University  
Cleveland, Ohio 44106

## **ABSTRACT**

An experimental and theoretical research program is described herein to study bubble generation in a liquid flow in a pipe under reduced gravity conditions. The objective of the work is to study the bubble size and frequency of the generation and the resulting two-phase flow but it also concerns the fluid mechanical aspects of boiling in forced flow in microgravity. By injecting a gas into a liquid flow in a pipe through a small hole in the pipe wall we will investigate how the bubble expands and detaches from the wall, without involving the complexities of boiling. The experiments will be conducted both under isothermal conditions and with heat transfer from the wall. In the experiments with heat transfer the effect of thermocapillarity on the bubble formation and detachment will be the main subject.

## **INTRODUCTION**

Two-phase systems including gas/liquid and liquid/liquid contacting systems are common phenomena encountered in many space applications, such as spacecraft thermal control systems, propulsion systems, power generation systems, cryogenic transfer and storage systems, life support systems, and other chemical/material process engineering systems. The design of two-phase systems for space applications requires a knowledge of heat- and mass-transfer processes under microgravity. The distribution and size of the dispersed phase are very essential for the analysis of heat and mass transfer, pressure drop and flow pattern in two-phase systems. Therefore, there is a great need to study how the bubble size and frequency can be controlled in microgravity.

Under microgravity conditions, the body force becomes negligible and surface tension effects become more important, thus very large and more spherical bubble or drop formation is expected. For control of bubble size and frequency, an additional force is needed for detachment of the bubble or drop. One practical way to obtain this additional force is to use the drag force of a flowing liquid near a confined solid boundary (such as the wall of a pipe). There have been numerous experimental and theoretical studies of bubble and drop formation in a quiescent continuous phase in normal gravity. In spite of the fact that in most industrial equipment applications, bubbles and drops are formed in the continuous phase moving past nozzles and orifices, the formation of bubbles and drops in a flowing continuous phase has received much less attention. Kim et al. (ref. 1) reviewed available work on the subject. However, all the empirical correlations developed in normal gravity cannot be applied directly to a microgravity environment by simply setting "g" equal to a low value. Therefore, in refs. 1 and 2 we have developed a theoretical model for the process of bubble and drop formation in flowing liquids, applicable for both terrestrial and microgravity environments. The model deals with two different flow systems; a co-flow and a cross-flow system. The model predictions agree well with available experimental results in normal gravity. They also evaluated the effects of the important dimensionless parameters on bubble and drop size in microgravity based on the model. We are currently conducting experiments in microgravity to test the model.

The current work is an extension of the ongoing work and we will study the process of bubble expansion and detachment from a wall surface which is also related strongly to the basic fluid mechanical phenomena involved in

boiling in forced flow. The power demand of spacecraft is expected to increase in the future. The high operating power levels for future space applications require very efficient thermal transport techniques. Two-phase flow systems are considered to be effective in transporting heat in spacecraft where, traditionally, a single-phase flow loop, solid conductor, and heat pipe have been used for thermal management. Two-phase systems take advantage of the heat of vaporization of the cooling liquid. Thus, in order to design efficient two-phase systems for thermal transport we must understand boiling in forced flow in microgravity. A major area of concern deals with how the presence and eventual detachment of vapor bubbles from a solid surface affect heat transfer characteristics in microgravity. Boiling in forced flow is a complex subject and much work is needed to understand the phenomenon. The bubble formation and the detachment from the heating surface during boiling in microgravity are generally quite different from those in normal gravity. Therefore, we will study that aspect of boiling without getting involved directly in the mechanism of boiling.

Another important aspect of boiling in microgravity is that thermocapillarity becomes important under some conditions but the effect of thermocapillarity on boiling in microgravity has not been investigated in detail. Thermocapillarity is usually overwhelmed by buoyancy in normal gravity. However, it is an important driving force for fluid flow in microgravity and we have conducted space experiments on thermocapillary flows (refs. 3 and 4). During boiling the wall is superheated so that the liquid temperature is lower than the wall temperature and there exist interfaces between the liquid and vapor. Then, in the absence of buoyancy, thermocapillary force could become important in the process of bubble generation and detachment. The thermocapillary force is caused by the variation of surface tension along the interface. Since surface tension decreases generally with increasing temperature, the liquid near the interface is pulled toward the colder region, namely away from the wall. The resultant liquid flow near the wall may have an important effect on the bubble behavior.

The thermocapillarity is represented by the dimensionless parameter called surface tension Reynolds number,  $R\sigma = \sigma_T \Delta T D_p / \mu_c v_c$ , where  $\sigma_T$  is the temperature coefficient of surface tension,  $\Delta T$  the overall temperature variation in the flow, and  $v_c$  the kinematic viscosity. Then the ratio of the liquid flow inertia to thermocapillary forces can be expressed as  $Re_p / R\sigma$ . Using the properties of water, the ratio is computed to be about 0.1 for the aforementioned liquid velocity of 10 cm/s and  $\Delta T = 10^\circ\text{C}$ , which means that the thermocapillary flow actually overwhelms the main liquid flow. Therefore, it is very important to consider the effect on boiling in microgravity. Besides, this thermocapillary effect gives us an additional option to control the size of bubbles in other applications. For example, in case where both the liquid and gas velocities cannot be changed easily because of flow rate constraints, the temperature difference between the wall and the liquid can be adjusted to obtain a desired bubble shape.

## DESCRIPTION OF WORK

### Experimental Work

In normal gravity one important dimensionless parameter for bubble generation in a flowing liquid is the Froude number,  $Fr = \rho_c U_{LS}^2 / ((\rho_c - \rho_d)g D_p)$ , where  $U_{LS}$  is the superficial liquid velocity,  $D_p$  the pipe diameter,  $\rho_c$  the liquid density,  $\rho_d$  the density of the gas, and  $g$  gravitational acceleration.  $Fr$  represents the ratio of the inertia forces of the liquid flow to buoyancy. When  $Fr$  is much larger than unity, the inertia dominates over buoyancy and thus the flow and the bubble behavior are essentially the same both in one-g and in microgravity. The difference becomes important when  $Fr$  is about unity or smaller and that is the situation we will study in microgravity. For example, for a liquid/gas system with a pipe diameter of 2.5 cm in one-g, the liquid velocity is on the order of 50 cm/s or smaller to satisfy the  $Fr$  condition. Moreover, we will focus on the laminar flow regime to simplify our analysis, which means the Reynolds number of the liquid flow must be below about 2,500. The Reynolds number is defined as  $Re_p = \rho_c U_{LS} D_p / \mu_c$ , where  $\mu_c$  is the viscosity of the liquid. Then, for water flow through a 2.5 cm dia. pipe, for example, the liquid velocity should not go beyond 10 cm/s. As for the gas velocity range, the momentum flux of the gas flow  $\rho_d U_G^2$  ( $U_G$  = gas velocity at



nozzle exit) must be smaller than that of the liquid flow  $\rho_l U_{LS}^2$ , otherwise the gas flow comes out as a jet. Then, for a water-air system with a liquid velocity of 10 cm/s, the air flow velocity must be less than 3 m/s and if the nozzle diameter is about one-fifth of the pipe diameter, for example, the superficial gas velocity is less than 10 cm/s. For such ranges of liquid and gas superficial velocities the two-phase flow will be in the bubble-flow or slug-flow regime in microgravity. For those flow regimes it is important to understand how an individual bubble is formed and how the bubbles coalesce.

The experimental part is an extension of our current effort. We are conducting microgravity experiments on bubble generation aboard the DC-9 Reduced Gravity Research aircraft at NASA Lewis. In that work, air is injected from a nozzle into water flow in a pipe. The air injection is either in the direction of the water flow (co-flow configuration) or normal to the flow (cross-flow configuration) as illustrated in Fig.1. For both configurations plexiglass pipes of inner diameters 1.27, 1.9, and 2.54 cm are used. Nozzle diameters are 10 and 20 % of a given pipe inner diameter. Superficial gas and liquid velocities are in the range of 5 to 70 cm/s for the 1.27 cm test section and in the range of 5 to 40 cm/s for the 1.9 and 2.54 cm test sections

The main objective of the work is to study the final dimensionless bubble size (ratio of bubble dia. to pipe dia.) under various ranges of the important dimensionless parameters of the problem (ratio of pipe dia. to nozzle dia., ratio of superficial gas velocity to superficial liquid velocity, liquid flow Reynolds number ( $Re_p$ , defined earlier), and Weber number). The Weber number is defined as  $We_p = \rho_l U_{LS}^2 D_p / \sigma$ , where  $\sigma$  is the surface tension. In normal gravity the Froude number defined earlier is also important. The process of bubble expansion and detachment is studied mainly photographically. The results will be compared with our model predictions.

The present work will be expanded to study how a bubble is removed from the pipe wall to simulate the conditions during boiling and in other applications. In our present study the injection nozzle tip is placed above the pipe wall in the cross-flow configuration (Fig.1) to minimize the effect of the wall. However, in the proposed work the nozzle tip will be flush with the pipe wall so that the bubble interacts directly with the wall (Fig.2). The experiment will be conducted with and without heating a portion of the pipe wall. Both tests are described below.

Bubble generation without heat transfer---First we will study bubble generation under isothermal conditions. We will investigate the most basic configuration, namely the generation of a single bubble. By using a single hole we will investigate the process of bubble formation and detachment under various conditions as in the present work. We will vary the pipe diameter, the hole diameter, the liquid velocity, and the gas velocity to cover ranges of the dimensionless parameters. The test fluids will be mainly water and air. We will also use a silicone oil-air system in conjunction with the heat transfer experiment discussed later. The process will be videotaped and analyzed. The size and shape of detached bubbles will be determined and compared with the prediction of our model. Since the mechanism of bubble detachment is not well understood in microgravity, the experimental information will help us refine the theoretical model. We will also investigate the relationship between the detached bubble size (relative to the pipe diameter) and the downstream two-phase flow regime. In ref. 2 we have conjectured that if the bubble size relative to the pipe diameter becomes larger than a certain value, the downstream two-phase flow regime changes from the bubble-flow to slug-flow, which seems to agree with available experimental data. Since it is an important transition for two-phase flow, we will study the transition condition in detail. Most of the isothermal experiments will be conducted in parabolic flights using mostly the existing NASA Lewis two-phase flow facilities.

Bubble generation with heat transfer---With bubble generation from a heated wall (without boiling) our main interest will be the effect of thermocapillarity on the process of bubble formation and detachment. In order to study mainly the fundamental nature of the effect, we will use only the single hole arrangement in the proposed experiment. A portion of the pipe around the hole will be heated by heating elements attached to the pipe outside wall. The air injected from the nozzle will have the same temperature as the heated wall. An important new dimensionless parameter in the problem is the aforementioned surface tension Reynolds number,  $Ro$ . Marangoni number,  $Ma = Ro/Pr$  ( $Pr$  = Prandtl number), is also used in thermocapillary flow study. In normal gravity buoyancy is also important but we will focus on

reduced gravity conditions. Since it is known that a water-air interface is very sensitive to surface contamination, we will use silicone oil (2 or 5 centistokes kinematic viscosity) as the test liquid in conjunction with air. In addition to the study of bubble expansion and detachment, we will investigate the flow around the bubble in detail. The main diagnostic tool will be flow visualization. For that we will mix a small amount of tracer particles into the test liquid and the flow near the nozzle will be illuminated by a laser light sheet. We will study their motion by a video camera. The motion of individual particle will be analyzed by a PIV technique, from which the flow field will be constructed. The same technique has been used in the aforementioned space experiment on thermocapillary flows. The flow field study will be done with and without heating to see the effect of thermocapillarity on the flow. Also, the size and shape of detached bubble will be compared. The work will be guided by the theoretical analysis discussed below. One complication associated with the flow visualization with heat transfer is that the flow field near the nozzle is blocked from our view by the heating elements. One way to see the flow field is to use thin metallic film heaters through which we can observe the flow field, similar to the heating elements used by Merte (ref.5). We will also investigate other options for the visualization. Experimentally, the pipe diameter will be fixed at about 2.54 cm (1") and the nozzle diameter, the liquid flow rate, the gas flow rate and  $\Delta T$  will be varied to cover ranges of velocity ratio, diameter ratio,  $Re_p$ ,  $We_p$ , and  $Ro$ .

Although some tests with heat transfer will be conducted in parabolic flights, we will need a longer duration of microgravity to study the effect of thermocapillarity accurately. The reason is that with heating buoyancy flow will be generated during the pull-back period of parabolic flights (the acceleration is about 2-g) and it will interfere with the thermocapillary flow during most of reduced gravity periods.

### Theoretical Work

A theoretical modeling is an important part of our bubble generation work. From the modeling work we can learn the basic physical process of bubble expansion and detachment. After an accurate model is developed, it can be used to predict the bubble behavior in other experiments and also, very importantly, it helps us to design a practical system which requires controlled bubble size. We have developed a theoretical model to predict the size of a bubble after its detachment for the configurations illustrated in Fig.1. The model is partly based on available experimental information obtained in one-g tests. We are going to test the model in our ongoing work. The bubble detachment condition from the nozzle is very important in determining the final bubble size. In the current model it is based on observations of bubble detachment under various conditions in one-g. We will study the detachment in the current experiment and, if necessary, we will modify the condition used in the model in this proposed work. We will also analyze the detachment mechanism for the injection from a hole in the pipe wall and develop a theoretical model for bubble expansion and detachment for that situation. The bubble detachment from a wall is different from that from a nozzle because the contact line of the gas bubble is fixed at the nozzle in the latter configuration but it can move along the wall during the bubble expansion in the former configuration. The difference must be taken into account in the modeling.

We will first modify our present model on bubble generation. It is based on a global force balance. The current model will be tested in our ongoing work and will also be used to design the present experiment. In the present model the injected bubble does not interact with the pipe wall and is held at the nozzle tip by surface tension. The bubble is assumed to be spherical in the present model. In the modified model the bubble will be attached to the wall with its neck size independent of the nozzle diameter (Fig.2). Therefore, the bubble shape during the expansion stage is not generally spherical and depends, among other factors, on the contact angle. Also, the condition at the bubble neck at the time of detachment is very important in the model. The current detachment model is based on available ground-based experimental information about bubble detachment from a nozzle without the wall effect. Therefore, we need experimental information regarding the shape of a bubble during the whole process in microgravity to modify our current model. Based on that information we will modify the formula to compute the net hydrodynamic drag on the

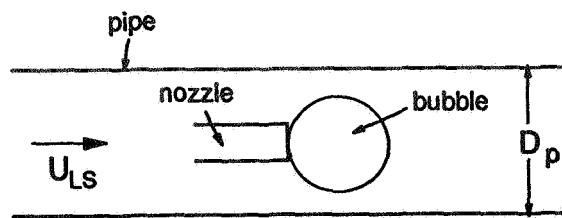
bubble and the net surface tension force at the contact line between the gas and the wall following the procedure described below.

First, we will characterize the bubble shape under various conditions based on the experimental information. From that information we will develop a formula to compute the net drag on the bubble including the effect of the wall. In the development process we will perform potential flow analysis to obtain information regarding the pressure distribution around the bubble. As for the net surface tension force, we will first characterize the contact line motion during the bubble expansion from the experimental information; we will need information regarding the neck size and contact angle. This contact line characterization is generally a difficult problem because it deals with dynamic contact angle. Since we will be performing a global force balance in this work, it is not necessary to characterize the contact line behavior in detail, so we will develop an approximate model for the contact line behavior. The detachment condition is also complex generally but for the detachment from a nozzle in one-g relatively simple conditions seem to work, namely by checking the bubble neck length relative to the nozzle diameter or the location of the bubble center relative to the nozzle location it is possible to identify the detachment (ref. 2). We will develop a detachment condition based on similar criteria from the data. Finally, we will put those information into the model and compute the final bubble size under various conditions, compare with the experimental data, and refine the model further, if necessary.

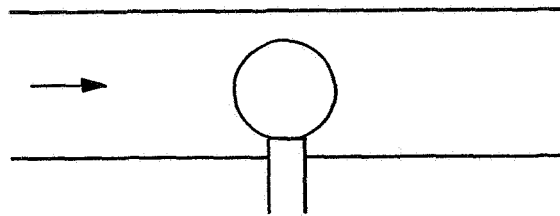
With heat transfer we will analyze the effect of thermocapillarity by scaling analysis. We have done scaling analyses in the past on various subjects including thermocapillary flows (e.g. ref. 6). We will follow basically the same procedure as in our past studies to find the important velocity and length scales in various regions and to determine the important forces at various locations. The information will be used to guide the above experimental measurement and also will help us analyze the experimental data. The result from the scaling analysis will also be used in the global force balance to develop a model for bubble generation with thermocapillarity. The procedure for developing the model will be the same as the procedure described above for the isothermal conditions. As mentioned above, the experiments with heat transfer require an extended microgravity of space and the modeling needs the experimental information, so only preliminary work will be done for the model development with thermocapillarity in the proposed four-year period.

## REFERENCES

1. Kim, I., Kamotani, Y., and Ostrach, S; Modeling Bubble and Drop Formation in Flowing Liquids in Microgravity, *AIChE Journal*, Vol.40, 1994, pp. 19-28.
2. Kim, I., Kamotani, Y., and Ostrach, S; Modeling of Bubble and Drop Formation in Flowing Liquids in Terrestrial and Microgravity Environments, Report EMAE/TR-92-207, Department of Mechanical and Aerospace Engineering, Case Western Reserve University, Cleveland, Ohio, 1992.
3. Kamotani, Y., Ostrach, S., and Pline, A.; A Thermocapillary Convection Experiment in Microgravity, *Journal of Heat Transfer*, Vol. 117, 1995, pp. 611-618.
4. Kamotani, Y., Ostrach, S., and Pline, A.; Analysis of Velocity Data Taken in Surface Tension Driven Convection Experiment in Microgravity, *Physics of Fluids*, Vol.6, 1994, pp. 3601-3609.
5. Merte, H.Jr.; Pool and Flow Boiling in Variable and Microgravity, *Proceedings of Second Microgravity Fluid Physics Conference*, NASA CP-3276, 1994, pp. 265-272.
6. Kamotani, Y., Chang, A. and Ostrach, S.; Effects of Heating Mode on Steady Axisymmetric Thermocapillary Flows in Microgravity, *Journal of Heat Transfer*, Vol. 118, 1996, pp. 191-197.



(a) Co-flow system



(b) Cross-flow system

Figure 1. Bubble injection from a nozzle.

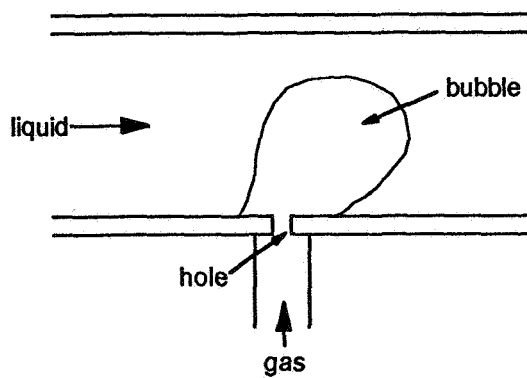


Figure 2. Bubble injection from a hole.

# Production of Gas Bubbles in Reduced Gravity Environments

Hasan N. Oğuz

Department of Mechanical Engineering  
The Johns Hopkins University, Baltimore, MD 21218

Shu Takagi

Department of Mechanical Engineering  
The University of Tokyo

7-3-1, Hongo, Bunkyo-ku,

Tokyo 113, Japan

and

Masaki Misawa

Mechanical Engineering Laboratory  
1-2, Namiki, Tsukuba, Ibaraki 305, Japan

## Introduction

In a wide variety of applications such as waste water treatment, biological reactors, gas-liquid reactors, blood oxygenation, purification of liquids, etc., it is necessary to produce small bubbles in liquids. Since gravity plays an essential role in currently available techniques, the adaptation of these applications to space requires the development of new tools.

Under normal gravity, bubbles are typically generated by forcing gas through an orifice in a liquid. There is a large number of studies on this topic and a comprehensive review is given by Kumar & Kuloor (1970). In this reference and many other subsequent publications the common approach is to take the bubble as an isolated object and apply a force balance. In general, the relevant forces can be

- gravitational
- surface tensional
- inertial
- viscous
- due to stagnation pressure of the injected gas
- of Marangoni type (due to temperature field or surfactants)
- due to an applied electric field.

When a growing bubble becomes large enough, the buoyancy dominates the surface tension force causing it to detach from the orifice. In the case of small growth rates, the radius of the detached bubble,  $R$ , can be determined by a static force balance between surface tension and buoyancy (Fritz 1935)

$$R_F = \left( \frac{3\sigma a}{2\rho g} \right)^{1/3} \quad (1)$$

where  $\sigma$  is the surface tension,  $a$  the orifice radius,  $\rho$  the liquid density,  $g$  the gravitational acceleration. Although the radius given by (1) is of limited accuracy, it serves as a good reference point for a given orifice size. As the growth rate is increased,  $R$  remains relatively constant up to a certain critical rate beyond which it is approximately given by

$$R_Q = \left( \frac{9Q^2}{8\pi^2 g} \right)^{1/5} \quad (2)$$

where  $Q$  is the gas flow rate (Oguz & Prosperetti 1993).

In space, the process is quite different and the bubble may remain attached to the orifice indefinitely. To *simulate* gravity, any one of the forces listed above can be used to promote bubble detachment. For instance, Pamperin & Rath (1995) found that very high gas injection velocities can lead to bubble



Figure 1: Selected frames from a high speed video film showing six cases of bubble growth and detachment from a needle in a tube. The inner diameter of the tube is 1.6 mm, and the inner and outer diameter of the needle is 0.58 and 0.90 mm. The air flow rate is 5 ml/mn and the water flow rates are from left to right 25, 50, 75, 99, 130, 162 ml/mn.



Figure 2: Selected frames from a high speed video film showing six cases of bubble growth and detachment from a needle in a tube. The inner diameter of the tube is 1.6 mm, and the inner and outer diameter of the needle is 0.58 and 0.90 mm. The air flow rate is 29 ml/mn and the water flow rates are from left to right 25, 50, 75, 99, 112, 130 ml/mn.

formation even under weightlessness conditions. Conceivably, one can also impose an electric field or a temperature field to replace the buoyancy force. However, the most practical approach seems to impose an ambient flow to force bubbles out the orifice (Kim et al 1994). The usefulness of this idea has been recognized a long time ago (Chuang & Goldschmidt 1970). In this paper, we are interested in the effect of an imposed flow in 0 and 1 *g*. Specifically, we investigate the process of bubble formation subject to a parallel and a cross flow. In the case of parallel flow, we have a hypodermic needle in a tube from which bubbles can be produced. On the other hand, the cross flow condition is established by forcing bubbles through an orifice on a wall in a shear flow. The first series of experiments have been performed under normal gravity conditions and the working fluid was water. A high quality microgravity facility has been used for the second type and silicone oil is used as the host liquid.

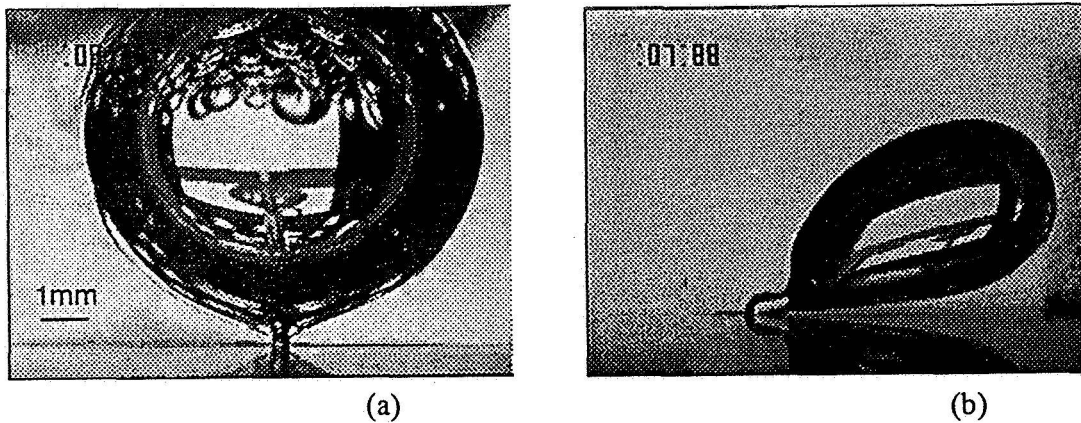


Figure 3: Images of a bubble growing from an orifice of diameter 1.7 mm in 0.0005 g under (a) quiescent conditions and (b) a shear flow of  $U/L=15$  cm/s.cm. Average growth rate of the bubble is about  $1.5$  cm<sup>3</sup>/s.

## 1 Experiments

Here we report on some preliminary experiments of air bubble formation from a needle in a plexiglass tube filled with water. In Fig. 1 we show selected frames from a series of high speed movies. In all the cases shown in the figure the gas flow rate is held constant at  $0.083$  cm<sup>3</sup>/s and the water flow rate is increased from  $0.42$  cm<sup>3</sup>/s (left) to  $2.7$  cm<sup>3</sup>/s (right). We have observed a substantial reduction in bubble size as the water flow rate is increased while the gas flow rate is kept constant. This behavior is common to other gas flow rates as well (Fig. 2). For sufficiently low water flow rates, bubble formation is quite regular with little or no variation from one bubble to another. This regime is ideal for reliable production of bubbles of specified size. However, above a certain critical flow rate an elongated bubble is seen to remain attached to the needle.

As the liquid flow rate is increased further the size of the detached bubbles starts showing substantial variance and the average bubble size tends to be higher than the minimum size of the regular regime. The lower part of the bubble is stable while the upper part oscillates and sheds occasional bubbles much like a flame and hence we use the term “bubble flame” to refer to it. This phenomenon can be explained in light of the studies by Frankel & Weihs (1985, 1987). They investigated the effect of stretching for inviscid and viscous jets. In the present case, the axial velocity at the top of the bubble is higher than at its bottom causing a fair amount of stretching that stabilizes the bubble. Although we have a gas jet in a confined geometry, the analysis of Frankel & Weihs is applicable to our case at least qualitatively. It must be noted that theoretical models that rely on the sphericity of the bubble will fail in this regime.

If the object is to minimize bubble size, the liquid flow rate must be maintained at the critical level that defines the boundary between the regular formation and the bubble flame regimes. We have found that the minimum bubble radius is always greater than the needle radius and increases with increasing gas flow rates.

## Microgravity experiments

In the second set of experiments the effect of a shear flow on a bubble growing from an orifice is investigated. This situation is of particular interest to two-phase flow studies in relation to boiling heat transfer.



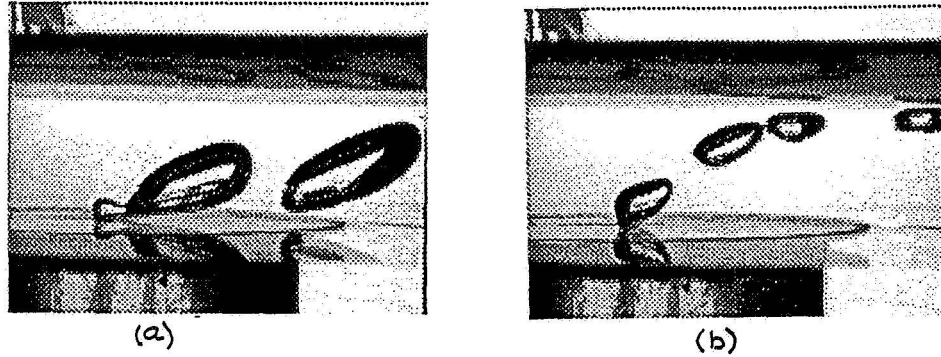


Figure 4: Comparison of bubble growth and detachment from an orifice of diameter 1.7 mm in (a) 0.0005  $g$  and (b) 1  $g$  subject to a shear flow of  $U/L=15$  cm/s.cm. Average growth rate of the bubble is about  $1.5$  cm<sup>3</sup>/s.

A series of experiments have been performed under normal and micro gravity conditions in Japan and more are planned for this year.

The system consists of a small plexiglass reservoir filled with silicon oil. A thin belt tensioned between two solid cylinders is installed in the middle of the reservoir providing a shear flow across the 15mm gap between the moving belt and the bottom wall of the reservoir. Bubbles are injected into silicone oil from the bottom through a hole of diameter 1.7 mm.

The apparatus has been installed in a bus module at the Japan Microgravity Center (JAMIC: Hokkaido, Japan) and subjected to a series of experiments with gravity levels as low as  $10^{-4}g$  for 10 seconds. Such a long duration of high quality microgravity has been achieved during free fall in a mine shaft about 710 m deep.

A number of free fall experiments have been conducted and bubble growth and detachment has been recorded by means of a CCD camera. The details of this experiment will be published elsewhere. Here, we give a brief summary of the important features of this experiment. Figure 3 shows snapshots of the bubble formation process with and without an imposed shear flow under 0.0005  $g$ . It is noted that when both the gravity and the flow are absent, detachment does not take place. This is consistent with Pamperin & Rath (1995) who reported that no detachment is possible when the Weber number

$$We = \frac{2u_g^2 a \rho_g}{\sigma} < 8, \quad (3)$$

where  $u_g$  is the gas velocity at the orifice. Another factor inhibiting bubble departure is viscosity of the liquid which is much higher in our experiments. However, when a shear flow is applied, viscous forces are acting favorably to promote detachment (see panel (b) of fig. 3). In this case, bubble pinchoff seems to be triggered by the deformation of the bubble under viscous drag and inertial forces.

## Theory

We have carried out boundary-integral simulations of the formation of a bubble in a tube. Comparison with the experiment is favorable when the water flow rate is sufficiently small. In fig. 5 we show two sequences of computed bubble shapes corresponding to the cases (c) of fig. 1 and (c) of fig. 2. At



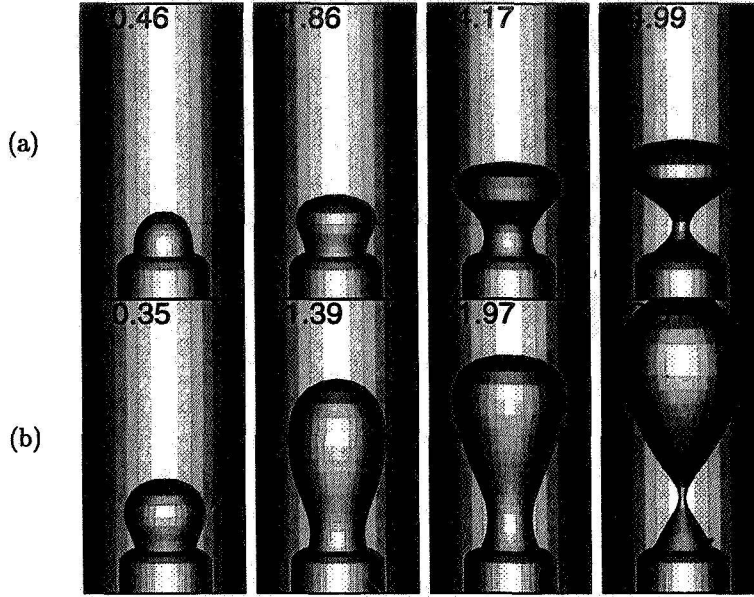


Figure 5: Axisymmetric boundary integral simulations of bubble growth and detachment from a needle in a tube. The inner diameter of the tube is 1.6 mm, and the inner and outer diameter of the needle is 0.58 and 0.90 mm. The air flow rate is (a) 5 and (b) 29 ml/mn. The water flow rate is 75 ml/mn. Times in ms.

higher flow rates the experimentally observed behavior cannot be duplicated by the boundary integral simulations because the inviscid flow assumption leads to numerical artifacts. For instance, our present simulations indicate that the needle wall thickness causes the bubble to detach prematurely. This may be due to the high stagnation pressures generated by the corner flow around the needle. In reality, flow separation prevents high speed corner flows. There are other discrepancies between the simulations and the experiments especially for small bubbles. The neglect of viscous drag is the primary cause. Despite these difference, a very good agreement between the experiment and the numerical simulations has been obtained for cases with relatively low liquid flow rates.

Within the framework of the assumptions, potential-flow boundary-integral method is very accurate but of limited use due to reasons stated above. Ultimately, one needs solve the Navier-Stokes equations with a free surface. There are several approaches to this problem and, most notably, the front tracking method of Unverdi & Tryggvason (1992) is particularly appealing to us because the bubble liquid interface is discretized in the same way as in the boundary integral method. In fig. 6 we show front tracking simulations of gas injection in a shear flow. The main problem with this type of code is the limitation for the viscosity and density ratios and the inaccurate way with which the surface tension effects are handled. These factors inhibit the pinchoff and an elongated bubble is predicted by the simulation. By the use of higher resolution and better algorithms we hope to solve this problem in the future.

## Acknowledgment

HNO gratefully acknowledges support from the National Science Foundation grant CTS 9318724 and equipment grant CTS 9506077. The microgravity experiment has been supported by the Japan Space Utilization Promotion Center (JSUP).

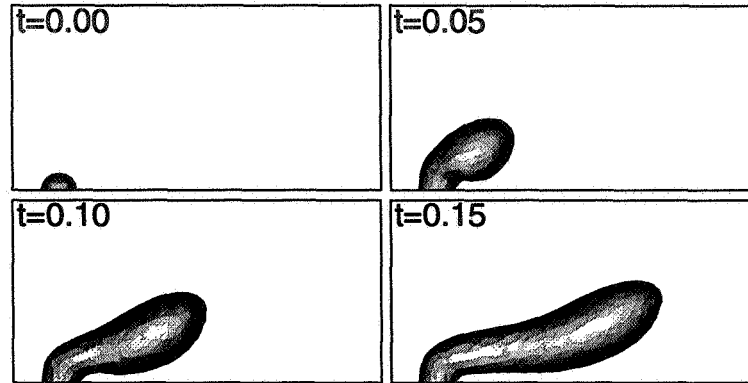


Figure 6: Simulations of bubble injection in a shear flow of 37 cm/s.cm as computed by a front tracking code based on Unverdi & Tryggvason (1992). The orifice diameter is 1.5 mm and the injection rate is 1.5 cm<sup>3</sup>/s. The surface tension is 21 dyn/cm. The viscosity of the liquid is 0.49 gm/cm.s and the viscosity/density ratios are 100. Times in seconds.

## References

- [1] S.C. Chuang and V.W. Goldschmidt. Bubble formation due to a submerged capillary tube in quiescent and coflowing streams. *ASME J. Basic Engng.*, 92:705–711, 1970.
- [2] I. Frankel and D. Weihs. Stability of a capillary jet with linearly increasing axial velocity (with application to shaped charges). *J. Fluid Mech.*, 155:289–307, 1985.
- [3] I. Frankel and D. Weihs. Influence of viscosity on the capillary instability of a stretching jet. *J. Fluid Mech.*, 185:361–383, 1987.
- [4] W. Fritz. Berechnung des maximale volume von dampfblasen. *Phys. Z.*, 36:379–384, 1935.
- [5] I. Kim, Y. Kamotani, and S. Ostrach. Modeling bubble and drop formation in flowing liquids in microgravity. *AIChE Journal*, 40:19–28, 1994.
- [6] R. Kumar and N.R. Kuloor. The formation of bubbles and drops. *Adv. Chem. Engng, Edited by Drew, T.B. et al*, 8:256–368, 1970.
- [7] H.N. Öğuz and A. Prosperetti. Dynamics of bubble growth and detachment from a needle. *J. Fluid Mech.*, 257:111–145, 1993.
- [8] O. Pamperin and H. Rath. Influence of buoyancy on bubble formation at submerged orifices. *Chem. Eng. Sci.*, 50:3009–3024, 1995.
- [9] S.O. Unverdi and G. Tryggvason. A front-tracking method for viscous, incompressible, multi-fluid flows. *J. Comp. Phys.*, 100:25–37, 1992.

# Phase Distribution Phenomena for Simulated Microgravity Conditions: Experimental Work

Maneesh Singhal, Fabian J. Bonetto, R.T. Lahey Jr.

Center For Multiphase Flow, Rensselaer Polytechnic Institute  
Troy, NY 12180

## 1.0 INTRODUCTION

This report summarizes the work accomplished at Rensselaer to study phase distribution phenomenon under simulated microgravity conditions. Our group at Rensselaer has been able to develop sophisticated analytical models to predict phase distribution in two-phase flows under variety of conditions. These models are based on physics and data obtained from carefully controlled experiments that are being conducted here. These experiments also serve to verify the models developed.

## 2.0 ANALYSIS

### 2.1 Conservation Equations

The generic conservation equation for each phase is given by:

$$\frac{\partial}{\partial t} \rho \Psi + \nabla \cdot \rho \Psi \mathbf{v} = \nabla \cdot \mathbf{J} + \rho f \quad (1)$$

The corresponding jump condition between components  $k$  and  $l$  is:

$$[(\rho \Psi (\mathbf{v} - \mathbf{v}_i) + \mathbf{J}) \cdot \mathbf{n}]_{kl} = M_i \quad (2)$$

where:

$\Psi$  ... conserved quantity

$\mathbf{J}$  ... conserved quantity's flux

$f$  ... conserved quantity's source density

$M_i$  ... conserved quantity's interfacial source

Typical state variables are given in Table I.

TABLE I State variables in generic conservation equations and jump conditions

Balance Principle	$\Psi$	$\mathbf{J}$	$f$	$M_i$
Mass	1	0	0	0
Momentum	$\mathbf{v}$	$\mathbf{T}$	$\mathbf{g}$	$\mathbf{m}_i^s$
Energy	$u + 0.5 \mathbf{v}^2$	$\mathbf{T} \cdot \mathbf{v} - \mathbf{q}$	$\mathbf{g} \cdot \mathbf{v} + r$	$e_i^s$
Enthalpy	$h$	$-\mathbf{q}''$	$r + \frac{1}{\rho} \left( \frac{dp}{dt} + \tau : \nabla \mathbf{v} \right)$	$h_i^s$

To obtain the conservation equations which govern the

motion of turbulent dispersed solid/fluid flows, the generic equation is first multiplied by the phase indicator function,  $X_k$ , defined as:

$$X_k = \begin{cases} 1, & \text{if } \mathbf{x} \in k \\ 0, & \text{otherwise} \end{cases} \quad (3)$$

and then averaged over all the possible realizations (ensembles). Drew et. al. [1995] define ensemble averaging of a function  $F$  at position  $\mathbf{x}$  and time  $t$ , for some particular realization  $\mu$ , as:

$$\bar{F}(\mathbf{x}, t) = \int_{\epsilon} F(\mathbf{x}, t; \mu) d\mu(\mu) \quad (4)$$

where  $\epsilon$ , ensemble, is the set of all the possible realizations. Also, if we consider a point on the interface while moving with it, we see that the phase indicator function,  $X_k$ , is a constant jump discontinuity. Therefore, its material derivative must be zero. That is,

$$\frac{D_t X_k}{Dt} = \frac{\partial X_k}{\partial t} + \mathbf{v}_i \cdot \nabla X_k = 0. \quad (5)$$

By using the above equation and procedure, ensemble-averaged conservation equations for adiabatic two-phase flow are obtained. These have been described in detail elsewhere [Alajbegovic 1994].

### 2.2 Closure

#### 2.2.1 The interfacial momentum source

The interfacial momentum source can be partitioned into drag and non-drag components [Lahey & Drew, 1990], as:

$$\mathbf{M}_k = -\mathbf{T} \cdot \nabla X_k = \mathbf{M}_k^{(D)} + \mathbf{M}_k^{(ND)} \quad (6)$$

For drag we may assume:

$$\mathbf{M}_c^{(D)} = -\mathbf{M}_d^{(D)} = \frac{1}{8} \rho_c C_D |\mathbf{v}_r| \mathbf{v}_r A_i''' \quad (7)$$

The non-drag component may be obtained assuming inviscid flow around spherical particles [Arnold, 1988; Park, 1992]. The average quantities were obtained using cell-averaging techniques [Nigmatulin, 1979], which are an approximation to ensemble averaging. The resulting expression includes virtual mass effects and a lateral force induced by the

non-uniform flow field around a spherical particle. The latter force is called lift force and is given by [Drew & Lahey 1987; 1990]:

$$\mathbf{M}_c^L = C_L \varepsilon_d \rho_c \nabla_r \times \nabla \times \nabla_c \quad (8)$$

The effects of the liquid turbulence interaction with particles/bubbles are included in the turbulent dispersion force:

$$\mathbf{M}_c^{(ND),TD} = -\mathbf{M}_d^{(ND),TD} = C_{TD} \rho_c k_c \nabla \alpha_d \quad (9)$$

### 2.2.2 Binary Collisions between the particles and the particle-wall collisions

Alajbegovic [1994] has developed closure laws for the stress induced in the dispersed phase and the transfer of the kinetic energy. For brevity only the procedure used to derive the expressions is described here. The following assumptions were made: collisions between more than two particles at the same instant are negligible; all collisions are elastic with negligible rotational effects. Starting from the expression for the average stress inside the dispersed phase given by Batchelor, [1970] an integral expression for the collision-induced shear stress is obtained by evaluating the probabilities of collisions of particles moving with given velocity, position and size. This expression is similar to that obtained by Chapman and Cowling [1970]. This was further integrated to obtain the final expressions. Similar procedure was used to calculate particle-wall collision-induced force.

### 2.2.3 Turbulent Interfacial Work

The interaction between the dispersed particles and the eddies is governed by the following equations:

$$\frac{dv'}{dt} p_{,i} = -\frac{1}{\tau_R} (v'_{p,i} - v'_{c,i}) \quad (10)$$

$$\frac{d}{dt} (m_c v'_c + m_p v'_p) = 0 \quad (11)$$

The interfacial work due to particle interactions with the continuous phase turbulence is:

$$W'_{d,ij} = \frac{\rho \alpha}{\tau_R} (C_1^W \overline{v'_{c,i} v'_{c,j}} - C_2^W \overline{v'_{p0,i} v'_{p0,j}}) \quad (12)$$

where,

$$\tau_R = \frac{4\rho_d D_p}{3\rho_c C_D |\nabla_p - \nabla_c|} \quad (13)$$

### 2.2.4 Algebraic Stress model for the dispersed phase Reynolds Stress

Starting with the assumption that:

$$\frac{v'_i v'_j}{k} \equiv \text{const.} \quad (14)$$

and negligible collisions and small gradients in the dispersed phase's mean velocity, we obtain

$$\overline{v'_{d,i} v'_{d,j}} = C_{R,ij} \frac{k_d}{k_c} \overline{v'_{c,i} v'_{c,j}} \quad (15)$$

The above models have been tested against experimental data obtained at Rensselaer and elsewhere for various flow situations, and show remarkable accuracy.

## 3.0 Solid/Liquid Experiments

In a two-phase mixture for low volume fractions, the lift force is one of the most important phenomena affecting the radial distribution of the flow. This effect is due to the relative velocity between the two phases. Serizawa et. al. [1988] demonstrated that this lift force pushes bubbles towards the wall in upward flows and towards the center of the conduit for downward flows.

Figure-1 shows how the gravity affects the hydrodynamic behavior of a turbulent two-phase flow. We may eliminate the buoyancy force by using a dispersed phase of same density as that of continuous phase. Assad et. al. [1995] measured the liquid and dispersed phase distribution in a solid/liquid two-phase flow in a horizontal pipe using a Laser Doppler Anemometer (LDA). The dispersed phase consisted of ~2.0 mm average diameter size expanded polystyrene particles with specific gravity of 1.03. The test section was 30.6 mm in diameter and the pipe was made out of a special optically clear material (FEP, Fluorinated Ethylene Propylene) with the same index of refraction as water. Measurements for the velocity profile, turbulent structure and the volume fraction for each phase were made for various flow rates and global volume fractions.

The two-fluid model described above was incorporated into the PHOENICS code to test it against the data for neutrally buoyant particles. Although the model was developed for vertical flows, only, the neutral buoyant particle data for horizontal flows can still be compared against the calculations. Figure 3 shows that the agreement with data is good.

## 4.0 Liquid/Liquid Experiments

The particles which were used by Assad [1995] were solid spheres with a non-deformable, non-slip interface. The flow dynamics around them are well understood and documented. In case of bubbles and droplets, there is no solid interface; the fluid outside interacts with the fluid inside giving rise to internal circulations and deformations. Pressure differentials can deform the surface so that they are no longer spherical. All this affects the interfacial momentum transfer and the turbulence structure in a significant way. However, if the droplets/bubbles are small enough, the deformations are very small compared to their size and hence can be neglected. The liquid/liquid experiments allow us to further verify our models and

collect data to guide us in further enhancements.

Butyl benzoate was chosen as the dispersed phase for simulating microgravity. It has a specific gravity of 1.0 at 20° C. Also, it is more sensitive to temperature as compared to water. This makes it convenient to gravity separate the oil from water by heating the mixture by 20°C. It has since been shown to have satisfactory optical properties for Phase Doppler measurements.

The closed loop mode of operation was found to be unsuitable for obtaining mono-dispersed droplet flows. This motivated us to consider open loop operation with an injector to produce a mono-dispersed suspension. A droplet injector was designed and has been constructed with the following characteristics: (i) ability to control the flow rate of water, (ii) ability to control the diameter of the oil droplets, (iii) ability to control the relative flow rates of water and oil to obtain desired global void fraction, and (iv) most importantly, the droplet size distribution should be as small as possible. Indeed, we want a mono-dispersed flow so that a correlation between the size of the droplet and the phase distribution phenomenon may be established. The obvious choice to achieve the above objectives is to have capillary tubes as injection units. A preliminary calculation was done to predict the size of the droplets as a function of oil volume flow rate, velocity of the stream trying to shear off the droplets from the tips and the size of the capillary. This was guided by the work done by several researchers [Hayworth et. al., 1950; Null et. al., 1958] where a balance between the drag on the spherical droplet being formed at the tip due to the fluid motion and the cohesion forces due to surface tension yielded a correlation between the droplet size and the capillary size with fluid velocity as a parameter. This droplet injector has been tested and appears to be functioning as predicted.

During initial tests, LDA data was found to be inadequate to estimate the size of the droplets accurately. This inadequacy stems from the method of interpreting the transit time of a burst as an indicator of the size of the droplets. This mode of droplet size estimation can only be used to get an approximate idea of the size distribution. For more accurate data we may use a Fiber Phase Doppler Anemometer (FPDA) which relies on the phase difference between the reflected light detected by two detectors, a fixed distance apart, to determine the size of the droplet. A FEP conduit was used as the test section and both the probes were submerged under water so that the optical path length does not change when traverses are made.

## 5.0 The Experimental Facility

A batch mode oil/water loop was built and tested as shown in figure-2. To avoid the realignment of the FPDA probe at each measurement location, the probes and the FEP test section are all immersed in water so that no correction or alignment has to be done for measurements at different locations.

The oil droplet injector was tested to find out the effect of

oil and water flow rates on the size distribution of droplets. A small test loop was constructed outside of the main test facility for ease of observation and control. Following conclusions were drawn from the data obtained:

- (1). The droplet size decreases with an increase in water flow rate.
- (2). The average droplet size increases with the increase in oil flow rate and at the same time the spread in the size distribution increases.

## 6.0 Results and Discussion

A study was done to verify that an FPDA can measure oil droplet size. This was necessary to optimize the setup variables and verify the optical properties of oil in the context of the FPDA measurements. Figure-4 below shows the experimental facility used for this purpose. A small glass tank was filled with a known amount of water. It was determined that the reflection mode of diameter measurement is most suited for actual measurements. Two void fractions were measured: 0.07% and 0.21%. Larger void fractions could not be tried because of the formation of an emulsion by the stirrer. This increased the turbidity of the mixture to such a large extent that the measurement rate decreased by a factor of 10.

Figure-5(a) shows the seeding size distribution in which 3.5 cc of the seeding was used to seed 19.6 liters of water. A sample of the seeding was analyzed under a travelling microscope to determine the sizes present. The glass seeding sizes were found to be in the range 5  $\mu$ m to 100  $\mu$ m, with most of them in 25 to 50  $\mu$ m range. Although the data is not statistically representative of the distribution, it gave us the bounds on size. The histogram in figure-5(a) is accurate to that extent with most particles the same range as above. Optimization of the alignment and different parameters led to different trials with most of them resulting in the similar distribution.

Figure-5(b) shows the particle size distribution in unseeded water. The particles measured are the natural seeding suspended in the water supply. Most of the particles are in range 0 to 20  $\mu$ m. Figure-5(c) shows the oil droplet size distribution for a volume fraction of 0.07%. Immediately after the measurements were done with unseeded water, 15.5 cc of oil was added. The stirrer immediately broke up the oil globules into small droplets and a delay of about 10 minutes was allowed before measuring to allow the system to stabilize. The histogram in figure-5(c) shows the range of sizes present is 0 to 340  $\mu$ m. Most of the particles are below 100  $\mu$ m in diameter. If this is compared with the figure-5(b), it is practically impossible to say which of the data belong to the droplets and which to the natural seeding especially in the 0-25  $\mu$ m range. This is the case with low volume fraction, however at higher volume fraction, the data percentage in this range must be small to be able to neglect the influence of natural seeding. This was confirmed by adding more oil to the tank, the resulting void fraction being 0.2%. Figure-5(d) shows a typical data set obtained

at this volume fraction. Here most of the droplets are in range 40 to 100  $\mu\text{m}$  and the fraction of particles/droplets less than 20  $\mu\text{m}$  is very small. With the injector in the main loop, we should be able to keep the global void fraction relatively large enough without any emulsification. Thus we are confident that with large sample sizes, the data will be representative of the true droplet size distribution.

## 7.0 Proposed future work

The main thrust of the future work is to put an experiment aboard the space shuttle. The objective of the experiment is to measure phase separation in an air/water mixture. The emphasis is on simplicity and efficiency in conducting the experiment and to provide adequate instrumentation of acquire a complete set of data. These data can then be used for further understanding the dynamics of bubbly flows in space. The instrumentation will consist of: (i) a two-dimensional pen Laser Doppler probe; (ii) a Phase Doppler Anemometer; (iii) a real time Fast Fourier Transform system, a phase discriminator, a high voltage generator and a demodulator, all fitted on a single PC card; (iv) a one-dimensional hot film anemometer; (v) a traversing mechanism, and (vi) a CCD camera. We will measure two-dimensional velocities with the LDA, one dimensional velocities and the local void fraction with the hot film probe, size distribution of the bubbles with the CCD camera and the FPD. All these will be measured as a function of radial position for two axial locations: one close to the inlet and one close to the outlet. These data will allow us to compute bubble coalescence and breakup as well as the developing phase distribution. These instruments will be progressively tested and calibrated in experiments in drop-towers and parabolic flights in Lear Jets. The loop itself will be a recirculating loop. A sine pump will circulate the mixture. For monodispersed experiments, we will separate the water from air using a centrifuge. For a arm length of 10 cm we will need about 600 rpm to simulate normal gravity. A specially designed injector will be used to generate the bubbles.

## 8.0 Bibliography

- Alajbegovic, A., "Phase Distribution and Turbulence Structure for Solid/Fluid Upflow in a Pipe", Ph.D. Thesis, Rensselaer Polytechnic Institute, Troy, New York, 1994.
- Arnold, G.S., "Entropy and Objectivity as Constraints Upon Constitutive Equations for Two-Fluid Modeling of Multiphase Flow", Ph.D. Thesis, Rensselaer Polytechnic Institute, Troy, New York, 1988.
- Assad, A., "An Experimental Study of Phase Distribution and Turbulence Structure for Solid/Liquid Flow in Horizontal and Vertical Pipes", Ph.D. Thesis, Rensselaer Polytechnic Institute, Troy, New York, 1995.
- Batchelor, G.K., "The Stress System in a Suspension of Force-Free Particles", *J. Fluid Mechanics*, Vol. 14, pp. 545-570, 1970.
- Chapman, S. Cowling, T.G., "The Mathematical Theory of Non-Uniform Gases", Cambridge University Press, Cambridge, 1970.
- Drew, D.A., Lahey, R.T., Jr., "The Virtual Mass and Lift Force on a Sphere in Rotating and Straining Inviscid Flow", *Int. J. Multiphase Flow*, vol. 13(1), pp. 113-121, 1987.
- Drew, D.A., Lahey, R.T., Jr., "Some Supplemental Analysis on the Virtual Mass and Lift Force on a Sphere in Rotating and Straining Inviscid Flow", *Int. J. Multiphase Flow*, vol. 16(6), pp. 1127-1130, 1990.
- Drew, D.A., Passman, S.L., "Theory of Multicomponent Fluids", To be published, 1995.
- Hayworth, Curtis B. and Treybal, Robert E., "Drop Formation in Two-Liquid-Phase Systems", *Industrial and Engineering Chemistry*, Vol. 42, No. 6, June 1950.
- Lahey, R.T., Jr., Drew, D.A., "The Current State-of-the-Art in the modelling of Vapor/Liquid Two-Phase Flows", *ASME 90-WA/HT-13*, 1990.
- Nigmatulin, R.I., "Spatial Averaging in the Mechanics of Heterogenous and Dispersed Systems", *Int. J. Multiphase Flow*, vol. 5, pp. 353-385, 1979.
- Null, Harold R., and Johnson, Homer F., "Drop Formation in Liquid/Liquid Systems from Single Nozzles", *A.I.Ch.E. Journal*, Vol. 4, No. 3, Sept. 1958.
- Park, J-W., "Void Wave Propagation in Two-Phase Flow", Ph.D. Thesis, Rensselaer Polytechnic Institute, Troy, New York, 1992.
- Serizawa A., Kataoka I., "Phase Distribution in Two-Phase Flow", *Transient Phenomena in Multiphase Flow*, Ed. Afghan, N.H., Hemisphere Pub. Corp., New York, pp. 179-225, 1988.

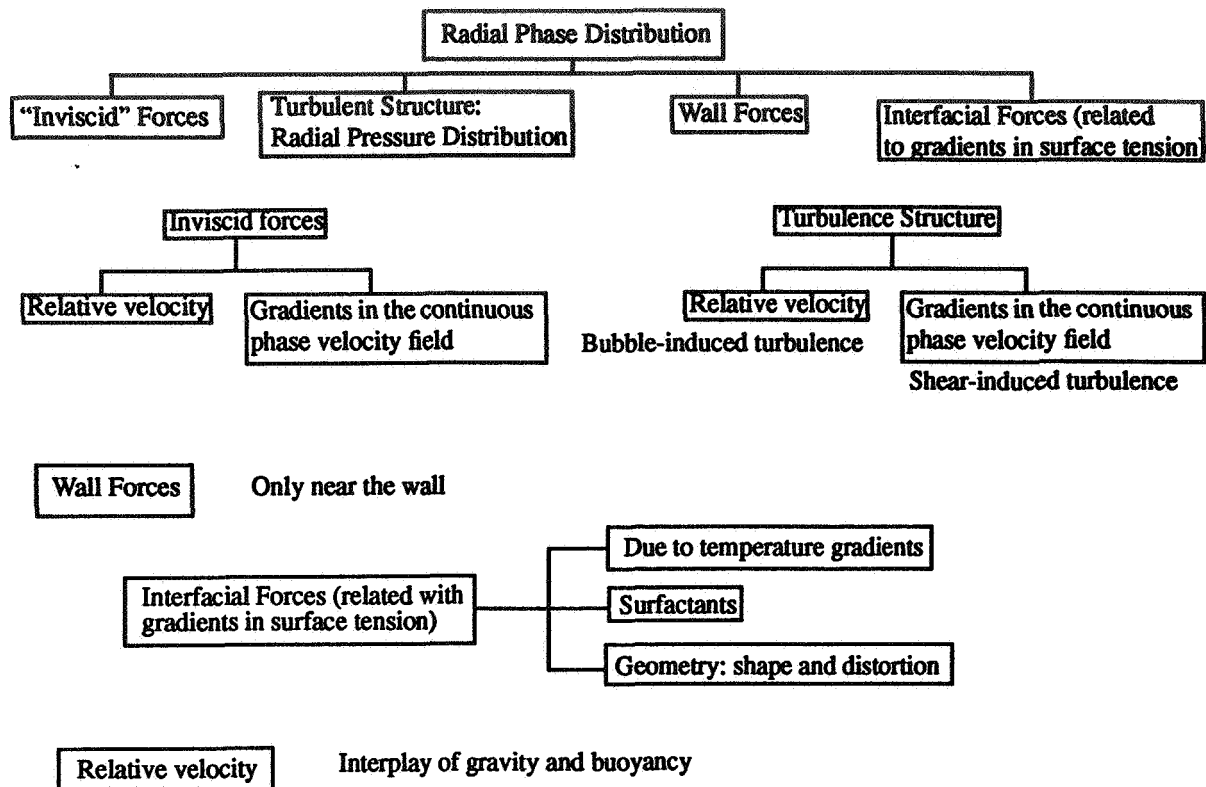


Fig. 1. Parametric dependence of two fluid models

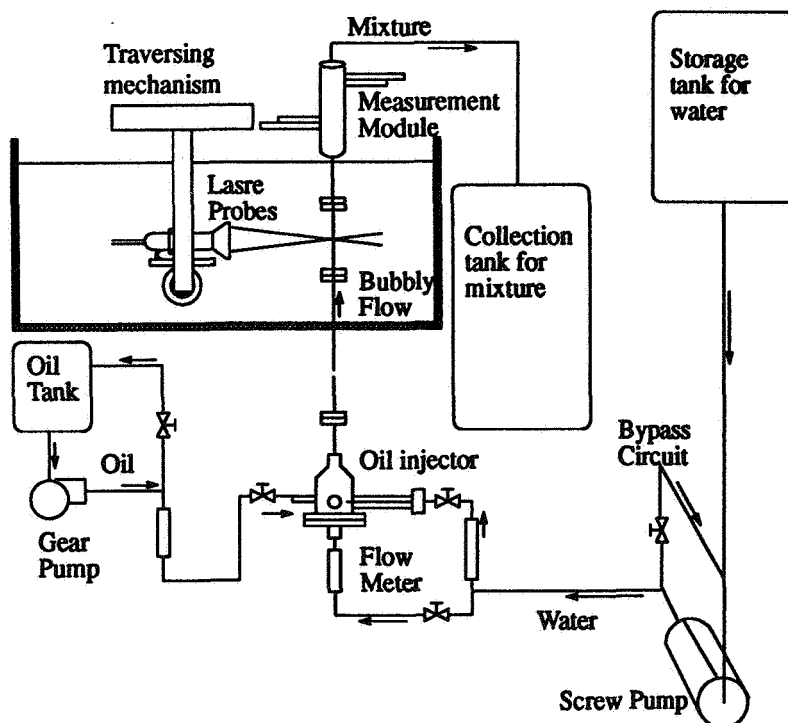


Fig. 2. Schematic of the new facility.

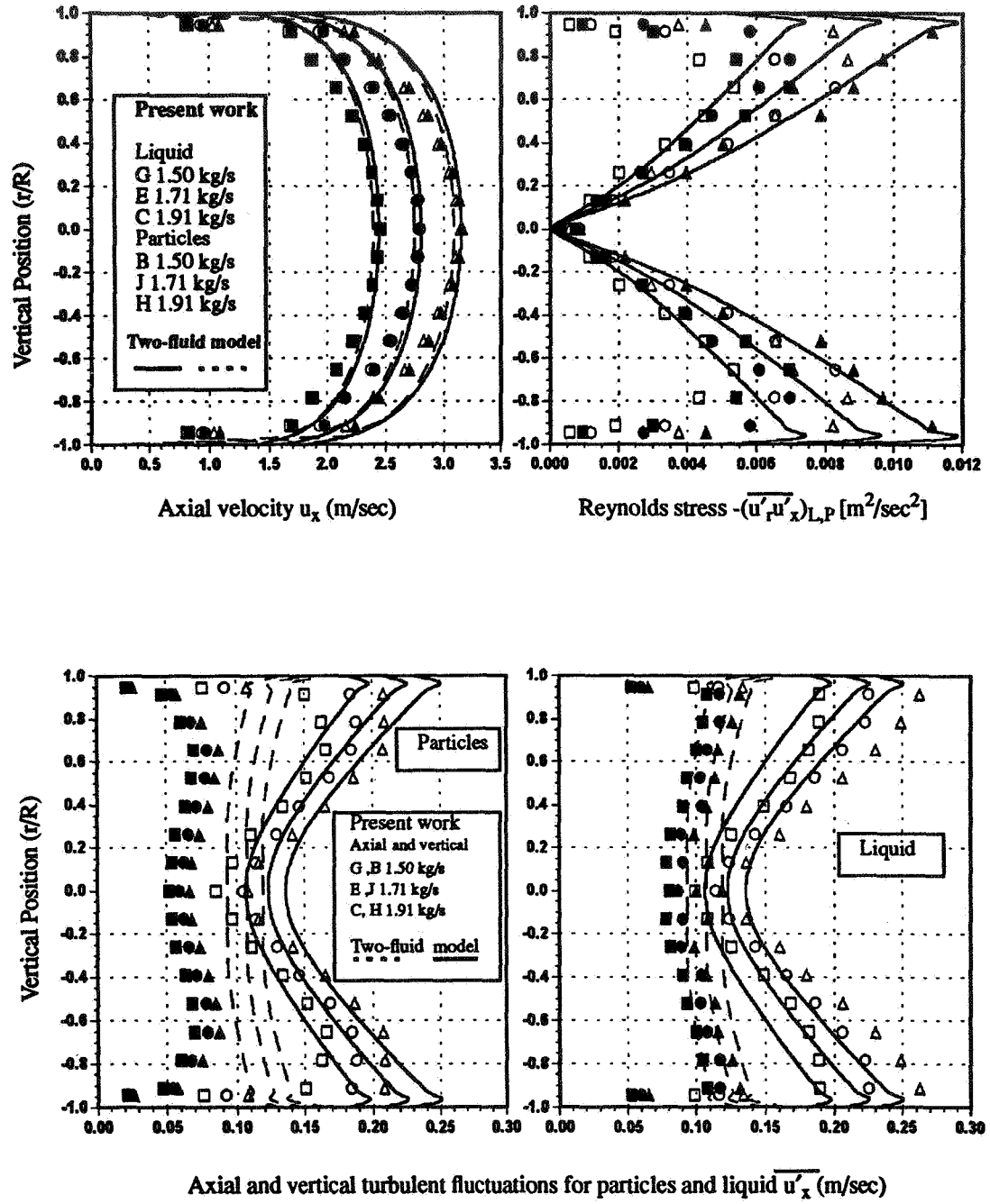


Fig. 3. Comparison between measured and predicted velocity and turbulence quantities for neutral particles.



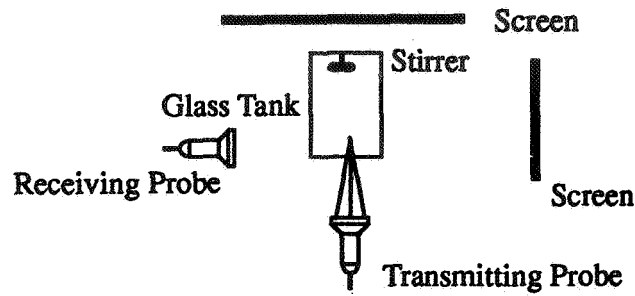
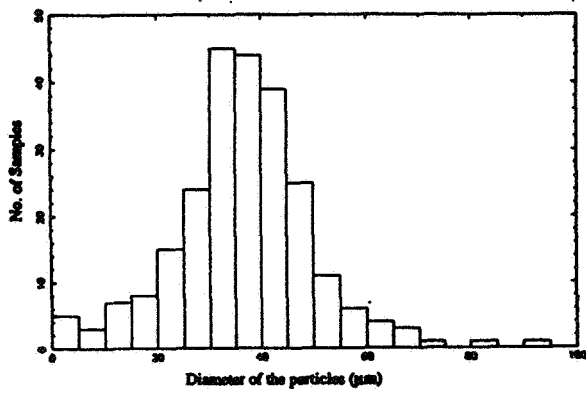
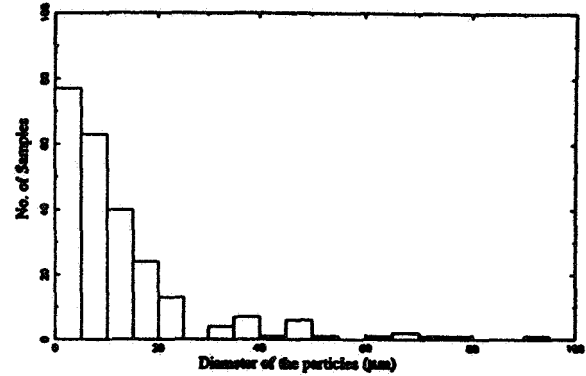


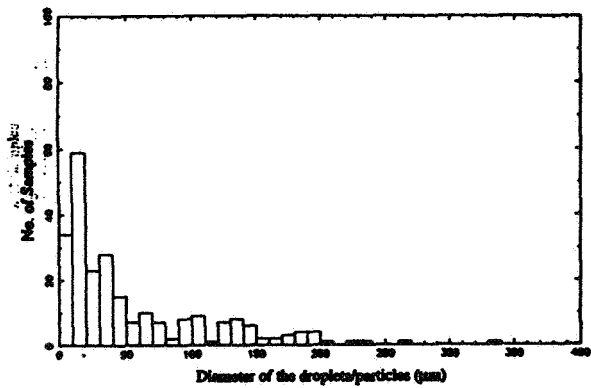
Fig 4. Schematic of the FPDA trial setup.



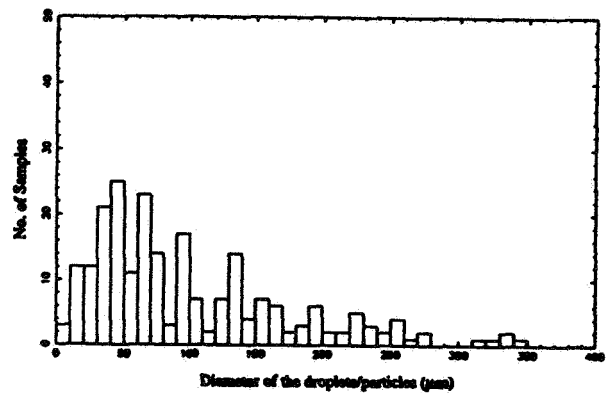
(a) With glass seeding



(b) Unseeded Water



(c) Oil droplets, Global void fraction=0.08%



(d) Oil droplets, Global void fraction=0.21%

Fig. 5. Particle/droplet size distributions.



# BUBBLE DYNAMICS, TWO-PHASE FLOW, AND BOILING HEAT TRANSFER IN MICROGRAVITY

Jacob N. Chung  
School of Mechanical and Materials Engineering  
Washington State University  
Pullman, WA 99164-2920

## ABSTRACT

The objective of the research is to study the feasibility of employing an external force to replace the buoyancy force in order to maintain nucleate boiling in microgravity. We have found that a bulk velocity field, an electric field and an acoustic field could each play the role of the gravity field in microgravity. Nucleate boiling could be maintained by anyone of the three external force fields in space.

## INTRODUCTION

The thermo-fluid dynamics of a two-phase system in microgravity encompasses a wide range of complex phenomena that are not well understood for engineering design to proceed. Therefore, there is an urgent need to explore these phenomena for future spacecraft design and space mission. Predicting the two-phase flow and boiling heat transfer phenomena under microgravity environment requires a thorough understanding of a multitude of fundamental physical processes including bubble dynamics, fluid dynamics, heat transfer, and interfacial transport. Significant gains in microgravity boiling science may result from investigating both the complexities of these phenomena in isolation and when acting in concert. The current research concentrates on the bubble nucleation, bubble dynamics and heat transfer mechanism under microgravity. Specifically, we intend to study the transport mechanisms when the dominance of gravity field is replaced by a bulk velocity field, an electric field or an acoustical field under the microgravity condition.

### I. Bulk Velocity Field

In highly subcooled and high-velocity forced-convection nucleate boiling, bubbles grow, slide, and collapse on the heater surface; therefore, buoyancy is of minimum reliance. In order to obviate the masking effect of buoyancy, our experiment was performed under low-velocity and microgravity conditions such that the physical phenomenon was more clearly recorded by our experimental system.

#### I.1 Experiment

The flow boiling apparatus consists of a pump, preheater, boiling test section, condenser, lighting, and video and data acquisition system. The maximum pump capacity maintained a single-phase mean velocity of  $7.7 \pm 0.1$  cm/s over the heater surface. Due to the physical limitations, the experimental system was open to the atmosphere. The bulk fluid temperature in the experiment was conveniently set to approximately the room temperature. This resulted in a relatively constant subcooling of  $17 \pm 2^\circ\text{C}$  for our experiment. Spectrophotometric grade Freon-113 (1,1,2 trichlorotrifluoroethane 99+ percent) was chosen as the test fluid. Because of the high solubility of dissolved gases in Freon-113 a typical degassing procedure was followed. Data acquisition was performed at 100 Hz for 500 scans: Three seconds of data were recorded before the release to obtain the 1g data, and two seconds of data recorded after the release, which captured the microgravity portion and the deceleration. A semitransparent, 400-Å-thick gold-film heater ( $2.54\text{cm} \times 2.54\text{cm}$ ) was built and used in the experiment. This heater design allowed us to maintain a relatively constant heat flux during the experiment and also provided the average surface temperature. The uncertainty in the heater resistance, surface temperature, and heat flux are  $\pm 0.00148$  ohms,  $\pm 1.16^\circ\text{C}$ , and  $\pm 380$  W/m<sup>2</sup>, respectively. This resulted in an uncertainty in heat transfer coefficient of  $\pm 96$  W/m<sup>2</sup> K.

## I.2 Results and Discussion

A. The heat transfer coefficient - The heat transfer coefficients are invariably higher during microgravity for both pool and flow boiling except at the highest heat flux. The present findings for the case of pool boiling are in good agreement (both quantitative and qualitative) with some previously published results (Ref. 1), which showed that nucleate pool boiling heat transfer is enhanced as the buoyancy normal to the heater surface is reduced (including microgravity) and that it is degraded as the buoyancy normal to the heater surface is increased. The next result is the sharp decline in the heat transfer coefficient during microgravity for the highest heat flux case ( $7.58 \times 10^4 \text{ W/m}^2$ ). The forced flow only delayed the drop in heat transfer coefficient. The drop in the heat transfer coefficient is thought to have been caused by the drying-up of some portion of the heater surface due to the formation of vapor slugs, which stuck to the surface. The forced flow lost its effectiveness when the vapor agglomerates grew to a certain size and this will be further verified later in the flow visualization study.

Owing to the fact that the forced velocity is constant in all the cases, it is apparent that the forced convection is only effective for the lowest heat flux case ( $2.88 \times 10^4 \text{ W/m}^2$ ), whereas for the other cases the differences in heat transfer coefficient are negligible between pool and forced convection boiling. For the lowest heat flux, the differences in heat transfer coefficient grew even larger during microgravity, which is believed to be due to the ability of the flow to prevent the formation of vapor agglomerates and to maintain single and sliding bubbles. For the other cases, the heating is so high that the bubbles merge into vapor slugs before the flow can move them. The flow visualization, presented later, will also confirm the above-suggested mechanism for the forced-convection boiling.

B. Visualization study - Based on a side-by-side comparison between pool and forced-convection boiling flow patterns in the vicinity of the heater surface for heat fluxes ranging from  $2.88 \times 10^4$  to  $7.5 \times 10^4 \text{ W/m}^2$ , we found the following general trends after examining the visualization figures. During microgravity pool boiling, the bubbles did not rise off the heater surface, and as a result, they coalesced to form what might be called "vapor agglomerates." These large bubbles of various shapes have very rough surfaces and tend to cover up the heater surface, which appeared to cause some portions of the surface to become unwetted during the trailing portion of microgravity. The drying-up of the surface due to vapor agglomerates contributed to the drop in heat transfer coefficient for the heat flux of  $7.58 \times 10^4 \text{ W/cm}^2$ , as discussed above. Therefore, under microgravity the bubble swarm of terrestrial boiling was, in general, replaced by bubble slugs and chunk. The average size of the bubbles was seen to increase with the heat fluxes.

The second finding is concerned with the differences between pool and forced convection boiling under microgravity. With forced flows, the bubbles experienced a shear force along the flow direction. In the absence of gravity, the bubble dynamics depends on the balance between the drag due to the forced flow and the surface tension. The surface tension force would prevail if the contact area between the bubble and the heater surface is larger than the bubble frontal surface area experiencing the forced flow, otherwise the drag force would dominate. For the former, a hemispherical bubble would tend to stick to the surface while a spherical bubble, which belongs to the latter case, would most likely slide on the heater surface. Based on the visualization photographs, we found that for medium to high heat fluxes, the coalesced vapor agglomerates tend to form hemispherical or dome shapes with large base areas as a result of rapid vapor generation. Therefore at medium and high heat fluxes ( $4\text{--}7 \times 10^4 \text{ W/m}^2$ ) in the vicinity of the heater surface, the surface tension dominated, which left the forced flow with negligible effects on the bubble dynamics and heat transfer. The heat transfer coefficients discussed previously also support this conclusion.

For the lowest heat flux case under microgravity, the two-phase pattern of the forced-convection boiling was fundamentally different from that of the pool boiling. Owing to the low heating rate, the bubbles did not have any opportunity to coalesce and form vapor agglomerates, which resulted in the dominance of the flow drag over the surface tension. Basically, it was found that the bubbles are spherical and most of them are isolated from another. Based on our image analysis, the average individual bubble size was calculated at 1 to 2 mm while those of the vapor chunks were on the order of 1 cm and up. Strong evidence was found that the isolated spherical bubbles were "sliding" on the heater surface. It is our conclusion that the significantly higher heat transfer coefficient for forced-convection boiling than that for pool boiling in microgravity for the lowest heat flux is apparently due to the combination of the prevention of vapor agglomerate formation by the flow and the sliding of individual spherical bubbles on the heater surface.

**C. Implications to space application** - Based on the measured heat transfer coefficient data and the flow visualization, it is reasonable to suggest that for a given heat flux, if the forced-flow field is strong enough to prevent bubble agglomeration and to maintain single and sliding bubbles, subcooled forced-convection nucleate boiling would be a feasible and efficient heat transfer mechanism in microgravity.

## II. ELECTRIC FIELD

The purpose of study in this section is to understand the effects of a dielectrophoretic (DEP) force that is produced by an electric field on the boiling heat transfer in microgravity. The DEP force on a spherical bubble in an electric field is given as

$$\mathbf{F}_{DEP} = 2\pi R^3 \epsilon_l \left( \frac{\epsilon_v - \epsilon_l}{\epsilon_v + 2\epsilon_l} \right) \nabla |\mathbf{E}|^2 \quad (1)$$

where  $R$  is the radius of the bubble,  $\mathbf{E}$  is the strength of the electric field,  $\epsilon_l$  and  $\epsilon_v$  are the dielectric permittivity for the liquid and vapor phase, respectively. The buoyancy force on a bubble is

$$\mathbf{F}_b = \frac{4}{3}\pi R^3 (\rho_l - \rho_v) \mathbf{g} \quad (2)$$

where  $\rho_l$  and  $\rho_v$  are densities of the liquid and vapor phase, respectively. The gravitational acceleration is represented by  $\mathbf{g}$ . In our design, the DEP force is either pointing in the direction of gravity or against gravity. For the bubbles in the system, a parameter,  $g'_{(b,e)}$ , is defined to delineate the net external force effects.

$$g'_{(b,e)} = b + e, b = \frac{|\mathbf{F}_b|}{|\mathbf{F}_b^*|} \text{ and } e = \pm \frac{|\mathbf{F}_{DEP}|}{|\mathbf{F}_b^*|} \quad (3)$$

In the above  $\mathbf{F}_b^*$  is the buoyancy force under terrestrial gravity level. For our experiment  $b$  is either unity or nearly zero representing terrestrial and microgravity conditions, respectively. The plus sign in the definition of  $e$  represents that the electric force is in the direction of earth gravity and the minus sign indicates that the electric force is in the opposite direction of earth gravity. The selected values for  $e$  in our experiment are 0, -1, -0.5 and -0.1.

### II.1 Experiment

A 1.91 cm platinum wire, 0.025 cm in diameter with a resistance between approximately 0.045Ω to 0.05Ω (depending on the wire temperature) was used as the heater. The heat flux was calculated from the power given to the heater and the heater surface area. The temperature in the heater was measured using the standard resistometry technique.

Two finite-sized, square plates (2.54cm × 2.54cm) separated by an angle of 13 degrees were used as the electrodes. A 600 Å gold film was sputtered on the surface of the plates and was utilized as the electrically conducting surface. Also, two electrode dimensions were used so that a 23kV potential could correspond to both a 1g and a 2g DEP force, thus eliminating the voltage as a variable. The distance from the imaginary intersection for electrode geometry #1 and #2 were 2.0cm and 1.25cm respectively. In order to control whether the DEP force aided or opposed buoyancy, the direction of the buoyancy force was changed relative to the electrodes. This was done because it was much simpler to invert the experiment than to move the electrodes.

The platinum heater wire was placed at the lower edge of the diverging plates. The platinum heater wire was positioned along the equipotential line at zero potential located at the midplane of the two electrodes. This eliminated nearly all of the coupling effects between the wire and the electric field.

A pool boiling test channel constructed of thick aluminum was used with bulk temperature control obtained from surface mounted KAPTON heaters. A temperature controller and a number of series-T thermocouples were used at various locations to control and monitor the fluid temperature. A diaphragm metal bellows was used in conjunction with a thin-film pressure transducer to monitor and control the system pressure. Composite video (30Hz) was used for visualization and the electric potential was generated with a Hipotronics high-voltage DC power pack. FC-72 was used as the working fluid for

this study because it is an insulating dielectric. A degassing procedure was followed according to the 3M Product manual recommendations.

## II.2 Results and discussion

**A. Visualization study** - Video pictures are given in Figure 1 for two-phase bubbly flows around the heater wire under microgravity condition. Therefore the parameter  $b$  was zero and three electric field strengths were investigated which correspond to  $e$  of -0.1, -0.5 and -1. The parameter  $e$  is zero without any electric field. The applied heat flux is  $12.1 \times 10^4 \text{ W/m}^2$ . A general trend is that the average sizes of the bubbles are decreased as the voltage is increased. Film boiling is actually taking place on the wire in the absence of an electric field under microgravity ( $b=0, e=0$ ). It is apparent from these images that the DEP force did provide a sufficient external force to remove the vapor bubbles from the heater surface. The application of a relatively small DEP force ( $e=-0.1$ ) resulted in a relatively strong enough force to revert the film boiling back to the nucleate boiling.

**B. Critical heat flux** - Many correlations have indicated that the critical heat flux (CHF) depends on  $g^{1/4}$  (Ref. 2). This can be normalized with terrestrial-gravity conditions and written as

$$\frac{Q_c''(g)}{Q_c''(g^*)} = \left( \frac{g}{g^*} \right)^{1/4} \quad (4)$$

Where  $Q_c''$  is the critical heat flux at terrestrial gravity ( $g^*$ ) and variable gravity conditions ( $g$ ) respectively. This assumes that the fluid properties are not significantly influenced by gravity reductions. An analogy can be formed by simply replacing the gravity field ratio ( $g/g^*$ ) in Equation (4) with the  $g'_{(b,e)}$ , the DEP and buoyancy effective gravity, which yields

$$\frac{Q_c''(g_{eq})}{Q_c''(g^*)} = \left( |g'_{(b,e)}| \right)^{1/4} \quad (5)$$

where  $g_{eq}$  is the equivalent acceleration due to all external forces. The need for an absolute value sign in Equation (5) will be explained next.

Experimental CHF data is given in Figure 2 along with the curve based on Equation (5). First, we note that the data point for the microgravity conditions without any electric field ( $g'(b=0, e=0)=0$ ) is closely matched by the point representing a conditions where the terrestrial buoyancy is completely counter balanced by the DEP force ( $g'(b=1, e=-1)=0$ ). Second, the cases of  $g'(b=1, e=-2)=-1$  and  $g'(b=1, e=0)=1$  give similar CHF values. It means that for the wire, a net force downward or upward relative to the wire would not make any difference for the CHF, which explains the absolute value sign in Equation (5). In general, the concept of an effective gravity which represents the net force of all external forces is verified for the case where gravity and DEP force coexist for the boiling system.

## III. ACOUSTIC FIELD

Pool boiling heat transfer experiments from a platinum wire heater in FC-72 liquid were conducted under terrestrial and microgravity conditions, both with and without the presence of a high intensity acoustic standing wave within the fluid.

### III.1. Experiment

The acoustic-driven boiling system consists of an acoustic resonator, a fluid chamber, and a platinum wire heater. A DC power supply, a personal computer with an A/D card, a frequency generator, and an acoustic amplifier are connected to the boiling system. Lighting and video system is also an integral part of the system. The natural frequency of the acoustic resonator and the fluid chamber must be carefully matched. The fluid level in the chamber was adjusted for the highest acoustic pressure amplitude, and the cleanest sinusoidal pressure distribution in the vertical direction. The pressure was measured with a hydrophone. Both the hydrophone and the resonator were carefully calibrated.

The average heater surface temperature was determined from the measurement of the electrical resistance of the wire. The heat flux was estimated by the power dissipated by the heater wire. The temperature stratification of the fluid was eliminated by the mixing due to acoustic streaming and the bulk temperature was measured by a copper-constantine thermocouple. The microgravity environment was obtained in our 0.6-second and 2.1-second drop towers. All experiments were conducted under atmospheric pressure which corresponded to a saturation temperature of 54.5°C for FC-72. The resonator driving frequency was always set at 10.18 kHz. The acoustic pressure amplitude is 2.6 atm. gauge.

### III.2. Results and Discussion

The effects of acoustics on the heat transfer coefficient (HTC) and vapor bubble movement in pool boiling depend on many factors. The properties of the experiment that can be controlled were the heat flux, acoustic pressure amplitude, heater position within the sound field, and the gravity level.

A. Terrestrial Gravity - The placement of the heater within the sound field was shown to be critical. The heater was placed at several positions within the sound field. Specially attention was given to the following heater positions within the sound field: pressure node, pressure antinode, and halfway between the pressure node and antinode where the acoustic force is the highest. The HTC increased when the heater was positioned anywhere within the sound field. However, the HTC had the highest increase when the heater was placed at the acoustic pressure antinode. The minimum increase in the HTC occurred when the heater was at the acoustic pressure node.

Acoustics had the largest effect on the HTC at the inception of boiling and close to burnout. The temperature of the heater surface dropped by approximately 10 degrees Celsius at the inception of boiling. At larger heat fluxes (46.4 W/cm<sup>2</sup>) the surface temperature dropped over 200°C. The most significant finding is that the incipience superheat excursion is eliminated with the acoustic field on. The effects of acoustics on the HTC diminished in the regime of vapor slugs and columns.

B. Microgravity - As shown in Figure 3, the heat transfer is more efficient in the presence of a sound field. Without an acoustic field, the degree of superheat was increased during microgravity. The heater surface temperature remained unaffected, when the system went from terrestrial gravity to microgravity under an acoustic field. Without a sound wave, the vapor bubbles tend to stay on the heater surface during microgravity, which increases the heater surface temperature. The acoustic field helps remove the bubbles during microgravity, which seems to maintain the heater surface temperature at a relatively constant value.

The effect of acoustics on vapor bubbles in pool boiling was investigated by video visualization. When the heater is placed at the acoustic pressure antinode the vapor bubbles were driven toward the pressure node. Only a few bubbles were seen along the heater surface. When the heater was located at the acoustic pressure node the bubbles were levitated around the heater. The vapor bubbles varied in size and they were not equally spaced along the heater. It is reasonable to conclude that it is feasible to maintain nucleate boiling in microgravity by placing the heater wire at the acoustic pressure antinode.

### ACKNOWLEDGMENT

The work was supported by NASA Grant No. NAG3-1387. The author is grateful for the assistance and support of Dr. Fran hiamionte at the NASA Lewis Research Center. The 3M Company donated the FC72 for our research.

### REFERENCES

1. Merte, H., Jr., Lee, H.S. and Ervin, J.S., Transient Nucleate Pool Boiling in Microgravity - Some Initial Results, Int. Symp. Microgravity Science and Applications, Paper J-5, 1993.
2. Zuber, N., On the Stability of Boiling Heat Transfer, J. Heat Transfer, Vol. 80, 1958, pp. 711-718.

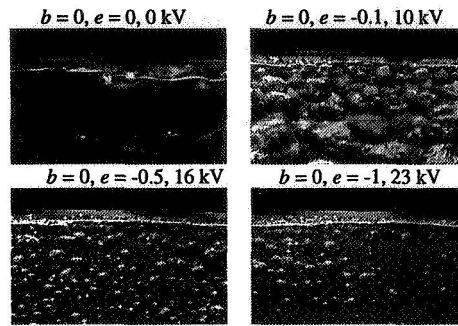


Figure 1 - Microgravity boiling ( $b=0$ ) with various DEP forces ( $e=-1, -0.5, -0.1, 0$ ), Heat Flux =  $12.1 \times 10^4 \text{ W/m}^2$

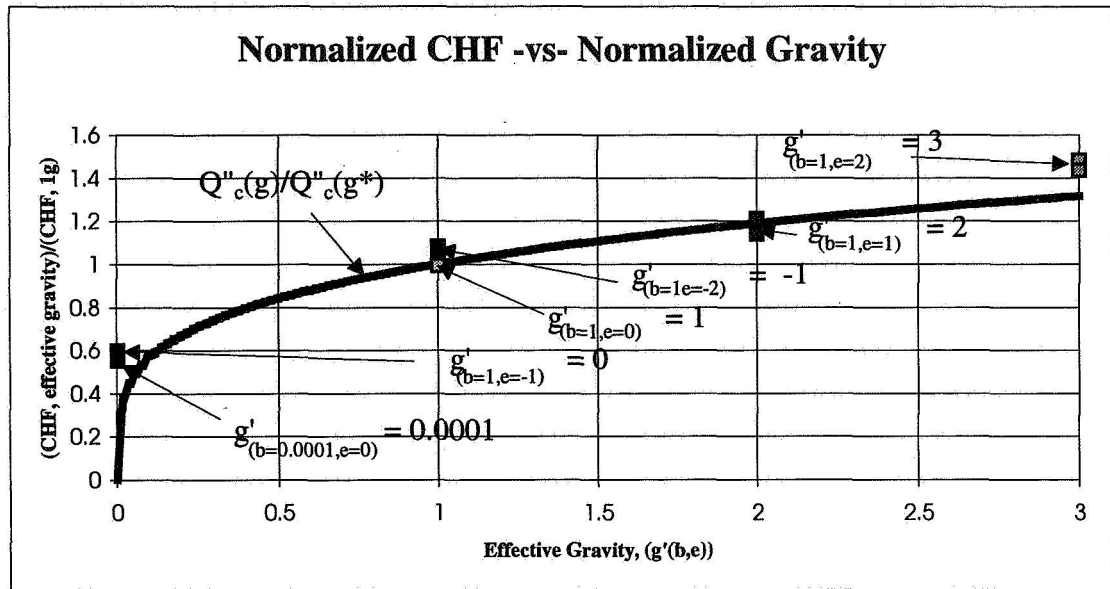


Figure 2 - Normalized CHF -vs- Effective Gravity

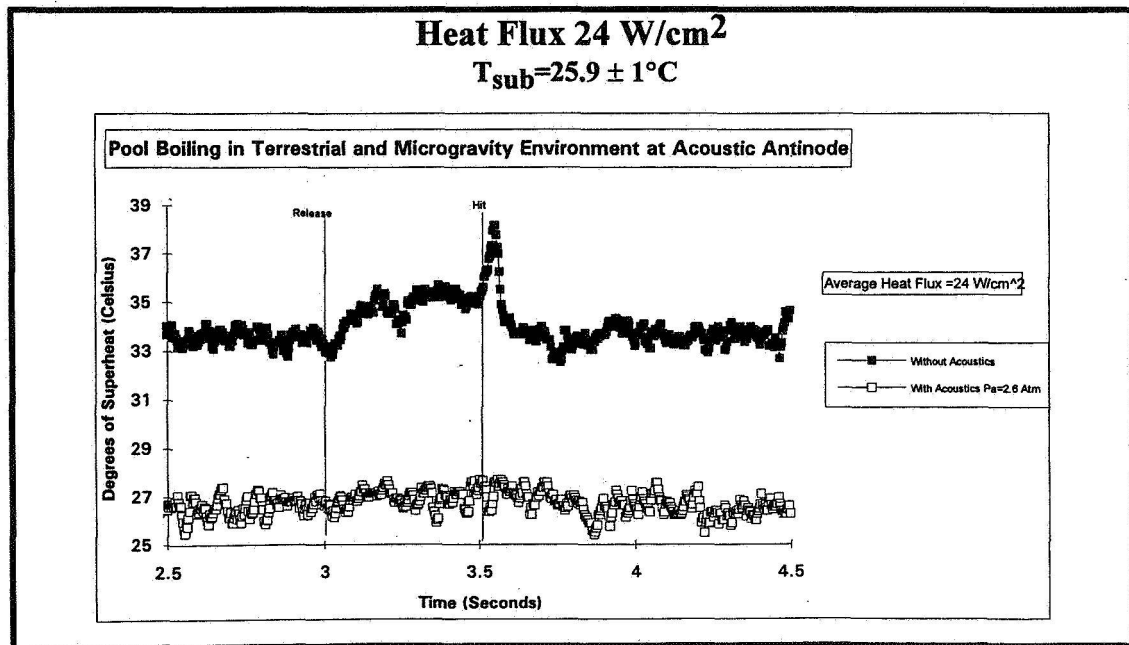


Figure 3



# NON-ISOTHERMAL EXPERIMENTAL STUDY OF THE CONSTRAINED VAPOR BUBBLE THERMOSYPHON

Muthu Karthikeyan, Jianming Huang, Joel Plawsky, and Peter Wayner, Jr.  
The Isermann Department of Chemical Engineering  
Rensselaer Polytechnic Institute  
Troy, New York 12180-3590

## ABSTRACT

Experimental and theoretical techniques to study non-isothermal transport processes in the constrained vapor bubble thermosyphon (CVBT) were developed using a pentane/quartz system. The transport processes can be evaluated by measuring the liquid film profile, which gives the pressure field, and the temperature field. The axial variation in the capillary pressure was measured using an image-analyzing interferometer that is based on computer-enhanced video microscopy of the naturally occurring interference fringes. Thermoelectric coolers were used to control the temperature level in the condensation region and, therefore, the length of the approximately "adiabatic" surface region which is a function of the temperature difference between the CVBT surface and the surroundings. High values for the axial thermal conductance in the "adiabatic" surface region were demonstrated under certain conditions.

## INTRODUCTION

In order to study the details of transport processes in heat pipes, we report on our investigation of a larger version of Cotter's micro heat pipe (1) in the form of a 3 x 3 x 40 mm fused quartz cell of square cross-section. In this case, the capillary driving force in a portion of the cell is of the same order of magnitude as the gravity force unlike a micro heat pipe for which the capillary force is sometimes much larger than the gravity force. Hence, we call this cell a Constrained Vapor Bubble Thermosyphon (CVBT). From a fundamental point of view, the CVBT conveniently permits the study of interfacial transport concepts. In particular, we are concerned with the experimental study of the generic CVBT presented in Fig. 1 for a micro-gravity environment. For a completely wetting system, the liquid will coat all the walls of the chamber. For a finite contact angle system, some of the walls will have only a small amount of adsorbed vapor that changes the surface properties at the solid-vapor interface. Liquid will fill a portion of the corners in both cases. If temperature at End (2) is higher than End (1) because of an external heat source, energy flows from End (2) to End (1) by conduction in the walls and by a combined evaporation, vapor flow, and condensation mechanism. Heat applied to End (2) vaporizes the liquid in this region and the vapor is forced to move to End (1) where it condenses, releasing the latent heat of vaporization in the process. The curvature of the liquid-vapor interface changes continually along the cell because of viscous losses, and the vaporization/condensation process. This capillary pressure difference between the evaporator and the condenser regions causes the working fluid to flow back to End(2) from End(1) along the right-angled corner regions. These corner regions act as liquid arteries and hence replace the wicking structure of a conventional heat pipe. Herein, we present the results of our initial ground-based non-isothermal studies which are a prologue to micro-gravity studies.

In order for the CVBT to operate, the maximum available capillary pumping head must be greater than the total pressure drop in the CVBT in a gravitational field. This pressure drop is made up of three components: The pressure drop  $\Delta P_l$  required to return the liquid from the condenser to the evaporator; The pressure drop  $\Delta P_v$  necessary to cause the vapor to flow from

the evaporator to the condenser ; The gravitational head  $\Delta P_g$  which may be zero, positive or negative.

$$(\Delta P_c)_{\max} \geq \Delta P_l + \Delta P_v + \Delta P_g \quad (1)$$

where the difference between the augmented Young-Laplace equations at locations (2) and (1) is

$$(\Delta P_c) = \sigma_l \left[ \frac{1}{r_2} - \frac{1}{r_1} \right] + \Pi_2 - \Pi_1 \quad (2)$$

The first term accounts for the change in the capillary force and  $\Pi$  is the disjoining pressure. A discussion concerning the use of this equation for the shape dependent stress field is given by DasGupta, et al. (2). In general, the performance of the CVBT is based on the chemical potential profile, which is a function of the temperature and pressure profiles. The pressure profile is connected to the film thickness profile by the augmented Young-Laplace equation, Eq. (2). Therefore, we need to measure the temperature and thickness profiles.

## EXPERIMENTAL PROCEDURE AND OBSERVATIONS

The CVBT experimental setup consists mainly of the quartz cell, a resistance heater, and four miniature (5 x 5 x 2.4mm) thermoelectric coolers. The heater was a hollow cylinder of *Garrolite* approximately 60 mm long on which high-resistivity nichrome wire was tightly wound. A 4.76 mm diameter, stainless steel rod of 85 mm length was inserted into the heater in such a way that 25 mm of the rod projected out of one end of the heater. The contact resistance between the heater and the stainless steel rod was reduced by using a layer of thermally conductive paste between the contact surfaces. The projecting end of the stainless steel rod was then attached to the cell using high thermal conductivity silver epoxy. The heater and the projected portion of the rod were thoroughly insulated to minimize heat loss. This arrangement enables us to estimate the heat input into the cell by measuring the temperature profile of the stainless steel rod. A simple fin equation can then be fitted to the temperature data to yield the rate of heat transport from the end of the rod to the cell. The whole assembly was mounted on the mechanical stage of a high-power light microscope. This enables the movement of the assembly on the stage so that any part of the cell could be viewed under the microscope, and the liquid film thickness profile measured at that location. The pentane (99.9% purity) working fluid used in the vapor bubble thermosyphon experiments was de-aerated and stripped of higher boiling substances by a single vacuum distillation step.

The temperature profiles of both the rod and the quartz cell were measured using closely spaced micro-scale (40 AWG) Chromel-Alumel thermocouple beads. These were attached to the side of the cell and the rod using conductive silver epoxy and the beads were then coated with regular epoxy to reduce the error in the measured temperature due to the effect of the surroundings. The coolers were firmly pressed against the edges of end (1) of the cell. A thin coating of thermally conductive paste ensures good thermal contact between the cell and the coolers. It should be pointed out that, although the coolers were primarily designed to help retain the bubble within the cell by maintaining a constant low temperature at the cooler end, they were found to have an additional important function. We found that the length of the adiabatic region could be changed by using the coolers to lower the temperature in the middle portion of the cell to a value close to that of the surroundings. A drawing of a corner of the CVBT, where the thickness profile was measured, is presented in Fig. 2. Details of this film thickness measurement, known as Image Analyzing Interferometry (IAI) are elaborated elsewhere

(DasGupta, 1995). The cell had roughly 40 to 50% of liquid by volume while the remaining volume was occupied by pentane vapor. We established the vapor bubble at the heater end by slightly tilting the setup in such a way that liquid flowed out of the heated end.

Prior to the experiments, the CVBT cell and the connecting tubes were thoroughly cleaned in an ultrasonic bath and dried in an oven. The cell alone was rinsed for 1 minute with a dilute (1%) solution of Hydrofluoric acid to remove a thin layer of quartz along with the contaminants adhering to the surface. This proved quite effective although it rendered the inner surface of the cell considerably rougher than it was before. A final rinse with de-ionized water was performed and the cell was blow dried in a stream of ultra-clean, dry nitrogen. The cell was attached to the liquid feeder/vacuum assembly by means of heat shrink Teflon tubing. The whole assembly was evacuated and a sufficient amount of pentane was distilled into the cell from the holding Squibb funnel. The pressure inside the system was continuously monitored using an *Omega* Pressure transducer/Digital meter combination, to ensure the lack of contamination by air.

## EXPERIMENTAL RESULTS AND DISCUSSION

Figure 3 shows a plot of the temperature difference between the surface of the CVBT and the room,  $\theta$  versus the axial distance,  $x$ , for a CVBT and the corresponding dry quartz cell. The electrical power input to the heater was 1.5 W in both cases. The difference between the two profiles is not dramatic because the coolers at the end of the CVBT remained off during the course of these experiments. Data presented below for different heater and cooler power settings indicate that a flat temperature profile in the middle of the CVBT could be obtained for a particular combination of these power settings.

The stainless steel rod was designed to evaluate the heat input into both the CVBT and the dry cell. The measured steel rod temperatures were fitted to the following fin solution equation, with the overall effective heat transfer coefficient  $U$  between the steel rod and the environment evaluated as a variable parameter.

$$\frac{\theta}{\theta_b} = \frac{(\theta_i / \theta_b) \sinh mx + \sinh m(l_s - x)}{\sinh ml_s} \quad (3)$$

where  $\theta_{1s}$  and  $\theta_b$  are the temperature differences between the CVBT and the room at the beginning and at the thermocouple location just before the end of the stainless steel rod. For the purposes of this analysis, the temperature differential at the end of the steel rod (at the interface between the rod and the cell) was omitted since this reading might not be accurate.  $l_s$  is the distance between the first and the last measured points used for calculation, which in this case is 20 mm, and  $m$  is defined by the following equation.

$$m^2 = \frac{UP}{kA_c} \quad (4)$$

where  $P$ ,  $k$ , and  $A_c$  are the perimeter, the thermal conductivity and the cross-sectional area of the stainless steel rod, respectively. Least squares method was used to obtain  $U$  from the best fit of the data. Then, the heat going out from the end of the steel rod,  $Q_{out}$ , was calculated from the fin equation.

Sets of CVBT experiments and corresponding dry cell experiments (same  $Q$  in both cases) were run at different heater power inputs. Using the same  $Q$ , a fin solution was obtained for a hypothetical solid quartz rod of similar length and cross-sectional area. The results for these

three cases are compared in Fig. 4 for  $Q=0.1$  W. As seen from this figure, the dry cell data can also be modeled as a fin with an appropriate value for the heat transfer coefficient,  $h$ . It is obvious that, for  $Q=0.1$  W, the CVBT has the lowest resistance. The local heat flux was calculated as follows: First, the heat transfer coefficient,  $h$  was calculated by fitting the dry cell data to a fin equation. Then, the local axial heat flux at different locations in the CVBT were calculated using the following equation:

$$q(x) = \frac{Q - \int_0^x P h \theta dx}{A} \quad (5)$$

where  $Q$  is the heat input to the CVBT,  $P$  the perimeter of the CVBT and  $A$  the cross-sectional area of the CVBT. Assuming that the value of the heat transfer coefficient between the surface of the CVBT and the room,  $h$ , is equal to the value obtained with the dry cell at approximately the same temperature, the surface heat flux was obtained. The integration was performed numerically with the cubic spline fit data. We found that, in this case, the heat rate from the CVBT obtained through integration of the temperature of the CVBT equaled the heat input  $Q$  to within 1%. The temperature profile of the CVBT in Fig. 4 was fitted as a smoothed cubic spline and the local slopes of the profile  $d\theta/dx$  were obtained numerically. Therefore, the local effective thermal conductivity can be obtained using the equation below:

$$k_{eff}(x) = -\frac{q(x)}{\frac{d\theta}{dx}(x)} \quad (6)$$

The local effective thermal conductivity distribution in the CVBT, with coolers off for  $Q=0.1$  W is shown in Fig. 5. As seen, the local heat flux decreases along the cell. But the effective thermal conductivity goes through a maximum value in the middle of the cell where the slope of the temperature profile becomes very small. For this portion of the CVBT, the effective thermal conductivity is comparable to that of the stainless steel rod. The results presented next demonstrate that the performance can be dramatically improved by using the thermoelectric coolers. Experiments with the coolers on at the end of the CVBT were also conducted. A comparison of two cases, one with the coolers on and the other with the coolers off, is presented in Fig. 6. We find that, for the same power input to the heater, a CVBT with coolers to remove the heat from the end performs much better (higher  $k_{eff}$ ) than the one with only natural convection to remove the heat. Also, the CVBT with the coolers on has a long distinct horizontal temperature region and a smaller base temperature. It is obvious that the efficiency of the CVBT reaches the maximum in this region. In essence, we were able to expand the "adiabatic" length by lowering  $\theta$ .

If the vapor pressure gradient is negligible, the liquid pressure gradient is due to the curvature gradient.

$$\frac{dP_l}{dP_x} = -\sigma_l \frac{dK}{dx} \quad (7)$$

As mentioned earlier, the liquid film thickness measurements were carried out. A plot of the curvature distribution of CVBT(coolers off) for  $Q=0.1$  W is shown in Fig. 7. This figure shows that the curvature decreases from the high temperature region to the low temperature region. Although, the analysis and data are incomplete, a rough calculation shows that this curvature gradient gives the correct order of magnitude for  $Q$ .

## CONCLUSIONS

Based on the experiments and subsequent analysis of the data gathered we reach the following conclusions:

1. Experimental and theoretical techniques to study non-isothermal transport processes in the constrained vapor bubble thermosyphon(CVBT) were developed.
2. The transport processes can be evaluated by measuring the liquid film profile using an image-analyzing interferometer, which gives the pressure field, and the temperature field.
3. Thermoelectric coolers can be used to *control* the temperature level in the condensation region and, therefore, the length of the approximately "adiabatic" surface region.
4. High values for the axial thermal conductance in the "adiabatic" surface region were demonstrated under certain conditions.

## ACKNOWLEDGMENT

This material is based on work supported by the National Aeronautics and Space Administration under grant # NAG3-1399. Any opinions, findings, and conclusions or recommendations expressed in this publication are those of the authors and do not necessarily reflect the view of NASA.

## REFERENCES

1. Cotter, T. P., 1984, "Principles and Prospects of Micro Heat Pipes", Proc 5th Int Heat Pipe Conf, Tsukuba, Japan, pp. 328-335.
2. DasGupta, S., Plawsky, J. L., and Wayner, P. C., Jr., 1995, "Interfacial Force Field Characterization in a Constrained Vapor Bubble Thermosyphon", AIChE Journal, 41(9), pp. 2140-2149.

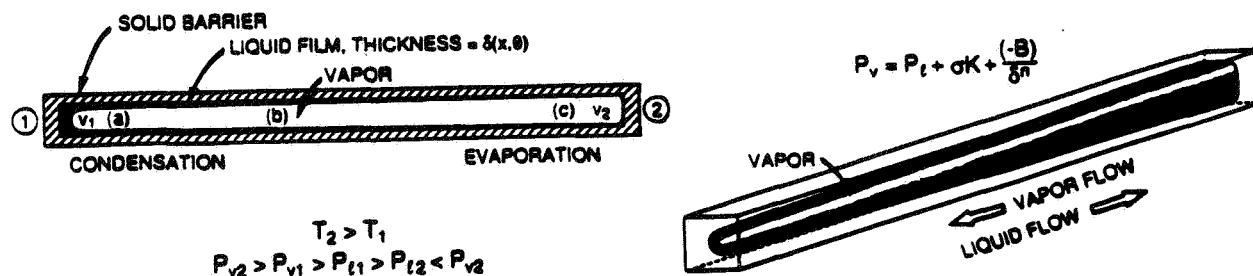


Figure 1. Constrained Vapor Bubble Thermosyphon Concept.

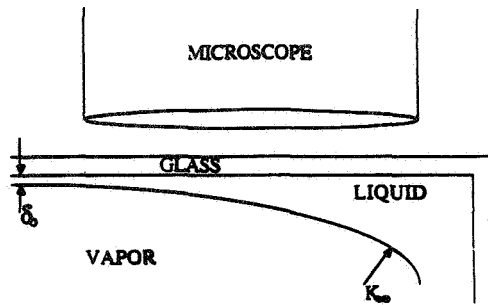


Figure 2. Location of microscope.

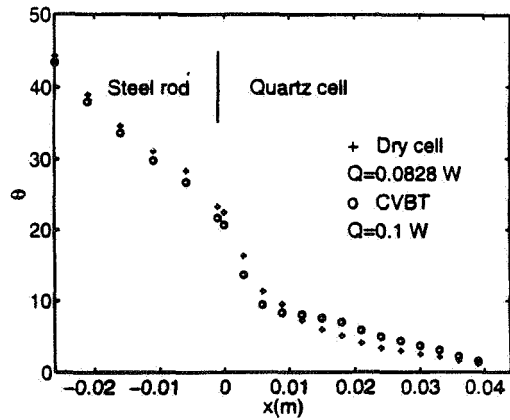


Figure 3. Comparison of  $\theta$  profile for CVBT and dry cell.

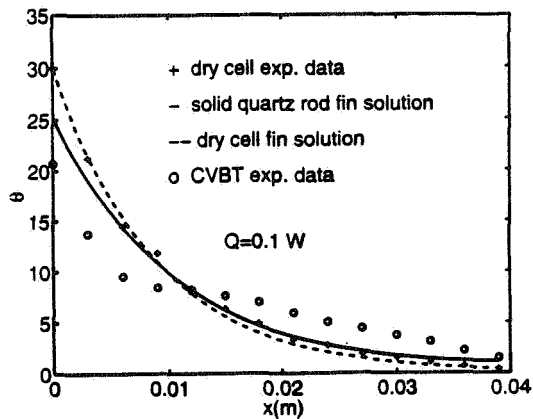


Figure 4. Comparison of the  $\theta$  profiles for the CVBT(coolers off), dry cell and solid quartz rod.

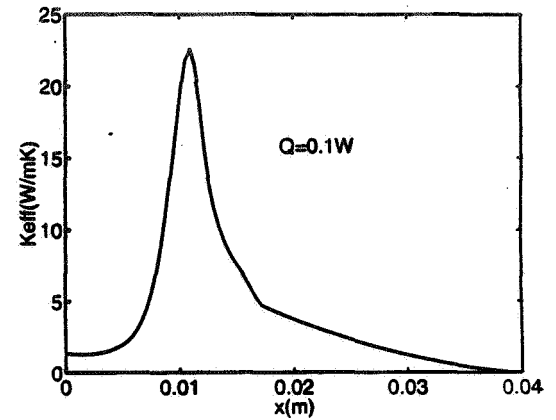


Figure 5. Local axial effective thermal conductivity distribution in CVBT for  $\theta(x)$  given in Figure 4.

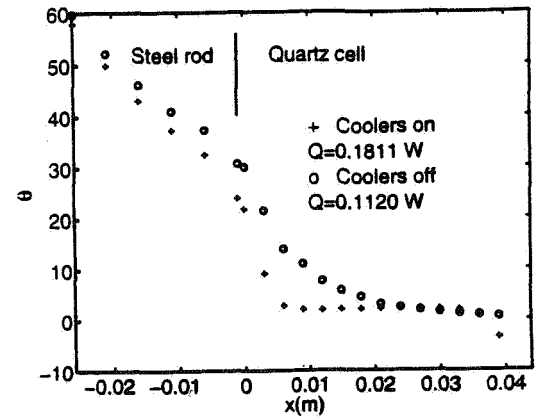


Figure 6. Comparison of CVBT with or without cooler on at same power input to heater, 2.2W.

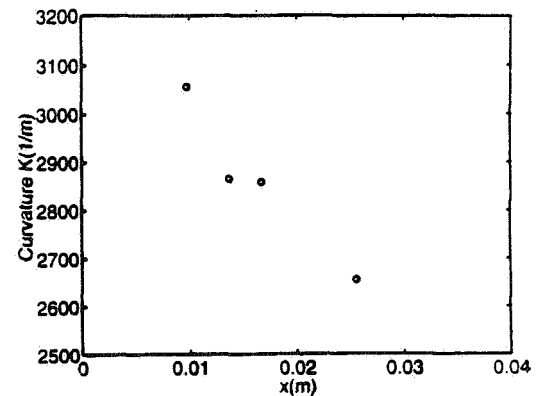


Figure 7. Curvature distribution in CVBT for data given in Figure 4 ( $Q=0.1$  W, coolers off).

# INVESTIGATION OF MECHANISMS ASSOCIATED WITH NUCLEATE BOILING UNDER MICROGRAVITY CONDITIONS

V.K. Dhir

Mechanical and Aerospace Engineering Department  
University of California, Los Angeles  
Los Angeles, CA 90095-1957

## ABSTRACT

The focus of the present work is to experimentally study and to analytically/numerically model the mechanisms of growth of bubbles attached to, and sliding along, a heated surface. To control the location of the active cavities, the number, the spacing, and the nucleation superheat, artificial cavities will be formed on silicon wafers. In order to study the effect of magnitude of components of gravitational acceleration acting parallel to, and normal to the surface, experiments will be conducted on surfaces inclined at different angles including a downward facing surface. Information on the temperature field around bubbles, bubble shape and size, and bubble induced liquid velocities will be obtained through the use of holography, video/high speed photography and hydrogen bubble techniques, respectively. Analytical/numerical models will be developed to describe the heat transfer including that through the micro-macro layer underneath and around a bubble. In the micro layer model capillary and disjoining pressures will be included. Evolution of the interface along with induced liquid motion will be modelled. Subsequent to the work at normal gravity, experiments will be conducted in the KC-135 or the Lear jet especially to learn about bubble growth/detachment under low gravity conditions. Finally, an experiment will be defined to be conducted under long duration of microgravity conditions in the space shuttle. The experiment in the space shuttle will provide microgravity data on bubble growth and detachment and will lead to a validation of the nucleate boiling heat transfer model developed from the preceding studies performed at normal and low gravity (KC-135 or Lear jet) conditions.

## INTRODUCTION

Boiling is known to be a very efficient mode of heat transfer, and as such, it is employed in component cooling and in various energy conversion systems. For space applications boiling is the heat transfer mode of choice, since for a given power rating the size of the components can be significantly reduced. For any space mission the size, and in turn, the weight of the components plays an important role in the economics of the mission.

Applications of boiling heat transfer in space can be found in the areas of thermal management, fluid handling and control, and power systems. For space power systems based on the Rankine cycle (a representative power cycle), key issues that need to be addressed are the magnitude of nucleate boiling heat transfer coefficient and the critical heat flux under low-gravity conditions. Knowledge of nucleate boiling heat transfer coefficients is necessary to determine the overall resistance for transfer of heat from a source to a sink. The critical heat flux represents the upper limit of safe heat removal since for heat fluxes greater than critical heat flux, the surface will be covered with a vapor film which, in turn, will result in a rapid rise in the temperature or failure of the component.

Understanding and quantification of boiling heat fluxes at low-gravity conditions are also important for other space power systems such as thermionic reactors operating under transient conditions (see e.g., von Arx and Dhir<sup>1</sup>). Design of on-orbit storage and of supply systems for cryogenic propellants and life support fluids also requires quantitative data for boiling heat transfer. Additionally, an assessment of the cooling of electronic packages or power supply systems associated with various instrumentation and control systems requires a knowledge of boiling heat transfer coefficients.

Studies of boiling heat transfer for space applications impose unique constraints in terms of the number of experiments that can be conducted under microgravity conditions, the duration of the experiments and expense and difficulties involved in performing the experiments. Thus for space applications, it is even more important that a better understanding of the boiling mechanism be developed so that space experiments are needed only for confirmation of the predictions.

The objective of the present work is to delineate through experiments and analysis, the contributions of some of the key mechanisms to total heat transfer rate during nucleate boiling under microgravity conditions. This includes the contribution of micro/macro layer evaporation on single and merged bubbles attached to a heated wall, heat transfer during sliding of a bubble along a heater wall and heat transfer due to fluid motion resulting from bubble growth and Marangoni effect. The effect of fluid motion induced by a growing bubble on its detachment from the surface will also be considered.

Under microgravity conditions the early data of Keshock and Siegel<sup>2</sup> and Siegel and Keshock<sup>3</sup> on bubble growth and heat transfer show that the effect of reduced gravity is to reduce the buoyancy and inertia forces acting on a bubble. As a result, under reduced gravity bubbles grow larger and stay longer on the heater surface. This in turn leads to merger of bubbles on the heater surface and existence of conditions similar to fully developed nucleate boiling. Thus, under microgravity conditions partial nucleate boiling region may be very short or non-existent. Figure 1a compares photographs taken by Zell et al<sup>4</sup> for nucleate boiling on a wire under 1-g and  $\mu$ -g conditions. It is interesting to note from Fig. 1b that data obtained under  $\mu$ -g condition is described well by curves fared through the data obtained at 1-g. This is consistent with the conclusion of Siegel<sup>5</sup> that the effect of reduced gravity on nucleate boiling heat transfer coefficient under saturated and subcooled conditions is small.

Ervin et al<sup>6</sup> and Ervin and Merte<sup>7</sup> have studied transient nucleate boiling on a gold film sputtered on a quartz plate by using a 5-second drop tower ( $10^{-5} g_e$ ) at NASA Lewis Research Center. In the experiments R-113 was used as the test liquid. From the Experiments it was found that time or temperature for initiation of nucleate boiling was greater for a pool at near saturation temperature than that for a subcooled pool. They also noted the occurrence of energetic boiling at relatively low heat fluxes. The energetic boiling in which vapor mass rapidly covered the heater was postulated to be associated with an instability at the wrinkled vapor-liquid interface. Hasan et al<sup>8</sup> have studied nucleate pool boiling of R-113 during the tank pressure control experiment (TPCE) under the low gravity environment of the space shuttle. They noted that at very low heat fluxes stable nucleate boiling could be sustained over a long period of time. The wall superheats accompanying the relatively low nucleate boiling heat fluxes were rather large. Recently Merte<sup>9</sup> has reported results of pool boiling experiments conducted in the space shuttle for the same surface that was used in the drop tower tests. Subcooled boiling during long periods of microgravity was found to be unstable. The surface was found to dryout and rewet. Average heat transfer coefficients during the dryout and rewetting periods were, however, found to be about the same. The nucleate boiling heat fluxes were higher than those obtained on a similar surface at earth normal gravity conditions.

Experimental studies of flow boiling under low gravity conditions are far fewer and limited than those for pool boiling. The earliest study of flow boiling under reduced gravity conditions is that of Cochran<sup>10</sup>. The experiments were conducted in drop towers with flow velocities varying from 4.2 to 11.5 cm/s. These short-duration (2.2 second) low gravity tests were focused on the boiling process near inception. In comparison to normal gravity tests, it was found that in microgravity, bubbles tended to stay on the heating surface, became large enough to coalesce with neighboring bubbles and acquired irregular shapes. The size of bubbles along the heating surface was found to correlate with thickness of the thermal layer. Very recently Saito et al<sup>11</sup> have studied flow boiling of water on a heater rod placed in a square channel. The experiments were conducted in Japanese low gravity experimental aircraft (MU-300) at  $0.01 g_e$  for 20 seconds. In the experiments, subcooled nucleate boiling heat transfer data for water were taken at velocities varying from 3.7 - 22.9 cm/s and pressures in the range of 0.9 to 2.40 bars. Nucleate boiling heat transfer coefficients were found to increase slightly in the direction of flow and the magnitudes of the heat transfer coefficients were about the same as at normal gravity. Figure 1c shows their photographs of nucleate boiling at a flow velocity of 6 cm/sec under both normal and microgravity conditions. Existence of relatively large bubbles on the heated surface is evident. These bubbles slide along the heater surface over long distances.

Finally, it appears that recent studies of nucleate boiling under microgravity have shed light on this complex phenomena, however, the studies are non-conclusive. Questions remain on the stability of nucleate boiling, the equivalence of magnitudes of heat transfer coefficients at normal gravity and low gravity conditions and on the physics that underlies the phenomena. As such there is no mechanistic model that describes the observed physical behavior and the dependence of nucleate boiling heat flux on wall superheat.

## DESCRIPTION OF PROPOSED RESEARCH

It is evident from the review of the current literature carried out in the previous section, an important question that needs to be answered, but has not yet been answered, is how does microgravity affect nucleate boiling heat transfer under pool and low velocity forced flow conditions? As such the main objective of the present work is to develop a physical understanding of the key phenomena and to advance mechanistic models so that development of a model for nucleate boiling under microgravity conditions is facilitated. The work is both experimental and analytical/numerical in nature. Experiments are to be performed both at normal gravity as well as at low gravity conditions in the KC-135 or the Lear jet and in the space shuttle.

To be able to predict nucleate boiling heat transfer under microgravity conditions, a quantitative understanding of the following is needed.

1. Number density of active nucleation sites.



2. Heat transfer to a single bubble including that associated with micro/macro layer evaporation.
3. Bubble merger process and heat transfer to vapor stems supporting a large bubble (may be mushroom type) attached to heater wall.
4. Detachment process of small as well as large mushroom type of bubbles.
5. Flow field induced by bubbles during growth and detachment including that due to Marangoni effect.
6. Heat transfer and flow field for a bubble sliding along a heated wall.

Number density of active nucleation sites at a given superheat is a very important parameter. However, this is an extremely untractable parameter because of the random nature of the size and shape of the cavities on a commercial surface and their gas/vapor trapping ability. Although significant progress has been made in recent years (see Wang and Dhir<sup>12</sup>) in a priori prediction of number of sites that can become active at a given superheat, in the present work the number of cavities that nucleate and their spacing will be a control variable. This will be done by using the surface of a silicon wafer as the test surface. On the wafer surface, single and multiple artificial cavities of a specified geometry (cylindrical) and mouth diameter will be formed. Isolated bubbles will be studied on a single cavity formed on the surface, whereas bubble merger and bubble-bubble interactions will be studied by adjusting the spacing of the artificial cavities (2 or more). Figure 2a shows the typical cavity spacings that will be studied.

Thus the present work will focus only on items 2-6, identified above. Experiments in support of items 2, 3, 5, and 6 will be conducted at normal gravity. The Lear jet or KC-135 aircraft will be used to conduct experiments in support of items 4 and 5. Finally, an experiment combining all aspects of items 2-6 will be defined to be carried out in the space shuttle. In this experiment a "designed" surface, rather than a commercial surface, will be used. The designed surface will have a pre-specified distribution of artificial cavities that can nucleate at a given superheat.

Initially, the experiments at normal gravity will be performed on a downward facing surface. The downward facing surface is chosen so as to stabilize the bubbles and to create temperature field in the liquid solely determined by diffusion of heat from the wall. However, the experiments will subsequently be conducted, when the surface is inclined at different angles with the horizontal. This will provide different magnitudes of gravitational acceleration normal and parallel to the surface. Figure 2b shows the type of orientations that will be investigated. Holographic interferometry will be used to determine the temperature field in the liquid at the wall and around the bubble. Reflections from the liquid-vapor interface of the micro layer and plane surface will be used to create interference fringes. The fringe spacing will be used to determine the thickness of the micro layer at various radial locations

For merged bubbles, the holographic technique will provide information of the temperature field in the upper outer region of the bubbles only. Inner details will be missing. However, interference patterns still could be used to determine the microlayer thickness under each bubble. Knowing the total evaporation rate and heat transfer from the microlayer and along the outer portion of the bubbles, an assessment of the heat flux in the blocked region of the hologram will be made. This evaluation will be confirmed with that determined from single bubble studies. Video/high speed movies will provide information on the growth rate and shape of the bubbles. Liquid motion during bubble growth will be determined by using the hydrogen bubble technique. Any distortions and limitations on bubble size and shape by the heater and test section dimensions will be identified. A cross check on the calculated evaporation rate will be made by comparing the heat input rate obtained by using the information from the temperature field in the liquid, and thickness of the micro layer with that obtained from the observed bubble growth rate. To simulate low velocity flow boiling, a positive displacement pump will be used to create flow parallel to the heater surface. Experiments will be conducted with water and PF-5050 ( $C_5F_{12}$ ). The test liquid PF-5050 is environmentally safe and has properties similar to R-113. The use of liquids with different wetting characteristics will allow us to determine the effect of wettability (contact angle) on microlayer thickness, and bubble growth and departure behavior.

## EXPERIMENTS

The objective of the experiments is to provide in a very clean manner, the basic information that is needed to develop a mechanistic model for prediction of nucleate boiling heat flux as a function of wall superheat. With the presumption that dependence of cavity site density on wall superheat is known, (true for designed surface) the prediction of heat flux requires a knowledge of interfacial area per cavity, interfacial heat flux, and thickness of micro/macro layers. Size of bubbles at breakoff, bubble release frequency and the number of bubble release sites influence the time and area

averaged heat transfer and also determine the vapor removal rate. Three types of experiments are proposed in the present work. These include experiments at normal gravity, in the KC-135 or the Lear jet and in the space shuttle.

### Normal Gravity Experiments

The first set of experiments will be conducted on a downward facing rectangular surface. A silicon wafer attached to a copper block with a high thermal conductivity cement will serve as the test surface. A silicon wafer is used to eliminate cavities other than the prescribed artificial cavities. The copper block will be divided into three sections so that the central portion can have a heat flux different than that on the bounding or auxiliary surfaces and end effects are minimized. Figure 3 shows a schematic diagram of the apparatus. Heat input to the copper block will be controlled with several cartridge heaters embedded in the block. The heat flux on the central and the auxiliary surfaces will be determined from several 36 gage chromel-alumel thermocouples located discretely in the copper block. Silicon wafers with a thickness of 50  $\mu\text{m}$  and a width and length of 1 and 3 cm respectively will be acquired commercially. Wafers will be visually inspected with an optical microscope to exclude surfaces having any pre-existing cavities. Artificial cavities in the shape of square cylinders will be formed on the surface with an etching process in the clean rooms of the School of Engineering and Applied Science at UCLA.

The test section will be mounted on one side of a liquid holding and viewing chamber. Four sides of the liquid chamber will have glass windows so that the boiling process can be viewed from two sides as well as from the bottom. On the sixth side of the viewing chamber, connection will be made to a positive displacement pump to create forced flow conditions on the heater surface. A provision will exist to orient the test surface at different angles to the gravitational acceleration vector.

The heat flux at the test surface will be determined from the output of the thermocouples embedded in the copper block. The temperature distribution in the liquid adjacent to the heated surface and the vapor liquid interface will be determined through holographic interferometry.

Interference fringe pattern obtained from laser beams reflected from the heater surface and from the liquid-vapor interface of the micro-layer will be used to determine the thickness of the micro-layer at various radial positions. Liquid velocity field created by the vapor bubble during its growth or by the liquid moving past the bubbles will be determined by using the hydrogen bubble technique. The hydrogen bubbles will be created on a copper electrode placed in the test liquid (water). The frequency of the pulse and the voltage difference will be varied until a well defined succession of bubble rows is observed. The size of the hydrogen bubbles is expected to be around 0.02 mm. For bubbles of this diameter, the rise velocity due to buoyancy will be less than 0.7 mm/s. Data for bubble growth and detachment process and bubble trajectory will be obtained from the video pictures.

Experiments will be conducted with saturated and subcooled water and PF-5050 ( $\text{C}_5\text{F}_{12}$ ). Use of two fluids with different wetting characteristics will allow scaling of the effect of contact angle both at microscopic (through disjoining pressure) and macroscopic (experiments) levels.

### Experiments in the KC-135 or the Lear Jet

Since at normal gravity, there is always a gravitational component parallel to and perpendicular to an inclined surface, the bubble shape and detachment, which are sensitive to magnitude of gravitational acceleration, must be studied under low gravity conditions. As such, it is proposed that during the later part of the third year and early part of the fourth year of the project, experiments be conducted in the KC-135 or the Lear jet. Although experiments will mainly focus on the bubble detachment process, the data for nucleate boiling heat transfer on designed surfaces will also be taken. The data will be very helpful in assessment of the overall heat transfer model, and in extrapolating it to microgravity conditions of the space shuttle. The experimental apparatus will be the same as used in the normal gravity experiments, except a few modifications will be made to accommodate the constraints of the aircraft facility. The holography facility will not be used in these experiments.

### Experiments in the Space Shuttle

To further quantify the effect of significantly reduced gravity ( $0.5g_e$ ) on the bubble detachment process in particular, and on the heat transfer in general, it is necessary that boiling experiments be carried out on the "designed" surface. These experiments will not only provide data on the scaling effect of gravity on various processes, including bubble growth and departure, but will also be valuable in validating the predictive model for nucleate boiling heat transfer under microgravity conditions. The experiments will be defined during the first two years of the project.

## ANALYSIS

Along with the experimental work, attention will be focused on the modeling of the important thermal hydrodynamic processes. These include:

- i. Shape of the vapor liquid interface, the thickness of the micro/macro layer and critical size of the bubble base.
- ii. Heat Transfer across the micro/macro layers and evaporation at the interface.
- iii. Bubble growth, breakoff and associated flow field including flow created by Marangoni effect.
- iv. Flow field and heat transfer associated with a bubble sliding along a heated wall.
- v. Generalization of results.

The shape and evolution of the vapor liquid interface of the micro-layer supporting a single bubble or a vapor stem, and heat transfer across the layer will be determined by solving two dimensional axi-symmetric transient momentum and energy equations for the liquid layer. The pressure gradient to overcome the drag experienced by the liquid in the microlayer will be provided by capillary force resulting from the change in the shape of the interface and from the disjoining pressure. The solution of governing equations for micro-layer will be coupled with the solution of transient two dimensional momentum equations for the liquid in the pool and the vapor pocket supported by the micro-layer. The governing equations will be solved in transformed variables using the finite difference method. Grids will be generated numerically. Significant experience exists in the group (e.g. see Son and Dhir<sup>13</sup>) in this area. Either constant temperature or constant heat flux conditions will be applied at the wall. Constant heat flux conditions will provide confirmation of a drop in temperature that may occur during a high rate of evaporation from the microlayers. Bubbles formed on inclined surfaces will not be symmetric. As a result, augmented two dimensional equations will have to be solved. Model predictions will be compared with the data.

## REFERENCES

1. Von Arx, A., and Dhir, V.K., (1993). System Simulation of a Thermionic Reactor, Paper No. 93-HT-24., presented at the National Heat Transfer Conference, Atlanta, GA.
2. Keshock, E.G., and Siegel, R., (1964). Focus Acting on Bubble in Nucleate Boiling Under Normal and Reduced Gravity Conditions, NASA TN-D-2999.
3. Siegel, R. and Keshock, E.G., (1964). Effect of Reduced Gravity on Nucleate Bubble Dynamics in Water, *AIChE J.*, Vol. 10, No. 4, pp. 509-516.
4. Zell, M., Straub, J., and Vogel, B., (1989). Pool Boiling Under Microgravity. Proc. Eurotherm Seminar, No. 8 On Advances in Pool Boiling Heat Transfer, Paderborn, Germany, pp. 70-74.
5. Siegel, R., (1967). Effects of Reduced Gravity on Heat Transfer, *Adv. in Heat Transfer*, Vol. 4, pp. 143-228.
6. Ervin, J.S., Merte, H., Kellers, R.B., and Kirk, K., (1992). Transient Pool Boiling in Microgravity, *Intl. J. Heat Mass Transfer*, Vol. 35, No. 3, pp. 659-674.
7. Ervin, J., and Merte, H., (1993). Boiling Nucleation and Propagation in Microgravity, *Heat Transfer in Microgravity*, ASME-HTD Vol. 269, pp. 131-138.
8. Hasan, M.M., Lin, C.S., Knoll, R.H., Bentz, M.D., Meserole, J.S., (1993). Nucleate Pool Boiling in the Long Duration Low Gravity Environment of the Space Shuttle, AIAA Paper No. 93-0465, 31st Aerospace Sciences Meeting and Exhibit, Reno, NV January 11-14.
9. Merte, H., (1994). Pool and Flow Boiling in Variable and Microgravity," 2nd Microgravity Fluid Physics Conference, Paper No. 33, Cleveland, OH, June 21-23.
10. Cochran, T.H., (1970). Forced-Convection Boiling Near Inception in Zero Gravity, NASA TN D-5612.
11. Saito, M., Yamaoka, N., Miyazaki, K., Kinoshita, M., and Abe, Y., (1994). Boiling Two-Phase Flow under Microgravity, *Nuclear Engineering Design*, Vol. 146, pp. 451-461.
12. Wang, C.H., and Dhir, V.K., (1993). On the Gas Entrapment and Nuclear Site Density During Pool Boiling of Saturated Water, *J. Heat Transfer*, Vol. 115, pp. 670-679.
13. Son, G., and Dhir, V.K., (1995). Two Dimensional Numerical Simulation of Saturated Film Boiling on a Horizontal Surface," 4th ASME JSME Thermal Engineering Joint Conference, Maui, Hawaii.

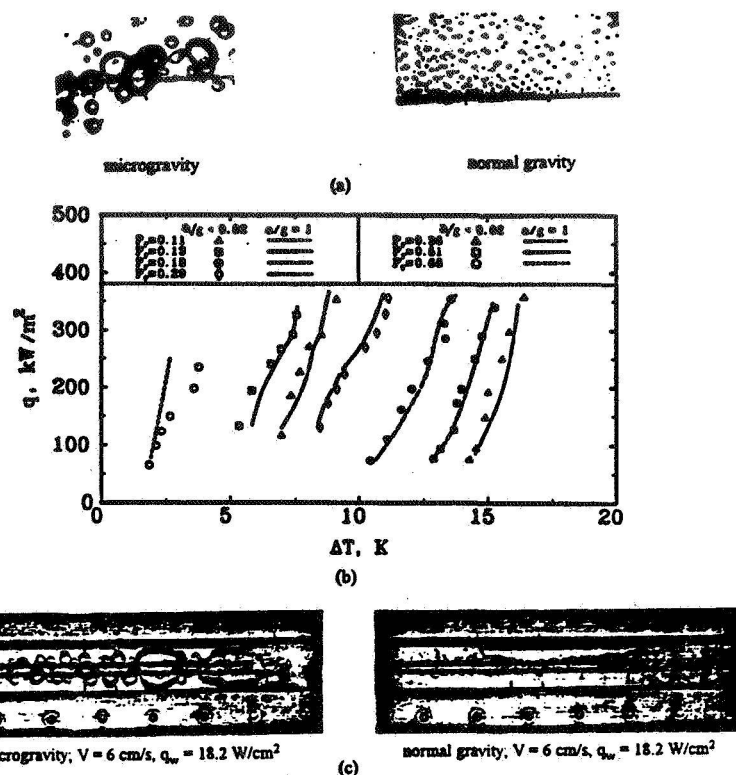
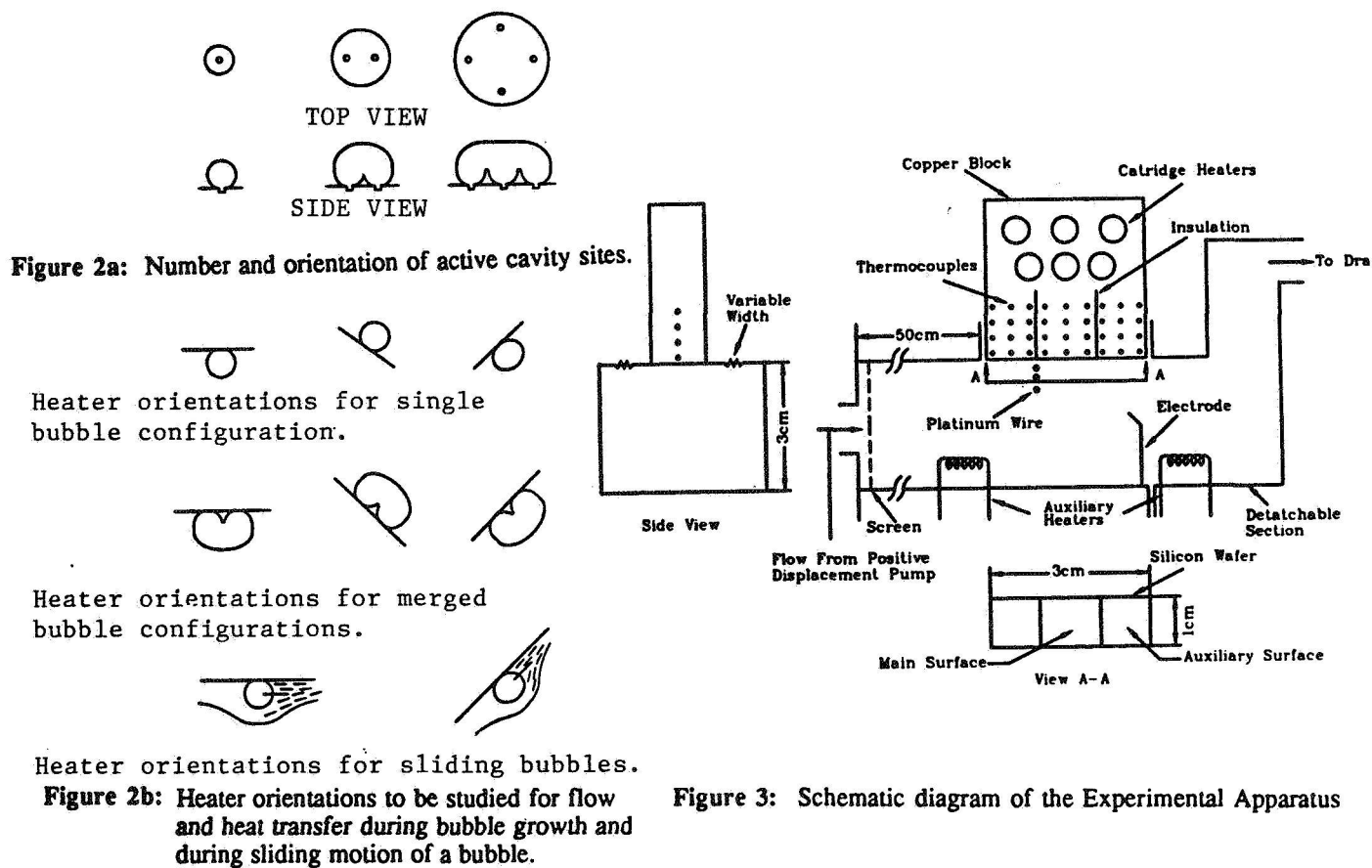


**Figure 1:** Comparison of normal and microgravity results: (a) pool boiling bubble size<sup>4</sup>, (b) pool boiling heat transfer coefficient<sup>4</sup>, (c) flow boiling bubble size<sup>11</sup>.



## ACOUSTIC BEHAVIOR OF VAPOR BUBBLES

A. Prosperetti and H.N. Oğuz  
Department of Mechanical Engineering  
The Johns Hopkins University  
Baltimore MD 21218

### Abstract

In a microgravity environment vapor bubbles generated at a boiling surface tend to remain near it for a long time. This affects the boiling heat transfer and in particular promotes an early transition to the highly inefficient film boiling regime. This paper describes the physical basis underlying attempts to remove the bubbles by means of pressure radiation forces.

## 1 Introduction

At normal gravity, the effectiveness of boiling as a heat transfer mechanism relies in no small measure on the rapid removal of vapor bubbles from the heated surface. This process has a two-fold benefit, as it both aids in removing latent heat and in promoting microconvective motion near the surface. On the basis of this remark, one would be led to believe that boiling at reduced gravity would be very inefficient. Somewhat surprisingly, at small to moderate heat fluxes, this statement is only partly true as shown by several experiments (Siegel 1967; Clark 1968; Zell et al. 1989; Oka et al. 1992, and others). Two major differences between micro- and normal-gravity boiling are however evident: (i) The bubble shape, size, and general dynamics is radically different; (ii) The critical heat flux is reduced severalfold at low gravity. As first shown by Siegel and Keshock (1964), a major heat removal mechanism in low gravity is the fact that a detaching bubble does not go far from the heated surface so that subsequent bubbles feed into it until the bubble leaves. At this point another bubble grows, detaches, is fed by smaller ones, and the cycle repeats. This process compounds with vigorous surface instabilities (Ervin et al. 1992) to produce a substantial heat transfer.

While the hovering of large bubbles near the nucleation site is beneficial at low to moderate heat fluxes, it is also at the root of the observed reduction in critical heat flux, where the heating surface is surrounded by a vapor blanket (Oka et al. 1992; Chung 1994). In order to increase the critical heat flux at low gravity it is therefore desirable to remove bubbles from the heated surface providing a substitute for buoyancy. Electric fields have been used for this purpose (Chung 1994), but it is too early to judge their effectiveness. The same author, Merte, and ourselves are also planning to use acoustic techniques.

The purpose of the present paper is to review the physical framework in which these acoustic bubble-removal techniques may be expected to operate.

The action of acoustic radiation forces on gas – rather than vapor – bubbles is well known (see e.g. Crum and Eller 1970; Crum and Nordling 1972; Crum 1971, 1975; Agrest and Kuzetsov 1972, 1973; Weiser and Apfel 1982; Barmatz and Collas 1985; Trinh and Hsu 1986; Holt and Crum 1992; Lee and Wang 1993a). For example, radiation forces are a major factor in acoustic cavitation where they promote violent translational motion and spatial reorganization of the gas that evolves from the liquid in an intense sound field. These and other aspects of pressure radiation forces have been extensively studied both experimentally and theoretically (see e.g. Yosioka and Kawasima 1955; Eller 1968; Foster et al. 1968; Wu and Du 1990; Löfsted and Putterman 1991; Lee and Wang 1993). In particular, Dr. E. Trinh (JPL) has carried out experiments on the Space Shuttle USML-1 demonstrating the action of these forces on drops and gas bubbles (Marston et al. 1993).

Gas bubbles are attracted or repelled by the pressure antinodes according as to whether they are driven below or above their resonance frequency. Furthermore, in the linear regime, neighboring bubbles repel each other when one is driven above and one below the natural frequency while they attract otherwise.

The resonance frequencies of bubbles thus play a major role for gas bubbles. While the situation may be expected to be similar for vapor bubbles, comparatively less work has been carried out on these systems. At

first sight, it may even come as an unexpected fact that a resonance frequency – that presupposes a restoring force – exists at all. To compound the surprise, it appears that *two* linear resonances exist in the case of vapor bubbles (Finch and Neppiras 1973; Khabeev 1976; Hsieh 1979; Marston and Greene 1978; Marston 1979; Nagiev and Khabeev 1979). The effect of this secondary resonance on pressure radiation forces is unknown.

## 2 Vapor bubble resonances

In a certain sense, the process that provides vapor bubbles with stiffness is very different from that at work in the case of bubbles containing a permanent gas. In the latter case, it is the compression and expansion of the gas that provides a restoring force opposing the deformation. For a vapor bubble, on the other hand, the vapor pressure essentially follows the saturation line and it rises and falls in response to the heating and cooling of the bubble wall due to latent heat effects.

An alternative argument can be made, however, according to which the stiffnesses of gas and vapor bubbles are very similar. Indeed, they both depend on diffusive processes in the liquid, in the former case of mass, and of heat in the latter one. In this view, the critical difference is merely a consequence of the fact that the diffusivity for mass is typically two orders of magnitude smaller than that of heat.

An estimate of the order of magnitude of the fundamental resonance of a vapor bubble can be readily found by the following argument. Consider a vapor bubble the radius  $R$  of which decreases by an amount  $\Delta R$ . This tends to cause the condensation of an amount of vapor (density  $\rho_V$ ):

$$\Delta m_V = 4\pi R^2 \rho_V \Delta R. \quad (1)$$

If the process occurs with a frequency  $\omega$ , the latent heat  $L\Delta m_V$  liberated by the condensation increases the temperature of a shell of liquid of thickness  $\sim \sqrt{D_L/\omega}$ , where  $D_L$  is the liquid thermal diffusivity, by an amount

$$4\pi R^2 \sqrt{\frac{D_L}{\omega}} \rho_L c_L \Delta T = L\Delta m_V, \quad (2)$$

with  $\rho_L$  the liquid density and  $c_L$  the specific heat. This heating of the bubble surface increases the saturation pressure by an amount  $\Delta p = (dp_V/dT)\Delta T$ , where the derivative is taken along the saturation line. A force tending to resist compression is generated in this way:

$$F = 4\pi R^2 \Delta p = -k\Delta R \quad (3)$$

where the following expression for “stiffness parameter”  $k$  follows from the previous argument:

$$k = 4\pi R^2 \sqrt{\frac{\omega}{D_L}} \frac{L\rho_V}{c_L\rho_L} \frac{dp_V}{dT} = 4\pi R^2 \sqrt{\frac{\omega}{D_L}} \frac{(L\rho_V)^2}{c_L\rho_L}. \quad (4)$$

The Clausius-Clapeyron relation has been used in the second step. The added mass for a sphere in radial motion is given by  $M_A = 4\pi R^3 \rho_L$ , and therefore (4) enables one to estimate the resonance frequency  $\omega_0$  of the vapor bubble by  $\omega_0 = \sqrt{k/M_A}$  or

$$\omega_0^2 = \sqrt{\frac{\omega}{D_L}} \frac{(L\rho_V)^2}{R c_L \rho_L^2}. \quad (5)$$

If  $\omega \neq \omega_0$ , this relation gives the position of the pole of the response function of  $\Delta R(t)$  when the bubble is driven at the frequency  $\omega$ . By setting  $\omega = \omega_0$ , on the other hand, we find the natural frequency of the bubble as

$$\omega_0^3 R^2 \simeq 11.8 \frac{L^4 \rho_V^4}{\rho_L^3 c_L^2 T^2 k_L}, \quad (6)$$

where  $k_L$  is the liquid thermal conductivity and a numerical constant has been introduced to account for the approximate nature of the derivation. With this adjustment, the previous argument gives results in reasonable

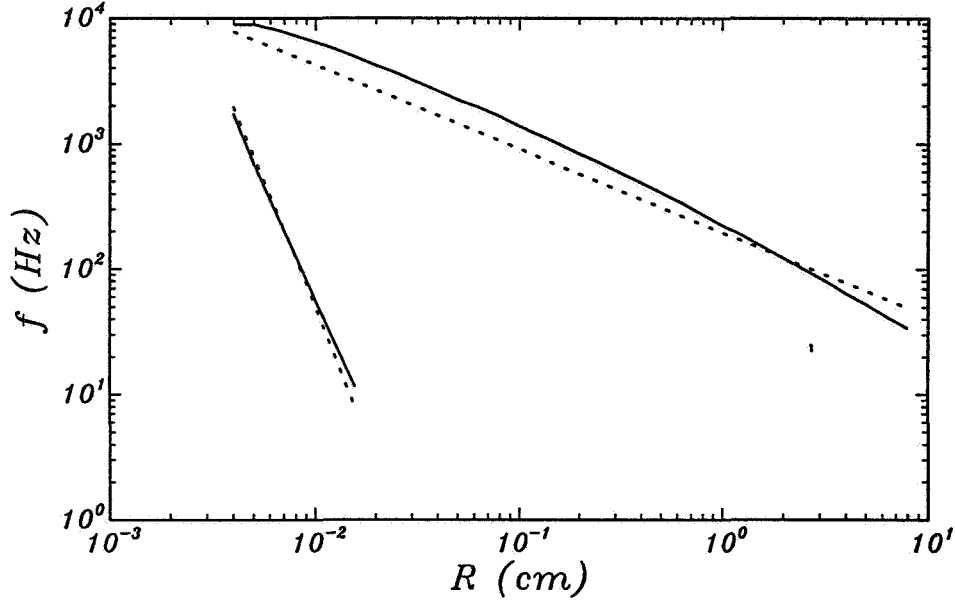


Figure 1: Graph of the resonance frequencies of vapor bubbles in water at 100 °C as a function of bubble radius  $R$ . The dashed lines show the results given by the simplified arguments.

agreement with the more detailed ones of Marston (1979) as shown by the upper pair of lines in Fig. 1 for the case of water at 100 ° and 1 atm.

For comparison, it may be recalled that the natural frequency of a gas bubble in adiabatic oscillation at a pressure  $P_\infty$  is given by

$$\omega_0^2 R^2 = \frac{3\gamma P_\infty}{\rho_L}, \quad (7)$$

where  $\gamma$  is the ratio of specific heats of the gas. This expression – and in particular its dependence on the bubble size – is very different from (6).

Figure 1 shows another remarkable fact, namely that in water, at 100 ° and 1 atm, bubbles larger than about 30  $\mu\text{m}$  possess *two* resonance frequencies. While the higher one is that predicted by the previous argument, the other one is much lower. The mechanics of this second resonance – that is one of the distinctive features of this system – can be described in physical terms as follows. At low frequency, inertia and damping effects are small and can be ignored. The main effects are the restoring force previously described and the surface tension force

$$-k\Delta R \simeq 4\pi R^2 \Delta \left( \frac{2\sigma}{R} \right), \quad (8)$$

where  $\sigma$  is the surface tension coefficient. These two forces tend to oppose each other and, in suitable conditions, they can balance. This circumstance leads to an oscillating system forced by the sound field, but with a very small restoring force. The oscillation amplitude is then evidently large, and this is the second resonance. Proceeding as before, equating (3) and (8), and again adjusting a numerical constant, we find

$$\omega_0 R^4 = 2.94 D_L \left( \frac{2\sigma c_L \rho_L T}{(L\rho_V)^2} \right)^2. \quad (9)$$

This result is compared with the precise one of Marston (1979) in Fig. 1 (lower pair of lines).

### 3 Pressure radiation

In a sound field, an inhomogeneity whose response to the pressure perturbation is different from that of the surrounding fluid is subject to a pressure-radiation force (King 1934; Yosioka and Kawasima 1955; Gor'kov 1962; Nyborg 1967; Barmatz and Collas 1985; Trinh and Hsu 1986; Wu and Du 1990; Löfsted and Putterman 1991).

For the case of a bubble the component of this force due to the monopole (volume pulsation) is much stronger than that due to the dipole (translational oscillation) and is approximately given by (Eller 1968; Wu and Du 1990; Löfsted and Putterman 1991; Lee and Wang 1993)

$$\mathbf{F} = - \langle V \nabla p \rangle, \quad (10)$$

where the angle brackets denote the average over one period of the sound,  $V$  is the bubble volume, and the gradient of the total pressure  $\nabla p$  is evaluated at the position occupied by the bubble. In a linear approximation, if we write

$$p = p_0 - p'(\mathbf{x}) \cos \omega t, \quad V = V_0 [1 + \delta \cos(\omega t + \phi)], \quad (11)$$

we find

$$\mathbf{F} = \frac{1}{2} V_0 \delta \cos \phi \nabla p'. \quad (12)$$

In a standing wave, for a bubble driven below resonance,  $\cos \phi \geq 0$  and the force is in the direction of the pressure antinode, while the converse occurs above resonance.

The physical basis for this phenomenon is readily explained as follows. A bubble, being lighter than the host liquid, is subject to a buoyancy force in a direction opposite that of the local pressure gradient. Consider a bubble driven below resonance, that expands during the low-pressure phase of the wave and compresses during the high pressure phase. When it is in the expanded state, the acoustic pressure is negative and the bubble migrates toward the pressure minimum, i.e. the acoustic antinode. When the bubble is compressed, the acoustic pressure is positive and the bubble is driven towards the pressure node. Since, however, the force is proportional to the bubble volume, the migration during the antinode in the expanded state is stronger than the one in the opposite direction during the high-pressure phase, and the net effect is a drift toward the pressure antinode. A similar argument applied to a bubble driven above resonance shows that the drift is toward the pressure node in this case.

One can appeal to this intuitive argument to deduce the bubble behavior near the secondary resonance. Below this frequency, the pressure stiffness force (which increases with frequency, see Eq. 4) is smaller than the surface tension force, which implies that the bubble compresses during the expansion half-cycle of the sound and will therefore be driven toward a pressure node.

These considerations are based on linear theory. A rigorous analysis of pressure forces in the case of nonlinear oscillations is not available. On the basis of an approximate model, we have found that, for gas bubbles, the force can have a sign opposite to that expected on the basis of the linear theory in the neighborhood of a nonlinear resonance (Oğuz and Prosperetti 1990). Whether this is indeed so, and whether the result also applies to vapor bubbles, is at present unknown.

### 4 Acoustic forces in boiling

The physical principles described in the previous sections indicate that it may be possible to enhance the removal of boiling bubbles from boiling surfaces under microgravity conditions by acoustic methods. A likely sequence of events may be the following.

Consider a standing sound wave in the presence of a heated boundary on which boiling takes place. Acoustically this boundary will behave nearly rigidly and therefore it will give rise to a pressure antinode in its



neighborhood. Consider then a growing vapor bubble. Initially it is small and its resonance frequency correspondingly high (Eq. 6), above that of the sound field. The pressure radiation force tends therefore to keep the bubble near the wall. When the bubble grows past the size such that it is resonant at the driving sound frequency, however, the radiation force changes sign and the bubble will tend to be pushed away from the wall toward a node of the sound field. Since the closest node will be at a distance of the order of  $1/4$  of the wavelength from the wall, frequencies between 2 and 20 kHz, in water, would tend to remove the bubble at distances between  $\sim 2$  and 20 cm from the wall. This is far enough that even a low-speed flow will be sufficient to carry the bubble away.

The previous chain of events can be influenced – positively or adversely – by acoustic streaming that could be a significant factor at the higher frequencies. Such flows have been extensively analyzed by Nyborg and other researchers (Nyborg 1965, Zarembo 1971, Lighthill 1978; Qi 1993), although Rayleigh – once again – was an early investigator of the phenomenon (Rayleigh 1898).

Another factor, the importance of which it is difficult to quantify a priori, is the effect of the “image” bubble. If the wall is acoustically rigid, the image bubble pulsates in phase with the real bubble and would tend therefore to attract it working against the primary pressure force of the sound field.

These considerations are based on a somewhat idealized model of the actual phenomena. The entire situation could be considerably more complex due to nonlinear effects, bubble distortion, and gas diffusion.

## References

- [1] E.M. Agrest and G.N. Kuznetsov. Migration of gas-filled cavities in an inhomogeneous sound field. *Sov. Phys. Acoust.*, 18:143–147, 1972.
- [2] E.M. Agrest and G.N. Kuznetsov. Instantaneous parameters of the motion of a cavitation bubble in an inhomogeneous sound field. *Sov. Phys. Acoust.*, 19:212–215, 1973.
- [3] M. Barmatz and P. Collas. Acoustic radiation potential on a sphere in plane, cylindrical, and spherical standing wave fields. *J. Acoust.Soc. Am.*, 77:928–945, 1985.
- [4] J.A. Clark. Gravic and agravic effects in cryogenic heat transfer. In K.J. Bell, editor, *Advances in Cryogenic Heat Transfer - Chemical Engineering Progress Symposium Series Vol. 64, No. 87*, pages 93–102. American Institute of Chemical Engineers, 1968.
- [5] L.A. Crum. Acoustic force on a liquid droplet in an acoustic stationary wave. *J. Acoust.Soc. Am.*, 50:157–163, 1971.
- [6] L.A. Crum. Bjerknes forces on bubbles in a stationary sound field. *J. Acoust.Soc. Am.*, 57:1363–1370, 1975.
- [7] L.A. Crum and A.I. Eller. Motion of bubbles in a stationary sound field. *J. Acoust.Soc. Am.*, 48:181–189, 1970.
- [8] L.A. Crum and D.A. Nordling. Velocity of transient cavities in an acoustic stationary wave. *J. Acoust.Soc. Am.*, 52:294–301, 1972.
- [9] A.I. Eller. Force on a bubble in a standing acoustic wave. *J. Acous. Soc. Am.*, 43:170–171, 1966.
- [10] J.S. Ervin, Merte H. Jr., R.B. Keller, and K. Kirk. Transient pool boiling in microgravity. *Int. J. Heat Mass Trans.*, 35:659–674, 1992.
- [11] R.D. Finch and E.A. Neppiras. Vapor bubble dynamics. *J. Acoust. Soc. Am.*, 53:1402–1410, 1973.
- [12] J.M. Foster, J.A. Botts, A.R. Barbin, and R.T. Vachon. Bubble trajectories and equilibrium levels in vibrated liquid columns. *J. Basic Eng.*, 90:125–132, 1968.
- [13] L.P. Gor'kov. On the forces acting on a small particle in an acoustic field in an ideal fluid. *Sov. Phys. Acoust.*, 6:773–775, 1962.
- [14] R.G. Holt and L.A. Crum. Acoustically forced oscillations of air bubbles in water: Experimental results. *J. Acoust. Soc. Am.*, 91:1924–1932, 1992.
- [15] D.Y. Hsieh. On oscillation of vapor bubbles. *J. Acoust. Soc. Am.*, 66:1514–1515, 1979.

- [16] Chung, J.N. Bubble dynamics, two-phase flow, and boiling heat transfer in a microgravity environment. In B.S. Singh, editor, *Second Microgravity Fluid Physics Conference*, pages 259–264. NASA No. 3276, 1994.
- [17] N.S. Khabeev. Heat transfer and phase-transition effects in the oscillation of vapor bubbles. *Sov. Phys. Acoust.*, 21:501–505, 1976.
- [18] L.V. King. On the acoustic radiation pressure on spheres. *Proc. Roy. Soc. London*, A147:212–240, 1934.
- [19] C.P. Lee and T.G. Wang. Acoustic radiation force on a bubble. *J. Acoust.Soc. Am.*, 93:1637–1640, 1993.
- [20] J. Lighthill. Acoustic streaming. *J. Sound Vib.*, 61:391–418, 1978.
- [21] R. Löfsted and S. Putterman. Theory of long wavelength acoustic radiation pressure. *J. Acous. Soc. Am.*, 90:2027–2033, 1991.
- [22] P.L. Marston. Evaporation-condensation resonance frequency of oscillating vapor bubbles. *J. Acoust. Soc. Am.*, 66:1516–1521, 1979.
- [23] P.L. Marston and D.B. Greene. Stable microscopic bubbles in helium i and evaporation-condensation resonance. *J. Acoust. Soc. Am.*, 64:319–321, 1978.
- [24] H. Jr. Merte. Pool and flow boiling in variable and microgravity. In B.S. Singh, editor, *Second Microgravity Fluid Physics Conference*, pages 265–272. NASA No. 3276, 1994.
- [25] F.B. Nagiev and N.S. Khabeev. Heat-transfer and phase-transition effects associated with oscillations of vapor-gas bubbles. *Sov. Phys. Acoust.*, 25:148–152, 1979.
- [26] W.L. Nyborg. Radiation pressure on a small rigid sphere. *J. Acoust. Soc. Am.*, 42:947–952, 1967.
- [27] W.L.M. Nyborg. Acoustic streaming. In W.P. Mason, editor, *Physical Acoustics*, volume II-B, pages 265. Academic Press, 1965.
- [28] H.N. Oğuz and A. Prosperetti. A generalization of the impulse and virial theorems with an application to bubble oscillations. *J. Fluid Mech.*, 218:143–162, 1990.
- [29] T. Oka, Y. Abe, K. Tanaka, Y.H. Mori, and A. Nagashima. Observational study of pool boiling under microgravity. *JSME Int. J.*, II-35:280–286, 1992.
- [30] Q. Qi. The effect of compressibility on acoustic streaming near a rigid boundary for a plane travelling wave. *J. Acoust. Soc. Am.*, 94:1090–1098, 1993.
- [31] Lord Rayleigh. *Theory of Sound*. Dover, 1945.
- [32] R. Siegel. Effects of reduced gravity on heat transfer. In J.P. Hartnett and T.F. Jr. Irvine, editors, *Advances in Heat Transfer - Vol. 4*, pages 143–228. Academic Press, 1967.
- [33] R. Siegel and E.G. Keshock. Effects of reduced gravity on nucleate boiling bubble dynamics in saturated water. *A.I.Ch.E. J.*, 10:509–517, 1964.
- [34] E.H. Trinh and C.J. Hsu. Acoustic levitation methods for density measurements. *J. Acoust.Soc. Am.*, 80:1757–1761, 1986.
- [35] M.A.H. Weiser and R.E. Apfel. Extension of acoustic levitation to include the study of micron-size particles in a more compressible host liquid. *J. Acoust.Soc. Am.*, 71:1261–1268, 1982.
- [36] J. Wu and G. Du. Acoustic radiation force on a small compressible sphere in a focused beam. *J. Acous. Soc. Am.*, 87:997–1003, 1990.
- [37] K. Yosioka and Y. Kawasima. Acoustic radiation pressure on a compressible sphere. *Acustica*, 5:167–178, 1955.
- [38] L.K. Zarembo. Acoustic streaming. In L.D. Rozenberg, editor, *High Intensity Ultrasonic Fields*, volume III, pages 137–199. Plenum, 1971.
- [39] M. Zell, J. Straub, and B. Vogel. Pool boiling under microgravity. *PCH*, 11:813–823, 1989.

# DESIGN OF AN IMPROVED HEATER ARRAY TO MEASURE MICROSCALE WALL HEAT TRANSFER

Jungho Kim and Choon Ping Ch'ng  
Department of Engineering  
University of Denver  
Denver, Colorado 80208

T.S. Kalkur  
Department of Electrical and Computer Engineering  
University of Colorado, Colorado Springs  
Colorado Springs, CO 80933-7150

## ABSTRACT

An improved array of microscale heaters is being developed to measure the heat transfer coefficient at many points underneath individual bubbles during boiling as a function of space and time. This heater array enables the local heat transfer from a surface during the bubble growth and departure process to be measured with very high temporal and spatial resolution, and should allow better understanding of the boiling heat transfer mechanisms by pinpointing when and where in the bubble departure cycle large amounts of wall heat transfer occur. Such information can provide much needed data regarding the important heat transfer mechanisms during the bubble departure cycle, and can serve as benchmarks to validate many of the analytical and numerical models used to simulate boiling. The improvements to the heater array include using a silicon-on-quartz substrate to reduce thermal cross-talk between the heaters, decreased space between the heaters, increased pad sizes on the heaters, and progressive heater sizes. Some results using the present heater array are discussed.

## INTRODUCTION

Boiling is an attractive heat transfer mechanism because large amounts of heat can be removed with relatively small temperature differences. Due to the difficulty of making measurements underneath bubbles, however, there is still much controversy regarding the relative contribution of the above mechanisms to the overall heat transfer. For example, estimates for the contribution of the microlayer heat flux to the overall heat transfer range from less than 20 percent to almost 100 percent depending on the boiling conditions. The great majority of the experimental data to date have been obtained using heater surfaces that were comparable to, or much larger than, the bubbles, enabling only average heat transfer rates over the entire heated surface to be obtained. Little experimental data is available regarding the *local* heat transfer rates from the wall under and around the bubbles as they grow and depart from the surface. Local heat flux measurements can provide much needed information regarding the relevant wall heat transfer mechanisms during the bubble departure cycle by pinpointing when and where in the cycle large amounts of heat are removed. Cooper and Lloyd (1) used a microthermocouple to obtain temperature fluctuations beneath a growing bubble, and demonstrated the existence of the microlayer. Some more recent work measured the local heat flux from a surface using laser interferometry to obtain contours of the microlayer thickness vs. time (refs 2-6). The rate of change of the microlayer thickness was related to the wall heat transfer through a simple energy balance.

The objective of the present work is to obtain direct measurements of the local heat transfer underneath single bubbles as they grow and depart from the surface so that the contribution of the various heat transfer mechanisms to the overall heat flux can be measured. This study should also provide benchmark data against which numerical codes can be compared. A novel heater surface consisting of an array of microscale heaters will be used to accomplish this. Each individual heater in the array is much

smaller than a single bubble, although the heater array is of the same order, or larger than, a single bubble. Each heater represents one resistance in a bridge, and is kept at constant temperature by an electronic feedback loop. By measuring the power required to keep each individual heater at a constant temperature, two dimensional maps of the heat transfer coefficient from the heater surface to the bulk liquid can be obtained. This heater array enables the heat transfer to a surface during the bubble growth and departure process to be measured with high temporal and spatial resolution. Data can also be obtained in the critical heat flux and transition boiling regions without the danger of heater burnout because the heaters are operated in constant temperature mode.

## HEATER CONSTRUCTION

The improved heater array is to be constructed on a highly doped silicon layer deposited on a quartz substrate using VLSI techniques. A schematic of the heater construction is shown on Figure 1. The quartz substrate prevents thermal cross-talk between the heaters. The thin Si layer electrically grounds one side of the heaters. A layer of SiO<sub>2</sub> is grown on the Si layer so that the heaters can be electrically insulated. Vias cut into this layer allow electrical connections from the heaters to the wafer. The vias are filled with metal, and an array of platinum resistance heaters in a serpentine pattern is then deposited onto the SiO<sub>2</sub>. Another layer of SiO<sub>2</sub> is deposited on top of the platinum resistance heaters as insulation. Vias cut into the top SiO<sub>2</sub> layer allow connections between the power leads and the heaters. The vias are filled with metal and the aluminum power leads are deposited. Below the Si wafer is a guard heater at the same temperature as the heaters, thereby eliminating heat conduction within the substrate--all power flowing into the heaters is transferred to the fluid. A photo of a single heater is shown on Figure 2. The new heater array will have about 240 of these heaters within a 4 mm diameter circle. The resistance heater, the power lead, and the vias are all clearly visible. Although the size of the heaters precludes measurement of the local heat transfer during bubble initiation (which occurs on submicron length scales), wall heat transfer during bubble growth and departure can be measured easily. The heater lines are 5  $\mu\text{m}$  wide and about 6000  $\mu\text{m}$  in total length, with spacing between heater lines of 5  $\mu\text{m}$ . The heaters have a nominal resistance of about 1000  $\Omega$ . This is large enough to prevent parasitic resistances due to the leads, contacts, etc. from significantly affecting the measurement, but small enough that the required output voltage of the op-amps do not exceed their rail voltage.

Changes in the new heater array are numerous. First the via size has been increased greatly so that the contact resistance between the Pt and the silicon wafer that plagued earlier heaters has essentially been eliminated. Second, the space between the heaters has been decreased to reduce the heat leakage from the heater to the unheated portions of the substrate. Third, the heater sizes will become progressively larger with radial distance in the next generation heater and the number of heaters will be increased, enabling increased resolution at the center of the array where the bubble will be smallest. The fourth improvement is the use of a low thermal conductivity quartz substrate. This will greatly reduce the thermal cross-talk between the heaters that would result if the heaters were made directly on a high thermal conductivity silicon wafer, and greatly increase the frequency response of the heaters.

## FEEDBACK LOOP

A schematic of a feedback control circuit used to keep a heater at a constant temperature (constant resistance) is shown in Figure 3. The circuit is similar to the feedback loops used for constant temperature hot-wire anemometers. Each circuit provides a driver voltage to its respective heater that corresponds to the power being dissipated by the heating element, and uses an input signal to select the desired temperature of the heating element. Because the heater is so thin ( $\sim 2.0 \mu\text{m}$ ), the frequency response of the heaters ( $10^6$ - $10^7$  Hz) is much higher than the bubble departure frequency ( $10^2$ - $10^3$  Hz). No frequency compensation circuitry is therefore needed. The resistance of the heater is controlled using a voltage controlled resistor (VCR) from Siliconix. A VCR was chosen instead of a manual potentiometer so the heaters resistance could be computer controlled. VCRs with resistance ranges from 250 to 650  $\Omega$  were chosen for this circuit.

The frequency response of the circuit was measured to be in excess of 20,000 Hz by removing the

heater, inputting a square wave, and measuring the circuit output. This is much faster than the frequencies expected during the bubble growth and departure cycle. The next generation feedback control circuit will include provision for calibration of the heater array on the same PCB used for control, and the VCRs may be replaced by IC chips that act as VCR's.

## COMPUTER CONTROL CIRCUIT

A microprocessor circuit is used to set the temperatures of the individual heaters in the array using computer control. The microprocessor controls the temperature of each heating element by controlling the voltage applied to the VCRs. The use of a separate system for heater control maximizes the data acquisition capabilities of the main computer since it will not need to share processing time for the heater control process. The microcontroller communicates with the main computer through a standard RS-232 serial data port at 9600 baud.

## DATA ACQUISITION SYSTEM

The data acquisition system consists of low-pass filters at the output of each bridge, a high speed multiplexer, and a 16 bit A/D converter sampled by a personal computer. Separate channels are used to measure the time, and the bulk liquid temperature and pressure. The Daqbook 216 from IO Tech was chosen due to its low cost, high resolution (16 bits), high data acquisition rate (100 kHz), portability, and expandability (256 channels maximum).

## RESULTS

Heater calibration.--Shown on Figure 4 are some resistance vs. temperature calibrations for sixteen heaters. The data were taken over a period of three days and a temperature range of 28 to 60 °C. It is seen that the curves are very linear, and that all the heaters have approximately the same slope. No drift in the heater resistances were seen over the three day calibration period. The observed resistivity of approximately  $2 \times 10^{-3} \text{ K}^{-1}$  differs from the published value for bulk platinum of  $3.9 \times 10^{-3} \text{ K}^{-1}$ . The difference in the two values is not surprising however, since thin film properties are often different from bulk properties.

Heater performance with feedback loop.--The case where only one of the heaters was powered was investigated. The heater resistance (heater temperature) was set so that the bridge output was nominally 1.4 V in air. When acetone was dropped onto the heater, the bridge output was observed to rise with time. As the acetone evaporates, its temperature decreases and the energy required to keep the heater at constant temperature increases, resulting in an increase in the output of the bridge. The response was relatively slow, since the heater is supplying energy to the high-conductivity silicon substrate which acts as a heat sink. Much faster response is expected if the array is constructed on a quartz substrate and all the heaters are powered.

The case where two adjacent heaters are powered is shown in Figure 5. The resistance of heater 14 was varied, and the response of heater 15 was observed. As expected, the responses are negatively correlated, i.e., an increase in the power supplied to heater 14 results in a decrease in the power supplied to heater 15, and vice versa. This thermal cross-talk between heaters can be greatly reduced by decreasing the thermal conductivity of the substrate, again by constructing the heater array on a quartz substrate.

Heater burnout.--To determine the heater burnout point, the current through the heater was measured as the voltage across the heater was increased while the heater was in still air. From these two measurements, the heater resistance/temperature and the power supplied to the heater were calculated. The heater temperature as deduced from the resistance measurements was observed to increase from 28 to 51 °C at the maximum voltage of 20 V. The temperature was not higher since the the substrate served as a heat sink for the heaters. The heat flux from the heaters at 20 V was calculated to be in excess of 600 W/m<sup>2</sup>.

The heaters should easily be able to handle the maximum expected local heat transfer coefficient ( $\sim 200 \text{ W/m}^2$ ).

## CONCLUSIONS

An improved heater array for wall heat transfer measurements during nucleate boiling has been designed and will be constructed this fiscal year. The improvements include increased via size, decreased spacing between heaters, a progressive heater size, and the use of a low thermal conductivity substrate. Upgrades to the feedback loops are also planned.

## REFERENCES

- (1) Cooper M.G., and Lloyd, A.J.P. "Transient Local Heat Flux in Nucleate Boiling", International Journal of Heat and Mass Transfer, Vol. 12, pp. 895-913, 1969.
- (2) Fath, H.S., and Judd, R.L. "Influence of System Pressure on Microlayer Evaporation Heat Transfer", Journal of Heat Transfer, Vol. 100, pp. 49-55, 1978.
- (3) Judd, R.L. and Hwang, K.S. "A Comprehensive Model for Nucleate Pool Boiling Heat Transfer Including Microlayer Evaporation", Journal of Heat Transfer, November, 1976, pp. 623-629.
- (4) Koffman, D. and Plesset, M.S. "Experimental Observations of the Microlayer in Vapor Bubble Growth on a Heater Solid", Journal of Heat Transfer, Vol. 105, pp. 625-632, 1983.
- (5) Shoukri, M., Judd, R.L. "Nucleation Site Activation in Saturated Boiling", Journal of Heat Transfer, February, 1975, pp. 93-98.
- (6) Voutsinos, C.M. and Judd, R.L. "Laser Interferometric Investigation of the Microlayer Evaporation Phenomenon", Journal of Heat Transfer, February, 1975, pp. 88-92.

## ACKNOWLEDGMENTS

Funding for this work was provided by the NASA, Microgravity Science and Applications Division under Grant No. NAG3-1609. Their support is gratefully acknowledged. The contract monitor is Mr. John McQuillen.

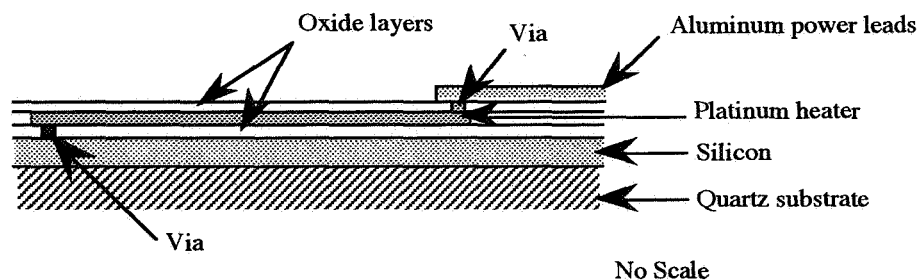


Figure 1--Schematic of heater construction.

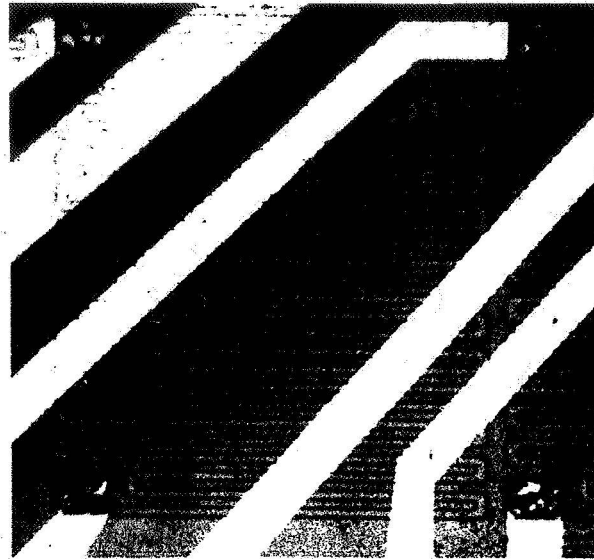


Figure 2--Photograph of single element showing the resistance heater, the power lead, and the vias.

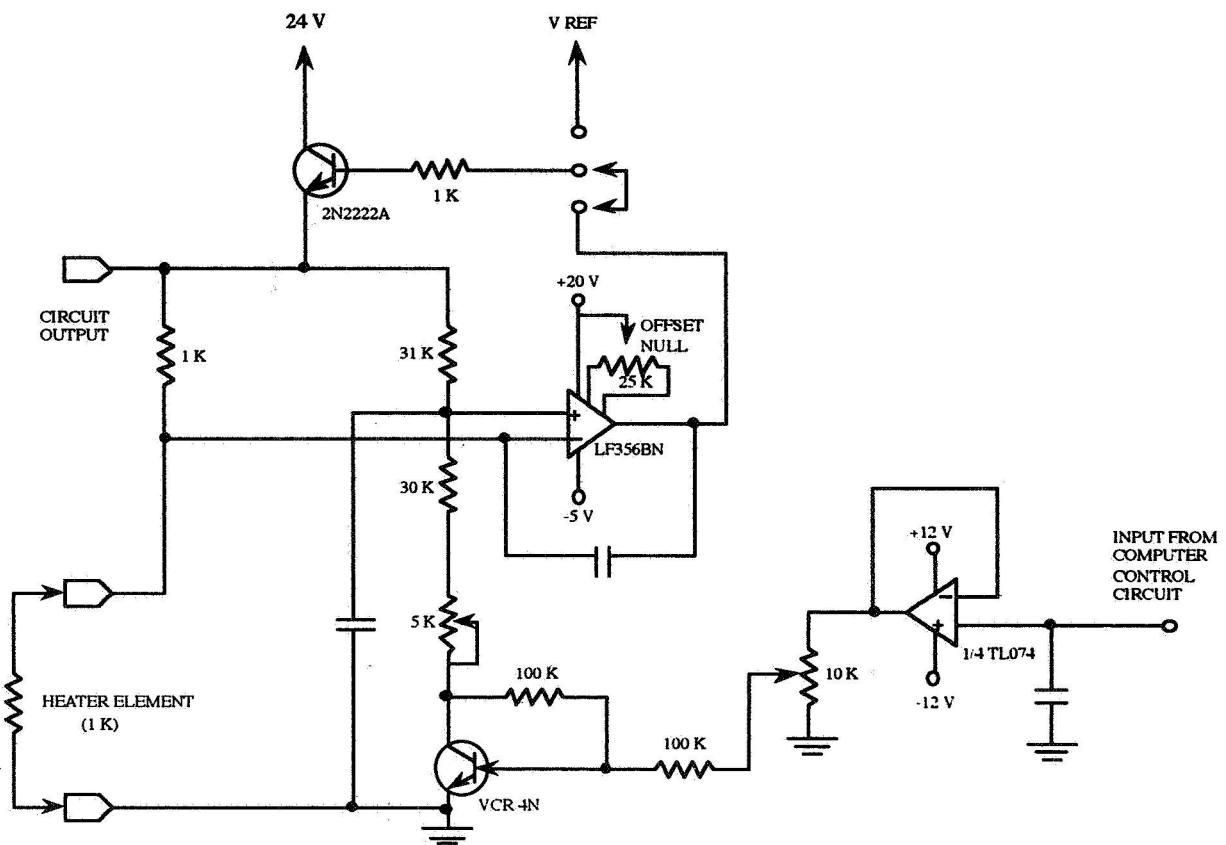


Figure 3--Schematic of feedback loop.

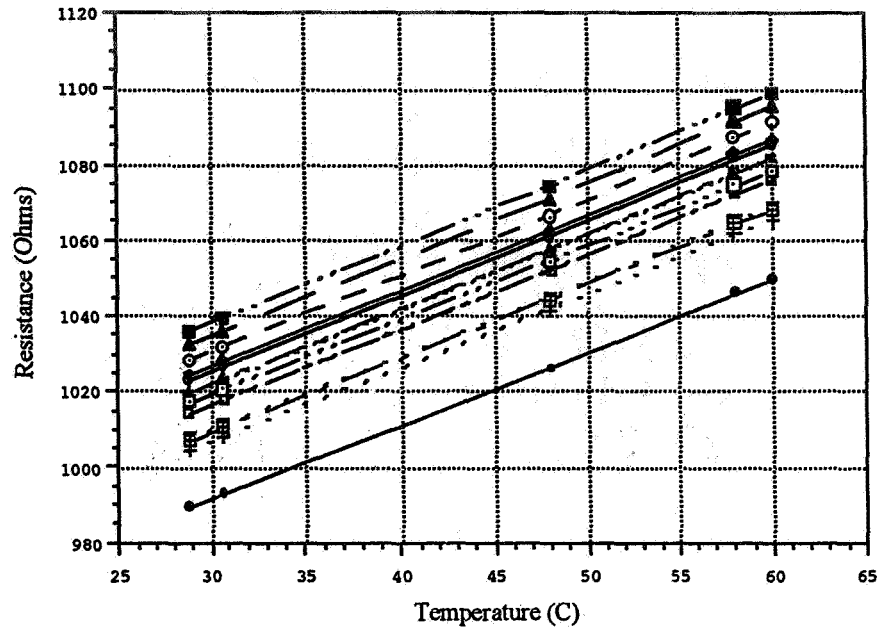


Figure 4--Typical calibration curves for heaters.

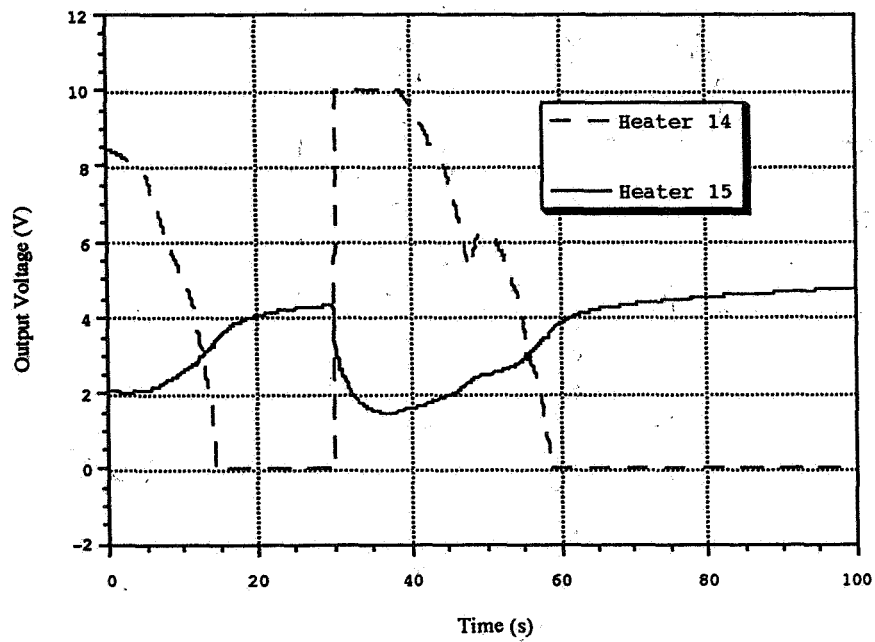


Figure 5--Output for two side by side heaters.



# **The Development of Novel, High-Flux, Heat Transfer Cells for Thermal Control in Microgravity**

**Marc K. Smith and Ari Glezer**

The George W. Woodruff School of Mechanical Engineering  
Georgia Institute of Technology  
Atlanta, GA 30332-0405

## **Abstract**

In order to meet the future needs of thermal management and control in space applications such as the Space Lab, new heat-transfer technology capable of much larger heat fluxes must be developed. To this end, we describe complementary numerical and experimental investigations into the fundamental fluid mechanics and heat-transfer processes involved in a radically new, self-contained, heat transfer cell for microgravity applications (patent pending). In contrast to conventional heat pipes, the heat transfer in this cell is based on a forced droplet evaporation process using a fine spray. The spray is produced by a novel fluidic technology recently developed at Georgia Tech (patent pending). This technology is based on a vibration induced droplet atomization process. In this technique, a liquid droplet is placed on a flexible membrane and is vibrated normal to itself. When the proper drop size is attained, the droplet resonates with the surface motion of the membrane and almost immediately bursts into a shower of very fine secondary droplets. The small droplets travel to the opposite end of the cell where they impact a heated surface and are evaporated. The vapor returns to the cold end of the cell and condenses to form the large droplets that are fragmented to form the spray. Preliminary estimates show that a heat transfer cell based on this technology would have a heat-flux capacity that is an order of magnitude higher than those of current heat pipes designs used in microgravity applications.

## **I. Introduction**

Thermal management is a critical technology in the microgravity environment because it affects so many different areas in the operation of spacecraft. Power plants must be cooled properly for efficient operation and the living environment must be maintained within the proper temperature range. Sensitive scientific instruments used in space, such as low temperature CCD imagers, must be maintained at a constant uniform temperature in order to work effectively. In addition, there is an ever increasing demand for power in space missions, such as the Space Lab. Increasing the size of power plants aboard such spacecraft brings with it an even larger thermal management problem associated with the waste heat that is generated. Thus, more efficient methods to remove this heat are required.

One popular method for thermal control in a microgravity environment is the heat pipe. These devices can accommodate a wide range of operating temperatures, can transport large amount of heat, and can operate independently of gravity. The high heat transfer rates that can be achieved are typical of phase-change heat transfer devices. However, heat pipes have their own limitations, as described by Dunn and Reay (1994). One major limit is that the amount of heat transfer carried by these devices is governed by the liquid flow rate produced by capillary pumping in the wicking material of the heat pipe.

In this paper, we introduce a radically new, self-contained heat-pipe-like cell for microgravity applications (patent pending) that may overcome this traditional limitation of the heat pipe. The heat transfer in this cell is based on forced two-phase convection using a novel fluidic technology called VIDA (Vibration Induced Droplet Atomization) that has been recently developed at Georgia Tech (patent pending). Inside the cell, the VIDA technology creates a fine spray of droplets from the liquid condensate layer at the cold end of the cell. The fine droplets of the spray travel to the opposite hot end of the cell where they impact the hot surface and are evaporated. This evaporation

produces a large vapor pressure that forces the vapor back down the cell toward the cold end where it recondenses to form the liquid condensate layer used to supply the spray.

## II. VIDA Technology

The VIDA technology that forms the basis of the design for this heat transfer cell is the result of a recent observation at Georgia Tech of a novel droplet instability. Consider a droplet of a condensed liquid attached to a metal diaphragm that is continuously vibrated normal to itself. As long as the diameter of the droplet is below a critical value, the liquid motion induced by the vibrations of the diaphragm are damped, ostensibly by viscosity and contact-line dissipation effects. As we increase the size of the droplet, the diameter soon reaches a critical value and an instability of the liquid-gas interface occurs due to disturbances at the vibrational frequency of the diaphragm. The instability manifests itself as a set of nonlinear surface waves that rapidly grow in amplitude. When the wave amplitude is of the order of the droplet height, the droplet breaks up and is *completely* drained into a spray of smaller (between one and two orders of magnitude) secondary droplets that is directed away from the diaphragm. The jet velocity near the surface appears to depend on the vibrational energy of the primary droplet prior to its breakup.

Figure 1 shows a sequence of snapshots of this droplet breakup. A water droplet having a planform diameter of 5 mm is placed on a horizontal circular metal diaphragm with a diameter of 25 mm and a thickness of 0.2 mm. As the diaphragm vibrates in its fundamental axisymmetric mode, droplet resonance and breakup is achieved as the amplitude of the vibration reaches a critical limit. The evolution of the droplet instability and breakup were recorded using a video camera. Figure 1a shows the unforced droplet for reference. As the excitation level is increased, waves first appear around the perimeter of the droplet near its contact line with the surface (Figure 1b). The waves then increase in amplitude and progress towards the crest of the droplet (Figure 1c). In this figure we also see that a few secondary droplets have already been ejected from the large droplet. Finally, in Figure 1d, the breakup is complete and the ejected secondary droplets have landed on the surface of the diaphragm under gravity. Figure 2 is a side view of a similar event. The unforced droplet is shown in Figure 2a and the droplet in the middle of the spray process is shown in Figure 2b. The black disk at the bottom of Figure 2b is the holder of the diaphragm and it is approximately 25 mm in diameter. This scale shows that most of the secondary droplets are within 5 cm of the surface.

Once the droplets are formed, they are propelled upwards at speeds that can exceed 50 cm/s near the surface. If the primary liquid droplet is continually replenished, then the small secondary droplets form a continuous spray. The mass flow rate of this spray can be significantly larger than the flow rate possible in the wick of a heat pipe and so a phase-change heat-transfer device based on this principle will have significantly better performance than conventional heat pipes.

## III. The VIDA Heat Transfer Cell

A prototypical cell based on the VIDA technology described above is shown in Figure 3 (patent pending). It is a completely sealed rectangular container with one end attached to a surface being cooled while the other is attached to a hot surface. The lateral surface of this cell would be insulated or slightly heated to prevent condensation. The cold end of the cell is vibrated at a specific frequency and amplitude. As the vapor in the cell condenses on the cold surface at specifically constructed condensation sites, the condensation droplets will begin to grow. When these droplets reach a critical size, the free-surface instability produced by the vibration will cause the droplets to disintegrate into a spray of smaller secondary droplets that will be propelled across the cell. When these droplets impact the opposite heated surface, they spread out and are vaporized. The vapor produced by this process travels back across the cylinder and condenses on the cold end to complete the heat transfer cycle in the cell.

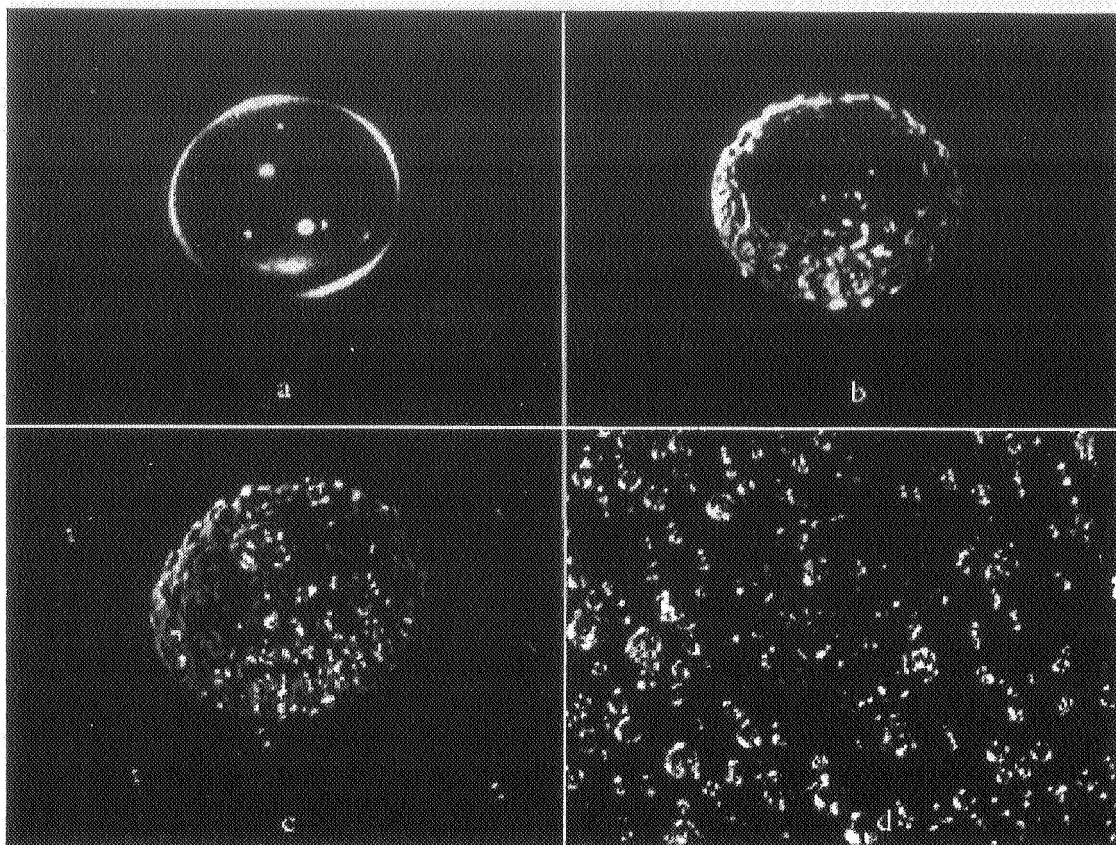


Figure 1: Four views of a liquid droplet on a vibrating diaphragm. a) The undisturbed droplet, b) the appearance of waves around the periphery, c) small waves over the entire droplet surface and the shedding of a few secondary droplets, and d) the total disappearance of the initial droplet.

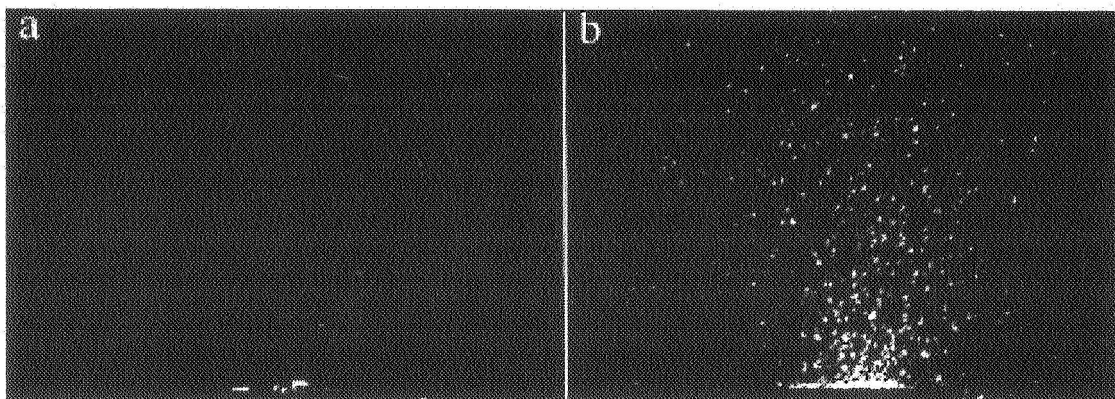


Figure 2: A side view of the droplet on a vibrating diaphragm. a) The undisturbed droplet, and b) the spray produced by the droplet resonance. Figure 2b is for a time somewhere between that of Figures 1c and 1d.

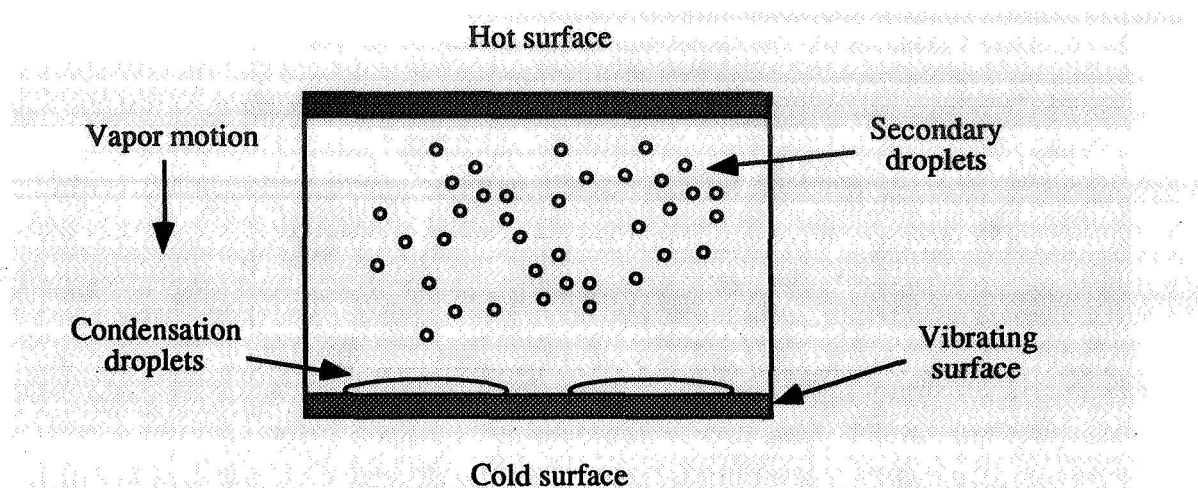


Figure 3: A schematic of the VIDA heat transfer cell.

#### IV. Physical Mechanisms

The physics associated with this droplet breakup instability must be understood in order to optimize the design of a heat transfer device based on this effect. The mechanism that causes the droplet instability is not well-known at this time, but there are a number of possibilities. The first is that the waves seen on the large droplet are a form of Faraday wave, similar to those seen when a container of liquid is vibrated vertically. (Faraday waves have recently been reviewed by Miles and Henderson, 1990.) At some specific frequency, the system goes into resonance and the Faraday waves on the droplet grow in amplitude and eventually pinch off to form the droplets. These waves are essentially a capillary wave and so their wavelength is related to the capillary length scale and the resonant frequency of the system. Thus, it is reasonable to assume that the size of the secondary droplets shed in the spray is also related to this wave length.

Despite the similarity with Faraday waves, there are several differences. The first is that classical Faraday waves are produced when a whole container of liquid is vibrated (an effective oscillation of the gravitational field). For the droplet, only the lower surface is oscillated and the liquid is not even contained at all. The second difference is that the resonant frequency of the droplet is larger than the frequencies typically used to explore Faraday waves.

A second possibility is that the waves on the large droplet are cross waves. Such waves were studied by Miles (1988). They are formed when a rigid plate is inserted part way into a liquid and then vibrated across the free surface. This causes an oscillatory motion of the contact line along the plate that in turn produces short stubby waves normal to the rigid plate. For the droplet, the contact-line motion is produced by the action of the surface vibration as it tends to periodically flatten and extend the droplet. In Figure 1b, we see that the first indications of wave motion seems to occur around the periphery of the droplet.

A third speculation on the cause of the droplet instability is that it is the result of high frequency pressure fluctuations that occur inside the droplet due to the vibrating diaphragm. When these pressure fluctuations resonate with the capillary waves on the surface of the droplet, they produce a large amplitude surface wave that pinches off at the crest to eject a small secondary droplet from the surface. This may be somewhat related to the mechanism for the atomization process of liquid jets as studied by Kang and Lin (1990) and Dressler and Kraemer (1990). However, for these jets the oscillation is along the axis of the jet parallel to the free surface, not normal to the free surface as in our droplets.

In order to fully examine the capability of this heat transfer cell, our current work is directed towards an understanding of the spray formation process. We are examining a small droplet on a



solid surface in which the surface vibrates vertically at a fixed frequency. From the frame of reference of a coordinate system moving with the plate, the system looks like a droplet subjected to an oscillatory gravitational body force. The flow is governed by the Navier-Stokes equations with the relevant free-surface boundary conditions. In addition, we pose a dynamic contact-line boundary condition and slip at the contact line. Although there is a great deal of similarity between this problem and the classical Faraday wave problem, one crucial difference is that a flat surface is not an equilibrium solution for the droplet problem. Thus, we can not treat this as a normal instability problem and use the standard weakly nonlinear techniques in the way discussed by Miles and Henderson (1990). The obvious inertial effects and nonlinearities exhibited by the droplet in Figure 1 indicate that we will most likely have to solve the full Navier-Stokes equations. We shall solve these equations numerically. We anticipate some difficulty in this calculation when the resonant frequency is approached and the wave amplitudes become very large. This difficulty is associated with the extremely fine scale at which the primary droplet breaks down into the spray. Another difficulty will be the precise model and computation for the motion of the contact line on the flat solid surface. One approximation that may be effective is to assume very small viscosity in the liquid. This seems reasonable in the light that we are examining a resonance phenomena in which damping may not play very much of a role. A perturbation analysis applied to this problem for small damping will produce the inviscid model to leading order. Solving this should be considerably easier than the fully-viscous problem, and it should simplify the difficulties associated with slip at the contact line. First-order effects of viscosity can be found using the usual regular perturbation methods.

The experimental work on this problem will investigate the effect of the liquid and surface properties on the evolution of the droplet instability, and, in particular, on the breakup of the primary droplet and the formation of the spray. Important parameters include the surface tension, density, and viscosity of the liquid, the wetting characteristics of the solid surface, and the amplitude of the surface vibration. The effect of liquid properties and droplet size on the amplitude threshold of the surface motion that is necessary for the onset of the breakup will be investigated. The time constants associated with the amplification of the instability and on the onset of primary droplet breakup and ejection of secondary droplets will be measured. The breakup and ejection process will be studied using high-speed and time exposure photography. The effect of liquid properties and primary droplet size on the size and density of the ejected secondary droplets will be investigated. Laser sheet illumination will be used to study the distribution, concentration and size of the secondary (ejected) droplets in planes that are vertical to and normal to the surface. Of particular interest is the nominally axisymmetric angular distribution in a plane that is normal to the surface and passing through the axis of the primary droplet. We will obtain estimates of velocity distributions (and thus of linear momentum) of the secondary droplets by using fast double shuttering of the laser sheet similar to what is done in PIV (particles image velocimetry) techniques. This can be accomplished using either video imaging or photographic film.

## V. Conclusions

Our work on the VIDA technology has indicated that our proposed heat transfer cell design will lead to an order of magnitude increase in heat-flux performance over conventional heat pipes used in current microgravity applications. The primary reason for this performance is that the proposed heat transfer cell uses a forced phase-change convection process that breaks through the capillary wicking limit of conventional heat pipes. Our current program of ground-based research is directed towards support of the conceptual design and the construction of a prototype of the heat transfer cell discussed above. Once constructed and tested, we believe that the heat transfer cell will be ready for direct use in a space experiment designed to demonstrate its performance in a microgravity environment.

## References

Dressler, J. L. & Kremer, G. O. (1990) "A multiple drop-size drop generator for calibration of a phase-doppler particle analyzer," *Liquid Particle Size Measurement Techniques: 2nd Volume*,

ASTM STP 1083, E. Dan Hirlman, W. D. Bachalo, and Philip G. Felton, Eds., American Society for Testing and Materials, Philadelphia, pp. 30-44.

Dunn, P. D. & Reay, D. A. (1994) "Heat Pipes," Elsevier Science Ltd.

Kang, D. J. & Lin, S. P. (1990) "Navier-Stokes flow for the initial stage of atomization," J. Colloid Interface Sci. 134, pp. 74-81.

Miles, J. (1988) "Parametrically excited, standing cross-waves," J. Fluid Mech. 186, pp. 119-27.

Miles, J. & Henderson, D. (1990) "Parametrically Forced Surface Waves," Ann. Rev. Fluid Mech. 22, pp. 143-65.

# THE DEVELOPMENT OF A FULL FIELD THREE-DIMENSIONAL MICROSCALE FLOW MEASUREMENT TECHNIQUE FOR APPLICATION TO NEAR CONTACT LINE FLOWS

Qun He and Kevin Hallinan  
University of Dayton  
Department of Mechanical and Aerospace Engineering  
Dayton, Ohio 45460-0210

## BACKGROUND

The goal of this paper is to present details of the development of a new three-dimensional velocity field measurement technique which can be used to provide more insight into the dynamics of thin evaporating liquid films (not limited to just low heat inputs for the heat transfer) and which also could prove useful for the study of spreading and wetting phenomena and other microscale flows.

Traditional velocity measurement techniques, such as hot-wire and laser Doppler anemometry (LDA) and standard Particle Image Velocimetry (PIV), are unable to provide velocity information in such thin films. The Forward Scattering Particle Image Velocimetry (FSPIV) technique developed by Ovrzyn and Hovenac (1993) offers the most promise. In this scheme, shown schematically in Figure 1, a partially coherent light beam back illuminates a mono-disperse suspension of spherical particles seeded in a fluid which ideally follow the fluid pathlines. A video microscopy system is used to view and record the forward scattered and transmitted light. Ovrzyn et al. has demonstrated that the light scattering produces a unique diffraction like image of the particle in the image plane for each de-focus position of the particles. This characteristic was exploited to determine the particle de-focus distance and the paraxial velocity if the time between the video frames is known. Simultaneously the transverse velocity (normal to the optical axis) was calculated by finding the particle centroid trajectories over time.

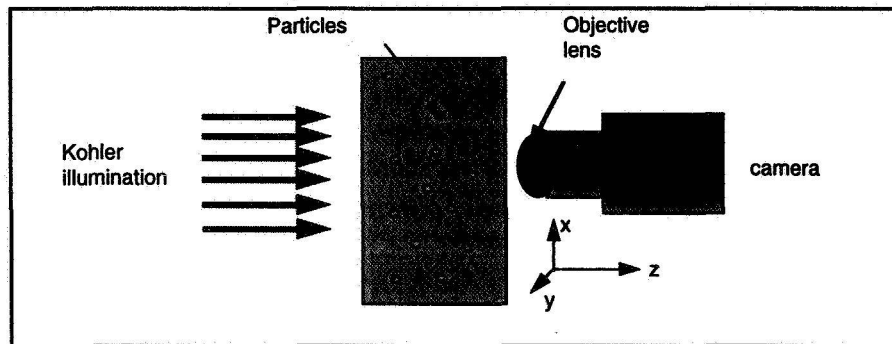


Figure 1. - Schematic of FSPIV.

Figure 2(a)-(c) show some examples of the scattered/transmitted light patterns of a spherical PMMA particle with a diameter of 0.325 micron in liquid methanol. Figure 2(d)-(e) are the intensity profiles of the diffraction images along the rows shown in the images. Apparent from these figures is that the diffraction patterns are different for equal and opposite paraxial defocus distance ("+" means closer to the objective, "-" means further away from the objective). The reason for this asymmetry has been shown in yet unpublished work by Khaydarov and Ovrzyn to be due to the transmission of light through the particles.

To obtain particle velocities, after acquiring the active particle images and ignoring any agglomerated particle images, the centroids of the scattered light images associated with each of the particles are first identified

in each frame<sup>1</sup>. The next step is to track individual particle centroids from frame to frame. The most widely used method is a two frame cross-correlation approach. Determining the particle centroids displacement over time provides the transverse velocity<sup>2</sup>. The axial velocity can be determined by identifying the rate of change of the defocus distance of each particle.

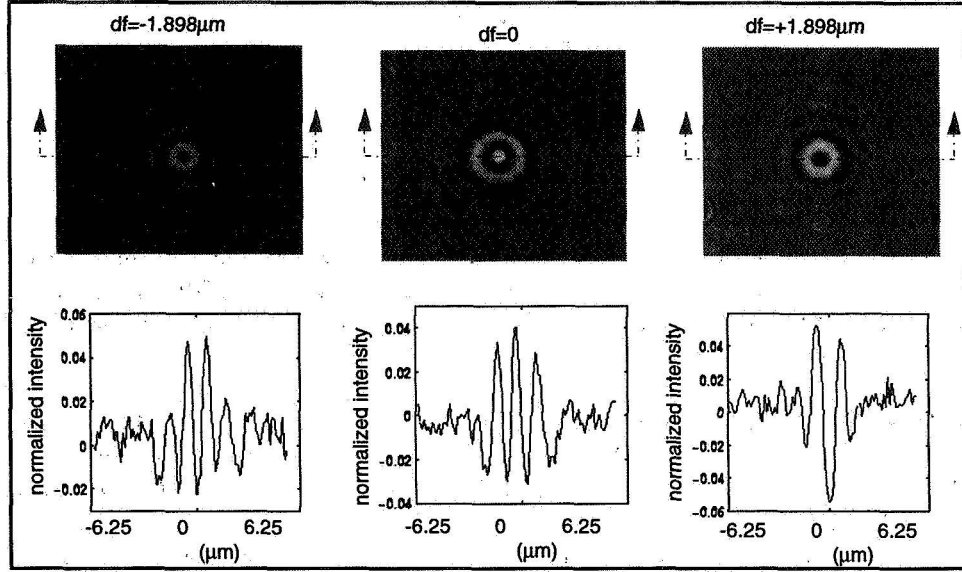


Figure 2. - Diffraction pattern and cross sectional intensity profile.

Establishing a relationship between the defocus of the particles and their scattering pattern is the most crucial aspect of this technique. A theoretical determination of this relationship is possible using Lorenz-Mie scattering theory. However, using theoretical predictions as a standard to compare to experimental measurements presumes an a priori knowledge of the optical aberrations of the experimental imaging and illumination systems. Alternatively, an experimental standard of 'calibration' images can be created and used. These 'calibration' images require that the image of near focus particles be obtained at known and different defocus distances. Then, the defocus distance of an active can be determined by comparison to a look-up-table (LUT) of calibration images using a correlation based pattern recognition technique. The active particle de-focus position is identified with the defocus of the calibration image which produces the best correlation.

The correlation involves integrating over space the product of the active particle image intensity,  $f(x, y)$  and the intensity of each image in the bank of calibration images,  $g(x, y)$ . Before correlating, however, the calibration and input images must first be normalized. This first requires the average intensity of the entire image to be determined as:

$$f_{average} = \frac{1}{M * N} \sum_{i=1}^M \sum_{j=1}^N f(i, j)$$

where  $M$  and  $N$  are the total number of pixels in the image in  $x$  and  $y$  directions. The analogous discrete normalized pixel intensity is defined as:

$$f_{normalization}(i, j) = \left( f(i, j) - f_{average} \right) \cdot \left( \sum_i \sum_j (f(i, j) - f_{average})^2 \right)^{-1/2}$$

<sup>1</sup>The centroid is easily found by identifying the center of the intensity profile.

<sup>2</sup>One of the limitations associated with cross-correlation particle tracking techniques for traditional PIV (i.e., the production of noise if the particles move out of the sampling region through three-dimensional motions) is not present for FSPIV.



The numerical approach for achieving the correlation is via the Fourier transform. The correlation process has a frequency space realization that involves Fourier transforming both signals and multiplying them. The correlation function is the inverse Fourier transform of this product. The mathematical representation of this process is shown below:

$$f * g = F^{-1} (F G)$$

where  $F$  and  $G$  are the Fourier transforms of  $f$  and  $g$ .

Figure 3 demonstrates the correlation pattern recognition procedure. In this figure, the active input image intensity and the bank of calibration images are shown. Each column in the bank of calibration images represents the normalized intensity profile of a particle image of known defocus. The input intensity plot is the normalized intensity of an image with unknown defocus. The correlator box shown represents the computer algorithm which makes the comparison of the unknown image to each of the calibration images. For the input image shown, the resulting correlation plot shows that the peak correlation is achieved at a defocus of  $-9 \mu\text{m}$ . Therefore, the input image is identified to be at a defocus of  $-9 \mu\text{m}$  relative to the focal plane of the imaging system, equal to the true defocus position of the active image for this example.

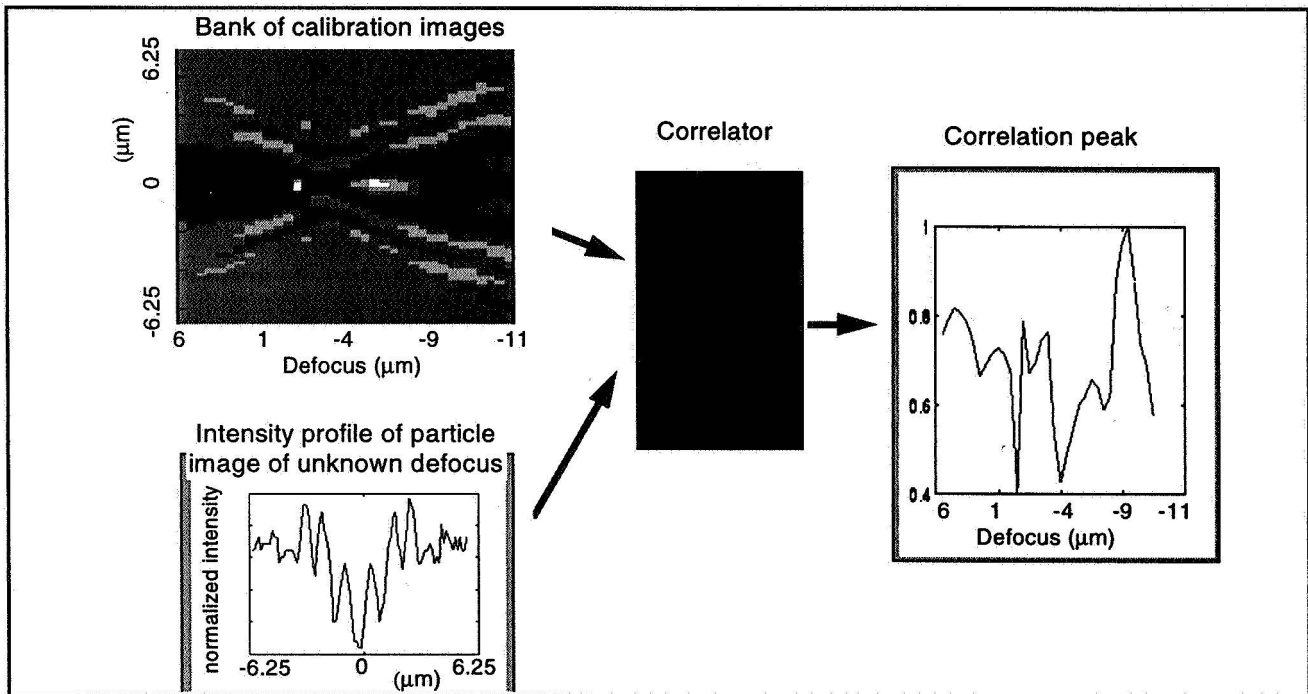


Figure 3. - Pattern recognition of diffraction images

## EXPERIMENTS

It has been a challenge to configure the hardware needed to implement this technique to measure fluid velocity in the near contact line region because of the small lengthscales associated with the region of interest (300 microns in length and up to 100 microns in film thickness). The small dimensions forced the use of micron or sub-micron size particles to minimize the disturbance of the particles to the flow. This requirement dictated the use of both a high Numerical Aperture imaging lens and a highly coherent light source in order to collect the scattered light around the particles. A long working distance imaging lens was also required to compensate for the thickness of the optical window separating the seeded liquid from the imaging lens. Alignment of the light source with the

optical axis of the objective lens was found to be extremely critical for producing repeatable results. Further, the development of a bank of calibration images required a very fine stage translation and accurate stage displacement micrometer since these affect the accuracy of both the determination of the particle position and paraxial velocity. Finally, the sampling time was required to be small enough to effectively freeze the particles in each frame to eliminate blurring.

Figure 4 shows a schematic of the final hardware setup for the three dimensional full field PIV technique which has been configured. A Labophot-2A microscope by Nikon with a built-in Kohler illumination system is used to view particles in a test cell mounted on the microscope stage. The light was filtered to minimize infrared heating of the liquid within the test cell. Experimental details are presented in the figure.

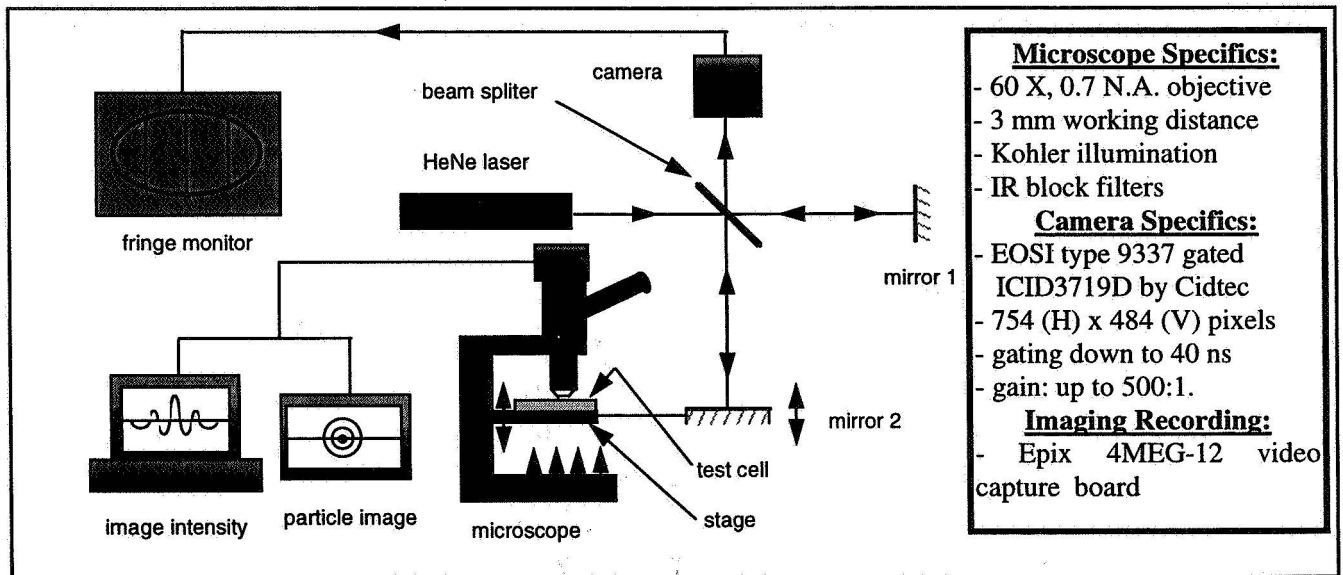


Figure 4. - Experimental setup.

The 80 mm x 80 mm x 10 mm deep test cell shown in Figure 5 is a rectangular and transparent enclosure partially filled with particle seeded liquid methanol (HPLC grade, 99.9% pure). The particles are 3.1 microns in diameter and are PolyMethylMethAcrylate (PMMA) in make-up. The enclosure is comprised of a Teflon spacer which separates two pieces of 1 mm borosilicate glass windows. There are two ports in the test cell used to inject fluid and particles into the cell. Heat input via a resistance heater (Minco) mounted to the top of the test cell and heat removal via a cooling water heat exchanger attached to the bottom of the test cell determine the thermal state within. The heat input causes the liquid to evaporate from the near contact line region of the meniscus on the upper window. The cooling causes the vapor to condense on the bottom window. Thermocouples mounted within the cell and along the upper wall of the cell are used to identify the thermal conditions present near the contact line and within the bulk of the liquid and vapor.

The calibration images were obtained by imaging a particle fixed on the test cell wall after liquid was added. The imaging optics were then adjusted to obtain the best 'focus' of the particle. The stage was then translated both up and down by known distances to move the particle in and out of focus. The resulting particle images were recorded for these known de-focus distances. The stage translation was measured with an accuracy of  $\pm 0.06$  microns using the Michelson interferometer shown schematically in Figure 4.

To establish the viability of the three dimensional full field forward scattering particle image velocimetry technique and apply it to the velocity measurement in an evaporating extended meniscus, velocity measurement experiments were conducted on the thin film region of a meniscus formed along a heated inclined plate. Tests were conducted for variable heat input and inclination angle. Temperatures were monitored until equilibrium was established. At this point, active particle images were recorded.

## RESULTS AND DISCUSSION

The initial experiments demonstrated that in the curved thin film region near the contact line, the image of the particle was found to be asymmetric such as shown in Figure 6. Figure 6(a) is the image of a particle at the flat adsorbed film region of the meniscus. Figure 6(b) is the image of a particle within the slightly curved thin film region approximately 70 microns away. Figure 6(c) is the image of a particle another 200 microns upstream. The asymmetry is due to the refraction of the incident light by the liquid-vapor interface before it interacts with the particles. When the liquid-vapor interface is not parallel with the focal plane of the imaging lens, the wave incised upon the particles is no longer planar relative to the focal plane. Also, the refraction angle of the incident wave is clearly different at different film slope. Consequently, calibration images at known film locations (i.e., for known local film slope) were generated and used to compare active images. Therefore, at discrete film slopes, a calibration Look-up-Table (LUT) similar to that shown in Figure 3 was generated.

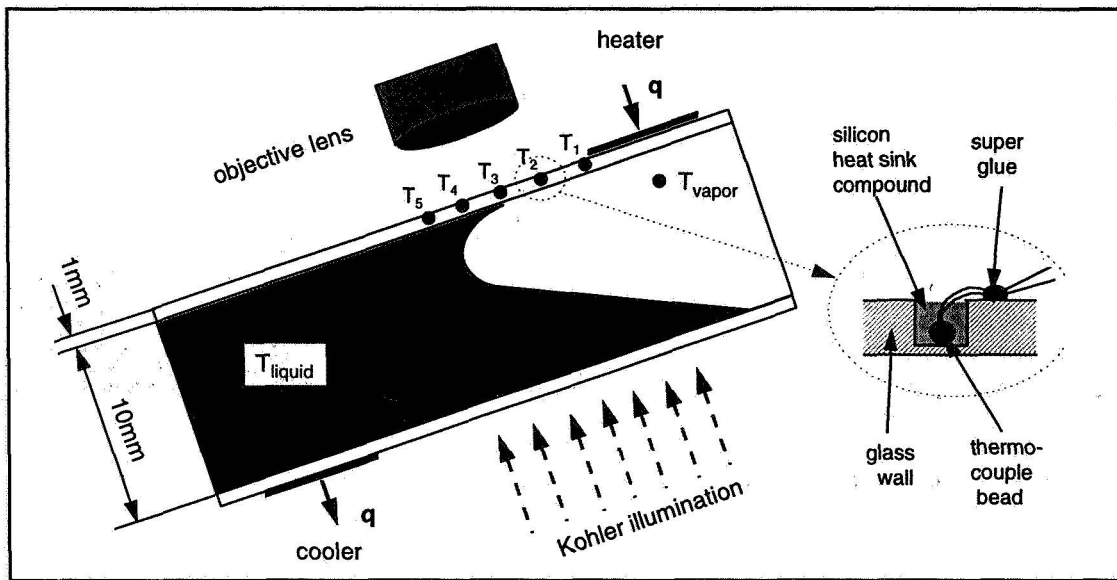


Figure 5: Schematic of test cell.

Figure 7(a) shows the trajectory of a single particle at a distance of 240 microns from the actual contact line for test conditions of 0.6 W heat input and a  $4.1^\circ$  inclination angle. (1/30 second interval between images). In this image, the background illumination of the image was subtracted. The centroid was computed for each particle position. From this particle trajectory, the velocity field was determined. Figure 7(b) shows the liquid through the cross-section of the liquid film. It is clear from the figure that thermocapillary stresses cause the flow to reverse near the contact line. The uncertainty of the velocity measurement is:  $u \pm 9.3 \mu\text{m/s}$ ,  $v \pm 7.5 \mu\text{m/s}$  and  $w \pm 15 \mu\text{m/s}$ .

## CONCLUSIONS

The FSPIV technique has been employed and used to measure the three-dimensional velocity field near the contact line of a curved and evaporating meniscus on a heated plate. While a significant amount of work remains to be done, its potential for application to dynamic near contact line flows has been demonstrated.

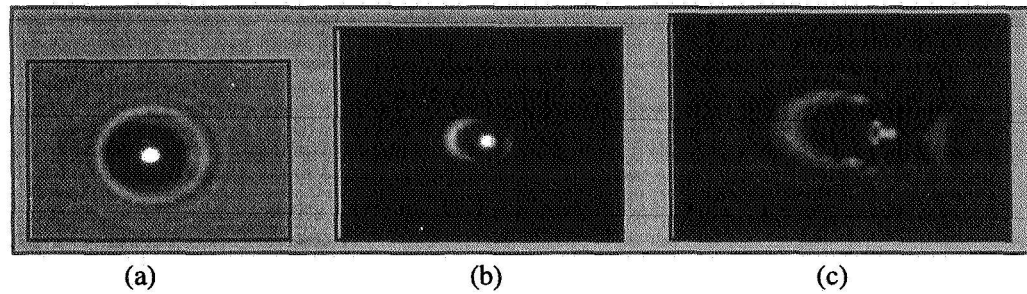


Figure 6. - Diffraction of particles in curved thin liquid film

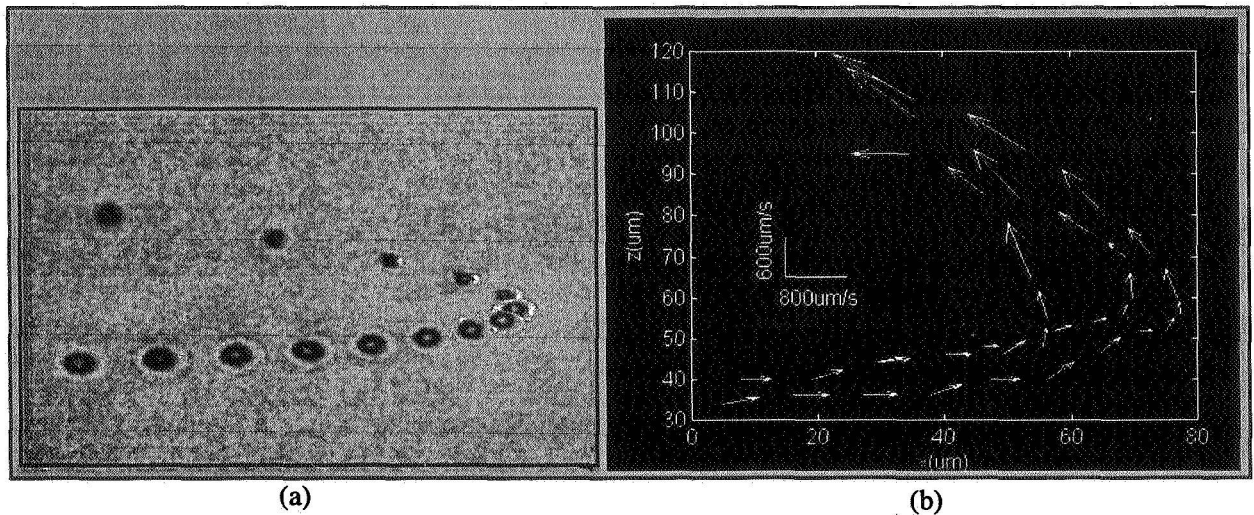


Figure 7. - (a) Images of a moving particle in thin film region with inclination angle:  $4.1^\circ$  and heat input 0.6 watt and (b) resulting film velocity profile.

## ACKNOWLEDGMENT

Thanks are due to Dr. B. Ovrn of NYMA, Inc. for his suggested use of the FSPIV technique. We would also like to acknowledge the support for this research by NASA through grant NAG3-1391.

## BIBLIOGRAPHY

Ovrn, B. and Hovenac, E.A., "Coherent forward scattering particle image velocimetry: application of Poisson's spot for velocity measurements in fluids," SPIE 2005, 338-348 (1993).

# **A Study of Nucleate Boiling with Forced Convection in Microgravity**

Herman Merte, Jr.  
Professor of Mechanical Engineering  
The University of Michigan  
Ann Arbor, Michigan

## **Introduction**

Boiling is a rather imprecise term applied to the process of evaporation in which the rate of liquid-vapor phase change is large. In seeking to determine the role and significance of body forces on the process, of which buoyancy or gravity is just one agent, it becomes necessary to define the term more precisely. It is generally characterized by the formation and growth of individual vapor bubbles arising from heat transfer to the liquid, either at a solid/liquid or liquid/liquid interface, or volumetrically. The terms "bubble" boiling and "nucleate" boiling are frequently used, in recognition of the interactions of surface tension and other forces in producing discrete bubbles at distinctive locations (although not always).

Primary considerations are that evaporation can occur only at existing liquid-vapor interfaces, so that attention must be given to the formation of an interface (the nucleation process), and that the latent heat for this evaporation can come only from the superheated liquid, so that attention must also be given to the temperature distributions in the liquid.

The elements that constitute the nucleate boiling process - nucleation, growth, motion, and collapse of the vapor bubbles (if the bulk liquid is subcooled) - are common to both pool and flow boiling. It is well known that the imposition of bulk liquid motion affects the vapor bubble behavior relative to pool boiling, but does not appear to significantly influence the heat transfer. Indeed, it has been recommended in the past that empirical correlations or experimental data of pool boiling be used for design purposes with forced convection nucleate boiling [1, 2]. It is anticipated that such will most certainly not be the case for boiling in microgravity, based on preliminary observations to be described below. In earth gravity buoyancy will act to remove the vapor bubbles from the vicinity of the heater surface regardless of how much the imposed bulk velocity is reduced, depending, of course, on the geometry of the system. The major so-called forces governing the motion of the bubbles are buoyancy, liquid momentum and viscosity. With sufficiently high flow Reynold's Numbers, it can be intuited that the latter two forces will outweigh the first, and the process will be the same whether at earth gravity or microgravity. However, as the Reynold's Number is reduced the magnitude of the liquid momentum and viscous forces are correspondingly reduced, and in microgravity buoyancy cannot take over as a "back-up" mechanism for vapor removal, leaving only the reduced levels of liquid momentum and viscous forces. Vapor bubbles have been observed to dramatically increase in size in the limit of pool boiling in microgravity [3], but will be bounded in size by the action of the liquid momentum and viscous forces of forced convection in microgravity.

Certain other effects that can be neglected at normal earth gravity, such as surface tension, both at the solid-liquid-vapor contact line and at the liquid-vapor surface associated with the interface temperature variation, will be of consequence at microgravity conditions. The net quantitative effect of these on the vapor bubble behavior is unknown, at present, as are the related effects on the heat transfer, and provides one of the motivations for the study of the flow boiling process in microgravity. As a case in point, the departure size of vapor bubbles at low velocities in microgravity will be an important parameter in the design of vaporizing heat exchangers for space applications, since its size relative to that of the flow passage has a significant influence on the mechanisms and magnitudes of the local heat flux.

The ultimate objective of the basic studies of flow boiling in microgravity is to improve the understanding of the processes involved in boiling, as manifested by the ability to predict its behavior. This is not yet the case for boiling heat transfer even in earth gravity, despite the considerable research activity over the past 30 years. Hahne et al [4], for example, compared 7 different correlations with their own R12 forced convection boiling data, for both up and down flow, with quite disparate results. With changes in the dimensional and time scales of boiling arising due to microgravity, more detailed observations of its elements will be possible, and perhaps disclose or clarify certain phenomena. For example, a source of the dynamic vapor bubble growth observed with pool boiling in microgravity [3] has been disclosed [5]. Figure 1, from [5], shows computed spherical vapor bubble dynamics beginning from the initial critical size nucleus, along with the time interval during which the bubble growth is predicted to become

unstable. This instability conforms to observations, in which a "roughened" liquid vapor interface is formed. The accompanying increase in the liquid-vapor interfacial area produces a significant increase in the bubble growth rates, as reported in [6], leading to so-called vapor explosions.

### Effects of Velocity

In the absence of buoyancy, a bulk liquid being heated at a solid surface can undergo dramatic changes in temperature distributions due to externally imposed velocities. This in turn influences both the nucleation characteristics and the subsequent vapor bubble growth. The latter effect is illustrated in the computed spherical vapor bubble growths in Figure 1, from [7, 8]. The heavy curves apply to the case where the bulk liquid is taken to be uniform at the measured heater surface temperature at nucleation, while the light curves show the results where the actual one-dimensional temperature distribution in the liquid, as heated from the plane surface, is taken to be the initial one dimensional radial distribution about the critical size vapor bubble. It is noted that differences between the two only become manifest during the later stages of growth, which conforms to comparisons with measurement.

One of the unique advantages of transient heating of liquids in microgravity, utilized in the pool boiling studies to date and anticipated to be equally applicable in future "low velocity" flow boiling studies, is the ability to predict with reasonable certainty the temperature distributions in the liquid. This permitted a quantitative description of what is defined as homogeneous nucleation, even though taking place in the immediate vicinity of the heater surface. Figure 2, from [3, 9] show the analytic predictions of homogeneous nucleation in the presence of transient temperature gradients, based on classical homogeneous nucleation theory, as a function of the imposed heat flux and the system pressure, which was varied as a means of conveniently changing the initial bulk liquid subcooling. Measurements from several sets of space experiments are superimposed, and confirm that decreasing the imposed heat flux results in a reduction in the heater surface superheat at nucleation. The measurements from the space experiments at the highest level of heat flux, to the right in Figure 2, are considered to be heterogeneous nucleations, since they all were initiated at precisely the same location on the heater surface, whereas those at the lower levels of heat flux occurred at various apparently random locations.

A tentative conclusion at this time is that it appears that nucleation conforming to the predictions of homogeneous nucleation here also result in the unstable or explosive type of vapor bubble growths characterized by roughened interfaces, described above. Although anticipated, it remains to be demonstrated that corresponding behaviors will take place in the presence of imposed liquid velocities. The nucleation process appears to be governed by local conditions, not in the sense of state functions, and hence should be influenced by the prior history.

Measurements with long term pool boiling in microgravity [3] have demonstrated that the heat transfer is enhanced considerably over that in earth gravity at the lower levels of heat flux, but that the heat flux at which dryout takes place is substantially reduced. This comparison is made in Figure 3, from [10]. The behavior in microgravity in what might normally be termed the film boiling domain is the consequence of a combination of dryout and bubble boiling taking place simultaneously over the heater surface, with the measurements of heat flux and surface temperature representing the spacially integrated mean values. The enhancement in the nucleate boiling domain in Figure 3 is attributed to the steady existence of a "macrolayer" between the heater surface and a large vapor bubble which remains suspended in the vicinity of the heater. This layer serves as a boundary across which evaporation takes place, as well as a mechanism for the efficient removal of vapor bubbles from the heater surface, due to vapor pressure differences arising from surface tension.

It is expected that any bulk liquid motion imposed parallel to the heater surface in microgravity would further enhance the heat transfer process by what has been termed sliding bubbles, in a manner similar to that produced by buoyancy in earth gravity [11] and by forced flow in short term reduced gravity [12]. These result in the continuous renewal of the thin liquid layers beneath the bubbles. The departure size of the vapor bubble is an important constituent in the microlayer evaporation process taking place in such circumstances, and the drag forces in forced convection boiling provide a vehicle for this departure in microgravity. A description of the relation between the buoyancy dominant and inertial dominant regimes for bubble departure has been provided in terms of a "two-phase Richardson number" [13].

### Experimental Results to Date

A schematic of a low velocity forced convection boiling loop for proposed studies in microgravity is shown in Fig. 4. Velocities can be varied from 0.5 cm/s to 60 cm/s by pump speed control combined with changes in test



section height, from 2.54 cm (1 inch) to 0.318 cm (0.125 inch). The use of a flow loop permits the study of boiling under steady conditions as well as under transients, and thus can accommodate the use of metallic surfaces which, while representative of engineering surfaces, also introduce complications with transients, associated with heat capacity effects. The flow loop proper occupies a volume of about  $1.22 \times .61 \times .46$  m ( $48 \times 24 \times 18$  inches). The flat heater surface used is rectangular in shape, 1.91 cm by 3.81 cm ( $0.75 \times 1.5$  inches), consisting of a 400 Angstrom thick semi-transparent gold film sputtered either on a quartz substrate which serves simultaneously as a heater and a resistance thermometer, or a copper substrate of the same size. The heater substrate is a disc which can be rotated so that the heated length in the flow direction can be changed from 1.91 to 3.81 cm (0.75 to 1.5 inches). Variable buoyancy normal to the heater surface is achieved by rotation of the entire loop relative to earth gravity. Of course, this is at the expense of varying the buoyancy parallel to the heater surface. The  $0^\circ$  reference for orientation is taken with the flat heater surface horizontal facing upward, while the angle increases such that  $90^\circ$  implies a vertical heater surface with the fluid flow direction upward.

The enhancement of the boiling process taking place with low velocities for those orientations, producing the "sliding" vapor bubbles described above, has been demonstrated and presented previously [14, 15]. A further confirmation of this effect is seen in Figure 5, from [16], in which the heated length in the flow direction was changed from 1.91 cm (0.75 inches) to 3.81 cm (1.50 inches). The orientation angle is  $\theta = 180^\circ$ , with the heater horizontal facing downward, so that buoyancy holds the vapor bubbles against the surface as they slide along with the higher velocity of 32.4 cm/sec here. Both polished quartz and copper heater surfaces of identical sizes were used, with similar enhancements as noted.

It was noted in Figure 3 that heater surface dryout takes place at a considerably lower heat flux with pool boiling in microgravity, as compared to earth gravity. With the imposition of fluid flow it can be anticipated that this dryout (CHF-Critical Heat Flux) will increase, depending, of course, on the velocity. The onset of the dryout depends on the ability of the liquid to make contact with the heater surface which depends, in turn, on the circumstances under which the vapor departs from the vicinity of the heater surface. Results of the influence of both heater surface orientation and velocity were reported previously [14, 17], for the flow loop in Figure 4. Recent work, in which void fraction measurements were made in the vicinity of the heater surface with the various orientations which tend to keep the vapor near the heater, indicate that a distinct relationship exists between the CHF and the vapor bubble residence time at the heater. The residence times were measured with hot wire anemometry, with the comparisons shown in Figure 6, from [18]. The residence time is related to the mechanisms producing departure of the vapor from the heater surface, as well as the geometry of the heater, including the heated length along the flow direction. It is anticipated that the description of the residence time will provide the analytical basis for predicting the flow boiling heat transfer in microgravity.

## References

1. Bergles, A. E., and Rohsenow, W. M., "The Determination of Forced-Convection Surface Boiling Heat Transfer," *J. Heat Transfer*, 86, 1964, 365-382.
2. Bartolini, R. et al, "Experimental Study on Nucleate Boiling of Water in Vertical Upflow and Downflow," *Int. J. Multiphase Flow*, 9, 1983, 161-165.
3. Merte, H., Jr., Lee, H. S., and Keller, R. B., "Report on Pool Boiling Experiment Flown on STS-47 (PBE-IA), STS-57 (PBE-IB), and STS-60 (PBE-IC). NASA CR 198465 prepared for Lewis Research Center under Contract NAS3-25812. March, 1996.
4. Hahne, E., et al, "Fully Developed Nucleate Boiling in Upflow and Downflow," *Int. J. Heat Mass Transfer*, 32, 1989, 1799-1808.
5. Lee, H. S., and Merte, H., Jr., "The Origin of the Dynamic Growth of Vapor Bubbles Associated with Vapor Explosions," submitted for presentation at session on "Heat Transfer in Microgravity Systems," to be held at the ASME-IMECE in Atlanta, GA on Nov. 17-22, 1996.
6. Ervin, J. S., Merte, H., Jr., Keller, R. B., and Kirk, K., "Transient Pool Boiling in Microgravity," *Int. J. Heat Mass Trans.*, 35, March, 1992, pp. 659-674.
7. Lee, H. S., and Merte, H., Jr., "Spherical Vapor Bubble Growth in Uniformly Superheated Liquids," accepted for publication in *Int. J. Heat Mass Transfer*, 1996.
8. Lee, H. S., and Merte, H., Jr., "Hemispherical Vapor Bubble Growth in Microgravity: Experiments and Model," accepted for publication in *Int. J. Heat Mass Transfer*, 1996.
9. Merte, H., Jr., and Lee, H. S., "Homogeneous Nucleation in Microgravity at Low Heat Flux: Experiments and Theory," ASME Paper 95-WA/HT-41 presented at Session "Heat Transfer in Microgravity Systems" at the ASME-IMECE in San Francisco, CA on Nov. 12-17, 1995.

10. Lee, H. S., Merte, H., Jr., and Chiaramonte, F., "The Pool Boiling Curve in Microgravity," AIAA Paper 96-0499 presented at 10th Annual Symposium on Microgravity Science and Space Processing, AIAA 34th Aerospace Science Meeting, Jan. 15-18, 1996, Reno, NV.
11. Cornwell, K., "The Role of Sliding Bubbles in Boiling on Tube Bundles," Heat Transfer 1990 - Vol. 3, *Proc. 9th Int. Heat Transfer Conf.*, Jerusalem, Israel, Aug. 19-24, 1990, 455-460.
12. Cooper, M., et al, "Behavior of Vapour Bubbles Growing at a Wall with Forced Flow," *Int. J. Heat Mass Transfer*, 26, 1983, 1489-1507.
13. Kirk, K. M., and Merte, H., Jr., "A Mixed Natural/Forced Convection Nucleate Boiling Heat Transfer Criteria," Heat Transfer 1994, Vol. 7, pp. 479-484. *Proceedings of the 10th International Heat Transfer Conference*, Brighton, England, August 14-18, 1994.
14. Merte, H., Jr., "Pool and Flow Boiling in Variable and Microgravity," *2nd Microgravity Fluid Physics Conference*, June 21-23, 1994, NASA-Lewis, Cleveland, OH.
15. Kirk, K. M., Merte, H., Jr., and Keller, R. B., "Low Velocity Subcooled Nucleate Flow Boiling at Various Orientations," *ASME J. of Heat Trans.*, Vol. 117, 2, pp. 380-386, May, 1995.
16. Nestel, S. U., and Merte, H., Jr., "The Effects of Heater Surface Length in Forced Convection Nucleate Boiling," Report No. UM-MEAM-95-07, University of Michigan, Department of Mechanical Engineering and Applied Mechanics conducted under NASA Grant NAG3-1310, July 1995.
17. Brusstar, M. J., and Merte, H., Jr., "The Effects of Buoyancy on the Critical Heat Flux in Forced Convection," *AIAA J. of Thermo-physics and Heat Transfer*, 8, April - June 1994, pp. 322-328.
18. Brusstar, M. J., and Merte, H., Jr., Keller, R. B., "The Role of Buoyancy Orientation on Bubble Residence Times and the Related Critical Heat Flux," 1995 *National Heat Transfer Conference, Proc. of Symposium "Heat Transfer in Microgravity Systems"*, ASME HTD-Vol. 305, pp. 15-27. Portland, Oregon, August 5-9, 1995.

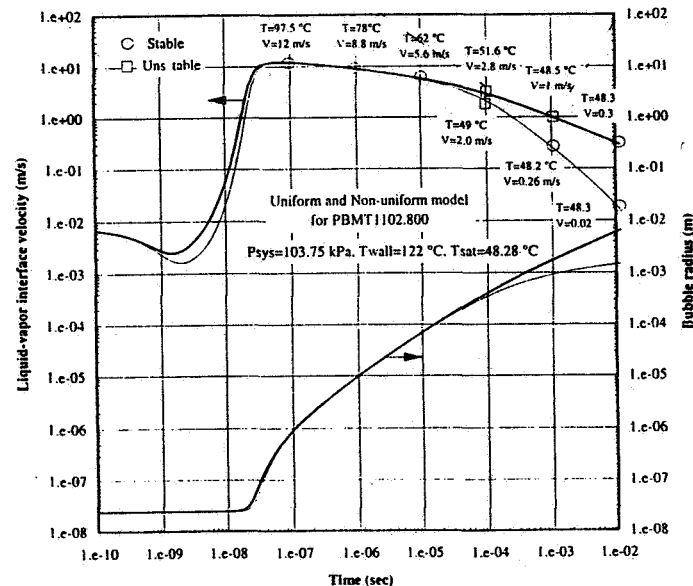


Figure 1. Prediction of onset of unstable vapor bubble growths in microgravity [5].



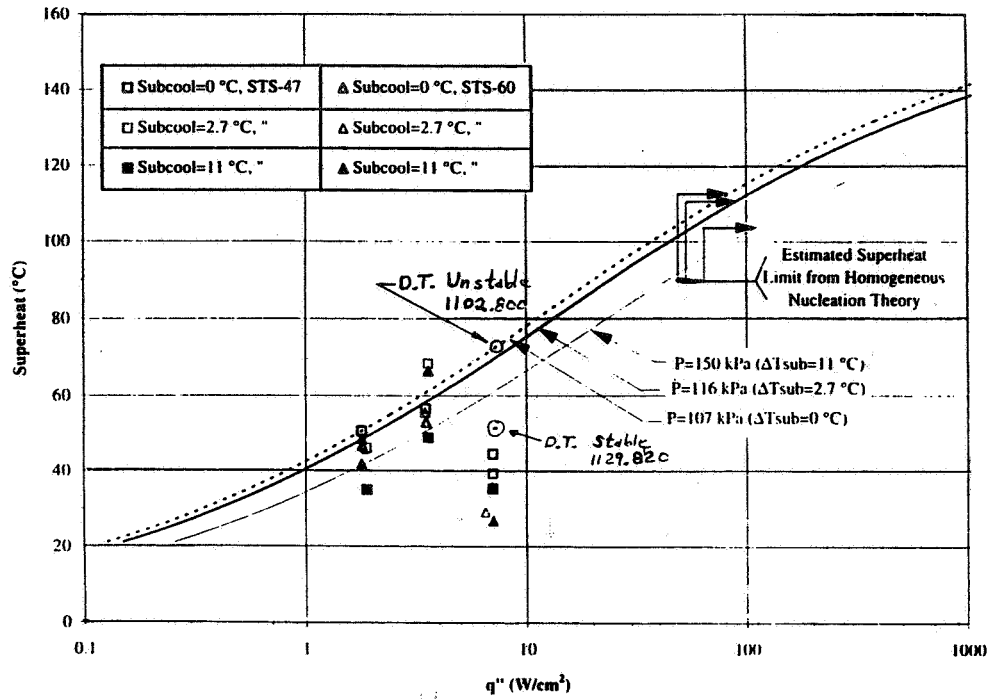


Figure 2. Homogeneous nucleation model for R-113 with transient heating in microgravity. Measurements with PBE-IA - IC (STS-47-60)  
 $K^* = 2.57 \times 10^6$  evaluated for PBE-IA: Run No. 9.

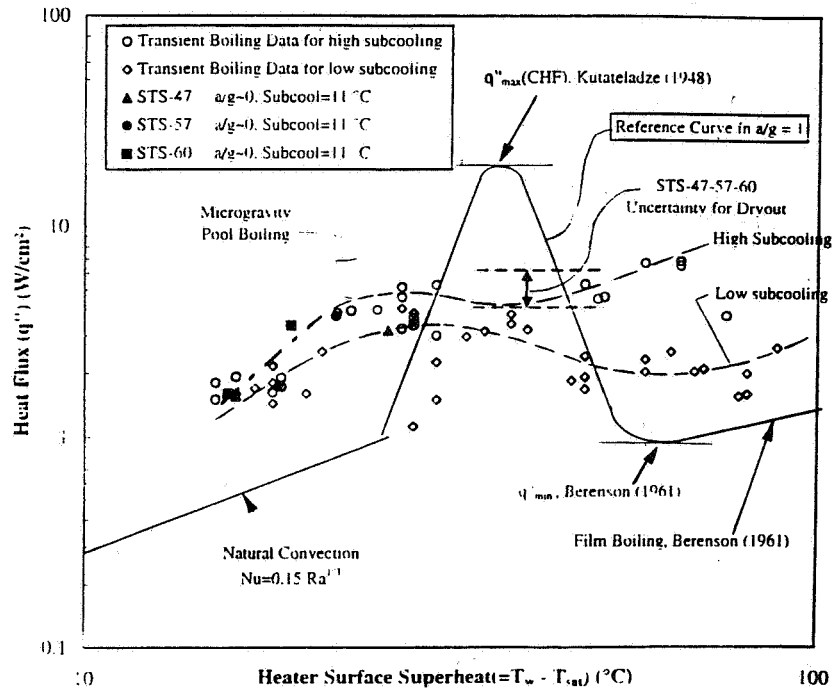


Figure 3. Composite microgravity pool boiling curves for R-113 from PBE-GAS space experiments compared with Reference Curve for  $a/g = 1$ . From [10].

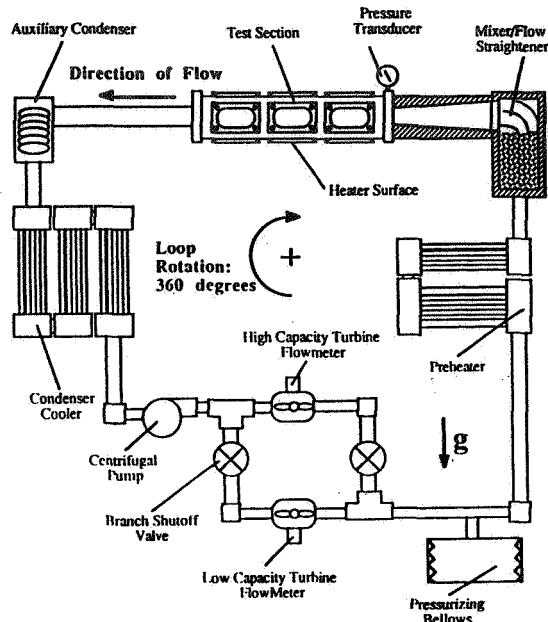


Figure 4. Schematic of flow loop for study of boiling in microgravity.

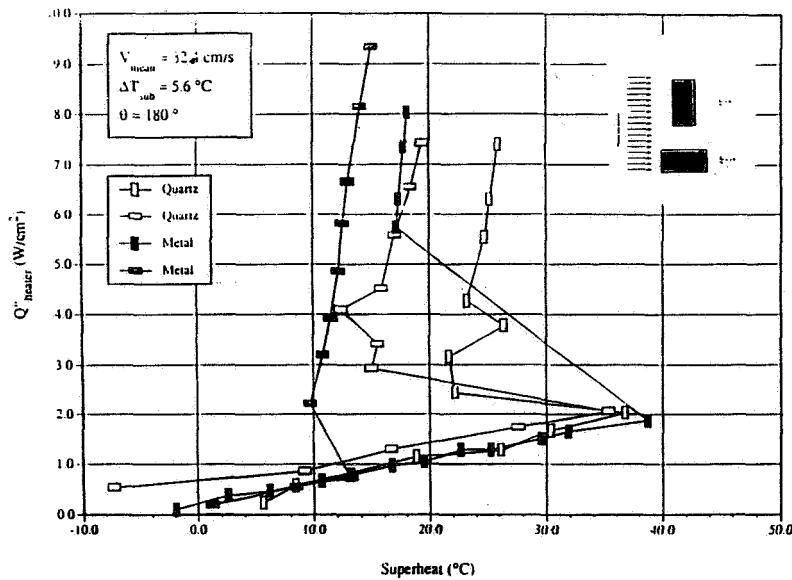


Figure 5. Steady forced convection nucleate boiling on flat heater surfaces. Horizontal down. R-113.  $\Delta T_{\text{sub}} = 5.6^\circ\text{C}$ .

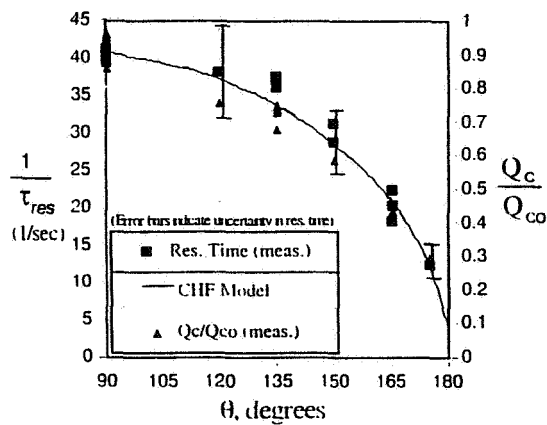


Figure 6. Comparison of Flow Boiling Measurements of Vapor Bubble Residence Time and Critical Heat Flux with Model Predictions at Various Orientation Angles. From [18].

# EVAPORATION ON/IN CAPILLARY STRUCTURES OF HIGH HEAT FLUX TWO-PHASE DEVICES

Amir Faghri and Dmitry Khrustalev

Department of Mechanical Engineering  
University of Connecticut, Storrs, Connecticut 06269

## ABSTRACT

Two-phase devices (heat pipes, capillary pumped loops, loop heat pipes, and evaporators) have become recognized as key elements in thermal control systems of space platforms (ref. 1). Capillary and porous structures are necessary and widely used in these devices, especially in high heat flux and zero-g applications, to provide fluid transport and enhanced heat transfer during vaporization and condensation. However, some unexpected critical phenomena, such as dryout in long heat pipe evaporators and high thermal resistance of loop heat pipe evaporators with high heat fluxes, are possible and have been encountered in the use of two-phase devices in the low gravity environment. Therefore, a detailed fundamental investigation is proposed to better understand the fluid behavior in capillary-porous structures during vaporization at high heat fluxes. The present paper addresses some theoretical aspects of this investigation.

## INTRODUCTION

Miniature flat heat pipes with axial micro grooves, shown in figure 1, are intended for the cooling systems of electronic components (ref. 2). Both capillary and boiling limitations are found to be important for flat miniature copper-water heat pipes with external dimensions of  $2 \times 7 \times 120$  mm and plain axial micro grooves on the inner surface which can have width of only 0.1 mm. Flat miniature heat pipes are capable of withstanding heat fluxes on the order of  $40 \text{ W/cm}^2$  applied to the evaporator wall (refs. 3 and 4). Higher heat fluxes are possible with the use of porous materials in addition to grooved structures as shown in figure 1(c). The enhanced copper-water flat heat pipe with axial grooves and a porous coating on the lands between the grooves can operate at a maximum heat flux in the evaporator of  $80 \text{ W/cm}^2$  in the horizontal orientation (ref. 5). Heat fluxes of up to  $200 \text{ W/cm}^2$  on evaporator walls of miniature heat pipes are achievable with the "inverted meniscus"-type evaporators (refs. 6 and 7).

While heat transfer during evaporation of liquid from capillary-grooved surfaces was considered by many investigators (refs. 8 to 11), their analyses were done for comparatively small heat fluxes. In all above mentioned papers, the variation of temperature of the liquid free surface along the microfilm in modeling of evaporative heat transfer on capillary-grooved surfaces was emphasized. Khrustalev and Faghri (ref. 11) took into consideration the existence of surface roughness and its influence on evaporative heat transfer. The film surface curvature,  $K$ , was expressed in terms of the solid surface curvature,  $K_w$ , and film thickness and formation of the thin liquid evaporating film was considered. Accounting for the roughness of the solid surface in the thin evaporating film region resulted in a decrease of the heat transfer coefficient by up to about 30% in comparison to

that obtained for a smooth surface for the case when the accommodation coefficient was set equal to unity. For  $\alpha \ll 1$  the influence of surface roughness on the evaporative heat transfer coefficient was insignificant. The simplified model of evaporative heat transfer, where it was assumed that the free film surface curvature in the microfilm region was equal to that in the meniscus region, predicted values of the heat transfer coefficient only up to 5% smaller in comparison to the case where the curvature variation along the film was taken into account (for  $\alpha = 1$ ). The value of the local evaporative heat transfer coefficient (for a fixed meniscus contact angle) was practically independent of the heat flux on the evaporator external wall. It should also be noted that Khrustalev and Faghri (refs. 4 and 11) found that their predictions of the effective evaporative heat transfer coefficient matched the existing experimental data only for very small values of the accommodation coefficients, for example,  $\alpha = 0.05$ . With small accommodation coefficients, the role of the thin-film region of the evaporating meniscus is smaller than with  $\alpha = 1$  because of the interfacial thermal resistance.

### HIGH FLUX EVAPORATION FROM LIQUID-VAPOR MENISCI

The main objective of the proposed theoretical effort is to identify the importance of various physical phenomena in initiating critical mechanisms in capillary structures with high heat fluxes. With high heat fluxes, some additional physical phenomena can be important in evaporative heat transfer from liquid-vapor menisci. Some examples include:

1. Fluid flow effects, neglected in the previous evaluations of the effective evaporative heat transfer coefficient, can significantly alter its value.
2. Shear stresses induced on the liquid-vapor interface by thermocapillarity and complex two- or three-dimensional vapor flow can cause the recession of the evaporating liquid meniscus in a groove (or pore) and lead to an unstable mode of operation in the axially-grooved evaporator.
3. The existence of thick liquid films attached to the extended evaporating meniscus in a capillary tube, recently observed in the experiments by Belonogov and Kiseev (ref. 12), can significantly change the existing methods in the prediction of dryout in capillary-driven devices.

In the zero-gravity environment, these phenomena can be more important than in the gravity field.

### Fluid flow in evaporating films and liquid-vapor menisci

A cross section of the liquid-vapor evaporating meniscus is given in figure 2(a). In the previous attempts, the liquid flow in the meniscus region and the vapor flow were neglected. The evaporation of liquid from the meniscus liquid-vapor interface mainly takes place in the thin-film region. This means that the corresponding injection of mass into the vapor space can induce recirculation of vapor over the interface due to strong asymmetry of the hydrodynamical problem in consideration, as shown in figure 3. The vapor flow along the liquid-vapor interface causes a shear stress in the liquid which can be as important as that produced by thermocapillarity.

For an incompressible fluid with constant vapor and liquid viscosities and densities depending on temperature, two-dimensional continuity and momentum equations for both vapor and liquid should be solved along with the energy equation. The mass, energy, and momentum energy balances should be satisfied at the liquid-vapor interface. Such two-dimensional problems, describing the evaporating meniscus in a narrow slot between two parallel walls, should include the evaporating microfilm model by Khrustalev and Faghri (ref. 11). A special control volume should be developed

in the numerical model containing the liquid evaporating microfilm. The liquid flow in this microfilm is driven mainly by the surface tension and the disjoining pressure.

$$\frac{dp_\ell}{ds} = -\sigma \frac{dK}{ds} + \frac{dp_d}{ds} - K \frac{d\sigma}{dT_\delta} \frac{dT_\delta}{ds} + \frac{d}{ds}(\rho_v^2 u_{v,\delta}^2) \left( \frac{1}{\rho_v} - \frac{1}{\rho_\ell} \right) \quad (1)$$

where  $K$  is the local interface curvature,  $p_d$  is the disjoining pressure and the last term is the kinetic reaction of the evaporating fluid pressure.

The temperature of the interface,  $T_\delta$ , is affected by the disjoining and capillary pressures, and also depends on the value of the interfacial resistance. The relation between the vapor pressure over the thin evaporating film,  $(p_{\text{sat}})_\delta$ , affected by the disjoining pressure, and the saturation pressure corresponding to  $T_\delta$ ,  $p_{\text{sat}}(T_\delta)$ , is given by the extended Kelvin equation (ref. 1). The liquid free surface saturation pressure,  $(p_{\text{sat}})_\delta$ , is different from the normal saturation pressure,  $p_{\text{sat}}(T_\delta)$ , and varies along the thin film (or  $s$ -coordinate). This is also due to the fact that  $T_\delta$  changes along  $s$ .

### Formation of thick liquid evaporating films

In the recent experiment by Belonogov and Kiseev (ref. 12), thick evaporating films ( $\delta > 1\mu\text{m}$ ) attached to the evaporating menisci of various liquids in a glass capillary tube were observed using a microcamera (figure 2(b)). The length of these thick films were several diameters of the capillary tube. This discovery can have a significant influence on the understanding of the evaporation of liquid from capillary tubes or porous structures. Explanation of the thick films existence by Belonogov and Kiseev (ref. 12) was consistent with that by Volintine and Wayner (ref. 13) where a mixture of two liquids was investigated with a surface tension gradient along the evaporating thick liquid film. Present efforts, however, are focused on evaporation of a pure liquid in a circular microchannel in the vicinity of a hemispherical liquid-vapor meniscus as shown in figure 2(b). It is assumed that thick liquid films can exist due to frictional vapor-liquid interaction at high rates of evaporation. A steady state mathematical model developed includes coupled vapor and liquid flows. The momentum conservation for viscous flow in a liquid film is expressed by the Stokes approximation.

$$\frac{1}{r} \frac{\partial}{\partial r} \left( r \frac{\partial w_\ell}{\partial r} \right) = \frac{1}{\mu_\ell} \frac{dp_\ell}{dz} \quad (2)$$

The boundary conditions are a no-slip condition at  $r = R$  and shear stresses at the liquid-vapor interface due to the frictional liquid-vapor interaction and surface tension gradient related to the interfacial temperature gradient along the channel.

$$w_\ell|_{r=R} = 0 \quad \frac{\partial w_\ell}{\partial r}|_{r=R-\delta} = \frac{1}{\mu_\ell} \left( -\frac{d\sigma}{dT} \frac{dT_\delta}{dz} - \mu_v \frac{\partial w_v}{\partial r}|_{r=R-\delta} \right) \quad (3)$$

Note that thick films inevitably end with the microfilm, therefore the microfilm model should be included in the thick-film problem. One essential feature of the thick film model should be mentioned here: due to the cylindrical geometry, the equation for the local curvature of the liquid-vapor interface contains the term directly related to the thickness of the liquid film. The pressure difference between the vapor and liquid phases is due to capillary and disjoining pressure effects.

$$p_v - p_\ell = \sigma \left\{ \frac{d^2 \delta}{dz^2} \left[ 1 + \left( \frac{d\delta}{dz} \right)^2 \right]^{-3/2} + \frac{1}{R - \delta} \cos(\text{atan} \frac{d\delta}{dz}) \right\} - p_d \quad (4)$$

The cosine term in the right-hand side of this equation is due to the second principal radius of the interfacial curvature for a cylindrical film. Therefore, the film surface curvature  $K$  increases with the liquid film thickness while the local heat flux through the liquid film decreases, which can make thick liquid films stable. It is possible that the existence of these thick films can directly affect thermal resistance of high heat flux evaporators in the zero-gravity environment. This problem is also important because it is closely related to the concept of the available capillary pressure developed by a porous structure and supporting fluid circulation in capillary-driven devices.

## CONCLUSION

High flux evaporation from liquid-vapor menisci can result in some additional effects compared to the low flux case such as recirculation zones in vapor, changes in effective heat transfer coefficients, and thick liquid films attached to the evaporating meniscus. Investigation of these effects is needed to better understand critical mechanisms in high heat flux capillary-driven devices.

## Nomenclature

$K$	curvature [1/m]
$p$	pressure [Pa]
$p_d$	disjoining pressure [Pa]
$s$	coordinate along the liquid-solid interface [m]
$T$	temperature [K]
$T_w$	temperature of the solid-liquid interface [K]
$u_{v,\delta}$	vapor blowing velocity [m/s]
$v$	velocity along the $y$ -coordinate [m/s]
$w$	velocity along the $z$ -coordinate [m/s]
$x, y, z$	coordinates [m]

### Greek symbols

$\delta$	film thickness [m]
$\mu$	dynamic viscosity [Pa-s]
$\rho$	density [kg/m <sup>3</sup> ]
$\sigma$	surface tension [N/m]

### Subscripts

$\ell$	liquid
$v$	vapor
$w$	wall
$\delta$	liquid film free surface

## References

1. Faghri, A., 1995, *Heat Pipe Science and Technology*, Taylor & Francis.
2. Faghri, A., and D. Khrustalev, D., 1995, "Advances in Modeling of Miniature Axially-Grooved Heat Pipes," *Proceedings of the Symposium on Thermal Science and Engineering in Honor of Chancellor Chang-Lin Tien*, Nov., 1995, pp. 391 – 398.
3. Plesch, D., Bier, W., Seidel, D., and Schubert, K., 1991, "Miniature Heat Pipes for Heat Removal from Microelectronic Circuits." In *Micromechanical Sensors, Actuators, and Systems* (Edited by D.Cho, R.Warrington, Jr., et al.), DCS-Vol. 32, pp. 303–313, ASME, New York.
4. Khrustalev, D., and Faghri, A., 1995a, "Thermal Characteristics of Conventional and Flat Miniature Axially-Grooved Heat Pipes," *ASME Journal of Heat Transfer*, Vol. 117, November, No. 4, pp. 1048-1054, 1996.
5. Khrustalev, D., and Faghri, A., 1996, "Enhanced Flat Miniature Axially-Grooved Heat Pipe," *ASME Journal of Heat Transfer*, Vol. 118, pp. 261–264.
6. Khrustalev, D., and Faghri, A., 1995, "Heat Transfer in the Inverted Meniscus Type Evaporator at High Heat Fluxes." *International Journal of Heat and Mass Transfer*, Vol. 38, No. 16, pp. 3091–3101, 1995.
7. Khrustalev, D., and Faghri, A., 1996, "Estimation of the Maximum Heat Flux in the Inverted Meniscus Type Evaporator of the Flat Miniature Heat Pipe," *International Journal of Heat and Mass Transfer*, Vol. 39, No. 9, pp. 1899-1909.
8. Kamotani, Y., 1978, "Evaporator Film Coefficients of Grooved Heat Pipes," *Proc. 3rd Int. Heat Pipe Conf.*, Palo Alto, pp. 128–130.
9. Holm, F.W., and Goplen, S.P., 1979, "Heat Transfer in the Meniscus Thin-Film Transition Region," *ASME J. Heat Transfer*, Vol. 101, No. 3, pp. 543–547.
10. Stephan, P.C., and Busse, C.A., 1992, "Analysis of the Heat Transfer Coefficient of Grooved Heat Pipe Evaporator Walls," *Int. J. Heat Mass Transfer*, Vol. 35, No. 2, pp. 383–391.
11. Khrustalev, D., and Faghri, A., 1995a, "Heat Transfer During Evaporation on Capillary-Grooved Structures of Heat Pipes." *ASME Journal of Heat Transfer*, Vol. 117, August, No. 3, pp. 740 – 747.
12. Belonogov, A.G., and Kiseev, V.M., 1995, "Evaporation Problems in Wetting Film Theory," *Proceedings of the 30th National Heat Transfer Conference (Portland)*, AIChE Symposium Series, Vol. 91, pp. 333–336.
13. Volintine, B.G., and Wayner, P.C., Jr., 1986, "Fluid Flow and Evaporation in an Ultra-Thin Film of a Binary Mixture," in *Thin Liquid Film Phenomena*, AIChE Symposium Series, Vol. 82, No. 252, pp. 157 – 166.

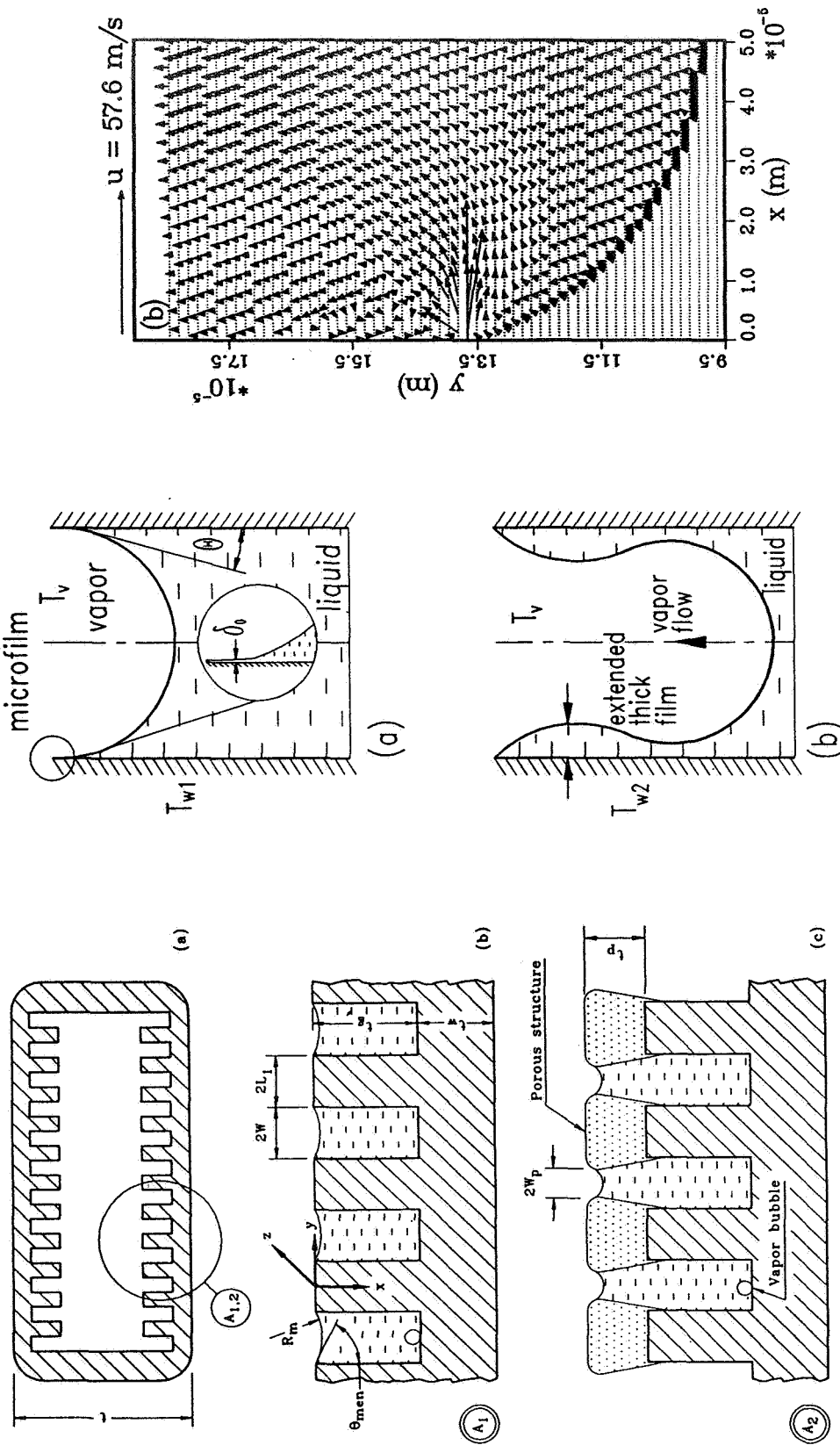


Fig. 1: Cross sections of high heat flux heat pipes: (a) flat miniature heat pipe, (b) plain capillary grooves, and (c) grooves with porous coating

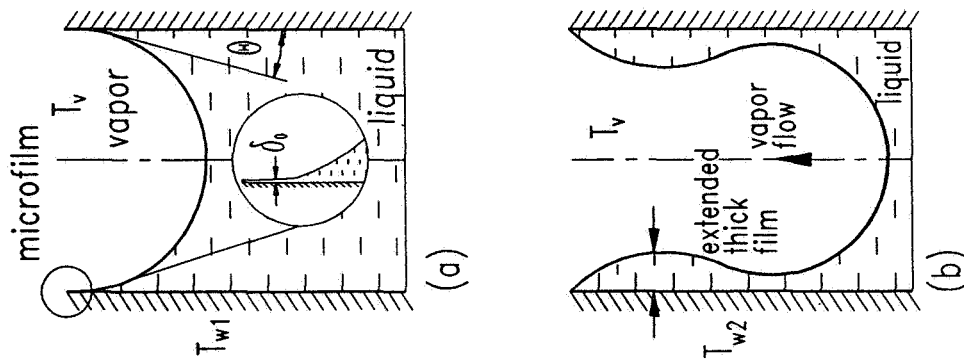


Fig. 2: Evaporation of liquid from cylindrical pores: (a) at low evaporation rates, and (b) at high evaporation rates

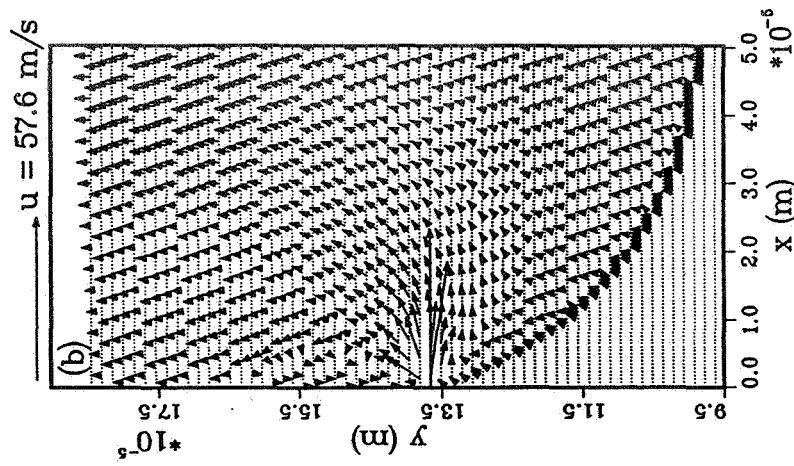


Fig. 3: Vapor flow over evaporating liquid-vapor meniscus (water,  $T_w - T_v = 10 \text{ K}$ )



# EXPERIMENTAL INVESTIGATION OF POOL BOILING HEAT TRANSFER ENHANCEMENT IN MICROGRAVITY IN THE PRESENCE OF ELECTRIC FIELDS

Cila Herman

Department of Mechanical Engineering  
The Johns Hopkins University, Baltimore, MD 21218

## 1. INTRODUCTION

Boiling is an effective mode of heat transfer since high heat flux levels are possible driven by relatively small temperature differences. The high heat transfer coefficients associated with boiling have made the use of these processes increasingly attractive to aerospace engineering. Applications of this type include compact evaporators in the thermal control of aircraft avionics and spacecraft environments, heat pipes, and use of boiling to cool electronic equipment. In spite of its efficiency, cooling based on liquid-vapor phase change processes has not yet found wide application in aerospace engineering due to specific problems associated with the low gravity environment.

After a heated surface has reached the superheat required for the initiation of nucleate boiling, bubbles will start forming at nucleation sites along the solid interface by evaporation of the liquid. Bubbles in contact with the wall will continue growing by this mechanism until they detach. In terrestrial conditions, bubble detachment is determined by the competition between body forces (e.g. buoyancy) and surface tension forces that act to anchor the bubble along the three phase contact line. For a given body force potential and a balance of tensions along the three phase contact line, bubbles must reach a critical size before the body force can cause them to detach from the wall. In a low gravity environment the critical bubble size for detachment is much larger than under terrestrial conditions, since buoyancy is a less effective means of bubble removal (*Zell (1991), Ervin et al. (1992)*).

Active techniques of heat transfer enhancement in single phase and phase change processes by utilizing electric fields have been the subject of intensive research during recent years. The field of electrohydrodynamics (EHD) deals with the interactions between electric fields, flow fields and temperature fields. Previous studies (*Yabe et al. (1995)*) indicate that in terrestrial applications nucleate boiling heat transfer can be increased by a factor of 50 as compared to values obtained for the same system without electric fields. Imposing an external electric field holds the promise to improve pool boiling heat transfer in low gravity, since a phase separation force other than gravity is introduced. The goal of our research is to experimentally investigate the potential of EHD and the mechanisms responsible for EHD heat transfer enhancement in boiling in low gravity conditions.

## 2. BACKGROUND

### 2.1 Boiling in low gravity environment

Numerous investigators have studied transient nucleate pool boiling both in earth gravity and microgravity. *Ervin et al. (1992)* used high-speed cameras to record two orthogonal views across and through the heating surface, and analyzed boiling spread across the heater surface. The heater surface was relatively large compared to the bubble dimensions at the onset of boiling and their experiments allowed the observation of six distinct categories of bubble dynamics as function of gravity for different surface orientations. In the absence of buoyancy, the initially stagnant fluid remains motionless while heated up to the onset of boiling. The high speed recordings of the boiling process indicate that bubbles grow larger under reduced gravity conditions, they begin to coalesce to a greater extent thus forming groups of larger bubbles (*Lee (1992)*). Coalescence increases with time and patterns are formed by small bubbles. The bubbles also increase in size at a certain distance from the heater (*Zell and Straub (1985), Zell (1991)*).

### 2.2 Influence of electric fields on heat transfer in boiling

A large amount of theoretical and experimental research has been done on EHD enhanced pool boiling in terrestrial conditions, that has potential applications in cryogenic engineering and heat exchangers (*Karayiannis et al. (1989), Ohadi (1991), Singh et al. (1993)* and others ...). *Grassi and DiMarco (1992)* reviewed the effects of gravity and electric fields on pool boiling. They showed that the improved heat transfer performance is commonly related to the change in the boiling curve, as illustrated in Figure 1 by the dashed lines. As a result of the

superposition of the electric field, the natural convection and peak heat fluxes are increased, transition boiling can be suppressed, resulting in a more monotonous increase of the boiling curve. These authors emphasize that tests of EHD enhanced pool boiling in reduced gravity can also improve the comprehension of the basic underlying physics of boiling. To our knowledge, the effects of electric fields on boiling in microgravity have not yet been investigated experimentally.

The magnitude of the body force acting on the fluid in the presence of an electric field,  $\vec{F}_e$  is obtained as

$$\vec{F}_e = \rho e \vec{E} - \frac{1}{2} E^2 \nabla \epsilon + \frac{1}{2} \nabla \left( E^2 \rho \left( \frac{\partial \epsilon}{\partial \rho} \right) \right)$$

In this equation  $\rho e$  is the electric charge density, obtained as the sum of the charges of positive and negative ions and the electrons in a unit volume,  $\epsilon$  is the dielectric constant of the fluid and  $E$  the electric field strength. The first term on the right hand side of the equation represents the Coulomb force acting on the net charges, the second term describes the force caused by the spatial change of the dielectric constant  $\epsilon$ , and the third component, called electrostriction, is the force caused by the inhomogeneity of the electric field strength.

To account for the influence of electric fields on the transport of momentum and heat, the body force term  $\vec{F}_e$  has to be added to the external force term in the Navier-Stokes equations. Thus, the sets of equations describing EHD phenomena consist of the continuity, momentum and energy equations accounting for flow and thermal phenomena, and the Maxwell equations (Yabe *et al.*, 1995) that describe the influence of the electric field. The complexity of EHD phenomena is partly caused by the coupling of the governing equations. Examples of such coupling are the presence of the electric body force term in the Navier-Stokes equation as well as the presence of the fluid velocity in the term describing the convective component of the electric current.

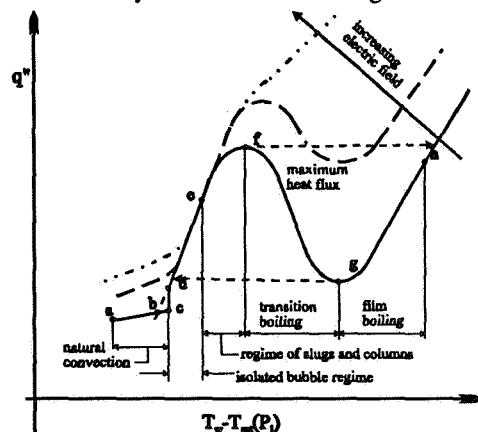


Figure 1. Pool boiling curve and changes due to the influence of the electric field

The presence of bubbles significantly increases the complexity of EHD phenomena, and causes dramatic changes of the boiling cycle, as discussed earlier (Figure 1). Several basic mechanisms involved in the boiling process, such as bubble growth on the wall and detachment, electric charging of bubbles, bubble buoyancy and rise velocity as well as the liquid vapor interface stability are expected to be influenced by the presence of electric forces. The process of EHD enhanced boiling in terrestrial conditions was analyzed experimentally using high-speed cinematography as well as by numerical simulation. One component of the force acting on a bubble in the presence of electric fields caused by the Maxwell stress is perpendicular to the surface and it presses the bubble against it. The radial component of the Maxwell stress parallel to the heated surface causes the motion of the bubble over the surface, characteristic for the presence of electric field.

### 3. METHOD OF STUDY

#### 3.1 Visualization of temperature fields using real-time holographic interferometry

Holographic interferometry was introduced into heat transfer measurements some 30 years ago (Hauf and Grigull (1970)). It allows the visualization of complex steady and unsteady, two or three dimensional temperature fields (Herman, Mewes, Mayinger, (1992)) without disturbing the investigated physical process. In the past, some attempts were made to implement it in the investigation of phase change processes, such as boiling, melting and solidification of ice, as well as in sublimation processes. Beer *et al.* (1977), Nordmann (1980) and Mayinger and Chen (1986) investigated nucleate pool boiling using holographic interferometry combined with high-speed cinematography. The fringe patterns recorded in their experiments allowed the reconstruction of temperature fields around the bubbles, the analysis of bubble dynamics, and measurements of local heat transfer along the liquid-vapor interface. Due to the complexity of these highly unsteady heat transfer processes and the limitations of the equipment and techniques used in the evaluation of the visualization images, relatively little quantitative information was obtained from those studies. Although the first results of interferometric experiments were promising, measurements of boiling heat transfer by means of holographic interferometry were later abandoned, and nowadays bubble shape, size and frequency are commonly measured.

Holographic interferometry combined with high-speed cinematography, the measurement technique chosen for our study, has not yet been applied to analyze EHD processes in boiling and we expect that our research will yield a new quantitative and qualitative understanding of the phenomenon. Details of real-time holographic interferometry will not be discussed in this paper and the interested reader is referred to specialized literature (Herman, Mewes, Mayinger (1992)).

### 3.2 Thermochromatic liquid crystals

Thermochromatic liquid crystals respond to changes of temperature by changing color. When the heat transfer surface is coated with a layer of such crystals, the local surface temperature can be visualized and measured. This methodology was successfully applied to determine surface temperatures during the process of boiling by Kenning (1992). In our laboratory the same technique was implemented to measure local surface temperatures during boiling. The visualized temperature fields were recorded on photographic film and the colors converted into temperatures by digital image processing techniques. Simultaneously, bubble distributions in the liquid phase were recorded with a second camera. Typical temperature patterns along the heated surface, reconstructed temperature fields as well as bubble distributions, recorded during our preliminary experiments, are shown in Figure 2. This approach will be used in our experimental study of EHD phenomena simultaneously with holographic interferometry.

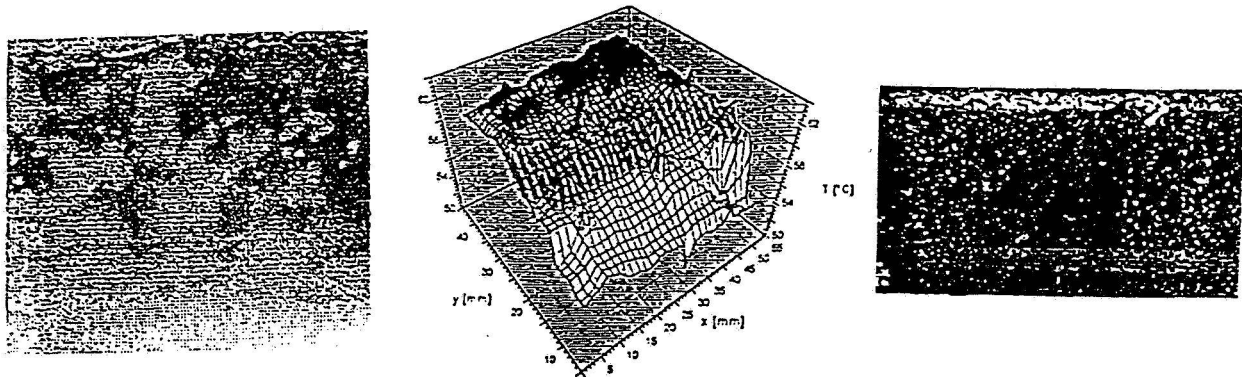


Figure 2. Temperature patterns along the heated surface, reconstructed temperature fields as well as bubble distribution in the liquid

### 3.3 Digital image processing

The availability of powerful computers and digital image processing techniques nowadays opens new possibilities in the study of high-speed heat transfer processes during boiling. A method for analyzing oscillating temperature fields in a sequence of images in communicating channels has been developed in our laboratory (Herman (1992)). By superimposing images after data reduction, the temporal development of an event can be reconstructed. This approach will be implemented to our studies of boiling.

## 4. EXPERIMENTS

We plan to conduct a systematic experimental investigation of pool boiling in microgravity to gain insight into the influence of electric fields on the boiling process and to perform a quantitative study of heat transfer enhancement in microgravity. We plan to simultaneously visualize and measure the temperature of the heated surface by coating it with thermochromatic liquid crystals and the temperature distribution in the liquid by holographic interferometry. A flat heater surface will be used in the experiments, because it resembles practical applications and it is convenient from the standpoint of optical visualization. This surface will simultaneously serve as one of the electrodes.

The experiments will be conducted in three phases characterized by increasing complexity of the boiling surface geometry. (i) In the first phase of our study the influence of the electric field on the behavior of a single bubble will be investigated. More details about these experiments are given in Section 4.1. (ii) In the second phase, a special heater surface allowing the forming of preferential nucleation sites at specified locations will be designed.

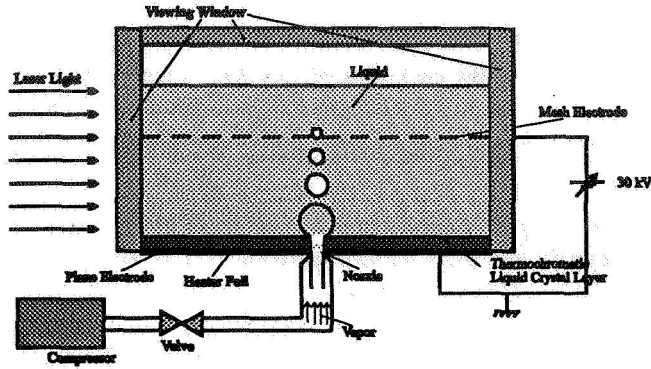


Figure 3. Schematic of the experimental setup used to study the behavior of a single bubble

Bubble generation on a heated surface in experimental studies corresponds well to general technical applications. The conditions in the thermal boundary layer along the heated surface and along the surface of the bubble are characterized by high temperature gradients and are difficult to evaluate and control. The exact location and time of bubble formation on a heated surface is generally not known and accurate alignment and focusing of the optical measurement equipment is difficult. As described by Webb (1994), by puncturing the foil glued to a grooved surface at specified locations, reentrant cavities acting

as preferential nucleation sites are formed on the heater. The surface with a controlled number of nucleation sites allows the study of boiling under more realistic conditions than nozzle injection and this approach was selected for the second phase of the research. The presence of a limited number of bubbles in the vessel allows the analysis of the interaction of bubbles with each other and the thermal boundary layer. (iii) In the third phase of the experimental research, smooth as well as enhanced boiling surfaces will be used. Since interferometric measurements are not possible when several bubbles are aligned along the path of the light beam, in the third phase data on bubble size, distribution and frequency can be obtained from high-speed visualization experiments.

#### 4.1 Behavior of a single bubble

In the first series of experiments the influence of the electric field on a single bubble will be investigated. Pool boiling is simulated by injecting a single bubble through a nozzle into the subcooled liquid (heater off) or into the thermal boundary layer developed along the flat heater surface, as illustrated in Figure 3. Injection of individual bubbles into the liquid has been proven to be a technique suitable to simulate a physical situation similar to that in subcooled nucleate boiling, as discussed in several studies (Nordmann (1980), Mayinger and Chen, (1986), Ogata and Yabe (1993)). The advantage of this approach is that the conditions in the vicinity of the growing bubble can be controlled by the experimenter. Conversely to the situation on the heated surface, the conditions in the vicinity of the developing bubble are generally steady. The bubble grows in a uniformly subcooled liquid. Condensation begins immediately and it takes place over the whole perimeter of the bubble. Bubble growth will be possible as long as the amount of vapor introduced into the bubble through the nozzle is larger than the amount of vapor condensing on the bubble surface. When there is no superheated boundary layer present along the solid surface (heater off), Marangoni convection will be absent. The accurate location of bubble formation is known and thus the optical equipment can be aligned and focused accurately, which is an essential requirement for precision measurements of bubble shape, size and deformation, as well as visualization by holographic interferometry. The size of the bubble and the frequency of bubble departure can be controlled by suitable selection of nozzle diameter and mass flow rate of vapor. In this approach effects due to the presence of the electric field can be separated from effects caused by the temperature gradients in the thermal boundary layer initially, and the influence of the thermal boundary layer can be included after activating the heater at a later stage of the research. All these features of the experimental setup offer the advantage of yielding clear and unambiguous results depending on a limited number of controlled process parameters.

#### 4.2 Experimental setup

The cross section of the experimental setup to be used in the first phase of the research is presented in Figure 3. Vapor is supplied to the bubble through the central cylinder of a coaxial nozzle. Vapor is also supplied to the outer annulus to prevent the cooling down of vapor when passing through the injection nozzle. The plane metal surface around the nozzle serves as one of the electrodes, and it is equipped with an electric heater that provides heating to the electrode, when required. The second brass mesh electrode is positioned above the heated surface and it is parallel to the first one. Later during the course of the project, the influence of the form of electrodes and the direction and form of electric field lines on the bubble motion and heat transfer enhancement will be

investigated. Apart from the (i) parallel mesh wire electrode, we will use (ii) one and (iii) more cylindrical electrodes in these experiments as well.

#### 4.3 Measurements

The temperature fields in the thermal boundary layer in the vicinity of the heated surface and around the growing bubble will be analyzed using holographic interferometry combined with high speed cinematography. Since typical time scales for boiling are of the order of ms, we will use a rotating prism high-speed 16 mm film camera that can achieve recording rates up to 6000 frames per second. This approach was successfully implemented to measure local Nusselt numbers along the perimeter of the growing bubble as function of position and time by Nordmann (1980). We expect to be able to achieve similar or better accuracy, since Nordmann's evaluations were conducted manually. Local heat transfer along a heated wall and heat transfer enhancement will also be measured.

Investigations of bubble behavior in the vicinity of the heated surface by Ogata and Yabe (1993) indicated that bubbles were pressed against the heated electrode and moved violently around it, when either positive or negative voltage was applied. Such a behavior can initiate a whole range of interactions with the thermal boundary layer. The increased momentum transfer in the boundary layer due to bubble motion can yield an enhancement of heat transfer as result of the "massaging" of the thermal boundary layer, similar to that observed in barbotage. If the bubbles move close enough to the surface, heat transfer through the microlayer may be an important mechanism of enhancement. The bubbles "touching" the heater may generate additional nucleation sites and thus also contribute to the enhancement of heat transfer. These questions will be addressed in our study. The visualization of surface temperatures by thermochromatic liquid crystals will allow us to quantify these effects. In order to photograph the heated surface, the cover plate of the test section is manufactured of glass and the mesh electrode has to be semi-transparent as well.

We propose to vary the heater surface orientation from downward to upward. A properly applied electric field with downward facing heater geometry could allow one to obtain a region in the boiling liquid where the electric force approximately balances the gravity force. This experiment may answer the question regarding the possibility to achieve conditions of low gravity in earth-based experiments.

Precision measurements of bubble size during growth and after detachment, visualization of the local flow structure in the wake region by holographic interferometry, and the impact of the bubble on the thermal boundary layer in this simple and idealized situation will yield both qualitative insight and quantitative data.

#### 4.4 Selection of the working fluid

Different substances, gases and liquids, as well as combinations of fluids have been used as working fluids in electrohydrodynamic studies. Dielectric liquids are required in electronic cooling applications. The commonly utilized refrigerants are suitable for our experiments, since their boiling point is achieved at relatively low temperatures, and thus power requirements on the heater are not excessive. An important property of a liquid that determines the magnitude of heat transfer enhancement in EHD applications is the relaxation time of electric charges,  $t_c$ , defined as  $t_c = \epsilon / \sigma_e$ . In this definition,  $\epsilon$  is the dielectric constant of the fluid and  $\sigma_e$  denotes its electrical conductivity. The relaxation time is the measure of the time period required to reach steady state in an electric field. The ratio of  $t_{EHD}$ , the time scale typical for the investigated EHD phenomenon, and the relaxation time determines if the fluid can be assumed to be a dielectric (for  $t_{EHD} \ll t_c$ ) or an electrically conducting (for  $t_{EHD} \gg t_c$ ) substance. The EHD boiling heat transfer enhancement effect increases with increasing electrical conductivity of the liquid, as discussed by Yabe *et al.* (1995). The effect is most pronounced when the relaxation time of electric charges in the liquid is less than the characteristic time for bubble detachment from the surface, which is known to be of the order of milliseconds. This criterion is satisfied by HCFC 123, mixtures of CFC 11 and ethanol, as well as other CFC alternatives. The orders of magnitude of the relaxation times are 1 s for insulating liquids, such as CFCs, 1ms for low conductivity liquids (HCFCs and HFCs) and 1  $\mu$  s for electrically conductive liquids, respectively. Apart from selecting one from the class of "semi-conducting" liquids, the final choice of the working fluid will also depend on the refractive index value, which has to be suitable for interferometric measurements.

## 5. CONCLUDING REMARKS

Heat transfer rates achieved in boiling under normal gravity and microgravity, as well as with and without electric fields, will be compared. System pressure will be varied as one of the parameters of the experiment. One of the expected results of this study will be the better understanding of the basic mechanisms of boiling and the dominating forces by separating the gravity dependent and gravity independent effects. Earlier studies of bubble growth, bubble dynamics, departure diameter and frequency under imposed electric fields of different intensities indicate that when high field intensities are reached, bubbles become smaller and move more violently around the heat transfer surface. This observation leads to the question if control of bubble diameter at detachment may be achieved in pool boiling under microgravity by controlling the intensity of the applied electric field. This hypothesis can be verified through our study. Another important question that remains to be answered is the possibility of the existence of steady state boiling and nucleate boiling under microgravity, as strong electric fields could prevent the coalescence of bubbles in low gravity conditions as well.

## 6. ACKNOWLEDGMENTS

This research is supported by the NASA research grant NAG3-1815.

The author gratefully acknowledges the motivating discussions with Dr. Ralph Webb and Dr. George Dulikravich.

## 7. REFERENCES

- Beer, H., Burow, P., Best, R., 1977, Bubble Growth, Bubble Dynamics and Heat Transfer in Nucleate Boiling, Viewed with a Laser Interferometer, in Heat transfer in Boiling, eds. E. Hahne and U. Grigull, Hemisphere Publishing Corp., Washington, pp. 21-52.
- Ervin, J. S., Merte, H., JR., Keller, R. B., Kirk, K., 1992, Transient Pool Boiling in Microgravity, Int. J. Heat Mass Transfer, Vol. 35, No. 3, pp. 659-674.
- Grassi, W., Di Marco, P., 1992, Gravity and Electric Field Effects on Pool Boiling Heat Transfer, Proc. VIIIth European Symp. on Materials and Fluid Sciences in Microgravity, Brussels, ESA SP-333, pp. 783-788.
- Hauf, W., Grigull, U., 1970, Optical Methods in Heat Transfer, in Advances in Heat Transfer, Vol. 6, Academic Press Inc., New York.
- Herman, C., 1992, Heat Transfer in Single and Communicating Grooved Channels (in German), Dissertation.
- Herman, C. V., Mewes, D., Mayinger, F., 1992, Optical Techniques in Transport Phenomena, Advances in Transport Processes VIII, Editors A. S. Mujumdar, R. A. Mashelkar, Elsevier Science Publishers, Amsterdam and New York, pp. 1-58.
- Karayiannis, T.G., Collins M.W., Allen P.H.G., 1989, Electrohydrodynamic Enhancement of Nucleate Boiling Heat Transfer in Heat Exchangers, J. of Heat Technology, Vol. 7, No.2, pp. 263-274
- Kenning, D. B. R., 1992, Wall Temperature Patterns in Nucleate Boiling, Int. J. Heat Mass Transfer, Vol. 35, No. 1, pp. 73-86.
- Lee, D. J., 1992, Bubble Departure Radius under Microgravity, Chem. Eng. Comm., Vol. 117, pp. 175-189.
- Mayinger, F., Chen, Y. M., 1986, Heat Transfer at the Phase Interface of Condensing Bubbles, Proc. 8 Int. Heat Transfer Conf., San Francisco, California, USA, pp. 1913-1918.
- Nordmann, Dieter, 1980, Temperatur, Druck und Wärmetransport in der Umgebung kondensierender Blasen, Dissertation, Technische Universität München.
- Ogata, J., Yabe, A., 1993, Augmentation of Boiling Heat Transfer by Utilizing the EHD Effect - EHD Behaviour of Boiling Bubbles and Heat Transfer Characteristics, Int. J. Heat Mass Transfer, Vol. 36, No. 3, pp. 783-791.
- Ohadi, M. M., 1991, Heat Transfer Enhancement in Heat Exchangers, ASHRAE Journal, Dec., pp. 42-50.
- Singh, A., Kumar, A., Dessiatoun, S., Faani, M. A., Ohadi, M. M., Ansari, A. I., 1993, Compound EHD-Enhanced Pool Boiling of R-123 in a Liquid-to-Refrigerant Heat Exchanger, ASME Paper - 93-WA/HT-40.
- Yabe, A., Mori, Y. and Hijikata, K., 1995, Active Heat Transfer Enhancement by Utilizing Electric Fields, In : Annual Review of Heat Transfer, Vol. 7, Begell House Publishing.
- Zell, M., 1991, Untersuchung des Siedevorgangs unter reduzierter Schwerkraft (Investigations of boiling under reduced gravity), Dissertation, Technische Universität München, Germany.
- Zell, M., Straub J., 1985, Experimentelle Untersuchung des Wärmeübergangs und seiner Transportmechanismen unter reduzierter Schwerkraft, Jahrbuch 1985 der Technischen Universität München, Germany.
- Webb, R. L., 1994, Principles of Enhanced Heat Transfer, John Wiley & Sons, New York.



# MARANGONI EFFECTS IN THE BOILING OF BINARY FLUID MIXTURES

Sayeed Ahmed\*, Van P. Carey\* and Brian Motil\*\*

\*Department of Mechanical Engineering; University of California; Berkeley, California 94720

\*\*NASA Lewis Research Center; Cleveland, Ohio 44135

## ABSTRACT

Results of very recent experimental studies indicate that during nucleate boiling in some binary mixtures, Marangoni effects augment the gravity driven flow of liquid towards the heated surface. With gravity present, it is impossible to separate the two effects. The reduced gravity environment gives an unique opportunity to explore the role of Marangoni effects on the boiling mechanisms free of gravitational body forces that obscure the role of such effects. However, recent experimental results suggest that under reduced gravity conditions, Marangoni effects is the dominant mechanism of vapor-liquid exchange at the surface for some binary mixture.

To further explore such effects, experiments have been conducted with water/2-propanol mixtures at three different concentrations under normal gravity with different orientations of the heater surface and under reduced gravity aboard the DC-9 aircraft at NASA Lewis Research Center. The system pressure was sub atmospheric ( $\sim 8$  kPa at  $1g_n$ ) and the bulk liquid temperature varied from low subcooling to near saturation. The molar concentrations of 2-propanol tested were 0.015, 0.025 and 0.1. Boiling curves were obtained both for high gravity ( $\sim 2g_n$ ) and reduced gravity ( $\sim 0.1g_n$ ). For each concentration of 2-propanol, the critical heat flux has been determined in the flight experiments only for reduced gravity conditions. Comparison of boiling curves and CHF obtained under  $1-g_n$  and reduced gravity indicates that boiling mechanism in this mixtures is nearly independent of gravity. The results also indicate that the Marangoni mechanism is strong enough in these mixtures to sustain the boiling under reduced gravity conditions.

## INTRODUCTION

In many technological applications, vaporization of a working fluid is critically important. It facilitates the heat input in Rankine power systems, the cooling effect in vapor compression heat pumps and high heat flux removal in thermal control applications. When the working fluid is a pure substance, as is often the case, the characteristics of the vaporization process can be predicted with reasonable accuracy using the results of extensive research on boiling of pure liquids over the past 60 years. Recent efforts to improve component or system performance have lead some developers to consider the use of binary working fluids. In general, researchers have found that some binary mixture working fluids offer the potential for improved thermodynamic efficiency, or superior heat transfer performance. The advantages of using binary mixture working fluids in heat pump systems have been explored by several investigators (see, for instance, Domanski (ref. 1)). This type of investigation invariably points out the fact that the current limited capability to accurately predict the transport processes for boiling of binary mixtures is a major obstacle to the development of heat pump systems using binary working fluids. Another perspective on the significance of Marangoni effects during binary mixture boiling can be obtained by considering two-phase thermal management systems for spacecraft. Systems of this type using pure working fluids have been extensively studied by Degroff et al.(ref. 2) and others.

Results of some very recent studies suggest that it may be possible to enhance the ability of the system to resist dryout and/or the onset of film boiling by using a binary coolant than a pure working fluid. McGillis and Carey (ref. 3) experimentally examined the pool boiling of mixtures of water and alcohol at low pressure on a small, 1.3 cm square heated surface. Boiling curves and the critical heat flux were determined for several different alcohol-water mixtures at a number of pressure and concentration combinations. Methanol/water, 2-propanol/water and ethylene glycol/water mixtures were tested. These experiments were done in a closed thermosiphon system so that concentrations in the liquid pool can be accurately maintained at a predetermined level throughout the test. At low concentrations of 2-propanol in water, these investigators have found that the critical heat flux (CHF) may be enhanced above that for either of the pure fluid components under comparable conditions. Interestingly, at low concentrations of ethylene glycol in water, the critical heat flux is observed to be lower than that of water. McGillis and Carey (ref. 3) found that the variation of the critical heat flux with concentration correlates strongly with the surface tension gradient or the Marangoni effect. 2-propanol/water is a positive mixture where the more volatile component has a lower surface tension than the surface tension of the less volatile component and the surface tension

gradients arising from the preferential evaporation of the more volatile component at the heated surface act to enhance the liquid motion towards the surface. Conversely, ethylene glycol/water is a negative mixture where the surface tension gradients act to decrease the liquid motion towards the heated surface. Beginning with the well-known Zuber correlation for the critical heat flux for an upward-facing flat heated surface, these investigators replaced the restoring effect of buoyancy in the Zuber correlation with the combined effect of buoyancy and surface tension gradients. McGillis and Carey (ref. 3) found that by adjusting a constant in the correlation, they could match critical heat flux data for both their water alcohol mixtures as well as the ethanol and water data of Reddy and Lienhard (ref. 4). Agreement is quite good over the entire range of concentrations tested, and this model correlates these data better than any other currently available schemes.

The important point here is that for certain binary fluid mixtures, there is abundant evidence that surface tension gradients resulting from concentration differences act to enhance the fluid motion towards the heated surface. For some mixtures the effect on the critical heat flux is so great that this effect appears to be substantially stronger than the normal buoyancy effect at 1- $g_n$ . It is difficult, however, to fully gauge the strength of the Marangoni effect because it is always combined with buoyancy. By conducting binary mixture nucleate boiling studies under reduced gravity conditions, the buoyancy effect would be removed, and the ability of Marangoni forces to induce liquid motion towards the surface would be directly observable. In addition, reduced gravity binary boiling experiments may also pave the way for the use of binary coolants in spacecraft thermal control applications. The present study is intended to investigate the Marangoni mechanism in the boiling of binary mixtures in a reduced gravity environment. Boiling of 2-propanol and water mixtures at three different concentrations have been investigated in a DC-9 reduced gravity aircraft which provides 20-25 seconds of reduced gravity. The gravity level attained by the aircraft is about 0.01 $g_n$ .

Siegel and Usiskin (ref. 5) conducted the first reduced gravity boiling experiment in a 0.7-second drop tower. Siegel (ref. 6) published a comprehensive summary of the early studies up to the mid-1960s. Recently, the effects of variable gravity on boiling heat transfer were summarized by Merte (ref. 7). Straub et al. (ref. 8) conducted microgravity boiling experiments for more than 15 years. Most of the studies conducted under reduced gravity or variable gravity were for pure liquids. However, Abe et al. (ref. 9) recently conducted pool boiling experiments with water-ethanol mixtures under microgravity conditions. These investigators found that the heat transfer was enhanced under microgravity and they ascribed this enhancement to the Marangoni flow due to surface tension gradient.

## SYMBOLS

$^{\circ}\text{C}$	Degree centigrade	CHF	Critical heat flux	$g$	Instantaneous Acceleration
$g_n$	Normal gravitational acceleration	$P$	Pressure	$q''$	Heat Flux
$t$	Time	$X_p$	Molar concentration of 2-propanol		

## EXPERIMENTAL SETUP AND PROCEDURE

The test section used in our experiments is a 12" long square (3") channel made of stainless steel. The top plate and the two side plates are 1/4" thick and the bottom plate is 1/2" thick. The bottom plate has a rectangular cut-out to accommodate replaceable heated surface element. The heater element is made of oxygen-free, high purity copper to ensure that the thermophysical properties of the element are defined to high accuracy. The copper heating element is silver soldered to the stainless steel holder. The contact area between the stainless steel and the copper is minimized to avoid heat loss. The heat loss is computed from a simple model and it is less than 5% of the heat input. Electric cartridge heaters fitted into the bottom of the copper element provide the heat input which flows along the bar of circular cross section to the flush end exposed to the flow in the test section. The flush end of the copper heater element is a 1.2 cm diameter circular finger. Miniature thermocouples installed along the copper bar allow measurement of the temperature gradient in the bar, and hence the heat flux to the surface exposed to the flow. Lateral side walls of the test section have rectangular windows made of transparent polycarbonate for flow visualization. The system pump delivers fluid to the inlet header of the test section. A porous plate in the inlet header helps provide even flow distribution in the test section. Flow exiting the test section is piped to the system condenser. A Validyne pressure transducer installed in the test section is used to monitor the pressure in the system. During reduced gravity flight test, a high speed video camera was mounted in front of the window of the test section for visual recording of the boiling process. Figure 1 shows the layout of the experimental hardware.



The experimental setup consists of two flow circuits; one for the binary mixture and the other for the coolant flow in the condenser. The components of the binary mixture circuit are the test section, a pump and the tubes in the condenser. The heater element at the bottom of the test section heats up the binary mixture. The purpose of the pump is to maintain a constant flow in the test section and the condenser. The intention of this design is to provide a weak bulk convective motion that will not affect the nucleate boiling process on the heated surface, but will carry vapor bubbles that leave the surface during the boiling process to the condenser. The objective is to sustain a steady nucleate boiling process while maintaining constant pressure and bulk concentration in the test section. The coolant circuit consists of coolant pump, a coolant tank and the shell of the condenser. A support structure for the test system is built by using 13/16" aluminum Unistrut bar. The test system along with its support structure is mounted in one of two Learjet racks provided by NASA. The computer, data acquisition system and all the electrical components are mounted on another Learjet rack. The thermocouple and pressure data are monitored using a PC-based data acquisition system.

The binary mixture circuit is evacuated by a vacuum pump. The fill port is opened and the binary mixture flows from the charging tank to fill the system. The pressure of the system can be lowered by bleeding vapor from the evacuation tank or can be increased by filling the system with more liquid mixture. When pressure becomes steady, the pumps are turned on. Electrical power is supplied to the cartridge heater and the heat flux to the binary mixture is controlled by a variac. The heat flux is obtained from a least-square fit of the five thermocouples embedded along the heater element and the surface temperature is computed by extrapolation. The experiment is continued until the system reaches the critical heat flux. 1-g<sub>n</sub> experiments were conducted at two different heater surface orientations, upward facing and downward facing. At first, the system pressure and temperature are stabilized for the upward facing heater surface and the experiment is conducted for this orientation. At the end of the experiment, there is a cool down period when the system pressure and temperature are re-stabilized. At this point, the rack is oriented to conduct experiments for the downward facing configuration. During the flight experiment, pressure was maintained constant in each flight experiment. At the beginning of every other parabola, the heat flux was set and the temperature profile in the heater element was monitored and recorded. When the flight experiences a transition from 2g<sub>n</sub> to reduced gravity, the gravitational part of the heat flux is expected to approach zero while the heat flux due to Marangoni effect becomes the dominant mechanism to sustain nucleate boiling. Therefore the system experienced a transient heat transfer mode and restabilized at a new heat flux value which can be monitored from the thermocouple readings. The normal gravity experiments for the boiling of binary mixture were performed in the Multiphase Transport Laboratory at the University of California at Berkeley and the reduced and elevated gravity experiments were performed in the DC-9 reduced gravity aircraft of NASA Lewis Research Center.

## RESULTS AND DISCUSSIONS

Figure 2 shows the boiling curve for 2-propanol/water binary mixture at two different orientations of the heater surface; upward facing and downward facing. The molar concentration of 2-propanol in the mixture is 0.015. Also shown in the plot are the critical heat fluxes for water at same orientation and same system pressure. It is evident from the plot that the critical heat flux of 2-propanol/water ( $X_p=0.015$ ) is greater than that of pure water under the same condition by a factor of three at same system pressure and same orientation. Another interesting point to note is that the critical heat flux of 2-propanol/water at downward facing heater configuration is substantially more than that of pure water at upward facing configuration. The trends of this normal gravity curve clearly suggests that there is additional mechanism in the boiling of 2-propanol/water mixture which is responsible for this higher critical heat flux.

The transient wall superheat and the g-level during an experimental cycle in DC-9 reduced gravity flight are shown in figure 3. The molar concentration of 2-propanol in water was 0.015 and the heat flux increased from 89 W/cm<sup>2</sup> to 98 W/cm<sup>2</sup> during this experimental cycle. Although the DC-9 aircraft is used for reduced gravity environment for 20-25 second, there is an elevated gravity (1.8g<sub>n</sub>~2.0g<sub>n</sub>) part during each parabolic maneuver which also lasts 20-25 seconds. During this change in gravity level, the hydrostatic pressure of the system changes by 2 kPa/1g<sub>n</sub> and causes a shift in the saturation temperature of the binary mixture by 4 - 5°C/1g<sub>n</sub>. The wall superheat changes during this change in gravity level but reaches a steady state value within 1°C during both elevated gravity period and reduced gravity period. Therefore, the data represented in the boiling curves are essentially steady state value for the system.

The temperature profiles along the heater were studied in detail to ensure the steady state condition of the system. Figures 4 and 5 show the transient temperature profile along the copper heater element obtained from five thermocouples embedded in the element for the same condition as in figure 3. The transient temperature profile during

low g to high g transition is shown in figure 4 where the system reaches steady state at a higher gravity level (i.e. higher saturation temperature) by establishing a higher wall temperature. Interestingly, the heat flux stays almost constant during this transition. The system moves towards a lower wall temperature during high g to low g transition as is evident in figure 5. However, the heat flux changes slightly from  $94.8 \text{ W/cm}^2$  to  $98 \text{ W/cm}^2$ .

The boiling curves at reduced gravity for three different concentrations are plotted in figure 6. The molar concentrations of the 2-propanol/water binary mixtures are 0.015, 0.025, 0.1 and the surface tension gradients of these mixtures decrease with concentration. The log-log plots show that the boiling curves roughly follow the general  $1/3$  power law. The boiling curves also show that the higher the surface tension gradient the higher the critical heat flux. It is evident here that the critical heat flux correlates strongly with the surface tension gradient and hence the Marangoni effect. At the heater surface, alcohol evaporates preferentially which has a lower surface tension. Therefore, the surface tension of the liquid close to the solid-liquid-vapor interface is higher than the bulk surface tension around liquid-vapor interface. This surface tension gradient apparently causes more liquid to flow towards the heater surface and delays the onset of dry-out. Figure 7 shows that the boiling heat transfer was virtually the same under reduced gravity and terrestrial conditions. However, the critical heat flux of the mixture under reduced gravity decreased by about 10% for 0.015 mole fraction mixture compared to the terrestrial level. Similar reduced gravity boiling characteristics of binary mixtures were reported by Abe et al. (ref. 9)

## CONCLUDING REMARKS

The data obtained in this investigation imply that the Marangoni effect arising from the surface tension gradients due to concentration gradients is an active mechanism in the boiling of binary mixtures such as 2-propanol/water. At a molar concentration of 0.015 of 2-propanol in water, where the surface tension gradient is highest among the concentration tested, the critical heat flux is a factor of three greater than that of pure water for similar conditions under normal gravity. Comparing the results of normal gravity and reduced gravity of the order of  $0.01g_n$ , it is found that the boiling curves and the corresponding critical heat fluxes are almost independent of the gravity level. The effect of gravity on the boiling curves of binary mixtures found in this investigation are consistent with that reported by Abe et al. (ref. 9)

## ACKNOWLEDGMENT

Support for this research provided by NASA's Office of Life and Microgravity Sciences and Applications under grant No. NAG 3-1633 is gratefully acknowledged. The co-operation of John Yanice of NASA Lewis Research Center during the reduced gravity experiments is greatly appreciated.

## REFERENCES

1. Domanski, P.: Modeling of a Heat Pump Charged with a Non-Azeotropic Refrigerant Mixture, NBS Technical Note 1218, National Bureau of Standards, 1986
2. Degdroff, W.T., Pietruszewski, C.S. and Downing, R.S.: Development Status of a Two-Phase Thermal Management System for Large Spacecraft, AIAA Paper 88-2703, 1988.
3. McGillis, W. R. and Carey, V. P.: On the Role of Marangoni Effects on the Critical Heat Flux for Pool Boiling of Binary Mixtures, ASME Journal of Heat Transfer, Vol. 118, No. 1, Feb. 1996, pp 103-109.
4. Reddy, R.P. and Lienhard, J.H.: The Peak Boiling Heat Flux in Saturated Ethanol-Water Mixtures, J. of heat transfer, Vol 111, No. 2, May 1989, pp. 480-486.
5. Siegel, R. and Usiskin, C.: A photographic Study of Boiling in the Absence of Gravity, J. of Heat Transfer, Vol 81, 1959, pp. 230-236.
6. Siegel, R.: Effect of Reduced Gravity on Heat transfer, Advances in Heat Transfer, Vol. IV, Academic Press Inc., New York, 1967, pp. 143-228.
7. Merte, H. Jr.: Nucleate Pool Boiling in Variable Gravity, Low Gravity Fluid Dynamics and Transport Phenomena, Progress in Astronautics and Aeronautics, Vol. 130, AIAA, Washington DC, pp. 15-69.
8. Straub, J., Zell, M. and Vogel, M.: What We Learn from Boiling Under Microgravity, Microgravity Science and Technology, Vol. VI, No. 4, 1993, pp. 239-247.
9. Abe, Y. Oka, T., Mori, Y.H. and Nagashima, A.: Pool Boiling of a Non-azeotropic Binary Mixture under Microgravity, Int. J. of Heat and Mass Transfer, Vol. 37, No. 16, November 1994, pp. 2405-2414.

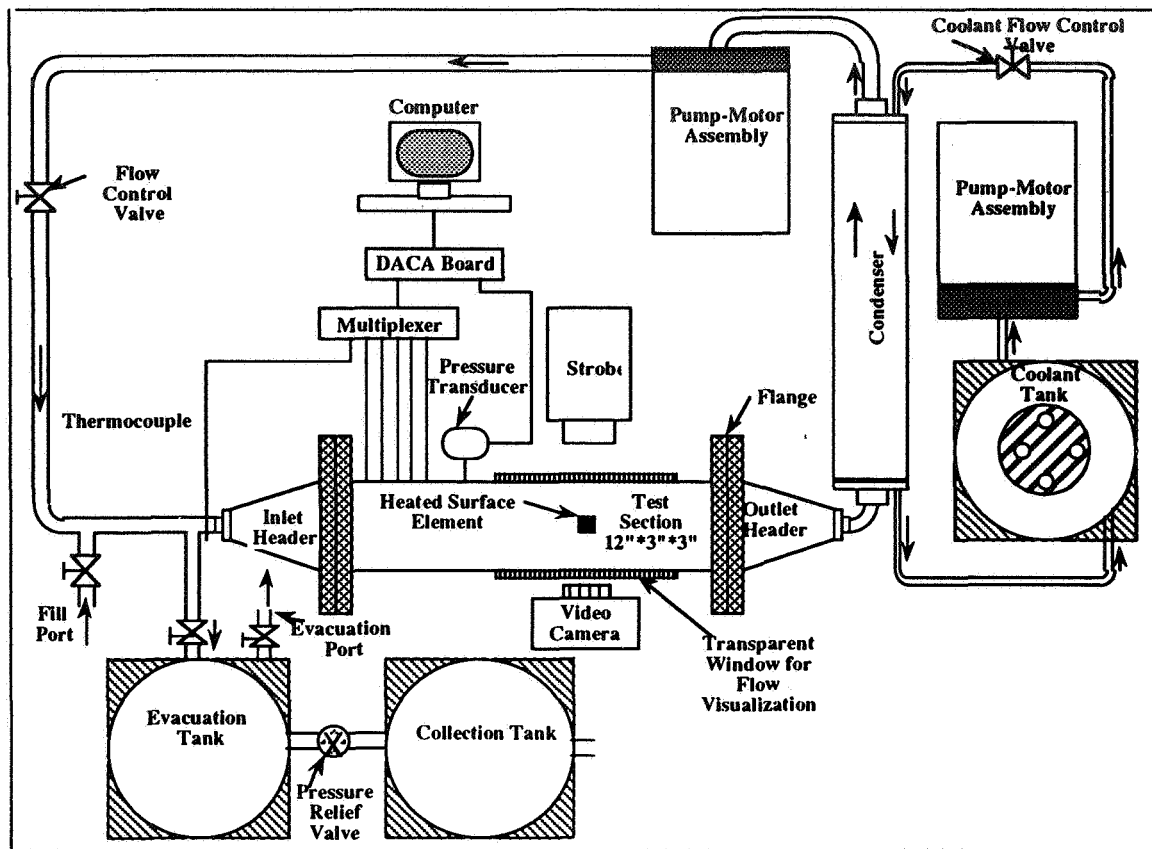


Figure 1.- Layout of the experimental system.

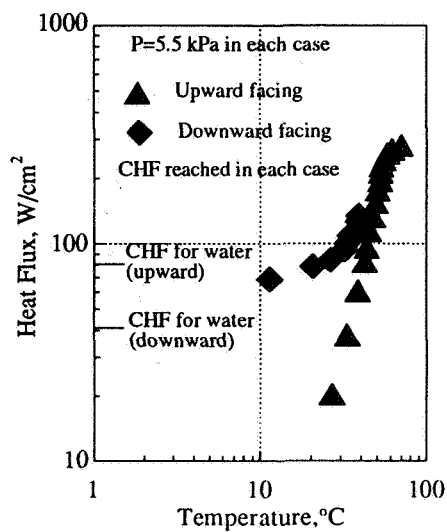


Figure 2.- Boiling curves for 2-propanol/water mixture ( $X_p=0.015$ ) at different orientations.

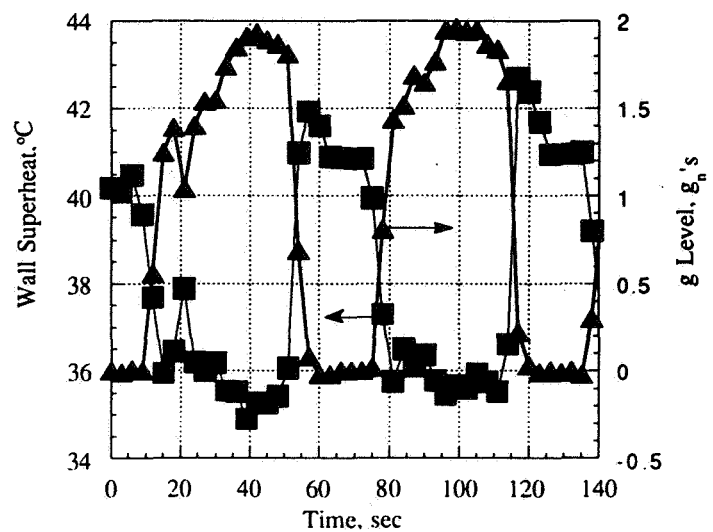


Figure 3.- Transient wall superheat and  $g$ -level during an experimental cycle for  $X_p=0.015$ .

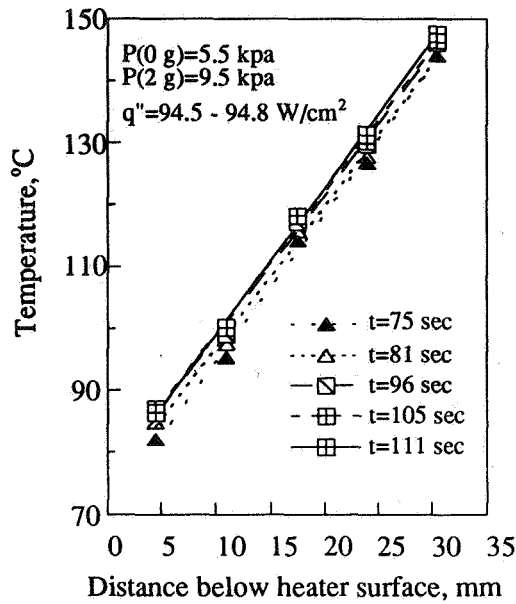


Figure 4.-Transient temperature profile along the heater during low g-high g transition for  $X_p=0.015$ .

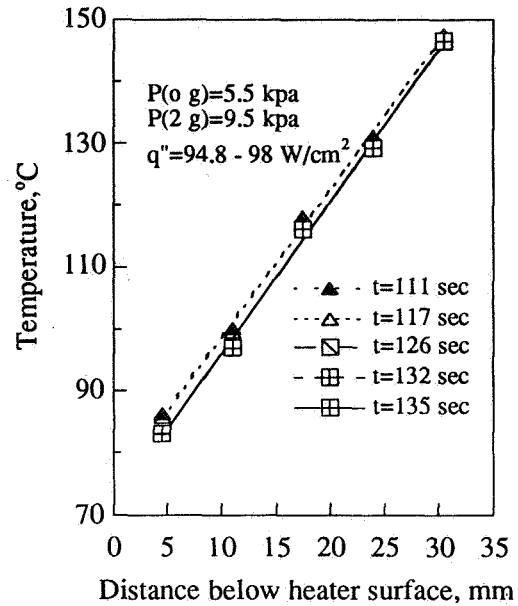


Figure 5.- Transient temperature profile along the heater element during high g-low g transition

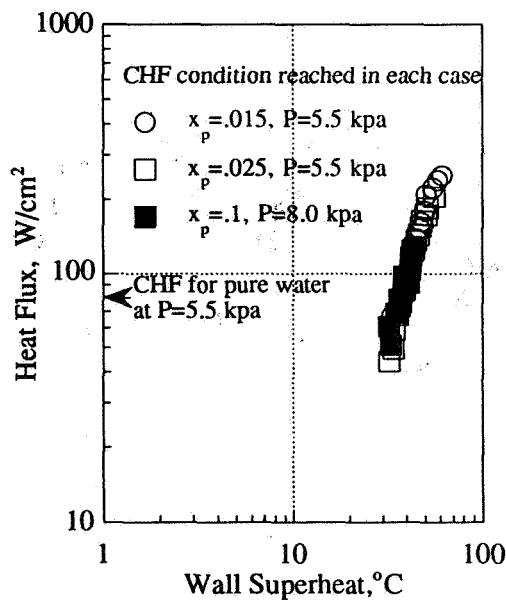


Figure 6.- Reduced gravity boiling curves for various concentrations of 2-propanol

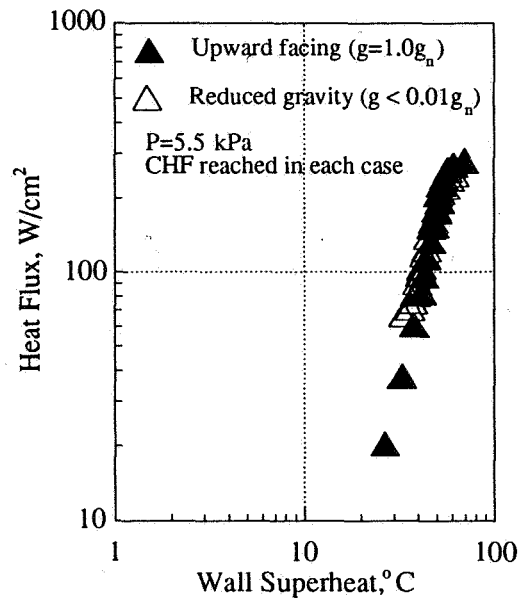


Figure 7.- Comparison of boiling curves between reduced gravity and terrestrial gravity

# REWETTING OF MONOGROOVE HEAT PIPE IN SPACE STATION RADIATORS

S. H. Chan, Ting Rong Shen and John Blake  
Department of Mechanical Engineering  
University of Wisconsin-Milwaukee  
Milwaukee, Wisconsin 53211

## ABSTRACT

Experimental investigation of the rewetting characteristics of a uniformly heated grooved surface was performed, the results of which are presented in this work. It was found that, for a rewetting fluid of 2-propanol, the rewetting temperature was 93~96 °c for the upward-facing case and about 2 °c lower for the downward-facing case. When the initial plate temperature was higher than the rewetting temperature, the rewetting speed decreased with the initial plate temperature. The rewetting speed is also faster in the upward-facing case than in the downward-facing case for the same initial plate temperatures, which indicates a gravitational effect on rewetting. This trend is found to be consistent with the previously investigated end heating condition. The rewetting distance that is predicted by the conduction controlled model is found to be in fair agreement with the experimental data. Also, an apparatus that enables experiments to be performed in a reduced gravitational environment has been built and experiments are currently being performed. The design of this apparatus is presented along with preliminary data.

## INTRODUCTION

The design of space station radiators uses efficient two-phase monogroove heat pipes (ref. 1), the inner surfaces of which are made up of capillary grooves. Such capillary grooved surfaces are widely used in other space-based applications as well. When the heat pipes are thermally overloaded, dryout of the grooved surface occurs. It is essential that the dry surface be rewetted in a timely manner to prevent the malfunction of the related thermal management system.

The section of the circumferential grooves in the monogroove heat pipe that is located away from the region of two-phase thermal loading was the subject of our *prior* investigation (ref. 2). It was equivalent to rewetting of a grooved plate with one end heated and maintained at a constant elevated temperature. The objective of *this* work is to investigate the rewetting characteristics of the groove section that is in direct contact with the thermal loading. The equivalent to this is the rewetting of a grooved plate that is subjected to uniform heating throughout its length. The effects of gravity are examined by placing the grooved plate in upward and downward-facing positions. Both the theoretical and experimental results are presented and compared. In addition, the design of the newly completed drop tower are also reported and preliminary data is presented.

## REWETTING WITH UPWARD AND DOWNWARD ORIENTATIONS

Experiment. -The experimental apparatus consists of the following components (fig. 1); a grooved copper plate with a flexible silicone rubber heater (10 W/in<sup>2</sup>) glued to the bottom, ten surface thermocouples spaced along the groove direction with spring loading towards the groove land, a multiplexed data acquisition system to simultaneously read and record the thermocouple signals, a temperature controller and a by-pass

switch that allows electric power to go either through the controller or directly to the heater, a variable flow rate liquid supply system and a video recording system for recording the liquid movement.

The plate was chemically cleaned and then uniformly heated to the desired initial temperature. The video camera was activated and a signal was recorded to indicate the commencement of computer data acquisition. The heater was turned on to allow the plate to undergo a continuous uniform heat flux during the rewetting process. Working fluid (2-propanol) was then introduced to the plate and the rewetting process was recorded. Rewetting experiments were conducted with the grooved plates at various initial temperatures and with the plate facing upward or downward.

**Results and Discussion.** -Experiments were first performed at high initial plate temperatures ( $>130\text{ }^{\circ}\text{C}$ ) for different flow rates in both the upward and the downward orientations to investigate the flow rate effect, as the fluid delivery system is such that there is overflow from the end of the plate. Thus, only fluid that was carried by the capillary action rewetted the plate. It was found that increasing the flow rate to above  $41\text{ ml/min}$ . had little effect on the rewetting of the plate for both the upward and downward orientations. After this finding, the rewetting tests were performed at the flow rate of  $41\text{ ml/min}$ .

Figure 2 and figure 3 show the rewetting front profiles and plate temperature profiles with initial temperature larger than  $110\text{ }^{\circ}\text{C}$ ,  $120\text{ }^{\circ}\text{C}$  and  $130\text{ }^{\circ}\text{C}$  for the grooved plate facing upward and downward respectively. The presented temperature profiles are contour plots that depict the plate temperature in relation to time and location. The location of the liquid front, as observed from the video, is superimposed on these plots. From figure 2 and figure 3 it can be seen that, with initial plate temperatures greater than  $110\text{ }^{\circ}\text{C}$  and  $120\text{ }^{\circ}\text{C}$ , the rewetting temperature (the plate temperature at the liquid front) is about  $93\text{--}95\text{ }^{\circ}\text{C}$  for the upward facing case and about  $2\text{ }^{\circ}\text{C}$  lower for the downward facing case. It can also be seen from that in the case of an initial plate temperature greater than  $130\text{ }^{\circ}\text{C}$ , the rewetting temperature is about  $94\text{--}96\text{ }^{\circ}\text{C}$  for the upward facing case and is, again, about  $2\text{ }^{\circ}\text{C}$  lower for the downward facing case. Figure 2 and figure 3 also give the experimental data of rewetting distance versus time for the upward and downward facing cases with continuous uniform heating at different initial temperatures. It is clear that the rewetting velocity decreases with the initial plate temperature and that rewetting is faster in the upward facing case than in the downward facing case for the same initial plate temperature. This trend is consistent with the previously investigated end heating condition (ref. 2). The results of research that has been performed under much lower than  $1\text{-}g_e$  conditions can help explain why the downward facing cases show a lower rewetting velocity. When the grooved plate is flipped from the upward to the downward-facing orientation, the gravity force exerted on the liquid in the groove is switched from a compressive to an expansive effect against the groove bottom surface. This is equivalent to switching from a positive to the negative gravity condition. Thus, analogous to previous finding (refs. 3-5), the boiling heat transfer rate should be lower in the negative gravity case and consequently the transient rewetting distance should be lower in the downward-facing condition as is shown in figure 2 and figure 3. The difference in boiling heat transfer rates may also account for the slight difference between the upward and downward-facing rewetting temperatures.

**Predictions.** -Prior study (ref. 2) has shown that rewetting goes from a hydrodynamically controlled to a heat conduction controlled mechanism when the initial plate temperature exceeds its rewetting temperature. The experimental data that is reported in figure 4 depicts a case in which the initial plate temperature exceeded the rewetting temperature. Thus, the heat conduction controlled model was used to predict the rewetting distance versus time for a grooved plate facing upward under continuous uniform heating with different initial temperatures. The rewetting temperatures and heat transfer coefficient must be prescribed when using the model to make calculations. The actual measured rewetting temperatures were used in calculations. The heat transfer coefficient is estimated in terms of the pool boiling diagram of 2-propanol by (ref. 6). It is noticed that the Leidenfrost temperature (temperature at CHF) from the diagram is about  $102\text{ }^{\circ}\text{C}$ , while the measured rewetting temperature is much lower than  $102\text{ }^{\circ}\text{C}$ . Therefore, it was necessary to make some adjustments in the evaluation

of the average heat transfer coefficient. The value of the average heat transfer coefficient is such that the actual heat transfer rate in the wet region is in accordance with the boiling diagram. The values are given in table I.

The predicted distances are given in figure 4. The predicted rewetting distances are found to be in fair agreement with experimental data, with (maximum) discrepancies of about 20%. From both experimental and calculated results it can be seen that the transient rewetting distance decreases with the plate initial temperature.

## DROP APPARATUS DESIGN AND REDUCED GRAVITY EXPERIMENTS

Introduction. -The research that we are currently involved with is the study of the wetting characteristics of heated capillary grooved surfaces under various environmental conditions. In our previous studies, the plate orientation and temperature were the varied conditions. The current phase of our research involves the study of wetting characteristics in various accelerational reference frames. To achieve this, it is necessary to devise experiments and equipment that will perform as needed to yield good data under these conditions. To this end, we have built a device that achieves an average relative accelerational frame of about 0.1 g for a period of ~0.9 sec. This is sufficient time to observe and measure the transient temperature and wetting velocity under some thermal conditions. This also allows us to test our experimental designs prior to attempting to run them in more expensive and hazardous environments such as NASA's microgravity research aircraft.

Drop Apparatus. -The purpose of a drop apparatus is to perform experiments at a near free-fall for as long as possible. Also, the experiments should be repeatable and non-destructive. Figure 5 is a schematic of the drop apparatus design. A rigid cage encloses the experimental device(s). The cage can be raised to a height of up to 4.3 meters from where the cage is released. The cage's descent is guided by four cables and at the bottom of travel is an airbag to cushion the cage's impact and bring it to rest. The drop apparatus consists of five major components: the lifting and dropping mechanism, the guide and anchoring assembly, the airbag, the state logic controller and the experimental platform. The lifting and release mechanism consists of: a rectangular frame that carries the platform along the guide cables to the top anchor bracket and a latch that connects to the experimental platform. When the latch is released, the platform falls away from the lifting mechanism. After the platform is dropped, the lifting mechanism is lowered and reconnected to the platform. As the platform drops, the frame experiences a change in relative gravitational acceleration from  $\ddot{x} = g_e$  prior to the drop to  $\ddot{x} \approx 0.1g_e$  during the drop. When the platform impacts with and is slowed by the airbag, it goes through a deceleration  $\ddot{x} \approx -3g_e$  until it comes to rest at  $\ddot{x} = g_e$ . Since the experiments are to be performed at a reduced acceleration frame  $\ddot{x} \approx 0.1g_e$ , a mechanism has been devised to initiate the experiment just after the platform and lifting mechanism de-couple, and terminate the experiment just prior to impact with the airbag. The controller contains a Set-Reset flip flop for the logic operation and receives inputs from the operator and the position of the cage. The control signals interface with and operate the experimental apparatus through a series of relays and solenoids. A block logic diagram of the controller is shown in figure 6.

Experimental Apparatus. - The current experiments observe the wetting velocity under reduced acceleration frames with the plate at various temperatures. In addition, equipment designs are being tested for functionality and resilience. The components in the current experiment are: a positioning mechanism, grooved plates that are heated either at the end or on the bottom, a temperature controller, a fluid reservoir which is also being tested for functionality, a data acquisition system to record the signals from thermocouples arrayed along the bottom of the plates, a video camera to monitor the fluid position within the grooves and laser line generator which provides a height measurement on the video data. The positioning mechanism is a two state system that operates through solenoids which are selectively activated by the controlling logic system. The mechanism positions the plate in the reservoir while the experimental platform is dropping and removes the plate from the

reservoir as the platform ends its descent. The grooved plate is fashioned from oxygen free copper and has 0.4 mm capillary grooves machined into the surface. Flexible heaters are glued either to the plate's bottom or end, the power to which is controlled by a PID temperature controller. An array of T-type thermocouples (36 gauge) is located on the bottom of the plates and the corresponding temperature signals are gathered by the data acquisition system. The reservoir contains the fluid (2-propanol) and is slotted on top to accommodate the plate. The slot is gasketed with condom latex. The video camera is a pinhole micro chip CCD. A laser line generator provides a non-invasive reference point for determining vertical position during close up video observations.

Discussion.-Experiments are currently being performed with this apparatus. A preliminary example of the data that is obtained from these experiments is given in figure 7, which depicts the change of the rewetting front position and the plate temperature profile with time.

## CONCLUSION

The rewetting of a grooved plate that is subjected to uniform heating with an initial temperature that is higher than the rewetting temperature was investigated and the completion of a drop apparatus design and construction was reported. The following conclusions can be reached; (i) The rewetting temperature is 93 °c~ 96 °c for the upward-facing case and about 2 °c lower for the downward-facing case when 2-propanol is used as a rewetting fluid. The rewetting temperature is a few degrees lower than prior findings for the end heating case. (ii) The rewetting speed decreases with the initial plate temperature. (iii) The rewetting speed is also faster in the upward-facing case for the same initial temperature conditions, thus indicating a gravity effect on rewetting. (iv) The prediction of the transient rewetting distance using the conduction controlled model is in fair agreement with experimental data. (v) A drop apparatus is ready to conduct rewetting tests under a reduced gravity environment ( $\sim 0.1 g_e$ ) for a duration of  $\sim 0.9$  s.

## ACKNOWLEDGMENT

Thanks are due to Dr. S. Jayawardena and Dr. B. Singh of NASA Lewis Research Center for valuable advise regarding this work.

## REFERENCES

1. Alario, J; Brown, R.; and Kosson, R.: Monogroove Heat Pipe Development for the Space Constructable Radiator System. AIAA paper 83-1431, 1983.
2. Chan, S.H.; Blake, J.D.; Shen, T.R.; and Zhao, Y.G.: Effects of Gravity on Rewetting of Capillary Groove Surface at Elevated Temperatures-Experimental and Theoretical Studies. ASME Journal of Heat Transfer, Vol. 117, Nov. 1995, pp. 1042-1047.
3. Kawaji, M.; and Westbye, C.J.: Microgravity Experiments on Two Phase Flow and Heat Transfer During Quenching of a Tube and Filling a Vessel. AIChE Journal, Vol. 11, 1991, pp. 403-419.
4. Lyon, D.N.; Jones, M.C.; Ritter, G.L.; Chiladakis, C.; and Kosky, P.G.: Peak Nucleate Boiling Fluxes for Liquid Oxygen on a Flat Horizontal Platinum Surface at Boyancies Corresponding to Acceleration Frames Between -0.03 and 1 g. AIChE Journal, Vol. 11, 1965, p. 773.



5. Merte, H.; and Clark, J.A.; Boiling Heat Transfer with Cryogenic Fluids at Standard, Fractional and Near-Zero Gravity. ASME Journal of Heat Transfer, Vol. 86, 1964, pp.351-359.
6. Ungar, E.K.; Saturated Pool and Flow Boiling From Horizontal Cylinders. PhD. dissertation, University of Wisconsin-Milwaukee, 1987, p. 71.

Table 1 Average Heat Transfer Coefficients Adjusted for Different Rewetting Temperatures

Rewetting Temperature (°C)	91	92	93	94	95	96
Average Heat Transfer Coefficient ( $\text{W/m}^2 \text{ } ^\circ\text{C}$ )	29,682	26,558	24,028	21,939	20,184	18,689

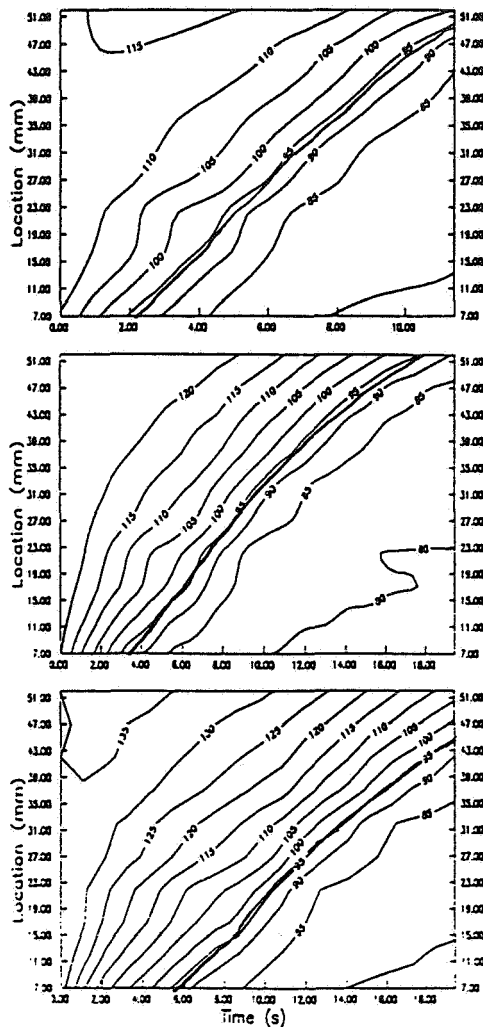


Figure 2. Rewetting Front and Temperature Profiles for the Grooved Plate Facing Upward Under Uniform Heat Flux ( $10 \text{ W/in}^2$ ).

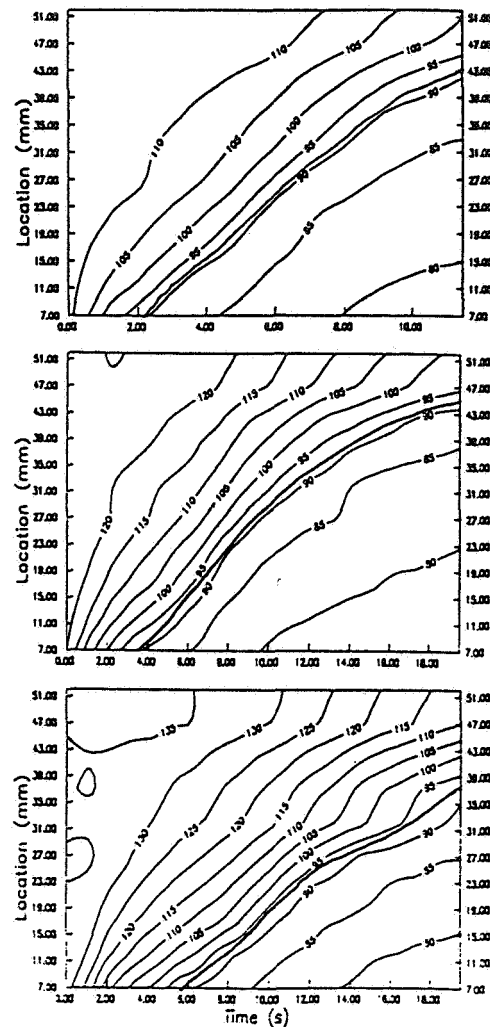


Figure 3. Rewetting Front and Temperature Profiles for the Grooved Plate Facing Downward Under Uniform Heat Flux ( $10 \text{ W/in}^2$ ).

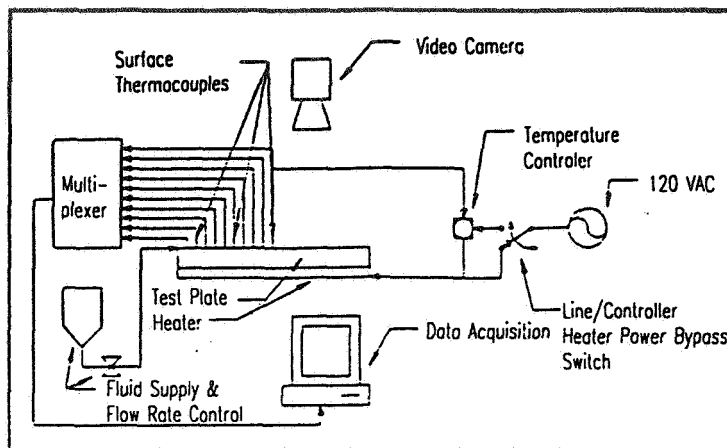


Figure 1. Schematic Diagram of Experiment Setup.

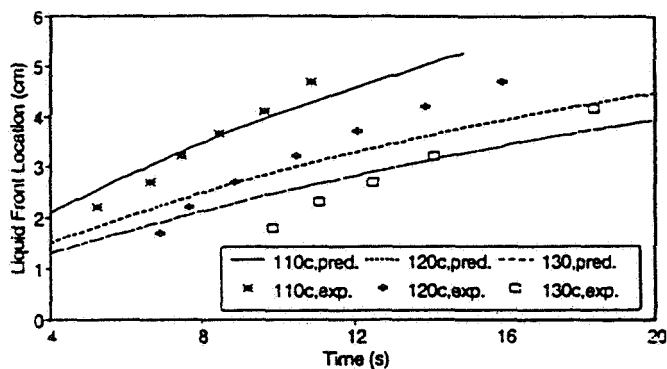


Figure 4. Predictions and Experimental Data of the Rewetting Front Locations Versus Time for the Grooved Surface Facing Upward at Different Initial Temperatures Under Uniform Heat Flux ( $10 \text{ W/in}^2$ ).

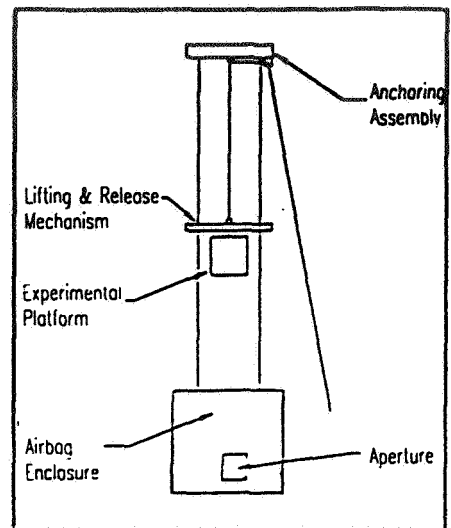


Figure 5. Drop Apparatus Schematic.

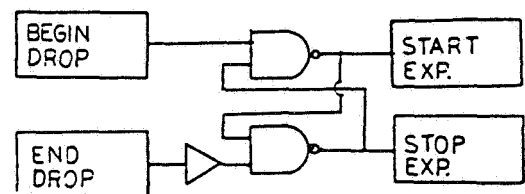


Figure 6. Controller Block Logic Diagram.

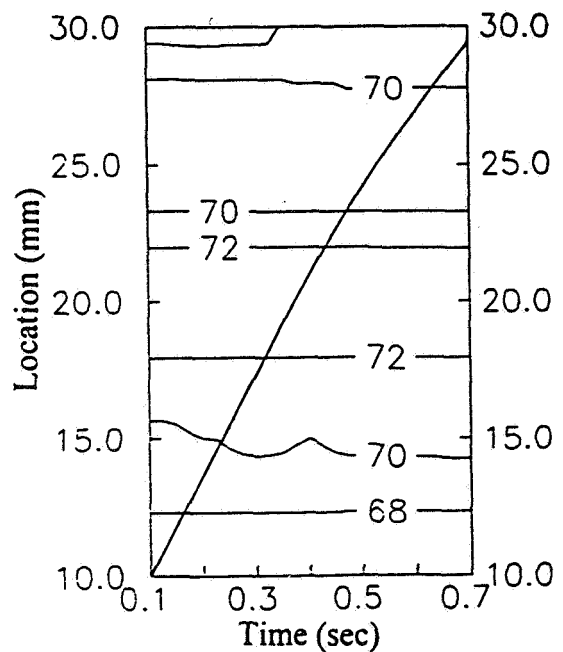


Figure 7. Preliminary Drop Data.

# ELECTROHYDRODYNAMIC POOL BOILING IN REDUCED GRAVITY

Principal Investigator: B. D. Shaw

Graduate Student: S. L. Stahl

Mechanical and Aeronautical Engineering Department  
University of California  
Davis, CA 95616-5294

## ABSTRACT

This research is concerned with studying the effects of applied electric fields on pool boiling in a reduced-gravity environment. Experiments are conducted at the NASA Lewis 2.2 sec Drop tower using a drop rig constructed at UC Davis. In the experiments, a platinum wire is heated while immersed in saturated liquid refrigerants (FC-72 and FC-87), or water, causing vapor formation at the wire surface. Electric fields are applied between the wire surface and an outer screen electrode that surrounds the wire. Preliminary normal-gravity experiments with water have demonstrated that applied electric fields generated by the rig electronics can influence boiling characteristics. Reduced-gravity experiments will be performed in the summer of 1996. The experiments will provide fundamental data on electric field strengths required to disrupt film boiling (for various wire heat generation input rates) in reduced gravity for a cylindrical geometry. The experiments should also shed light on the roles of characteristic bubble generation times and charge relaxation times in determining the effects of electric fields on pool boiling. Normal-gravity comparison experiments will also be performed.

## INTRODUCTION

Pool boiling heat transfer is important in a number of applications. There are several different regimes in pool boiling, e.g. nucleate boiling and film boiling [1]. Nucleate boiling is characterized by formation of individual bubbles at a heated surface. The bubbles leave the surface, allowing fresh liquid to come into contact with the surface. This fresh liquid forms more bubbles, and the cycle repeatedly occurs, promoting high heat transfer rates. It has been observed, however, that critical surface heat fluxes ( $q''_{\max}$ ) can exist such that nucleate boiling can no longer be sustained, leading to the formation of a layer of vapor which remains deposited on the heat transfer surface; this corresponds to the film boiling regime [1]. Heat transfer coefficients are generally much lower in the film boiling regime than for nucleate pool boiling, and surface temperatures are typically substantially higher. With pool boiling heat transfer, it is generally desirable to operate in the nucleate boiling regime so that: (i) high heat transfer coefficients, and therefore small heat transfer surface areas, may be realized; and (ii) acceptably-low surface temperatures may be attained (e.g., for safety reasons). As a result, it is important to be able to predict  $q''_{\max}$ .

Theory and experiment suggest that gravity, when it is the only body force present, plays an important role in determining  $q''_{\max}$ . Theoretically, it is predicted [1] that the critical heat flux scales with the gravitational acceleration raised to the one-fourth power (i.e.,  $q''_{\max} \sim g^{1/4}$ , where "g" is the gravitational acceleration). Experimental data [2] tend to support this scaling with gravity. Physically, as g decreases, buoyancy forces become less effective at removing bubbles from surfaces. Hence, in reduced gravity the critical heat flux  $q''_{\max}$  may be substantially

decreased. This results in a penalty of larger heat transfer areas to safely transfer a given amount of heat. In space-based systems, as well as earth-based systems, there are substantial cost and size advantages to be gained by increasing  $q''_{\max}$ . It is thus desirable to study ways of enhancing boiling heat transfer so that  $q''_{\max}$  may be increased.

One method for increasing  $q''_{\max}$  involves applying electric fields in the region where bubble nucleation and growth (boiling) occurs. Nucleate boiling in the presence of electric fields has been the subject of numerous studies. Electric fields have been shown (in 1-g) to be capable of increasing  $q''_{\max}$  in a controllable manner by an order of magnitude or more. A 1978 review of the subject may be found in Ref. [3]. More recent studies have also been reported [4-9] (though no reduced-gravity data has been found). Ground-based studies have shown that electric fields can substantially increase  $q''_{\max}$ , basically by causing film boiling to become unstable and by strongly affecting bubble motions. Vapor blankets associated with film boiling are destabilized by sufficiently-strong electric fields, thus promoting nucleate boiling at high heat fluxes.

Electric fields influence bubble and liquid behaviors in several ways. For example, convective flows are induced in liquids by electric fields; these flows tend to increase heat transfer rates, and may actually delay the onset of nucleate boiling. Effects of electric fields on bubbles can be dramatic, splitting larger bubbles into smaller ones and inducing significant bubble velocities through the action of electrical forces [4,5]. The time  $t_c = \epsilon/\sigma_e$ , where  $\epsilon$  is liquid dielectric permittivity and  $\sigma_e$  liquid electrical conductivity, is a characteristic time for charge relaxation (accumulation) to occur around a bubble under the action of an applied electric field. The magnitude of  $t_c$  has been shown to be important in determining pool boiling behavior [5,6]. Physically, it seems reasonable that if  $t_c$  is small relative to a characteristic time  $t_{res}$  for bubble residence time in the electric field zone, electric fields may significantly affect bubble behaviors. Conversely, if  $t_c \gg t_{res}$ , electric fields may not be significant. Such phenomena have been noted in 1-g experiments with R-11 ( $\text{CCl}_3\text{F}$ ) [9]. In these experiments,  $t_{res}$  may have been strongly influenced by buoyancy forces.

In reduced gravity, buoyant residence times may become quite large, suggesting that electric field effects may be significant for liquids with large values of  $t_c$ . It is noted, however, that 1-g experiments have suggested that the characteristic bubble generation time  $t_b$  (i.e., the time to generate a bubble at the surface) is also important [4,5]; electric field effects (e.g., on  $q''_{\max}$ , heat transfer coefficients, and bubble behaviors) were strong when  $t_c \ll t_b$ , and weak when  $t_c \gg t_b$  (it was also shown that varying the electric field magnitudes allowed control of heat transfer [4,5]). These works, however, did not take buoyant residence times into account. It seems plausible that electric field effects should be important if  $t_c \ll t_{res}$ , regardless of whether  $t_c \gg t_b$  or  $t_c \ll t_b$ , that is, so long as the residence time is sufficient for electric effects to occur. Reduced-gravity experiments (which will greatly increase  $t_{res}$ ) with liquids that have  $t_c \gg t_b$  or  $t_c \ll t_b$ , should thus delineate whether  $t_b$  or  $t_{res}$  is more important in determining the effects of electric fields.

Available theory suggests that  $q''_{\max}$  should scale linearly with applied electric field magnitudes when gravity is negligible [8]. It is noted, however, that this theory assumes liquids are perfect conductors, the film exists over a flat plate, and uniform DC fields are present. Any or all of these assumptions may be violated in an application. Many refrigerants, e.g. fluorocarbons, have very low electrical conductivities.

## SCIENTIFIC OBJECTIVES

This research is focused upon investigating the effects of electric fields on reduced-gravity pool boiling. The following areas are addressed:

It is expected that it will be shown that electric fields will significantly (and controllably) increase reduced-gravity nucleate boiling heat transfer rates and maximum heat fluxes for the cylindrical geometry considered.

It will be investigated whether available theory will predict  $q''_{\max}$  (critical heat fluxes) when electric fields are applied in reduced gravity.

It will be investigated whether bubble dynamics will be significantly affected by electric fields. It is expected that electric fields will produce smaller bubbles, and will strongly affect their motions, as observed in 1-g experiments. Contrary to 1-g experiments, these trends are expected to apply as long as  $t_c \gg t_{\text{res}}$ , regardless of whether  $t_c \gg t_b$  or  $t_c \ll t_b$ .

### SCIENTIFIC AND TECHNICAL SIGNIFICANCE

Scientifically, this research will advance knowledge of the effects of electric fields on boiling heat transfer. Reduced-gravity studies will decrease buoyancy forces to negligible levels, allowing investigation of the relative importances of liquid charge relaxation times ( $t_c$ ) and characteristic bubble production times ( $t_b$ ), both of which are considered to be of fundamental importance. Physically, it seems reasonable to expect that a bubble must be exposed to an electric field for at least the time  $t_c$  for the field to affect the bubble. Normal-gravity studies have suggested that electric field effects are strongest when  $t_c \ll t_b$  and weak when  $t_c \gg t_b$ . However, buoyant bubble residence times ( $t_{\text{res}}$ ) were generally small relative to  $t_c$  when the  $t_c \gg t_b$  studies were performed, suggesting that buoyancy may have played a critical role. It seems likely that electric field effects will be important if  $t_c$  is small relative to bubble residence times in the electric field zone, regardless of whether  $t_c \ll t_b$  or  $t_c \gg t_b$ . Reduced-gravity experiments will be performed with liquids for which  $t_c \ll t_b$  or  $t_c \gg t_b$ . The experiments will render buoyant residence times large relative to  $t_c$ , and will allow this hypothesis to be evaluated. In addition, quantitative data will be obtained on the effects of electric fields on heat transfer coefficients and critical heat fluxes in reduced-gravity.

Technically, this research will help in the development of pool boiling heat transfer devices for use in space as well in terrestrial applications. A major obstacle to utilizing pool boiling in space is the fact that the critical heat flux decreases with decreasing gravity levels. Electric fields may act as a substitute for gravity, increasing critical heat fluxes and boiling heat transfer rates in controllable manners. This may help to lead to space-based (and earth-based) applications of this technology. Space applications are especially significant, in view of the possible weight savings involved; small reductions in weight generally lead to substantial cost savings associated with putting a system in orbit.

### RESEARCH APPROACH

A pool boiling apparatus has been constructed at UC Davis for use in the 2.2 sec drop tower at the NASA Lewis Research Center (see Fig. 1 for a schematic). Liquids at saturation conditions (at one atm) will be studied. This apparatus consists of a chamber initially filled with liquid. Inside the chamber is a circular platinum wire ( $\approx 0.1$  mm diameter and 70 mm in length) surrounded by a concentric screen about 70 mm in length and 10 - 30 mm in diameter (variable). Boiling is caused to occur by passing electrical current from a DC-DC convertor through the wire. Measurements of wire voltage drop and current allow the average wire resistance to be calculated. Since wire resistance is a known function of temperature, the average wire temperature can thus be

calculated; because the wire is thin, wire temperature gradients should be small (these gradients will be estimated). The average surface heat flux  $q''_s$  will also be easily calculated from knowledge of the platinum wire voltage drop and current.

The platinum wire and outer concentric screen is connected to an on-board high voltage power supply (a DC-DC convertor). If cylindrical symmetry is assumed, the electric field  $E$  between the screen and the platinum wire is approximately given by  $E = (V/r)/\ln(r_2/r_1)$ , where  $V$  is the voltage difference between the wire and screen,  $r$  the radial coordinate, and  $r_1$  and  $r_2$  denote the wire and screen radii, respectively. For  $V = 1$  kV (attainable with the DC-DC convertors used),  $r_1 = 0.05$  mm and  $r_2 = 5$  mm,  $E \approx 4$  MV/m near the wire. These field strengths significantly increase boiling rates and  $q''_{\max}$  in 1-g conditions [3-6,8,9].

For pressure control, a balloon has been mounted inside the chamber such that one side of the balloon is exposed to the test liquid while the other side is open to the atmosphere (see Fig. 2 for a schematic). The balloon simply collapses as bubbling ensues, maintaining the test-cell volume very closely to local atmospheric pressure. A thermal control system to maintain the bulk fluid at saturation conditions has also been implemented.

Some drop tower experiments will proceed by stabilizing boiling for a few seconds in 1-g at the top of the drop tower, before the drop occurs. The package will then be dropped, providing the reduced-gravity environment. Other experiments will involve initiating boiling while in  $\mu$ g. The experiment package is computer-controlled while in reduced gravity. Platinum wire currents and voltages are continuously monitored and recorded with an on-board data acquisition system. The high voltage applied between the wire and the screen is monitored and recorded, as is the DC-DC convertor current. Three thermistors are used for liquid temperature measurements, and a pressure transducer is used for test-cell pressure measurements; the temperature and pressure of the liquid are recorded by an on-board data acquisition system. After each drop, data will be downloaded to a computer for later analysis. On-board video cameras, orthogonally aligned, provide visual records of the experiments. One camera shows a close-up of the platinum wire, while the other provides a wider field of view showing the wire as well as the screen. Details of bubble nucleation and growth, as well as bubble behavior after detachment will be observed.

Experiment procedures will involve setting  $q''_s$  and  $V$  to specific values. Data will be evaluated to determine if a transition to film boiling occurs during a drop or whether existing film boiling can be disrupted in  $\mu$ g after the electric field is activated. The parameters  $q''_s$  and  $V$  will be systematically varied from drop to drop so that  $q''_{\max}$  and wire heat transfer coefficients may be determined as a function of the applied voltage. For comparison, the same experiments will be performed in 1-g using the same apparatus. This should shed light on the effects of gravity on boiling phenomena, for example characteristic bubble sizes and heat transfer rates.

## RESULTS TO DATE

Preliminary experiments in normal gravity (using water) have shown that the drop rig is functional. These experiments have demonstrated that electric fields applied by the drop rig circuitry can influence boiling heat transfer in normal gravity. Figure 3 shows experimental values of wall heat fluxes vs. wall superheat with and without electric fields. In each case, the wire diameter was 125  $\mu$ m and the screen electrode diameter was 20 mm in diameter (both were about 70 mm in length). As is evident in these figures, applied electric fields increased heat transfer rates. These preliminary experiments utilized voltage gradients of about 1 kV/cm in the vicinity of the wire; future experiments in both normal gravity and reduced gravity will involve voltage gradients that will be up to about 10 times larger. In addition, the screen diameters will be varied in order to assess effects on finite-length wires and screen electrodes.

## RESEARCH PLAN

The next phase of the work will involve performing reduced-gravity experiments at the NASA Lewis Research Center during the summer of 1996. Following this, comparison experiments in normal gravity will be performed at UC Davis using the same apparatus.

## ACKNOWLEDGEMENTS

The contributions of R. Brodeur, T. Brodeur, R. Kapesser, T. Ferrel, A. Jenkins, N. Smith, J.-B. Wei, G. Wilson, and the UCD Engineering Shop Personnel in helping to design and construct the apparatus are gratefully acknowledged. Technical supervision was provided by Dr. F. Chiaramonte of the NASA Lewis Research Center.

## REFERENCES

1. F. P. Incropera and DeWitt, *Fundamentals of Heat and Mass Transfer*, 3rd edition, Chapter 10, Wiley, New York, 1990.
2. A. E. Bergles, "Elements of Boiling Heat Transfer," in Boiling Heat Transfer, Modern Developments and Advances, R. T. Lahey, Jr., ed., pp. 389- 445, Elsevier, New York, 1992.
3. T. B. Jones, "Electrohydrodynamically Enhanced Heat Transfer in Liquids - A Review," Advances in Heat Transfer 14: pp. 107-148, 1978.
4. J. Ogata and A. Yabe, "Basic Study on the Enhancement of Nucleate Boiling Heat Transfer by Applying Electric Fields," International Journal of Heat and Mass Transfer 36: pp. 775-782, 1993.
5. J. Ogata and A. Yabe, "Augmentation of Boiling Heat Transfer by Utilizing the EHD Effect - EHD Behavior of Boiling Bubbles and Heat Transfer Characteristics," International Journal of Heat and Mass Transfer 36: pp. 783-791, 1993.
6. P. Cooper, " EHD Enhancement of Nucleate Boiling," Journal of Heat Transfer 112: pp. 458-464, May 1990.
7. M. L. Bologna and F. M. Sazhin, "Electroconvection and Heat Exchange in Dispersed Gas-Liquid Systems," Journal of Engineering Physics 59: pp. 419-431, 1990.
8. J. Berghmans, "Electrostatic Fields and the Maximum Heat Flux," International Journal of Heat and Mass Transfer 19: pp. 791-797, 1976.
9. H. Kawahira, Y. Kubo, T. Yokoyama, and J. Ogata, "The Effect of Electric Field on Boiling Heat Transfer of Refrigerant-11 - Boiling on a Single Tube," IEEE Transactions on Industry Applications 26: pp. 359-365, March/April 1990.

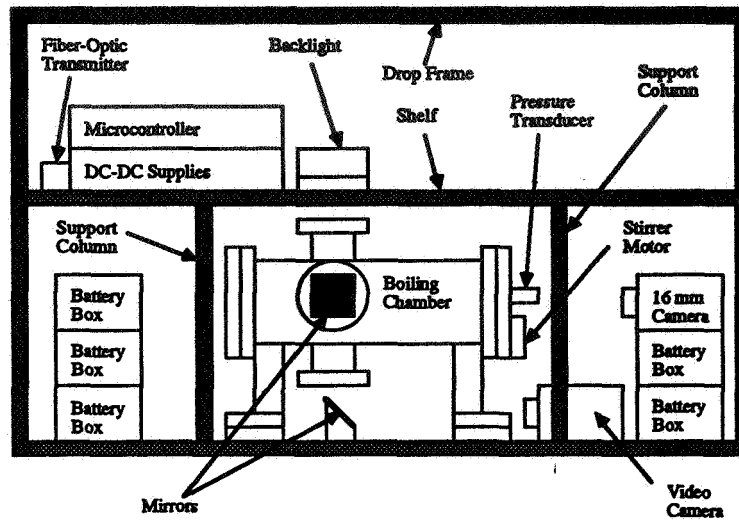


Figure 1. Drop Rig Schematic

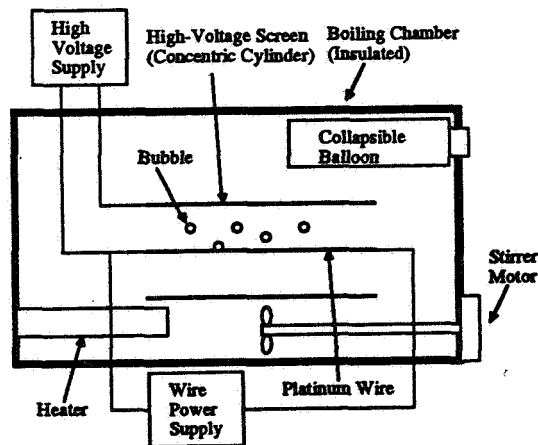


Figure 2. Boiling chamber schematic.

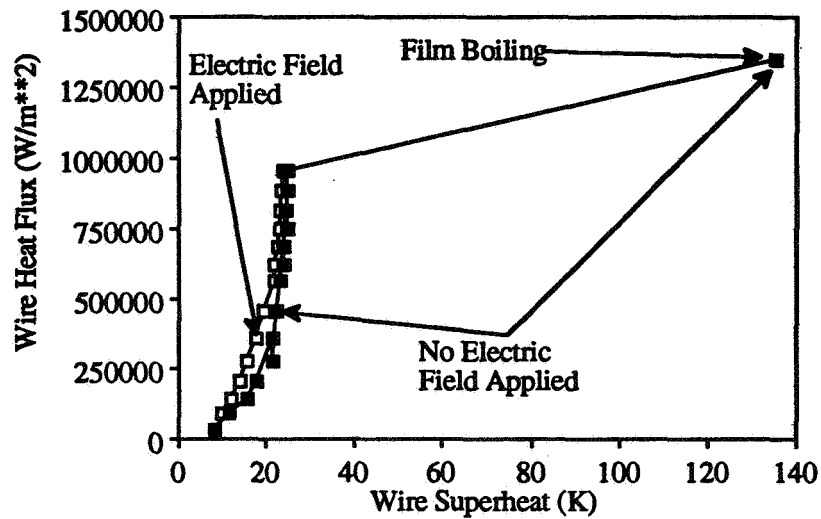


Figure 3. Heat flux from the wire surface for boiling in water (normal gravity).



# ANALYSIS OF THE HYDRODYNAMICS AND HEAT TRANSFER ASPECTS OF MICROGRAVITY TWO-PHASE FLOWS

Kamiel S. Rezkallah  
Department of Mechanical Engineering  
University of Saskatchewan  
Saskatoon, SK S7N 5A9  
CANADA

## ABSTRACT

Experimental results for void fractions, flow regimes and heat transfer rates in two-phase, liquid-gas flows are summarized in this paper. The data was collected on-board NASA's KC-135 reduced gravity aircraft in a 9.525 mm circular tube (i.d.), uniformly heated at the outer surface. Water and air flows were examined as well as three glycerol/water solutions and air. Results are reported for the water-air data.

## INTRODUCTION

Two-phase thermal transport systems have been utilized and researched in the nuclear and petrochemical industries for many decades. Despite the numerous efforts (experimentally, analytically and numerically), two-phase flow models still lack essential information on the interface dynamics and flow characteristics to provide for closure solutions. The microgravity environment provides a good tool to examine the flow without the masking effects of gravitational forces on ground. Flow regimes are basically divided into three regions, namely surface tension dominated region (bubbly and slug flows), inertia dominated region (annular flow) where minimum differences exist between 1-g and  $\mu$ -g, and an intermittent region (which is mostly occupied by a frothy slug-annular flow). These regions are shown in Figure 1 on a map with dimensionless coordinates in terms of the phase Weber number.

While there is a substantially large body of information on two-phase, gas-liquid flows at 1-g (both adiabatic and in boiling/condensing systems), the knowledge-base for their use in space hardware has only recently been growing. Early experimental studies of two-phase convective heat transfer under microgravity conditions were reported by Papell [1] and Feldmanis [2]. In the first study, Papell [1] reported a 15% increase in the heat transfer rate for a sub-cooled water system during reduced gravity. Feldmanis [2], on the other hand, did not explicitly determine heat transfer coefficients. Instead, based on the temperature measurements made during his experiment, he predicted that for forced convective condensation gravity would have little influence on heat transfer.

More recently, Reinharts, Best and Hill [3] worked with a boiling and condensing Refrigerant-12 test loop on-board NASA's KC-135. They reported that the condensation heat transfer coefficients were 26% lower for  $\mu$ -g conditions as opposed to 1-g condition. Boiler temperatures remained constant throughout the KC-135 flights. Thus, no conclusions could be drawn on the effect of gravitational acceleration on the boiling heat transfer coefficients. Ohta *et al.* [4] completed a study of convective boiling system with Refrigerant-113 flow through a 8 mm ID circular tube. They reported that while boiling was occurring in the bubbly and annular flow regimes, there was no difference in the heat transfer coefficients between 1-g and  $\mu$ -g conditions. However, when boiling was suppressed due to the high flow rates and low heat flux, the heat transfer coefficients were lower at  $\mu$ -G compared with 1-g. With such conflicting results, it is clear that further experimental investigation into the heat transfer behavior of two-phase flows under  $\mu$ -g is warranted.

## SYMBOLS

A	annular flow regime	VSG	superficial gas velocity, m/s
B	bubbly flow regime	x	gas quality
g	earth's gravitational acceleration	<i>Greek Symbols:</i>	
h	heat transfer coefficient, W/m <sup>2</sup> .K	$\alpha$	gas void fraction (volumetric)
Nu	Nusselt number (dimensionless)	$\mu$	"micro"
PDF	Probability Density Function		
S	slug flow regime		
VSL	superficial liquid velocity, m/s		

## TEST APPARATUS AND PROCEDURE

A forced-convective two-phase test apparatus was designed and built for testing aboard NASA's KC-135 Zero-G aircraft. The apparatus is instrumented such that simultaneous measurements of pressure drop, void-fraction and heat transfer data can be made, with continuous observation and recording of the two-phase flow patterns. In order to cover a wide range of test conditions, the facility allows for the independent control of three separate parameters during testing: air flow rate, water flow rate, and temperatures of the two-phase mixture in the flow loop. A schematic of the test apparatus is shown in Figure 2.

On-board the plane the apparatus was situated such that the observation and heated test sections were oriented vertically with respect to the floor of the aircraft. A complete discussion of the flow loop may be found in Rite and Rezkallah [5]. Data were mostly gathered for air-water mixtures. In addition, data were also collected with three air-glycerol/water solutions of 50%, 59%, and 65% glycerol (by weight), respectively. These mixtures were used to examine the effect of changing the liquid viscosity on the heat transfer rates and flow transitions/pressure drops. The data were also used in the development of a set of empirical heat transfer correlations.

Quasi-steady-state conditions were obtained during the short  $\mu$ -g duration. This was investigated experimentally, first on-ground and later during flight. It was determined that in a worst case scenario, after approximately ten seconds quasi-steady-state conditions were achieved for all flow rates. It was decided therefore that data for only the last ten seconds of each parabola would be included in the average heat-transfer values. More complete details on the above mentioned tests can be found in Rite and Rezkallah [6,7]. In addition, an analytical study by Zhao and Rezkallah [8] confirmed these results.

## EXPERIMENTAL RESULTS

### Average Heat Transfer Coefficients

Sample results are shown in Figures 3(a) and 3(b) for the two-phase flow Nusselt numbers versus the gas quality,  $x$ . The superficial liquid velocity " $V_{SL}$ " ranged from 0.07 to 2.5 m/s. The flow regime for each data point is also marked besides each point. The abbreviations for the various flow regimes are as follows: "B" for bubbly, "S" for slug, and "A" for annular flow.

It can be seen that at low gas qualities (mainly in the bubbly and slug flow regions), the 1-g Nusselt number values are much greater than those measured at  $\mu$ -g for the same liquid flow rates. As the gas flow rate increases (thus moving to annular flow conditions with high gas inertia), the 1-g and  $\mu$ -g data points approach one another. This suggests that the difference between 1-g and  $\mu$ -g behavior is flow regime dependent. Complete results for all fluids tested are given in Rite [9].

### Local Heat Transfer Coefficients

The results of the local heat-transfer coefficients are shown in Figures 4(a) and 4(b). In these figures, the local heat transfer coefficients,  $h_{local}$ , were calculated from each of the 12 surface measurements on the heated test section using the following equation:

$$h_i = \frac{E}{\pi LD (T_{s,i} - T_{b,i})} \quad (1)$$

where  $E$  is the total heat input into the test section (W),  $L$  is the length of the heated test section (m), and  $T_{b,i}$  is the average bulk fluid temperature at the  $i$ -th section of the heated tube ( $^{\circ}\text{C}$ ). Integration with respect to length then provided an average heat transfer coefficient ( $h_{TP}$ ).

Figures 4(a) and 4(b) show the local heat transfer measurements at a constant liquid superficial velocity  $V_{SL}$  of 0.10 m/s ( $Re_{SL} \approx 1200$ ). In these figures, slug flow is present at each gas velocity, and the 1-g data shows an increase in the local heat transfer coefficient from inlet to exit, while the  $\mu$ -g results show a decrease in  $h_{local}$  similar to what is commonly seen with single-phase

flows in the viscous flow region. The local minima and maxima in the local heat transfer coefficient, shown in the figures at locations 2&10, are in fact due to overlap in the heater wire at those locations.

The 1-g results described above for slug flow agree well with the findings of Vijay, Savic, and Sims [10]. They hypothesized that the effect of buoyancy forces on the gas bubbles caused the gas to have a greater velocity than the surrounding liquid. This "slip" between the phases led to a breakdown in the laminar sub-layer near the tube wall, thus leading to a movement away from laminar flow-type behavior (i.e., a relatively long thermal entry length). However, under  $\mu$ -g conditions this does not happen. The reduction of gravity greatly lessens the buoyancy forces and therefore the turbulence-generating ability of the gas bubbles; Elkow & Rezkallah [11]. The bubble movement at  $\mu$ -g do not largely interfere with the maintenance of the laminar sub-layer. Further analysis based on the flow regime associated with the flow were made, and results can be found in Rite [9].

## VOID-FRACTION RESULTS

Void fraction measurements ranging from approximately 0.1 to 0.9, and covering flow regimes from bubbly to annular flow were simultaneously obtained during flight testing. The results for slug flow are presented here. Complete results over the entire range of flow regimes can be found in Elkow [12]. In a comparison of the overall average void fraction values, it was found that small differences exist between the 1-g and  $\mu$ -g cases only for bubble and slug flows. The overall average void fraction for slug flow was approximately 10% higher at  $\mu$ -g conditions when compared to 1-g. However, instead of only considering the average values, the temporal fluctuations were analyzed with the use of Probability Density Function (PDF) plots.

### Slug Flow Results

The PDF plots are shown for slug flow in Figures 5(a) and 5(b) for  $\mu$ -g and 1-g, respectively. For these figures, the flow rates were  $V_{SL} = 0.24$  m/s and  $V_{SG} = 0.19$  m/s. The PDF plots show that there is a greater fluctuation in void fraction at 1-g. For this type of flow, the predominant forces include those due to buoyancy, surface tension, and turbulent stresses. At 1-g, forces due to gravitational acceleration tend to accelerate the bubbles and hence increase the probability of their interactions and coalescence.

Slug flow is characterized by the presence of "bullet shaped" bubbles, commonly known as Taylor bubbles. Due to buoyancy effects at 1-g, smaller bubbles will eventually "catch-up" with the Taylor bubble and hence increase  $\alpha$ . An additional factor at 1-g is due to slip. Since there is a relative velocity between the liquid and gas phases, a low pressure region in the wake of the Taylor bubble exists. Therefore, smaller bubbles are drawn into the trailing end of the Taylor bubble, causing coalescence to occur due to the high turbulent mixing. Thus, at 1-g, as shown in Figure 5(a), fluctuations can be seen from  $\alpha=0.0$  to approximately 0.75. With buoyancy negligible at  $\mu$ -g, turbulence is lower, resulting in a more structured flow. For this case the void fraction fluctuations were between  $\alpha = 0.3$  to 0.55.

Further discussion and interpretation of the PDF results can be made based on the flow images shown in Figures 6(a) and 6(b). Taylor bubble like flows at  $\mu$ -g are more uniform in length (Figure 6b). The Taylor bubbles at  $\mu$ -g vary from only 1 to 3 tube diameters, whereas at 1-g the Taylor bubble for the same flow rates ranges from 1 to 6 tube diameters. Further evidence of the effects of buoyancy can be seen in the flatter trailing end of the Taylor bubble at 1-g (Figure 6a), whereas the trailing end of the Taylor bubble at  $\mu$ -g (shown in Figure 6b) where buoyancy is negligible, is seen to be more rounded.

Buoyancy causes a relative velocity difference between the liquid and gas phases. With the gas phase having the higher velocity, a low pressure region at the tail of the Taylor bubble would occur. From the video recordings in this region, it has been observed that coalescence is enhanced when another Taylor bubble approaches this low pressure region. However, at  $\mu$ -g there is essentially no slip, thus a low pressure region at the tail of a Taylor bubble does not exist. It has been observed from video recordings that Taylor bubbles within close proximity to each other rarely coalesce at  $\mu$ -g.

Heat transfer measurements in slug flow, shown earlier in Figure 3(a), indicate that the heat transfer coefficients at 1-g can be 28 to 40% higher than their counterparts at  $\mu$ -g (corresponding to

a void fraction increase from approximately 0.3 to 0.65). This could be perhaps explained in terms of the results shown in Figures 6(a)&(b). The wider fluctuations at 1-g enhance mixing due to the greater turbulence, resulting in higher heat transfer coefficients.

## SUMMARY AND CONCLUSIONS

It was found that for low liquid flow rates reduced gravity retards the heat transfer coefficient by up to 50% at the lowest gas qualities (bubbly and slug flow regimes). As the gas quality is increased (transition to annular flow), the difference between the 1-g and  $\mu$ -g heat transfer coefficients becomes smaller. At higher liquid velocities, an increase in the gas quality results in the  $\mu$ -g heat transfer coefficients being greater than those at 1-g by approximately 10%, which is within the uncertainty of the measurements. The influence of gravity was found to be both a single-phase effect and a two-phase effect. Mixed convection in the liquid phase affects the heat transfer coefficients, and reduced gravity has a substantial influence on the interfacial surface between the two phases.

Using a capacitance void fraction sensor, volumetric void fraction measurements were obtained for adiabatic two-phase, water-air flows at 1-g and  $\mu$ -g. Comparisons of the void fraction signals at both gravity levels were made using PDF plots. It was found that a greater fluctuation in void fraction for slug flow existed at 1-g. At ground conditions fluctuations were in the range,  $0 < \alpha < 0.75$ , while at  $\mu$ -g the fluctuations were within a much narrower range;  $0.3 < \alpha < 0.55$ . The PDF histograms for annular flow were found to be similar for both 1-g and  $\mu$ -g flows. A very narrow fluctuation from approximately  $0.8 < \alpha < 0.9$  was observed. This is expected since the flow in this regime is highly inertia dominated.

## Acknowledgments

The authors acknowledge the financial assistance of the Microgravity Science Program of the Canadian Space Agency (CSA), and NSERC.

## REFERENCES

- [1] Papell, S.S. (1962) An instability effect on two-phase heat transfer for subcooled water flowing under conditions of zero gravity *American Rocket Society 17th Annual Meeting and Space Flight Exposition*.
- [2] Feldmanis, C.J. (1966) Pressure and temperature changes in closed loop forced convection boiling and condensing processes under zero gravity conditions *Institute of Environmental Sciences' 1966 Annual Technical Meeting Proceedings*.
- [3] Reinarts, T., Best, F.R., and Hill, W.S. (1992) Definition of condensation two-phase flow behaviors for spacecraft design *AIP Conference Proc.*, Vol. 246, pp.1216-1225.
- [4] Ohta et al.(1994) Microgravity flow boiling in a transparent tube *10th International Heat Transfer Conference*, Brighton, England, No. 111.
- [5] Rite, R.W., and Rezkallah, K.S. (1993) An investigation of transient effects on heat transfer measurements in two-phase gas-liquid flows under microgravity conditions *ASME Heat Transfer in Microgravity Systems - 1993*, pp. 49-57.
- [6] Rite, R.W. and Rezkallah, K.S. (1994a) Heat transfer in two-phase flow through a circular tube at reduced gravity *Journal of Thermophysics and Heat Transfer*, Vol. 8, No. 4, pp. 702-708.
- [7] Rite, R.W., and Rezkallah, K.S. (1994b) The influence of liquid viscosity on heat transfer coefficients in gas-liquid flows under microgravity conditions *AIP Conference Proc.*, Vol. 301, pp. 1129-1136.
- [8] Zhao, L. and Rezkallah, K.S. (1993) The transient effects on the two-phase flow heat transfer at microgravity, *29th National Heat Transfer Conference*, Paper No. 93-3905, Atlanta, GA.
- [9] Rite, R.W. (1995) *Heat Transfer in Gas-Liquid Flows through a Vertical, Circular Tube under Microgravity Conditions*, Ph.D. Thesis, Saskatoon: University of Saskatchewan.
- [10] Vijay, M. M., Savic, P., and Sims, G. E., 1978, "The Graetz Problem for Two-Phase Two-Component Gas-Liquid Flow in Vertical Tubes," *Proc. 6th Int. Heat Transfer Conf.*, Vol. 1, pp. 493-497.
- [11] Elkow, K.J., 1995, "Void-Fraction Measurements and Analysis at Normal and Microgravity Conditions, M.Sc. Thesis, University of saskatchewan, saskatoon, Canada.
- [12] Elkow, K.J., and Rezkallah, K.S., 1996, " Void-Fraction Measurements in Gas-Liquid Flows Using capacitance Sensors, *J. Measurement Science & Technology*, (in press).

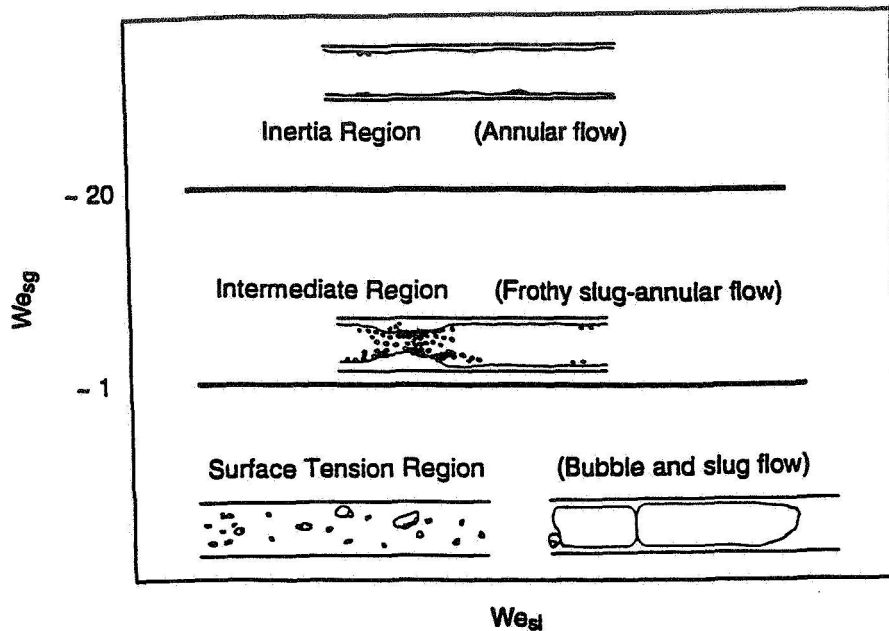


Figure 1. Weber Number based Flow Pattern Map for Two-Phase Flows at Microgravity

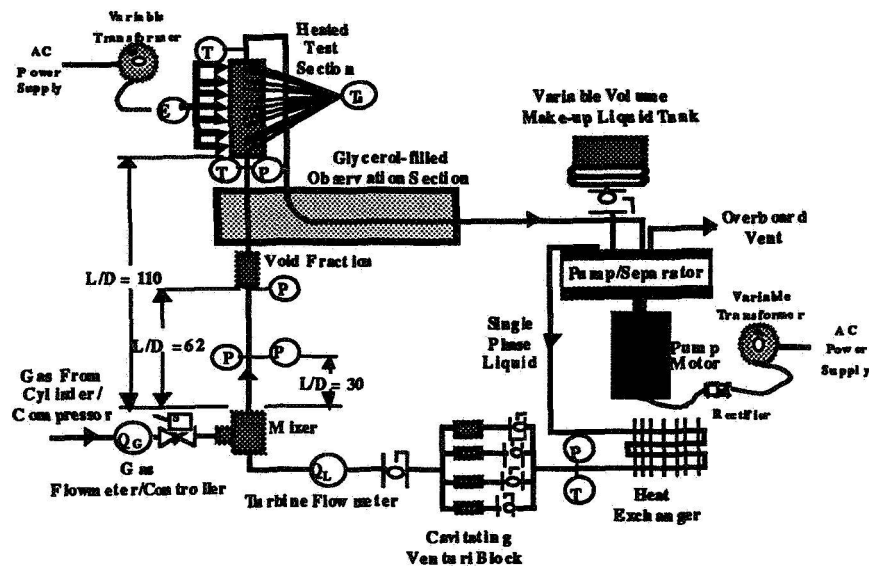


Figure 2. A Schematic of the Two-Phase Flow Loop

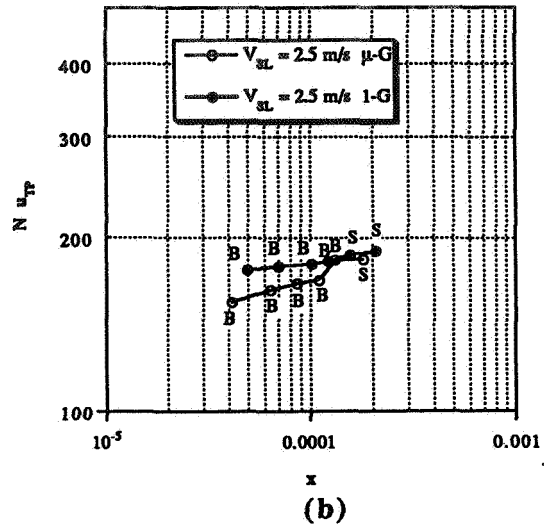
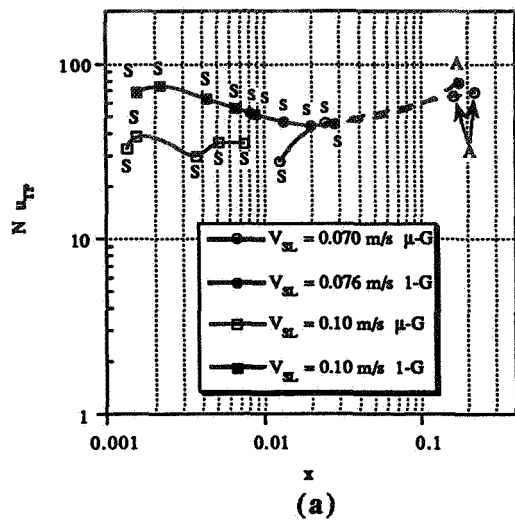


Figure 3. Mean Heat Transfer Results at Microgravity; (a)  $V_{sl}=0.07\&0.1$  m/s, (b)  $V_{sl}=2.5$  m/s

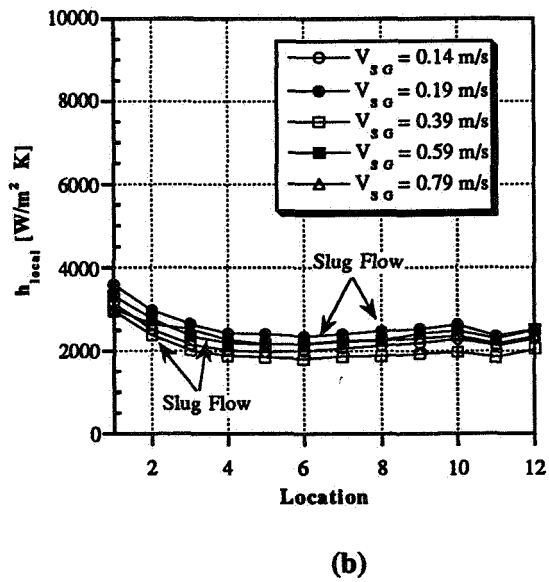
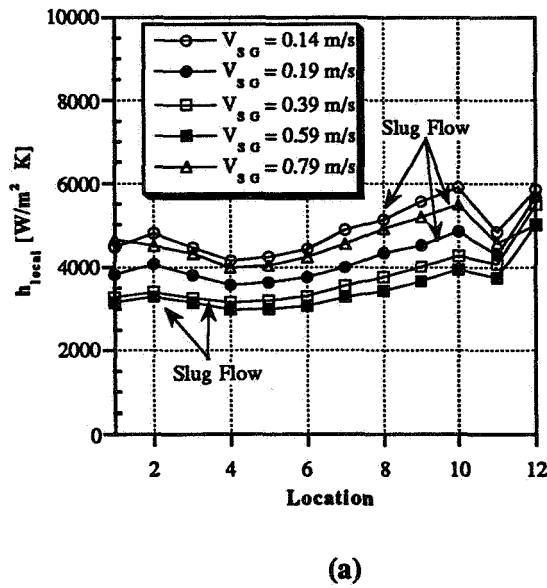
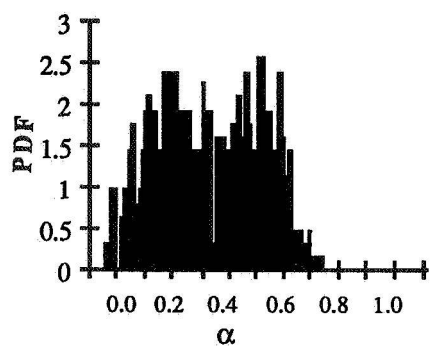
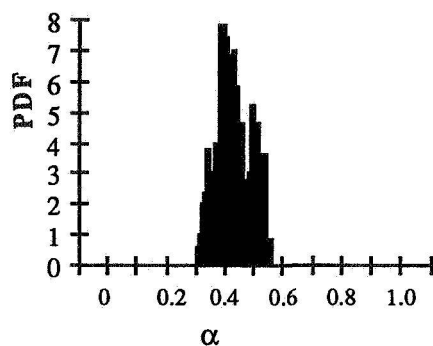


Figure 4. Local Heat Transfer Coefficients at  $V_{SL}=0.10$  m/s; (a) 1-g, (b)  $\mu$ -g

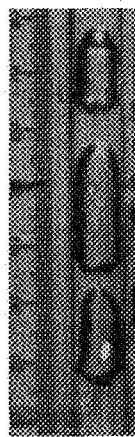
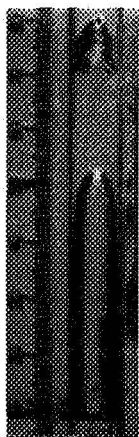
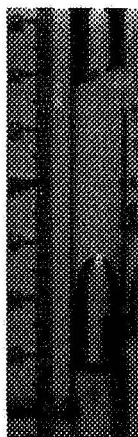


(a)



(b)

Figure 5. Propability Density Functions for Slug Flow; (a) at 1-g, (b) at  $\mu$ -g



(a)

(b)

Figure 6. Flow Images of Slug flow; (a) at 1-g, (b) at  $\mu$ -g





## MICROGRAVITY PARTICLE DYNAMICS

Ivan O. Clark, NASA Langley Research Center, Hampton, Virginia, 23681

Edward J. Johnson, Lockheed Martin, Hampton, Virginia, 23666

### ABSTRACT

The physical scales of velocity, length, time, thermal gradient magnitude, and velocity gradient magnitude likely to be involved in laminar gas-solid multiphase flight experiments are assessed for 1-100  $\mu\text{m}$  particles.

### INTRODUCTION

This research seeks to identify the experimental design parameters for future flight experiments to better resolve the effects of thermal and velocity gradients on gas-solid flows. By exploiting the reduced body forces and minimized thermal convection currents of reduced gravity experiments, features of gas-solid flows normally masked by gravitationally induced effects can be studied using flow regimes unattainable under unigravity.

A complex interaction of forces normally governs the motion of solid particles which are conveyed pneumatically [1]. Forces due to viscous drag, gravity, inertia, velocity gradients, rotation, buoyancy, thermal gradients and several other causes may be present depending on the physical environment. The present research focuses on the effects of thermal and velocity gradients on the motion of solid particles in a laminar flow field. Thermal gradients induce an additional force on the particles, known as a thermophoretic force, which causes the particle trajectory to deviate from the fluid streamlines [2]. This force is dependent on the strength of the thermal gradient, the size of the particle, and the thermophysical properties of both the particle and the fluid. Many numerical simulations rely on simple empirical expressions or an interpolation scheme based on Knudsen number developed by Talbot [2] to provide an expression for the thermophoretic force acting on a particle. Numerical investigations in laminar tube flows [3] and investigations of thermophoretic effects in stagnation point flows [4] show that additional terms must also be considered in these non-isothermal systems to adequately characterize the motion of suspended particles. The adverse effects of thermophoresis on particle-based velocimetry instrumentation is also of concern [5].

Particles transiting a flow field containing a velocity gradient or shear will experience an additional force causing them to deflect from the surrounding fluid streamlines if they deviate from the local velocity of the fluid. Saffman [6] demonstrated, for laminar flows, that the physical origins of this force lie in the variation of the pressure distribution acting on the surface of the particle. This force causes the particle to migrate to specific regions of shear. Segré and Silberberg [7] observed that small, neutrally buoyant spheres in Poiseuille flow migrate to a position 0.6 tube radii from the axis. Experimental observations of liquid droplets in Poiseuille flow demonstrated that lift forces may direct the particles toward or away from the centerline depending on the particle and shear properties [8]. Lift forces acting on freely rotating particles in close proximity to walls have been investigated [9] and the effects of nonuniform particle concentrations in compressible shear flows and particle inertia on the accuracy of particle-based velocimetry instrumentation have also been studied [10].

### EXPERIMENTAL CONSIDERATIONS

A uniformly accepted mathematical treatment for the motion of a solid particle through a compressible gas containing both velocity and thermal gradients does not exist in a simple form. For experiment planning, one can assume that any experiment package suitable for flight or drop tower tests will require that the experiment be contained in an enclosure: either in an enclosed space or in a tube or duct. For experiments involving a flowing gas or liquid, some entry length and characteristic time is required for the system to reach hydrodynamic and thermal equilibrium. A discussion of the characteristic lengths and times associated with a large enclosure is quite complex. Restricting discussions to enclosure sizes more likely to be encountered in flight experiments reduces this complexity. For example, analysis of laminar flow in a tube provides a great deal of insight into the length and time scales likely to be encountered in a wide class of flight experiments. This is the classic Poiseuille flow

for which hydrodynamic and thermal entry lengths are well established. The hydrodynamic and thermal entry length equations are derived from conservation of momentum and energy equations by Kays and Crawford [11] in the following forms, neglecting axial conduction:

$$\begin{array}{llll} \text{Hydrodynamic entry length, } x & x = \frac{Re D}{20} & \text{Reynolds number} & Re = \frac{U D}{\nu} \\ \text{Thermal entry length, } x & x = \frac{Re Pr D}{20} & & \end{array}$$

where  $x$  is the axial location of fully developed flow,  $U$  is the fluid velocity,  $D$  is the tube diameter,  $Re$  is the Reynolds number based on the tube diameter,  $\nu$  is the kinematic viscosity of the fluid, and  $Pr$  is the Prandtl number. The Prandtl number is the ratio of the momentum diffusivity to the thermal diffusivity. In fluids with  $Pr > 1$ , the hydrodynamic profile develops faster than the thermal profile. The thermal entry length solution above applies to cases where  $Re Pr > 100$ .

By selecting Reynolds numbers and tube diameters, the equations above may be used to estimate the hydrodynamic and thermal entry lengths and the characteristic velocity of the system. A worst-case time scale can also be derived by dividing the maximum of the two length scales above by the characteristic velocity scale. Table I presents the results of such calculations for some common materials whose Prandtl numbers span four orders of magnitude at 300K. The Reynolds numbers are fixed at 1000 and 500 to maintain a laminar flow. For comparison, a Reynolds number of 2300 would normally indicate a turbulent flow in a tube. Tube diameters are selected to be 2.54 cm and 1.27 cm. Selection of  $Re$  and  $D$  fixes the hydrodynamic entry length scale independent of the fluid under consideration. As expected from the linear relations above, reducing the Reynolds number for a given diameter reduces the fluid entry length, thermal entry length and characteristic velocity but maintains the same time scale. Reducing the diameter at a given Reynolds number reduces the fluid entry length, thermal entry length and time scale but increases the velocity scale. For enclosed laminar experiments involving gases, it is desirable to reduce the Reynolds number and increase the tube diameter. Among the possible costs of this solution are that the desired fluid dynamic regime may not be attained and/or gravitational terms may become significant in the transport of solid particles relative to the reduced hydrodynamic drag.

It is possible to assess the response of a solid particle to an abrupt change in the fluid velocity, in a general way, by consideration of the so-called particle relaxation time. That is, the time required for a particle to adjust its velocity to match a change in the fluid velocity to within a very small percentage. Neglecting gravity, an expression for the particle relaxation time is derived by Hinds [12] in the following form for particle motion in the Stokes region and  $Re$  (based on the particle diameter) less than one:

$$\text{Relaxation time, } \eta \quad \eta = \frac{\rho_p d^2 C_c}{18 \mu} \quad \text{with} \quad C_c = 1 + \frac{\lambda}{d} [2.514 + 0.800 \exp(-0.55 \frac{d}{\lambda})]$$

where  $d$  is the particle diameter,  $\rho_p$  the particle density,  $\mu$  the fluid dynamic viscosity,  $C_c$  the Cunningham slip correction factor, and  $\lambda$  is the mean free path of a fluid molecule at the temperature and pressure under consideration. In all that follows, atmospheric pressure will be assumed and the focus will be on the gas-solid flow case. A nondimensional parameter known as the Knudsen number may be defined as  $Kn = 2\lambda/d$  which relates the mean free path to the particle radius. By selecting specific particle and gas parameters, the equations above and the Reynolds condition for Stokes flow provide a means to calculate a particle relaxation time and determine the maximum velocity for which Stokes hydrodynamic drag applies. The results of such calculations are presented in Table II for two types of particles in a size range from 1-100  $\mu\text{m}$  in both hydrogen and air over a range of temperatures. The specific particles used in these calculations are alumina ( $\text{Al}_2\text{O}_3$ ) with a density of 3970  $\text{kg/m}^3$  and polystyrene latex (PSL) with a density of 1050  $\text{kg/m}^3$ . The diameters used are assumed to be equivalent spherical diameters and the intent is for the PSL particle to represent a low density particle and for the alumina to represent a medium density particle. Both materials are in common use as seed particles for particle-based velocimetry instruments. These simple calculations of the Knudsen number and the maximum velocity for which Stokes drag applies contain no particle properties other than the diameter. Hence, the results for alumina and PSL, or any other particle type, depend only on the thermodynamic properties of the fluid at the local

temperature and pressure. The results indicate that maximum velocity for Stokes conditions on the particle is highly dependent on the local temperature and fluid properties. It may range from a few meters per second through supersonic velocities depending on the local conditions. These simple calculations also indicate that small particles may be expected to adapt to changes in the fluid velocity extremely rapidly. An incorrect conclusion may be drawn from such an analysis that the motion of sufficiently small particles in laminar flow is governed solely by hydrodynamic drag for a given fluid and temperature. Indeed, hundreds of successful numerical models and particle-based experiments have been conducted based on this assumption. However, there are many forces besides drag which may be present in a given situation and which may impact the particle motion.

As described by Soo [13] and others, Tchen is generally credited with deriving the first widely accepted Lagrangian equation for the motion of a solid particle in an unsteady gas flow field. In what follows, the discussion of Tchen's equation parallels Nichols [14]. The basic equation, in index notation, takes the form:

$$m_p \frac{dv_i}{dt} = -3 \pi \mu d (v_i - u_i) + m_f \frac{Du_i}{Dt} - \frac{1}{2} m_f \frac{d}{dt} (v_i - u_i) - \frac{3}{2} \frac{d^2}{dt^2} \sqrt{\pi \rho_f \mu} \int_0^t \frac{d}{d\tau} (v_i - u_i) d\tau - g_i (m_p - m_f)$$

with

$$\frac{Du_i}{Dt} = \frac{\partial u_i}{\partial t} + u_j \frac{\partial u_i}{\partial x_j} \quad \frac{du_i}{dt} = \frac{\partial u_i}{\partial t} + v_j \frac{\partial u_i}{\partial x_j}$$

where  $v_i = v_i(t)$ ,  $u_i = u_i(t)$  and  $g_i$  are respectively the component at time  $t$  in the  $x_i$  direction of the particle velocity, fluid velocity, and gravitational acceleration;  $m_p$  is the mass of the particle;  $m_f$  is the mass of a volume of fluid equal to the particle volume; and  $\rho_f$  is the fluid density. The terms on the right represent forces acting on the particle associated with Stokes drag, the pressure distribution, the additional mass of fluid which must be accelerated along with the particle, a Basset history integral over time  $\tau$  (related to the acceleration history of the particle), and gravity.

An idealized, quasi-one-dimensional problem provides a convenient way to assess the relative contributions of the various forces acting on a solid particle in a gas flow field. The case of the gas flow undergoing a step change in velocity is considered. For this case the Tchen equation is solved either numerically using a 4th order Runge-Kutta technique, if the Basset term is included, or analytically if the Basset term is dropped. The analytic solution for the relative velocity between the particle and the gas is in the form of a decaying exponential which provides a more exact determination of the particle relaxation time than the expression above. For this case, the force terms in the Tchen equation are supplemented with expressions for a shear-induced lift force and a thermophoretic force arising from thermal gradients in a laminar flow. As noted by Nichols [14], the shear-induced lift force or Saffman force has the form:

$$\text{Shear-induced lift, } F_{L,i} \quad F_{L,i} = 1.6125 d^2 \sqrt{\rho_f \mu} \left| \frac{\partial u_i}{\partial x_j} \right|^{1/2} (v_i - u_i)$$

while Talbot [2] provided an expression for the force due to a thermal gradient in the form:

$$\text{Thermophoretic force, } F_{T,i} \quad F_{T,i} = \frac{\pi \mu v d}{2 |T|} \alpha(Kn) \frac{\partial T}{\partial x_i} \quad \text{with} \quad \alpha(Kn) = 12 C_s \frac{k_f / k_p + C_i Kn}{(1 + 3 C_m Kn)(1 + 2 k_f / k_p + 2 C_i Kn)}$$

representing a thermophoretic correction factor based on the Knudsen number. Thermal conductivities of the gas and particle are  $k_f$  and  $k_p$ , respectively, and  $C_s=1.147$ ,  $C_i=2.20$  and  $C_m=1.146$  are empirically derived constants.

The equations for shear-induced lift and thermophoretic force combined with a solution to Tchen's equation for the one-dimensional step change in gas velocity provide a means to quantify the relative contributions of the force terms. By selecting the gas, temperature, magnitude of the step change in velocity, particle size, and particle type, the magnitudes of the velocity and thermal gradients required to produce a lift or thermophoretic force equal to the drag, gravitational, or Basset force acting on the particle may be determined. Table III presents the results of such a calculation for a 1  $\mu\text{m}$  particle experiencing a 1 mm/s relative velocity in both hydrogen and air over a range of temperatures. Table IV presents similar calculations for the case in which the temperature is held fixed and the particle diameter is varied for the case of an alumina particle in hydrogen at 300K. Table V presents the case in which the gas, temperature, particle size and particle type are fixed and the

relative velocity is varied from 1 mm/s to 10 m/s. Experimental flow and thermal field measurements for chemical vapor deposition reactors at the NASA Langley Research Center indicate that thermal gradients consistent with these calculations can be easily established and that appropriate velocity gradients can be achieved [15].

## CONCLUSIONS

The following observations may be made from these calculations. First, the thermodynamic properties of the gas under consideration are extremely important in determining the contributions of the various force terms. Second, for small relative velocities, the magnitude of the velocity gradient required to produce a lift force equal to either the hydrodynamic drag or gravitational force are quite large. However, at higher relative velocities, it is possible for relatively modest velocity gradients to result in lift forces which exceed the gravitational forces acting on a particle. Third, thermal gradients are much more likely to produce a significant force acting on the particle relative to drag and gravity. This is especially true for small particles in high temperature flows. The exact conditions for maximum thermally-induced forces are not linear in temperature and depend on the gas under consideration. Resolution of the physics involved in gas-solid flows could be expected to improve significantly from experiments in microgravity where access to experimental conditions involving low speed flows with small velocity and/or thermal gradients and unrestricted particle size is not precluded by ground-based convection and sedimentation effects.

## REFERENCES

- [1] Barnett, D.O.: Seeding Requirements for Laser Velocimeter Utilization in Fluid Dynamics Facilities, Arnold Eng Dev Center, Arnold Air Force Station, TN, Final Report, Contract F40600-80-C-0002, Jan., 1981.
- [2] Talbot, L., Chen, R.K., Schefer, R.W., and Willis, D.R.: "Thermophoresis of particles in a Heated Boundary Layer," *J. Fluid Mechanics*, Vol. 101, Part 4, 1980, pp. 737-758.
- [3] Pratsinis, S.E., and Kim K.: "Particle Coagulation, Diffusion and Thermophoresis in Laminar Tube Flows," *J. Aerosol Sci.*, Vol. 20, No. 1, 1989, pp. 101-111.
- [4] Turner, J.R., Fissan, H.J., and Liguras, D.K.: "Particle Deposition from Plane Stagnation Flow: Competition between Electrostatic and Thermophoretic Effects," *J. Aerosol Sci.*, Vol. 19, No. 7, 1988, pp. 797-800.
- [5] Johnson, E.J., Hyer, P.V., Culotta, P.W. and Clark, I.O.: "Laser Velocimetry Measurements in Non-isothermal CVD Systems," *Laser Anemometry: Advances and Applications*, Vol. 2, 1991, eds., A. Dibbs and B. Ghorashi, ASME, pp. 483-489.
- [6] Saffman, P.G.: "The Lift on a Small Sphere in a Slow Shear Flow," *J. Fluid Mech.*, Vol. 22, part 2, 1965, pp. 385-400.
- [7] Segré, G. and Silberberg, A.: "Behavior of Macroscopic Rigid Spheres in Poiseuille Flow: Part 2. Experimental Results and Interpretation," *J. Fluid Mech.*, Vol. 14, No. 115, 1962, pp. 136-157.
- [8] McLaughlin, J.B.: "The lift on a small sphere in wall-bounded linear shear flows," *J. Fluid Mech.*, Vol. 246, 1993, pp. 249-265.
- [9] Cherukat, Pradeep, and McLaughlin, J.B.: "The inertial lift on a rigid sphere in a linear shear flow field near a flat wall," *J. Fluid Mech.*, Vol. 263, 1994, pp. 1-18.
- [10] Samimy, M. and Lele, S.K.: "Motion of Particles in a Compressible Free Shear Layer," *Phys. of Fluids A*, Vol. 3, No. 8, 1991, pp. 1915-1923.
- [11] Kays, W.M., and Crawford, M.E.: Convective Heat and Mass Transfer, McGraw-Hill, NY, 1980.
- [12] Hinds, W. C.: Aerosol Technology, John Wiley & Sons, NY, 1982.
- [13] Soo, S.L.: Multiphase Fluid Dynamics, Gower Technical, 1990.
- [14] Nichols, R.H.: The Effect of Particle Dynamics on Turbulence Measurements with the Laser Doppler Velocimeter, Ph.D. Dissertation, University of Tennessee, Knoxville, June, 1986.
- [15] Clark, I.O., Jesser, W.A., Hyer, P.V., and Johnson, E.J.: Microgravity Chemical Vapor Deposition, Proc. Microgravity Materials Science Conf., Huntsville, AL, June 10-11, 1996.

**Table I:** Characteristic times, thermal entry lengths and velocities associated with combinations of Reynolds numbers and length scales for some common liquids and gases.

	Prandtl number 300K	Time scale (s)	Tube diameter 0.0254 m				Tube diameter 0.0127 m			
			Re 1000 Fluid scale 1.27 m		Re 500 Fluid scale 0.635 m		Re 1000 Fluid scale 0.635 m			
			Thermal entry length (m)	Velocity scale (m/s)	Thermal entry length (m)	Velocity scale (m/s)	Time scale (s)	Thermal entry length (m)	Velocity scale (m/s)	
Mercury	2.48E-02	2.87E+02	3.15E-02	4.40E-03	1.57E-02	2.21E-03	7.17E+01	1.57E-02	8.86E-03	
Hydrogen	7.01E-01	2.91E-01	8.90E-01	4.37E+00	4.45E-01	2.19E+00	7.27E-02	4.45E-01	8.74E+00	
Air	7.07E-01	2.03E+00	8.98E-01	6.23E-01	4.49E-01	3.13E-01	5.07E-01	4.49E-01	1.25E+00	
Freon	3.50E+00	5.78E+02	4.44E+00	7.70E-03	2.22E+00	3.84E-03	1.45E+02	2.22E+00	1.54E-02	
Water	5.83E+00	2.20E+02	7.40E+00	3.37E-02	3.70E+00	1.68E-02	5.50E+01	3.70E+00	6.73E-02	
Ethylene Glycol	1.51E+02	3.45E+02	1.92E+02	5.55E-01	9.59E+01	2.78E-01	8.64E+01	9.59E+01	1.11E+00	

**Table II:** Relaxation times, maximum velocities which maintain Stokes conditions and Knudsen number for 1, 10 and 100  $\mu\text{m}$  alumina and polystyrene latex (PSL) particles.

Temp.	HYDROGEN				AIR			
	Alumina Relax. time	PSL Relax. time	Stokes Maximum Velocity	Kn	Alumina Relax. time	PSL Relax. time	Stokes Maximum Velocity	Kn
PARTICLE DIAMETER - 1 $\mu\text{m}$								
K	(s)	(s)	(m/s)		(s)	(s)	(m/s)	
100	5.84E-05	1.55E-05	1.76E+01	1.03E-01	3.18E-05	8.40E-06	2.32E+00	4.65E-02
300	3.65E-05	9.66E-06	1.10E+02	3.73E-01	1.51E-05	3.98E-06	1.53E+01	2.02E-01
500	3.35E-05	8.85E-06	2.59E+02	6.78E-01	1.22E-05	3.22E-06	3.70E+01	3.83E-01
1000	3.55E-05	9.38E-06	8.25E+02	1.53E+00	1.13E-05	2.98E-06	1.22E+02	8.56E-01
1500	3.96E-05	1.05E-05	1.62E+03	2.46E+00	1.18E-05	3.12E-06	2.45E+02	1.37E+00
2000	4.37E-05	1.16E-05	2.63E+03	3.44E+00	1.26E-05	3.32E-06	4.02E+02	1.97E+00
PARTICLE DIAMETER - 10 $\mu\text{m}$								
K	(s)	(s)	(m/s)		(s)	(s)	(m/s)	
100	5.24E-03	1.39E-03	1.76E+00	1.03E-02	3.02E-03	7.99E-04	2.32E-01	4.65E-03
300	2.59E-03	6.85E-04	1.10E+01	3.73E-02	1.23E-03	3.26E-04	1.54E+00	2.02E-02
500	1.91E-03	5.04E-04	2.59E+01	6.78E-02	8.57E-04	2.27E-04	3.70E+00	3.84E-02
1000	1.31E-03	3.47E-04	8.25E+01	1.53E-01	5.75E-04	1.52E-04	1.22E+01	8.56E-02
1500	1.10E-03	2.91E-04	1.62E+02	2.46E-01	4.67E-04	1.23E-04	2.45E+01	1.37E-01
2000	9.95E-04	2.63E-04	2.63E+02	3.44E-01	3.99E-04	1.06E-04	4.02E+01	1.97E-01
PARTICLE DIAMETER - 100 $\mu\text{m}$								
K	(s)	(s)	(m/s)		(s)	(s)	(m/s)	
100	5.18E-01	1.37E-01	1.76E-01	1.03E-03	3.00E-01	7.94E-02	2.32E-02	4.65E-04
300	2.49E-01	6.57E-02	1.10E+00	3.73E-03	1.20E-01	3.18E-02	1.54E-01	2.02E-03
500	1.77E-01	4.68E-02	2.59E+00	6.78E-03	8.22E-02	2.17E-02	3.70E-01	3.84E-03
1000	1.12E-01	2.97E-02	8.25E+00	1.53E-02	5.25E-02	1.39E-02	1.22E+00	8.56E-03
1500	8.65E-02	2.29E-02	1.62E+01	2.46E-02	4.05E-02	1.07E-02	2.45E+00	1.37E-02
2000	7.22E-02	1.91E-02	2.63E+01	3.44E-02	3.28E-02	8.67E-03	4.02E+00	1.97E-02

**Table III:** Magnitude of velocity and thermal gradients required to produce a lift or thermophoretic force equal in magnitude to the drag or gravitational force acting on a 1  $\mu\text{m}$  alumina particle experiencing a 1.0 mm/s relative velocity in hydrogen and air.

Temp. K	HYDROGEN				AIR			
	Velocity gradient		Thermal gradient		Velocity gradient		Thermal gradient	
	Drag (1/s)	Gravity (1/s)	Drag (K/m)	Gravity (K/m)	Drag (1/s)	Gravity (1/s)	Drag (K/m)	Gravity (K/m)
100	6.02E+08	1.24E+04	2.15E+04	1.09E+04	7.91E+07	2.49E+03	2.57E+05	7.55E+04
300	3.77E+09	1.49E+04	8.68E+03	2.11E+03	5.25E+08	2.76E+03	6.13E+04	7.21E+03
500	8.86E+09	1.62E+04	7.47E+03	1.28E+03	1.26E+09	2.91E+03	4.35E+04	3.48E+03
1000	2.82E+10	1.81E+04	7.57E+03	8.18E+02	4.17E+09	3.28E+03	3.56E+04	1.81E+03
1500	5.55E+10	1.94E+04	8.29E+03	6.82E+02	8.38E+09	3.52E+03	3.54E+04	1.38E+03
2000	9.00E+10	2.03E+04	9.06E+03	6.14E+02	1.37E+10	3.65E+03	3.75E+04	1.18E+03

**Table IV:** Magnitude of velocity and thermal gradients required to produce a lift or thermophoretic force equal in magnitude to the drag or gravitational force acting on an alumina particle experiencing a 1.0 mm/s relative velocity in hydrogen at 300K.

HYDROGEN				
Particle diameter (m)	Velocity gradient		Thermal gradient	
	Drag (1/s)	Gravity (1/s)	Drag (K/m)	Gravity (K/m)
5.0E-07	1.51E+10	7.44E+03	1.10E+04	6.67E+02
1.0E-06	3.77E+09	1.49E+04	8.68E+03	2.11E+03
1.0E-05	3.77E+07	1.49E+05	1.84E+04	4.45E+05
1.0E-04	3.77E+05	1.49E+06	1.09E+05	2.63E+08

**Table V:** Magnitude of velocity and thermal gradients required to produce a lift or thermophoretic force equal in magnitude to the drag or gravitational force acting on a 1  $\mu\text{m}$  alumina particle over a range of relative velocities in hydrogen at 300K.

HYDROGEN				
Relative velocity (m/s)	Velocity gradient		Thermal gradient	
	Drag (1/s)	Gravity (1/s)	Drag (K/m)	Gravity (K/m)
1.0E-03	3.77E+09	1.49E+04	8.68E+03	2.11E+03
1.0E-02	3.77E+09	1.49E+03	8.68E+04	2.11E+03
1.0E-01	3.77E+09	1.49E+02	8.68E+05	2.11E+03
1.0E+00	3.77E+09	1.49E+01	8.68E+06	2.11E+03
1.0E+01	3.77E+09	1.49E+00	8.68E+07	2.11E+03

# **Mechanics of Granular Media**





# MICROGRAVITY SEGREGATION IN BINARY MIXTURES OF INELASTIC SPHERES DRIVEN BY VELOCITY FLUCTUATION GRADIENTS

James T. Jenkins and Michel Y. Louge,  
Cornell University, Ithaca, NY 14853

## ABSTRACT

We are interested in collisional granular flows of dry materials in reduced gravity. Because the particles interact through collisions, the energy of the particle velocity fluctuations plays an important role in the physics. Here we focus on the separation of grains by properties - size, for example - that is driven by spatial gradients in the fluctuation energy of the grains.

The segregation of grains by size is commonly observed in geophysical flows and industrial processes. Segregation of flowing grains can also take place based on other properties, e.g. shape, mass, friction, and coefficient of restitution. Many mechanisms may be responsible for segregation; most of these are strongly influenced by gravity. Here, we outline a mechanism that is independent of gravity. This mechanism may be important but is often obscured in terrestrial grain flows. It is driven by gradients in fluctuation energy.

In microgravity, the separation of grains by property will proceed slowly enough to permit flight observations to provide an unambiguous measurement of the transport coefficients associated with the segregation. In this context, we are planning a microgravity shear cell experiment that contains a mixture of two types of spherical grains. The grains will be driven to interact with two different types of boundaries on either sides of the cell. The resulting separation will be observed visually.

## BACKGROUND

The size segregation of flowing or shaken grains is a commonly observed phenomenon in industrial processes and in nature. In many industrial processes a homogeneous aggregate is desired; in these, size segregation is undesirable. However, in the mining industry, segregation by size is exploited in some crushing operations. When observing natural grain deposits, grain segregation provides an indication of whether an aggregate of grains was deposited dry (larger grains above) or under water (larger grains below).

In systems that do not involve much agitation of the grains, several mechanisms that involve gravity have been identified as leading to such segregation. These include the preferential downward percolation of smaller particles in relatively slow inclined shear flows (e.g. Savage and Lun, 1988), the upward frictional ratcheting of large particles (e.g. Haff and Werner, 1986), and the preferential filling of space beneath larger particles by smaller particles in a system that is occasionally shaken (e.g. Rosato, Strandburg, Prinz and Swendsen, 1986, 1987).

In highly agitated flows there is a mechanism independent of gravity that is available to drive separation. This is associated with spatial gradients in the energy of the velocity fluctuations of the grains. Collisional interaction between and among different species of grains require that, in general, spatial gradients of concentration exist to balance spatial gradients of the particle fluctuation energy.

In sheared or vibrated collisional systems, gravity also influences mixtures of different size grains. Here, buoyant forces act to separate grains that differ in size and the local volume that they displace. The competition between buoyancy and gradients in concentration and energy may then

result in convection cells in which particles with different properties separate (e.g. Knight, Jaeger and Nagel, 1993).

In reduced gravity, such convection is suppressed and attention can be focused on the simpler balance between gradients in concentration and the gradients in fluctuation energy. Reduced gravity also eliminates the possibility that a collisional flow will condense into a slower, denser flow dominated by enduring contacts rather than by collisions.

Because collisions between grains inevitably dissipate energy, collisional granular shear flows are usually of limited extent in the direction transverse to the flow. One consequence is that shear flows are strongly influenced by their boundaries. Because grains, on average, slip relative to boundaries, a bumpy or frictional boundary can provide energy to the velocity fluctuations. However, because collisions between grains and the boundary dissipate fluctuation energy, there is a competition between production and dissipation.

In principle, it is possible to design the geometry of the boundary - for example, the size and spacing of regular bumps - so that the boundary either produces or dissipates fluctuation energy (e.g. Jenkins and Askari, 1993). This permits the control of the component of the spatial gradient of the fluctuation energy that is normal to the boundary. The gradients in fluctuation energy established by such boundaries may be exploited to drive the separation by size or other properties in a binary mixture of spherical grains.

We note here that microgravity makes the visual observations possible by permitting us to employ moderate rates of shear. On earth, the effects of gravity can be minimized by shearing so rapidly that the particle pressure overwhelms gravity. However, in this event, separation takes place too rapidly for visual observation, buoyancy and/or condensation associated with the centripetal acceleration must be accounted for, and the particles can be severely damaged.

Here we sketch the existing theory for collisional shear flows of binary mixtures of smooth, nearly elastic spheres (Jenkins and Mancini, 1987, 1989) and introduce the numerical simulations of the complete flow in the microgravity shear cell (Hopkins and Louge, 1991; Louge, 1994). The link between theory, simulations and experiments is provided by measurements of collision parameters in the apparatus described by Foerster, Louge, Chang and Allia (1994).

## THEORY

Rather than providing here an exhaustive description of the complete theory, we introduce the governing equations for an unsteady, rectilinear shearing flow of a binary mixture of frictionless spheres, in which the gradient of the mixture velocity is vertical. These equations govern the time dependent response of an initially steady shearing flow to an increment in boundary velocity. This example provides an indication of how unsteadiness and gravity influence the theory for segregation.

In this case, the horizontal and vertical components of the balance of momentum for the mixture as a whole may be written as

$$\rho \dot{u} = S' \text{ and } 0 = -P' - \rho g,$$

where  $\rho$  is the mixture mass density,  $u$  is the horizontal component of the mixture velocity,  $S$  and  $P$  are the mixture shear stress and pressure,  $g$  is the gravitational acceleration, and overdots and primes indicate derivatives with respect to time and vertical coordinate, respectively. The shear stress  $S$  is proportional to  $u'$  and the pressure  $P$  is proportional to the mixture fluctuation energy  $T$ . The coefficients in these expressions are given by Jenkins and Mancini (1989) for frictionless spheres as explicit, but extremely complicated, functions of the number densities, masses, radii, and coefficients of restitution of the two types of spheres.

Similarly, the balance of fluctuation energy for the mixture is

$$(3/2) \rho \dot{T} = -Q' + S u' - \rho \gamma,$$

where  $Q$  is the flux of mixture fluctuation energy, and  $\gamma$  is the rate of mixture dissipation of fluctuation energy due to the inelasticity of the collisions. The flux of fluctuation energy is proportional to  $T'$  and the rate of collisional dissipation  $\gamma$  is proportional to  $T^{3/2}$ . Jenkins and Mancini (1989) again provide the explicit forms of the coefficients. The presence of the collisional dissipation in the energy balance distinguishes the macroscopic system from its molecular counterpart.

Time dependent segregation of the spheres is described by an expression related to an approximate form of the difference between the balance of momentum for each species:

$$v_A - v_B = -n^2 D_{AB} (d_A + K_T T') / n_A n_B,$$

where  $v_A$  and  $v_B$  are the vertical components of the diffusion velocities,  $n_A$  and  $n_B$  the number densities of the two species,  $n$  is their sum,  $D_{AB}$  and  $K_T$  are, respectively, the coefficients of ordinary and thermal diffusion, and  $d_A$  is the vertical component of the diffusion force. It has the form

$$d_A = B_A P' + C_A T' + D_A n_A' + E_A n_B',$$

where the explicit forms for these and the diffusion coefficients are provided by Jenkins and Mancini (1989). When  $v_A - v_B$  is different from zero, segregation is taking place; when  $v_A - v_B$  vanishes, a steady balance between the gradients of fluctuation energy and gradients of species number density is attained. Segregation is influenced by gravity through the presence of  $P'$  in  $d_A$ .

Boundary conditions are obtained by calculating the collisional exchange of momentum and energy at the boundary. An expression for the slip velocity of the mixture results from balancing the sum of the collisional production of momentum with the mixture shear stress. The energy balance at the wall equates the normal component of the flux of mixture fluctuation energy to the working of the mixture shear stress less the sum of the species' collisional dissipation. Mancini's (1986) derivation of boundary conditions for bumpy, frictionless boundaries will be extended to include friction, and boundaries that produce fluctuation energy will be distinguished from boundaries that dissipate it.

In Figure 1 we show concentration profiles of two phases in a steady, fully-developed flow driven by the relative motion of identical, parallel, bumpy boundaries in the absence of gravity. These were obtained by Mancini (1986) as numerical solutions of the governing equations and boundary conditions for spheres of different diameters made of the same material. The boundary spheres were of the same diameter as the spheres of phase B and were assumed to be affixed in an hexagonal close-pack to two flat wall that were separated by a distance of 6.5 diameters of phase B. The spheres of phase A had a diameter 0.7 that of phase B, the average concentration of both species was taken to be 0.25, and the coefficients of restitution for all collisions were equal to 0.9. The full line in the figure is the concentration profile for a single phase of species B.

## COMPUTER SIMULATIONS

The computer simulations are carried out to guide the design of the microgravity shear cell and inform the development of theory. The idea is to follow the dynamics of an ensemble of spheres interacting with the boundaries and among themselves through individual impacts. The

impacts are characterized by the three-parameter model that we establish for real spheres using the experiment described later.

Particle simulations are extensively used to perform numerical granular flow experiments. Chief among these simulations are the deformable particle simulations, in which the inter-particle forces are modeled during every impact (Walton 1983; Walton and Braun, 1986; Walton, Braun, Mallon and Cervelli, 1989) and the rigid particle simulations in which only the collisional impulses are modeled (Campbell, 1982, 1989).

Unlike earth-bound granular flows, bounded shear flows under low gravity do not readily condense into amorphous regions of negligible agitation. Without such condensation, the forces are primarily impulsive. In this case, Hopkins and Louge (1991) describe an efficient algorithm that permits simulations involving up to a hundred thousand spheres on a workstation of relatively modest size.

In their algorithm, collisions occur when a sphere overlaps slightly with another sphere or with the wall. The algorithm adjusts its time step periodically to ensure that the mean overlap is kept below a negligible tolerance. In addition, a search grid is superimposed on the flow domain to permit fast identification of near neighbors. Because this method makes it superfluous to maintain a list of future impacts, its computing time is merely proportional to the number of spheres  $N$ , unlike other algorithms that grow as  $N \ln N$  or even  $N^2$ . Figure 2 is an example of a microgravity shear cell geometry that we contemplate.

#### ACKNOWLEDGMENTS

The preparation of this manuscript was supported by NASA's Microgravity Science and Applications Division.

#### REFERENCES

- Campbell, C S, 1982 Shear Flows of Granular materials. Ph.D. Dissertation, California Institute of Technology, Pasadena, California.
- Campbell, C S, 1989 The stress tensor for simple shear flow of a granular material. *J. Fluid Mech.* 203, 449-73.
- Foerster, S, M Y Louge, H Chang and K Allia 1994 Measurements of the Collision Properties of Small Spheres. *Phys. Fluids* 6, 1108-15.
- Haff, P K, and B T Werner 1986 Computer simulation of the mechanical sorting of grains. *Powder Tech.* 48, 239-45.
- Hopkins, M A and Louge M 1991 Inelastic Microstructure in Rapid Granular Flows of Smooth Disks. *Phys. Fluids A* 3, 47-57.
- Jenkins, J T, and Askari, E 1993 Rapid granular shear flows driven by identical, bumpy, frictionless boundaries. In *Powders and Grains 93* (C Thornton, Ed.) Balkema, Rotterdam, pp. 295-300.
- Jenkins, J T, and F Mancini 1987 Balance laws and constitutive relations for plane flows of a dense, binary mixture of smooth, nearly elastic disks. *J. Appl. Mech.* 109, 27-34.
- Jenkins, J T, and F Mancini 1989 Kinetic theory for binary mixtures of smooth, nearly elastic spheres. *Phys. Fluids A* 1, 2050-7.
- Knight, J B, H M Jaeger and S R Nagel 1993 *Phys. Rev. Lett.* 70, 3728-31.

- Louge, M Y, 1994 Computer simulations of rapid granular shear flows of spheres interacting with a flat, frictional boundary. *Phys. Fluids* 6, 2253-69.
- Mancini, F, 1986 Transport Theory for Dense Binary Mixtures of Smooth, Round, Nearly Elastic Particles. Ph.D. Dissertation, Cornell University, Ithaca, NY.
- Rosato, A, K J Strandburg, F Prinz and R H Swendsen 1986 Monte Carlo simulation of particulate matter segregation. *Powder Tech.* 49, 59-69
- Rosato, A, K J Strandburg, F Prinz and R H Swendsen 1987 Why the Brazil nuts are on top: size segregation of particulate matter by shaking. *Phys. Rev. Lett.* 58, 1038-40.
- Savage, S B and C K K Lun 1988 Particle size segregation in inclined chute flow of dry cohesionless granular solids. *J. Fluid Mech.* 189, 311-35.
- Walton, O R, 1983 Particle-dynamics calculations of shear flow. In *Mechanics of Granular Materials - New Models and Constitutive Relations*, (J T Jenkins and M Satake, Eds.) Elsevier, Amsterdam, pp. 327-38.
- Walton, O R, and R L Braun. 1986 Viscosity, granular-temperature, and stress calculations for shearing assemblies of inelastic, frictional disks. *J. Rheol.* 30, 949-80.
- Walton, O R, R L Braun, R G Mallon and D M Cervelli 1989 Particle-dynamics calculations of gravity flow of inelastic, frictional spheres. In *Micromechanics of Granular Materials* (M Satake and J T Jenkins, Eds.), Elsevier, Amsterdam, pp. 153-62.

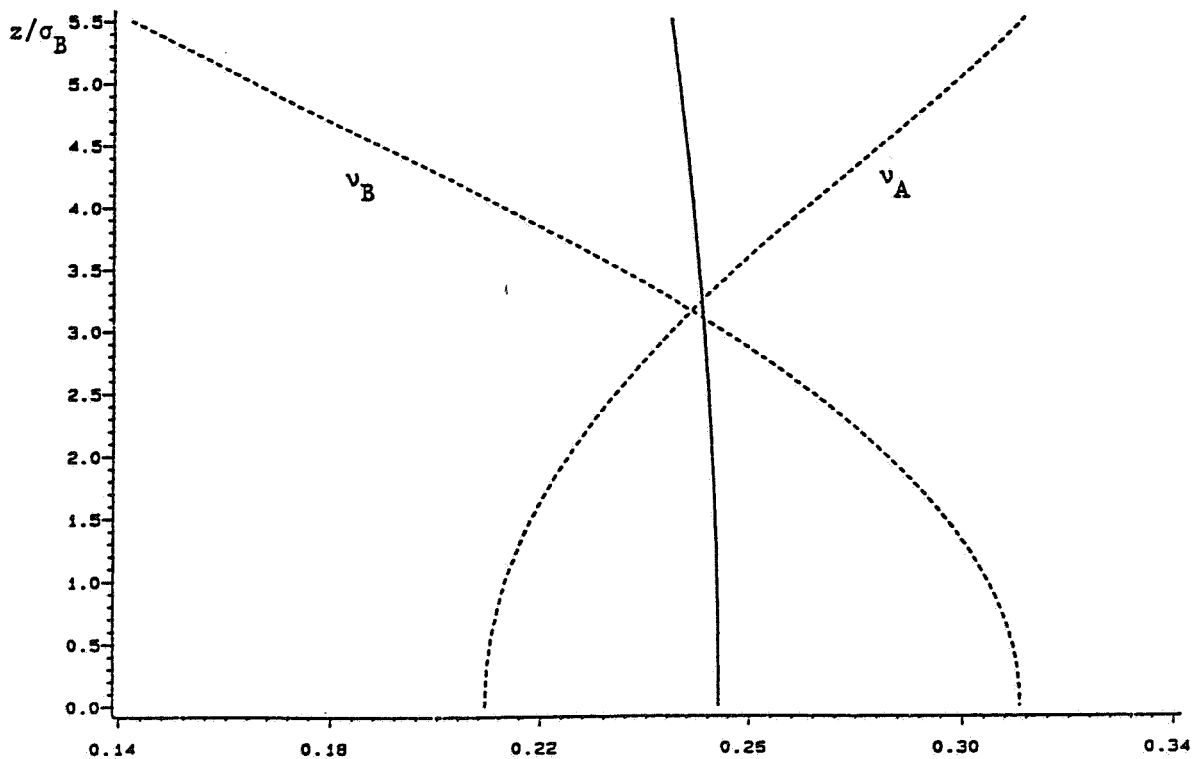


Figure 1. Concentration profiles of two species in the upper half of a shear flow driven by the relative motion of identical, parallel, bumpy boundaries in the absence of gravity.

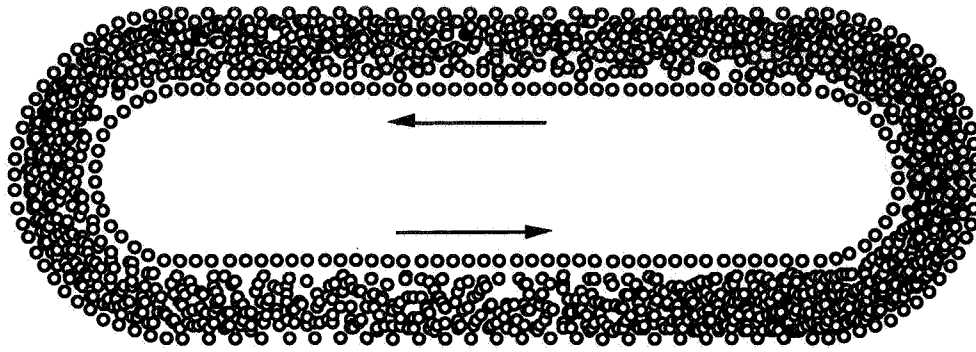


Figure 2. Snapshot from a numerical simulation of a microgravity shear cell involving identical boundary and interior spheres at an overall solid volume fraction of 30%. The inner boundary moves in the direction shown. The size of interior spheres is reduced for clarity.

# MIGRATIONAL INSTABILITIES IN PARTICLE SUSPENSIONS

J. D. Goddard  
Department of Applied Mechanics  
and Engineering Sciences  
University of California, San Diego  
La Jolla, CA 92093-0411

## ABSTRACT

This work deals with an instability arising from the shear-induced migration of particles in dense suspensions coupled with a dependence of viscosity on particle concentration. The analysis summarized here treats the inertialess ( $Re = 0$ ) linear stability of homogeneous simple shear flows for a Stokesian suspension model of the type proposed by Leighton and Acrivos (1987). Depending on the importance of shear-induced migration relative to concentration-driven diffusion, this model admits short-wave instability arising from wave-vector stretching by the base flow and evolving into particle-depleted shear bands. Moreover, this instability in the time-dependent problem corresponds to loss of ellipticity in the associated static problem ( $Re = 0, Pe = 0$ ).

While the isotropic version of the Leighton-Acrivos model is found to be stable with their experimentally determined parameters for simple shear, it is known that the stable model does not give a good quantitative description of particle clustering in the core of pipe flow (Nott and Brady 1994). This leads to the conjecture that an appropriate variant on the above model could explain such clustering as a two-phase bifurcation in the base flow.

## INTRODUCTION

The general theme of the present work is *material instability*, whose recent history, from the 1950s onwards, mainly resides in solid mechanics. There one encounters a wide variety of "strain-softening" phenomena giving rise to spatial localization of strain in the form of "shear bands" or "necks". By comparison, there is a much smaller literature dealing with related instabilities in fluid-like materials, such as non-monotone viscous stress in particulate suspensions and polymeric fluids or dissipative clustering in rapid granular flows.

A recent report (Goddard 1996) contains a brief review and fairly extensive bibliography whose common thread is the "short-wavelength" instability of homogeneous deformations and the associated "change of type" in the underlying field equations, *e.g.* loss of static ellipticity or of dynamic hyperbolicity (Joseph 1990).

The present paper deals with a class of material instabilities in which diffusional scalar transport plays a crucial rôle. Prior related studies involve the effects of heat conduction on thermally-softening media, where mechanical dissipation (having no direct counterpart here) gives rise to phenomena such as bifurcation in liquid flows or "adiabatic" shear bands in solids.

## MODEL AND ANALYSIS

We consider a neutrally-buoyant "Stokesian" suspension (*cf.* Leighton and Acrivos, 1987) with stress:

$$\mathbf{T} = 2\eta(\phi)\mathbf{D} - p\mathbf{1} \quad (1)$$

and particle flux:

$$\mathbf{j} = -\{\kappa(\phi, \dot{\gamma})\nabla\phi + \nu(\phi, \dot{\gamma})\nabla\dot{\gamma}\} \quad (2)$$

where  $\phi$  denotes particle volume fraction,

$$\mathbf{D} := \frac{1}{2}\{\nabla\mathbf{v} + (\nabla\mathbf{v})^T\}, \quad \dot{\gamma} := \left\{2\text{tr}(\mathbf{D}^2)\right\}^{\frac{1}{2}} \quad (3)$$

and  $\mathbf{v}$  is mixture velocity. The quasi-static mechanics ( $Re = 0, Pe \geq 0$ ) is governed by the above constitutive equations, the balances

$$\nabla \cdot \mathbf{T} = \nabla p \quad \text{with} \quad \nabla \cdot \mathbf{v} = 0, \quad (4)$$

and

$$\partial_t\phi + \mathbf{v} \cdot \nabla\phi + \nabla \cdot \mathbf{j} = 0, \quad (5)$$

together with suitable boundary conditions (compatibility with the base state and/or regularity of perturbed states in unbounded domains).

For planar infinitesimal perturbations  $\mathbf{v}^{(1)}, \phi^{(1)}$  of the uniform base state:

$$v_x^{(0)} = \dot{\gamma}^{(0)}y \quad \text{and} \quad \{v_y^{(0)}, v_z^{(0)}, \nabla\dot{\gamma}^{(0)}, \nabla\phi^{(0)}\} = 0, \quad (6)$$

the standard stream-function *cum* Fourier representation in the x-y plane,  $\Psi(k_x, k_y, t)$ ,  $\Phi(k_x, k_y, t)$ , must satisfy

$$k^4\Psi + \alpha(k_x^2 - k_y^2)\Phi = 0 \quad (7)$$

and

$$\partial_t\Phi - k_x\partial_{k_y}\Phi = -k^2\{\nu(k_x^2 - k_y^2)\Psi + \kappa\Phi\} \quad (8)$$

where we let

$$k^2 = k_x^2 + k_y^2 \quad \text{and} \quad \alpha = \dot{\gamma}^{(0)} \left( \frac{d\log\eta}{d\phi} \right)^{(0)} \quad (9)$$

and adopt the change of notation

$$\dot{\gamma}^{(0)}t \rightarrow t, \quad \frac{\kappa^{(0)}}{\dot{\gamma}^{(0)}} \rightarrow \kappa, \quad \frac{\nu^{(0)}}{\dot{\gamma}^{(0)}} \rightarrow \nu \quad (10)$$

The stream function  $\Psi$  is readily eliminated from (7)-(8), which are easily seen to be elliptic for  $\kappa > \nu\alpha$  and otherwise hyperbolic, with the possibility of singular surfaces.

### Wave-Vector Shearing

With  $\Psi$  eliminated, (7)-(8) become

$$\partial_t\Phi - k_x\partial_{k_y}\Phi = \sigma\{\mathbf{k}\}\Phi \quad (11)$$

where

$$\sigma\{\mathbf{k}\} = -k^2\left\{\kappa - \frac{\nu\alpha}{k^4}(k_x^2 - k_y^2)^2\right\} \quad (12)$$

Were it not for the term  $k_x\partial_{k_y}$ , representing a wave-vector shearing (Thomson 1887, Savage 1992, Wang *et al.* 1996) that becomes dominant for large time, the preceding relation would immediately



provide the dispersion relation for mode  $\mathbf{k}$  which, incidentally, is identical with that given by the simplified 1-D treatment in the concluding section of Nott and Brady (1994).

We note that wave-vector stretching in an arbitrary isochoric homogeneous flow, with  $\nabla \mathbf{v} = \mathbf{L}^T = \text{const.}$  and  $\text{tr}\{\mathbf{L}\} \equiv \nabla \cdot \mathbf{v} = 0$ , can be concisely represented by the respective transformations between material ("embedded") coordinates  $(\hat{\mathbf{x}}, \hat{\mathbf{k}})$  in physical space and "reciprocal" space:

$$\hat{\mathbf{x}} = \mathbf{F}^{-1} \mathbf{x}, \quad \text{with } (\partial_t)_{\hat{\mathbf{x}}} = (\partial_t)_{\mathbf{x}} + (\mathbf{L}\mathbf{x}) \cdot \partial_{\mathbf{x}} \quad (13)$$

and

$$\hat{\mathbf{k}} = \mathbf{F}^T \mathbf{k}, \quad \text{with } (\partial_t)_{\hat{\mathbf{k}}} = (\partial_t)_{\mathbf{k}} - (\mathbf{L}^T \mathbf{k}) \cdot \partial_{\mathbf{k}} \quad (14)$$

where

$$\mathbf{F}(t) = e^{\mathbf{L}t} \quad (15)$$

is the physical-space deformation gradient.

For the simple shear at hand, the transformation (14) gives  $\mathbf{k}(\hat{\mathbf{k}}, t)$  as

$$k_x \equiv \hat{k}_x \quad \text{and} \quad k_y = \hat{k}_y - \hat{k}_x t \quad (16)$$

and converts (11) into the o.d.e.

$$\frac{d \log \Phi}{dt} = \sigma\{\mathbf{k}(\hat{\mathbf{k}}, t)\} \quad (17)$$

where  $\sigma\{\mathbf{k}\}$  is given by (12).

While (17) can be integrated subject to (16), asymptotic stability is determined by its limiting form for large  $t$ , and there are two cases to consider,  $\hat{k}_x \neq 0$  and  $\hat{k}_x = 0$ , for which, respectively, one easily finds from (16)-(17) that

$$\log \Phi \sim (\nu\alpha - \kappa) \frac{\hat{k}_x^2 t^3}{3} \sim (\nu\alpha - \kappa) \frac{k_y^2 t}{3} \quad (18)$$

and

$$\log \Phi \equiv (\nu\alpha - \kappa) k_y^2 t \quad (19)$$

for  $t \rightarrow \infty$ . Thus,  $\kappa < \nu\alpha$  implies short-wavelength instability in the form of a ("Kelvin-mode") shear-band structure, with  $k_y \gg k_x$ , representing particle-depleted strata lying perpendicular to the y-direction.

### A Special Case

To describe the particle distribution in a fully-developed rectilinear shear flow, Leighton and Acrivos (1987) employ (1) together with the 1-D form for particle flux :

$$j_y = -\phi^2 \left\{ K_1 \frac{d\dot{\gamma}}{dy} + K_2 \alpha \frac{d\phi}{dy} \right\} \quad (20)$$

where

$$\alpha = \dot{\gamma} \frac{d \log \eta}{d \phi} \geq 0 \quad (21)$$

and where the coefficients  $K_1 \geq 0$  and  $K_2 \geq 0$  are constants, or only weakly dependent on  $\phi$  (and proportional to particle diameter squared).

Taking (2) as the obvious extension of (20) to 3D (*i.e.* ignoring shear-induced anisotropy), one can easily deduce from the above stability analysis that linear stability (against planar disturbances) requires that

$$K_2 > K_1, \quad (22)$$

plainly satisfied by the empirically assigned values of Leighton and Acrivos (1987), for which  $K_2 \approx 2K_1$  over a relatively broad range of  $\phi$ .

Recently Nott and Brady (1994) have made the interesting observation that the stable form of (20) does not give a particularly good quantitative description of the dense "plug-flow" clustering of particles in the core of pipe flow. While they propose a more elaborate constitutive theory, this author wonders whether a mere adjustment of the coefficients  $K_1, K_2$ , to impart instability near the state of maximum packing  $\phi_{max}$ , might not suffice to explain the above clustering as a flow bifurcation with two-phase, core-annular structure.

## CONCLUSIONS

Depending on its coefficients, the above particle-migration model can exhibit instability in simple shear, the dominant linear mode being particle-depleted shear bands. While the empirical form proposed by Leighton and Acrivos is linearly stable, an unstable version might allow for a better description of particle clustering in pipe flow.

It is plausible that the migrational instability considered here would be enhanced by non-Newtonian rheology, as in shear-thinning suspensions of colloidal or deformable particles, thereby accentuating the tendency towards clustering or phase separation.

For the simple constitutive model of the present work, loss of ellipticity in the static problem is directly connected with time-dependent instability. This broaches an interesting and unresolved mathematical question as to the precise relation between material stability and static ellipticity for materials with long-range memory.

Several of the above issues are the subject of further work in progress.

## ACKNOWLEDGEMENT

Partial support from the U.S. AFOSR, NASA and NSF and from the 1996 Programme on the Dynamics of Complex Fluids, Isaac Newton Institute of Mathematical Sciences, University of Cambridge, U.K., is gratefully acknowledged.

## BIBLIOGRAPHY

1. Goddard, J.D. (ed.) 1996 *Workshop on Material Instabilities*, Report No. 95-20, Institute for Mechanics and Materials, University of California, San Diego.
2. Joseph, D.D. 1990 *Fluid Dynamics of Viscoelastic Liquids*, Springer-Verlag.
3. Leighton, D. T. & Acrivos, A. 1987, *J. Fluid Mech.*, 181, 415.
4. Nott, P.R. & Brady, J.F. 1994, *J. Fluid Mech.*, 275, 157.
5. Savage, S.B. 1992, *J. Fluid Mech.*, 241, 109.
6. Thomson, W. (Lord Kelvin) 1887, *Phil. Mag.*, 24, 188.
7. Wang, C.-H., Jackson, R. & Sundaresan, S. 1996, *J. Fluid Mech.*, 308, 31.

# Dynamics of Granular Materials

R. P. Behringer

Department of Physics and Center for Nonlinear and Complex Systems  
Duke University

Granular materials exhibit a rich variety of dynamical behavior, much of which is poorly understood. Fractal-like stress chains, convection, a variety of wave dynamics, including waves which resemble capillary waves,  $1/f$  noise, and fractional Brownian motion provide examples. Work beginning at Duke will focus on gravity driven convection, mixing and gravitational collapse. Although granular materials consist of collections of interacting particles, there are important differences between the dynamics of a collections of grains and the dynamics of a collections of molecules. In particular, the ergodic hypothesis is generally invalid for granular materials, so that ordinary statistical physics does not apply. In the absence of a steady energy input, granular materials undergo a rapid collapse which is strongly influenced by the presence of gravity. Fluctuations on laboratory scales in such quantities as the stress can be very large—as much as an order of magnitude greater than the mean.

## I. Introduction

In this paper, I briefly given an overview of important aspects of granular flows. I then focus on recent experiments on gravity-driven convective flows. I conclude by indicating future directions.

Granular materials<sup>1-3</sup> are collections of macroscopic particles or grains typically having inelastic interactions and often surrounded by a fluid, such as air or water. The interactions between granular materials are governed chiefly by the local elastic and frictional forces between particles, or between particles and a wall. The surrounding fluid may also play an important role in the dynamics of the system. For instance, when granular materials are shaken, then can “convect” in a manner which is reminiscent of ordinary convection, and the surrounding gas can profoundly affect the nature of the flow. Although models for granular materials are often predicated on the assumption that the particles are spheres, in many practical situations, the particles are decidedly nonspherical. This means that both the local and collective properties of granular dynamics will have features associated with particle shape.

One might expect that granular materials behave like a gas or fluid, but on a larger scale. This expectation is usually not met for a variety of reasons. Granular interactions are inelastic. If a system starts with with nonzero kinetic energy, it very rapidly loses that energy— in a finite length of time. In the process, clustering occurs, and the system becomes inhomogeneous.<sup>4</sup> Here, gravity almost surely plays a key role—causing collapse in a finite time even for a single particle bouncing on a smooth surface. At this point, it is very difficult to sort out the role of gravity from clustering effects which would occur in the absence of gravity.

Non-transient granular flow requires the constant input of energy, from gravity, shaking, or other sources. Often, the ergodic hypothesis of statistical mechanics fails: the system comes nowhere near sampling the possible microstates for given macroscopic parameters. One of the complications of many granular flows is that part of the system is in a frozen state

while nearby regions are moving. Finally, the interaction between grains and a boundary is typically very different for a granular material versus a conventional viscous fluid. In the latter case, the appropriate boundary condition at the wall is that of "sticking"—the fluid is at rest relative to the wall. But, there is no such condition for granular materials—grains can and do slip along a wall. In addition, it is possible to transfer stresses from deep within a granular material to the walls through friction and the mechanism of stress chains. A dramatic consequence of this is that columns of granular materials do not demonstrate hydrostatic head effects, such as those seen in a column of water.

Models of granular dynamics typically try to capture one of two extremes. In one extreme, the grains are compacted and remain in enduring contact with each other and the walls. In the other extreme, the grains move about rapidly and collide randomly like the molecules of a gas. The experiments described here pertain chiefly to the second regime in which energy is provided through shaking.

There are also many technical applications of granular materials, ranging from the commonplace transport of coal and grain to the high-tech handling of pharmaceutical powders, fluidized beds, and the preparation of sinters for advanced materials. The total cost involved in the handling of these materials is enormous.<sup>5</sup> A modest improvement in our understanding of granular flow properties could lead to significant savings.

The current understanding of the statistical properties and dynamics of these materials lags far behind the understanding of the dynamics of conventional fluids. Current models, although useful and sophisticated, all show weaknesses which invite alternative models. In no case is there a model which is as firmly established as the Navier- Stokes equations of Newtonian fluid mechanics.

## II. Shaken Granular Materials

Work beginning at Duke will focus on shaken granular materials, on mixing of these materials, and on gravitational collapse. These aspects of granular flows are all highly sensitive to gravitational fields. Indeed, various aspects of these phenomena are so dominated by the presence of gravity that only in a very low- $g$  environment will it be possible to sort out the different aspects of the relevant physics.

Because the work at Duke is only beginning, I will chiefly note here some of the basic phenomena involved in shaken granular materials. I will also note a novel coarsening effect which we have recently discovered in the Duke lab. I will then comment briefly on future directions of study.

The observation of granular convection can be dated at least to the time of Faraday, who noticed organized motion of powders sprinkled on vibrating plates. Broadly, in a gravitational field,  $g$ , grains subject to vertical vibrations which have accelerations exceeding  $g$ , undergo a kind of large scale convective flow, in which a heap may also form. However, the qualitative nature of these flows can depend on several parameters, and until recently, the relative importance of these parameters was not clear. Indeed, several important control parameters for these flows were only recently identified. Several groups,<sup>6,8,7,9-11</sup> including the one at Duke, have been recently involved in characterizing granular convection. In general, the detailed mechanisms responsible for granular convection are only partially clarified, and much work remains before we can say that this system is understood.

The recent work at Duke has been focused on mapping out a “phase diagram” for granular convection. This means identifying and characterizing important dynamical states, followed by determining the relevant control parameters, and the ranges of these parameters over which the states occur. For the present discussion, I assume that the material is contained in a box of width  $W$ , height,  $H \gg W$ , and length  $L \gg W$ . In most of the Duke experiments, the shaker has an annular geometry, for reasons having to do with the wall friction. The material generally cannot fill the container, since otherwise, no convection occurs; hence, the actual fill height of the container is  $h < H$ . The grains are assumed to have a typical grain diameter,  $d$ . In general, the grains need not be spherical; indeed grain “roughness”, can play a key role in the overall convective flow, although this is not generally appreciated. In most experiments, the grains are surrounded by air at  $1\text{Atm}$ , but in general, the gas pressure is  $P$ . By assumption, the containing box is shaken in a purely vertical direction with a sinusoidal displacement,  $z = A \cos(\omega t)$ . One of the most important control parameters is then the dimensionless peak acceleration  $\Gamma = A\omega^2/g$ . In general, granular convection can only occur for  $\Gamma > 1$ ; for smaller  $\Gamma$ 's, the material will relax slowly to a uniform height.

Two primary mechanisms have been proposed for the origins of convection under uniform shaking (The case of nonuniform shaking is clearly different.) These mechanisms are friction with the sidewalls, and lift effects associated with the surrounding gas. Recent molecular dynamics (MD) studies and experiments have helped to clarify the role of friction. Roughly, the idea is that when the granular material is shaken, it exists in both a compacted state and a dilated state during different phases of each shake. Typically, the compacted state occurs when the material is being accelerated upward by the shaker, whereas the dilated state occurs as the shaker accelerates downward. It is during the dilated stage that the grains are most free to move. The expectation is that friction with the vertical walls will then drag the outermost grains down more strongly than the inner grains, resulting in a convection loop which circulates downward at the vertical sidewalls and upward in the interior. This is indeed the case for smooth spherical particles, but curiously, not the case for rough particles of comparable size. In the rough case, circulation consists of an upward motion of the grains towards the top of a heap, followed by strong downward avalanching along the slope of this heap. And, the frictional convection mechanism does not suggest the formation of a significant heap. This heap is, nevertheless, a common feature of the flow.

The surrounding gas pressure can also play a significant role, particularly if the particles have  $d \leq 1\text{mm}$ . Recent experiments at Duke<sup>9</sup> in which the pressure is carefully controlled over  $0 \leq P \leq 1\text{Atm}$ , have shown that the heaping/convection is strongly suppressed when  $P$  falls below about  $10\text{Torr}$ . The Duke observations settled an ongoing dispute<sup>6,7</sup> about the role of gas pressure on granular convection. The physical mechanisms which lead to the reduction of heaping/convection at  $10\text{Torr}$  are still under study at Duke. Gas effects can also be very dramatic for relatively small  $d$  and large  $\Gamma$ , where a bubbling instability occurs.<sup>9</sup>

Interestingly, the height  $h$  of the granular layer is also important in determining the state of shaken granular materials. If  $h$  is small, say less than  $1\text{cm}$ , the convective flow does not occur. Rather, there occur a variety of different parametric wave states.<sup>7,11,9</sup> If the layer is tall enough that the convection and heaping occurs, then these parametric states still likely occur. However, a different kind of wavy instability, discovered at Duke, dominates. These are traveling waves which propagate up the slope of the heap.

A recent aspect of work at Duke has been studies to characterize the fluctuations for shaken granular materials. This is interesting because it may be possible to relate these fluctuations to kinetic theory models,<sup>12</sup> in which the fluctuations are characterized by a granular temperature—a quantity which is analogous to, but not to be confused with, the ordinary temperature for thermodynamic systems.

Another issue of interest is the pattern forming mechanism which leads to the formation of a single heap for granular convection. We have found that this process has two apparent aspects. In some cases—i.e. for certain particle sizes, shaker amplitudes, etc. the evolution of the heaping/convection state occurs via the relatively early formation of only a few (one or two, typically) large heaps which then merge into a single heap. However, we have recently found that in some circumstances, the initial instability is to a relatively small wavelength spatial oscillation which then coarsens, so that in the end there is only a single heap. An example of this novel state is given in Figure 1.

### III. Conclusions and Directions

The discussion above gives a brief overview of some of the key phenomena associated with granular convection. This system is particularly relevant here because of the dominance of gravity. It seems clear, however, that the availability of a low gravity environment would lead to significant new insights into granular dynamics. In particular, shaken granular systems would appear more like granular “gases”, and convection might or might not occur. In particular, low-g access would mean that we could test recent theories of inelastic collapse which are not easily tested in an earth-bound environment. In addition, granular materials also exhibit interesting mixing and segregation phenomena in a gravitational field. Segregation by size can occur if there is a distribution of grain sizes.<sup>13,14,10,17</sup> Typically, larger particles rise to the top, even if they are heavier than the smaller particles. Important mechanisms for segregation include geometric effects<sup>16</sup> (small particles fall more easily into the “cracks”) and convection.<sup>10,15</sup> This kind of segregation can be either useful or detrimental in commercial applications. A particularly interesting prospect would be the study of size effects in a low-g environment.

### ACKNOWLEDGMENTS

Support for this work is beginning under a new NASA grant.

## References

- <sup>1</sup>For a review see H.M. Jaeger and S. R. Nagel, *Science* **255**, 1523-1531 (1992); H.M. Jaeger, S.R. Nagel, and R.P. Behringer, *Physics Today*, April, 1996; and to appear, *Rev. Mod. Phys.*
- <sup>2</sup>C. S. Campbell, *Ann. Rev. Fluid Mech.* **22** 57-92 (1990).
- <sup>3</sup>For a review see R. P. Behringer, *Nonlinear Science Today*, **3**, 1 (1993).
- <sup>4</sup>S. McNamara and W. R. Young, *Phys. Fluids A* **4** 496-504 (1992); *Phys. Fluids A* **5** 34-45 (1993); *Phys. Rev. E* **50**, R28-31 (1994).
- <sup>5</sup>B.J. Ennis, J. Green and R. Davis, *Particle Tech.* **90**, 32 (1994).
- <sup>6</sup>P. Evesque and J. Rajchenbach, *Phys. Rev. Letters* **62**, 44 (1989).
- <sup>7</sup>S. Douady, S. Fauve and C. Laroche, *Europhysics Lett.* **8**, 621-627 (1989).
- <sup>8</sup>E. Clement, J. Duran, and J. Rajchenbach, *Phys. Rev. Lett.* **69**, 1189-1192 (1992).
- <sup>9</sup>H. K. Pak and R. P. Behringer, *Phys. Rev. Lett.* **71**, 1832 (1993); in the *Proceedings of the First International Conference on chaos*, p. 91, ed. H. Lee (1993); *Pattern formation of vertically vibrated granular materials*, to be published (1996); *Nature* **371**, 231 (1994); H. K. Pak E. Van Doorn, and R. P. Behringer, *Phys. Rev. Lett.* **74**, 4643 (1995).
- <sup>10</sup>J. B. Knight, H. M. Jaeger, and S. R. Nagel, *Phys. Rev. Lett.* **70**, 3728 (1993).
- <sup>11</sup>F. P. Melo, P. Umbanhowe and H. Swinney, *Phys. Rev. Lett.* **72**, 172 (1994).
- <sup>12</sup>P. K. Haff, *J. Fluid Mech.* **134**, 401-430 (1983). S. Ogawa in *Proceedings US-Japan Seminar on Continuum-Mechanical and Statitital Approaches in the Mechanics of Granular Materials*, S. C. Cowin and M. Satake eds, Gakujutsu Bunker Fukyukai, Tokyo, Japan, 1978. J. T. Jenkins and S. B. Savage, *J. Fluid Mech.* **130**, 186-202 (1983)
- <sup>13</sup>A. Rosato, K.J. Strandburg, F. Prinz, and R.H. Swendsen, *Phys. Rev. Lett.* **58**, 1083 (1987).
- <sup>14</sup>R. Jullien, P. Meakin, and A. Pavlovitch *Phys. Rev. Lett.* **69**, 640 (1992).
- <sup>15</sup>R. Khosropour, J. Zirinsky, H.K. Pak and R. P. Behringer, to be published, 1996.
- <sup>16</sup>J. E. S. Socolar, *Europhysics Lett.* **18**, 39-44 (1992). R. Jullien and P. Meakin, *Nature* **344**, 425-427 (1990).
- <sup>17</sup>G. Metcalfe, T. Shinbrot, and J. Ottino, *Nature* **374**, 39 (1995).

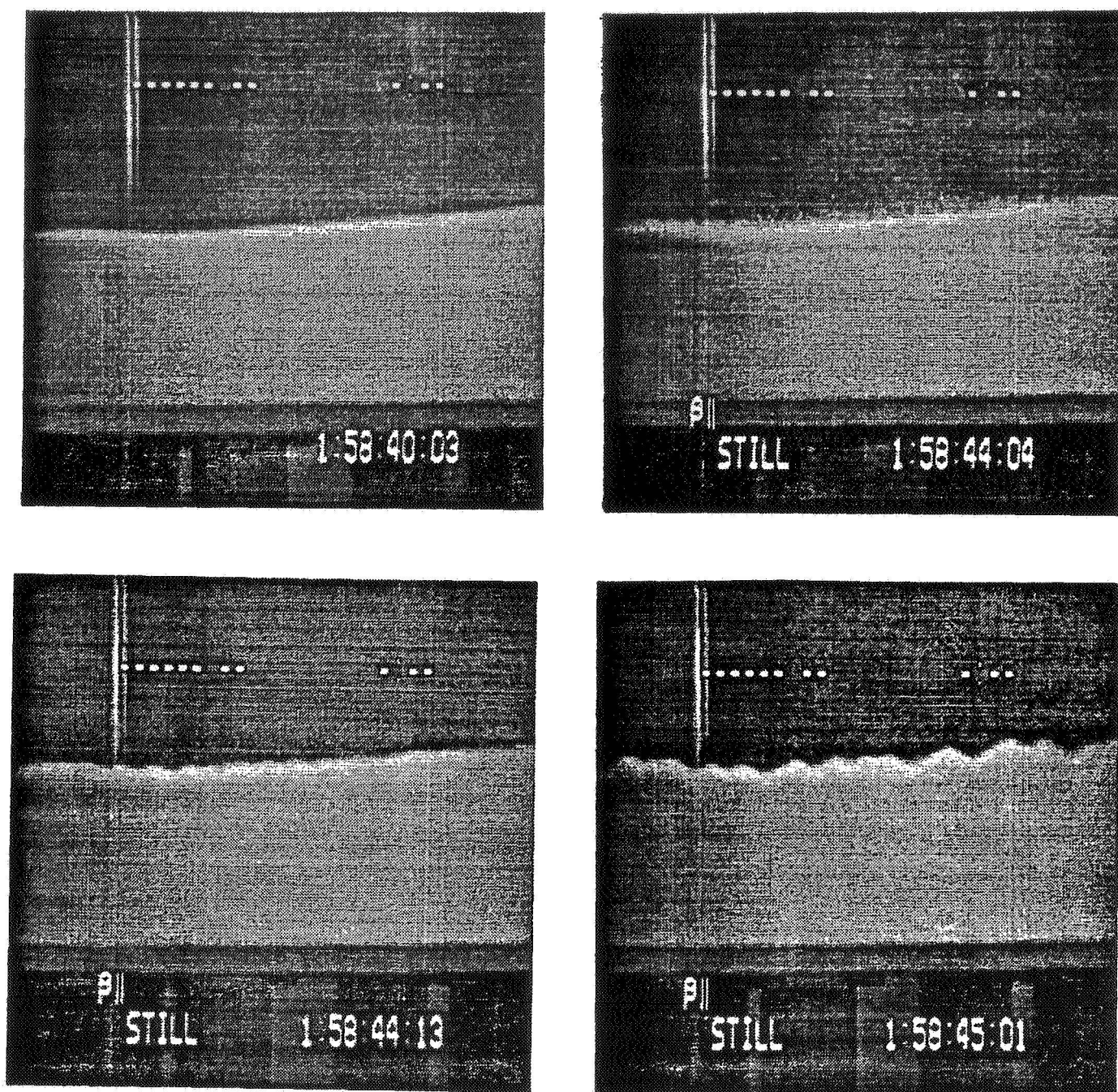


Figure 1: A time sequence showing the initial formation of the wavy disturbance. Here  $f = 10.16\text{Hz}$ ,  $a = 5.13\text{mm}$ . The grains are glass, spherical particles of diameter  $d = 0.15\text{mm}$ . The container has an annular geometry, with an gap width  $w = 4.5\text{mm}$ . The container is open to the surrounding air.



## NMRI MEASUREMENTS OF FLOW OF GRANULAR MIXTURES

Masami Nakagawa\*, R. Allen Waggoner\*\* and Eiichi Fukushima\*\*

\*Sandia National Laboratories, P.O. Box 5800, Albuquerque  
New Mexico 87185-0709

\*\* The Lovelace Institutes, 2425 Ridgecrest Dr. SE, Albuquerque  
New Mexico 87108-5127

### ABSTRACT

We investigate complex 3D behavior of granular mixtures in shaking and shearing devices. NMRI can non-invasively measure concentration, velocity, and velocity fluctuations of flows of suitable particles. We investigate origins of wall-shear induced convection flow of single component particles by measuring the flow and fluctuating motion of particles near rough boundaries. We also investigate if a mixture of different size particles segregate into their own species under the influence of external shaking and shearing disturbances. These non-invasive measurements will reveal true nature of convecting flow properties and wall disturbance. For experiments in a reduced gravity environment, we will design a light weight NMR imager. The proof of principle development will prepare for the construction of a complete spaceborne system to perform experiments in space.

### INTRODUCTION

Particle technology is a science in its infancy and models capable of predicting the behavior of dry granular systems over the range of observed phenomena are generally unavailable. Consequently, engineers are forced to design systems based only on experience and this sometimes leads to failure and breakdown of systems at a tremendous economic cost. There is a clear need to obtain an understanding of the fundamental physics governing these complex materials in order to advance the science of particle technology so that predictive models and scaling laws can be developed.

One of the most intriguing and ubiquitous phenomenon which occurs in particulate mixtures is segregation. When subjected to various mechanical disturbances which typically occur in industrial handling processes, a bulk solid tends to segregate and this is generally an undesirable effect which could have serious implications on the integrity of end products. While several mechanisms of segregation have been proposed, a clear relationship between them has not been established. Convective motions of particles due to vertical vibration has captured some of the great minds including Faraday (ref.1). Furthermore, convection flows due to wall-shear have recently attracted researchers from different disciplines (refs. 2, 3, 4, 5).

Traditionally, granular flow properties have been measured non-invasively from outside the flow by optical methods or high performance video cameras, or invasively by electronic sensors. All non-invasive methods fail when the particle concentration is high. In the proposed experiment we employ Nuclear Magnetic Resonance Imaging (NMRI) which does not suffer concentration related opacity problems and can measure concentration and velocity anywhere and in any orientations in the flow. Emphasis will be placed on ground based experiments to lay the groundwork for future microgravity experiments. In parallel with ground-based NMRI experiments, we will design/construct a light weight NMRI device which can be transported into a reduced gravity environment.

### NUCLEAR MAGNETIC RESONANCE IMAGING

#### NMRI Basics

An atomic nucleus with a magnetic moment, for example, protons, the nuclei of hydrogen atoms, precesses around the magnetic field like a spinning top precesses about the direction of gravity. There is a unique precession frequency called the Larmor frequency for each atomic nucleus in a particular strength of magnetic field. A known spatial variation of the magnetic field will cause the nucleus at each point to precess at a different Larmor frequency. MRI measures the distribution of signals as a function of this frequency and relates it to the spatial distribution of nuclear spins. This technique is now widely used for non-invasive diagnosis in clinical medicine.

The use of MRI for studying flowing samples is more complex than it is for measuring static samples but it offers a unique technique for non-invasively studying the detailed concentration and flow behavior anywhere in the flow regardless of optical or acoustic opacity. For the evaluation of velocities, we use the so-called phase method in this work. It works on the principle that the phase of the macroscopic magnetization comprised of the aggregate nuclear moments in an element of volume evolves in a manner depending on its motion in the presence of a magnetic field-gradient. We obtain the velocity information from the measured phase behavior of the magnetization in each image voxel. By applying the magnetic field gradient in a certain sequence, we make the phase shift proportional to the average velocity in the voxel with the proportionality factor an experimentally controllable parameter called the first moment of the gradient. This is in addition to phase-encoding which is a procedure to encode a spatial dimension in the image. Basics of MRI for studying flowing fluids have been described elsewhere (refs. 6 and 7).

#### Previous NMRI Flow Measurements of Granular Flow

##### Granular Flows in a Rotating Cylinder

In our rotating horizontal cylinder experiment, we demonstrated the feasibility to measure steady-state granular flows by MRI (ref.7). The cylinder is half-filled with particles, inserted into the bore, and rotated with the long nonmagnetic shaft which is required to keep the motor far from the magnet. Most of the particles undergo solid body translation with the cylinder without slipping while the shear flow takes place along the free surface which is inclined at the dynamic angle of repose. At these rotation rates, no transient effects, such as wave propagation, were seen through the acrylic cylinder or end caps and this was supported by MRI evidence as discussed below.

Protons are best suited for MRI because of their strong signal as well as their abundance in nature. We have used mustard seeds which yield excellent proton NMR signals from their oils. Based on measurements of a few hundred representative seeds, their average diameter is 1.5 mm, the average density is  $1.3 \text{ g/cm}^3$ , and the average coefficient of restitution is 0.75 when they are dry and at room temperature.

An acrylic cylinder of length 300 mm with an inner diameter of 70 mm was half-filled with mustard seeds and inserted into a larger cylinder with an inner diameter of 88 mm. The gap between the concentric cylinders was packed with mustard seeds which formed a ring undergoing rigid body rotation with uniform concentration and predictable velocity profiles. These profiles could then be used as velocity and concentration references at each rotation speed.

Our MRI experiment, the Cartesian components of the velocity,  $V_x$  and  $V_y$ , were measured in two independent experiments with a total measurement time of approximately 15 minutes. MRI measures average flow properties over this time within each voxel

averaged over the 8mm thick slice. Figure 1 shows NMR images of velocity components parallel and perpendicular to the free surface of particles flowing at different rotation speeds. Figure 2 shows a schematic view of particle motion in a rolling mode at 17 rpm with the corresponding velocity profile along a line A-B.  $f$  is at the free surface and  $r$  at the cylinder wall.  $F$  is the sliding layer consisting of a constant shear portion  $f-f'$  and a variable shear portion  $r'-f'$ . The particles from  $r'$  to  $r$  do not flow but rotate as a solid body.

### Proposed NMRI Research

#### NMRI experiments

We propose to investigate the origins of segregation due to external shearing disturbances, first on the ground and then in space. It has been observed that the radial segregation occurs very quickly and axial segregation occurs in a much longer time scale under the influence of gravity. In a reduced gravity environment, however, other mechanisms may amplify and segregation phenomena may take different forms. By decoupling gravity effects, we hope to investigate mechanisms of segregation which are important in a reduced gravity environment where, in future, many materials are expected to be handled in particulate forms.

NMRI experiments will be conducted using non-magnetic shaking and shearing devices inside the limited bore space of the magnet. Figures 3 and 4 show possible construction designs for shaking and shearing devices, respectively. For the ground experiments, various variations of the shaking design shown in fig.3 will be used to investigate convection flow, the propagation depth of wall disturbances, and the effects of the vertically shaking bottom wall. Some of the same designs will be used to investigate transverse and longitudinal shaking in the basket. The inner walls are roughened to provide enough shearing effects on the flowing particles.

In the above experiments, we first use monosize particles in order to establish a link between boundary conditions and convection flows with and without gravity effects. Measurable flow properties include concentration, mean velocity, and fluctuation velocity anywhere in the sample, near and far from the boundary. Control parameters include the solid volume fraction, particle properties (size, elasticity, and shape), wall roughness, shaking amplitudes and frequencies, and shearing rates. Since particles' motions in a convection flow are influenced by both the mean flow and velocity fluctuations, the above results provide, for the first time, non-invasive information connecting particle fluctuations due to shaking/wall-shearing to global convective motion. For the Couette shearing experiments, we will also measure the slip velocity by detecting the difference in the average velocity of the particles glued on the inner wall and that of flowing particles adjacent to the wall. We will then use a mixture of two different size particles to investigate conditions where convections cause size-segregation. We will make an effort to find particles whose mechanical properties are identical but NMR signals are not. For example, particles encapsulated with different liquids with distinguishable NMRI signals will be sought. As stated earlier, segregation processes are essentially nonsteady and their time durations depend on many parameters. For the slower segregation process, NMRI will provide concentration, mean velocity and fluctuation velocity continuously. For the faster evolving processes, we stop the flow periodically to image dynamically induced static structures of each segregating constituent. With distinguishable particles, it will be possible to investigate spatio-temporal distribution patterns of each segregating component.

#### Development of Spaceborne NMRI Components

We propose a proof-of-principle project to demonstrate the feasibility of a spaceborne NMRI apparatus. The proposed ground based laboratory NMRI represents necessary

preludes to spaceborne experiments and the demonstration of a low-power, light weight, magnet capable of making NMR images must precede the actual spaceborne unit. After our success with the proposed magnet, it will be easy to predict how to scale it up for any experiment with particular utility and space limitations. The requirements for such an apparatus are: 1) relatively light weight; 2) low electrical power consumption; 3) no cryogenic fluids; and 4) adequate sample space, signal to noise ratios and spatial resolution.

Non-imaging NMR apparatus, based on permanent magnets, have been known but such magnets were unsuitable for NMR imaging or too massive for spaceborne uses. We will design and build a cylindrical permanent magnet system (ref.8) with an opening of roughly 5 cm and a field strength of around 0.4T. That would give a respectable proton Larmor frequency of 17 MHz. The best candidate for the material is NdFeB which, in addition to its superior magnetic properties, is more than 10% lighter than SmCo. A 6 inches od, 2 inches id, and 6 inches long NdFeB Halbach magnet will weigh 40 pounds.

Figure 5 is a sketch of the proposed magnet. It consists of axial segments of magnetic material with their transverse magnetizations rotated between segments as shown. The magnetic field is transverse and the return flux is confined to the volume of the magnet, eliminating the need for a separate iron return path. The homogeneity depends on the number of segments used as well as the quality of each segment of magnetic material. The Halbach magnet has several advantages:

- Its cylindrical shape with a transverse magnetic field is ideal because efficient longitudinal solenoid rf coils can be used for the NMRI experiment.
- The magnet will be fairly light because of the lack of an iron field-return path.
- There will be little or no stray magnetic field.
- No electrical power is required.
- Fast and accurate Fourier images will be possible because of the switching gradients will not induce eddy currents in the poorly conducting magnetic material.

One of the problems to be solved is how to optimally shim such a magnet with the least weight including that of the shim/gradient current supplies. The best results may require ferromagnetic shims together with basic current shimming with auxiliary coils. Take the cylindrical axis to be z, the field along y, and the mutually perpendicular direction to be x. The geometry for the shim/gradient coil providing the gradient along y (the magnet field) can be a simple quadrupole type with four axial wires (ref.9). The four wires are placed 90 degrees apart so, for example, in the 8-segment Halbach magnet, they can be in the centers of the four segments located 45 degrees off axis, as shown in fig.5.

The transverse gradients are more difficult. The x coils can be some variant of the longitudinal wire coil like the quadrupole but with different symmetry of the wire placement which will create a field that is odd with respect to x with a field that vanishes at center. The currents and the wire placements must be adjusted for the best field linearity. The y coils can be a variant of axially displaced saddle coils which create a field that is odd with respect to z. Again, the wire placement must be optimized for best effects.

In order to save weight, we will make a dedicated image sequencer "on a board" with a computer (ref.10). Imaging parameters for density and velocity images will be preset for the experiments. Because this will be a dedicated proton imager with no need for other frequencies, the rf transmitter and receiver circuits can be narrow-banded at the Larmor frequency to save weight.

The NMRI apparatus will be developed as a hybrid of portable and laboratory components. The portable components, i.e., the magnet assembly and the NMRI

electronics including the microprocessor, which are the truly novel items, will be developed by us while standard items such as power supplies and audio amplifiers for driving the magnetic field gradients will be of the ready-made laboratory variety.

### ACKNOWLEDGMENT

The work presented here was sponsored, in part, by the U.S. Department of Energy, Pittsburgh Energy Technology Center via Contract # DE-AC22-90PC90184 and the U.S. Department of Energy, Office of Basic Energy Science via Contract #DE-FG04-90ER14087. We would like to thank NASA for selecting our proposed project of NMR measurements of particle segregation for funding through the program: Microgravity Fluid Physics: Research and Flight Experiment Opportunities, NRA-94-OLMSA-05.

### REFERENCES

1. Faraday, M., "On a peculiar class of accoustical figures assumed by groups of particles upon vibrating elastic surfaces," *Phil.Trans. Soc. London* **52**, 299(1831).
2. Knight, J.B., H. M. Jaeger and S. M. Nagel, "Vibration-Induced Size Separation in Granular Media: The Convection Connection," *Phys. Rev. Lett.* **70**, 3728 (1993).
3. Gallas, J. A. C., Herrmann, H. J. and S. Sokolowski, "Convection Cells in Vibrating Granular Media," *Phys. Rev. Lett.* **69**, 1371 (1992).
4. Rosato, A. D. and Y. Lan, "Granular Dynamics Modeling of Vibration-Induced Convection of Rough Inelastic Spheres," *Proceedings of the AIChE First International Particle Technology Forum*, pg. 446-453, Aug. 17-19, Denver, CO (1994).
5. Taguchi, Y-h., "New Origin of Convective Motion: Elastically Induced Convection in Granular Materials," *Phys. Rev. Lett.* **69**, 1367 (1992).
6. Caprihan, A and Fukushima, E., "Flow Measurements by NMR", *Phys. Rep.* **198**, 95 (1990).
7. Nakagawa, M., Altobelli, S. A., Caprihan, A.C., Fukushima, E., & Jeong, E.-K., "Non-invasive measurements of granular flows by magnetic resonance imaging," *Exp. in Fluids* **16**, 54-60 (1993).
8. Halbach, K., *Nucl. Instrum. Methods* **169**,1 (1980).
9. Assink, R.A., *J. Magn. Reson.* **22**, 165(1976).
10. Kose, K. and Inouye, T., *Meas. Sci. Technol.* **3**, 1161 (1992).

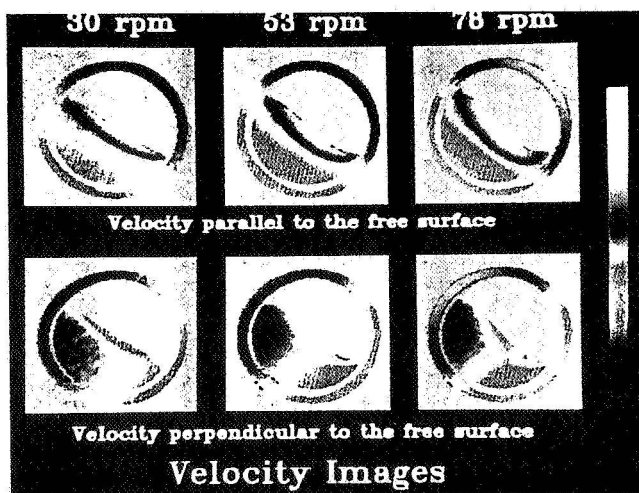


Figure 1. NMR velocity images.

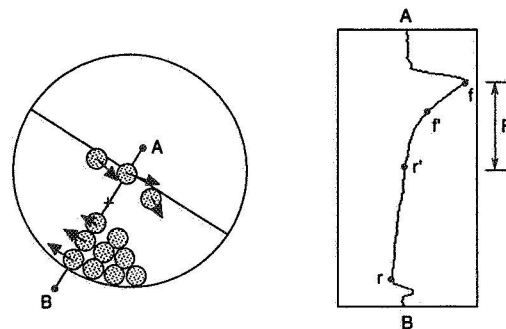


Figure 2. Schematic view of particle motion and velocity profile.

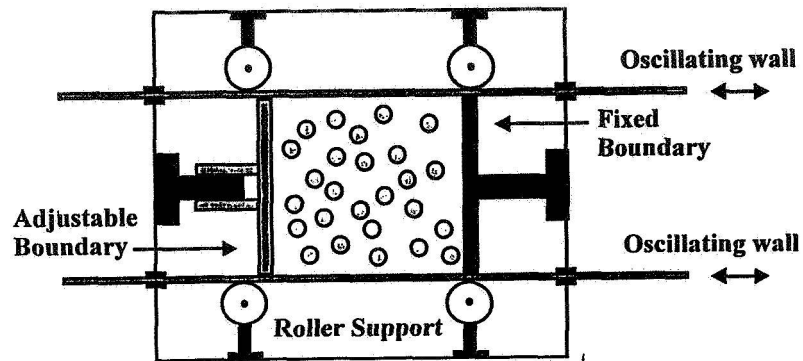


Figure 3. A schematic drawing of the shaking apparatus. Parts colored in black are non-moving components. Parts colored in gray are moving components including particles. Oscillating walls are roughened by gluing particles that are identical to flowing ones.

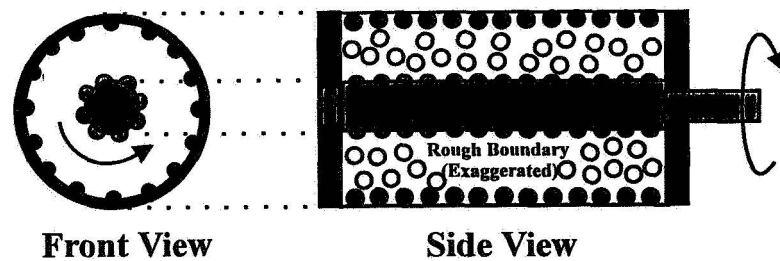


Figure 4. A schematic drawing of the Couette shearing device. Moving parts are shown in gray. Inner walls are roughened by glued particles in order to assure rigorous interactions between the walls and flowing particles.

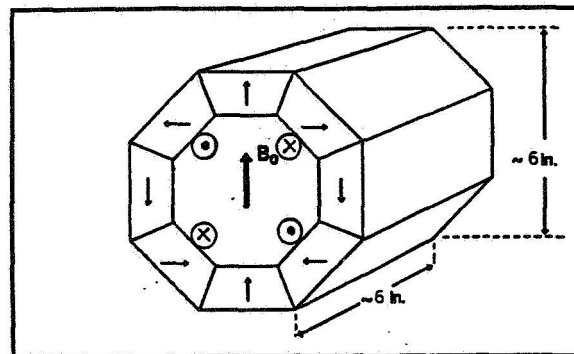


Figure 5. A sketch of the proposed magnet.

# **Pattern Formation, Flow Instability, and Thermocapillary Flows**





# EXPERIMENTAL STUDY OF BUOYANT-THERMOCAPILLARY CONVECTION IN A RECTANGULAR CAVITY

Manfred. G. Braunsfurth and George. M. Homsy  
Department of Chemical Engineering,  
Stanford University, Stanford, CA 94305

## ABSTRACT

The problem of buoyant-thermocapillary convection in cavities is governed by a relatively large number of nondimensional parameters, and there is consequently a large number of different types of flow that can be found in this system. Previous results give disjoint glimpses of a wide variety of qualitatively and quantitatively different results in widely different parts of parameter space. In this study, we report experiments on the primary and secondary instabilities in a geometry with equal aspect ratios in the range from 1 to 8 in both the direction along and perpendicular to the applied temperature gradient. We thus complement previous work which mostly involved either fluid layers of large extent in both directions, or consisted of investigations of strictly two-dimensional disturbances. We observe the primary transition from an essentially two-dimensional flow to steady three-dimensional longitudinal rolls. The critical Marangoni number is found to depend on the aspect ratios of the system, and varies from  $4.6 \times 10^5$  at aspect ratio 2.0 to  $5.5 \times 10^4$  at aspect ratio 3.5. Further, we have investigated the stability of the three-dimensional flow at larger Marangoni numbers, and find a novel oscillatory flow at critical Marangoni numbers of the order of  $6 \times 10^5$ . We suggest possible mechanisms which give rise to the oscillation, and find that it is expected to be a relaxation type oscillation.

## INTRODUCTION

Buoyant-thermocapillary convection occurs in a variety of different applications, including crystal growth. We choose to study buoyant-thermocapillary convection in a simplified geometry and under carefully controlled experimental conditions, where the link between the observed dynamics and the underlying mechanisms can be made. The geometry of the system considered in this study is shown schematically in figure 1. A horizontal temperature gradient is applied by heating and cooling two opposite sidewalls. The remaining two sidewalls and the bottom are taken to be rigid and insulating, and the top surface of the fluid is free. There are two physical mechanisms which drive fluid flow in this system, buoyancy and thermocapillarity. For fluids with surface tension decreasing with increasing temperature, these mechanisms reinforce each other to drive the convection, but with differing scaling dependence (see Carpenter & Homsy, ref. 1).

The system is characterized by a set of nondimensional parameters, which are the aspect ratios  $A_x = \frac{d}{h}$ ,  $A_y = \frac{w}{h}$ , the Marangoni number  $Ma = \frac{\gamma_T \Delta T d}{\mu \kappa}$ , the Raleigh number  $Ra = \frac{g \alpha \Delta T h^3}{\nu \kappa}$ , the Prandtl number  $Pr = \frac{\nu}{\kappa}$ , the Capillary number  $Ca = \frac{\gamma_T \Delta T}{\gamma}$ , and the dynamic Bond number  $G = \frac{Ra A_x}{Ma} = \frac{g \alpha \rho h^2}{\gamma_T}$ . The dynamic Bond number  $G$ , while not independent of these groups, is often used as a measure of the relative strength of thermocapillarity to buoyancy driving forces. Finally, there is the contact angle of the fluid with the wall, which is given by the contact angles appropriate for acetone on glass and acetone on copper, and no attempt was made to change these values.

The results of previous studies give disjoint glimpses of a wide variety of qualitatively and quantitatively different results in widely different parts of parameter space. Four different transitions have been seen: from a two-dimensional steady single-cellular flow to (i) steady two-dimensional transverse rolls, (ii) to two-dimensional oscillatory rolls, (iii) to a three-dimensional flow of longitudinal rolls, (iv) to three-dimensional oblique rolls. In this study, we consider a container with equal values for the aspect ratios  $A_x$  and

$A_y$  in the range of 1 to 8. This choice of aspect ratios will allow us to complement previous studies. On the one hand, we are considering a system with a moderate aspect ratio  $A_x$ , similar to the ones studied by Peltier & Biringen, Xu, Mundrane & Zebib, Schwabe, Moeller, Schneider, & Scharmann, and by Villers & Platten (refs. 2 to 5). On the other hand, due to the fact that  $A_x=A_y$ , we are not restricting the system to only transverse modes of instabilities, in contrast to those studies. The geometry will also allow fully three-dimensional flows, such as the ones considered by for example Gillon & Homsy and by Mundrane & Zebib (refs. 6, 7). Our results in fact indicate a first instability to longitudinal rolls, as seen by Gillon & Homsy and by Mundrane & Zebib, and we investigate the dependence of the critical Marangoni number for this transition on the aspect ratios. A further aim of our study is to investigate the stability of the longitudinal rolls, and to identify the mechanisms by which time dependence occurs in this flow.

## EXPERIMENTAL SETUP

The working section of the experiment is constructed from pieces of glass and two copper blocks, bonded together using silicone rubber sealant, as this is resistant to acetone. The resulting chamber has a width perpendicular to the applied temperature gradient of  $10.18 \text{ mm} \pm 0.1 \text{ mm}$ , and a length along the temperature gradient of  $10.61 \text{ mm} \pm 0.06 \text{ mm}$ . The top of the chamber is covered with another piece of glass and a silicone rubber seal, to limit evaporation of the acetone. The thermal conductivity of copper is  $400 \text{ W m}^{-1}\text{K}^{-1}$ , which is 3 orders of magnitude better than that of acetone, which is  $0.16 \text{ W m}^{-1}\text{K}^{-1}$ . This ensures a uniform temperature over the whole of the copper side walls. The chamber is insulated from the surroundings, and the temperature stability of the fluid inside the apparatus is measured to be better than  $\pm 0.05 \text{ K}$  over the period of a day.

Measurements of the fluid flow are performed using small tracer particles suspended in the fluid. The tracer particles are illuminated by a light sheet, which is provided by a slide projector. The fluid motion can hence be observed either with the eye using a traveling telescope, or can be recorded for later analysis using a CCD camera and high resolution video recorder. In order to obtain quantitative measurements of velocity we employ a particle tracking velocimetry algorithm which was specifically developed for the present setup.

The fluid used in the experiments is acetone. Two experimental parameters were changed between different observations of the flow, the fluid height, and the temperature difference between the side walls. The physical properties of acetone at  $14^\circ\text{C}$  lead to the following expressions for the nondimensional groups,  $\text{Pr} = 4.44$ ,  $\text{Ra} = 3.4 \times 10^{11} \text{ K}^{-1}\text{m}^{-3} \times \Delta T \text{ h}^3$ ,  $\text{Ma} = 4.00 \times 10^4 \text{ K}^{-1} \times \Delta T$ , and  $G = 9.03 \times 10^4 \text{ m}^{-2} \times h^2$ . It is important to note that by varying only two experimental parameters, we are always on one particular two-dimensional sub-section of a higher-dimensional parameter space. The aspect ratios in the experiment cover a range from 1 to 8, with an associated range in  $G$  from 4 to 0.17. The Marangoni number can be varied between 0 and  $8.2 \times 10^5$ , and the Rayleigh number can cover a range from 0 to  $7.1 \times 10^5$ .

## STEADY FLOWS

At small applied temperature differences, i.e. small Marangoni number and small Rayleigh number, the convective flow is essentially two-dimensional. An example of the velocity field for aspect ratio  $A_x=1.81$ , Marangoni number  $\text{Ma}=7.67 \times 10^4$ , Rayleigh number  $\text{Ra}=1.31 \times 10^5$ , and thus  $G=3.10$  is shown in figure 2. We observe a single closed convection circulation, rising at the hot wall and hot fluid flowing on the top half of the container towards the cold wall, where the fluid sinks, and flows back along the bottom, thus closing the loop.

A transition from the two-dimensional flow to a steady three-dimensional flow is observed when the temperature difference is increased. The velocity field on the center section of the flow at an aspect ratio of  $A_x=2.35$ , Marangoni number  $\text{Ma}=3.44 \times 10^5$ , and Rayleigh number  $\text{Ra}=2.71 \times 10^5$  is shown in figure 3. In this case, we see evidence of three-dimensional flow. In the top left corner of the flow domain, at the top of the cold wall, we see that fluid flows into the center plane from regions outside the plane of view. Somewhat surprisingly, this fluid is driven against the expected direction of both the buoyancy forces and of surface tension effects. Where this fluid meets with the main circulation, the velocity components in the plane of the section goes to zero, and here fluid is leaving the center plane. The velocity field was found to be symmetric with respect to reflection about the center plane of the container, and suggests a circulation in the form of two counter-rotating eddies in the plane perpendicular to the temperature gradient. These circulations have

upwelling flow at the sides of the container, and downwelling flow at the center. This type of flow has been observed previously by Gillon & Homsy, and by Mundrane & Zebib (refs. 6, 7).

In figure 4 we show the critical Marangoni number for the onset of the three-dimensional flow as a function of the aspect ratio  $A_x$ . The points drawn as triangles represent combinations of the experimental parameters where the flow was found to be two-dimensional in nature, and the circles represent points where the flow is three-dimensional. The line separating the two-dimensional flow and the three-dimensional flow in this aspect ratio - Marangoni number projection lies along  $Ma \approx 10^6 - 2.7 \times 10^5 A_x$ .

## OSCILLATORY FLOW

Above Marangoni numbers of  $7 \times 10^5$  we observe the onset of a novel oscillatory flow, representing a secondary instability of the fully three-dimensional flow described in the last section. As the Marangoni number is increased beyond the onset of the three-dimensional flow, the region in the center section where the fluid is driven in the direction opposite to the expected direction of buoyancy and surface tension forces grows in size, until it fills as much as half of the center section. This is a typical base flow, on which the new oscillatory flow develops in a two-step process, as we will describe next. Upon further increase of the Marangoni number, a small but fast, steady eddy forms in the top right corner, at the top edge of the hot wall. This eddy rotates in the same direction as the main circulation of the convective flow. For example, at an aspect ratio of  $A_x = 3.56$ , the eddy is at first steady and confined to a small region of typical size less than 0.5 mm close to the hot wall. With an increase in Marangoni number from  $Ma = 6.70 \times 10^5$  where it first becomes observable to  $Ma = 6.79 \times 10^5$ , it grows to a typical size of 1.2 mm, with characteristic fluid speeds of  $2 \text{ mm s}^{-1}$ . A further increase in the Marangoni number to  $Ma = 6.81 \times 10^5$  results in the onset of an oscillation of the eddy, during which it begins to oscillate in both size and strength. This scenario is typical for the onset of oscillation at all the aspect ratios considered. The strength of the eddy and the amplitude of its oscillation is largest in the center section of the container, and it diminishes towards the sidewalls in a fashion which is symmetric with respect to reflection about the center plane.

The critical curve of the onset of oscillation in parameter space is shown in figure 4. The circles in figure 4 denote the parameter combinations where the flow was found to be three-dimensional and steady, and the crosses indicate time-dependent flow. At small aspect ratios, the critical Marangoni number for the onset of oscillation is around  $Ma_c = 7 \times 10^5$ . At an aspect ratio of  $A_x = 4.5$  we see a sharp drop in the critical Marangoni number, to a value of  $Ma_c = 5.3 \times 10^5$ , followed by a smooth rise to  $Ma_c = 6.6 \times 10^5$  at an aspect ratio of  $A_x = 7$ . The frequency of the oscillation is around 0.7 Hz.

To understand the onset of oscillations, we consider mechanisms in which small disturbances would amplify themselves, and the system would be unstable. We can state that the total temperature difference across the container is constant, since this is applied externally. Thus, the total amount of driving due to surface tension gradients is constant when integrated over the whole length of the container. If now for some reason there is a small temperature fluctuation in the region of the eddy increasing the temperature gradient and leading it to grow, there would be an associated reduction in surface driving in the rest of the flow. In the remainder of the center plane of the flow, the fluid is propelled against the driving due to surface tension forces, and thus a reduction in surface tension forces in this region would be associated with an increase in the flow from the cold wall to the stagnation point. This would increase the temperature gradient across the eddy, and thus lead it to grow further. This argument can also be used to show that a reduction in size would amplify itself, and is a mechanism for positive feedback, which can provide the driving for an oscillation. Once the eddy grows large on the other hand, there will be stronger advection of heat from the hot wall through the eddy to the stagnation point, thus lowering the temperature gradient and reducing the driving. In addition, when the eddy becomes large, the stagnation point moves away from the hot wall, and thus the local temperature gradient decreases, and the eddy will no longer be able to sustain itself. This scenario bears some similarity to the one described by Kayser & Berg (ref. 8) for the case of convection due to solute concentration gradients. If we assume that the lifetime of the eddy or the period of the oscillation is determined by the advection of heat through the eddy, we can make an estimate of the time scale of such a mechanism. This is the transit time of fluid through the eddy multiplied by the Peclet number to the half power, which is of the order of 2 s, and compares favorably with the frequency of the oscillation, which is of the order of 1 Hz.

## CONCLUSIONS

We have investigated experimentally the primary and secondary mechanisms of instability in buoyant-thermocapillary convection, in a rectangular configuration with equal length and width. In this system, we have observed the transition from an essentially two-dimensional flow at small Marangoni numbers to a steady, three-dimensional flow as seen previously by Gillon & Homsy and by Mundrane & Zebib (refs. 6, 7). In addition, we traced the aspect ratio dependence of the critical Marangoni number, and found a strong decrease of the critical  $Ma$  with an increase in the aspect ratio. In view of the results of Peltier & Biringen and Xu, Mundrane & Zebib (refs. 2, 3), which find a lower critical aspect ratio for the onset of two-dimensional steady rolls, we speculate that our system becomes three-dimensional before the expected onset of two-dimensional rolls, and that we hence never observe those.

We have further investigated the stability of the three-dimensional flow at larger Marangoni numbers, and have observed a transition to oscillatory behavior. Oscillation takes place in a small confined region, and is driven by the strongly developed three-dimensional flow. We were able to suggest the underlying physical mechanism which gives rise to the oscillation, which consists of a positive feedback mechanism leading the eddy to grow, and a mechanisms by which the eddy eventually destroys itself. This scenario is consistent with a relaxation type oscillation. The appearance of the oscillation may be localized to a section of the three-dimensional cellular flow structure, and may well be very sensitive to the value of the contact angle of the fluid with the wall.

## ACKNOWLEDGMENTS

We wish to acknowledge the support of NASA through Contract No. NAG-3-1475.

## REFERENCES

1. B. M. Carpenter, G. M. Homsy, "Combined buoyant-thermocapillary flow in a cavity", *J. Fluid Mech.* **207**, (1989), pp. 121-132.
2. L. J. Peltier, S. Biringen, "Time-dependent thermocapillary convection in a rectangular cavity: numerical results for a moderate Prandtl number fluid", *J. Fluid Mech.* **257**, (1993), pp. 339-357.
3. J. Xu, M. Mundrane, A. Zebib, personal communication, (1995).
4. D. Schwabe, U. Moeller, J. Schneider, A. Scharmann, "Instabilities of shallow dynamic thermocapillary liquid layers", *Phys. Fluids A* **4** 11, (1992), pp. 2368-2381.
5. D. Villers, J. K. Platten, "Coupled buoyancy and Marangoni convection in acetone: experiments and comparison with numerical simulations", *J. Fluid Mech.* **234**, (1992), pp. 487-510.
6. P. Gillon, G. M. Homsy, personal communication, (1996).
7. M. Mundrane, A. Zebib, "Two- and three-dimensional buoyant thermocapillary convection", *Phys. Fluids A* **5** 4, (1992), pp. 810-818.
8. W. V. Kayser, J. C. Berg, "Spontaneous convection in the vicinity of liquid menisci", *Ind. Eng. Chem. Fundam.*, **10** 3, (1971), pp. 526-529.

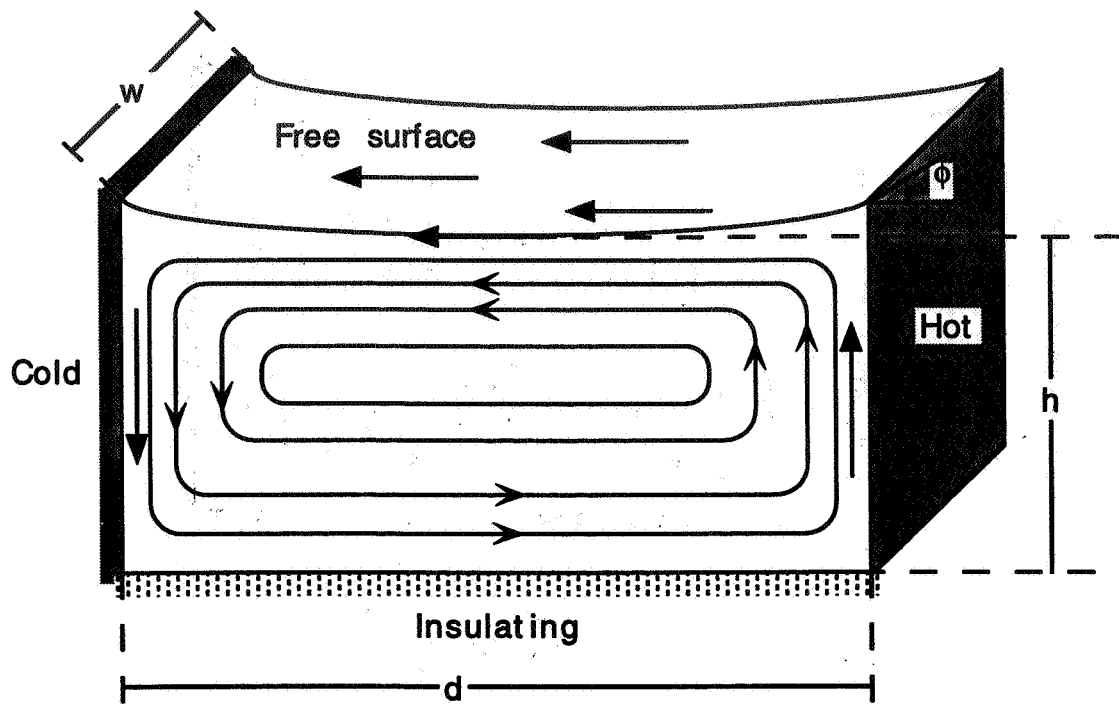


Figure 1: Schematic view of the geometry

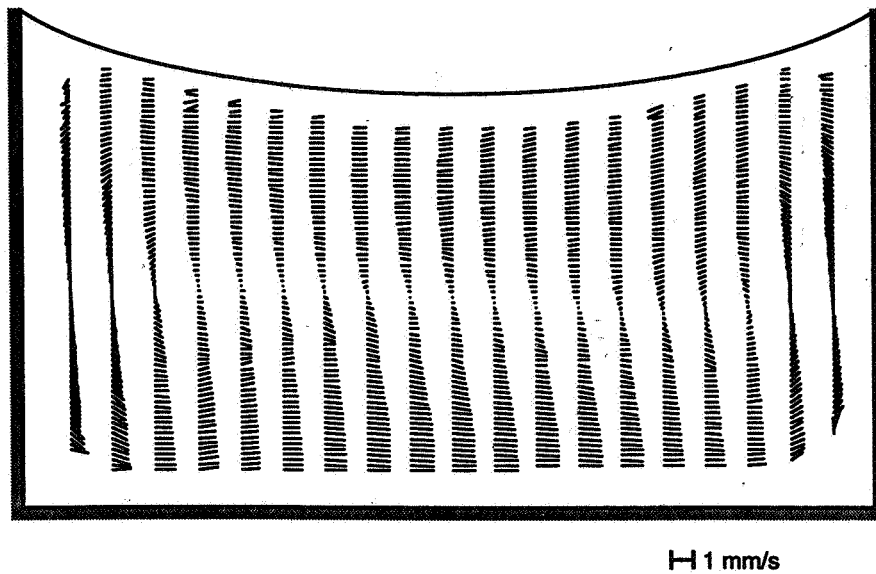


Figure 2: Velocity field on the center section of the cell, at  $A_x=1.81$ ,  $Ma=7.67 \times 10^4$ ,  $Ra=1.31 \times 10^5$ ,  $G=3.10$ .

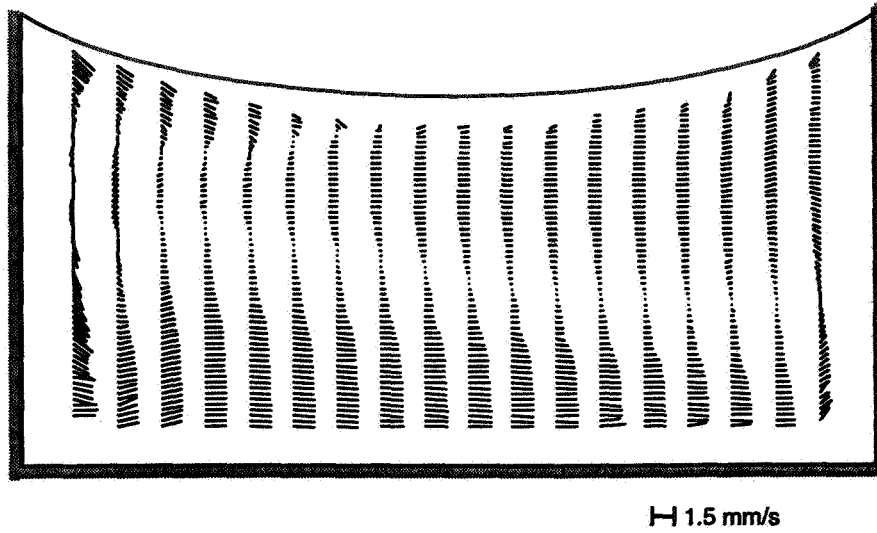


Figure 3: Velocity field on the center section of the cell, at  $A_x=2.35$ ,  $Ma=3.44 \times 10^5$ ,  $Ra=2.71 \times 10^5$ ,  $G=1.85$ .

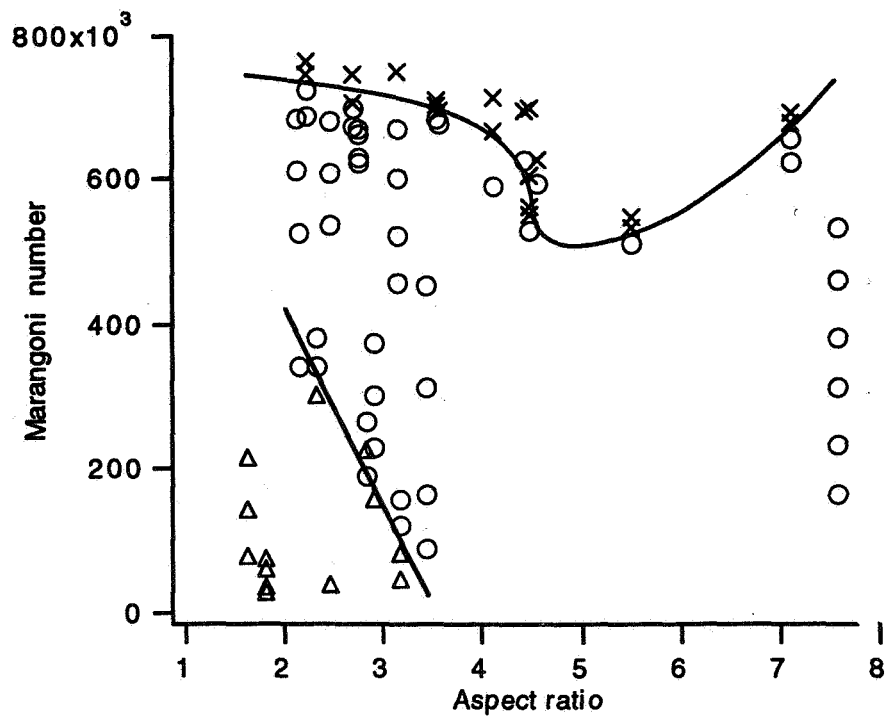


Figure 4: Overview of parameter space.  $\Delta$ : steady 2-D flow,  $O$ : steady 3-D flow,  $X$ : oscillatory flow.

# LONG-WAVELENGTH INSTABILITY IN MARANGONI CONVECTION

Stephen J. Van Hook, Michael F. Schatz, Jack B. Swift,  
W. D. McCormick and Harry L. Swinney  
Center for Nonlinear Dynamics and Department of Physics  
The University of Texas at Austin  
Austin, TX 78712

## ABSTRACT

Our experiments in thin liquid layers ( $\sim 0.1$  mm thick) heated from below reveal a well-defined long-wavelength instability: at a critical temperature difference across the layer, the depth of the layer in the center of the cell spontaneously decreases until the liquid-air interface ruptures and a dry spot forms. The onset of this critical instability occurs at a temperature difference across the liquid layer that is 35% smaller than that predicted in earlier theoretical studies of a single layer model. Our analysis of a two-layer model yields predictions in accord with the observations for liquid layer depths  $\geq 0.15$  mm, but for smaller depths there is an increasing difference between our predictions and observations (the difference is 25% for a layer 0.06 mm thick). In microgravity environments the long-wavelength instability observed in our terrestrial experiments is expected to replace cellular convection as the primary instability in thick as well as thin liquid layers heated quasistatically from below.

## INTRODUCTION

An understanding of thermocapillary flows and other surface-tension-driven phenomena will be critical for successful containerless processing in microgravity. Surface-tension-driven Bénard (Marangoni) convection (see Fig. 1), in which a liquid with a free upper surface is heated from below, is a classic example of such thermocapillary flows. The temperature gradient on the free surface that initially drives the fluid flow can originate from both temperature fluctuations and deformational perturbations. The former are stabilized by diffusion, the latter by gravity. When gravity is sufficiently strong to stabilize deformational perturbations, the primary instability leads to the short-wavelength hexagonal convection cells first observed by Bénard [1]. This instability forms when the Marangoni number ( $M \equiv \sigma_T \Delta T d / \rho \nu \kappa$ ), the non-dimensionalized  $\Delta T$  across the liquid, exceeds a critical value  $M_c$ . Recent experiments have yielded  $M_c = 83$  [2], in accord with linear stability theory [3]. In microgravity, however, another instability can arise; the liquid is particularly vulnerable to deformational instabilities since gravity (characterized by the Galileo number,  $G \equiv g d^3 / \nu \kappa$ , where  $g$  is the gravitational acceleration) is not strong enough to prevent thermocapillarity (characterized by  $M$ ) from pulling liquid from warm, depressed regions of the interface to cool, elevated regions. The suppression of curvature by surface tension causes this deformational instability to appear with a long wavelength.

This long-wavelength instability was predicted to exist in the 1960's [4, 5], but the present experiments are the first to demonstrate the existence of this instability [6]. Both linear [7-9] and nonlinear [10-13] theories have used a one-layer model, with the effect of the air layer modeled by use of a heat transfer coefficient, the Biot number, which in the long-wavelength limit is  $H = k_a d / k d_a$ , where  $k$  and  $k_a$ , respectively, are the liquid and air thermal conductivities and  $d$  and  $d_a$  are the layer thicknesses. The one-layer model predicts onset of the instability at  $M = (2/3)G(1 + H)$ . To study this long-wavelength instability in terrestrial experiments, we achieve small  $G$  by using very thin depths,  $d \sim 0.1$  mm; a 0.1-mm-thick layer of liquid in terrestrial gravity has the same  $G$  as a 1.0-mm-thick layer for  $g = 10^{-3}g_E$ .

## EXPERIMENTAL METHODS

We study a thin layer of silicone oil that lies on a heated, gold-plated aluminum mirror and is bounded above by an air layer (see Fig. 1). A single-crystal sapphire window (0.3-cm-thick) above the air is cooled by a temperature-controlled chloroform bath. The temperature drop across the liquid layer is calculated assuming conductive heat transport and is typically 0.5–5 °C. We use a distilled polydimethylsiloxane silicone oil with a viscosity of 10.2 cS at 50 °C [14]. The circular cell (3.81 cm inner diameter) has aluminum sidewalls whose upper surface is made non-wetting with a coating of Scotchgard. The liquid layers are sufficiently thin that buoyancy is negligible; the experiments are performed with  $0.005 \text{ cm} < d < 0.025 \text{ cm}$  (with aspect ratios ranging from 150 to 750) and  $0.023 < d_g < 0.080 \text{ cm}$  (typically  $d_g = 0.035 \text{ cm}$ ); the corresponding fundamental wavevectors are in the range  $0.008 < q = 2\pi d/L < 0.040$  ( $\ll 1$ ). We visualize the layer using interferometry, shadowgraph and infrared imaging ( $256 \times 256$  pixel InSb staring array, sensitive in the range 3–5  $\mu\text{m}$ ). The gap between the sapphire window and the mirror is uniform to 1%, as verified interferometrically. The liquid surface is initially flat and parallel to the mirror to 1% in the central 90% of the cell, with a boundary region near the sidewalls due to contact line pinning. This initial depth variation is accentuated by thermocapillarity as  $\Delta T$  is increased; measurements of depth variation show a 10% surface deformation in the central 90% of the cell at 3% below onset.

## EXPERIMENTAL RESULTS

**Instability Onset** Above a critical  $\Delta T$ , the liquid layer becomes unstable to a long-wavelength draining mode that eventually forms a dry spot [see Figs. 2(left) and 5(left)]. The drained region takes several hours (of order a horizontal diffusion time,  $L^2/\kappa$ ) to form. Although we refer to the drained region as a “dry spot”, it is not completely dry since an adsorbed layer  $\sim 1 \mu\text{m}$  thick remains. The size of the drained region is typically one-quarter to one-third the diameter of the entire cell. As Fig. 3(left) shows, our measurements of onset are consistently 35% below in  $\Delta T$  (or  $M$ ) the prediction of linear stability for the one-layer model that appears in the literature [7–13]. We do not believe this discrepancy is due to systematic errors in the characterization of our experiment (*e.g.*, geometry, fluid properties) or nonuniform heating of the liquid because experiments in the same convection cell using thicker liquid layers find onset of hexagons uniform across the cell at a  $\Delta T$  that agrees with another experiment [2] and linear stability theory [3].

**Mode Competition** The long-wavelength and the hexagonal modes become simultaneously unstable at a critical liquid depth  $d_c$ . Near this critical depth, both modes of instability compete and influence the formation of the pattern. The two modes are not mutually exclusive, but there is a fundamental imbalance in their relationship: the presence of the hexagons suppresses the long-wavelength mode, while the presence of long-wavelength deformation may induce the formation of hexagons. One-layer linear stability theory predicts  $d_c = (120\nu\kappa/g)^{1/3} = 0.023 \pm 0.001 \text{ cm}$ ; we observe the exchange of primary instabilities at  $d_c = 0.025 \pm 0.001 \text{ cm}$ . For  $d > d_c$ , hexagons are the primary instability [see Fig. 2(right)]; the hexagons smooth the large-scale temperature variations that would allow formation of the long-wavelength mode as a secondary instability when  $M$  exceeds  $M_c$ .

For  $d < d_c$ , the long-wavelength mode is the primary instability. The liquid expelled from the forming dry spot increases the local height  $h(x, y, t)$  and thus the local Marangoni number [ $\propto h(x, y, t)$ ] in the newly formed elevated region; for  $0.017 \text{ cm} < d < d_c$ , hexagons form in the elevated region since the local  $M$  in this region exceeds  $M_c$  for the onset of hexagons [see Fig. 2(center)]. For  $d < 0.017 \text{ cm}$ , hexagons do not form at the onset of the long-wavelength mode [see Fig. 2(left)], but can form in the elevated region for  $\Delta T$  sufficiently far above onset. Similar mode



competition phenomena have been studied theoretically for solutocapillary convection [15]. Rapid instead of quasistatic ramping can lead to the formation of the hexagons where the long-wavelength is predicted to be the primary instability since the timescale for formation of hexagons (the vertical diffusion time,  $d^2/\kappa$ ) is much shorter than the timescale for formation of the long-wavelength mode (the horizontal diffusion time,  $L^2/\kappa$ ). When  $d \ll d_c$ , increasing  $\Delta T$  far above  $\Delta T_c$  increases the area of the dry spot until the remaining layer is thick enough to form hexagons, which then halts any further advance of the dry spot. At fixed  $\Delta T$ , the dry spot is stable.

## TWO-LAYER MODEL

The evolution of the instability can be studied using a nonlinear evolution equation derived from the Navier-Stokes equations in the limit of long-wavelengths. Several authors [10-13] have derived evolution equations using a one-layer model. We have developed a two-layer model which takes into account the change in the temperature profile in the air due to deformation of the interface. The appropriate heat transfer coefficient then becomes  $F = (d/d_a - H)/(1 + H)$ . The two-layer model reduces to the one-layer model in the limit  $d/d_a \rightarrow 0$ . The two-layer evolution equation for the surface height  $h(x, y, t)$  is:

$$\frac{3}{G}h_t + \nabla \cdot \left\{ \frac{3M}{2G} \frac{(1+F)h^2 \nabla h}{(1+F-Fh)^2} - h^3 \nabla h + \left( \frac{2\pi d}{L} \right)^2 \frac{h^3}{B_L} \nabla^2 \nabla h \right\} = 0$$

where time is scaled by  $d^2/\kappa$  and  $B_L$  is a modified static Bond number,  $B_L \equiv \rho g(L/2\pi)^2/\sigma > 0$ .  $B_L \sim 30$  for our experiments. The first term in curly brackets describes the effect of thermocapillarity; the second, gravity; and the third, surface tension.

Analysis A linear stability analysis of the above equation predicts onset of the instability at

$$M = \frac{2G}{3(1+F)},$$

which is smaller than predicted by the one-layer model. As  $d/d_a$  increases, the difference between the two theories becomes more pronounced. A weakly nonlinear analysis of the evolution equation reveals that the bifurcation is subcritical for all  $B_L$  and  $F$ , with squares being more unstable than rolls. We solved for all the steady states in one dimension (rolls) and discovered that no stable, deformed states exist; that is, the bifurcation curve continues backwards in  $M$ , never turning over in a saddle-node bifurcation. The shape of the (unstable) steady states changes at  $F = 1/2$ , and thus the two-layer model suggests a qualitative change in behavior at  $F = 1/2$ . The two-layer model reduces to the one-layer model when  $d/d_a = 0$  and thus  $F \leq 0$ , so the one-layer model cannot make this prediction.

Numerical Simulations We performed numerical simulations of the evolution equation, both with a one-dimensional and a two-dimensional surface. The simulations employed a pseudospectral method to handle the extreme nonlinearity of the equations. Because of the fourth-order nonlinearity, a 2/5 rule was required to prevent aliasing (e.g., for 256 spatial locations in one dimension, only 103 spectral modes from -51 to +51 were used). At each time-step, the power in the remaining 3/5 of modes was exponentially damped. We used periodic boundary conditions (a square box in two-dimensions) with a Fourier series as a basis set. The simulations find the same bifurcation curve as the analytical theory found. When the system is unstable, it forms either a dry spot ( $F < 1/2$ ) or an elevated region ( $F > 1/2$ ), as Fig. 4 illustrates. The evolution equation gives good qualitative agreement to the experiments for  $F < 1/2$  (see Fig. 5).

## CONCLUDING REMARKS

Terrestrial experiments produce the first observation of a long-wavelength deformational instability in surface-tension-driven Marangoni convection. The experimental results do not agree with a one-layer model in the literature, but do agree with a two-layer model for certain liquid depths. The source of the deviation from the two-layer model is being investigated.

The two-layer model predicts a qualitatively different state, one with an elevated region, for sufficiently large  $d/d_a$  ( $F > 1/2$ ); we are currently testing this prediction. Employing gases other than air (*e.g.*, helium) allows us to vary  $F$  without changing the geometry of the experiment or the liquid layer thickness.

## ACKNOWLEDGMENTS

We thank S.H. Davis and R.E. Kelly for helpful discussions. This research is supported by the NASA Microgravity Science and Applications Division (Grant No. NAG3-1382). S.J.V.H. is supported by the NASA Graduate Student Researchers Program.

## REFERENCES

- [1] H. Bénard, *Rev. Gén. Sci. Pure Appl.* **11**, 1261 (1900).
- [2] M. F. Schatz, S. J. VanHook, W. D. McCormick, J. B. Swift and H. L. Swinney, *Phys. Rev. Lett.* **75**, 1938 (1995).
- [3] J. R. A. Pearson, *J. Fluid Mech.* **4**, 489 (1958).
- [4] L. E. Scriven and C. V. Sternling, *J. Fluid Mech.* **19**, 321 (1964).
- [5] K. A. Smith, *J. Fluid Mech.* **24**, 401 (1966).
- [6] S. J. Van Hook, M. F. Schatz, W. D. McCormick, J. B. Swift, and H. L. Swinney, *Phys. Rev. Lett.* **75**, 4397 (1995).
- [7] M. Takashima, *J. Phys. Soc. Japan* **50**, 2745 (1981).
- [8] D. A. Goussis and R. E. Kelly, *Int. J. Heat Mass Trans.* **33**, 2237 (1990).
- [9] C. Pérez-García and G. Carneiro, *Phys. Fluids A* **3**, 292 (1991).
- [10] S. H. Davis, in *Waves on Fluid Interfaces*, edited by R. E. Meyer (Academic Press, New York, NY, 1983), p. 291.
- [11] S. H. Davis, *Annu. Rev. Fluid Mech.* **19**, 403 (1987).
- [12] B. K. Kopbosynov and V. V. Pukhnachev, *Fluid Mech. Sov. Res.* **15**, 95 (1986).
- [13] A. Oron and P. Rosenau, *J. Phys. II (France)* **2**, 131 (1992).
- [14] M. F. Schatz & K. Howden, *Exp. in Fluids* **19**, 359 (1995).
- [15] A. A. Golovin, A. A. Nepomnyashchy and L. M. Pismen, *Phys. Fluids* **6**, 34 (1994).

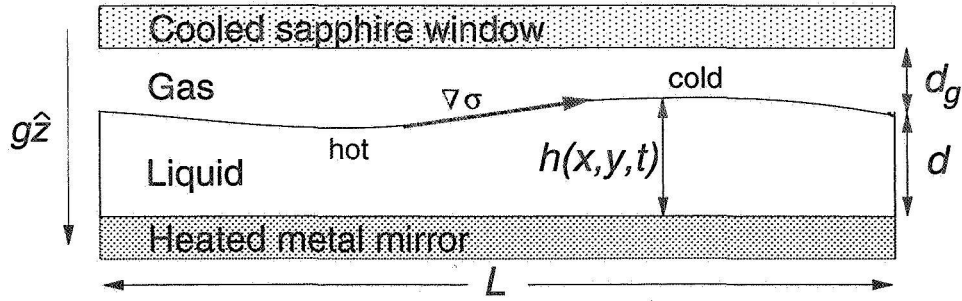


Fig. 1. Sketch of Marangoni convection experiment. Silicone oil (depth  $d$ ) is heated from below and is bounded above by an air layer (depth  $d_a$ ). The air layer is cooled from above and the mean temperature drop across the liquid layer is  $\Delta T$ . In the presence of deformation, a temperature-gradient-induced surface-tension gradient pulls liquid against gravity up the interface. The liquid has density  $\rho$ , kinematic viscosity  $\nu$ , thermal conductivity  $k$ , thermal diffusivity  $\kappa$ , and temperature coefficient of surface tension  $\sigma_T \equiv |d\sigma/dT|$ .

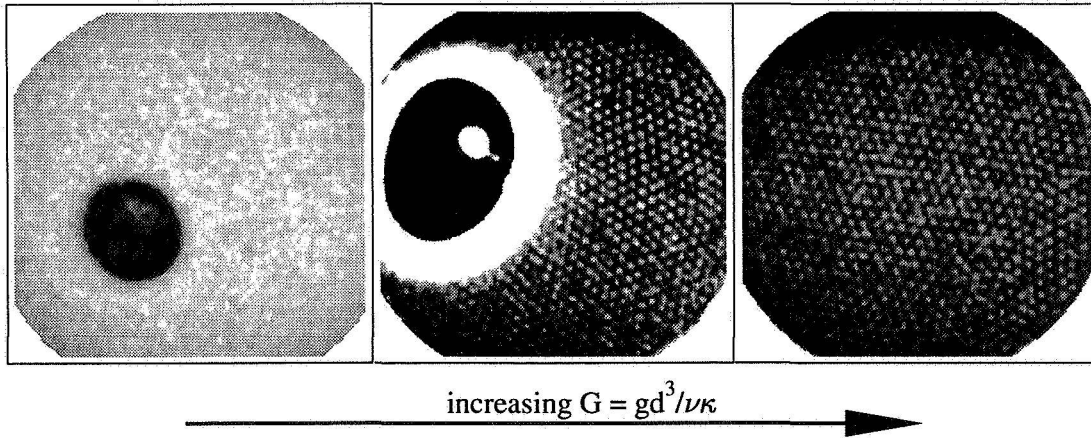


Fig. 2. Infrared images from experiments with increasing liquid depth (increasing  $G$ ). Left: For  $d = 0.011$  cm, the long-wavelength mode is the primary instability. The dark region is the dry spot. Center: At  $d = 0.022$  cm, the long-wavelength and hexagonal modes coexist. A droplet (white circle) is trapped within the dry spot (dark oval); the liquid layer is strongly deformed (white annulus) between the dry spot and the hexagonal pattern. Right: For  $d > 0.025$  cm (in air), hexagons are the primary instability (here  $d = 0.033$  cm).

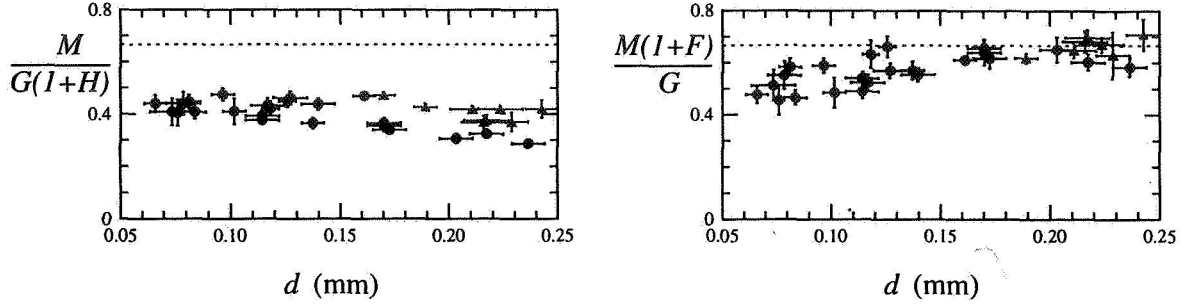


Fig. 3. Comparison of the observed instability onset to both (left) one- and (right) two-layer linear stability theory (dashed line). Circles correspond to dry spots, triangles to dry spots with hexagons. For  $d > 0.18$  mm, the circles are from experiments in which He, not air, was used as the gas. The data agree well with the two-layer theory for thick liquid depths, but not for thin liquid depths.

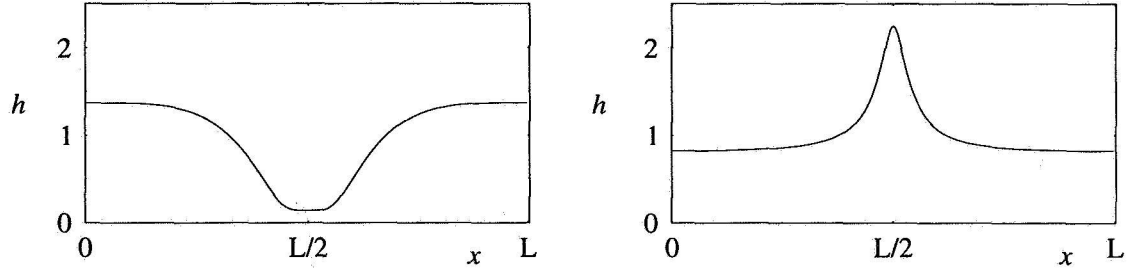


Fig. 4. The height of the layer as a function of position in the cell as determined by one-dimensional numerical simulations for two values of  $F$  at 0.33% above the onset of linear instability. Left:  $F = 1/3$ ,  $B_L = 30$ . A dry spot forms where the depth of the liquid nearly approaches zero in the drained region. Right:  $F = 2/3$ ,  $B_L = 30$ . The system forms a localized elevated region instead of a dry spot. It continues to evolve until it ‘hits’ the top plate.

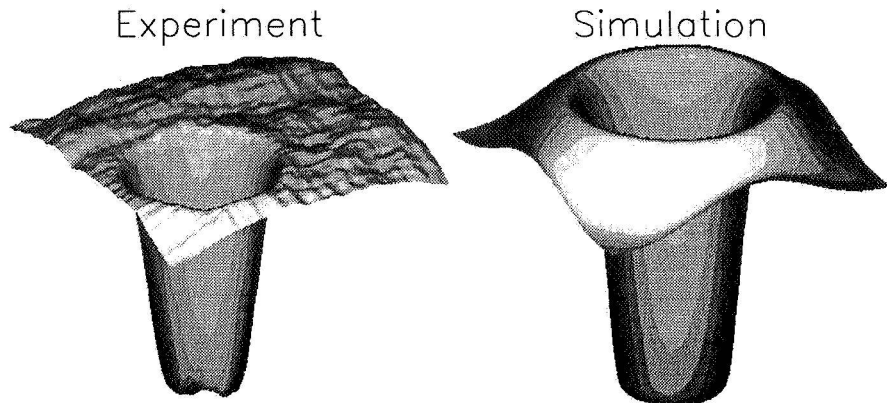


Fig. 5. Dry spot in both experiment and numerical simulation. The experimental picture shows the measured brightness temperature as a function of position along the interface about 10% above onset of instability;  $d = 0.011$  cm ( $F \sim 0.2$ ). Numerical simulation of a long-wavelength evolution equation ( $F = 0$ ,  $B_L = 30$ ) shows the depth as a function of position for 1% above onset of linear instability. The depth of the liquid approaches zero in the drained region.

# AN EXPERIMENTAL STUDY OF RICHTMYER-MESHKOV INSTABILITY

Jeffrey W. Jacobs and Charles E. Niederhaus  
Department of Aerospace and Mechanical Engineering  
University of Arizona  
Tucson, AZ 85721

## ABSTRACT

Richtmyer-Meshkov (RM) instability occurs when a planar interface separating two fluids of different density is impulsively accelerated in the direction of its normal. It is one of the most fundamental of fluid instabilities and is of importance in fields ranging from astrophysics to materials processing. Because RM instability experiments are normally carried out in shock tubes, where the generation of a sharp well controlled interface between gases is difficult, there is a scarcity of good experimental results. The experiments presented here utilize a novel technique which circumvents many of the experimental difficulties that have previously limited the study of RM instability. In this system, the instability is generated by bouncing a thin rectangular tank containing two liquids off of a fixed spring. Results obtained from these experiments yield particularly well visualized images of the nonlinear development of the instability. However, because the run time in these experiments is limited, new experiments capable of achieving longer run times are planned.

## INTRODUCTION

Richtmyer-Meshkov (RM) instability is the instability of an impulsively accelerated planar interface separating two fluids of different density. For example, RM instability causes small perturbations on a flat interface, accelerated by a passing shock wave, to grow in amplitude and eventually become a turbulent flow. It is closely related to Rayleigh-Taylor (RT) instability which is the instability of a planar interface undergoing constant acceleration, such as caused by the suspension of a heavy fluid over a lighter one in the earth's gravitational field. Therefore, RM instability is often referred to as impulsive or shock-induced Rayleigh-Taylor instability. Like the well known Kelvin-Helmoltz instability, RM instability is a fundamental hydrodynamic instability which exhibits many of the nonlinear complexities that transform simple initial conditions into a complex turbulent flow. Furthermore, the simplicity of RM instability (in that it requires very few defining parameters), and the fact that it can be generated in a closed container, makes it an excellent testbed to study nonlinear stability theory as well as turbulent transport in a heterogeneous system.

Richtmyer-Meshkov instability is of importance in fields ranging from astrophysics to materials processing. For example, RM instability is believed to occur when the outward propagating shock wave generated by the collapsing core of a dying star passes over the helium-hydrogen interface. Observations of the optical output of the recent supernova 1987A seem to indicate that the outer regions of the supernova were much more uniformly mixed than expected, indicating significant RM mixing had occurred (ref. 1). RM instability is of critical importance to inertial confinement fusion. In this case, the shell which encapsulates the deuterium-tritium fuel becomes RM unstable as it is accelerated inward by the ablation of its outer surface by laser or secondary X-

ray radiation. The degree of compression achievable in laser fusion experiments is ultimately limited by RM and RT instability. Thus, these instabilities represent the single most significant barrier to attaining positive-net-yield fusion reactions in laser fusion facilities (ref. 2). RM instability is also of importance to high speed combustion applications, where, for example, the interaction of a shock wave with a flame front can be unstable, thereby greatly enhancing mixing and significantly altering the burning rate (ref. 3). In addition, RM instability has been identified as one of the phenomena which allows dissimilar metal alloys to be bonded together in explosive welding processes (ref. 4).

The evolution of RT instability from small amplitude perturbations to fully turbulent flow has been well documented by numerous experimental investigations (refs. 5 and 6). However similar experimental verification for RM instability is noticeably lacking. In particular, there is a scarcity of well visualized experimental results. RM instability experiments have traditionally been carried out in shock tubes. Shock tube experiments have had some success in verifying the linear stability theory, and in determining the bulk properties of the final turbulent flow. However, visualizations of the nonlinear transition process in these experiments are virtually nonexistent. The major difficulty in these experiments is in maintaining a well controlled sharp boundary between two gases. One solution to this problem has been to initially separate the two gases with a thin membrane which is then broken by the passing shock wave (refs. 7 and 8). Under the best of circumstances, the membrane is broken into small pieces which produce a minimal effect on the larger scale initial perturbation imposed by the initial shape of the membrane; however, the broken membrane fragments generate uncontrolled small scale perturbations which can seed turbulence production. Under the worst of circumstances, the membrane breaks into larger fragments which disturb even the growth of the initial perturbation. Under all circumstances the presence of membrane fragments impedes Schlieren or shadowgraph visualization, obscuring both the interface and the resulting turbulent mixing region. Other shock-tube experiments have attempted to avoid membrane effects by initially separating the two gases by a solid barrier which is removed immediately prior to firing the shock tube (refs. 9 and 10). Because the diffusion coefficients of gases are large, this technique generates diffuse interfaces (typically 1 cm thick). In addition, because the interfacial disturbance left behind by removing the barrier is used as the initial perturbation, the resulting instability is nonuniform and difficult to characterize, thus severely limiting the usefulness of the experimental results.

The use of liquids instead of gases eliminates the problems with generating a sharp well defined interface because the very low diffusion coefficients of liquids allow for the easy generation of sharp interfaces. Low speed liquid phase experiments are, however, complicated by the fact that gravity strongly influences the flow development. RM instability involves the flow evolution and turbulent mixing of a system of two fluids of different density. However, the effects of body forces must be kept small except during the impulsive acceleration. In shock tube experiments, the flow induced by the earth's gravitational acceleration is negligible when compared with the high fluid velocities of the induced RM instability. However, in low speed liquid experiments the earth's gravitational influence is much more dominant, and can stabilize (or destabilize) the developing RM instability. Furthermore it can strongly effect the turbulent flow development. Thus, these types of experiments must be carried out in a low gravity environment.

Recently, we have developed a novel experimental technique to study the RM instability of a liquid system (ref. 11). In these experiments a tank containing two stably stratified liquids is impulsively accelerated by bouncing it off of a stationary spring. These experiments represent a significant advancement in the study of RM instability because: (1) a sharp liquid/liquid interface is easy to form and visualize, and (2) the relatively low speed of the flow allows for the use of standard video imaging. The problems with gravity in liquid phase RM

instability experiments are solved in these experiments by keeping the fluids essentially in free-fall during the evolution of the instability.

## EXPERIMENTAL DESCRIPTION

The experimental apparatus (figure 1) consists of a thin rectangular tank with inside dimensions of 2.54 cm x 11.75 cm x 25.4 cm which is mounted to a linear rail system oriented so that the tank is free to move in the vertical direction with approximately 1.25 m of travel. This system utilizes a set of 4 linear bearings which ride with very little friction on a pair of 1.91 cm diameter rails. At the bottom of the rail system is a vertical fixed spring which is secured at one end. The rails are mounted to a steel plate which is pinned at the top, thus allowing it to pivot in the lateral direction. The bottom half of the tank is initially filled with a colored salt water solution, and the top half with clear fresh water, while the tank is held at a position approximately 0.5 m above the spring using an electromagnet. A nearly saturated salt solution is used, consisting of  $\text{Ca}(\text{NO}_3)_2$  ( and water and having specific gravity of approximately 1.35. This combination produces an Atwood number (i.e. the difference of the densities divided by their sum) of approximately 0.15.

An initial surface shape is given to the system by sinusoidally oscillating the rail system in the horizontal direction to produce standing waves on the interface. This is accomplished using an eccentric circular cam mounted to a stepper motor which rides on the side of the steel plate. The sinusoidal motion generated by the rotating cam generates a sinusoidal surface pattern. The wavelength of this surface pattern can be controlled by properly specifying the input signal to the stepper motor. In addition, the amplitude of the initial shape can be controlled by changing the amplitude of oscillation through adjustment of the degree of eccentricity of the cam. Note that initial conditions produced by this technique are ordinarily not motionless. However, in the present experiments the electromagnet release can be synchronized with the container oscillation. Therefore, the experiments can be timed so that the initial velocity is zero.

At the start of each experiment, the tank is released by disconnecting the power to the electromagnet, thus allowing the tank to fall and bounce off of the fixed spring. Because the container is nearly in free-fall before and after bouncing, the only body force that it experiences is during the bouncing event, which lasts for approximately 30 ms. The experiment therefore generates an impulsive acceleration without using a shock wave. After bouncing, the system travels upward and downward again before the experiment ends on the second bounce. During the entire event, the interface is viewed using a shuttered CCD camera which is mounted to the moving container. The video signal from the camera is fed to a computer system with a frame grabber where it is stored for later viewing. The time between bounces is approximately 0.5 s. The camera is operated in an interlaced mode so that it effectively acquires 60 frames per second, thus yielding 30 pictures of the evolving interface per experiment. The camera also views a vertical scale attached to the stationary rails which allows for measurement of the instantaneous position of the tank. In addition an accelerometer mounted to the tank records the acceleration history of the fluid system.

## EXPERIMENTAL RESULTS

Figure 2 is a sequence of photographs showing the evolution of the instability as viewed by the video camera. Figure 2(a) was taken immediately before the container contacts the spring. Thus, it represents the initial surface shape. Figure 2(b) was taken during the time the container was in contact with the spring, and figures 2(c)-(j) span the period of free fall between the first two bounces. Figures 2(k) and (l) were taken during and after

the time of the second bounce. The impulsive acceleration in these experiments is directed from the heavier fluid into the lighter fluid. Thus the sinusoidal initial surface shape inverts phase before growing (figure 2b). The instability initially retains its sinusoidal shape. However, with time, vortices begin to form at points midway between the crests and troughs (figure 2d), yielding the symmetric mushroom pattern typical of RT and RM instability of fluids with small density differences. These vortices eventually roll the interface around their cores to form a spiral pattern. This large amplitude interfacial pattern is reminiscent of that observed in Kelvin-Helmholtz experiments. However, in Kelvin-Helmholtz instability the vortices all have the same sign, while in this case the vortices alternate in sign. Note that, characteristic of the instability with small density differences, the surface shape retains its top to bottom symmetry well into the nonlinear regime.

The container bounces a second time, and thus receives a second acceleration beginning at a point between figure 2(j) and 2(k). In 2(k), one can see a dramatic change in the interfacial pattern in which the mushroom features rapidly collapse and erupt into turbulence. In 2(l) mushrooms are no longer detectable in what appears to be a fully turbulent flow.

## CONCLUSIONS

The experiment described above represents a significant advancement in the study of RM instability in that extremely well visualized results are obtained. However, the run times achievable in the present experimental apparatus are obviously limited. Previous shock tube experiments and computational studies have shown that turbulent flows can be obtained with a single impulsive acceleration. But because of the limited run time of the current apparatus, it appears that a turbulent flow will not be attainable in this set up. The low gravity environment of space allows a unique opportunity to develop an experiment of this type which could be carried out in earth orbit. If achievable this would provide effectively unlimited run times, and as a result yield valuable information about this fundamental and important fluid instability.

## REFERENCES

1. Arnett, W. D., Bahcall, J. N., Kirshner, R. P. & Woosley, S. E. "Supernova 1987A," *Annu. Rev. Astron. Astrophys.* **27**, 629-700 (1989).
2. Lindl, J. D., McCrory, R. L. & Campbell, E. M. "Progress Toward Ignition and Burn Propagation in Inertial Confinement Fusion," *Physics Today*, **45** (9) 32-50 (1992).
3. Markstein, G. H. "A Shock Tube Study of Flame Front-Pressure Wave Interaction," Sixth Symposium (International) on Combustion. Reinhold. 387-398 (1957).
4. Shaner, J. W. "Pattern Formation by Shock Processes," *Physica D* **12**, 154-162 (1984).
5. Emmons, H. W., Chang, C. T., & Watson, B. C. "Taylor Instability of Finite Surface Waves," *J. Fluid Mech.* **7**, 177-193 (1960).
6. Read, K. I. "Experimental Investigation of Turbulent Mixing by Rayleigh-Taylor Instability," *Physica D* **12**, 45-58 (1984).



7. Meshkov, E. E. "Instability of the Interface of Two Gases Accelerated by a Shock Wave," *Izv. Akad. Nauk. SSSR Mekh. Zhidk. Gaza* 4, 151-157.(1969) [Russian: *Izv. Acad. Sci. USSR Fluid Dyn.* 4, 101-104]
8. Benjamin, R. F. "Experimental observations of shock stability and shock-induced turbulence," in *Advances in Compressible Turbulent Mixing, Proceedings of the First International Workshop on the Physics of Compressible Turbulent Mixing*, Edited by W. P. Dannevik, A. C. Buckingham, C. E. Leith, Published by Lawrence Livermore National Laboratory, Conf-8810234, 341-348 (1992) .
9. Brouillette, M. and Sturtevant, B. "Experiments on the Richtmyer-Meshkov instability: single-scale perturbations on a continuous interface," *J. Fluid Mech.* 263, 271-292 (1994).
10. Cavailler, C., Mercier, P., Rodriguez, G. & Haas, J. F., "A new vertical shock tube for Rayleigh-Taylor instability measurements," *Proceedings of the 17th ISSWST at Bethlehem PA; Current Topics in Shock Waves*, Y. Kim editor, 564 (1990).
11. Jacobs, J.W., and Sheeley, J.M., "Experimental Study of Incompressible Richtmyer-Meshkov Instability," *Phys. Fluids* 8, 405-415 (1996).

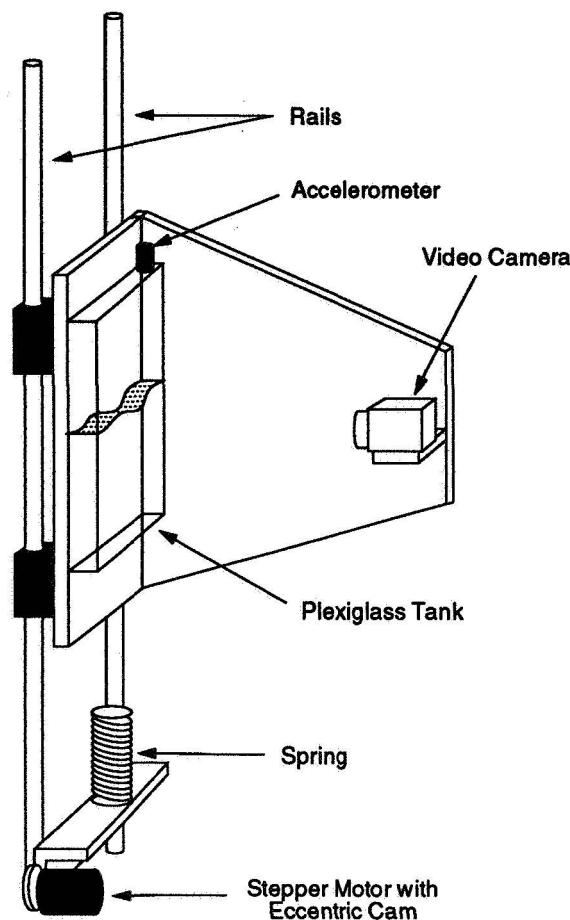


Figure 1. The experimental apparatus.

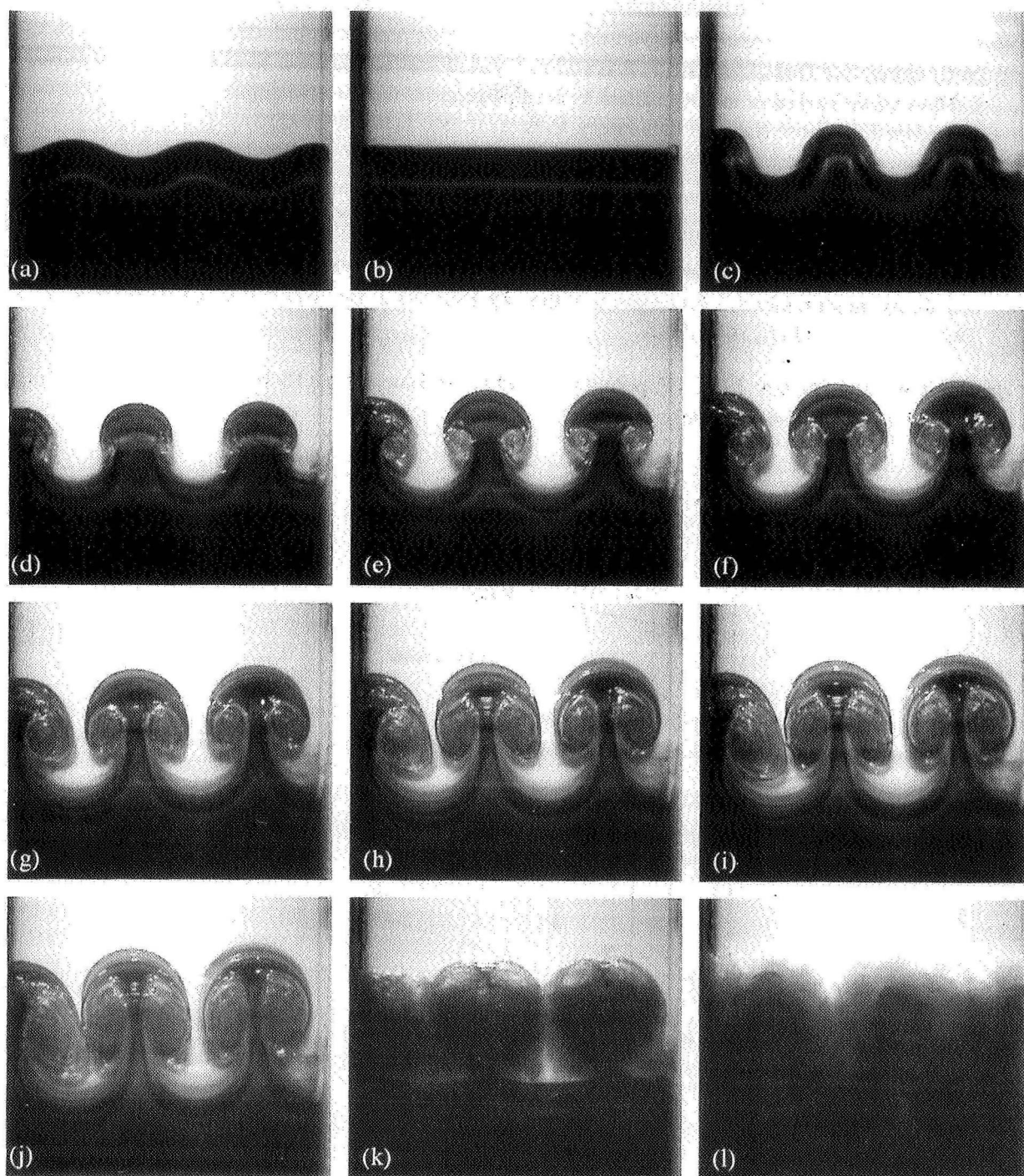


Figure 2. A sequence of images showing the development of the instability in a typical experiment. Times relative to the point of first contact with the spring are: (a) -15 ms, (b) 18 ms, (c) 68 ms, (d) 118 ms, (e) 185 ms, (f) 235 ms, (g) 285 ms, (h) 352 ms, (i) 402 ms, (j) 452 ms, (k) 519 ms, (l) 569 ms. The second spring contact occurs between (j) and (k).

# ABSOLUTE AND CONVECTIVE INSTABILITY OF A LIQUID JET IN MICROGRAVITY

S.P. Lin, I. Vihinen, A. Honohan and M. Hudman  
Mechanical and Aeronautical Engineering Department  
Clarkson University  
Potsdam, New York 13699-5725

## ABSTRACT

The transition from convective to absolute instability is observed in the 2.2 second drop tower of the NASA Lewis Research Center. In convective instability the disturbance grows spatially as it is convected downstream. In absolute instability the disturbance propagates both downstream and upstream, and manifests itself as an expanding sphere. The transition Reynolds numbers are determined for two different Weber numbers by use of Glycerin and a Silicone oil. Preliminary comparisons with theory are made.

## INTRODUCTION

The capillary instability of an infinitely long inviscid jet in vacuum with respect to temporally growing disturbances was investigated by Rayleigh (ref. 1). The instability of a viscous liquid jet with respect to spatially growing disturbances was investigated by Leib and Goldstein (ref. 2). They demonstrated that the disturbance in the jet may grow spatially as it is convected downstream or grow both in the upstream and downstream directions depending on the flow parameters. The former is called convective instability and the latter is called absolute instability. They determined the critical Weber number below which the flow is absolutely unstable as a function of Reynolds number. Lin and Lian (ref. 3) showed that the critical Weber number may be increased for a given Reynolds number by increasing the density of the ambient gas which was neglected by previous workers. The effect of gas viscosity was investigated by Lin and Lian (ref. 4). In the above referenced theories, gravity is neglected. Therefore, the good comparison of experiments on earth with theoretical results (ref. 5) may be fortuitous. Moreover the phenomenon of the jet absolute instability has never been observed. The observation of jet instability in the NASA Lewis drop tower facility allows us to elucidate the phenomenon of absolute instability. The comparison of experiments with theory is still in a preliminary stage, however.

## THEORY

The linear stability analysis of the jet instability results in the characteristic equation (ref.6)

$$\mathbf{D}(\mathbf{k}, \omega) \cdot \mathbf{A}(\mathbf{k}, \omega) = \mathbf{S}(\mathbf{k}, \omega)$$

where  $\mathbf{D}$  is the coefficient matrix,  $\mathbf{k}$  is the complex wavenumber vector,  $\omega$  is the complex frequency and  $\mathbf{S}$  is the Laplace-Fourier transform of the source vector arising from the initial condition. The eigenvector  $\mathbf{A}$  in the physical space may be obtained from the inverse Laplace-Fourier transform (ref. 6)

$$\mathbf{A}(\mathbf{r}, \tau) \int_L \frac{d\omega}{2\pi} \exp(\omega\tau) \int_F \frac{d\mathbf{k}}{(2\pi)^2} \exp(i\mathbf{k}\tau) \mathbf{D}^{-1} \mathbf{S},$$

where  $\mathbf{r}$  is the position vector,  $\tau$  is time,  $\mathbf{k}$  is the complex wavenumber assumed to be two-dimensional, and the subscripts L and F denote suitably chosen integration paths in the Laplace and Fourier space respectively. The singularities of the integrand are given by

$$D(\mathbf{k}, \omega) = 0,$$

which is the characteristic equation for the unforced natural disturbances. When the singularity is a saddle point in the Fourier space the jet may become absolutely unstable, and the axisymmetric disturbance grow asymptotically as (ref. 6).

$$\lim_{\tau \rightarrow \infty} A \sim \exp(ik_0 y) \exp(\omega_0 \tau) / \tau^{1/2}$$

when  $k_0$  and  $\omega_0$  denote respectively the location of the saddle point in the Fourier space and the branch point in the Laplace space, and  $y$  denote any point along the jet axis. When the singularity of the integrand is a simple zero of  $D=0$ , the jet may become convectively unstable. Then the disturbance which is convected downstream with the group velocity  $V_g$  behave asymptotically as (ref. 6)

$$\lim_{\tau \rightarrow \infty} A(V_g \tau, \tau) \sim \frac{1}{\sqrt{\tau}} \exp[k_{im}(\omega_s) V_g \tau],$$

where  $k_{im}$  is the maximum of  $k_i$  for  $\omega_r=0$ , and  $\omega_s$  is the corresponding frequency of oscillation.

## EXPERIMENTS

A series of experiments to investigate the transition between absolute and convective instability in a liquid jet were performed at the 2.2 second drop tower at NASA Lewis Research Center. A preliminary round of ten tests, performed with Glycerin, showed that it was possible to identify the transition with the existing drop rig. A second round of eighteen tests, performed with Dow Corning 200 Series 1000 cSt Silicone Oil, were completed with additional sensors to identify the transition point more accurately.

To investigate absolute and convective instabilities in liquid jets, one needs to be able to produce a liquid jet, induce a disturbance, photograph it, and record important flow parameters. Hence, the experimental drop rig consists of four main systems: a pressure delivery system to drive the liquid jet, a piezoceramic forcing system, a high speed photographic system, and a sensory and data acquisition system. From the preliminary round of tests it was found that the forcing system was not necessary for testing absolute instability as the vibrations from the start of the drop were sufficient to introduce a disturbance into the liquid jet. Compressed helium gas, controlled by a pressure regulator, was used to pressurize and drive the test fluid at a constant rate through the system to the solenoid valve and one millimeter nozzle. A high speed Milliken DBM-45 16mm motion picture camera was used in conjunction with a Quadtec 1538-A strobe light, synchronized at 200 frames per second, to photograph the jet. Pressure, velocity, and temperature in the second round of tests were measured by a Setra model C206 pressure transducer, AWCO model ZHM-01 flowmeter, and Omega type T thermocouple and model TX903 transmitter. These three channels of analog data were recorded by a 12-bit tattletail digital data acquisition system, whose sampling rate was controlled by the flowmeter.

To find the transition point in each round of tests, a trial and error procedure was used. Although the transitional Reynolds and Weber numbers can be obtained from theory and used to determine starting velocities and pressures, determining whether or not the instability will be visible in the test section during the 2.2 seconds of microgravity is not as trivial. Consequently, the first few tests were conducted over a broad range of pressures to get a general idea of our operating range, followed by a second set of tests to pinpoint the transition from absolute to convective instability.

Analysis of our 16mm films was performed with the TRACKER software and digital object tracking system at NASA Lewis Research Center. This tracking system included a Mekel 16mm film transport system, a Kodak Megaplug digitizing camera, a Matrox Image series framegrabber, two high resolution monitors, and a Pentium PC, among other devices for other input media. Representative images at one g and microgravity were also digitized and archived for future study.

The classification of a test as absolute or convective was determined by observing the microgravity images. In all tests, the basic state is a quiescent liquid jet at one g, the disturbance is the vibration introduced at the start of the drop, and the perturbed state is the result which exists in microgravity. In convective instability, the disturbance would be rapidly convected downstream, leaving behind a quiescent, constant diameter jet, as shown in Figure 1. In absolute instability, the disturbance would cause the liquid jet to bifurcate into an upstream and downstream section. The upstream section would snap back towards the nozzle and achieve a new dynamic equilibrium which resembled an expanding sphere, as shown in Figure 2. The sphere remains connected to the nozzle by a neck, which grows in diameter in the downstream axial direction. The downstream portion would either disappear from view or float back and coalesce with the upstream portion. At the transition, the jet breaks into two parts, but the neck grows significantly in length and can be observed as a jet whose diameter increases in the downstream direction, as shown in Figure 3.

Absolute and convective instability can also be qualitatively thought of as a balance between surface tension and inertial forces. Looking at a balance of forces in the axial flow direction for absolute instability, the inertial force acts in the downstream direction while the net force of surface tension acts in the upstream direction. In absolute instability, surface tension is stronger, enabling the disturbance to break the jet into two and containing the upstream section so that it remains local to the nozzle. Fluid particles exit the nozzle and decelerate as they enter the expanding sphere, increasing the size of this section. In the transitional case, the downstream inertial force has grown such that it balances with the upstream surface tension force. The surface tension force is still able to break the jet into two parts, but the increased inertial force has lengthened the neck between the nozzle and the sphere, signifying that the transition is about to occur, much like an elastic metal in a uniaxial tension test at its yield stress undergoing plastic deformation just before failure. For convective instability, the inertial force completely overpowers the surface tension force. The upstream surface tension force is effectively reduced to zero so that surface tension now acts solely to maintain the diameter of the jet. Fluid particles travel freely downstream as if they were still contained by the walls of the nozzle.

Figure 4 shows the experimental versus theoretical transition points. Glycerin with surface tension 63.3 dynes/cm, viscosity 1182 cSt, specific gravity 1.26 and Dow Corning 200 Series Silicone oil with surface tension 21.2 dynes/cm, viscosity 1000 cSt, and specific gravity 0.972 were used as test fluids. Due to the limited dimension of the test section and short test time of 2.2 seconds, some uncertainty as to the precise transition point remains. More refinement of our experiments is being planned.

## CONCLUDING REMARKS

The transition from convective to absolute instability in a liquid jet is demonstrated experimentally for the first time. The comparison between theory and experiments is far from complete.

## ACKNOWLEDGMENT

This work was supported by Grant NAG3-1402, NGT-51142 of NASA. We are grateful to Myron Hill, the staff of the 2.2 second drop tower, and the people of the Imaging Technology Center of NASA Lewis Research Center for their valuable assistance, without which, this research would not have been possible.

## REFERENCES

1. Lord Rayleigh, W.S., On the Instability of Jets, London Math Soc. Vol. 10, 1879, p. 361.
2. Leib, S.J. and Goldstein, M.E., Convective and Absolute Instability of a Viscous Liquid Jet, Phys. Fluids, Vol. 29, 1986, p. 952.
3. Lin, S.P. and Lian, Z.W., Absolute Instability of a Liquid Jet, Phys. Fluids A Vol. 1 (3) 1989, 490.
4. Lin, S.P. and Lian, Z.W., Absolute and Convective Instability of a Viscous Liquid Jet Surrounded by a Viscous Gas in a Vertical Pipe, Vol. 5, 1993, p. 771.
5. Lin, S.P. and Ibrahim, E.A., Instability of a Viscous Liquid Jet Surrounded by a Viscous Gas in a Vertical Pipe, J. Fluid Mech. Vol. 218, 1991, p. 641.
6. Bers, A., Handbook of Plasma Physics (North-Holland, Amsterdam, 1983), Vol. 1, pp. 452-516.

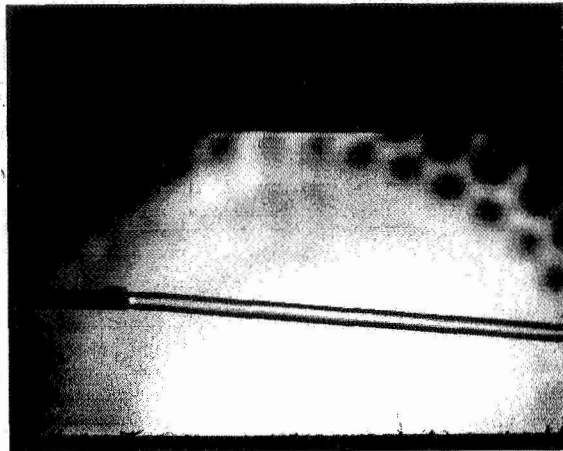


Figure 1. Convective Instability, ( $Re=0.233$ ,  $We=0.215$ )

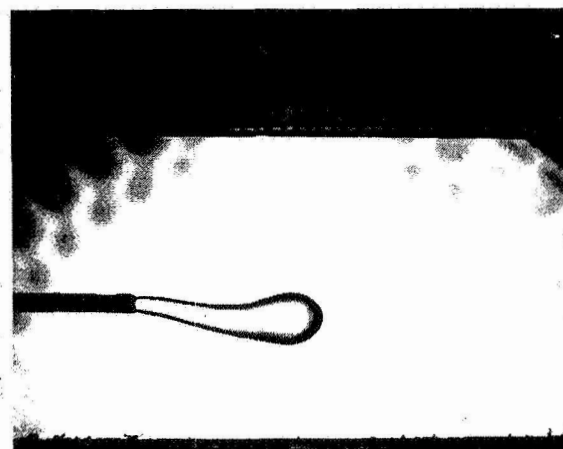


Figure 2. Absolute Instability, ( $Re=0.070$ ,  $We=2.365$ )

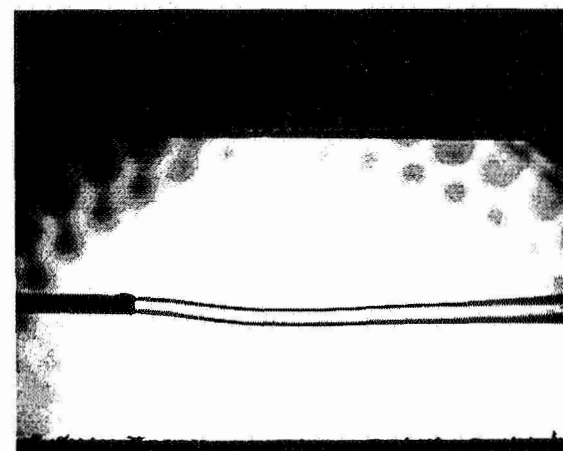


Figure 3. Transition Regime, ( $Re=0.158$ ,  $We=0.466$ )

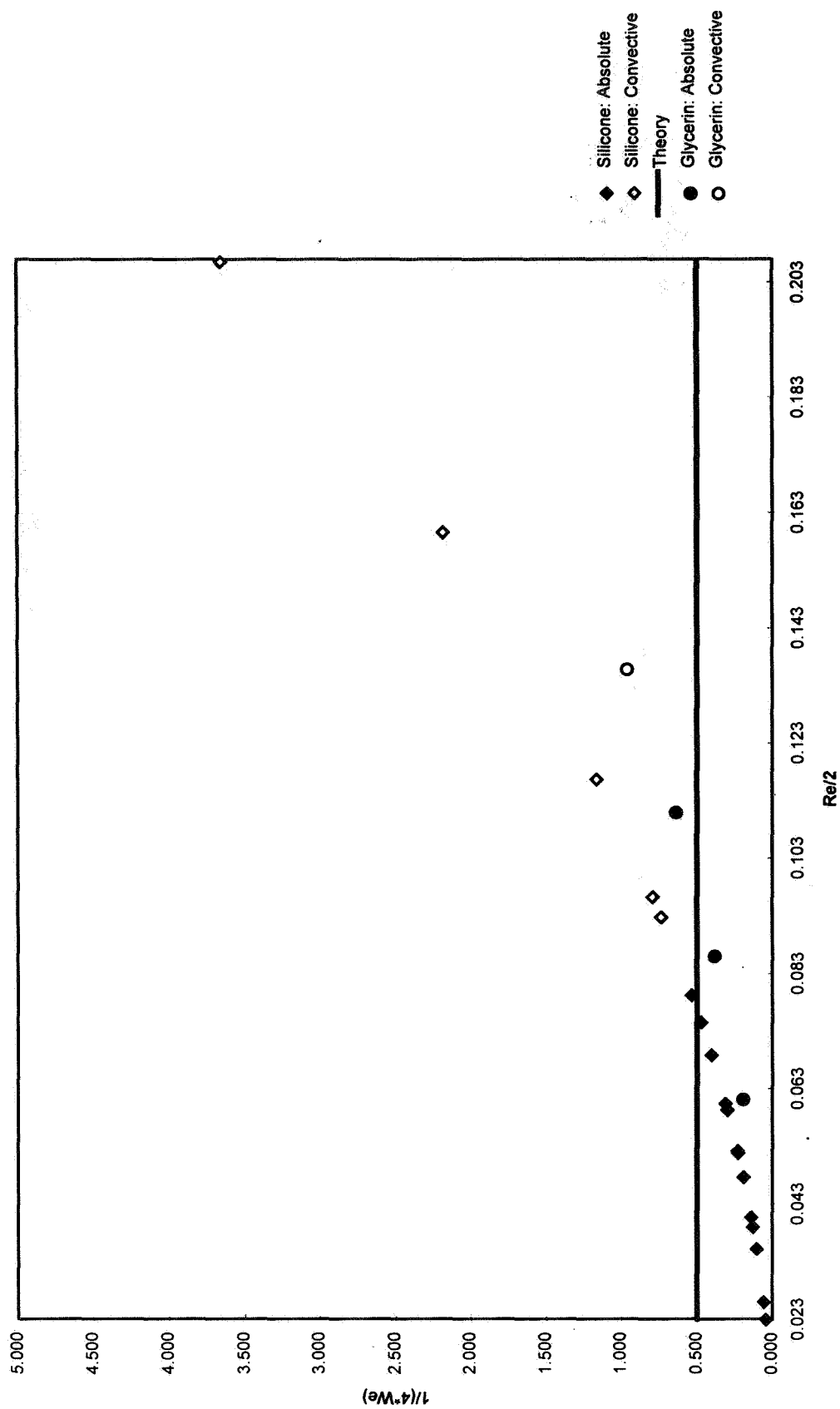


Figure 4. Absolute and Convective Instability



# NON-COALESCENCE EFFECTS IN MICROGRAVITY

G. Paul Neitzel

The George W. Woodruff School of Mechanical Engineering  
Georgia Institute of Technology  
Atlanta, GA 30332-0405

## Abstract

It has been observed experimentally that two drops (or a single drop and a planar surface) of the *same liquid* can be made to resist coalescence under certain conditions which lead to relative motion of the interfaces. Such relative motion may be brought about through the mechanism of thermocapillarity or forced convective motion of one of the interfaces. Such non-coalescence phenomena have been observed to persist for hours, indicative of the stability of the phenomena. This stability, in turn, implies that such non-coalescence may be put to use in a microgravity environment. One potential application is the development of easily formed, low-friction, self-centering bearings for microgravity experimentation.

## A. Introduction

When two drops of liquid are brought into contact with each other, one of several things may happen. If the two liquids are *miscible*, they may quickly coalesce and form a single drop, after the fluid originally between them has drained away. A description of coalescence events can be found, for example, in the works of Marrucci (1969), Anilkumar, Lee & Wang (1991), Tambe & Sharma (1991). Coalescence is of great importance, for example, in the separation of emulsions of immiscible liquids (where the droplets of a single phase coalesce with each other) or in determining the distribution of droplet sizes in aerosols. If the two liquids are *immiscible*, when they come into contact, they may reciprocally experience adhesion forces and form a liquid-liquid interface according to their spreading coefficient. If the conditions for non-coalescence are satisfied, whether the two liquids are miscible or not, they do *not* mix and do not experience any direct adhesion over one another. Two non-coalescing drops can be pressed against one another, deformed under pressure, and then detached without any sticking. If they are pressed together strongly enough, they can even slip over one another.

Although the subject has been of interest for some time, non-coalescing systems are not yet completely understood. Rayleigh (1899) examined the behavior of water jets that bounce over one another as early as 1879. A century later, Walker (1978) still referred to matter as a "scientific curiosity." While observation of a drop of liquid floating upon the surface of the same liquid is indeed curious, being able to *control* the coalescence process is yet another matter.

Recently, Dell'Aversana, Banavar & Koplik (1996) described some experimental techniques which are able to produce systems formed by liquid bodies which behave like solid elastic objects when pressed against one another, in a surrounding medium of air. What makes this work particularly interesting, technologically and scientifically, is that *i*) coalescence can be purposely induced provided that well-defined conditions are attained, and *ii*) these systems are stable in time, even when they are subjected to noticeable mechanical stresses.

One mechanism for accomplishing noncoalescence between drops of a single liquid is to maintain a temperature difference between the two liquid bodies. Figure 1 is a photograph of two non-coalescing drops of silicone oil, differentially heated, and pressed together. The features of the contact interface are quite impressive: the interface is stable both in time and with respect to surface deformation, so that two drops of liquid can safely be squeezed together for (at least)

several hours without coalescing; a time limit associated with this behavior, if one exists, is still to be determined.

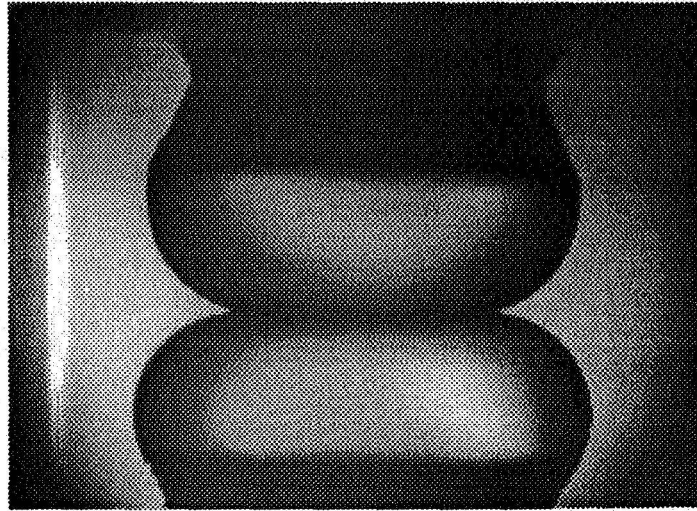


Figure 1. Non-coalescence of differentially heated drops of the same liquid (silicone oil). The rods have a diameter of 2 mm while the temperature difference between them is roughly 20 °C.

#### B. Physical Mechanisms

Consider again the situation depicted in Figure 1. The lower, cold drop induces a cold spot on the free surface of the upper, hot drop and vice versa. For liquids whose surface tension decreases with increasing temperature, the induced thermocapillary convection pulls the free surface of the upper drop *toward* the symmetry axis and that of the lower drop *away* from this same axis.

The motion of the interfaces induces not only motion in the bulk liquid, but also in the gas surrounding the system. It has been hypothesized that a thin film of gas exists between the two drops, serving as a lubricating layer; work by Dell'Aversana *et al.* (1996) suggests that lubrication theory is suitable to explain the phenomenon. Interfacial motion draws the surrounding gas into the thin space between the drops, forming a streamline pattern which, in a highly expanded view, might resemble the sketch in Figure 2. Furthermore, the stability of these configurations,

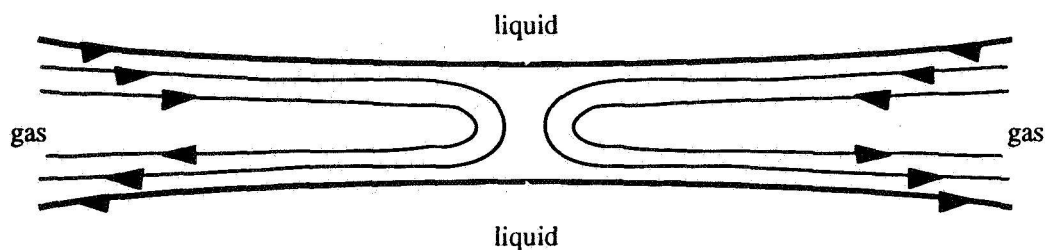


Figure 2. Expanded view of the gap between two immiscible drops showing lubrication layer.

even when purposely subjected to disturbances, suggests that this thin film maintains its integrity and does not permit the liquids to come into contact with one another. Neither would the continuum hypothesis appear to fail, since a layer thickness on the order of the mean-free path of the gas molecules would most certainly lead to coalescence. Experiments have been conducted in which one of the drops was dyed prior to pressing the two together; no dye was observed to migrate into the neighboring drop.

Additional evidence in support of this mechanism has been provided by experiments which demonstrate that differential heating is *not* necessary to prevent coalescence, but that relative motion will suffice. In these experiments, a layer of silicone oil was brought to a state of rigid-body rotation on a turntable and a drop of the same liquid *at the same temperature* was brought into contact with the rotating surface near the periphery of the apparatus. As long as the rotational speed was maintained above a particular value, coalescence was prevented, although at very high speeds, or when deformed sufficiently, the drop begins to oscillate and often breaks.

The pressure distribution established in the gas layer by the surface motion must be sufficiently large to keep the liquid surfaces apart, implying, in turn, that the free-surface motion must be sufficiently vigorous. For the rotating case described in the previous paragraph, coalescence occurs when the speed is reduced; for the differentially heated case; the drops coalesce when  $\Delta T$ , the temperature difference between them, *decreases below a certain critical threshold*.

### C. Proposed Research

#### 1. Theoretical

Assuming that the mechanism preventing coalescence is accurately described in the preceding section, the most rational theoretical approach to pursue is the use of lubrication theory to describe the flow and pressure distribution in the gas layer as well as the interactions between the gas and the liquid. This has been done previously for drops *prior* to coalescence by Charles & Mason (1960). For a situation with two surfaces between which a gas flows in a *single direction*, lubrication theory may yield a complete solution. For the pair of drops at different temperatures, however, lubrication theory alone may not be able to accomplish the entire task, due to the presence of what might be termed a *stagnation region* in the middle of the gap where the two gas streams change direction. This region is depicted in the center of the sketch in Figure 2. In this region, a *numerical* solution might be necessary, since the assumptions of lubrication are violated there, while away from this region, lubrication theory continues to hold. A similar approach was used by Ruschak (1982), who analyzed a coating-flow problem in this fashion, employing a numerical matching procedure to match the numerical solution to that obtained from lubrication theory.

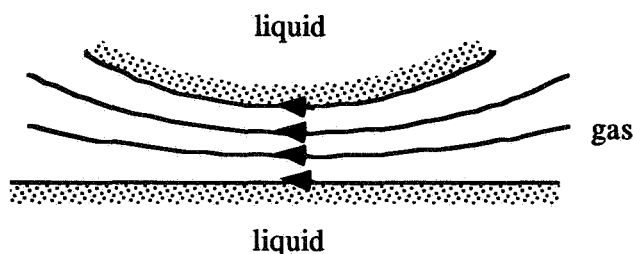


Figure 3. Two-dimensional model lubrication problem.

The first analysis to be attempted will examine the case of two, *two-dimensional* free-surfaces (one curved) with a gas film between them driven by the motion of the planar surface (see Figure 3 above). This is a more-or-less standard lubrication-theory problem with the additional complication of flexible "bearing" surfaces.

Following the treatment of this problem, the more difficult problem associated with the flow depicted in Figure 2 will be studied, first for two-dimensional flow, and then for the problem with spherical droplets. The latter case is complicated by the geometry, suggesting a formulation in terms of bispherical coordinates. The two-dimensional problem serves as more than just a model problem, however, from the standpoint of potential technological utilization of the effect. If the technology were to be developed for a microgravity-bearing application, one could easily conceive of applications for which a long, nearly two-dimensional drop would be desirable.

Although, for large relative velocities (driven by thermocapillarity in the one case), the preliminary experiments have found the situation to be very stable, there is a state of relative motion, below which, coalescence will occur. The *stability* of these flows in the vicinity of such thresholds is therefore a subject of interest, which can be examined with the aid of the lubrication (or combined lubrication/numerical) solutions.

## 2. Experimental Studies

A large number of experiments demonstrating the phenomenon of non-coalescence have already been performed (Dell'Aversana *et al.* 1996) but there are more questions to be answered from careful experiments. A sampling of some of these are:

- How is the coalescence threshold affected by the characteristics of the surrounding medium?
- How does the threshold change with changes in "contact" area? How large can this area be made on earth and in microgravity?
- Is there an *upper* limit to the temperature gradient that the lubricating layer can sustain?
- How long can a non-coalescing system sustain a mechanical stress of a given magnitude without occurrence of interface rupture? Is the stability of the interface a function of this stress?

Experiments to be conducted at Georgia Tech and the MARS Center in Naples, Italy will attempt to answer many of these. The apparatus to be used for spherical-droplet cases is that employed by Dell'Aversana *et al.* (1996).

Experiments will also be conducted at Georgia Tech for the case of a nearly two-dimensional droplet. Once the contact line position has been established, it is possible to either inject or withdraw liquid from the "drop" to cause the interface to either bulge or flatten. This then becomes a good experiment for examining the influence of interface curvature, and curvature mismatch, on non-coalescence.

Some possible experiments which can be conducted in either, or in some cases both, of these devices are suggested here:

*Measurement of the film local thickness.* This measurement can be performed by interferometric means with great precision; related measurements with interferometry have been performed at MARS.

*Interface resistance as a function of the lubricating gas parameters.* Important parameters which enter the functioning of non-coalescing systems are those of the surrounding medium.

*Load measurements.* The load the interface between non-coalescing liquids can carry can be directly measured and compared with the data obtained from the theoretical calculations based upon the film shape measured in the Experiment 1.

*Measurements of friction.* Together with the preceding experiment, these measurements will allow us to assess the coefficient of friction, i.e., the ratio of friction to load, for gas-lubricated liquid bearings.

*Non-coalescence achieved by induced surface vibrations.* It has been demonstrated (Walker 1978) that quasi-stable non-coalescence is achievable by means of vibrations of suitable frequency of the liquid surfaces. Lubrication theory seems to be able to explain this kind of phenomenon as well, in the context of squeezing films.

*Interface curvature effects.* Interface curvature will profoundly affect the ability of the non-coalescing system to sustain a load. Experiments to determine non-coalescence thresholds for different curvatures and curvature mismatches will be performed in the two-dimensional apparatus, as well as measurements of sustainable loads for various curvature configurations.

The actual experiments to be performed will, of course, be dictated by results obtained both from experiments and theoretical results, and the effects to be investigated. However, the existence of apparatus for both spherical and two-dimensional geometries, as well as a facility for investigating the effects of high tangential speeds will allow many of the questions posed above to be answered.

#### D. Summary and Outlook for Applications

The project teams at Georgia Tech and the MARS Center possess complementary and overlapping talents for the investigation of the non-coalescence phenomena described above. A possible collection of experiments was identified, to indicate the wide realm of scientific questions and possibilities present within these systems. These, in turn, suggest several potential applications of the results of this work, a couple of which have already been alluded to.

Potential space applications include the containerless confinement, shaping, and transfer of liquids. From the standpoint of scientific applications, non-coalescing systems could provide useful tools for the study of electro-chemical forces at the surface of liquids, for the study of lubricated systems, etc. As already mentioned, non-coalescing systems could be employed as liquid bearings in microgravity. In fact, because of the extremely low friction which is generated at the interface between two non-coalescing liquids, they could be employed as quasi-friction-free joints for high-precision devices in microgravity. The attractiveness of such bearings is increased by the fact that, due to the elasticity of liquid surfaces, non-coalescing bodies are self aligning and their surfaces are naturally and perfectly smooth under any conditions, eliminating the need for difficult technological efforts. Thus, liquid bearings would not present alignment, tolerance or roughness problems, would not be noisy, would not be affected by wear, would not generate heat which, in common bearings, can produce distortions, and would provide support with minimum friction and torque.

On the other hand, it must be observed that the loading capability of a liquid bearing is limited by the possibility that the liquid may spread outside its own support when the liquid surface undergoes deformation with respect to its minimum-energy shape. Therefore, one must consider coatings with outstanding anti-wetting capabilities and particular support shapes able to maximize the normal stress when determining the limits of mechanical stability of liquid bearings under load. In microgravity, however, where loads are much smaller, such bearings could find several practical applications.

Although the phenomenon is of broader scientific interest, the bulk of the proposed research will be aimed at the future exploitation of non-coalescing systems features in microgravity, since this environment seems to hold the most promise for exploitation of the effect. Due to the weak nature of surface-tension forces, these systems obtain the utmost, in terms

of versatility, in a weightless environment, where a number of configurations are possible which would be unthinkable on ground.

#### References

- Anilkumar, A. V., Lee, C. P. & Wang, T. G. 1991 Surface-tension-induced mixing following coalescence of initially stationary drops. *Phys. Fluids A* **3**, 2587.
- Charles, G. E. & Mason, S. G. 1960 The coalescence of liquid drops with flat liquid/liquid interfaces. *J. Colloid Sci.* **15**, 236.
- Dell'Aversana, P., Banavar, J. R. & Koplik, J. 1996 Suppression of coalescence by shear and temperature gradients. *Phys. Fluids* **8**, 15.
- Marrucci, G. 1969 A theory of coalescence. *Chem. Eng. Sci.* **24**, 975.
- Rayleigh, L. 1899 Investigations in capillarity. *Phil. Mag.* **36**, 321.
- Ruschak, K. J. 1982 Boundary conditions at a liquid-air interface in lubrication flows. *J. Fluid Mech.* **119**, 107.
- Tambe, D. E. & Sharma, M. U. 1991 Hydrodynamics of thin liquid films bounded by viscoelastic interfaces. *J. Colloid Int. Sci.* **147**, 137.
- Walker, J. 1978 Drops of liquid can be made to float on the liquid. What enables them to do so? *Sci. Amer.* 123.

# Time-dependent thermally-driven interfacial flows in multilayered fluid structures

H. Haj-Hariri<sup>1</sup> and A. Borhan<sup>2</sup>

<sup>1</sup>Dept. of Mechanical & Aerospace Engineering, *University of Virginia, Charlottesville, VA*

<sup>2</sup>Dept. of Chemical Engineering, *The Pennsylvania State University, University Park, PA*

## Abstract

A computational study of thermally-driven convection in multilayered fluid structures will be performed in order to examine the effect of interactions among deformable fluid-fluid interfaces on the structure of time-dependent flow in these systems. Multilayered fluid structures in two model configurations will be considered: the differentially heated rectangular cavity with a free surface, and the encapsulated cylindrical liquid bridge. An extension of a numerical method developed as part of our recent NASA Fluid Physics grant will be used to account for finite deformations of fluid-fluid interfaces.

## 1 Introduction

In growing crystals from a melt containing volatile components (such as GaAs or InP), stringent control of the stoichiometry is crucial in order to avoid crystallographic defects and degradation of electronic properties of the resulting product. Two approaches have been devised to minimize evaporation of the volatile component from the melt during processing of these materials: pressurization of the growth chamber with the volatile component's vapor, and encapsulation of the melt in an amorphous liquid glass phase. The former approach often requires precise temperature control to avoid deposition of the volatile material on surfaces of the components inside the growth chamber. Furthermore, the pressurized vapor is often reactive (e.g., arsenic) and poses a safety hazard which represents a major drawback of this approach, particularly in connection with space-based processing. The second approach wherein the melt is encapsulated in a low melting point amorphous molten glass, such as boron oxide ( $B_2O_3$ ) or pyrolytic boron nitride (PBN), holds more promise for implementation in space. The viability of this technique was originally demonstrated by Metz et al. [25] who encapsulated germanium, PbTe, and PbSe single crystals with molten  $B_2O_3$ . Liquid-encapsulated crystal growth (abbreviated LEC growth) has since been used in the Bridgman and Czochralski configurations by researchers. Integration of this approach into the float zone process on earth has been impractical due to severe limitations on the maximum diameter of a stable molten zone (including the encapsulant) that can be supported by interfacial tension forces in the presence of destabilizing buoyancy forces. In addition, any electromagnetic levitation of the molten zone provided by RF heating coils would be lost upon encapsulating the floating zone since the encapsulant is typically nonconductive (e.g.,  $B_2O_3$ ). Johnson [19] used a liquid-encapsulated float-zone (LEFZ) technique to produce 10 mm diameter ingots of polycrystalline GaAs by pulling a GaAs rod through  $B_2O_3$  contained in a quartz tube. He estimated the maximum attainable crystal diameter in that process to be about 15 mm as compared with commercially useful diameters of 50 mm or more. Under microgravity conditions, however, the molten zone (including the encapsulant) will be affected predominantly by interfacial tension forces, and the limitations imposed on the maximum crystal diameter by *capillary* instabilities are not as severe as those dictated by buoyancy-driven instabilities on earth. In addition, there have been a number of interesting attempts aimed at controlling interfacial instabilities through encapsulation of the bridge in an annular liquid column (cf. Metz et al. [25], and Barocela and Jalilevand [1]), and the introduction of a coflow in the encapsulating layer (cf. Lowry and Steen [23]). Hence, the LEFZ technique represents a promising approach for space-based production of monocrystalline semiconductors with a volatile component.

The main distinction between the unencapsulated and LEC growth techniques is the presence of the additional liquid-liquid interface between the melt and the encapsulant in LEC growth. The addition of this new interface in a highly nonisothermal environment can be a source of new and complex dynamics that may critically affect crystal quality. It is well-known that nonuniform distributions of temperature on the interface between two fluids can cause variations in interfacial tension across the interface. Such interfacial tension gradients act like tangential stresses on the interface and drive a surface flow from regions of low interfacial tension to those of high interfacial tension. The resulting surface flow can penetrate into the bulk phases on the two sides of the interface through the action of viscosity and, in turn, induce bulk fluid motions which are called *Marangoni* or *thermocapillary* convection. In general, thermocapillary convection will be significant when buoyancy effects are negligible, as in systems involving small scales or under microgravity conditions.

Two of the most widely studied model problems in the analysis of thermocapillary convection have been the differentially-heated rectangular cavity with one free surface, and the cylindrical liquid bridge consisting of a liquid drop fixed between two coaxial circular disks (cf. review by Kuhlmann [21]). The former represents an idealization of the open-boat crystal growth technique while the latter is a model for the upper or lower half of the liquid domain in the float-zone process (cf. Ostrach [27]). For thermocapillary convection in a single fluid layer, the structure of the steady, linear and nonlinear, two-dimensional and axisymmetric flow and temperature distributions are well understood. Though significant progress has been made in understanding the nature of time-dependent flows, the role of interface deformations as well as the nonlinear dynamics of time-dependent and three-dimensional thermocapillary flows still provide challenges for future numerical investigations.

In comparison with the unencapsulated process, modeling of LEC growth has received considerably less attention. Recent numerical simulations of steady thermocapillary convection in liquid encapsulated Czochralski growth [37, 11, 34] have predicted multicellular flow patterns in the two liquid phases. There have also been a few studies of *steady* thermocapillary convection in double layers of immiscible liquids within differentially heated rectangular cavities, with the imposed temperature gradient parallel to the free surface. Villers and Platten [38] performed a one-dimensional analysis assuming a constant temperature gradient across the cavity, while others [32, 12, 7, 22] obtained numerical solutions of the two-dimensional problem for low to moderate aspect ratios. The results of these studies show that under microgravity conditions, the strength of the thermocapillary flow in the layer in contact with the solid boundary can be significantly reduced, suggesting that the liquid encapsulation method can be used as a means of suppressing thermocapillary convection in the melt. Since the encapsulant in LEC growth is typically very viscous (e.g.,  $B_2O_3$ ), a reduction in the strength of the thermocapillary convection in the melt by the encapsulant is consistent with the experimental results of Eyer and Leiste [10], who showed that a solid encapsulation technique can eliminate striations in silicon crystals. Most recently, Prakash and Koster [30, 31] extended the above analyses to include a third immiscible liquid layer. They performed both a one-dimensional analysis similar to that of Villers and Platten [38] and an asymptotic analysis for shallow rectangular cavities similar to the single layer analysis of Sen and Davis [36]. The results of their analysis indicate that for equal layer heights and encapsulant viscosities, the flow in the middle (encapsulated) layer is qualitatively similar to, but weaker than, that obtained by Sen and Davis for a single layer. However, when the middle layer is much thicker than the encapsulant, the interface deformations are quite different from those for the single layer. Hence, the flow pattern in the encapsulated layer strongly depends on the encapsulation thickness.

All of the above studies of thermocapillary convection in multilayered fluid structures have been limited to steady convection. Furthermore, aside from a few exceptions [37, 12, 31], previous studies have neglected deformations of the fluid-fluid interfaces in order to avoid the complexity associated with the determination of the unknown interface shapes. Recent numerical simulations of thermocapillary flows accounting for finite deformations of the free surface indicate that the shape of the interface may strongly influence the flow and temperature fields [24, 3, 4, 6, 20, 5, 2]. Some studies [28, 3, 20] have even suggested that oscillatory flows may be established as a consequence



of a coupling between interface deformation and thermocapillary convection. Another example of the importance of interface deformability in determining the dynamics of thermocapillary flows in LEC growth is the recent flight experiment of Koster [35] involving a three-layer fluid structure in a container differentially heated parallel to the free surface. The goal of the experiment was to identify the criteria for reducing thermocapillary convection in the middle liquid layer which is presumed to be representative of the encapsulated melt of an electronic material in LEC growth. Upon initial operation of the experiment, when two curtains separating the three fluid layers were drawn, the layers collapsed. Although the cause is not fully understood, the growth of capillary instabilities present at the fluid-fluid interfaces—as well as the contact-line region—can provide a plausible explanation for the failure of the experiment.

Based on the limited available results, it is reasonable to expect the presence of multiple deformable fluid-fluid interfaces in LEC growth to lead to interesting new dynamics which can play an important role in determining the quality of the resulting crystals grown under microgravity conditions. Thus, the effect of interactions among deformable fluid-fluid interfaces on the structure of time-dependent thermocapillary convection in these systems remains an open question that warrants further investigation. It is the purpose of this study to address this issue for thermocapillary convection in multilayered fluid structures in the cavity and bridge configurations. We intend to remove the limitations associated with the assumption of nondeformability of interfaces in previous studies of this problem by using an extension of a numerical method developed as part of our recent NASA Fluid Physics grant [15, 16] to allow interface shapes to evolve in accordance with the physics of the problem. The results will help extend our knowledge of the dynamics and stability of multilayered fluid systems, and will provide insight into the governing physics of the LEC growth process.

## 2 Formulation

In what follows, the subscript ‘*s*’ denotes an interface-specific quantity, while a plain symbol or one with a caret references a property of the bulk phase on one or the other side of the interface. The interfacial tension,  $\sigma$ , is taken to depend on the temperature,  $T$ , as well as the surface concentration of surface-active contaminants,  $\Gamma$ . The temperature dependence of other fluid properties can also be easily included. Using the velocity scale  $U \equiv (GL/\mu)\sigma_T$ , obtained through a tangential stress balance at an interface, the following well-known parameters arise in the equations governing the various transport processes in each phase:

$$Re = UL/\nu, \quad Ma = UL/\alpha, \quad Ca = \mu U/\sigma, \quad Bi = hL/k, \quad Br = (\mu U^2/kGL),$$

where  $G$  denotes the imposed temperature gradient and  $h$  is the heat-transfer coefficient at the liquid-vapor interface. In addition to the above dynamic and thermal parameters, there are also a number of geometric and physical property ratios for the various fluid phases. The vector-invariant forms of the governing equations in each fluid phase are given by

$$\mathbf{u}_{,t} + \nabla \cdot (\mathbf{u}\mathbf{u}) = \frac{1}{Re} \nabla \cdot \mathbf{\Pi}, \quad \nabla \cdot \mathbf{u} = 0, \quad T_{,t} + \nabla \cdot (\mathbf{u}T) = \frac{1}{Ma} \left[ \nabla^2 T + Br \tau : \nabla \mathbf{u} \right],$$

where  $\mathbf{\Pi} = -p\mathbf{I} + \boldsymbol{\tau}$  is the Newtonian stress tensor with  $\boldsymbol{\tau} = \nabla \mathbf{u} + (\nabla \mathbf{u})^\dagger$ .

The interfacial boundary conditions on  $\mathbf{x} = \mathbf{x}_s(t)$  include

$$\hat{\mathbf{n}} \cdot (\mathbf{\Pi} - \lambda \hat{\mathbf{n}}\hat{\mathbf{n}}) + \nabla_s \sigma = \sigma (\nabla_s \cdot \hat{\mathbf{n}}) \hat{\mathbf{n}}, \quad \mathbf{u} = \hat{\mathbf{u}}, \quad d\mathbf{x}_s/dt = \mathbf{u}, \quad T = \hat{T}, \quad \hat{\mathbf{n}} \cdot \nabla T = \beta \hat{\mathbf{n}} \cdot \nabla \hat{T},$$

where  $\hat{\mathbf{n}}$  denotes the unit normal vector at the interface. The thermal boundary condition at the liquid-vapor interface is  $-\hat{\mathbf{n}} \cdot \nabla T = Bi(T - T_o)$  for some ambient temperature  $T_o$ . The solid-liquid boundary conditions are standard, except in the vicinity of the contact line, where a multi-valued

velocity gives rise to a stress singularity (cf. Dussan V. and Davis [8]). This singularity will be regularized through the introduction of a slip coefficient,  $a$ , according to (Huh and Scriven [18])

$$\hat{\mathbf{b}} \cdot \Pi \cdot \hat{\mathbf{e}} = a \mathbf{u} \cdot \hat{\mathbf{e}}, \quad (a \ll 1),$$

where  $\hat{\mathbf{b}}$  and  $\hat{\mathbf{t}}$  are the unit vectors normal to the solid-liquid boundary and tangent to the contact line, respectively, and  $\hat{\mathbf{e}} = \hat{\mathbf{t}} \wedge \hat{\mathbf{b}}$ .

In the presence of bulk-insoluble surface contamination, the concentration  $\Gamma$  of the surface-active impurity on a fluid-fluid interface is governed by

$$\frac{\partial \Gamma}{\partial t} + \nabla_s \cdot (\mathbf{u}_s \Gamma) + (\mathbf{u} \cdot \hat{\mathbf{n}})(\nabla_s \cdot \hat{\mathbf{n}})\Gamma = \frac{1}{Pe_s} \nabla_s^2 \Gamma,$$

where  $Pe_s$  denotes a surface Peclet number. This surface convective-diffusion equation will be converted into a volumetric one and treated as such (cf. [17]):

### 3 Method

As part of a previous MSAD-funded effort, a computer code for the simulation of flows driven, or affected, by interfacial forces was developed; its main features are:

- \* Solution of the three-dimensional, incompressible Navier-Stokes equation,
- \* Temperature-dependent properties,
- \* Automatic adaptive grid refinement near fluid-fluid interfaces,
- \* Determination of surface topology (e.g.  $\hat{\mathbf{n}}$ , curvature, etc.), and normal distance to the interface via the solution of the level-set<sup>1</sup> equations (cf. Osher and Sethian [26]),
- \* Smearing of the interfacial forces into a body force occupying a thin band about the original crisp interface, via a mollified delta function (cf. Peskin [29]) in the interface-normal direction.

This code has been well calibrated and tested, and is being parallelized in order to achieve significantly faster speeds. The adaptive local refinement of the underlying grid in the vicinity of fluid-fluid interfaces is an essential feature of the code (cf. Haj-Hariri et al. [14]), and has been achieved using an oct-tree data structure.

Briefly, the computational approach involves the treatment of interfacial forces as body forces, and smearing of all fluid properties across the interface, resulting in an effectively single-phase flow problem. For example, the momentum equation involves a body-force concentration,  $\mathbf{f}$ , accounting for the effect of an interface:

$$\mathbf{f} = [(\mathbf{I} - \hat{\mathbf{n}}\hat{\mathbf{n}}) \cdot \nabla \sigma - (\nabla \cdot \hat{\mathbf{n}})\sigma \hat{\mathbf{n}}] \delta(\phi).$$

In the above expression,  $\delta$  denotes a mollified Dirac delta function (cf. Peskin [29]) and  $\phi$  is the 'distance' from the interface, obtained via the level-set construction of Osher and Sethian [26]:

$$|\nabla \phi| = 1, \quad \phi_s = 0.$$

The gaussian curvature of the interface,  $\nabla \cdot \hat{\mathbf{n}}$ , is then obtained using  $\hat{\mathbf{n}} = \nabla \phi$ . The treatment of the surface convective-diffusion equation (arising when an interface is contaminated with surface-active impurities) is more challenging, as the physical quantity  $\Gamma$  is genuinely a surface quantity and its treatment as a volume quantity generates ambiguity for its behavior in the normal direction. To avert the ambiguity, it is shown that  $\Gamma$  should be extended away from the interface using

$$\hat{\mathbf{n}} \cdot \nabla \Gamma = 0,$$

<sup>1</sup>The concept of the level sets is not new; it is akin to the constant-phase surfaces which are obtained via the solution of the Eikonal equation in monochromatic wave-propagation problems

so that the surface convective-diffusion equation is then equivalent to a volumetric one.

Another point requiring special treatment is the contact-line area. The slip-coefficient formulation is used to regularize the force singularities. However, one needs to further implement a model accounting for the contact-angle hysteresis as well as the general dependence of the advancing and receding contact angle on the in-plane normal speed of the contact line (e.g. power-law dependence  $U = \kappa(\theta - \theta_{eq})^m$ ; cf. Ehrhard and Davis [9]). This information is incorporated into the formulation through the imposition of the interface normal on the interface at the contact line, i.e.  $\hat{n}$  is determined such that  $\hat{n} \cdot \hat{b} = \cos \theta$  (while  $\hat{n} \cdot \hat{t} = 0$ ). This specification supercedes the definition  $\hat{n} = \nabla \phi$ , which is applied at all other points within the computational domain.

While the stability problem will be addressed via a complete time-dependent solution, a linear stability analysis in the spirit of Ramanan and Homsy [33] will also be performed in order to illuminate the energetics of the flow. Namely, any physical quantity,  $q$ , will be expanded about its value at time  $t$ :

$$q(t + \delta t) = q(t) + \delta q,$$

and a linearized equation for  $\delta q$ , as well as an evolution equation for an energy-like quadratic, will be determined. The latter equation will provide further insight into the nature of the otherwise purely-numerical solution by indicating the main contributions to the production and dissipation of energy; this information will be helpful in understanding and controlling the behavior of the solution.

## References

- [1] E. Barocela and A. Jalilevand. Liquid encapsulated float zone method for microgravity production of gallium arsenide. Paper 87-0390, AIAA aerospace sciences meeting, Reno, 1987.
- [2] C. Chen and J. M. Floryan. On the thermocapillary convection in liquid layers. In *Fluid Mechanics Phenomena in Microgravity*, edited by D. A. Siginer, R. L. Thompson, and L. M. Trefethen, ASME, 1993.
- [3] J. C. Chen and F. S. Hwu. Oscillatory thermocapillary flow in a rectangular cavity. *Int. J. Heat Mass Transfer*, 36(15):3743-3749, 1993.
- [4] J. C. Chen, J. C. Sheu, and S. S. Jwu. Numerical computation of thermocapillary convection in a rectangular cavity. *Numer. Heat Transfer A*, 17:287-308, 1990.
- [5] J. C. Chen, J. C. Sheu, and Y. T. Lee. Maximum stable length of nonisothermal liquid bridges. *Phys. Fluids A*, 2(7):1118-1123, 1990.
- [6] C. Cuvelier and J. M. Driessen. Thermocapillary free boundaries in crystal growth. *J. Fluid Mech.*, 169:1-26, 1986.
- [7] T. Doi and J. N. Koster. Thermocapillary convection in two immiscible liquid layers with free surface. *Phys. Fluids A*, 5(8):1914-1927, 1993.
- [8] E. B. Dussan V. and S. H. Davis. On the motion of a fluid-fluid interface along a solid surface. *J. Fluid Mech.*, 65:71-95, 1974.
- [9] P. Ehrhard and S. H. Davis. Non-isothermal spreading of liquid drops on horizontal plates. *J. Fluid Mech.*, 229:365, 1991.
- [10] A. Eyer and H. Leiste. Striation-free silicon crystals by float-zoning with surface-coated melt. *J. Crystal Growth*, 71:249-252, 1985.
- [11] J. P. Fontaine, A. Randriamampianina, G. P. Extremet, and P. Bontoux. Simulation of steady and time-dependent rotation-driven regimes in a liquid-encapsulated Czochralski configuration. *J. Crystal Growth*, 97:116-124, 1989.
- [12] J. P. Fontaine and R. L. Sani. Thermocapillary effects in a multilayered fluid system. paper 92-0689, AIAA aerospace sciences meeting, Reno, NV, 1992.
- [13] H. P. Greenspan and B. M. McCoy. On the wetting of a surface by a very viscous fluid. *Studies in Appl. Math.*, 64:95-12, 1981.
- [14] H. Haj-Hariri, Q. Shi, and A. Borhan. Effect of local property smearing on global variables : Implication for numerical simulations. *Phys. Fluids A*, 6(8):2555-2557, 1994.

- [15] H. Haj-Hariri, Q. Shi, and A. Borhan. Thermocapillary motion of deformable drops at finite Reynolds and Marangoni numbers. *J. Fluid Mech.*, submitted.
- [16] H. Haj-Hariri, Q. Shi, and A. Borhan. A continuum surface model for flows driven by interfacial tension gradients. *Proceedings of the 17th Boundary Element International Conference*, Madison, WI, 1995.
- [17] H. Haj-Hariri and A. Borhan. A computational model for surfactant transport on deformable two-phase boundaries based on interface mollification. To appear in *Proceedings of the 18th Boundary Element International Conference*, Braga, Portugal, 1996.
- [18] C. Huh and L. E. Scriven. Hydrodynamic model of steady movement of a solid/liquid/fluid contact line. *J. Colloid Interface Sci.*, 35:85–101, 1971.
- [19] E. S. Johnson. Liquid encapsulated float zone melting of GaAs. *J. Crystal Growth*, 30:249–256, 1975.
- [20] N. D. Kazarinoff and J. S. Wilkowski. Bifurcations of numerically simulated thermocapillary flows in axially symmetric float zones. *Phys. Fluids A*, 2:1797–1807, 1990.
- [21] H. C. Kuhlmann. Thermocapillary flows in finite-size systems. *Math. and Computer Modelling*, 20(10–1):145–173, 1994.
- [22] Q. S. Liu, G. Chen, and B. Roux. Thermogravitational and thermocapillary convection in a cavity containing two superposed immiscible liquid layers. *Int. J. Heat Mass Transfer*, 36(1):101–117, 1993.
- [23] B. J. Lowry and P. H. Steen. Stabilization of an axisymmetrical liquid bridge by viscous flow. *Int. J. Multiphase Flow*, 20(2):439–443, 1994.
- [24] W. Q. Lu. Boundary element analysis of thermocapillary convection with a free surface in a rectangular cavity. *Int. J. Heat Mass Transfer*, 37(7):1063–1071, 1994.
- [25] E. P. Metz, R. C. Miller, and R. Mazelsky. A technique for pulling single crystals of volatile materials. *J. Appl. Phys.*, 33:2016–2017, 1962.
- [26] S. Osher and J. A. Sethian. Fronts propagating with curvature-dependent speed: Algorithms based on hamilton-jacobi formulations. *J. Comp. Phys.*, 79:12–49, 1988.
- [27] S. Ostrach. Low-gravity fluid flows. *Ann. Rev. Fluid Mech.*, 14:313–345, 1982.
- [28] S. Ostrach, Y. Kamotani, and C. L. Lai. Oscillatory thermocapillary flows. *PCH PhysicoChem. Hydrodyn.*, 6:585–599, 1985.
- [29] C. S. Peskin. Numerical analysis of blood flow in the heart. *J. Comp. Phys.*, 25:220–252, 1977.
- [30] A. Prakash and J. N. Koster. Natural and thermocapillary convection in three layers. *Eur. J. Mech., B/Fluids*, 12(5):635–655, 1993.
- [31] A. Prakash and J. N. Koster. Convection in multiple layers of immiscible liquids in a shallow cavity. 1. steady natural-convection. *Int. J. Multiphase Flow*, 20(2):383–396, 1994.
- [32] N. Ramachandran. Thermal buoyancy and Marangoni convection in a two fluid layered system—a numerical study. Paper 90–0254, AIAA aerospace sciences meeting, Reno, NV, 1990.
- [33] N. Ramanan and G. M. Homsy. Linear stability of lid-driven cavity flow. *Phys. Fluids*, 6(8):2690–2701, 1994.
- [34] P. Sabhapathy and M. E. Salcudean. Numerical analysis of heat transfer in LEC growth of GaAs. *J. Crystal Growth*, 97:125–135, 1989.
- [35] G. Seibert. Early mission report on the four ESA facilities: Biorack; Bubble, Drop and Particle Unit; Critical Point Facility and Advanced Protein Crystallization Facility flown on the IML-2 Spacelab Mission. *Microgravity News from ESA*, 7(3):2–7, 1994.
- [36] A. S. Sen and S. H. Davis. Steady thermocapillary flows in two-dimensional slots. *J. Fluid Mech.*, 121:163–186, 1982.
- [37] P. D. Thomas, J. J. Derby, L. J. Atherton, R. A. Brown, and M. J. Wargo. *J. Crystal Growth*, 96:135–152, 1989.
- [38] D. Villers and J. K. Platten. Influence of interfacial tension gradients on thermal convection in two superposed immiscible liquid layers. *Appl. Sci. Res.*, 47:177–191, 1990.

# STUDIES IN THERMOCAPILLARY CONVECTION OF THE MARANGONI-BENARD TYPE

R. E. Kelly

A. C. Or

Mechanical and Aerospace Engineering Department

University of California

Los Angeles, CA 90095-1597

## ABSTRACT

The effects of an imposed nonplanar, oscillatory shear upon the onset of Marangoni-Benard convection, as predicted by linear theory, in a layer of liquid with a deformable free surface were reported upon by Or and Kelly (ref. 1) for small amplitude oscillations. Depending upon the operating conditions, either stabilization or destabilization might occur. The aim of the current paper is to report results for finite amplitude imposed oscillations so that the actual amount of stabilization or destabilization can be determined for prescribed operating conditions.

## INTRODUCTION

The small amplitude analysis of Or and Kelly (ref. 1) predicts that the finite wavelength mode of thermocapillary instability, which tends to be the critical mode on earth, can be stabilized by imposing an oscillatory, nonplanar shear on the fluid layer. However, the same shear has a destabilizing influence upon the long wavelength mode associated with surface deformation, which tends to be the most unstable mode under microgravity conditions. Although the small amplitude analysis is useful for an initial approach to the problem in view of the many nondimensional parameters involved, a fully numerical approach is necessary in order to predict how much stabilization or destabilization is obtained for finite amplitude oscillations. Therefore, an expansion of the solution was made in terms of a Fourier representation in a plane parallel to the bounding wall and Chebyshev functions in the direction normal to it (using the Tau method). This procedure yields a set of ordinary differential equations with time-periodic coefficients that is then investigated by use of Floquet theory in order to determine the stability boundaries. Only one figure showing some preliminary results was shown in 1994 (Fig. 5 of ref. 2); much more extensive results have since been obtained and are now reported.

## PROBLEM DESCRIPTION

A layer of Boussinesq fluid with mean thickness  $h$  rests above a solid horizontal plate that can perform simple harmonic motion along each of the axes defining the plane of the wall. A difference in phase ( $\delta$ ) between the two oscillations creates an oscillatory nonplanar shear field, as defined for the basic state by the well-known solution of Stokes. The layer is heated at the isothermal wall and, since viscous dissipation is neglected, the temperature of the basic state is governed by the steady conduction equation and so varies linearly with distance normal to the wall. The surface of the layer, in general, is allowed to deform in accordance with the free surface boundary conditions, and heat transfer there is characterized by a Biot number ( $Bi$ ).

The formulation of the problem has been given by Or and Kelly (ref. 1) for arbitrary amplitude oscillations and so is not repeated here. The numerical problem consists of solving eqs. (22) and (23) of ref. 1 subject to the boundary conditions given there as eqs. (24) - (28). For lack of space, neither these equations nor details of the numerical solution are given here. The governing nondimensional parameters will be described below.

## RESULTS

Besides the phase angle  $\delta$ , the other nondimensional parameters governing the basic state's velocity are the nondimensional frequency  $\beta = (\omega h^2 / 2\nu)$ , where  $\omega$  is the dimensional frequency and  $\nu$  is the fluid's kinematic viscosity, a Reynolds number (Re) that involves the magnitude of the wall's velocity in one direction, and a parameter  $\lambda$  that is a ratio of the magnitude of the two components of the wall's motion. For  $\delta = \pi/2$ , the effects of the nonplanar aspect of the fluid motion are the greatest, and  $\lambda$  is a parameter that governs the pattern selection, which will not be discussed here.

Additional nondimensional physical parameters entering into the equations are the Prandtl number  $Pr = \nu / \kappa$  ( $\kappa$  being the thermal diffusivity), the Rayleigh number  $Ra = \alpha g \Delta \bar{T} h^3 / \nu \kappa$  ( $\alpha$  being the coefficient of thermal expansion,  $g$  gravity, and  $\Delta \bar{T}$  the temperature difference across the layer in the basic state), the Marangoni number  $M = \gamma \Delta \bar{T} h / \rho \nu \kappa$  ( $\gamma$  being proportional to the rate of change of surface tension with temperature), the Bond number  $Bo = \rho g h^2 / \sigma$  ( $\sigma$  being the surface tension) and the Crispation number  $C = \rho \nu \kappa / \sigma h$ . We shall assume that  $Ra \ll 1$  so that the effects of buoyancy can be neglected.

As  $\beta \rightarrow 0$ , the shear in the basic flow vanishes whereas, for  $\beta \gg 1$ , the thickness of the Stokes layer is much less than  $h$ . In either case, no change occurs in, say, the critical value of  $M_c$  relative to the case  $Re = 0$ . Hence, an optimal value of  $\beta$  exists which has a value between one and two, as shown in Fig. 1.

Some typical values for a case typical of conditions on earth ( $Bo = 0.15$ ) are shown in Figure 2. For the given conditions, the finite wavenumber mode is critical when  $Re = 0$ . Fig. 1 indicates that this mode can be stabilized substantially as  $Re$  increases. However, the nearly vertical solid line near  $Re = 190$  indicates that a limit to the stabilization exists. This line is the stability boundary for long wavelength disturbances which are much more stable at low values of  $Re$ . We therefore conclude that stabilization of the system is limited by a pronounced destabilization of the long wavelength mode at sufficiently large values of  $Re$ . This destabilization is due to the action of the unsteady shear at the free surface and has been discussed for the isothermal case by Yih (ref. 3) and Or and Kelly (ref. 4).

As the value of  $g$  diminishes relative to the value on earth ( $g_0$ ), the nearly vertical line in Fig. 2 moves to the left and both the maximum amount of stabilization and the Reynolds number at which this is achieved diminish. These cut-off values are shown in Fig. 3 as a function of  $g/g_0$ . In particular, as  $g/g_0 \rightarrow 0$  stabilization becomes impossible and, instead, destabilization occurs for all  $Re > 0$ . A sequence of neutral stability boundaries for  $Bo = 0.01$  is given in Fig. 4 as  $Re$  increases. In Figs. (4a) and (4b),  $M_c$  increases with  $Re$  because the finite wavenumber mode is critical and tends to be stabilized by the oscillations. However, the long wavelength mode ( $k \rightarrow 0$ ) is also becoming less stable. When  $Re = 70$ , the long wavelength mode is already critical and destabilization of the layer occurs. For  $Re = 100$ , the layer is unstable even when the wall is cooled relative to the ambient.

Because the destabilization of the long wavelength mode is associated with the interfacial instability discussed first by Yih (ref. 3), the isothermal case was explored to a greater extent than done by Yih. As Fig. 5 indicates, more than one unstable, long wavelength region of instability occurs as  $\beta$  increases, but the regions are separated from each other. However, when finite wavelength disturbances are also considered, the corridors of stability

are eliminated. Current research is aimed at clarifying the connection between these new finite wavenumber modes existing for the isothermal case with the finite wavenumber modes already established for the thermocapillary case.

## REFERENCES

1. Or, A. C., and Kelly, R. E., *Int. J. Heat Mass Transfer* **38** (1995), 2269-2279.
2. Kelly, R. E., and Or, A. C., *NASA CP 3276* (1994), 15-20.
3. Yih, C. S., *J. Fluid Mech.* **31** (1968), 737-751.
4. Or, A. C., and Kelly, R. E., *Bull. APS* **40** (1995), 1949 (abstract only).

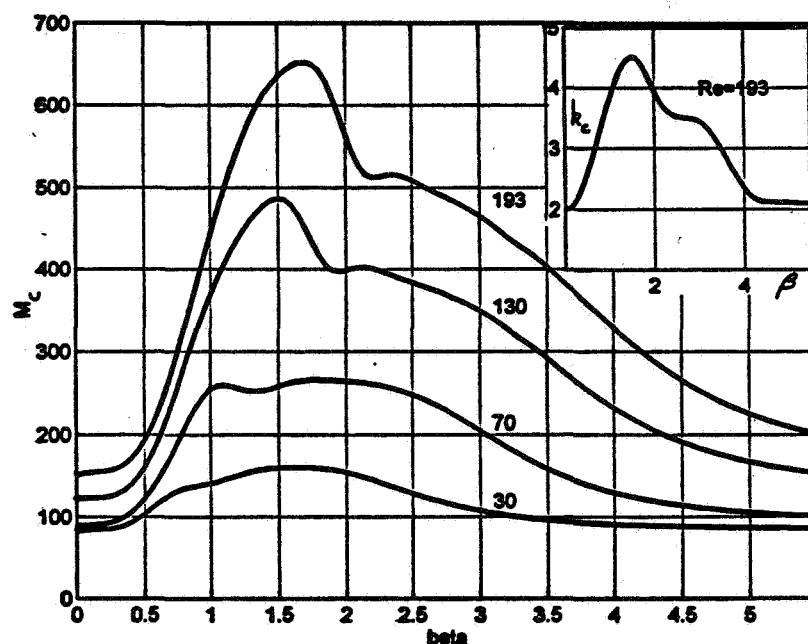


Figure 1: Critical Marangoni number versus nondimensional frequency for various  $Re$ ;  $Pr = 7$ ,  $Cr = 2 \times 10^{-6}$ ,  $Bo = 0.15$ ,  $Bi = 0.1$ . Insert shows variation of critical wavenumber with frequency for one Reynolds number.

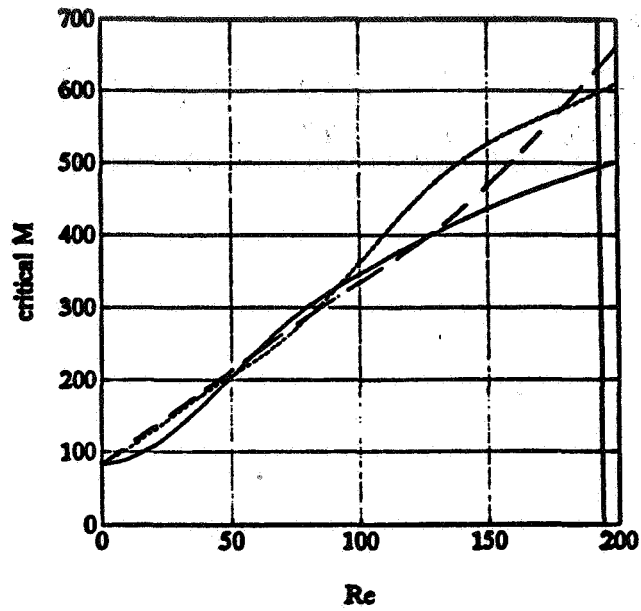


Figure 2: Critical Marangoni number as a function of Reynolds number for  $\beta = 1.1$  (solid), 1.4 (short dashes) and 1.7 (long dashes);  $Pr = 7$ ,  $Cr = 2 \times 10^{-6}$ ,  $Bo = 0.15$ ,  $Bi = 0.1$ .

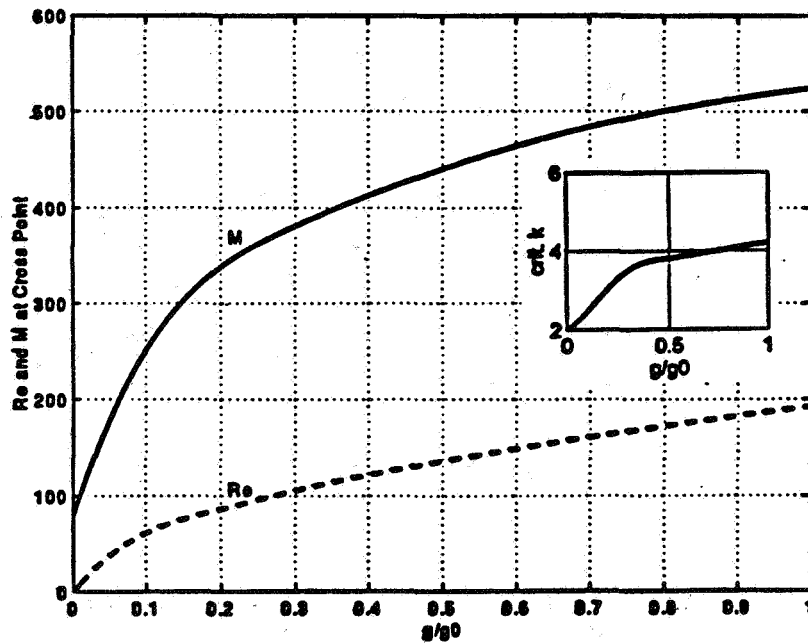


Figure 3: The cut-off values of Reynolds number (lower curve) and Marangoni number (upper curve) for maximum stabilization at  $\beta = 1.1$  as a function of  $g/g_0$ ;  $Pr = 7$ ,  $Cr = 2 \times 10^{-6}$ ,  $Bo = 0.15$  at  $g = g_0$ ,  $Bi = 0.1$ ,  $\beta = 1.1$ .



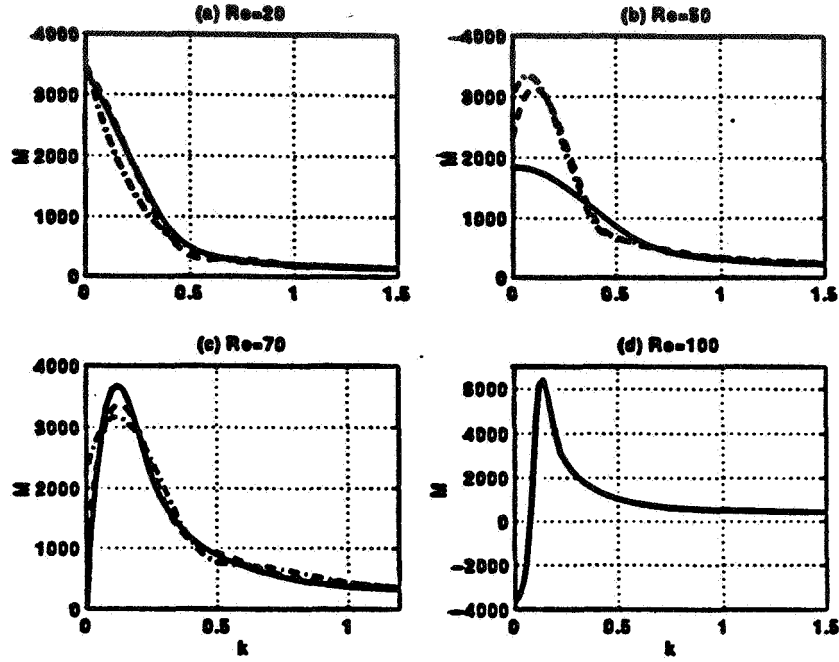


Figure 4: Critical Marangoni number as a function of wavenumber for various Reynolds numbers for  $\beta = 1.1$  (solid), 1.4 (dashes), 1.7 (dash-dot);  $Pr = 7$ ,  $Cr = 2 \times 10^{-6}$ ,  $Bo = 0.01$ ,  $Bi = 0.1$ .

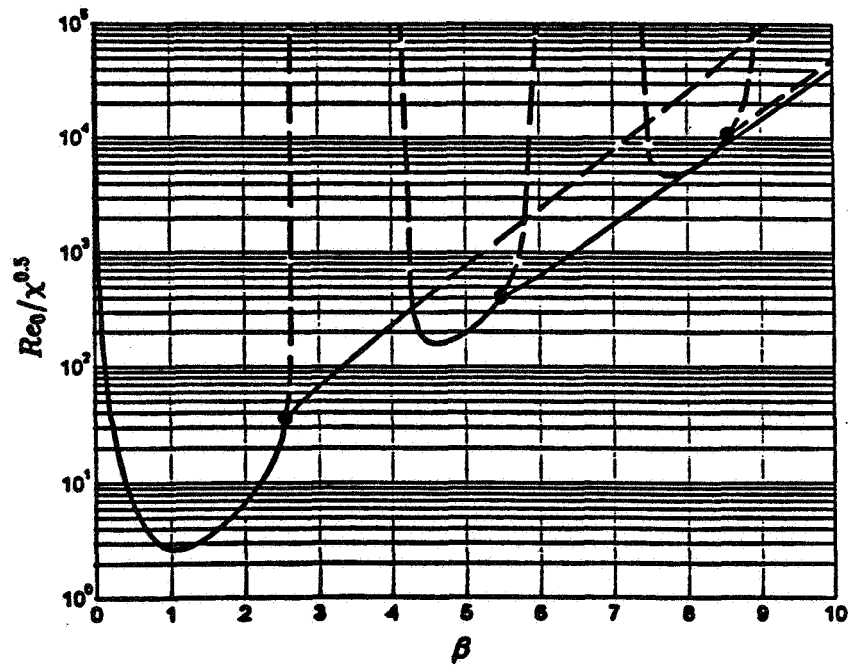


Figure 5: Scaled critical Reynolds number as a function of frequency for the isothermal case with  $Bo = 0.1$ ;  $\chi = gh^3/2\nu^2$ . Black dots mark points at which finite  $k$  neutral curves bifurcate from the  $k \rightarrow 0$  neutral curves shown as loops.



# **THERMOCAPILLARY CONVECTION IN A LOW $Pr$ MATERIAL UNDER SIMULATED REDUCED-GRAVITY CONDITIONS**

Y. Tao and S. Kou

Department of Materials Science and Engineering  
University of Wisconsin  
Madison, WI 53706

## **ABSTRACT**

A liquid bridge of tin was held between two vertical coaxial iron rods 4.5 mm in diameter and 4.6 mm apart. The temperatures at the top and bottom of the liquid bridge were 325 and 240°C, respectively. Flow oscillation was detected by a thermocouple in the liquid bridge. The amplitude and frequency of oscillation were around 1.3 °C and 5 Hz, respectively.

## **INTRODUCTION**

The surface tension  $\gamma$  of a fluid is a function of temperature  $T$  and the temperature coefficient of the surface tension  $\partial\gamma/\partial T$  is negative for most pure materials, e.g.,  $-0.28$  dyne  $\text{cm}^{-1}$  °C for silicon(1). Thermocapillary convection in a fluid is induced by the gradients of temperature and hence surface tension along the free surface of the fluid. It becomes significantly more important as gravity and hence gravity-induced buoyancy convection are reduced. It is often studied in the configuration of a liquid bridge, as shown in Fig. 1. A liquid bridge is sometimes called a half zone.

Numerous experiments have been conducted to study thermocapillary convection in high  $Pr$  materials, typically silicone oils. This is because these materials are transparent for convection to be observed and because they are easy to handle. Low  $Pr$  materials such as metals and semiconductors, on the other hand, are opaque and much more difficult to handle though they are also much more useful.

In the materials processing of low  $Pr$  materials, e.g., crystal growth and welding, thermocapillary convection can often play a significant role. In  $\mu\text{g}$  floating-zone crystal growth of silicon, for example, thermocapillary convection dominates in the molten zone. In fact, thermocapillary convection can be so strong as to become oscillatory, causing formation of dopant striations. Dopant striations are fluctuations in the dopant concentration and they cause the physical properties to vary in the crystal, thus degrading the crystal quality. They are caused by the growth rate fluctuations induced by flow oscillation.

In the present study thermocapillary convection in the liquid bridge of a low Pr material, tin, is investigated and the preliminary results are reported here. To the best of our knowledge, thermocapillary convection has not yet been studied in low Pr materials in the configuration of a liquid bridge.

## EXPERIMENTAL PROCEDURE

Tin was selected as the material for study in view of its relatively low melting point and well documented physical properties, as shown in Table 1(2-4).

The liquid tin bridge was held between two vertical coaxial iron rods of 4.5 mm diameter. Iron is chemically compatible with molten tin. The rods were heated by two independent heaters. The temperature difference across the liquid bridge was indicated by the two thermocouples at the ends of the rods. A third thermocouple was pushed with a micrometer screw into the liquid bridge from the side to detect temperature and hence flow oscillation. The temperature of the third thermocouple was recorded with a strip chart recorder. All three thermocouples were of the K type.

The experiment was conducted in a vacuum chamber (up to  $10^{-6}$  torr) in order to prevent oxidation.

More details of the experimental procedure will be reported elsewhere due to space limitation.

## RESULTS AND DISCUSSION

The tin liquid bridge was axisymmetric ; the molten tin wetted the iron rods properly. The liquid bridge was stable and its free surface was shiny.

Figure 2 shows the result of the temperature measurement in the liquid bridge. The distance between the rods was 4.6 mm. The temperatures of the upper and lower rods were 325 and 240°C, respectively. The tip of the thermocouple was 3 mm above the lower rod and 1 mm into the liquid bridge.

As shown in Fig. 2, the evidence of flow oscillation is clear. The temperature oscillates at the amplitude of around 1.3 °C and the frequency of around 5 Hz. Since the strip chart recorder was already running at its maximum paper speed, however, the time scale could not be enlarged further to reveal more details of the oscillation.

The Marangoni and Bond numbers are defined as follows:

$$Ma = -(\partial\gamma/\partial T)(L\Delta T/\mu\alpha) \quad (1)$$

$$Bo = -\beta\rho gL^2/(\partial\gamma/\partial T) \quad (2)$$

where  $\Delta T$  is the temperature difference between the upper and lower rods,  $L$  the characteristic length,  $\mu$  the viscosity of the fluid,  $\alpha$  the thermal diffusivity of the fluid,  $\beta$  the thermal expansion coefficient of the fluid,  $\rho$  the density of the fluid and  $g$  the gravitational acceleration.

Based on the physical properties given in Table 1 and the rod radius as the characteristic length  $L$ , the Marangoni and Bond numbers for the tin liquid bridge are 488 and 0.33, respectively.

In our previous studies(5-7) we have investigated thermocapillary convection in silicone oil bridges similar to the present liquid tin bridge in size. Computer simulation and flow visualization both confirmed that, as in  $\mu g$ , thermocapillary convection dominates under 1g in these silicone oil bridges. According to Eqns. (1) and (2), the Bond number for tin (0.33) is lower than that for silicone oil (0.79). As such, thermocapillary convection is expected to dominate in the tin liquid bridge in the present study.

## CONCLUSION

A liquid bridge of tin was held between two vertical coaxial iron rods 4.5 mm in diameter and 4.6 mm apart. Flow oscillation was observed at a temperature difference of 85°C. The amplitude and frequency of oscillation were around 1.3 °C and 5 Hz, respectively.

## FUTURE PLANS

Study on flow oscillation in tin liquid bridge will continue. A data acquisition and processing system will be used to better analyze the experimental results. The critical Marangoni numbers for the onset of flow oscillation will be determined.

## REFERENCES

1. S. C. Hardy, Journal of Crystal Growth 69(1984) 456.
2. T. Iida and R. I. L. Guthrie, The Physical Properties of Liquid Metals, Oxford University Press, Oxford, 1988.

3. Information about Dow Corning Silicone Fluids, Dow Corning Corp., Midland, MI(1990).
4. C. V. Burkersroda, A. Prakash and J. N. Koster, *Microgravity Quarterly* 4(1994) 93.
5. Y. Tao, R. Sakidja and S. Kou, *International Journal of Heat and Mass Transfer* 38(1995) 503.
6. Y. Tao, B. Xiong and S. Kou, *International Journal of Heat and Mass Transfer*, in press.
7. Y. Tao, B. Xiong and S. Kou, 2nd Microgravity Fluid Physics Conference, Cleveland, OH, June 21-23, 1994, NASA Conference Publication 3276, p. 45.

TABLE 1  
Physical Properties of Tin (2) and Silicone Oil (3,4)

Properties	Sn	Silicone Oil (5cs)
$T_m, ^\circ\text{C}$	232	-
$\gamma, \text{dyne cm}^{-1}$	560	18.7
$\rho, \text{g cm}^{-3}$	6.98	0.913
$\frac{\partial \gamma}{\partial T}, \text{dyne cm}^{-1} ^\circ\text{C}^{-1}$	-0.09	-0.06
$\beta = \frac{-1}{\rho} \frac{d\rho}{dT}, ^\circ\text{C}^{-1}$	$0.87 \times 10^{-4}$	$1.05 \times 10^{-3}$
$\mu, \text{g cm}^{-1} \text{sec}^{-1}$	$1.81 \times 10^{-2}$	$4.57 \times 10^{-2}$
$k, \text{W cm}^{-1} ^\circ\text{C}^{-1}$	0.34	$1.09 \times 10^{-3}$
$C_p, \text{J g}^{-1} ^\circ\text{C}^{-1}$	0.25	1.71
$\alpha = \frac{k}{\rho C_p}, \text{cm}^2 \text{sec}^{-1}$	0.195	$6.982 \times 10^{-4}$
$Pr = \frac{C_p \mu}{k}$	0.013	71.7

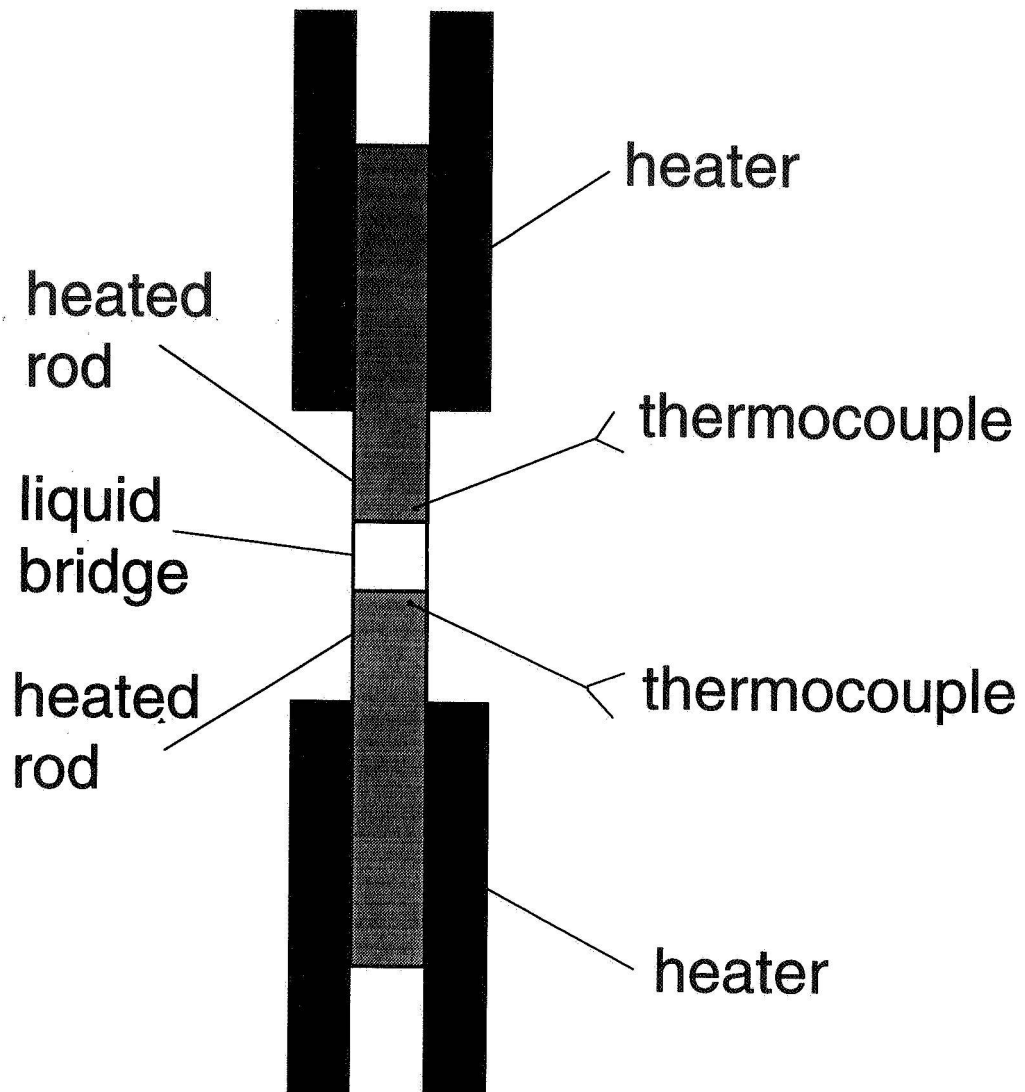


Fig. 1 Liquid bridge.

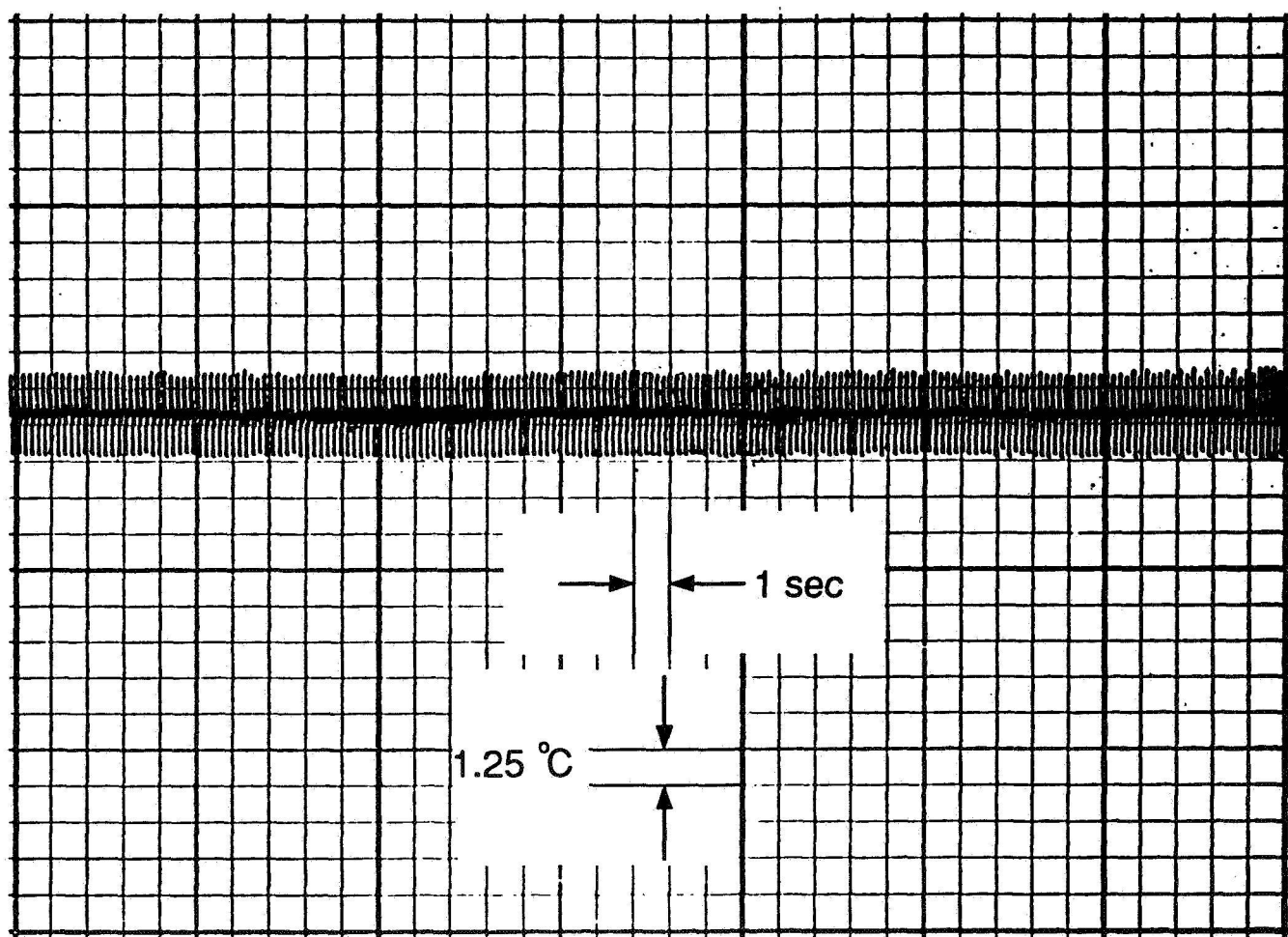


Fig. 2 Temperature oscillation detected in a tin liquid bridge.



# OSCILLATORY THERMOCAPILLARY CONVECTION

Jieyong Xu and Abdelfattah Zebib  
Department of Mechanical and Aerospace Engineering  
Rutgers University  
Piscataway, NJ08855-0909

## ABSTRACT

Stability analysis of thermocapillary convection in rectangular cavities is performed using direct numerical simulations. Influence of the Reynolds number( $Re$ ), the fluid Prandtl number( $Pr$ ) and cavity aspect ratio( $Ar$ ) on the motion is investigated. Neutral stability curves for transition to time-dependent convection are delineated in the  $Re - Ar$  plane for fluids with  $Pr=1.0, 4.4, 6.78$  and  $10$ . Several interesting features of these diagrams are discussed. One important conclusion is that  $Ar_{cr}$  increases as  $Pr$  decreases. Thus, large values of both  $Ar$  and  $Re$  are necessary to induce thermocapillary oscillations for small  $Pr$  fluids such as liquid metals and semiconductor melts. Energy analysis is also performed for the oscillatory flow in the neighborhood of critical points in order to gain insight into the mechanisms leading to instability.

## INTRODUCTION

Understanding fluid motion is crucial in some material processing technologies. In crystal growth from the melt, single crystals with uniform material properties are desired, but homogeneity in crystals can be destroyed if melt motion is unsteady [1]. In the terrestrial environment, buoyancy and thermocapillarity are two major causes for convection. However, in low gravity environment, thermocapillary convection becomes dominant[2].

Numerous experiments (for example, [3], [4] and [5]) have demonstrated the existence of instability of thermocapillary convection, i.e. when the Marangoni number( $Ma$ ) exceeds a critical value, the motion undergoes a transition from steady to oscillatory.

Thermocapillary flows have received considerable interest. A rich body of numerical investigations are available in the literature (see [6], [7] and [8]). Results of direct numerical simulation of oscillatory thermocapillary convection was reported in [9] by Peltier & Biringen. They provided a stability diagram in the  $(Ar, Ma)$  space for a  $Pr=6.78$  fluid, and found a minimum critical  $Ar$  near  $2.3$  and a minimum critical  $Ma$  near  $20,000$  within the parameter range of  $Ar \leq 3.8$ .

Discussions of instability mechanisms can be found in [10] and [11] for dynamic thermocapillary infinite liquid layers, and in [12] for thermocapillary liquid bridges. Description of the oscillatory instability is also provided in [9], relating the temporal evolution of large-scale structures in the flow and their interaction with the temperature sensitive free surface.

Here, we present a detailed stability diagram for fluids with  $Pr=10.0, 6.78, 4.4$  and  $1.0$ . Interesting features in the diagram are discussed. Comparison of flow patterns is provided to investigate the influence of  $Re$  and  $Ar$  on the motion of a  $Pr=10$  fluid. In addition, energy analysis results are also given for convection of a  $Pr=4.4$  fluid with  $Re$  near both higher and lower critical points of the unstable region at  $Ar=3.0$ .

## MODEL DESCRIPTION AND NUMERICAL PROCEDURE

The physical model considered is thermocapillary convection of incompressible and Newtonian fluid in a rectangular cavity with height  $H$  and width  $Ar \times H$  ( $Ar$  is the aspect ratio). Two vertical isothermal side walls are kept at  $T_h$  on the left and  $T_c$  on the right, respectively. Bottom boundary is rigid and adiabatic. Top boundary is a flat free surface open to a passive gas. Here, surface tension on the free surface is assumed to be a linear function of temperature as  $\sigma = \sigma_0 - \gamma(T - T_0)$ .

A dimensionless mathematical model in the stream function - vorticity formulation is used for numerical simulation, in which length, temperature, velocity and time are made dimensionless by use of scales  $H$ ,  $\Delta T = (T_h - T_c)$ ,  $\gamma \Delta T / \mu$  and  $H^2 / \nu$ , respectively. Dimensionless parameters are defined as:  $Pr = \frac{\mu}{\alpha}$  and  $Re = \gamma \frac{\Delta T H}{\mu \nu}$ , where  $\mu$ ,  $\nu$  and  $\alpha$  are dynamic viscosity, kinematic viscosity and thermal diffusivity, respectively.

The coupled equation system is solved by a finite volume based scheme, in which the Poisson equation for the stream function is solved by the SOR method. Both the vorticity transport and energy equations are solved by the alternating direction implicit (ADI) method. All time derivatives and spatial derivatives including boundary conditions are approximated in second order accuracy. Velocities are obtained as spatial derivatives of stream function. Uniform mesh is used in the solution procedure with mesh resolution of 50 to 90 points per dimensionless unit length, depending on the Reynolds number considered.

## RESULTS

For thermocapillary convection of a  $Pr=6.78$  fluid in rectangular cavities, Peltier & Biringen [9] constructed a stability diagram in the  $(Ar, Ma)$  plane for the region  $Ar \leq 3.8$  and  $Ma \leq 1.0 \times 10^5$ . Their  $Ma$  is equivalent to our  $RePrAr$ . Some interesting characteristics were found, including the existence of double valued stability limits, i.e. as  $Ma$  goes up, the flow first changes from stable to oscillating at  $Ma_{cr1}$ , and then becomes stable again when  $Ma_{cr2}$  is reached.  $Ma_{cr2}$  grows monotonically with  $Ar$ , however,  $Ma_{cr1}$  does not.

In the present work, we extend this investigation to fluids with  $Pr=1.0, 4.4$  and  $10.0$ , and construct the stability diagrams in the  $(Ar, Re)$  plane. A wider range of parameter space ( $0.0 \leq Ar \leq 7.0$  and  $0.0 \leq Re \leq 1.3 \times 10^4$ ) is considered as shown by Fig. 1, in which more interesting features are found. If we look at the particular fluid with  $Pr=4.4$ , the first critical aspect ratio is around 2.6. Unstable region exists for any  $Ar > 2.6$ , and more interestingly, there are more than one unstable regions with  $Ar > 6.0$ , i.e. if  $Re$  goes up from zero, one can find that the flow is steady at low  $Re$ , starts to oscillate at first critical point, goes back to steady state at second critical point, and becomes oscillatory again as  $Re$  reaches its third critical point. In addition, stability curves of fluids with different  $Pr$  do not cross each other. Neutral curves of smaller  $Pr$  fluids always locate inside curves of larger  $Pr$ , i.e. when  $Pr$  goes smaller, the critical aspect ratio always becomes larger, so does the lowest critical Reynolds number. From the trend given by these curves, we can draw a very important conclusion that, for fluids with very low  $Pr$ , large values of critical  $Ar$  and  $Re$  are expected for the transition to oscillatory thermocapillary convection.

The convective flow field is strongly influenced by  $Re$ ,  $Ar$  and  $Pr$ . For a  $Pr=10$  fluid, Fig. 2 gives three examples of streamlines at  $Ar=3.0$  and  $Ar=6.0$ . (a) shows the flow field at  $Re_{cr1}$  for  $Ar=3.0$ , in which one can see a bi-cellular structure with a stronger cell near the hot wall and a much weaker cell close to the cold wall. Increasing  $Re$  to  $Re_{cr2}$  at about 7400, one can find, in (b), that the previous strong hot wall cell moves to the center of the cavity, and the weak cell disappears. For a larger aspect ratio ( $Ar=6.0$ ), Fig. 2 (c) exhibits the flow pattern at  $Re_{cr1}$ , from which we find that three cells exist, with the strongest one

still near the hot wall. Further increase of  $Ar$  will result in more cellular structure in the flow field.

For convection of a  $Pr=10$  fluid at a large aspect ratio ( $Ar=20$ ), Fig. 3 displays the mean velocity profiles and snapshots of temperature fluctuation fields for three different values of  $Re=1012$ , 1025 and 1500, respectively. Comparison of these three mean velocity profiles shows almost identical patterns even when  $Re$  changes from 1012 to 1500, with most strong activities locating near two side walls. However, large difference can be found among the temperature fluctuation fields. At  $Re=1012$  (b-1), which is very close to  $Re_{cr1}$ , a *thermal wave* generates near the center of the cavity and starts to die at the right edge of the strong flow cell near the hot wall. Most area in the right part of the cavity remains pretty calm. The *wave* actually propagates toward the hot wall if we look at snapshots at different time instants, which is in agreement with [10]. As  $Re$  goes up a little bit to 1025, (b-2) shows that the starting point of the *thermal wave* moves toward the cold wall. Further increase  $Re$ , this starting point keeps moving to the right until it reaches the cold wall. Fig. (b-3) shows the case when  $Re=1500$ , in which one can see a *wave* generating at the cold wall, propagating actively, and dying at the right edge of the strong flow cell near the hot wall.

## ENERGY ANALYSIS

Energy analyses are performed for flows with Reynolds numbers in the neighborhoods of different critical points. The physical parameters of the oscillatory flows are decomposed into their mean and fluctuating components, and investigations are conducted on the behavior of the fluctuation kinetic energy ( $k$ ) and the fluctuation thermal energy ( $\theta = t^2/2$ ).

For the case  $Ar=3.0$  and  $Pr=4.4$ , results of the energy analysis are provided here for flows with Reynolds numbers near both lower ( $Re=1950$ ) and higher ( $Re=5020$ ) critical points of the unstable region. Temporal variations over one flow oscillation period are shown in Fig. 4(a-1) and (a-2) for the rate of change of the total fluctuation kinetic energy ( $dK/d\tau = \frac{d}{d\tau}(\int k d\Omega)$ ), as well as its components  $I_{k_1}$  (production),  $I_{k_2}$  (diffusion) and  $I_{k_3}$  (dissipation). It is seen that  $dK/d\tau$  oscillates with its time average being equal to zero, which means no kinetic energy is added to the flow over each period of oscillation. This is consistent with the fact that the flow field oscillates with a stable amplitude. If we look at  $I_{k_1}$ ,  $I_{k_2}$  and  $I_{k_3}$ , we find  $I_{k_1}$  and  $I_{k_3}$  providing two major contributions, with  $I_{k_1}$  always being positive (destabilizing) and  $I_{k_3}$  always being negative (stabilizing). Time averages of  $I_{k_1}$  and  $I_{k_3}$  are much larger than that of  $I_{k_2}$ , however, the phase difference between  $I_{k_1}$  and  $I_{k_3}$  is always near  $\pi$ , which means that  $I_{k_3}$  always cancels the effect of  $I_{k_1}$ . This gives the smaller term  $I_{k_2}$  a chance to influence the temporal behavior of  $dK/d\tau$ . In Fig. 4(a-2), which is for the higher critical point, one can clearly see that  $dK/d\tau$  oscillates at a very close amplitude and a very small phase difference with  $I_{k_2}$ , while the phase difference between  $I_{k_1}$  and  $I_{k_3}$  is almost  $\pi$ .

Variation of the rate of change of the total fluctuation thermal energy ( $d\Theta/d\tau = \frac{d}{d\tau}(\int \theta d\Omega)$ ) and its components ( $I_{t_1}$  and  $I_{t_2}$ ) are given in Fig. 4(b-1) and (b-2) for the lower and higher critical points, respectively. As expected,  $d\Theta/d\tau$  oscillates with its time average being equal to zero, since the temperature field oscillates in a limit cycle with stable amplitude. In addition, although the time averages of  $I_{t_1}$  and  $I_{t_2}$  have the same absolute value, the oscillation amplitude of  $I_{t_1}$  is much larger than that of  $I_{t_2}$ . Thus  $I_{t_1}$  dominates the oscillatory behavior of  $d\Theta/d\tau$ . In both cases, the phase difference between  $I_{t_1}$  and  $d\Theta/d\tau$  is very small. If we further compare the magnitude of the destabilizing fluctuation thermal energy component ( $I_{t_1}$ ) and the kinetic energy components ( $I_{k_1}$  and  $I_{k_2}$ ), we find that the magnitude of thermal energy production  $I_{t_1}$  is generally two to three orders larger than that of  $I_{k_1}$  or  $I_{k_2}$ . Thus,  $I_{t_1}$  appears to be the major driving source of flow instability.

## CONCLUSIONS

Direct numerical simulation is employed for stability analyses of thermocapillary driven convection in rectangular cavities. Stability boundaries are delineated in the  $Re - Ar$  plane, in which several interesting features are found. Influence of  $Re$  and  $Ar$  on the flow patterns and the temperature fields is briefly discussed. In addition, energy analyses are performed to gain insight into mechanisms involved in the onset of instability. Results are presented for a  $Pr=4.4$  fluid with  $Re$  near both higher and lower critical points at  $Ar=3.0$ . Investigations on 2D and 3D convection of lower  $Pr$  as well as larger  $Ar$  and  $Re$  are in progress.

## ACKNOWLEDGEMENT

This research is sponsored by NASA through grant No. NAG3-1453. We also acknowledge the Pittsburgh Supercomputing Center for providing CRAY C90 time through grant No. CTS950032P.

## References

- [1] Hurle, D. T. J. *Thermo-hydrodynamic oscillation in liquid metals: the cause of impurities striations in melt-grown crystals*. J. Phys. Chem. Solids, Suppl. no.1, 659-669(1967).
- [2] Ostrach, S. *Low-gravity fluid flows*. Ann. Rev. Fluid Mech., 14, 313-345(1982).
- [3] Chun, C. H. and Wuest, W. *Experiments on the transition from the steady to the oscillatory Marangoni convection of a floating zone under reduced gravity effect*. Acta Astronautica, 6, 1073-1082(1979).
- [4] Chun, C. H. *Experiments on the transition from the steady to the oscillatory temperature distribution in a floating zone due to Marangoni convection*. Acta Astronautica, 7, 479-488(1980).
- [5] Preisser, F., Schwabe, D., and Scharmann, A. *Steady and oscillatory thermocapillary convection in liquid columns with free cylindrical surface*. J. Fluid Mech., 126, 545-567(1983).
- [6] Zebib, A., Homsy, G. M. and Meiburg, E. *High Marangoni number convection in a square cavity*. Physics Fluids, 28(12), 3467-3476(May 1985).
- [7] Carpenter, Bradley M. and Homsy, G. M. *High Marangoni number convection in a square cavity: Part II*. Physics Fluids A, 2(2), 137-149(1990).
- [8] Ben Hadid, H. and Roux, B. *Thermocapillary convection in long horizontal layers of low-Prandtl number melts subject to horizontal temperature gradient*. J. Fluid Mech., 221, 77-103(1990).
- [9] Peltier, L. J. and Biringen S. *Time-dependent thermocapillary convection in a rectangular cavity: numerical results for a moderate Prandtl number fluid*. J. Fluid Mech., 257, 339-357(1993).
- [10] Smith, Marc K. and Davis, Stephen H. *Instabilities of dynamic thermocapillary liquid layers. Part 1. Convective instabilities*. Physics Fluids, 132, 119-144(1983).
- [11] Smith, Marc K. *Instability mechanisms in dynamic thermocapillary liquid layers*. Physics Fluids, 29(10), 3182-3186(1986).
- [12] Wanschura, M., Shevtsova, V. M., Kuhlmann, H. C. and Rath, H. J. *Convective instability mechanisms in thermocapillary liquid bridges*. Physics Fluids, 7(5), 912-925(May 1995).
- [13] Braunsfurth, M. G. and Homsy, G. M. *Experimental study of buoyant-thermocapillary convection in a rectangular cavity*. 48th annual meeting of APS-DFD, (presentation FG3), (1995).

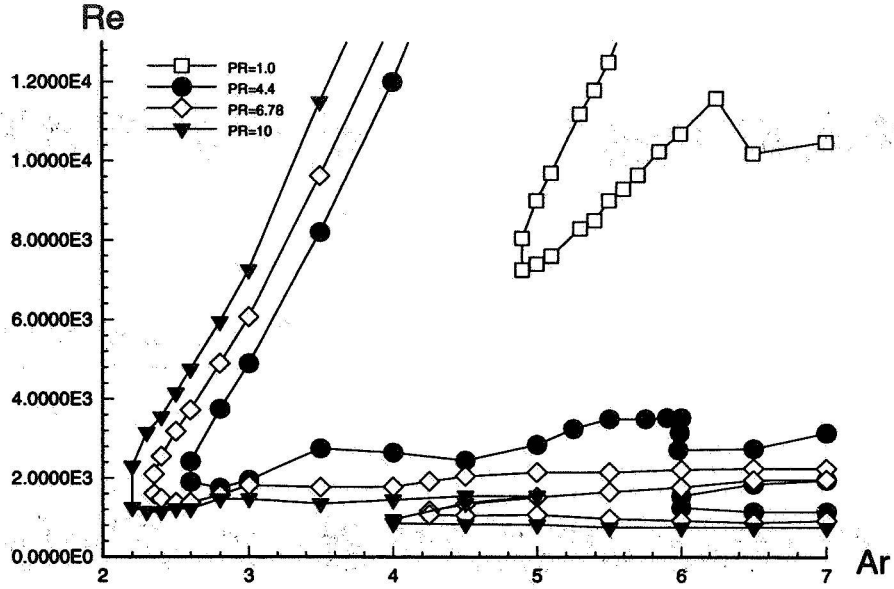


Figure 1: Stability diagrams in the  $Re - Ar$  plane for fluids with  $Pr=10.0$ ,  $6.78$ ,  $4.4$  and  $1.0$ .

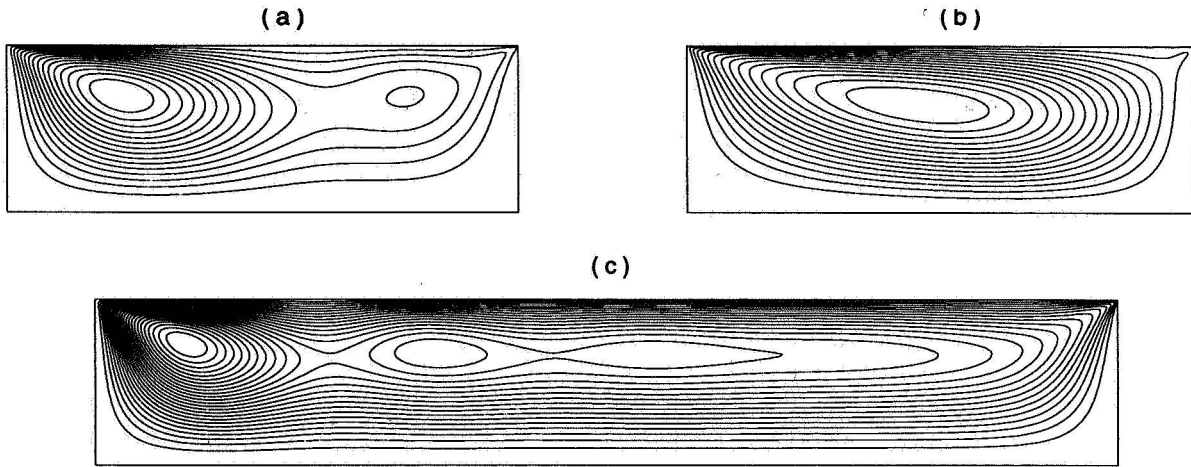


Figure 2: Examples of streamlines for convection of a  $Pr=10$  fluid. Case (a):  $Ar=3.0$ ,  $Re=1530$  ( $\approx$  the first critical number); Case (b):  $Ar=3.0$ ,  $Re=7400$  ( $\approx$  the second critical number); Case (c):  $Ar=6.0$ ,  $Re=700$  ( $\approx$  the first critical number).

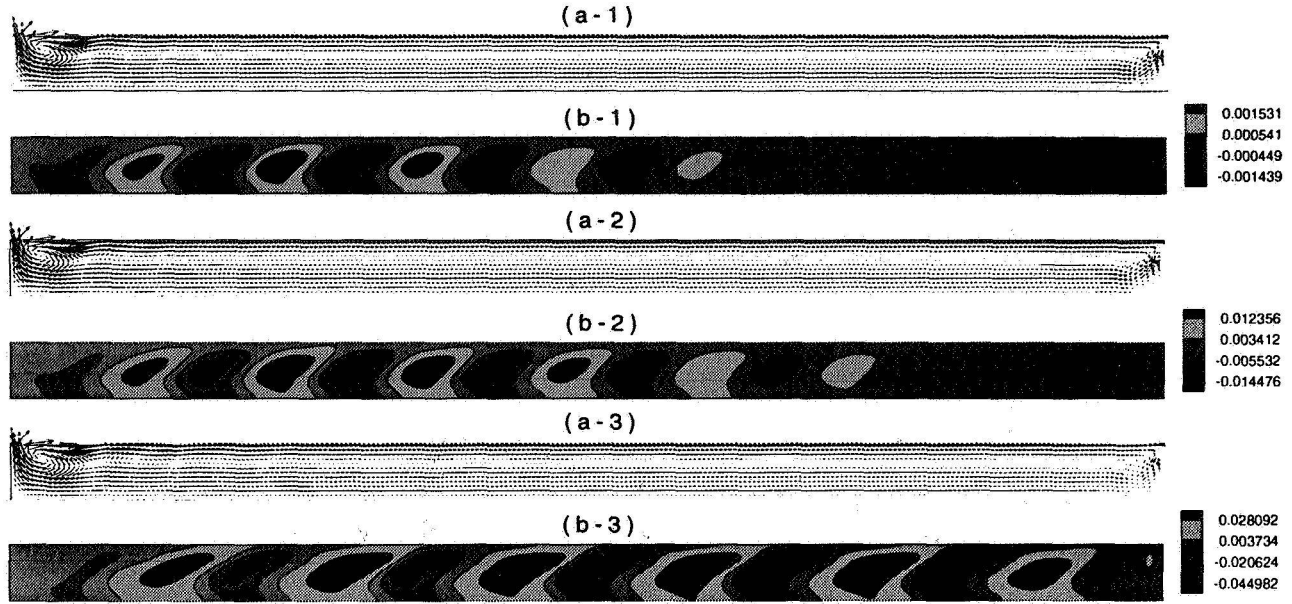


Figure 3: Comparison of mean velocity profiles and temperature fluctuation fields of a  $Pr=10$  fluid at large aspect ratio  $Ar=20$ . Case 1:  $Re=1012$ , which is approximately the first critical point; Case 2:  $Re=1025$ , which is slightly higher than the first critical point; Case 3:  $Re=1500$ , which is much higher than the first critical point.

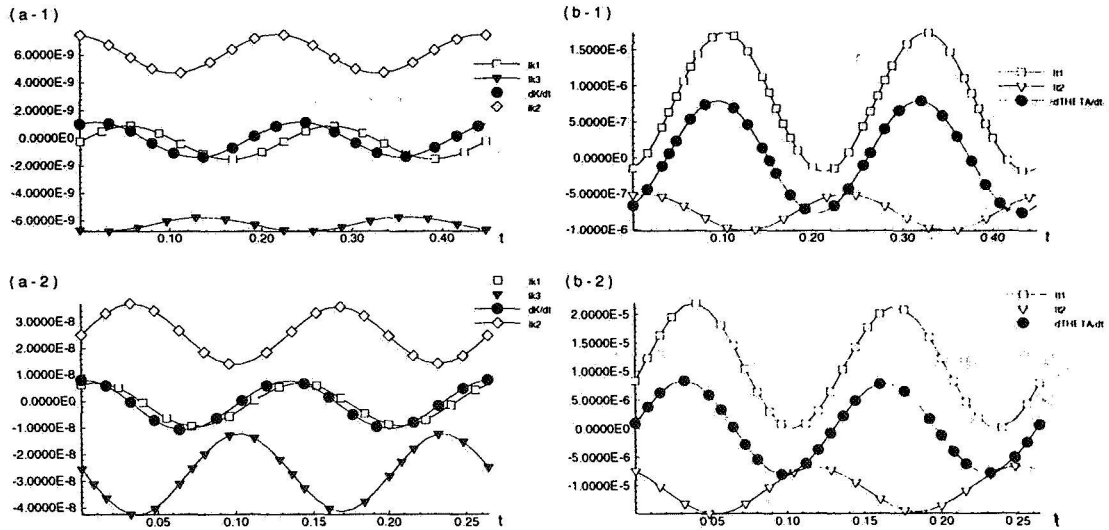


Figure 4: Temporal variation of the rate of change of the total kinetic energy  $\frac{dK}{dt}$ , the thermal energy  $\frac{d\Theta}{dt}$  and their components  $I_{k1}$ ,  $I_{k2}$ ,  $I_{k3}$ ,  $I_{t1}$  and  $I_{t2}$  for a  $Pr=4.4$  fluid at  $Ar=3.0$ . (a-1) and (b-1) give results for  $Re=1950$  (near the lower critical point), (a-2) and (b-2) provide results for  $Re=5020$  (near the higher critical point).

# OBSERVATIONS OF TIME-DEPENDENT BEHAVIOR IN THE TWO-LAYER RAYLEIGH-BÉNARD SYSTEM

C. David Andereck, Peter W. Colovas and Michael M. Degen  
Department of Physics  
The Ohio State University  
Columbus, OH 43210

## ABSTRACT

In this paper we present results from experiments with a system consisting of two immiscible fluid layers in rectangular and annular geometries, driven by a vertical temperature gradient. Time-dependent variations in the type of coupling observed between the two layers are described and characterized.

## INTRODUCTION

Rayleigh-Bénard convection is one of the oldest and most thoroughly studied of fluid dynamical systems. The basic system consists of a single fluid confined between parallel horizontal plates held at a temperature difference  $\Delta T$ , usually with the higher temperature being on the lower plate. If  $\Delta T$  is large enough, convection begins in the form of parallel rolls, the result of the destabilizing effect of the buoyancy force overcoming the stabilizing influences of viscous drag and thermal diffusion. The onset of convection in the one fluid Rayleigh-Bénard problem is simply characterized by the Rayleigh number

$$Ra = \frac{g\alpha\Delta T d^3}{\kappa\nu}, \quad (1)$$

the dimensionless temperature difference, and a ratio of the destabilizing force to the stabilizing forces. In equation (1),  $g$  is the acceleration of gravity,  $\alpha$  is the volume coefficient of expansion,  $d$  is the depth of the fluid layer,  $\kappa$  is the thermal diffusivity, and  $\nu$  is the kinematic viscosity of the fluid. Another nondimensional parameter, the Prandtl number  $P = \nu/\kappa$ , does not enter into the determination of the onset of convection. Thorough introductions to the stability analysis of the one fluid problem have been presented in the books by Chandrasekhar[1], and Drazin and Reid[2]. One result of these analyses is the fact that the equations are self-adjoint, and all the eigenvalues are real, leading to the "exchange of stability," i.e. the growth of small disturbances leads to steady cellular convection, there being no oscillatory modes at criticality. Fluids from water to liquid helium, and gases like air and  $CO_2$  have been used in experiments which explore the one fluid Rayleigh-Bénard problem.

If the upper surface is free, or bounded by another fluid, then surface tension may play a role in determining the onset of convection[3]. Various theoretical analyses have shown the possible existence of oscillatory modes at the onset of convection, for cases of both deformable and nondeformable interfaces[4, 5, 6, 7, 8, 9, 10, 11, 12, 13, 14, 15, 16, 17]

Gershuni and Zhukovitskii [9] described a possible mechanism for oscillations which can appear in the coupling between two convecting fluid layers. The basic types of coupling are *thermal* and *mechanical*. Thermal coupling is the alignment of the hot rising fluid in both layers, causing rolls that are aligned one above the other to turn with the same sense, either clockwise or counterclockwise. Mechanical coupling is the alignment of the cold falling fluid in one layer with the hot rising fluid in the other layer, with the result that the rolls turn with opposite senses, in a gear-like fashion. The oscillations were predicted to be periodic variations between thermal and mechanical coupling. Experimental work on the two-layer problem

has been reported by a number of groups [17, 10, 18, 19, 20], but none have found time-dependence in the coupling at the onset of convection. In this paper we show the results of our experimental investigation of a Rayleigh-Bénard system consisting of two immiscible fluids, concentrating on the search for oscillatory states.

## EXPERIMENTAL SYSTEM

The experimental system consists of two fluids confined between horizontal parallel plates and bounded on the sides by transparent walls. The lower fluid, here designated fluid 1, occupies a depth fraction  $l_1 = d_1/d$ , where  $d_1$  is the actual depth of fluid 1 and  $d$  is the total thickness of the cell. Fluid 2, the upper fluid, similarly occupies  $l_2 = d_2/d$ . Two different pairs of fluids were selected for use in our experiments. The first pair consists of a silicone oil, Rhone-Poulenc Rhodorsil 47v10, over a perfluorinated hydrocarbon, Fluorinert FC-70, from 3M. They were chosen because they are nearly immiscible, and because their properties are similar enough that convection in both layers should start at the same overall  $\Delta T$  for nearly equal depths. The other pair of fluids is 2 cs silicone oil, Rhodorsil 47v2, over water.

In the rectangular geometry, the fluids are confined within 9.5 mm thick glass walls. The interior horizontal dimensions of the cell are 78 mm x 21 mm, and the total height of the cell  $d = 12$  mm. The dimensions of the cell were chosen so that the onset of convection leads to a nearly one dimensional set of rolls in each layer. These rolls form parallel to the short dimension of the cell, as in single layer convection. The top and bottom of the cell are aluminum blocks. The blocks are thick to assure uniformity of temperature across the surfaces which contact the fluids. The top and bottom blocks are cooled and heated, respectively, by water which is conditioned by temperature controlled baths. In each circulation loop is a thermal low pass filter, which removes the short term fluctuations present in the bath. The system is shown in Figure 1. The annular cell has inner radius  $r_i = 44$  mm and outer radius  $r_o = 64$  mm. It has the same height as the rectangular cell, and is heated and cooled in the same manner.

The temperature difference between the plates is measured by thermistors embedded in the center of each block, approximately 1.2 cm from the contact surface. The long term stability  $\Delta T$ , is  $\pm 0.02$  C, while the horizontal variation in plate temperature is less than  $\pm 0.01$  C.

The thermal patterns in the rectangular system were observed using Schlieren and shadowgraph techniques, while only shadowgraph could be used for the annular cell. The measurement, while local along the length of the cell, is an integral over the width of the fluid layer. A representative Schlieren pattern is shown in Figure 2. The dark regions indicate rolls turning in one direction, while the light regions indicate rolls turning in the other direction. To analyze the space-time behavior of the system, a single horizontal line through the center of each layer was chosen, and the intensity recorded over a period of time encompassing several oscillations. A representative plot is shown for the rectangular cell in Figure 3, and for the annular cell in Figure 4. The resulting data can then be analyzed to find periods, wavelengths, wave speeds, etc. Our analysis comes primarily from this data.

## PROCEDURE

While the parameter space of the two-layer Rayleigh-Bénard problem is large [21], practical considerations simplify the experimental process considerably. Upon choosing the fluids, the only experimental variables are the depths of the layers,  $l_1$  and  $l_2$ , and the temperature difference,  $\Delta T$ , between the top and bottom plates. We proceed by filling the cell with the appropriate amount of each fluid to achieve the desired  $l_1$  and  $l_2$ . The depth of the lower fluid is measured precisely by an optical telescope, accurate to  $\pm 0.02$  mm. The full system is left to equilibrate for a period of 12 hours before the temperature ramping begins. The temperature is then ramped approximately  $0.1^\circ\text{C}$  at a time, starting from  $\Delta T = 0$ , and the system is left for at least three hours before data taking begins. As the period of oscillations is on the order of one hour,



a data run consists of one "frame" of a single data line in each layer, taken every 30 seconds over a period of 6 to 8 hours. This gives us an effective ramping rate of  $\approx 0.2^\circ\text{C}/\text{day}$ .

Wavelengths and frequencies are computed from power spectra in space and time, respectively. A time average at each spatial point is first subtracted from the data, to remove non-uniformities in lighting due to the system optics. A one-dimensional FFT is then performed on the resulting data to compute the desired spectrum. We report our results in terms of  $\Delta T$ , the temperature difference across the total height  $d$ .

## RESULTS AND DISCUSSION

We began our experiments with 47v10 over FC-70, at a depth fraction  $l_1 = 0.50$ , where calculations predicted the onset of convection to occur at nearly the same  $\Delta T$  in both layers. At this fraction, we found only mechanical coupling, at  $\Delta T$  values up to  $2.0^\circ\text{C}$ . From here, we systematically decreased  $l_1$  until we reached the value  $l_1 = 0.39$ , where we discovered oscillations slightly above the onset of convection. A plot of our results is shown in Figure 6. Oscillations near onset continue at lower fractions, until the value  $l_1 = .345$  is reached, where no oscillations are observed, and the coupling is predominantly thermal. We have calculated wavenumbers and frequencies for the oscillations in both the top and bottom layers from the power spectra. The results are close to those predicted by the numerical analysis of Y. Renardy (unpublished). Figure 6 shows that in order for time-dependent behavior to develop with this combination of fluids, the coupling at the onset of convection must be mechanical.

Our experiments with the combination of fluids 47v2 over water show different behavior at the onset of convection. Calculations predict simultaneous onset of convection for  $l_1 = 0.69$  in this system. Our work near this depth fraction shows that in the range  $0.71 \geq l_1 \geq 0.60$  the critical mode at onset is time dependent. A space-time plot of this behavior is shown in Figure 5. This is consistent with numerical work done by Y. Renardy, who describes a parameter

$$Y = \frac{\kappa_1 \alpha_1 \rho_1}{\kappa_2 \alpha_2 \rho_2}, \quad (2)$$

which should be far from one for the possibility of oscillations to be large. The 47v10/FC-70 system has  $Y = .776$ , while the 47v2/water system has  $Y = 0.374$ , implying that the range of depths where oscillations can be expected is much larger.

## CONCLUSIONS

Numerical studies done on the two-layer Rayleigh-Bénard problem predict that the coupling between the two layers at onset should be predominantly thermal for values of  $l_1$  just below the range where the onset should have oscillatory behavior, and predominantly mechanical for  $l_1$ , just above the oscillatory range. The size of the window of oscillations is determined by the parameter  $Y$ . Our work in the 47v10/FC-70 shows thermal coupling at low  $l_1$  and mechanical coupling at high  $l_1$ . In addition, this system shows oscillatory behavior above onset for a range  $0.39 \geq l_1 \geq 0.345$ . Further work with the 47v2/water system shows the occurrence of oscillations at the onset of convection for  $0.71 \geq l_1 \geq 0.60$ , supporting the usefulness of  $Y$  as a qualitative predictor for the range of  $l_1$  where oscillatory behavior may be expected.

## ACKNOWLEDGEMENTS

We would like to thank Y. Renardy for her discussions on the nature of the system and her numerical predictions. We would also like to acknowledge discussions with P. Kolodner and M. Schatz, and D. A. Campbell & Co. for supplying the silicone oils. This work was supported by NASA grant NAG3-1612.

## REFERENCES

- [1] S. Chandrasekhar, *Hydrodynamic and Hydromagnetic Stability* (Oxford University Press, Oxford, England, 1961).
- [2] P. G. Drazin and W. H. Reid, *Hydrodynamic Stability* (Cambridge University Press, Cambridge, England, 1981).
- [3] J. R. A. Pearson, *J. Fluid Mech.* **4**, 489 (1958).
- [4] F. M. Richter and C. E. Johnson, *J. Geophys. Res.* **79**, 1635 (1974).
- [5] L. Cserepes and M. Rabinowicz, *Earth Planet. Sci. Lett.* **76**, 193 (1985).
- [6] L. Cserepes, M. Rabinowicz, and C. Rosemberg-Borot, *J. Geophys. Res.* **93**, 12009 (1988).
- [7] F. M. Richter and D. P. McKenzie, *J. Geophys. Res.* **86**, 6133 (1981).
- [8] F. H. Busse, *Phys. Earth Planet. Inter.* **24**, 320 (1981).
- [9] G. Z. Gershuni and E. M. Zhukovitskii, *Sov. Phys. Dokl.* **27**, 531 (1982).
- [10] S. Rasenat, F. H. Busse, and I. Rehberg, *J. Fluid Mech.* **199**, 519 (1989).
- [11] Y. Renardy and D. D. Joseph, *Phys. Fluids* **28**, 788 (1985).
- [12] Y. Renardy and M. Renardy, *Phys. Fluids* **28**, 2699 (1985).
- [13] Y. Renardy, *Phys. Fluids* **29**, 788 (1986).
- [14] M. Renardy and Y. Renardy, *Physica (Amsterdam) D* **32**, 227 (1988).
- [15] P. Colinet and J. C. Legros, *Phys. Fluids* **6**, 2631 (1994).
- [16] Y. Renardy and D. D. Joseph, *Fundamentals of Two Fluid Dynamics*, Vol. 1 of *Interdisciplinary Applied Mathematics* (Springer-Verlag, Reading, Massachusetts, 1993).
- [17] R. W. Zeren and W. C. Reynolds, *J. Fluid Mech.* **53**, 305 (1972).
- [18] H. C. Nataf, S. Moreno, and P. Cardin, *J. Phys. France* **49**, 1707 (1988).
- [19] P. Cardin and H. C. Nataf, *Europhys. Lett.* **14**, 665 (1991).
- [20] P. Cardin, H. C. Nataf, and P. Dewost, *J. Phys. II* **1**, 599 (1991).
- [21] F. H. Busse, *Geophys. Res. Lett.* **9**, 519 (1982).

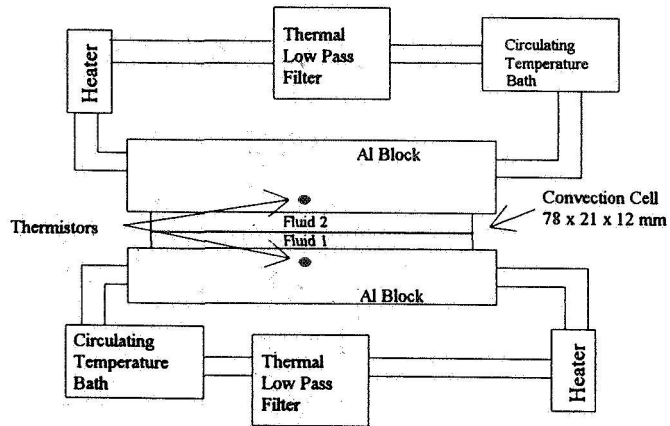


Figure 1: Schematic of the convection cell and temperature control, including thermal low pass filters and in-line active heaters

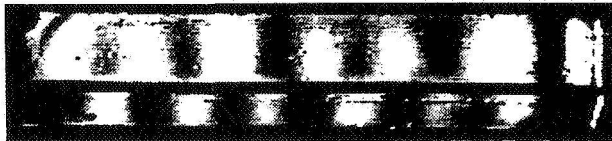


Figure 2: Schlieren image of the 47v10/FC-70 system. Light regions are rolls turning in one direction, Dark rolls turn in the opposite sense.  $\Delta T = 1.6$  C,  $I_1 = 0.38$ .

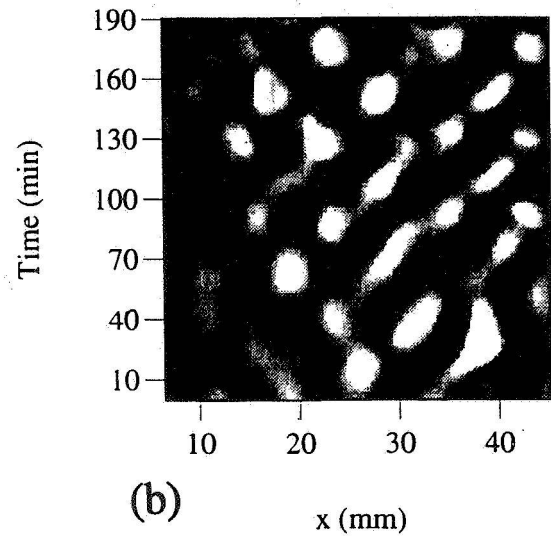
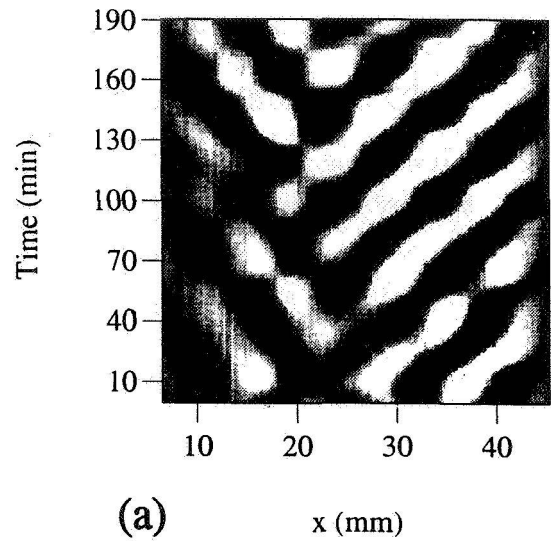
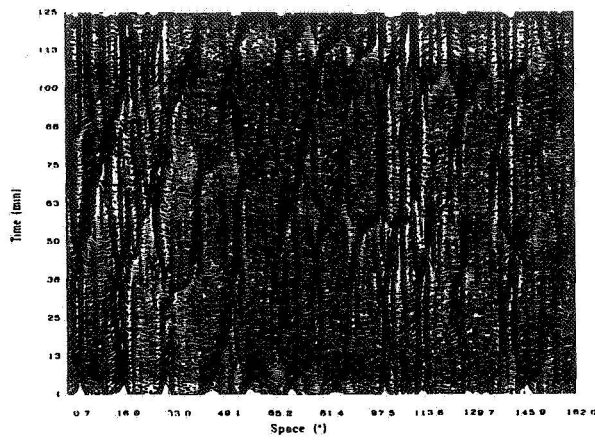
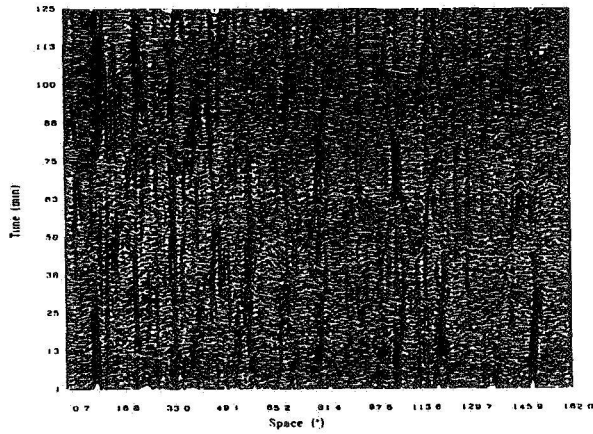


Figure 3: Space-time plot of the (a) top and (b) bottom layer in the rectangular cell, for the state shown in Fig. 2. Time advances up the vertical axis, and a time-averaged background has been subtracted.



(a)



(b)

Figure 4: Background subtracted space-time plot of the (a) top and (b) bottom layer in the annular cell, for  $\Delta T=2.0$  C,  $l_1=0.37$ . The horizontal axis units are degrees around the azimuthal dimension.

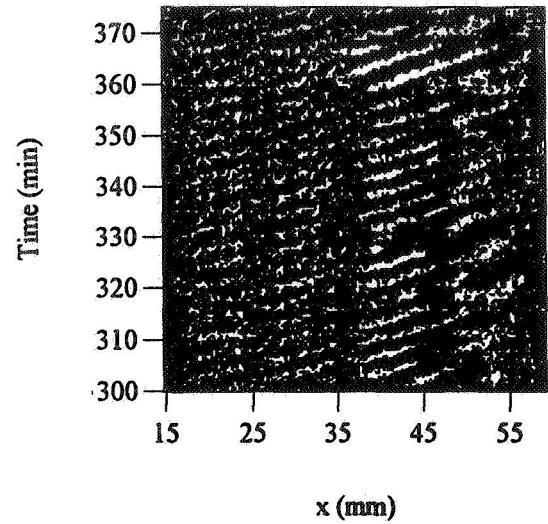


Figure 5: Background subtracted space-time plot of the upper layer in the 47v2/water system near the onset of convection, showing the time-dependent behavior of the rolls.  $\Delta T=0.74$  C,  $l_1=0.6$ .

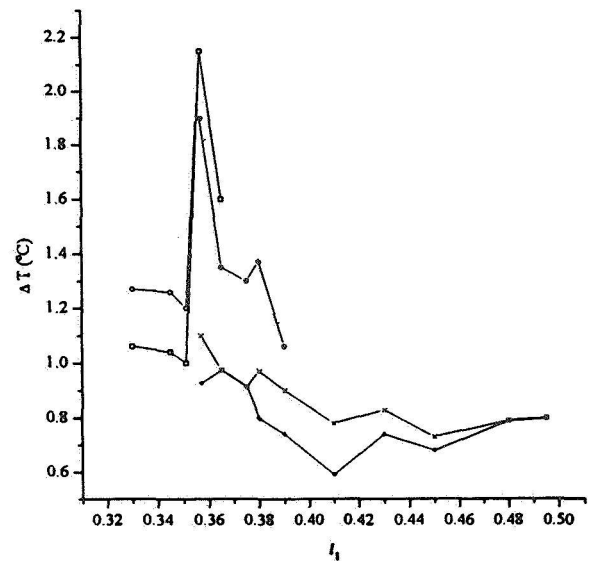


Figure 6: Plot of  $\Delta T$  vs.  $l_1$  showing the range of coupling and the onset of oscillations in the 47v10/FC-70 system. (X) and (+) indicate the onset of mechanically coupled convection in the top and bottom layers, respectively. (○) and (□) indicate the onset of thermally coupled convection in the top and bottom layers. (●) indicates the onset of oscillations.

# SALT-FINGER CONVECTION IN A STRATIFIED FLUID LAYER INDUCED BY THERMAL AND SOLUTAL CAPILLARY MOTION

C. F. Chen and Cho Lik Chan  
Department of Aerospace and Mechanical Engineering  
The University of Arizona  
Tucson, AZ 85721

## ABSTRACT

Salt-finger convection in a double-diffusive system is a motion driven by the release of gravitational potential due to differential diffusion rates. The normal expectation is that, when the gravitational field is reduced, salt-finger convection together with other convective motions driven by buoyancy forces will be rapidly suppressed. However, because the destabilizing effect of the concentration gradient is amplified by the Lewis number, with values varying from  $10^2$  for aqueous salt solutions to  $10^4$  for liquid metals, salt-finger convection may be generated at much reduced gravity levels. In the microgravity environment, the surface tension gradient assumes a dominant role in causing fluid motion. In this paper, we report some experimental results showing the generation of salt-finger convection due to capillary motion on the surface of a stratified fluid layer. A numerical simulation is presented to show the cause of salt-finger convection.

## INTRODUCTION

When a fluid contains two diffusing components with different molecular diffusivities, convective motion may be generated when potential energy is released owing to differential diffusion. In the case of a warm and solute-rich fluid overlying cold and fresher fluid with an overall density distribution that is gravitationally stable, convection will be generated through the finger instability mechanism of the double-diffusive system. The critical condition is given by Stern (ref. 1) for a free-free layer:

$$R_s Le = R_T + \frac{27\pi^4}{4} \quad (1)$$

in which the solute and thermal Rayleigh numbers are defined as

$$R_s = \frac{g\alpha_s \Delta S d^3}{\kappa \nu}, \quad R_T = \frac{g\alpha \Delta T d^3}{\kappa \nu} \quad (2)$$

with  $g$  the gravitational acceleration;  $\alpha_s$  and  $\alpha$  the volumetric expansion coefficients due to the solute and temperature, respectively;  $\Delta S$  and  $\Delta T$  the changes in solute and temperature across the fluid layer with thickness  $d$ ;  $\kappa$  the thermal diffusivity; and  $\nu$  the kinematic viscosity. The Lewis number, defined as  $Le = \kappa / \kappa_s$ , where  $\kappa_s$  is the mass diffusivity, is generally quite large, being  $\sim 10^2$  for aqueous salt solutions and  $\sim 10^4$  for liquid metals. The constant  $27\pi^4/4$  is for free-free boundary conditions only. For other conditions, it is of order  $10^3$ .

In laboratory experiments and in practice, the convecting cells are long and narrow (aptly named fingers), with upward and downward flow in alternating cells. Because of the large magnitudes of  $Le$ , the critical condition for the onset of finger convection can be exceeded under reduced gravity levels. Using the thermophysical properties for a lead-tin alloy as given by Coriell et al. (ref. 2) and letting  $g = \epsilon g_0$ , where  $g_0$  is the sea-level gravity, the critical condition for the onset of finger convection becomes

$$\varepsilon \Delta S d^3 > \frac{10^3 \kappa_s \nu}{g_0 \alpha_s} = 1.43 \times 10^{-5} \text{ wt\%-cm}^3 \quad (3)$$

in which  $\Delta S$  is in wt%. For  $d = 1$  cm and  $\Delta S = 1$  wt%,  $\varepsilon = 10^{-5}$ , or finger convection may be triggered at  $10^{-5} g_0$ . We note here that the thermal Rayleigh number at this gravity level is

$$R = 0.438 \times 10^3 \varepsilon \Delta T = 0.4 \times 10^{-2} \Delta T \quad (4)$$

which is negligible compared to  $LeR_s$  for reasonable values of  $\Delta T$ . For an ethanol-water solution with 98% ethanol, finger convection may occur at  $10^{-4} g_0$  for a comparable layer thickness and concentration difference. Under microgravity conditions, thermocapillary flow is easily generated. If this motion occurs on the surface of a stratified fluid layer, might not finger convection be caused to onset? We have made experimental investigations into this possibility and found the answer to be affirmative. Numerical simulations indicate that the thermocapillary effect is the main cause of this phenomenon.

In order to minimize the effect of buoyancy-driven convection, the experiment was conducted in a stratified ethanol-water solution with pure ethanol on the surface. A small  $\Delta T$  was imposed across the tank to generate the thermocapillary flow. It is known that when the  $\Delta T$  exceeds the critical value, a vertical array of nearly horizontal convection cells are generated. This problem of sideways heating of a solute gradient has been investigated experimentally by Thorpe et al., Chen et al., Tanny and Tsinober, and Lee et al. (refs. 3-6). Numerical simulations of this problem have been made by Wirtz et al. (ref. 7), Heinrich (ref. 8), and, more recently, by Lee and Hyun (ref. 9). In the experiments we conducted, the  $\Delta T$  was limited to  $1^\circ\text{C}$  or  $2^\circ\text{C}$ , well below the critical value of  $6^\circ\text{C}$ , and the fluid in the rest of the tank remained motionless, except in the layer near the bottom boundary where convection was induced by the end conditions.

## EXPERIMENTAL APPARATUS AND PROCEDURE

Experiments were carried out in a tank 5 cm wide  $\times$  10 cm high  $\times$  9.5 cm long. The two sidewalls (10 cm  $\times$  9.5 cm) are made of chrome-plated copper, with passages provided for circulating fluid from two constant-temperature baths. The two end walls are made of plexiglass, and the bottom of Bakelite. A thermocouple was mounted on a vertical transverse mechanism located at the center of the tank to measure the temperature distribution of the fluid. The fluid used was an ethanol-water solution; it was chosen because its free surface is not easily contaminated. The concentration varied from 100 wt% ( $\rho = 0.791 \text{ g cm}^{-3}$ ) at the top to 64 wt% ( $\rho = 0.883 \text{ g cm}^{-3}$ ) at the bottom. This relatively large stable density gradient was chosen so that the critical  $\Delta T$  for the onset of horizontal cellular convection would not be exceeded during our experiments. This value of  $\Delta T_c$  is  $6.4^\circ\text{C}$  according to the stability analysis carried out by Thorpe et al. (ref. 3). In our experiments, the  $\Delta T$  was obtained by increasing (decreasing) the temperature of the hot (cold) wall by  $\Delta T/2$ .

Flow visualization was carried out either by shadowgraph or by particle trace. For the latter, aluminum powder was added to the fluid. A 20-mW He-Ne laser with a cylindrical lens was used to provide a horizontal sheet of light through the tank. A CCD video camera was mounted vertically above the tank, and the image of the particle motion was viewed on a monitor and simultaneously recorded by a time-lapse VCR. The test tank was mounted on a platform capable of vertical motion. In this manner, particle traces could be viewed at any horizontal plane within the 10-cm height of the test tank.

Twenty-one layers, each containing  $21.5 \text{ cm}^3$  of solutions of decreasing density, were successively introduced into the tank to obtain the initial stratification. For the ethanol-water solution, the diffusivity varied nonlinearly with the concentration from  $0.41 \times 10^{-5} \text{ cm}^2/\text{s}$  at 64% ethanol to  $1.15 \times 10^{-5} \text{ cm}^2/\text{s}$  at 100% ethanol. Since we have no means of measuring the concentration of ethanol, the diffusion process was simulated by a one-dimensional calculation taking into account the effect of variable diffusivity. The concentration distribution at 1 hr after the start of the diffusion process was essentially linear with height, with nondiffusive effects near the top and bottom. With these results in mind, the test procedure followed was to begin all experiments 1 hr after completion

of the filling process. For flow visualization tests, aluminum particles were added to the prepared solutions for each layer prior to filling the tank.

## RESULTS AND DISCUSSION

Experiments were conducted with a free and a rigid top boundary. For the free-surface experiment, salt-finger convection was induced soon after the  $\Delta T$  was imposed. (These are illustrated in a series of four particle-trace photographs taken from the video display with an 8-sec exposure.) During this experiment, the first  $\Delta T$  step of  $0.8^\circ\text{C}$  was imposed at 10:10. Particles at a level 0.5 cm below the free surface were seen to move slowly from the hot wall toward the cold wall soon after the  $\Delta T$  was imposed. Fig. 1a shows a particle trace photograph taken at 10:14. Motion of the particles can be discerned, but there were no apparent salt fingers. At 10:18, Fig. 1b, finger convection was clearly exhibited. It is noted here that finger convection in the presence of shear, which is present in our experiments, appears in longitudinal sheets aligned with the direction of shear. This phenomenon, similar to the case of Rayleigh-Benard convection in the presence of shear, was clearly shown by Linden (ref. 10) in counterflowing streams of sugar and salt solutions. The onset of salt fingers near the cold rather than the hot wall is due to the large effect of solute concentration on surface tension, and this point is further discussed in the section on numerical simulation. By 10:32, Fig. 1c, fingers reached across approximately 3/4 of the width of the tank, and the transverse velocity became less, due to the smaller temperature gradient. At 11:20, the  $\Delta T$  was increased to  $1.9^\circ\text{C}$  and, at 11:55, Fig. 1d, the fingers were quite well organized across the entire width of the tank. In experiments conducted with the rigid top boundary, no finger convection was observed at comparable  $\Delta T$ 's.

The observed difference between the free-surface and the rigid-surface experiments can be explained in terms of the temperature and density distributions. Since there is no easy method of measuring the concentration of ethanol in situ, we infer its distribution from the measured temperature distribution by comparing the results obtained in our earlier experiments with salt solution in which concentration and temperature were simultaneously measured. In the present experiments, temperature was measured along the vertical centerline of the tank at 2.5 mm intervals. The results for the free-surface case and the rigid-surface case are shown in Fig. 2. In both cases, the temperature distributions at  $\Delta T = 1^\circ\text{C}$ ,  $2^\circ\text{C}$ , and  $3^\circ\text{C}$  are shown. For the free-surface case, it is seen that, at  $\Delta T = 1^\circ\text{C}$ , temperatures in the top 1 cm are slightly higher than the rest of the fluid because of the motion at the surface due to the surface tension gradient. The temperature difference between the surface and the rest of the fluid became larger as  $\Delta T$  was increased. One also notes that there was a layer of fluid at the top, 2-4 mm in thickness, in which the temperature was constant, indicating that the fluid was well mixed due to finger convection. The results for the rigid surface show a small, positive temperature gradient near the top. The characteristics of temperature distribution at  $\Delta T = 2^\circ\text{C}$  were quite similar to the data obtained at  $\Delta T = 2.1^\circ\text{C}$  with the salt solution, in which the concentration measurement at the same time indicated a stable gradient essentially unchanged from the initial distribution. In fact, this stable concentration gradient persisted to  $\Delta T = 3.8^\circ\text{C}$ . From these results, we infer that, in the comparable experiment with a rigid top surface at  $\Delta T$  up to  $2^\circ\text{C}$ , the initial stable ethanol gradient still persisted and the fluid was motionless. At  $\Delta T = 3^\circ\text{C}$ , the temperature distribution indicates there was motion but, because of the stable concentration and temperature gradients, no fingers were observed.

## NUMERICAL SIMULATION

Numerical simulation using a transient two-dimensional finite difference method (FDM) was performed. The geometry simulated is a  $1 \times 5$  rectangular domain. The fluid is initially at uniform temperature, with stably stratified ethanol-water solution. The initial concentration distribution is essentially linear, with nondiffusive effects near the top and bottom. At time zero, nondimensional temperatures at the left and right sidewalls are set and maintained at 0.5 and -0.5, respectively. The relevant dimensionless parameters are  $R_T = 100$ ,  $R_S = 1000$ ,  $M_T = 8000$ ,  $M_S = 40,000$ ,  $\text{Pr} = 17$ , and  $\text{Le} = 85$ . These correspond to  $\Delta T = 1^\circ\text{C}$ ,  $\Delta S = 4 \text{ wt\%}$ , and a 1-cm height scale. The gravitational field is  $10^{-3} g_0$ . The two-dimensional simulation clearly captured the mechanism that led to salt fingers.

The imposed temperature conditions at the sidewalls established very strong temperature gradients near the upper corners, as shown in Fig. 3a. Consequently, two counter-clockwise vortices are established due to thermocapillarity. These vortices bring high-concentration solution to the free surface, creating a nonuniform concentration on the free surface, as shown in Fig. 3b. Near the hot wall (left), the concentration on the free surface

produces a surface tension force opposing the thermocapillarity. However, the concentration on the free surface near the cold wall (right) reinforces the thermocapillarity. This can be seen clearly in Fig. 3c, where the total surface tension effect  $[(M_S/M_T)S - T]$  is plotted. Consequently, the vortex near the hot wall decays while the vortex near the cold wall grows, which greatly distorts the temperature and concentration fields. The vertical temperature distribution near the cold wall ( $x = 4.75$ ), as shown in Fig. 4a, is stabilizing. The vertical concentration distribution, shown in Fig. 4b, is initially stably stratified. However, at later times, the rotation brings high-concentration solution to the top, creating a destabilizing effect. Based on the temperature and concentration distributions and the corresponding length scale, we estimated that  $R_S = 167$  and  $R_T = 15$ . According to Eq. (1), this is in the supercritical regime for salt-finger instability. The total vertical density  $[(R_S/R_T)S - T]$  distribution is plotted in Fig. 4c. The top-heavy situation can be seen clearly. This unstable situation is responsible for the onset of salt fingers near the cold wall and their propagation throughout the tank as observed in our experiments.

## CONCLUSIONS

When a fluid layer is stratified by a solute concentration and has a top free surface, thermocapillary motion is generated as soon as a small  $\Delta T$  across the tank is imposed. Due to the initial density stratification, no motion is induced in the rest of the fluid at this small  $\Delta T$ . The capillary motion near the cold wall brings the warmer and solute-rich fluid to the surface and causes the onset of finger convection. This is an effective means of generating finger convection in a microgravity environment. Since the conditions at onset are likely to be in the neighborhood of the critical state, finger convection would appear in rolls, with lateral dimensions comparable to the layer thickness.

## ACKNOWLEDGMENT

This research was funded by NASA through Microgravity Science and Application Grant NAG-1328.

## REFERENCES

1. Stern, M. E., "The 'Salt-Fountain' and Thermohaline Convection," *Tellus*, Vol. 12, pp. 172-175, 1960.
2. Coriell, S. R., Cordes, M. R., and Boettinger, W. J., "Convective and Interfacial Instabilities During Unidirectional Solidification of a Binary Alloy," *J. Crystal Growth*, Vol. 49, pp. 13-28, 1980.
3. Thorpe, S. A., Hutt, P. K., and Soulsby, R., "The Effects of Horizontal Gradients on Thermohaline Convection," *J. Fluid Mech.*, Vol. 38, pp. 375-400, 1969.
4. Chen, C. F., Briggs, D. G., and Wirtz, R. A., "Stability of Thermal Convection in a Salinity Gradient Due to Lateral Heating," *Int. J. Heat Mass Transfer*, Vol. 14, pp. 57-65, 1971.
5. Tanny, J. and Tsinober, A. B., "The Dynamics and Structure of Double-Diffusive Layers in Sidewall Heating Experiments," *J. Fluid Mech.*, Vol. 196, pp. 135-156, 1988.
6. Lee, J., Hyun, M. T., and Kang, Y. S., "Confined Natural Convection Due to Lateral Heating in a Stably Stratified Solution," *Int. J. Heat Mass Transfer*, Vol. 33, pp. 869-875, 1990.
7. Wirtz, R. A., Briggs, D. G., and Chen, C. F., "Physical and Numerical Experiments on Layered Convection in a Density-Stratified Fluid," *Geophys. Fluid Dyn.*, Vol. 3, pp. 265-288, 1972.
8. Heinrich, J. C., "A Finite Element Model for Double-Diffusive Convection," *Int. J. Num. Meth. Eng.*, Vol. 20, pp. 447-464, 1984.
9. Lee, J. W. and Hyun, M. T., "Time-Dependent Double Diffusion in a Stably Stratified Fluid Under Lateral Heating," *Int. J. Mass Heat Transfer*, Vol. 34, pp. 2409-2415, 1991.
10. Linden, P. F., "Salt Fingers in a Steady Shear Flow," *Geophys. Fluid Dyn.*, Vol. 6, pp. 1-27, 1974.



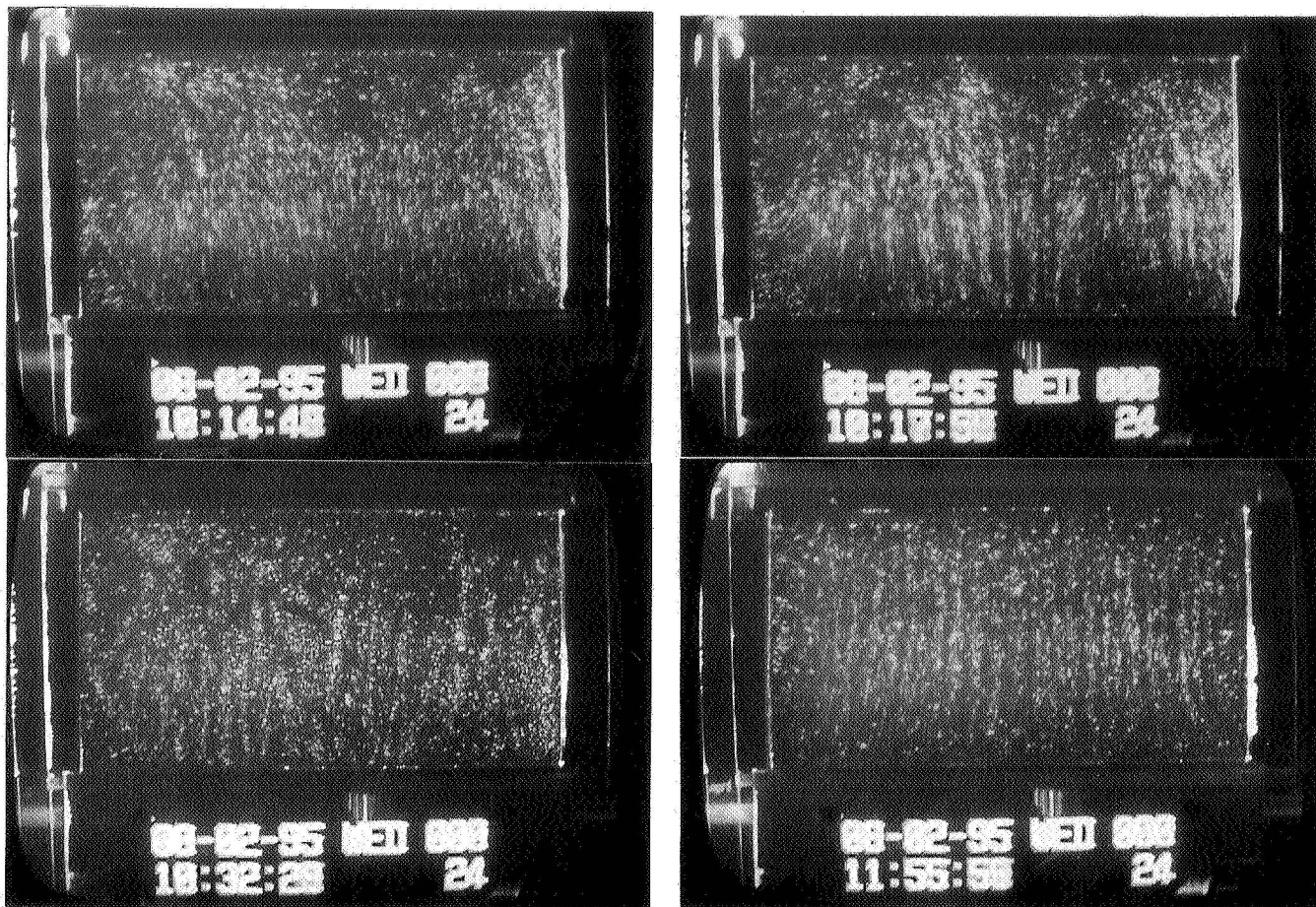


Fig. 1. Particle trace at 0.5 cm below the free surface, 8-sec exposure. Cold wall at bottom. Experiment started with  $\Delta T = 0.8^\circ\text{C}$  at  $t = 10:10$ .  $\Delta t$  increased to  $1.9^\circ\text{C}$  at  $t = 11:20$ .

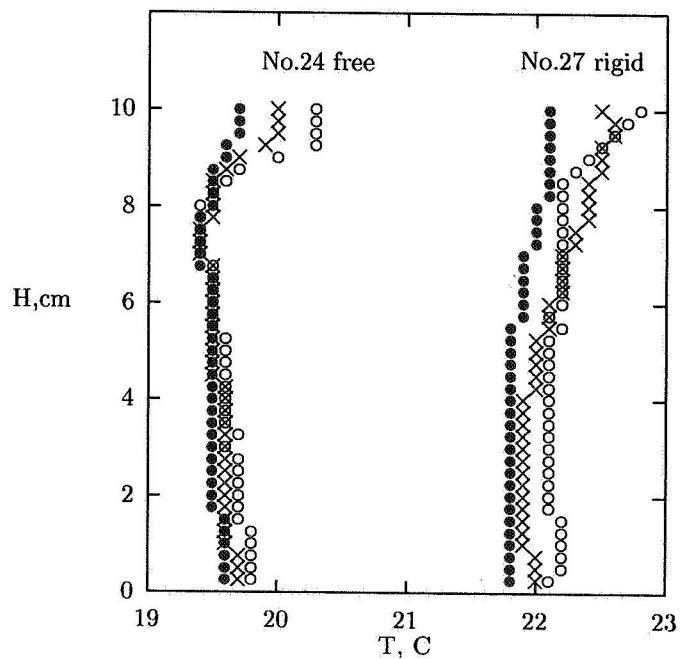


Fig. 2. Vertical temperature distribution for the free and rigid top surfaces.

- $\Delta T = 1^\circ\text{C}$
- ×  $\Delta T = 2^\circ\text{C}$
- $\Delta T = 3^\circ\text{C}$

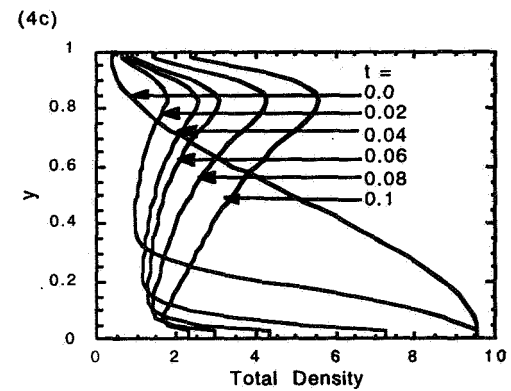
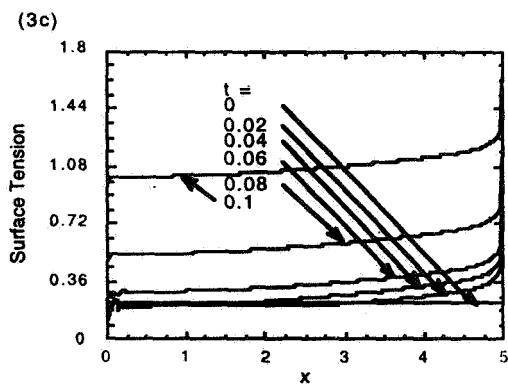
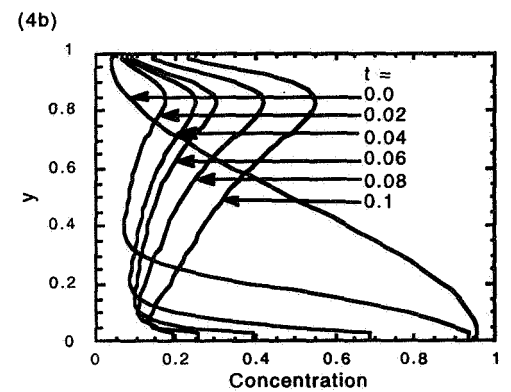
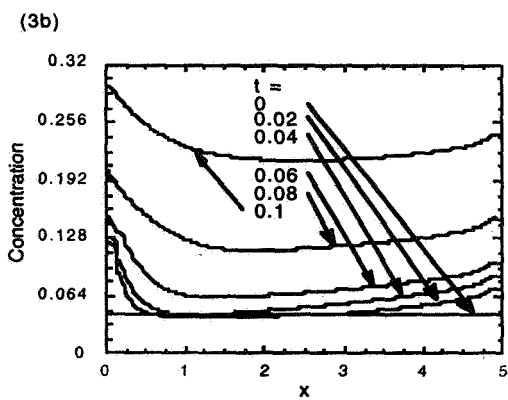
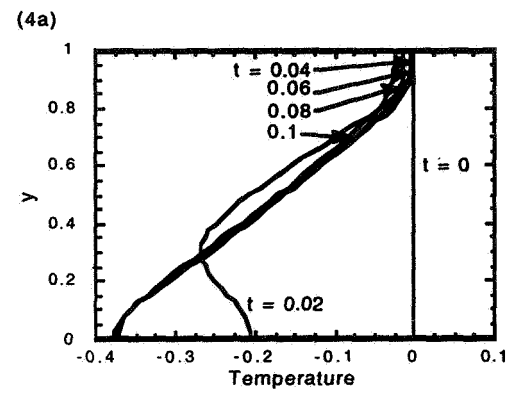
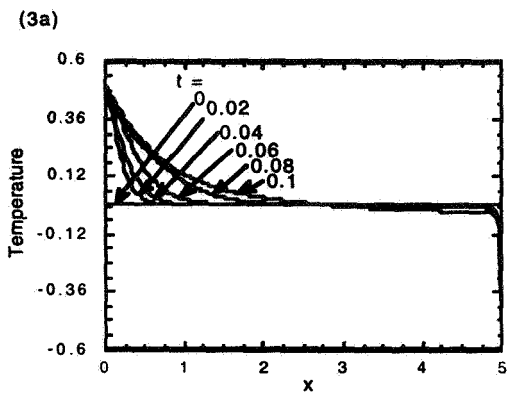


Fig. 3. Temperature, concentration, and surface tension distributions on the free surface.

Fig. 4. Temperature, concentration, and total density distributions (vertical) near the cold wall ( $x = 4.75$ ).

# LOW-DIMENSIONAL DYNAMICAL MODELS OF THERMAL CONVECTION

A. Liakopoulos

Department of Mechanical Engineering and Mechanics

Lehigh University

Bethlehem, Pennsylvania, 18015

## ABSTRACT

A low-dimensional dynamical model for transitional buoyancy-driven flow in a differentially heated tall enclosure is presented. The full governing partial differential equations with the associated boundary conditions are solved by a spectral element method for a cavity of aspect ratio  $A = 20$ . Proper orthogonal decomposition is applied to the oscillatory solution at Prandtl number  $Pr = Pr_o = 0.71$  and Grashof number  $Gr = Gr_o = 3.2 \times 10^4$  to construct empirical eigenfunctions. Using the four most energetic empirical eigenfunctions for the velocity and temperature as basis functions and applying Galerkin's method, a reduced model consisting of eight nonlinear ordinary differential equations is obtained. Close to the "design" conditions  $(Pr_o, Gr_o)$ , the low-order model (LOM) predictions are in excellent agreement with the predictions of the full model. In particular, the critical Grashof number at the onset of the first temporal flow instability (Hopf bifurcation) as well as the frequency and amplitude of oscillations at supercritical conditions are in excellent agreement with the predictions of the full model. Far from the "design" conditions, the LOM predicts the existence of multiple stable steady solutions at large values of  $Gr$ , and a unique stable steady solution at small values of  $Gr$ , and exhibits hysteretic behavior that is qualitatively similar to that observed in direct numerical simulations based on the full model.

## INTRODUCTION

Thermally driven cavity flows provide a wealth of paradigms for the study of flow instabilities and transition to turbulence. A classical problem is concerned with the motion in a rectangular cavity when the vertical boundaries are maintained at fixed but distinct temperatures and the upper and lower horizontal surfaces are adiabatic. For a Newtonian fluid, subject to the Boussinesq approximation, the flow field is governed by three dimensionless parameters: the aspect ratio  $A$  (height/width), the Prandtl number  $Pr$ , and the Grashof number  $Gr$  (based on the cavity width). At moderate  $Gr$ , the base flow corresponds to a single unicellular state. As  $Gr$  increases, both time-dependent and stationary bifurcations can occur, depending on the aspect ratio and Prandtl number. In the present study we investigate the possibility of developing low-dimensional dynamical models of oscillatory multicellular convection in a rectangular cavity of aspect ratio  $A = 20$ .

The method of weighted residuals can be used to transform evolution partial differential equations (PDEs) to systems of ordinary differential equations (ODEs). Most frequently, trigonometric or orthogonal polynomials are used as basis functions (e.g., Gottlieb and Orszag, 1977). Other basis functions, e.g., spline functions (Liakopoulos, 1985, Liakopoulos and Hsu, 1984) have also been used successfully. In practice, the infinite dimensional problem is truncated to a finite dimensional space of dimension  $n$ . To ensure that the dynamic behavior described by the resulting finite dimensional system converges to that of the original infinite dimensional problem, the required dimension  $n$  is typically high. A large reduction in the dimension of the resulting system of ODEs is accomplished by expanding the unknown functions in terms of basis functions that are constructed specifically for each flow system and reflect the behavior of the flow in the vicinity of some values of the controlling parameters. Proper Orthogonal Decomposition (POD) is a rigorous methodology for obtaining a set of optimal basis functions (Berkooz et al., 1993). POD systematically identifies the most energetic eigenmodes that contain enough information for accurate description of the flow dynamics. Consequently, one is able to compress numerical or experimental data by retaining a small number of modes that capture most of the flow and temperature "energy".

In this paper, we consider the buoyancy-driven flow in a laterally heated enclosure of aspect ratio  $A = 20$ . Direct numerical simulations are performed for  $Pr = 0.71$  and  $10^3 \leq Gr \leq 10^5$ . Proper Orthogonal Decomposition and Galerkin's version of the method of weighted residuals are employed to derive low-order dynamical models of the flow in the transitional regime.

### FULL MODEL

The flow domain consists of a two-dimensional rectangular cavity in which the upper and lower surfaces are adiabatic and the vertical walls are maintained at constant but different temperatures. Subject to the Boussinesq approximation, the continuity, momentum, and energy equations are written in dimensionless form:

$$\nabla \cdot \vec{V} = 0, \quad (1)$$

$$\frac{\partial \vec{V}}{\partial t} + (\vec{V} \cdot \nabla) \vec{V} + \nabla P = \Theta \vec{j} + \frac{1}{\sqrt{Gr}} \nabla^2 \vec{V} \quad (2)$$

$$\frac{\partial \Theta}{\partial t} + \vec{V} \cdot \nabla \Theta = \frac{1}{Pr\sqrt{Gr}} \nabla^2 \Theta \quad (3)$$

with boundary conditions  $\vec{V} = 0$  along the walls,  $\Theta(x = 0, y) = 1$ ,  $\Theta(x = 1, y) = 0$ , and  $\frac{\partial \Theta}{\partial y}(x, \pm \frac{A}{2}) = 0$ . The dimensionless variables are defined as

$$(x, y) = (x^*, y^*)/l, \quad t = \frac{u_c}{l} t^*, \quad \vec{V} = \frac{\vec{V}^*}{u_c} \quad (4)$$

$$P = \frac{p^*}{\rho u_c^2}, \quad \text{and} \quad \Theta = \frac{T - T_1}{T_2 - T_1}.$$

Here  $T_1$  and  $T_2$  are the cold and hot wall temperatures, respectively,  $l$  is the cavity width,  $Pr = \nu/\alpha$  is the Prandtl number,  $Gr = \frac{\beta g (T_2 - T_1) l^3}{\nu^3}$  is the Grashof number,  $\nu$  is the kinematic viscosity,  $\alpha$  is the thermal diffusivity,  $\beta$  is the thermal expansion coefficient,  $g$  is the acceleration of gravity,  $\vec{j}$  is the unit vector in the direction opposite to gravity, and  $u_c = \sqrt{\beta g l (T_2 - T_1)}$ . Note that the characteristic velocity  $u_c$  has been determined by balancing the inertia and buoyancy forces in the momentum equation and the pressure has been scaled by two times the dynamic pressure. These are appropriate scales for the high Grashof number thermal convection considered in the present study.

For high  $Gr$  the IBVP (full model) has multiple stable solutions that can be computed by assigning appropriate initial conditions. For example, if we start with a three-cell time-independent solution at  $Gr = 4 \times 10^4$  and gradually decrease  $Gr$ , different solution branches can be reached. At  $Gr = 3.2 \times 10^4$ , a stable three-cell time-independent solution is found. This contrasts the four-cell time-dependent flow that is found when  $Gr$  is gradually increased. Reducing  $Gr$  further, we obtain a sequence of time-independent solutions that may belong to the same steady solution branch. At  $Gr = 10^4$  a steady multicellular solution is computed. Note that the multiplicity of solutions is a property of the full model for large values of  $Gr$  only. At  $Gr = 5 \times 10^3$ , the solution to the IBVP computed by decreasing  $Gr$  is identical to the one computed for increasing  $Gr$ . We have found no evidence of multiple solutions as  $Gr$  was decreased further. Although an exhaustive search for all possible solutions is prohibitively expensive, we may conclude with a reasonable degree of confidence that the full model has a unique stable steady solution for  $Gr \leq 8 \times 10^3$ .

## DERIVATION OF THE LOW-ORDER MODEL

In the context of transitional thermal convection, we assume that, for some values  $(Pr_o, Gr_o)$ , we have obtained spontaneously oscillatory flow and temperature fields. We refer to these values of the parameters as “design” parameters or “design” conditions. Furthermore, it is assumed that  $M$  snapshots of each field have been experimentally measured or computed based on the full model for  $Pr = Pr_o$  and  $Gr = Gr_o$ . Following the procedure described in Liakopoulos and Gunes (1996), we construct the stationary empirical eigenfunctions. Expanding the unknown functions in terms of the eigenfunctions, applying Galerkin method, and making use of the orthonormality property of the empirical eigenfunctions, we obtain a system of non-linear ODEs for the temporal expansion coefficients

$$\frac{da_k}{dt} = A_k + \frac{1}{\sqrt{Gr}} B_k + C_{ki} a_i + \frac{1}{\sqrt{Gr}} D_{ki} a_i + E_{kij} a_i a_j + R_{ki} b_i \quad (5)$$

$$\frac{db_k}{dt} = F_k + \frac{1}{Pr\sqrt{Gr}} G_k + H_{ki} a_i + \frac{1}{Pr\sqrt{Gr}} I_{ki} b_i + J_{kij} a_i b_j + K_{ki} b_i.$$

## EIGENVALUES AND EMPIRICAL EIGENFUNCTIONS

Twenty snapshots ( $M = 20$ ) of the oscillatory solution for  $Gr = Gr_o = 3.2 \times 10^4$  and  $Pr = Pr_o = 0.71$  provide the input data for the extraction of the empirical eigenfunctions. A list of the eight largest eigenvalues is given in Table I. The eigenvalues have been normalized so that their sum equals unity, and their cumulative contribution to the total flow and temperature fluctuation “energy” is given in the last column of Tables Ia and Ib, respectively. The first four eigenmodes capture 99.83% of both flow and temperature fluctuation “energy”. However, the energy distribution among the four most energetic modes is slightly different for temperature than for velocity. The principal eigenvalue contributes 63.07% of the total fluctuation “energy” for temperature as opposed to 55.83% for velocity. Furthermore, for the temperature eigenvalues  $\lambda_2 \approx \lambda_1/2$  and  $\lambda_4 \approx \lambda_3/2$ .

Isotherms and streamlines for the four most energetic empirical eigenfunctions are shown in Figure 1. Note that although the direct numerical simulations and the proper orthogonal decomposition are performed in terms of primitive variables  $(u, v, P, \Theta)$ , the velocity eigenfunctions are presented here in terms of the corresponding streamfunction. The velocity and temperature eigenfunctions are both centro-symmetric. The two most energetic eigenfunctions are localized in the central part of the cavity where velocity and temperature fluctuations are most vigorous. Higher order eigenfunctions capture features in the entire cavity, including regions close to the horizontal end walls. Repeated flow and temperature structures can be seen in the middle part of the cavity. These repeated structures form patterns that are characteristic of the early transition process of convection in laterally heated tall cavities. Preliminary results reveal that the most energetic eigenmodes exhibit the same spatial patterns in the middle part of a cavity of aspect ratio  $A = 40$ .

## RESULTS BASED ON THE LOW-ORDER MODEL

In developing a reduced model, it is desired to keep the dimensionality of the system sufficiently low so that the methods of the dynamical systems theory can be effectively applied. On the other hand, enough modes should be retained so that the field variables are reconstructed accurately, most of the flow and temperature fluctuation “energy” is captured, and the potentially important information hidden in the small scale features of higher modes is not lost. For the problem at hand, at least four modes for each field variable need to be retained in order to obtain oscillations of correct amplitude at “design” conditions  $(Gr_o, Pr_o)$ . Retaining fewer than four modes leads to unrealistically large modal amplitudes. The results summarized below are obtained using eight ODEs (four from the momentum equation and four from the energy equation). The critical points (fixed points, steady solutions) of the low-order model are found by setting the

right hand side of equation (5) to zero and solving the resulting nonlinear algebraic equations. The stability of a steady solution is then determined by the eigenvalues of the associated Jacobian matrix evaluated at the critical point under consideration. Note that the Jacobian matrix is real and non-symmetric. Several steady solution branches are found for  $1 \leq Gr \leq 2 \times 10^5$  using a Newton-Raphson method with random initial guesses for the solution components. For  $Gr < 2.63 \times 10^4$ , a unique branch of stable fixed points is found. We refer to this branch as the primary solution branch. It is denoted by A in Figure 2 where the norm  $(a_i a_i + b_i b_i)^{1/2}$  of the fixed points is plotted against  $Gr$ . For  $Gr \geq 2.63 \times 10^4$ , multiple steady solutions are found. Since we are interested in solutions that are potentially relevant to the solutions of the original system of PDEs, we discard fixed points whose norm is several orders of magnitude larger than the norm of the primary branch. In Figure 2, we present only fixed points with a norm smaller than 3 in the range  $1 \leq Gr \leq 10^5$ . Thick lines represent stable fixed points while thin lines correspond to unstable fixed points. Two stable steady solutions exist for  $2.63 \times 10^4 \leq Gr \leq 3.11 \times 10^4$ . At  $Gr = 3.11 \times 10^4$ , the fixed point on the primary branch undergoes a Hopf bifurcation that marks the onset of periodic oscillations in time. For  $3.11 \times 10^4 \leq Gr \leq 4.14 \times 10^4$ , we find one stable steady solution (branch B) while for  $4.14 \times 10^4 \leq Gr \leq 9.87 \times 10^4$ , two stable steady solutions exist (branches B and C). The fixed point along branch C becomes unstable at  $Gr = 9.87 \times 10^4$ . For  $Gr > 9.87 \times 10^4$ , we find only one stable steady solution that maintains its stability at least up to  $Gr = 2 \times 10^5$ . These stability results have been confirmed by solving equations (5) with suitable initial conditions using a fourth order Runge-Kutta ODE solver.

A detailed quantitative comparison of the low-order model predictions with the full model is beyond the scope of the present work. However, we mention some encouraging observations both quantitative and qualitative in nature. The low-order model prediction of a Hopf bifurcation along the primary branch is in excellent agreement with the full model prediction. The low-order model predicts a Hopf bifurcation at  $Gr = Gr_H = 3.11 \times 10^4$ , while the full model predicts the onset of spontaneously oscillatory convection at  $Gr \simeq 3.1 \times 10^4$ . The frequency of oscillations at the onset of the temporal instability is successfully predicted by the low-order model. Turning our attention to values of  $Gr$  far from the design conditions, we find qualitative agreement between the low-order model and the full model. For example, the low-order model predicts a stationary bifurcation at  $Gr < Gr_H$  in qualitative agreement with the full model which predicts that a stationary instability certainly precedes the onset of oscillatory convection for  $A = 20$  and  $Pr = 0.71$ . The low-order model predicts a unique stable steady solution for small values of  $Gr$  and multiple stable steady solutions for large values of  $Gr$  in agreement with the direct numerical simulation results based on the full model. However, the critical values of  $Gr$  at which the multiple stable solutions emerge or lose their stability are at variance with the PDE-based calculations. More research is needed in documenting the multiplicity of solutions of the PDEs before a meaningful quantitative comparison with the ODE predictions can be accomplished. This is a demanding task since direct numerical studies based on the full model are computationally intensive and are complicated by the presence of hysteresis effects.

## CONCLUSIONS

A low-dimensional dynamical model for transitional buoyancy-driven flow in a differentially heated enclosure of aspect ratio  $A=20$  has been presented. Empirical eigenfunctions have been determined by applying the snapshot version of the proper orthogonal decomposition at “design” conditions  $Pr_o = 0.71$  and  $Gr_o = 3.2 \times 10^4$ . The computed eigenfunctions are centro-symmetric. Using the four most energetic eigenmodes of the velocity field and the four most energetic eigenmodes of the temperature field, a Galerkin procedure leads to an eight-equation nonlinear dynamical model. Close to the “design” conditions, the low-order model predictions are in excellent agreement with the predictions of the full model. Conditions at the onset of the first temporal instability (Hopf bifurcation) of the flow are in excellent agreement with the full model predictions in terms of the critical Grashof number, the frequency of oscillations, and the amplitude

of oscillations at supercritical conditions. Far from the "design" conditions, the LOM predicts a unique steady solution at small values of  $Gr$ , and multiple stable steady solutions at large values of  $Gr$ , and exhibits hysteretic behavior that is qualitatively similar to that observed in direct numerical simulations based on the full model. It is believed that low-order models have the potential of becoming a viable tool in the study of complex transitional flows. Note, however, that the governing equations have been scaled appropriately in order to widen the range of applicability of the resulting low-order model. The possibility of improving the performance of the LOM by constructing empirical eigenfunctions that take into account the behavior of the flow system at multiple values of  $Gr$  is under investigation.

#### ACKNOWLEDGMENT

This work was partially supported by NASA /LeRC under contract No. NAG3-1632.

#### REFERENCES

- Berkooz, G., P. Holmes, and J. L. Lumley (1993), "The Proper Orthogonal Decomposition in the Analysis of Turbulent Flows," *Ann. Rev. Fluid Mech.* 25, 539-575.
- Gottlieb, D. and S. A. Orszag (1977), "Numerical Analysis of Spectral Methods," Society for Industrial and Applied Mathematics, Philadelphia, PA.
- Liakopoulos, A. and Gunes, H. (1996), "Low-Dimensional Description of Oscillatory Thermal Convection: The Small Prandtl Number Limit," submitted, *Theoretical and Computational Fluid Mechanics*.
- Liakopoulos, A. (1985), "Computation of High Speed Turbulent Boundary Layer Flows Using the  $k-\epsilon$  Turbulence Model," *Int. J. Num. Meth. Fluids*. 5, No. 1, 81-97.
- Liakopoulos, A. and C. C. Hsu (1984), "On a Class of Compressible Laminar Boundary-Layer Flows and the Solution Behavior Near Separation," *J. Fluid Mech.* 149, 339-353.
- Lumley, J. L. (1967), "The Structure of Inhomogeneous Turbulent Flows," In *Atmospheric Turbulence and Radio Wave Propagation*, A. M. Yaglom and V. I. Tatarski, ed. 166-178 (Nauka, Moscow).

Table I

##### a) Velocity eigenvalues

Modes	Normalized Eigenvalue	Cumulative Energy Contribution (%)
1	0.5583	55.83
2	0.3424	90.07
3	0.0658	96.65
4	0.0317	99.83
5	$0.921 \times 10^{-3}$	99.92
6	$0.707 \times 10^{-3}$	99.99
7	$0.603 \times 10^{-4}$	99.99
8	$0.293 \times 10^{-4}$	100.0

##### b) Temperature eigenvalues

Modes	Normalized Eigenvalue	Cumulative Energy Contribution (%)
1	0.6307	63.07
2	0.3163	94.70
3	0.0345	98.15
4	0.0168	99.83
5	$0.881 \times 10^{-3}$	99.92
6	$0.677 \times 10^{-3}$	99.99
7	$0.696 \times 10^{-4}$	99.99
8	$0.524 \times 10^{-4}$	100.0

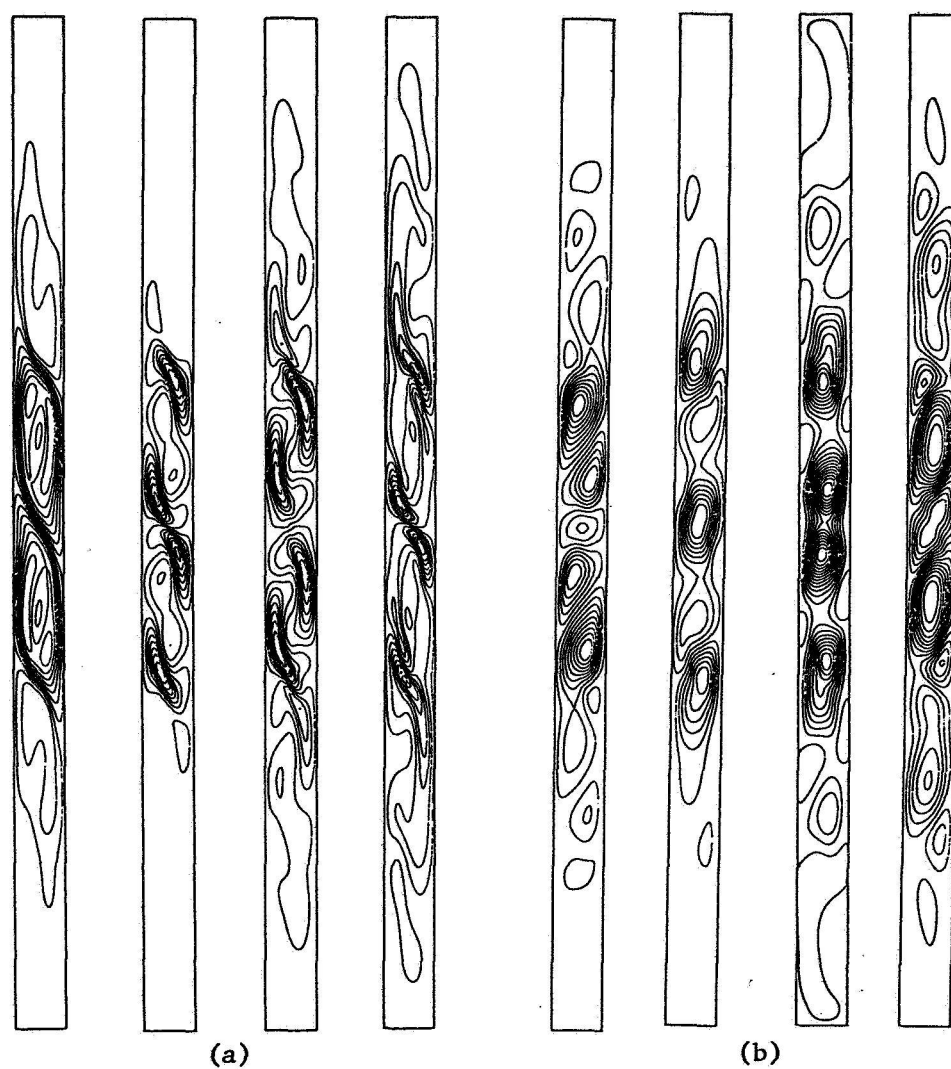


Figure 1. Temperature (a) and velocity (b) empirical eigenfunctions.

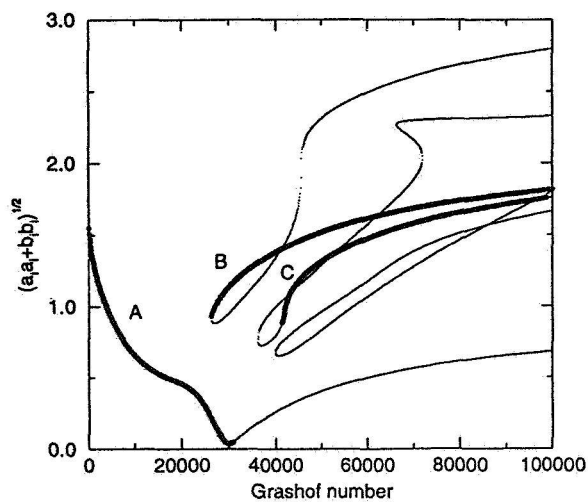


Figure 2. Fixed points of the LOM and their stability.  $Pr = 0.71$ .



## SURFACE TENSION DRIVEN CONVECTION EXPERIMENT-2 (STDCE-2)

Simon Ostrach and Yasuhiro Kamotani  
Department of Mechanical and Aerospace Engineering  
Case Western Reserve University  
Cleveland, Ohio, 44106

### ABSTRACT

The Surface Tension Driven Convection Experiment-2 (STDCE-2) was conducted aboard the USML-2 Spacelab which was launched on October 20, 1995. The main objective of the experiments was to study oscillatory thermocapillary flows in microgravity. Thermocapillary flows were generated in cylindrical test chambers filled with 2 centistokes silicone oil. Six modules were used to study three different chamber diameters and two different heating modes. Tests with both flat and curved free surfaces were conducted. The flow field was studied by flow visualization and an infrared imaging system recorded the oil free-surface temperature. An optical (Ronchi) system was used to measure the oil free-surface deformation and motions. A total of 55 tests were conducted and oscillations were found in most of them. The data are currently being analyzed.

### INTRODUCTION

Thermocapillary flow is known to become oscillatory under certain conditions. However, its cause and the dimensionless parameter(s) to characterize the onset of oscillations are not yet fully understood despite the fact that many investigators studied the phenomenon for many years. One major reason for the lack of understanding is that some of the available experimental data on oscillatory thermocapillary flows taken in one-g environments are confusing or contradictory because of buoyancy. For that reason we have conducted a series of thermocapillary flow experiments in microgravity.

The first experiments, called the Surface Tension Driven Convection Experiment (STDCE), were performed aboard the USML-1 Spacelab in 1992 and the results were reported by Kamotani et al. (refs. 1 and 2). The experiments were mainly for steady thermocapillary flows. One important finding was that the flow did not become oscillatory despite the fact that its Marangoni number ( $Ma$ , to be defined later) was several times larger than the critical  $Ma$  for the onset of oscillations found in our one-g tests using smaller test chambers (refs. 3 and 4). Since  $Ma$  is the main dimensionless parameter representing the flow driving force in the absence of buoyancy, the results implied that there must be other factors to characterize the onset. Our past theoretical and experimental work suggested that the additional parameter is associated with the free surface deformation. Based on that concept we designed the second series of experiments in microgravity.

The second experiments, called the Surface Tension Driven Convection Experiment-2 (STDCE-2) were performed during the USML-2 mission in October-November, 1995. Oscillations were found in those experiments and the conditions for the onset of oscillations were investigated under various conditions. Since a large amount of data was gathered in the STDCE-2 their analysis is not yet complete.

## DESCRIPTION OF STDCE-2

### Apparatus

Cylindrical containers of 1.2, 2.0, and 3.0 cm diameters were used in the STDCE-2. 2 centistokes silicone oil was the test fluid. The test fluid was stored in a reservoir attached to each container. The oil was put into the container before each test through a small filling hole at the bottom of the container and withdrawn to the reservoir after the test. The side wall of each container was maintained at a uniform temperature by circulating cooling water around it. Two different heating modes were employed (see Fig. 1). A submerged heater system was used to study flows over a range of imposed temperature differences (called the constant temperature (CT) mode). The heater diameter was 10 % of the container diameter. In addition, a surface heating system (a CO<sub>2</sub> laser system) was employed to study flows generated by various heat fluxes distributed across the surface of oil (called the constant flux (CF) mode). The CO<sub>2</sub> laser beam was absorbed within 0.1 mm from the oil free surface. The laser beam diameter at the oil surface was adjustable.

The oil free surface shape was varied by adjusting the total volume of the oil in the container. The free surface shapes are shown in Fig. 1. In all cases the fluid free surface was anchored at the top edge of the container side wall. For that purpose the side wall had a sharp edge and was barrier-coated. In the CT mode there were three shapes (flat, shallow concave, and deep concave), while in the CF mode a convex shape was also studied. In the CF mode each shape is a part of a spherical surface but in the CT mode the shape is more complex because two orthogonal radii of curvature at any point on the surface are different.

The flow field was studied by flow visualization. 70 micron pliolite particles were added to the fluid and they were mixed uniformly in the reservoir before the filling by shaking the whole test module. A video camera recorded the motions of the particles from above the container. The experimental arrangement is sketched in Fig. 2.

An infrared scanner (IR imager) was used to measure the free surface temperature distribution. It operated in the wavelength range from 8 to 14  $\mu\text{m}$ . Our ground based tests had shown that the technique was a very useful tool to study the thermocapillary oscillation phenomenon. The IR imager developed for the present experiments is described in detail by Pline et al. (ref. 5)

An optical method called Ronchi system was employed to measure the free surface deformations and motions. It was designed to measure the slope of the free surface up to 20  $\mu\text{m}/\text{mm}$ , from which the surface shape was to be constructed after the flight. It was used only for flat free surface tests. Various types of grating were tried during the tests to find the optimum setting to measure a given oscillation pattern.

Three thermistors were placed along the length of each heater to monitor its temperature. One thermistor monitored the side wall temperature near its top edge and another thermistor recorded the air temperature above the oil surface. The fluid temperature was measured by a movable thermistor probe placed near the mid-radius of each container (see Fig. 1). Its bead diameter was 0.5 mm. Its vertical position was adjusted manually and placed close to the free surface usually. The effect of the probe on the oscillation phenomenon was investigated by comparing the data with the probe out and those with the probe completely withdrawn. The probe was also used to determine the position of the free surface.

In conjunction with the STDCE-2, a glovebox experiment called the Oscillatory Thermocapillary Flow Experiment-2 (OTFE-2) was conducted. The OTFE-2 experiments were performed only in the CT mode and the test chamber design was similar to the CT chambers in the STDCE-2. The flow visualization was the main diagnostic technique in the OTFE-2.

## Parametric Ranges

The important dimensionless parameters for steady thermocapillary flow in the present configuration with flat free surface are:  $Ma$  (Marangoni number) =  $\sigma_T \Delta T H / \mu \alpha$ ,  $Pr$  (Prandtl number) =  $\nu / \alpha$ ,  $Ar$  (aspect ratio) =  $H/R$ ,  $Hr$  (relative heater size) =  $D_H/D$ , where  $\sigma_T$  is the temperature coefficient of surface tension,  $\Delta T$  the overall temperature variation along the fluid free surface,  $\nu$  the fluid kinematic viscosity,  $\mu$  the dynamic viscosity,  $\alpha$  the thermal diffusivity,  $H$  the container depth,  $R$  container radius,  $D$  the container diameter, and  $D_H$  the heating zone diameter (the heater diameter in the CT mode). In the case of curved free surfaces the shape is specified by the relative total fluid volume (total fluid volume/total fluid volume for flat free surface).

Since  $Ma$  is the only parameter that contains  $\Delta T$  (the driving force for the flow) in the above list, the conditions for the onset of oscillations should be specified by  $Ma$  for a given  $Ar$ ,  $Hr$ , and  $Ar$ . However, in our earlier work we have shown that  $Ma$  is not sufficient to specify the onset conditions. One objective of the present experiments is to confirm that in the reduced gravity conditions of space. Our past work suggested that free surface deformation plays an important role in the oscillation mechanism. In that case a parameter such as capillary number ( $Ca = \mu U_c / \sigma$ , where  $U_c$  is the characteristic velocity scale of the flow and  $\sigma$  the surface tension) is also important. In fact, our first space experiments (STDCE) were designed based on  $Ma$  but no oscillations were found even though the range of  $Ma$  was much larger than the range of  $Ma$  where oscillations were found in our ground-based tests. Therefore, the STDCE-2 experiments had been designed based not on  $Ma$  but on our concept of the oscillation mechanism.

The test conditions in the STDCE-2 and OTFE-2 experiments are summarized in Table 1. In all, 55 tests were conducted (13 CT tests and 42 CF tests) in the STDCE-2, and 4 tests were performed in the OTFE-2.

Silicone oil with  $\nu = 2$  centistokes at  $25^\circ\text{C}$  was the test fluid. In the temperature range of the STDCE-2 tests its Prandtl number varied from 18 to 28. The aspect ratio was unity in the baseline tests but in some additional tests in the CF mode  $Ar$  was changed to 0.5 by inserting a circular disk into the test cell to raise its bottom.  $Hr$  was fixed at 0.1 in the CT tests but varied from 0.05 to 0.4 in the CF tests. The range of  $Ma$  was  $Ma < 5 \times 10^5$ . In the OTFE-2 the container aspect ratio was set at 0.5 and 2.0 to study the effect of  $Ar$  on the onset of oscillations.

## Operation of STDCE-2

One important feature of the STDCE-2 was that the tests were run interactively. All three video images (flow visualization, IR images, and Ronchi patterns) were downlinked simultaneously using the HIPAC system to the Payload Operation Command Center (POCC) at Huntsville, Alabama. We followed the tests at the POCC, communicated with the astronaut who was conducting the test, and helped him or her identify the onset of oscillations. The astronaut also followed the test from the start to the end and was very much involved in the experiments. The astronaut setup each test, filled the container, ramped the heating power up manually based on his or her flow observation, stopped the ramping whenever something interesting was observed, and changed the grating for the Ronchi system as the oscillation pattern changed. The data obtained in one test were analyzed by us immediately after the test and the test conditions for the subsequent test were determined and uplinked. This interactive operation was very useful and many interesting phenomena were found as a result.

## PRELIMINARY RESULTS

All tests were completed successfully, with every test, except one, producing oscillatory flow. We conducted all of the pre-mission defined tests as well as several tests that were re-runs to establish repeatability. The quality of all the data (video and digital) was excellent. All of our onboard Hi-8 video tapes (about 120 tapes) and RAM memory cartridges (20) were used. We are still analyzing those tapes and data. We are also conducting numerical analysis of the flows to supplement the experimental information.

Preliminary analysis shows the following trends. (1) The critical temperature differences and heat fluxes for the onset of oscillations for the 1.2 cm chambers with flat free surfaces were close to those found in our ground-based tests. However, for the 2 and 3 cm chambers the critical values were much lower than those found on the ground, showing the effect of buoyancy in the latter. (2) The largest critical Marangoni number in the STDCE-2 tests was nearly three to four times larger than that found in our ground based-tests with using smaller chambers, which means that there is no fixed critical Marangoni number to specify the onset of oscillations. (3) The critical values increased as the free surface was made more concave. The critical values also increased when the chambers were made shallow.

## REFERENCES

1. Kamotani, Y., Ostrach, S., and Pline, A. ; Analysis of Velocity Data Taken in Surface Tension Driven Convection Experiment in Microgravity, *Physics of Fluids*, Vol.6, 1994, pp. 3601-3609.
2. Kamotani, Y., Ostrach, S., and Pline, A.; A Thermocapillary Convection Experiment in Microgravity, *J. Heat Transfer*, Vol. 117, 1995, pp. 611-618.
3. Kamotani, Y., Lee, J. H., Ostrach, S., and Pline, A.; An Experimental Study of Oscillatory Thermocapillary Convection in Cylindrical Containers, *Physics of Fluids*, Vol. 4, 1992, pp. 955-962.
4. Kamotani, Y., Maud, J., and Pline, A.; Oscillatory Convection due to Combined Buoyancy and Thermocapillarity, *J. Thermophysics and Heat Transfer* Vol. 10, 1996, pp. 102-108.
5. Pline, A. and Butcher, R. L. ; Spacelab Qualified Infrared Imager for Microgravity Science Applications, *Thermosense XII*, SPIE, Vol.. 1313, 1990, pp. 250-258.

Table 1. Summary of STDCE-2 and OTFE-2 tests.

No. of CT tests with  $Ar = 1$

DIA. (CM)	FLAT	S.C.	D.C.
1.2	2	2	1
2	2	2	1
3	1	1	1

Total 13 CT tests with  $Ar = 1$

(S.C.=shallow concave surface, D.C.=deep concave surface, see Fig. 1)

No. of CF tests with  $Ar = 1$

CONTAINER DIA. (CM)	BEAM DIA. (CM)	FLAT	S.C.	D.C.	CONVEX
1.2	0.12	1	1	1	
	0.24	1	1	1	
	0.4	1			
	0.6		1	1	
2	0.1	1	1	1	1
	0.2	1	1	1	1
	0.4	1	1	1	1
	0.6				1
3	0.15	1	1	1	
	0.3	3	1		
	0.6	1	1	1	

Total 32 CF tests with  $Ar = 1$

Additional 10 CF tests with  $Ar = 5$

No. of OTFE tests (CT tests only)

DIA. (CM)	$Ar=0.5$	$Ar=2$
1.2	1	1
2	1	1

Total 4 OTFE tests

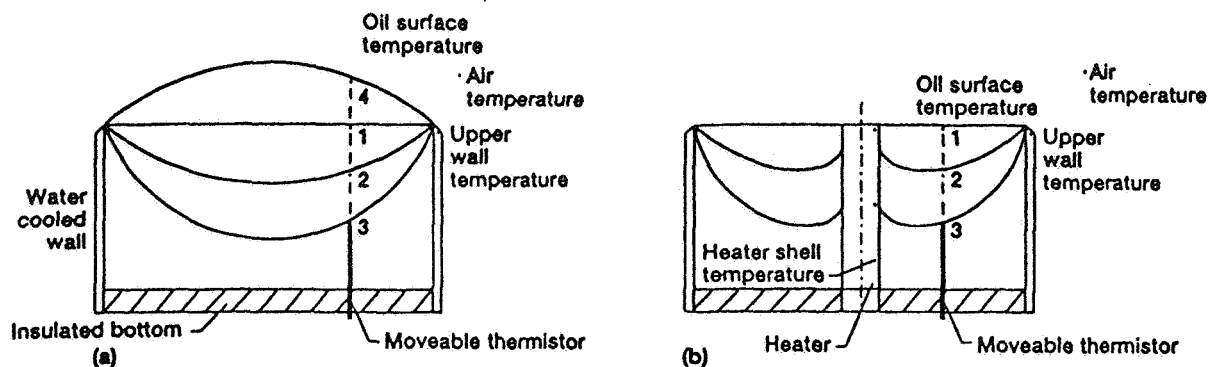


Figure 1. Free surface shapes in STDCE tests: (a) CF cells, (b) CT cells.

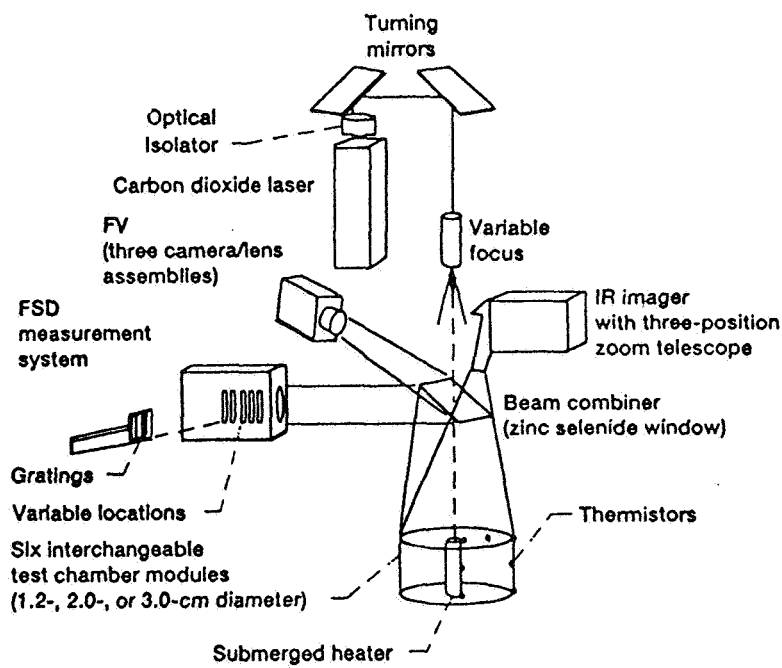


Figure 2. Test setup of STDCE.

# THERMOCAPILLARY MOTION IN AN EMULSION

Vladislav V. Pukhnachov

Lavrentyev Institute of Hydrodynamics, Lavrentyev prospect 15, Novosibirsk 630090, Russia,  
and Oleg V. Voinov

Institute for Mechanics of Multiphase Systems, Taimyrskaya 74, Tyumen 625026, Russia

## ABSTRACT

The phenomenological model for the motion of an emulsion or a gas-liquid mixture exposed to the thermocapillary forces and microaccelerations is formulated. The analytical and numerical investigation of one-dimensional flows for these media is fulfilled, the structure of discontinuous motion is studied. The stability conditions of a space-uniform state and of the interface between an emulsion and a pure liquid are obtained.

## MAIN ASSUMPTIONS

Let us consider the motion of a liquid with inclusion of small drops of another liquid immiscible with the first one. It is supposed that the system is in local thermodynamic equilibrium. The relative phase motion is primarily due to the nonuniformity of the temperature field which produces the thermocapillary effect by virtue of the dependence of the coefficient of the surface tension  $\sigma$  on the temperature  $T$ . For simplicity, we suppose that this dependence is linear,  $\sigma = \sigma_0 - \sigma_T(T - T_0)$  where  $\sigma_0, T_0$  and  $\sigma_T$  are some positive constants. In addition to the thermocapillary forces, the system is exposed to the microgravity with acceleration  $\vec{g}$ .

Further, it is supposed that the drops or bubbles have the spherical form, that they are of equal radius  $R$ , and that the volume concentration  $c$  of the disperse phase is small. Moreover, we assume that the mean distance between the drops  $l$  satisfies the inequalities  $R \ll l \ll \text{diam}\Omega$ , where  $\Omega$  is the volume containing the liquid. In this case, the concepts of mechanics of heterogeneous media are applicable to describe the motion of such a system. Besides, below the Peclet numbers for the liquid matrix and disperse phase are assumed small. This allows us to restrict ourselves to the medium model with the single temperature.

## GOVERNING EQUATIONS.

The system of governing equations involves the following unknown functions:  $T, c$ , averaged velocity of drops or bubbles  $\vec{u}$ , and carrying phase  $\vec{v}$ , pressure of carrying phase  $p$ . Let us use the indices  $d$  and  $m$  to denote the parameters of the disperse phase and liquid matrix, correspondingly. The thermal conductivity of the mixture is determined from the Maxwell formula, whereas, the dynamic viscosity coefficient from the Taylor formula. The resulting system is as follows

$$c_i + \text{div}(c\vec{u}) = 0, \quad (1)$$

$$(1-c)_i + \text{div}[(1-c)\vec{v}] = 0, \quad (2)$$

$$\begin{aligned} & \rho_d c (\vec{u}_i + \vec{u} \cdot \nabla \vec{u}) + \rho_m (1-c) (\vec{v}_i + \vec{v} \cdot \nabla \vec{v}) = \\ & = -\nabla p + \text{div} \left\{ \mu_m \left[ 1 + c \frac{\mu_m + 5\mu_d/2}{\mu_m + \mu_d} \right] [\nabla \vec{v} + (\nabla \vec{v})^*] \right\} + \rho_d c \vec{g} + \rho_m (1-c) \vec{g}, \end{aligned} \quad (3)$$

$$\rho_d \lambda_d (T_i + \vec{u} \cdot \nabla T) + \rho_m \lambda_m (1-c) (T_i + \vec{v} \cdot \nabla T) = \text{div} \left\{ k_m \left[ 1 - c \frac{3(k_m - k_d)}{2k_m + k_d} \right] \nabla T \right\}, \quad (4)$$

$$\vec{u} - \vec{v} = \frac{2R(\mu_m + \mu_d)}{3\mu_m(2\mu_m + 3\mu_d)} \times \left[ (\rho_d - \rho_m)R\vec{g} + \frac{3k_m\mu_m\sigma_T\nabla T}{(2k_m + k_d)(\mu_m + \mu_d)} \right], \quad (5)$$

where  $\rho, \mu, \lambda, k$  stand for density, dynamic viscosity, heat capacity, and thermal conductivity of the corresponding phase. These coefficients are assumed constant.

System (1) - (5) was obtained in [1]. It should be noticed that this system does not contain any empiric parameter. Equations (1) and (2) are the exact forms (within the framework of the approach of heterogeneous mechanics) of the mass conservation law for the disperse and carrying phases. When deriving the momentum equation (3) and the energy equation (4) we neglected the terms of the second order with respect to  $c$  in viscous stresses, and the diffusion heat flow, correspondingly. Besides, we omitted the dissipation function in (4) taking into account the smallness of the arising velocities of the motion.

The completing equation of system (1) - (5) requires a special comment. This relation gives an approximate value of the relative phase velocity in the equation (5) we neglected the effect of added masses and Basset's hereditary force, which is inefficient for the flow with low Reynolds numbers calculated from the drop radius and for smoothly changing external conditions. The coefficients in the right-hand part of (5) correspond to the known dependences in the Hadamard-Rybczynski, [2,3], and Young-Goldstein-Block, [4], formulas. In this connection, it is worth mentioning work [5] where the problem of creeping motion of a small drop with the gravity acceleration collinear to the temperature gradient at infinity was solved explicitly. Also, this paper discussed limits of applicability of formula (5).

Let us consider now the motion of a gas-liquid mixture under the effect of thermocapillary forces and microaccelerations. In the case when the gas is the disperse phase we have  $\rho_d \ll \rho_m$ ,  $\mu_d \ll \mu_m$ ,  $k_d \ll k_m$ . The corresponding system of governing equations can be obtained from (1) - (5) by a simple limiting procedure. Historically, the model of a gas-liquid motion in weak force fields was derived before in work [6]. Its further analytical and numerical investigation was fulfilled in [7] where, in particular, self-similar solutions and travelling waves were studied.

### STABILITY OF SPACE - UNIFORM STATE

The simplest solution of system (1)-(5) corresponds to a uniform relative phase motion with a constant concentration and the temperature distribution being linear function of Cartesian coordinate  $x$  in the absence of gravity:

$$\begin{aligned} c &= c_0, \quad T = Gx + Ht, \quad p = \text{const}, \\ u &= (1 - c_0)LG, \quad v = -c_0LG \end{aligned} \quad (6)$$

where  $c_0 \in (0, 1)$  and  $G$  are given constants,

$$\begin{aligned} H &= c_0(1 - c_0)LG^2(\rho_m\lambda_m - \rho_d\lambda_d)[\rho_d\lambda_dc_0 + \rho_m\lambda_m(1 - c_0)]^{-1} \\ L &= 2Rk_m\sigma_T(2\mu_m + 3\mu_d)^{-1}(2k_m + k_d)^{-1}; \end{aligned} \quad (7)$$

$u$  and  $v$  designate projections of vectors  $\vec{u}$  and  $\vec{v}$  on the direction  $x$ .

The linear analysis of the stability of solution (6) with respect to the 3D disturbances proportional to  $\exp(\alpha t + i\vec{\beta} \cdot \vec{x})$  where  $\alpha$  is the complex frequency and  $\vec{\beta}$  is the wave vector leads to a cubic equation for  $\alpha(\vec{\beta})$ . It turns that two of its roots,  $\alpha_2$  and  $\alpha_3$ , always have the negative real part. As for the first one, the real part of  $\alpha_1$  has no definite sign. For the small concentration  $c_0$  we have

$$\text{Re } \alpha_1 = \frac{c_0(LG)^2\chi_m|\vec{\beta}|^2}{(LG\beta)^2 + \chi_m^2|\vec{\beta}|^4} \times \left( \frac{5k_m - 2k_d}{2k_m + k_d}\beta^2 - \frac{\rho_d\lambda_d}{\rho_m\lambda_m}|\vec{\beta}|^2 \right) + O(c_0^2),$$

where  $\chi_m = k_m/\rho_m\lambda_m$  is the thermodiffusion coefficient of the carrying phase,  $\beta$  is  $x$ -component of the vector  $\vec{\beta}$  and  $L$  is defined by formula (7). Therefore, the stability conditions is



$$2\left(\frac{\rho_d \lambda_d}{\rho_m \lambda_m} + \frac{k_d}{k_m}\right) + \frac{\rho_d \lambda_d k_d}{\rho_m \lambda_m k_m} \geq 5, \quad (8)$$

moreover one-dimensional disturbances are the most dangerous ones.

It follows immediately from condition (8) that the uniform distribution of bubbles in the liquid ( $\rho_d \ll \rho_m$ ,  $k_d \ll k_m$ ) under the constant gradient of temperature is unstable. The mentioned instability is of the heat nature. It disappears when  $\chi_m \rightarrow 0$  and  $\chi_m \rightarrow \infty$  and has no analogy among the flows in the two-phase media.

On the other hand, given a liquid matrix, we can point out such properties of the disperse phase that inequality (8) will be fulfilled. An example of such a situation is delivered by the emulsion "aluminium-lead" with aluminium as the carrying phase. We also note that the emulsion having the same coefficients of the carrying and disperse phases is neutrally stable in the sense indicated above.

## ONE - DIMENSIONAL MOTION

System (1)-(5) is very complicated due to its nonlinearity, high order and mixed type. However, in the case of the one-dimensional motion with plane waves it can be simplified radically. (In this case, we suppose that vectors  $\vec{g}$  and  $\nabla T$  are collinear and parallel to the axis  $x$ ). In fact, the two first equations of (1)-(5) provide the integral

$$cu + (1-c)v = f(t) \quad (9)$$

where  $f(t)$  is the mean volume velocity of the mixture. Now we can express  $u$  and  $v$  from (9) and the last equation of system (5) in terms of  $c$ ,  $T$  and  $f$ . As a result, we obtain a system to determine  $T$  and  $c$ :

$$c_t + \left\{ [c(\mathcal{K}g + LT_x) - f](1-c) \right\}_x = 0; \quad (10)$$

$$[\rho_d \lambda_d c + \rho_m \lambda_m (1-c)](T_t + f T_x) + (\rho_d \lambda_d - \rho_m \lambda_m) c (1-c)(\mathcal{K}g + LT_x) = k_m [(1-Mc) T_x]_x \quad (11)$$

Here we introduce the following notations:

$$\mathcal{K} = \frac{2R^2(\rho_d - \rho_m)(\mu_m + \mu_d)}{3\mu_m(2\mu_m + 3\mu_d)}, \quad M = \frac{3(k_m - k_d)}{2k_m + k_d};$$

parameter  $L$  is defined by formula (7) and  $g = |\vec{g}|$ .

System (10), (11) should be completed with appropriate initial and boundary conditions. An additional boundary condition is necessary to determine the new sought function  $f(t)$  (for example,  $f = 0$  in the motion possessing a plane of symmetry). The typical problem of such kind was set up in [6]. The gas-liquid mixture is restricted by two parallel solid impermeable walls. The initial distributions of concentration and temperature are given. The heat flux at both walls is prescribed as a function of time. In addition, the impermeability condition for liquid phase is fulfilled at boundaries of the flow domain. The solvability of formulated problem is proved in [8].

## DISCONTINUOUS SOLUTIONS

System (10), (11), as well as the original one, does not have a definite type. In some sense, it contains both hyperbolic and parabolic parts. This peculiarity leads to a special structure of discontinuities in its solutions. Namely, the concentration has a jump across the line of discontinuity  $x = X(t)$ , while the temperature and heat flux are continuous across this line. The jump of concentration gives rise to a jump of the phase velocities. Proceeding in the standard way and using the notation  $D = X'(t)$  for the jump velocity, we obtain the conditions on the line of discontinuity:

$$\begin{aligned} [c]D &= \left\{ [c(\mathcal{K}g + LT_x) - f](1-c) \right\}, \\ [T] &= 0, \quad [(1-Mc) T_x] = 0. \end{aligned} \quad (12)$$

Here the symbol  $[r]$  denotes the difference of values of the function  $r$  in front and behind the jump.

One of the important cases of concentration discontinuity is a boundary that separates the emulsion and the pure liquid ( $c=0$ ). In this case  $D=u^+$  where  $u^+$  is a velocity of drops in the emulsion (after a jump). Symbol "+" denotes below the emulsion characteristics. The problem of the thermocapillary motion of a single drop near the moving boundary of the emulsion at weightlessness is considered on the base of relations (12) and the Young-Goldestein-Block formula. The difference of the velocities of the boundary  $u^+$  and the drop  $u^-$  equals

$$u^+ - u^- = L(k_m - 4k_d)(2k_m + k_d)^{-1} c^+ T_x^+. \quad (13)$$

If  $T$  increases in the direction from the boundary of emulsion into the pure liquid, then the drop is absorbed by the emulsion when  $k_m > 4k_d$  and it runs away from the boundary when  $k_m < 4k_d$ . If the sign of  $T_x$  is the opposite, the effect also changes its sign. The loss or the absorption of a drop by the weighted layer is important for its stability. Either lower or upper boundary is unstable. Correspondingly, the suspended layer will occur near a heated or a cooled wall of the vessel. The formula (13) shows where exactly.

Let us consider now the problem of the motion of a single drop relatively the boundary of a stationary weighted layer of drops. The equilibrium of this layer is possible if  $KG = -LT_x^+$ . The absence of coalescention of drops is important for the realization of such a layer. The conditions of "attraction" or "repulsion" of the drop from the layer differs in this case from that given above. Namely, if  $k_m > k_d$ , the single drops are absorbed by the lower boundary of the layer and run away from the upper one (the direction of the increasing of temperature is denoted as the upper one). If  $k_m < k_d$ , the single drops run away from the upper boundary and, on the contrary, are absorbed by the lower boundary. In the first case the layer is located at the bottom of the vessel, and in the second case it is positioned overhead.

#### EXAMPLE OF NUMERICAL SOLUTION

Nonlinear initial boundary value problem for system (10), (11) was solved numerically for different combinations of disperse and carrying phases and for different initial distributions of temperature and concentration. We present here the results of its solution in case when the carrying phase is a melted aluminium and the disperse one is a liquid lead. Initial distributions of temperature and concentration are shown on Figures 1 and 2, correspondingly; two other pairs of curves on these figures demonstrate profiles of temperature and concentration at moments  $t=90$  sec and  $t=180$  sec. The boundary conditions are the following:  $T=T_0=1000$  K if  $x=0$ ,  $T_x=0$  if  $x=10$  cm;  $c=0.03$  if  $x=0$ . The gravity is absent, the parameter  $\sigma_T R$  entering into the definition (7) of the coefficient  $L$  is chosen as  $0.001$  gram · cm / sec · K.

#### CONCLUDING REMARKS

In the process of derivation of system (1)-(5), we supposed that all drops or bubbles are of the equal radius. This assumption allows us to minimize dispersion effects. The equations of motion of a polydisperse emulsion or gas-liquid mixture can be obtained using the procedure described above.

A specific trait of the space-uniform state (6) is the dependence of temperature distribution of time. Namely this peculiarity, together with the dependence of mixture heat conductivity coefficient of concentration, lead to the origin of a non-zero real part of the first root in the dispersion equation. Ignoring these factors, we obtain the neutral stability of the convective mode corresponding to the root  $\alpha_1$ .

The conclusion concerning the instability of uniform distribution of bubbles in a gradient temperature field correlates with the results of numerical simulation of 1D thermocapillary motion in a gas-liquid mixture [7]. Here we mention one of them. Let us suppose that initial distribution of concentration is like to a smoothed shelf while initial distribution of temperature is close to a linear one, moreover, the derivatives of both functions are of the same sign. Nonlinear development of process brings to the steepening of the concentration profile and to the loss of its monotonicity: after passing the region of large gradients, the concentration peak appears and this peak is growing rapidly. At the same time, the temperature profile remains close to linear and deforms slightly in the zone where the concentration changes abruptly.

As for stability conditions of the interface "emulsion-pure liquid", they were obtained on the base of conservation laws on the discontinuity. In spite of that, an intrinsic mechanism of instability of two-phase flow was not taken into account. Therefore, the mentioned conditions of stability should be considered as the necessary ones.

In conclusion, we remark that system (1)-(5) can be used for the study of solidification process of an emulsion. To this end, we have to add to these equations appropriate Stefan-type conditions at the front of solidification as well as, in the simplest case, the heat equation in the solid phase. Generally speaking, the solidification temperature of disperse phase is not the same with one of liquid matrix. This circumstance leads to complication of the problem under consideration due to possible appearance of two fronts of solidification. On the other hand, the situation is feasible when drops are driven back from the front of solidification of the pure liquid. Besides the direct problem, the inverse one has an interest: to get the given (for example, constant) distribution of inclusions in the solid material by the control of the boundary regime of cooling.

#### ACKNOWLEDGEMENT

The authors thank NASA for the support of this work in the framework of Contract NAS15-10110.

#### REFERENCES

1. Pukhnachov, V.V.; and Voinov, O.V.: Mathematical model of motion of emulsion under effect of thermocapillary forces and microacceleration. Abstracts of Ninth European Symposium on Gravity Dependent Phenomena in Physical Sciences, Berlin, 1995, pp.32-33.
2. Hadamard, J.: Mouvement permanent lent d'une sphere liquide visqueuse un liquide visqueux. C. R. Acad. Sci. Paris, Vol.152, 1911, pp. 1735-1738.
3. Rybczynski, M.: Uber die fortschreitende Bewegung einer flussigen Kugel in einen zahren Medium. Bull. Intern. Acad. Polon. Sci. Cracovie, Ser. A, Vol.1, 1911, pp.40-46.
4. Young, N.O.; Goldstein, J.S.; and Block, M.J.: The motion of bubbles in a vertical temperature gradient. J. Fluid Mech., Vol.6, 1959, pp. 350-356.
5. Antanovskii, L.K.; and Kopbosynov, B.K.: Non-stationary thermocapillary drift of a drop in a viscous liquid. J. Appl. Mech. and Techn. Phys., Vol.2, 1986, pp. 59-64.
6. Voinov, O.V.; and Pukhnachov, V.V.: Thermocapillary motion in the gas-liquid mixture. J. Appl. Mech. and Techn. Phys., Vol.5, 1980, pp. 38-45.
7. Kopbosynov, B.K.: One-dimensional thermocapillary motion in the gas-liquid mixture. Dinamika Sploshnoi Sredy, Novosibirsk, Vol.74, 1986, pp. 25-37 (in Russian).
8. Pukhnachev, V.V.: Two inverse problems of continuum mechanics. Ill-posed problems of mathematical physics and analysis. Nauka, Novosibirsk, 1984, pp. 113-118 (in Russian).

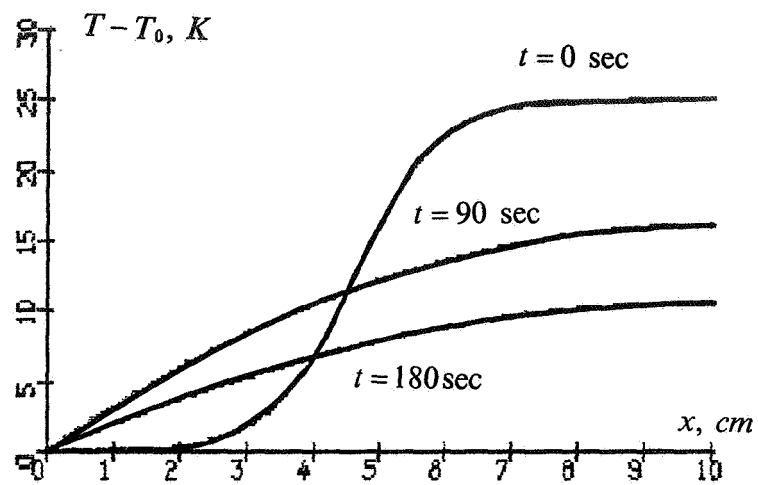


Fig.1

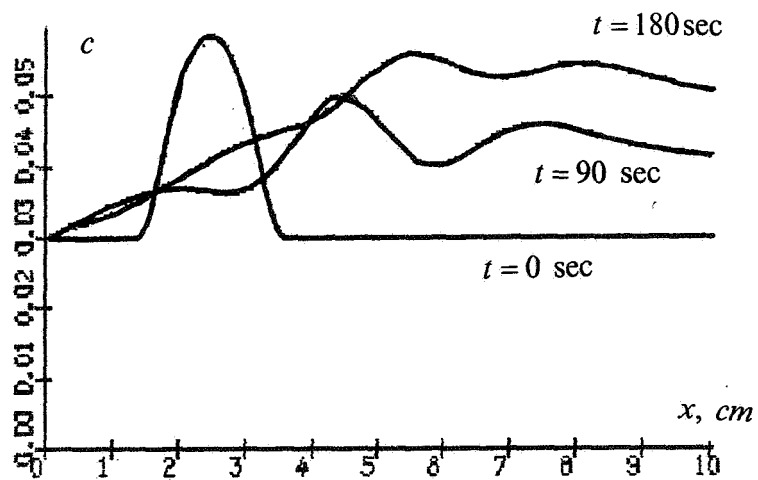


Fig.2

Nonlinear evolution of temperature (Fig. 1) and concentration (Fig.2) in the process of the motion of lead droplets ( $\sigma_T R = 0.001 \text{ gram} \cdot \text{cm} / \text{sec} \cdot \text{K}$ ) in a melted aluminium.

# **Solidification**



## INTERFACE MORPHOLOGY DURING CRYSTAL GROWTH: EFFECTS OF ANISOTROPY AND FLUID FLOW

S. R. Coriell, B. T. Murray, A. A. Chernov<sup>1</sup>, and G. B. McFadden  
National Institute of Standards and Technology  
Gaithersburg, MD 20899 USA

### ABSTRACT

The effect of a parallel shear flow and anisotropic interface kinetics on the onset of instability during growth from a supersaturated solution is analyzed. The model used for anisotropy is based on the microscopic picture of step motion. A shear flow (linear Couette flow or asymptotic suction profile) parallel to the crystal-solution interface in the same direction as the step motion decreases interface stability. A shear flow counter to the step motion enhances stability and for sufficiently large shear rates the interface is absolutely morphologically stable. For large wave numbers, the perturbed flow field can be neglected and a simple analytic approximation for the stability-instability demarcation is found.

### INTRODUCTION

During crystal growth or solidification of a binary alloy from a liquid phase, temperature and solute gradients are inherently present. In a gravitational field, these gradients can give rise to fluid flow in the melt. The interaction of fluid flow with the crystal-melt interface [1, 2] plays an important role in determining the properties of the solidified material. Convection in the melt and interface instability may both produce solute inhomogeneities. In the absence of fluid flow, the conditions for the onset of morphological instability are well established. However, the coupling between morphological instability and fluid flow can be complicated; interfacial instabilities depend on temperature and solute gradients which may be strongly influenced by the flow field. The flow field, in turn, may be influenced by the morphology of the interface.

Previously, we have carried out a number of theoretical investigations relevant to the experimental studies in space by J. J. Favier and colleagues (Centre d'Etudes Nucleaires de Grenoble) and R. Abbaschian and colleagues (University of Florida) utilizing the MEPHISTO apparatus [3]. In the MEPHISTO space experiments, dilute alloys of tin containing bismuth (USMP-1 & 3) and bismuth containing 0.1 at.% tin (USMP-2) were directionally solidified for growth conditions in the vicinity of the planar-cellular transition. While tin is fairly isotropic, bismuth is extremely anisotropic forming facets during growth. We first discuss recent results on the morphological stability of highly anisotropic materials.

During alloy solidification, a smooth crystal-fluid interface may become unstable, leading to cellular or dendritic growth. Linear morphological stability theory [4, 5] describes the conditions under which the interface becomes unstable. The original treatment of morphological stability by Mullins and Sekerka assumed local equilibrium at the crystal-melt interface and isotropy of the crystal-melt surface tension; this is an excellent approximation for many metals at low growth velocities. However, many materials, including semiconductors and metals such as gallium and bismuth, grow with facets indicating strong anisotropy and deviations from local equilibrium. The stability of faceted growth has also been reviewed [6]. The effect of anisotropy of surface tension and interface kinetics on morphological stability has been treated in a quasi-static approximation to the diffusion field; kinetic anisotropy causes traveling waves along the crystal-melt

---

<sup>1</sup>Universities Space Research Association and NASA Marshall Space Flight Center, 4950 Corporate Drive, Suite 100, Huntsville, AL 35806 USA, On leave from the Institute of Crystallography, Russian Academy of Sciences, Leninsky Prospekt, 59, 117333 Moscow, Russia

interface [7]. Yuferev [8] showed that for growth in which the interface is near a singular orientation (an atomically smooth orientation), there is an enhancement of morphological stability; more detailed calculations for a binary alloy [9] and for growth into a supersaturated solution [10] and supercooled melt [11] have been carried out. Recently, we have considered the effect of shear flows and anisotropic interface kinetics on the morphological stability of a binary alloy growing from the melt [12].

The motion of elementary steps is the essence of layerwise growth and decrystallization (dissolution, melting, or evaporation). Step motion has the well-known tendency for not always proceeding as regular step trains, i.e., keeping the interstep distance constant and producing homogeneous crystals. Instead, under a wide range of conditions, the elementary steps cluster into step bunches. In other words, the interface is morphologically unstable with respect to step bunching. The step bunches trap impurities in amounts which depend on the local step densities, and therefore the impurity distribution differs from that formed by regular step trains. As a result, bands enriched or depleted in point-defects appear in the grown crystal [13]. Step bunches themselves may, in turn, lose their stability and trap inclusions of solvent. Growth conditions under which these instabilities are less likely typically require experimental determination; they are not well understood quantitatively and in some cases not even qualitatively. It is well known, however, that fluid flow in the solution, crystal growth rate, and impurities are of great importance for the onset of step bunching. This is the motivation for analyzing the effect of flow on step bunching, i.e., on the morphological stability of vicinal faces in solution and melt growth. If the role of flow effects is understood, the influence of other factors on crystal quality may be better discerned.

Experiments and theory indicate that a solution flowing above a vicinal face of a crystal can either enhance or prevent the development of step bunches [6, 14, 15, 16]. In the absence of flow, anisotropic kinetics arising from the motion of steps on the crystal surface provides an important self-stabilization mechanism [8, 9, 10, 11].

In this manuscript, we treat the effect of shear flows on the morphological stability of a crystal growing from solution by a step mechanism at a given constant velocity  $\bar{V}$ . In the absence of flow the self-stabilization due to anisotropic kinetics has been treated [10] and we employ the same model here. The effect of flow on morphological stability of stepped surfaces has been treated previously ignoring the perturbed flow field [15]. We will explore this approximation and show that it is valid for a range of growth conditions.

## THEORY

In order to phenomenologically treat anisotropic kinetics, we assume that growth is by the motion of elementary steps, which leads to a macroscopic anisotropic kinetic law. The interface kinetic coefficient  $\beta(p)$ , defined as the ratio of the solute flux and the deviation ( $C_I - \bar{C}_e$ ) of the interface concentration  $C_I$  from the equilibrium solution concentration  $\bar{C}_e$ , is given by  $\beta(p) = \beta_{st}|p|$ ,  $p = \tan \theta$ , where  $\theta$  measures the deviation of the slope of the interface from a singular orientation [6]. If the planar interface is a singular interface ( $p = 0$ ), its kinetic coefficient vanishes and in this model there is no growth. In reality, a singular interface becomes macroscopically or locally vicinal due to a screw dislocation or a two-dimensional nucleation mechanism, which generates steps. A locally finite value of  $p$  at any macroscopic area of the interface results. The unidirectional step motion introduces anisotropy and we will only consider perturbations along the direction of the step motion. Further, we assume that the perturbations are sufficiently small that the quantity  $p$  does not change sign.

Our sign convention is such that positive  $p$  corresponds to step motion to the left (negative  $x$  direction, see Figure 1a). If we consider a small sinusoidal perturbation of a planar interface characterized by a constant positive value of  $p = \bar{p}$ , then regions of the perturbed interface with positive slopes will have larger values of  $p$  and therefore larger kinetic coefficients and larger step densities. Thus for the same supersaturation, regions of the interface with positive slopes will grow faster than regions with negative slope; this leads to a translation of the sinusoidal perturbed interface in the direction of the step motion.



As previously discussed [9, 10, 15, 16], both this lateral translation of the sinusoidal interface perturbation and the lateral flow of liquid can move a depression in the interface to a solute-enriched region of solution where it can grow faster and thus provide a stabilizing mechanism.

A shear flow in the opposite direction from the step motion tends to move fluid into the steps and is somewhat equivalent to a faster translation of the perturbations in a stagnant fluid; therefore, one expects such a flow to further stabilize the interface. Conversely, a shear flow in the direction of the step motion will destabilize the interface. Thus, the key physics behind the stabilization or destabilization is the phase shift between the perturbation of the interface shape (characterized by alternation of higher and lower step density running tangentially along the interface) and the concentration waves induced by these step bunches (also traveling parallel to the interface). This phase shift is influenced by both the motion of the step bunches and the solution flow.

We have carried out a linear stability analysis for constant velocity growth in the  $z$ -direction into a supersaturated solution. We solve the incompressible Navier-Stokes equations for the fluid velocity  $u$  and the convection-diffusion equation for solute concentration  $C(x, z, t)$  in the absence of gravity. We consider a two-dimensional problem and assume all quantities are independent of the coordinate  $y$ . The basic equations and boundary conditions are given in references [10] and [12].

For the linear stability analysis of the base state, the variables are written as the superposition of the base state component and a perturbation. The perturbed quantities are Fourier analyzed in the lateral direction and exponential time-dependence is assumed, so that the perturbed variables are proportional to  $\exp(\sigma t + ik_x x)$  where  $\sigma = \sigma_r + i\sigma_i$  is the complex temporal growth rate, and  $k_x$  is the wavenumber in the  $x$ -direction. The numerical solution procedures used to solve the resultant differential eigenvalue problem have been described previously [12].

## RESULTS and DISCUSSION

We have carried out a series of calculations using the following parameters: diffusion coefficient  $D = 1.0 \times 10^{-5} \text{ cm}^2/\text{s}$ , capillary parameter  $\Gamma = 5.0 \times 10^{-8} \text{ cm}$ ,  $C_s/\bar{C}_e = 5$ ,  $\beta_{st} = 0.1 \text{ cm/s}$ ,  $\nu = 0.01 \text{ cm}^2/\text{s}$ , and  $\rho = 1$  [15], where  $C_s$  is the concentration in the crystal,  $\nu$  is the kinematic viscosity, and  $\rho = \rho_S/\rho_L$  is the ratio of the crystal and solution densities  $\rho_S$  and  $\rho_L$ . Numerical calculations were carried out for unperturbed flows corresponding to both linear Couette flow (in which the flow velocity increases linearly with distance from the interface and the shear rate is independent of distance) and the asymptotic suction profile (in which the flow velocity attains a constant value far from the interface and the shear rate decays exponentially). However, for a given shear rate  $S$  at the interface, the results for both profiles are essentially identical.

In Figure 2 for  $\bar{p} = 0.01$ , we plot (solid curves) the wavenumber  $k_x$  as a function of growth velocity  $\bar{V}$  for  $\sigma_r = 0$  for various shear rates. The result for zero shear is the same as previously given [10], with the system being stable for large velocities and large wavenumbers. Stability at large wavenumbers is a result of capillarity while anisotropic kinetics provides stability at intermediate wavenumbers. Negative shear (flow in the direction of the step motion) destabilizes the interface, particularly at small wavenumbers. The curve for  $S = -0.1 \text{ s}^{-1}$  has a minimum at small wavenumbers and large velocities. Below this minimum wavenumber the system is unstable for all velocities. Above this minimum wavenumber there is a region of stability at intermediate velocities. Positive shear (flow opposite to the direction of the step motion) stabilizes the interface. At a shear rate of  $0.1 \text{ s}^{-1}$ , the neutral curve forms a closed loop with instability occurring inside the loop. Above a shear rate of  $0.629 \text{ s}^{-1}$ , we have not found any modes with  $\sigma_r \geq 0$  indicating that the system is stable for shear rates greater than this value. Following Chernov [15], we have also solved the stability problem by neglecting the perturbed flow. The results for the same conditions are given by the dashed curves in Figure 2. The dashed curves are only visible for  $S = -0.1 \text{ s}^{-1}$  at low wavenumbers indicating that the perturbed flow field is unimportant at high wavenumbers.

Since it is a good approximation to neglect the perturbed flow field, the perturbed solute field can be obtained analytically in terms of Airy functions. For large wavenumbers, the Airy function can be simplified by using its asymptotic representation, and we can obtain a simplified stability criterion, namely

$$\left\{ \frac{\sigma_i}{k_x} \right\} \left\{ \frac{\sigma_i}{k_x} + \frac{S}{2k_x} \right\} > 2Dk_x \bar{V} \left\{ 1 - \frac{\bar{C}_e \Gamma D k_x^2}{(C_s - \bar{C}_e) \rho \bar{V}} \right\}, \quad (1)$$

with

$$\sigma_i = \frac{\bar{V} \beta_{st} \zeta^2}{D(1 + \zeta)}, \quad (2)$$

where  $\zeta = Dk_x/(\beta_{st}\bar{p})$ .

In the absence of capillarity, the above stability criterion can be written simply as

$$v_x + S/(2k_x) > 2\bar{p}(Dk_x + \beta_{st}\bar{p}), \quad (3)$$

where  $v_x = \sigma_i/k_x$  is the magnitude of the phase velocity.

To better understand the physics behind the stabilization mechanism, we consider the concentration field above the perturbed interface within the general framework employed earlier [10, 15]. The perturbed stepped interface is shown in Figure 1a, where the numbers 1-3 are used to indicate specific regions of the perturbed stepped interface. The solution is evidently depleted with respect to the average solute concentration above regions of the type 1 where the step density (and thus ability of the interface to incorporate solute) is higher than the average step density (for an unperturbed interface). Conversely, the solution is enriched above the low step density areas (type 2). The perturbed solute distribution as a function of  $x$  and  $z$  is shown schematically in Figure 1b; the lowest wavy line is in the immediate vicinity of the interface.

The amplitude of the concentration waves at a distance  $z$  from the interface decreases as  $z$  increases. The typical decay length is  $\approx k_x^{-1}$ . The decay of the amplitude is depicted by the upper wavy lines in Figure 1b. These concentration waves would be stationary if neither the solution nor the interface pattern moved, as would be the case for a non-stepped, isotropic rough interface in a stagnant solution. Actually, both the step bunches and the solution move with respect to the crystal lattice. Therefore, each solution layer parallel to the interface moves tangentially with respect to the step pattern. Correspondingly, the phase shift of the concentration wave in each layer increases with  $z$ . In Figure 1b, each neighboring concentration wave is shown shifted to the right, following the solution flow relative to the step bunches.

The flow-induced morphological stabilization or destabilization results from the influence of the solution flow on the phase shift between the concentration waves and the perturbed interface waves. The shift of the surface concentration maxima, say, points A and B in Figure 1b, to the right causes stabilization because enriched solution (region 2, Figure 1a) first comes to the interface valleys (region 3) while the depleted solution (originating from region 1) passes over the interface hills, thus diminishing the perturbation amplitude.

In summary, a theoretical and numerical analysis that includes perturbations of the hydrodynamic flow field in addition to the solute field above the perturbed vicinal interface has been carried out. It is found that the hydrodynamic perturbations are important only at low wave numbers. Ignoring the flow perturbation, we have found an analytic condition for stability. This condition predicts absolute (not relative, as in reference [15]) stability with respect to step bunching if the shear rate  $S$  is sufficiently large. The critical shear rate depends on both capillarity and kinetics.

## References

- [1] M. E. Glicksman, S. R. Coriell, and G. B. McFadden, Interaction of Flows with the Crystal-Melt Interface, *Ann. Rev. Fluid Mech.*, Vol. 18, 1986, pp. 307-335.

- [2] S. H. Davis, Effects of Flow on Morphological Stability, Handbook of Crystal Growth 1 Fundamentals, Part B: Transport and Stability, Ed. D. T. J. Hurle (North-Holland, Amsterdam, 1993) pp. 859-897.
- [3] J. J. Favier, J. P. Garandet, A. Rouzaud, and D. Camel, Mass Transport Phenomena during Solidification in Microgravity: Preliminary Results of the First Mephisto Flight Experiment, J. Crystal Growth Vol., 140, 1994, pp. 237-243.
- [4] W. W. Mullins and R. F. Sekerka, Stability of a Planar Interface during Solidification of a Dilute Binary Alloy, J. Appl. Phys., Vol. 35, 1964, pp. 444-451.
- [5] S. R. Coriell and G. B. McFadden, Morphological Stability, Handbook of Crystal Growth 1 Fundamentals, Part B: Transport and Stability, Ed. D. T. J. Hurle (North-Holland, Amsterdam, 1993) pp. 785-857.
- [6] A. A. Chernov and T. Nishinaga, Growth Shapes and Their Stability at Anisotropic Interface Kinetics: Theoretical Aspects for Solution Growth Morphology of Crystals, Ed. I. Sunagawa (Terra, Tokyo, 1987) pp. 207-267.
- [7] S. R. Coriell and R. F. Sekerka, The Effect of the Anisotropy of Surface Tension and Interface Kinetics on Morphological Stability, J. Crystal Growth, Vol. 34, 1976, pp. 157-163.
- [8] V. S. Yuferev, Stability of a Crystal-Melt Interface with a Lateral Growth Mechanism, Phys. Chem. Mech. of Surfaces, Vol. 2, 1983, pp. 1916-1925.
- [9] S. R. Coriell, B. T. Murray, and A. A. Chernov, Kinetic Self-Stabilization of a Stepped Interface: Binary Alloy Solidification, J. Crystal Growth, Vol. 141, 1994, pp. 219-233.
- [10] A. A. Chernov, S. R. Coriell, and B. T. Murray, Morphological Stability of a Vicinal Face Induced by Step Flow, J. Crystal Growth, Vol. 132, 1993, pp. 405-413.
- [11] A. A. Chernov, S. R. Coriell, and B. T. Murray, Kinetic Self-Stabilization of a Stepped Interface: Growth into a Supercooled Melt, J. Crystal Growth, Vol. 149, 1995, pp. 120-130.
- [12] S. R. Coriell, B. T. Murray, A. A. Chernov, and G. B. McFadden, Effects of Shear Flow and Anisotropic Kinetics on the Morphological Stability of a Binary Alloy, Metallurgical and Materials Trans., Vol. 27A, 1996, pp. 687-694.
- [13] E. Bauser, Atomic Mechanisms in Semiconductor Liquid Phase Epitaxy, Handbook of Crystal Growth 3 Thin Films and Epitaxy, Part B: Growth Mechanisms and Dynamics, Ed. D. T. J. Hurle (North-Holland, Amsterdam, 1994) pp. 879-939.
- [14] A. A. Chernov, Yu. G. Kuznetsov, I. L. Smol'sky, and V. N. Rozhansky, Hydrodynamic Effect in Growth of ADP Crystals from Aqueous Solutions in the Kinetic Regime, Soviet Phys.-Cryst., Vol. 31, 1986, pp. 705-709.
- [15] A. A. Chernov, How Does the Flow within the Boundary Layer Influence Morphological Stability of a Vicinal Face, J. Crystal Growth, Vol. 118, 1992, pp. 333-347.
- [16] A. A. Chernov, Formation of Crystals in Solutions, Contemp. Phys., Vol. 30, 1989, pp. 251-276.

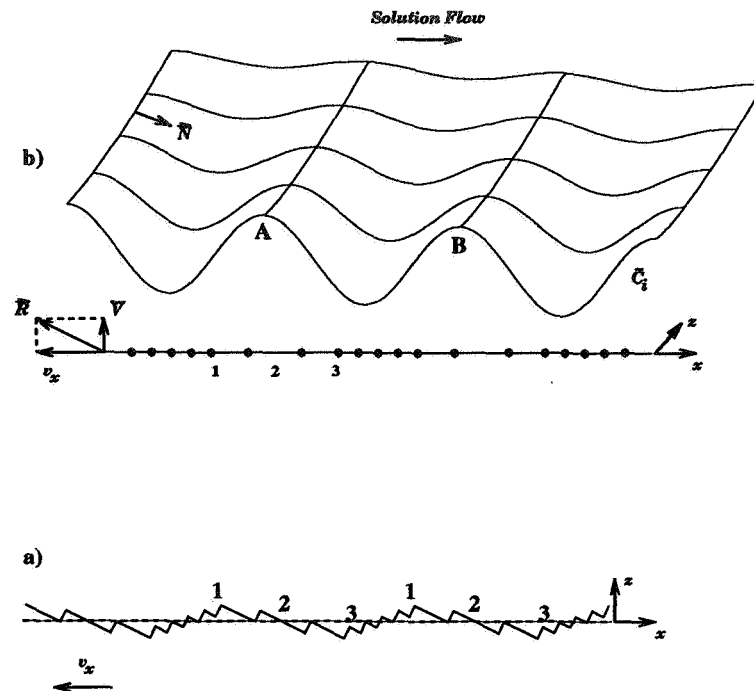


Figure 1: a) Profile of a periodically perturbed vicinal face with steps moving to the left at phase velocity  $v_x$ . The numbers indicate regions with different step densities. b) Surface plot of the perturbed concentration field. The solid circles show the relative location of the step train with respect to the concentration wave.

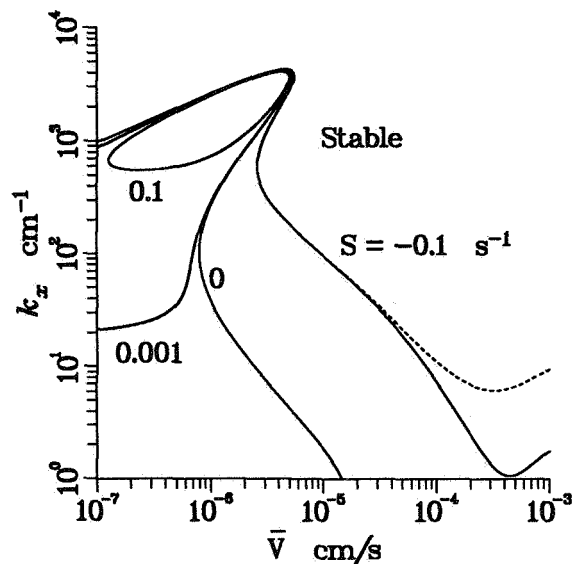


Figure 2: The spatial wavenumbers at which the system is neutrally stable as a function of growth velocity calculated numerically for  $\bar{p} = 0.01$  and shear rates of  $-0.1$ ,  $0.0$ ,  $0.001$ , and  $0.1$  for the linear Couette profile. The solid curves are numerical solutions of the complete linear stability equations while the dashed curves neglect the perturbed flow field.

# SHEAR STABILIZATION OF A SOLIDIFYING FRONT

Stephen H. Davis and Timothy P. Schulze<sup>1</sup>

Department of Engineering Sciences and Applied Mathematics  
Northwestern University, Evanston, IL 60208 USA

## ABSTRACT

The manufacturing of multi-component single crystals with uniform material properties is frequently hampered by the presence of morphological instabilities during the solidification. We discuss the influence of shear flows on the linear and nonlinear stability of the solid/liquid interface during the directional solidification of binary alloys. The flows are generated by nonplanar harmonic translations of the crystal parallel to the mean interface position. Oscillations with physically realizable amplitudes and frequencies are found to be useful for stabilization purposes.

## INTRODUCTION

*Directional solidification* is a processing configuration which lends itself to experimental observation and mathematical analysis. Here a liquid may be confined to a Hele-Shaw cell or to a fully three-dimensional region (inside a cylindrical tube, for example). The confined material, along with its container, is then pulled through a temperature gradient, so that the fluid solidifies as it moves from a heated region into a cooler one. If the material is pulled at constant speed, the solid-liquid interface will establish itself at a fixed position relative to the heat source and sink.

The instability of the planar front was first explained by Tiller et al [1] and a full linear-stability analysis, including the effects of surface energy, was first done by Mullins and Sekerka [2]. They found that the interface is stable for sufficiently low solute concentrations. For higher concentrations, the interface is unstable for a finite range of pulling speeds. Near the critical values of the pulling speed, the instability results in nearly sinusoidal cells.

When the instability is present, variations in the concentration along the interface are frozen into the solid, resulting in stripes of elevated solute concentration. A number of authors have attempted to use a forced fluid flow to extend the range of pulling speeds for which the interface remains flat (see Davis [3] for a summary of these). Schulze and Davis [4] investigated the effects of translating the crystal in elliptical orbits parallel to the interface, following the example of Kelly and Hu [5], who has found that the same flow has a stabilizing influence on Bénard convection. This nonplanar forcing will generate a three-dimensional version of a Stokes boundary layer in the fluid above the interface. Because the boundary layer will be compressed due to the flow normal to the interface generated by the pulling speed, we refer to this flow configuration as a three-dimensional Compressed Stokes Layer (3D CSL), or CSL for short.

Schulze and Davis [4] found that this flow can, on a linear theory basis, stabilize the interface, provided the pulling speed is sufficiently high. The success of this method requires that the frequency of the flow lie within a calculated range. The outermost curve in Figure 1 is a typical neutral curve for the no-flow system [2], showing the critical pulling speed as a function of the alloy concentration for a fixed temperature gradient. Also shown in this figure are neutral curves for the system when it is forced through the boundary to generate a CSL. As the amplitude of the forcing is increased, the upper branch of the neutral curve is lowered considerably and the nose of the curve moves to the right. For a pulling speed near the nose of the neutral curve, typical values for the frequency and amplitude of the lateral velocity oscillations would be  $10^4$  hertz and  $10^{-3}$  centimeters respectively. Such scales would lend themselves well to an acoustic forcing. The precise value of these parameters can vary over many orders of magnitude,

---

<sup>1</sup>Present address: Department of Applied Mathematics and Theoretical Physics, University of Cambridge, Cambridge, England CB3 9EW

but, as a rule, vary with the solute-diffusion length and time scales and are physically realizable for a sizable range of operating conditions.

In this paper the effect of CSL on the bifurcation structure for morphological instability will be investigated. Our principal aim is to discover under what conditions the flow may provide effective control of interfacial instability. Of particular concern is the possibility that subcritical instabilities could reduce, or even eliminate, the stabilization indicated by the linear theory. When the interface is unstable, there are a variety of potential patterns for the instability to take, including square, hexagonal and two-dimensional (roll) cells, and we shall discuss the use of this flow as a pattern-selection mechanism.

Our focus will be on the upper branch of the curve shown in Figure 1, for it is in this region that the CSL has a strong influence on the interfacial morphology. Along this portion of the neutral curve the critical wavelength of interfacial disturbances is long compared to the solutal boundary-layer thickness, and an analysis which exploits this fact was accomplished by Brattkus and Davis [6]. Our aim is to generalize this work to one in which the CSL is present.

## THE EVOLUTION EQUATION

The system is stable for all nondimensional surface tensions  $\Gamma > \Gamma_s = 1/k$ . We introduce the small parameter  $\epsilon$  as a measure of closeness to this point, which is known as the absolute stability limit:

$$\epsilon^4 = 1/k - \Gamma . \quad (0.1)$$

In this limit, the system becomes linearly unstable to long-wave disturbances when the morphological number becomes very large. In terms of physical variables, this limit can be thought of as large pulling speed.

The linear stability theory suggests the following slow space and time scales:

$$X = \epsilon^2 x , Y = \epsilon^2 y , T = \epsilon^4 t . \quad (0.2)$$

Near the absolute stability limit, the morphological number  $M$  scales like

$$\bar{M} \sim \epsilon^8 M , \quad (0.3)$$

with  $M \sim O(1)$ . With these scales one obtains the sought after generalization to the equation of Brattkus and Davis [6] valid for the case of the imposed CSL flow.

This equation has the form [7]

$$L[h_0] + R^2 f_0 \nabla^2 |r \cdot \nabla|^2 F^{-1} \left[ \frac{\hat{h}_0}{|k|} \right] + k \bar{M}^{-1} h_0 = N[h_0] , \quad (0.4)$$

where the operators  $L$  and  $N$  are defined by the Brattkus-Davis [6] equation  $L[h_0] = N[h_0]$ ,  $F^{-1}$  is the inverse Fourier transform,  $R$  is a scaled Reynolds number, and  $f_0$  is constant. Note that the correction is linear.

## RESULTS AND SUMMARY

We have derived [7] a strongly nonlinear evolution equation for the shape of a directionally solidifying interface in the presence of a three-dimensional compressed Stokes layer. We used a one-sided model, where diffusion of solute in the solid is neglected, and we invoked the frozen temperature approximation. The equation is valid when: the surface energy parameter  $\Gamma$  is near the absolute stability boundary  $\Gamma_s = 1/k$ ; and the imposed flow, as measured by  $R$ , is weak. In this limit, the critical disturbance

wavelength is long compared to the diffusion length scale  $D/V$  and the critical morphological number is large.

Linear theory shows that increasing the flow amplitude  $R$  could stabilize the interface, provided the frequency of the flow oscillations is within a calculated range. The stabilization is particularly effective in the long-wave regime. The two-dimensional bifurcation analysis [7] of the derived long-wave evolution equation shows that increasing the amplitude of the CSL will eventually change bifurcations from super- to subcritical when the flow is in the stabilizing parameter regime. Thus, at least some of the stabilization gained according to the linear theory is lost to subcritical instabilities if the flow is made too large; yet it is still possible to stabilize within a range of  $R$  values for which the bifurcation is supercritical and, presumably, one could increase  $R$  at least somewhat beyond this range before the subcritical instability would cancel the stabilization indicated by the linear theory. It appears that effective stabilization of the two-dimensional system using the CSL will require careful control of both the amplitude and frequency of the flow.

For the three-dimensional system we have examined [7] bifurcations to steady roll, square and hexagonal solutions. When the motion of the crystal is a noncircular elliptical pattern, rolls are the only bifurcating solution in the weakly nonlinear limit. This may be the best scenario for stabilizing the three-dimensional system, as there are fewer types of bifurcating solutions to suppress, at least near onset. However, for systems which are strongly supercritical or for systems forced by a nearly circular motion of the crystal, secondary bifurcations to rectangles and asymmetric hexagons are likely to occur.

When the motion of the crystal is in a circular pattern, the system is isotropic in the plane of the interface, and superposition states involving more than one set of obliquely positioned rolls are possible. This flow may be useful for selecting a preferred pattern among these states, allowing a crystal grower more control over crystal microstructure.

We have examined [7] the competition between roll and square solutions, and found that increasing the flow amplitude tends to reduce, and eventually eliminate, the range of segregation coefficients for which stable square solutions are possible. Increasing the flow amplitude favors subcritical instabilities for both squares and rolls. Unlike the no-flow case, unstable, supercritically bifurcating square solutions are possible for a small range of  $R$  values.

We have examined [7] the competition between roll and hexagonal solutions. For values of  $k$  away from unity, unstable hexagons bifurcate transcritically and are the only bifurcating solution in the weakly nonlinear limit. When  $k$  is sufficiently close to unity, the cubic and quadratic nonlinearities in the evolution equation are balanced, and a complicated bifurcation structure emerges. As with the square and roll solutions, bifurcations to rolls are supercritical when  $R$  is sufficiently small, but switch to subcritical as  $R$  is increased. Hexagons bifurcate transcritically, but with very shallow subcritical turning points for small  $R$ . When  $R$  is increased, the bifurcation for the hexagons changes direction, and they become essentially subcritical. So, in general, increasing the flow amplitude favors subcritical instability for all types of solutions examined.

In general, we have found that the flow has little impact on the system when the frequency and Schmidt number are in the destabilizing range. Clearly, this is an effect of the weak-flow limit, as microstructure will be significantly altered by a stronger version of this flow any time the interface remains unstable in its presence. The steady rolls, squares and hexagons indicated by the analysis of this chapter are leading-order approximations for the interface shape in a specific limit. Higher-order corrections to the evolution equation would indicate time-periodic variations of these patterns as one moves vertically through the crystal, and a large amplitude flow would likely render the patterns unrecognizable.

When the flow parameters are in the stabilizing range, we have found that the bifurcation structure for all types of solutions (rolls, squares, hexagons and mixed modes) changes only in scale until a critical value of  $R$  is surpassed. Beyond these transition points, which are distinct for each solution type, bifurcations

switch from super- to subcritical. In general, lowering the frequency  $\Omega$  lowers these transitions, and increasing the frequency raises them.

### ACKNOWLEDGEMENTS

This work was supported by grants from the National Aeronautics and Space Administration through the Graduate Student Researchers Program (TPS) and the Program on Microgravity Science and Applications (SHD).

### REFERENCES

- [1] Tiller, W. A., Jackson, K. A., Rutter, J. W. and Chalmers, B.: The Redistribution of Solute Atoms during the Solidification of Metals, *Acta Metall.* Vol. 1, 1953, 428.
- [2] Mullins, W. W. and Sekerka, R. F.: Stability of a Planar Interface during Solidification of a Dilute Binary Alloy, *J. Appl. Phys.*, Vol. 35, 1964, 444.
- [3] Davis, S. H.: Effects of Flow on Morphological Stability, in "Handbook of Crystal Growth" (Ed. D.T.J. Hurle) North-Holland Press. Amsterdam (1993), 859.
- [4] Schulze, T. P. and Davis, S. H.: Shear Stabilization of Morphological Instability during Directional Solidification, *J. Cryst. Growth*, Vol. 149, 1995, 253.
- [5] Kelly, R. E. and Hu, H.-C.: The Onset of Rayleigh-Bénard Convection in Non-planar Oscillatory Flows, *J. Fluid Mech.*, Vol. 249, 1993, 373.
- [6] Brattkus, K. and Davis, S. H.: Cellular Growth near Absolute Stability, *Phys. Rev. B* 38, 1988, 11452.
- [7] Schulze, T. P. and Davis, S. H.: Shear Stabilization of a Solidifying Front: Weakly Nonlinear Analysis in the Long-Wave Limit, *Phys. Fluids*, 1996, in press.



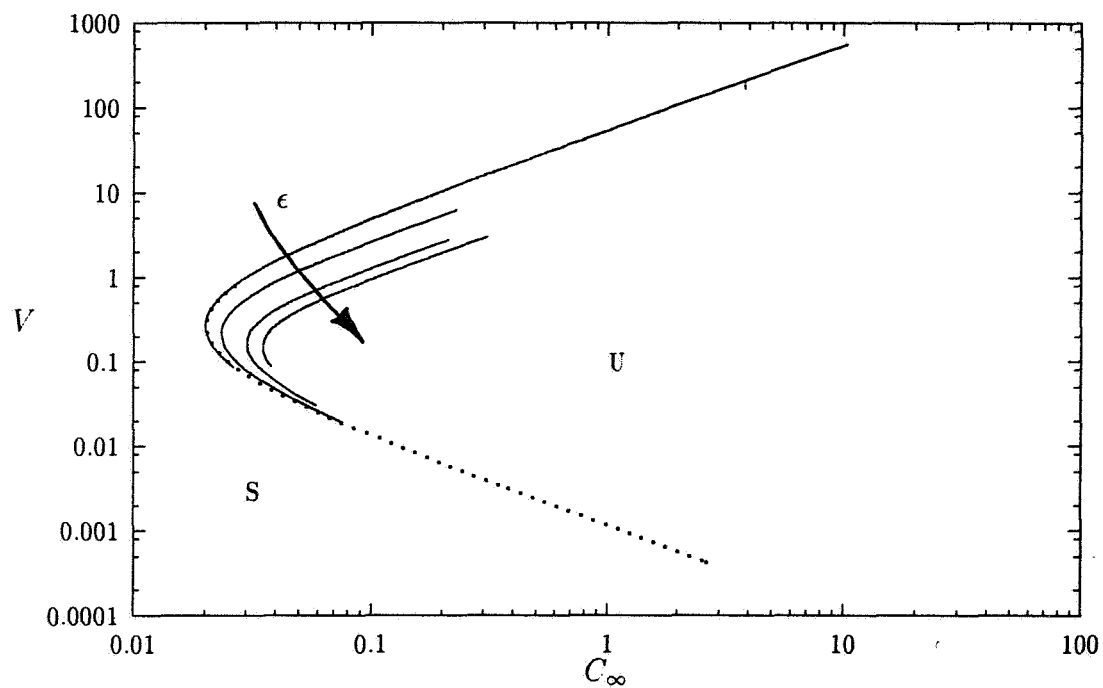


Figure 1: Plot of a typical neutral curve in dimensional form— $V$  versus  $C_\infty$  for with a fixed temperature gradient. All of the curves extend infinitely along tangents to the portions shown. The interface is linearly stable (S) when the far-field concentration is to the left of the neutral curve. The no-flow (outermost) curve is divided into a portion corresponding to subcritical instability (dashed portion) and a portion corresponding to supercritical instability (solid portion).



# FLUID DYNAMICS AND SOLIDIFICATION OF MOLTEN SOLDER DROPLETS IMPACTING ON A SUBSTRATE IN MICROGRAVITY

Dimos Poulikakos, Constantine M. Megaridis  
Department of Mechanical Engineering (M/C 251)  
University of Illinois at Chicago  
Chicago, IL 60607-7022

M. Vedha-Nayagam  
Analex Corporation  
3001 Aerospace Parkway  
Brook Park, Ohio 44142

## ABSTRACT

This program will investigate the fluid dynamics and simultaneous solidification of molten solder droplets impacting on a flat substrate. The problem of interest is directly relevant to the printing of microscopic solder droplets in surface mounting of microelectronic devices. The study consists of a theoretical and an experimental component. The theoretical work uses axisymmetric Navier-Stokes models based on finite element techniques. The experimental work is performed in microgravity in order to allow for the use of larger solder droplets that make feasible the performance of accurate measurements while maintaining similitude of the relevant fluid dynamics groups ( $Re$ ,  $We$ ) and keeping the effect of gravity negligible.

## INTRODUCTION

A schematic of the two distinct stages (flight and impact) of the problem examined is shown in Fig. 1. The primary application of interest (solder microdroplet dispensing) employs solder droplets approximately 50 to 100  $\mu m$  in diameter, which collide, spread, recoil and eventually solidify on the substrate. Due to the small size of the droplets and the relatively high surface tension coefficient of solder, gravity effects are negligible. This solder application technology has shown great promise in microelectronic packaging and assembly, therefore, the development of a good understanding of the pertinent fluid dynamics and solidification phenomena is essential for its successful commercial implementation. However, progress in this area has been hindered by the small length scales of the problem (50 to 100  $\mu m$ ), which have made experimental measurements of the relevant transport phenomena difficult. Alternative approaches, which employed much larger (mm-size) droplets, yielded results that were affected by the masking effects of gravity. Hence, even though mm-size droplets yield significantly improved resolution, the applicability of the obtained results for much smaller droplets remains suspect. Conducting experiments in a microgravity environment eliminates the unwanted influence of gravity and makes the experimental investigation of large droplet dispersion directly relevant.

The Reynolds, Weber and Froude numbers characteristic of the process shown in Fig. 1 are defined by

$$Re = V_0 r_0 / \nu, We = \rho V_0^2 r_0 / \gamma, Fr = V_0^2 / r_0 g \quad (1)$$

where  $V_0, r_0$  denote droplet impact velocity and radius, while  $\rho, \nu, \gamma$  correspond to the density, kinematic viscosity and surface tension coefficient of the liquid. To exemplify the disparity in the importance of gravity in the dispersion of large and small droplets, the values of  $Re, We$  and  $Fr$  were calculated for a set

of parameters corresponding to the real dispensing process in normal gravity (50 micron diameter solder droplet impacting on a flat surface with a velocity 1m/s). These values were  $Re=78.5$ ,  $We=0.6$ ,  $Fr=4077$ , and illustrate the importance of inertia and surface tension, as well as the insignificance of gravity effects. If a larger (1mm) drop is used in normal gravity experiments, a slower impact velocity  $V_0$  is required for similitude based on  $Re$ . In turn, similitude in terms of the Weber number requires a smaller surface tension coefficient. To maintain similitude in this specific example, the surface tension coefficient as well as the impact velocity of the larger droplets need be reduced by twenty-fold. The resulting values of the above dimensionless groups are then  $Re=78.5$ ,  $We=0.6$ ,  $Fr=0.5$ . Clearly, the drastic decrease in the value of the Froude number proves that gravity effects become significant for mm-size droplets, and that the presence of a microgravity environment is necessary in large solder-droplet impact experiments.

## OBJECTIVE

The study will be aimed at identifying the degree of influence of the dominant process parameters on specific aspects of solder droplet dispensing. These parameters are: droplet size and velocity; droplet, substrate and ambient gas temperatures; and contact angle between the solder and substrate before and after solidification. The sensitivity of the final bump shape and size to variations in the above parameters is critical because solder bump volume, position, and height variation are key metrics for solder jet technology. The data produced in this program will be analyzed to define the domains of solder microdroplet dispensing operational parameters that result in optimal and consistent production of solder bumps as needed for specific industrial applications. At the same time, through a series of numerical simulations, the effect of the dimensionless groups defined in Eq. (1) (and the physics they represent) will be thoroughly documented.

## METHODOLOGY

The research consists of both a theoretical and an experimental component. The theoretical component investigates the fluid dynamics and solidification of a molten solder droplet during its impact on the substrate, in order to attain an understanding of the miniature solder deposition process. The experimental component tests the numerical predictions and provides necessary input data (such as wetting angles) for the theoretical model. Details of both components are given below.

### Theoretical

A schematic description of the impacting droplet problem was presented earlier in Fig. 1. In this figure, a microscopic liquid-metal droplet is shown after impact, while it spreads on the substrate. Cooling of the liquid metal takes place almost entirely by conduction through the substrate, and solidification ensues some time during this process. The theoretical model for the fluid dynamics, which uses a Lagrangian formulation to solve the axisymmetric Navier-Stokes equations accounting for surface tension effects, has been outlined and tested in [1, 2]. The model takes into account the important effect of wetting in the advancement of the contact line, if the dynamic contact angle is known from experiments.

**Wetting:** In order to model the wetting phenomenon, knowledge of the contact angle  $\psi_C$  is necessary. A number of issues relevant to static and dynamic contact lines on solid surfaces have been reviewed by Dussan [3] and de Gennes [4] who showed that a clear distinction exists between the static and the dynamic values of contact angle. The value of the contact angle in this work will be measured experimentally. With the contact angle known, the following boundary condition is satisfied at the contact line

$$\vec{\sigma} \cdot \vec{n} = -(2\gamma H_C + p_0)\vec{n} \quad (2)$$

where  $\tilde{\sigma}$  is the stress tensor,  $\gamma$  the surface tension coefficient,  $p_0$  a reference pressure,  $H_C$  the mean surface curvature, and  $\vec{n}$  the normal vector (Fig. 2). The mean curvature of the free surface is defined by

$$H = \frac{r^2(r'z'' - z'r'') + [(r')^2 + (z')^2]rz'}{2r^2[(r')^2 + (z')^2]^{3/2}} \quad (3)$$

All symbols in Eq. (3) are defined in Fig. 2 with the primes denoting differentiation with respect to the free surface coordinate,  $s$ . At the contact line  $r' = -\cos\psi_C$ ,  $z' = \sin\psi_C$ , thus the mean curvature expression becomes

$$H_C = \frac{1}{2}(-z''\cos\psi_C - r''\sin\psi_C + \frac{\sin\psi_C}{r}) \quad (4)$$

**Solidification:** With the velocity field provided by the fluid dynamics simulation, the axisymmetric energy equation will be solved both in the liquid metal droplet and the substrate, in order to attain the temperature field. Convection will be taken into account in the energy equation for the liquid solder and conduction in the substrate. Typically, the substrate consists of a number of layers each of different material, parallel to the exposed surface (Fig. 1), a fact that will also be taken into account in the substrate conduction model. Continuity of temperature and heat flux will be imposed at the substrate/droplet interface. After the initiation of solidification, the contact resistance at this interface will be taken into account to the extent allowed by the currently existing limited data for relevant contact resistance values [5].

The solidification modeling will focus on eutectic solders (for example Sn63/Pb37 which is commonly used by manufacturers of microelectronic components) to circumvent additional complexities associated with the possible presence of a mushy zone in non-eutectic solders. When solidification is initiated during the impact process, it does so in the presence of undercooling and recalescence. Several issues regarding the modeling of solidification with undercooling and recalescence are discussed in [6]–[9]. Given the parametric domain of the solder dispersion process (low to moderate impact velocities and temperature differences), it is speculated that the effect of undercooling will not be significant. In the absence of undercooling, the freezing front velocity will be determined from an energy balance at the interface, with the interface temperature being the freezing temperature of the eutectic solder.

For the finite element implementation of the solidification process the exact specific heat method proposed by Bushko [10] will be adopted. This method demonstrated superior accuracy over the enhanced specific heat method in energy conservation tests. It is especially suited for materials with specific heat functions that can be represented by Dirac delta functions in the neighborhood of phase transition

$$C(T) = [C_s(T), C_l(T)] + L\delta(T - T_m) \quad (5)$$

where  $C$  is the specific heat,  $L$  the latent heat of fusion,  $T$  the temperature, the subscripts  $s, l$ , and  $m$  denote the solid phase, liquid phase and melting point, respectively, and  $\delta$  is the Dirac delta function [10]. Many metals and alloys, including solders, exhibit this characteristic which makes this method attractive for the planned research. Figure 3 shows a bump shape as obtained during experiments in 1-g utilizing an initially  $50\mu m$ -diameter Sn63/Pb37 solder droplet. This picture depicts the final state of a single droplet after complete solidification. The ripples on the surface of both solidified bumps may be explained as follows: After impact the droplet spreads and recoils (oscillates) several times prior to achieving its sessile state. As the droplet oscillates, solidification initiates at the bottom of the splat and advances upward. The dynamic interaction between the flow oscillations and the advancement of the solidification front yields the ripples on the surface of the solder bump shown in Fig. 3.

## Experimental

Since this is a new program, the experiments have not commenced yet. Molten-metal single droplet impaction tests will be conducted in a low-gravity environment. The 2.2 second drop tower at the NASA

Lewis Research Center will be used to conduct these studies. Our estimates of the characteristic times for the various stages involved (droplet deployment, oscillations decay, impaction and solidification) have shown that 2.2 seconds of microgravity are sufficient for the single droplet experiments. In addition to the direct information obtained from the experimental results, this component of the study will serve to generate wetting-angle information, necessary to the theoretical work, and will provide specific criteria to validate the model predictions.

Measurements of the wetting angles and the splat dimensions will be made from high-speed films. The films will be used also to calculate the droplet preimpact velocity required for the simulations. A photoelectric method (Fig. 4) will be used as a means of providing data on the transient behavior of splat radius and spreading velocity for comparisons with theoretical predictions. This technique has been proven feasible in 1-g laboratory environments and does not involve recording of the droplet image; yet it is accurate, despite the short time scales of the experiment.

## References

- [1] Fukai, J.; Zhao, Z.; Poulikakos, D.; Megaridis, C. M.; and Miyatake, O.: Modeling of the Deformation of a Liquid Droplet Impinging Upon a Flat Surface. *Physics of Fluids A*, Vol. 5, 1993, pp. 2588-2599.
- [2] Fukai, J.; Shiiba, Y.; Yamamoto, T.; Miyatake, O.; Poulikakos, D.; Megaridis, C. M.; and Zhao, Z.: Wetting Effects on the Spreading of a Liquid Droplet Colliding with a Flat Surface: Experiment and Modeling. *Physics of Fluids A*, Vol. 7, 1995, pp. 236-247.
- [3] Dussan V., E. B.: On the Spreading of Liquids on Solid Surfaces: Static and Dynamic Contact Lines. *Ann. Rev. Fluid Mech.*, Vol. 11, 1979, p. 371.
- [4] de Gennes, P. G.: Wetting: Statics and Dynamics. *Rev. Mod. Phys.*, Vol. 57, 1985, p. 827.
- [5] Bennett, T.; and Poulikakos, D.: Heat Transfer Aspects of Splat-Quench Solidification: Modeling and Experiment. *Journal of Materials Science*, Vol. 29, 1994, pp. 2025-2039.
- [6] Clyne, T. W.: Numerical Treatment of Rapid Solidification. *Metallurgical Transactions B*, Vol. 15B, 1984, pp. 369-381.
- [7] Cahn, J. W.; Hillig, W. B.; and Sears, G. W.: *Acta Metal.*, Vol. 12, 1964, pp. 914-922.
- [8] Wilson, H. A.: *Phil. Mag.*, Vol. 50, 1900, pp. 238-246.
- [9] Frenkel, J.: *Physik. Z. Soviet Union*, Vol. 1, 1932, pp. 498-503.
- [10] Bushko, W. C.: M.S. Thesis, Mechanical Engineering Department, University of Massachusetts, 1990.

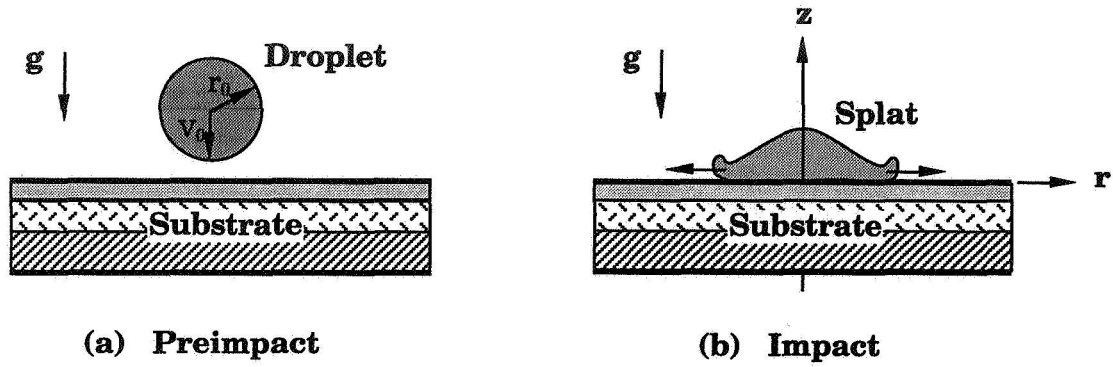


**Figure 1:** Schematic of the problem of interest. a) Flight stage, b) Impact stage. The multiple layers of the substrate represent practical situations of interest.

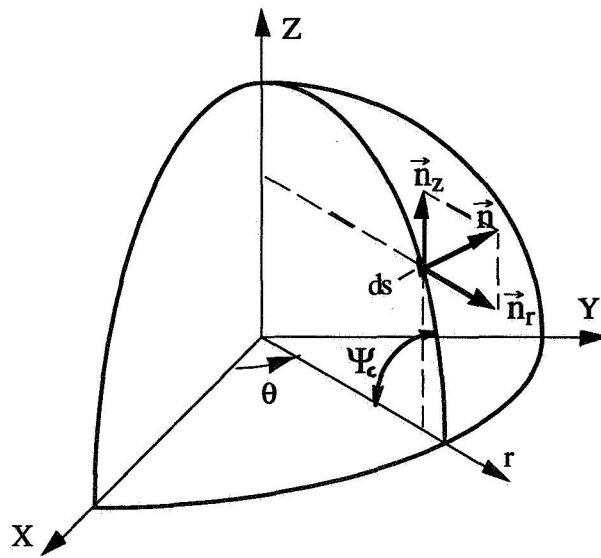


**Figure 2:** Schematic defining various symbols in the mathematical formulation of a droplet impacting on the X-Y plane in a direction parallel to the Z axis.

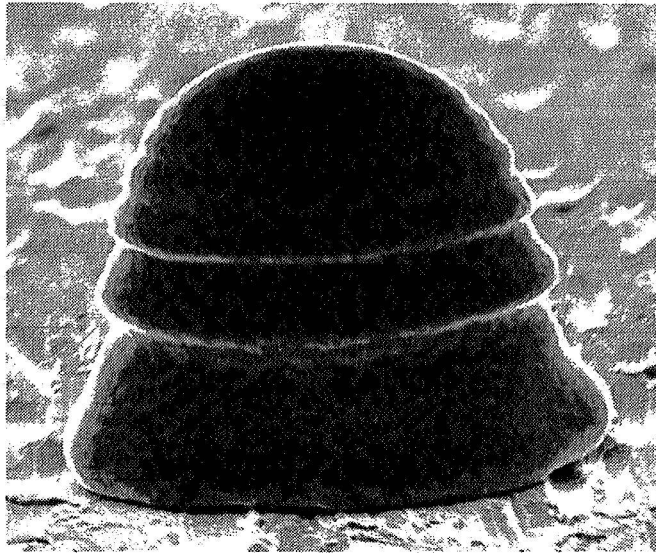


**Figure 3:** Solder microbump obtained experimentally in normal gravity. The solidified bump was produced by the deposition of a single 50  $\mu\text{m}$ -diameter droplet.

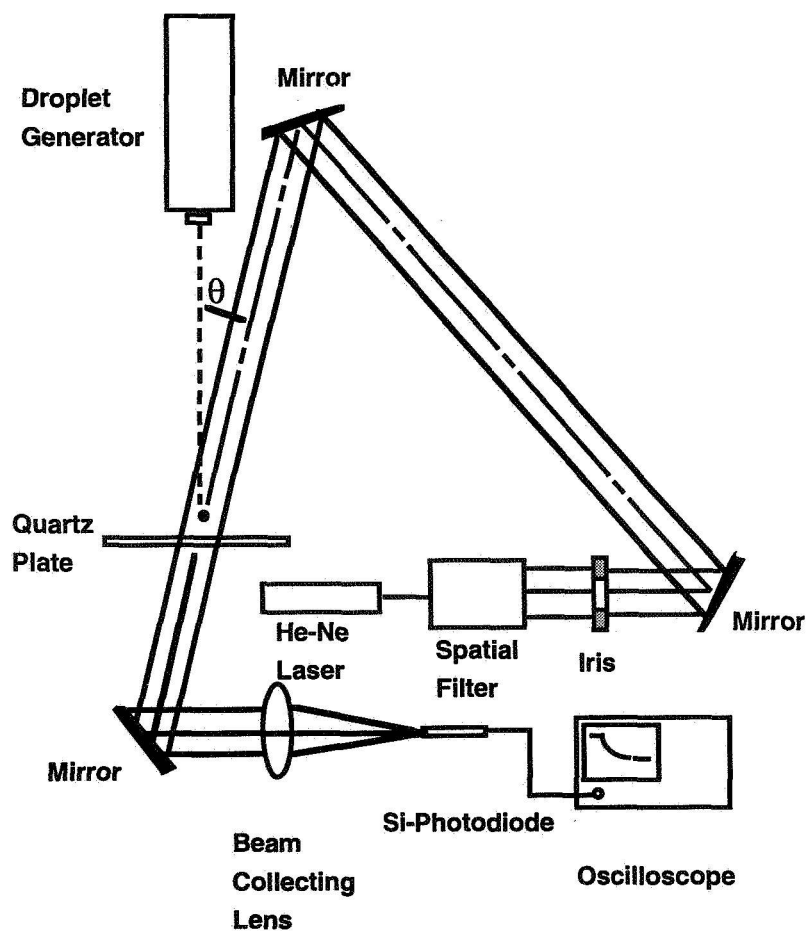


**Figure 4:** Photoelectric droplet spreading measurement system.



# CRYSTAL GROWTH AND FLUID MECHANICS PROBLEMS IN DIRECTIONAL SOLIDIFICATION

S. Tanveer,

G.R. Baker & M. R. Foster

The Ohio State University, Columbus, OH 43210

May 1996

## 1 Scientific objectives

The following is an outline of the directions of our efforts;

- A. A more complete theoretical understanding of convection effects in a vertical Bridgman apparatus, looking toward doing the following:
  - A1 Construct analytical solutions for interfacial shape and fluid velocity in mathematically sensible and physically meaningful limit cases. It appears that Biot number, Prandtl number and the Rayleigh numbers are crucial. Certain canonical nonlinear problems may be treated as well.
  - A2 Numerically verify and extend asymptotic results from A1 to other ranges of parameter space with a view to a broader physical understanding of the general trends.
  - A3 Numerically and analytically investigate the nature of the initial-value problem for the melt/solid combination, paying special attention to the end conditions. Are the often tacitly-assumed quasi-steady states in fact realizable?
- B. A clear understanding of scalings of various features of dendritic crystal growth in the case that both the surface energy and undercooling are small. We need to answer the following questions:
  - B1 Are there unsteady dendritic solutions in two dimensions to the fully nonlinear, time-evolving dynamical equations in the small-surface-energy limit (with small undercooling as well), for which there is a steady tip region with well defined tip radius and velocity, but with persistent unsteadiness in the side-branching? Most importantly, is anisotropic surface energy necessary for the existence of such solutions, as it is for a true steady-state needle crystal? How does the size of such a tip region depend on capillary effects, anisotropy and the undercooling?
  - B2 What is the source of noise in the dendrite problem? How does the linear theory of amplification of noise differ from a theory that includes nonlinear effects? How do nonlinear effects determine dendrite coarsening ?

## 2 Scientific and technological relevance

The vertical Bridgman apparatus is useful for the directional solidification of certain molten binary alloys. Such alloys, which are often components in semi-conductor devices, require minimal material segregation and minimal crystalline defects to be useful. The problem with the device is that the significant heat loss through the side walls of the material ampoule, necessary to avoid constitutional supercooling, produces significant convection in the melt and its concomitant variation in solutal concentration along the crystal-melt interface, and hence frozen in to the solid product. A clear understanding of the dependence of segregation and interfacial deformation on the numerous non-dimensional parameters of the device/melt combination is likely to lead to improved design and control of this industrially relevant process. Brown<sup>1</sup> has reviewed much of the important prior theoretical/numerical work, and since we have further discussed it in our 1994 report, we do not repeat it here.

Dendritic crystal growth is an important problem in pattern formation, (See References [2-4] for reviews.) but the connection with problems in directional solidification is that dendrites may arise in the context of solidification when the drawing speed in a Bridgman device, for example, exceeds some critical value that determines a "cell-to-dendrite transition". In this case, the dendrite growth is controlled by solutal diffusion rather than thermal. Nonetheless, the equations are similar to those for pure needle-crystal growth. Appearance of dendritic structures in directional solidification leads to undesirable striations of solute rich material in the crystal. Further understanding of the basic process of dendritic crystal growth, comparing and contrasting with existing theories<sup>2,3,5,6</sup>, can be both scientifically and technologically rewarding.

## 3 Research approach

### 3.1 Bridgman problem

#### 3.1.1 Analytical approaches

One method of approach is to explore various asymptotic solutions of the Bridgman equations for extreme values of particular parameters. We utilize a number of differing methods to uncover something of the dependence of the exact solutions on these parameters, including the WKBJ technique and matched asymptotic expansions. The advantage of the former technique is that the scales of velocities, temperature, *et al*, come out naturally from the analysis—without any *ad hoc* prescriptions of the gauge functions. Scaling guidance from such a procedure allows matched asymptotics methods to be used. The advantage of the latter technique is that certain canonical, parameter-free, weakly nonlinear problems may be formulated and solved—gaining an entrance into the nonlinear regime without resort to full numerical computations. A number of significant results are reported in the next section.

The efficacy of analytic approaches has already been demonstrated<sup>7,8</sup> in simple optimization conditions for minimization of interfacial deflection, and hence material segregation. It appears now that in a wide range of Rayleigh numbers such optimization is possible<sup>9</sup>.

### 3.1.2 Numerical approaches

Our approach to seeking optimal operating conditions for a Bridgman device is divided into two Parts. First, we seek steady-states<sup>10</sup> in which the crystal grows steadily inside the insulation zone. The solution is a quasi-stationary state in that the top and bottom of the ampoule are assumed to be sufficiently far away as to have no effect on the local behavior near the interface and insulation zone. We utilize Newton's method to solve the discrete system. Secondly, we investigate the transient development of the flow in the ampoule, paying special attention to the end boundary conditions, and differences between behavior in finite and infinitely-long ampoules. We use an ADI technique to advance the temperature and a semi-implicit method to advance the interface in time.

## 3.2 The dendrite problem at small Peclet number

We consider the time evolving aspects of a one-sided model for two-dimensional dendritic growth in a weakly undercooled melt that corresponding to small Peclet number. Further, our focus is almost exclusively to the case when the surface energy effects are appropriately small. It is to be noted that for a dendrite that is approximately parabolic, surface energy effects are reduced further away from the tip due to decreasing curvature and this makes the small surface energy limit of obvious relevance. We combine analytical and numerical methods to shed light on this limiting dynamics.

The essence of the approach rests on that of Tanveer<sup>11</sup> in solving the problem of the evolution of a Hele-Shaw finger, *viz.*, extending the domain into a complex plane, thereby making well-posed a mathematical problem for the interfacial evolution that is ill-posed in the physical plane as surface energy goes to zero. The sensitivity to noise in the laboratory setting is then seen as having its origin in the motion of a distribution of singularities in the complex plane. A variety of such initial distributions correspond to essentially identical laboratory initial conditions—but lead to quite different behaviors in time.

## 4 Discussion of results

### 4.1 Bridgman problem

We have carefully studied the nature of the asymptotic solutions for flow/solidification in the Bridgman device, under a 'quasi-steady' approximation, in the case that the Biot number is small and one or both of the inverse Rayleigh numbers (for temperature or solutal concentration) are small<sup>7,8,9</sup>. Matched asymptotic expansion techniques have provided particular information about the flow: The boundary- and shear-layer regions are shown schematically as Figure 1, where the dashed lines indicate the boundaries of the insulation zone that brackets the crystal/melt interface. The flow in the side-wall boundary layer drives the motion, with details of the material segregation being rather different depending on the relative sizes of the two Rayleigh numbers. Our most recent results<sup>9</sup> depend to some extent on the analysis of Brattkus & Davis<sup>12</sup>, but to a much greater extent build on the foundation of the WKBJ studies of Tanveer<sup>7,8</sup>, in which the essential scale analysis has

been given. The two approaches have proved to be complementary, each reinforcing the results of the other.

Numerical approaches outlined above have also yielded important insights into the non-linear steady-state solutions<sup>10</sup>, but also some preliminary information with regard to what circumstances must exist at the ampoule ends in order that anything like a 'steady state' can be attained. Below is an itemized summary of our conclusions to date, in both analytical and computational arenas.

- Imposition of a no-stress rather than no-slip on the side walls of the Bridgman ampoule makes no difference to the leading-order flow/segregation at large Rayleigh numbers and small Biot numbers.<sup>9,10</sup>
- A minimization of material segregation can be achieved at small Biot number, if either the thermal Rayleigh number, or the solutal Rayleigh number are large, or both are large and of comparable order<sup>7,8,9</sup>. Simple optimization formulae can be found in both axisymmetric<sup>7,8</sup> and two-dimensional cases<sup>9</sup> in the two limit cases, but not when both Rayleigh numbers are of comparable size, though optimization has been demonstrated in this case as well<sup>9</sup>. Small interfacial surface tension has no effect on the optimization<sup>9</sup>.
- For Biot numbers that are comparable to the largest Rayleigh number to the '1/6' power, the flow becomes nonlinear in the melt boundary layer that is adjacent to the solid interface—remaining linear elsewhere. Such nonlinearity can also arise even at small Biot numbers if the Prandtl number in the melt is small—which is often the case for materials of interest.
- The usual quasi-steady hypothesis employed by countless investigators in analyzing the flow in the melt is problematic. The thermal boundary conditions at the top and bottom of the moving ampoule must be arranged in a particular way in order to establish such a quasi-steady state. Numerical and analytical results indicate that such a steady state may be difficult to achieve in practice. We have found that the Biot numbers play a crucial role in determining when an ampoule is long enough so that the interface will grow steadily without feeling the influence of the conditions at the top and bottom of the ampoule<sup>13</sup>.

## 4.2 Dendrite problem

Results for the temporal evolution of a dendrite in a weakly undercooled melt, in the limit as the surface energy goes to zero involve three papers, which incorporate material from the PhD Dissertation of Kunka<sup>14</sup>, but also include a great deal of additional material. We summarize below the principal points of those three papers, all of which we expect to submit for publication by the end of the summer of 1996.

- In Part I we first carry out a formal asymptotic expansion for small Peclet number,  $P$ , and determine where such an assumed expansion ceases to be consistent. For a dendrite that is initially Ivantsov-like in the far-field, we show that there are three asymptotic regions at small  $P$ , with different governing equations and scales to the

leading order. For an  $O(1)$  region around the tip, the temperature is harmonic to the leading order in Peclet number, with boundary and far-field conditions are very similar to those for the problem of unstable viscous fingering in a Hele-Shaw cell. When initial shape deviation (not necessarily small or localized) from an Ivantsov parabola is confined to the tip region, the temperature and interfacial shape in other regions, to the leading order, remains that given by the Ivantsov solution—at least so long as the time,  $t \ll P^{-1}$ . For  $t$  satisfying this constraint, the growth and advection of initially localized disturbances superposed on an arbitrary time evolving state is investigated, in both linear and nonlinear regimes. The linear results essentially agree with previous well known results of Barber, Barbeiri & Langer<sup>15</sup>, though careful examination of the fully nonlinear problem indicates that the results of the linearized analysis give a false impression of the dynamics of dendrite evolution. That is because the dynamical equations for the interface evolution without surface energy are mathematically ill-posed, so it cannot be deduced that the solutions for surface energy tending to zero are necessarily solutions of the zero-surface-energy equations<sup>16,17</sup>.

To understand and predict dendritic evolution properly, one is therefore, as in the Hele-Shaw case, to investigating the dynamics in an extended complex plane, where the zero-surface-energy equations are well-posed<sup>18</sup>. The complex plane specification of initial conditions, while apparently artificial from the viewpoint of an experimentalist who is only in a position to determine initial interface shape to a finite precision, has the theoretical advantage of removing all sensitivity of the dynamics to initial condition. In this formulation, the actual results of an experiment are to be understood by studying a random ensemble of initial conditions in the complex plane subject to the constraint that the corresponding initial interface shapes for each of these initial conditions are the same interface shape, to within errors of measurement.

- In Part I, we restrict discussion to the various features of the zero-surface-energy dynamics in the complex plane, and the corresponding features observed at the interface. In terms of complex-plane zero-surface-energy dynamics involving particular classes of singularities, we also present a possible mechanism for nonlinear coarsening. However, in Part II, surface-energy effects are considered in the extended complex plane, examining in particular the nature of the singularity structure at finite, but small, surface energy, and the response of the dendritic interface as singularities approach the real domain.
- In Part III, we identify and amplify a specific mechanism for how dynamics in the limit of small surface energy differ from the zero-surface-tension dynamics. We also consider the effect of anisotropy on the impact of ‘daughter singularities’. We determine that, unlike the case for isotropic surface energy, where no locally-steady tip region forms, the impact time of a daughter singularity can theoretically predict the formation of a locally-steady tip region, at the same time that the rest of the dendrite continues to be unsteady. A scaling analysis complements a highly accurate computation that supports the scalings, in the context of both the dendrite and the mathematically analogous Hele-Shaw finger, with anisotropic surface energy.

## References

1. R. A. Brown (1988) *AICHE J.* **34**, 881.
2. D. Kessler, J. Koplik & H. Levine (1988) *Adv. Phys.*, **37** 255.
3. P. Pelce (1988) *Dynamics of Curved Fronts*, Academic Press, NY.
4. W. Kurz & R. Trivedi (1990) *Acta Metall. Mater.* **38**, 1.
5. E. Coutsias & H. Segur (1991) In *Asymptotics Beyond All orders*, NATO ARW Proceedings (Ed. Segur et al), Plenum.
6. J.J. Xu, (1991) *Phys. Rev. A* **43**, 930.
7. S. Tanveer (1994) *Phys. Fl* **6**, 2270..
8. S. Tanveer (1995) *Phys. Fl*, under review.
9. M.R. Foster (1996), submitted to *J. Crystal Growth*.
10. G. Koester (1996) PhD Dissertation, The Ohio State University.
11. S. Tanveer (1993) *Phil. Trans. R. Soc. London A* **343**, 155.
12. K. Brattkus & S.H. Davis (1988) *J. Crystal Growth* **91**, 538-556.
13. G. R. Baker & D. Vompe (1996), in preparation.
14. M. Kunka (1995) PhD Dissertation, The Ohio State University.
15. Barber, Barbieri & Langer (1987) *Phys Rev A* **36** 3340.
16. M. Siegel & S. Tanveer (1996) *Phys Rev Lett*, to appear.
17. M. Siegel, S. Tanveer & W.S. Dai (1996) *J. Fluid Mech*, to appear.
18. G.R. Baker, Michael Siegel & S. Tanveer (1995) *J. Comp. Phys.*, **120**, 348.

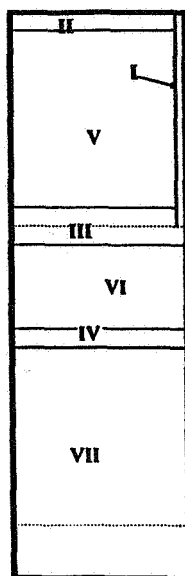


**Figure 1** Flow structure in the Bridgman ampoule at large Rayleigh number and small Biot number,  $\beta$ . If  $Ra$  represents the larger of the thermal and solutal Rayleigh numbers, then the region I boundary layer scales with  $Ra^{-1/4}$ , and regions II, III and IV scale with  $Ra^{-1/6}$ . The solid occupies region VII. The flow in V and VI is inviscid but diffusive. The deflection at the IV-VII interface scales with either  $Ra^{-1/6}$  (Solutal dominance<sup>8,9</sup>) or with  $\beta Ra^{-1/6}$  (Thermal dominance<sup>7,9</sup>).

# NONLINEAR CONVECTION IN MUSHY LAYERS

M. Grae Worster<sup>1</sup>, D.M. Anderson<sup>2</sup> & T.P. Schulze<sup>1</sup>

<sup>1</sup>Institute of Theoretical Geophysics, Department of Applied Mathematics and Theoretical Physics, Silver Street, Cambridge CB3 9EW, ENGLAND.

<sup>2</sup>Applied and Computational Mathematics Division, National Institute of Standards and Technology, Gaithersburg, MD 20899, USA.

## INTRODUCTION

When alloys solidify in a gravitational field there are complex interactions between solidification and natural, buoyancy-driven convection that can alter the composition and impair the structure of the solid product. The particular focus of this project has been the compositional convection within mushy layers that occurs in situations where the lighter component of the alloy is rejected into the melt during solidification by cooling from below. The linear stability of such a situation was described at the 2nd Microgravity Fluid Physics Conference [1] and has been further elucidated in a number of published articles [2–4]. Here we describe some recent developments in the study of the nonlinear evolution of convection in mushy layers.

The system under consideration is illustrated in figure 1. A two-component alloy is solidified upwards at a constant rate  $V$ . It is completely solid at temperatures below the eutectic temperature  $T_E$  in the region  $z < 0$ , where  $z$  is the vertical coordinate in a frame of reference moving with the solidification rate. Between the eutectic front ( $z = 0$ ) and the liquidus isotherm (at  $z = h(x, y, t)$ ), solid and liquid coexist in close proximity within a mushy layer. At temperatures above the liquidus temperature the alloy is completely molten. The mush–liquid interface is a free boundary whose position  $z = h(x, y, t)$  has to be calculated. We have studied convecting states that are steady in the moving frame of reference and have analyzed the stability of those states.

The dimensionless governing equations in the mushy layer are

$$\left(\frac{\partial}{\partial t} - \frac{\partial}{\partial z}\right)(\theta - S\phi) + \mathbf{u} \cdot \nabla \theta = 0, \quad (1)$$

$$\left(\frac{\partial}{\partial t} - \frac{\partial}{\partial z}\right)[(1 - \phi)\theta + C\phi] + \mathbf{u} \cdot \nabla \theta = 0, \quad (2)$$

$$\mathbf{u} = -\Pi(\phi)(\nabla p + R_m \theta \hat{\mathbf{z}}), \quad (3)$$

$$\nabla \cdot \mathbf{u} = 0, \quad (4)$$

where

$$\theta = \frac{T - T_L(C_0)}{\Delta T} = \frac{C - C_0}{\Delta C}, \quad (6)$$

$\Delta T = T_L(C_0) - T_E$ ,  $\Delta C = C_0 - C_E$ , represents both the dimensionless temperature and the dimensionless liquid composition, since they are coupled by the liquidus relationship  $T = T_L(C)$  throughout the mushy layer. The mushy layer is treated as a porous medium with locally isotropic permeability  $\Pi(\phi)$  that is a function of the local solid fraction  $\phi$ . Convection in the system is

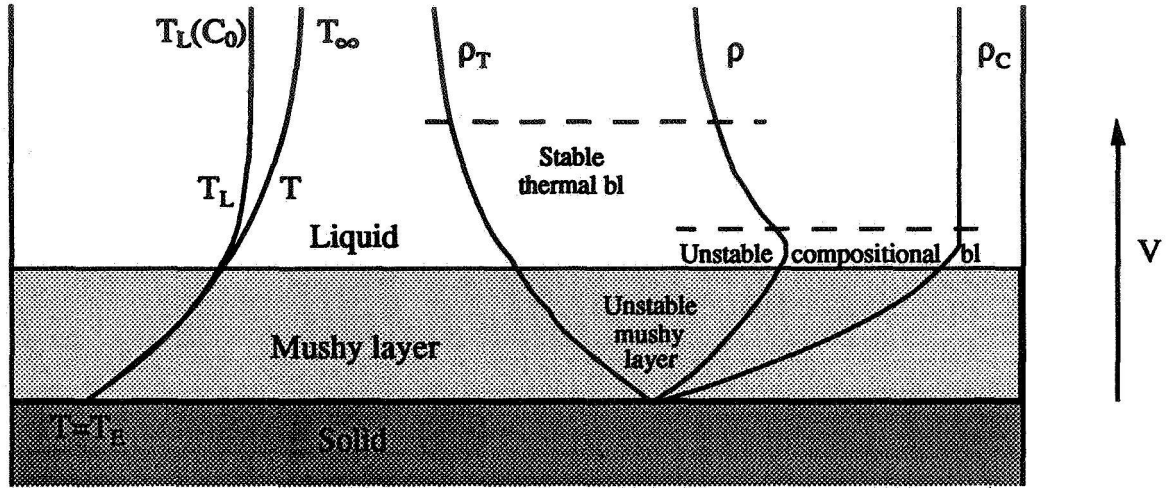


Figure 1. A schematic diagram showing the steady upwards solidification of an alloy at speed  $V$ . On the left is shown the steady temperature profile  $T$  and the profile of liquidus temperature  $T_L(C)$ , which is proportional to the local concentration of the liquid  $C$ , in the absence of flow. These give rise to the density profiles shown on the right. The overall density  $\rho = \rho_T + \rho_C$  is unstably stratified throughout the mushy layer and can give rise to convection in the mushy layer leading to the formation of chimneys.

controlled by the Rayleigh number

$$R_m = \frac{\beta \Delta C g \Pi^*}{\nu V} \quad (7)$$

mediated by the dimensionless parameters

$$S = \frac{L}{C_p \Delta T}, \quad C = \frac{C_s - C_0}{C_0 - C_E} \quad \text{and} \quad \theta_\infty = \frac{T_\infty - T_L(C_0)}{\Delta T}. \quad (8, 9, 10)$$

Interactions between the liquid and mushy regions are further influenced by the Darcy number

$$\mathcal{H} = \frac{\kappa^2 / V^2}{\Pi^*}, \quad (11)$$

which is proportional to the square of the ratio of macroscopic lengthscales to the interstitial lengthscale of the mushy layer and is typically very large. One effect of this is that the dynamic boundary condition at the mush-liquid interface is simply that the pressure is continuous.

## WEAKLY NONLINEAR ANALYSIS

We have determined the evolution of small, finite-amplitude perturbations to the steady state with no fluid flow. The coupled equations in the mushy and liquid regions are extremely complex so we have analysed a simpler system in which the mush-liquid interface is assumed to be horizontal, fixed in the moving frame and impermeable to fluid flow. This greatly simplifies the analysis without compromising the modelling of processes that are internal to the mushy layer. The fixed dimensionless height of the mushy layer  $\delta$  replaces  $\theta_\infty$  as a controlling parameter. In the basic, steady state of the full system,  $\delta = 1/\theta_\infty$ .

The dependent variables are expanded in the form

$$\theta = \theta_B(z) + \epsilon \hat{\theta}(x, y, z, t) \quad (12)$$



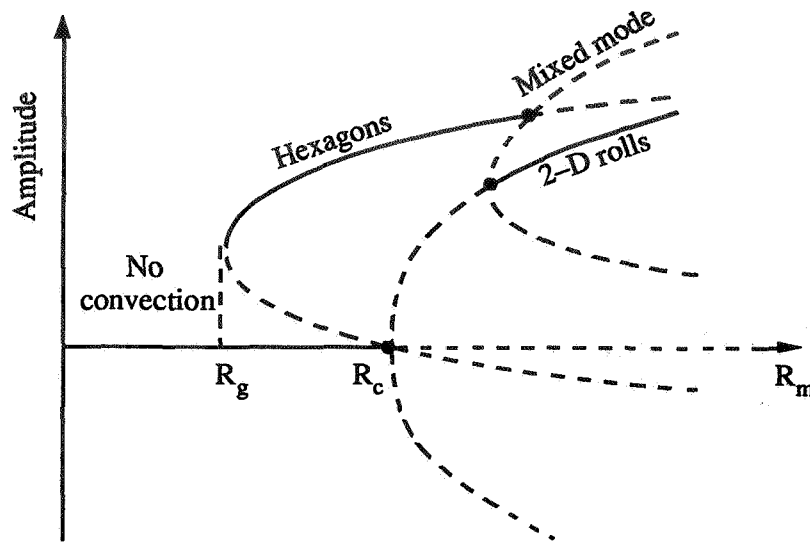


Figure 2. The nonlinear bifurcation diagram determined from the small-amplitude expansions. Solid curves indicate stable steady states of the system, while dashed curves indicate unstable steady states. In the parameter regime investigated, convection with a hexagonal planform bifurcates sub-critically while convection in the form of two-dimensional rolls bifurcates super-critically. The analysis has determined the global stability limit  $R_g$  and its explicit dependence on the various dimensionless parameters of the system. When the Rayleigh number  $R_m < R_g$  no convection can occur in the mushy layer.

(with similar expressions for  $\phi$  and  $u$ ), where  $\epsilon \ll 1$  measures the perturbation amplitude. To simplify the analysis further we employed the near-eutectic approximation [5], which amounts to taking the distinguished asymptotic limit  $\delta \ll 1$ , with  $C = O(\delta^{-1})$  and  $S = O(\delta^{-1})$ . To leading order in this limit one recovers the analysis of convection in a passive porous medium [6]. Phenomena intrinsic to a mushy layer are then reintroduced at  $O(\delta)$ .

The central result of this analysis is a set of coupled evolution equations

$$a\dot{A}_1 = 2\pi R_2 A_1 + bA_2 A_3^* - cA_1 |A_1|^2 - dA_1 (|A_2|^2 + |A_3|^2), \quad (13)$$

$$a\dot{A}_2 = 2\pi R_2 A_2 + bA_1 A_3^* - cA_2 |A_2|^2 - dA_2 (|A_1|^2 + |A_3|^2), \quad (14)$$

$$a\dot{A}_3 = 2\pi R_2 A_3 + bA_2 A_1^* - cA_3 |A_3|^2 - dA_3 (|A_2|^2 + |A_1|^2), \quad (15)$$

for the amplitudes of three intersecting two-dimensional rolls oriented at  $120^\circ$  to each other. Using these equations one can determine steady two-dimensional convection by setting two of the amplitudes to zero, or steady convection with hexagonal planform by setting the three amplitudes to be equal. Such steady states were analysed by Amberg & Homsy [7]. The fully coupled equations allow interactions between these modes of convection and their stability to be determined. The structure of the nonlinear bifurcation diagram in the vicinity of the linear critical point  $R_m = R_c$  is illustrated in figure 2.

The figure is drawn for the case  $b > 0$  in which the first stable steady convecting state has hexagonal planform with upflow in the centres of the hexagons. This is the case when the nonlinear interactions are dominated by the variation in the permeability with solid fraction [7], which has long been thought to be the primary interaction leading to focusing of the flow. However, experiments [8] have indicated that convection in mushy layers is initiated in the form of hexagons with downflow at their centres. Our analysis [9] has shown that  $b$  can have either sign, i.e. that hexagons

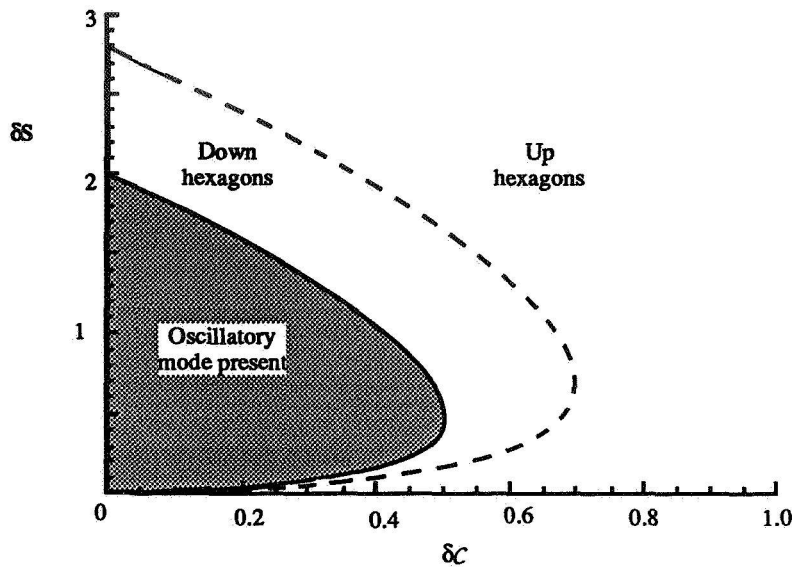


Figure 3. A diagram showing the regions of parameter space where convection in the form of either up-flowing or down-flowing hexagons are the preferred stable mode. The shaded region shows the parameter values where oscillatory convection is predicted to occur.

with either upflow or downflow at their centres can be the preferred, stable mode, depending on the dimensionless parameters of the system, as indicated in figure 3.

## OSCILLATORY CONVECTION

A surprising result of the nonlinear analysis is the fact that the coefficient of the time derivative,  $a$ , can be negative for certain parameter values. This signals the existence of a hitherto unsuspected oscillatory mode of convection. A detailed linear analysis [10] has revealed such an oscillatory instability, in which the convection can take the form of travelling rolls. Although these might be difficult to observe directly, they leave a signature in the solid in the form of slanted regions of compositional alteration. Perhaps more importantly, the discovery of the oscillatory mode has highlighted a significant interaction between convection and solidification within mushy layers that has previously been neglected in asymptotic analyses.

## THE FORMATION OF CHIMNEYS

The small-amplitude perturbation analysis shows that the solid fraction becomes zero inside the mushy layer when the upward velocity becomes sufficiently large. It suggests the formation of narrow, vertical channels of zero solid fraction — chimneys. Chimneys have been observed in many laboratory experiments, particularly those in which ammonium chloride is crystallized from solution [11–13] and those in which metallic alloys are solidified from below [14].

An important question is, following the nonlinear bifurcation from the linear critical point, does a chimney form first on the lower, unstable branch or on the upper, stable branch. In the latter case, finite-amplitude, steady convection can exist without the formation of chimneys. In the

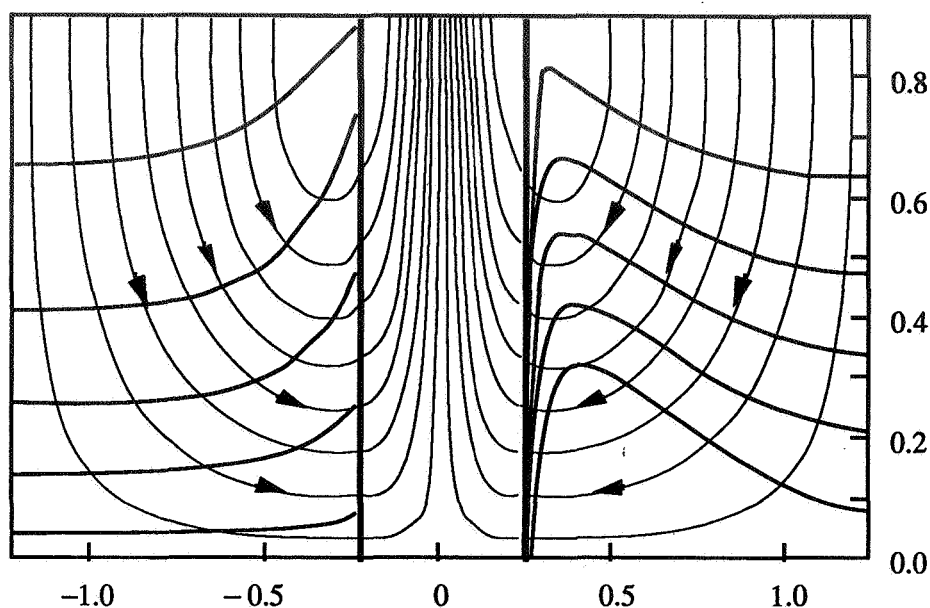


Figure 4. The thin lines show the streamlines through the mushy layer and up through a chimney (the central portion). Superposed on the left, in thicker curves, are isotherms. Superposed on the right are contours of solid fraction. The width of the chimney and the aspect ratio of the mushy layer are not to scale. The width of the chimney is inversely proportional to the cube root of the Darcy number  $\mathcal{H}$  and so is typically much narrower than its height.

former case, any triggering of convection must lead inexorably to the formation of chimneys. The weakly nonlinear analysis reveals that either can occur depending on the dimensionless parameters of the system. Our recent numerical study of the fully nonlinear system has confirmed this finding.

## FULLY DEVELOPED CHIMNEYS

In many systems, chimneys may be difficult to avoid. It then becomes important to be able to assess their effect on the structure of and compositional variations within a casting. To this end, models have been proposed for convection through fully developed chimneys. Roberts & Loper [15] developed a framework for such a model in which each chimney is treated as a vertical cylinder of possibly varying radius in which the liquid flows in response to its own buoyancy and the pressure at the chimney wall. The wall pressure and the heat and mass fluxes through the chimney wall couple to the flow and heat transfer in the rest of the mushy layer. This idea was adopted by Worster [16], who presented a scaling analysis, valid for  $R_m \gg 1$ , that revealed the structure of the flow and the temperature distribution in the mushy layer. We have recently used this same idea in a numerical evaluation of steady convecting states in a mushy layer with fully developed chimneys. The calculations performed to date have been two-dimensional. The flow in the chimney is solved using an approximate analysis based on lubrication theory. This analysis provides dynamic boundary conditions for the flow, temperature distribution and solid fraction in the mushy layer, which are calculated numerically.

Typical results are shown in figure 4. The depth of the mushy layer was allowed to vary dynamically, controlled in an average way by the heat transfer from the overlying liquid region.

However, the mush–liquid interface was kept horizontal. Nevertheless, the contours of solid fraction are strongly indicative that the mush–liquid interface should be raised to form a conical vent around the chimney, as has been observed in experiments. It is also apparent from figure 4 that the solid fraction at first increases towards the chimney before decreasing sharply to zero very close to the wall.

From calculations such as these we shall be able to extend the weakly nonlinear bifurcation diagram (figure 2) into strongly nonlinear regimes. From a practical point of view, we are able to calculate the solute fluxes from the mushy layer to the liquid region and hence to calculate macrosegregation in castings. Further, we plan to investigate the stability of such fully convecting states in order to determine the mean spacing between chimneys.

## CONCLUSIONS

Studies of nonlinear convection in mushy layers have elucidated the parametric controls on the plan form of convection and the global stability limit for convection leading to chimney formation. Depending on parameter values, finite-amplitude convection can exist in a mushy layer without chimneys forming or the onset of convection can lead inexorably to the formation of chimneys. Numerical analyses of convection in mushy layers with fully developed chimneys have revealed the internal structure of a convecting mushy layer and promise to yield important results concerning macrosegregation in cast alloys.

## REFERENCES

1. Worster, M.G. (1994) *Proc. 2nd Microgravity Fluid Physics Conf. NASA Conference Publication 3276* 193–198.
2. Worster, M.G. (1992). *J. Fluid Mech.* **237** 649–669.
3. Emms, P. & Fowler, A.C. (1994) *J. Fluid Mech.* **262**, 111–139.
4. Chen, F., Lu, J.W. & Yang, T.L. (1994) *J. Fluid Mech.* **276**, 163–187.
5. Fowler, A.C. (1985) *IMA J. Appl. Maths* **35**, 159–174.
6. Palm, E., Weber, J.E. & Kvernfold, O. (1972) *J. Fluid Mech.* **54**, 153–161.
7. Amberg, G. & Hornsy, G.M. (1993) *J. Fluid Mech.* **252**, 79–98.
8. Tait, S., Jahrling & Jaupart, C. (1992) *Nature* **359**, 406–408.
9. Anderson, D. & Worster, M.G. (1995) *J. Fluid Mech.* **302**, 307–331.
10. Anderson, D. & Worster, M.G. (1996) *J. Fluid Mech.* **307**, 245–267.
11. Copley, S.M., Giamei, A.F., Johnson, S.M. & Hornbecker, M.F. (1970) *Metall. Trans.* **1**, 2193–2204.
12. Chen, F. & Chen, C.F. (1991) *J. Fluid Mech.* **227**, 567–586.
13. Tait, S. & Jaupart, C. (1992) *J. Geophys. Res.* **97**(B5), 6735–6756.
14. Sample, A.K. & Hellawell, A. (1984) *Metallurgical Transactions A* **15A**, 2163–2173.
15. Roberts, P. & Loper, D.E. (1983) In *Stellar and Planetary Magnetism*, ed. AM Soward 329–349.
16. Worster, M.G. (1991) *J. Fluid Mech.* **224**, 335–359.

# **Complex Fluids**



# THE EXTENSIONAL RHEOLOGY OF NON-NEWTONIAN MATERIALS

Stephen H. Spiegelberg and Gareth H. McKinley

Division of Engineering and Applied Sciences  
Harvard University  
Cambridge, MA 02138

## ABSTRACT

The evolution of the transient extensional stresses in dilute and semi-dilute viscoelastic polymer solutions are measured with a filament stretching rheometer of a design similar to that first introduced by Sridhar et al. (1991). The solutions are polystyrene-based (PS) Boger fluids that are stretched at constant strain rates ranging from  $0.6 \leq \dot{\epsilon}_0 \leq 4 \text{ s}^{-1}$  and to Hencky strains of  $\epsilon > 4$ . The test fluids all strain-harden and Trouton ratios exceeding 1000 are obtained at high strains. The experimental data strain-hardens at lower strain levels than predicted by bead-spring FENE models. In addition to measuring the transient tensile stress growth, we also monitor the decay of the tensile viscoelastic stress difference in the fluid column following cessation of uniaxial elongation as a function of the total imposed Hencky strain and the strain rate. The extensional stresses initially decay very rapidly upon cessation of uniaxial elongation followed by a slower viscoelastic relaxation, and deviate significantly from FENE relaxation predictions. The relaxation at long times  $t \geq 5 \text{ s}$  is compromised by gravitational drainage leading to non-uniform filament profiles.

For the most elastic fluids, partial decohesion of the fluid filament from the endplates of the rheometer is observed in tests conducted at high strain rates. This elastic instability is initiated near the rigid endplate fixtures of the device and it results in the progressive breakup of the fluid column into individual threads or 'fibrils' with a regular azimuthal spacing. These fibrils elongate and bifurcate as the fluid sample is elongated further. Flow visualization experiments using a modified stretching device show that the instability develops as a consequence of an axisymmetry-breaking meniscus instability in the nonhomogeneous region of highly deformed fluid near the rigid endplate.

## INTRODUCTION

In recent years, concerted effort has been focused on the behavior of polymer solutions when subjected to strong extensional deformations. Extensional flows are found in most polymer-processing operations such as fiber-spinning, extrusion, and coating flows. Hence, rheological measurements of the appropriate materials under idealized extensional flow fields would be extremely valuable for comparison with theoretical model predictions. The parameter of interest is the uniaxial extensional stress growth coefficient  $\bar{\eta}^+$ , or the *transient extensional viscosity*, which is defined as

$$\tau_{zz}(t) - \tau_{rr}(t) = \bar{\eta}^+(t, \dot{\epsilon}_0) \dot{\epsilon}_0 \quad (1)$$

where  $\tau_{zz}(t) - \tau_{rr}(t)$  is the time-dependent normal or tensile stress difference, and  $\dot{\epsilon}_0$  is the constant imposed extensional strain rate. When the polymer chains reach maximum extension, the transient extensional viscosity reaches a constant steady-state value termed the *asymptotic extensional viscosity* denoted by  $\bar{\eta}(\dot{\epsilon}_0)$ .

Recent developments in extensional rheometer design have led to a greater understanding of the complexities of the behavior of polymer solutions in extensional flow. The filament stretching device first introduced by Cogswell [1] for melts has undergone several transformations throughout the years, the most significant recent contributions originating from Sridhar and co-workers [2, 3], who demonstrated the ability to generate a uniaxial extensional flow at a constant strain rate  $\dot{\epsilon}_0$  while measuring the small tensile forces exerted on the endplate by the deforming filament of fluid. In this design, a small, cylindrical sample of fluid is held between two rigid circular plates, which are then separated at a known rate. By measuring the force on one of the endplates, one can calculate the transient extensional viscosity growth function of the fluid as the Hencky strain  $\epsilon \equiv \dot{\epsilon}_0 t$  of the filament is increased.

With this design, Sridhar and co-workers have examined the extensional behavior of polyisobutylene-based Boger fluids [3] plus a shear-thinning polyisobutylene solution [4] and attained steady-state values in both systems.

The effects of the non-homogeneous kinematics on the measured material functions have been considered by Spiegelberg *et al.* [5]. Muller and co-workers [6] have examined the dependence of extensional behavior on solvent quality in polystyrene-based Boger fluids. In all these studies, the physical size of the sample and the minimum stretch rate attainable are constrained by gravitational body forces acting on the deforming filament, and the dimensionless quantity  $Bo/Ca = \rho g R_0^2 / \eta_0 \dot{\epsilon}_0$  must typically be less than unity. In a microgravity environment, larger samples and higher sample aspect ratios can be used which permit (i) the use of lower extension rates closer to the coil-stretch transition; (ii) larger sample aspect ratios that result in homogeneous kinematics, and (iii) application of other non-invasive diagnostic techniques for probing molecular structure, *e.g.* flow-induced birefringence.

In this paper we present ground-based measurements of the extensional viscosity for dilute polystyrene (PS) solutions obtained under normal gravitational conditions. These results are compared with models that predict the transient stress growth of pure elastic systems. These comparisons outline the need for microgravity conditions in order to further understand the complex response of these viscoelastic fluids in an extensional flow.

## EXPERIMENTAL

### Test Fluid Rheology

A series of three polystyrene-based Boger fluids with almost constant shear viscosities have been studied in the present work. High molecular weight polystyrene with a narrow polydispersity index (Scientific Polymer Products,  $M_w = 2.25 \times 10^6$  g/mole, P.D.I. = 1.02) was dissolved in oligomeric styrene (Hercules Piccolastic A5) with concentrations ranging from 0.05 wt.%  $< c < 0.2$  wt.% (500 – 2000 wppm). Simple molecular calculations for the high molecular weight PS species show that the critical concentration for chain overlap is  $c^* = 0.06$  wt.% [7] and the experimental test fluids therefore span the dilute and semi-dilute regime.

The viscometric material functions for these ‘Boger’ fluids were measured in a cone-and-plate geometry with a TA instruments controlled shear rheometer and have been discussed in detail elsewhere [5]. The viscometric properties of the fluids in steady and transient shear-flows can be quantitatively described by the bead-spring model of Zimm and can also be approximately modeled in strong flows by the simpler Chilcott-Rallison constitutive equation. In this model, the dilute solution of monodisperse polystyrene chains are considered to act as a non-interacting suspension of dumbbells connected by a finitely extensible nonlinear elastic (FENE) spring. The finite extensibility of the dumbbells is estimated to be  $L \approx 37$  by using the specified molecular properties of the monodisperse polystyrene to calculate the r.m.s. length and contour length of the statistically equivalent freely-jointed Kuhn (bead-rod) chain [5]. The key viscometric parameters for all three fluids, along with the oligomeric styrene forming the athermal, viscous Newtonian solvent, are listed in Table I.

### Experimental Apparatus

The filament-stretching rheometer used in this work is described in detail in [5]. Tests were conducted in air under normal gravitational conditions at  $T = 25^\circ\text{C}$ . Small samples with an initial diameter  $D_0 = 0.3$  or  $0.7$  cm and lengths ranging from  $0.05 \leq L_0 \leq 0.3$  cm were used to ensure that for the sample at rest, surface tension forces would dominate gravitational body forces. An example of the sequence of video-images obtained from the extensional deformation of a non-Newtonian fluid sample is shown in Figure 1. Modified endplate velocity profiles were used to ensure a constant effective strain rate as measured from the minimum diameter [3, 5]. The latter approach is used to compensate for the no-slip boundary conditions that exist at the fixed endplates and the resulting nonhomogeneous kinematics that arise at short times. Upon completion of stretching, the force on the bottom plate was monitored until significant gravitational drainage was apparent. For the strongly strain-hardening materials examined here, the force could be monitored for 2-3 seconds. As we discuss below, these measurements provide valuable information about the relaxation behavior of the polymer chains from an initial configuration close to full extension, and provide an indication of the relaxation spectrum of the material.

## RESULTS AND DISCUSSION

Experimental results for a Newtonian polystyrene oil ( $\dot{\epsilon}_0 = 4.5 \text{ s}^{-1}$ ) and a non-Newtonian 0.05 wt.% PS/PS Boger fluid solution ( $\dot{\epsilon}_0 = 3.3 \text{ s}^{-1}$ ,  $De = 2.8$ ) subjected to an extensional deformation are shown in Figure 2, where the transient Trouton ratio  $Tr \equiv \bar{\eta}^+ / \eta_0$  is plotted as a function of the Hencky strain  $\epsilon$ . The results demonstrate that the response of the non-Newtonian fluid is initially very similar to the Newtonian oil for strains  $\epsilon < 2$ . At higher levels of stretch, the polymer molecules approach maximum extension, the connector force between the chain ends becomes increasing nonlinear and the polymer chains begin to undergo non-affine



deformation. The fluid stress begins to rise, and increases several orders of magnitude at high Hencky strains. In the Newtonian fluid, however, the dimensionless stress approaches a constant value of  $Tr = 3$ , and remains invariant with Hencky strain. The initial overshoot in both fluids is a result of the non-ideal flow kinematics which occur at the solid endplates [5], and is well-described by the one-dimensional model shown with the experimental data.

The non-Newtonian predictions for two simple constitutive models are shown together with the experimental data in Figure 2. The polymer chain is considered to be a simple dumbbell in both models. The Oldroyd-B model assumes that the polymer chain is infinitely extensible ( $L \rightarrow \infty$ ) and the extensional viscosity increases without bound. The Chilcott-Rallison model incorporates finite chain extensibility and the Trouton ratio is predicted to approach an asymptotic value that scales as  $\bar{\eta} \sim L^2$ . Both models underpredict the transient response observed in the experimental data, which grows at a rate faster than that expected from affine extensional deformation of a Hookean dumbbell. It is possible that there is an additional ‘viscous’ or dissipative contribution to the total tensile stress in the fluid which arises from conformation-dependent drag on the deforming polymer chains [9], and which is not captured by simple FENE models that only account for the recoverable ‘elastic’ contribution to the stress arising from the loss of configurational entropy of the polymer chains. An alternative explanation is that the internal relaxation modes of the actual macromolecule give rise to a spectrum of relaxation times which lead to modifications of the dynamical processes by which the chains unravel during transient uniaxial elongation.

The discrepancy between the theoretical predictions and experimental results leads to the need for two additional sets of measurements to be conducted during the extensional test. Firstly, to decouple the two sources of measured stress, an independent measure of the microstructural deformation at the molecular-level is required. Phase-modulated birefringence measurements can provide the appropriate time-resolved non-invasive indication of the degree of orientation of the polymer chains [10]. As the degree of orientation is directly related to the level of elastic or ‘entropic’ stress experienced by the polymer chains, *in situ* birefringence measurements will probe the elastic contribution to the total measured stress, and the measured response should compare well with the FENE models.

Secondly, in addition to birefringence measurements, it is instructive to monitor the stress relaxation behavior of the polymer chains upon cessation of flow. As the deformation stops, any viscous or ‘dissipative’ component of the measured stress should disappear immediately, followed by a gradual viscoelastic decay of the residual elastic stresses. This stress relaxation may be measured both with birefringence and independently with the overall endplate force measurement. An example of stress relaxation following extensional deformation is shown in Figure 4 for a 0.05 wt.% PS/PS solution stretched at a single fixed extension rate to differing levels of strain. For comparison, the relaxation prediction of the Chilcott-Rallison model for a strain level of  $\epsilon = 4.08$  is also shown. The single mode relaxation predicted by the CR model decreases at a much lower rate than the experimental results. The initial drop in stress is convoluted with the deceleration time of the mechanical system; thus it is unclear at present if the initial drop is instantaneous or has a small finite relaxation time. In either case, it is evident from these preliminary results that a single-relaxation mode model lacking any viscous component is insufficient to predict the relaxation behavior of these materials when subjected to a strong extensional flow.

Both of the latter experiments are complicated by the presence of gravitational body forces. To make successful birefringence measurements, samples with large initial radii are required to prevent refraction of the polarized laser light beam that passes through the deforming column. As the diameter increases, however, the susceptibility of the fluid column to gravitational sag increases dramatically. Similarly, analysis of the stress relaxation studies require that a uniform cylindrical fluid column is maintained for several seconds. As the stress relaxes in the fluid, however, the fluid motion begins to reverse as the sample drains away from the upper plate under the influence of gravity. Therefore, for successful completion of these tests and hence complete understanding of the behavior of these materials under extensional deformation, access to an extended reduced-gravity environment is required.

An additional complication in the measurements of extensional viscosity results from the endplate conditions. As we have reported in [5], the rigid endplates lead to the partial decohesion of the filament from the endplates. A rigorous investigation shows that the axial curvature of the fluid filament at the endplates and the resulting adverse pressure gradient in the fluid lead to the formation of an elastic instability, which grows as the Hencky strain increases [11]. This instability only appears in samples that exhibit significant strain-hardening; however, the instability can lead to erroneous interpretation of the experimental data, as the appearance of the instability coincides with a leveling of the measured stress, which under normal circumstances could be interpreted as the attainment of steady-state extension. Two images at the onset of the instability are shown in Figure 4. The first image shows an axial side view of a 0.05 wt.% solution subjected to a strain rate  $\dot{\epsilon}_0 = 2 \text{ s}^{-1}$  after a strain of  $\epsilon \approx 4.3$ . The second image shows the spatial plan-form of the non-axisymmetric disturbance to the free-surface of the fluid

column using a camera that is focused axially upwards through a lower plate made of glass. At the onset of the instability, the cylindrical column breaks up into 3-5 lobes typically, which grow in a dendritic pattern exhibiting 'tip-splitting' and the formation of tertiary side-lobes.

Although this phenomenon is hydrodynamically interesting, it results in nonhomogeneous fluid deformations and prohibits determination of the extensional viscosity of the material. Such disturbances can not be eliminated by microgravity conditions, and in order to prevent onset of such elastic instabilities, it is necessary to impose the correct fluid boundary conditions at the endplates of the test device. Following the concept proposed and implemented by Kröger *et al.*[12], 'adaptive endplates' are being constructed that will inhibit axial curvature of the fluid interface at the endplates, and will thus eliminate the dynamical mechanism for instability.

## CONCLUSIONS

Ground-based experimental measurements of extensional viscosities for polystyrene-based viscoelastic solutions demonstrate a large increase in the transient extensional viscosity with strain, and dimensionless Trouton ratios increasing by three orders of magnitude. Comparisons with FENE models demonstrate that the single mode models do not capture the rapid increase in tensile stress with Hencky strain. Simultaneous birefringence measurements, coupled with stress relaxation studies following extension, will provide further information regarding the source of the discrepancy between model and experiment. Non-idealities in the flow characteristics of the filament-stretching rheometer result in partial decohesion of highly strain-hardening fluids. The non-idealities may be addressed with an adaptive endplate that imposes the correct radial velocity, rendering the fluid sample a cylinder for the majority of the test.

## REFERENCES

- (1) Cogswell, F. N. *Plast. Polym.*, **36**, 109 (1968).
- (2) Sridhar, T.; Tirtaatmadja, V.; Nguyen, D. A.; Gupta, R. K. *J. Non-Newtonian Fluid Mech.*, **40**, 271-280 (1991).
- (3) Tirtaatmadja, V.; Sridhar, T. *J. Rheol.*, **37**, 1081 (1993).
- (4) Ooi, Y. W.; Sridhar, T. *J. Non-Newtonian Fluid Mech.*, **52**, 153-162 (1994).
- (5) Spiegelberg, S. H.; Ables, D. C.; McKinley, G. H. *J. Non-Newtonian Fluid Mech.*, **to appear**, (1996).
- (6) Solomon, M. J.; Muller, S. J. *submitted to J. Rheology*, (1996).
- (7) Flory, P. J. *Principles of Polymer Chemistry*; Cornell University Press: Ithaca, 1953.
- (8) James, D. F.; Sridhar, T. *J. Rheol.*, **39**, 713-724 (1995).
- (9) Hinch, E. J. *J. Non-Newtonian Fluid Mech.*, **54**, 209-230 (1994).
- (10) Fuller, G. G. *Ann. Rev. Fluid Mech.*, **22**, 387-417 (1990).
- (11) Spiegelberg, S. H.; McKinley, G. H. *J. Non-Newtonian Fluid Mech.*, **to appear**, (1996).
- (12) Berg, S.; Kröger, R.; Rath, H. J. *J. Non-Newtonian Fluid Mech.*, **55**, 307-319 (1994).

Table 1. Zero-shear rate viscometric properties for three polystyrene-based Boger fluids denoted PS-05 (0.05 wt.%), PS-1 (0.1 wt.%), and PS-2 (0.2 wt.%) and a viscous polystyrene (PS) oil. All data at  $T_0 = 25^\circ\text{C}$ .

Measured Material Property	PS-05	PS-1	PS-2	PS Oil
$\eta_0$ [Pa.s]	47.7	52.0	70.4	
$\eta_s$ [Pa.s]	37.2	37.9	36.7	37.0
$\Psi_{10}$ [Pa.s <sup>2</sup> ]	18.3	42.5	122.6	
$\sigma$ [N/m]	$29 \times 10^{-3}$	$29 \times 10^{-3}$	$29 \times 10^{-3}$	$29 \times 10^{-3}$
Computed Model Parameters				
$\lambda_s = \Psi_1 / 2(\eta_0 - \eta_s)$ [s]	0.87	1.52	1.82	
$\beta = \eta_s / \eta_0$	0.78	0.73	0.52	

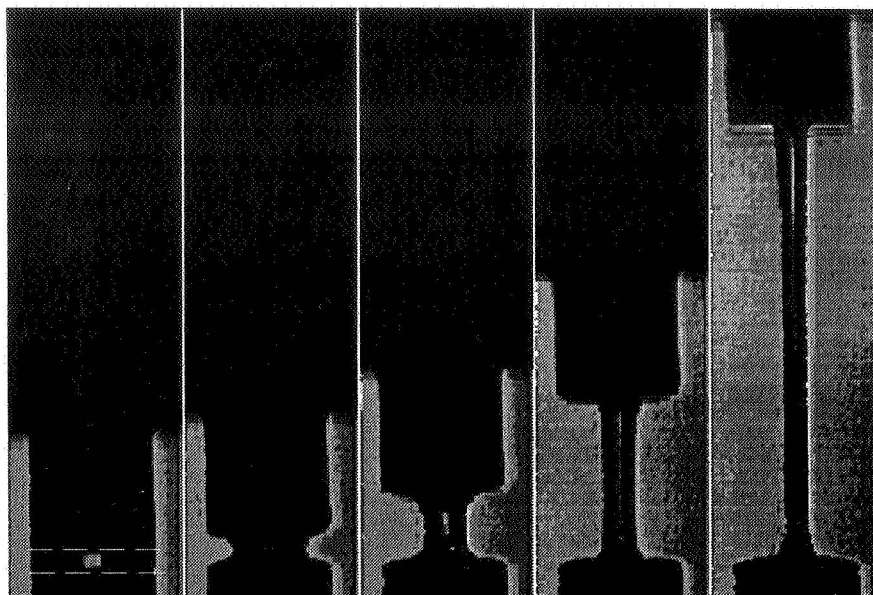


Figure 1: Evolution of a cylindrical fluid sample of 0.05 wt.% PS/PS solution stretched at a constant strain rate  $\dot{\epsilon}_0 = 2.0 \text{ s}^{-1}$ , corresponding to  $De = 1.4$ . Images are spaced 0.4 seconds apart. Sample aspect ratio  $\Lambda_0 = L_0/R_0 = 0.33$ , where  $R_0 = 0.15 \text{ cm}$ . The dashed lines show the initial sample length  $L_0$ .

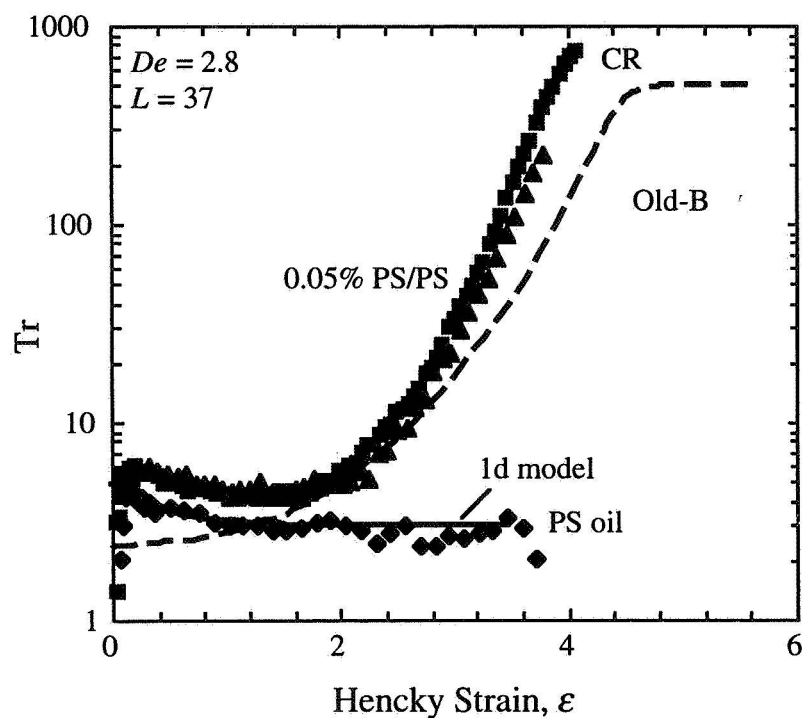


Figure 2: Strain-hardening in the transient tensile stress growth coefficient ( $Tr = \bar{\eta}^+/\eta_0$ ) of 0.05 wt.% PS/PS solutions stretched at a Deborah number  $De = 2.8$ . The predictions for two dumbbell-like models are shown for comparison, together with the response for a Newtonian PS oil.

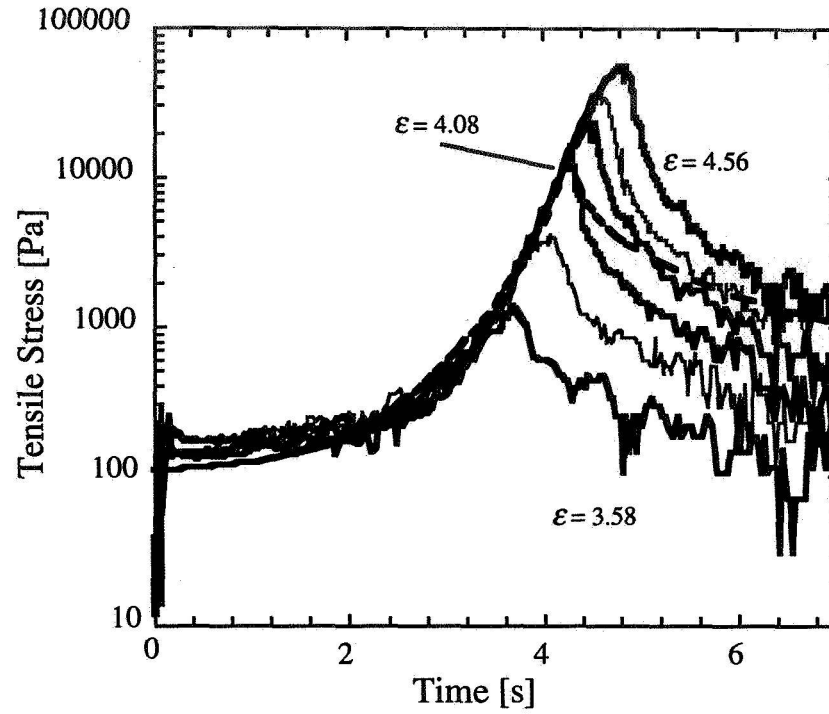


Figure 3: Stress relaxation behavior of 0.05 wt.% PS/PS solutions subjected to the same extensional strain rate  $\dot{\epsilon}_0 = 0.92 \text{ s}^{-1}$  for Hencky strains  $\epsilon = 3.58, 3.87, 4.08, 4.29, 4.32,$  and  $4.56$ . The relaxation behavior of the Chilcott-Rallison model for  $\epsilon = 4.08$  is shown for comparison as a dashed line.

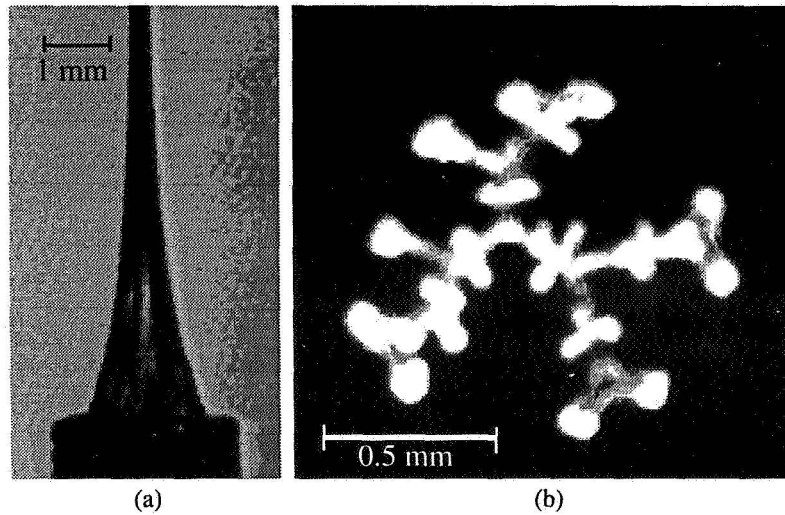


Figure 4: Onset of elastic instability in 0.05 wt.% PS/PS solution in extensional flow,  $\epsilon = 4.6$  and  $\dot{\epsilon}_0 = 2.0 \text{ s}^{-1}$  for  $\Lambda_0 = L_0/R_0 = 0.33$ . (a) Side view, (b) plan view. Images are taken from 2 different experiments at identical kinematic conditions.

# THE MELTING OF AQUEOUS FOAMS

Douglas J. Durian, Anthony D. Gopal, Moin U. Vera  
UCLA Department of Physics & Astronomy  
Los Angeles, CA 90095-1547

Stephen A. Langer  
National Institute of Standards and Technology  
Gaithersburg, MD 20899-0001

## ABSTRACT

Diffusing-wave spectroscopy measurements show that ordinarily solid aqueous foams flow by a series of stick-slip avalanche-like rearrangements of neighboring bubbles from one tight packing configuration to another. Contrary to a recent prediction, the distribution of avalanche sizes do not obey a power-law distribution characteristic of self-organized criticality. This can be understood from a simple model of foam mechanics based on bubble-bubble interactions.

## INTRODUCTION

Foams are nonequilibrium dispersions of discrete gas bubbles in a smaller, continuous, volume of liquid which contains surface-active macromolecules [1, 2]. They are familiar in everyday life from cleaning, food, and cosmetic products, and are important in a truly wide variety of industrial and research settings, whether fabricated for specific applications or inhibited and destroyed where undesirable. A hierarchy of structure and self-organization at progressively smaller length scales, as shown schematically in Figure 1, is ultimately responsible for the unique properties which make foams such fascinating and useful materials. The largest structural length scale, above which the foam appears homogeneous, is set by the average bubble size and can typically vary from 1 cm to 10  $\mu\text{m}$  depending on method of preparation and foam age. At the very smallest structural length scale, surface-active molecules are preferentially adsorbed at the gas/liquid interfaces and give rise to several physical-chemical effects which deter the coalescence of neighboring bubbles and thereby lend stability to the foam. An important intermediate length scale is the thickness of the liquid film separating neighboring gas bubbles; its value depends on details of the interfacial forces, and hence on the molecular composition of the liquid, but is typically on the order of 100 nm as is familiar from the colorful interference patterns in isolated soap films.

The Long-Range Goal: is to exploit rheological and multiple-light scattering techniques, and ultimately microgravity conditions, in order to quantify and elucidate the unusual elastic character of foams in terms of their underlying microscopic structure and dynamics. Special interest is in determining how this elastic character vanishes, i.e. how the foam melts into a simple viscous liquid, as a function of both increasing liquid content and shear strain rate.

General Approach: The unusual elastic character of foams will be quantified macroscopically by measurement of the shear stress as a function of static shear strain, shear strain rate, and time following a step strain; such data will be analyzed in terms of a yield stress, a static shear modulus, and dynamical time scales. Microscopic information about bubble packing and rearrangement dynamics, from which these macroscopic non-Newtonian properties presumably arise, will be obtained non-invasively by novel multiple-light scattering diagnostics such as diffusing-wave spectroscopy (DWS). Quantitative trends with materials parameters, such as average bubble size, and liquid content, will be sought in order to elucidate the fundamental connection between the microscopic structure and dynamics and the macroscopic rheology.

Need For Microgravity: Aqueous foams are intrinsically nonequilibrium systems; with time, the gas and liquid components inexorably separate by some combination of coarsening (gas diffusion from smaller to larger bubbles), film rupture, and the gravitational drainage of liquid from in between gas bubbles. While coarsening is often slow and film rupture can be eliminated, gravitational drainage cannot be prevented on earth since it is not possible to density match gas and liquid; furthermore, the rate of drainage increases rapidly with liquid content. This fundamentally precludes the possibility of ground-based study of foams near the melting transition. Microgravity

conditions are therefore required in order to eliminate drainage for experimental study of the intrinsic structure, dynamics, and rheology of foams with liquid content varying up to, and beyond, the melting transition.

**Significance:** The utility and fascination of foams are derived largely from the surprising fact that they have a solid-like elastic character in spite of being mostly gas with a few percent volume fraction of liquid, but can nevertheless flow under shear. The physical origin of such unusual rheology in terms of microscopic structure and dynamics is poorly understood and remains a subject of basic scientific interest. The planned research promises important new insight into these issues, and could also have significant consequences for our understanding of flow in other dense randomly-packed systems such as emulsions, colloidal suspensions, slurries, bubbly liquids, and granular materials. Furthermore, all foam applications are empirically based and the proposed research may generate valuable fundamental guidance for the development of materials with more desirable rheology and better stability.

**In this paper:** we focus on recent results regarding the melting of foams, not as a function of liquid content, but rather as a function of shear rate. Foam is confined between parallel glass plates which have been roughened to impose a no-slip condition as one plate is slid relative to the other. To study the dynamics of bubble rearrangements induced by the applied shear, we employ DWS and thus measure fluctuations in the transmitted intensity of light from a coherent laser. This yields a normalized electric field autocorrelation function,  $g_1(\tau)$ , which is subsequently analyzed using the formalism of diffusing-wave spectroscopy (DWS). We begin with a discussion of technical advances in the DWS technique followed by application to our specific foam system under shear. Lastly the experimental results are understood using a new model of foam mechanics.

## ADVANCES IN DIFFUSING-WAVE SPECTROSCOPY (DWS)

To extract useful information from DWS measurements requires that the propagation of light through the multiple-scattering sample be accurately modeled. Traditionally, this is done using a diffusion approximation wherein the number density of photons is assumed to have no direction dependence and to obey the diffusion equation [3]. This approach neglects the ballistic nature of photon transport between successive scattering events, and requires that additional assumptions be made about the treatment of the source terms and boundary conditions. The traditional formalism thus fails near the source and boundary, for strong absorption, and for samples that are not optically thick. Even within the range of validity, the accuracy can still be unacceptably poor if the source terms and boundary conditions are not properly treated. Furthermore, there is no means within diffusion theory to incorporate the effects of scattering anisotropy. By use of computer simulation and experiment, we have shown how best to implement the source terms [4] and boundary conditions [5, 6] within diffusion theory, and have quantified the accuracy of the resulting predictions [7]. In particular, we have shown how to average the penetration depth over an appropriate distribution and that the extrapolation length can be deduced from the angular dependence of diffusely transmitted light.

We have also proposed a two-stream theory of DWS that makes no diffusion approximations but can be solved analytically [8]. It provides a natural means of incorporating the effects of boundary reflections and, for the first time, ballistic propagation and scattering anisotropy. Predictions are compared with simulation in Figure 2, showing that these effects are of considerable magnitude in typical experimental situations and that they now can be accurately accounted for. These developments help transform DWS into a quantitative tool on the same level of accuracy as traditional single-scattering techniques, and will thus be crucial to the ultimate success of our approach.

## DWS APPLIED TO A FLOWING FOAM

The nature and rate of bubble-switching rearrangements in a coarsening foam can be measured using DWS [9]. Here, experimental electric field correlation functions are shown in the inset of Figure 3 before, during, and after imposed shear strain [10]. Also shown are excellent fits using the formalism of DWS and the assumption that events have a characteristic size and occur at random with a characteristic rate. This gives a nearly-exponential form for the decay with a time scale set by the optical thickness and the rearrangement rate. The main plot shows the ratio of this rate to that in a quiescent sample as a function of applied strain rate. At low strain rates, the ratio is one, implying that coarsening induced events dominate the dynamics. At high strain rates, the ratio is well-described by the form  $1 + A(V/L)\tau_{oq}$ , where  $V/L$  is the strain rate, plate speed divided by separation,  $\tau_{oq}$  is the time

between rearrangements in the quiescent sample, and  $A$  is an adjustable parameter. This implies that rearrangements are induced by shear at a rate given by the shear strain rate. From the value of  $A$ , we deduce that the events consist of a small core of bubble, approximately four across, undergoing sudden topology change. Macroscopic deformation and flow of foams are thus accomplished by a series of these sudden stick-slip, locally avalanche-like, events of neighboring bubbles from one configuration to another.

## BUBBLE-MODEL SIMULATIONS

Sudden rearrangement of bubbles during flow has been predicted in several models of foam rheology. In the classic Princen-Prud'homme model of the foam as a periodic hexagonal network, the happen simultaneously throughout the entire system [11, 12]. However, all foams are naturally disordered and this significantly changes the nature of actual events, as shown in the models of Weaire and Kawasaki and their co-workers [13, 14]. Weaire's model is based on a caricature of individual soap films separating adjacent bubbles. It thus allows for liquid content to be varied over a small range, but is strictly quasi-static and difficult to implement in higher than two dimensions. Kawasaki's model is based on a caricature of the vertices where three films meet and the dissipation that occurs when the films move, but is strictly limited to two dimensional foams with zero liquid content. Both models predict that avalanche-like rearrangement events can be triggered by small strain increments, and that the distribution of these events is sufficiently broad to be considered as a deterministic example of self-organized criticality. Our experiments seem to rule this out, however, and so here we present an alternative microscopic model of foam rheology.

Rather than focus on interfaces, films, or vertices, we focus instead on entire bubbles and their interactions [15]. If two bubbles in a sea of liquid are pushed together, then their shapes will distort away from spherical and the increase in surface area will give rise to a repulsive central force. And any relative motion of the two interacting bubbles will be retarded by a viscous drag in approximate proportion to their velocity difference. We seek the simplest possible model that includes these two crucial ingredients. Our new model is thus constructed by summing pair-wise interactions between neighboring gas bubbles as approximated in terms of their center positions  $\{\bar{r}_i\}$ , velocities  $\{\bar{v}_i\}$ , and radii  $\{R_i\}$ . No degrees of freedom are introduced for details of the bubble shapes. The equation of motion for bubble  $i$  can then be written as

$$\bar{v}_i = \langle \bar{v}_j \rangle + \frac{F_o}{b} \sum_j \left[ \frac{1}{|\bar{r}_i - \bar{r}_j|} - \frac{1}{R_i + R_j} \right] (\bar{r}_i - \bar{r}_j) + \frac{\bar{F}_i^a}{b}, \quad (1)$$

where  $F_o$  is set by surface tension,  $b$  is set by viscous drag, where the sum includes only neighboring bubbles  $j$  that satisfy  $|\bar{r}_i - \bar{r}_j| < R_i + R_j$ , and where  $\bar{F}_i^a$  is an externally applied force for edge bubbles. The first term represents viscous dissipation due to relative motion, and the second represents a repulsive spring force due to shape distortion. By contrast with all other models, ours is trivial to implement for foams of arbitrary dimensionality and liquid content. It is also complementary in being a closer approximation to reality in the limit of wet foams, whereas previous models are closer in the limit of dry foams.

Like previous models, ours predicts sudden avalanche-like rearrangements to be triggered by small strain increments during slow, steady shear. Unlike previous models, however, we do not find a broad distribution of event sizes characteristic of self-organized criticality. Figure 4 shows the bubble configuration before and after the very largest rearrangement event seen, as measured in terms of energy release. Just as in our DWS experiments, the event does not span the system but instead involves only a small core of bubbles undergoing topology change. We speculate that a combination of finite liquid content, which allows bubbles to rearrange more readily, and viscous dissipation, which slows down the bubble motion and hence hinders event propagation, are responsible for setting an upper limit on the event size and thus preventing self-organized criticality.

## CONCLUSIONS

Foams are familiar and important materials which remain of basic scientific interest due to lack of microscopic understanding of their fascinating and unusual properties. We have formulated, and are now implementing, a comprehensive research program which will overcome traditional experimental difficulties and serve to elucidate the fundamental interrelationships between foam composition, structure, dynamics, stability, and rheology. Progress is now being made in the ground-based component of our approach in which new multiple light scattering techniques are developed and used to noninvasively probe foam structure and dynamics. The second key component to our approach will be the use of microgravity conditions in order to examine sequences of foams with fixed composition and topology but increasing liquid content. The need for microgravity is clear and compelling: It is crucial to vary the liquid content towards the rigidity loss transition, however this cannot be done on earth due to the intrinsic density mismatch of the liquid and vapor portions of foam and the rapidly increasing rate of drainage on earth as the transition is approached.

## ACKNOWLEDGMENTS

We thank Andrea J. Liu and Sriram Ramaswamy for helpful discussions, and are grateful to NASA for encouraging and supporting this work.

## REFERENCES

- [1] J. H. Aubert, A. M. Kraynik and P. B. Rand, "Aqueous foams," *Sci. Am.* **254**, 74 (1989).
- [2] D. J. Durian and D. A. Weitz, "Foams," in *Kirk-Othmer Encyclopedia of Chemical Technology* J. I. Kroschwitz, Eds. (Wiley, New York, 1994), vol. 11, pp. 783.
- [3] D. A. Weitz and D. J. Pine, "Diffusing-wave spectroscopy," in *Dynamic Light Scattering: The Method and some Applications* W. Brown, Eds. (Clarendon Press, Oxford, 1993) pp. 652.
- [4] D. J. Durian, "Penetration depth for diffusing-wave spectroscopy," *Applied Optics* **34**, 7100 (1995).
- [5] D. J. Durian, "The influence of boundary reflection and refraction on diffusive photon transport," *Phys. Rev. E* **50**, 857 (1994).
- [6] M. U. Vera and D. J. Durian, "The angular distribution of diffusely transmitted light," *Phys. Rev. E* **53**, 3215 (1996).
- [7] D. J. Durian, "Accuracy of diffusing-wave spectroscopy theories," *Phys. Rev. E* **51**, 3350 (1995).
- [8] D. J. Durian, "Two-stream theory of diffusing-light spectroscopies," to appear in *Physica A* (1996).
- [9] D. J. Durian, D. A. Weitz and D. J. Pine, "Multiple light scattering probes of foam structure and dynamics," *Science* **252**, 686 (1991).
- [10] A. D. Gopal and D. J. Durian, "Nonlinear bubble dynamics in a slowly driven foam," *Phys. Rev. Lett.* **75**, 2610 (1995).
- [11] H. M. Princen, "Rheology of foams and highly concentrated emulsions. I. Elastic properties and yield stress of a cylindrical model system," *J. Col. I. Sci.* **91**, 160 (1983).
- [12] R. K. Prud'homme, Ann. Meet. Soc. Rheol., Louisville KY., Foam Flow (1981).
- [13] S. Hutzler, D. Weaire and F. Bolton, "The effects of Plateau borders in the two-dimensional soap froth III. Further results," *Phil. Mag. B* **71**, 277 (1995).
- [14] T. Okuzono and K. Kawasaki, "Intermittent flow behavior of random foams: A computer experiments on foam rheology," *Phys. Rev. E* **51**, 1246 (1995).
- [15] D. J. Durian, "Foam mechanics at the bubble scale," *Phys. Rev. Lett.* **4780** (1995).



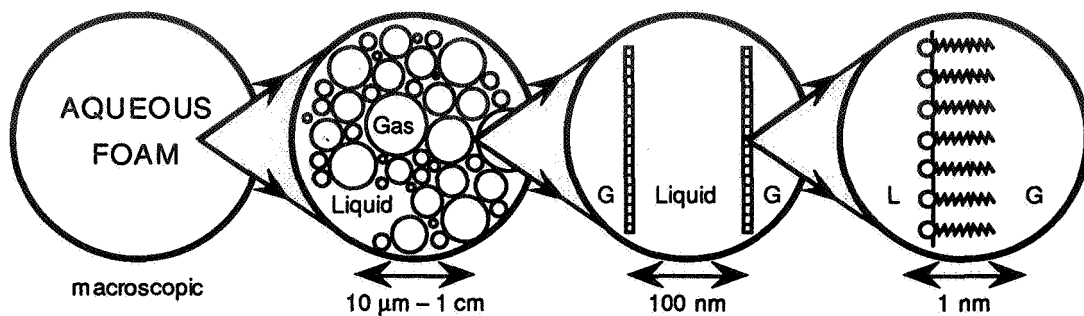


Fig. 1 – Hierarchy of structure and self-organization in an aqueous foam. Large gas bubbles are separated by thin liquid films which are stabilized against rupture by physical-chemical effects arising from the presence of adsorbed surfactants.

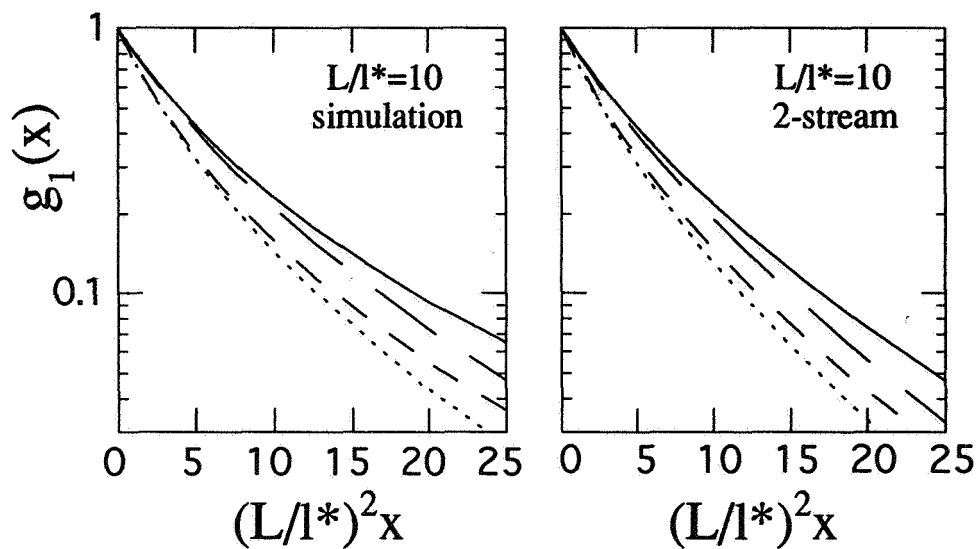


Fig. 2 – DWS correlation function as a function of the dynamical variable  $x = k^2 \langle \Delta r^2(\tau) \rangle$  for a trasmission through a slab of thickness ten transport mean free paths. The boundary reflectivity and scattering anisotropy are signified by curve type: solid for  $R = 0$  and  $l^*/l_s = 1$ ; long dash for  $R = 0$  and  $l^*/l_s = 10$ ; short dash for  $R = 1/2$  and  $l^*/l_s = 1$ ; dotted for  $R = 1/2$  and  $l^*/l_s = 10$ .

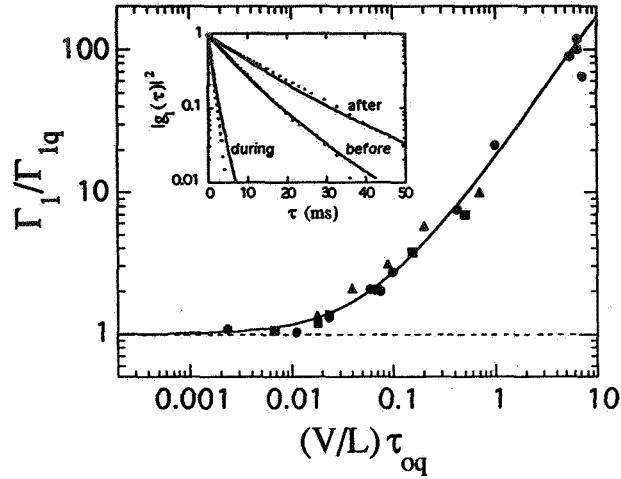


Fig. 3 – Inset: Typical DWS correlation functions for foam before, during, and after application of shear along with fits for the rate of rearrangements. Main: the ratio of rearrangement rate in sheared to quiescent samples as a function of plate speed, separation, and time between events in quiescent sample. Triangles, circles, and squares are for samples of thickness 6, 8, and 10 mm. The solid curve is a fit to  $1 + A(V/L)\tau_{oq}$ , from which we deduce that rearrangement events involve topology changes with in small core region only 4 bubbles across.

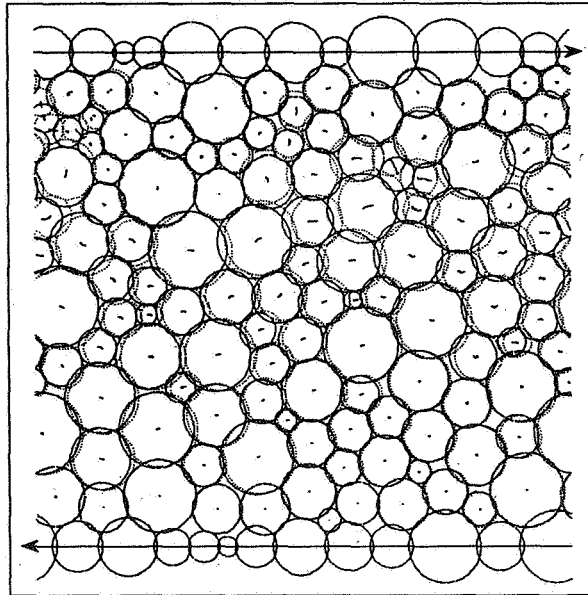


Fig. 4 – Bubble configurations before (light) and after (heavy) a simulated rearrangement; the dotted curves show the bubble center positions during motion. This particular event produced the largest observed energy release, but only involves topology change to a small core of bubbles, consistent with experiment.

# CHAIN DYNAMICS IN A DILUTE MAGNETORHEOLOGICAL FLUID

Jing Liu and Martin Hagenbuchle  
Department of Physics and Astronomy  
California State University Long Beach  
Long Beach, CA 90840

## ABSTRACT

The structure formation and dynamics of dilute, monodisperse ferrofluid emulsions in an external magnetic field have been investigated using dynamic light scattering techniques. In the absence of the magnetic field, the emulsion particles are randomly distributed and behave like hard spheres in Brownian motion. An applied magnetic field induces a magnetic dipole moment in each particle. Dipolar interaction between particles align them into chains where correlation function shows two decay processes. The short-time decay shows the motion of straight chains as a whole where the apparent chain length increases with the applied magnetic field and the particle volume fraction. Good scaling results are obtained showing that the apparent chain length grows with time following a power law with exponent of 0.6 and depends on the applied field, particle volume fraction and diffusion constant of the particles. The long-time decay in the correlation function shows oscillation when the chains reach a certain length with time and stiffness with threshold field. This result shows that chains not only fluctuate but move in a periodic motion with a frequency of 364 Hz at  $\lambda = 15$ . It may suggest the existence of phonons. This work is the first step in the understanding of the structure formation especially chain coarsening mechanism of MR fluids at higher volume fractions.

## INTRODUCTION

Magnetorheological (MR) fluids are suspensions of magnetizable particles of roughly a micrometer in diameter in a non-magnetizable liquid. Without magnetic field, the particles are hard-sphere like and are in Brownian motion. An applied magnetic field induces a magnetic dipole moment in each particle. Dipolar interaction between particles align them into chains which may further coalesce to other larger structures. This microscopic structural transition changes viscosity dramatically and reversibly upon the removal of the field, leading to many potential applications from active shock absorbers and clutch controls for cars to seismic damage controls for bridges and buildings (Ref. 1). The key to these novel rheological properties are the structures induced by the applied magnetic field. While the goal of the research is to understand the mechanism of the structure formation of MR fluids, this work focuses on the initial stage of the structural transition: dynamic properties of chain formation in a dilute model MR fluid.

The dipolar interaction is anisotropic. It is attractive if the two dipoles is aligned within  $55^\circ$  relative to the applied field direction and it is repulsive if they are aligned outside this angle. When two dipoles are aligned head to tail with the field, the attractive force is the strongest. Thus if exposed to a magnetic field, the first reaction of randomly distributed dipoles is to form many separated chains. The chains then aggregates to form columns or worm-like wall structures depending on the volume fraction of the particles, the field strength and rate that was applied, and the sample geometry (Ref. 2-3). Theoretical calculation has shown that two-straight chains have a very short-range interaction which is typically two-particle diameters for our ferrofluid emulsion and the field applied ( $<400$  G) (Ref. 4-5). However, we still observed the aggregation of chains to columns under this situation. A chain-fluctuation model for the chain-coarsening mechanism has been proposed by Halsey recently (Ref. 6). No one has quantitatively measured and studied the chain fluctuation.

In this paper we present the first measurement of chain formation and chain fluctuation with dynamic light scattering technique. We chose dilute MR fluids and weak applied fields to focus on the chain dynamics where no coarsening of the chains into columns occurs.

## EXPERIMENTS

A ferrofluid emulsion (Ref. 7) was used as a model MR fluid. It consists of small ferrofluid droplets dispersed in water. The droplets are stabilized against irreversible aggregation and coalescence by the

surfactant *sodium dodecyl sulfate (SDS)*. The ferrofluid itself is a suspension of iron oxide grains in kerosene where the grains have an average diameter of 90 Å. Each of these grains possess a permanent dipole moment. Yet, there is no net dipole moment of the whole droplet since thermal motion keeps the orientation of the grains random. Only when an external magnetic field is applied, the grains orient and thus induce a dipole moment in each droplet which depends on the strength of the applied field. The distribution of droplet sizes in an emulsion is generally very broad. We obtained a monodisperse emulsion by applying the fractionated crystallization scheme which is described elsewhere (Ref. 8). Two particle sizes were used in the experiments with radius  $a$ :  $233 \pm 17$  nm and  $80 \pm 24$  nm measured by dynamic light scattering. The sample was diluted to a volume fraction in the range of  $\phi \sim 10^{-4}$ - $10^{-6}$  to avoid multiple light scattering and chain coarsening.

We used an air-cooled Argon-ion laser at a wavelength of 514.5 nm and a He-Ne laser at 632.8 nm for our light scattering experiments. A lens was used to focus the laser beam into a cylindrical glass tube of 20 mm outer diameter which contained about 10 ml of the sample. This sample cell was surrounded by an index-match bath to reduce reflections and to keep the temperature of the sample constant. A Helmholtz coil with the sample in its center provided a homogeneous magnetic field. After passing the detector optics, the scattered light was detected by a photo-multiplier tube at different scattering angles in a plane normal to the field direction. The photon counts were then sent to a digital correlator (BI-9000AT) for processing, from which the averaged scattered light intensity  $I$  and the homodyne intensity autocorrelation function  $\langle I(\tau)I(0) \rangle$  were obtained. Using the Siegert relation (Ref. 9) we converted the intensity autocorrelation function into the normalized field autocorrelation function  $g^{(1)}(q, \tau) = \langle E(\tau)E(0) \rangle / \langle |E(0)|^2 \rangle$  from which the diffusion coefficients were derived as described below.

## RESULTS

### 1. Chain Formation

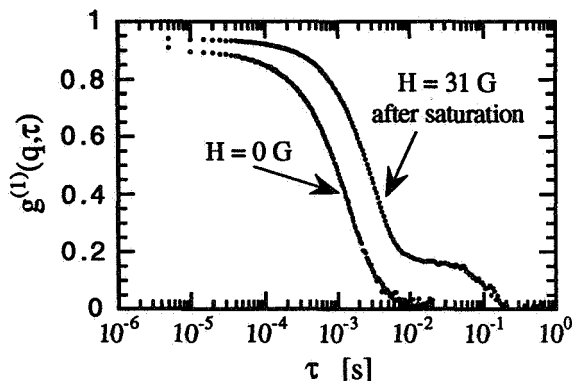


Fig. 1

**Fig. 1.** Normalized field autocorrelation function  $g^{(1)}(q, \tau)$  without magnetic field ( $H = 0$ ) and after saturation ( $H = 31$  G,  $\lambda = 9.4$ ,  $t = 110$  min.). Here particle radius  $a = 233$  nm, Scattering angle  $\theta = 90^\circ$ , and volume fraction  $\phi = 7.65 \times 10^{-5}$ .

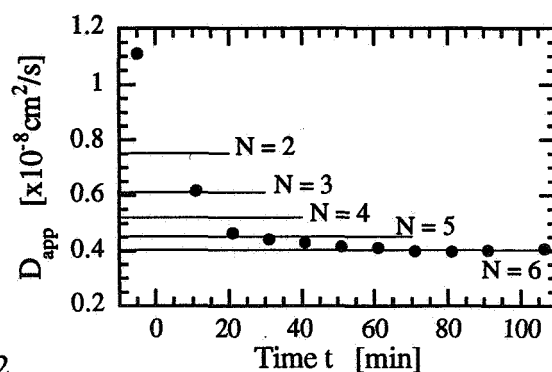


Fig. 2

**Fig. 2.** Short-time self diffusion coefficient during chain formation at  $H = 31$  G for the same conditions as in Fig. 1. The constant levels are calculated diffusion coefficients for a chain consisting of  $N$  particles.

Fig. 1 shows the comparison of the normalized field autocorrelation function  $g^{(1)}(q, \tau)$  at applied magnetic field  $H = 0$  G and  $H = 31$  G for  $\phi = 7.7 \times 10^{-5}$ ,  $a = 233$  nm and scattering angle  $\theta = 90^\circ$ . The correlation function with applied magnetic field was measured after the chain formation had stopped which means after the scattered intensity  $I(t)$  had saturated. The differences between the two correlation functions is clearly shown in Fig. 1. The correlation function at zero field can essentially be described by a single exponential. Due to the high dilution the emulsion behaves like a system of non-interacting particles. The small deviation from an exponential function is caused by the small size polydispersity of the droplets. In contrast,  $g^{(1)}(q, \tau)$  with applied magnetic field decays generally slower and shows two distinct decay times at

H=31G. At this field, the dipolar interaction energy between two dipoles in contact is 9.4 time of the thermal energy, i.e. the coupling constant  $\lambda = 9.4$ . The main decay time at this earlier time is of the same order of magnitude as the zero-field decay time. Compared to this short-time decay the long-time decay is about two orders of magnitude slower.

In the following we focus only on the short-time behavior of  $g^{(1)}(q, \tau)$ . The short-time dynamics is usually described in terms of the first cumulant  $\Gamma_1(q)$  (Ref. 10):

$$\Gamma_1(q) = -\frac{\partial}{\partial \tau} \ln g^{(1)}(q, \tau) \Big|_{\tau=0} \quad (1).$$

The first cumulant defines an apparent diffusion coefficient through:

$$\Gamma_1(q) = q^2 D_{app}(q) \quad (2).$$

Therefore,  $D_{app}(q)$  can be obtained from Fig. 1 using Eqs. 1 and 2. In general  $D_{app}(q)$  contains both self and collective diffusion. However, there are two arguments that in our experiment  $D_{app}(q)$  is solely determined by the self diffusion of the particles. First, since the threshold distance, which is a measure of the magnetic interaction range, is about two-particle diameters ( $2a$ ) and the dilution is so high that the initial distance  $d_i$  between neighboring particles are about  $20 \times 2a$ , after saturation we have essentially a system of non-interacting chains. Without interaction there are no correlations between different chains. Thus,  $D_{app}(q)$  reduces to  $D_{app}^{self}(q)$ . Second, it has been pointed out by several authors (Ref. 10-11) that for  $q \gg q_{max}$ ,  $D_{app}(q)$  reduces to  $D_{app}^{self}(q)$  even in interacting colloidal suspensions. Here,  $q_{max} = 2\pi/d_{max}$  with  $d_{max}$  the nearest neighbor distance between chains and  $q = 2\pi/l_q$  is the scattering wavevector employed in our experiment where  $l_q = 273 \text{ nm} \sim 2a$ . Since  $d_{max} \gg l_q$ , the above mentioned condition  $q \gg q_{max}$  is well fulfilled.

Figure 2 shows  $D_{app}^{self}(q)$  during the chain formation for the same sample as the one used in Fig. 1. The magnetic field was switched on at time 0 and kept constant at 31 G. The time to measure a correlation function was two minutes. The first and the last point in Fig. 2 correspond to the two correlation functions presented in Fig. 1. The diffusion coefficient of a chain of particles decreases with increasing number of particles in the chain. Thus, Fig. 2 directly reflects the chain formation. Due to our scattering geometry where the scattering wavevector is normal to the field direction, we are sensitive only to the motion of the chains perpendicular to their axes. Using the Stokes Einstein relation and the appropriate friction coefficient  $F_{chain}^\perp$  (Ref. 12), we can calculate the diffusion coefficient  $D_{chain}^\perp$  normal to the field direction:

$$D_{chain}^\perp = \frac{kBT}{F_{chain}^\perp}, \quad F_{chain}^\perp = \frac{4N}{3 \ln 2N + \gamma^\perp} \cdot F_{sphere} \quad (3).$$

Here,  $F_{sphere}$  is the Stokes friction coefficient of a single particle,  $N$  is the number of particles in the chain, and for  $\gamma^\perp$  a value of - 0.418 was reported (Ref. 13). The calculated values for  $N = 2$  to 6 are presented in Fig. 2 as constant levels. Comparing the diffusion coefficients calculated from Eq. 3 with the extrapolated values from measurements based on Eq. 1-2, we can estimate the apparent number of particles in an average chain. We find that at saturation the chain consists of approximately six particles. Here we do not expect one single chain length but a distribution of chain lengths to be induced by the applied field. Therefore the diffusion coefficient we measure is actually an averaged diffusion coefficient corresponding to an average chain length. The estimate for the number of particles in a chain from Eq. 3 is based on straight chains in the sample. Therefore, we call it apparent chain length. In reality, dynamic light scattering is

sensitive to all kinds of motion. Thus if there are bending modes or chain fluctuations as we will show later, they will affect  $D_{app}^{self}(q)$  to some degree.

## 2. Influence of Applied Field and Volume Fraction on Short-Time Dynamics

If we increase the field strength, the interaction range between particles will increase. This leads to the formation of longer chain lengths. Therefore, the measured diffusion coefficient at short time will be reduced. Figure 3 shows the growth of the apparent chain lengths with time at different fields from 52 to 195 G corresponding to  $\lambda = 26$  to 228. The same sample as in Fig. 1 was used with  $\phi = 1.4 \times 10^{-5}$  and  $\theta = 90^\circ$  using He-Ne laser of wavelength 632.8 nm. When the field is ramped up quickly and held at a constant value, the short-time self diffusion coefficient similar to Fig. 2 is observed which decreases with time as chains build up. The stronger the applied field, the faster the diffusion coefficient decreases, and therefore, a longer chain length is formed. The apparent chain length is obtained the same way as the one in Fig. 2 by comparing calculated diffusion coefficient for straight chains with experimental data.

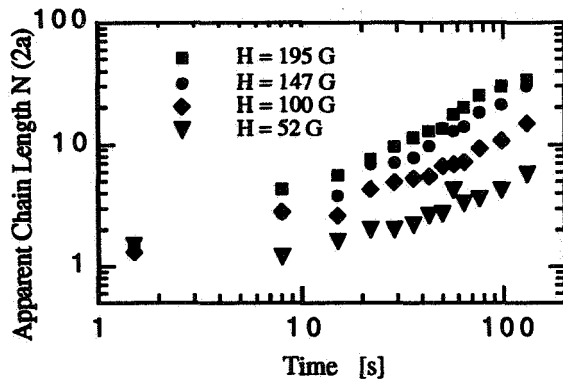


Fig.3

Fig. 3. Apparent chain length in units of particle diameters vs. time measured for different applied field strengths which correspond to  $\lambda = 26, 85, 156, 228$ . The field is turned on at  $t=0$ .  $\phi = 1.4 \times 10^{-5}$ .

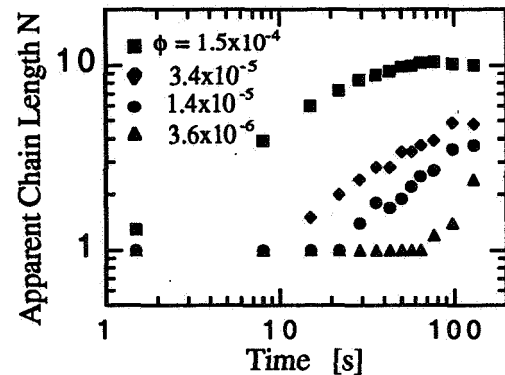


Fig.4

Fig. 4. Apparent chain length vs. time measured for different particle volume fractions at  $H=50$  G and  $\lambda=24$ . Both figures correspond to  $a=233$  nm and  $\theta = 90^\circ$ .

Figure 4 shows the results of changing particle volume fractions for the same sample at a constant field of 50 G ( $\lambda=24$ ) and  $\theta = 90^\circ$  using  $\text{Ar}^+$  laser of wavelength 514.5 nm. If we increase the particle volume fraction  $\phi$ , the initial distance between particles is reduced which shortens the diffusion time for particles to enter each other's interaction range which is defined by  $\lambda \geq 1$  and more particles are within that range to form chains. Therefore, a longer chain is formed as compared to that at low  $\phi$  for the same time after the field is applied. Specifically, at  $\phi=3.6 \times 10^{-6}$ , a dimer forms after the field is turned on for one hour. Whereas at  $\phi=1.5 \times 10^{-4}$ , it takes only 1 minute. However, they both increase with time at a similar rate on this log-log scale once dimers are formed and  $N$  starts to increase. The slowing down of  $N$  at  $\phi=1.5 \times 10^{-4}$  at later time might be due to the sedimentation of long chains and the long-time decay influence to the short-time behavior in the correlation function. The ferrofluid emulsion is nearly density matched but not exactly. When chain gets longer, sedimentation becomes more obvious.

Figure 5 shows the apparent chain length from Fig. 3 and 4 plotted as a function of rescaled time on a log-log scale. The normalization factor is a characteristic time scale,  $t_{BW}$ , for particles to aggregate. This time factor originates from the Brownian motion weighted by the stability factor  $W$  to take into account of dipolar interaction:  $t_{BW}=t_B W=9.16 a^2/(6D\phi\lambda^{4/3})$  (Ref. 14). All the data collapse to follow a power law  $N = (t/t_{BW})^z$  where  $z=0.6$  as shown in Fig. 5. For  $\lambda \geq 9$ , the aggregation process is non-equilibrium or irreversible for the

volume fractions used in our experiments (Ref. 15). At lower  $H$  or  $\phi$ , it takes a longer time for two particles to move into each other's interaction range to form a dimer. However, the growth rate of average chains for each sample measured follows the same relation:  $dN/dt \sim \lambda^{0.8} \phi^{0.6} D^{0.6} t^{-0.4}$ . The larger the interaction strength and diffusion constant or the closer the initial particle distance, the faster the chains grow.

A power-law behavior shows that the chain formation can be described by the Smoluchowski's equation for irreversible aggregation. It means that the formation of a  $N$ -particle chain is due to a combination of two short chains at any given time. Earlier study of ER fluid by Fraden et al. has shown a similar behavior with  $z=0.6$  (Ref. 16).

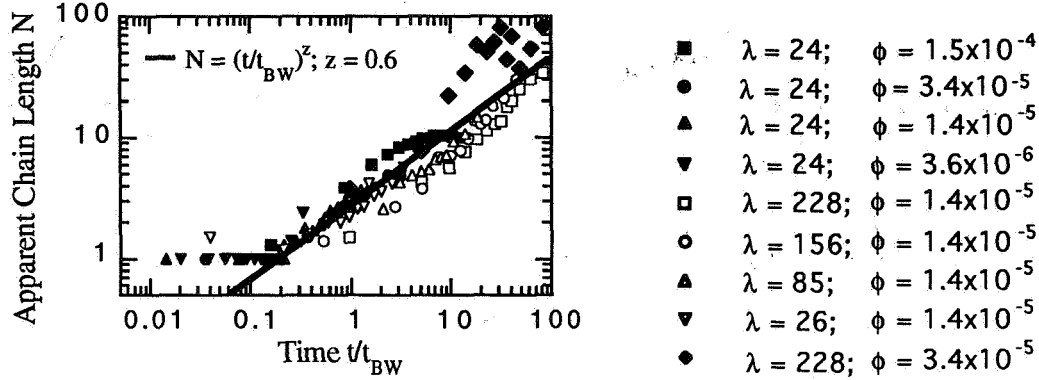


Fig. 5. Apparent chain length in units of particle diameter vs. normalized time for the data shown in Fig. 3 and 4. All the measurements show the same power-law growth.

### 3. Long-Time Dynamics

Figure 1 shows that an additional decay appears at long time when the field is applied. As the short time decay reflects the diffusing motion of a straight chain, the long time decay may reflect additional motion of a chain. On a closer look at the long-time behavior one finds surprising results. Figure 6 shows correlation functions measured at different angles when the same field is turned on for about two hours. In this case, smaller size particles with  $a=80$  nm are used at a higher field ( $H=310$  G and  $\lambda = 15$ ) than that used in Fig. 1. Now an average chain consists of about 300 particles which is at least a factor of 10 more than the particles in a typical chain formed with larger particles used in obtaining Fig. 1-4. A little bump at the decay slope in Fig. 6a indicates that an additional motion may exist and overlaps with the short-time decay. Dramatic results are seen at the scattering angle of  $150^\circ$  where oscillation is observed. The first oscillation peak of the correlation function in Fig. 6b occurs at a time about 2.7 ms which corresponds to a frequency of 364 Hz. Oscillation in the correlation function indicates that chains fluctuate regularly at this characteristic frequency. If plotted in a linear scale, the interval between oscillations are constant. This shows the possibility of existence of phonons which is surprising to see in a heavily damped system.

The differences between Fig. 6a and 6b is the length scale or window used to measure transverse motion:  $l_q = 1/q = 1.5 \times 2a$  for  $\theta = 150^\circ$ , whereas  $l_q = 2.1 \times 2a$  for  $\theta=90^\circ$ . This indicates that the fluctuation amplitude,  $A_f$ , is about two-particle diameters. If  $l_q > A_f$ , the fluctuation is averaged out as seen by the detector. If  $l_q < A_f$ , the fluctuation can be detected. This observation is consistent with other measurements at smaller angles of  $30^\circ$  and  $60^\circ$  where the bump becomes less obvious.

The oscillation does not occur at all the times. It appears about 15 minutes after the field is turned on which depends on the field applied, the particle volume fractions, and the particle size. The oscillation amplitude increases and the peak width narrows down with time. If we reduce the field step by step after saturation is reached, the oscillation in the correlation function generally reduces with field and disappears at low field where no chain exists. Thus a certain threshold-field strength is required to see oscillation. This

indicates that a certain length and stiffness of chains is required to support oscillation. It is consistent with the picture of phonon propagating along a chain in a damped environment.

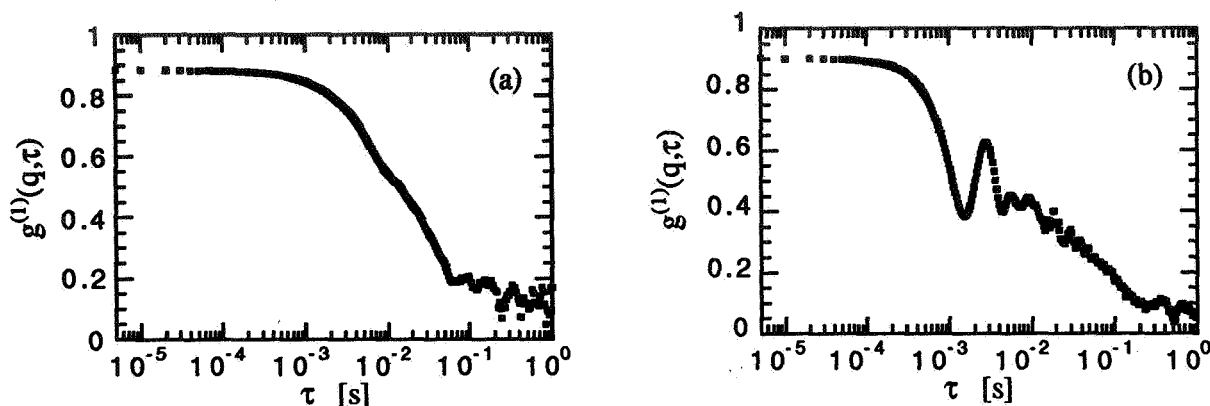


Fig. 6. Correlation function measured at scattering angles of (a)  $90^\circ$  and (b)  $150^\circ$  corresponding to a length scale  $l_q = 1/q = 2.1 \times 2a$  and  $1.5 \times 2a$ . Oscillation is observed and becomes pronounced at  $150^\circ$ . Here  $H=310\text{G}$  ( $\lambda = 15$ ),  $\phi=3.6 \times 10^{-5}$ ,  $a=80\text{ nm}$ .

## CONCLUSION

In summary, we have presented initial dynamic-light-scattering measurements on a dilute model magnetorheological fluid. Field-induced chain formation was observed for  $\lambda > 1$ . The motion of chains can be described by two processes: the diffusive motion of straight chains as a whole and the fluctuation of chains. The straight-chain motion corresponds to a diffusion constant which decreases with the increase of applied field and particle volume fraction. The chain fluctuation shows a surprising periodic oscillation at a time scale of a few ms when the chains reach a certain length with time and stiffness at a threshold field. This result may suggest the existence of phonons along chains. The observed chain fluctuation supports the basis of Halsey's theory for the chain-coarsening mechanism.

## ACKNOWLEDGMENT

We thank Dr. Yun Zhu and Dr. Mark Gross for helpful discussion and gratefully acknowledge the support by NASA, NAG 3-1634.

## REFERENCES

1. J. D. Carlson, et al, *Proc. of 5th Int. Conf. on Electro-Rheological Fluids and Magneto-Rheological Suspensions*, University of Sheffield, UK, 10 - 14 July 1995, Bullough ed. (World Scientific, 1996).
2. E.M. Lawrence, et al, *Int. J. Mod. Phys. B*, **8**, 2765 (1994).
3. J. Liu, et al, *Phys. Rev. Lett.* **74**, 2828 (1995).
4. R. Tao and J. M. Sun, *Phys. Rev. Lett.* **67**, 398 (1991).
5. B. Murakami, APS March Meeting, St. Louis, 1996.
6. T.C. Halsey and W. Toor, *J. Stat. Phys.*, **61**, 1257 (1990).
7. J. Bibette, *J. Magnetism and Magn. Materials* **122** (1993) 37.
8. J. Bibette, *J. Coll. Int. Sci.* **147** (1991) 474.
9. B. J. Berne and R. Pecora, *Dynamic Light Scattering* (Wiley, New York, 1976).
10. P. N. Pusey, *J. Phys. A: Math. Gen.* **11** (1978) 119.
11. K. J. Gaylor, I. K. Snook, W. J. van Megen, and R. O. Watts, *J. Phys. A: Math. Gen.* **13** (1980) 2513.
12. K. Zahn, R. Lenke, and G. Maret, *J. Phys. II France* **4** (1994) 555.
13. H. Yamakawa, *J. Chem. Phys.* **53** (1970) 436.
14. M. Fermigier and A. P. Gast, *J. Coll. Int. Sci.* **154** (1992) 522.
15. P. G. de Gennes and P. Pincus, *Phys. Kondes, Mater.* **11**, 189 (1970).
16. S. Fraden, A. J. Hurd, and R.B. Meyer, *Phys. Rev. Lett.* **63**, 2373 (1989).



**Growth and morphology of crystals made of hard spheres**

Bruce Ackerson, Oklahoma State University

**Paper not available**



## Dynamics of Disorder-Order Transitions in Hard Sphere Colloidal Dispersions in $\mu g$

J.X. Zhu, M. Li, S.E. Phan, W. B. Russel, P.M. Chaikin, Princeton  
R. Rogers, W. Meyers, NASA Lewis  
Crew of Shuttle Columbia, STS-73

### Abstract

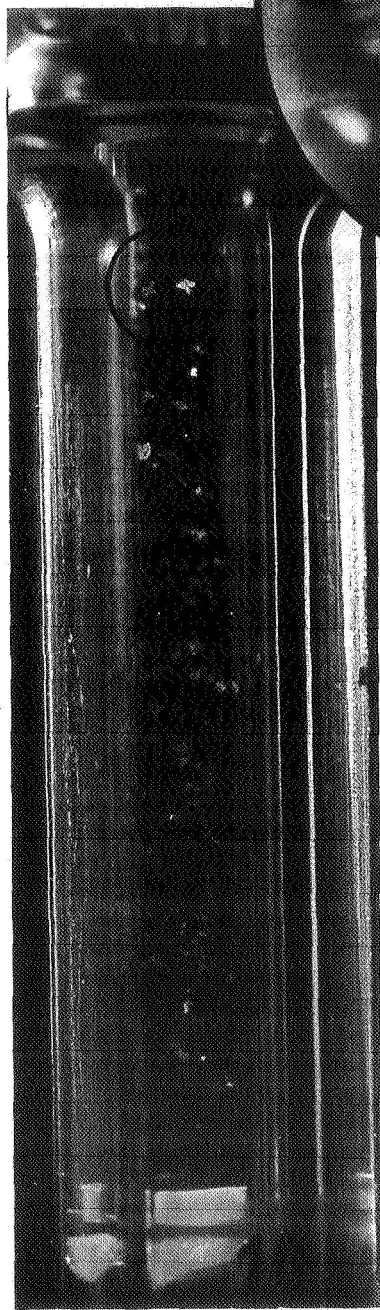
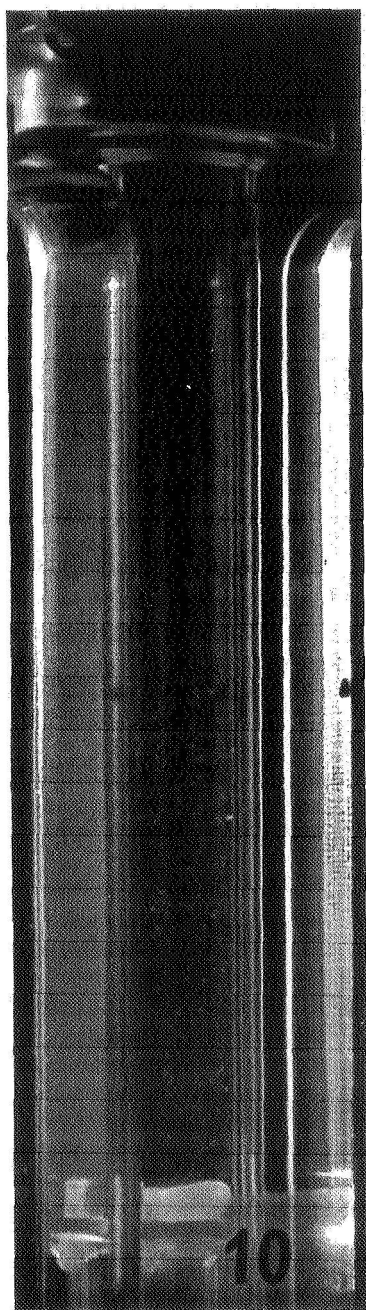
We have performed a series of experiments on  $0.518\mu m$  PMMA spheres suspended in an index matching mixture of decalin and tetralin in the microgravity environment provided by the Shuttle Columbia on mission STS-73. The samples ranged in concentration from 0.49 to 0.62 volume fraction ( $\phi$ ) of spheres, which covers the range in which liquid, coexistence, solid and glass phases are expected from earth bound experiments. Light scattering was used to probe the static structure, and the particle dynamics. Digital and 35mm photos provided information on the morphology of the crystals. In general the crystallites grew considerably larger (roughly an order of magnitude larger) than the same samples with identical treatment in one g. The dynamic light scattering shows the typical short time diffusion and long time caging effects found in one g. The surprises that were encountered in  $\mu g$  include the preponderance of RHCP (Random Hexagonal Close Packed) structures and the complete absence of the expected Face Centered Cubic (FCC) structure, existence of large dendritic crystals floating in the coexistence samples (where liquid and solid phases coexist) and the rapid crystallization of samples which exist only in glass phase under the influence of one g. These results suggest that colloidal crystal growth is profoundly effected by gravity in yet unrecognized ways. We suspect that the RCHP structure is related to the nonequilibrium growth that is evident from the presence of dendrites. An analysis of the dendritic growth instabilities is presented within the framework of the Ackerson - Schatzel equations.

### Introduction

The CDOT (Colloidal Disorder-Order Transition) experiment consisted of two parts, 1) photographic investigation of the phase diagram (liquid, crystal, glassy regimes) and crystallite morphology and 2) light scattering and shear modulus measurements of the monodispersed samples in the CDOT hardware operated in the shuttle glovebox. A detailed description of the CDOT hardware is to be found elsewhere in this conference. The samples were mixed each day prior to liftoff to prevent sedimentation. A day after orbit was achieved the samples were unstored and mixed in  $\mu g$ . Photographs and further experiments were performed after the samples had been in  $\mu g$  for three or more days after the  $\mu g$  mix. The mix was performed using a magnetic stirbar drawn through the sample in a prearranged series of translations and rotations and the samples were visually inspected by the astronauts after mixing to assure homogeneity and the absence of any remnant crystals.

### Dendritic growth

Figure 1 shows photos of a sample in the coexistence region with volume fraction  $\phi=0.52$ . The left photo is taken on earth and shows liquid solid phase separation in gravity with the denser crystalline phase occupying the lower half of the tube and liquid in the upper half. In  $\mu g$  the crystallites remain suspended in the liquid phase. In addition to the larger crystallite size, an enlargement of part of the photo shows the existence of branched or dendritic crystals with dimensions  $\sim 2$  mm and characteristic structure on the scale  $100\mu$ . Although there have been hints of dendritic growth observed during nucleation experiments[1], and for soft potentials on a lower surface[2], this is the first clear evidence that the dominant growth mode of the hard sphere colloid is dendritic. In the following section we study why this phenomena is related to  $\mu g$  and whether the crystalline growth is intrinsically unstable.



◀ **In Microgravity**  
In the low gravity environment of space, the spheres remain evenly dispersed in the cell and large crystallites formed in many of the samples. The shapes of many of these large crystallites indicate dendritic growth.

▲ **On Earth**

Gravity-driven sedimentation produces a volume fraction gradient from top to bottom. The liquid phase at the top appears transparent while crystallites can be observed in the lower portion of the cell.

In comparing the effects of gravity to thermal processes, whether equilibrium or kinetic, a relevant quantity is the gravitational length,  $h = kT/mg$  ( $\sim 6\mu$  or 12 particle diameters for our particles), the height over which thermal energy can support a particle. Now consider nucleation and growth in the presence of gravity. If the solid phase is energetically favored then fluctuations can produce a crystallite in the liquid phase which will grow if it is larger than the critical nucleation radius. The crystalline droplet has a higher density than the surrounding fluid and will begin to sediment. The Stokes drag on the crystallite produces a stress proportional to the weight and inversely proportional to the cross section. When this stress exceeds the yield stress  $\sigma_{crit}$  of the crystallite, then the surface (and particularly any dendrites) will be sheared off. The condition can be written as  $\frac{\Delta Mg}{4\pi R^2} = \sigma_{crit} \sim G \sim \frac{\alpha kT}{a^3}$ ,  $\Delta M = \frac{4}{3}\pi R^3 \Delta\phi\Delta\rho$ , where  $\Delta\rho$  is the density difference between PMMA and the solvent,  $\Delta\phi$  is the volume fraction difference between liquid and solid in coexistence,  $\alpha$  is a constant of order unity,  $G$  is the shear modulus and the yield stress is taken in its limiting form relative to  $G$ . The upper limit for the size of freely sedimenting crystals is then:

$$R_{crit} = \frac{\alpha kT}{\frac{4}{3}\pi a^3 g \Delta\phi \Delta\rho} = \frac{h}{\Delta\phi} \sim 20h$$

which amounts to about  $100\mu$  for our samples.

A more severe limitation on the observation of dendritic growth relates to whether the particle flux around the sedimenting crystallite is determined by convection or diffusion. This ratio is the Peclet number which for a single particle is simply the ratio of the particle radius to the gravitational length:

$$Pe_0 = \frac{vl}{D} = \frac{\left(\Delta\rho g \frac{4}{3}\pi a^3 / 6\pi\eta a\right)a}{kT/6\pi\eta a} = \frac{mga}{kT} = \frac{a}{h}$$

For a falling crystallite of dimension  $R$  the Peclet number becomes:

$$Pe_{crist} = \frac{\left(\Delta\rho g \frac{4}{3}\pi R^3\right)\Delta\phi / 6\pi\eta R}{kT/6\pi\eta R} R = \frac{a}{h} \frac{R^4}{a^4} \Delta\phi = Pe_0 \Delta\phi \frac{R^4}{a^4}$$

Thus in order to observe dendritic growth at one  $g$  we would be limited to growth below

$$Pe_{crist} \sim 1 \Rightarrow R_{crit} = a \left(\sqrt[4]{h/a\Delta\phi}\right) \sim 5a$$

We would expect dendrites to anneal from both self and gradient diffusion processes. The characteristic times for these processes vary as  $\frac{1}{\tau} \propto \frac{D_s}{R^2}$  and  $\frac{1}{\tau} \propto \frac{\gamma}{\eta R}$  where  $D_s$  is the self diffusion constant and  $\gamma$  is the surface tension. For our parameters self diffusion dominates and leaves structures of dimensions  $100\mu$  rough (unannealed) after three days.

#### Ackerson and Schatzel Growth Model

In order to model their pioneering experiments of the growth of hard sphere colloidal crystals Ackerson and Schatzel[3] wrote down the following equations governing the growth of the interface separating solid and liquid regions and solved them numerically for a spherical droplet.

$$\Pi_s(\phi_s) = \Pi_f(\phi_f) + \frac{2\gamma}{R} \quad \text{pressure balance}$$

$$\frac{dR}{dt} = \alpha \left[ \frac{D_s(\phi_f)}{2a} \right] \left[ 1 - \exp\left( \frac{(\mu_f(\phi_f) - \mu_s(\phi_s))}{kT} \right) \right] \quad \text{growth kinetics}$$

$$\frac{dR}{dt} (\phi_s - \phi_f) = n \cdot [D_c^f \nabla \phi_f - D_c^s \nabla \phi_s] \quad \text{flux balance}$$

Briefly, the first equation equates the osmotic pressure inside the droplet to the exterior pressure plus the Laplace pressure generated by the curvature  $1/R$ , and the surface tension  $\gamma$ . The second term weights the rate at which particles collide with the surface by the sticking probability. The third term says that the additional particle density accumulating at the growing interface is supplied by the net particle diffusion to the interface from the neighboring fluid and solid regions. These equations are then combined with the continuity equations in the solid and fluid phases.

$$\frac{\partial \varphi_s}{\partial t} = \nabla \cdot (D_c^s(\varphi_s) \nabla \varphi_s) \quad \frac{\partial \varphi_f}{\partial t} = \nabla \cdot (D_c^f(\varphi_f) \nabla \varphi_f)$$

These equations bear resemblance to the equations often used in the study of the dendritic instability:  $\frac{dR}{dt}(\varphi_s - \varphi_f) = n \cdot [D_c^f \nabla \varphi_f - D_c^s \nabla \varphi_s]$  and  $\mu - \mu_{equil} = -\frac{\gamma}{\Delta C} \kappa$  where  $\kappa$  is the local curvature. The second equation is the Gibbs-Thomson relation which is an approximation to the actual pressure discontinuity and the actual chemical potential equality for equilibrium. The growth kinetics are absent in this model under the assumption that the kinetic coefficient is so large the growth rate is self consistently limited by the Gibbs-Thomson relation which controls the the growth exponential.

With dimensionless definitions for kinetic coefficient,  $\delta = l D_s^0 / 2a D_0$ , critical radius,  $l = \frac{8\pi\gamma a^3}{3\varphi_s(\mu_f - \mu_s)}$ , chemical

potential,  $\mu = \mu/kT$ , and surface tension  $K = \gamma a^3 / l kT$  and with cooperative diffusion at high volume fraction approximately equal to the Stokes-Einstein diffusion constant we have the dimensionless growth equations as:

$$\begin{aligned} \Pi_s &= \Pi_f + 2\kappa K \\ \frac{dX}{dt} &= \delta [1 - e^{\Delta\mu}] \\ \frac{dX}{dt} &= \frac{n \cdot [D_c^f \nabla \varphi_f - D_c^s \nabla \varphi_s]}{(\varphi_s - \varphi_f)} \end{aligned}$$

The nature of the growth process depends only on the initial volume fraction  $\phi_0$  and particularly on the depth to which the sample is quenched into the solid phase as characterized by the undercooling parameter  $\Delta = \frac{\varphi_0 - \varphi_{freeze}}{\varphi_{melt} - \varphi_{freeze}}$ . Here  $\varphi_{freeze}$

is the lowest volume fraction at which hard spheres start to form crystals from the liquid ( $\varphi_{freeze}=0.49$ ) and  $\varphi_{melt}$  is the highest volume fraction at which the crystal phase begins to melt ( $\varphi_{melt}=0.54$ ). Physically the "quench" is accomplished by forcing the sample into the fluid state by vigorous shear melting. Generally we[5] follow the spirit of the treatments of Ackerson and Schatzel[3] and Langer[4]. With the dimensionless growth equations and the boundary conditions:

$$\varphi_s(0, \tau) = const, \quad \varphi_f(\infty, \tau) = \varphi_0, \quad \varphi_f(\rho, 0) = \varphi_0, \quad \rho > 1$$

there are pseudo-steady solutions corresponding to rapid growth for large undercooling ( $\Delta \gg 1$ , a quench deep into the solid regime) and slow growth (for  $\Delta < 1$ , in the coexistence region near the fluid phase).

The profile for rapid growth is described by:

$$\varphi_s = \varphi_{si} = \varphi_0, \quad \varphi_f \approx \varphi_0 - (\varphi_0 - \varphi_{fi}) e^{-\frac{dX}{dt}(p-x)}, \quad \frac{dX}{dt}(\varphi_{si} - \varphi_{fi}) = \nabla \varphi_f - \nabla \varphi_s = \frac{dX}{dt}(\varphi_0 - \varphi_{fi})$$

and is illustrated in figure 2 left. The equation and profile are the same as for a plane interface.

The profile for slow growth is described by:

$$\varphi_f \approx \varphi_0 - (\varphi_{freeze} - \varphi_{f0}) \frac{X}{\rho}, \quad X^2 = 2\Delta t$$

$$\frac{dX}{dt}(\varphi_{\text{melt}} - \varphi_{\text{freeze}}) = \nabla \varphi_f = \frac{-X}{\rho^2}(\varphi_{\text{freeze}} - \varphi_0) = \frac{(\varphi_0 - \varphi_{\text{freeze}})}{X}$$

$$\frac{XdX}{dt} = \frac{\varphi_0 - \varphi_{\text{freeze}}}{\varphi_{\text{melt}} - \varphi_{\text{freeze}}} = \Delta$$

and is illustrated in figure 2 right.

### Rapid Growth

### Slow Growth

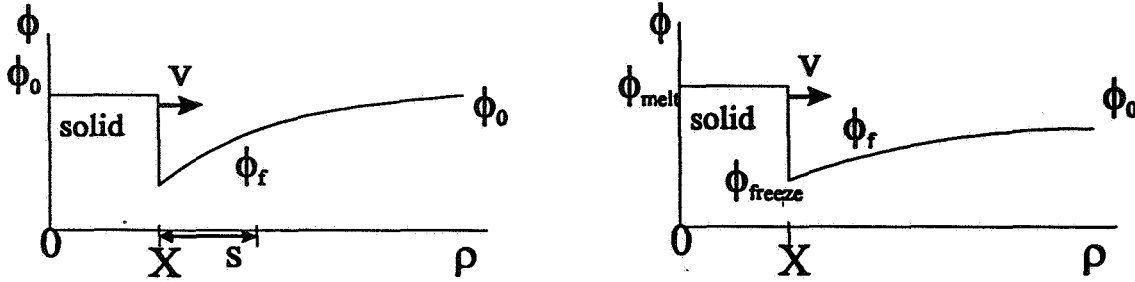


Fig. 2 Volume fraction (concentration) profiles for the pseudo steady solutions to the spherical growth model of references[3] and [5]. Left for rapid growth (strong undercooling). Right for slow growth.

These solutions describe the growth of spherical crystallites. We wish to see whether they are linearly stable to a perturbation which distorts the surface as a spherical harmonic.

The surface is taken as:  $\rho = x + \varepsilon Y_{jm}(\Theta, \Phi)e^{\omega_j t}$ . The volume fraction is perturbed with a similar symmetry and a coefficient  $\phi_j^1$  for which we must self consistently solve.

$$\varphi = \varphi^0(\rho, \tau) + \varepsilon \phi_j^1(\rho, \tau) Y_{jm}(\Theta, \Phi) e^{\omega_j t} \text{ the curvature is } \nabla^2 Y_{jm} = -\frac{j(j+1)Y_{jm}}{X^2}$$

or "rapid growth" the rate at which the perturbation develops,  $\omega_j$ , is given

$$\text{by: } \omega_j = \frac{j}{X} \dot{X} \left\{ 1 - \frac{K}{\Delta \varphi \Pi_s \dot{X}} \frac{j^2}{X^2} \frac{\pi'_j / \varphi_f + \pi'_j / \varphi_s}{\pi'_j / \varphi_f - \pi'_j / \varphi_s} \right\} \text{ or } \omega_j = kv \frac{l^2}{D_0} \left\{ 1 - (1 + \beta) k^2 \frac{D_0 \gamma}{v(\Delta C)^2 (\partial \mu / \partial c)} \right\} \text{ with } kl = j/X$$

which is the same form in detail as the Mullins-Sekerka instability. Likewise for "slow growth" the perturbation develops

$$\text{with rate: } \omega_j = \frac{(j-1)}{X} \dot{X} \left\{ 1 - \frac{(J+2)}{\Delta \varphi \Pi_s \dot{X}} \frac{K}{X^2} \frac{\pi'_j / \varphi_f + (j+1)\pi'_j / \varphi_s}{\pi'_j / \varphi_f - \pi'_j / \varphi_s} \right\} \text{ or}$$

$$\omega_j = (j-1) \frac{v}{R} \left\{ 1 - \frac{((1+\beta)j+1)(j+2)}{R^2} \frac{D_0 \gamma}{v(\Delta C)^2 (\partial \mu / \partial c)} \right\} \text{ with } v = \dot{X} \frac{D_0}{l} \text{ and } \beta = \frac{\pi'_j / \varphi_f}{\pi'_j / \varphi_s} \text{ which is the same as for the}$$

simpler growth model and is unstable when the crystallite grows to more than about 7 critical radii or about  $49a \sim 13\mu$  for our samples.

These results indicate that the spherical growth is linearly unstable to the formation of a modulated surface early in the growth. Presumably these modulations will develop into the dendritic arms which we observe. However, as in most cases of dendritic growth, the characteristic size of the dendrites is determined by the growth velocity which depends itself on the

finger width typically as:  $v_R = \frac{D}{R} \left( \Delta - \frac{2d_0}{R} \right)$ . The equations allow for a variety of velocities and tip radii. If we take the

Glickman result that  $v \sim v_{\max}/50$  and use the number shown in table 1 we find that the dendrite size is  $\lambda \sim 140\mu$  as in our CDOT experiment.

Table 1. definitions and values for lengths used in the dendritic growth calculations

	Definition	value at $\phi=0.52$ $a=\text{particle}$ radius
critical nucleus	$\frac{\Gamma^*}{a} = \frac{8\pi\gamma a^2}{3\phi_s(\mu_f - \mu_s)}$	$\sim 7a$
capillary length	$d_0 = \frac{\gamma}{(\Delta C)^2 \left( \frac{\partial \mu}{\partial C} \right)}$	$\sim 2a$
diffusion length	$l = \frac{2D}{v} \sim \frac{2D_c(\phi)}{\left( D_s(\phi) / 2a \right) (1 - e^{-\Delta\mu/kr})}$	$> 80a$
dendrite size	$\lambda = 2\pi\alpha\sqrt{ld_0}$	$\sim 80a \quad \sim 20\mu$

### Conclusions

In this paper we have addressed a few of the aspects of the CDOT experiment concentrating on the dendritic growth. We also observed that all of the samples which were supposed to be in the glassy state, and never crystallized on the ground, did form crystals in orbit. The static light scattering exhibited very strong narrow "streaks" indicating large crystallites with a RHCP structure and none of the FCC observed on ground. The absence of a glass phase or an FCC phase are unexpected effects of  $\mu g$  which deserve further attention and point to some very subtle effects of gravity on crystal nucleation and growth.

Research supported by NASA under grant NAG3-1762.

### References

- [1] K. Schatzel and B. J. Ackerson, Phys. Rev. Lett. **68**, 337 (1992).
- [2] A. P. Gast and Y. Monovoukas, Nature, **351**, 553 (1991).
- [3] B. J. Ackerson and K. Schatzel, Phys. Rev. **B52**, (1995).
- [4] J. S. Langer, Rev. Mod. Phys. **52**, 1 (1980).
- [5] W. B. Russel et al., to be published.



# DYNAMIC LIGHT SCATTERING FROM COLLOIDAL GELS

A.H. Krall and D.A. Weitz

*Department of Physics and Astronomy  
University of Pennsylvania  
209 S33 rd St.  
Philadelphia, PA 19104-6396*

## Abstract

We present a brief, preliminary account of the interpretation of dynamic light scattering from fractal colloidal gels. For small scattering angles, and for high initial colloid particle volume fractions, the correlation functions exhibit arrested decay, reflecting the non-ergodic nature of these systems and allowing us to directly determine the elastic modulus of the gels. For smaller initial volume fractions, the correlation functions decay completely. In all cases, the initial decay is not exponential, but is instead described by a stretched exponential. We summarize the principles of a model that accounts for these data, and discuss the scaling behavior of the measured parameters.

When colloidal particles are destabilized and made to aggregate, highly tenuous and disordered structures result. However, despite their disorder, the structure of these colloidal aggregates can be quantitatively described as fractals, allowing relatively simple yet quantitative characterization of their structure [1]. In particular, the growth of their mass with their size follows a power law,  $M \sim R^{d_f}$ , where the exponent is the fractal dimension,  $d_f$ , which characterizes the structure, and reflects how tenuous it is; a lower fractal dimension corresponds to a more tenuous structure. The scaling behavior of fractal aggregates is not limited to their structure; fractal objects are also predicted to have other scaling properties. For example, their internal dynamics should also exhibit scaling properties, but should be sensitive to a different scaling exponent reflecting the connectivity of the structure [2]. Thus, measurement of the internal dynamics of fractal objects should provide both new information about their properties as well as their structure.

An ideal experimental method for studying the internal dynamics of a colloidal aggregate is dynamic light scattering. It probes the motion of an object over length scales comparable to the wavelength of light, which is ideal for the internal dynamics of colloidal aggregates. Unfortunately, however, dynamic light scattering probes all motion of the aggregates, and the normal contribution due to the diffusive motion of the aggregates dominates all other contributions, precluding the measurement of their internal dynamics [3]. However, if the aggregates can be held rigidly in place, and not allowed to undergo translational diffusion, the remaining dynamics would allow the determination of their internal dynamics. This is possible by exploiting a unique property of colloidal aggregates; since their density decreases as their size grows, if a colloid system is allowed to aggregate,

and if it continues to form fractal structures indefinitely, the aggregates will ultimately fill all space to form a colloidal gel [4]. This will pin the individual aggregates in place, allowing dynamic light scattering to be used to measure their internal dynamics. To form such gels, it is essential for the fractal aggregates to continue to grow unimpeded. The major limitations to continued growth is the sedimentation of the aggregates as their mass increases. This can be reduced by slowly tumbling the sample, but true gelation is still not observed. There is, however, one system that can be made to gel. This is polystyrene latex particles; their density is only about 5% above that of water, and thus they can be buoyancy matched by the addition of heavy water to the solution, obtaining isopicnic conditions [4]. This allows colloidal gels to be made and their properties to be studied.

Ultimately, the challenge will be to adjust the important parameters of these colloidal gels. These include the strength of the bonds between the individual particles, which must scale the overall strength and properties of the fractals, and the scattering properties of the individual particles, which determine the range over which they can be studied using light scattering. The control of these different features will require the use of different materials. For example, one fundamental question to be addressed is whether there is a fundamental limit on the extent of a fractal cluster, and hence on the lowest initial volume fraction of particles that can be used to form a gel. The experimental limitation in the investigation of this question is the time it takes for the gel to form. Since the gelation is ultimately limited by diffusion, and since the diffusion coefficient of the growing clusters decreases as their radius increases, the gelation time increases rapidly as the initial volume fraction is decreased, and can soon exceed any reasonable length of experiment. However, the gelation time also depends on the size of the initial particles, and much lower initial volume fractions can be explored using very small colloidal particles. In addition, because their scattering cross section is reduced, the use of very small particles will also allow higher initial volume fractions to be studied with light scattering without running into the problems of multiple scattering. A particularly useful material to use to meet these criteria is silica, which is available in the form of very small particles. Finally, for the study of very low volume fraction gels, it will also become essential to use particles that have very strong interparticle bond strengths, and metallic particles may provide the optimum choice. However, both the silica and the metallic particles are too dense to allow them to be buoyancy matched. Thus, these studies must be performed in microgravity. The study of the properties of these gels will be accomplished using light scattering, and thus it is essential to establish the theoretical underpinnings for the correct interpretation of the light scattering by using gels made with buoyancy matched polystyrene. Here, we summarize

some preliminary results of these studies, and will provide a more complete account elsewhere [5].

We use polystyrene colloids with a radius of  $a = 9.5$  nm, suspended in a mixture of H<sub>2</sub>O and D<sub>2</sub>O to buoyancy match the particles as much as possible. Their aggregation is initiated by adding a solution of MgCl<sub>2</sub> to make the final concentration 6 mM. While the ultimate aggregation process is diffusion-limited, we adjust the salt concentration to slightly slow the rate to allow sufficient time to prepare the sample and study its behavior before it gels. Thus, for the higher initial volume fractions, the aggregation is initially in the reaction-limited regime, although it ultimately becomes limited by diffusion [1]. Our preliminary experiments focus on initial volume fractions of  $1 \times 10^{-4} \leq \phi_0 \leq 5 \times 10^{-3}$ , and measurements performed after the sample had been allowed to aggregate for several days, so that the properties no longer changed with time, and a gel had been formed. We measure the intermediate structure factor,  $f(q, t)$ , as a function of scattering wave vector,  $q$ , properly performing an ensemble average where required. We find that the method suggested by Pusey and van Megen [6] was preferable to that used by Xue et al [7], as the former method enabled decays at longer time scales to be discerned, limited only by the total measurement time, rather than by the rotation rate.

The measured  $f(q, t)$  depend strongly on the initial volume fraction of the particles, and on the scattering vector. For the higher concentrations, the samples were non-ergodic for all  $q$ , in that  $f(q, t)$  did not decay to zero. By contrast, as the initial volume fraction decreased, the total decay in  $f(q, t)$  increased, with the higher  $q$  becoming ergodic first. Finally, for the lowest volume fraction samples,  $f(q, t)$  decayed completely for all scattering wave vectors measured. Interestingly, for all cases, the initial decay of the correlation function was not exponential, but instead was well described by a stretched exponential, decaying as  $\exp[-(t/\tau)^p]$ , where the stretching exponent,  $p$ , was approximately 0.7 and was essentially independent of both  $\phi_0$  and  $q$ . For the lower volume fraction samples, the stretched exponential form provided a good description of  $f(q, t)$  over the full range of its decay. By contrast, for the higher volume fraction samples, it provided a good description only for the early time decay, as  $f(q, t)$  saturated at a non-zero values at longer times.

We found empirically that  $f(q, t)$  could be well fit for all  $q$  and all  $\phi_0$  using a functional form reminiscent of that which describes a harmonically bound Brownian particle. Thus, we fit the data to

$$f(q, t) = \exp \left\{ -q^2 \delta^2 \left[ 1 - e^{-(t/\tau)^p} \right] \right\} \quad (1)$$

where the characteristic decay time,  $\tau$ , and the maximum excursion,  $\delta^2$ , were used self-consistently as fitting parameters for each value of  $\phi_0$ . This described the data quite well.

Although empirical, this functional form can be derived with a simple model that describes the dynamics of a fractal aggregate [5]. We assume that the scattering probes the motion of small subunits within each aggregate, of size  $q^{-1}$ . The motion of each of these subunits is determined by the total motion of all the other portions of the aggregate to which it is attached, up to the motion of largest fractal cluster which makes up the gel. Because of the contribution of motions of many different length scales, the initial decay is comprised of many different time scales, leading to the observed non-exponential behavior. By performing an appropriate sum over all the contributions, we find a functional form that is empirically similar to Eq. (1). The value of the stretching exponent depends on  $d_s$ , the bond or connectivity fractal dimension, which determines the scaling of the connected regions [2]. Thus, this provides the only experimental measure of this dimension for a colloidal gel. When  $f(q,t)$  does not decay to zero, the extent of the total decay,  $\delta^2$ , provides a measure of the effective spring constant of the gel,  $\kappa = k_B T / \delta^2$  [7]. This spring constant also determines the effective time constant of the decay, provided we know the size of the characteristic cluster in the gel,  $R_c$ . This can be determined directly from the position of the peak of the ring of the static scattering pattern; alternatively this can be calculated from the initial volume fraction of particles, assuming that the gelation process is diffusion-limited cluster aggregation [4]. Then, the time constant is given by  $\tau = 6\pi\eta R_c / \kappa$ . Thus, both the time constant and the spring constant of the colloidal gel are determined. Finally, we can also determine the elastic modulus of the gel; it is related to the spring constant through an additional length scale, which we again take as the characteristic cluster size, giving  $G = \kappa / R_c$ .

An important question about the scaling of these quantities is their dependence on  $\phi_0$ . We can directly determine the scaling of the modulus for those gels whose correlation functions are non-ergodic, allowing  $\delta^2$  to be measured. For the lower volume fraction samples, we can only determine the time constant, and from it infer the modulus. We find that the modulus scales as  $G \sim \phi_0^{3.9}$ , which is consistent with expectations. This is the first experiment measure of this scaling behavior for these low volume fraction colloidal gels. In addition, this establishes our ability to measure the mechanical properties of colloidal gels through light scattering alone. This is of particular importance as the moduli of the colloidal gels become very weak and mechanical measurement would be strongly biased by the contribution of the surrounding fluid, making it difficult to measure the contributions of the colloidal gel network itself.

These light scattering experiments establish the essential theoretical basis required to interpret the dynamic light scattering from colloidal gels. This will enable these studies to be performed in microgravity. Furthermore, it will be possible to use light scattering measurements, rather than mechanical measurements, to determine the elastic modulus of these colloidal gels.

We thank Robin Ball, Mike Cates and Tom Witten for useful discussions and suggestions. Z. Huang performed some of the measurements.

## References

1. M.Y. Lin, H.M. Lindsay, D.A. Weitz, R. Klein, R.C. Ball and P. Meakin, *Proc. Roy. Soc. London A* **423**, 71 (1989).
2. Y. Kantor and I. Webman, *Phys. Rev. Lett.* **52**, 1891 (1984).
3. D.A. Weitz, J.S. Huang, M.Y. Lin and J. Sung, *Phys. Rev. Lett.* **54**, 1416 (1985).
4. M. Carpineti and M. Giglio, *Phys. Rev. Lett.* **68**, 3327 (1992).
5. A. Krall and D.A. Weitz, *to be published*.
6. P.N. Pusey and W. van Megen, *Physica A* **157**, 705 (1989).
7. J.-Z. Xue, D.J. Pine, S.T. Milner, X.-L. Wu and P.M. Chaikin, *Phys. Rev. A* **46**, 6550 (1992).



**Structure, hydrodynamics, and phase transition  
of freely suspended liquid crystals**

Noel Clark, University of Colorado

**Paper not available**





**Behavior of rapidly sheared bubbly suspensions**

Ashok Sangani, Syracuse University

**Paper not available**



# POLYMER-INDUCED DEPLETION INTERACTION AND ITS EFFECT ON COLLOIDAL SEDIMENTATION IN COLLOID-POLYMER MIXTURES

Penger Tong

Department of Physics, Oklahoma State University, Stillwater, OK 74078

The study of motions of small particles suspended in a fluid has always been an interesting subject in physics.<sup>1</sup> The dynamics of the particles is determined by the statistical properties of the random forces resulting from interactions between the particle and the surrounding fluid molecules. Brownian diffusion of small particles in a fluid at thermal equilibrium is one of the classical and best understood examples. Sedimentation, wherein heavy particles fall under the action of gravity through a fluid in which they are suspended, on the other hand, represents a "self-induced hydrodynamic diffusion".<sup>2</sup> The character of the sedimentation depends upon the interplay between long-range hydrodynamic forces, random Brownian forces and direct inter-particle forces.<sup>3</sup> The main objectives of our NASA research projects carried out at Oklahoma State University are: (1) study motions of colloidal particles under different random forces in the carrier fluid, and (2) understand the effect of gravity on the particle motion when the density of the particles is different from the carrier fluid.

In this paper we focus on the polymer-induced depletion attraction and its effect on colloidal sedimentation in colloid-polymer mixtures. We first report a small-angle neutron scattering (SANS) study of the depletion effect in a mixture of hard-sphere-like colloid and non-adsorbing polymer. Then we present results of our recent sedimentation measurements in the same colloid-polymer mixture. A key parameter in controlling the sedimentation of heavy colloidal particles is the inter-particle potential  $U(r)$ , which is the work required to bring two colloidal particles from infinity to a distance  $r$  under a given solvent condition. This potential is known to affect the average settling velocity of the particles,<sup>3</sup> and experimentally one needs to have a way to continuously vary  $U(r)$  in order to test the theory. The interaction potential  $U(r)$  can be altered by adding polymer molecules into the colloidal suspension. In a mixture of colloid and non-adsorbing polymer, the potential  $U(r)$  can develop an attractive well because of the depletion effect<sup>4</sup>, in that the polymer chains are expelled from the region between two colloidal particles when their surface separation becomes smaller than the size of the polymer chains. The exclusion of polymer molecules from the space between the colloidal particles leads to an unbalanced osmotic pressure difference pushing the colloidal particles together, which results in an effective attraction between the two colloidal particles. The polymer-induced depletion attraction controls the phase stability of many colloid-polymer mixtures, which are directly of interest to industries.

It has been shown that the potential  $U(r)$  has the form<sup>4</sup>

$$U(r) = \begin{cases} +\infty & r \leq \sigma \\ -\Pi_p V_0(r) & \sigma < r \leq \sigma + 2R_g \\ 0 & r > \sigma + 2R_g \end{cases} \quad (1)$$

where  $\sigma$  is the particle diameter,  $\Pi_p$  is the osmotic pressure of the polymer molecules, and  $R_g$  is their radius of gyration. The volume of the overlapping depletion zones between the two colloidal particles is given by<sup>4</sup>

$$V_0(r) = v_p \left( \frac{\lambda}{\lambda - 1} \right)^3 \left[ 1 - \frac{3}{2} \left( \frac{r}{\sigma\lambda} \right) + \frac{1}{2} \left( \frac{r}{\sigma\lambda} \right)^3 \right], \quad (2)$$

where  $v_p = (4\pi/3)R_g^3$  is the volume occupied by a polymer chain and  $\lambda = 1 + 2R_g/\sigma$ . In the experiment, we measure the colloidal (partial) structure factor,  $S_c(Q)$ , which is directly related to the interaction potential  $U(r)$ . An advantage of using SANS is that one can eliminate the undesirable scattering from the polymer chains by using isotopically mixed solvents. (In the discussion below the subscripts c and p will be used to refer to colloid and polymer, respectively.)

The colloidal particles used in the experiment consisted of a calcium carbonate ( $\text{CaCO}_3$ ) core with an adsorbed monolayer of a randomly branched calcium alkylbenzene sulphonate surfactant. These particles have been well characterized previously using SANS and small-angle X-ray scattering (SAXS) techniques.<sup>5</sup> Our recent SANS and SAXS measurements revealed that the particle has a core radius,  $R_0 = 2.0 \text{ nm}$ , and a monolayer thickness,  $\delta = 2.0 \text{ nm}$ . Previous dynamic light scattering experiment<sup>6</sup> has shown that the colloidal particles are relatively monodispersed with  $\sim 10\%$  standard deviation in particle radius. The polymer used in the study was hydrogenated polyisoprene (poly-ethylene-propylene or PEP), a stable model polymer. The molecular weight of the PEP was  $M_p = 26,000$ . Decane has been found to be a good solvent for both the colloid and PEP.<sup>6</sup> Because decane and PEP are both protonated, the polymer chains in the mixture are invisible to neutrons. Our Zimm analysis of the SANS data from the pure PEP/deuterated-decane solution has shown that the polymer chains have a radius of gyration  $R_g = 8.3 \text{ nm}$  and their second virial coefficient  $A_2M_p = 44.4 \text{ (cm}^3/\text{gm)}$ . With the measured  $A_2$  one can define an effective hard sphere radius  $R_{hs}$  via  $4(4\pi/3)R_{hs}^3 = A_2M_p^2$ . Thus we have  $R_{hs} = 4.8 \text{ nm}$ , which agrees well with our previous light scattering measurement.<sup>6</sup> The light scattering experiment has revealed that the PEP chains do not adsorb onto the colloidal surfaces, and the phase separation in the colloid-PEP mixture samples occurs at the concentrations very close to the depletion prediction.<sup>6</sup> Because the basic molecular interactions are tuned to be simple, the SANS measurements in the colloid-PEP mixture can be used to critically examine the current depletion theory. The SANS measurements were performed at the High Flux Beam Reactor in the Brookhaven National Laboratory. The incident neutron wavelength  $\lambda_0 = 7.05 \pm 0.4 \text{ \AA}$ , and the usable range of the scattering wave number  $Q [= (4\pi/\lambda_0)\sin(\theta/2)]$ , with  $\theta$  being the scattering angle] was  $0.007 \text{ \AA}^{-1} \leq Q \leq 0.15 \text{ \AA}^{-1}$ . The structure factor  $S_c(Q)$  was obtained using the equation  $S_c(Q) = I(Q)/[\rho_c P_c(Q)]$ , where  $I(Q)$  is the scattered intensity of the mixture samples,  $\rho_c$  is the colloid number density, and  $P_c(Q)$  is the scattering intensity per unit concentration measured in a dilute pure colloidal suspension, in which  $S_c(Q) = 1$ . All the scattering measurements were conducted at room temperature.

To reduce the fitting ambiguity and pinpoint the control parameters for the depletion effect we prepared three series of mixture samples with the colloid volume fraction  $\phi_c = 0.146, 0.08$  and  $0.038$ , respectively. For each series of the samples,  $\phi_c$  was kept the same and the polymer concentration  $C_p \text{ (gm/cm}^3\text{)}$  was increased until the mixture became phase separated (except for the series with  $\phi_c = 0.038$ ) with a visible interface, which separates the dark brown colloid-rich phase from the light brown colloid-poor phase. Fig. 1 compares the measured  $S_c(Q)$  for three values of  $C_p$  when (a)  $\phi_c = 0.146$  and (b)  $\phi_c = 0.086$ . It is seen that the main effect of adding PEP into the colloidal suspension is to increase the value of  $S_c(Q)$  in the small- $Q$  region, whereas the large- $Q$  behavior of  $S_c(Q)$  remains nearly unchanged. The solid curves in Fig. 1 show the calculated  $S_c(Q)$  using  $U(r)$  in Eq. (1). Note that there are four fitting parameters in the calculation: the diameter  $\sigma$ , the volume fraction  $\phi_c$ , the dimensionless interaction amplitude  $\tilde{P} = \Pi_p v_p / k_B T$ , and the range parameter  $\lambda$ . The first two parameters are used to describe the hard core part of  $U(r)$  and the last two parameters are used for the attractive tail. It is found from the fitting that for a fixed colloid concentration, the fitted values of  $\sigma$  and  $\phi_c$  for the mixture samples do not change

very much with  $C_p$ , and they are very close to those obtained from the corresponding pure colloidal suspensions. Furthermore, the fitted  $\lambda$  also remains constant for different  $\phi_c$  and  $C_p$ , and its best fit value is  $\lambda = 2.9$ . This value is close to the calculated  $\lambda = 1 + R_g/(R_0 + \delta) = 3.07$ . With the above three fitting parameters fixed, we were able to fit all the scattering data from different mixture samples (19 samples in total) with only one free parameter - the interaction amplitude  $\tilde{P}$ .

Figure 2a shows the fitted  $\tilde{P}$  as a function of the effective polymer volume fraction  $\phi_p = C_p/C^*$ , where  $C^* = M_p/[(4\pi/3)R_g^3]$  is the polymer overlap concentration. It is seen that  $\tilde{P}$  first increases linearly with  $\phi_p$  up to  $\phi_p \simeq 1$  and then it levels off. For a given  $\phi_p$ ,  $\tilde{P}$  also depends upon  $\phi_c$ . If the polymer molecules in the mixture are treated as an ideal gas, their osmotic pressure  $\Pi_p = n_p k_B T$  and hence  $\tilde{P} = \Pi_p v_p / (k_B T) = \phi_p$ . Recently, Lekkerkerker et al.<sup>7</sup> pointed out that the polymer number density  $n_p$  should be defined as  $n_p = N_p/V_f$ , where  $N_p$  is the total number of the polymer molecules and  $V_f = \alpha(\phi_c)V$  is the free volume not occupied by the colloidal particles and their surrounding depletion zones. They have calculated  $\alpha(\phi_c)$  as a function of  $\phi_c$ . It is seen from Fig. 2b that once  $\phi_p$  is scaled by the calculated  $\alpha(\phi_c)$ ,<sup>8</sup> the three curves in Fig. 2a collapse into a single master curve. The solid curve in Fig. 2b is the fitted function  $\tilde{P} = -0.054 + 0.178(\phi_p/\alpha) - 0.0245(\phi_p/\alpha)^2$ .

The fitted  $\tilde{P}$  consists of three terms. The small negative intercept indicates that there is a weak repulsive interaction between the soft surfactant shells of the colloidal particles. (To have a meaningful comparison with the fitted  $\tilde{P}$  for the mixture samples, we used the same  $U(r)$  as in Eq. (1) but change the sign of  $U(r)$  for  $r > \sigma$  to fit the repulsive tail for the pure colloidal samples.) The linear coefficient should be unity for non-interacting polymer chains (an ideal gas), but our fitted value is 0.178. One plausible reason for the deviation is that with the effective potential approach, the polymer molecules are assumed to be smaller than the colloidal particles and their number density should be much higher than that of the colloidal particles. In our experiment, however, these two assumptions are not strictly satisfied, and thereby the overlap volume  $V_0(r)$  in Eq. (2) is over-estimated. As a result, the fitted  $\tilde{P}$  becomes smaller than its actual magnitude, because  $U(r)$  in Eq. (1) is proportional to the product of  $V_0(r)$  and  $\tilde{P}$ . Another possibility is that in calculating  $\phi_p$ , a smaller characteristic length than  $R_g$  should be used for the polymer chains. For example, if  $R_{hs}$  is used to compute  $\phi_p$ , the linear coefficient will be increased by a factor of  $(R_g/R_{hs})^3 \simeq 5.2$ . The polymer-polymer interaction, which gives rise to the quadratic term in the fitted  $\tilde{P}$ , can have two competing effects on the depletion attraction. It may either increase the osmotic pressure (and hence  $\tilde{P}$ ) because the polymer chains have a positive second virial coefficient, or reduce the depletion attraction because it requires the system to do more work to expel the polymer molecules from the depletion zones. Fig. 2b clearly shows that the polymer-polymer interaction tends to reduce the depletion attraction. Similar suppression effects are also found in recent theoretical calculations of the depletion attraction between two parallel plates immersed in an interacting polymer (or particle) solution.<sup>9</sup>

The above SANS measurements clearly demonstrate the effectiveness of using a non-adsorbing polymer to control the magnitude as well as the range of the interaction between the colloidal particles. It is shown that the amplitude of the potential  $U(r)$  is controlled by the polymer concentration  $C_p$ , and the range of  $U(r)$  is proportional to the radius of gyration  $R_g$  of the polymer chains. Because the depletion potential  $U(r)$  can be continuously varied in the experiment, the colloid-PEP mixture becomes an ideal system for the study of the interaction effect on the colloidal sedimentation. In the experiment to be described below, we measure the average settling velocity  $v_c(C_p)$  of the colloidal particles as a function of  $C_p$ . The addition of the polymer molecules into

the colloidal suspension can have two competing effects on  $v_c(C_p)$ . It can either reduce  $v_c(C_p)$  because the viscosity of the mixture solution is increased, or increase  $v_c(C_p)$  because the depletion attraction between the particles is increased. Experimentally, one can separate the two effects by changing the colloid concentration. For sufficiently dilute colloidal mixtures, the distance between the colloidal particles is so large that their mutual interaction can be ignored. In this case, adding polymer into the colloidal suspension only affects the viscosity of the solution. The effect of  $U(r)$  on  $v_c(C_p)$  can be studied in the concentrated colloidal mixtures, once the sedimentation of the individual particles through a polymer solution is understood.

We now discuss the measurements of  $v_c(C_p)$  in the dilute colloidal mixtures. The  $\text{CaCO}_3$  particles have a hydrodynamic radius,  $R_h = 5.0 \text{ nm}$ , and their density  $d_c \simeq 2.0 \text{ gm/cm}^3$ . The density of the PEP is  $d_p = 0.856 \text{ gm/cm}^3$ . The solvent (decane) density is  $d_s = 0.73 \text{ gm/cm}^3$  and its viscosity  $\eta_0 = 0.84 \text{ cp}$  (at  $T = 25^\circ\text{C}$ ). The Stokes velocity of the particle, determined by the balance between the accelerational force and the viscous drag, is

$$v_c(C_p) = \frac{2R_h^2(d_c - d_s)\mathcal{A}}{9\eta_c(C_p)}, \quad (3)$$

where  $\mathcal{A}$  is the acceleration and  $\eta_c(C_p)$  is the viscosity experienced by the colloidal particles in the polymer solution at the concentration  $C_p$ . Because the particles are very small, their sedimentation under earth gravity ( $\mathcal{A} = g$ ) is unobservable. To increase the settling velocity of the particles, we used a commercial ultracentrifuge, Beckman Model L8-70M. The sample cells were made of Ultra-Clear solid polymer and their size (diameter  $\times$  height) was  $14 \times 95 \text{ mm}$ . The distance between the middle of the sample cell and the center of rotation was  $\bar{r} = 11.3 \text{ cm}$ . All the samples were centrifuged at the rotation speed  $f = 35,000 \text{ rpm}$  for 4 to 6 hours depending on the sample viscosity. The corresponding centripetal acceleration  $\mathcal{A} = (2\pi f)^2 \bar{r}$  was  $1.5 \times 10^8 \text{ cm/s}^2$  ( $1.5 \times 10^5 g$ ), which was large enough to cause the colloidal particles to settle 1 to 6 cm towards the bottom of the cell. After the centrifugation, a clear interface could be observed by eye in the initially uniform solution. This interface separated the upper clear solvent region from the lower dark-brown colloid-rich region. The travelling distance  $h$  of the interface was measured by a low-magnification microscope mounted on a translational stage controlled by a micrometer. The settling velocity was computed from the measured  $h$  via  $v_c(C_p) = h/t$ , where  $t$  is the running time. All the measurements were conducted at  $22^\circ\text{C}$ . Because the polymer density is very close to that of the solvent, the sedimentation of the polymer molecules was negligible. Therefore, the colloidal particles settled through a uniform PEP/decane solution at rest. To reduce systematic errors in the experiment, we present the sedimentation data in terms of the velocity ratio  $R_c \equiv v_c(C_p = 0)/v_c(C_p)$ . As shown in Eq. (3),  $R_c = \eta_c(C_p)/\eta_0$  for the dilute colloidal mixtures.

Figure 3 shows the measured  $R_c$  as a function of  $C_p$  at  $\phi_c = 0.014$ . The molecular weight of the PEP was  $M_p = 17,500$  and its  $R_g \simeq 5.8 \text{ nm}$ .<sup>10</sup> It is seen that the measured  $R_c(C_p)$  first increases linearly with  $C_p$  up to  $C_p^c \simeq 0.07 \text{ gm/cm}^3$  and then it turns up sharply. Similar behavior was also observed for the measured  $R_c(C_p)$  with other molecular weights. The crossover concentration  $C_p^c$  is found to be independent of  $M_p$ . With this value of  $C_p^c$ , we estimate the correlation length (or the mesh size) of the polymer solution to be  $\xi \simeq R_g(C_p/C^*)^{-3/4} \simeq 3.5 \text{ nm}$ , which is close to the size of the colloidal particles. The solid curve in Fig. 3 shows the macroscopic viscosity of the same polymer solution measured independently by Davison et al. with a capillary viscometer.<sup>10</sup> The functional form of the solid curve is  $\eta_p/\eta_0 = 1 + [\eta]C_p + k_H([\eta]C_p)^2$ , with the coefficients  $[\eta] = 25 \text{ cm}^3/\text{gm}$  and  $k_H = 0.335$ . The dashed line is the linear plot  $\eta_p/\eta_0 = 1 + [\eta]C_p$ . Fig. 3 thus

reveals that the colloidal particles in the polymer solution feel the single-chain viscosity when their size is smaller than  $\xi$ . The particles experience the macroscopic viscosity of the polymer solution when their size become much larger than  $\xi$ .

We now discuss the effect of the colloidal interaction on  $R_c(C_p)$ . Fig. 4 shows the measured  $R_c$  vs.  $C_p$  for different  $\phi_c$ . It is seen that for the two lowest colloid concentrations ( $\phi = 0.014$  and  $0.02$ ), the measured  $R_c(C_p)$ 's superimpose with each other, indicating that the interaction between the colloidal particles is negligible and thus the velocity ratio  $R_c$  equals the viscosity ratio  $\eta_c(C_p)/\eta_0$ . As  $\phi_c$  increases, the colloidal particles feel more and more depletion attraction and, therefore, their settling velocity at a fixed  $C_p$  is increased ( $R_c$  is reduced). For a fixed  $\phi_c$ , the depletion attraction between the particles also increases with increasing  $C_p$ . Consequently, the colloidal settling velocity is increased. This is seen in Fig. 4 once the effect of increasing viscosity is divided out from the measured  $R_c$  vs.  $C_p$ . For the first time, the experiment provides a quantitative relationship between the settling velocity  $v_c(C_p)$  and the inter-particle potential  $U(r)$ . Further theoretical calculation of  $v_c(C_p)$  using the depletion potential  $U(r)$  is underway. The above measurements reveal a great potential of using sedimentation to measure the interaction between the colloidal particles and other macromolecules in complex fluids.

## ACKNOWLEDGMENT

I gratefully acknowledge the enjoyable collaboration with X. Ye, T. Narayanan, B. J. Ackerson and J. S. Huang. I have benefitted from discussions with T. A. Witten, B. J. Ackerson, J. H. H. Perk, and W. B. Russel. Thanks are also due to D. Schneider, M. Y. Lin, B. L. Carvalho for their assistance with the SANS and SAXS measurements and to L. J. Fetters for providing me the polymer samples. I also acknowledge the Brookhaven National Laboratory for granting neutron beam times. This work was supported by the National Aeronautics and Space Administration under Grant No. NAG3-1613.

## REFERENCES

- <sup>1</sup>see, e.g., J-P. Bouchaud and A. Georges, Phys. Report, **194**, 127 (1990).
- <sup>2</sup>R. H. Davis and M. A. Hassen, J. Fluid Mech., **196**, 107 (1988).
- <sup>3</sup>W. B. Russel, D. A. Saville and W. R. Schowalter, *Colloidal Dispersions* (Cambridge University Press, Cambridge, 1989).
- <sup>4</sup>S. Asakura and F. Oosawa, J. Chem. Phys., **22**, 1255 (1954); A. Vrij, Pure Appl. Chem., **48**, 471 (1976).
- <sup>5</sup>I. Markovic et al., Colloid and Polymer Sci. **262**, 648 (1984); *ibid.*, **264**, 65 (1986); T. P. O'Sullivan and M. E. Vickers, J. Appl. Cryst. **24**, 732 (1991).
- <sup>6</sup>P. Tong, T. A. Witten, J. S. Huang, and L. Fetters, J. Phys. (France), **51**, 2813 (1990).
- <sup>7</sup>H. N. W. Lekkerkerker et al., Europhys. Lett., **20**, 559 (1992); S. M. Ilett et al., Phys. Rev. A, **51**, 1344 (1995).
- <sup>8</sup>In the calculation of  $\alpha(\phi_c)$ , we have used the fitted value of  $\sigma/(2R_g)$ , instead of  $2R_g/\sigma$ , as the size ratio. This is because our polymer chains are larger than the colloidal particles.
- <sup>9</sup>P. B. Warren et al., Phys. Rev. E, **52**, 5205 (1995); Y. Mao et al., Physica A, **222**, 10 (1995).
- <sup>10</sup>N. S. Davison et al., Macromolecules, **20**, 2614 (1987).

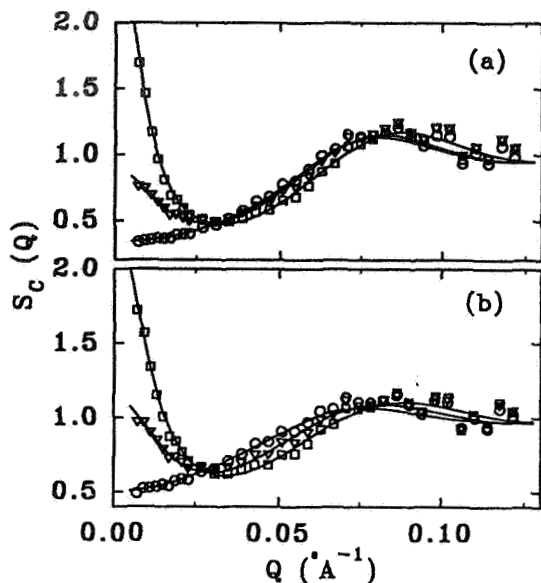


Fig. 1 - Measured  $S_c(Q)$  of the colloid-PEP mixtures for different  $C_p$  when (a)  $\phi_c = 0.146$  and (b)  $\phi_c = 0.086$ . The values of  $C_p$  ( $\text{gm}/\text{cm}^3$ ) in (a) are: 0.0039 (circles), 0.0165 (triangles), 0.0308 (squares), and those in (b) are: 0.0038 (circles), 0.0233 (triangles) and 0.0652 (squares). The solid curves are the calculated  $S_c(Q)$  using  $U(r)$  in Eq. (1).

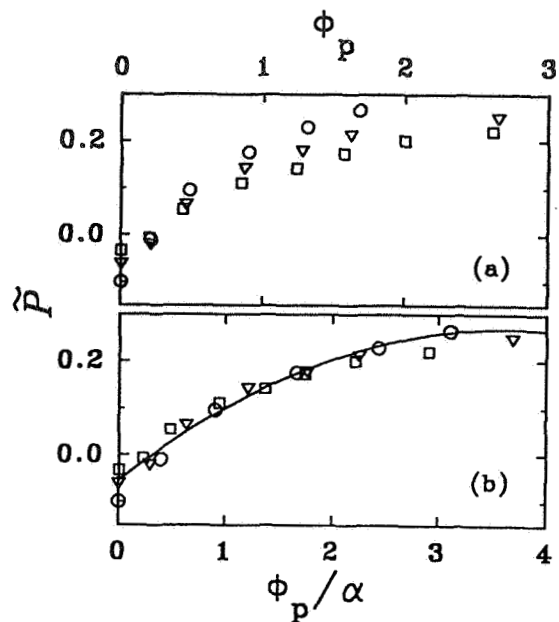


Fig. 2 - Fitted  $\tilde{P}$  as a function of (a)  $\phi_p = C_p/C^*$  and (b)  $\phi_p/\alpha$ . The values of  $\phi_c$  in the mixture samples are: 0.146 (circles), 0.086 (triangles) and 0.038 (squares). The solid curve in (b) is the fitted function  $\tilde{P} = -0.054 + 0.178(\phi_p/\alpha) - 0.0245(\phi_p/\alpha)^2$ .

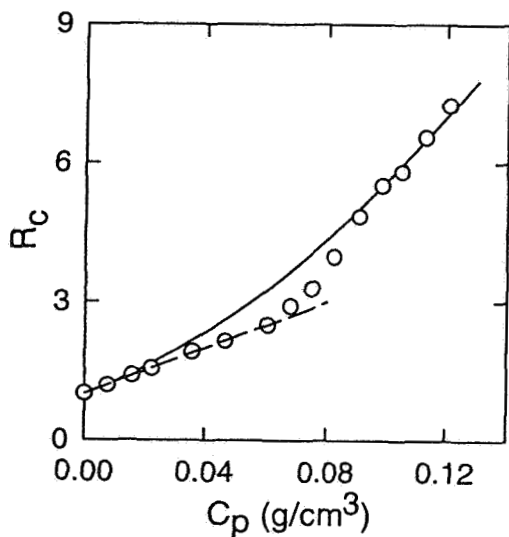


Fig. 3 - Measured  $R_c$  as a function of  $C_p$  at  $\phi_c = 0.014$ . The solid curve is  $\eta_p/\eta_0 = 1 + [\eta]C_p + k_H([\eta]C_p)^2$  with  $[\eta] = 25 \text{ cm}^3/\text{gm}$  and  $k_H = 0.335$ . The dashed line is the linear plot  $\eta_p/\eta_0 = 1 + [\eta]C_p$ .

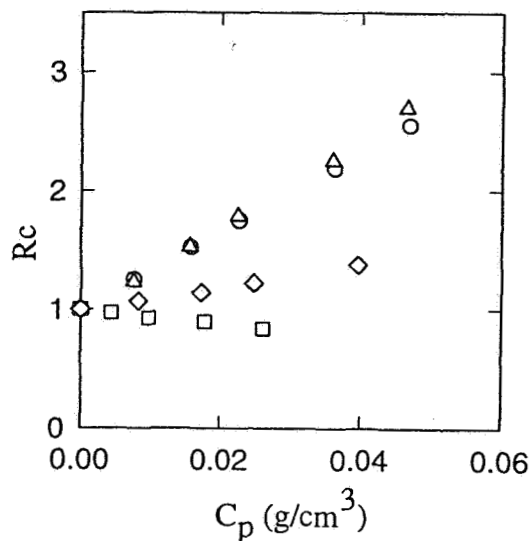


Fig. 4 - Measured  $R_c$  vs.  $C_p$  for different  $\phi_c$ . The values of  $\phi_c$  are: 0.014 (triangles), 0.02 (circles), 0.086 (diamonds), and 0.146 (squares).



## CHIRAL SYMMETRY BREAKING IN CRYSTAL GROWTH IS HYDRODYNAMIC CONVECTION RELEVANT?

B. Martin, A. Tharrington, and X-l. Wu

*Department of Physics, University of Pittsburgh, Pittsburgh, PA 15260*

### ABSTRACT

The effects of mechanical stirring on nucleation and chiral symmetry breaking have been investigated for a simple inorganic molecule, sodium chlorate ( $\text{NaClO}_3$ ). In contrast to earlier findings, our experiment suggests that the symmetry breaking may have little to do with hydrodynamic convection. Rather the effect can be reasonably accounted for by mechanical damage to incipient crystals. The catastrophic events, creating numerous small "secondary" crystals, produce statistical domination of one chiral species over the other. Our conclusion is supported by a number of observations using different mixing mechanisms.

### INTRODUCTION

Question about origins, whether of the Universe, of the Earth or of life, have always held great fascination. One intriguing problem of this type is to explain chiral symmetry-breaking in nature; how for example, it came to be that nearly all the optically active amino acids of biological significance are levo- rather than dextro-rotatory. One of the compelling explanations is the process of auto-catalysis: the enhancement of the rate of growth of a population as that population increases. In the early 90's auto-catalysis was demonstrated for the first time by Kondepudi et al. <sup>1</sup> on crystallization of an inorganic salt in the presence of a hydrodynamic flow. In a simple, yet elegant experiment Kondepudi obtained some interesting data on the distribution of optical activity among crystals precipitating from a supersaturated solution of sodium chlorate under different mixing conditions. The handedness of the crystals was established visually, using crossed polarizers.

What Kondepudi established is the following: (1) When the solution was not stirred, of 1,000 crystals collected from 17 different crystalizations, 525 were of levo (left-handed) and 475 of dextro (right-handed) chirality; that is, the total numbers were statistically equal, as were the numbers in each individual experiment. (2) When the solution was stirred at 100 r.p.m. during the crystalization process, the total numbers for the 11,829 crystals were consistent with a 50-50 distribution of D- and L-crystals. One exception, however, was that each of the 32 individual crystalizations gave rise to a set of crystals that were more than 99% levo- or 99% dextro-rotatory.

This observation is remarkable in that it suggests that the system undergoes a transition from a totally symmetric (achiral) state to a totally asymmetric (chiral) state simply by introducing a hydrodynamic flow, without careful control of temperature and other conditions. The authors attribute the observed selectivity to an autocatalytic effect arising from the rapid production of secondary nuclei from a single primary nucleus in the stirred system. Namely, the first primary nucleus (or micro-crystal) serves as a chiral template which is convected by the flow, triggering secondary nucleations that have the same chirality as the primary one.

Kondepudi's work has stimulated considerable interest in the scientific community. Metcalfe and Ottino have modeled the experiments by a simple autocatalytic reaction scheme combined with a chaotic mixing flow <sup>2</sup>. Due to repetitive stretching and folding of fluid elements chirality initially associated with an incipient seed spreads rapidly throughout the entire system. The symmetry breaking was also considered as one of many examples of imperfect mixing in autocatalytic chemical and biological systems <sup>3</sup>.

Kondepudi's experiment touches upon a number of issues including nucleation, convective diffusion, chaotic mixing, and autocatalysis. All of these are of considerable current interest. However, the experiment also raises many questions that need to be answered before the effect can rest on firm ground. The most pressing question is the physical origin of the secondary nucleation and its relationship to hydrodynamic convection. For this reason we have designed and carried out a series of experiments aimed at better control of interactions between the flow and the precipitated micro-crystals. Two flow geometries are used, mechanical stirring and electro-convection. In the mechanical-stirring experiments each sample contains approximately a single vortex and the flow is chaotic even at low stirring rate. The simple mechanical setup allows mass production of crystals under nearly identical conditions, ensuring adequate counting-statistics. On the other hand, in the electro-convection experiments, large numbers of vortices are generated and the flow characteristics can be tuned continuously. A critical finding of our experiment is that the degree of chiral symmetry breaking depends on the location as well as the speed of the magnetic mixer. In electro-convection, which has no mechanical moving part, there is no chiral symmetry breaking. Our experiment, therefore, suggests that mechanical damage to incipient crystals, rather than hydrodynamic flow, is responsible for the chiral symmetry breaking.

## EXPERIMENTAL

The crystallization experiments were performed using a  $\text{NaClO}_3$  solution with a weight fraction of 50%<sup>4</sup>. The  $\text{NaClO}_3$  was first dissolved in distilled water and constantly stirred at room temperature for 8 hours to ensure complete dissolution of the solute. The solutions were then filtered through a  $0.2\mu\text{m}$  filter before usage. The crystal growth was initiated by slow evaporation. At the given concentration, the nucleation occurs approximately 4-6 hours after the samples were prepared, and this time interval appears to be independent of the flow rate. In the experiments the crystals were grown to an average size of  $\sim 1\text{ mm}$ ; this takes an additional a couple of hours for quiescent samples and less than an hour for stirred samples.

Crystals of different chiralities can be distinguished by their optical activity. A right-handed crystal will rotate polarized light clockwise while a left-handed crystal will rotate light counter-clockwise. A long-working-distance microscope with a pair of polarizers allows us to visually determine the handedness of the crystals even when they are only  $\sim 100\mu\text{m}$  in size. Under the transmission of a white light source, the two different crystal species appear blue and brown by slightly un-crossing the polarizers a few degrees. Since in some cases thousands of crystals were produced in a single sample, only a representative region of a few hundred crystals were analyzed.

Two different flow geometries were employed in the experiments. In the first experiment,  $\text{NaClO}_3$  solution was contained in a cylindrical dish of  $\sim 5\text{ cm}$  in diameter. A small Teflon coated magnetic mixer (1 cm long and 0.2 cm diameter) was used to stir the solution. The light weight of the magnetic mixer and the large surface tension of the solution kept the mixer floating on the liquid-vapor interface while driven by a horse-shoe magnet. The field gradient of the horse-shoe magnet kept the mixer centered on the interface, providing effective mixing near the surface as well as in the interior of the solution. To improve statistics, twenty identical samples were run simultaneously with the horse-shoe magnets connected in tandem, driven by a single DC motor. Flow visualization using Kallirosopic fluid indicated that flow was spatiotemporally chaotic even at a very low stirring rate,  $\sim 1/30\text{ hz}$ . In this experiment, the stirring rate  $f$  as well as the volume of the solution  $V$  are the control parameters. As we shall see, the volume  $V$ , which essentially determines the distance between the stirrer and the bottom of the dish, plays an important role for the outcomes of the experiment.

In the second experiment, flow was produced by electro-convection. In this geometry all the moving parts were eliminated, preventing mechanical damage to the precipitated crystals. The flow cell has a dimension of  $12 \times 20\text{ cm}^2$  with a biased ac current flowing along the long dimension of the cell. The electrodes are made of platinum to reduce contamination of the solution. Directly underneath the cell is an array of 400 cylindrical magnets each having a field of  $\sim 0.4\text{ T}$  near the surface of the magnets. The magnets are arranged in a square lattice with alternating poles pointing vertically. When a current passes through a thin layer of  $\text{NaClO}_3$  solution, an array of counter rotating vortices are formed. Depending on the strength of the current, both localized and delocalized vortices can be generated. Since the thickness of the fluid is small,  $\sim 3\text{ mm}$ , compared to the width of the cell, the flow is approximately two dimensional.

## EXPERIMENTAL OBSERVATION

### 1. Nucleation in Quiescent Solutions

To ascertain that nucleation behaves normally with no substantial bias towards either species, a set of quiescent measurements were carried out. Here, our finding was rather similar to that of Kipping and Pope<sup>5</sup>, and Kondepudi<sup>1</sup>. In a total of 5395 crystals obtained from 94 crystallization, 2523 were right handed and 2872 were left handed. The difference between the two species is about 6%. We noted that similar bias was also observed in Kondepudi's experiment at the level of  $\sim 10\%$ . If an order parameter is defined as  $O = (N^L - N^R)/(N^L + N^R)$ , we can plot the distribution function  $P(O)$  for all 94 runs. Figure 1 shows  $P(O)$  for the quiescent samples ( $f = 0\text{ hz}$ ). For a comparison a binomial distribution with the width comparable to our measurements is also shown by the solid line. The bias (6%) towards left-handed crystals, as illustrated in the graph, is statistically significant since the standard deviation predicted by the bimodal distribution is  $\sim 1\%$  for the number of the crystals produced. The observation suggests that the formation of crystals is likely due to heterogeneous nucleation. The chirality of the crystals may somehow be influenced by the impurities already existing in the solution or coming from air. This conjecture seems to be supported by a set of independent measurements where carefully filtered, concentrated sodium chlorate solutions were flame sealed in ampules. These samples can be supercooled by as much as  $100^\circ$  without crystallization!

### 2. Nucleation in Stirred Solutions

To have a "quality control" to the experiment, we simultaneously run quiescent samples (typically four) together with the stirred samples. If these reference samples showed notable bias in the chirality of the crystals, which rarely occurred due to contamination, the entire run is discarded.

Systematic measurements were carried out for samples containing  $V = 5$  and  $7.5\text{ cc}$  of solutions. For samples with  $V = 5\text{ cc}$ , the magnetic bars touch the bottom of the dishes when the nucleation occurs, whereas for samples with  $V = 7.5\text{ cc}$ , the magnetic bars always stay afloat.

Mechanical stirring has a dramatic effect on the population of two chiral species for samples containing small amount of solutions ( $V = 5$  cc). In this case we found that for  $f \gg 1$  Hz, each sample is populated either by the left or by the right-handed crystals, yielding high chiral purity with a great certainty. The situation is different at low speeds,  $0 < f \leq 1$  Hz. The degree of chiral symmetry breaking, in this case, depends on the rotation speed of the magnetic mixer. Figure 2 shows a series measurements with different  $f$ , ranging from 0.02 hz to 1 hz. For each stirring frequency, twenty samples were examined. The total number of crystal counts are of the order of 10,000 for the high frequency end and of the order of 1,000 for the low frequency end. We note that even at very low frequencies, such as  $f \sim 0.02$  hz, the probability distribution function, PDF, is already significantly different from that of a quiescent solution as shown in Fig. 1. The broadening of the central peak indicates the chiral symmetry in these samples is partially broken. As the stirring rate increases, the PDF starts to peak around the two chirally pure state with  $O = \pm 1$ . For instance, at  $f = 1$  hz, among the twenty samples, eight of them are left-handed with  $O \sim +0.99$ , twelve samples are right-handed with an average order  $O \simeq -0.95$ .

To characterize the order of an assemble of samples by considering  $O > 0$  and  $O < 0$  to be degenerate, we define an ensemble averaged order parameter:  $O_{avg} = [\sum_O O^2 P(O) / \sum_O P(O)]^{1/2}$ . By this definition we understand that  $O_{avg}$  is non-zero even for runs with no stirring. According to Fig. 1, the finite width in the PDF gives  $O_{avg} \simeq 25\%$ . Figure 3 shows  $O_{avg}$  as a function of stirring frequency  $f$  ranging from 0.01 to 3 hz. Here the data are plotted as solid squares. As can be seen, for  $f > 1$  hz the samples are almost completely ordered with optical purity approaching nearly 100%, while for  $f < 1$  hz only partial ordering were observed. The variation of  $O_{avg}$  vs.  $f$  appears to be smooth, and for all the runs  $O_{avg}$  is significantly higher than the background level of 25%. The large statistical noise seen in the data, particularly for the partially ordered samples, is also interesting, and it reflects the fact that the distribution function is extremely broad in the range between  $-1 < O < 1$ .

An interesting observation, which was caused by an unintended event, was that the chiral ordering reduced notably for samples containing slightly larger volumes of solution, while the mixing condition remained the same. We pursued the matter systematically. Fig. 4 shows the PDF for samples containing 7.5 cc solution. The stirring frequency is varied between 0.01 to 4.0 hz. The distribution is in remarkable contrast with runs having a small sample volume, see Fig. 2. A fair comparison is perhaps for  $f = 1$  hz. Here we observed that the PDF is essentially flat with little or no enhancement at  $O = \pm 1$ . To convince ourselves that the effect we were observing was real, we repeated the measurement many times. Instead of using 20 samples, in this set of measurements ( $f = 1$  hz) 92 samples were used. Increasing the stirring frequency to 2 or 4 hz does not change the PDF drastically, and the chiral symmetry is only weakly broken. In Fig. 3 we also show  $O_{avg}$  vs.  $f$  for samples with  $V = 7.5$  cc. As shown by open circles, here we find that the data has only a weak frequency dependence, and the overall value of the order is not much greater than the background value of 25%. We note that if PDF is a flat distribution,  $O_{avg}$  is approximately 60%, which is comparable to what we observed at high stirring frequencies. At best, the chiral symmetry is only weakly broken in this case.

### 3. Nucleation in Electro-convection

The nucleation experiment was also carried out in an electro-convection cell with different flow characteristics. For low currents, the vortices are localized in space and form a fairly regular lattice. For a high current, however, the vortices become delocalized and the flow is nearly turbulent. The local velocity in the electro-convection cell can be a few cm/s which is at least comparable to the mechanical stirring experiments. It is anticipated, therefore, that if hydrodynamic flow is responsible for the symmetry breaking, we would see localized patches of crystals with broken symmetry. In the strong flow regime, a single chiral species may even dominate the entire population in the cell. This is not what has been observed experimentally. For all different flow rates, no strong evidence of chiral symmetry breaking was observed in this set of experiments.

### INTERPRETATION

It should be noted that in our experiments, both with and without stirring, the initial nucleation almost always occurs on the liquid-vapor interface. Typically one sees several crystals float on the surface, and their chirality is not dominated by either handedness. As the crystals grow to a fraction of a millimeter, they fall to the bottom due to gravity. The surface nucleation itself is not surprising in that it is well known that impurities and surfaces can significantly lower the energy barrier of nucleation. However, surface nucleation can explain the unexpected volume dependence seen in the experiment. For a small volume, the magnetic stirring bar makes contact with the bottom of the dish. A settled crystal can be caught between the surfaces of the mixer and the dish, and can be crushed. A single catastrophic event like this, if it could produce a large number of small crystals, can severely bias the population since the initial number of the crystals is very small due to a large activation energy for nucleation,  $\sim 100k_B T$ . For a large volume, there still is a small amount of mechanical contact between the mixer and the crystals on the liquid surface, but the crushing of settled crystals between the mixer and dish is practically eliminated.

Quantitatively it is not difficult to show that hydrodynamic interaction alone is not sufficient to cause a rapid production of the secondary nuclei. To see this we estimate the stress on a nucleus due to hydrodynamic shear,  $\sigma = \eta\gamma$ , where  $\eta(=0.1 \text{ poise})$  is the shear viscosity of the solution and  $\gamma$  is the shear rate. In our experiment  $\gamma \sim f \sim 1 \text{ hz}$ , we found  $\sigma \sim 10^{-1} \text{ erg/cm}^3$ . This is very small compared to the energy density  $\epsilon$  of a fully-grown crystal,  $\epsilon = k_B T \rho \sim 10^9 \text{ erg/cm}^3$  for  $\rho \sim 10^{23} \text{ cm}^{-3}$ . However, it is easy to show that stress produced by the weight of the magnetic bar  $\sigma[\equiv mg/a^2] \simeq 10^6$  is not insignificant compared to  $\epsilon$ . Here  $m = 0.1 \text{ g}$  is the weight of the mixer,  $g \simeq 1000 \text{ cm/s}^2$  is the gravitational acceleration, and  $a = 0.01 \text{ cm}$  is the size of the crystal. We note that  $\epsilon$  estimated above is for a bulk crystal material, which may not be applicable to micro-crystals, or to the edges and the corners of a fully-grown crystals. The mechanical strength of those parts can be significantly lower than  $\epsilon$ , and they are prone to mechanical damage by either the weight or the impact of the magnetic mixer. Indeed, a close inspection of crystals for some of our samples reveals clear signs of mechanical damage. Unlike those crystals grown from a quiescent solution, under stirring conditions, the shape of certain crystals is highly irregular, with missing corners and rounded edges. The null result observed in our electro-convection experiment is also consistent with our interpretation.

The effects of mechanical damage on the chiral symmetry breaking of  $\text{NaClO}_3$  crystals can be mimicked by the following simple growth model. A difference equation for the growth of each crystal species can be formulated where in each time step, one crystal is nucleated from the solution. This crystal will be either left or right handed. In addition to nucleation, crystals can be created by crushing. If we denote the crushing rate by  $\lambda$ , the the population of right handed,  $N^R$ , and left handed,  $N^L$ , crystals at any time step,  $i$ , is given by:

$$\begin{aligned} N_{i+1}^R &= N_i^R + k + \lambda N_i^R \\ N_{i+1}^L &= N_i^L + !k + \lambda N_i^L, \end{aligned}$$

where  $i = 1 \dots N_{max}$ . Here  $k$  is randomly chosen to be either 0 or 1 per step, and  $!k$  is the opposite of  $k$ . That is, if  $N^R$  grows one crystal,  $N^L$  does not grow one. The iteration continues until the solution is depleted (i.e.  $i = N_{max}$ ). It is obvious that this scheme produces a binomial distribution when  $\lambda=0$ . Figure 5 shows the symmetry breaking when  $\lambda$  is varied from 0 to 10. For each value of  $\lambda$  the PDF is plotted against the order parameter  $O$ . All distribution functions were calculated using 100 independent runs, and each run evolved for  $N_{max}=1000$  steps.

Despite its simplicity, with no hydrodynamics or thermodynamics, our model nonetheless captures some basic features seen in the experiment. Namely, in the absence of the mechanical damage  $\lambda = 0$ , the PDF is strongly peaked at  $O = 0$ . The introduction of a small crushing parameter immediately broadens the distribution function. As the crushing parameter increases, the distribution shifts continuously towards the states with  $O = \pm 1$ , in a similar fashion as our experiments with small samples.

## CONCLUSIONS

In conclusion, using different flow geometries we find that the chiral symmetry breaking in super-saturated  $\text{NaClO}_3$  solutions cannot be explained by hydrodynamic convection as suggested by a number of earlier experiments <sup>1,6</sup> and theories <sup>2,3</sup>. The effect appears to be purely mechanical, resulting from mixer-crystal interaction. In effect, the phenomenon is not much different from seeding the solution with numerous micro-crystals created from a single "mother" crystal. This mechanism of generating secondary nuclei was previously considered by Kondepudi and Sabanayagam <sup>7</sup>. However, its severity and extent have not been fully appreciated. We emphasize that by eliminating mechanical contacts with the precipitated crystals, even in the presence of a chaotic flow, there will be no chiral symmetry breaking. Using a simple growth model, we demonstrate that the phenomenon is essentially controlled by a single parameter, the rate of crushing  $\lambda$ . By varying  $\lambda$ , the system can be in either non-chiral, weakly chiral, or strongly chiral symmetry breaking state. The PDF generated from our simple model is also in good agreement with our measurements.

## ACKNOWLEDGMENTS

We would like to thank W.I. Goldburg and C. Yeung for many helpful discussions during the course of this research. This research is supported by NASA under grant No. NAG8-959.

## REFERENCES

- <sup>1</sup>D. Kondepudi, R. Kaufman, and N. Singh, *Science* **250**, 975 (1990).
- <sup>2</sup>Guy Metcalfe and J.M. Ottino, *Phys. Rev. Lett.* **72**, 2875 (1994).
- <sup>3</sup>Irving R. Epstein, *Nature* **374**, 321 (1995).
- <sup>4</sup>The sodium chlorate,  $\text{NaClO}_3$ , was purchased from Fisher Scientific. The chemical is 99.9% pure and was used without further purification.
- <sup>5</sup>F.S. Kipping and W.J. Pope, *J. Chem. Soc. Trans.* **73**, 606 (1898).
- <sup>6</sup>X-l. Wu, B. Martin, and A. Tharrington, *Proceeding of "Second Microgravity Fluid Physics Conference,"* 319 (1994).
- <sup>7</sup>D.K. Kondepudi and C. Sabanayagam, *Chem. Phys. Lett.* **217**, 364 (1994).

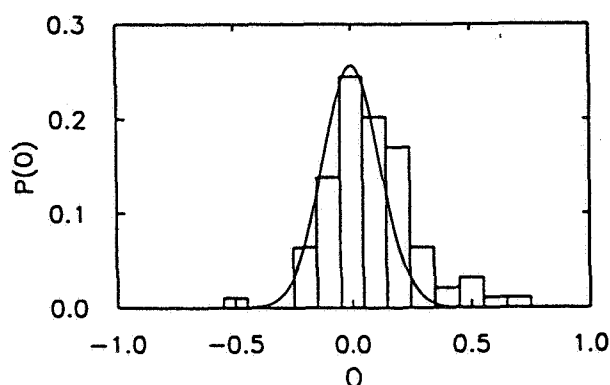


Figure 1. The order-parameter probability distribution function  $P(O)$  for quiescent samples.

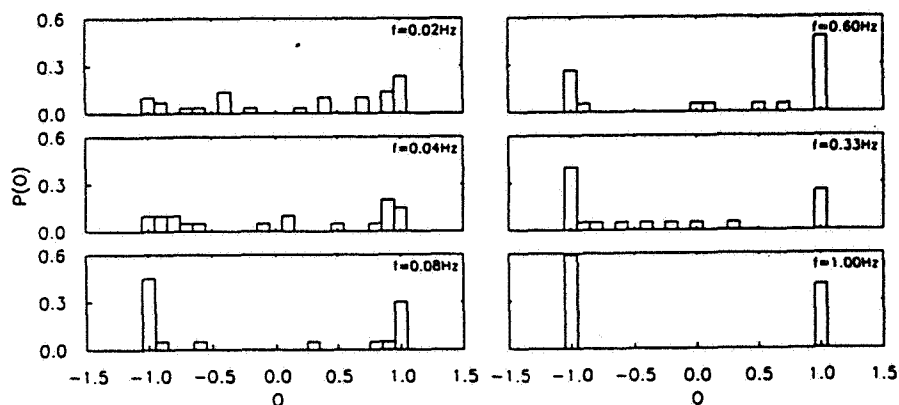


Figure 2. The order parameter probability distribution functions with different stirring rates. The volume of the solution is  $V = 5.0$  cc.

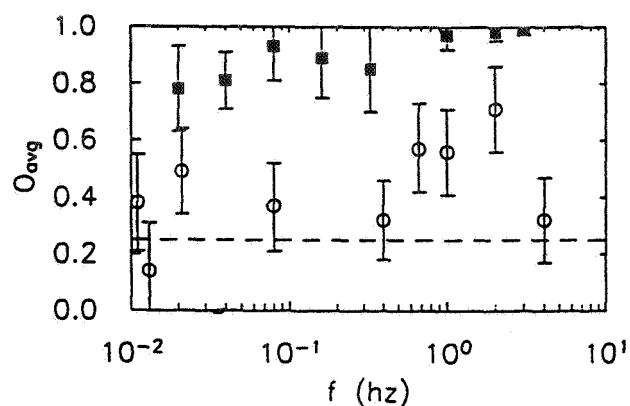


Figure 3. The solid squares are for samples with  $V = 5.0$  cc and the open circles are for samples with  $V = 7.5$  cc. The error bars are due to statistical errors. The dashed line is the background, see text for details.

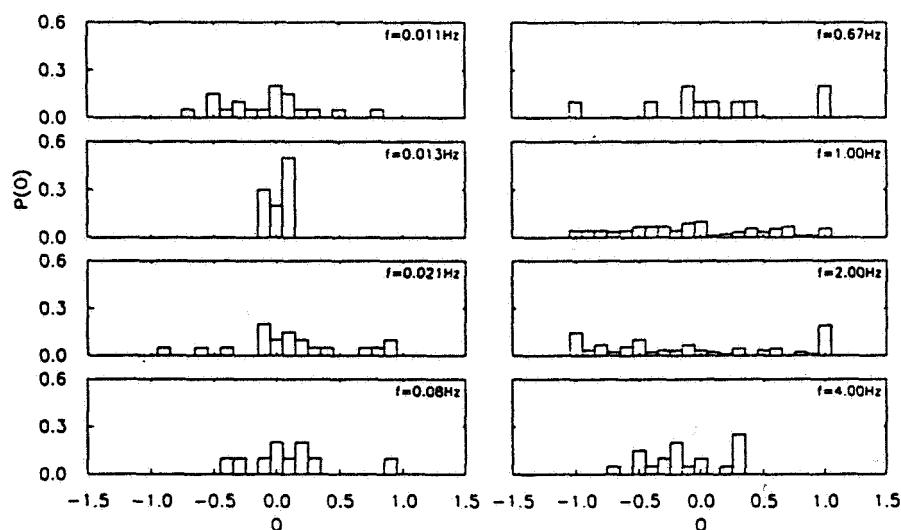


Figure 4. The order parameter probability distribution functions with different stirring rates. The volume of the solution is  $V = 7.5$  cc.

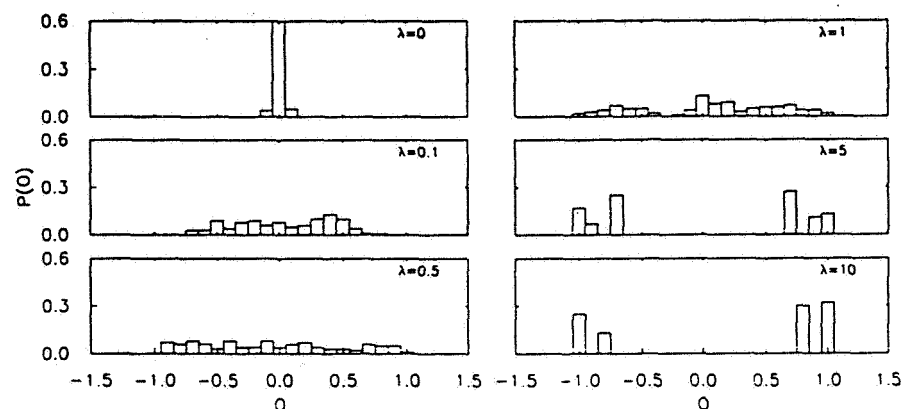


Figure 5. Model calculations for probability distribution functions with different crushing rates.

**Plasma dust crystallization**

John Goree, University of Iowa

**Paper not available**





# **G-Jitter Induced and Stochastic Flows**



# FLUID PHYSICS IN A FLUCTUATING ACCELERATION ENVIRONMENT

J. Ross Thomson, François Drolet and Jorge Viñals  
Supercomputer Computations Research Institute  
Florida State University  
Tallahassee FL 32306-4052

## ABSTRACT

We summarize several aspects of an ongoing investigation of the effects that stochastic residual accelerations ( $g$ -jitter) onboard spacecraft can have on experiments conducted in a microgravity environment. The residual acceleration field is modeled as a narrow band noise, characterized by three independent parameters: intensity  $\langle g^2 \rangle$ , dominant angular frequency  $\Omega$ , and characteristic correlation time  $\tau$ . Realistic values for these parameters are obtained from an analysis of acceleration data corresponding to the SL-J mission, as recorded by the SAMS instruments. We then use the model to address the random motion of a solid particle suspended in an incompressible fluid subjected to such random accelerations. As an extension, the effect of  $g$ -jitter on coarsening of a solid-liquid mixture is briefly discussed, and corrections to diffusion controlled coarsening evaluated. We conclude that  $g$ -jitter will not be significant in the experiment "Coarsening of solid-liquid mixtures" to be conducted in microgravity. Finally, modifications to the location of onset of instability in systems driven by a random force are discussed by extending the standard reduction to the center manifold to the stochastic case. Results pertaining to time-modulated oscillatory convection are briefly discussed.

## STOCHASTIC MODEL OF G-JITTER

We have introduced a stochastic model [1] to describe in quantitative detail the effect of the high frequency components of the residual accelerations onboard spacecraft (often called  $g$ -jitter) on fluid motion [2, 3, 4]. Each Cartesian component of the residual acceleration field  $\vec{g}(t)$  is modeled as a narrow band noise characterized by three independent parameters: its intensity  $\langle g^2 \rangle$ , a dominant frequency  $\Omega$ , and a characteristic spectral width  $\tau^{-1}$ . Specifically,  $g(t)$  is a Gaussian random process, of zero mean, and autocorrelation

$$\langle g(t)g(t') \rangle = \langle g^2 \rangle e^{-|t-t'|/\tau} \cos[\Omega(t-t')]. \quad (1)$$

The power spectrum for this autocorrelation function is,

$$P(\omega) = \frac{1}{2\pi} \langle g^2 \rangle \tau \left( \frac{1}{1 + \tau^2(\Omega + \omega)^2} + \frac{1}{1 + \tau^2(\Omega - \omega)^2} \right). \quad (2)$$

Each realization of narrow band noise can be viewed as a temporal sequence of periodic functions of angular frequency  $\Omega$  with amplitude and phase that remain constant only for a finite amount of time ( $\tau$  on average). At random intervals, new values of the amplitude and phase are drawn from prescribed distributions. This model is based on the following mechanism underlying the residual acceleration field: one particular natural frequency of vibration of the spacecraft structure ( $\Omega$ ) is excited by some mechanical disturbance inside the spacecraft, the excitation being of random amplitude and taking place at a sequence of unknown (and essentially random) instants of time.

From a theoretical standpoint, narrow band noise provides a convenient way of interpolating between monochromatic noise (akin to more traditional studies involving a deterministic and periodic gravitational field), and white noise (in which no frequency component is preferred). In the limit  $\tau \rightarrow 0$  with  $D = \langle g^2 \rangle \tau$  finite, narrow band noise reduces to white noise of intensity  $D$ ; whereas, for  $\tau \rightarrow \infty$  with  $\langle g^2 \rangle$  finite, monochromatic noise is recovered.

In order to ascertain the validity of this model, and to determine the values of the parameters defining the noise, we have analyzed actual  $g$ -jitter data collected during the SL-J mission (SAMS-258), and studied in detail the time series of head A between MET 0017 and MET 0023, or roughly six hours. First, a scaling analysis has been performed to determine the existence of deterministic or stochastic components in the time series. Figure 1 shows the power spectrum of  $g$ -jitter calculated over a window of size  $N$ , and then averaged over the six-hour period (the values of  $g$  are sampled at 250 Hz). With the normalization of the

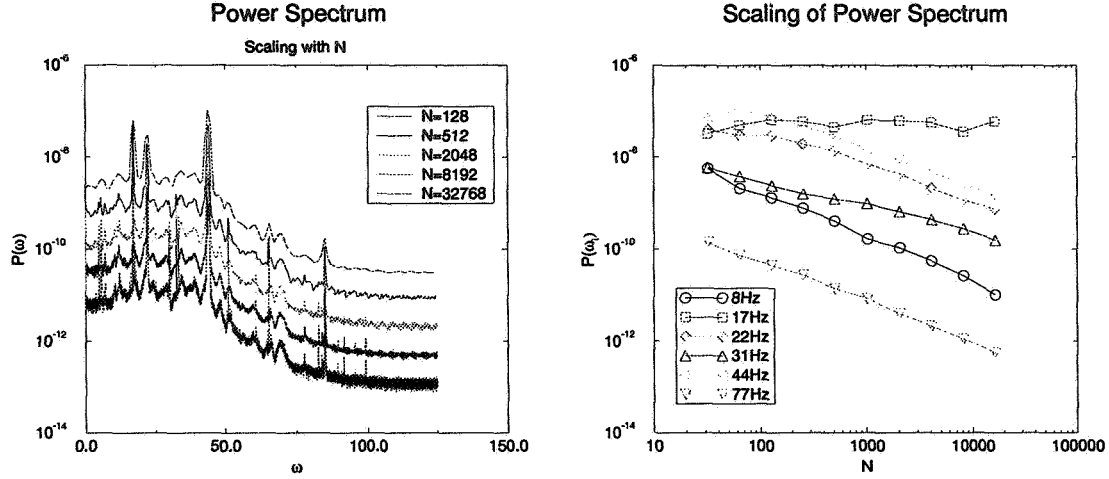


Figure 1: Left, power spectrum as a function of frequency for a six-hour interval during the SL-J mission. The various curves shown correspond to spectra calculated over the window of indicated size. Right, intensity versus window size for a few selected frequencies.

spectrum used, the power spectrum of a deterministic time series ought to be independent of  $N$ , whereas for a stochastic signal, it should decay as  $1/N$  when the window size is much larger than the correlation time  $\tau$ . Figure 1 (right) shows the dependence of the power of a selected set of frequencies as a function of the window size, displaying its scaling with  $N$ . During this period of six hours, there appears to be a monochromatic contribution at 17 Hz with an amplitude  $\sqrt{\langle g^2 \rangle} = 3.56 \times 10^{-4} g_E$ , where  $g_E$  is the intensity of the gravitational field on the Earth's surface. There are two additional components that have a finite correlation time: For the component at 22 Hz we estimate  $\sqrt{\langle g^2 \rangle} = 3.06 \times 10^{-4} g_E$  and  $\tau = 1.09$  s, whereas for 44 Hz we find,  $\sqrt{\langle g^2 \rangle} = 5.20 \times 10^{-4} g_E$  and  $\tau = 0.91$  s. As an estimate of the white noise background, we obtain from the slope of the intensity of the 8 Hz component versus  $N$  the value  $D = 8.61 \times 10^{-4} \text{cm}^2/\text{s}^3$ .

## RANDOM MOTION OF BUOYANT PARTICLES; COARSENING OF SOLID-LIQUID MIXTURES

We study here the motion of a particle suspended in an incompressible fluid of different density, when the fluid is subjected to an effective acceleration field like the one described above. This type of motion has been termed inertial random walk because of the similarity with Brownian motion [5]. The difference, of course, is that the random motion of the particle is not due to thermally induced collisions with the molecules of the fluid, but results from an effective random buoyant force acting on the particle. The asymptotic mean squared velocity of a particle subjected to narrow band noise is found to be,

$$\langle v^2 \rangle_\infty = \frac{\Delta \rho^2 \langle g^2 \rangle (\gamma + \frac{1}{\tau})}{\gamma \left[ (\gamma + \frac{1}{\tau})^2 + \Omega^2 \right]},$$

where  $\Delta \rho = (\rho_p - \rho_f)/\rho_p$ ,  $\gamma = 9\pi\eta/2\rho_p R^2$ , with  $\eta$  the shear viscosity of the fluid,  $\rho_p$  and  $\rho_f$  the density of the particle and fluid respectively, and  $R$  the radius of the particle. The particle undergoes diffusive motion (the mean squared displacement is proportional to time), with an effective diffusion coefficient that is proportional to the intensity of the fluctuating acceleration. On the other hand, if the acceleration field were periodic in time (deterministic case), the mean squared displacement of the particle would remain bounded.

We have also performed an asymptotic analysis away from the deterministic limit ( $\tau \rightarrow \infty$ ) to illustrate the emergence of diffusive behavior as the correlation time becomes finite. We have found an effective diffusion coefficient given by,

$$D_{\text{eff}} = \frac{\Delta \rho^2 \langle g^2 \rangle \gamma}{(\gamma^2 + \Omega^2)^2} \left( 2 + \frac{\Omega^2}{\gamma^2} + \frac{\gamma^2}{\Omega^2} \right) \frac{1}{\tau} + \mathcal{O}(\tau^{-2}).$$

Therefore, from a measure of the autocorrelation function of the particle displacement, it should be possible in principle to determine independently the parameters that define  $g$ -jitter. Knowledge of this sort could conceivably lead to the construction of an instrument that would complement the data set provided by accelerometers.

A residual acceleration field can produce a number of deleterious effects on otherwise purely diffusive controlled coarsening. We have focussed on two such effects: random motion of the suspended particles induced by the effective (random) buoyant force and the concomitant increase in the likelihood of particle coalescence, and additional flow in the fluid phase caused by  $g$ -jitter and its effect on solute mass transport. Numerical estimates have been obtained for a solid-liquid mixture of Sn-rich particles in a Pb-Sn eutectic liquid, the system that will be used in a forthcoming microgravity experiment [6, 7].

Neglecting inter-particle interactions, precipitate particles will execute a random motion of the type described above. For the case of monochromatic noise (fixed frequency and random phase), the average quadratic displacement of each particle remains bounded. For values of the parameters appropriate for a Pb-Sn eutectic liquid and the conditions of the planned microgravity experiment,  $\gamma = 260s^{-1}$ , and by using the amplitude of the 17 Hz component of the power spectrum, we find that  $\max \{ \langle x^2 \rangle \} \approx 10^{-8}cm^2$ , and hence negligible. At the other extreme, we find that for white noise the mean squared displacement after five hours is  $\langle x^2 \rangle (t = 5 \text{ hr.}) = 8.85 \times 10^{-6}cm$  or  $\sqrt{\langle x^2 \rangle} \approx 30\mu m$ . Clearly the average square displacement induced by the white noise component of the residual acceleration field is much larger than that induced by the monochromatic component, but it is still about one half of the expected average particle size at the end of the coarsening experiment. Therefore Brownian motion induced by  $g$ -jitter will not lead to appreciable motion of the precipitate particles relative to their size.

Estimating the effect of  $g$ -jitter on mass transport in the fluid phase is far more complex. In the limit of Stokes flow and non-interacting solid particles, (the former is appropriate for the size of the coarsening particles involved),  $g$ -jitter induced flow acts to renormalize the solute diffusivity. We find an effective diffusion coefficient given by,

$$D_{eff} = D_s + \frac{\Delta\rho^2 D}{\gamma^2}, \quad (3)$$

where  $\Delta\rho$  is the relative difference in density between the liquid and solid phases, and  $D_s$  is the solute diffusivity. We find that

$$\frac{\Delta\rho^2 D}{\gamma^2 D_s} = 5 \times 10^{-5} \ll 1, \quad (4)$$

and therefore negligible.

Finally, the effect of particle-particle interaction can be estimated in the overdamped limit. We find that although it would be asymptotically dominant in the limit of large particles (or long coarsening times), the interaction terms also remain small within the range of coarsening times to be explored in the experiment.

## CENTER MANIFOLD REDUCTION FOR STOCHASTICALLY DRIVEN SYSTEMS

The onset of oscillatory instabilities in stochastically driven systems is also being studied. The approach that we follow applies to systems consisting of a "slow" variable  $u$  coupled to one (or more) "fast" variable(s)  $v$  [8]. In the classical deterministic case, one simplifies the dynamics of the problem close to onset of instability through the adiabatic elimination of the fast variable. The stochastic analog of this reduction scheme consists in assuming a probability distribution of the form  $\mathcal{P}(u, v, t) = P(u, t)\delta(v - v_o(u))$ , with  $v = v_o(u)$  is the center manifold of the associated deterministic problem (in the weak noise limit). The resulting Fokker-Planck equation is then integrated over  $v$ , yielding an equation for  $P(u, t)$ . Using this procedure, a generic system of the form

$$\partial_t \begin{bmatrix} u \\ v \end{bmatrix} = \begin{bmatrix} \alpha & 0 \\ 0 & -\lambda \end{bmatrix} \begin{bmatrix} u \\ v \end{bmatrix} + \begin{bmatrix} f(u, v) \\ g(u, v) \end{bmatrix} + \xi(t) \begin{bmatrix} k_{11} & k_{12} \\ k_{21} & k_{22} \end{bmatrix} \begin{bmatrix} u \\ v \end{bmatrix} \quad (5)$$

where  $\lambda, \alpha > 0$ , and  $k_{ij}$  are known constants, reduces to the Fokker-Planck equation,

$$\begin{aligned} \partial_t P(u, t) = & -\partial_u [(\alpha u + f(u, v_o(u)))P(u, t)] + D\partial_u [(k_{11}u + k_{12}v_o(u)) \\ & (k_{11} + 2k_{12}\partial_u v_o(u))P(u, t) - k_{12}(k_{21}u + k_{22}v_o(u))P(u, t) \\ & + (k_{11}u + k_{12}v_o(u))^2 \partial_u P(u, t)]. \end{aligned} \quad (6)$$

The value  $\alpha = 0$  corresponds to the deterministic threshold, while the functions  $f(u, v)$  and  $g(u, v)$  involve terms of the form  $u^a v^b$  ( $a + b \geq 2$ ). The random process  $\xi(t)$  is assumed to be Gaussian and white, of zero mean and intensity  $2D$  ( $\langle \xi(t)\xi(t') \rangle = 2D\delta(t - t')$ ).

As an illustration of the procedure, consider the Van der Pol oscillator

$$\partial_t^2 x = \alpha x - \gamma \partial_t x - ax^3, \quad (7)$$

with the driving force having a stochastic component (i.e.,  $\alpha \rightarrow \alpha + \xi(t)$ ),  $\gamma$  is a constant damping coefficient and  $a > 0$  a nonlinear coupling constant. The problem can be mapped to Eq. (5) by first defining  $y = \partial_t x$  and then letting  $u = x + y/\gamma$  and  $v = -y/\gamma$  [8]. Assuming  $u, D \ll 1$ , the resulting Fokker-Planck equation yields the stationary distribution

$$P(u) = \mathcal{N}|u|^{-2+\frac{\alpha\gamma}{D}} \exp\left(-\frac{a\gamma}{2D}u^2\right), \quad (8)$$

which is normalizable as long as  $\alpha \geq D/\gamma$ . The theory thus predicts a shift in the threshold from  $\alpha = 0$  to  $\alpha = D/\gamma$ . This result agrees with that obtained by Lücke [9] by other methods, but contradicts earlier work of Knobloch and Wiesenfeld. The probability density can either be unimodal ( $\alpha \geq 2D/\gamma$ , Fig. 2 (left)) or monotone with an infinite peak at zero ( $D/\gamma < \alpha < 2D/\gamma$ , Fig. 2 (right)).

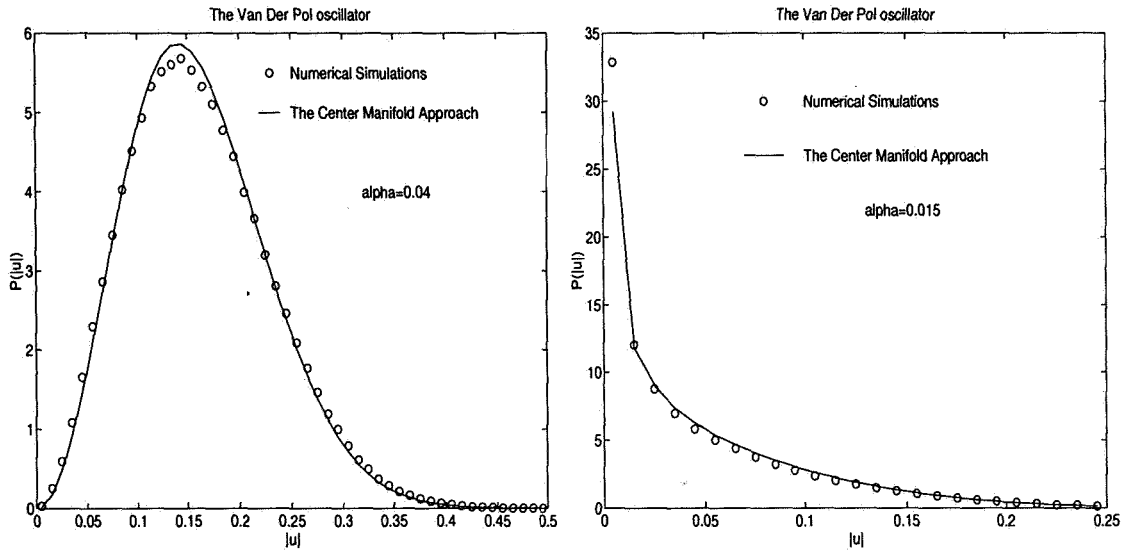


Figure 2: Probability density distribution for the Van der Pol oscillator with noise intensity  $D = 0.01$  ( $\alpha = \gamma = 1$ ).

The procedure can also be used to study the influence of fluctuations on time-modulated oscillatory convection. The left and right traveling waves appearing at large Rayleigh numbers have been modeled by a set of equations for their amplitude ( $x$  or  $y$ ) and phase difference ( $\chi$ ) [10]. In the parameter regime in which both waves have equal amplitude (thus corresponding to the emergence of standing waves), the system of equations can be shown to reduce to

$$\partial_t \begin{bmatrix} A \\ \theta \end{bmatrix} = \begin{bmatrix} a_R + \sqrt{b^2 - a_i^2} & 0 \\ 0 & -2\sqrt{b^2 - a_i^2} \end{bmatrix} \begin{bmatrix} A \\ \theta \end{bmatrix} + \begin{bmatrix} \frac{n_R}{4} A^3 - a_i \theta A \\ \frac{n_i}{2} A^2 + a_i \theta^2 \end{bmatrix} \quad (9)$$

close to onset. In Eq. (9),  $A = x + y$ ,  $\theta = \chi - \arcsin(a_i/b)$  and the other quantities are constant parameters entering the model. The effect of fluctuations in the Rayleigh number can then be studied by letting  $a_R \rightarrow a_R + \xi(t)$ . The center manifold approach predicts changes in the various moments of  $A$ , but no shift in the position of the threshold for this instability. This has been verified numerically, as shown in Fig. 3.

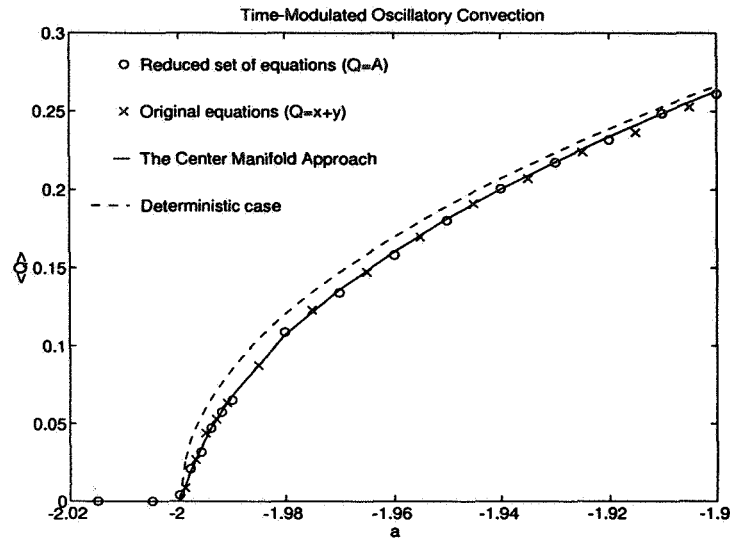


Figure 3: Standing Wave bifurcation in time-modulated oscillatory convection.

## CONCLUSIONS

A stochastic model of the residual acceleration environment onboard spacecraft has been introduced. It provides a realistic description of the various contributions to the acceleration environment, as exemplified by the power spectrum recorded during the SL-J mission. During the time window analyzed, the signal has a deterministic component at 17 Hz (with a correlation time longer than 65 s), two other major components at 22 and 44 Hz that can be modeled as narrow band noise of short correlation time (of the order of one second), and a significant white noise background. Since the stochastic model used can smoothly interpolate between the deterministic and white noise limits, it represents a useful tool for numerical analysis and statistical predictions concerning the effect of  $g$ -jitter on a number of phenomena.

In particular, we have briefly discussed our results concerning three different situations. First, random displacements of buoyant particles result in diffusive motion that could be used in passive accelerometer devices to have an independent measurement of  $g$ -jitter intensity. This random motion and the concomitant fluid flow have been estimated in connection with the experiment "Coarsening of solid-liquid mixtures". The effect of  $g$ -jitter has been shown to be of the same order as ordinary Brownian motion and therefore negligible, except possibly for experiments of long duration (over ten hours). Finally, the effect of noise on the onset of oscillatory instabilities, such as in double diffusive convection, is being examined by extending the classical center manifold reduction to the stochastic case. Two examples are briefly discussed that exhibit the main qualitative features of the phenomenon, with particular emphasis being paid to possible shifts in the instability point relative to the deterministic (noiseless) case.

## ACKNOWLEDGMENTS

This work has been supported by the Microgravity Science and Applications Division of the NASA under contract No. NAG3-1284. This work is also supported in part by the Supercomputer Computations Research Institute, which is partially funded by the U.S. Department of Energy, contract No. DE-FC05-85ER25000.

## References

- [1] W. Zhang, J. Casademunt, and J. Viñals, *Phys. Fluids A* **5**, 3147 (1993).
- [2] *Fluid Sciences and Materials Sciences in Space*, edited by H. Walter (Springer Verlag, New York, 1987).

- [3] E. Nelson, NASA Technical Report No. TM 103775, 1983.
- [4] G. Martin, C. Baugher, and F. Henderson, NASA Technical report, Acceleration Characterization and Analysis Project, 1992.
- [5] L. Regel, A. Vedernikov, R. Ilinski, and I. Melikhov, in *Proceedings of the Sixth European Symposium on Materials Sciences under Microgravity Conditions* (European Space Agency, Paris, 1987), ESA Publication SP-256.
- [6] S. Hardy and P. Voorhees, *Met. Trans. A* **19A**, 2713 (1988).
- [7] S. Hardy *et al.*, *J. Crystal Growth* **114**, 467 (1991).
- [8] E. Knobloch and K. Wiesenfeld, *J. Stat. Phys.* **33**, 611 (1983).
- [9] M. Lücke and F. Shank, *Phys. Rev. Lett.* **54**, 1465 (1985).
- [10] H. Riecke, J. Crawford, and E. Knobloch, *Phys. Rev. Lett.* **61**, 1942 (1988).



# RESOLVING HIGH AMPLITUDE SURFACE MOTION WITH DIFFUSING LIGHT

W. Wright, R. Budakian & S. J. Putterman  
Physics Department, University of California, Los Angeles, CA 90095

**Abstract:** A new technique has been developed for the purpose of imaging high amplitude surface motion. With this method one can quantitatively measure the transition to ripple wave turbulence. In addition one can measure the phase of the turbulent state. These experiments reveal strong coherent structures in the turbulent range of motion.

The high amplitude motion of a fluid surface exhibits a remarkable range of broken symmetries ranging from quasi-crystals to quantum scars to ripple turbulence<sup>1</sup>). Key to a quantitative investigation of these states is a means of measuring the surface height as a function of location.

Figure 1 shows the apparatus that we have used to excite and measure the large amplitude distortions of a fluid surface<sup>2</sup>). A vibration exciter oscillates a container of fluid in the vertical direction at sufficient amplitude that instabilities determined by the Matthieu equation come into play. The resulting surface motion is made visible by suspending into the water a .04% solution of polyballs. This concentration is sufficiently dense that light traveling through the water is so strongly scattered that it diffuses. A charge coupled device (CCD) records the light to exit the fluid. Typically the surface is broken up into one million pixels [1024x1024] where each pixel is capable of recording a dynamic range of 65,000 gray scales [or 16 bits]. This image is converted into the surface height with the help of a calibration plot shown in Figure 2. This plot shows the amount of light to exit the surface as a function of fluid depth. The deeper the fluid the smaller is the amount of light to make it to the surface at that location. An example of a photo and its rendition as obtained with the use of the calibration plot is shown in Figure 3.

The surface height as a function of time at a single point in the fluid can be obtained by reading out the calibrated signal from a single pixel as a function of time. From this measurement one can obtain the power spectrum of surface motion as shown in Figure 4. At low amplitudes of excitation the motion is sinusoidal at half the frequency of the drive. Harmonics of this frequency are also present. But as the amplitude of sinusoidal excitation is increased the fluid motion shows a transition to a broad band response. We claim that this is the state of wave turbulence of propagating ripples<sup>3</sup>). When plotted on a log-log scale the slope which we find is -3.2 which is close to the value of -17/6 predicted by the Kolmogorov scaling law<sup>4</sup>) for interacting ripples<sup>3</sup>). The small deviation which we find can be due to a) the finite size of the container, b) the limited range of the broad band distribution that can be obtained with our apparatus, and c) mistakes in the physical assumptions<sup>5,6</sup>) that underlie the theoretical analysis of turbulence in propagating capillary waves. Problems a) and b) are of experimental origin and can be addressed by carrying out this experiment in microgravity.

Theories which are based upon a random phase approximation yield a power spectrum in agreement with the Kolmogorov dimensional analysis and of course also yield a description of turbulence that is devoid of intermittency. Since phase is a physical quantity of importance equal to power [or amplitude squared] we have used the instantaneous photos [e.g. Figure 3] to investigate the phase coherence, if any, of the turbulent state. To do this we digitally filtered the photo to include only the contributions from a range of wavelengths. In this case those wavelengths corresponding to the frequency range 373Hz to 429Hz. From this filtered photo we then constructed the dissipation function which is proportional to the square of the Laplacian of the surface height. A rendition of this data is shown in Figure 5. Note that the turbulence is localized onto surfaces. It is not uniformly spread out. According to these experiments the turbulent state is filled with structures or so-called "intermittency".

It will be interesting to see if these effects persist when the turbulence cascades over a wider range

of frequencies and the effects of boundaries are eliminated. This will be achieved in those arrangements where one images ripples that interact on the surface of a large drop of liquid such as can be achieved in microgravity. Mathematically, it is essential to determine the appropriate way to analyze and quantify the structures shown in Figure 5.

#### THE SUPPORT OF NASA MICROGRAVITY IS ACKNOWLEDGED

#### REFERENCES

- 1) N.B. Tufillaro, R. Ramshankar, J.P. Gollub; Order-Disorder Transition in Capillary Waves: Phys. Rev. Lett. 62, 422-425, (1989).  
A.B. Ezersky, S.V. Kiyashko, P.A. Matusou, M.I. Rabinovich; Domain Walls and Dislocations in Capillary Ripples: Europhys. Lett. 26, 183-188 (1994).  
S.T. Milne; Square Patterns and Secondary Instabilities in Driven Capillary Waves: J. Fluid Mech. 225, 81-100, (1991). B. Christianson, P. Alstrom, M. T. Levinsen; Ordered Capillary Wave States: Quasicrystals, Hexagons and Radial Waves: Phys. Rev. Lett. 68, 2157-2160 (1992).  
R.Blümel, I.H. Davidson, W.P. Reinhardt, H. Lin, M. Sharnoff; Quasilinear Ridge Structures in Water Surface Waves: Phys Rev A45, 2641-2644, (1992).  
B.J. Gluckmen, P. Marq, J. Bridges, J.P. Gollub; Time-Averaging of Chaotic Spatiotemporal Wave Patterns: Phys. Rev. Lett. 71, 2034-2037 (1993).  
E. Bosch, W. van de Water; Spatiotemporal Intermittency in the Faraday Experiment: Phys Rev Lett: 70, 3420-3423 (1993).
- 2) W. Wright, R. Budakian, S. Putterman, Diffusing Light Photography of Fully Developed Isotropic Ripple Turbulence: Physical Review Letters, June 1996. W. Wright, R. Budak, S. Putterman; Diffusing Light Photography of Solitons and Capillary Wave Turbulence: J. Acoust. Soc. Am. 96, 3322-3323 (1994).
- 3) V.E. Zakharov, V.S. L'vov, G. Falkovich; Kolmogorov Spectra of Turbulence: [Springer-Berlin] 1992. R.Z. Sagdeev; Turbulence and Nonlinear Waves: Rev. Mod Phys. 51, 1-9, (1979). G.E. Falkovich, I. Ya Shapiro, L. Shtilman; Decay Turbulence of Capillary Waves: Europhys Lett 29, 1-6, (1995).
- 4) A.N. Kolmogorov; The local Structure of Turbulence in an Incompressible Fluid for Very Large Reynolds Numbers: Dokl. Akad. Nauk. SSSR 30, 301-305, (1941). A.M. Oboukhov; On the Distribution of Energy in the Spectrum of Turbulent Flow: Dokl. Akad. Nauk. SSSR 32, 19, (1941).
- 5) S.J. Putterman, P.H. Roberts; Fokker-Planck Equation for Interacting Waves: Dispersion Law Renormalization and Wave Turbulence: Phys. Rep. 168, 209-263, (1988). A.C. Newell, The Closure Problem in a System of Random Gravity Waves: Rev. Geophys. 6, 1-13 (1968).
- 6) A.N. Pushkarev, V.E. Zakharov, Turbulence of Capillary Waves: Phys. Rev. Lett. 76, 3320-3323, (1996).

#### FIGURES

**Figure 1;** Apparatus for imaging the instantaneous high amplitude displacement of a fluid surface. A flash from a strobe diffuses through the fluid and exits the top surface where it is imaged onto a CCD. Higher regions are darker. The fluid is sinusoidally excited by a shake table. Above a critical threshold the surface motion sets in. The light diffuses as a result of multiple scattering by a .04% concentration of polyballs suspension in the water.

**Figure 2;** Relative intensity of light to exit fluid surface as a function of depth. Each of the one million pixels of the CCD is calibrated. From this calibration the local height is determined.

**Figure 3;** An actual photo of the turbulent state and its scaled and calibrated rendition as obtained from use of Figure 2.

**Figure 4;** Power spectrum of surface motion. Displayed is the Fourier Transform of the time dependent motion as recorded at a single pixel. At high drive levels the harmonic response [characteristic of low drive] turns into a broad band spectrum. The solid line has a slope of -3.2. The threshold for turbulence [reference 2] is indicated by the dashed line.

**Figure 5;** Digitally filtered photo of the motion in the turbulent state. The photo shown in Figure 3 is first filtered in the range 373Hz-429Hz. Then the dissipation function is calculated [this is the square of the Laplacian and gives the local dissipation of ripple motion due to viscosity. The structure shown in this photo is indicative of intermittency. This is data, not simulation!]

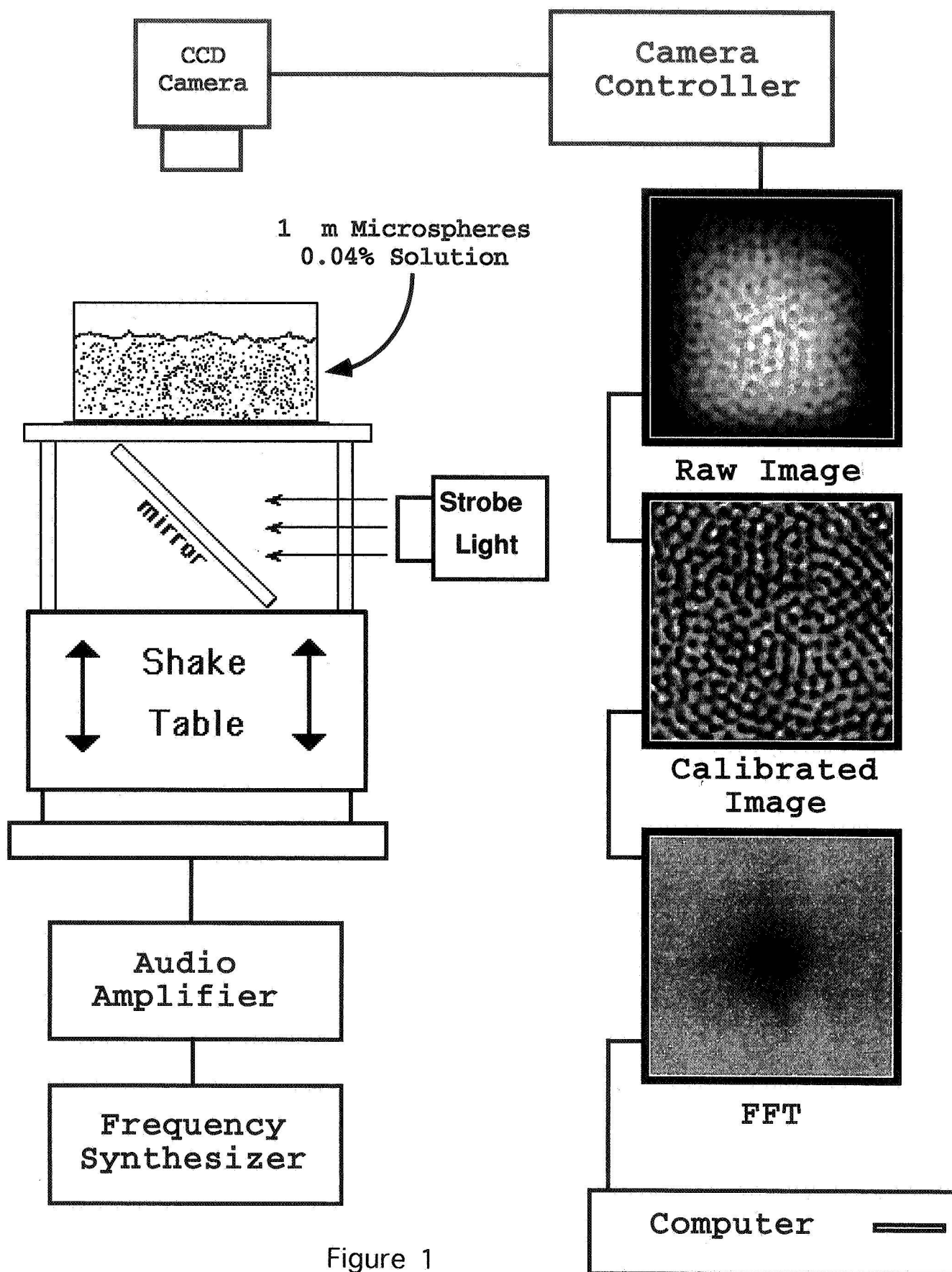
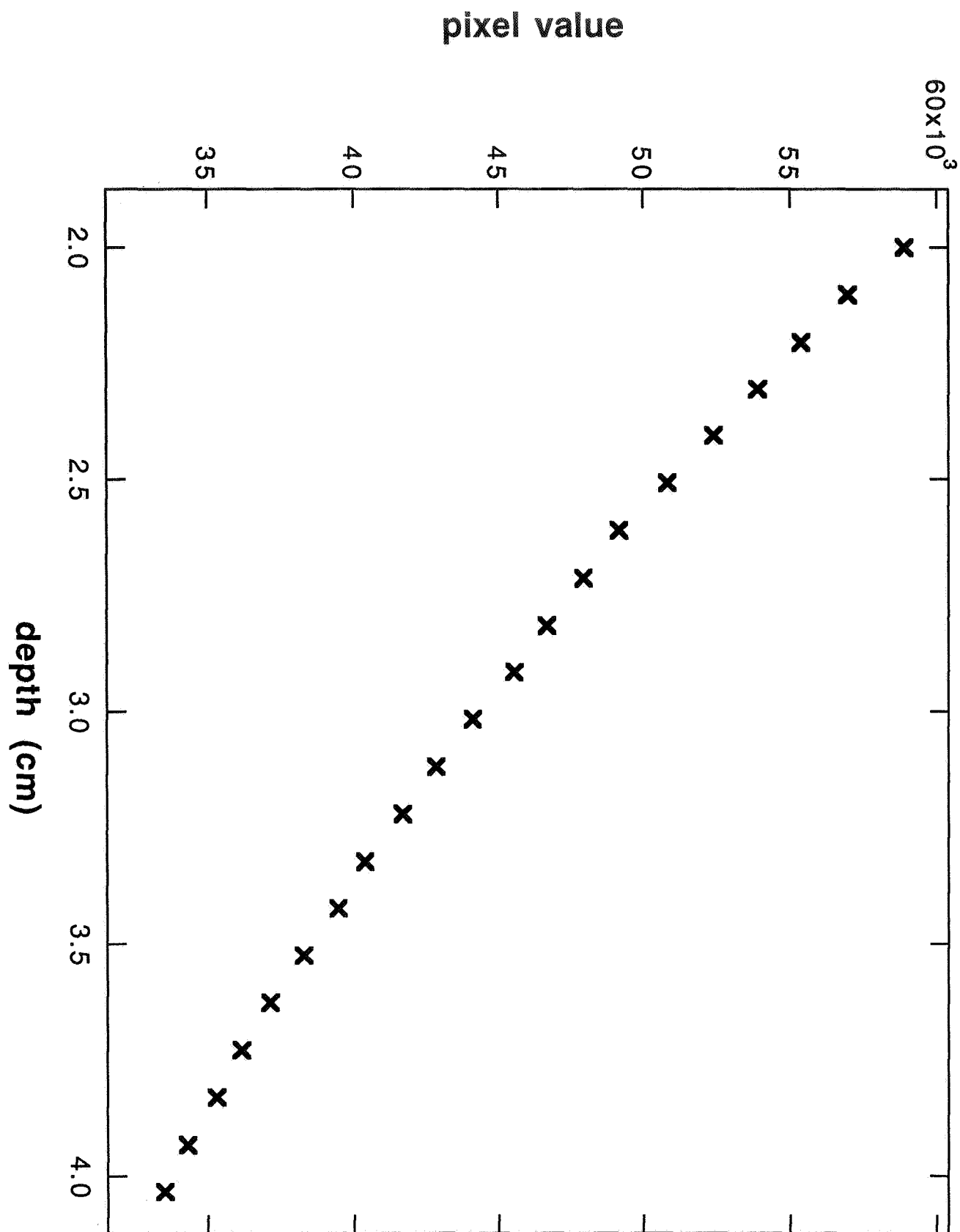


Figure 1



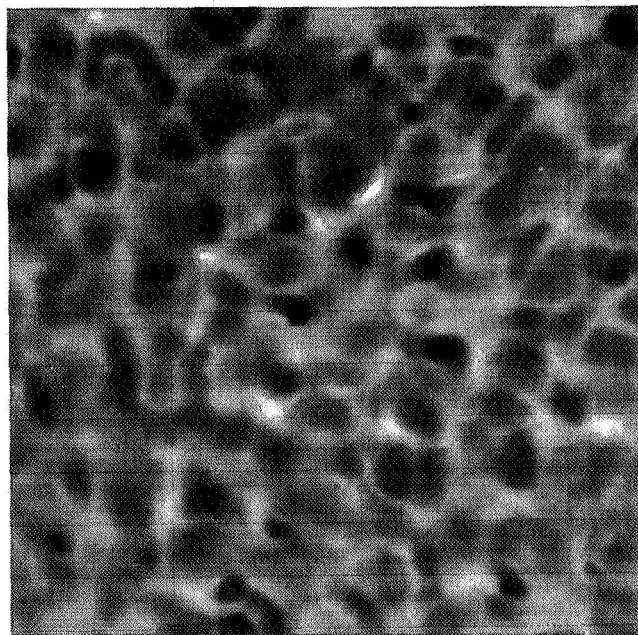


Figure 3

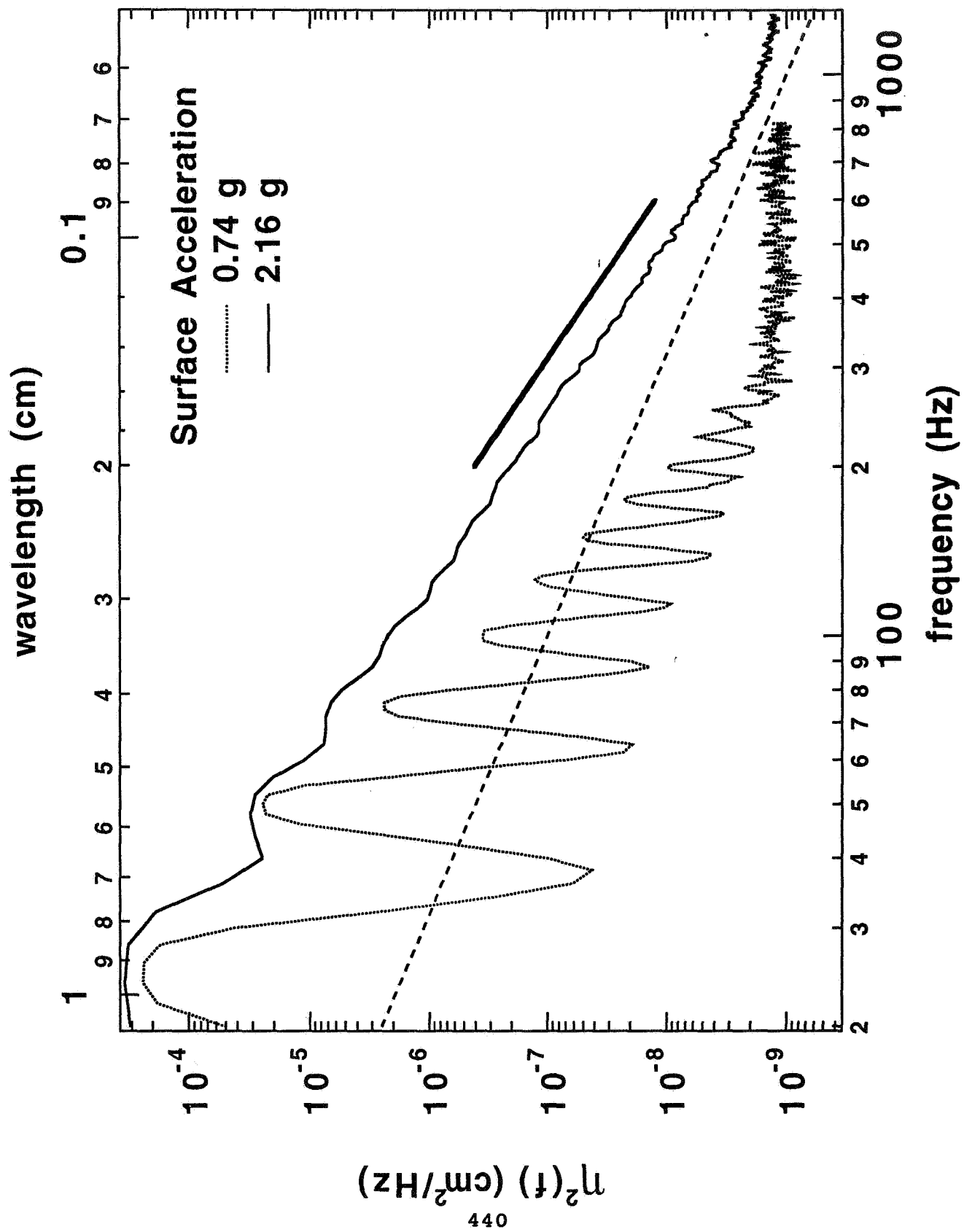


Figure 5







# EFFECTS OF GRAVITY ON SHEARED TURBULENCE LADEN WITH BUBBLES OR DROPLETS

Said Elghobashi and Juan Lasheras\*\*

Mechanical and Aerospace Engineering Department  
University of California, Irvine, California 92717

\*\* Applied Mechanics and Engineering Sciences Department  
University of California, La Jolla, California 92093

## ABSTRACT

This is a new project which started in May 1996. The main objective of the experimental/numerical study is to improve the understanding of the physics of *two-way coupling* between the dispersed phase and turbulence in a prototypical turbulent shear flow – homogeneous shear, laden with small liquid droplets (in gas) or gaseous bubbles (in liquid). The method of direct numerical simulation (DNS) is used to solve the full three-dimensional, time-dependent Navier-Stokes equations including the terms describing the two-way coupling between the dispersed phase and the carrier flow. The results include the temporal evolution of the three-dimensional energy and dissipation spectra and the rate of energy transfer across the energy spectrum to understand the fundamental physics of turbulence modulation, especially the effects of varying the magnitude of gravitational acceleration. The mean-square displacement and diffusivity of the droplets (or bubbles) of a given size and the preferential accumulation of droplets in low vorticity regions and bubbles in high vorticity regions will be examined in detail for different magnitudes of gravitational acceleration. These numerical results which will be compared with their corresponding measured data will provide a data base from which a subgrid-scale (SGS) model can be developed and validated for use in large-eddy simulation (LES) of particle-laden shear flows. Two parallel sets of experiments will be conducted: bubbles in an immiscible liquid and droplets in air. In both experiments homogeneous shear will be imposed on the turbulent carrier flow. The instantaneous velocities of the fluid and polydispersed-size particles (droplets or bubbles) will be measured simultaneously using a two-component Phase-Doppler Particle Analyzer (PDPA). Also, the velocity statistics and energy spectra for the carrier flow will be measured.

## INTRODUCTION

Turbulent, dispersed, two-phase flows occur in a wide range of manufacturing and processing applications. Often, the efficiency of the process depends directly on the degree of uniformity of dispersion of one phase into the other, e.g. the dispersion of droplets in a gas, or gaseous bubbles in a liquid. Thus, when the influence of gravity is reduced or eliminated, it is expected that the efficiency of many of these manufacturing or chemical processes could be greatly enhanced. However, at present, no existing two-phase mathematical model is accurate enough to be used for the design, operation and control of processes involving turbulent, dispersed two-phase flows. The keystone in the characterization of these flows still remains to be the modeling of the two-way interaction between the dispersed-phase and the turbulent carrier flow.

The main objective of our experimental/numerical study is to improve the understanding of the

fundamental physics of *two-way coupling* between small particles (droplets or bubbles) and a turbulent carrier flow. This two-way coupling encompasses the dispersion of the discrete particles (droplets or bubbles) by the turbulent fluid motion and the simultaneous modulation of the turbulence structure of the carrier flow by the dispersed-phase.

Our approach is to conduct a well-controlled set of ground-based and reduced-gravity experiments to measure the instantaneous velocities of the carrier flow and polydispersed-size droplets (or bubbles) using a two-component Phase-Doppler Particle Analyzer (PDPA) in a homogeneous-shear-turbulence wind tunnel (or water channel) where the air (or water) is laden with small droplets (or bubbles) of a known size-distribution. Although a flow laden with polydispersed-size particles (drops or bubbles) represents an added complexity to the experimental study, we have intentionally selected these conditions for two reasons. First, these conditions closely resemble those in practical applications. Second, this flow enables us to perform a full parametric study of the particle size effects on the turbulence kinetic energy exchange between the two phases *with a single experiment*. The parallel numerical study employs direct numerical simulation (DNS) to solve, for the same flow, the full three-dimensional, time-dependent Navier-Stokes equations including the two-way coupling terms. The choice of this uniform-shear flow avoids the unnecessary complexities resulting from inhomogeneities of the mean velocity or pressure as in jets and mixing layers.

The results of our study will directly impact the development of *subgrid scale*, SGS, models for *large eddy simulation*, LES, of particle-laden turbulent shear flows. At present, **there is no SGS model for particle-laden flows with two-way coupling**. It is important to note that an SGS model represents a *local spatial average of the instantaneous small scale turbulence*. This *instantaneous spatial average* is quite different from what is modeled in the conventional *time-averaged* transport equations (e.g. in the  $k - \epsilon$  model) where there is no distinction between large- and small-scale motions, and, by definition, the instantaneous motion cannot be retrieved. Therefore, all existing closure models of particle-laden turbulent shear flows provide little or no assistance in developing SGS models for LES of the same flows. The needed information can be obtained *only* from well-controlled experiments and DNS studies like those considered here.

It is true that DNS is not expected to predict engineering flows in complex geometries in the next few decades. However, DNS is the *only method that can provide new physical insights at all scales of turbulence*. Furthermore, DNS has provided excellent agreement with measurements in wind tunnels at comparable values of  $R_\lambda$  [3].

The scientific merit of the present study is that it will enhance the understanding of the basic physics of particle-laden turbulent shear flows and especially the effects of gravity on the two-way interaction between the dispersed phase and the carrier flow. Furthermore, the newly acquired experimental and numerical results will be used to improve the current mathematical models of these flows.

This project started in May 96 and thus this paper presents only a description of the numerical method, the experimental facility and the quantities to be measured.

## NUMERICAL STUDY

The three-dimensional Eulerian instantaneous velocity field for the fluid will be obtained by the method of direct numerical simulation (DNS) described by Elghobashi et al [2], Gerz et al. [5],

Elghobashi and Truesdell [3] [4] and thus only the main features are outlined here.

We consider a cubical domain with side-length  $L$  which is usually about eight times the initial integral length scale of turbulence ( $\ell_o$ ). Gravity acts downward in the negative  $x_3$  (or  $z$ ) direction. The two other coordinates  $x_1$  (or  $x$ ) and  $x_2$  (or  $y$ ) are in the horizontal plane. The fluid is incompressible and has a constant kinematic viscosity,  $\nu$ . The equations governing fluid motion are the instantaneous, three-dimensional Navier-Stokes, and continuity equations which can be written in a dimensionless form as :

$$\frac{\partial u_i}{\partial t} + \frac{\partial}{\partial x_j} (u_j u_i) + S x_3 \frac{\partial u_i}{\partial x_1} + S u_3 \delta_{i1} = \frac{1}{Re} \frac{\partial^2 u_i}{\partial x_j^2} - \frac{\partial p}{\partial x_i} - f_i, \quad (1)$$

$$\frac{\partial u_j}{\partial x_j} = 0. \quad (2)$$

In the above equations,  $u_i$  are the deviations of the instantaneous velocity  $U_i$  from their respective reference profiles:  $u_i(x, y, z, t) = U_i(x, y, z, t) - U_{ref}(z) \delta_{i1}$ , where  $U_{ref}(z) = z(dU_1/dz)_{ref}$  and  $(dU_1/dz)_{ref}$  is a fixed reference velocity gradient. The nondimensional shear  $S$  is defined as  $S = (L/\Delta U)(dU_1/dz)_{ref}$ , where  $\Delta U$  is the difference in the mean velocity at the top and bottom of the domain. The characteristic quantities used in nondimensionalizing eqs. (1)-(2) are  $L, \Delta U$  and a reference density  $\rho_o$ . The dimensionless time,  $t$ , is defined as  $t = (\tau \Delta U)/L$ , where  $\tau$  is the real time. The last term in eq.(1) is the force exerted on the fluid by  $N$  particles (droplets or bubbles) per unit mass of fluid, in the  $x_i$ - direction, and calculated from :  $f_i = \sum_{m=1}^N f_{m,i}$ , where  $f_{m,i}$  is the instantaneous local sum, in the  $x_i$ - direction, of the forces which act on one particle  $m$ . These are represented by the first four forces on the RHS of the equation (3) of particle motion described in the next subsection. Normalization of  $f_i$  is consistent with the other terms in eq. (1).  $N$  is the instantaneous number of particles,  $[N = N(x_1, x_2, x_3, t)]$ , within the control volume at which eq. (1) is integrated. The direct effect of the particles presence on the continuity equation of the fluid, eq. (2), is assumed negligible since the volume fraction of the particles is less than  $10^{-3}$ . It should also be emphasized that if the volume fraction of the particles exceeds  $10^{-3}$ , particle-particle collision may occur, thus resulting in *four-way coupling* [1] which is not considered in the present study.

The instantaneous velocity of a spherical particle,  $v_i$ , in the  $x_i$  direction, is obtained by time integration of the following Lagrangian equation of particle motion :

$$m_p (dv_i/dt_p) = m_p (u_i - v_i)/\tau_p + m_f (Du_i/Dt) + \frac{1}{2} m_f (Du_i/Dt - dv_i/dt_p) + 6a^2 (\pi \rho \mu)^{1/2} \int_{t_p}^{t_p} \frac{d/d\tau (u_i - v_i)}{(t_p - \tau)^{1/2}} d\tau + (m_p - m_f) g_i. \quad (3)$$

Equation (3) describes the balance of forces acting on the particle as it moves along its trajectory. The term on the left hand side is the inertia force acting on the particle due to its acceleration. The terms on the right side are respectively the forces due to viscous and pressure drag, fluid pressure gradient and viscous stresses, inertia of virtual mass, viscous drag due to unsteady relative acceleration (Basset) and buoyancy. As mentioned in the previous section, the negative of the sum of the first four terms on the RHS of (3) is the force exerted by one particle on its surrounding fluid. The response time  $\tau_p$  is the time for momentum transfer due to drag and is given, for the case of Stokes flow, as :  $\tau_p = (2a^2 \rho_p)/(9\nu \rho)$ .

The quantities,  $a, m_p, \rho_p$ , are, respectively, the particle radius, mass and material density. The fluid density and dynamic viscosity are  $\rho$  and  $\mu$ .  $m_f$  is the mass of the fluid displaced by the particle and equals  $m_p(\rho/\rho_p)$ . The derivative,  $d/dt_p$ , is with respect to time following the moving particle, whereas  $Du_i/Dt$  is the total acceleration of the fluid as seen by the particle, evaluated at the particle position  $\vec{x}_p$ . The integration of (3), via a second order Adams-Bashforth scheme

provides the new velocity,  $v_i(t)$ , in the  $x_i$ - direction for each droplet as a function of time. The new position,  $x_{p,i}(t_n)$ , along the particle trajectory is calculated from:

$$x_{p,i}(t_n) = x_{p,i}(t_{n-1}) + \Delta t[v_i(t_n) + v_i(t_{n-1})]/2 + \Delta t[U_{ref}(x_{p,i}, t_{n-1})]\delta_{i1}, \quad (4)$$

where  $t_n$  and  $t_{n-1}$  are the times at the current and previous time-steps, and  $\Delta t = t_n - t_{n-1}$ . The last term in (4) is the displacement of a particle due to the imposed mean velocity  $U_{ref}(x_3)$  of the carrier flow in the  $x_1$  direction.

The fluid velocity  $u_i[x_{p,i}(t)]$  at the particle location, which is needed to integrate eq. (3), is obtained by a fourth-order, two-dimensional, four-point Hermitian polynomial interpolation scheme between the adjacent Eulerian fluid velocity values. This scheme is applied in the three coordinate directions at the particle location. It should be mentioned that eq. (3) must be solved simultaneously with the Navier-Stokes equ.(1) and the continuity equ.(2) in order to evaluate the coupling terms  $f_i$ .

## EXPERIMENTAL STUDY

In order to examine the complex interactions between the particles and the turbulent flow, simultaneous measurement of the velocity fields of the two phases is required. For this purpose, detailed phase Doppler velocity and size measurements will be conducted at locations downstream along the evolving turbulence using an Aerometrics phase Doppler particle analyzer (PDPA) system. Due to the relatively large concentration of particles (void fraction) required for our particle-turbulence two-way interaction study, these measurements represent a particularly challenging problem. Therefore we will to conduct each experimental study in two stages. The first stage considers the modification of decaying homogeneous (grid-like) turbulence in a uniform flow by the presence of particles of a known size distribution. The second stage concerns the more general case of homogeneous turbulence in a uniform-mean-gradient shear flow. The following sections describe the experimental set-ups for the studies of both inertial particles (droplets in air) and particles with negligible inertia (bubbles in water).

### Uniform mean-velocity facilities

#### a) Wind tunnel

The blow-down wind tunnel to be used in the first part of experiments (water droplets in air) already exists in our laboratory at UCSD. The basic facility is described in detail by Lázaro and Lasheras [6] [7]. By extending the splitter plate an additional 4m and by building both top and bottom surfaces of the test sections out of movable belts, this facility permits the study of the decay of the particle-laden turbulent flow over extended distances. The facility is rather versatile since it allows not only for the variation of the mean velocity and rms of the air flow, but also the systematic variation of both the droplet size distribution, and the droplet volumetric flow rate.

#### b) Water channel

The water channel used in the second set of experiments also exists in our laboratory at UCSD. Conceptually this facility is identical to the above described wind tunnel with the exception of the bubble generation section.

### Droplet and bubble generation

#### a) Droplet generation

A polydispersed size spray of droplets generated through an array of air blast atomizers is used in our wind tunnel to inject droplets into the shear flow and control their size and void fraction. The humidity of the carrier gas prior to the droplet injection section is always kept equal to the

equilibrium saturation value. Thus, evaporation effects in the test section are quite negligible [6] [7].

Each atomizer consists of two 22G (0.406mm inner diameter) stainless steel tubes placed together in an inverted U configuration [6]. The bent tube is fed with compressed air whereas the straight one is fed with distilled water from a pressurized tank. The high velocity air jet issuing from the bent tube impinges and breaks the capillary water jet emanating from the straight needle. This design allows, within a certain range, control over the mean diameter and droplet density. The diameter is controlled by varying the air supply pressure while the density can be regulated by adjusting the water flow rate. The atomizer is then introduced in the air stream with the compressed air jet issuing in the streamwise direction. The resulting droplet volume-size probability density function shows that 99% of the number pdf is contained within the range  $2\mu\text{m} < D < 100\mu\text{m}$ .

To ensure uniform particle concentration in the cross-section of the free stream, several hundred atomizers are distributed along the atomization region, forming an equidistant triangular mesh in the plane perpendicular to the streamwise direction. Every atomizer can be separated from its neighboring ones at a preset distance. The overlapping of the resulting array of sprays in the mesh results in the desired uniform free-stream droplet size and density (void fraction) distribution.

Our experimental set-up and flow conditions ensure that there is negligible droplet collision and evaporation and thus are ideal for the study of particle/turbulence interaction.

#### **b) Bubble generation**

The bubbles are created using the "novel" injection scheme. Water, saturated with  $\text{CO}_2$  at 90 psi by a water carbonator, is expanded as a jet through small holes drilled into a grid of brass tubes. The resulting negative pressure step experienced by the carbonated water causes homogeneous nucleation to occur in the jet. Due to the rapid mixing with non-carbonated water flow in the water channel, the bubble growth is limited, resulting in a small polydispersed bubble size distribution. Bubble production is not uniform in the vertical direction due to varying pressure steps along the small brass tubing, however, the mixing induced by the jets homogenizes the bubble sizes throughout the stream. Any bubbles produced that are too large rise rapidly and are removed by the free surface just downstream of the injection location. Bubbles that accumulate on the underside of the splitter plate in the slow moving flow prior to the contraction are removed by suction.

#### **Uniform-mean-shear flow facilities**

Recently, Piccirillo [8] has successfully extended Rohr's multi-layer concept [9] to air flow. This new facility is currently used in our laboratory at UCSD to study the evolution of turbulence in a uniform-mean-shear, thermally stratified flow. The facility consists of a blow-down, open-loop, multi-layered wind tunnel. The facility is supplied by an array of ten independent blowers connected to individual diffusers and turbulent management sections, and thus allows for the generation of ten layers of air at a pre-determined velocity and temperature. The merging of the ten parallel layers results in a uniform-mean-shear flow at the beginning of the test section. This multi-layered design allows for a relatively simple way to generate a large variety of uniformly-sheared turbulent flows in which water droplets can be added to produce a flow of uniform  $\Phi_v$ .

For our droplet-laden air flow turbulence experiments and for the bubble-laden water flow, both multilayer facilities will be modified by simply placing at the end section of each layer an array of atomizers or micronozzles in a similar way as is currently done in the uniform-velocity facilities described above. To minimize the wake effects resulting from the boundary layers on the plates separating each layer, a set of screens are placed downstream of the merging section. To produce uniform volumetric flow rate of droplet loading ( $\Phi_v$ ) throughout the whole cross-stream length of the test section, the number of individual atomizers placed in each array will be adjusted depending

on the mean air velocity in each layer.

### Quantities to be measured

The polydispersed drop size distribution will be discretized into five size families. Similarly, for the bubble case, the bubble size distribution will be discretized in the same number of families. For each drop size, we will measure the three components of their velocity along the centerline ( $u_d, v_d, w_d$ ). The size range between  $1\ \mu m$  and  $2\ \mu m$  will be used as markers to extract the velocity of the carrier gas ( $u_a, v_a, w_a$ ). We will conduct a parametric study of the effect of  $\Phi_v$  and the strain parameter  $\frac{1}{U_a} \frac{dU_a}{dz}$  for a fixed droplet size distribution.

The following turbulence quantities will be extracted from the measurements.

**Carrier flow (Air or Water):** The turbulent stresses (normal and shear), the production rate of turbulence kinetic energy, the streamwise dissipation rate of turbulence energy, the energy spectrum, the turbulence length scales (Taylor microscale, the integral length scale by integrating the corresponding autocorrelation coefficient).

**Dispersed phase (Droplets and Bubbles):** For each family  $D_i$  of the discrete size distribution we will compute: the probability density distribution function of the three components of the particle velocity, the turbulence kinetic energy of each particle family,  $\overline{q_{D_i}^2} = \frac{1}{2} (\overline{u_{D_i}'^2} + \overline{v_{D_i}'^2} + \overline{w_{D_i}'^2})$ , the mean volume flow rate of each droplet size,  $\Phi_{v_{D_i}}$ , and the total mean volume flow rate of droplets,  $\Phi_v = \sum_{i=1}^5 \Phi_{v_{D_i}}$ .

## REFERENCES

- [1] S.E. Elghobashi. On predicting particle-laden turbulent flows. *Appl. Sci. Res.*, 52, 1994.
- [2] S.E. Elghobashi, T. Gerz, and U. Schumann. Direct simulation of turbulent homogeneous shear flow with buoyancy. *Fifth International Symposium on Turbulent Shear Flows, Cornell Univ.*, pages 227-233, 1985.
- [3] S.E. Elghobashi and G.C. Truesdell. Direct simulation of particle dispersion in decaying isotropic turbulence. *J. Fluid Mech.*, 242:655-700, 1992.
- [4] S.E. Elghobashi and G.C. Truesdell. On the two-way interaction between homogeneous turbulence and dispersed solid particles, part 1: turbulence modification. *Phys. Fluids*, A5:1790-1801, 1993.
- [5] T. Gerz, U. Schumann, and S. Elghobashi. Direct simulation of stably stratified homogeneous turbulent shear flows. *J. Fluid Mech.*, 200:563-594, 1989.
- [6] B.J. Lazaro and J.C. Lasheras. Particle dispersion in the developing free shear layer. part 1. unforced flow. *J. Fluid Mech.*, 235:143-178, 1992.
- [7] B.J. Lazaro and J.C. Lasheras. Particle dispersion in the developing free shear layer. part 2. forced flow. *J. Fluid Mech.*, 235:179-221, 1992.
- [8] P.S. Piccirillo. Evolution of stratified shear turbulence. *Ph.D. Thesis*, University of California, San Diego, AMES Dept., 1993.
- [9] J. J. Rohr, E. C. Itsweire, K. N. Helland, and C. W. Van Atta. An investigation of the growth of turbulence in a uniform-mean-shear flow. *J. Fluid Mech.*, 187:1, 1988.

# TRANSPORT PHENOMENA IN STRATIFIED MULTI-FLUID FLOW IN THE PRESENCE AND ABSENCE OF GRAVITY

Norman Chigier and William Humphrey  
Carnegie Mellon University  
5000 Forbes Avenue  
Pittsburgh, Pennsylvania 15213

## ABSTRACT

Experiments are being conducted to study the effects of buoyancy on planar density-stratified shear flows. A wind tunnel to generate planar flows separated by an insulating splitter plate, with either flow heated, which emerge from a two-dimensional nozzle. The objective is to isolate and define the effect of gravity and buoyancy on a stratified shear layer. To this end, both stably and unstably stratified layers will be investigated. This paper reports on the results of temperature and velocity measurements across the nozzle exit plane and downstream along the nozzle center plane.

## INTRODUCTION

The objective of this research is to separate the effects of molecular and turbulent diffusion from the effect of buoyancy in the mixing of two fluid layers. This fundamental phenomenon is encountered in many applications. The use of reduced gravity will allow the elimination of buoyant body forces in a flow which contains density gradients.

Transport processes in multi-fluid flows with and without gravity have been studied by several researchers. However, most of these studies concerned themselves with the initiation of convection and diffusion in small, bounded fluid volumes initially at rest (e.g., Refs. 1 & 2). These experiments, with forced flows of variable velocity and buoyancy and stable or unstable density stratification, will provide the means to identify the effect of buoyancy on shear flow.

This research will contribute to the understanding of the fundamental processes involved in the mixing of fluids of different densities. The effects of orientation and the sign of the velocity and density gradients on the mixing process can be individually examined. The reduced gravity environment will also allow the isolation of the effect of density gradients on mixing separate from the effect of buoyancy caused by such gradients in earth gravity.

## EXPERIMENTAL APPARATUS AND METHODS

The two-dimensional shear layer is generated by a low-velocity facility similar to a wind tunnel. Fig. 1 shows a sketch of the apparatus and Fig 2 shows the nozzle exit dimensions with the coordinate system used in the experiments. The two flow passages in the tunnel are separated by an insulating plate. The air supplies are independently controlled. The temperature of each stream can be controlled by a 7.5 kW coil heater with a feedback control system. Uniform exit velocities are provided by high contraction ratio two-dimensional nozzles.

The insulating splitter plate between the two flow passages is critical to the performance of the system. The plate must minimize both heat transfer between the flows and flow disturbances. Minimum thickness with adequate insulation properties was achieved thanks to Owens-Corning Corporation, who provided prototype vacuum super-insulation panels. These were faired into a smooth plate by lamination with high-temperature castable ceramic. The final 2° wedge in the nozzle section, used to bring the two flows together at the nozzle exit nearly parallel, was formed from Marinite-I.

Each flow passage has an independently regulated air supply. Air supply flow rate limitations only allow exit velocities of up to 2 m/s. The large expansion ratio diffusers allow a low air velocity in the heater section to ensure a uniform temperature downstream.

The density of the air stream is controlled by temperature. Either stream can be heated to produce stable (top heated) or unstable (bottom heated) stratification in the shear layer. The heater output is regulated by an SCR

power controller with feedback provided by a T-type thermocouple and a digital electronic proportional-integral-derivative feedback controller. This system achieves excellent temperature stability of  $\pm 2^\circ\text{C}$  at  $200^\circ\text{C}$ . The vertical temperature gradient across the plane of the splitter plate (at  $z=0$ ) is approximately  $6.5^\circ\text{C}/\text{mm}$ . The temperature is nearly uniform (within  $\pm 5^\circ\text{C}$ ) across more than 50% of the width of the nozzle (Fig. 3).

The flows are accelerated to the desired exit velocity by the one-sided high contraction ratio two-dimensional nozzles. The cross-sectional area distribution was chosen to minimize length and, therefore, heat transfer as well as provide highly uniform flow. Excellent uniformity along the vertical axis is achieved (except for the inevitable boundary layers) and the flow across nearly 50% of the width can be considered two-dimensional (Fig. 4).

Temperature measurements are made using 15 fine-wire Type-K thermocouples. The thermocouples are mounted in a linear array which spans the width of the nozzle exit. A traversing mechanism allows the array to be moved vertically and axially.

Velocity measurements are made with a TSI two-component LDV system. Seeding particles generated by an atomizer are introduced into the flow via perforated tubes mounted horizontally across the flow immediately following the flow straighteners. The LDV system is operated in coincidence mode with the receiving optics placed  $30^\circ$  off-axis in a forward scatter arrangement. The LDV system provides mean and fluctuating velocity measurements as well as fluctuation correlations and the Reynolds shear stress. Due to geometric constraints, measurements cannot be made closer than 5 mm from the nozzle exit ( $x/H = 0.2$ ).

## RESULTS

In addition to the temperature and velocity maps of the nozzle exit plane, LDV measurements of the shear layer have been made for the unstratified, stably stratified and unstably stratified conditions. Mean and fluctuating components of axial and vertical velocity were measured simultaneously along the centerplane ( $y=0$ ) of the flow. In all experiments to date, the mean velocity of the upper flow was maintained at  $u_t = 1$  m/s and the lower flow at  $u_b = 0.5$  m/s. In all stratified cases, the mean temperature of the heated flow was maintained at  $T = 200^\circ\text{C}$ .

Fig. 5 shows the progression of the axial and vertical velocity profiles at progressive downstream locations of  $x/H = 0.2, 1, 2$ , and  $4$ , respectively in the unstratified case. At  $x/H = 0.2$  (effectively at the nozzle exit) the axial velocity profile shows nearly uniform velocity except for the boundary layers on the nozzle walls and on the splitter plate. The thickness of the central velocity defect is small and the gradient is steep, so the flow approaches the ideal step profile. At the nozzle exit, the vertical velocity has a sign opposite that of the vertical position. This is due to the slight wedge shape of the splitter plate. The maximum value of  $v$  is about 4% of the upper stream velocity,  $u_t$ , so the flows are essentially parallel. As the flow progresses downstream, the central velocity defect relaxes and the profile broadens due to entrainment.

Fig. 6 shows the progression of the velocity profiles at downstream locations  $x/H = 0.2, 1, 2$ , and  $4$ , respectively for the stably stratified case. At  $x/H = 0.2$ , the axial velocity profile differs little from the unstratified case. The vertical velocity profile shows the effect of buoyancy as the vertical velocity in the upper flow increases, changing sign. The vertical velocity in the lower flow also increases, and this increase is greatest nearest the splitter plate. This is primarily due to heat transfer through the splitter plate and the accompanying thermal boundary layer. The axial velocity profiles demonstrate the same behavior as the unstratified profiles with the exception that the entire profile rises with distance due to the buoyant nature of the upper flow.

Fig. 7 & 8 show the axial and vertical velocity profiles at downstream locations of  $x/H = 0.2$  &  $1$ , and  $x/H = 2$ , respectively, for the unstably stratified case. The axial velocity is not grossly changed from the previous, stable, case. The vertical velocity profile at the nozzle exit ( $x/H = 0.2$ ) also does not change appreciably from the stably stratified case. However, as the flow moves downstream, the vertical velocity profile quickly moves towards a nearly uniform upward motion. The magnitude of the vertical velocity is also lower overall than in the stably stratified case.

The data in Fig. 7 was collected with the entire flow seeded. Due to decreasing data rates due to sparse seeding as axial distance from the nozzle increases, conditional sampling was explored. In conditional sampling the two streams are each seeded alone. Velocity profiles are measured twice, once for each condition of seeding. Fig. 8



shows the velocity profiles from each case on the same axes. The vertical positions at which data can be collected overlap due to diffusion and mixing of the seeding particles. The axial velocities show some disparity between the conditions of sampling. The mean velocities in each condition do not represent the mean velocity of the flow at the point in question. Rather, they represent the mean velocity of turbulent eddies which carry seeding particles through the probe volume. However, the vertical velocities agree well in this region. The mean vertical velocity observed is the bulk velocity of the entire flow; it is reasonable to expect that the average vertical velocity of fluctuating eddies about the mean vertical velocity would be zero, and thus not appear in the time-averaged data.

## CONCLUSIONS

The low speed stratified shear layer wind tunnel has been built and shown to meet all of the performance criteria required. LDV measurements of an unstratified shear layer were made as a baseline for comparison.

LDV measurements in both stably and unstably stratified shear layers have also been made. As expected, the axial mean velocity profiles do not show a significant dependence on the sign of the density gradient beyond the translation of the whole flow. The vertical velocity profile at the nozzle exit shows great dependence on the existence of a density gradient. The downstream vertical velocity profiles do show some dependence on the sign of the density gradient. For the unstably stratified case, the ascent of the mixing layer is less and the vertical velocity is more nearly uniform across the layer.

Further experiments are underway to determine if this effect of density gradient on the vertical velocities is also dependent on the sign of the velocity gradient. In addition, evidence regarding the existence of large scale structures (Refs. 3 & 4) in the layer is being sought. Both LDV data and flow visualization (using laser sheet photography) will be employed. It is expected that the unstably stratified shear layer will not support such organized structures due to the higher level of turbulence generated.

Initial attempts to ascertain the effect of gravity on the buoyant shear layer will be made in the earth-based low velocity facility. The experiment will be arranged so that the gravity vector is perpendicular to the dimensions of interest, by rotating the tunnel about its long axis by 90°.

## ACKNOWLEDGMENT

This work was supported by a grant from the NASA Microgravity Science and Applications Division (NASA Grant NAG3-1505).

## REFERENCES

1. Koster, J.N. and Sani, R.L. (Ed.), "Low Gravity Fluid Dynamics and Transport Phenomena", Progress in Astronautics and Aeronautics, AIAA, Washington, D.C., Vol. 130, 1990
2. Prakash, A. et al, "Convective Instabilities in a Two-Layer Fluid System", AIAA Paper 91-0313, 1991
3. Brown, G. and Roshko, A., "On the Density Effects and Large Structures in Turbulent Mixing Layers", J. Fluid Mechanics, Vol. 64, pp. 775-816, 1974
4. Chandrsuda, R. et al, "Effects of Free-stream Turbulence on Large Structure in Turbulent Mixing Layers", J. Fluid Mechanics, Vol. 85, pp. 693-704, 1978

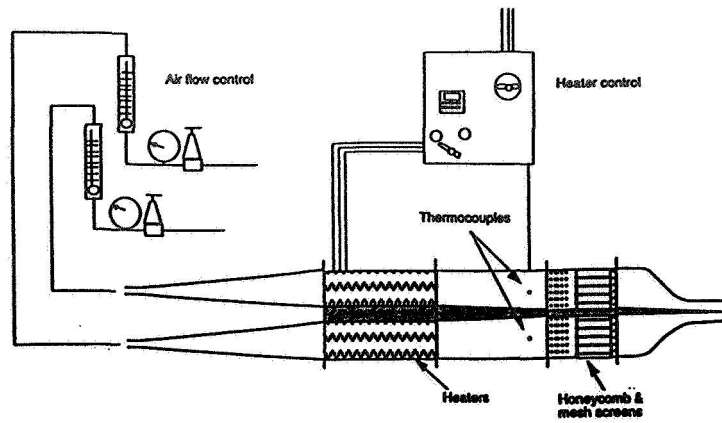


**Fig. 1: Two-dimensional Shear Layer Wind Tunnel Schematic**

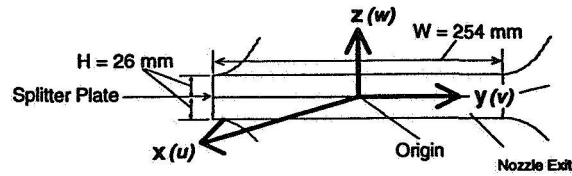


**Figure 2: Nozzle Dimensions and Coordinate System**

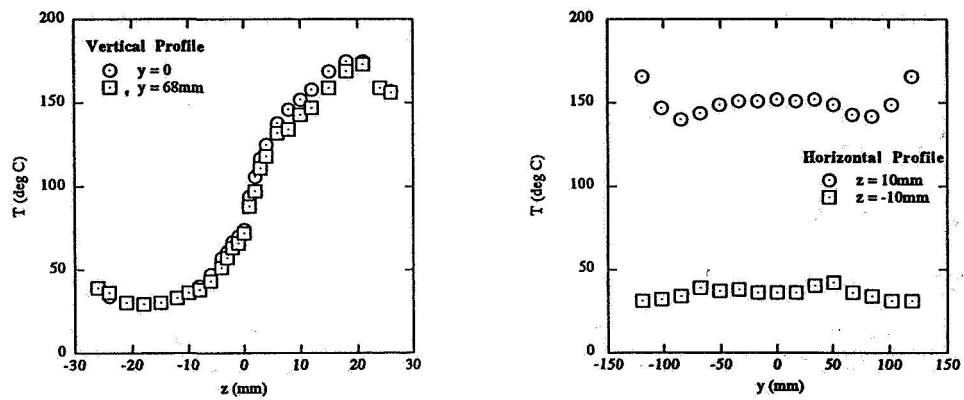


**Fig. 3: Nozzle Exit Plane Temperature Profiles (top stream heated to 200°C)**

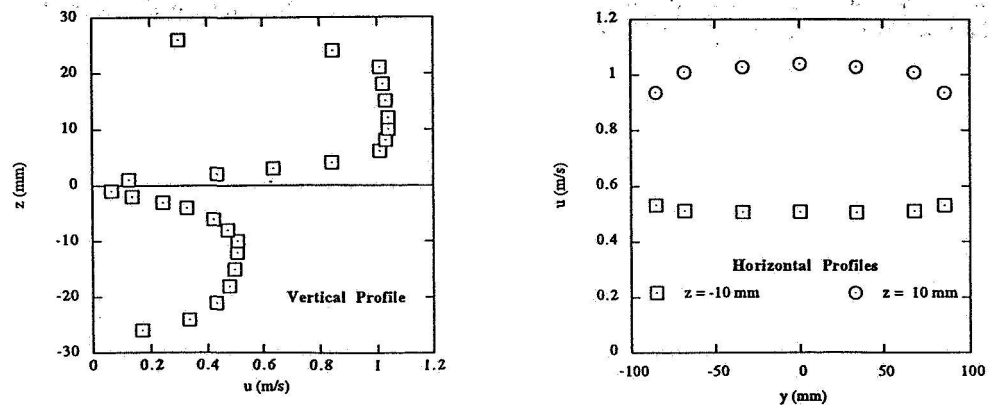


**Fig. 4: Nozzle Exit Plane Axial Velocity Profiles (unheated flow)**

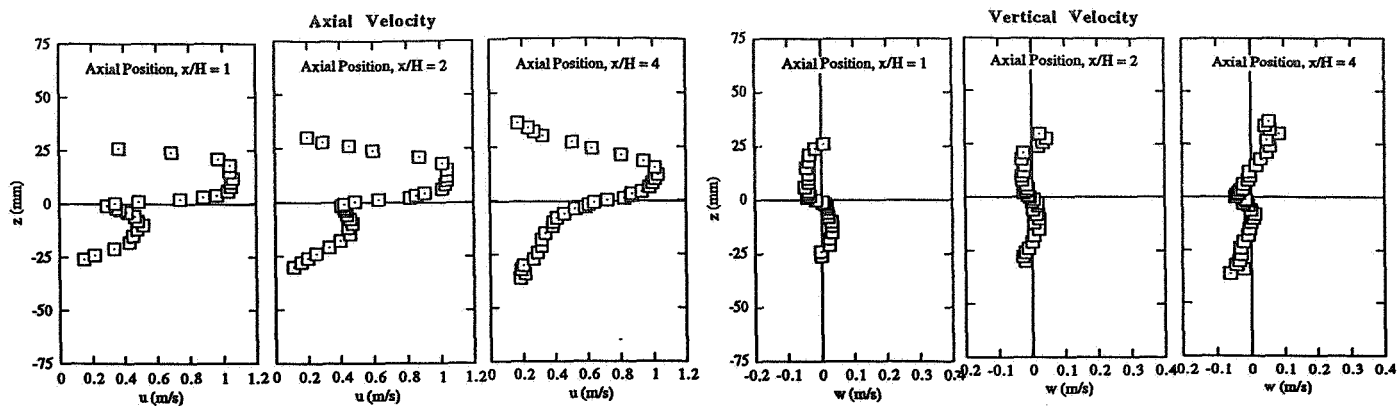


**Fig. 5: Downstream Velocity Profiles (unheated flow)**

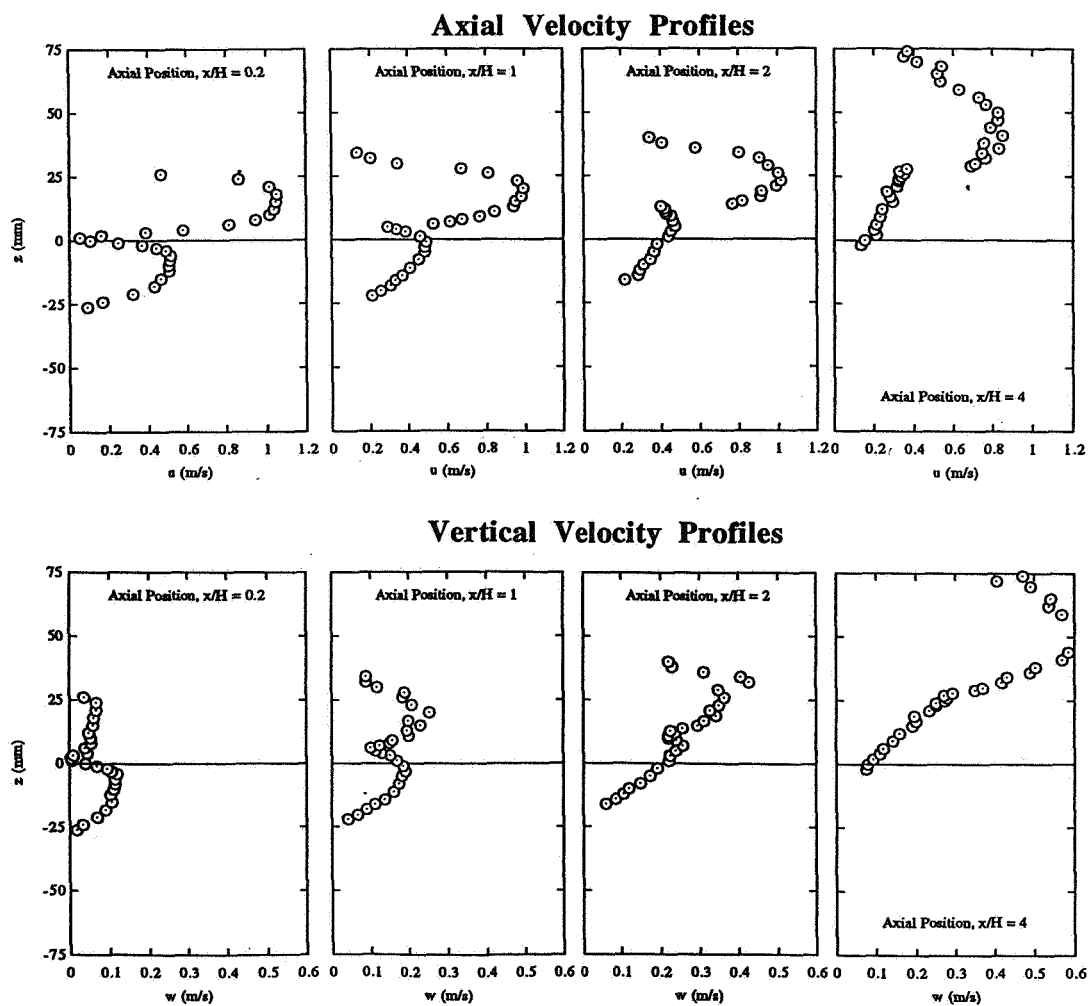


**Fig. 6: Velocity Profiles (stably stratified, top stream  $T=200^{\circ}\text{C}$ )**

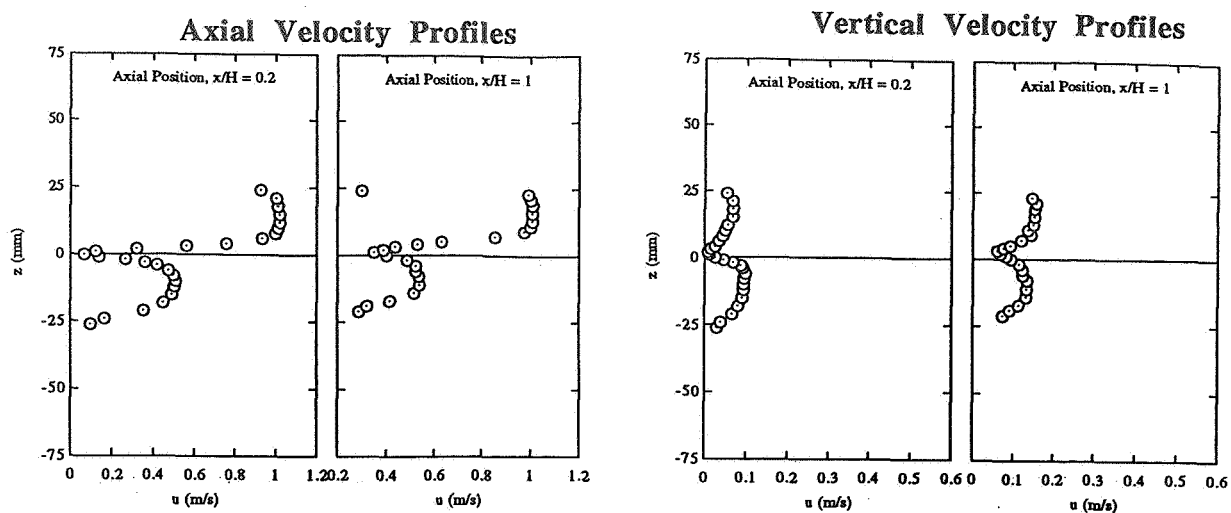


**Fig. 7: Velocity Profiles (unstably stratified, bottom stream  $T=200^{\circ}\text{C}$ )**

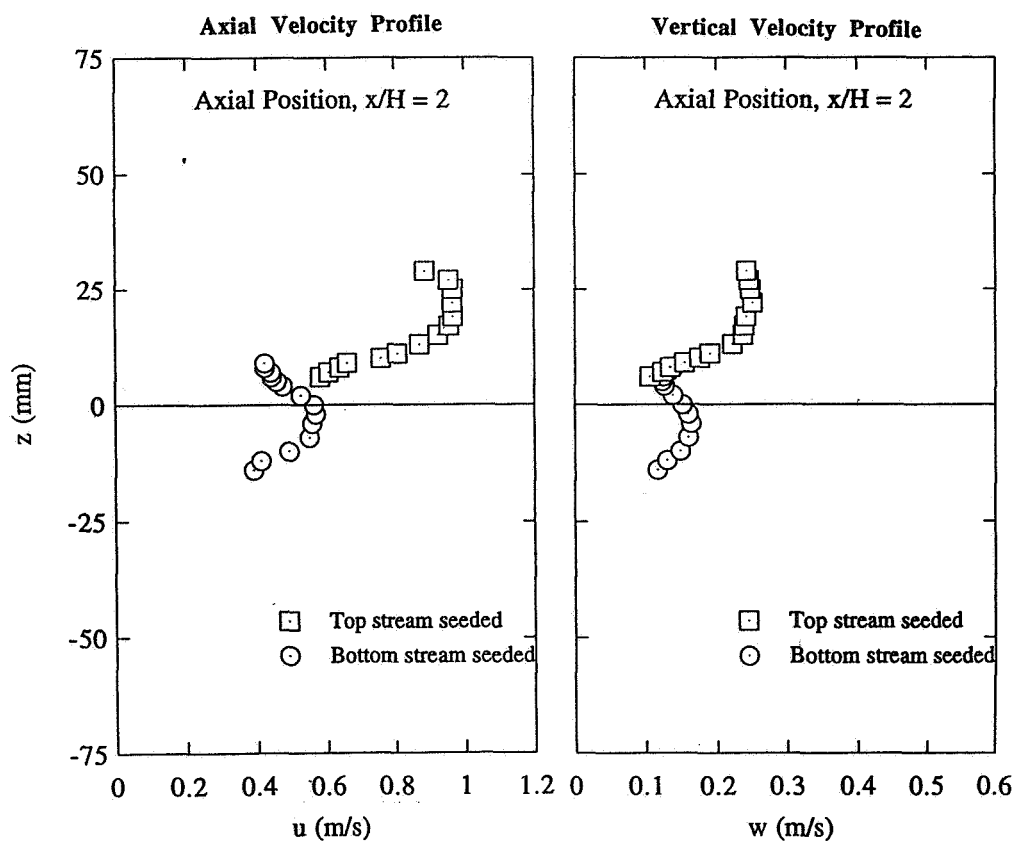


**Fig. 8: Velocity Profiles (unstably stratified, bottom stream  $T=200^{\circ}\text{C}$ )  
Conditional Sampling**

# Decoupling The Role Of Inertia And Gravity On Particle Dispersion

*Chris Rogers  
Tufts University  
Medford, MA 02155*

*and  
Kyle Squires  
University of Vermont  
Burlington, VT 05405*

## **Abstract**

Turbulent gas flows laden with small, dense particles are encountered in a wide number of important applications in both industrial settings and aerodynamics applications. Particle interactions with the underlying turbulent flow are exceedingly complex and, consequently, difficult to accurately model. The difficulty arises primarily due to the fact that response of a particle to the local environment is dictated by turbulence properties in the reference frame moving with the particle (particle-Lagrangian). The particle-Lagrangian reference frame is in turn dependent upon the particle relaxation time (time constant) as well as gravitational drift. The combination of inertial and gravitational effects in this frame complicates our ability to accurately predict particle-laden flows since measurements in the particle-Lagrangian reference frame are difficult to obtain.

Therefore, in this work we will examine separately the effects of inertia and gravitational drift on particle dispersion through a combination of physical and numerical experiments. In this study, particle-Lagrangian measurements will be obtained in physical experiments using stereo image velocimetry. Gravitational drift will be varied in the variable-g environments of the NASA DC-9 and in the zero-g environment at the drop tower at NASA-Lewis. Direct numerical simulations will be used to corroborate the measurements from the variable-g experiments. We expect that this work will generate new insight into the underlying physics of particle dispersion and will, in turn, lead to more accurate models of particle transport in turbulent flows.

## **Introduction**

In modeling particle-laden flow, one must have a fundamental understanding of how the particle responds to local turbulence. Defining this turbulence is probably the greatest difficulty in deriving an accurate model. The difficulty arises from the fact that each particle navigates a unique path through the flow: a path dictated by its inertia and gravitational drift. This path, dubbed the particle-Lagrangian reference frame, is neither the purely Lagrangian path of a fluid point, nor the conventional stationary Eulerian reference frame. Particle inertia affects the turbulence experienced by the particle as particles are flung from one fluid neighborhood to another, and gravity affects the path

by pulling the particle through the turbulence. To accurately model the behavior of the particle, one must decouple the effects of the gravitational drift from those resulting from the inertia of the particle: this is the goal of the proposed research.

If one imagines a turbulent fluid field consisting of a random assortment of various size eddies, then the turbulence can be partially characterized by a power spectrum: a measure of the distribution of the turbulent kinetic energy among these eddies. The behavior of an individual particle will depend on how quickly a particle can respond to these fluctuations in the fluid velocity. For instance, small (high frequency) eddies will have little effect

on particles with slow response times (large time constants) and, conversely, large (low frequency) eddies will have little difficulty in influencing all but the most sluggish particles. The apparent frequency of the eddy experienced by the particle, however, will be a function of the particle velocity. Similar to an acoustic Doppler shift, as the particle moves through an eddy, the frequency it responds to will be a function of the particle velocity as well. Finally, to further complicate modeling, as it crosses the eddies due to its gravitational drift, it moves from one fluid neighborhood to another. This is known as the "crossing-trajectories" effect<sup>1</sup>, and plays an active role in the particle dispersion<sup>2</sup>.

#### *Previous Work*

Although there has been a substantial effort to better understand and model the transport of a dilute particle species in a turbulent field<sup>3,4</sup>, accurate modeling has been hindered by the inability to transform the Eulerian (or Lagrangian) fluid models into the particle-Lagrangian reference frame. Csanady<sup>5</sup> assumed a simplified particle transport equation

$$\frac{d\vec{V}_p}{dt} = \frac{1}{\tau_p} (\vec{U}_f - \vec{V}_p) - \vec{g} \quad [1]$$

where  $U_f$  and  $V_p$  are the fluid and particle velocities and  $\tau_p$  is the particle time constant. This equation is the transport equation for particles whose density is much greater than that of the carrier fluid. The particle time constant is a measure of the response time and for Stokesian particles is

$$\tau_p = \frac{\rho d^2}{18\mu} \quad [2]$$

where  $\rho$  and  $d_p$  are the particle density and diameter,

respectively, and  $\mu$  is the viscosity of the fluid. Finally, a Stokesian particle is one whose Reynolds number is less than 0.1. The particle Reynolds number is simply defined as

$$Re_p = \frac{U_s d}{\nu} \quad [3]$$

where  $U_f$  is the fluid velocity relative to the particle and  $\nu$  is the fluid kinematic viscosity.

From this transport equation, Csanady showed that if one examined the fluctuating component of equation 1 (Reynolds decomposition) and replaced the particle and fluid velocity by a Fourier series, one could estimate the fluid power spectrum by

$$E_p(\nu) = \frac{1}{1 + 4\pi^2 \tau_p^2 \nu^2} E_f(\nu) \quad [4]$$

where  $E_p$  and  $E_f$  are the particle and fluid power spectra,  $\nu$  is the eddy frequency (in Hz), and  $\tau_p$  is the particle time constant.<sup>6</sup> Csanady assumed that  $E_f$  is the fluid power spectrum in the particle-Lagrangian coordinate system. If one could accurately transform measurements made in the Eulerian reference frame to the particle-Lagrangian, one could then use the above analysis to estimate the particle response - and - from there - the particle autocorrelation. Once one has the particle autocorrelation, one can then predict the particle dispersion ( $y_2(t)^2$ ) with a Taylor-like analysis<sup>7</sup>:

$$\overline{y_2(t)^2} = 2\overline{v_2^2} \int_0^t \int_0^\eta \overline{R_L(\tau)} d\tau d\eta \quad [5]$$

where  $R_L(\tau)$  is the particle velocity autocorrelation and  $v_2^2$  is the average square particle velocity fluctuation for homogeneous stationary turbulence.

To date, there have been three approaches to trying

to decouple gravity and inertia to model this transformation. The first is by charging the particles and then using an electric field to essentially remove the effects of gravity (the Wells and Stock experiment<sup>2</sup>), the second is through numerical simulations, and the third is a combination of the two.

#### The Wells and Stock Experiment

Wells and Stock were able to make similar measurements to the ones proposed here by electrically charging the particles and using a electric field to vary the particle drift velocity. They introduced electrically charged two different diameter glass beads (5 and 57  $\mu\text{m}$ ) into a near-homogeneous flow. They found that the effect crossing-trajectories on particle dispersion was negligible for particles with drift velocities that were less than the r.m.s. velocity of the fluid. This would correspond to particles that almost follow the fluid and therefore will not experience the crossing trajectories effect. Particles with drift velocities equal to the r.m.s. velocity of the fluid reduced the dispersion coefficient by about 10%. They had some difficulty, however, with particle charge and shape non-uniformity affecting their results. This, in turn, led to a difficulty in making conclusions on the effects of inertia.

They did, however, demonstrate that the crossing trajectories effect reduces particle dispersion. The dispersion decreases because as the particle moves through fluid neighborhoods, the fluid fluctuations experienced by the particle lose correlation more rapidly and therefore (from equation 4) reduce the

particle velocity correlation and hence a decrease in dispersion (equation 5). They were also able to show that the magnitude of the gravitational drift directly affects the particle behavior in a non-linear way.

Unfortunately, in their work they were only able to examine two particles and had difficulties in retaining uniform charge on the particles. In the future experiments, we would first extend their work in two ways: (1) examine a greater range of particle time constants and (2) examine the effect of inertia on particle dispersion. The latter could not be accurately ascertained using their experimental setup. The last stage of the work would be to correlate instantaneous particle behavior to the instantaneous fluid behavior, making it easier to extend the results to a wider class of applications.

#### Numerical Work

As mentioned above, the majority of “purely numerical” studies of particle dispersion in turbulence have been performed using direct numerical simulation. In DNS the Navier-Stokes equations are solved without approximation (other than those associated with the numerical method) and the results from a DNS calculation may be analyzed in much the same fashion as measurements from a laboratory experiment. The main disadvantage of DNS is that it remains limited to calculation of moderate Reynolds number canonical flows. However, given the extremely detailed description of the flow in a DNS computation, it provides a powerful tool for simulation and analysis.

Several investigators have used DNS to examine particle transport in isotropic turbulence (e.g., see Squires and Eaton<sup>8</sup>, Elghobashi and Truesdell<sup>9</sup>, Wang and Maxey<sup>10</sup>). Each of these investigations have demonstrated the utility of DNS for examination of fundamental aspects of particle dispersion in canonical flows. Squires and Eaton found good agreement between particle dispersion in DNS and the theory of Csanady<sup>5</sup>. Elghobashi and Truesdell also obtained good agreement between DNS predictions and the experimental measurements of Snyder and Lumley<sup>11</sup>. Wang and Maxey demonstrated that increases in particle settling velocities obey Kolmogorov scaling. While each of these previous efforts are relevant to this study, the principal aim of the DNS calculations proposed in this work is to corroborate the measurements obtained from the variable-g measurements. The parameter combinations required in the proposed simulations are not directly available from previous work.

### **Plan of Action**

In this work we will decouple the effects of gravity and inertia in particle dispersion. With a better understanding of how one can estimate the fluid turbulence in the reference frame of a moving particle, one can better estimate the particle response to its environment. The work will be divided into six segments: (1) development of the laboratory experiment, (2) computer simulations of the expected particle behavior for variable-g, (3) quasi-simulations tracking an imaginary particle through the measured fluid velocity field, (4) experimental

tests on a local aircraft for small time durations to verify and hone the experimental techniques, (5) variable-g experiments in the NASA DC-9 and drop tower, and (6) final data analysis and model development. First we will develop, build and test a sample experimental setup at Tufts - testing out the stereo-imaging velocimetry system (SIV) and refining the particle/fluid discrimination system. In tandem, we will run simulations of our flow at low Reynolds numbers. We will compare the simulation results with the measurements made in the laboratory. Next, using a local airplane, we will test the experiment in a near-zero-g environment. Combining these results, we will then run a series of experiments in the NASA DC-9 at variable-g. We will compare these results to both the full simulations and the quasi-simulations, and to the results of Wells and Stock. These final data will serve two purposes; (1) be the basis for our modeling effort and (2) quantify the accuracy of our quasi-numerical scheme, from which we can numerically examine a large number of particle parameters.

### **Experiment Design; Ground-Based: Laboratory**

#### **Experimental**

The experimental apparatus will be a simple suction tunnel with a variable-sized entrance grid to generate the various turbulence scales (see figure 1). The idea is to track particles in three dimensions through the simplest turbulent flow. This tunnel design is based on Corrsin's<sup>13</sup> and Pope's work<sup>14</sup> and should provide a relatively homogeneous turbulent flow. The honeycomb at the exit reduces the effects of the fan blades propagating upstream and the particle injector at the tunnel entrance allows us to



control the particle initial conditions. Turbulence properties (such as the energy spectrum) will also be measured at the injection location and will therefore permit comparison to simulations. The total height of the tunnel should be about 2 meters - this allows for roughly 20 particle time constants in the test section and another 10 for the entrance.

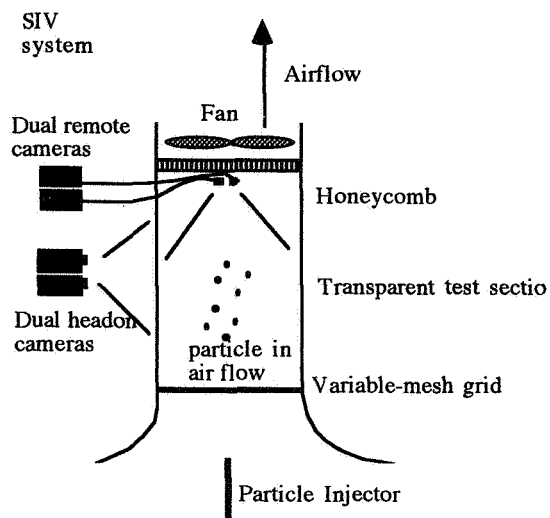


Figure 1: Experiment Schematic

The particle injection system for the ground-based experiment will be a single injection vacuum system so that we can control the particle injection time and speed to accurately compare with simulation results. For the flight experiments, we will use a continuous particle injection system that will allow us to track numerous particles in a given run (due to the time limitations of the flight experiments). We will distinguish particles from fluid tracers by using fluorescent particles (we can therefore discriminate based on reflected color). The air will be seeded with micron-size particles for the stereo image velocimetry (SIV) system using a simple paint-sprayer and talcum powder suspended

in alcohol. This seeding technique has been successfully used for seeding for LDV measurements - it relies on the alcohol evaporating before the talcum powder enters the test section.

#### Experiment Design: Numerical

The proposed simulations of particle-laden isotropic turbulence are direct numerical simulations. DNS of the incompressible Navier-Stokes equations shall be performed using the pseudo-spectral method of Rogallo (1981). In this method the dependent variables are represented using Fourier series expansions. Aliasing errors are eliminated using a combination of coordinate shifts and truncation. The discrete system of equations is time advanced using second-order Runge Kutta.

Treatment of a dispersed second phase of heavy particles is performed through numerical integration of the equation of motion for a large ensemble of particles. For particles with material densities much larger than the surrounding carrier flow the most significant forces governing motion are drag and gravity. The code uses equation 1 to describe the motion of a particle. Advancement of (1) requires the fluid velocity along the particle trajectory. Since it is unlikely particles are located at grid points where the turbulence velocity is available, calculation of the drag force requires interpolation of the fluid velocity from the grid to the instantaneous particle position. A recently developed B-spline method will be used for velocity interpolation.

The material properties of the particles will be identical to those used in the experiments. Previous investigations have shown that the sample size

necessary for adequate convergence of statistical quantities such as particle mean-square dispersion and the velocity autocorrelations is approximately 4,000. Similar sample sizes will be used in this work.

### **Conclusions**

In conclusion, the work we will be performing will look at how particle inertia gravity independently affect its motion. An accurate understanding of these effects will allow for accurate modeling of particle motion in a large number of industrial flows, including those being performed in zero-g environments. Work on this project will begin June 1.

### **References**

1. Yudine, M.I. 1959 Physical considerations on heavy-particle diffusion. In *Atmospheric Diffusion and Air Pollution: Adv. Geophys.*, **6**, pp. 185-191.
2. Wells, M.R. and D.E. Stock 1983 The effects of crossing trajectories on the dispersion of particles in a turbulent flow. *Jrnl. Fluid Mech.*, **136**, pp. 31-62.
3. Crowe, C., J.N. Chung, T.R. Troutt 1988 Particle mixing in free-shear flows, *Prog. Energy Combust Sci* **14**, 171-194.
4. Crowe, C., J.N. Chung, T.R. Troutt 1993 Particle dispersion by organized turbulent structures, In *Particulate Two-Phase Flow*, Butterworth-Leinemann, ed. M. Roco.
5. Csanady, G.T. 1963 Turbulent diffusion of heavy particles in the atmosphere. *J. Atmos. Sci.* **20**, 201-208.
6. Rogers, C.B., Eaton, J.K. 1989 The Interaction Between Dispersed Particles and Fluid Turbulence in a Flat-Plate Turbulent Boundary Layer in Air, *Report No. MD-52, Thermosciences Division, Stanford University, Stanford, CA.*
7. Taylor, G.I. 1921 Diffusion by continuous movements. *Proc. R. Soc. Lond. A* **151**, 421-478.
8. Squires, K.D. & Eaton, J.K. 1991 Measurements of particle dispersion obtained from direct numerical simulations of isotropic turbulence. *J. Fluid Mech.*, **226**, pp. 1--35.
9. Elgobashi S. and G.C. Truesdall 1992 Direct simulation of particle dispersion in a decaying isotropic turbulence *J. Fluid Mech.*, **242**, pp. 655-790
10. Wang, L.P. and M.R. Maxey 1993 Settling velocity and concentration distribution of heavy particles in homogenous-isotropic particles, *J. Fluid Mech.*, **256**, pp. 27-68
11. Snyder, W.H. and J.L. Lumley 1971 Some Measurements of Particle Velocity Autocorrelation Functions in a Turbulent Flow, *J. Fluid Mech.*, **48**, pp. 41-71.
12. Beckel, D., S. Ainley, J. Thompson, C.B. Rogers, and J.K. Eaton *Measurements in the Particle-Lagrangian Reference Frame*, ASME FED-Vol.228, p. 147-155. 1995.
13. Corrsin, S. 1963 Turbulence: experimental methods. In *Handbuch der Physik*, **812**, pp. 115-145.
14. Pope, A. 1961 Wind-tunnel calibration techniques, NATO Advisory Group for Aeronautical Research and Development, AGARDograph 54, 55-62.
15. Rogallo, R.S. 1981 Numerical experiments in homogenous experiments NASA TM 81315
16. Zimin, V. and F. Hussain 1994 High-aperture raster holography for particle imaging, *Optics Letters*, **19**, 15, pp. 1158-1160.

# **Analysis of residual acceleration effects on transport and segregation during directional solidification of tin-bismuth in the MEPHISTO furnace facility**

J. Iwan D. Alexander, Arnaud Lizée  
Center for Microgravity and Materials Research  
University of Alabama in Huntsville  
Huntsville, Alabama 35899

J.-J. Favier, J.-P. Garandet,  
CEA-Grenoble, France

## ***Objectives***

The object of this work, started in March of 1995, is to approach the problem of determining the transport conditions (and effects of residual acceleration) during the plane-front directional solidification of a tin-bismuth alloy under low gravity conditions. The work involves using a combination of 2- and 3-D numerical models, scaling analyses, 1D models and the results of ground-based and low-gravity experiments. The experiments conducted in the MEPHISTO furnace facility during the USMP-3 spaceflight which took place earlier this year (February 22 through March 6, 1996). This experiment represents an unprecedented opportunity to make a quantitative correlation between residual accelerations and the response of an actual experimental solidification system

## ***Introduction***

Real-time Seebeck voltage variations across a Sn-Bi melt during directional solidification in MEPHISTO on USMP-1 showed a distinct variation which can be correlated with thruster firings. The Seebeck voltage measurement is related to the response of the instantaneous average melt composition at the melt-solid interface. This permitted a direct comparison of numerical simulations (and acceleration data) with the Seebeck signals obtained on USMP-1. Motivated by the results of the comparison we used numerical simulations to predict the response of the Seebeck signal to composition changes at the interface caused by convective disturbances produced by thruster firings of various magnitudes and durations. These simulations were carried out for different solidification rates. The results of the simulations were used to plan a subset of the USMP-3 MEPHISTO experiments dedicated to the evaluation of g-jitter effects. There were several differences between the USMP-3 experiments as compared to USMP-1. Firstly, a more concentrated alloy was solidified on USMP-3, and, secondly, Primary Reaction Control System (PRCS) thruster burns were requested at particular times during four separate growth runs. This allowed us to monitor the Seebeck signal response under well-characterized growth conditions. This allowed for quantification of the effects of "g-jitter" on convective-diffusive transport in the melt through the real-time changes in average interfacial composition obtained from the Seebeck measurement. In addition, guided by SAMS acceleration data, we carried out simulations during the experiment in order to obtain a better comparison of predicted responses with the actual Seebeck signal. Preliminary results are described below.

## ***Approach***

Our approach relied primarily on the use of numerical models to simulate the response of transport behavior in the directionally solidifying tin-bismuth to particular types of g-jitter. In particular, since specific accelerations (corresponding to unidirectional acceleration of a given fixed magnitude, orientation and duration) were requested at specific times during the experiments, the modeling focused primarily on "impulse"-type acceleration.

A sketch of the experiment set-up is shown in Fig. 1. There are two furnaces, one is fixed, the other is translated through a temperature gradient. The applied temperature profile shown in Fig. 1 leads to a central cylindrical melt volume bounded by a moving and a stationary (or reference) solid-liquid interface. The melt composition at the moving and the stationary reference interfaces is not the same. For Sn-Bi there is a dependence of melting temperature on concentration. Thus, it follows that the melting temperature at the two interfaces will not be the same. The Seebeck effect gives rise to a small but measurable voltage difference between these two interfaces. Measurement of this voltage difference

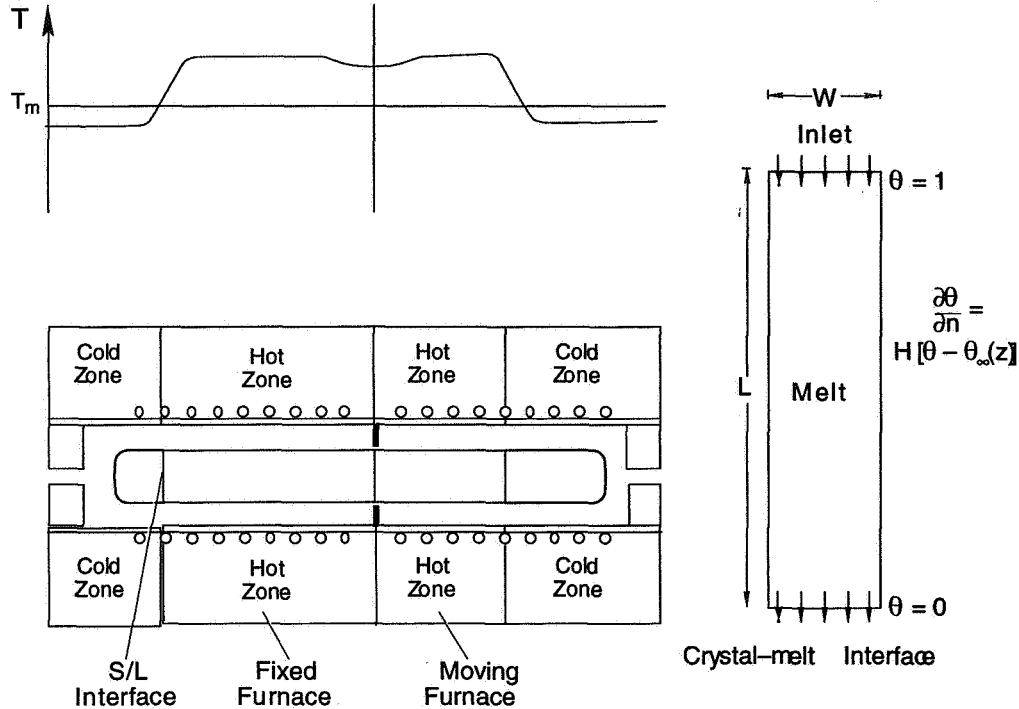


Fig. 1 The MEPHISTO set-up (bottom-left), temperature profile (top left) and computational model (right).  $T_m$  denotes the melting temperature.

allows the determination of the average temperature and, thus, the average composition of at the growing interface. The MEPHISTO set-up and the Seebeck measurements are discussed in more detail in [1].

The basic model system used for the simulations has been described elsewhere [2,3]. The essential features are outlined below. Solidification takes place as the ampoule is translated along a temperature gradient. For this model system, translation of the ampoule is simulated by supplying a doped melt of bulk composition  $c_\infty$  at a constant velocity  $V_g$  at the top of the computational space (inlet), and withdrawing a solid of composition  $c_s = c_s(x, t)$  from the bottom. The crystal-melt interface is located at a distance  $L$  from the inlet; the width of the ampoule is  $W$ . The temperature at the interface is taken to be  $T_m$ , the melting temperature of the crystal, while the upper boundary is held at a higher temperature  $T_h$ . The ampoule wall temperatures are prescribed according to the particular situation to be modeled. Since we wish to confine our attention to compositional nonuniformities caused by buoyancy-driven convection, rather than variations resulting from non-planar crystal-melt interfaces, the interface is held flat. We expect that, given the large ( $175 - 195 \text{ K cm}^{-1}$ , temperature gradient) that changes in melting temperature due to compositional non-uniformity will not lead to significant changes in interface shape due to interfacial compositional inhomogeneity. In addition, because of the melt's low Prandtl

number together with the low magnitude accelerations, convection does not lead to significant deviations of the temperature from the conductive state and, thus, changes in the interface shape due to changes in the thermal field will be negligible. The governing equations governing coupled convective-diffusive heat mass and species transfer in the melt are taken to be the Oberbeck-Boussinesq equations which are solved using a Chebyshev spectral method.

In an actual experiment, owing to the finite length of the ampoule, there is a gradual decrease in length of the melt zone during growth. In this model, transient effects related to the change in melt length are ignored. Since the MEPHISTO experiments involves melt lengths that are far in excess of the ampoule diameter, this does not preclude us from calculating the compositional transient. That is, we can start the calculations by solidifying from an initially uniform composition melt. Our results, when compared to experiment, reveal that this assumption is justified. The thruster firings are simulated using impulsive accelerations which are introduced through a time-dependent body-force term  $g$ . During the first year of this grant we calculated the response of the system to impulsive accelerations of various magnitudes and durations. Preliminary results are described in [4].

During the recent USMP-3 experiments the first quantitative experimental results concerning the effects of microgravity disturbances on the directional solidification. Comparison of the real-time (raw, uncorrected) Seebeck signals with the predicted Seebeck signal calculated from the evolution of the simulated composition profiles showed excellent agreement. Selected examples of the results obtained during the USMP-3 mission will be discussed in more detail the workshop.

### ***Ongoing work***

Detailed analysis of the experimental results (by the Grenoble group) is currently in progress and we are coordinating our ongoing work accordingly.

In addition to the work specifically related to the USMP-3 experiment, we have undertaken an extensive analysis of the effects of vibration (coupled with steady acceleration) on convection, heat and mass transport. For the case of thermovibrational convection of a Boussinesq fluid contained in a closed differentially heated rigid-walled 2D cavity we have found that chaotic flow responses occur at high vibration amplitudes. In the absence of vibration a steady (intermediate Rayleigh number,  $Ra$ ) buoyancy-driven flow occurs. The simulations were undertaken by direct solution of the Navier-Stokes-Boussinesq equations using a pseudo-spectral Chebyshev collocation method. Four basic regimes are recognized: quasi-static, oscillatory, asymptotic and a fourth regime, which appears for certain values of the vibrational Rayleigh number as a wedge-shaped region which separates the oscillatory and asymptotic regimes. This region is characterized by two-periodic, sub-harmonic cascades and chaotic behavior and represents that region of parameter space where the vibrating fluid behaves as an unstable dissipative oscillator. Here the vibration of the cavity results in a parametrically excited motion that exhibits a variety of nonlinear behavior depending on the relationship between the forcing frequency and the resonant frequency of the fluid system. At twice the Brünt-Väisälä frequency of the system a continuous transition from simple periodic oscillations to a subharmonic cascade toward chaotic responses is observed as the vibration amplitude is increased. In the absence of vibrational motion, chaotic motion would be expected to occur only at very large values of the Rayleigh number. Thus, it appears that simple translational low frequency oscillations of the cavity can lead to transitions to chaos at relative low values of  $Ra$ . A brief overview of these results will also be presented at the workshop.

### ***References***

- [1] J.-J. Favier and A. Rouzaud, *Revue Phys. Appl.* 22 (1987) 713.
- [2] J.I.D. Alexander, J. Ouazzani and F. Rosenberger, *J. Crys. Growth* 97 (1989) 285.

- [3] J.I.D. Alexander, S. Amiroudine, J. Ouazzani and F. Rosenberger, *J. Crys. Growth* 113 (1991) 21.
- [4] J.I.D. Alexander, in *Materials and Fluids under Low Gravity*, L. Ratke, H. Walter and B. Feuerbacher, eds.(Springer, Berlin, 1995) p. 95-102.

**Reliability of numerical solutions and two-dimensional turbulence  
in the problem of Rayleigh-Benard convection**

Olga Rodicheva and Evgeny Rodichev, Moscow State University

**Paper not available**





# **Dynamics and Stability of Liquid Bridges**



## Dynamics and Statics of Nonaxisymmetric Liquid Bridges

J. Iwan D. Alexander, Andrew H. Resnick and L. A. Slobozhanin  
Center for Microgravity and Materials Research, University of Alabama in Huntsville,  
Huntsville, AL 35899

### Objectives

- Theoretical and experimental investigation of the stability of nonaxisymmetric and nonaxisymmetric bridges contained between equal and unequal radii disks as a function of Bond and Weber number with emphasis on the transition from unstable axisymmetric to stable nonaxisymmetric shapes.
- Numerical analysis of the stability of nonaxisymmetric bridges between unequal disks for various orientations of the gravity vector
- Experimental and theoretical investigation of large (nonaxisymmetric) oscillations and breaking of liquid bridges.

### Introduction

A liquid bridge, or captive drop, is a mass of liquid held by surface tension between two or more solid supports. Liquid bridges occur in a variety of physical and technological situations and a great deal of theoretical and experimental work has been done to determine axisymmetric equilibria for various disk configurations, bridge aspect ratios and rotations (for example, see [1-6]). There have also been numerous investigations of the dynamics of axisymmetric liquid bridges subject to different excitations (impulses, vibration, etc.). Such investigations have been motivated both by practical considerations and basic scientific interest. Liquid bridges and drops are important factors when considering propellant management in liquid fuel chambers and in the positioning of liquid masses using surface tension forces. In crystal growth, they are associated with the floating-zone growth technique. Their oscillation and relaxation properties can also be used for viscosity and surface tension measurements of molten materials at high temperatures [7]. Pendular liquid bridges occur widely in the powder technology industry and are a major influence on powder flow process and mechanical properties [8]. In porous media flow, liquid-liquid displacement can lead to evolution of pendant and sessile lobes or lenticular bridges. The formation of liquid bridges from the gel that coats lung micro-airways results in occlusion of the bronchioles and is a precursor to respiratory problems and lung collapse [9].

In addition to the above, we note that liquid bridges have been involved in a number of past microgravity experiments. In addition to the primary objectives listed above, our research will provide results useful for the quantitative assessment of g-jitter effects on such experiments.

### Research approach

#### Experiments

The Plateau or neutral buoyancy method [3] works on the following principle: if two immiscible liquids of equal density are configured such that one envelops the other then the curvature of the equilibrium interface is a constant. That is, despite the fact that gravity creates a hydrostatic pressure gradient in each liquid, the interface between the two liquids behaves as if gravitational acceleration is zero. In each liquid the pressure  $p_i$ ,  $i=1,2$ , satisfies

$$\text{grad } p_i^* = 0,$$

where  $p_i^* = p_i + \rho_i gz$ ,  $p_i^*$  is reduced pressure and  $\rho_i$  is the density. At the interface between the two fluids

$$p_1^* - p_2^* = (\rho_1 - \rho_2)gz + 2\gamma K.$$

Here  $K$  is the mean curvature of the surface. When  $\rho_1$  and  $\rho_2$  are equal, the curvature is a constant, and equivalent zero-gravity conditions are obtained. In general, the shapes and stability of liquid bridges are governed by the following dimensionless numbers

$$\begin{aligned} Bo &= \Delta\rho R^2 g / \gamma && \equiv \text{Bond number} \\ V &= V_0 / \pi R^2 L && \equiv \text{relative volume} \\ \Lambda &= L / 2R && \equiv \text{slenderness} \\ We &= \Delta\rho R^3 \Omega^2 / \gamma && \equiv \text{Weber number} \\ K &= R_1 / R_2 && \equiv \text{Ratio of supporting disk radii.} \\ \phi_1, \phi_2 &&& \equiv \text{lower and upper contact angles} \end{aligned}$$

Here  $\Delta\rho$  is the density difference between the liquid bridge and the surrounding liquid or gas,  $R$  is the characteristic length associated with the bridge (usually the radius of the supporting disk),  $g$  is the gravitational acceleration,  $\gamma$  is the surface (or interfacial) tension,  $L$  is the distance between the disks,  $V_0$  is the actual liquid volume and  $\Omega$  is the angular rotation rate of the disks.  $Bo$  is a measure of the ratio of buoyancy to surface tension forces. The Weber number represents a balance between centrifugal and surface tension forces. For a non-zero  $Bo$  the outer bath density can be changed by adjusting the bath composition or temperature [5].

Figure 1 schematically depicts our Plateau chamber. Liquid bridges are formed between rigid sharp-edged 1 cm diameter circular disks. The disks are mounted on supports that allow for independent rotation and lateral and vertical translation. These motions are facilitated through two 3-axis precision motor/drive systems. This provides for vertical oscillation, rotation and small amplitude lateral oscillation (the slip-ring gasket constrains the allowable lateral motion of the lower disk). The upper disk is supported by an injection tube. The disks are made from stainless steel. The bridge liquid is injected or removed through an injection tube which terminates in a 4 mm-diameter hole in the center of the upper disk. A calibrated syringe driven by a variable speed electric motor is used for the injection of a fixed volume of liquid. The bridge is simultaneously lengthened by slowly moving the disks apart to the required separation distance. This distance can be determined to within 1-2  $\mu\text{m}$ . A 3-way purge valve is suitably positioned to trap air bubbles.

Each support can be independently vibrated at frequencies less than 10 Hz. Bridge injection is automated with simultaneous recording of precise volume data ( $\pm 0.1 \text{ mm}^3$ ). We use two imaging methods. Video images are obtained from two orthogonal cameras. A high quality Fourier transform imaging system is used for edge detection. The important physical parameters are the aspect ratio of the bridge, the liquid volume and the static and dynamic Bond numbers. The liquid volume and the slenderness (aspect ratio) of the bridge depend on the precision with which lengths can be determined. The disk diameters are known to within 10  $\mu\text{m}$ . The length of the bridge is set by the positioning device and can be determined with a precision of 1-2  $\mu\text{m}$ . Thus, for bridges of 2.5 cm length the slenderness,  $\Lambda = L/2R_0$ , can be determined to within  $\pm 0.04\%$ . Volume can be measured with a precision of 0.1  $\text{mm}^3$  and an accuracy of 0.1%. The liquid bath is a methanol-water solution. Variation of the methanol concentration changes the density difference between the Dow Corning 200<sup>®</sup> silicone oil bridge and the bath. We control the bath temperature and change the methanol concentration to adjust  $Bo$ . At 83% water concentration a condition of neutral buoyancy is obtained.

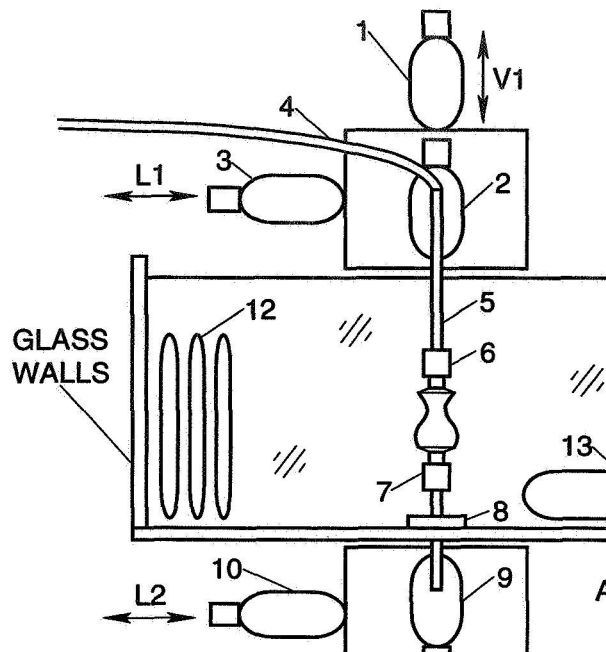


Fig. 1 Plateau Chamber: (1) upper vertical displacement motor  $V_1$ ; (2) upper rotational motor; (3) upper lateral displacement motor,  $L_1$ ; (4) bridge fluid injection line; (5) upper spindle; (6) upper feed disk; (7) lower feed disk; (8) slip-ring gasket; (9) lower rotational motor; (10) lower lateral displacement motor,  $L_2$ ; (11) lower vertical displacement motor  $V_2$ ; (12) cooling coils; (13) bath circulator.

### Theoretical work

Our theoretical work will focus on the numerical modeling of the oscillation and breaking of bridges subject to axial and lateral forcing. The problem of stability of bridges subject to steady axial and nonaxial gravity will be examined through a combination of analytical and numerical work (see discussion below).

### Results to date

#### *Stability of nonaxisymmetric configurations subject to axial and nonaxial gravity.*

We have examined the stability of nonaxisymmetric shapes of liquid bridges (with a fixed volume  $V_0$ ) held between equidimensional coaxial disks of radius  $R$ . The disks are separated by a distance  $L$  and subject to lateral acceleration. We employed *Surface Evolver* [11] to find the minimum energy configurations of the bridges. In comparison, for axisymmetric bridges subject to axial gravity, the stability limits correspond to a situation when the axisymmetric bridge breaks, or when the axisymmetric bridge loses stability to a stable nonaxisymmetric shape. The lateral acceleration stability limit is defined solely in terms of loss of stability by breaking. This limit is determined for both large and small values of the relative volume. The stability limit can be divided into two basic segments (stable regions are to the left of the curves, see Fig. 2). One segment appears to be indistinguishable from part of the margin for the zero-Bond number case. The other segment belongs to a one-parameter ( $Bo$ ) family of curves which, for a given  $Bo$  and a fixed value of  $\Lambda$ , have a maximum and minimum stable relative volume. Each of these curves is asymptotic to another part of the minimum volume zero-Bond number limit up to a point determined by the particular value of  $Bo$  and has a turning point corresponding to a maximum value of  $\Lambda$ . For  $V \gg 1$ , the maximum volume stability limit tends to infinity as  $\Lambda \rightarrow 0$ . For any given lateral Bond number, the minimum volume

stability limit is decreased and becomes indistinguishable from the zero Bond number limit when  $\Lambda$  becomes sufficiently small. For unstable bridges in the vicinity of the stability limit a consistent sequence of shapes can be readily identified and are recognizable by their overall shape and the number of necks.

In a recent bifurcation analysis for  $V = 1$  bridges subject to lateral gravity (Laveron et al. [10]) it was speculated that, because the eigenfunction associated with a subcritical bifurcations for  $\Lambda > \Lambda_c$  is antisymmetric with respect to the  $z = 0$  plane, the bridge would break into two drops of unequal volumes. Likewise it was speculated that, for  $\Lambda < \Lambda_c$ , loss of stability would lead to equal size drops since destabilization occurs through a turning point and the associated eigenfunction is symmetric. Our results confirm this, although we note that, when breaking occurs, three drops form. Two of these remain attached to the disks while the third is a smaller, free, satellite drop.

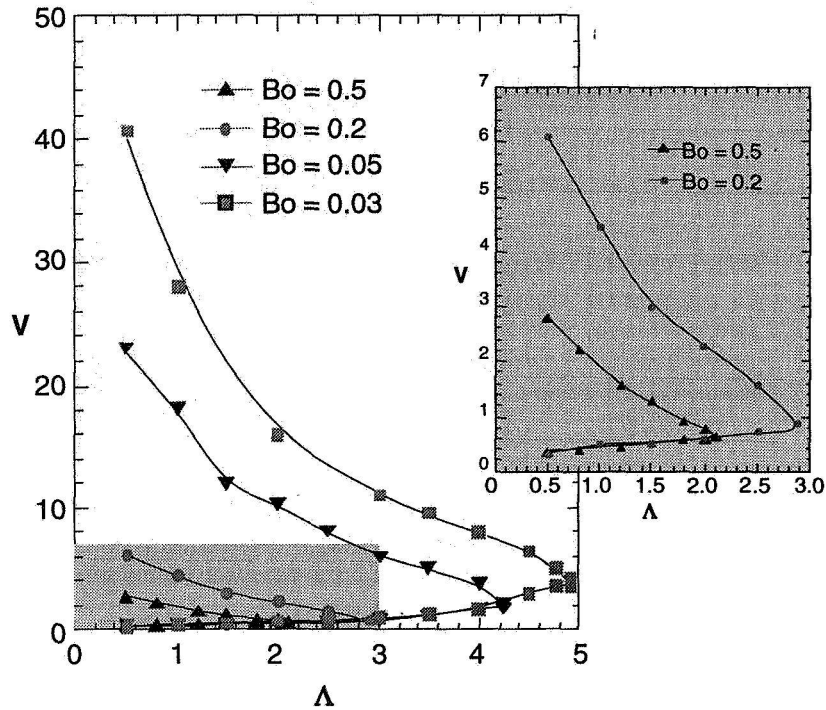


Fig. 2 Stability limits of liquid bridges held between equidimensional coaxial circular disks and subject to lateral gravity. (Points shown are stable bridges close to the stability limit). From [12].

#### *Stability of equilibrium of axisymmetric bridges subject to arbitrary perturbations*

The stability problem for an isorotating bridge between equal disks in an axial gravity field has been solved under constraints typical for the materials purification processes and growth of single crystals by the floating zone technique. For the constraint that the relative volume,  $V$ , is equal to 1, the critical values of the slenderness,  $\Lambda$ , have been determined for a wide range of the  $Bo$  and  $We$  numbers. For a prescribed value of the liquid contact angle at the upper or the lower disk (the chosen values correspond to growing angle values of  $0^\circ$  and  $15^\circ$ ), the dependencies of critical  $\Lambda$  and  $V$  values on  $Bo$  and  $We$  have been calculated. The influence of unequal radii disks on the boundary of the stability region in the  $(\Lambda, V)$ -plane has also been investigated for the case of finite axial gravity [13]. Unlike earlier work, arbitrary (not only axisymmetric) perturbations are accounted for and the entire stability boundary is constructed. The approach taken is

described in [14]. This work is still in progress and selected results will be presented at the workshop.

### ***Numerical modeling***

When a liquid bridge is at, or exceeds, its stability limit it will either change its shape, (for example, from an axisymmetric to a nonaxisymmetric shape) detach from the support disks, or break up into smaller drops. The process of breaking involves the decay of the bridge radius to zero at some points. When this occurs the bridge separates. This means that the governing equations must be singular at this point. Linear stability theory fails to describe this situation adequately and cannot predict the shape of the surface as breaking is approached, nor does it account for the non-uniform break-up of the bridge, i.e. that separation of the bridge into two or more large drops is accompanied by the formation of much smaller "satellite drops". The breaking of liquid bridges has been studied using 1D models [15]. Numerical treatment of the breaking of liquid jets beyond the singularity has been studied recently by Eggers and Dupont [16] using a 1D model, and Shulkes [17] has compared the predictions of 1D models of inviscid bridges as breaking is approached with the results of a 2D axisymmetric velocity-potential calculation for which no simplifying assumptions were made. At early times the differences between the three are small, however, as the bridge deformation became severe, the 1D models deviated significantly from the trends exhibited by the 2D velocity-potential results. The major shortcomings of 1D models are their inability cope with the bending of the bridge well below the lower disk edge. The velocity-potential model was able to handle this degree of deformation. Recently, we have applied a modified Volume of Fluid (VOF) method to the dynamical problem of breaking of viscous axisymmetric and non-axisymmetric bridges. Selected results will be presented at the workshop.

### ***References***

- [1] Mason, G. C., An experimental determination of the stable length of cylindrical liquid bubbles, *J. Colloid Interface Sci.* 32 (1970), 172-176.
- [2] Meseguer, J. & Sanz, A., Numerical and experimental study of the dynamics of axisymmetric liquid bridges, *J. Fluid Mech.* 153 (1985), 83-101.
- [3] Meseguer, J., Mayo, L. A., Llorente, J. C. & Fernández, A., Experiments with liquid bridges in simulated microgravity, *J. Crystal Growth* 73 (1985), 609-621.
- [4] Bezdenezhnykh, N. A. & Meseguer, J., Stability limits of minimum volume and breaking of axisymmetric liquid bridges between equal disks. Presented at the International Symposium on Hydromechanics and Heat/Mass Transfer in Microgravity (1991), Perm.
- [5] Sanz, A., 1985 The influence of the outer bath on the dynamics of axisymmetric liquid bridges, *J. Fluid Mech.* 156 (1985), 101-140.
- [6] Meseguer, J., Stability of slender, axisymmetric liquid bridges between unequal disks, *J. Crystal Growth* 67 (1984), 141-143.
- [7] Tsamopoulos, J., Chen T. & Borkar, A., Viscous oscillations of capillary bridges, *J. Fluid Mech.*, 225 (1992) 579-609.
- [8] Ennis, B.J., Li, J., Tardos, G. & Pfeffer, R., The influence of viscosity on the strength of an axially strained pendular bridge, *Chem. Eng. Sci.*, 45 (1990) 3071-3088.
- [9] Newhouse, L. A. & Pozrikidis, C., The capillary instability of annular layers and thin liquid threads, *J. Fluid Mech.*, 242 (1992) 193-209.
- [10] Laveron, A. & Perales, J.M., Equilibrium shapes of nonaxisymmetric liquid bridges, *Phys. Fluids*, 17 (1995) 1204-1213.
- [11] Brakke, K. Experimental Mathematics, 1 (1992) 141.
- [12] Alexander, J.I.D., Delafontaine, S. & Carter, C., Stability of liquid bridges subject to lateral acceleration, to be published (1996).

- [13] Slobozhanin, L., Alexander, J.I.D. & Resnick, A.H., Stability of liquid bridges under low gravity conditions, to appear in the Proceedings of the 2nd Symposium on Fluids in Space, Naples, Italy, 1996.
- [14] Myshkis, A.D., Babitskii, V.G, Kopachevskii, N.D. Slobozhanin, L.A. & Tyuptsov, A.D., Low Gravity Fluid Mechanics (1987) Springer Verlag, Berlin.
- [15] Meseguer, J., The breaking of axisymmetric slender liquid bridges, *J. Fluid Mech.* 130 (1983) 123-151.
- [16] Eggers, J. & Dupont, T.F., Drop formation in a one dimensional approximation of the Navier-Stokes equations, *J. Fluid Mech.* 262 (1994) 205.
- [17] Shulkes, R.M.S.M., Nonlinear dynamics of liquid columns: A comparative study, *Phys. Fluids A* (1993) 2121-2130.



# STABILIZATION AND LOW-FREQUENCY OSCILLATION OF CAPILLARY BRIDGES WITH MODULATED ACOUSTIC RADIATION PRESSURE

P. L. Marston, M. J. Marr-Lyon, S. F. Morse, and D. B. Thiessen  
Physics Department, Washington State University  
Pullman WA 99164-2814

## I. Introduction

Liquid bridges between two solid surfaces have applications in low gravity such as the solidification of floating zones. It has been known since the research of Plateau (1866) and Rayleigh (1879) that a cylindrical liquid bridge will become unstable when it is longer than a critical length. Long bridges naturally become unstable to a symmetric mode by bulging near one end while the opposite end thins. For a cylindrical bridge in low gravity of radius  $R$  and length  $L$ , the slenderness  $S = L/2R$  has a natural (Rayleigh) limit of  $\pi$  beyond which the bridge breaks. In the presence of gravity (which causes a static distortion of a bridge from a cylindrical shape) the critical length is known to be even shorter. This instability places practical limitations on the management of liquids in low gravity and on the earth. For example, stabilization of liquid bridges may facilitate a reduction of temperature gradients in the float-zone method of crystallization. Various methods have been investigated for overcoming the Rayleigh-Plateau (RP) instability, however the methods studied by other researchers may turn out to have limited value for fluids applications of general interest. These include effects of electric fields on dielectric bridges [1], magnetic fields on bridges of high electrical conductivity [2], and hydrodynamic stabilization due to flow of a viscous fluid parallel to a bridge [3]. The objectives of the current research effort are to utilize modulated acoustic radiation pressure to stabilize bridges against breakup and to obtain quantitative information about the frequency and decay time of bridge oscillations.

In the work reported here it is demonstrated that acoustic radiation pressure may be used in simulated low gravity to produce stable bridges significantly beyond the Rayleigh limit with  $S$  as large as 3.6. The bridge (PDMS mixed with a dense liquid) has the same density as the surrounding water bath containing an ultrasonic standing wave. Modulation was first used to excite specific bridge modes [4]. In the most recent work reported here the shape of the bridge is optically sensed and the ultrasonic drive is electronically adjusted such that the radiation stress distribution dynamically quenches the most unstable mode. This active control simulates passive stabilization suggested for low gravity [5]. Feedback increases the mode frequency in the naturally stable region since the effective stiffness of the mode is increased.

## II. Acoustic Stabilization Methods

The first step in the investigation of acoustic stabilization was to demonstrate the selective excitation of bridge modes in a Plateau tank using the radiation pressure of modulated ultrasound. Results demonstrating that objective were already published [4]. The next step was Marston's analysis [5] of the effect of a selected radiation pressure squeezing of a bridge on the natural frequency and stability of an inviscid bridge. It was

assumed that the acoustic radiation pressure  $\langle p_r \rangle$  could be increased with increasing local bridge radius  $R$  in such a way that the sound field (on the average) squeezed harder on the fat portions of the bridge than on the slender portions. The control is expressed in terms of an *acoustic parameter*

$$q = (R^2/\sigma) d\langle p_r \rangle/dR \quad (1)$$

where  $\sigma$  denotes the surface tension of the bridge. The analysis is equally applicable to the situation of passive feedback as it is in the active control case. In the passive case, the acoustic field is designed such that the radiation pressure automatically squeezes more on the fatter parts of the bridge even without active adjustment of the acoustic field. Results are summarized subsequently in the discussion of Fig. 2.

In the next stage of development measurements were made of the natural frequency of the most unstable bridge mode for a bridge in a Plateau tank both with and without active stabilization. Figure 1 shows a diagram of the apparatus. The instantaneous left-right asymmetry of the bridge was sensed by detection of an optical signal with a split photodetector. The resulting voltage difference  $V_d$  represents an error signal which is multiplied by a gain constant  $k$  and used to control the frequency of the high-frequency oscillator used to excite the ultrasonic transducer. The typical acoustic frequency is 120 kHz. The transducer was designed in such a way that shifting the frequency of the drive shifts the left-right asymmetry of the radial component of radiation pressure on the bridge. The natural frequency of oscillation was measured by superposing on the error signal a weak low-frequency modulation which could be used to excite the  $N = 2, m = 0$  (left/right asymmetry) bridge mode which is the most unstable mode. The frequency of the modulation was adjusted to maximize the response of the desired mode. The measurements of the increase in natural frequency due to active stabilization were carried out with the same kind of silicone-oil/TBE bridge mixture for a neutral density bridge in water as described in [4].

### III. Results

#### A. Frequency Measurements of the Most Unstable Mode

Figure 2 shows an example of the normalized frequency data (as a function of the slenderness  $S = L/2R$ ) for an experiment where the feedback "gain level"  $k$  was set to three different values. The data for the case  $k = 0$  is shown as the squares. The corresponding theory curve is calculated from the one-dimensional inviscid slice (ODIS) approximation applied by Marston [5]. Here  $\bar{\omega}$  is a normalized frequency as described in [4]. The theory curve intercepts  $\bar{\omega} = 0$  at the Rayleigh-Plateau natural limit of  $\pi$  and the data, which could be taken up to  $S = 3$ , follow the curve.

The circles correspond to data taken with  $k = 4$  which is the appropriate feedback sign to increase the stability of the bridge. In each case the natural frequency of the bridge is increased indicating that the "spring" of the bridge mode oscillator has been "stiffened" by the feedback. This is exactly what is required for enhanced stability. The curve labeled  $q = 0.2$  was obtained by adjusting the value of the acoustic parameter  $q$  to fit the data. Here  $q$  is the parameter in Eq. (1). The fit suggests that with the strength of feedback achieved, it would be possible to extend the bridge to the modified slenderness limit of  $S_L \approx 3.5$

which is significantly greater than  $\pi$ . The triangles were taken with  $k = -4$  which correspond to the sign of feedback to reduce the stability of this mode. The frequency is reduced in comparison to the no-feedback ( $k = 0$ ) values. The corresponding curve shows the case of  $q = -0.2$  which reduces the slenderness limit to 2.86, below the natural value of  $\pi$ .

## B. Acoustic Stabilization Beyond the Rayleigh Limit

The next stage of the research was to demonstrate acoustic stabilization as described in the abstract [6]. Several experimental improvements were made to facilitate this objective including (a) improved stability and control of the liquid deployment system and (b) greater bandwidth of the amplifier in the electronic feedback system (Fig. 1). With those improvements, stabilization up to a slenderness  $S$  of 3.7 has been achieved. Figure 3 shows frames from a CCD camera video record showing deployment and active acoustic stabilization of a bridge with  $S = 3.6$ . Figures 3(a) - (d) show the initial bridge deployment and extension to a length of  $S = 3.5$ . In (e) the supports are set and left at  $S = 3.6$  and the bridge volume is adjusted to give a circular cylinder. The bridge length  $L$  and diameter  $D$  are 15.8 mm and 4.32 mm. The active control of the ultrasonic drive based on an optical error signal (Fig. 1) is implemented throughout the sequence except at the end as explained below. Note that (e) is at an elapsed time of 19 seconds as displayed on the counter. The bridge remains stable until (j), elapsed time of 42 seconds, where the sound field is turned off. The bridge becomes unstable and breaks in less than 1 second in (k) and (l). The viscosity of the bridge liquid was small, only 5 cs, so viscous dissipation was not an important stabilization mechanism. While the stabilization sequence in Fig. 3 is less than 1 minute in duration, similar observations show that  $S = 3.6$  may be maintained for an arbitrarily long time. Comparison with results of an investigation of viscous flow-induced stabilization of capillary bridges [3] indicates that the acoustic stabilization method is superior even at this early stage of development.

## IV. Conclusions

The research described here has demonstrated that modulated acoustic radiation pressure can be coupled to the natural oscillation modes of a capillary bridge. This effect has been used both to excite these modes in order to measure the natural frequency and damping characteristics of the modes as well as to modify these characteristics in order to enhance the stability of the bridge. Stabilization has been demonstrated to a slenderness ratio of 3.7 using active feedback control of the acoustic field. This is a significant increase in the slenderness ratio over the natural limit of  $\pi$ .

## Acknowledgment

This research was supported by NASA Grant NAG3-1622.

## References

- [1] S. Sankaran and D. A. Saville, Experiments on the stability of a liquid bridge in an axial electric field," *Phys. Fluids A* **5**, 1081-1083 (1993).
- [2] J. A. Nicolás, "Magnetohydrodynamic stability of cylindrical liquid bridges under a uniform axial magnetic field," *Phys. Fluids A* **4**, 2573-2577 (1992).
- [3] B. J. Lowry and P. H. Steen, "Flow-influenced stabilization of liquid columns," *J. Coll. Inter. Sci.* **170**, 38-43 (1995).
- [4] S. F. Morse, D. B. Thiessen, and P. L. Marston, "Capillary bridge modes driven with modulated ultrasonic radiation pressure," *Phys. Fluids* **8**, 3-5 (1996).
- [5] P. L. Marston, "Capillary bridge stability in an acoustic standing wave: Linearized analysis of passive stabilization with radiation pressure (abstract)," *J. Acoust. Soc. Am.* **97**, 3377 (1995) and *Bull. Am. Phys. Soc.* **40**, 1923 (1995).
- [6] M. J. Marr-Lyon, D. B. Thiessen, and P. L. Marston, "Active acoustic stabilization of capillary bridges significantly beyond the Rayleigh limit: experimental confirmation (abstract)," *J. Acoust. Soc. Am.* **99**, 2540 (1996).

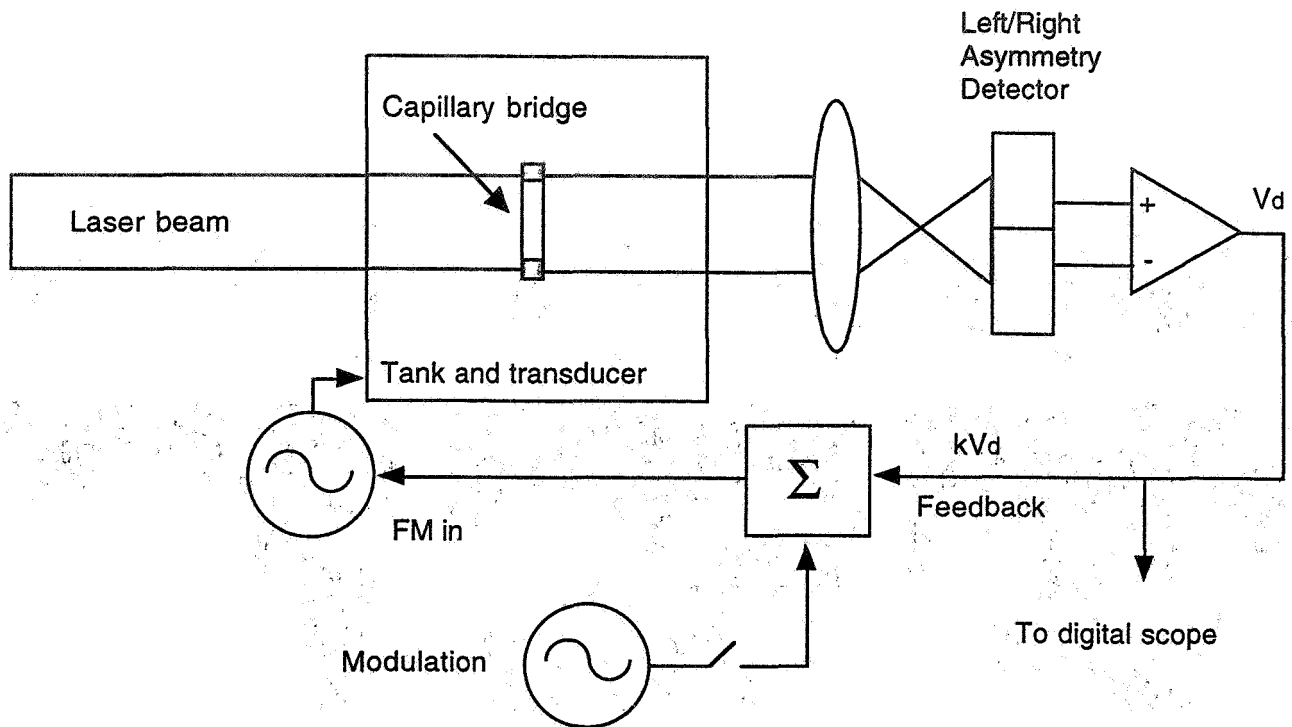


Figure 1. Apparatus to actively stabilize and measure the frequency of maximum response of a capillary bridge.

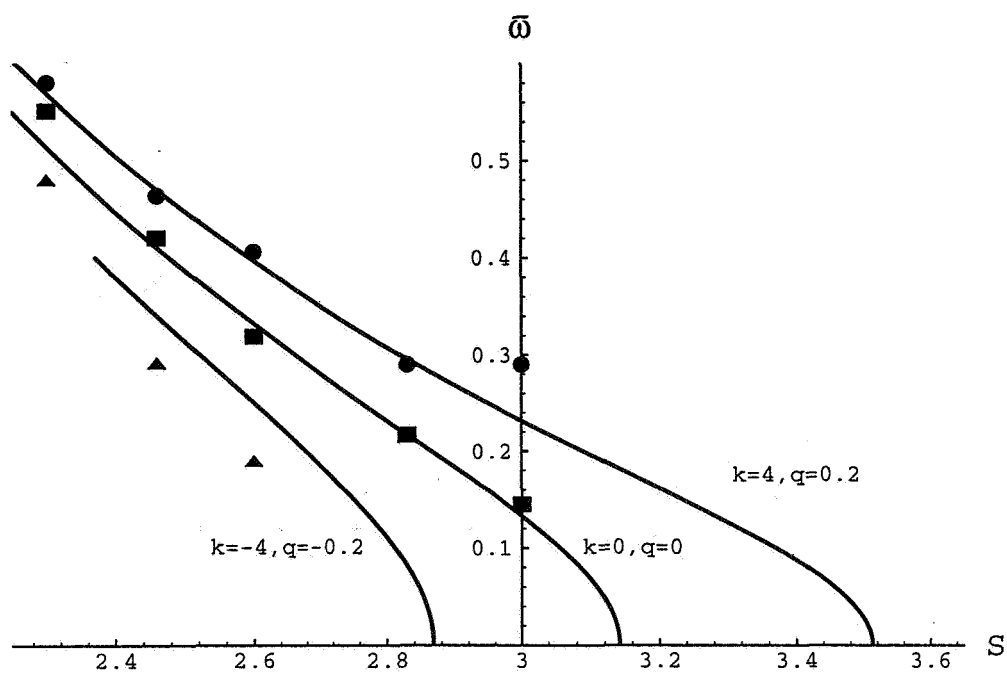


Figure 2. Normalized natural frequency vs. Slenderness ratio.

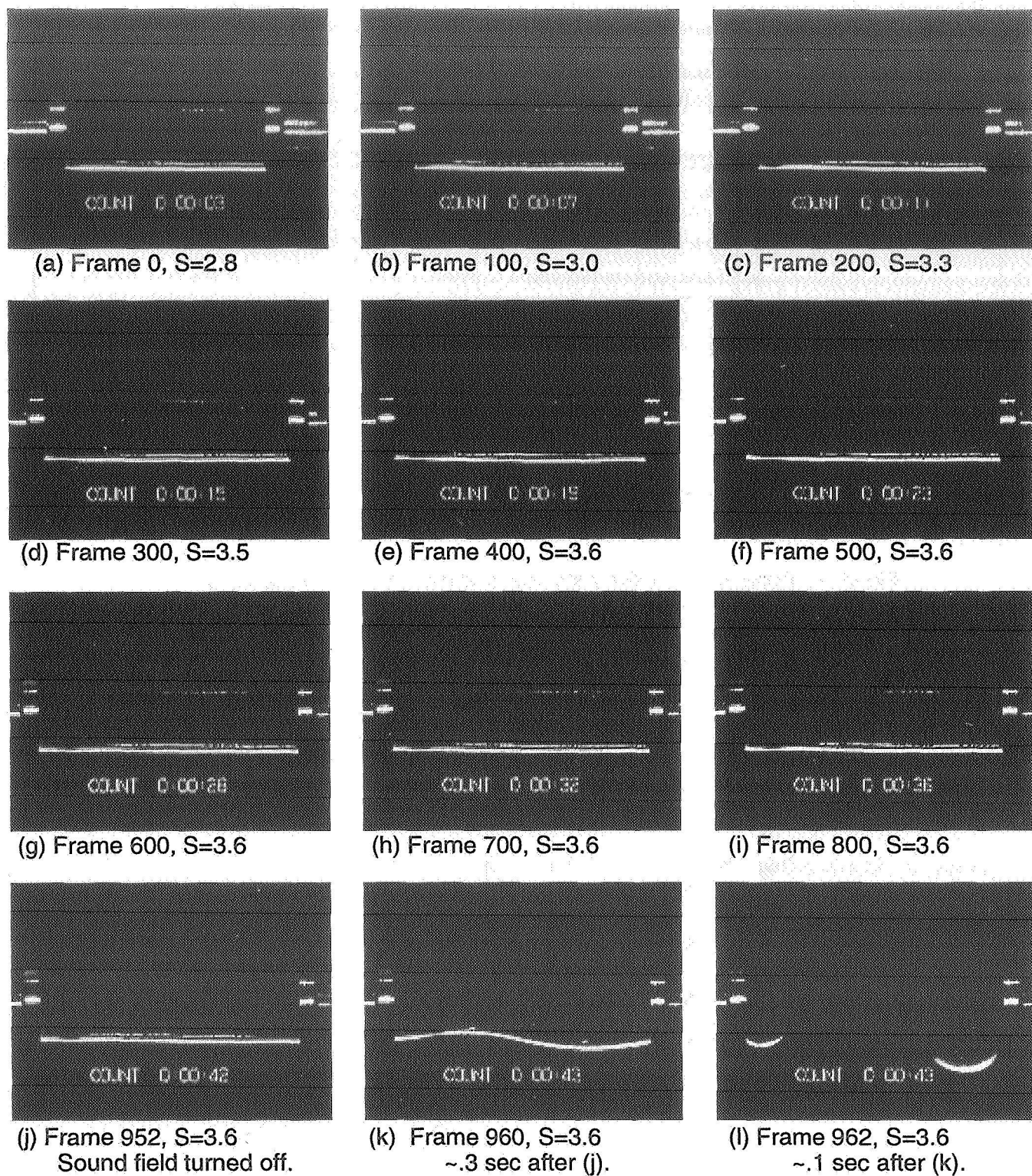


Figure 3. Sequence of CCD images of the evolution of a stabilized capillary bridge.

# INFLUENCE OF THERMOCAPILLARY FLOW ON CAPILLARY STABILITY: LONG FLOAT-ZONES IN LOW GRAVITY

Yi-Ju Chen and Paul H. Steen  
School of Chemical Engineering  
Cornell University  
Ithaca, NY 14853

## ABSTRACT

A model problem is posed to study the influence of flow on the interfacial stability of a nearly cylindrical liquid bridge for lengths near its circumference (the Plateau-Rayleigh limit). The flow is generated by a shear stress imposed on the deformable interface. The symmetry of the imposed shear stress mimics the thermocapillary stress induced on a float-zone by a ring heater (i.e. a full zone). Principal assumptions are i) zero gravity ii) creeping flow and iii) that the imposed coupling at the free surface between flow and temperature fields is the only such coupling. A numerical solution, complemented by a bifurcation analysis, shows that bridges substantially longer than the Plateau-Rayleigh limit are possible. An interaction of the first two capillary instabilities through the stress-induced flow is responsible. Time-periodic standing waves are also predicted in certain parameter ranges. Motivation comes from extra-long float-zones observed in MEPHISTO space lab experiments (June 1994).

## INTRODUCTION

Observation of several float-zones (MEPHISTO, 1994) shows lengths much longer than their average circumference (up to 50 % longer)[1]. Since knowledge of precise experimental conditions is lacking, there is room for a variety of explanations. The results of the simple model problem posed below suggest one possible mechanism.

In the absence of flow ( $c = 0$ ), the pinned cylindrical interface exhibits, with increasing length, a sequence of shape instabilities due to surface tension. Destabilizing shapes that are antisymmetric (eigenvalues  $p_n$ ) are interlaced with those that are symmetric about the mid-plane (eigenvalues  $q_n$ , where  $n = 1, 2, \dots$ ). The instability at the Plateau-Rayleigh limit is antisymmetric and corresponds to eigenvalue  $p_1$ .

If the quiescent bridge is perturbed by a flow that is symmetric about the midplane ( $c > 0$ ), the symmetry of the bifurcations corresponding to  $p_n$  are preserved giving a steady-streaming-like effect. In particular, that effect on  $p_1$  gives stabilization (figure 1a). At the same time, bifurcations  $q_n$  are broken (figure 1b). Symmetry plays a key role in the analysis. Previous studies, including those by Ribicki & Floryan[2], Chen & Shen & Lee[3] and Dijkstra[4], have largely been numerical simulations.

A brief sketch of the model problem is given first. A concise formulation is then set down and symmetry issues are discussed followed by an identification of the underlying mathematical structure (the universal unfolding).

## MODEL SKETCH

Figure 2 shows the schematic. Fluid surface tension is assumed to be a linear function of surface temperature  $\sigma = \bar{\sigma} + \frac{\partial \sigma}{\partial T}(T - \bar{T})$  and is nowhere zero along the fluid surface. The aspect ratio

$A \equiv (r_o - r_i)/r_o$  models a possibly solidified core and provides a potential unfolding parameter in the analysis. The temperature field of the ambient is approximated by a sinusoidal function  $T_a = \Delta T \sin(\pi z)$  to simulate the effect of external heating. Normal stress induced by thermocapillary flow is calculated by the lubrication approximation. Figure 3 plots a typical bifurcation diagram (schematically) obtained by a numerical continuation method [5]. The two state variables,  $\varepsilon_1 \equiv \langle u, \phi_1 \rangle$  and  $\varepsilon_2 \equiv \langle u, \psi_1 \rangle$ , are used to measure the solutions in an appropriate function space (see FORMULATION for symbol definitions). The dimensionless parameter  $c$  controls the thermocapillary strength,  $c \equiv -\frac{\partial \sigma}{\partial T} \Delta T / \bar{\sigma}$ .

The bifurcation structure near the singular points  $p_1$  and  $q_1$  is predicted by the symmetry issues alluded to above and discussed in detail in the next section. The first bifurcation point is shifted from the classical limit ( $2\pi$ ) by an amount proportional to  $c$  — the  $\mathbf{Z}_2$ -invariant branch may be stable even for bridge length  $\ell > 2\pi$ . By further increasing  $c$  it is possible to turn the pitchfork bifurcation over — i.e. to make it supercritical. The trivially-invariant branch may be stabilized.

## FORMULATION AND SYMMETRY ISSUES

The model assumes zero Bond, small Reynolds and small Peclet numbers. The imposed tangential stress at the interface drives the flow. The normal stress balance, however, determines the shape stability and is our focus. Incorporating appropriate boundary conditions, the normal stress balance is set-up as a map

$$\mathcal{F}(u, \ell, c) \equiv \sigma \, 2\mathcal{H}(u, \ell) - P_s + \mathcal{N}(u, \ell, c). \quad (1)$$

The normal stress induced by thermocapillary flow  $\mathcal{N}(u, \ell, c)$  is balanced by the mean curvature  $2\mathcal{H}(u, \ell)$ , with surface deflection function  $u(z)$ , and static pressure  $P_s$ .

Note that at  $c = 0$ ,  $\mathcal{N}(u, \ell, 0) \equiv 0$  and the classical Young-Laplace equation is recovered. The linear map  $\partial_u \mathcal{F}(0, \ell, 0)$  has two distinct categories of null space ( $n = 1, 2, \dots$ ) [6]:

$$(I) \quad \phi_n = \sin(p_n z), \quad p_n = 2n\pi. \quad (2)$$

$$(II) \quad \psi_n = \frac{2}{q_n} (\cos(q_n z) + \frac{q_n}{2} \sin(q_n z) - 1), \quad \tan(\frac{q_n}{2}) = \frac{q_n}{2}. \quad (3)$$

The branching solutions tangent to class (I) form a subcritical pitchfork bifurcation at  $\ell = p_n$ ; the solutions branching from the class (II) form a transcritical bifurcation at  $\ell = q_n$ . The bridge loses its stability at  $\ell = 2\pi$ . We shall demonstrate that, when  $c \neq 0$ , the nonlinear interaction of  $\{\phi_1\}(p_1 = 2\pi)$  and  $\{\psi_1\}(q_1 = 8.98)$  modes may stabilize an otherwise unstable bridge.

The map  $\mathcal{F}$  has reflection symmetry ( $\mathbf{Z}_2$ ) inherited from heating at the midplane

$$\mathcal{F}(\gamma u, \ell, c) = \gamma \mathcal{F}(u, \ell, c), \quad (4)$$

where the flip transformation  $\gamma \in \mathbf{Z}_2$  is defined as  $\gamma u(z) = u(1 - z)$ . Here,  $z$  is normalized by  $\ell$ . Two remarks are in order:

(i) By the equivariant property (4) one can show that the projection  $g \equiv \langle \mathcal{F}(\varepsilon \phi + w, \lambda, c), \phi^* \rangle$  preserves the symmetry, where  $w$  is in the complement of  $\text{span}\{\phi\}$ , ie.

$$g(-\varepsilon, \ell, c) = -g(\varepsilon, \ell, c), \quad \forall n. \quad (5)$$

Generically, (5) shows a pitchfork bifurcation (c.f. figure 1(a)).

(ii) Since  $\langle \partial_c \mathcal{N}(u, \ell, 0), \psi^* \rangle \neq 0$ , there exists a unique branch of solutions  $c = \hat{c}(\varepsilon, \ell)$  near  $\ell = q_n$  by the implicit function theorem. The transcritical breaks to a limit point bifurcation [7] (c.f. figure 1(b)).



## UNIVERSAL UNFOLDING

The analytical structure and stability of the bifurcation diagram is now considered. Solutions of the nonlinear problem (1) are obtained by the Lyapunov-Schmidt method near the singular points. The bifurcation equation is obtained by the projection of  $F$  onto  $\phi_1^*$  and  $\psi_1^*$  [8,9]:

$$\mathbf{g} = \left( -\frac{1}{2(8.98)}\varepsilon_2^2 - \frac{1}{4}\lambda_2\varepsilon_2 - \delta_1 c, \left(-\frac{3}{32} + \xi_3 c\right)\varepsilon_1^3 + \left(-\frac{1}{4}\lambda_1 + \xi_1 c\right)\varepsilon_1 \right), \quad (6)$$

where  $\lambda_1 = 1 - (2\pi/\ell)^2$ ,  $\lambda_2 = 1 - (8.98/\ell)^2$  measure the deviation of the bridge length from the classical bifurcation points, and the coefficients  $\xi_1(A)$ ,  $\xi_3(A)$  and  $\delta_1(A)$  are obtained through the reduction. A straightforward evaluation using (6) gives the positions of the two bifurcation points (the pitchfork and the limit point), and criteria that turn the trivially-invariant solutions supercritical.

## DISCUSSION

Results of numerical continuation and the reduction equations may be summarized. The problem falls into the class of a bifurcation problem in two state variables with  $\mathbf{Z}_2$  symmetry  $(x, y) \mapsto (x, -y)$ . By appropriate coordinate transformations the bifurcation equations may be fitted into a normal form with the topology of a  $\mathbf{Z}_2$ -codimension 2 bifurcation:

$$\mathbf{g}(x, y) = (x^2 + y^2 - \lambda, (\mu x^2 - \beta x + y^2 - \alpha)y), \quad (7)$$

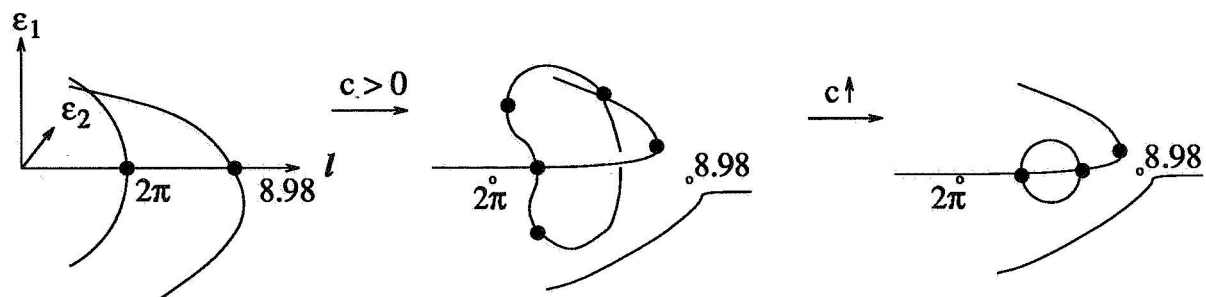
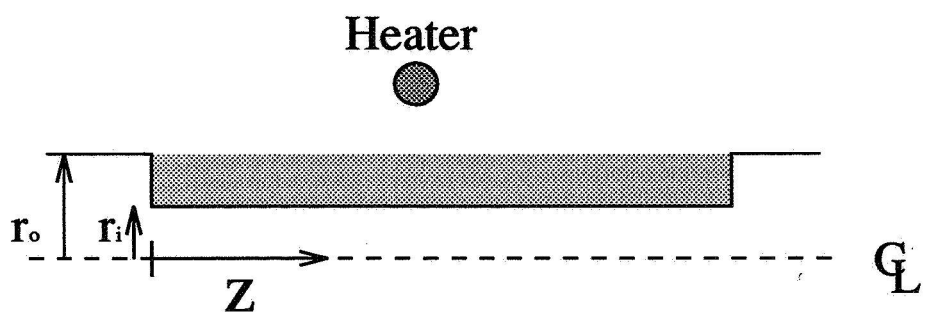
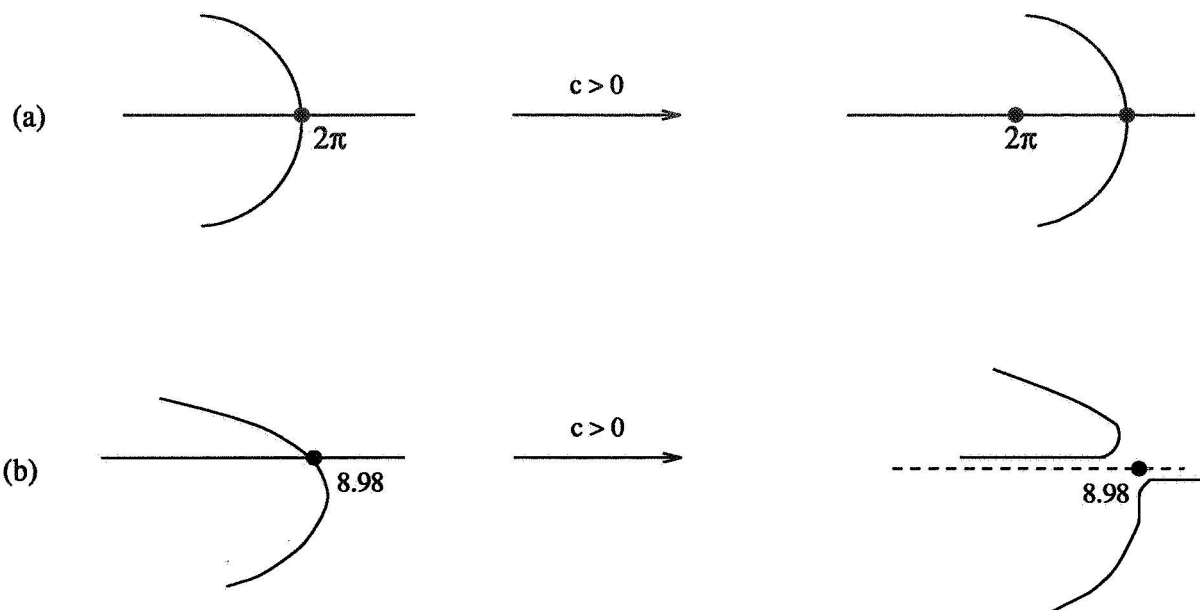
$\mu > 0$ . The normal form renders stability of the branching solutions within the limitation of negligible Reynolds and Peclet numbers. The unfolding diagram is given in [9, p.441]. A somewhat surprising result, as seen from that diagram, is that the two-mode interaction may lead to a Hopf bifurcation. A standing wave solution is possible. Predicting the stability of such solution is beyond the present model.

Good estimates from the space experiment, of the strength of the perturbation from zero gravity (relative to the thermocapillary perturbation) and the amplitude of the interface deformation, are most important in assessing the relevance of this model.

## REFERENCES

1. Abbaschian, R. 1995, private communication.
2. Ribicki, A. and Floryan, J.M. 1987 "Thermocapillary Effects in Liquid Bridges I. Thermocapillary Convection," *Phys. Fluids* 30(7), p.1956.
3. Chen, J.C., Sheu, J.C. and Lee, Y.T. 1990 "Maximum Stable Length of Nonisothermal Liquid Bridges," *Phys. Fluids A* 2(7), p.1118.
4. Dijkstra, H.A. 1993 "On the Shear Stabilization of Capillary Break-up of Finite Liquid Bridges," *Microgravity Science and Tech. IV*, p.13.
5. Dodel, E.J. 1981 AUTO: A Program for the Automatic Bifurcation Analysis of Autonomous Systems. *Congressus Numerantium* 30, p.265 (*Proceeding of the 10th Manitoba Conference on Numerical Mathematics and Computation, University of Manitoba, Winnipeg, Canada, 1980*)

6. Brown, R.A. and Scriven, L.E. 1980 "The Shape and Stability of Captive Rotating Drops," *Phil Trans. R. Soc. Lond. A*, 297, p.51.
7. Iooss, G. and Joseph, D.D. 1981 *Elementary Stability and Bifurcation Theory*. Springer-Verlag, New York.
8. Sattinger, D.H. 1979 *Group Theoretic Methods in Bifurcation Theory*, Lecture Notes in Mathematics, vol. 762. Springer-Verlag, Berlin.
9. Golubitsky, M., Stewart, I. and Schaeffer, D.G. 1988 *Singularities and Groups in Bifurcation Theory*, vol.2, Springer-Verlag, New York.





# EXPERIMENTAL CONTROL OF THERMOCAPILLARY CONVECTION IN A LIQUID BRIDGE

Valery Petrov, Michael F. Schatz\*, Kurt A. Muehlner,  
Stephen J. Van Hook, W. D. McCormick, Jack B. Swift  
and Harry L. Swinney

Center for Nonlinear Dynamics and Department of Physics  
The University of Texas at Austin  
Austin, TX 78712

## ABSTRACT

We demonstrate the stabilization of an isolated unstable periodic orbit in a liquid bridge convection experiment. A model independent, nonlinear control algorithm uses temperature measurements near the liquid interface to compute control perturbations which are applied by a thermoelectric element. The algorithm employs a time series reconstruction of a nonlinear control surface in a high dimensional phase space to alter the system dynamics.

## INTRODUCTION

Hydrodynamic instabilities arise frequently in materials processing and can significantly impact the quality of the resulting products; these instabilities can be present even in a microgravity environment where buoyancy effects are suppressed. In float-zone refinement, for example, the appearance of time-dependent thermocapillary convective flow induces undesired variation in the chemical composition of crystals processed either on Earth or in microgravity [1]. Recent experimental and theoretical studies have explored hydrodynamic instabilities in model systems such as liquid bridges [2-5]; these studies are an important first step toward devising strategies for improving process outcomes.

There has been much progress in the control of dynamics in low-dimensional nonlinear systems [6]. These efforts, popularly known as “control of chaos”, have succeeded in stabilizing various physical systems including lasers [7], chemical reactions [8], and cardiac tissue [9]. Unfortunately, these methods fail when the goal dynamics for the controlled system is distant in phase space from the autonomous system behavior. Recently, however, an algorithm that targets goal dynamics anywhere in the phase space was proposed [10]. The algorithm requires no knowledge of the underlying, possibly nonlinear, governing equations; instead, time series of the system response to random perturbations is used to construct a control law in a time-delay space.

## EXPERIMENTS AND CONTROL ALGORITHM

**Convection Cell** A liquid bridge is formed by a drop of silicone oil (tetradecamethylhexasiloxane with > 95% purity [11]) confined between two coaxial cylindrical stainless steel rods (radius  $r = 0.3$  cm) that are separated vertically by a gap  $l = 0.3$  cm [Fig. 1(a)]. The rods differ in temperature by  $\Delta T > 0$  with the upper rod warmer than the lower; the mean temperature of the bottom rod is  $15.0^\circ\text{C}$  and  $\Delta T$  is computer-controlled to a precision of  $\pm 0.05^\circ\text{C}$ . The volume of liquid in the drop is  $0.065\text{ cm}^3$ . The dimensionless number that characterizes the surface tension driving is the Marangoni number ( $M \equiv \sigma_T \Delta T d / \rho \nu \kappa$ , with the liquid surface tension  $\sigma$ , density  $\rho$ , kinematic viscosity  $\nu$ , thermal diffusivity  $\kappa$ , and  $\sigma_T \equiv |\frac{d\sigma}{dT}|$ ).

The flow is measured and controlled by, respectively, a single temperature sensor and single feedback element. The temperature sensor is a 0.03 cm diameter thermistor that is placed approximately  $l/2$  above the lower rod and 0.03 cm from the surface of the drop. The sensor yields a measurement that is determined primarily by the local temperature of the nearby liquid interface. The feedback element is a 0.1 cm  $\times$  0.2 cm  $\times$  0.3 cm thermoelectric device which is placed at the same relative location as the temperature sensor on the opposite side of the liquid bridge [Fig 1 (a)]. The temperature of the feedback element can be increased or decreased by applying a voltage of the proper polarity; these temperature changes, in turn, impose a localized temperature perturbation at the surface of the drop, thus altering the thermocapillary forces that drive the flow.

**Control Algorithm** A representation of the system state is obtained by selected sampling of the temperature sensor output and the applied perturbations. Samples are recorded at local maxima of the sensor output; differences between adjacent maxima are taken to filter out the influence of slow temperature drifts. The resulting sequences of temperature differences  $x_i$  and applied perturbations  $p_i$  (which are held constant between samples  $i - 1$  and  $i$ ) are used to construct a simplified map description of the dynamics through the use of difference equations.

For an  $m$ -dimensional system at time step  $i$ , the next applied perturbation  $p_{i+1}$  is determined from the history (subscript  $h$ ) and target (subscript  $t$ ) dynamics:

$$p_{i+1} = C[x_h(i), p_h(i), x_t(i+1), p_t(i)]$$

where  $C$  is a single-valued mapping into a time-delay space with  $x_h(i) \equiv (x_i, \dots, x_{i-m+1})$ ,  $p_h(i) \equiv (p_{i-d}, \dots, p_{i-m-d+2})$ ,  $x_t(i) \equiv (x_{i+m+d}, \dots, x_{i+2m+d-1})$ , and  $p_t(i) \equiv (p_{i+m+1}, \dots, p_{i+2m-1})$ . This formulation assumes that measurements are recorded from a single sensor; therefore, a given system state can be determined by sequence of  $m$  measurements and  $m$  perturbations. Only one control parameter is available to change the system dynamics; thus, a minimum of  $m$  successive perturbations are required to reach the target dynamics, which, for stabilization of an unstable periodic orbit, is given by  $x_t(i+1) = 0$  and  $p_t(i) = 0$ . Additionally,  $d$  is a delay time which includes the time to compute  $p_{i+1}$  and the time before an applied perturbation affects the measurements.

If  $C$  is linear,  $4m$  unknown coefficients are required to determine  $p_{i+1}$ . For the liquid bridge,  $C$  is nonlinear and is approximated by a tangential (linear) interpolation in the delay space constructed from time series. Typically, one thousand random perturbations are first applied to the liquid bridge. The applied perturbations and resulting measurements from this "identification stage" are stored as a reference set. When control is activated at time step  $i$ , the reference set is searched for  $8m$  readings (a minimum of  $4m$  are required) that are nearest in the delay space to the history and target dynamics  $[x_h(i), p_h(i), 0, 0]$ . The best linear least squares fit to the  $4m$  coefficients of  $C$  is obtained by singular value decomposition of the (overdetermined)  $8m$  system of selected reference readings and the next applied perturbation for each reading. With the determination of  $C$ , the perturbation  $p_{i+1}$  is computed and applied. The entire computation procedure takes approximately 0.1 sec on a 120 MHz Pentium PC; this forces a one iteration delay (2.3 s) before the perturbation is applied.

## RESULTS

The control scheme is applied for  $M = 17750$  where the unperturbed system exhibits a two frequency state. For  $M > \sim 14000$ , the flow becomes time-dependent with a single fundamental frequency [Fig. 1(b)]; for  $M \approx 16500$ , a second frequency appears and is locked to the first. When the control algorithm is applied, the second oscillation is rapidly suppressed [Fig. 2(a)]. Initially,

the applied perturbations are large; however, once the system approaches the target dynamics, only small perturbations are required to keep the system under control [Fig. 2(b)]. After the control is turned off, the system rapidly returns to the two-frequency dynamics of the unperturbed state.

Effective control is obtained when  $C$  is computed for several different values of  $m$  and  $d$ ; however, the fastest convergence is achieved for  $m = 4$  and  $d = 2$ . This result implies the dimensionality of the unperturbed dynamics is  $m = 4$ . Two dimensions are required to describe the second frequency present in the unperturbed system; the other two dimensions effectively describe the decay of stable modes in the liquid bridge and the thermal relaxation of the feedback element. The delay  $d = 2$  is approximately equal to the sum of the calculation delay and the time for waves with azimuthal wavenumber 2 and period of 2.3 s to propagate from the feedback element location to the sensor location.

Figure 3 demonstrates that our control method is effective for stabilizing states which lie far from the unperturbed dynamics in the phase space. Previous methods for controlling periodic orbits relied on the unperturbed dynamics to carry the system close to the target dynamics before the application of control [6]. The target dynamics for our control method can lie in any region of phase space that can be accessed by the random perturbations applied during the “identification” period when the reference set is constructed. The control scheme fails for  $M > \sim 19000$  because the dynamics become highly nonlinear, and the one thousand points in our reference set become insufficient for good interpolation. More sophisticated methods developed for nonlinear time series predictions (*e.g.*, neural networks) may help extend the parameter range for control [12].

## CONCLUSIONS

Our experiments demonstrate that a single local measurement and feedback perturbation are sufficient to control liquid bridge convection in parameter regimes where the dynamics are sufficiently low-dimensional. For other flow states, however, the spatial structure cannot be ignored. In particular, we have attempted to stabilize unstable time-independent states using the present experiment. Oscillations can be suppressed at the sensor location; nevertheless, infrared imaging reveals the presence of standing waves with antinodes between the feedback element and the sensor. In this case, multiple spatially distributed measurements and perturbations will be required for control; we are presently modifying our control algorithm and experiment to include two sensors and two feedback elements. In this way, liquid bridge convection serves as an ideal proving ground for developing methods for controlling spatially extended nonlinear systems.

## ACKNOWLEDGMENTS

This research is supported by the NASA Microgravity Science and Applications Division (Grant No. NAG3-1382). S.J.V.H. is supported by the NASA Graduate Student Researchers Program.

## REFERENCES

- \* Author to whom correspondence should be directed—email: schatz@chaos.ph.utexas.edu
- [1] A. Croll, W. Muller, and R. Nitsche, *Microgravity Sci. Tech.* **3**, 204 (1991).
- [2] R. Velten, D. Schwabe, and A. Scharmann, *Phys. Fluids A* **3**, 267 (1991).
- [3] G. P. Neitzel, K. T. Chang, D. F. Jankowski, and H. D. Mittelman, *Phys. Fluids A* **5**, 108 (1993).

- [4] M. Wanschura, V. M. Shevtsova, H. C. Kuhlmann, and H. J. Rath, *Phys. Fluids* **7**, 912 (1995).
- [5] M. Levenstam and G. Amberg, *J. Fluid Mech.* **297**, 357 (1995).
- [6] E. Ott, C. Grebogi, and J. A. Yorke, *Phys. Rev. Lett.* **64**, 1196 (1990).
- [7] R. Roy, T. W. Murphy, T. D. Maier, Z. Gillis, and E. R. Hunt, *Phys. Rev. Lett.* **68**, 1259 (1992).
- [8] V. Petrov, V. Gáspár, J. Masere, and K. Showalter, *Nature*, **361**, 240 (1993).
- [9] A. Garfinkel, M. L. Spano, W. L. Ditto, and J. N. Weiss, *Science*, **257**, 1230 (1992).
- [10] V. Petrov and K. Showalter, *Phys. Rev. Lett.* **76**, 3312 (1996).
- [11] M. F. Schatz and K. Howden, *Exp. in Fluids* **19**, 359 (1995).
- [12] H. D. I. Abarbanel, R. Brown, J.J. Sidorowich, and L. S. Tsimring, *Rev. Mod. Phys.*, **65**, 1331 (1993).



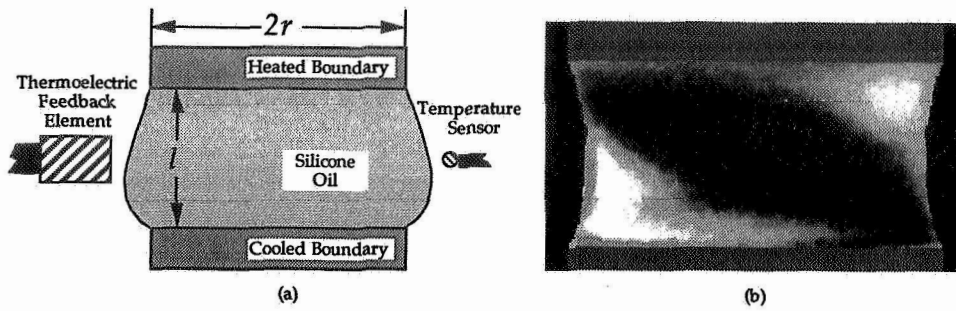


Fig. 1. (a) Sketch of liquid bridge convection experiment. (b) Infrared image of the brightness temperature (darker shading for colder temperatures) for time-periodic liquid bridge convection. The “barber-pole” structure of the temperature corresponds to two waves that propagate azimuthally (right to left in the figure).

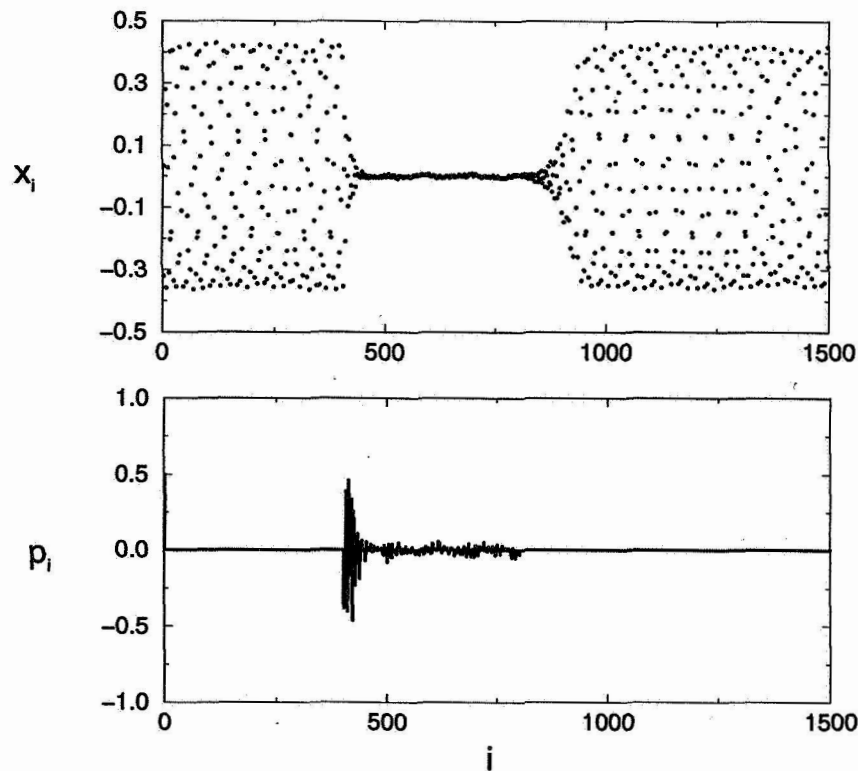


Fig. 2. The application of control is illustrated for discretized dynamics by time series of temperature differences  $x_i$  (top) and applied perturbations  $p_i$  (bottom). The control is applied at time step  $i = 300$  and the second oscillation in the two frequency state is rapidly suppressed. Releasing the control at time step  $i = 800$  caused the system to rapidly return to the unperturbed dynamics.

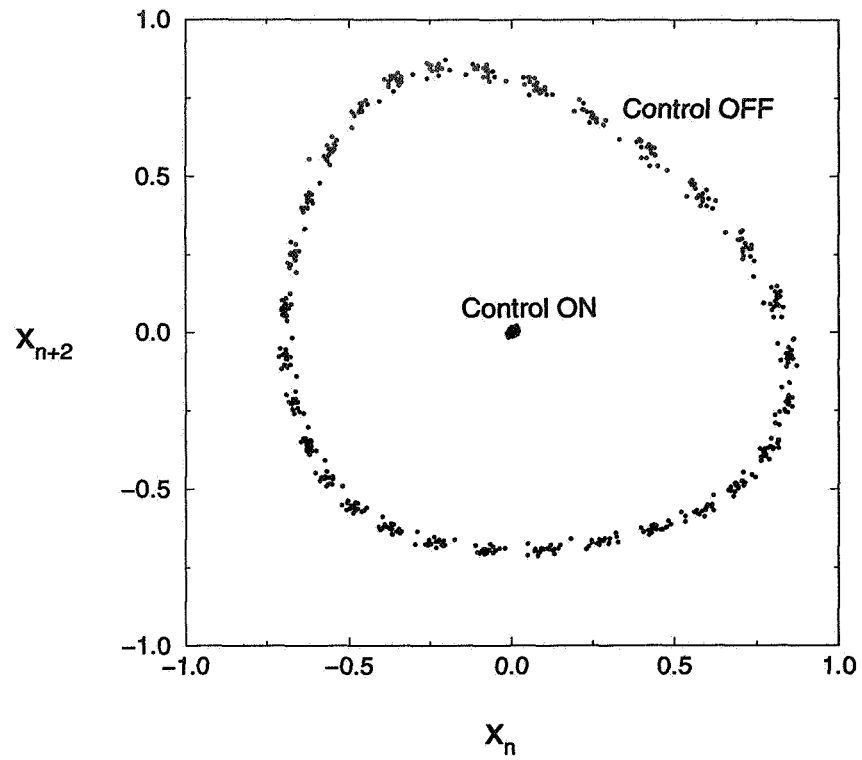


Fig. 3. Second return map constructed from experimental time series illustrating both the torus dynamics (control "off") and the stabilized periodic orbit (control "on").

# DEFORMATION OF FLUID COLUMN BY ACTION OF AXIAL VIBRATION AND SOME ASPECTS OF HIGH-RATE THERMOCAPILLARY CONVECTION

Alexander I. Feonychev, Irina S. Kalachinskaya\*, and Victor I. Pokhilko<sup>+</sup>

Moscow Aviation Institute, 4 Volokolamskoe sh. , GSP-47, 125810, Moscow, Russia

\* Moscow State University

<sup>+</sup> Institute for Mathematical Modelling of Russia Academy of Sciences

## ABSTRACT

The deformation of the fluid column by an action of a low-frequency vibration is considered. It is shown that behaviour of the free fluid surface depends from the frequency of applied vibration and its amplitude. In the area of very low frequencies when fluid has time to comment on travel of bounding solid walls limiting column the harmonical oscillations of free surface with given frequency are observed. With increase of vibration frequency the steady - state relief on free fluid surface is formed. If the amplitude of vibration is very small and the frequency corresponding to the first peak in the vibration spectrum on the Mir orbital station the deformation of free surface tends to zero. Fluid flow induced thermocapillary effect on deformed free surface is more unstable as in the case of smooth cylindrical surface. It was shown that width of heating zone affects very essentially on flow pattern and on transition to oscillatory regime of thermocapillary convection.

## INTRODUCTION

A fluid column has been the subject of investigation over a long term of years. Currently these investigations had expanded still more in connection with necessities of space materials science, in particular of crystal growth by floating zone method. Complex process of crystal growth under action of vibrations set being aboard the spacecrafts and of thermocapillary convection has been broken up into two groups of problems which was solved earlier separately and by different methods. The problem of stability and deformation of fluid column under vibration was solved only for isothermal fluid by analytical methods. Thermocapillary convection and its effect on crystallization process were studied by numerical simulation and without vibration perturbations. Attempt to combine the both problems had been undertaken in (ref.1) using the known analitical solutions about fluid column deformation by action of axial vibration (refs. 2 and 3).

The undertaken investigation of complex problem, especially under action of frequencies set, and also the unexpected and conflicting results obtained in experiments during the SL - D1 and SL - D2 (ref. 4) have had a stimulating influence on beginning of this work.

From the outset presenting work had been planed so as to combine the both lines of investigations. In this connection, exact calculations of free surface deformation would be carried out with the help of the Navier - Stokes equations and a study of thermocapillary convection ought to be extended to the area of the high Marangoni numbers existing in real technological processes. The two circumstances favoured the realization of this plan:

- development of new finite-difference scheme of the third order of accuracy and of new very effective algorithm for numerical solution of the Navier-Stokes equations in velocity-pressure variables (ref. 5);
- obtaining of financial support of NASA allowed to purchase Pentium PC.

Presenting work is the first stage of plan having for an object to create a computer program for calculation of complex process of crystal growth by floating zone method with regard for deformation of free fluid surface on account of vibration, thermocapillary flow and control magnetic field (ref. 6).

## OUTLINE

Consider the fluids flow in a circular cylindrical zone of height  $L$  and radius  $R$  with free sides surface. The temperature is constant. The cylinderes foots are oscillate in the axial direction. The fluid equations to be solved are the Navier-Stokes equation:

$$\frac{\partial u}{\partial t} + u \frac{\partial u}{\partial r} + v \frac{\partial u}{\partial z} = -\frac{\partial p}{\partial r} + \nu \left[ \frac{\partial}{\partial r} \left( \frac{1}{r} \frac{\partial(ru)}{\partial r} \right) + \frac{\partial^2 u}{\partial z^2} \right] \quad (1)$$

$$\frac{\partial v}{\partial t} + u \frac{\partial v}{\partial r} + v \frac{\partial v}{\partial z} = -\frac{\partial p}{\partial z} + \nu \left[ \frac{1}{r} \frac{\partial}{\partial r} \left( \frac{\partial(rv)}{\partial r} \right) + \frac{\partial^2 v}{\partial z^2} \right] + Re_\omega \sin \Omega t \quad (2)$$

$$\frac{\partial u}{\partial r} + \frac{\partial v}{\partial z} + \frac{u}{r} = 0 \quad (3)$$

where  $u, v$  are velocity components,  $p$  is pressure,  $\nu$  is kinematic viscosity,  $Re_\omega = \omega Ra/\nu$  is vibrational Reynolds number,  $a$  is amplitude of displace,  $\Omega = \omega R^2/\nu$ ,  $\omega$  is frequency of vibration,  $t$  is time. Fluid density has been normalised to unity. The equation system (1)-(3) is completed with boundary condition:

- on solid bodies ( $z = 0, L$ )  $u = v = 0$
- on the free fluid surface ( $R = \xi(z)$ )  $u = \partial \xi / \partial t$
- tangential viscous stresses are zero  $\partial v_n / \partial n + \partial v_s / \partial s = 0$
- normal stresses  $p - 2\partial v_n / \partial n - K_\sigma (R_1^{-1} + R_2^{-1}) = 0$

where  $n$  and  $s$  are normal and tangent to free surface respectively,  $K_\sigma = \sigma R / \rho \nu^2$  is capillary constant,  $\sigma$  is surface tension.  $R_1$  and  $R_2$  are the principal radii of curvature.

In the preset work the basic idea of VOF method (Ref. 7) is adapted to solving above problem.

## NUMERICAL RESULTS

The deformation of free fluid surface. The deformation of free fluid surface. The three different regimes of vibration had been considered. For the least frequency (Fig. 1) when fluid is able to respond to oscillations of solid ends such point on free fluid surface oscillates with frequency of applied force. This result agrees qualitatively with experiment (Ref. 8) and with the approximate analytical solutions (Refs. 2,3). Under more high frequency of vibration fluid in every point cannot - finish complete cycle of oscillations. As a result oscillations in every point on free surface decay (Fig. 2b). and steady - state relief is formed. For the first peak of vibration spectrum on the Mir orbital station (ref. 9) oscillations in every point on free fluid surface die out after transition from the vibration beginning. As an axample, the oscillations in point on free fluid surface with the coordinate  $z = L/4$  had been presented in Fig. 3.

Thermocapillary convection under the high Marangoni numbers. It seems reasonable to say that vibration will have impact on stability of thermocapillary flow. Influence of free fluid surface form on temperature field and flow pattern under the large Marangoni numbers had been considered for case when deformation free fluid surface is held steady-state (Fig. 4).

Thermocapillary effect is characterized by kinematic condition on free fluid surface

$$\partial v_n / \partial n = Ma Pr^{-1} \partial \theta / \partial s$$

where  $Ma = \gamma \Delta T L / \rho \nu a$  is the Marangoni number,  $\Delta T = T_1 - T_0$  is characteristic temperature difference,  $\theta = (T - T_0) / \Delta T$ ,  $\gamma = -\partial \sigma / \partial T$ ,  $Pr = \nu / a$  is the Prandtl number.

A heating of fluid zone proceeds on the source side of free fluid surface in the form of exponential curve  $\partial \theta / \partial r = A \exp(-B(z - L/2)^2)$  where  $A$  and  $B$  are selected constants.

Crystallization is imitated on the end  $z = 0$  with impurity balance according to equation

$$\partial c / \partial z = -Sc(1 - k_0) Re_{cr} c,$$

here  $Sc = \nu/D$  is the Schmidt number,  $Re_{cr} = v_{cr}L/\nu$  is dimensionless crystallization rate,  $k_0$  is equilibrium coefficient of dopant distribution ( $k_0 < 1$ ),  $c$  is concentration,  $D$  is diffusion coefficient; "s" falls into crystallization boundary.

Previously we found out physical cause of oscillatory regime advent for thermal gravitational convection, the Kelvin - Helmholtz's instability (Ref. 10). Similar search for thermocapillary convection showed that one of cause inducing oscillations can be form of heat flux on free fluid surface. The wide zone of heating induces oscillatory regime of thermocapillary convection (Fig. 5b, where  $A = 0.8$ ,  $B = 0.3$ ), whereas oscillations are absent under narrow zone of heating (Fig.5a, where  $A = 5$ ,  $B = 15$ ).

## CONCLUDING REMARKS

Conducted investigation on vibration effect on fluid column gave quantitative configuration about high sensitivity of fluid column to vibrations especially in the area of low frequencies and for small-viscous fluids (semiconducting materials, for example). Unexpected phenomenon of steady-state relief formation on free fluid surface for vibrating column had been discovered. It is planned to carry out the series of the experiments on the Mir orbital space station for a verification of the obtained data.

## ACKNOWLEDGMENTS

This research was carried out by the NASA Microgravity Science and Application Division support within the framework of the NASA - RSA agreement, contract NAS 15 - 10110. We are also thankful to M.J. Wargo and B.M. Carpenter for possibility to participate in the NASA conferences in Huntsville, AL and Cleveland, OH at June 1996.

## REFERENCES

1. Feonychev A. I. ; and Dolgikh G. A. : Influence of vibration on heat and mass transfer in microgravity conditions. Microgravity Quarterly, Vol. 4, No 4, pp. 233 - 240.
2. Meseguer J. ; and Perales J. M. : Non - steady phenomena in the vibration of viscous cylindrical long liquid bridges. Microgravity Science and Technology, Vol. 5, 1992, pp: 69-72.
3. Bauer H. F. : Axial response and transient behavior of a cylindrical liquid column in zero gravity. ZFW, 14, 1990, S. 174-182. Forschungsbericht : LRT-WE-9-FB-4 1991. Munchen.
4. Martinez I. ; Perales J. M. ; and Meseguer J. : Stability of long liquid columns; in: Scientific results of the German Spacelab Mission D2. P. R. Sahm, M. H. Keller, B. Schiwe (Eds.), DLR, Koln, Germany 1995, p. 220.
5. Pokhilko V. I. : Finite-Difference Method For Solution of Navier-Stokes Equations in Natural Variables With Using Conditional-Monotone Approximation. Moscow, Inst.Math.Model., 1994, prepr. No. 8
6. Feonychev A. I. ; and Dolgikh G. A. : Effect of magnetic field on crystal growth process under action of gravity and capillary force. Ninth European Symposium "Gravity Dependent Phenomena in Physical Sciences". Berlin, Germany, 2 - 5 May 1995. Abstracts, p. 246.
7. C.W.Hirt and B.D.Nicols. Volume of fluid ( VOF ) method for the dynamics of free boundaries. J. Comp. Phys. 1981, Vol.39, pp. 201-205.
8. Martinez I. ; Perales J. M. ; and Meseguer J. : Response of a liquid bridge to an acceleration varying sinusoidally with time; in : Materials and Fluid Under Low Gravity. Proceedings. L. Ratke, H. Walter, B. Feuerbacher (Eds.) . Berlin, Germany, Springer, 1995, pp. 271-279.
9. Feonychev A. I.; Tillotson B. J. ; Torre L. P. ; and Willenberg H. J. : Characterization of the microgravity environment on the Salyut and Mir space stations. SPIE Intern. Symp. On Aerospace Sensing, Orlando, FL, April 4 - 8, 1994.
10. Feonychev A. I. : Comparative analysis of thermocapillary convection in one- and two-layer systems. Problem of oscillatory convection. Advances in Space Research, Vol. 16, No 7, 1995, pp. 59-65.

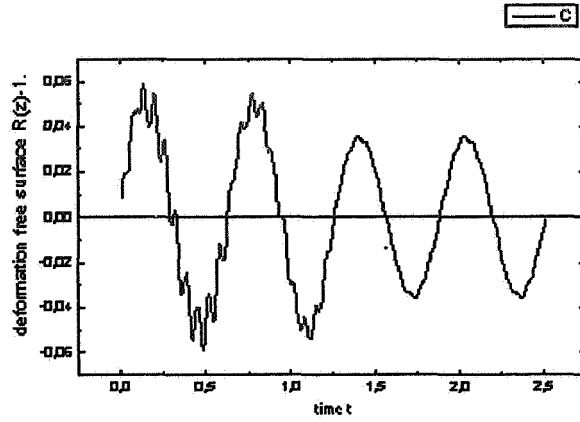


Fig.1. Free surface deformation at  $z = L/4$  by  $Re_\omega = 10.$ ;  $L/R = 1.$ ;  $\Omega = 10.$ ;  $K_\sigma = 3.26 \cdot 10^3$

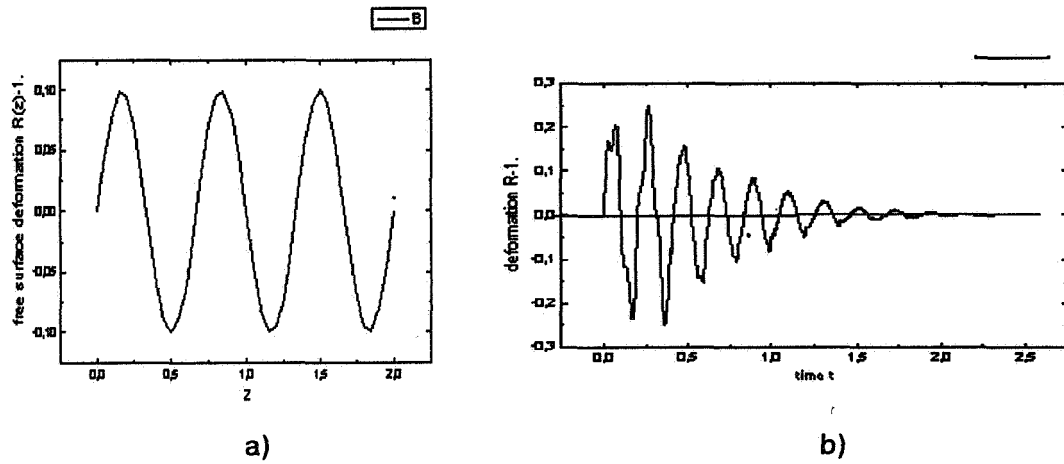


Fig 2. Shape (a) and deformation at  $z=L/8$  (b) of free fluid surface by  $Re_\omega = 30.$ ;  $L/R = 2.$ ;  $\Omega = 30.$ ;  $K_\sigma = 3.26 \cdot 10^3$

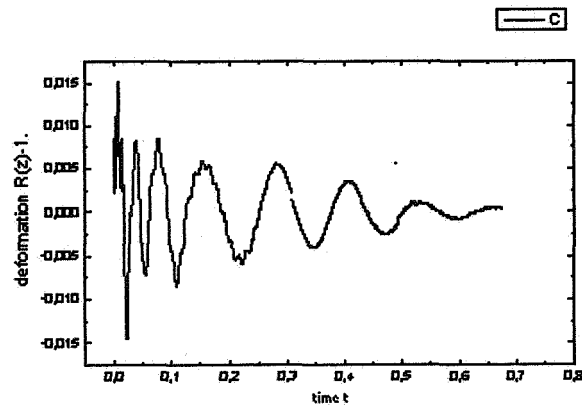


Fig. 3. Free surface shape at  $z = L/4$  by  $Re_\omega = 3.12.$ ;  $L/R = 1.$ ;  $\Omega = 200.$ ;  $K_\sigma = 3.26 \cdot 10^3$

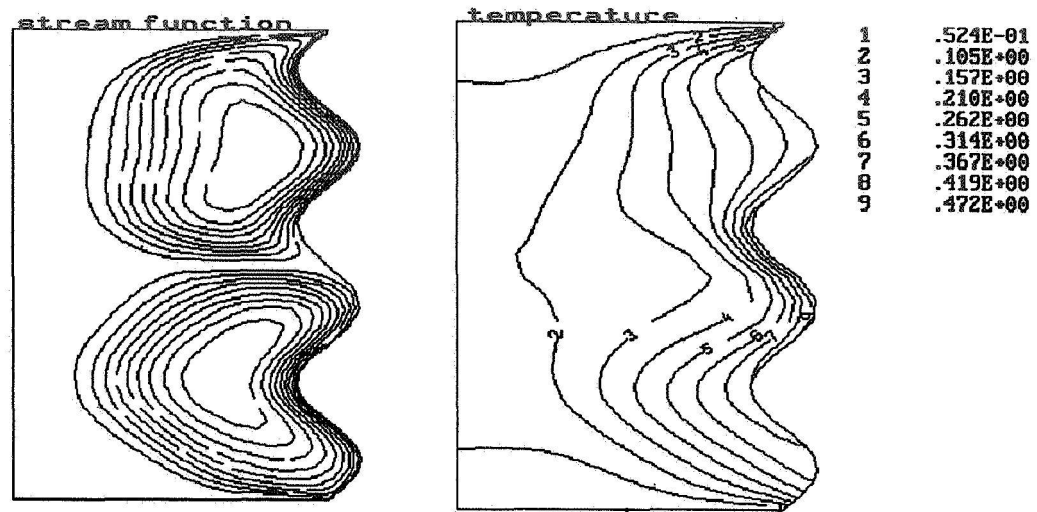
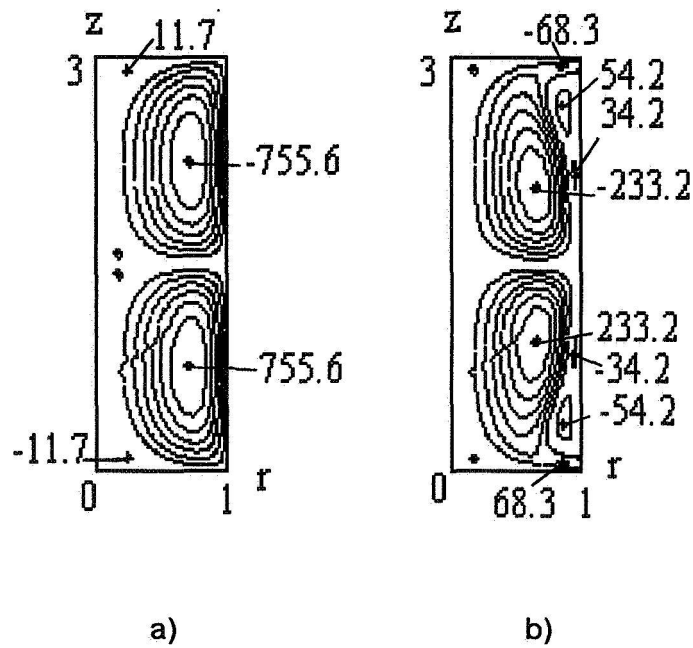


Fig. 4. Stream function and isotherms for goffed free fluid surface similar to data in Fig. 2 by  $Ma=2600$ ,  $Pr=0.018$ ,  $A=3$ ,  $B=10$



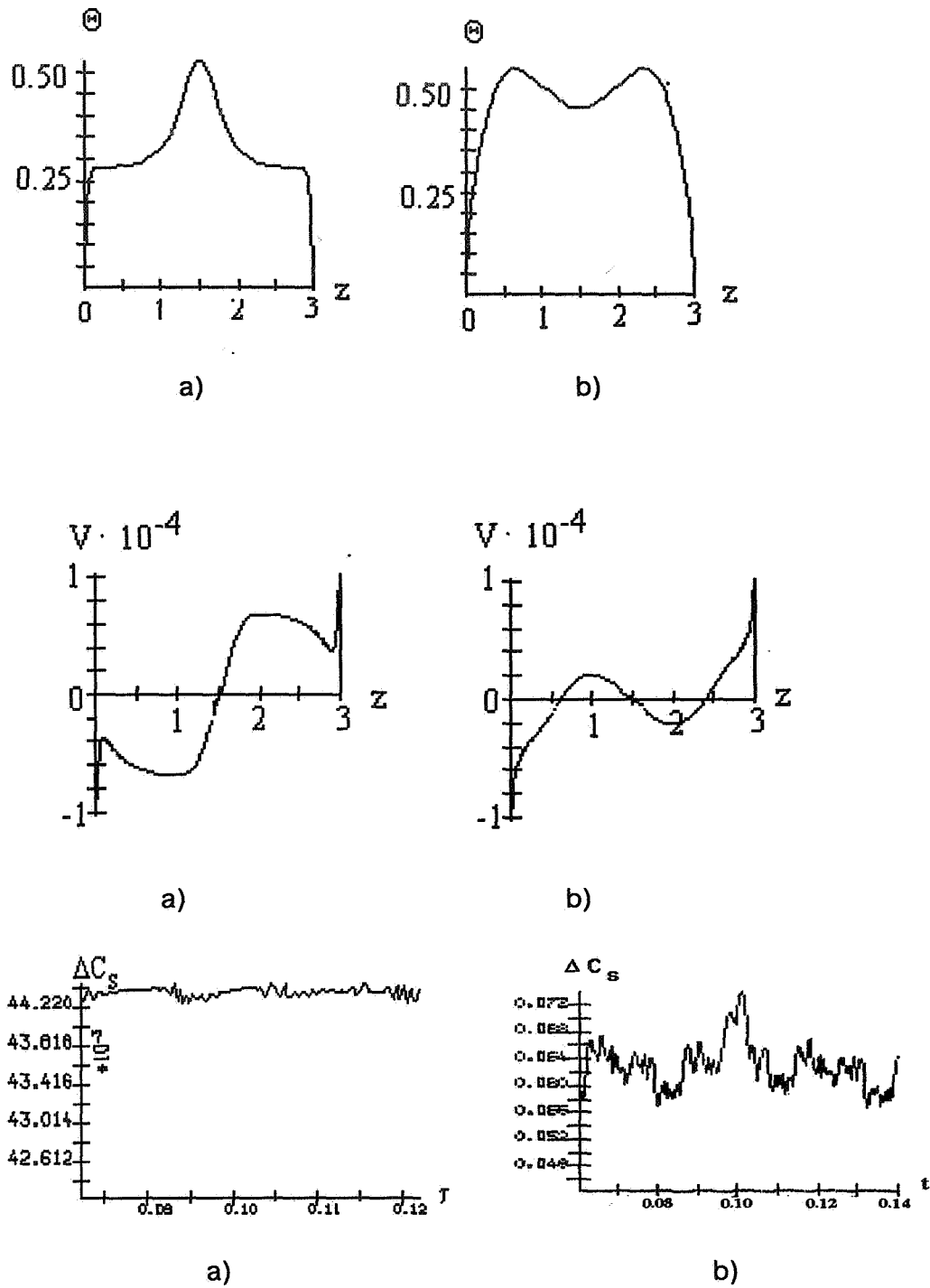


Fig. 5. Temperature distribution on free fluid surface ( $r = 1$ ), stream function, distribution of velocity on free surface and impurity concentration difference on phase boundary ( $z = 0$ ) for narrow (a) and wide (b) zones of heating.  $Ma = 5400$ ;  $Pr = 0.018$ ;  $Sc = 10$ ;  $Re = 0.2$ ;  $k = 0.023$ .



# **Dynamics and Interaction of Bubbles and Drops**



# INVESTIGATION OF DROP FORMATION BY A VORTEX RING IN MICROGRAVITY

Luis P. Bernal and Pepi Maksimovic  
Department of Aerospace Engineering  
University of Michigan  
Ann Arbor, Michigan 48109-2118

## ABSTRACT

An investigation of drop formation by a vortex ring propagating through one or more fluid interfaces in microgravity is described. The main goal of the research is to determine the dynamics of drop formation by vortical flows in the capillary limit with large density change across the interface. Dimensional analysis shows that in microgravity experiments the capillary limit can be studied using a relatively large vortex ring diameter to facilitate experimental characterization of the interaction. Results obtained in density matched systems are reviewed to illustrate the complex nature of these interactions.

## INTRODUCTION

We consider the propagation of a vortex ring through one or more fluid interfaces. The flow configuration is shown schematically in Figure 1. It consists of a vortex ring formed in the liquid below the interface moving toward one or more fluid interfaces (Figure 1a). If the vortex ring has sufficient impulse the collision of the vortex ring with the interface(s) will result in the formation of a drop (Figure 1b). If the initial condition consisted of several liquid layers the resulting drop is expected to have a layered structure as well. The size of the drop is determined by the volume of fluid carried by the vortex ring. The fluid motion inside the drop is determined by the vorticity distribution in the vortex ring. This relatively simple flow problem captures important dynamical processes relevant to the evolution of fluid interfaces in microgravity and in other flow systems. For a review of the flow characteristics of vortex rings see the review paper by Shariff and Leonard.<sup>1</sup>

The dynamics of fluid interfaces in the case of surface-tension-dominated evolution is important in many practical problems. Atomization of liquid fuels is influenced by the interfacial properties of the fuel as well as by fluid motion within the liquid. For example, several investigators have found important effects of liquid turbulence on the spray characteristics of a nozzle.<sup>2-4</sup> Wu *et al.*<sup>5</sup> investigated primary breakup of a turbulent liquid jet. They used holographic imaging to measure the drop size distribution. The spatial and temporal resolution in these experiments was not adequate to capture the evolution of the breakup process. However they developed a phenomenological model of turbulent breakup that is illustrated in the sketch in Figure 2. In this model the size of the drop is assumed to be of the order of the size of eddies in the turbulent liquid. They obtained good correlation between the measured mean drop size at several Weber numbers and the predictions of the model. The interaction of the vortex ring with a fluid interface resulting in the formation of a drop is viewed as an idealization of the interaction of a turbulent eddy with the liquid surface. These flow processes in typical atomization systems are very difficult to investigate experimentally because of the small size of the droplets. As shown below the limit of interests is the capillary limit, i.e., finite Weber number and infinite Froude number, that is the same as in microgravity. It follows that experiments in microgravity can provide valuable new insights on the dynamics of flow induced atomization.

The study of the interaction of a vortex ring with multiple fluid interfaces is motivated in part by problems in encapsulation technology. The goal of this technology is to produce small drops of a drug solution coated with a membrane of suitable chemical and biological properties. The fluid dynamic processes encountered in this technology have been reviewed by Kendall *et al.*<sup>6</sup> Lin and Wang<sup>7</sup> proposed an encapsulation system using a droplet generator based on the Rayleigh instability of a liquid column. Microgravity experiments of a vortex ring propagating through multiple fluid interfaces can provide new insights on these problems and should contribute to the development of improved encapsulation technology.

The interaction of a vortex ring with a fluid interface in microgravity is a relatively simple flow configuration where the balance between capillary, viscous and inertia forces is similar to that found in a variety of flow problems of practical interest. It is a relatively simple flow configuration that can be easily implemented in existing microgravity facilities. The vortex ring flow has been used frequently to study the dynamics of the interaction of vortical flows with miscible and immiscible fluid interfaces.<sup>9-20</sup> The present experiments extend this work to the case of surface-tension-controlled interface dynamics.

## DIMENSIONAL ANALYSIS

To help clarify the role of various parameters in the flow we use dimensional analysis for the case of a single interface.<sup>21</sup> The initial state is characterized by the vortex ring diameter,  $a$ , and circulation,  $\Gamma$ . The interface is characterized by the densities  $\rho_1$  and  $\rho_2$ , the viscosities  $\mu_1$  and  $\mu_2$ , and the interfacial tension  $\sigma$ . The ring moves toward the interface with speed  $U$  and collides with it. The collision and the subsequent evolution of the drop depend on fluid inertia, viscosity and surface tension. Therefore the nondimensional numbers characterizing the phenomena are the Weber number, the Froude number and the Reynolds number. These are defined as:

$$We = \frac{\rho_1 \Gamma^2}{\sigma a}, \quad Fr = \frac{\rho_1 \Gamma^2}{(\rho_1 - \rho_2) g a^3}, \quad Re = \frac{\rho_1 \Gamma}{\mu_1},$$

respectively. In addition, the density ratio  $r = \rho_2 / \rho_1$  and the viscosity ratio  $\lambda = \mu_2 / \mu_1$  must be specified. Here, the subscript 1 denotes the fluid below the interface and inside the drop and 2 the fluid above the interface. In the experiments of Bernal *et al*<sup>21</sup>  $r = 0.99$  and for a typical liquid/gas interface  $r \approx 10^{-3}$ .

The effect of the gravitational acceleration is best illustrated by a plot of  $We$  versus  $Fr$  as shown in Figure 3. For fixed vortex ring diameter and interface properties, all possible vortex ring strengths (i.e. circulation  $\Gamma$ ) define a straight line. The slope of the line is the Bond number,

$$Bo = \frac{We}{Fr} = \frac{\rho_1 - \rho_2}{\sigma} g a^2.$$

Shown in Figure 3 are two lines for 1g. These lines correspond to the interaction of a 1 cm diameter vortex ring with a water/air interface ( $r \approx 10^{-3}$ ) and with a silicon-oil/water-methanol interface ( $r = 0.99$ ). These are conditions typical of what can be obtained in 1g with density matched systems. The corresponding Bond numbers are 14 and 0.4 respectively.

In microgravity experiments the gravitational acceleration is very small, approximately  $10^{-5}g$  in the 2.2 sec drop tower, and consequently the Bond number is at least four orders of magnitude smaller than in 1g. The corresponding lines in Figure 4 coincide with the horizontal axis. This condition corresponds to the capillary limit of finite Weber number and infinite Froude number. Using Bond number scaling it follows that an experiment in microgravity with a vortex ring diameter of 1 cm would be equivalent to an experiment in 1g with a vortex ring diameter of 32  $\mu m$ . In the experiments of Wu *et al*.<sup>5</sup> the drop size varied from 350  $\mu m$  to 34  $\mu m$  as the jet speed was increased.

## RESULTS FOR DENSITY MATCHED SYSTEMS

Bernal *et al*<sup>21</sup> studied the interaction of vortex rings with a fluid interface. They consider the case of small density change across the interface. Figure 4 shows the evolution of the interaction as determined by Laser Induced Fluorescence (LIF) flow visualization pictures (first row) and the results of numerical simulations at the same flow conditions (second and third row). These experiments show that at sufficiently high Froude and Weber number the vortex ring penetrates the interface and forms a drop. Before breakup the interface is highly stretched and vorticity is left behind along the liquid column. The location where the interface breaks depends on the strength of the vortex ring. It occurs near the vortex ring at high Froude/Weber number and away from the vortex ring, near the undisturbed interface at low Froude/Weber number. They observed the formation of satellite drops during the interaction that are

observed the formation of satellite drops during the interaction that are associated with concentrations of vorticity along the stretched interface. The numerical simulations are in good agreement with the experiments. Computation at several Froude and Weber numbers suggest that in the capillary limit drops form at Weber number greater than  $\approx 4$ . An interesting observation is the formation of a reflected vortex ring propagating in the direction opposite to the drop motion.

Bernal & Maksimovic<sup>22</sup> studied the propagation a vortex ring through two immiscible interfaces. The top and bottom layer were mixtures of water and methanol and the middle layer was silicone oil. Figure 5 shows the evolution of a relatively weak vortex ring. The Froude and Weber number based on the lower interface properties are 100 and 49 respectively. The thickness of the middle layer is  $H/a = 3.7$ . The initial evolution is similar to that reported by Bernal *et al*<sup>21</sup> for a single interface. In this case however, the vortex ring reaches the second interface before the liquid column breaks. The third image in the sequence captures the flow after the vortex ring has penetrated the second interface and the liquid column breakup. The final image in the sequence shows the vortex ring in the liquid layer on top. At these conditions the vortex ring does not carry any silicone oil from the middle layer. Because the top and bottom layer are made of the same components, namely water and methanol, the vortex ring structure that forms in the top liquid layer is not a drop. In this case fluid from the lower layer is transferred to the top layer without a silicone oil coating. The pictures also show the formation of smaller satellite drops below the main vortical region.

Figure 6, also for a three layer system, shows the evolution of a stronger vortex ring and a larger depth of the middle layer. The Froude and Weber number based on the lower interface properties are 324 and 144 respectively. The thickness of the middle layer is  $H/a = 5.9$ . In this case the vortex ring penetrates the interface and forms a drop of liquid from the lower layer in the middle layer. The drop forms before reaching the second interface in the first image. The last three images show that the interaction with the second interface results in the formation of a drop of dyed fluid in the top layer covered by a layer of silicone oil. The dyed liquid originated in the lower layer while the silicone oil originated in the middle layer. This "drop-within-a-drop" structure indicates that at these flow conditions the drop engulfs a significant amount of silicone oil as it moves through the middle layer.

## SUMMARY

Microgravity experiments could be used to study flow induced atomization processes at a larger scale than in 1g experiments and, consequently, detailed measurements can be obtained more easily. The vortex ring flow is a useful model for the interaction of vortical flows with fluid interfaces. Experiments in density matched systems show several interesting phenomena. The results show that regions of concentrated vorticity play an important role in the formation of satellite drops.

## REFERENCES

1. K. Shariff & A. Leonard "Vortex rings" *Ann. Rev. Fluid Mech*, vol. 24, pp. 235-79, 1992.
2. R.D. Reitz & F.V. Bracco. Mechanism of atomization of a liquid jet. *Phys. Fluids*, vol. 25 (1982), pp. 1730-1742.
3. G.A. Ruff, L.P. Bernal, & G.M. Faeth, "Structure of the near-injector region of non-evaporating pressure-atomized sprays," *Journal of Propulsion and Power*, vol. 7, no. 2, pp. 221-230, March-April 1991.
4. G.A. Ruff, P.-K. Wu, L.P. Bernal, & G.M. Faeth, "Continuous- and Dispersed-Phase Structure of Dense Non-Evaporating Pressure-Atomized Sprays," *Journal of Propulsion and Power*, vol. 8, no. 2, pp. 280-9, March-April 1992.
5. P.-K. Wu, L.-K. Tseng & G.M. Faeth, "Primary breakup in gas/liquid mixing layers for turbulent liquids," *Atomization and Sprays*, vol. 2, pp. 295-317, 1992.
6. J.M. Kendall, M. Chang, & T.G. Wang, "Fluid and chemical dynamics relating to encapsulation technology," AIP Proceeding 197, Int'l Colloquium on drops and bubbles, Monterey, CA. 1988.

7. K.C. Lin & T.G. Wang, "A novel method for producing microspheres with semipermeable polymer membranes," AIAA paper 92-0118, AIAA 30nd Aerospace Sciences Meeting & Exhibit. Reno, NV. January 6-9, 1992.
8. P.F. Linden. The interaction of a vortex ring with a sharp density interface. *J Fluid Mech.* (1973), pp 467 - 480
9. Dahm, W.J.A., Scheil, C.M. & Tryggvason, G. Dynamics of Vortex Interaction with a Density Interface. *J. Fluid Mech.*, **205**, 1-43, (1989).
10. T. Sarpkaya & D. O. Henderson. Free surface scars and striations due to trailing vortices generated by a submerged lifting surface. AIAA paper 85-0445
11. Hirsa, A. 1990 An experimental investigation of vortex pair interaction with a clean or contaminated free surface. Ph.D. Thesis, University of Michigan.
12. Kwon, J.T. 1989 Experimental study of vortex ring interaction with a free surface. Ph.D. Thesis, University of Michigan.
13. Kachman, N.J. 1991 The interaction of a vortex ring with a contaminated free surface. Ph.D. Thesis, University of Michigan.
14. L.P. Bernal, & J.T. Kwon, "Vortex ring dynamics at a free surface," *Phys. Fluids A*, vol. 1, no. 3, pp 449-451, March 1989.
15. N.J. Kachman, E. Koshimoto, & L.P. Bernal, "Vortex ring interaction with a contaminated surface at inclined incidence," in *Dynamics of Bubbles and Vortices Near a Free Surface*, Ed: I. Sahin, G. Tryggvason and H.L. Schreyer, AMD - vol. 119, pp 45-58, ASME Applied Mechanics Division, 1991.
16. J. G. Telste. Potential flow about two counter-rotating vortices approaching a free surface. *J. Fluid Mech.*, **201**, 283-296, (1989).
17. Yu, D. & Tryggvason, G. The Free Surface Signature of Unsteady, Two-Dimensional Vortex flows. *J. Fluid Mech.*, **218**, 547-572, (1990).
18. Song, M., Bernal, L.P. & Tryggvason G. Head-on Collision of a Large Vortex Ring with a Free Surface. *Phys. of Fluids A* **4**, 1457-1466, (1992).
19. S. Ohring & H.J. Lugth. Interaction of a viscous vortex pair with a free surface. *J. Fluid Mech.*, **227**, 47-70, (1991).
20. Tryggvason, G., Abdollahi-Alibeik, J., Willmarth, W. and Hirsa, A. Collision of a Vortex Pair with a Contaminated Free Surface. *Phys. of Fluids A* **4**, 1215-1229, (1992).
21. L.P. Bernal, P. Maksimovic, F. Tounsi & G. Tryggvason. "An experimental and numerical investigation of drop formation by vortical flows in microgravity," AIAA paper 94-0244, AIAA 32nd Aerospace Sciences Meeting & Exhibit. Reno, NV. January 10-13, 1994.
22. L.P. Bernal & P. Maksimovic, "The Propagation of a Vortex Ring through Multiple Liquid Interfaces in Microgravity," AIAA paper 96-0593, AIAA 34th Aerospace Sciences Meeting & Exhibit. Reno, NV. January 15-18, 1996.

# FIGURES

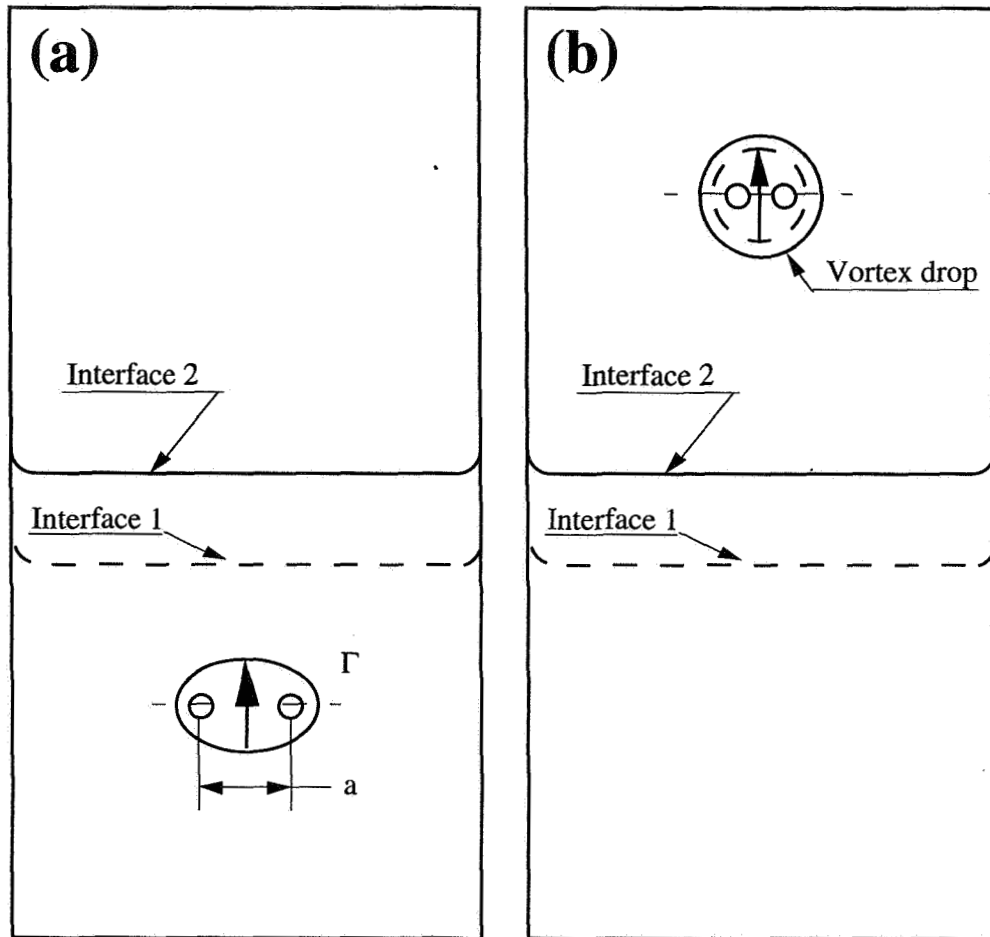


Figure 1 Schematic diagram of the interaction of a vortex ring with fluid interfaces. (a) Idealized picture before the interaction. (b) Idealized picture after the interaction. Note that the multiple interface structure in (a) is expected to result in a layered structure of the drop in (b).

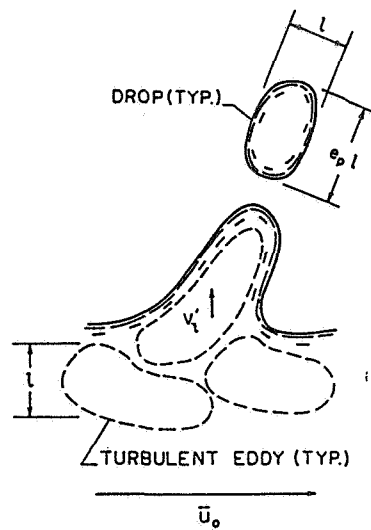


Figure 2 Sketch of turbulent primary breakup at a liquid surface (from Wu *et al*<sup>5</sup>)

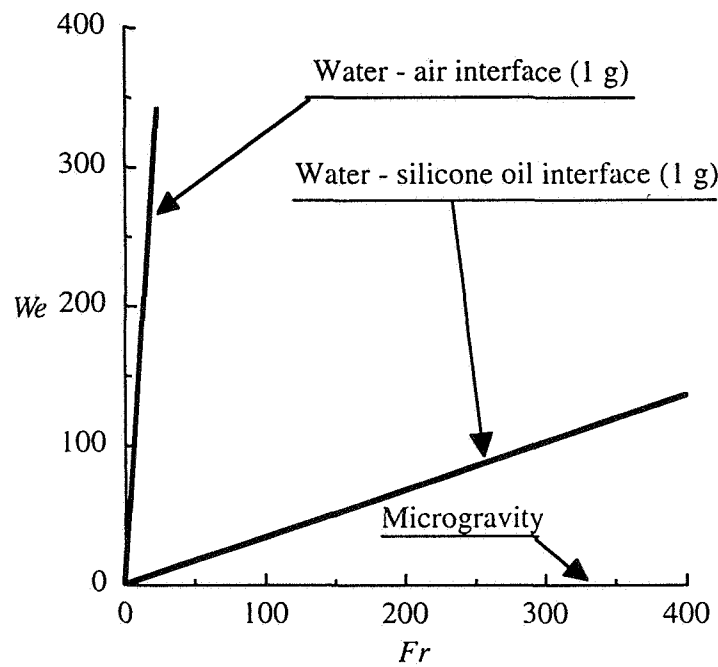


Figure 3. Plot of the Weber number vs the Froude number for typical interfaces on earth based systems (1 g) and in microgravity.



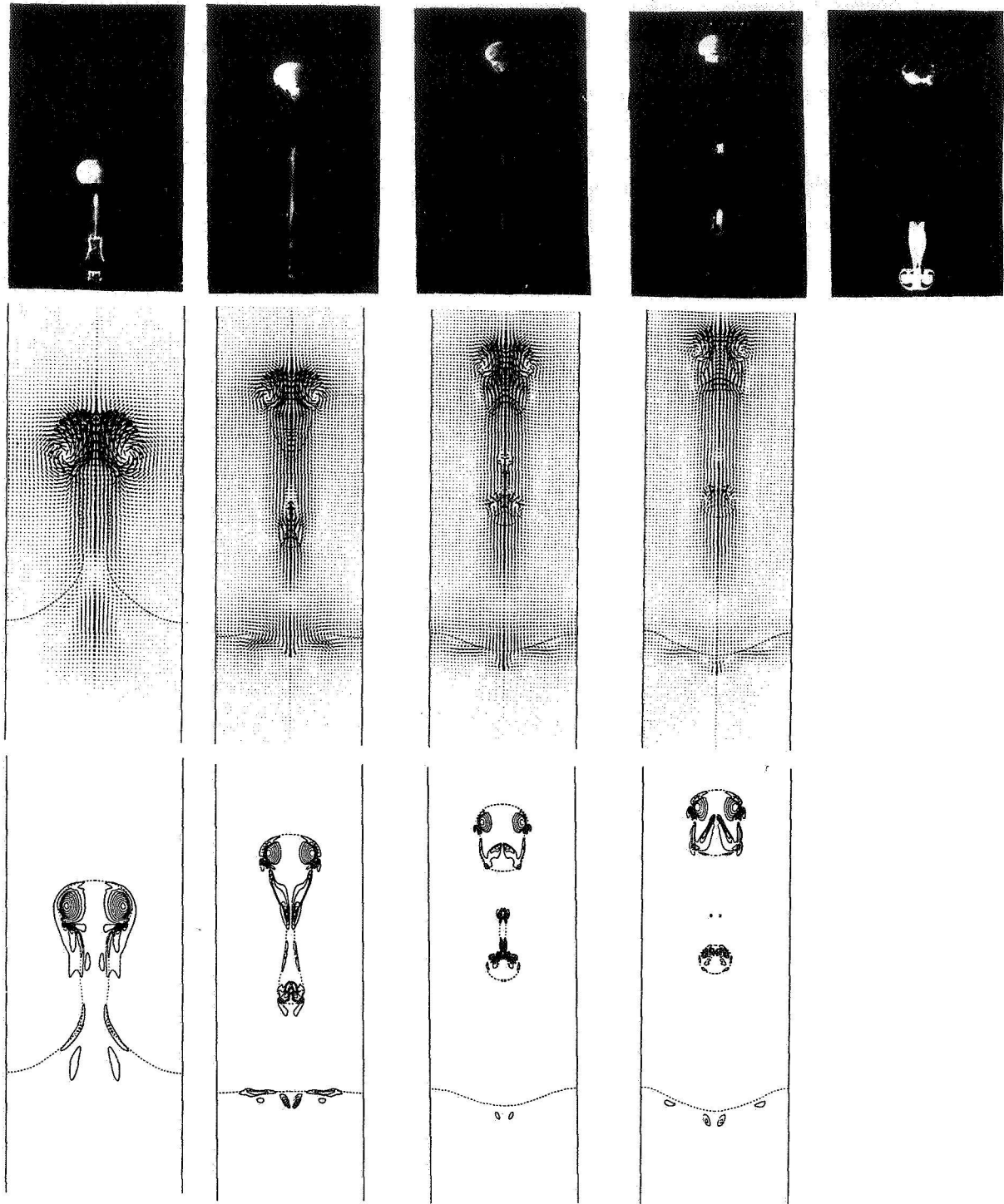


Figure 4. Interaction of a vortex ring with a fluid interface at  $Fr = 63$ ,  $We = 22$  and  $Re = 1200$ . First row flow pictures obtained at  $U/a = 7.1, 10.34, 11.88, 12.35, 16.66$  (from left to right). Second and third row - Computational results obtained at  $U/a = 6.26, 9.22, 10.3, 11.48$  (from left to right). Second row - velocity vector plot and interface elevation. Third row - vorticity contours. (From Bernal et al.<sup>21</sup>)

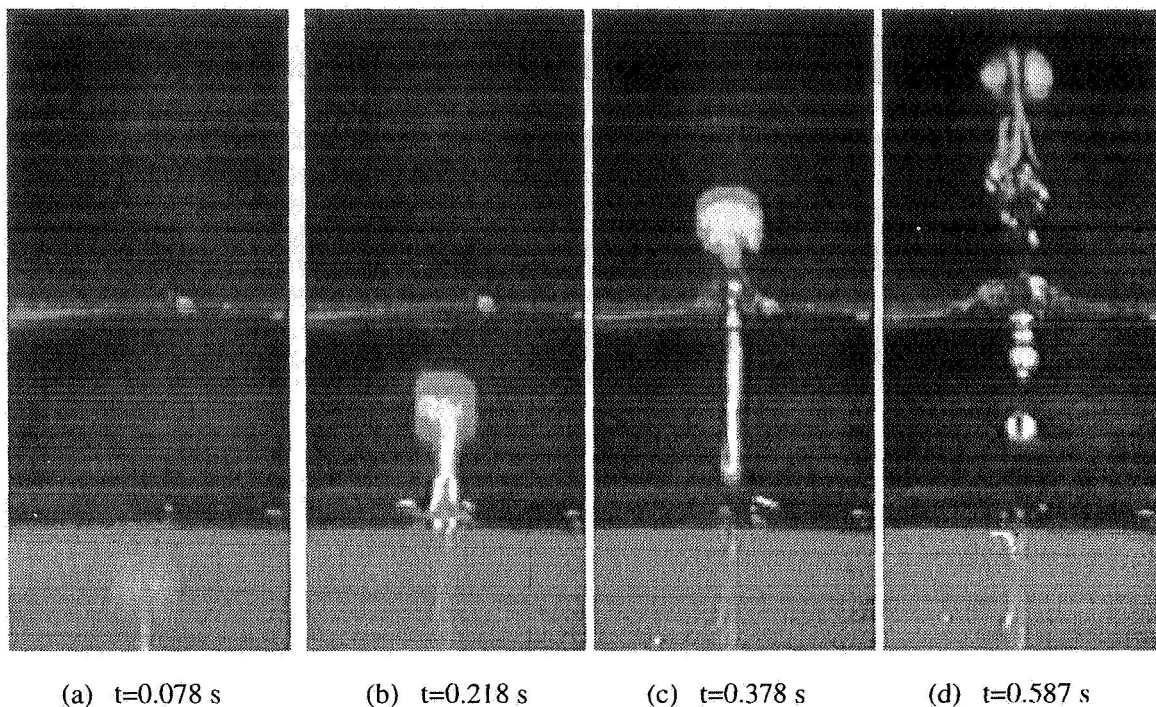


Figure 5. Propagation of a vortex ring through two fluid interfaces. Froude number  $Fr_1 = 100$ , Weber number,  $We_1 = 49$ , Reynolds number 1920.

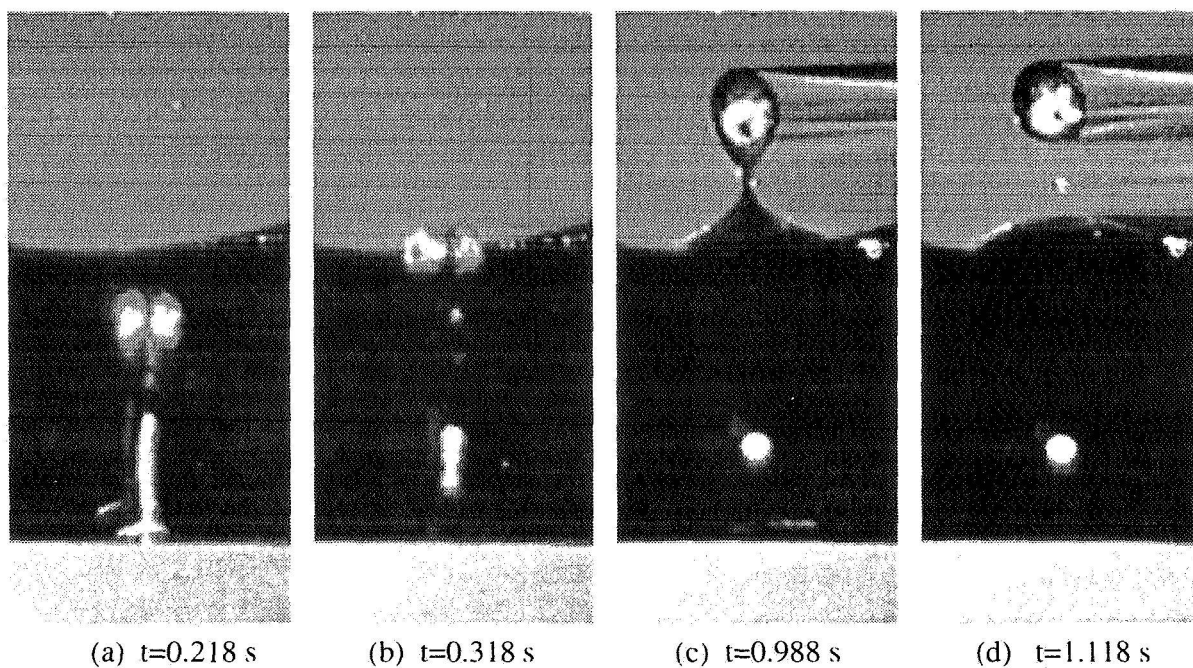


Figure 6. Propagation of a vortex ring through two fluid interfaces. Froude number  $Fr_1 = 324$ , Weber number,  $We_1 = 144$ , Reynolds number 3373.

# Droplet Deformation in an Extensional Flow: The Role of Surfactant Physical Chemistry

Kathleen J. Stebe, Chemical Engineering Department, Johns Hopkins University, Baltimore, MD 21218

## Abstract

Surfactant-induced Marangoni effects strongly alter the stresses exerted along fluid particle interfaces. In low gravity processes, these stresses can dictate the system behavior. The dependence of Marangoni effects on surfactant physical chemistry is not understood, severely impacting our ability to predict and control fluid particle flows. A droplet in an extensional flow allows the controlled study of stretching and deforming interfaces. The deformations of the drop allow both Marangoni stresses, which resist tangential shear, and Marangoni elasticities, which resist surface dilatation, to develop. This flow presents an ideal model system for studying these effects.

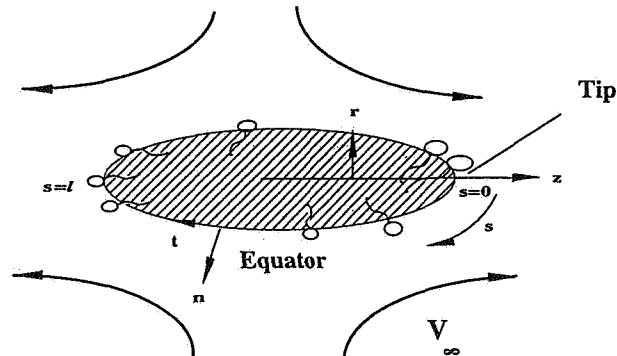
Prior surfactant-related work in this flow considered a linear dependence of the surface tension on the surface concentration, valid only at dilute surface concentrations, or a non-linear framework at concentrations sufficiently dilute that the linear approximation was valid. [1-3] The linear framework becomes inadequate for several reasons. The finite dimensions of surfactant molecules must be taken into account with a model that includes surface saturation. Nonideal interactions between adsorbed surfactant molecules alter the partitioning of surfactant between the bulk and the interface, the dynamics of surfactant adsorptive/desorptive exchange, and the sensitivity of the surface tension to adsorbed surfactant. For example, cohesion between hydrocarbon chains favors strong adsorption. Cohesion also slows the rate of desorption from interfaces, and decreases the sensitivity of the surface tension to adsorbed surfactant. Strong cohesive interactions result in first order surface phase changes with a plateau in the surface tension vs surface concentration. Within this surface concentration range, the surface tension is decoupled from surface concentration gradients.

We are engaged in the study of the role of surfactant physical chemistry in determining the Marangoni stresses on a drop in an extensional flow in a numerical and experimental program. Using surfactants whose dynamics and equilibrium behavior have been characterized in our laboratory, drop deformation will be studied in ground-based experiment. In an accompanying numerical study, predictive drop deformations will be determined based on the isotherm and equation of state determined in our laboratory. This work will improve our abilities to predict and control all fluid particle flows.

## Introduction

When an initially spherical drop suspended in an immiscible fluid is subject to an extensional flow, it elongates. The flow field is governed by Stokes' equations for an incompressible fluid, continuity of velocity, the interfacial stress balance, and a far-field imposed pure straining motion. In the absence of surfactant adsorption, two dimensionless groups determine the extent of the deformation; the viscosity ratio of the drop to the suspending phase  $\lambda$ , and the capillary number  $Ca$ , which is the ratio of characteristic viscous stresses, which tend to deform the drop, to surface tension, which resists deformation. For weak flows, (small  $Ca$ ), the drop deforms only slightly from a spherical geometry.[4,5] As  $Ca$  increases, the steady shapes are more elongated. If the flow is strong enough ( $Ca$  in excess of a critical value  $Ca^{cr}$ ), the drop will not attain a steady shape, but will continue to elongate and ultimately fragment into smaller drops. The viscosity ratio  $\lambda$  affects both the steady shapes observed and the values of  $Ca^{cr}$ . Drops of low viscosity ( $\lambda < 1$ ) exhibit shapes that have pointed ends which break off into satellite drops, a phenomenon called "tip-streaming"; highly viscous drops have bulbous ends. The role of  $\lambda$  is well documented both theoretically [4,5] and experimentally [6-8].

Figure 1



Surfactants present in either phase adsorb on the drop interface and reduce the surface tension. Their effect on the flow can be understood by considering the flow geometry, shown in Figure 1. An initially spherical drop with a uniform concentration of adsorbed surfactant is centered in an extensional flow which creates a stagnation ring at the drop equator and stagnation points at either tip. Surface convection sweeps adsorbed surfactant toward the poles. The resulting non-uniform surfactant distribution alters the interfacial stress balance: [9]

$$[ [\mathbf{n} \cdot \mathbf{T}] ] = -\nabla_s \gamma \mathbf{t} + 2H\gamma \mathbf{n}$$

where  $\mathbf{T}$  is the Cauchy stress tensor,  $\mathbf{n}$  is the surface normal, and the bracketed term on the left hand side of (1) represents the stress jump at the interface. The tangent vector to the surface is denoted  $\mathbf{t}$ ,  $\gamma$  is the surface tension,  $\nabla_s$  is the surface gradient operator, and  $2H$  is the mean curvature of the interface. This expression can be made dimensionless by scaling the viscous stresses by  $\mu G$ , (where  $G$  is the applied strain rate, and  $\mu$  is the viscosity of the external fluid), scaling lengths with the initial drop radius  $a$ , the surface tension with its value in equilibrium with the initial, uniform surface concentration  $\gamma_{eq}(\Gamma_{eq})$ , and using the chain rule to express the dependence of the surface tension on the surface concentration:

$$Ca [ [\mathbf{n} \cdot (\mathbf{T}' - \lambda \hat{\mathbf{T}}')] ] = -E \left[ \frac{\partial \gamma'}{\partial \Gamma'} \frac{1}{R'/T'} \right] \nabla_s \Gamma' \mathbf{t} + 2H' \gamma' (\Gamma') \mathbf{n} \quad (1)$$

The derivative of the surface tension with respect to the surface concentration is made dimensionless by  $RT$ , the product of the ideal gas constant and the temperature;  $\Gamma_\infty$  is the maximum surface packing of surfactant on the interface. Two dimensionless groups appear;  $Ca$  is the capillary number,  $E$  is a Gibbs elasticity number, a characteristic magnitude of the dependence of the surface tension on the surface concentration, defined as:

$$Ca = \frac{\mu G a}{\gamma_{eq}} ; E = \frac{RT \Gamma_\infty}{\gamma_{eq}}$$

The greater is  $E$ , the more sensitive is the flow to non-equilibrium surfactant distributions.

These non-equilibrium distributions alter the flow in two ways. The interface will pull from the low surface tension zone at the poles toward the elevated tension at the equator, exerting a Marangoni stress which resists the viscous shear. In addition, since regions of low surface tension require higher curvatures to balance the normal stress jump across the interface, low tension regions become elongated and curved, leading to higher deformations in the surfactant-rich regions of the interface. This elongation serves to dilute the surface concentration, further perturbing the surfactant distribution. This is accompanied by a flattening of the surfactant-poor regions, which strongly resist surface dilatation. This effect in the normal stress balance is the Marangoni elasticity.

The surfactant distribution is determined by the relative rates of surface convection and surface dilatation, which disturb the surfactant distribution from equilibrium, to the rates of surface diffusion, bulk diffusion and adsorption-desorption, all of which tend to restore interfacial equilibrium. The diffusion and sorption kinetics are determined by the chemical structure of the surfactant and the bulk fluids. The surface tension dependence on the surface concentration is determined by the interfacial thermodynamics including the adsorption isotherm and the surface equation of state. Non-ideal interactions between surfactant molecules (e.g. cohesion or repulsion) strongly impact the form of these expressions [10,11]. The required data are scarce in the literature. The measurement of these kinetic and thermodynamic parameters has been the emphasis of a recent studies in our laboratory.[12,13]. The role of surface saturation and surfactant interactions has not been explored previously in terms of their impact in dynamic immiscible fluid systems. We are currently engaged in studying the role of the surfactant physical chemistry in drop deformation and break-up in a two part study. In the first part, the flow field is studied numerically. The location of the drop interface is not known *a priori*. A time-marching numerical scheme is employed starting from an initially spherical drop and tracing its shape evolution as a function of the capillary number,  $Ca$ , until either a steady drop shape is attained or the surface velocity diverges, indicating drop fragmentation. For work completed to date on bulk insoluble surfactants, (Pawar and Stebe, in press, Physics of Fluids) [14] the coupled Stokes' flow and mass transfer equations are solved numerically using the Boundary Element Method for the instantaneous velocity and an explicit Euler scheme to advance the surfactant distributions. Our results in this limit are briefly described. Future work will focus on bulk soluble surfactants with finite convective transport using the front tracking technique [15].

In the second part of the research, ground-based experiment is used to test the accuracy of these models

in predicting the drop shape evolution and break-up. Surfactant molecules which exhibit non-ideal interactions are identified as part of an ongoing project in our laboratory. Using these surfactants, we will measure the deformation of liquid drops in surfactant solutions in a computer-controlled four roll mill apparatus. Digitized images of the deforming drop are recorded. These images will be used to calculate the deformations as a function of Ca which will be compared with theoretical predictions.

Below, the relevant surfactant physical chemistry and dynamics, along with our insoluble surfactant work in this flow field are briefly reviewed. Thereafter, a brief discussion of the research objectives for the theoretical and experimental parts of this study is given.

### Surfactant Mass Transfer

Non-uniform surfactant distributions develop when the rates of surface convection and dilatation which disturb the surfactant concentration  $\Gamma$  from equilibrium are rapid compared to the rate of surface diffusion and the rate that surfactant is supplied from the bulk fluid. The balance of these competing fluxes is given by: [16]

$$\frac{\partial \Gamma}{\partial t} + \nabla_s \cdot (\Gamma \mathbf{v}_s) - D_s \nabla_s^2 \Gamma = -\mathbf{n} \cdot \mathbf{j} \quad (2)$$

where  $D_s$  is the surface diffusivity, and  $\mathbf{v}_s$  is the surface velocity which has both a normal component which stretches the interface and a tangential component which sweeps surfactant along the surface.

The bulk concentration  $C$  is determined by the balance of convection and diffusion in the bulk:

$$D \nabla^2 C = \frac{\partial C}{\partial t} + \mathbf{v} \cdot \nabla C \quad (3)$$

The normal flux of surfactant from the bulk to the interface takes place via two steps in series. Surfactant diffuses from the bulk to the fluid sublayer immediately adjacent to the interface. The diffusive flux toward an interface with normal  $\mathbf{n}$  into the fluid is given by:

$$-\mathbf{n} \cdot \mathbf{j}_D = \mathbf{n} \cdot D \nabla C|_s \quad (4)$$

where  $C$  is the bulk concentration,  $D$  is the diffusivity of the surfactant in solution, and the subscript  $s$  indicates that the flux is evaluated at the interface. Subsequently, surfactant adsorbs/desorbs from this sublayer onto the interface. Using a reaction-kinetic framework, the adsorptive-desorptive flux is given by:

$$-\mathbf{n} \cdot \mathbf{j}_{ads} = \beta e^{(-E_a/RT)} C_s (\Gamma_\infty - \Gamma) - \alpha e^{(-E_d/RT)} \Gamma \quad (5)$$

The constants  $\beta$  [ $\text{cm}^3 \text{mol}^{-1} \text{s}^{-1}$ ] and  $\alpha$  [ $\text{s}^{-1}$ ] are the kinetic constants for adsorption and desorption, respectively. The symbol  $\Gamma_\infty$  [ $\text{mol cm}^{-2}$ ] is the maximum packing of surfactant along the interface, and  $\Gamma$  [ $\text{mol cm}^{-2}$ ] denotes the surface concentration of adsorbed surfactant. The energy terms  $E_a$  and  $E_d$  [erg] are the energies of activation for adsorption and desorption, respectively, and  $RT$  is the product of the ideal gas constant and the absolute temperature.

Defining  $\Gamma'$  and  $C'$  as dimensionless surface and bulk concentrations scaled with their respective values at equilibrium,  $\Gamma_{eq}$  and  $C_{eq}$ , scaling time with the inverse rate of strain  $G^{-1}$ , and using the quantity  $\Gamma_{eq} G$  to scale the flux from the bulk, the dimensionless bulk balance becomes:

$$\nabla^2 C' = Pe \left\{ \frac{\partial C'}{\partial t'} + \mathbf{v}' \cdot \nabla C' \right\} \quad (6)$$

The dimensionless surface mass balance is:

$$\frac{\partial \Gamma'}{\partial t'} + \nabla_s \cdot (\Gamma' \mathbf{v}'_s) - \frac{1}{Pe_s} \nabla_s^2 \Gamma' = -\mathbf{n} \cdot \mathbf{j}' \quad (7)$$

where the primes indicate a dimensionless quantity. The dimensionless normal flux expressions can be written:

$$-\mathbf{n} \cdot \mathbf{j}'_D = \frac{1}{h Pe} \mathbf{n} \cdot \nabla C' \quad (8)$$

and

$$-n \cdot \mathbf{j}'_{ads} = Bi \left( k C'_s \left( \frac{\Gamma_\infty}{\Gamma_{eq}} - \Gamma' \right) - \Gamma' \right) \quad (9)$$

In these expressions, the following dimensionless groups appear:

(i.) The surface Peclet number,  $Pe_s$  and the bulk Peclet number  $Pe$ , which give the ratio of characteristic convective to surface diffusive or bulk diffusive fluxes, respectively.

$$Pe_s = \frac{a^2 G}{D_s}; \quad Pe = \frac{a^2 G}{D}$$

(ii.) The adsorption depth, which is the depth beneath the interface depleted to populate the interface.

$$h = \frac{\Gamma_{eq}}{C_{eq} a}$$

(iii.) The Biot number, which is a measure of sorption rate to surface convective rate.

$$Bi = \frac{\alpha}{G}$$

(iv.) The adsorption number, which is the ratio of the characteristic rates of adsorption to desorption.

$$k = \frac{\beta C_{eq}}{\alpha} \exp \left( - \frac{(E_a - E_d)}{RT} \right)$$

### Mass Transfer Regimes to be Studied Numerically

In order to realistically model bulk soluble surfactants, the regime of finite  $Pe$  must be considered. This will be the focus of our numerical work. The ratio  $1/hPe$  is the characteristic diffusive flux to the interface relative to the surface convective flux, and  $Bi$  is the adsorptive flux to convective flux. Therefore,

$$\eta = \frac{DC_{eq}}{\Gamma_{eq} a \alpha}$$

is the ratio of the characteristic diffusive to sorptive flux. The magnitude of this group determines the surfactant mass transfer regime. For fixed surfactant physical chemistry, these regimes can be spanned by varying the bulk concentration.

- $\eta \sim 0$ , and the normal flux to the interface goes to zero. The surfactant behaves as an insoluble layer on the interface. Equation (7), with the right hand side set to zero governs  $\Gamma'$ . This limit has been explored in Pawar and Stebe.
- For small  $\eta$  the diffusive flux is rate limiting;  $C'_s$  is determined according to (6) and (8). Surfactant partitions instantaneously between the sublayer and the interface according to the adsorption isotherm  $\Gamma'(C'_s)$  obtained by setting (9) to zero.
- For  $\eta$  of  $O(1)$ , the system has mixed kinetic-diffusion control. At finite  $Pe$ , diffusion and convection determine  $C'$  according to (6). The diffusive flux (8) determines  $C'_s$ , and the sorption flux (9) regulates  $\Gamma'$ . These fluxes are equal, and give the right hand side of (7).
- Finally, for large  $\eta$ , the sorption flux (9) is rate controlling; diffusion instantaneously maintains  $C'$  at unity.

### Non-ideal interactions among adsorbed surfactants

The energies terms that appear in the Arrhenius factor in (5) determine the form of the equilibrium adsorption isotherm obtained by setting (9) to zero. For example, if they are constant, the Langmuir adsorption isotherm is obtained. Through the Gibbs-Duhem equation for the interface, the corresponding surface equation of state is found.

For long chain saturated surfactants (e.g. the n-alcohols, [10]) the energies for adsorption and desorption

depend upon the surface concentration because of cohesive interactions among the saturated chains. For bulky sidechains, repulsive interactions have been observed. If this dependence is assumed to be linear,

$$E_i = E_{io} + \nu_i \Gamma_{eq} \quad (10)$$

where  $i = a, d$  respectively, the corresponding adsorption isotherm and surface equation of state are given by the Frumkin equations:

$$\frac{\Gamma_{eq}}{\Gamma_{\infty}} = \frac{k_f}{e^{\left(\frac{K\Gamma_{eq}}{\Gamma_{\infty}}\right)} + k_f} \quad (11)$$

$$\gamma = \gamma_o + RT\Gamma_{\infty} \left( \ln \left[ 1 - \frac{\Gamma_{eq}}{\Gamma_{\infty}} \right] - \frac{K}{2} \frac{\Gamma_{eq}^2}{\Gamma_{\infty}} \right) \quad (12)$$

where the adsorption constant is:

$$k_f = \frac{\beta C_{eq}}{\alpha} e^{\frac{-(E_{ao} - E_{do})}{RT}} \quad (13)$$

and the interaction parameter is:

$$K = \frac{(\nu_a - \nu_d) \Gamma_{\infty}}{RT} \quad (14)$$

which is negative for cohesion, i.e. as  $\Gamma$  increases, the energy required for surfactant to desorb also increases. For  $K=0$ , the surfactants have no non-ideal interactions, and the Langmuir case is recovered. In this expression,  $\gamma_o$  and  $\gamma_{eq}$  are the surface tension of the clean interface and that in equilibrium with  $\Gamma_{eq}$ , respectively. These non-ideal interactions strongly alter the partitioning of surfactant between the bulk and the interface. For example, for a given  $C_{eq}$ , the  $\Gamma_{eq}/\Gamma_{\infty}$  which result are greater for cohesion, and smaller for repulsion when compared to the Langmuir case. In addition, for a given  $\Gamma_{eq}$ ,  $\gamma_{eq}$  reduces less for cohesion and more for repulsion relative to the Langmuir case. The comparison between the Frumkin and Langmuir frameworks is somewhat subtle in terms of  $C_{eq}$ , however, since surfactant partitioning is also effected.

For the case of cohesion,  $\nu_d > 0$ , and the net desorption coefficient as  $\Gamma$  increases:

$$\alpha_{eff} = \alpha (\Gamma=0) \exp \frac{-\nu_d \Gamma}{RT}$$

slowing the effective Biot number, and thereby leading to more pronounced surface concentration gradients. The converse effect is expected for repulsive interactions.

The effect of the  $\Gamma$  distribution on the flow is determined by the surface equation of state. Figure 2 depicts the dimensionless surface pressure vs. a normalized area per molecule  $\Gamma_{eq}^{-1}\Gamma_{\infty}$  for repulsion ( $K=2.52$ ); no interactions, ( $K=0$ , Langmuir); for moderate cohesion ( $K=-2.52$ ) and for the elevated cohesion ( $K=-4.0$ ) case where an interface exhibits a significant flattening in the surface pressure-area per molecule isotherm. The case of stronger cohesion, where the interface undergoes a phase transition from a surface expanded to a condensed state is also shown. This requires a more sophisticated treatment of the equation of state. First order phase changes are discussed in the insoluble limit by Pawar and Stebe.

### Droplet Deformation for Insoluble Surfactants with of Non-Ideal Interactions

One set of results from the study of Pawar and Stebe are briefly described here. At fixed surface concentration, the drop deformation is shown to vary with  $K$  in Figure 3 for an insoluble surfactant. Deformations are defined in terms of the drop length  $L$  and breadth  $B$ , and are plotted vs.  $Ca$  are diagrammed. First, compare the  $K=0$  case which accounts for surface saturation to the linear framework. Saturation generates strong Marangoni stresses as surfactant is swept to the poles, preventing the surface concentration from attaining its maximum value. More uniform surface concentration profiles result, with reduced tip stretching when compared to the linear case.

Thus, smaller deformations are realized. For nonzero  $K$ , drop deformations were found to decrease with  $K$ , i.e. repulsive interactions gave the least deformations, while cohesive interactions between molecules gave the greatest.

### Research Objectives

In the numerical part of the work, we will explore the role of repulsion/cohesion and strong cohesion resulting in surface phase changes for bulk soluble surfactants with diffusion control or mixed kinetic-diffusion control at finite  $Pe$ . The aim of the experimental aspect of the research program is to investigate whether the trends predicted by the theoretical study can be observed experimentally. A four roll mill device suitable for surfactant related work will be constructed to simulate a pure straining flow, based on the design of Bentley and Leal.[7] Drop deformation will be recorded using a CCD camera, allowing the shapes to be digitized and analyzed as a function of surfactant type, concentration, and applied strain rate.

### Bibliography

1. Stone, H. A. and Leal, L. G., J. Fluid Mech, **220**, 161 (1990)
2. Milliken, W. J., Stone, H. A. and Leal, L. G., Phys. Fluids A **5**, 69 (1993)
3. Milliken, W. J. and Leal, L. G., J. Coll. Int. Sci., **166**, 275 (1994)
4. Barthes-Biesel, D. and Acrivos, A., J. Fluid Mech, **61**, 1 (1973)
5. Rallison, J. M. and Acrivos, A., J. Fluid Mech., **89**, 191 (1978)
6. Taylor, G. I., Proc. R. Soc. London Ser., **A146**, 501 (1934)
7. Bentley and Leal J. Fluid Mech. **167**, 219 (1986)
8. Bentley and Leal J. Fluid Mech., **167**, 241 (1986)
9. Levich, V.G. Physicochemical Hydrodynamics Prentice-Hall, Englewood Cliffs, N.J. (1962)
10. Fainerman, V.B. and Lylik, Kolloidnyi Zhurnal, **44**, 598 (1982)
11. Lin, S.Y., McKeigue, K. and Maldarelli, C., Langmuir **7**, 1055 (1991)
12. Johnson, D.O. and Stebe, K.J., J. Colloid Int. Sci **168**, 21-31 (1994)
13. Johnson, D.O. and Stebe, K.J., J. Colloid Int. Sci, in press
14. Pawar and Stebe, Physics of Fluids, in press
15. Unverdi, S. and Tryggvason, G. J. Comp. Phys. **100**, 25, (1992)
16. Aris, R. Vectors, Tensors, & Basic Equations of Fluid Mechanics, Prentice-Hall, Englewood Cliffs, N.J. (1962)

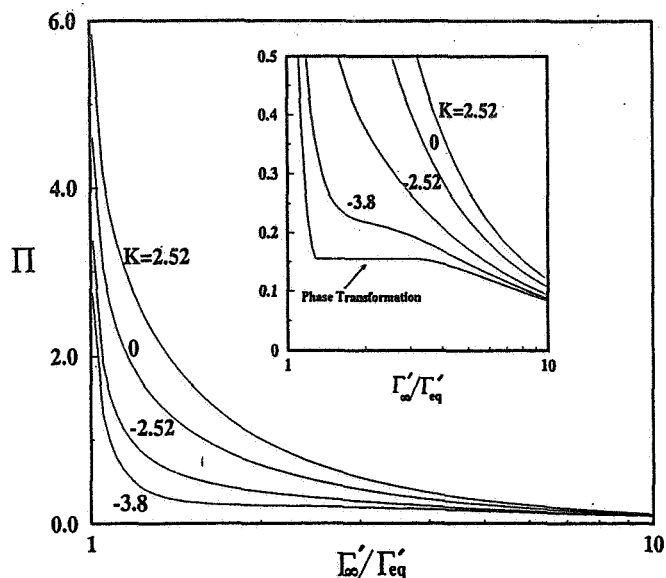


Figure 2

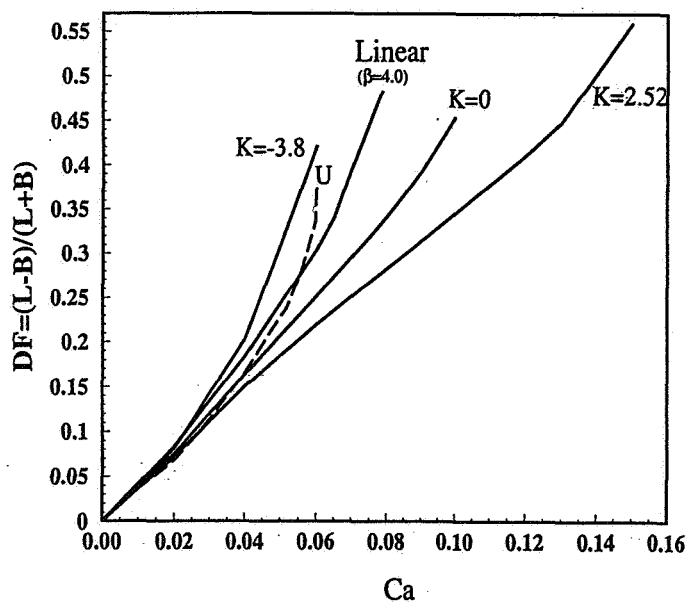


Figure 3



# GROUND BASED STUDIES OF THERMOCAPILLARY FLOWS IN LEVITATED DROPS

Satwindar Singh Sadhal  
Department of Mechanical Engineering  
University of Southern California  
Los Angeles, CA 90089-1453

Eugene H. Trinh  
Jet Propulsion Laboratory  
4800 Oak Grove Drive  
Pasadena, CA 91109

**ABSTRACT:** Ground-based experiments together with analytical studies are presently being conducted for levitated drops. Both acoustic and electrostatic techniques are being employed to achieve levitation of drops in a gaseous environment. The scientific effort is principally on the thermal and the fluid phenomena associated with the local heating of levitated drops, both at 1-*g* and at low-*g*. In particular, the thermocapillary flow associated with local spot heating is being studied.

Fairly stable acoustic levitation of drops has been achieved with some exceptions when random rotational motion of the drop persists. The flow visualization has been carried out by light scattering from smoke particles for the exterior flow and fluorescent tracer particles in the drop. The results indicate a lack of axial symmetry in the internal flow even though the apparatus and the heating are symmetric.

The theoretical studies for the past year have included fundamental analyses of acoustically levitated spherical drops. The flow associated with a particle near the velocity antinode is being investigated by the singular perturbation technique. As a first step towards understanding the effect of the particle displacement from the antinode, the flow field about the node has been calculated for the first time. The effect of the acoustic field on the interior of a liquid drop has also been investigated. The results predict that the internal flow field is very weak.

## INTRODUCTION

One of the important uses of containerless processing is deep undercooling which can promote certain types of crystal growth and at the same time provide homogeneity of the product. In this regard, there is a strong interest in understanding the basic thermodynamics of such processes as well as the measurement of properties such as thermal conductivity and thermal diffusivity. In this regard, the potential for fundamental advancement in materials processing through containerless experimentation is well recognized.

With ground-based studies, the acoustic and electrostatic levitation offer suitable alternatives to zero- and low-gravity levitation. However, the level of undercooling achievable with the latter is considerably higher but at a much greater cost. Under microgravity conditions, the levitation apparatus is used to stabilize the drops with weak acoustic or electrostatic fields which can afford a lower level of deformation and other disturbances.

## OBJECTIVES

### EXPERIMENTAL STUDIES

The principal objectives were first to develop the experimental capability to quantitatively characterize thermocapillary flows within freely suspended and spot-heated droplets under the full effect of gravity. The second experimental objective was to identify the direct and indirect effects of the gravitational field on the thermocapillary flow fields internal to the drop. The direct effects are related to the interference by the gravitationally-induced convection, while the indirect effects originate from the additional external convection and the solid body and differential motions induced by the high intensity levitation fields.

## ANALYTICAL STUDIES

The theoretical objectives consist of the development of models that appropriately account for the acoustic field interference and predict the thermocapillary flows for the imposed thermal stimuli. Under the current program for ground-based studies, analytical models of acoustically levitated drops with thermal interaction are being developed with the final aim of having a comprehensive model that would work in conjunction with the experiments. For this purpose, numerical and perturbation solutions for the combined thermal and acoustic fields are being developed.

## SIGNIFICANCE

As stated earlier, containerless processing is useful for deep undercooling which facilitates the production of certain types of crystals with a high degree of uniformity. In particular, there is high potential for the production of technologically useful new materials. The ongoing research will provide fundamental understanding of the Marangoni flows associated with localized heating of levitated drops. In addition, a comprehensive theoretical and experimental system is being developed for the thermodynamic measurement and analysis of materials in containerless environments. For ground based studies where there is interference from the acoustic field, a sound numerical model will provide significant new information about the behavior of these complex systems. Most importantly, the model development along with the experimental studies will represent fundamental groundwork for the measurement of thermophysical properties of undercooled liquids.

## RESEARCH APPROACH

### EXPERIMENTS

The experimental approach is based on Earth-based single-drop levitation using a unique ultrasonic-electrostatic hybrid technique and fluorescent particles suspended in the drop. These tracer particles are illuminated by a laser sheet (or a collimated beam) at the fluorescence excitation wavelength, and the scattered signal is detected at the fluorescence emission wavelength. The particle motion is tracked through CCD cameras and the optically-corrected flow fields are digitally analyzed. The hybrid ultrasonic-electrostatic levitation approach allows the experimental parametric evaluation of the effects of drop distortion and external flows due to acoustic radiation stresses and streaming, and the assessment of the influence of a net electrical charge on the drop surface in the presence of a high static electric field.

### ANALYSIS

The relevant problems can be mathematically described by the Navier-Stokes equations and the energy equation in a coordinate system suitable to the spherical or the spheroidal geometries. With a defined acoustic field and a quantified heat source, approximate analytical methods and numerical methods will be employed.

*Asymptotic Methods:* The perturbation expansions are useful when a small parameter can be identified. Among the various approximations being used include the high frequency acoustic field limit for which various large and small dimensionless parameters have been identified. In particular,  $\varepsilon = U_0/a\omega \ll 1$  and  $M^{-1} \ll 1$ , with  $M^2 = a^2\omega/\nu$ , serve as suitable perturbation parameters. Here,

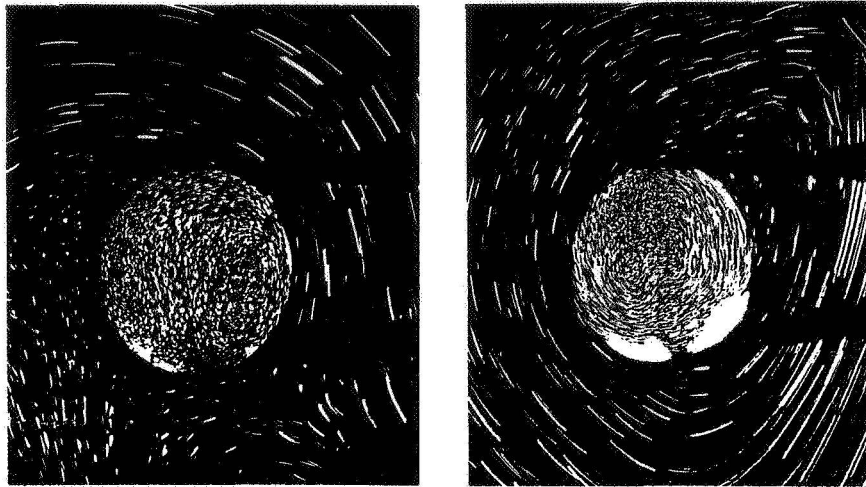


FIGURE 1: Entrained internal flows within droplets suspended in a liquid medium where external streaming flows have been generated.

$U_0$  is the velocity amplitude,  $\omega$  is the frequency,  $\nu$  is the kinematic viscosity and  $a$  is the particle length scale.

*Numerical Methods:* Outside the range of the above approximations, numerical treatment is necessary. In fact, even for the perturbation methods used, some cases of asymptotic matching required numerical procedures. Finite difference techniques would be the most suitable for full numerical treatment of the Navier-Stokes and the energy equations.

## RESULTS

### EXPERIMENTS

*Studies of Acoustic Streaming:* Flow visualization studies of the external forced convective fields generated by the high intensity ultrasound used to levitate millimeter-size droplets under the full effect the Earth gravitational field have been previously reported. The increase in the heat and mass transfer coefficients between a levitated liquid drop and the surrounding gas has been quantitatively evaluated. In addition to affecting the transport process, external flows also induce low velocity internal flows due to entrainment. Arising from the time-varying acoustic motion and from the steady streaming flow component, this entrained flow field is weak for the case of a liquid drop levitated in a gas. It can be substantial, however, for a drop levitated in an immiscible liquid host (see Figure 1). In summary, the assessment is that it will be possible to quantitatively evaluate the influence of external convection on thermocapillary flows in a microgravity environment where the controlled introduction of such external convection can be obtained from a zero base state.

*Internal Flow Visualization in Levitated Drops in 1 G:* An apparatus described in Figure 2 has been used to record the motion of fluorescent tracer particles suspended in the drop liquid. Polystyrene particles of Florida Yellow G from Bangs Laboratories having 0.405 microns in average diameter have been visualized using an Argon Ion (488 nm) laser sheet with variable orientation (the sheet thickness is about 200-300 microns). The scattered light is gathered along two orthogonal views using holographic notch filters to block the elastically scattered light from the drop surface. The liquid used was an aqueous mixture of glycerin and silicone oil (Polydimethylsiloxanes) and

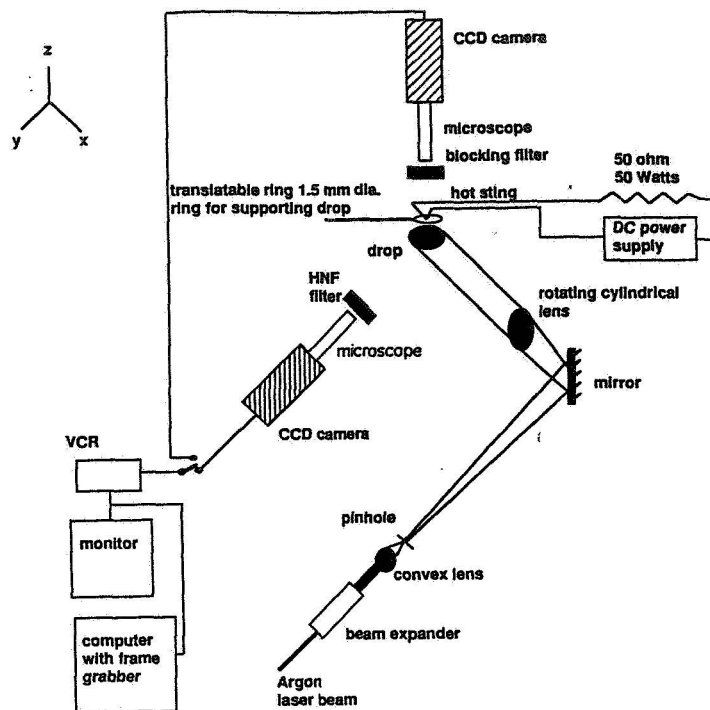


FIGURE 2: Apparatus for flow visualization in a levitated drop.

a focused  $\text{CO}_2$  laser was used to spot heat the levitated drop. The results show that although it was possible to accurately measure the internal flows of isothermal drops, the combination of Earth-based levitation and spot heating induces an uncontrolled torque which drives a random rotational motion of the drops. The digital image processing required in the deconvolution of this rotational motion in order to extract the thermocapillary and buoyancy-driven flows requires substantial computational power, and will be pursued by this experimental effort. Figure 3 shows photographs of time-exposures of the residual motion within a spot-heated drop after heating has stopped. In general, all the recorded flow fields have lacked axial symmetry although both the levitation apparatus and the heating direction are axially symmetrical. Control of drop evaporation has been implemented by maintaining the drop environment at a high humidity, and the Marangoni convection contribution due to evaporation can thus be neglected. Ongoing and future studies will include the measurement of flows within drastically flattened drops to constrain the flows in a two dimensional plane, the implementation of total electrostatic levitation of charged droplets, and an automated digital data reduction and analysis.

*Glovebox Low-Gravity Demonstration:* A Glovebox flight investigation tentatively scheduled for April 1997 has been initiated to assess the capability for ultrasonic positioning in microgravity for drop internal flow measurement. A compact ultrasonic positioner has been designed and integrated with laser diode illumination in order to experimentally demonstrate the rotation control of freely suspended drops in low gravity and to obtain preliminary flow field measurements for sting-heated droplets. A laboratory breadboard is already available, and the flight unit is currently nearing design completion.

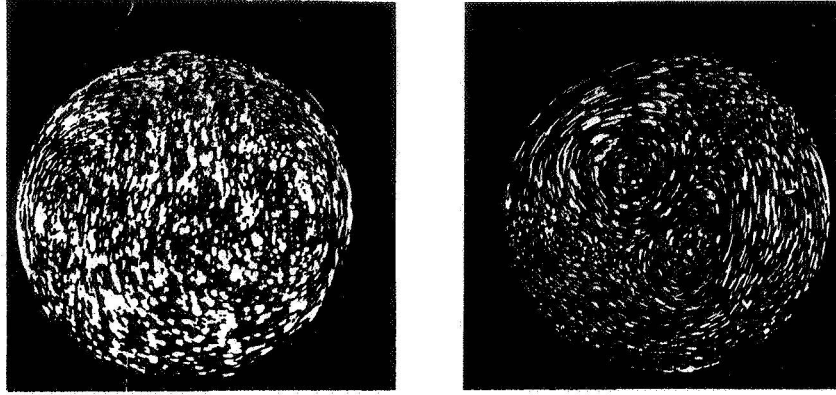


FIGURE 3: Time exposure (10 sec) photographs of slow internal flows in levitated drops containing tracer particles. These are residual flows observed after the spot heating has been terminated.

### ANALYSIS

The theoretical analysis of the flow field associated with a levitated spherical particle requires a detailed study of the fluid mechanics of streaming flows. In particular, the disturbance due to the presence of the particle needs to be investigated. Riley [2] has given a singular perturbation solution which may be used for the flow associated with a solid particle at the velocity antinode. Presently, this has been extended to the case of a fluid particle. In addition, the technique has been used to calculate the flow for a solid particle at the velocity node.

*Spherical Particle in an Acoustic Field:* As mentioned before, Riley [2] gave the solution for the flow field associated with a sphere oscillating in a fluid. This solution is applicable to a particle at the velocity antinode of a standing wave. Attempts are being made to derive a rigorous solution for the flow with a particle displaced from the antinode. For a particle of radius  $a$  and a displacement  $Z_0$ , with the limiting approximation  $ka \ll 1$ , the 'far-field' velocity field is given by

$$u = A \cos[k(z + Z_0)] e^{i\tau} = A [\cos kZ_0 + (kz) \sin kZ_0 + \dots], \quad (1)$$

$$\psi = (A \cos kZ_0) \psi^{(0)} + (Ak \sin kZ_0) \psi^{(1)} + \text{nonlinear terms} \quad (2)$$

where  $R = U_\infty a / \nu$ ,  $M = i\omega a^2 / \nu$ ,  $\psi^{(0)}$  is the stream function for the case when the particle is at the velocity antinode and  $\psi^{(1)}$  for the antinode. The expression for  $\psi^{(0)}$  is already available for the limit  $\varepsilon = R|M|^{-2} \ll 1$ . The new results include the perturbation solution for  $\psi^{(1)}$  which has been calculated to the second order. However, only the first order results are presented here.

Outer Solution:

$$\begin{aligned} \psi^{(1)} \rightarrow \phi^{(1)} &= \frac{1}{2}(r^3 - r^{-2})\bar{\mu}(1 - \bar{\mu}^2) \cos \tau \\ &+ \varepsilon r^{-4}\bar{\mu}(1 - \bar{\mu}^2) \left[ -\frac{5}{2}(R_s^{-\frac{1}{2}} r^2 \cos(\tau - \frac{1}{4}\pi) + \frac{75}{112}(r^2 - 1) \left\{ r^2 + \frac{3}{2}(7\bar{\mu}^2 - 3) \right\} \right] + \dots \end{aligned} \quad (3)$$

Within the Shear-Wave Layer:

$$\begin{aligned} \psi^{(1)} \rightarrow \Phi^{(1)} &= \bar{\mu}(1 - \bar{\mu}^2) \left\{ \frac{5}{2} \left[ \eta - \frac{1}{2}(1 - i) \left( e^{-(1+i)\eta} \right) \right] \cos \tau \right. \\ &+ \varepsilon \left[ \left( \frac{325}{32} - \frac{75}{16}\eta \right) - \frac{25}{16} \cos(2\tau + \frac{1}{4}\pi) \right. \\ &\left. \left. + \bar{\mu}^2 \left( -\frac{875}{32} + \frac{225}{16}\eta + \frac{275\sqrt{2}-225}{32\sqrt{2}} \cos(2\tau + \frac{1}{4}\pi) \right) \right] \right\} + \dots, \end{aligned} \quad (4)$$

where  $\varepsilon = R|M|^{-2}$ ,  $R_s = \varepsilon R$ ,  $\bar{\mu} = \cos \theta$ , and  $\eta = \frac{1}{2}(r-1)|M|$ .

*Internal Circulation in a Drop in an Acoustic Field:* The investigation of the internal flow in a drop at the antinode of a standing wave has been carried out by singular perturbation approach of Riley [2]. At the fluid-fluid interface, the stress and velocity continuity condition are applied. The results for the drop phase stream function to the leading order are as follows:

$$\hat{\psi}^{(0)} = c^* \left[ r^2 \left( \frac{1}{\widehat{M}} + 1 \right) e^{-\widehat{M}} - r^2 \left( \frac{1}{\widehat{M}} - 1 \right) e^{\widehat{M}} \left( \frac{1}{\widehat{M}r} + 1 \right) e^{-\widehat{M}r} + \left( \frac{1}{\widehat{M}r} - 1 \right) e^{\widehat{M}r} \right] (1 - \bar{\mu}^2) e^{i\tau}, \quad (5)$$

where

$$c^* \simeq \frac{\frac{3}{2} \left( 1 - \frac{\widehat{M}}{\widehat{M} + \lambda M} \right)}{-\widehat{M} e^{\widehat{M}}}, \quad \widehat{M}^2 = \frac{i\omega a^2}{\hat{\nu}},$$

$\hat{\nu}$  is the kinematic viscosity of the liquid phase, and  $\lambda = \mu/\bar{\mu}$  is the ratio of the gas to the liquid dynamic viscosities. It is observed that the strength of this internal flow behaves like  $\sim e^{-\widehat{M}}/\widehat{M}$ . For large  $\widehat{M}$ , this is very weak. The reason for such weak flow is mainly the recirculating Stokes layer which is very thin. Since there are opposing velocities within it, a very large shear stress is required to sustain its motion. The system cannot afford such a large shear stress at the interface and the result is weak internal circulation. The large drop viscosity as compared with the gas also has a role in weakening this circulation.

## CONCLUSION

The analytical and experimental studies of drops in an acoustic field have led to several new results. These are briefly summarized here.

1. The theoretical analysis of the flow field inside an acoustically levitated spherical drop shows that the internal circulation is quite weak. This is owing to the thin recirculating shear layer which cannot sustain the large stresses that would arise if there were substantial internal flow. While experimental studies also show a weak internal circulation, the magnitude has not yet been verified to be in agreement with the extremely low predictions. However, a liquid drop in a liquid host is seen to experience substantial internal circulation.

The external flow field associated with a particle between the velocity antinode and the node of a standing wave can be described as a combination of the independent fields about these point. In addition, there are some nonlinear interaction terms that are of the same order.

2. It has been possible to accurately measure the internal flows of isothermal drops. The results of the combination of the Earth-based levitation and the spot heating induces an uncontrolled torque that drives a random solid-body like rotational motion of the drops.

## REFERENCES

- [1] S.S. Sadhal, E.H. Trinh & P. Wagner, *Fluid Mechanics Phenomena in Microgravity*, ASME Publication No. AMD-Vol. 154 / FED-Vol. 142, (1992) 105–110.
- [2] N. Riley, On a sphere oscillating in a viscous fluid, *Quart. J. Mech. Appl. Math.*, **19** (1966) 461–472.

# MARANGONI-BÉNARD CONVECTION IN AN EVAPORATING LIQUID THIN LAYER

An-Ti Chai and Nengli Zhang<sup>1</sup>

NASA Lewis Research Center, Cleveland, Ohio 44135  
U.S.A.

## ABSTRACT

Marangoni-Bénard convection in evaporating liquid thin layers has been investigated through flow visualization and temperature profile measurement. Twelve liquids, namely ethyl alcohol, methanol, chloroform, acetone, cyclohexane, benzene, methylene chloride, carbon tetrachloride, ethyl acetate, n-pentane, silicone oil (0.65 cSt.), and freon-113, were tested and convection patterns in thin layers of these samples were observed. Comparison among these tested samples shows that some liquids are sensitive to surface contamination from aluminum powder but some are not. The latter is excellent to be used for the investigation of surface-tension driven convection through visualization using the tracer. Two sample liquids, alcohol and freon-113 were particularly selected for systematic study. It was found that the wavelength of Bénard cells would not change with thickness of the layer when it evaporates at room temperature. Special attention was focused on cases in which a liquid layer was cooled from below, and some interesting results were obtained. Convection patterns were recorded during the evaporation process and the patterns at certain time frame were compared. Bénard cells were observed in thin layers with a nonlinear temperature profile and even with a zero or positive temperature gradient. Wavelength of the cells was found to increase as the evaporation progressed.

## INTRODUCTION

The first systematic experimental study of the convection in a horizontal liquid thin layer was made by Henri Bénard [1,2]. Although the main portion of his report concerned spermaceti, Bénard also experimented with several different liquids and found that volatile liquids produced permanently unsteady cellular convection in shallow pools. In other words, Bénard actually experimented also with evaporating liquid layers. However, the convection observed in Bénard's experiments was believed to be driven by buoyancy and theoretically explained by Lord Rayleigh [3]. Nowadays it is referred to as Rayleigh-Bénard convection. Block [4] demonstrated the convection cells in a layer thinner than 1 mm with a free surface were produced by variations in surface tension instead of buoyancy. Under motivation of Block's work and others, J. R. A. Pearson [5] proposed a radically different theoretical model from Rayleigh's. In Pearson's model the fluid is assumed to be supporting an adverse linear temperature gradient and all the fluid properties except the surface tension are taken to be independent of temperature. Pearson analytically showed that the Bénard convection can be produced by the variation of surface tension with temperature. This surface-tension-driven convection is now referred to as Marangoni-Bénard convection. D. A. Nield [6] combined these two theories and found that the two agencies causing the Bénard convection ( i.e. buoyancy and surface tension forces ) reinforce one another and are tightly coupled. Pearson's and Nield's theories predict a critical thickness below which there is stability relative to convection induced by surface tension although Block reported there was no indication that a critical thickness had been reached at least until 50 microns. An open question is: whether or not actually there is a critical thickness? If a critical thickness exists as the theories predicted what is the limiting value and why? Analyses now available can not explain Block's experimental

---

<sup>1</sup> National Research Council Associate

results because no one really considered the effects of evaporation on the convection which may be the key point in the experiments conducted by Block. Pearson claimed: "The allied problem of a liquid cooling by evaporation may be treated in a similar fashion.....owing to the loss of fluid from the surface, the effect of evaporation may be reasonably well represented by a given heat loss from the surface,....." Actually, this masked the essential mechanism of the convection fueled by the evaporation. Another question dodged by most investigators is: what would happen when an evaporating liquid layer was cooled from below? Almost all relevant analyses presented until now based on the assumption that the liquid layer is heated from below except Castillo and Velarde [7]. Only a few experiments dealt with Bénard convection in an evaporating liquid layer and Block may have been the only one who conducted an experiment on an evaporating liquid layer cooled from below. Berg [8] described four principal patterns of evaporative convection and pointed out that cells appeared to be the dominant patterns in all liquids for depth of 2 mm or less. He reviewed the Bénard convection dealing with evaporation in detail and analyzed the mechanisms of Bénard convection but never touched upon the mechanism problem of the convection in a liquid layer cooled from below. Zhang and Chai [9] initiated to investigate the evaporative convection in a liquid thin layer cooled from below; some effects of evaporation on the convection were discussed. In the present work, more liquid samples were tested as liquid thin layers ( $\leq 1$  mm). More detailed experimental data for alcohol and Freon-113 were graphed and discussed. The effects of evaporation on the convection, including the structure of patterns and the size (wavelength) change of the convection cells, are experimentally studied.

## EXPERIMENTAL APPARATUS AND PROCEDURE

The apparatus used in the present study is the same as in reference [9]. It consisted of a test section with a cooling base, a refrigerated circulator, a thermocouple set, a computer data acquisition system, a CCD camera mounted on a microscope with zoom lens and connected to a video recorder, a color video printer and a color monitor. The test section is made by a flat polished copper base plate and four glass side plates. The four glass plates of 2 mm thick and 6 mm wide are glued on the copper plate of 1.5 mm thick to form a square trough of 50.8 x 50.8 mm. The side walls of 6 mm high are surrounded with expanded polystyrene of 5 mm thick for thermal insulation. The test section is sat on the aluminum top plate of the cooling base which is cooled through a refrigerated circulator. The circulator has a working temperature range of -23 to 150 °C, regulated by PID controller, with an accuracy of  $\pm 0.02$  °C. The convection patterns in the test layer can be recorded with the video recorder through the CCD camera mounted on the zoom microscope and monitored with the color monitor in the meantime. Any interesting picture shown on the monitor, either in real time or when playing back a recorded tape of an experiment, can be caught by the video printer and printed out within 30 sec. Eight thermocouples are connected to the computer data acquisition system to record the temperature profiles of the test liquid layer and of the air close to the liquid surface. The thermocouples were divided into two groups, four in each. Each group was mounted on a 3-Axis stage with differential micrometers and so can be moved in 3-D with an accuracy of 0.0005 mm. The thermocouples are made with fine CHROMEGA and ALOMEGA wires 0.0005 in. (0.0127 mm) in diameter and deployed one over another. The distances between the thermocouple tips can be accurately measured through the microscope. The lowest thermocouple of Group I (numbered from lowest one as #1, #2, #3, and #4) can be adjusted to touch to the bottom of the test section through the 3-Axis stage and can therefore measure the layer temperatures at the bottom, and at the positions of 0.278 mm, 0.496 mm, and 0.754 mm from the bottom. The lowest one in Group II (numbered from the lowest one as #5, #6, #7, and #8) was placed at 1.000 mm from the bottom and so can measure the temperature at the surface of the test liquid layer when the initial thickness of the layer is set 1.000 mm and the temperatures of the air at the positions of 0.258 mm, 0.555 mm, and 0.892 mm from the liquid surface can be measured by #6 to #8. All of the thermocouple tips were adjusted in a perfect alignment perpendicularly through the micrometers on the stages.



Although the thermocouple wires were already calibrated by the manufacturer, the divergence of the temperature measurements between the thermocouples was still more than  $0.5^{\circ}\text{C}$  due to the material inhomogeneities. Therefore a rigorous sifting was necessary. In order to obtain meaningful temperature profiles within very tiny distances, a measurement divergence among the eight thermocouples should not exceed  $0.05^{\circ}\text{C}$  in the temperature range of  $0$  to  $30^{\circ}\text{C}$ . Only one out of approximately 20 thermocouples was found to be qualified for use in the thermocouple set. The thermocouples in both Group I and II were also specially calibrated before and after every test was made to ensure the data obtained to be reliable. Test liquids mixed with aluminum powder of  $1 - 3\ \mu$  diameter are injected into the test section speedily and smoothly through a syringe and the convection patterns and the temperature profiles in the test liquid layer and in its vicinal air were recorded simultaneously.

## RESULTS AND DISCUSSION

Twelve liquids, namely ethyl alcohol, methanol, chloroform, acetone, cyclohexane, benzene, methylene chloride, carbon tetrachloride, ethyl acetate, n-pentane, silicone oil ( $0.65\ \text{cSt.}$ ), and Freon-113, were tested and convection patterns in the thin layers were observed. All of the samples were first tested at a thickness of  $1\ \text{mm}$  or less to observe surface-tension driven convection and then at thicknesses of  $1.5\ \text{mm}$  and  $2\ \text{mm}$ , respectively, to observe the buoyancy effects on the convection. Quite different convection patterns were found in the sample layers with a same thickness, for example  $1\ \text{mm}$ . Figure 1 shows the typical patterns in an  $1\ \text{mm}$  layer of silicone oil ( $0.65\ \text{cSt.}$ ), alcohol, freon-113, and n-pentane, respectively, which evaporate at room temperature ( $24^{\circ}\text{C}$ ). The wavelength  $\lambda$ , which equals to  $H/\delta$ , can be determined from the pictures shown in Fig.1, where  $H$  is the mean value of the distance between the centers of two neighboring cells, and  $d$ , the thickness of the layer. It is obvious that silicone oil and alcohol have more regular Bénard cells and the wavelengths are 2 and 3, respectively. Freon-113 has a kind of combination of cells and rolls, while more violent and complex motion appears in the n-pentane layer in which small cells are covered by large cells or rolls. It can be seen that cells in the freon-113 layer have a wavelength of about 6. Methanol layer has the same convection pattern as freon-113 has (not shown). However, some samples, such as acetone, benzene, and cyclohexane exhibited convection cells in an  $1\ \text{mm}$  layer only for very short period of time just after the liquid is deployed and then quieted down, while others, like carbon tetrachloride, ethyl acetate, chloroform, and methylene chloride never exhibited convection at this thickness. The reason may be that the surface of these liquids is very sensitive to the "contamination" caused by the aluminum powder. The liquids which are not sensitive to surface contamination from aluminum powder, such as alcohol, freon-113, n-pentane, silicone oil, and methanol, are excellent for the investigation of surface-tension driven convection in an evaporating thin layer through flow visualization using aluminum powder as the tracer. The wavelength of the cells depends on the liquid properties and the evaporation conditions but not the thickness of the layer. For example, alcohol layer evaporating at room temperature has the wavelength of about 3 for different layer thickness, while for freon-113 the value of  $\lambda$  is about 6. It is obvious that there is no critical thickness be reached until  $0.1\ \text{mm}$ . However, two evidences demonstrate the existence of a critical thickness: first, in the last stage of evaporation, no cells appeared in the rim of the layer which is drying out; second, the cells disappeared at about  $0.1\ \text{mm}$  thick when a thicker freon-113 layer evaporated and the thickness decreased with the evaporation.

More interesting results were obtained when an evaporating liquid thin layer was cooled from below. As described in reference [9], Bénard cells can be observed clearly in a liquid thin layer with a nonlinear temperature profile and even with zero or positive temperature gradient. More detail observation has found that the wavelength of the cells in the evaporating layers cooled from below changed with time during the cooling process in which the temperature profile varied. Generally, the wavelength would become larger and larger as the evaporation progresses. Figure 2 shows the temperature histories and convection patterns in an

evaporating freon-113 layer at different moments when its bottom is cooled to 11.14 °C. Moments A, B, and C correspond to 5, 15, and 45 seconds after the liquid deployment is finished. It can be seen that moment A is a converse point of the temperature profile in the layer from a negative to a positive temperature gradient and the temperature gradient at this moment is almost zero. However, active Bénard cells with wavelength  $\lambda = 1$  (the layer thickness  $\delta = 0.994$  mm) can be observed clearly, as shown in Fig. 2 (b). Even more brisk Bénard cells can be observed at moments B and C with a wavelength of 3.5 ( $\delta = 0.983$  mm) and 10 ( $\delta = 0.950$  mm), respectively, as shown in Fig. 2 (c) and (d). It can be seen that the cell construction tends to become more complex as the evaporation progresses. Apparently, the strong nonlinear profile of temperature in the layer could play a key role in these phenomena. An increase of the wavelength with evaporation was also found in a thin layer of alcohol even with a zero temperature gradient (when the layer bottom was cooled to 16.6 °C) and with a positive temperature gradient (when the layer bottom was cooled to 12.3 °C).

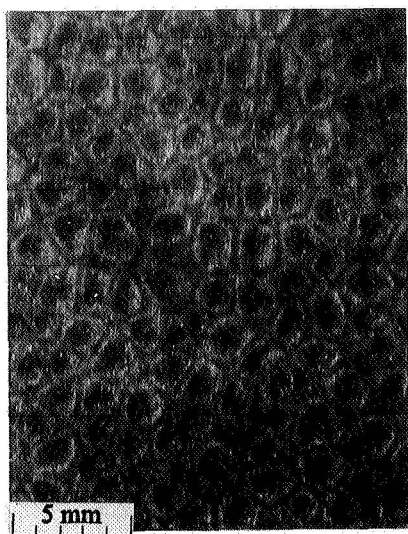
In reference [9], a modified form of Marangoni number,  $Ma = -\sigma m h \delta^2 / k \mu \alpha$  was introduced to take into consideration of the evaporation effects, where  $\sigma$  is the surface tension gradient with respect to temperature,  $m$ , evaporation rate,  $h$ , latent heat of the liquid,  $d$ , the layer depth;  $k$ ,  $\mu$ ,  $\alpha$  are thermal conductivity, viscosity, and thermal diffusivity, respectively. However, in view of the above discussed experimental results,  $\delta$ , the layer depth, may need to be modified to account for the effect of the nonlinear temperature gradient in the layer. It is conceivable that the depth of the temperature gradient conversion point in the layer could be used in place of  $\delta$  in defining a more meaningful Marangoni number.

## CONCLUSIONS

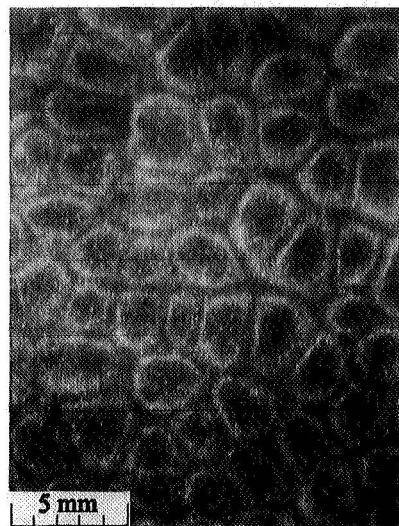
Studies of evaporating thin liquid layers clearly demonstrated that Bénard cells and similar thermocapillary flows can be triggered and sustained even if the layers were cooled from below. It is found that the wavelength of the cells depends on the liquid properties and the evaporation conditions but not the thickness of the layer when it evaporates at room temperature, while the wavelength would become larger and larger with the evaporation when the layer is cooled from below. Evaporation and nonlinear temperature profile may play an important role in the capillary convection. The traditional static instability theory and modeling of Marangoni-Bénard convection can no longer describe the complex phenomena involving a dynamic, evaporating free surface. Further study and more experimental data are needed to adequately account for both evaporation and temperature gradient conversion in an evaporating liquid layer.

## REFERENCES

1. H. Bénard, *Rev. Gen. Sci. Pure Appl.*, **11**, 1261, 1309 (1900)
2. H. Bénard, *Ann. Chim. Phys.*, **23**, 62 (1901)
3. Lord Rayleigh, *Phil. Mag.*, **32**, 529 (1916)
4. M. J. Block, *Nature*, **178**, 650 (1956)
5. J. R. A. Pearson, *J. Fluid Mech.*, **4**, 489 (1958)
6. D. A. Nield, *J. Fluid Mech.*, **19**, 341 (1964)
7. J. L. Castillo and M. G. Velarde, *J. Fluid Mech.*, **125**, 463 (1982)
8. J. C. Berg, A. Acrivos and M. Boudart, *Adv. Chem. Engng.*, **6**, 61 (1966)
9. Nengli Zhang and An-Ti Chai, *4th Intern. Sympos. on Heat Transfer, Beijing, China, 1996*, (in review)



**(a) Silicone oil (0.65 cSt.)**



**(b) Alcohol**

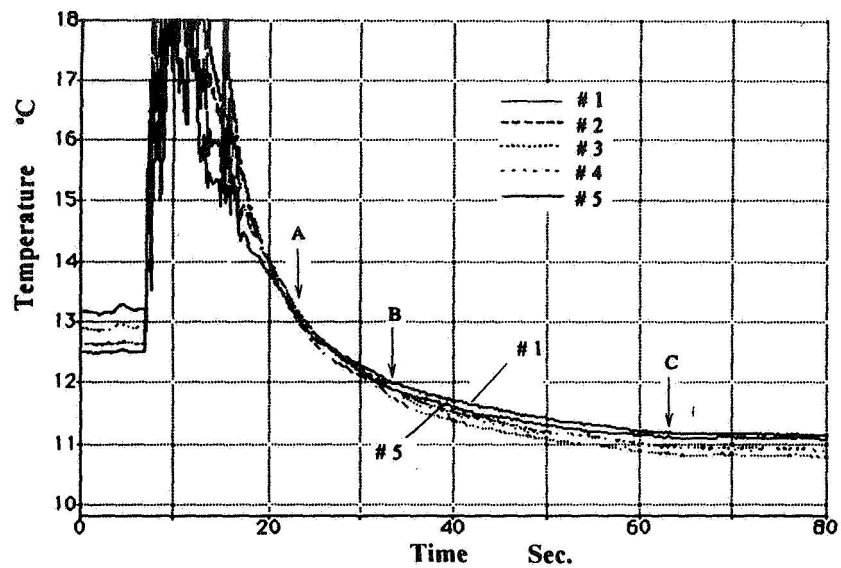


**(c) Freon-113**

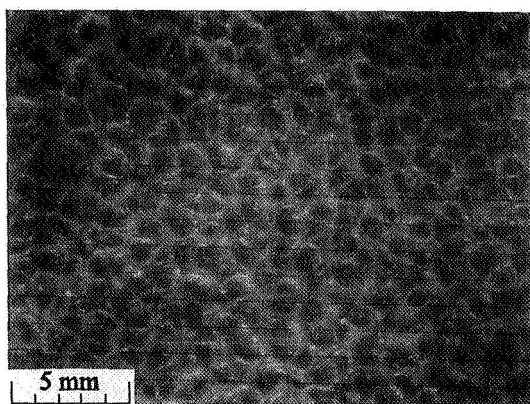


**(d) n-pentane**

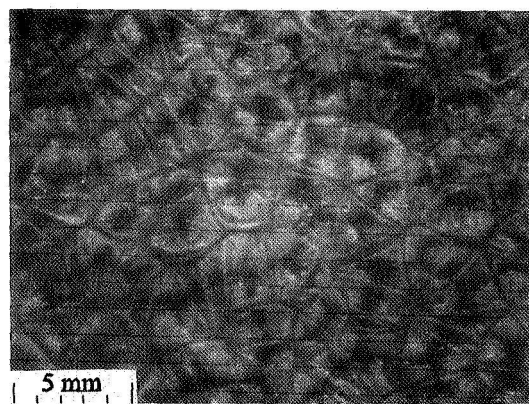
**Fig. 1 Convection patterns in an 1 mm layer evaporating at room temperature**



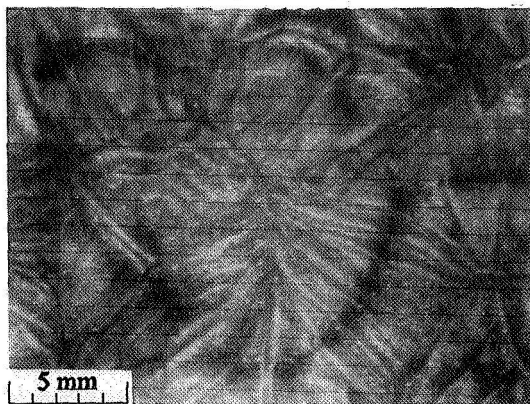
(a) Temperature histories



(b) Convection pattern at moment A



(c) Convection pattern at moment B



(d) Convection pattern at moment C

**Fig. 2 Temperature histories and convection patterns in a thin layer of freon-113 cooled from below**

# Bubble Dynamics on a Heated Surface

M. Kassemi\* and N. Rashidnia\*\*

NASA Lewis Research Center  
Cleveland, Ohio

## Abstract

In this work, we study the combined thermocapillary and natural convective flow generated by a bubble on a heated solid surface. The interaction between gas and vapor bubbles with the surrounding fluid is of interest for both space and ground-based processing. On earth, the volumetric forces are dominant, especially, in apparatuses with large volume to surface ratio. But in the reduced gravity environment of orbiting spacecraft, surface forces become more important and the effects of Marangoni convection are easily unmasked. In order to delineate the roles of the various interacting phenomena, a combined numerical-experimental approach is adopted. The temperature field is visualized using Mach-Zehnder interferometry and the flow field is observed by a laser sheet flow visualization technique. A finite element numerical model is developed which solves the two-dimensional momentum and energy equations and includes the effects of bubble surface deformation. Steady state temperature and velocity fields predicted by the finite element model are in excellent qualitative agreement with the experimental results. A parametric study of the interaction between Marangoni and natural convective flows including conditions pertinent to microgravity space experiments is presented. Numerical simulations clearly indicate that there is a considerable difference between 1-g and low-g temperature and flow fields induced by the bubble.

## Introduction

In many industrial situations which involve materials processing, manufacturing, boiling, and storage and management of liquids, the interaction between gas and vapor bubbles with the surrounding fluid is of great interest. This interaction is manifested by a fluid motion brought about by two co-existing and sometimes competing mechanisms; *natural convection* induced by the volumetric buoyancy force and *Marangoni convection* driven by the interfacial stresses along the bubble surface. Unlike natural convection which is driven by density differences generated by either temperature or concentration gradients in the bulk of the fluid, Marangoni convection is driven by surface tension forces brought about by temperature or concentration gradients (thermocapillary and solutocapillary convection, respectively) along the free surfaces of the fluid volume. On earth, the volumetric forces are dominant, especially, in apparatuses with large volume to surface ratio. But in the reduced gravity environment of orbiting spacecraft, surface forces become more important and the effects of Marangoni convection are easily unmasked.

In this work, we study the interaction between thermocapillary convection and natural convection generated by a bubble on a heated solid surface in both 1-g and low-g environments. In addition to its inherent scientific significance, this phenomenon is also of prime practical importance to materials processing and boiling processes. A Comprehensive review paper by Ostrach<sup>1</sup> drew attention to the importance of Marangoni convection in materials processing and fluid management in space. As a result, there has been a significant volume of published work investigating the role of thermocapillary flows in the past decade. A category which has received much less attention includes studies of the interaction of bubbles attached to heated or cooled surfaces with the surrounding fluid. Need for low-gravity research in this area was demonstrated by a series of low-g and 1-g solidification experiments by Papazian and Wilcox<sup>2</sup>. They demonstrated that while during ground-based tests bubbles were seen to detach from the interface easily and float to the top of the melt, in low-gravity tests no detachment from the interface occurred and large voids were grown in the crystal. Larkin<sup>3</sup> conducted the first numerical study of the thermocapillary effect around a hemispherical bubble placed on a solid wall subject to a constant heat flux. He obtained time-dependent numerical solutions for Marangoni numbers between 0 and 100,000 and Prandtl numbers between 1 and 5. The results indicate that the flow builds up quickly and then gradually declines with time. Unfortunately, Larkin was unable to continue the solution until steady-state was reached because of the enormous computer time required, nor was he able to predict an oscillatory flow. It should be mentioned that Larkin did not include the effect of natural convection in his numerical model. Kao and Kenning<sup>4</sup> extended the work of Larkin by taking into account heat transfer at the interface between a gas bubble and the surrounding liquid and studied the effect of surfactants on the flows. They covered a range of Marangoni numbers from 50 to 250,000 and Biot numbers from 0 to 5000. Although the effects of natural convection were included in their analysis, they still did not predict flow and temperature oscillations. The aforemen-

\* OAI/NASA Senior Research Scientist

\*\* NYMA/NASA Senior Research Scientist

tioned numerical results contradict recent experimental observations made by Raake et al.<sup>5</sup> and Chun et al.<sup>6</sup> and Rashidnia<sup>7</sup> who, using interferometry, visualized thermal oscillations in the fluid surrounding a bubble at Marangoni numbers above 12,000. The published numerical predictions are also not in accordance with the unsteady thermocapillary flow behavior reported at high Marangoni numbers in liquid bridges or free surface enclosures as described above.

### Mathematical Formulation

Consider an enclosure containing a liquid (silicone oil) with a bubble placed on the inside of the top wall as shown in Fig. 1. The side walls are insulated and the temperature of the top and bottom walls are uniformly maintained at  $T_h$  and  $T_c$ , respectively. Therefore, a thermally stratified state is established in the enclosure before the bubble is introduced. Once the bubble is positioned and the interface between the air and test liquid is formed, surface tension forces created by the temperature gradient along the interface will drive a thermocapillary convective flow. This thermocapillary flow disrupts the thermal stratification near the bubble resulting in significant temperature gradients and convection near the bubble surface.

A two dimensional model is developed to describe the fluid flow and heat transfer induced by the bubble. In this work, the Boussinesq approximation is used which is valid for small temperature differences ( $\Delta T = 4$ ). All the material properties, except for the surface tension coefficient are assumed to be constant. The dependence of surface tension on temperature is experimentally determined and incorporated into the model. Following these assumptions, the flow in the enclosure is described by the continuity and momentum equations which are written in dimensionless form as

$$\nabla \cdot \vec{v} = 0 \quad (1)$$

$$Re \left( \frac{\partial \vec{v}}{\partial t} + \vec{v} \cdot \nabla \vec{v} \right) = -\nabla P + \nabla^2 \vec{v} - \left( \frac{Gr}{Re} \right) \theta \hat{e}_s \quad (2)$$

These equations are subject to nonslip condition at the top, bottom, and left boundaries, and symmetry conditions along the central axis of the enclosure.

The normal and tangential stress balances along the surface of the bubble are written as.

$$\sigma_n = 2\gamma H - P_a \quad (3)$$

$$\sigma_t = \nabla_t \theta \quad (4)$$

Note that there are two driving forces for the flow. The first is due to the surface tension force which drives a vigorous tangential velocity along the bubble surface. The second is the buoyancy force which is driven by the density differences in the bulk of the fluid. Because both surface tension and density are functions of temperature, both of these driving forces couple the momentum equation to the energy equation.

The energy equation is written in dimensionless form as

$$Re \left( \frac{\partial \theta}{\partial t} + \vec{v} \cdot \nabla \theta \right) = \left( \frac{1}{Pr} \right) \nabla^2 \theta \quad (5)$$

This equation is subject to insulated boundary conditions at the wall, symmetry condition at the center and prescribed temperatures at the top and bottom walls respectively:

$$\theta = \theta_h \quad (6)$$

$$\theta = \theta_c \quad (7)$$

There are four important dimensionless parameters which govern the fluid flow and heat transfer in the enclosure. These are the  $Re$ ,  $Gr$ ,  $Pr$ , and  $Ca$  numbers. The first three dimensionless parameters can be combined using the definitions of Marangoni and Raleigh numbers as  $Ma = Re \cdot Pr$  and  $Ra = Gr \cdot Pr$ . The ratio of  $Ra$  and  $Ma$  numbers (most commonly referred to as the Bond number) is a measure of the relative importance of heat transfer by natural convection to heat transfer by thermocapillary convection.

To solve the problem numerically, a finite element model for the bubble is developed based on the simulation code



Fidap. In this two-dimensional steady heat transfer and fluid flow model the bubble is treated as a flexible free surface with a specified contact angle with the top wall. The position of the interface is an unknown variable which is updated as the solution evolves. The boundary conditions on the interface are written as continuities of normal and tangential stresses and the kinematic constraint that requires the interface to always remain an interface. According to this scheme which is sometimes referred to as *normal stress updating*, the kinematic constraint and the balance of tangential stresses are used to satisfy the boundary conditions for the momentum equation and the normal stress balance is applied to determine the position of the interface. As a result, during a pseudo-transient solution, the position of all the nodes is adjusted according to the updated position of the interface. The equations are solved using a segregated approach in which each degree of freedom is tackled individually and the equations are, therefore, only loosely connected. This results in convergence rates which are lower than coupled solvers but the method has a large radius of convergence and is also not demanding on computer resources such as storage allocation which can be prohibitive due to the clustering of the nodes near the bubble (which is needed in order to resolve the very thin boundary layers formed at high Ma numbers).

### **Experimental Setup and Procedures**

The experimental setup designed and constructed to quantify the thermocapillary flow generated by the bubble consists of three main components; the test cell and the injector, The Mach-Zehnder Interferometer (MZI), and the laser sheet flow visualization unit. The onset of the thermocapillary and natural convection flows is determined by observing the interferometric fringe patterns created by the temperature field and visualizing the velocity field near the bubble using a laser sheet. A schematic of the test cell which is made of large optical glass widows suitable for interferometric measurements is shown in Fig. 2. The enclosure has inside dimensions of 38mm x 19mm x 19mm (w x d x h). The transparent side walls are also suitable for laser light sheet illumination. The copper top and bottom walls are heated and cooled in order to establish the desired temperature gradients. Two reservoirs (not shown) are diagonally located in the corners of the upper copper wall to allow for expansion/contraction of the test liquid. These reservoirs are also used to supply and remove the fluid. There is a capillary opening with a connection to a syringe (not shown) at the center of the top plate for bubble injection. A depression is formed around the injection hole to hold various size bubbles. The chamber is filled with the test liquid. The fluid is heated from above and cooled from below by two independently controlled thermostatic circulation baths connected to the copper plates. When the desired temperature difference in the chamber is reached and steady-state conditions prevail, an air bubble of controlled size will be injected. Heat losses through the side walls and windows are negligible due to the vacuum in between the transparent double walls of the chamber (this can be confirmed from the flat interferometric fringe patterns shown in Fig 5). The entire diagnostic instrumentation and test cell, with the exception of the thermally controlled constant baths are installed on a vibration-isolation optical table for the ground-based experiments. The baths are connected to the test cell via flexible tygon tubing.

The flow fields are visualized with a low power (5 mW) HeNe laser light sheet at the meridian plane of the bubble. Neutrally buoyant particles, added to the test liquid, are used as flow tracers. The movement of the tracer particles are recorded by a time-lapse recorder on S-VHS. The temperature fields is visualized using MZI which has been successfully used in previous investigations with similar flow configurations<sup>6</sup>. This interferometric technique has been chosen because of its accuracy and sensitivity in pinpointing the different modes of oscillation. In this technique, light rays transversing through a phase object furnish an integral information about the refractive index distribution of the medium they have travelled through. For axisymmetric flow conditions the interferometric fringe patterns can be translated to temperature contours using Abel transformation<sup>7</sup>.

### **Results and Discussion**

#### **Numerical simulations**

In order to gain insight into the flow and temperature fields generated by the bubble in a typical ground-based situation, numerical simulations were performed for silicone oil ( $Pr = 8.4$ ) as the test fluid. The steady-state results for the base case ( $Re = 4300$ ,  $Gr = 2400$ ) is presented in Fig 3. The streamlines in Fig. 3a indicate that three vortices exist in the enclosure. The strongest vortex driven by the thermocapillary force fills the top portion of the enclosure next to the bubble. It carries the fluid down along the surface of the bubble creating a strong boundary layer flow which is revealed by the packing of streamlines near the interface. The temperature contours around the bubble are distorted significantly by this vigorous flow as indicated in Fig 3b. At steady-state, the primary thermocapillary vortex co-exists with two additional vortices below the bubble. These secondary and tertiary vortices are driven by the buoyancy force brought about by unstable density gradients created as the hot fluid from the top of the enclosure flows into the colder region by thermocapillary convection. It is important to note that the secondary vortex rotates in the opposite direction of the primary vortex and impedes the enlargement of this vortex and the free flow of fluid into the lower regions of the enclosure. These numerical predictions are in close qualitative agreement with our flow visualization results

shown in Fig. 6 and the experimental flow and temperature fields reported by Raake et al.<sup>4</sup>. Finally, Fig. 3c indicates that the steady-state shape of the bubble (as determined by the balance of forces at the interface) is quite different from the initial hemispherical shape assumed at the beginning of the simulation. Again, there is an extremely good qualitative agreement between the flattened bubble shape predicted by the model and the experimental observations in our laboratory (Fig. 6) and by Raake et al.<sup>4</sup>. Our results indicate that with increasing Re number, the temperature along the bubble becomes more uniform, and consequently, the velocity of the fluid along the bubble surface which is driven by the temperature-dependant surface tension force is significantly reduced. The largest  $u$  and  $v$  velocities at the interface occur for the  $Re=43$  case which has the highest level of thermal stratification. Moreover, for the  $Re=4300$  case, the flow attains its peak interfacial speed near the contact point between the bubble and the top wall, while for lower Re numbers, the peak speed shifts lower towards the central regions of the bubble.

Next, conditions pertinent to the microgravity environment are considered. Since, a low gravity environment is characterized by a reduced buoyancy force, decreased hydrostatic head, and negligible natural convection, the low-g shape of the bubble and the resulting thermocapillary flow and temperature fields will be also significantly different from the 1-g cases discussed above. Again, we use numerical simulations to underscore this fact.

The steady-state flow and temperature fields generated by the bubble in a low-g environment ( $g_0 = 10^{-4}g$ ) are shown in Fig. 4. Just as in the 1-g situation, a vigorous thermocapillary flow is generated next to the bubble surface. Again, this strong flow will drastically modify the temperature profiles in the enclosure. But in contrast to the terrestrial examples presented in Fig. 3, this time, a natural convective flow will not ensue due to the reduced buoyancy force. As a result, the recirculating thermocapillary vortex will grow unopposed until it nearly fills the entire enclosure at steady-state. The streamlines of Fig. 4a clearly show that the microgravity flow pattern resembles a jet-like flow emanating from around the bubble and flowing downwards into the enclosure. As a result of this intense recirculating flow, the temperature field is greatly altered as depicted in Fig. 4b. The low-gravity bubble shape is plotted in Fig. 4c. Comparison with the bubble shape presented in Fig. 3c clearly shows the significant difference between low-g and 1-g bubble shapes. In low gravity, the bubble is elongated rather than flattened (as in the 1-g case) from its originally assumed hemispherical shape. *Thus, in microgravity, the shape of the bubble, and the temperature and fluid flow fields are all drastically different from their terrestrial counterparts.*

#### Interferometric and Flow Visualization Results

The interferometric patterns established in the enclosure before the bubble is placed are shown in Fig. 5. When the bubble is introduced, both the flow and temperature fields are modified. At low Ma numbers the flow reaches steady-state conditions as discussed previously. An example of the steady-state interferometric patterns and flow field is included in Fig. 6 for  $Ma = 3.6 \times 10^4$ .

Our experimental results indicate that these steady state temperature and flow fields can be disrupted at higher Ma numbers. Initiation of periodic oscillations at larger Marangoni numbers is clearly indicated by again observing the basic thermocapillary flow and interferometric patterns. This periodic behavior is demonstrated by the sequence of interferometric fringe contours presented in Fig. 7 for  $Ma = 9 \times 10^4$ . The interferograms depict one full cycle of oscillation. Preliminary particle flow visualizations also show similar oscillations in the velocity distributions around the bubble. The flow and temperature fields for this case are axisymmetric. Our experience indicates that at still higher Marangoni numbers, the flow becomes nonperiodic and eventually will lead to chaotic patterns.

#### Conclusions

In this work a combined experimental numerical approach to investigate the fluid flow and temperature fields created by a bubble attached to a heated solid surface was presented. From the results obtained the following conclusions can be made.

1. Both experimental observation and numerical predictions indicate that the thermo-capillary flow induced by bubbles on earth is greatly influenced and affected by its inevitable interactions with buoyancy-driven convection.
2. steady-state numerical predictions indicate that the temperature and fluid fields generated by the bubble in low-gravity and its shape are significantly different from their ground-based counterparts. There has been no direct low-gravity experimental verification or confirmation of these numerical predictions.
3. Preliminary interferometric measurements in our laboratory demonstrate that the flow and temperature fields around the bubble can go through various oscillatory modes depending on the parametric space of the experiment. The nature and origin of these modes and their dependance on the interactions between natural and thermocapillary convection are as of yet not clearly known.

Results and conclusions obtained during ground-based experiments with regard to oscillatory convection cannot in any way be extrapolated to determine the behavior of the thermocapillary flow in space. *Therefore extensive hand-in-hand experiments and numerical modelling is required with fine steps of varying temperature gradient and bubble*



size in order to accurately delineate the parametric space and exact conditions for the onset of the various oscillatory modes for both space and ground-based applications.

### References

1. Papazian, J. M. & Wilcox, W. R., *Interaction of Bubbles with Solidification Interfaces*, AIAA J., Vol. 16, 447-451, 1978.
2. Larkin, B.K., *Thermocapillary Flow around Hemispherical Bubble*, AIChE J., Vol. 16, No. 1, pp. 101-107, 1970.
3. Kao, Y.S. and Kenning, D.B.R., *Thermocapillary Flow Near a Hemispherical Bubble on a Heated Wall*, J. F. Mech., Vol 53, pp. 715-735, 1972.
4. Raake, D, Siekmann, J., Chun, Ch.-H., *Temperature and Velocity Fields Due to Surface Tension Driven Flow*, Exp. in Fluids, Vol. 7, pp. 164-172, 1989.
5. Chun, C.-H., et al., *Oscillating Convection Modes in the Surroundings of an Air Bubble Under a Horizontal Heated Wall*, Experiments in Fluids, Vol. 11, 359-367, 1991.
6. Rashidnia, N., *Observation of Flow and Temperature Oscillations Around a Bubble on a Solid Surface Subject to a Vertical Temperature Gradient*, AIAA Paper, No. 95-0880, 1995.
7. Vest, C.M., *Holographic Interferometry*, Wiley, New York, 1979.

### Nomenclature

$Ca$	= Capillary number, $\frac{\gamma_T \Delta T}{\gamma_o} = \frac{\mu U}{\gamma_o}$	$U$	= characteristic velocity, $\left( \frac{\gamma_T \Delta T}{\mu} \right)$
$C$	= specific heat, (J / kg K)	$\vec{v}$	= velocity vector, $\left( \frac{V^*}{U} \right)$
$\vec{g}$	= gravitational vector, $(g_o \hat{e}_g)$	$w$	= width of the enclosure, (m)
$Gr$	= Grashof number, $\left( \frac{g_o \beta R^3 (T_h - T_c)}{\nu^2} \right)$	<i>Greek</i>	
$H$	= mean Gaussian curvature parameter	$\alpha$	= thermal diffusivity, $\left( \frac{\rho C}{k} \right)$
$h$	= height of the enclosure, (m)	$\beta$	= expansion coefficient, (1 / K)
$k$	= thermal conductivity, (W / m K)	$\Delta T$	= temperature difference, $(T_h - T_c)$
$\hat{n}$	= unit normal vector	$\gamma$	= surface tension
$Ma$	= Marangoni number, $Re \cdot Pr$	$\gamma_T$	= thermal coefficient of surface tension
$Pr$	= Prandtl number, $\left( \frac{\nu}{\alpha} \right)$	$\mu$	= dynamic viscosity, (N s / m <sup>2</sup> )
$P$	= pressure, (N/m <sup>2</sup> )	$\nu$	= kinematic viscosity, (m <sup>2</sup> /s)
$P_a$	= atmospheric pressure, (N/m <sup>2</sup> )	$\rho$	= density, (kg / m <sup>3</sup> )
$R$	= bubble radius, (m)	$\sigma$	= dimensionless stress, $\frac{\sigma^* R}{\gamma_T \Delta T}$
$Ra$	= Raleigh number, $Gr \cdot Pr$	$\theta$	= dimensionless temperature, $(T - T_c) / (T_h - T_c)$
$Re$	= Reynolds number, $\left( \frac{UR}{\nu} \right)$	<i>Subscripts</i>	
$t$	= time, (sec)	$n$	= normal
$T$	= temperature, (K)	$t$	= tangential
		$h$	= hot
		$c$	= cold
		<i>Superscripts</i>	
		*	= dimensional quantity

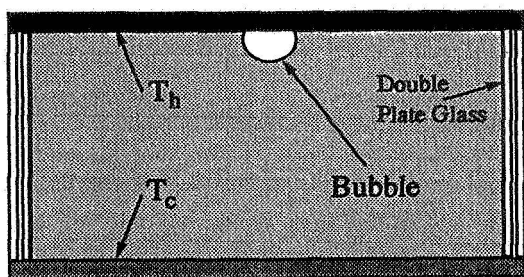


Figure 1. Schematic of The Test Enclosure.

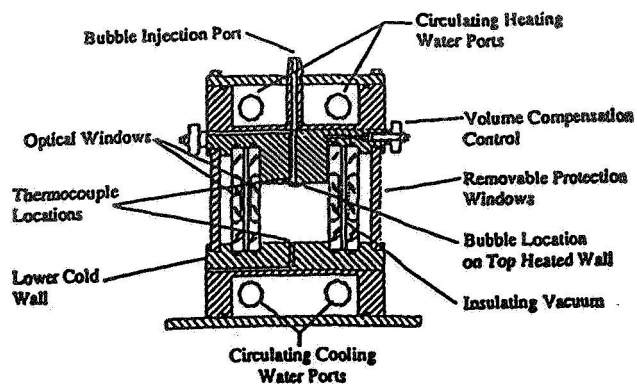
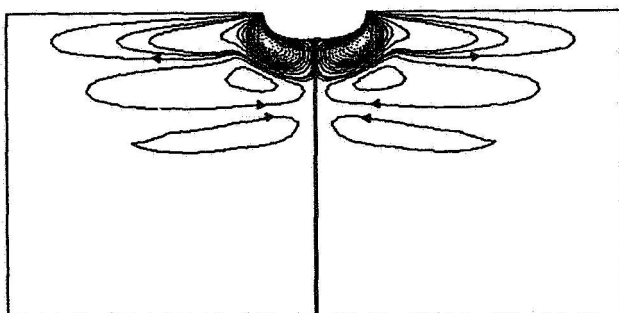
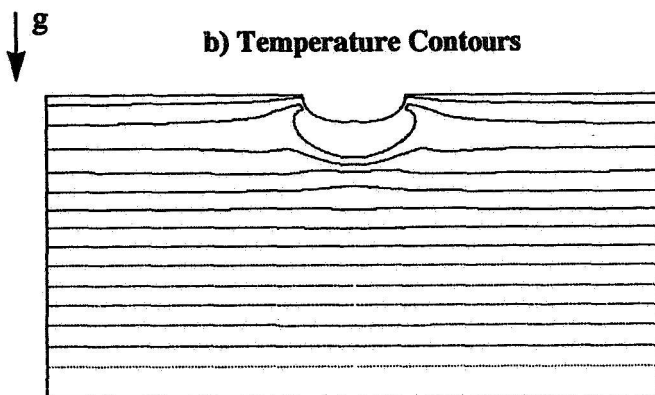


Figure 2. Schematic of The Test Cell

a) Streamlines



b) Temperature Contours



c) Bubble Shape

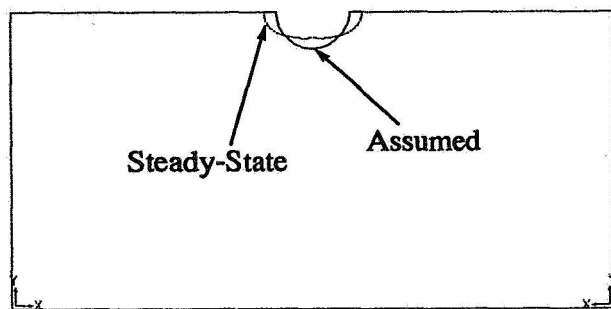
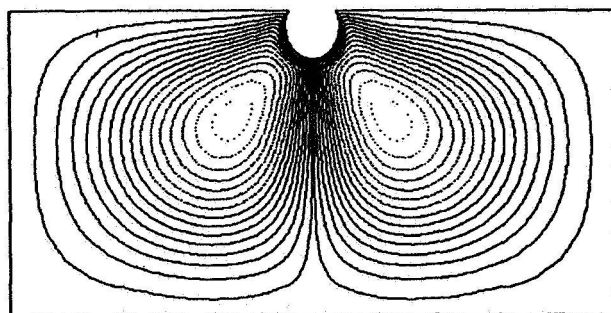
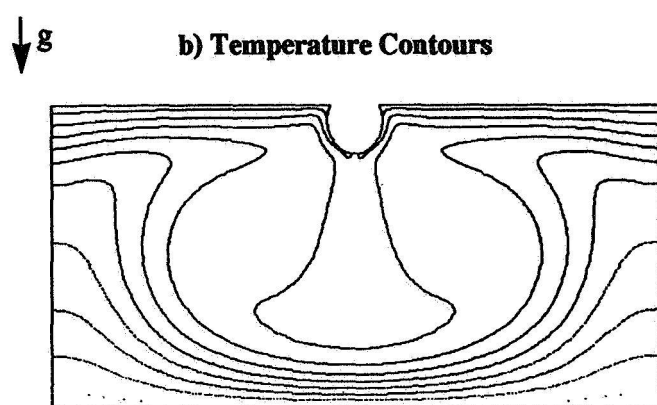


Figure 3. 1-G Numerical Predictions of Temperature and Flow Fields and Bubble Shape at Steady-State ( $Re = 4.3 \times 10^3$ ,  $Gr = 2.4 \times 10^3$ ).

a) Streamlines



b) Temperature Contours



c) Bubble Shape

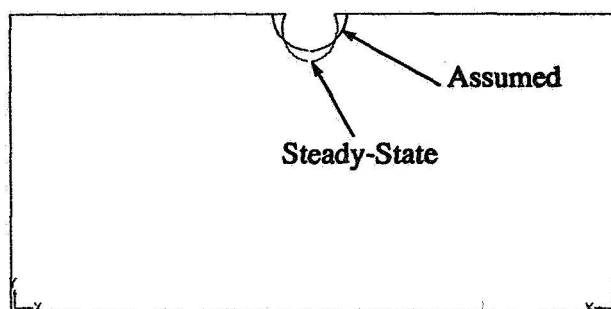
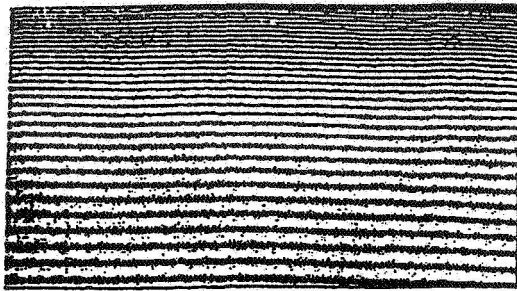
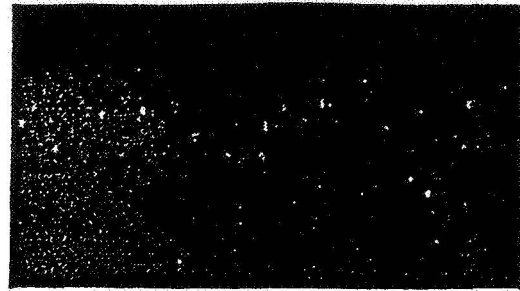


Figure 4. Low-G Numerical Predictions of Temperature and Flow Fields and Bubble Shape at Steady-State ( $Re = 430$ ,  $Pr = 8.4$ ).

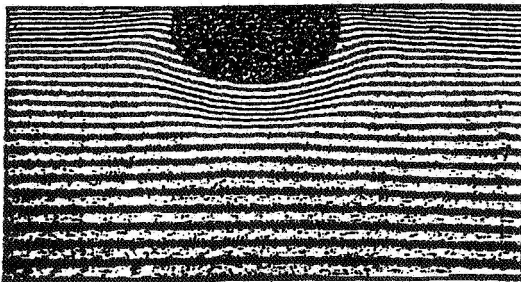


(a)

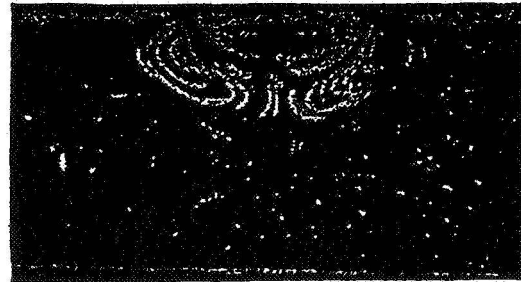


(b)

**Figure 5. Steady-State 1-G Interferometric Fringe Patterns (a) and Laser Sheet Images (b) Depicting The Thermally Stratified Conditions Before Bubble Placement.**



(a)



(b)

**Figure 6. Steady-State 1-G Interferometric Fringe Patterns (a) and Laser Sheet Images (b) After Bubble Placement ( $Ma = 3.6 \times 10^4$ ).**

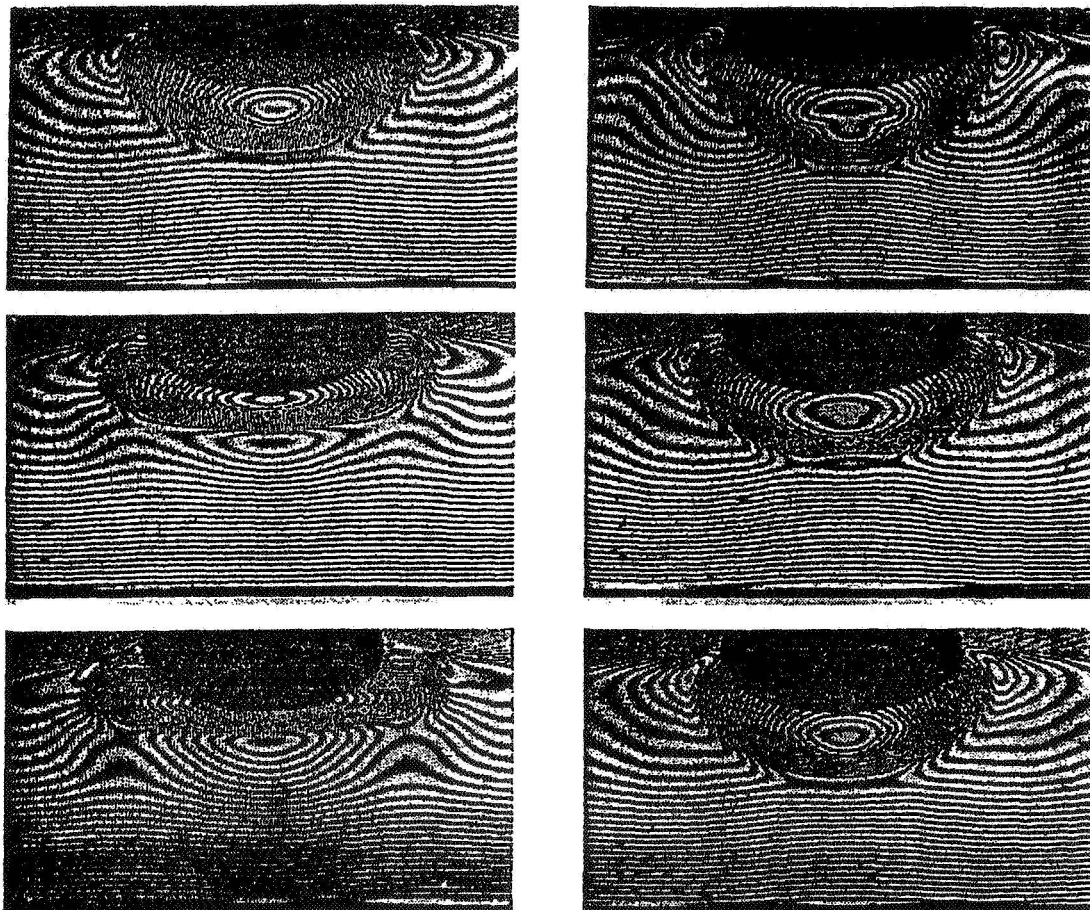


Figure 7. Sequence of Interferograms for Symmetric Oscillations of Temperature Field near the Bubble ( $Ma = 9 \times 10^4$ ).

# COMPUTATIONS OF DROP COLLISION AND COALESCENCE

Grétar Tryggvason, Damir Juric, Selman Nas, and Saeed Mortazavi  
Department of Mechanical Engineering  
The University of Michigan  
Ann Arbor, Michigan 48109

## ABSTRACT

Computations of drops collisions, coalescence, and other problems involving drops are presented. The computations are made possible by a finite difference/front tracking technique that allows direct solutions of the Navier-Stokes equations for a multi-fluid system with complex, unsteady internal boundaries. This method has been used to examine the various collision modes for binary collisions of drops of equal size, mixing of two drops of unequal size, behavior of a suspension of drops in linear and parabolic shear flows, and the thermal migration of several drops. The key results from these simulations are reviewed. Extensions of the method to phase change problems and preliminary results for boiling are also shown.

## INTRODUCTION

The presence of a free surface that is not constrained to be more or less flat due to the action of gravity is perhaps the most important aspect of fluid flow in microgravity. The absence of gravity generally makes surface tension effects important at much larger length scales than we are used to on earth. The large amplitude surface motion possible when gravity is small or absent is generally highly nonlinear and thus difficult to analyze by conventional means. Such surface motion is, nevertheless, to be expected in microgravity environment and it is necessary to understand it to be able to work with free surface systems. Experiments in microgravity are expensive, and usually difficult as well. It is therefore desirable to be able to predict the evolution of free surface systems numerically. Numerical simulations can replace experiments in some cases and complement experiments in other cases by providing information that are difficult to measure. Numerical simulations can also aid in the design of space experiments.

Numerical simulations of free surface flows have remained one of the frontiers of computational fluid dynamics since the beginning of large scale computations of fluid flow. Progress has however been much slower than for homogeneous flows and numerical simulations have not played the same role in multifluid and multiphase research as they have done for turbulence research, for example. Recently, however, a number of investigators have made considerable progress. We have been conducting simulations of multifluid and multiphase systems for several years and this paper reviews briefly those aspects of our work that are of particular relevance to microgravity fluid systems. We start by a description of the numerical methodology, since it is critical to the success of our work, and then review a few applications.

## NUMERICAL METHOD

The numerical method is based on writing one set of equations for the entire computational domain, independently of how many different fluids are involved. This is possible by allowing for different material properties in the formulation and adding singular terms at the phase boundaries to ensure that the correct boundary conditions are satisfied. The resulting "one-field" Navier-Stokes equations are:

$$\frac{\partial \rho \bar{u}}{\partial t} + \nabla \cdot \rho \bar{u} \bar{u} = -\nabla p + \bar{f} + \nabla \cdot \mu (\nabla \bar{u} + \nabla \bar{u}^T) + \int_F F_\sigma \delta(\bar{x} - \bar{x}_f) d\bar{a}$$

Here,  $\bar{u}$  is the velocity vector,  $p$  the pressure, and  $\rho$  and  $\mu$  are the discontinuous density and viscosity fields, respectively.  $\bar{f}$  is a body force that can be used to initiate the motion. The surface forces,  $F_\sigma$  act only on the interface between the different fluids and appears in the current formulation multiplied by a three-dimensional delta function,  $\delta$ . The integral is over the entire front. It is important to note that this equation contain no approximations beyond those in the usual Navier-Stokes equations. In particular, it contains implicitly the proper stress conditions for the fluid interface. The momentum equation is supplemented by an equation of mass conservation, which for incompressible flows is simply

$$\nabla \cdot \bar{u} = 0$$

Combining this equation with the momentum equation leads to an elliptic equation for the pressure. Since the density and the viscosity are different for the different fluids, it is necessary to track the evolution of these fields by solving the equations of state which simply specify that each fluid particle retains its original density and viscosity:

$$\frac{\partial \rho}{\partial t} + \bar{u} \cdot \nabla \rho = 0; \quad \frac{\partial \mu}{\partial t} + \bar{u} \cdot \nabla \mu = 0$$

The momentum equation is discretized on a regular staggered grid using second order, centered finite differences for the spatial derivatives and a second order time integration scheme. The continuity equation, when combined with the momentum equation results in a pressure equation that is not separable as for homogeneous flow and is solved by a multigrid package (MUDPACK from NCAR). To advect the material properties, and to evaluate the surface tension term in the momentum equation, we track the interface between the different phases explicitly by using a moving grid of lower dimension than what we use for the conservation equations. This grid is usually referred to as a front. The one-field formulation used here is common to other techniques for multifluid flows such as the VOF (Volume of Fluid) and level set methods. In these methods, however, the phase boundary is not tracked explicitly, but reconstructed from a marker function. Explicitly tracking the interface avoids the difficulty of advecting such marker function and allows accurate evaluation of surface forces.

Computing surface tension accurately is one of the most difficult part of methods intended for simulations of multifluid flows. Our current algorithm, which appears to be very satisfactory, is based on computing directly the force on each element by

$$\bar{F}_\sigma = \oint_{elem} \sigma \bar{n} \times \bar{t} ds$$

in a semi-implicit way. Here  $\bar{t}$  is a tangent to the boundary of the surface element,  $\bar{n}$  is the surface normal, and  $\sigma$  is the surface tension coefficient. By computing the surface forces this way, we explicitly enforce that the integral over any portion of the surface gives the right value, and for closed surfaces, in particular, we enforce that the integral of surface tension forces is zero. This is particularly important for long time simulations where a failure to enforce this constraint can lead to unphysical motion of bubbles and drops.

Since the boundary between the fluids (the front) usually undergoes considerable deformation during each run, it is necessary to modify the surface mesh dynamically during the course of the computations. The surface mesh is an unstructured grid consisting of points that are linked by elements. Both the points and the elements are arranged in a linked list, so it is relatively easy to change the structure of the front, including adding and deleting points and elements. Topological changes, such as when bubbles coalesce or drops break in two can also be accomplished by minimum effort. This is usually considered a major difficulty in implementing methods that explicitly track the front, but we have shown that with the right data structure these tasks become relatively straightforward. Although topology changes are easily done from a programming point of view, the physics is far from trivial. In reality, drops bounce off each other if the time when the drops are close is shorter than the time it takes to drain the film. Usually the film becomes very thin before it breaks and it would require excessive grid refinement to resolve the draining fully. At the moment we are dealing with this issue in a rather *ad hoc* way by simply changing the topology of the front at a prescribed time. However, considerable analytical work has been done on film draining and rupturing and we are currently exploring the possibility of combining such a model with our simulations.

The method has been implemented for two- and three-dimensional flows on regular grids and for axisymmetric geometries using stretched grids to allow local grid refinement. It has been applied to a number of multifluid problems and tested and validated in a number of ways, not only to check the implementation, but also to assess its accuracy. Those tests include comparisons with analytical solutions for simple problems, other numerical computations, and experiments. The actual resolution requirement varies with the parameters of the problem. High Reynolds numbers, for example, generally require finer resolution than lower ones, as in other numerical calculations. We have also found that for problems where the surface tension varies, such as for contaminated bubbles and drops moving by thermal migration we generally require finer resolution than for flows where the surface tension is constant. However, in all cases we have found that the method converges rapidly under grid refinement, and in those cases where we have other solutions we have found excellent agreement, even for modest resolutions. The method has also been extended in various ways to allow for simulations of heat transfer, surfactant effects, thermal migration, and phase changes. These effects can also be dealt with using the one-field formulation, thus allowing for a very efficient solution process. Examples of these validations are contained in various papers and dissertations listed at the end of this paper. Our work on other physical systems, such as bubbly flows are also discussed in these references.

## RESULTS

We have examined the collision and coalescence of two drops in considerable detail. The results of our investigation of the head-on collision of drops can be found in Nobari, Jan, and Tryggvason (1996). In this paper we examine how the collision modes changed as a function of Weber number, and how the exact time of coalescence, where the film between the drops ruptures, affected the outcome of the collision. Figure 1 shows one simulation from this paper. This work has now lead to a collaboration with Professor C.K. Law of Princeton University who has conducted extensive experimental studies of drop collisions and a detailed comparison between his experimental results and the simulations has shown excellent agreement. The interplay between experiments and simulations has also greatly improved our understanding of the boundaries between the various collision regimes. Three-dimensional simulations of off-axis collisions are described in Nobari and Tryggvason (1996). The results there show good agreement with experimental investigations, but the study is not yet as detailed as for the head-on collisions. For drops of unequal size, we have examined the coalescence of initially stationary drops that are driven together by surface tension. The results, which have been submitted for publication (Nobari and Tryggvason, 1994), show that considerable mixing can take place due to vorticity injected into the large drop by the smaller one.

With the collision of drops well under control, we have examined more complex problems. These include both large scale simulations of many drops as well as problems where additional physical effects have to be accounted for, such as heat transfer, thermal migration of drops, and phase changes. For isothermal drops we have examined the behavior of many drops in wall driven and pressure driven shear flows. In normal gravity such situations occur frequently in emulsions, for example, where the density of the drops is comparable with the continuous fluid. In microgravity, there is no restriction on the density difference and for finite Reynolds number flows we can expect significant effect due to the inertia of the drops. This investigation also has relevance to high pressure sprays where there are strong interactions between the drops and the continuous phase. In figure 2 we show several frames from a fully three-dimensional simulation of twelve drops in a periodic channel. The domain simulated is resolved by a  $64^3$  grid and the simulations are carried out for sufficiently long time so the drop distribution reaches an approximately steady state. Using both three-dimensional simulations with a models number of drops and two-dimensional simulations with larger number, the effect of the various governing parameters has been explored. The simulations generally show that the drops migrate away from walls, forming a denser core near the centerline. A single drop, however, generally takes up a position approximately half way between the wall and the centerline (the so-called Segre-Silberg effect) and for dilute distributions we find local maximum in the concentration at this position.

When gravity is absent, other effects, such as variable surface tension can dominate the dynamics. While thermal migration, where surface tension variations are brought about by variable temperature field, has been extensively studied for a single bubble or a drop, little is known about the interactions of many drops, particularly at finite Reynolds and Marangoni numbers. Figure 3 show an example of a fully three-dimensional simulation of two drops on a  $32$  by  $64$  by  $128$  grid. The drop surface and the temperature field in the centerplane are shown. The top and bottom boundaries are rigid walls at constant temperature, but the horizontal boundaries are periodic. This simulation, along with several two-dimensional ones of several drops show that the drops tend to form layers perpendicular to the temperature gradient. The simulations also show that even though surface tension is relatively low, the drops generally do not deform to any significant degree as they move.

The methodology used for the problems discussed above can be extended to much more complex physics in a relatively straight forward way. Application to the relatively simple problem of solidification of pure material in the absence of flow is discussed in Juric and Tryggvason (1995) where validation studies for simple problems and applications to the growth of dendrites can be found. Extension to binary alloys where it is necessary to follow the composition of the material can be found in Juric (1996). For full multiphase problems where fluid flow, heat transfer, and phase change are taking place simultaneously, we combine the method for the energy equation used for the solidification problems with the method for the Navier-Stokes equations. The resulting code has allowed us to simulate several boiling problems and in figure 4 we show a simulation of the growth of a vapor bubble in superheated fluid. The domain, which is resolved by a  $100$  by  $100$  grid, is open at the top, allowing fluid to escape as the bubble grows. The bubble shape is perturbed slightly at time zero and as the bubble expands, these perturbations grow. The bubble shape at time zero and several subsequent times is shown in the frame to the left. The right frame shows the bubble shape and temperature contours at an intermediate time. A simplified version of this method has also been used to simulate solidification of drops colliding with a wall in the case where the density of the melt and the solid are the same.

## CONCLUSIONS

We have discussed a numerical methodology to simulate multifluid and multiphase flows in microgravity and shown a few application of these methods. These simulations have already lead to a better understanding of some aspects of drop collisions and coalescence and also demonstrate the versatility of the method. Overall, it seems reasonable to state that the fluid problem is under good control with the exception of how to handle the rupture of thin films, although our current *ad hoc* strategy seems to work well in some cases. In most cases the fluid motion is only a part of an engineering application and heat transfer and phase change must be dealt with in order to establish the understanding needed for a completely predictive capability. We have taken preliminary steps in this direction and examined the thermal migration of drops and various phase change problems. The capability to examine the detailed evolution of boiling fluids, for example, promises to yield a dramatic new insight and understanding.

## ACKNOWLEDGMENTS

Our work on flows in microgravity has been supported under NASA grant NAG3-1317 and a NASA Graduate Student Fellowship NGT-51070 for D. Juric. We wish to thank Dr. D. Jacqmin at the NASA Lewis Research Center for many helpful discussions.

## REFERENCES

- S.O. Unverdi, G. Tryggvason, "A Front Tracking Method for Viscous Incompressible Flows." *J. Comput Phys*, 100, 25-37, (1992).
- S.O. Unverdi and G. Tryggvason, "Computations of Multi-Fluid Flows." *Physica D*, 60, 70-83, (1992).
- Y.-J. Jan. Ph.D. Dissertation, Computational Studies of Surfactant Effect on Bubble and Drop Dynamics. The University of Michigan, 1993.
- S. Nas and G. Tryggvason. Computational Investigation of the Thermal Migration of Bubbles and Drops. In *AMD 174/FED 175 Fluid Mechanics Phenomena in Microgravity*, Ed. Siginer, Thompson and Trefethen. 1993 ASME Winter Annual Meeting.
- M.R. Nobari. Ph.D. Dissertation, Numerical Simulation of Oscillation, Collision, and Coalescence of Drops. The University of Michigan, 1993, 155 pages.
- A. Esmaeeli. Ph.D. Dissertation, Numerical Simulations of Bubbly Flows. The University of Michigan, 1995.
- S. Nas. Ph.D. Dissertation, Computational Investigation of Thermocapillary Migration of Bubbles and Drops in Zero Gravity. The University of Michigan, 1995.
- S. Mortazavi. Ph.D. Dissertation, Computational Investigation of Particulate Two-Phase Flows. The University of Michigan, 1995.
- M.R. Nobari, Y.-J. Jan and G. Tryggvason. "Head-on Collision of Drops--A Numerical Investigation." *Phys. of Fluids* 8, 29-42 (1996).
- D. Juric and G. Tryggvason, "A Front Tracking Method for Dendritic Solidification." *J. of Comput. Phys.* 123, 127-148, (1996).
- M.R.H. Nobari, and G. Tryggvason, "Numerical Simulations of Three-Dimensional Drop Collisions." *AIAA Journal* 34 (1996), 750-755.
- A. Esmaeeli and G. Tryggvason, "An Inverse Energy Cascade in Two-Dimensional, Low Reynolds Number Bubbly Flows." *J. Fluid Mech.* 314 (1996), 315-330.
- Y.-J. Jan, and G. Tryggvason, "Computational Studies of Contaminated Bubbles." Submitted to *Phys. of Fluids*
- M.R. Nobari and G. Tryggvason, "Coalescence of Initially Stationary Drops." Submitted to *J. Fluid Mech.*
- A. Esmaeeli and G. Tryggvason, "Direct Numerical Simulations of Bubbly Flows. Part I—Low Reynolds Number Arrays" Submitted to *J. Fluid Mech.*
- D. Juric. Ph. D. Dissertation, Computations of Phase Change. The University of Michigan, 1996.
- D. Juric and G. Tryggvason, "A Front-Tracking Method for Liquid-Vapor Phase Change," in *Advances in Numerical Modeling of Free Surface and Interface Fluid Dynamics*, edit by Raad, Huang, and Tryggvason. FED-Vol. 234, ASME, pp. 141-148 (1995).
- D. Juric and G. Tryggvason, "Full Simulations of Flows with Phase Change," AIAA 95-0700. 3rd AIAA Aerospace Sciences Meeting, (1995).
- D. Juric and G. Tryggvason, "Direct Numerical Simulations of Flows with Phase Change," AIAA 96-0857eeting, (1996).



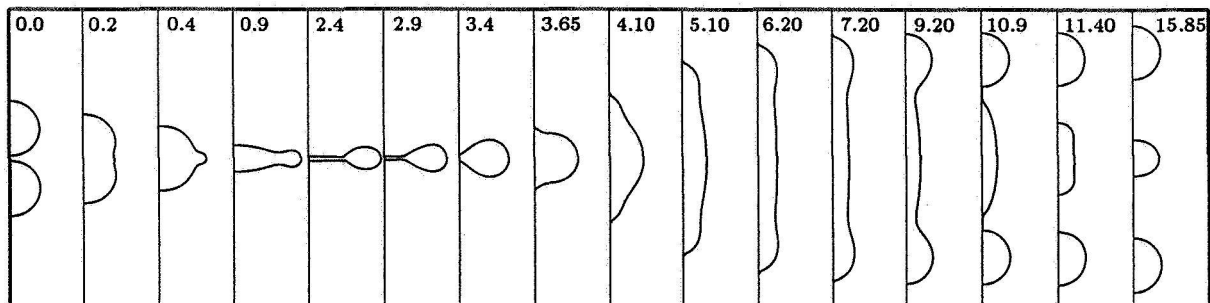


Figure 1. The head-on collision of two drops computed by an axisymmetric version of our method. Here  $We=115$  and  $Re=185$ . The drops are sufficiently energetic so they break up again after initial coalescence.

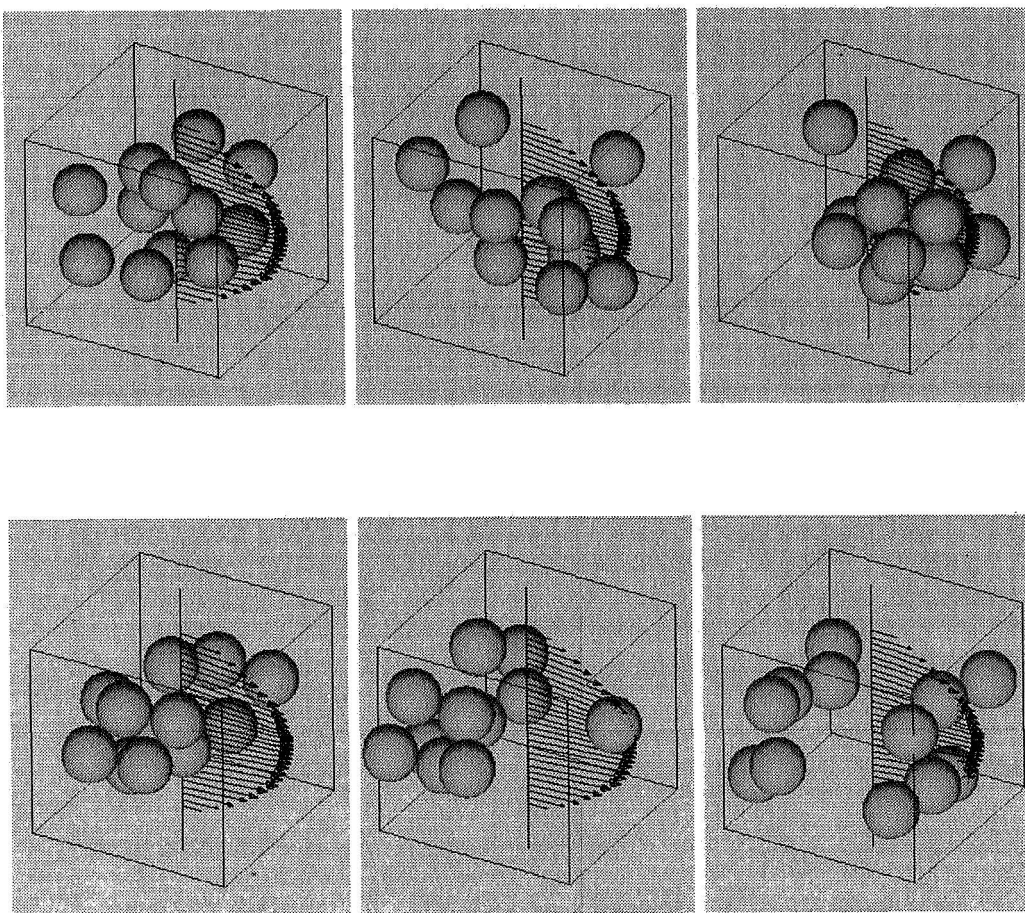


Figure 2. Simulation of the motion of twelve drops in a wall bounded/periodic pressure driven flow.  $Re=20$ ,  $We=0.125$  and the computational domain is resolved by a  $64^3$  grid.

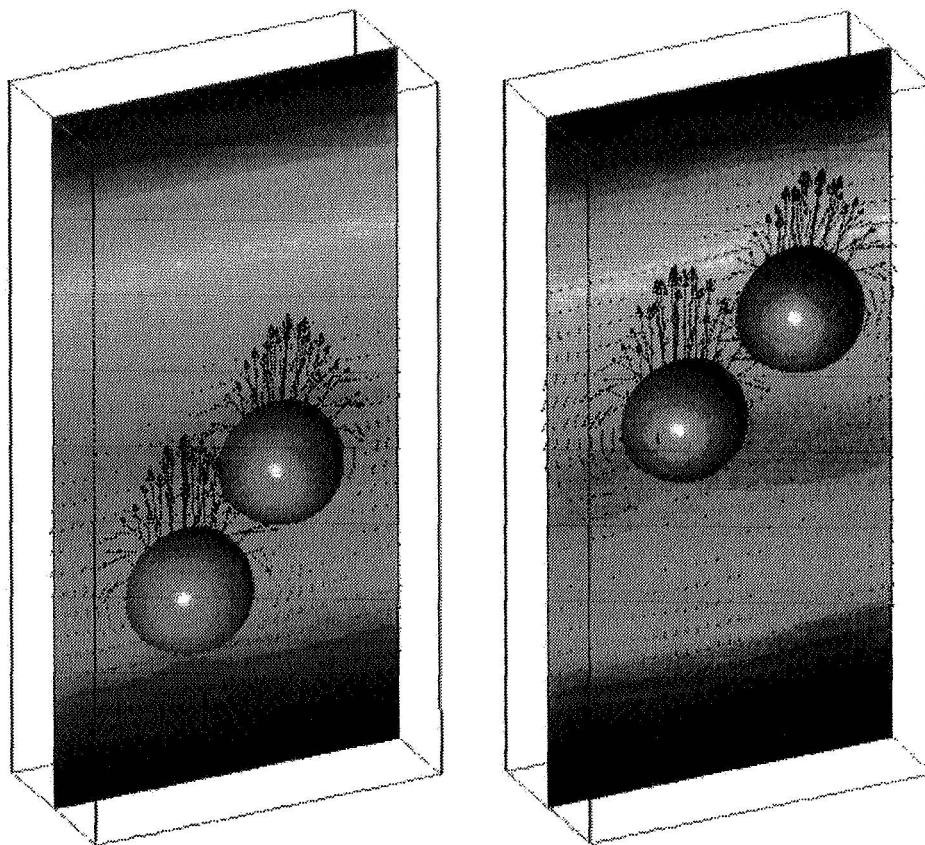


Figure 3. The thermal migration of several two three-dimensional drops simulated on a 64 by 32 by 128 grid. Here,  $Ca=20$  and  $Re=60$ . The initial conditions are to the left. The drops and the isotherms are shown.

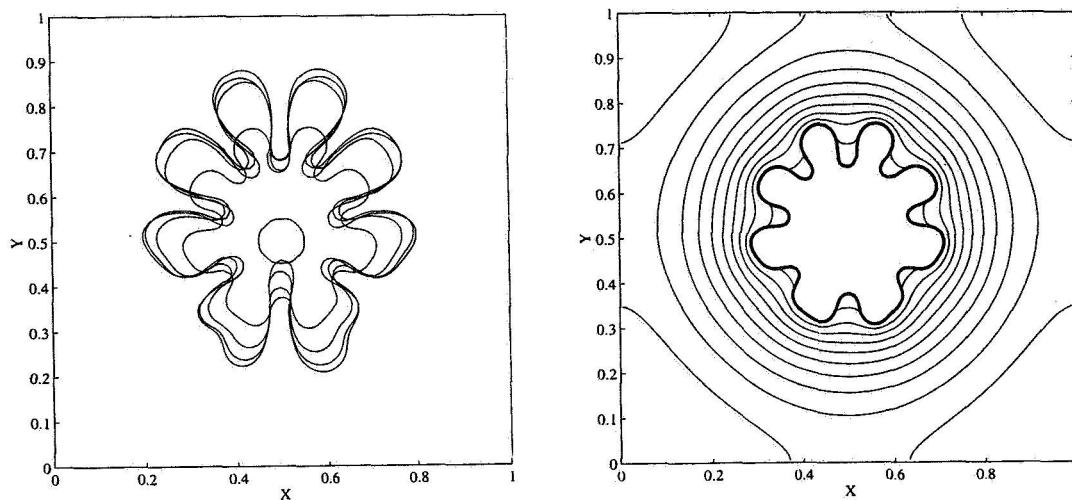


Figure 4. The evolution of a bubble grooving in superheated liquid. The bubble surface at several different times is shown in the frame to the left. The bubble surface and several isotherms at an intermediate time are shown on the right.

## **Marangoni Effects on the Bubble Dynamics in a Pressure Driven Flow**

**Chang-Won Park and S. R. K. Maruvada**

**Department of Chemical Engineering**

**University of Florida**

**Gainesville, FL 32611**

### **ABSTRACT**

The motion of air bubbles and water drops in a Hele-Shaw cell filled with a silicone oil has been studied experimentally and theoretically. By adding a predetermined amount of a surfactant to the water drops we attempted to investigate the surfactant influence systematically. While the motion of air bubbles was in reasonable agreement with the predictions of Taylor and Saffman [Q. J. Mech. Appl. Math. 12, 265 (1959)], water drops behaved quite differently in that the translational velocities were smaller by an order of magnitude and their shapes were very unusual as observed previously by Kopf-Sill and Homsy [Phys. Fluids 31, 18 (1988)]. Assuming that the surrounding fluid wets the solid wall and the bubble (or the drop) surface is rigid due to the surfactant influence, we have estimated the translational velocity of an elliptic bubble. The calculated velocities were in good agreement with the observations indicating that the surfactant influence could retard the bubble motion significantly. The present study also indicates that the unusual bubble shapes are also due to the surfactant influence.

### **INTRODUCTION**

Various physical systems involving the motion of bubbles or drops often show many unexpected flow phenomena which cannot be explained by existing theories. The unexpected flow characteristics of bubbly flows may include unusually high pressure drops, low bubble velocities, and perplexing bubble shapes. Furthermore, these flow characteristics are usually bubble-size dependent. While many of the unexpected flow phenomena may be attributed to the influence of surface active substances present in the system, details of such flows are yet to be fully understood.

When bubbles or drops are driven by a surrounding immiscible fluid, the flow may involve two characteristic velocities; the bubble velocity and the average velocity of the surrounding fluid. Although the bubble is driven by the surrounding fluid, the two characteristic velocities are not necessarily the same depending on the flow situations. If surface active substances are present, the flow becomes even more complicated since they affect the relative magnitude of the two characteristic velocities, resulting in various flow regimes. Although these complex flow situations may be encountered whether the gravity effect is present or not, the fundamental issue is in understanding the balance between the surface elasticity induced by the non-uniform surface tension and the viscous force under various flow conditions. Thus, in studying such flows it is desirable to minimize the gravity influence which introduces unnecessary complication. In ground-based experiments, the gravity effect may become negligible in a flow where the

characteristic length scale is very small. Examples may include the motion of bubbles in a capillary tube or in a Hele-Shaw cell. The motion of bubbles in a Hele-Shaw cell is especially rich in exhibiting various perplexing flow characteristics which are apparently caused by the surfactant influence.

The motion of a finite bubble moving in a Hele-Shaw cell which is filled with a viscous liquid was first analyzed by Taylor and Saffman (1959). Neglecting the surface tension and the wetting film between the bubble and the plates (Fig. 1), they predicted that a small elliptic bubble with its longer axis in the flow direction moves with a velocity  $U$  greater than  $2V$ . Here  $V$  is the average velocity of the surrounding fluid which drives the bubble (Fig. 1). When  $U < 2V$ , on the other hand, the shorter axis of the elliptic bubble is in the flow direction. If the bubble is circular,  $U=2V$ . In any case their solution indicates that the bubble velocity is always greater than the average velocity of the surrounding fluid (i.e.,  $U > V$ ).

Maxworthy (1986) conducted an experiment with bubbles that were driven by buoyancy rather than by a pressure gradient. He investigated air bubbles moving in an inclined Hele-Shaw cell which was filled with silicone oil. The bubbles in his experiment were ellipses elongated in the flow direction. While large bubbles moved somewhat faster than the Taylor-Saffman prediction, small bubbles moved slower than expected. Kopf-Sill and Homsy (1988) conducted similar experiments, but theirs was a pressure driven flow in which air bubbles in a horizontal Hele-Shaw cell were driven by a glycerin-water mixture. Unlike the experiments of Maxworthy, they observed a variety of unusual bubble shapes such as ovoids, long- and short-tailed bubbles. In addition, the bubble velocities were much smaller than expected by an order of magnitude. Considering the fact that aqueous systems are very prone to contamination by surface active substances, it may be possible that the perplexing observations by Kopf-Sill and Homsy may be due to the influence of surface-active contaminants.

In this paper, the results of an experimental study are presented in which water drops containing sodium dodecyl sulfate at a predetermined concentration were driven through a Hele-Shaw cell filled with a silicone oil. A theoretical calculation is also presented for the bubble velocity which accounts for the influence of surfactants. Both experimental and theoretical results show reasonable agreement with those of Kopf-Sill and Homsy indicating that surface active contaminants can be responsible for the observed retardation and for the perplexing bubble shapes.

## EXPERIMENTS

The Hele-Shaw cell consisted of two 1/2-in thick Pyrex glass plates separated by a rubber gasket of 0.9 mm or 1.8 mm in thickness. The effective cell dimension was 17.8 cm by 86.4 cm. A silicone oil with the measured viscosity and surface tension of 97 cp and 21 dyn/cm was used as the driving fluid. The cell had an injection port at one end of the top plate so that an air bubble or a water drop could be introduced into the cell using a syringe. The planform diameter of bubbles and drops was controlled to be at about 1.3 cm and 2.1 cm throughout the experimental

study. Water drops containing a surfactant at various concentrations were prepared by dissolving sodium dodecyl sulfate (SDS) in distilled water at a concentration of 5%, 10% and 20% of the critical micelle concentration (CMC), respectively. The CMC of SDS in water at 25°C is 8.2 mmol/l which is equivalent to 0.236% by weight. The interfacial tension at room temperature was 34.3, 32.1 and 25.9 dyn/cm at the prescribed concentrations of SDS.

Once an air bubble (or a water drop) of predetermined size was positioned at one end of the cell, the silicone oil was driven by a peristaltic pump at various flow rates to induce the bubble motion. The translational velocity and the shape of the bubble (or drop) were then recorded for each value of the oil flow rate. The measured velocities are plotted as a function of capillary number  $Ca$  in Fig. 2.  $Ca$  is defined as  $\mu U/\sigma$  where  $\mu$  is the viscosity of the surrounding fluid,  $U$  is the bubble velocity and  $\sigma$  the equilibrium value of the interfacial tension. Although some discrepancies existed, the air bubbles were moving with a velocity close to the prediction of Taylor and Saffman and their shapes were near circular with slight elongation in the flow direction. Water drops, on the other hand, were moving much slower than predicted, and they were elongated in the transverse direction unlike the air bubbles. At the prescribed concentrations of SDS, the data sets were indistinguishable from one another. Although not indicated in the figure, some drops showed a transition to a short-tailed shape at a higher capillary number in accordance with the observations of Kopf-Sill and Homsy. These differences between air bubbles and water drops are apparently due to the surfactant influence as supported by the theoretical calculation given in the following section. More details of the experimental study can be found in Park et al. (1994).

## ESTIMATION OF BUBBLE VELOCITY

In the absence of surface tension effect, the analysis of Taylor and Saffman predicts an elliptic shape when the bubble size is much smaller than the width of the cell. If surface active substances are present, the bubbles are not necessarily elliptical and may take on various interesting shapes depending on the flow condition. Nevertheless, we assume an elliptic plan form since the shape distortion is small at a low capillary number as observed experimentally. While the bubble shape should be determined as a part of solution, the current analysis is an approximation in which the bubble shape is assumed *a priori* in order to obtain an analytic progress.

As indicated in Figure 1, the two principal axes of the elliptic bubble are assumed to be aligned with the flow and the transverse directions with  $2a$  and  $2b$  denoting the bubble dimensions in the two principal axes. The surrounding fluid wets the solid surface thus forming a thin liquid film between the plates and the bubble. In the presence of surface active substances, the Marangoni effect resulting from the surface tension gradient may complicate the flow field near the bubble. When the bubble is small, however, it may be simplified since the entire bubble surface may become rigid (Davis & Acrivos, 1966; Park, 1992). Here we consider the case of a small bubble in which the entire bubble surface is assumed to be rigid.

The flow field slightly away from the bubble is known to be parabolic in the  $xz$ -plane (i.e., across the gap). Furthermore, it can be described as a potential flow in the  $xy$ -plane. Thus,

$$\mathbf{v} = 1.5 \mathbf{v}_{avg} \left( 1 - \frac{4z^2}{h^2} \right) \quad (1)$$

where  $\mathbf{v}_{avg}$  is the gap (or depth)-averaged velocity field described by the potential flow in  $xy$ -plane. In an elliptic cylindrical coordinate system  $(\zeta, \eta)$ , the complex potential  $\Omega$  for the flow past an elliptic cylinder in a bubble fixed frame of reference is given by

$$\Omega = \Phi + i\Psi = -b(V-U) \frac{(k+1)}{2} \sqrt{k^2-1} \left[ \frac{e^\gamma}{k+1} - \frac{e^{-\gamma}}{k-1} \right] \quad (2)$$

where  $\gamma = \xi + i\eta$  and  $k$  the shape factor defined as  $k = a/b$ .  $V$  and  $U$  are the magnitude of the average velocity of the surrounding fluid and the bubble, respectively. From the gradient of the velocity potential  $\Phi$  or the stream function  $\Psi$ , the velocity components in  $\xi$  and  $\eta$  directions (hence  $\mathbf{v}_{avg}$ ) can be obtained.

In the thin film region between the plates and the bubble, the flow field is represented by a Couette flow if the bubble surface is rigid. The previous analyses on the bubble motion in a capillary tube or in a Hele-Shaw cell provide an expression for the film thickness which is proportional to  $Ca^{2/3}$  (Park, 1992). Thus, the flow field in the thin film region is known. Eqns (1), (2) and the Couette flow in the film region represent the three-dimensional velocity field around the translating bubble excluding the small region of  $O(h)$  in the immediate vicinity the bubble rim. Using this velocity field, an analytic description of the translational velocity of the elliptic bubble can be obtained from an integral form of the  $x$ -directional momentum balance as follows:

$$F_D = \frac{12\mu}{h} \frac{\pi c^2}{4} \left\{ V \frac{k+1}{k-1} - \left[ (V-U) + U \frac{k-1}{k+1} \right] + (V-U) \frac{2}{k-1} \right\} - \frac{16\mu U(abI)}{2.122hCa^{2/3}} \quad (3)$$

Here  $c = \sqrt{a^2 - b^2}$  and  $I$  is a constant given as a definite integral which accounts for the film thickness variation in the transverse direction (i.e.,  $y$ -direction) for a given value of  $k$ .  $I$  varies from 0.79 to 1.29 for  $k$  changing from 0.1 to 3.0. For a circular bubble (i.e.,  $k = 1$ ),  $I = 0.91$ .  $F_D$  is the drag force acting on the bubble which is zero for a freely suspended drop. Consequently, the following expression for the bubble velocity can be obtained:

$$U = \beta(k+1)V \quad \text{where} \quad \beta = \frac{Ca^{2/3}}{Ca^{2/3} + 0.2kI} \quad (4)$$

Here  $\beta$  is the retardation factor introduced by the surfactant influence which is  $O(Ca^{2/3})$ . This order of magnitude decrease in the bubble velocity is due to the large drag in the thin film region where the bubble surface is rigid. Since this drag is proportional to the film thickness, the bubble velocity is also proportional to  $Ca^{2/3}$ . In the absence of Marangoni effect, the bubble surface in the thin film region is stress free, and the expression for the bubble velocity is equivalent to setting  $\beta = 1$ . Thus the result of Taylor and Saffman for elliptical bubbles is recovered.

In Figure 2, the calculated  $U/V$  using Eqn (4) has been overlaid for various value of  $k$  to compare with experimental results. It appears that the measured velocities are in reasonable agreement with the current predictions for ellipses which are elongated in the transverse direction (i.e.,  $k < 1$ ). While the drops in the experiment were not exactly elliptical, they were nearly elliptical and elongated in the transverse direction. Experiments indicate that the drops are elongated sideways at a low capillary number and their aspect ratio decreases with increasing capillary number. It is interesting to note that the data points show better agreement with the theoretical curve with smaller  $k$  at a lower  $Ca$ . With increasing  $Ca$ , the agreement becomes progressively better with the curves for larger  $k$  in accordance with the experimental observations.

## CONCLUSIONS

The present study indicates that surface active contaminants can influence the bubble dynamics significantly, and that most of the perplexing observations by Kopf-Sill and Homsy are probably due to the influence of surface active substance which may be present in the system as contaminants. As Kopf-Sill and Homsy anticipated, the significant retardation of bubble velocity and remarkable bubble shapes, in fact, result from the three-dimensional nature of the flow which cannot be explained by the two-dimensional Hele-Shaw equations.

## ACKNOWLEDGMENTS

The authors wish to acknowledge the financial support of NASA, Microgravity Science and Applications Division (Grant No. NAG3-1635) for this study.

## REFERENCES

- Davis, R. E. and Acrivos, A., *Chem. Engng Sci.* **21**, 681 (1966).
- Kopf-Sill, A. R. and Homsy, G. M., *Phys. Fluids* **31**, 18 (1988).
- Maxworthy, T., *J. Fluid Mech.* **173**, 95 (1986).
- Park, C.-W., *Phys. Fluids A*, **4**, 2335 (1992).
- Park, C.-W., Maruvada, S.R.K., and Yoon, D.-Y., *Phys. Fluids* **6**, 3267 (1994).
- Taylor, G. I. and Saffman, P. G., *Q. J. Mech. Appl. Maths* **12**, 265 (1959).

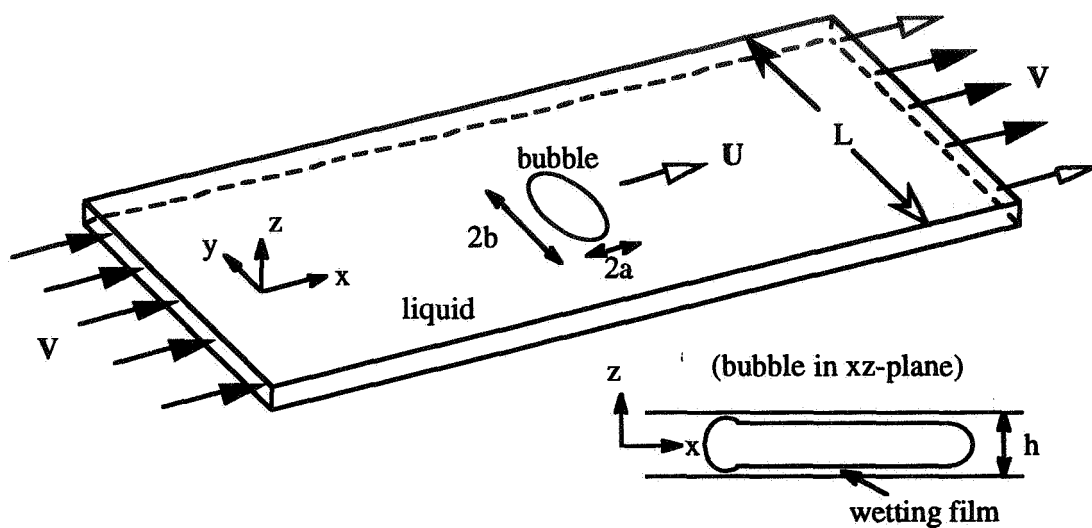


Figure 1 Schematic of a bubble moving in a Hele-Shaw cell

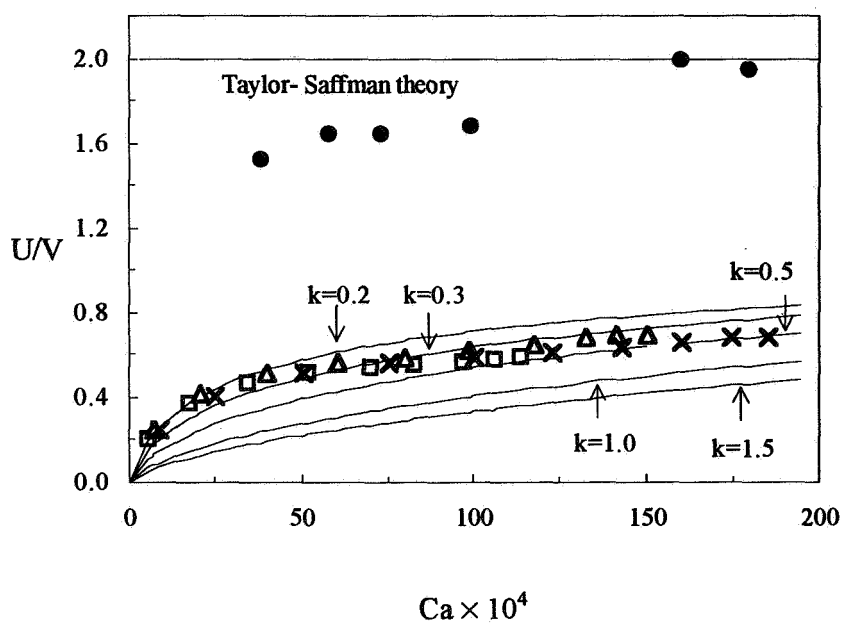


Figure 2 Comparison of experimental results and the theoretical estimate given by Eqn. (4) (●, air bubbles; Open symbols are for water drops at the SDS concentration of 5% (□), 10% (Δ), and 20% (×) of CMC.)



## FORCED OSCILLATIONS OF SUPPORTED DROPS

Edward D. Wilkes and Osman A. Basaran\*

School of Chemical Engineering, Purdue University  
West Lafayette, IN 47907-1283

### ABSTRACT

Oscillations of supported liquid drops are the subject of wide scientific interest, with applications in areas as diverse as liquid-liquid extraction, synthesis of ceramic powders, growing of pure crystals in low gravity, and measurement of dynamic surface tension. In this research, axisymmetric forced oscillations of arbitrary amplitude of viscous liquid drops of fixed volume which are pendant from or sessile on a rod with a fixed or moving contact line and surrounded by an inviscid ambient gas are induced by moving the rod in the vertical direction sinusoidally in time. In this paper, a preliminary report is made on the computational analysis of the oscillations of supported drops that have "clean" interfaces and whose contact lines remain fixed throughout their motions. The relative importance of forcing to damping can be increased by either increasing the amplitude of rod motion  $A$  or Reynolds number  $Re$ . It is shown that as the ratio of forcing to damping rises, for drops starting from an initial rest state a sharp increase in deformation can occur when they are forced to oscillate in the vicinity of their resonance frequencies, indicating the incipience of hysteresis. However, it is also shown that the existence of a second stable limit cycle and the occurrence of hysteresis can be observed if the drop is subjected to a so-called frequency sweep, where the forcing frequency is first increased and then decreased over a suitable range. Because the change in drop deformation response is abrupt in the vicinity of the forcing frequencies where hysteresis occurs, it should be possible to exploit the phenomenon to accurately measure the viscosity and surface tension of the drop liquid.

### 1. MOTIVATION, BACKGROUND, AND OBJECTIVES OF RESEARCH

A fundamental understanding of oscillations of both free and supported — pendant or sessile — liquid drops is of practical and scientific importance. A better understanding of oscillations of supported drops, the goal of this research and the subject of this brief research progress report, than that currently available is needed in areas as diverse as: (a) electric field-enhanced liquid-liquid extraction<sup>1,2</sup>, (b) electrospray methods for the synthesis of simple- and mixed-oxide ceramic precursor powders<sup>3</sup>, (c) growing of pure crystals in the reduced gravity environment of space<sup>4</sup>, and (d) measurement of dynamic surface tension by the pulsating bubble (drop) technique<sup>5,6</sup> and the growing drop technique<sup>7-9</sup>.

In (a) and (b), the energy required to break up and/or atomize supported drops can be minimized by taking advantage of the resonant coupling that can occur between the natural oscillations of the drop and the controlled oscillations of the driver. In (c), it is important to understand the effect of support vibrations on the quality of grown crystals. In a pulsating bubble (drop) surfactometer (PBS) (d), a bubble that is pendant from a tube and is surrounded by a surfactant solution is forced to undergo oscillations to infer the dynamic surface tension of the interface. In the growing drop technique (d), interfacial surface area is created either by impulsively growing out of a capillary tube an initially static pendant drop or repeatedly growing and detaching drops, viz. periodically dripping drops, from a tube by continuously flowing the drop liquid through it. In the experiments of Nagarajan and Wasan<sup>7</sup>, oscillations in drop shape and velocity and pressure fields arise after the static drop is impulsively set in motion. In the continuous flow experiments of MacLeod and Radke<sup>8</sup> and Zhang *et al.*<sup>9</sup>, similar oscillations occur after one drop detaches from the capillary and another one starts growing from it following the rupture of the liquid bridge connecting the former drop to the rest of the liquid in the capillary (cf. Zhang and Basaran<sup>10</sup>). The oscillations of pendant drops that arise during early times in these growing drop experiments not only create an uncertainty in the initial state

\*Corresponding author. Phone: 317-494-4061; Fax: 317-494-0805; E-mail: obasaran@ecn.purdue.edu.

of the system but also make it impossible to infer dynamic tension values for times lower than about 20 milliseconds despite the desirability of being able to do so in milliseconds and even in submilliseconds<sup>9</sup>.

However, while the dynamics of oscillating free drops have been studied for over a century since the time of Lord Rayleigh<sup>11</sup>, oscillations of supported drops had not been studied until recently and have received only limited attention to date. Previous studies of dynamics of supported drops<sup>12-19</sup> have been highly restrictive, including restriction to small-amplitude oscillations, irrotational oscillations of inviscid drops, and free oscillations. Moreover, in none of these previous studies has the effect of surfactants on finite-amplitude oscillations been considered. Given the widespread occurrence of applications that are enumerated above and the poor state of understanding of them that currently exists, the major goal of this research program is to develop a comprehensive understanding of the finite-amplitude forced oscillations of supported drops that either are pure liquids or contain surface-active species.

For the purpose of illustration, in this brief progress report attention is focused on forced oscillations of drops that are supported on a solid rod, as shown in Fig. 1. It is also taken here that the three-phase contact line where the drop liquid, ambient fluid, and rod meet remains pinned to the sharp edge of the rod throughout the drop motion and the drop is devoid of any surface-active species.

## 2. MATHEMATICAL FORMULATION

The system is an axisymmetric drop of an incompressible, Newtonian liquid of constant viscosity  $\mu$  and constant density  $\rho$  that is pendant from (or sessile on) a circular cylindrical rod of radius  $R$  that lies along the direction of the gravitational acceleration  $\underline{g}$ , as shown in Fig. 1. The drop is forced to oscillate by moving the rod in the vertical direction sinusoidally in time with frequency  $\tilde{\Omega}$  and amplitude  $\tilde{A}$  so that the instantaneous position of the rod tip is given by  $\tilde{z}' = \tilde{A} \sin \tilde{\Omega} \tilde{t}$  where  $\tilde{z}'$  is axial distance measured in an inertial frame of reference in the direction of (opposite to) gravity for a pendant (sessile) drop and  $\tilde{t}$  is time. The ambient fluid surrounding the drop has negligible density and viscosity and exerts a constant pressure and negligible drag on the drop as it oscillates. The drop/ambient fluid interface has constant surface tension  $\sigma$ . Throughout the motion, the three-phase contact line (circle) remains pinned to the edge of the face of the circular rod.

The problem is cast onto a moving frame of reference in which the rod is stationary by the transformation  $\tilde{z} = \tilde{z}' - \tilde{A} \sin \tilde{\Omega} \tilde{t}$ . The equations, boundary conditions, and initial conditions that govern the dynamics are put in dimensionless form by using the radius of the rod  $R$  as the length scale and the quantity  $\sqrt{\rho R^3 / \sigma}$  as the time scale. In what follows, variables with tildes over them are dimensional whereas the same variables without tildes are dimensionless.

The dimensionless groups that govern the forced oscillations of supported drops are (1) a Reynolds number  $Re \equiv (1/\nu)\sqrt{\sigma R/\rho}$ , (2) a gravitational Bond number  $G \equiv \pm \rho g R^2 / \sigma$ , (3) dimensionless forcing amplitude  $A$ , (4) dimensionless forcing frequency  $\Omega$ , and (5) dimensionless drop volume, which is parametrized by a parameter  $\alpha$  that varies between -1 and 1 such that  $\alpha = 0$  corresponds to a drop whose volume equals that of a hemisphere.

In this paper, two different types of initial conditions are considered. In one of these, a supported drop that is in static equilibrium for times  $t \leq 0$  is impulsively set into oscillation by moving the rod in the vertical direction sinusoidally in time for all time  $t > 0$  with a fixed forcing frequency  $\Omega$  and amplitude  $A$ . The transient Navier-Stokes system is then integrated in time until the drop motion approaches a time-periodic steady state or a limit cycle. With the other initial condition, once the drop attains a steady oscillatory state at frequency  $\Omega = \Omega_1$ , the forcing frequency is then changed by a finite amount to  $\Omega = \Omega_2 = \Omega_1 + \Delta\Omega$ . The transient system is then integrated until a new steady oscillatory state is reached. This procedure is then repeated by incrementing the forcing frequency. Indeed, frequency sweeps are carried out such that the forcing frequency is first increased over a range  $\Omega_{low} \leq \Omega \leq \Omega_{high}$  and then decreased over the same range.

## 3. RESULTS

Figure 2 shows the drop aspect ratio  $a/b$ , the ratio of the length of the drop along the axis of symmetry to the rod radius, and the instantaneous location of the rod tip in a fixed frame of reference after the drop has reached a state of steady oscillations during approximately one period for the situation in which the

equilibrium drop shape is a hemisphere ( $\alpha = 0$ ),  $Re = 10$ ,  $G = 0$ , and  $A = 0.1$ . The forcing frequency  $\Omega = 4$  so that the period of steady oscillations is  $\pi/2$ . The out of phase oscillations between the rod and the drop aspect ratio give rise to interesting fluid motions inside the drop (not shown but see Wilkes and Basaran<sup>20</sup>) in particular near maximum and minimum drop deformations and are due to the differences in the time scale of vorticity diffusion from the solid surface and the time scale of rod motion. This out of phase motion between the rod and the liquid underneath the fluid interface has also been observed by Chen and Tsamopoulos<sup>21</sup> in the forced oscillations of liquid bridges.

Whereas the eigenfrequency of infinitesimal amplitude oscillations is independent of the disturbance amplitude, increasing the forcing amplitude decreases the resonance frequency<sup>20</sup>. The downward shift of the resonance frequency with increasing forcing amplitude shows that oscillating supported drops exhibit a *soft* nonlinearity.

Were surface tension, density, and rod radius held fixed, a change in  $Re$  reflects a change in the viscosity of the drop liquid. Figure 3 shows the effect of  $Re$  on the variation of the maximum aspect ratio achieved during steady oscillations,  $(a/b)_m$ , with forcing frequency when  $\alpha = 0$  and  $G = 0$  for drops that are forced to oscillate at a value of the forcing amplitude fixed at  $A = 0.10$ . As with simple systems such as the Duffing oscillator, the results highlighted show that as viscosity ( $Re$ ) decreases (increases), the drop deformation increases and the resonance frequency decreases. Figure 3 shows that oscillation modes, in particular modes other than the primary oscillation mode, become easier to detect as  $Re$  increases. Within the range of forcing frequencies examined, a second peak in  $(a/b)_m$  could not be detected for  $Re \leq 5$  and no peaks could be detected for  $Re = 1$ .

During nonlinear oscillations of supported drops, as  $Re$  increases the dissipation of energy by viscous forces decreases relative to the the input of kinetic energy into the drop due to the rod motion which manifests itself as an increase in fluid inertia. As in the case of increasing forcing amplitude discussed previously, one can think of this roughly as increasing the relative importance of forcing to damping. The soft nonlinearity of the system is once again made plain by Fig. 3, which shows that as the forcing to damping ratio increases, the observed peaks in deformation amplitude  $(a/b)_m$  are skewed to the left or lower values of the forcing frequency. It is well known for the Duffing oscillator that as the ratio of forcing to damping further rises, the ascending side of the Duffing profile can actually turn back on itself. This yields a range of forcing frequencies over which two stable limit cycles exist. This jump phenomenon, also known as hysteresis, is exhibited by many nonlinear systems. For example, DePaoli *et al.*<sup>22</sup> have reported experimental observations of hysteresis in drop response for pendant drops that are forced to oscillate by carrying out frequency sweeps in which the forcing frequency is first increased over a range and then decreased over the same range. By continuously varying the forcing frequency, DePaoli *et al.* were able to observe both limit cycles.

Next the response of pendant drops to frequency sweeps were studied. The effect of increasing forcing amplitude on the dynamics of a pendant drop at the highest value of  $Re$  shown in Fig. 3 was investigated. When the forcing amplitude was sufficiently small, the computed value of  $(a/b)_m$  for increasing values of  $\Omega$  was the same as that for decreasing values of  $\Omega$ . However, Fig. 4(a) shows that the drop response is hysteretic when the forcing amplitude is increased to 0.05. Fig. 4(b) shows the phase portraits of the drop in the plane of velocity of the drop tip ( $v_0$ ) versus position of the drop tip ( $f_0$ ) at the same value of the forcing frequency albeit the portrait on the left corresponds to the upward part of the sweep whereas the one on the right corresponds to the downward part of the sweep. The phase portraits of Fig. 4(b) plainly demonstrate the existence of two stable limit cycles.

#### 4. CONCLUSIONS AND OUTLOOK

The abruptness of the transition in drop deformation at a well defined value of the forcing frequency that is typical of hysteretic response offers a potentially highly accurate method for making physical property measurements with oscillating supported drops and liquid bridges although no attempt has heretofore been made to take advantage of such drop<sup>19</sup> or bridge response<sup>21</sup>.

Oscillating bubbles and drops are widely used in measuring dynamic surface tension of gas-liquid interfaces (see, e.g., Chang & Franses<sup>5,6</sup>). However, the underlying flow field is always simplified in these studies to facilitate the solution of the surfactant transport problem. The methods and results reported in this

paper form the necessary preliminaries for analyzing rigorously the combined problems of flow and surfactant transport in and around oscillating drops and bubbles for making improved dynamic surface tension measurements. Such analyses and the requisite accompanying experimental studies are now underway in our laboratory.

## REFERENCES

- <sup>1</sup>T. C. Scott and R. M. Wham, "Surface area generation and droplet size control in solvent extraction systems utilizing high intensity electric fields," U. S. Patent 4,767,515 (August 30, 1988).
- <sup>2</sup>K. J. Ptasiński and P. J. A. M. Kerkhof, "Electric field driven separations: phenomena and applications," *Sep. Sci. Technol.* **27**, 995 (1992).
- <sup>3</sup>M. T. Harris, T. C. Scott, and C. H. Byers, "Method and apparatus for the production of metal oxide powder," U. S. Patent 5,122,360 (June 16, 1992).
- <sup>4</sup>M. Strani and F. Sabetta, "Free vibrations of a drop in partial contact with a solid support," *J. Fluid Mech.* **141**, 233 (1984).
- <sup>5</sup>C-H. Chang and E. I. Franses, "An analysis of the factors affecting dynamic tension measurements with the pulsating bubble surfactometer," *J. Colloid Interface Sci.* **164**, 107 (1994).
- <sup>6</sup>C-H. Chang and E. I. Franses, "Dynamic tension behavior of aqueous octanol solutions under constant-area and pulsating-area conditions," *Chem. Eng. Sci.* **49**, 313 (1994).
- <sup>7</sup>R. Nagarajan and D. T. Wasan, "Measurement of dynamic interfacial tension by an expanding drop tensiometer," *J. Colloid Interface Sci.* **159**, 164 (1993).
- <sup>8</sup>C. A. MacLeod and C. J. Radke, "A growing drop technique for measuring dynamic interfacial tension," *J. Colloid Interface Sci.* **160**, 435 (1993).
- <sup>9</sup>X. Zhang, M. T. Harris, and O. A. Basaran, "Measurement of dynamic surface tension by a growing drop technique," *J. Colloid Interface Sci.* **168**, 47 (1994).
- <sup>10</sup>X. Zhang and O. A. Basaran, "An experimental study of dynamics of drop formation," *Phys. Fluids* **7**, 1184 (1995).
- <sup>11</sup>J. W. S. Rayleigh, "On the capillary phenomena of jets," *Proc. R. Soc. Lond., Ser. A*, **29**, 71 (1879).
- <sup>12</sup>H. Rodot, C. Bisch, and A. Lasek, "Zero gravity simulation of liquids in contact with a solid surface," *Acta Astronaut.* **6**, 1089 (1979).
- <sup>13</sup>C. Bisch, A. Lasek, and H. Rodot, "Comportement hydrodynamique de volumes liquides spheriques semi-libres en apesanteur simulée," *J. Méc. Théor. Appl.* **1**, 165 (1982).
- <sup>14</sup>C. Bisch, "Les modes de vibrations axiales et tangentielles d'une sphère semi-libre," *C. R. Acad. Sc. Paris* **293**, 107 (1981).
- <sup>15</sup>C. Bisch, "Axial and tangential vibrational modes for semi-free liquid spheres in microgravity nodal circles and nodal points position," *35th Cong. Intl. Astronautica Federation*, Paper No. IAF-84-138, Lausanne, Switzerland, 1984.
- <sup>16</sup>M. Strani and F. Sabetta, "Viscous oscillations of a supported drop in an immiscible fluid," *J. Fluid Mech.* **189**, 397 (1988).
- <sup>17</sup>N. E. Bixler and R. E. Benner, "Finite element analysis of axisymmetric oscillations of sessile liquid drops," *Proc. 4th Intl. Conf. Numer. Meth. Laminar Turbulent Flow* (Swansea, UK, 1985), p. 1336.
- <sup>18</sup>T. Tsukada, M. Sato, N. Imaishi, M. Hozawa, and K. Fujinawa, "A theoretical and experimental study on the oscillation of a hanging drop," *J. Chem. Eng. Japan* **20**, 88 (1987).
- <sup>19</sup>O. A. Basaran and D. W. DePaoli, "Nonlinear oscillations of pendant drops," *Phys. Fluids* **6**, 2923 (1994).
- <sup>20</sup>E. D. Wilkes and O. A. Basaran, "Forced oscillations of pendant (sessile) drops," submitted to *Phys. Fluids* (1996).
- <sup>21</sup>T-Y. Chen and J. A. Tsamopoulos, "Nonlinear dynamics of capillary bridges: theory," *J. Fluid Mech.* **255**, 373 (1993).
- <sup>22</sup>D. W. DePaoli, J. Q. Feng, O. A. Basaran, and T. C. Scott, "Hysteresis in forced oscillations of pendant drops," *Phys. Fluids* **7**, 1181 (1995).

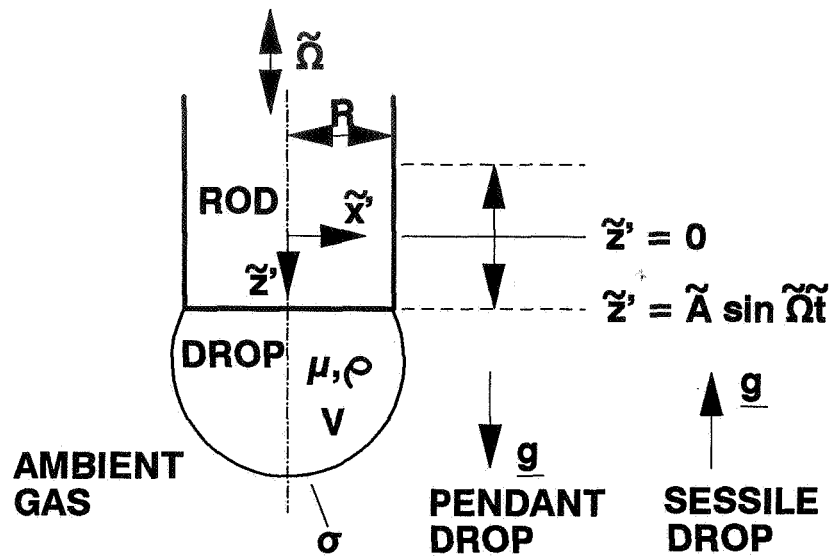


Figure 1. A liquid drop that is pendant from or sessile on a solid rod and undergoing forced oscillations in a vacuum or a gas of negligible density and viscosity.

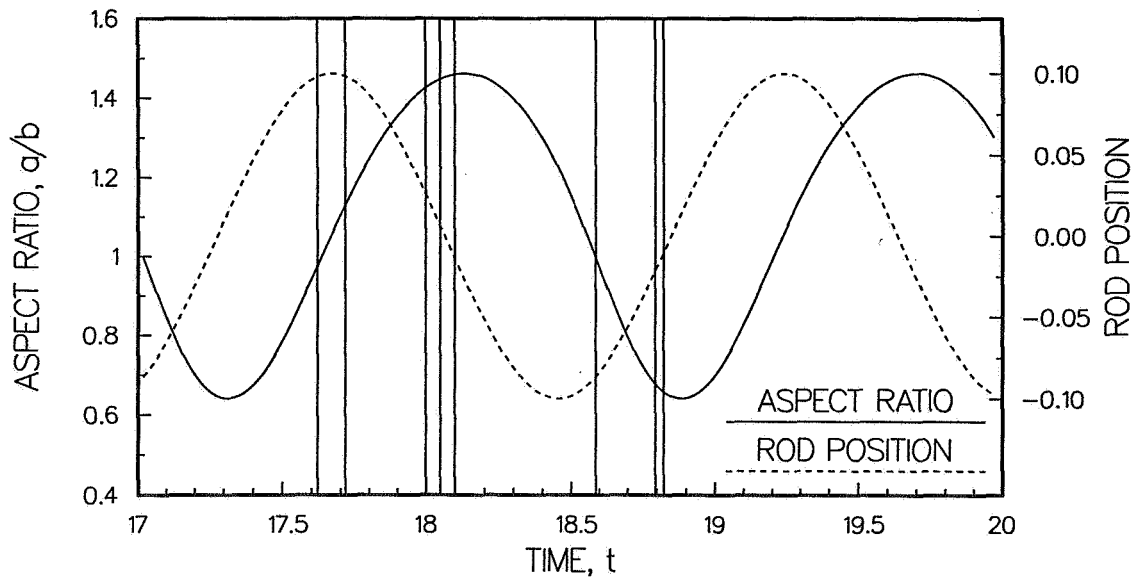


Figure 2. Variation in time of the drop aspect ratio and position of the rod tip. The vertical lines indicate times at which the flow field undergoes interesting transitions (see reference 20). For example, at  $t = 17.620$  and  $18.098$  fluid particles inside the drop are following the motion of the rod. However, due to finite inertia, at  $t = 17.717$  and  $18.588$ , some fluid particles are moving in the direction of the rod whereas others are moving in the opposite direction. At the remaining times, recirculating eddies are visible inside the drop.

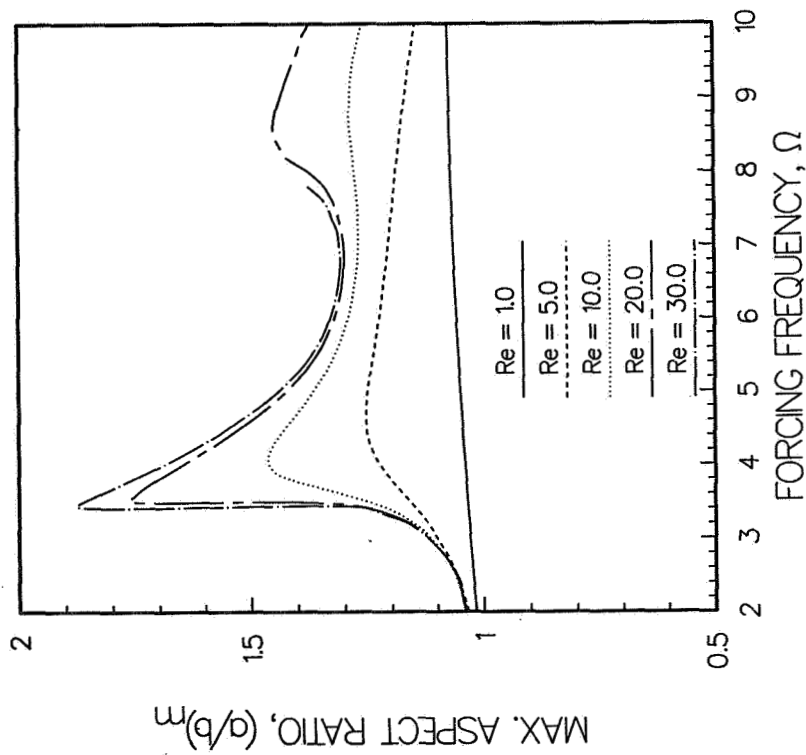
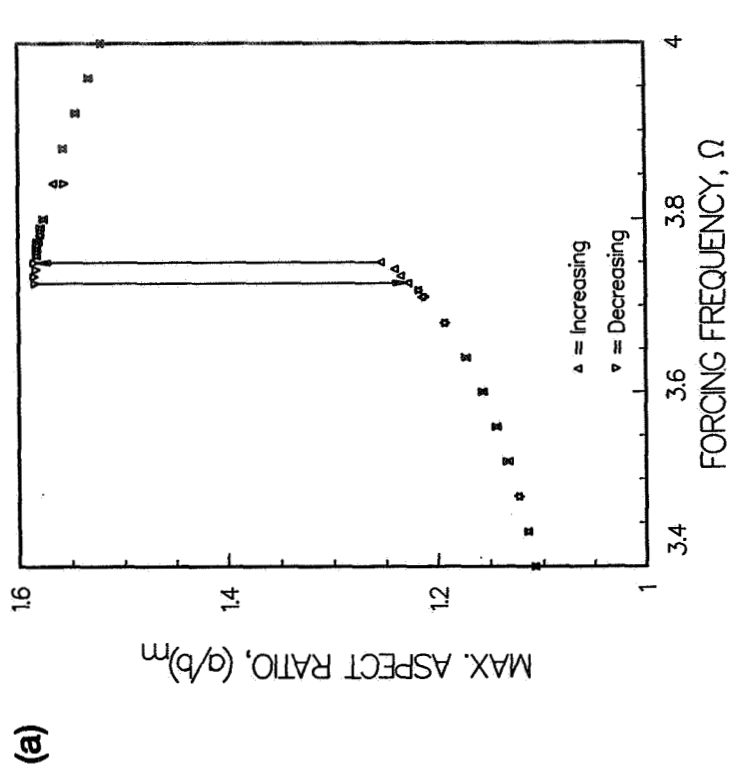


Figure 3. (Top) Effect of Reynolds number on the variation of the aspect ratio at maximum drop deformation during steady-state oscillations with the forcing frequency. The first resonance frequency equals 4.567 when  $Re=5$ , 4.079 when  $Re=10$ , 3.534 when  $Re=20$ , and 3.469 when  $Re=30$ .



(b)

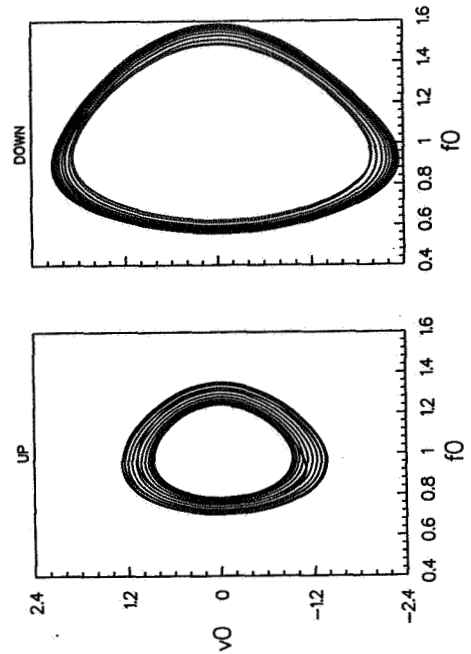


Figure 4. (Right) (a) Drop response to a frequency sweep. (b) Phase portraits at  $\Omega=3.742$ , showing the two limit cycles. In both (a) and (b),  $Re=30$ ,  $G=0$ ,  $\alpha=0$ , and  $A=0.05$ .

# THERMOCAPILLARY MIGRATION AND INTERACTIONS OF BUBBLES AND DROPS

R. Balasubramaniam  
NASA Lewis Research Center  
Cleveland, Ohio 44135

Claud E. Lacy<sup>1</sup>  
Box 5705  
Clarkson University  
Potsdam, New York 13699-5705

Günter Wozniak  
University of Freiberg, Germany

and

R. Shankar Subramanian  
Box 5705  
Clarkson University  
Potsdam, New York 13699-5705

## ABSTRACT

Results from experiments conducted in reduced gravity on the thermocapillary motion of bubbles and drops are discussed.

## INTRODUCTION

When a drop or bubble is placed in another fluid and subjected to the action of a temperature gradient, the drop will move [1]. Such motion is a direct consequence of the variation of interfacial tension with temperature, and is termed thermocapillary migration. The literature on both experimental and theoretical research in this field up to approximately 1989 has been adequately reviewed by Wozniak *et al.* [2] and Subramanian [3].

The movement of suspended objects such as drops and bubbles is relevant to situations that are likely to arise in low gravity experiments. Liquid drops may be encountered during the formation and solidification of alloys, and in separation processes such as extraction that might be used in long duration space voyages for recycling purposes. Also, a dispersion of vapor bubbles might be encountered in heat transfer fluids used in spacecraft which undergo phase change. Gas bubbles arise in crystallization where dissolved gases are rejected at the interface and also in separation processes such as gas absorption. In most applications, it is likely that a collection of drops or bubbles would be involved in which the individual members will influence the motion of each other, and also possibly coalesce leading to changes in size distributions over time.

The speed at which a drop migrates under the action of a temperature gradient can be obtained by solving the governing Navier-Stokes and energy equations along with the associated boundary conditions. When convective transport effects become important, the problems involved are nonlinear. The relative importance of convective transport of energy when compared to conduction can be judged from the magnitude of the Péclet number whereas a similar ratio for momentum transport is described by the Reynolds number,  $Re$ . When a velocity scale characteristic of thermocapillary migration is used, the Péclet number is known as the Marangoni number,  $Ma$ . The Capillary

---

<sup>1</sup>presently with Corning, Inc. Corning, New York 14831

number also is technically a parameter; however all observations to date involve no measurable deformation in shape. The relevant quantities are defined below.

$$Re = \frac{R v_o}{\nu}, \quad (1)$$

$$Ma = \frac{R v_o}{\kappa}. \quad (2)$$

Here,  $R$  is the radius of the drop or bubble,  $\mu$  is the dynamic viscosity of the continuous phase,  $\nu$ , its kinematic viscosity, and  $\kappa$ , its thermal diffusivity. The reference velocity,  $v_o$ , is defined below.

$$v_o = \frac{|\sigma_T| |\nabla T_\infty| R}{\mu}. \quad (3)$$

In the above,  $\sigma_T$  is the rate of change of interfacial tension with temperature, and  $\nabla T_\infty$ , the temperature gradient imposed in the continuous phase fluid.

In the linear limit when the Reynolds and Marangoni numbers are negligible, the contribution of thermocapillarity can be extracted from an experiment on the ground. Therefore, experiments designed to explore thermocapillary migration on the ground are subject to this important limitation; some of this experimental work is discussed in the above two reviews.

To fully explore the parameter space in the Reynolds and Marangoni numbers, investigators have attempted to carry out experiments in reduced gravity conditions. The literature is discussed in Balasubramaniam *et al.* [4]. The previous studies were subject to many limitations which raise questions regarding the utility of the data. Therefore, we performed thermocapillary migration experiments in reduced gravity under conditions closer to those assumed in theoretical models. The experiments were carried out aboard the IML-2 mission of the NASA Space Shuttle in the summer of 1994. Here a brief summary of the experiments is given. For more details, the reader is referred to [4].

## EXPERIMENTAL APPARATUS AND PROCEDURE

The experiments were performed in an apparatus labeled the BDPU (Bubble, Drop, Particle Unit) which was provided by the European Space Agency through a cooperative arrangement with the National Aeronautics and Space Administration. The apparatus consists of a "facility" which provided power, optical diagnostics and illumination, imaging facilities including a video camera and a motion picture camera, and other sundry support services. Within this facility, a test cell that was specific to the experiment was inserted by the payload specialist on the Shuttle when needed.

Conceptually, the experiments were simple. Within a test cell mounted in the facility and filled with a suitable liquid, a temperature gradient was established, followed by the introduction of a bubble or a drop as desired. The subsequent motion of the object, in the direction of the applied temperature gradient, was recorded for later analysis on videotape on the ground as well as on cine film on board the Shuttle in selected experiments. When a bubble or drop reached the hot wall, it was extracted and another was introduced after a small waiting period.

The heart of the experimental apparatus is the test cell shown schematically in Figure 1. Two rectangular test cells were available. Both were of identical dimensions, measuring 60 x 45 x 45 mm in the interior. This cavity was filled with a Dow-Corning DC-200 series silicone oil of nominal viscosity 50 centistokes in both cells. It was possible to maintain the two end walls (made of aluminum) in the long dimension of the cell at fixed known temperatures so that a temperature



gradient could be established in the z-direction. Within the cavity, an injection needle was available when needed. When not in use, the tip was flush with the cold aluminum surface at its center. It was possible to introduce air bubbles in one test cell, and Fluorinert FC-75 drops in the other cell. The diameters of the bubbles varied from approximately 2.1 mm to 14.8 mm, and those of drops ranged from 2.0 to 14.4 mm. After a bubble or drop completed its traverse, it was possible to extract it from the hot wall using an extraction tube mounted at the center of a net.

The equipment provided white background illumination and the opportunity to capture images of the interior of the test cell on videotape on the ground. Also, a limited amount of cine film was available, and was used to capture images during selected runs at 18 frames per second.

In any given run, the procedure was first to establish the desired temperature gradient over a period of 2 hours. This was followed by the injection, traverse, and subsequent extraction of a bubble or drop. This process was repeated until the allotment of real-time video capability was exhausted. The entire procedure was performed six times permitting the use of different temperature gradients, and allowing a total of approximately 6 hours of observation time. A total of 22 bubbles and 98 drops were recorded on videotape, and 16 of the bubbles and 65 of the drops on cine film. About one-third of the data were on isolated drops or bubbles. Multiple objects were encountered in most of the remaining runs. From the latter, a few usable runs on pairs of drops were identified; data on a representative pair will be presented and discussed in the next section.

## RESULTS AND DISCUSSION

### Isolated Bubbles and Drops

We observed from the data that the bubbles and drops were spherical to within the uncertainty of the diameter measurements made. Only one velocity per traverse, evaluated at a suitable location, is reported. Typically, the bubble or drop achieved a quasi-steady velocity, to within the uncertainty of our velocity measurements, after moving about half a radius from the injection location. To be conservative, we report data only when the object has moved at least one radius.

In Figure 2, the velocity data on isolated air bubbles are plotted in scaled form and compared with available predictions. The velocity of a bubble is scaled using the velocity it would have in the limit of negligible values of the Reynolds number and the Marangoni number. The various physical properties are evaluated at the estimated temperature in the undisturbed fluid at the x-y plane containing the center of the bubble. Typical uncertainty estimates are shown in the figure.

Included in the drawing for comparison is a theoretical prediction originally presented by Balasubramaniam and Lavery [5] who solved the governing momentum and energy equations for the quasi-steady velocity and temperature fields and bubble velocity when the Reynolds and Marangoni numbers are not negligible. The authors also assumed a spherical bubble in an infinite extent of fluid, and Newtonian and incompressible flow with constant physical properties, except for the interfacial tension which was assumed linear with temperature. Their finite difference code was used to develop the predictions shown. The Prandtl number varied between 370 and 575 in the bubble runs because of the change in temperature. The actual curve was prepared from theoretical predictions for a Prandtl number of 370, but the predictions are not very sensitive to the Prandtl number in the above range. Also included is the prediction of Balasubramaniam and Subramanian in the asymptotic limit of large Marangoni number for negligible Reynolds number.

It is evident from Figure 2 that the data support the qualitative trend predicted from the quasi-steady theory with the following discrepancies noted. First, for small values of Ma in the

approximate range 5 to 10, the observed velocities are significantly larger than those predicted. Second, while the four data points at values of Marangoni number between 250 and 800 are distributed around the asymptote for large values of  $Ma$ , it is not evident that the overall trend of the data is to achieve this asymptotic behavior; clearly we need to extend the observations to larger values of the Marangoni number for making a definitive statement. The discrepancies may be attributed to a variety of reasons which are discussed in [4]. The most plausible explanation appears to be that interactions of the walls with the migrating bubbles via the temperature fields can account for the observation.

In Figure 3, we show a drawing similar to Figure 2, but for Fluorinert FC-75 drops. These data display a trend very similar to that shown by bubbles in Figure 2. The reference velocity is once again the predicted velocity at negligible values of Reynolds and Marangoni number from Young *et al.*. Note the asymptotic trend displayed by the scaled velocity at values of  $Ma \geq 100$ . We do not have a theoretical prediction in this case so that no statements can be made with respect to agreement with predictions or lack thereof. The behavior of the scaled velocity as  $Ma$  approaches small values is similar to that observed in the case of bubbles. The curve shown in the figure is a fitted result and does not represent a prediction.

### Interacting Drops

A few usable runs were performed on pairs of Fluorinert drops. In these, the leading drop was smaller than the trailing drop. It was observed that the leading drop moved at approximately the velocity it would have if isolated, but the trailing drop was found to move at a reduced velocity compared to the value it would have if isolated. This remarkable observation can be explained qualitatively by recognizing the existence of a thermal wake behind the leading drop in which temperature gradients are weakened. The trailing drop moves into this region and therefore experiences a reduction in the driving force for its motion. We intend to explore this phenomenon in more detail and also extend the range of parameters obtained in IML-2 in follow-on flight experiments scheduled for conduct on the LMS mission of the Space Shuttle in summer 1996.

### CONCLUDING REMARKS

Results from observations made on isolated bubbles and drops moving in a temperature gradient in a space laboratory are reported. The results for the migration velocity of air bubbles qualitatively confirm the trend predicted by a theoretical model, but there are quantitative discrepancies. Some tentative explanations are offered to account for these discrepancies. The data for drops display similar trends. Experiments on pairs of drops revealed the remarkable feature that a small leading drop, which itself appears unaffected in its motion, can significantly influence the motion of a larger trailing drop almost twice its diameter. It is conjectured that this is a consequence of the thermal wake behind the leading drop.

### ACKNOWLEDGMENTS

The work described herein was supported by NASA's Microgravity Sciences and Application Division through NASA Grants NAG3-1122 and NAG3-1470 from the Lewis Research Center to Clarkson University. Also, support by the German Space Agency (DARA) through DARA Grant 50WM9434 to G. Wozniak is gratefully acknowledged.

### References

- [1] N. O. Young, J. S. Goldstein, and M. J. Block: The motion of bubbles in a vertical temperature

gradient, *J. Fluid Mech.*, Vol. 6, 1959, pp. 350-356.

- [2] G. Wozniak, J. Siekmann, and J. Srulijes: Thermocapillary Bubble and Drop Dynamics Under Reduced Gravity — Survey and Prospects, *Z. Flugwiss. Weltraumforsch.*, Vol. 12, 1988, pp. 137-144.
- [3] R. S. Subramanian: The Motion of Bubbles and Drops in Reduced Gravity, in *Transport Processes in Bubbles, Drops, and Particles*, edited by R. Chhabra and D. De Kee, Hemisphere, New York, 1992, pp. 1-41.
- [4] R. Balasubramaniam, C.E. Lacy, G. Wozniak, and R.S. Subramanian: Thermocapillary Migration of Bubbles and Drops at Moderate Values of the Marangoni Number in Reduced Gravity, *Phys. Fluids*, Vol 8, No. 4, 1996, pp. 872-880.
- [5] R. Balasubramaniam and J. E. Lavery: Numerical Simulation of Thermocapillary Bubble Migration Under Microgravity for Large Reynolds and Marangoni Numbers, *Num. Heat Transfer A*, Vol. 16, 1989, pp. 175-187.

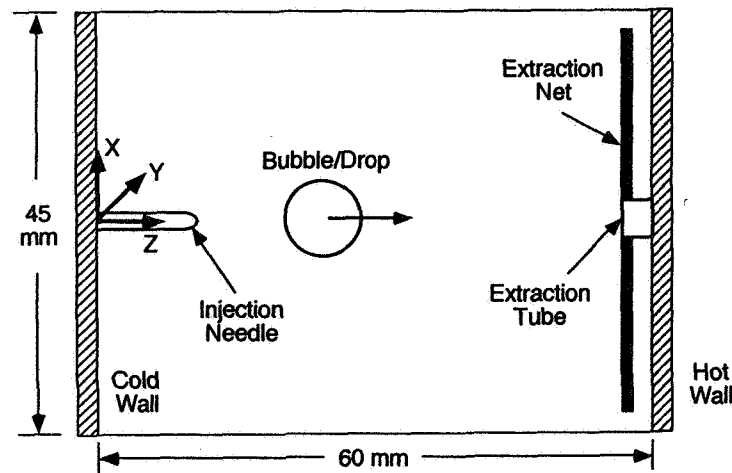


Figure 1. Sketch of test cell

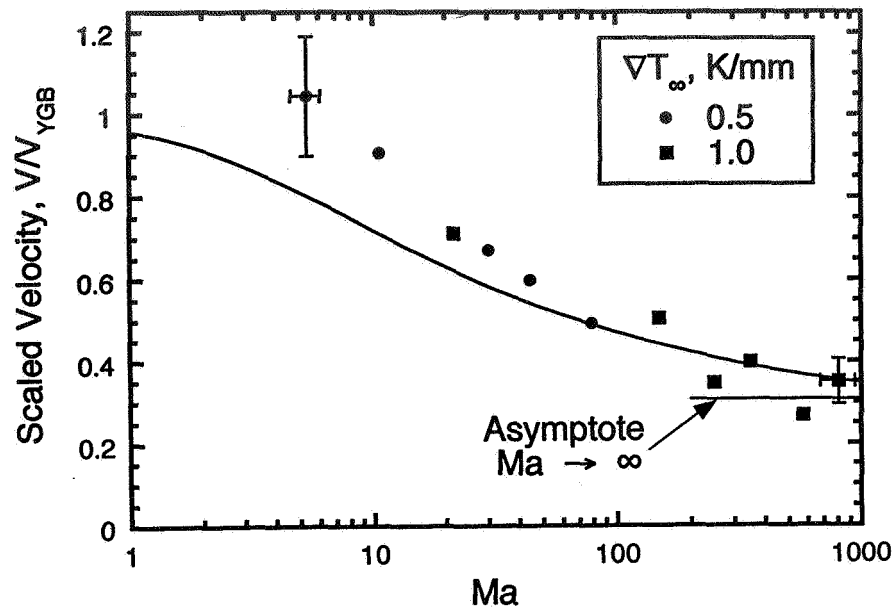


Figure 2. Scaled velocity of the bubbles versus the Marangoni number. The solid curve represents predictions from a numerical solution. The horizontal solid line is from a prediction for negligible Reynolds number and  $Ma \rightarrow \infty$  based on asymptotic analysis.

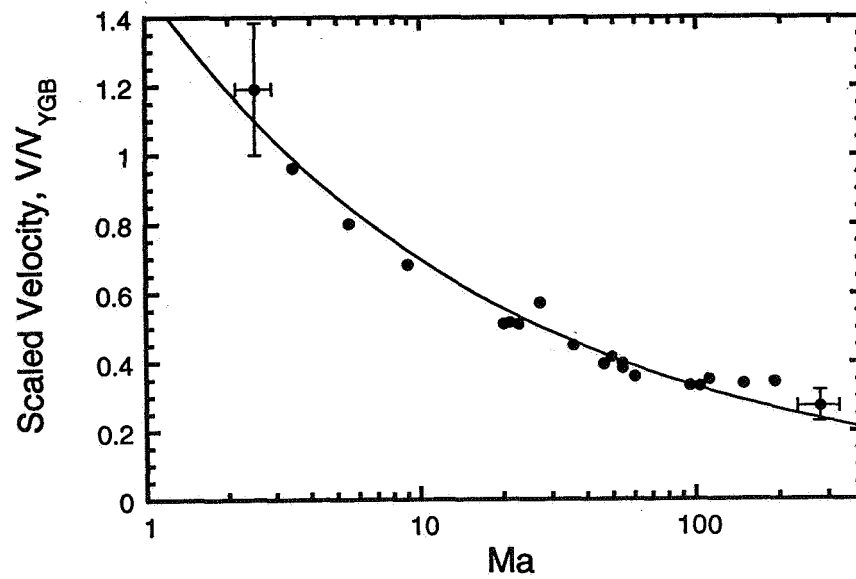


Figure 3. Scaled velocity of the Fluorinert FC-75 drops versus the Marangoni number. The solid curve represents an empirical curve fit of the data.

# STUDIES OF THE STABILITY AND DYNAMICS OF LEVITATED DROPS

A.V. Anilkumar, C.P. Lee, and T.G. Wang  
Center for Microgravity Research and Applications  
Vanderbilt University  
Nashville, TN 37235, U.S.A.

## ABSTRACT

This is a review of our experimental and theoretical studies relating to equilibrium and stability of liquid drops, typically of low viscosity, levitated in air by a sound field<sup>1,2,3</sup>. The major emphasis here is on the physical principles and understanding behind the stability of levitated drops. A comparison with experimental data is also given, along with some fascinating pictures from high-speed photography. One of the aspects we shall deal with is how a drop can suddenly burst in an intense sound field; a phenomenon which can find applications in atomization technology. Also, we are currently investigating the phenomenon of suppression of coalescence between drops levitated in intense acoustic fields.

## INTRODUCTION

In the past two decades, or so, acoustic levitation has gained prominence as a way to manipulate liquid samples in the microgravity environment of Space [4,5,6,7]. This is where the interest in the study of interactions between drops and sound arises. The central question is what happens when a liquid drop is introduced into a standing sound field.

The simplest interaction between the drop and the sound field is the force on the drop. If the drop surface is assumed to be rigid, then the force on the drop [8] is the summation of the normal force acting on the surface due to acoustic radiation pressure  $\langle \delta p \rangle$ , where [9,10]

$$\langle \delta p \rangle = \frac{\langle p'^2 \rangle}{2\rho_0 c_0^2} - \frac{\rho_0 \langle \mathbf{u} \cdot \mathbf{u} \rangle}{2}, \quad (1)$$

$p'$  is the acoustic pressure,  $\mathbf{u}$  is the particle velocity,  $\rho_0$  and  $c_0$  are the density and speed of sound of the ambient air, and  $\langle \rangle$  denotes average over an acoustic cycle.

A more complex kind of drop-sound interaction is the deformation of the liquid drop due to the acoustic radiation stress. This is resisted by the drop through its surface tension. The static deformation is described by the Young-Laplace equation

$$P_I - \langle \delta p \rangle = \sigma \nabla \cdot \mathbf{n}, \quad (2)$$

where  $\sigma$  is surface tension,  $P_I$  is the internal liquid pressure, and  $\nabla \cdot \mathbf{n}$  represents the total curvature of the drop surface [11]. Let us consider a drop, of spherical radius  $R_s$ , to be at the pressure node of a plane wave  $p' = A \sin kz \cos \omega t$ , where  $A$  is the pressure amplitude,  $k$  is the wavenumber,  $\omega$  is the angular frequency,  $z$  is the axial position and  $t$  is the time. For small amplitude  $A$ , the shape of the drop is given by [12,13]

$$f(\theta) = R_s \left[ 1 - \frac{3}{32} B_a \left( 1 + \frac{7}{5} \alpha^2 \right) P_2(\theta) \right], \quad (3)$$

where  $B_a = R_s A^2 / \sigma \rho_0 c_0^2$  is the acoustic Bond number,  $\alpha = k R_s < 1$  represents the spherical radius of the drop scaled by the acoustic wavelength  $\lambda = 2\pi/k$ , and  $P_2$  is a Legendre polynomial. Moderately larger static deformations have been studied numerically by expansion of the drop shape in Legendre polynomials [14]. Also, acoustic deformation can be an excitation source for drop oscillations, if the deforming sound field is modulated in amplitude, near a resonant frequency of the capillary oscillations of the drop [12,15].

## EXPERIMENTAL OBSERVATIONS

A common approach to ground-based study of liquid drops is to levitate a millimeter-sized drop in a single-axis acoustic levitator, which consists of a transducer at the bottom and a reflector at the top, providing a standing sound field that vibrates vertically and falls off laterally. It is known that the levitated drop ends up disintegrating in a burst if the sound pressure level (SPL) is raised too high [16]. Our goal is to understand why, when, and how the burst can occur. The first step is to study the phenomenon in detail, using high-speed photography. The observations are described as follows [1,2].

All drops levitated in a sound field become more flattened with increasing SPL, progressively attaining oblate spheroidal, and then flat disk shapes. Their subsequent evolution and stability can be differentiated based on their initial size. Two limiting scenarios can be identified. Whenever the drop is acoustically small ( $\alpha \leq 0.3$ ), flattening cannot exceed a critical point, beyond which the drop disintegrates. The manner of disintegration is a sudden horizontal expansion, in which the drop is pulled apart at the periphery (Fig.1). Acoustically large drops ( $\alpha \geq 0.5$ ), on the other hand, can sustain equilibrium beyond the critical point by actively lowering the sound pressure level in the levitator. A large flattened drop is an efficient scatterer of the acoustic wave and can induce a sufficiently large resonance frequency shift in the system, causing the levitator to lose power [17]. The SPL in the levitator first increases with flattening, as expected, but then decreases with flattening beyond the critical point. Here, the drop becomes concave and eventually drastically flattened to the point where the drop has a meridional cross-section resembling a dogbone, with a membrane in the middle surrounded by a donut-shaped periphery (fig. 2). Drops of intermediate size ( $0.3 \leq \alpha \leq 0.5$ ) lose equilibrium beyond the critical point and show sudden horizontal expansion, but they return to equilibrium following sufficient lowering of the sound pressure level through resonance frequency shift.

On continued flattening, the central membrane of a large drop may eventually buckle upward, with the ring-shaped periphery contracting and closing, leading to violent shattering (Fig.2 f,g,h). The buckling is always upward, such that it has to be related to the presence of gravity. For all low-viscosity drops, like water drops, as the central membrane vibrates in the sound field capillary ripples are excited parametrically on it. Here, unless buckling instability occurs first, the ripples become so intense that satellite droplets are ejected vertically in both directions. This phenomenon is conventionally referred to as atomization. For small drops, on the other hand, atomization takes place near the edge, during the sudden horizontal expansion, and is inherently nonsteady. A highly viscous drop does not atomize, by this route, because any ripple would be heavily suppressed by viscosity.

## STATIC EQUILIBRIUM

To understand these complex drop-sound interactions, the natural thing to do is to understand the equilibrium of the system, then find out when the system becomes unstable [1,2,3]. The poles of the drop are stagnation points of the oscillating flow of the sound field. In these regions, according to eq.(1), the radiation stress comes mostly from the acoustic pressure and is positive. At the equator, on the other hand, the particle velocity is most intense. The radiation stress here comes mostly from the particle velocity and is negative. The drop shape is determined by the compressive stress at the poles, the suction stress at the equator, together with surface tension, and the constant internal pressure inside the drop. When the central membrane is thin enough, it vibrates with sound a little. In our cases of interest, the vibration is not strong enough to significantly violate the rigid wall boundary condition. The membrane vibration leads to a Bernoulli correction in the internal pressure. The equilibrium shape, as a consequence of all these forces, changes from an oblate spheroid to one with flat poles, and then to one with concave poles.

Mathematically, the difficulty with the problem of a drastically deformed drop is that the drop shape depends on the wave, but the wave also depends on the shape. To handle the problem in a self-consistent manner, we have used a boundary integral method for solving the Helmholtz equation for the wave [3,18], given the shape. Then we use the resulting radiation pressure to solve for the shape using eq.(2). The two procedures are repeated alternatively until both the wave and the shape converge to their respective forms.

For a given drop size  $\alpha$ , if we plot the acoustic Bond number  $B_a$  versus the non-dimensional equatorial radius  $R^*$  ( $R^*=R/R_g$ ,  $R$ : equatorial radius), we find that  $B_a$  rises with  $R^*$  to a maximum, and then decreases with  $R^*$ , schematically as shown by the solid curve in Fig.3. Correspondingly, the SPL increases to a maximum and then decreases with flattening, in agreement with the observation for large drops. A large drop can bring about a downturn in SPL because it can easily induce the necessary resonant frequency shift. Therefore it stays on the solid equilibrium curve until buckling instability, or atomization, occurs. An intermediate sized drop has to expand sufficiently, before it can bring about the necessary lowering in sound intensity, to be on the equilibrium curve. Therefore the drop follows curve 1 (fig. 3) which jumps from the equilibrium curve, but returns to it later. A small drop on the other hand, cannot bring about a significant power loss by resonant frequency shift during expansion. Hence it follows a curve like 2 (fig. 3) to disintegration.

A typical  $B_a$ - $R^*$  curve for a large drop is shown in Fig.4, showing good agreement with experiment. When the central membrane of a large drop vibrates, the internal pressure in the membrane cannot be lowered much because the surface curvature of a thin membrane is close to zero. Thereby, the internal pressure has to be close to the external radiation pressure. The Bernoulli effect, due to membrane vibration, is manifested in the relative raising of the liquid pressure in the ring-shaped periphery. This tips the force balance at the edge, such that the drop loses equilibrium at a lower flattening than that for which central membrane does not vibrate. If the drop is viscous, vibration of the membrane is spread into the periphery too, such that Bernoulli effect is effectively nullified and can be ignored. The point here is that a viscous drop can be flattened more than a inviscid drop because of the absence of Bernoulli effect due to membrane vibration. This is consistent with experimental observations.

The actual occurrence of the downturn of the  $B_a$ - $R^*$  curve depends on the active involvement of the levitator. In practice, we may be more concerned with drops that are too small to cause any power loss, or a sound system that is too strong to allow for a significant power loss. Hence the peak of a  $B_a$ - $R^*$  curve is important because it represents the maximum sound intensity and maximum deformation a drop of size  $\alpha$  can sustain. In Fig.5, we plot the maximum  $B_a$ , denoted by  $B_{a,cr}$ , and the corresponding  $R^*$ , denoted by  $R_{cr}^*$ , versus  $\alpha$ . Experimental data are also displayed for comparison, showing good agreement between the two.

## INSTABILITIES

On the downturn side of the equilibrium curve (fig. 3), a large drop will lose equilibrium at the edge, beyond a certain degree of flattening. But before the drop reaches this point, instabilities will occur. These can be either: (i) the buckling instability [1] or, (ii) the parametric instability that gives rise to the ripples and the subsequent atomization [2, 19].

Buckling instability is explained as follows. When a drop is drastically flattened such that the membrane is thin enough to be forced into vibration, like a drumhead by the sound field, a dynamic pressure arises. The latter is given by  $\rho \langle v^2 \rangle / 2$ , where  $\rho$  is the density of the liquid, and  $v$  is the vibration velocity of the membrane. This pressure tends to push the liquid toward the periphery. If equilibrium is to be maintained, the hydrostatic pressure in the membrane has to become lower, as dictated by Bernoulli law. But the membrane surfaces are almost flat, such that there is limited room for readjustment. The membrane becomes more susceptible to acoustic vibration as it gets thinner with flattening. Ultimately, there is a point beyond which the hydrostatic pressure in the membrane can no longer withhold the dynamic pressure. If the membrane is perfectly symmetric about its mid-surface, there is still the relatively higher hydrostatic pressure in the thick periphery to contain the membrane liquid. But in the presence of gravity, the membrane is slightly buckled upward, to start with. In this case, the dynamic pressure can cause the membrane to expand and buckle upward, as shown in Fig.2 (f,g,h).

For a low viscosity drop, capillary ripples can be excited on the membrane through parametric instability, when the membrane vibrates in the sound field (frequency  $\omega$ ). In general, there can be two wave modes: a symmetric wave (frequency  $\omega_s$ ) in which the two surfaces vibrate in opposite directions, and an antisymmetric wave (frequency  $\omega_a$ ) in which they vibrate in the same direction [20]. For a vibrating membrane, of a given thickness, the wavelength of the disturbance is determined as a consequence of parametric instability [2,19]. Parametric excitation of a wavelength can occur only when the wavelength satisfies the synchronism condition:  $\omega = \omega_s + \omega_a$ . When the membrane is thick

$\omega_a = \omega_s = \omega/2$ , and the waves are known as Faraday ripples. When the ripples grow violent, they spit out satellite droplets as in conventional atomization. When the membrane is thin,  $\omega_a$  is much larger than  $\omega_s$ . A thin film will shatter as ripples grow because it will snap wherever its two surfaces come into contact. If a drop is very viscous, then ripples are suppressed. The easier route for a viscous drop to fragment is through a sudden horizontal expansion, in which the membrane is stretched so thin that it has to rupture and shatter due to van der Waals forces.

## CLOSING COMMENTS

In this article, we have addressed the issue of equilibrium and stability of a liquid drop, when introduced into an intense sound field. This complex problem has been primarily presented in a physical way, substantiating it with clear photographic evidence and a simple theoretical framework employing the acoustic Bond number and the drop equatorial radius ( $B_a$ - $R^*$  curve). Presently, we are trying to understand the mechanism of suppression of coalescence of drops in intense acoustic fields. Normally, when two drops are introduced into a levitating field, they coalesce to form a single drop. However, whenever the intensity of the acoustic field is high, the two drops do not coalesce, but instead form a stable doublet (fig. 6 a,b). They seem to contact along a line, and their contacting surfaces display a knife-edge feature. The reason for this stability has probably to do with the nature of the vibrating air flow in the narrow strait between the drops, and needs to be well understood<sup>21</sup>. The stable doublet can be rotated as a rigid body, without the two drops separating. The drops coalesce only when the intensity of the levitating field is reduced, thereby making the drops less flattened and more spherical.

## ACKNOWLEDGEMENTS

The work described in this article was carried out at the Center for Microgravity Research and Applications at Vanderbilt University, under funding by the Microgravity Science and Applications Division of the National Aeronautics and Space Administration. Figures 1 - 4 have been reproduced with permission of the Physics of Fluids journal, a publication of the American Institute of Physics.

## REFERENCES

1. Lee, C.P., Anilkumar, A.V., & Wang, T.G. 1991, Phys. Fluids A3, 2497.
2. Anilkumar, A.V., Lee, C.P., & Wang, T.G. 1993, Phys. Fluids A5, 2763.
3. Lee, C.P., Anilkumar, A.V., & Wang, T.G. 1994, Phys. Fluids 6, 3554.
4. Wang, T.G. 1979, In: IEEE, Ultrasonic Symposium Proceedings, page 471.
5. Wang, T.G., Anilkumar, A.V., Lee, C.P., & Lin, K.C. 1994, J. Fluid Mech. 276, 389.
6. Wang, T.G., Anilkumar, A.V., Lee, C.P., & Lin, K.C. 1994, J. Colloid Interface Sci. 165, 19.
7. Wang, T.G., Anilkumar, A.V., & Lee, C.P. 1996, J. Fluid Mech. 308, 1.
8. King, L.V. 1934, Proc. R. Soc. Lond. A147, 212.
9. Beyer, R.T. 1974, Nonlinear Acoustics, Naval Ship Systems Command, Department of the Navy.
10. Lee, C.P. & Wang, T.G. 1993, J. Acoust. Soc. Am. 94, 1099.
11. Lamb, H. 1945, Hydrodynamics, Dover, sixth edition.
12. Marston, P.L. 1980, J. Acoust. Soc. Am. 67, 15.
13. Trinh, E.H. & Hsu, C.J. 1986, J. Acoust. Soc. Am. 79, 1335.
14. Tian, Y., Holt, R.G., & Apfel, R.E. 1993, J. Acoust. Soc. Am. 93, 3096.
15. Marston, P.L. & Apfel, R.E. 1980, J. Acoust. Soc. Am. 67, 27.
16. Lierke, E.G., Leung, E.W., & Luhmann, D. 1988, In: Wang, T.G. (editor), AIP Conference Proceedings 197, Drops and Bubbles Third International Colloquium, Monterey, California, pg. 71.
17. Leung, E., Lee, C.P., Jacobi, N., & Wang, T.G. 1982, J. Acoust. Soc. Am. 72, 615.
18. Batchelor, G.K. 1967, An introduction to Fluid Dynamics, Cambridge.
19. Danilov, S.D. & Mironov, M.A. 1992, J. Acoust. Soc. Am. 92, 2747.
20. Taylor, G.I. 1959, Proc. R. Soc. Lond. A253, 296.
21. Dell'Aversana, P., Banavar, J.R., and Koplik, J. 1996 Phys. Fluids 8, 15.



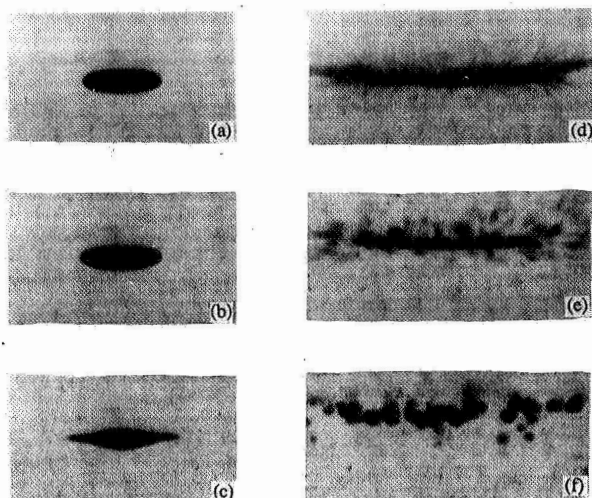


Fig. 1 The side view of a small water drop ( $\alpha=0.2$ ): (a) being flattened, (b) its rim getting sharper, (c) rim developing into a knife-edge, (d,e) expanding horizontally and instability occurring along the outermost edge, and (f) final breakup.

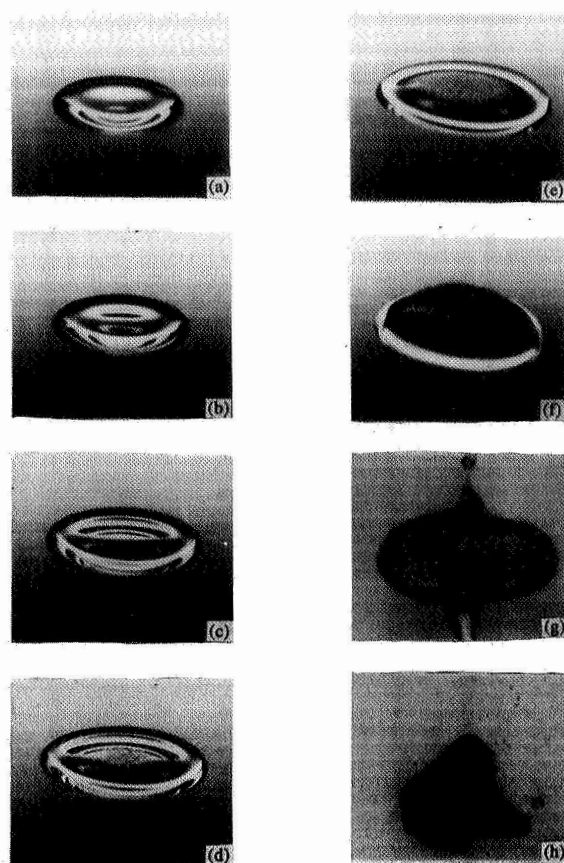


Fig. 2. The evolution of a large water drop ( $\alpha=0.8$ ) levitated in an acoustic field with increasing intensity: (a) being flattened and slightly dimpled, (b,c) becoming concave, (d,e) ripples formed on the central membrane, spreading throughout the latter, (f) buckling upward, (g) ballooning with two jets shooting in opposite directions at the bottom part that has just been closed, and (h) final breakup.

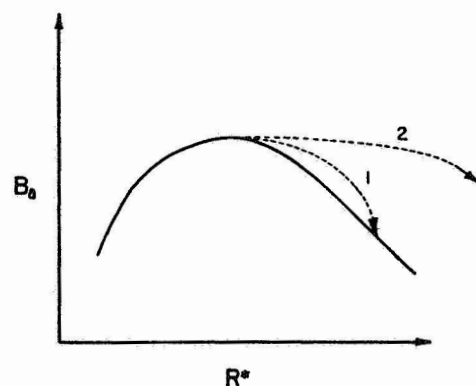


Fig. 3. Responses of a levitated drop to a continuous increase in input sound intensity.

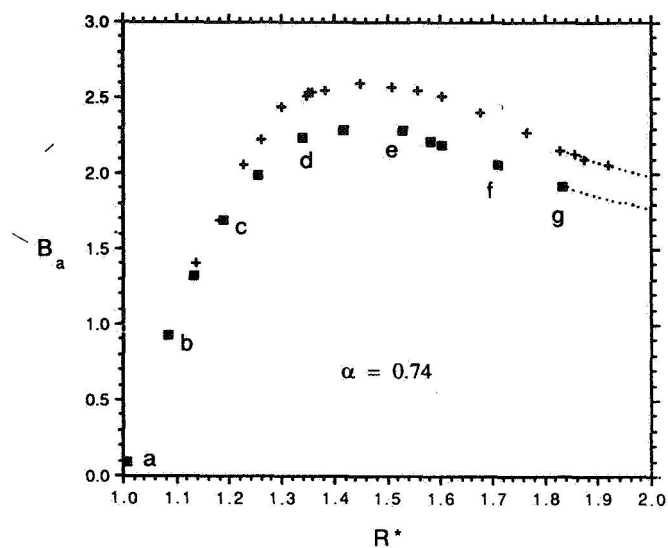


Fig. 4. Plot of  $B_a$  vs  $R^*$  for a water drop with  $\alpha=0.74$ . The crosses are experimental data and the solid squares are theoretical data. The dotted curves are asymptotic forms given by  $B_a=B_m^*/R^*$ , where  $B_m^*=3.52$  for the theory and 3.95 for the experiment.

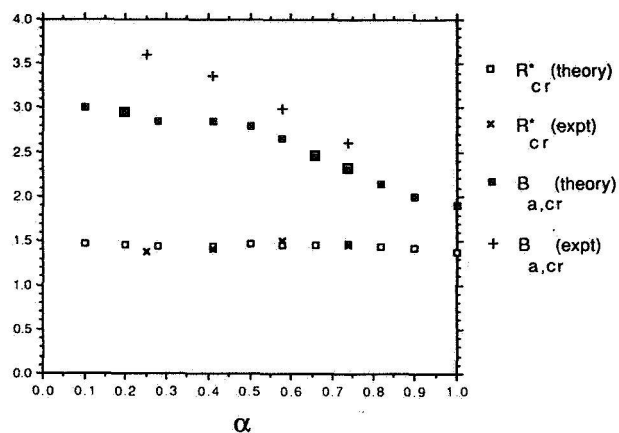


Fig. 5. The maximum  $B_a$  of the  $B_a$ - $R^*$  curve, denoted by  $B_{a,cr}$ , and the corresponding  $R^*$ , denoted by  $R_{cr}^*$ , for a range of  $\alpha$ . Theoretical data are given by squares and experimental data are given by crosses.

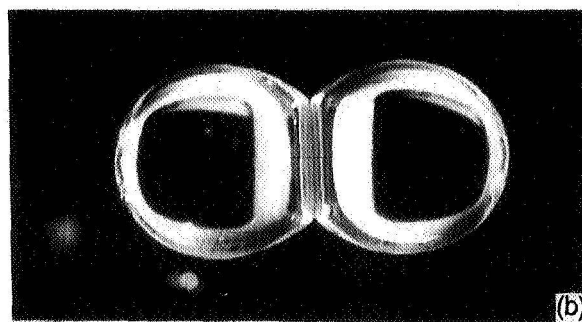
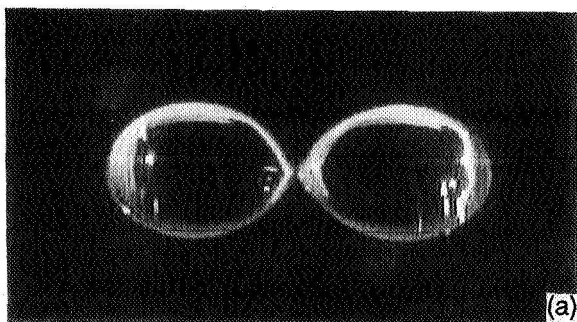


Fig. 6. Side (a) and top (b) views of a stable non-coalescing doublet in intense acoustic field.

# NONLINEAR BUBBLE INTERACTIONS IN ACOUSTIC PRESSURE FIELDS

Tiberiu Barbat, Nasser Ashgriz, Ching-Shi Liu  
Department of Mechanical and Aerospace Engineering  
State University of New York at Buffalo  
Buffalo, New York 14260

## I. INTRODUCTION

The systems consisting of a two-phase mixture, as clouds of bubbles or drops, have shown many common features in their responses to different external force fields. One of particular interest is the effect of an unsteady pressure field applied to these systems, case in which the coupling of the vibrations induced in two neighboring components (two drops or two bubbles) may result in an interaction force between them. This behavior was explained by Bjerknes [1] by postulating that every body that is moving in an accelerating fluid is subjected to a "kinetic buoyancy" equal with the product of the acceleration of the fluid multiplied by the mass of the fluid displaced by the body. The external sound wave applied to a system of drops/bubbles triggers secondary sound waves from each component of the system. These secondary pressure fields integrated over the surface of the neighboring drop/bubble may result in a force additional to the effect of the primary sound wave on each component of the system. In certain conditions, the magnitude of these secondary forces may result in significant changes in the dynamics of each component, thus in the behavior of the entire system. In a system containing bubbles, the sound wave radiated by one bubble at the location of a neighboring one is dominated by the volume oscillation mode and its effects can be important for a large range of frequencies. The interaction forces in a system consisting of drops are much smaller than those consisting of bubbles. Therefore, as a first step towards the understanding of the drop-drop interaction subject to external pressure fluctuations, it is more convenient to study the bubble interactions.

Effects of the secondary Bjerknes forces are reported in a study concerning cavitation by Kornfeld and Suvorov [2]. They describe a strange zig-zag motion of the bubbles ("dancing bubbles") near the surface of an oscillating piston, driven at high frequencies. The phenomenon received only a qualitative explanation, based on the instability of the motion dominated by the inertia forces. Crum [3] studies experimentally the interaction between air bubbles immersed in water contained by an oscillating vessel. The vessel is driven at low frequencies (60 Hz) by a mechanical shaker. The ambient pressure is reduced below atmospheric conditions in order to increase the natural frequency of volume oscillations of the bubbles. He provides also an simple model for the relative motion of the bubbles, using a first approximation for the sound field radiated by one bubble at the location of the other one and neglecting the inertial forces. His theoretical results compare well with his experimental data at low oscillation frequencies. However, his algebraic model overpredicts the relative velocity between the bubbles, showing only the trends of variation of this quantity.

The inviscid theoretical approach to secondary Bjerknes forces of Pelekasis [4] and the computational results of Pelekasis and Tsamopoulos [5,6] produce useful data for a specific range of frequencies, pressure amplitudes and bubble sizes due to the admissible values of Bond and Weber numbers. They predict repulsive secondary Bjerknes forces if the frequency of the disturbance is located between the two natural frequencies for volume oscillations of the unequal sized bubbles and attraction forces for any other case, including the equal size bubbles interaction. The relative motion of the two bubbles is found to be dependent on the frequency of the external acoustic field. When the Bond number  $B_o = (\rho \bar{a} R^2) / \sigma$ , based on the average acceleration  $\bar{a}$ , the radius  $R$  of the larger bubble and the properties of the liquid ( $\rho$  the density,  $\sigma$  the surface tension coefficient), lies above a critical value, spherical-cap shapes are predicted to appear with the deformation confined on the side of the bubbles facing away from the direction of acceleration. However, their results are affected quantitatively and qualitatively by the absence of the viscous

effects, especially important for the magnitude of the relative velocity and the time in which the two bubbles get to collide. This paper presents experimental results and theoretical predictions concerning the interaction and the motion of two levitated air bubbles in water in the presence of an acoustic field at high frequencies (  $22\text{--}23\text{kHz}$  ).

## II. EXPERIMENTAL SETUP

In order to obtain a stable position for the two bubbles within the tank (Figure 1), the dimensions, the quality and the amount of water used must be determined in such a way that a stationary sound wave is obtained inside the vessel; all these must be correlated with the signal frequency. The exact positions of the bubbles inside the tank are determined using an Edmund Scientific laser pointer ML-211 and a milimetric transparent grid. The oscillations are induced by a thin wall hollow cylinder piezoceramic transducer made of C-5400 material (Channel Industries) with the resonance frequency of  $22.5\text{kHz}$  . The maximum radius of the levitated bubbles with the present amplifier is  $3.5\text{mm}$  . The sinusoidal signal is generated by a Hewlett-Packard 33120A function generator and amplified by a Hewlett-Packard 6824A DC Power Supply Amplifier. The signal is checked with a Gould 4050 Oscilloscope (at the exit of the amplifier) against any kind of distortions. In these conditions, a stationary sound wave is formed inside the tank and the horizontal plane at approximately the middle of water depth corresponds to a pressure minimum. The bubbles are levitated at this location with different initial separations. Their motion is recorded and analyzed using a Kodak EktaPro 1000 Motion Analyzer, choosing the rate of frames per seconds between 60 and 1000 and adjusting the magnification with the Chinon - Hoya Zoom System of lens (  $18 - 108\text{mm}$  ).

In the principal experiment, two air bubbles of various radii are injected using clean plastic syringes and needles at different distances apart and their motion recorded and played back frame-by-frame. Figure 2 gives photos of the video screen for a typical experiment, recorded at a rate of 1000 frames per second. The reticle provided by the EktaPro system is used to determine the position of the center of mass of each bubble and their radii; a simple calibration is performed for each session in order to determine the magnification on the screen.

In order to properly study their Bjerknes interaction, small bubbles are injected and afterwards their sizes are increased gradually until the mutual forces triggered the relative motion. At the high frequency used in experiments, it is impossible to measure with accuracy the amplitude of the volume oscillations of the bubbles, this quantity being determined indirectly from the equilibrium of forces in the vertical direction. Perfect levitation of the two bubbles is obtained easily over the entire central region of the vessel, no significant vertical motion of the two bubbles is observed after the initial injection oscillations died down. The quality and stability of the levitation are controlled through small changes of the level of the water inside the vessel (around  $63\text{mm}$  ) and the intensity of the acoustic field (controlled from the function generator output voltage level with an accuracy of  $\pm 1\text{mV}$  ), the frequency of the signal being maintained constant at  $22.5\text{kHz}$  . This paper only presents the attracting bubble results. Other modes of bubble interactions will not be discussed here.

## III. MECHANISM AND DYNAMICS OF BUBBLE - BUBBLE INTERACTION

Consider now two gas bubbles of nominal radii  $R_{01}$  and  $R_{02}$  , which undergo volume oscillations:

$R_1(t) = R_{01}(1 + \varepsilon_1 \sin \omega_1 t)$  and  $R_2(t) = R_{02}(1 + \varepsilon_2 \sin(\omega_2 t + \varphi))$  , levitated in an external stationary sound wave

$p_A(z, t) = A_0 \sin(2\pi z/\lambda) \sin(\omega t) = A \sin(\omega t)$  , where  $A$  will be a notation for the amplitude of oscillation at a fixed location in the liquid column. Volume oscillations of bubble 1 determine the acoustic pressure field around bubble 2 to be modified with the additional wave (spherical symmetry is assumed) [7]:

$$p_1(r, t) = y_1(t)p_A + y_1(t)[1 - (y_1(t))^3](\rho U_1^2(t)/2)$$

$$+[1-(y_1(t))](U_1(t))(\rho U_1^2(t)-2p_A-R_1(t)(dp_A/(dR_1)))/c_0) \quad (1)$$

where:  $y_1(t) = (R_1(t))/r$ ,  $U_1(t) = (dR_1(t))/(dt)$  and  $c_0$  = sound velocity in the liquid. The secondary Bjerknes force on the bubble 2 due to sound field radiated by bubble 1 will be the average taken over one period of the integral of this pressure field on the surface of bubble 2:

$$F_{12} = \langle \int_{S_2} p_1(r, t) \hat{n}_2 dS_2 \rangle = \langle \int_{V_2} \nabla p_1(r, t) dV_2 \rangle \quad (2)$$

Assume that the frequencies  $\omega_1$  and  $\omega_2$  are both equal with the external applied frequency  $\omega$  (transient effects being very short); also, assume the bubbles having an in-phase oscillation  $\phi = 0$ . With these assumptions and by neglecting all terms of the order 3 and greater in  $\epsilon_i$ , equations (1) and (2) give us the following formulas:

$$|F_{ij}| = \frac{\pi}{3} R_{0i}^3 R_{0j}^3 \rho \omega^2 \left[ \frac{2A_i}{\rho \omega^2 R_{0i}^2} (\epsilon_i + 3\epsilon_j) + \epsilon_i^2 \right] \frac{1}{r^2} \quad (3)$$

where  $i, j = 1, 2$  ( $i \neq j$ ). The formulas give a better understanding on the parameters that govern the bubble-bubble interaction than the simplified model developed by Crum, whose results showed a pair of equal forces on the bubbles, depending directly only with frequency, radii and  $1/r^2$ . The validation of our formulas will stand in comparing the experimental data (velocities of bubbles) with our model predictions and with Crum's experiments and model results.

The forces which are considered in studying the motion of the bubbles in the horizontal plan are the secondary Bjerknes forces given by (3) and the drag forces:  $F_{Di} = (\rho v_i^2 S_i C_{Di})/2$ , where  $Re_i = (\rho v_i (2R_{0i}))/2$  is Reynolds number for bubble  $i$  based on the instantaneous velocities  $v_i$  and nominal radii  $R_{0i}$ , and  $S_i = \pi R_{0i}^2$  is the frontal area of the bubble. The drag coefficient is determined by the model proposed by Moore [8]:  $C_{Di} = 48 Re_i^{-1} (1 - 2.2 Re_i^{-0.5})$ . The forces generated by the gradient of pressure amplitude in the horizontal plane are neglected as the hydrophone measurements indicated a smooth distribution of the amplitude  $A$ . The differential equations governing the motion of the two bubbles are nonlinear, of second order with respect to time:

$m_i \ddot{r}_i = |F_{ji}| - |F_{Di}|$ , where  $m_i$  is the induced mass of bubble  $i$  which is equal to the half of the mass of the displaced liquid). This relation is transformed by changing the independent variable to  $r(t) \equiv r_1(t) - r_2(t)$  and choosing the unknown functions to be the velocities of each bubble,  $v_i$ . The amplitude of the pressure signal will be considered the same around each bubble:  $A_1 = A_2 = \rho \omega^2 R_{01}^2 \epsilon_1^2 = \rho \omega^2 R_{02}^2 \epsilon_2^2$  since  $\omega_0 \ll \omega^2$  for the investigated frequencies. Further substitution results in the following system:

$$(v_1 + v_2) v_i' = G_i r^{-2} - ((72\nu)/R_{0i}^2) v_i [1 - 2.2(\nu/(2v_i R_{0i}))^{0.5}]$$

where:  $G_i = 1.5 R_{0j}^3 \omega^2 [\epsilon_j (\epsilon_j + 2\epsilon_i)]$ ,  $i, j = 1, 2$  ( $i \neq j$ ),  $v_1' = (dv_1)/(dr)$ , and  $v_2' = -(dv_2)/(dr)$ . The length scale and the velocity scale used to non-dimensionalize (4) are:  $L = R_1$  and  $U = (\sigma/(\rho R_1))^{0.5}$ , where the larger bubble (index 1) is considered to be the left one. This nonlinear system is solved numerically with the initial conditions imposed by the initial velocities measured during each experiment:  $v_1(r=d_0) = v_{10}$  and  $v_2(r=d_0) = v_{20}$ . The solution of the system is used to compute and plot the relative velocity of the bubbles  $v(r) \equiv v_1(r) + v_2(r)$ .

## IV. RESULTS AND DISCUSSIONS

Figure 3 presents the results obtained by applying the model proposed by Crum and our model to our experimental data in order to compare the accuracy of both approaches. The comparison shows clearly that the simplified dynamics considered by Crum overpredicts the relative velocity even at large bubble separation. Neglecting the inertia forces and using a first order expression for the acoustic field radiated by one bubble in determining the secondary Bjerknes forces formulas are the principal causes for its limited accuracy. On the other hand, the new analytic model presently proposed gives results in good agreement with the experiments until the dimensionless distance between bubbles decreases below a minimum value:  $r_m \approx 3$  as shown in Fig. 3. The differences between theory and experiment become significant for  $r < r_m$ , where the two neglected effects mentioned before (drag modification and acoustic interference) are important. At the moment of collision, secondary Bjerknes forces attain the maximum magnitude, which is less than 40% of the buoyancy on the larger bubble. Based on the proposed model, we designate two new dimensionless parameters which determine the time in which the bubbles reach the impact point:  $\Gamma \equiv d_0^2/(R_{01}R_{02})$  (containing the geometrical conditions of the interaction) and  $\alpha \equiv A/(P_0(z))$  (related to the acoustical conditions). Figure 4 presents the experimental data translated in dimensionless variables. These plots of the coordinates of center of mass of each bubble in time show that:  $\Delta t \sim \Gamma^n \alpha^{-s}$  with positive values for  $n$  and  $s$ . The average values correlated from the experimental data are:  $\bar{n} \approx 4/3$  and  $\bar{s} \approx 1/2$ .

## V. ACKNOWLEDGMENTS

This work was supported by the NASA Microgravity Program under the grant number NAG3-1620.

## VI. REFERENCES

1. Bjerknes, V.F.K. *Fields of Force*, Columbia U.P., New York, 1906.
2. Kornfeld, M., Suvorov, L., "On the Destructive Action of Cavitation", *J. Appl. Phys.*, **15**, 495-506, 1944;
3. Crum, L.A., "Bjerknes forces on bubbles in a stationary sound field", *J. Acoust. Soc. Am.*, **57**(6) part I, 1975.
4. Pelekasis, N.A., *A Study on Drop and Bubble Dynamics via a Hybrid Boundary Element-Finite Element Methodology*, Ph.D. Thesis, State University of New York at Buffalo, 1991.
5. Pelekasis, N.A, Tsamopoulos, J.A., "Bjerknes forces between two bubbles. Part 1. Response to a step change in pressure", *J. Fluid Mech.*, **254**, 467-99, 1993.
6. Pelekasis, N.A, Tsamopoulos, J.A., "Bjerknes forces between two bubbles. Part 2. Response to an oscillatory pressure field", *J. Fluid Mech.*, **254**, 500-27, 1993.
7. Gilmore, F.R., *Report No 26-4*, Hydrodynamics Laboratory, California Institute of Technology, 1952.
8. Moore, D.W., "The boundary layer on a spherical gas bubble", *J. Fluid Mech.*, **16**, 161-176, 1963.

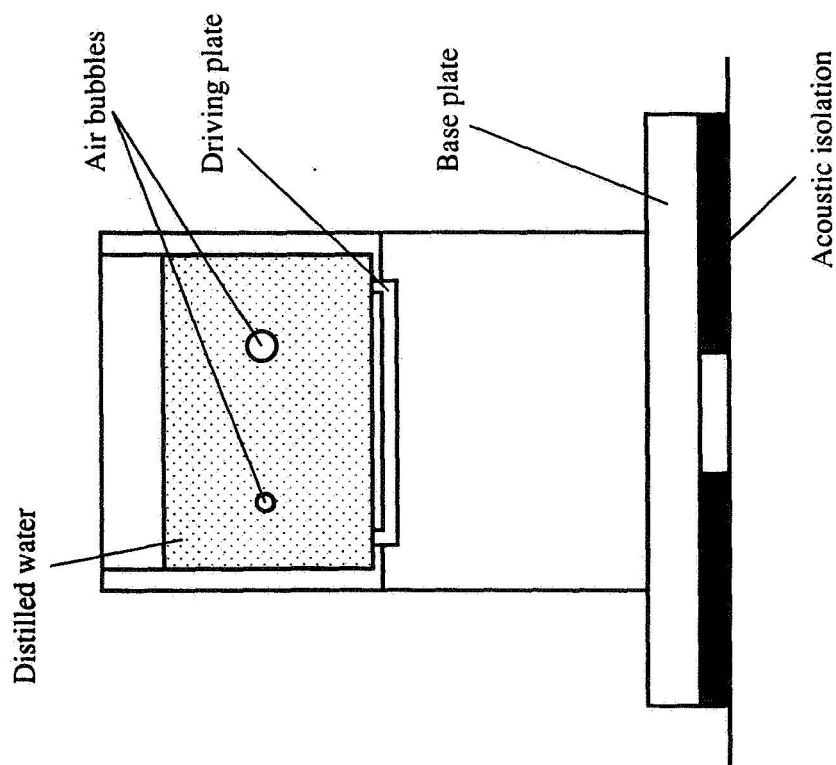


Fig. 1. The levitator.

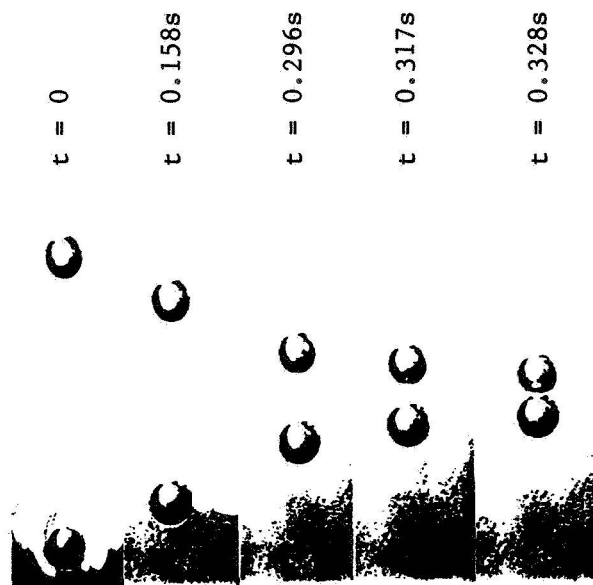


Fig. 2. Photos of a typical bubble motion under secondary Bjerknes forces interaction.

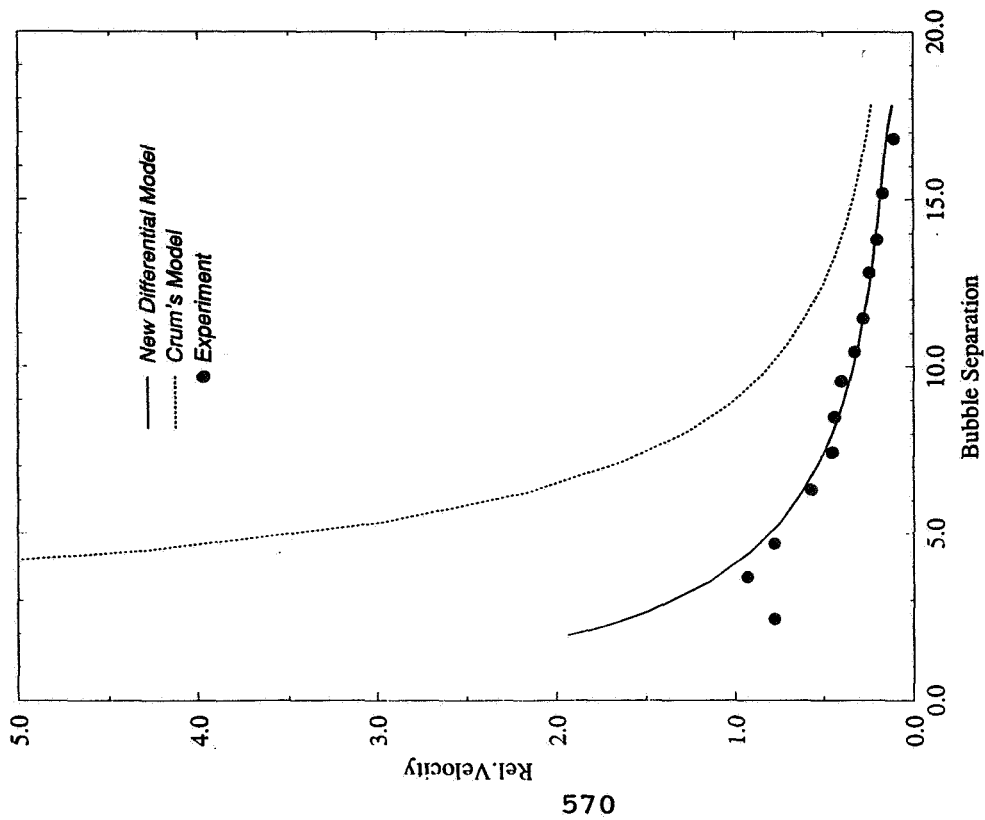


Fig. 3. Relative velocity of the bubbles. Comparison of new experimental data, Crum's model and new differential model:  $\Gamma=390.6$  and  $\alpha=0.49$

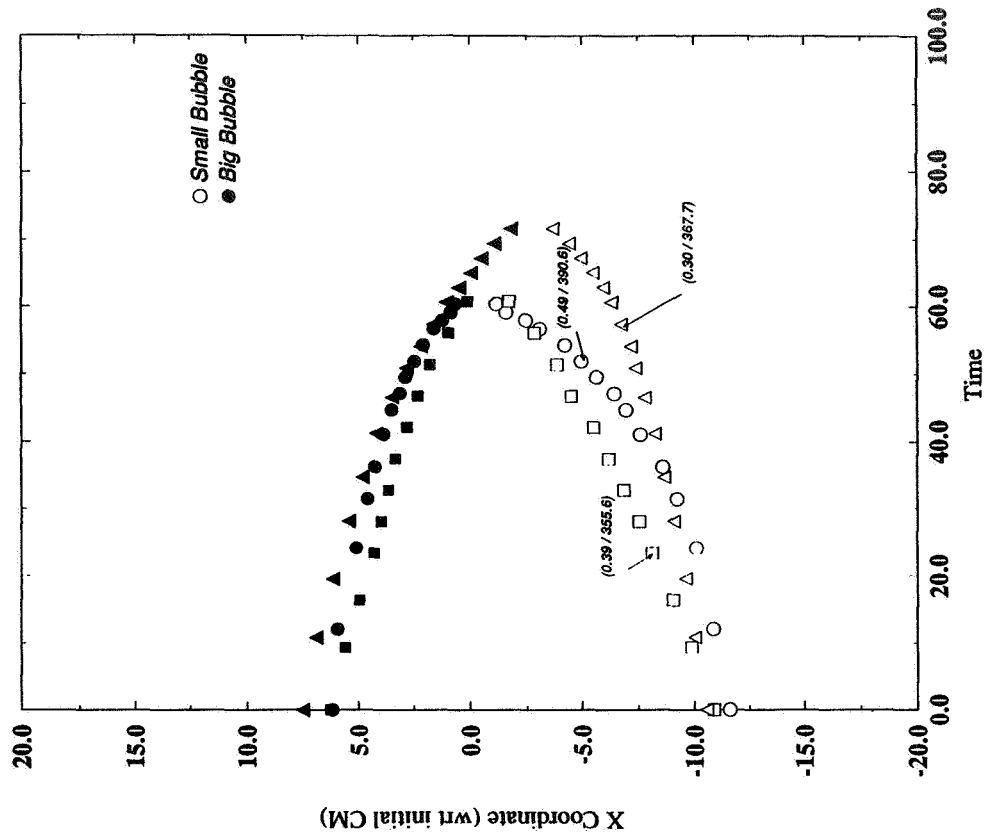


Fig. 4. History of x-coordinates of the centers of mass of each bubble  $\alpha$  between 0.30 and 0.49



# **A Theoretical Study of Remobilizing Surfactant Retarded Fluid Particle Interfaces**

Yanping Wang  
Dimitri Papageorgiou  
*Department of Mathematics*  
*New Jersey Institute of Technology*

Charles Maldarelli  
*Levich Institute and Department of Chemical Engineering*  
*City College of New York*

## **I. Introduction**

Microgravity processes must rely on mechanisms other than buoyancy to move bubbles or droplets from one region to another in a continuous liquid phase. One suggested method is thermocapillary migration in which a temperature gradient is applied to the continuous phase<sup>1</sup>. When a fluid particle contacts this gradient, one pole of the particle becomes warmer than the opposing pole. The interfacial tension between the drop or bubble phase and the continuous phase usually decreases with temperature. Thus the cooler pole is of higher interfacial tension than the warmer pole, and the interface is tugged in the direction of the cooler end. This thermocapillary or thermally induced Marangoni surface stress causes a fluid streaming in the continuous phase from which develops a viscous shear traction and pressure gradient which together propel the particle in the direction of the warmer fluid.

A significant and as yet unresolved impediment to the use of thermocapillary migration to direct bubble or drop motion is that these migrations can be significantly retarded by the adsorption onto the fluid particle surface of surface active impurities dissolved in the continuous or (if the particle is a liquid) droplet phases. Surfactant adsorbs onto the surface of a moving fluid particle, where it is convected by the surface flow to the particle's trailing end. Accumulation at the back end causes kinetic desorption into the bulk sublayer, and the sublayer concentration increases above the value far from the interface. This difference gives rise to a diffusive flux away from the trailing end. Similarly at the front end kinetic adsorption occurs from the sublayer since the front surface is swept clean of surfactant. The sublayer concentration adjacent to the leading end of the particle decreases creating a bulk diffusive flux from the bulk to the front end. Eventually a steady state develops: In this state, the surface concentration at the back end has increased to the point where the desorption rate, proportional to the difference between the surface and sublayer concentration, balances the convective rate. In addition, the sublayer concentration has increased sufficiently so that the diffusive flux away from the particle surface, proportional to the difference between the sublayer and far field concentration, balances the kinetic desorption. At the front end, the surface concentration becomes reduced enough so that kinetic adsorption balances convection, and the sublayer concentration becomes reduced enough so that diffusion to the surface balances adsorption. Consequently, in this steady state the surface concentration is considerably higher at the rear than at the front of the particle, and the interfacial tension is lower at the back relative to the front. This interfacial tension difference creates a surfactant Marangoni stress along the surface as the front end tugs at the rear. The direction of this surface stress is opposite to that of the surface flow caused by the thermocapillary driven motion of the particle, and thus the adsorption of surfactant onto the particle interface acts to reduce the surface flow and hinder the interfacial mobility. The less mobile an interface, the more drag is exerted by the continuous phase on the particle as it moves through the medium, and the smaller is the thermocapillary migration velocity.

This reduction in surface mobility and migration velocity due to retarding Marangoni gradients caused by the convective partitioning of surfactant has been studied extensively for the buoyancy driven

motion in which fluid inertia is negligible (low Reynolds number) and the fluid particles take the shape of spheres (small Weber number). For this case, the terminal velocity becomes reduced from the clean, mobile surface value (the Hadamard-Rybczynski velocity,  $U_{HR} = \frac{2}{3} \frac{\rho g a^2}{\mu}$  (for a bubble) where  $\rho$  and  $\mu$  are the continuous phase density and viscosity, respectively,  $g$  the gravitational acceleration, and  $a$  the particle radius) to the Stokes velocity ( $U_{ST} = \frac{2}{9} \frac{\rho g a^2}{\mu}$ ) of a sphere when the interface mobility is completely arrested. When either the kinetic or diffusive transport is slow relative to interfacial convection, surfactant collects at the trailing pole in a stagnant cap of surfactant, and the terminal velocity is a function of the cap angle which is determined by the steady amount of surfactant adsorbed.<sup>2-5</sup> Theoretical studies for finite kinetic and diffusive transport have also been studied<sup>6-10</sup>. The effect of surfactant adsorption on thermocapillary motion has only recently been studied: Kim and Subramanian<sup>11-12</sup> and Nadim and Borhan<sup>13</sup> have theoretically examined the reduction in thermocapillary migration velocity due to surfactant adsorption, and find that, for the same amount of surfactant adsorbed onto the surface, the reduction (relative to the value for a completely mobile interface) is much greater for thermocapillary driven movement than it is for buoyancy driven motion. The reason, as they point out, is that in thermocapillary migration the strength of the streaming flow around the particle which is driven by the surface tension gradient, and which is responsible for propelling the particle forward, is directly proportional to the interface mobility. The less mobile the surface, the more reduced is the streaming flow due to a fixed surface tension gradient, and the smaller is the particle velocity. Thus thermocapillary migration is very sensitive to the surfactant adsorption, and this adsorption, even arising from surfactants dissolved in trace amounts, can reduce the thermocapillary movement to near zero.

Most experimental evidence in tests both on earth and under microgravity conditions indicate that it is difficult to achieve significant thermocapillary migrations in agreement with the Young et al value, and many studies have attributed the reduced migrations to the retarding effect of surfactant impurities unavoidably present in the bulk phases (see the review article of Subramanian<sup>14</sup>). In addition, Barton and Subramanian<sup>15</sup> demonstrated directly the retardation by the intentional addition of surfactant to a liquid phase in which droplets were moving by thermocapillarity. To date the problem of retardation of thermocapillary driven particle motion due to surfactant impurities remains unresolved. Thermocapillary motions in agreement with the expression of Young et al<sup>1</sup> can only be achieved in systems in which extreme precautions have been taken to remove impurities (as, for example, in Barton and Subramanian's<sup>15</sup> experiments using ethyl salicylate drops in ethylene glycol).

In this paper, we provide a theoretical basis for remobilizing surfactant retarded fluid particle interfaces in an effort to make more viable the use of thermocapillary migrations for the management of bubbles and drops in microgravity. The retarding Marangoni stresses arise because the rate of convection of surfactant to the trailing pole is much larger than either the kinetic or diffusive flux away from the particle surface. The scale for the convective flux is  $\Gamma_0 U a$ , where  $U$  is the terminal velocity,  $a$  (as before) the radius and  $\Gamma_0$  is the surface concentration in equilibrium with the bulk concentration  $C_0$  far from the particle. In this study we will use Langmuir relations to describe surfactant exchange; thus the adsorption rate is  $\beta C_s (\Gamma_\infty - \Gamma)$  and the desorption rate is  $\alpha \Gamma$ ,  $C_s$  the surfactant concentration adjacent to the interface (the sublayer concentration),  $\Gamma_\infty$  is the maximum packing density, and  $\alpha$  and  $\beta$  are kinetic coefficients. At equilibrium, the sublayer concentration is equal to  $C_0$  and the equilibrium surface concentration  $\Gamma_0$  is

$$\frac{\Gamma_0}{\Gamma_\infty} = \frac{C_0 / b}{1 + C_0 / b} \quad (1)$$

where  $b$  is an adsorption parameter equal to  $\alpha/\beta$ . The scale for the diffusive flux is  $[D C_0 / a] a^2$ , where  $D$  is the bulk diffusion coefficient. We assume surfactant concentrations are below the critical micelle concentration, so no surfactant aggregates are present in the bulk liquid. The scale for the kinetic desorptive flux is  $\alpha \Gamma_0 a^2$ . Retarding surfactant gradients do not develop when

$$\begin{aligned} \alpha a / U &\gg 1 \\ \chi(1 + C_o / b) / Pe &\gg 1 \end{aligned} \quad (2a,b)$$

where  $\chi = ba/\Gamma_\infty$  and  $Pe$  is the Peclet number  $Pe = Ua/D_s$  because when these inequalities are met, kinetic and diffusive transport are sufficient to maintain the surface concentration uniform despite the action of convective redistribution. The diffusion criteria in (2) illustrates the reason impurity or small concentrations of surfactant tend to retard interfaces: The diffusion coefficient of surfactant monomers is of the order of  $10^{-6} \text{ cm}^2/\text{sec}$ , and  $b/\Gamma_\infty$  is of the order .01-1, so for typical values of  $a$  and  $U$  of  $10^{-3} \text{ cm} < a < 10^{-4} \text{ cm}$  and  $10^{-3} \text{ cm/sec} < U < 1 \text{ cm/sec}$ ,  $\chi/Pe$  is not larger than 1. Thus diffusion alone reduces the surface mobility. However, the criteria in (2) suggest a method for remobilizing interfaces which have been retarded by the adsorption of a surfactant impurity. Select a surfactant (which we term a remobilizing surfactant) whose kinetic desorption rate constant is larger than the convective rate  $U/a$ . There are not many reported measurements of surfactant kinetic rate constants, but the small amount of data derived from dynamic surface tension measurements indicates that  $\alpha$  can be as large as  $10^2 \text{ sec}^{-1}$ , so that for  $U/a < 10^2 \text{ sec}^{-1}$ , surfactants whose desorptive rate is fast enough so that (2a) is satisfied can be identified. The second criteria can be satisfied if the bulk concentration is large enough; typically  $C_o/b$  can be as large as  $10^3$  or more, before Micellar aggregation initiates. When the bulk concentration of the remobilizing surfactant is high, the impurity does not have an opportunity to adsorb onto the surface because of the faster transport of the remobilizing surfactant. Thus the interface consists only of the remobilizing surfactant, which keeps the interface mobile by maintaining a uniform surface concentration.

To verify the above scaling arguments, we undertake numerical simulations of the effect of increasing the bulk concentration on the steady velocity of a gas bubble in a continuous liquid phase. In this first effort, we assume that buoyancy drives the bubble motion, and that surface tension forces are larger than inertial and viscous forces (small Weber and capillary numbers) so that the bubble retains its spherical shape as it moves. The kinetic exchange is assumed to be fast enough to insure that the surface and the sublayer are in equilibrium, as we have observed that surfactants can have fast kinetic regimes, and Peclet numbers for the bulk surfactant mass transfer are assumed of order one, as observed above. In addition, we retain the effects of fluid inertia by developing order one Reynolds number solutions since the Reynolds number is not small for bubble motions in the most common of continuous phases, water. In the following sections we detail the Formulation and the Numerical Solution Algorithm (Sec. II), and the Results (Sec. III).

## II. Formulation and Solution Algorithm

We consider the axisymmetric, steady motion of a spherical bubble in an unbounded, Newtonian incompressible liquid in a spherical coordinate system  $(r, \theta)$  with the bubble fixed, and the coordinate angle  $\theta$  measured from the upstream pole. All fluid equations are written nondimensionally with the radial coordinate scaled by  $a$ , and the velocity by  $U$ , the terminal velocity. Because the fluid motion in the surrounding liquid is axisymmetric and incompressible, the velocities in the  $r$  ( $u_r$ ) and  $\theta$  ( $u_\theta$ ) directions can be specified in terms of a (nondimensional) stream function  $\Psi(r, \theta)$  (scaled by  $a^2 U$ ):

$$u_r = -\frac{1}{r^2 \sin \theta} \frac{\partial \Psi}{\partial \theta}; u_\theta = \frac{1}{r \sin \theta} \frac{\partial \Psi}{\partial r} \quad (3)$$

and the one component of the vorticity,  $w$  (in the azimuthal direction, scaled by  $U/a$ ) is

$$rw(r, \theta) = -\frac{1}{\sin \theta} \frac{\partial^2 \Psi}{\partial r^2} + \frac{1}{r^2} \frac{\partial}{\partial \theta} \left[ \frac{1}{\sin \theta} \frac{\partial \Psi}{\partial \theta} \right] \quad (4)$$

The fluid motion is governed by the Navier Stokes equations at order one Reynolds number, and we use the vorticity-stream function formulation to develop solutions:

$$\frac{\partial}{\partial r}(ru, w) + \frac{\partial}{\partial \theta}(u_\theta w) = \frac{1}{\text{Re}} \left[ \frac{\partial}{\partial r} \left( \frac{\partial}{\partial r} (rw) \right) + \frac{\partial}{\partial \theta} \left( \frac{1}{r \sin \theta} \frac{\partial}{\partial \theta} (w \sin \theta) \right) \right] \quad (5)$$

where Re is the Reynolds number ( $=\rho Ua/\mu$ ). The boundary conditions on the stream function and vorticity are the matching to the free stream velocity at infinity ( $r \rightarrow \infty$ )

$$\psi \rightarrow \frac{1}{2} r^2 \sin \theta \quad (6a, b)$$

$$w \rightarrow 0,$$

zero normal velocity, and the balance of the tangential stress with the Marangoni stress at the bubble interface  $r=1$ :

$$\begin{aligned} \psi &= 0 \\ w &= \frac{2}{\sin \theta} \frac{\partial \psi}{\partial r} + \frac{\text{Ma}}{1 - \Gamma} \frac{\partial \Gamma}{\partial \theta} \end{aligned} \quad (7a, b)$$

where  $\Gamma$  is the surface concentration (nondimensionalized by  $\Gamma_\infty$ ) and Ma is the Marangoni number  $RT\Gamma_\infty/\mu U$ . The surface concentration is obtained from the solution of the convective diffusion equation,

$$\mathbf{u} \cdot \nabla C = \frac{1}{\text{Pe}} \nabla^2 C \quad (8)$$

where  $C(r, \theta)$  is the bulk concentration (nondimensionalized by the far field value  $C_0$ ) and Pe the Peclet number, and the surfactant boundary conditions at the bubble surface  $r=1$ :

$$\begin{aligned} \Gamma &= \frac{kC_s}{1 + kC_s} \\ \frac{1}{\sin \theta} \frac{\partial}{\partial \theta} (\sin \theta \Gamma u_\theta) &= \frac{k\chi}{\text{Pe}} \frac{\partial C}{\partial r} \end{aligned} \quad (9a, b)$$

where  $k=C_0/b$  and  $\chi=ba/\Gamma_\infty$  as in Sec. I. The nondimensional concentration must match to 1 as  $r \rightarrow \infty$ .

We use a finite difference method to solve the above equations. The infinite boundary is truncated to a value  $r=20$ , and the annular region from the bubble surface  $r=1$  to the outer boundary  $r=20$  is mapped to a unit square  $(x, y)$  by the transformations  $x=\ln r/\ln r_\infty$  and  $y=\pi/\theta$ . The square is discretized with  $\Delta x=.01$  and  $\Delta y=.01$ . The discretized system is solved by using an ADI (Alternating Directions Implicit) scheme<sup>16</sup> in which the field equations (4, 5 and 8) and boundary condition (9b) are made pseudo-unsteady in time, and equal part time steps ( $\Delta t=.005$ ), implicit in either  $x$  or  $y$ , are taken. The convergence criteria in time is formulated in terms of the change in the maximum value of the vorticity and the stream function over  $\Delta t$   $10^2$ ; this change is required to be less than  $10^{-6}$ .

### III. Simulation Results

We begin by first examining the case without inertia ( $\text{Re}=0$ ). To illustrate remobilization, we fix the values of the Marangoni and Peclet numbers ( $\text{Ma}=5$ ,  $\text{Pe}=1$ ) and  $\chi (=1)$ , and we obtain solutions for increasing bulk concentrations by varying  $k$ . In Fig. 1, we plot the surface concentration profile for three different values of  $k$  ( $=.1, 1$  and  $5$ ) relative to the maximum packing concentration  $\Gamma_\infty$  (Fig. 1a) and the equilibrium concentration  $\Gamma_0$  (Fig. 1b). The convective partitioning of surfactant on the surface is evident for all values of  $k$ , as the surface concentration is higher at the downstream pole ( $\theta=\pi$ ) than the upstream pole ( $\theta=0$ ). We note that as  $k$  increases, Fig. 1a indicates clearly that the total amount of adsorbed surfactant increases. More importantly, as is evident in Fig. 1b, the surface concentration becomes more uniform as  $k$  increases: The ratio of bulk diffusion to convection ( $\chi(1+k)/\text{Pe}$ ) increases from 1.1 to 6 as  $k$  varies from .1

to 5, and diffusion therefore begins to outscale convection (see criteria 2b) to maintain a uniform surface concentration. The remobilization of the interfacial mobility is evident in Figs. 2 which plots the maximum interfacial velocity as a function of  $k$  over a much wider range of  $k$  ( $10^{-2} < k < 10^2$ ) with the same values of  $Ma$ ,  $Pe$  and  $\chi$  as in Fig. 1. Note that for a clean interface, the surface velocity is equal to  $(1/2)\sin\theta$ , so the maximum velocity at the equator ( $\theta=\pi/2$ ) is  $1/2$ . As  $k$  increases from 0 to 1, the interfacial velocity decreases from the clean value of  $1/2$ . This is the retardation that as we noted in the Introduction has been well documented in the literature. However, as  $k$  increases further and the surface concentration becomes uniform, the interfacial mobility is restored and the maximum surface velocity tends to  $.5$ .

As the bulk concentration increases and the surface concentration becomes more uniform, the sublayer concentration (in equilibrium with the surface) also becomes more uniform. In Fig. 2a, we plot the sublayer concentration for  $k=.1, 1$  and  $5$  (for  $Ma=5, Pe=1$  and  $\chi=1$ ), and the tendency towards a more uniform concentration with increasing  $k$  is evident. With the sublayer concentration approaching 1, the concentration in the bulk also approaches one as the diffusion driving force disappears. In Fig. 3, contours of constant bulk concentration are shown for  $k=.1$  (Fig. 3a),  $k=1$  (Fig. 3b) and  $k=10$  (Fig. 3c), and it is clear that as the interface remobilizes, the bulk concentration becomes uniform.

The effect of increasing the bulk concentration on the terminal velocity is examined in Fig. 4 which plots the drag on the nondimensional drag on the bubble (nondimensionalized by  $\pi\mu aU$ ) as a function of  $k$ , for  $Ma=5$  and  $\chi=1$  and a few values of  $Pe$  (.1, 1 and 10). In these nondimensional units, the drag on a clean bubble is 4 and the drag on a completely immobile surface (the Stokes drag) is equal to 6. For fixed  $Pe$ , we note that as  $k$  increases, the drag at first increases (corresponding to the decrease in interfacial mobility observed in Fig. 2b), but then decreases as the interface becomes remobilized. For fixed  $k$ , as  $Pe$  increases the drag increases. This elevation in drag, which begins to approach the Stokes value of 6 for  $Pe=10$ , can be directly attributed to the larger convective partitioning of surfactant on the surface relative to bulk diffusion; as  $Pe$  increases,  $\chi(1+k)/Pe$  decreases. Importantly, the larger drags at high Peclet numbers can also be reduced to clean surface drags if the bulk concentration is taken large enough so as to increase the ratio  $\chi(1+k)/Pe$ .

The above simulations have been for  $Re=0$ ; some preliminary results for a finite value of  $Re$  ( $Re=5$ ) are given in Fig. 5 in which the drag is plotted as a function of  $k$  for  $Pe=1$  and  $Ma=5$ . Again we note that as  $k$  increases, the drag can be reduced and the terminal velocity increased.

#### IV. References

- <sup>1</sup> Young, N, Goldstein, J., and Block, M. J. Fluid Mech., **6**, 350 (1959).
- <sup>2</sup> Davis, R.E. and Acrivos, A., Chem. Engr. Sci., **21**, 681 (1966).
- <sup>3</sup> Harper, J.F., J. Fluid Mech., **58**, 539 (1973).
- <sup>4</sup> Sadhal, S. and Johnson, R., J. Fluid Mech., **126**, 237 (1982).
- <sup>5</sup> He, Z, Maldarelli, C. and Dagan, Z., J. Colloid and Interface Sci., **146**, 442 (1981).
- <sup>6</sup> Saville, D., Chem. Engr. J., **5**, 251 (1973).
- <sup>7</sup> Levan, M. and Newman, J., AIChE J., **22**, 695 (1976).
- <sup>9</sup> Holbrook, J. and Levan, M., Chem. Engr. Commun., **20**, 191 and 273 (1983).
- <sup>10</sup> Chen, J. and Stebe, K., J. Colloid and Int. Sci., **178**, 144 (1996).
- <sup>11</sup> Kim, H. and Subramanian, R., J. Colloid and Int. Sci., **127**, 417 (1989).
- <sup>12</sup> Kim, H. and Subramanian, R., J. Colloid and Int. Sci., **130**, 112 (1989).
- <sup>13</sup> Nadim, A. and Borhan, A., PhysicoChem Hydodyn., **11**, 753 (1989).
- <sup>14</sup> Subramanian, R.S., in Transport Processes in Bubbles, Drops and Particles, Hemisphere Publishing, NY (1992).
- <sup>15</sup> Barton, K.D. and Subramanian, R.S., J. Colloid and Interface Sci., **133**, 211 (1990).
- <sup>16</sup> Ryskin, G. and Leal, L., J. Fluid Mech., **148**, 1 and 19 (1984).

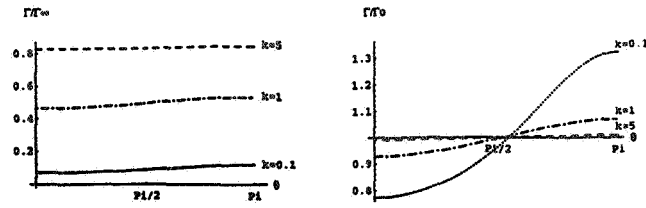


Fig. 1 Surface concentration distribution as a function of  $k$  for  $Re=0$ ,  $Ma=5$ ,  $\chi=1$  and  $Pc=1$ .

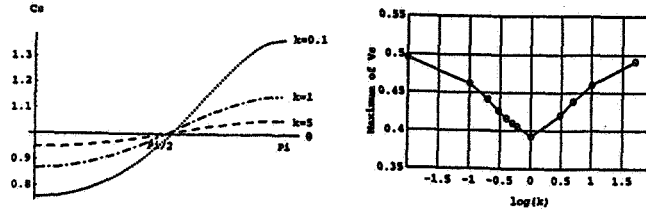


Fig. 2. The maximum interfacial velocity as a function of  $k$  and the sublayer concentration for  $Re=0$ ,  $Ma=5$ ,  $\chi=1$  and  $Pc=1$

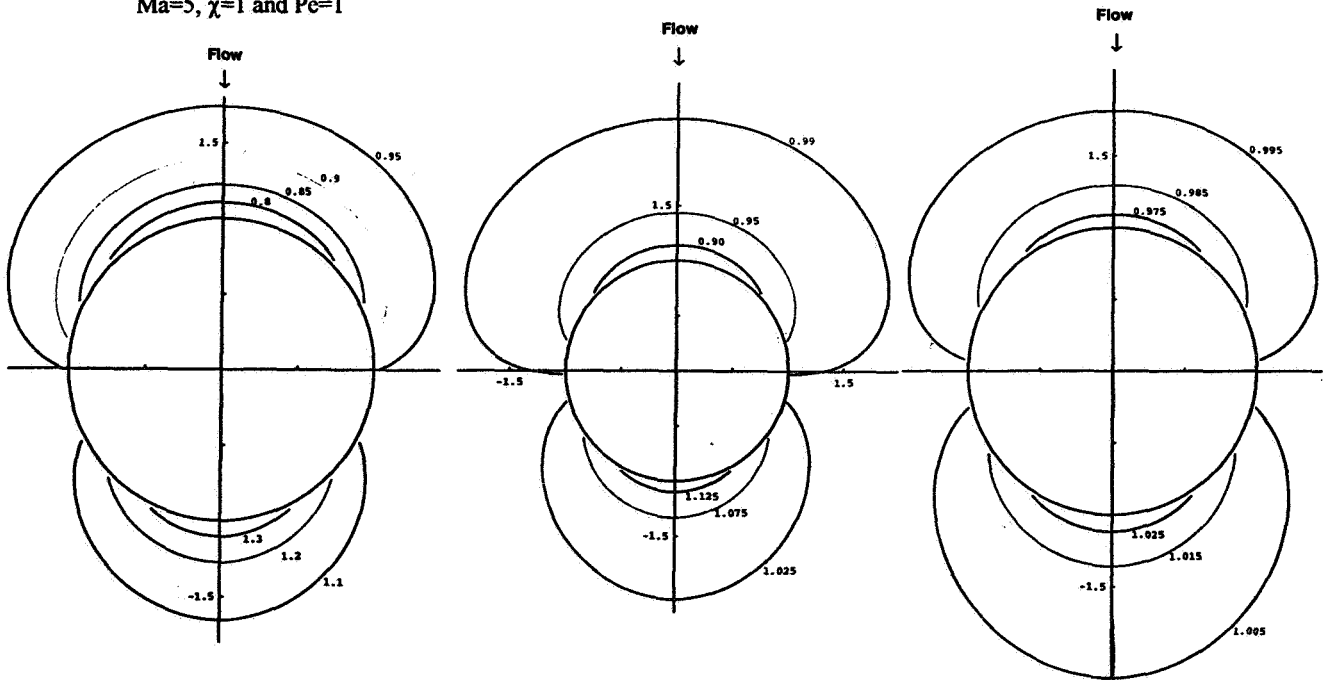


Fig. 3. Contours of constant concentration in the bulk for  $k=.1$ ,  $k=1$  and  $k=10$  and  $Re=0$ ,  $Ma=5$ ,  $\chi=1$  and  $Pc=1$

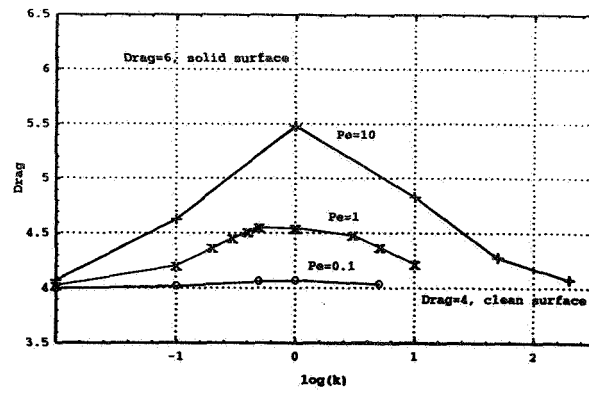


Fig. 4. Terminal velocity as a function of  $k$  for  $Re=0$

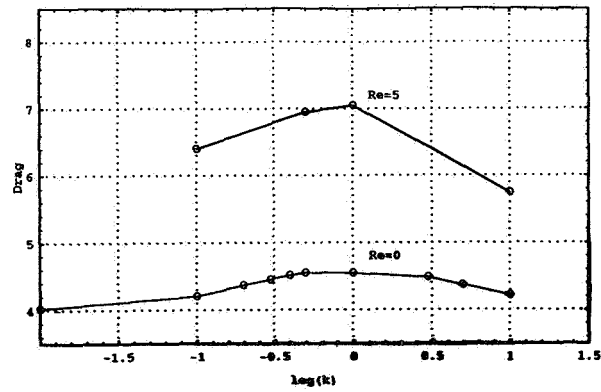


Fig. 5 Terminal velocity as a function of  $k$  for  $Re=5$





# SELF-DIFFUSION OF DROPS IN A DILUTE SHEARED EMULSION

M. Loewenberg<sup>†</sup> & E.J. Hinch<sup>\*</sup>

<sup>†</sup>Department of Chemical Engineering  
Yale University  
New Haven, Connecticut 06520-8286

<sup>\*</sup>Department of Applied Mathematics and Theoretical Physics  
University of Cambridge  
Cambridge CB3 9EW

## ABSTRACT

Self-diffusion coefficients that describe cross-flow migration of nonBrownian drops in a dilute sheared emulsion were obtained by trajectory calculations. A boundary integral formulation was used to describe pairwise interactions between deformable drops; interactions between undeformed drops were described with mobility functions for spherical drops. The results indicate that drops have large anisotropic self-diffusivities which depend strongly on the drop viscosity and modestly on the shear-rate. Pairwise interactions between drops in shear-flow do not appreciably promote drop breakup.

## INTRODUCTION

Shear-induced self-diffusion of nonBrownian drops in emulsions is important because it facilitates mixing. In the production of specialized polymer blends, macroscopic properties such as the mechanical strength rely on effective mixing of the emulsified melt to produce a uniform microstructure. In the absence of interfacial tension, the drop size in an efficient mixing device will continuously decrease until Brownian motion can effectively homogenize the fine droplets throughout the continuous phase.

However, interfacial tension places a lower bound on the drop size that can be obtained by mixing. For drops in shear-flow, significant deformation and breakup generally occur when the capillary number,  $Ca = \frac{\mu\dot{\gamma}a}{\sigma}$  is  $O(1)$ , where  $\dot{\gamma}$  is the imposed shear-rate,  $a$  is the undeformed drop radius,  $\mu$  is the continuous-phase viscosity, and  $\sigma$  is the interfacial tension. The numerical value of the critical capillary number depends on the dispersed- to continuous-phase viscosity ratio,  $\lambda$ , and the dispersed-phase volume fraction,  $\phi$ . For isolated drops with  $0 < \lambda < 4$ , the criterion  $Ca = O(1)$  provides a reasonable estimate of the drop size produced by a given shear-rate (Hinch & Acrivos 1980; Grace 1982). The effect of drop interactions on the critical capillary number has not been studied thus the effect of volume fraction is unknown. Simple scaling arguments indicate that typical mixing operations generate nonBrownian deformable drops; thus, self-diffusion of deformable drops is an important mixing mechanism in most emulsification processes.

The  $O(a)$  displacements and  $O(\dot{\gamma}a)$  relative velocities between interacting particles or drops produce self-diffusivities that are  $O(\dot{\gamma}a^2)$ . Shear-induced self-diffusion of rigid spherical particles has been experimentally observed (Eckstein *et al.* 1977; Leighton & Acrivos 1987) and numerically simulated (Brady & Bossis 1987). Pairwise interactions do not induce a net cross-flow displacement of smooth spheres; cross-flow self-diffusion results from multi-particle interactions. Wang *et al.* (1996) calculated the  $O(\phi^2\dot{\gamma}a^2)$  cross-flow self-diffusivity of smooth spheres in a sheared dilute suspension. Net cross-flow displacements can result from pairwise interactions between nonspherical particles or drops. Thus, nonspherical particles and drops have larger  $O(\phi\dot{\gamma}a^2)$  self-diffusivities in dilute suspensions that result from pair interactions. da Cunha & Hinch (1996) computed the self-diffusivity of rough spheres in a dilute suspension but there have been no studies on the self-diffusion of drops.

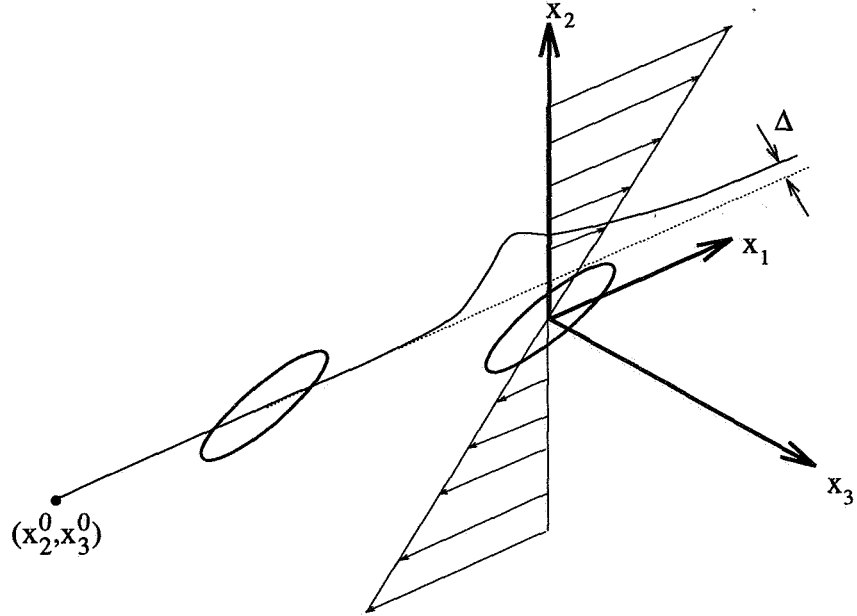
The aim of this article is to compute cross-flow self-diffusion coefficients of nonBrownian deformable drops in a sheared dilute emulsion. The effects of the capillary number and viscosity ratio were the focus

of our study. Neutrally buoyant drops, a monodisperse drop size distribution, and low Reynolds number conditions are assumed. Marangoni stresses on the drop interfaces that result from surfactant concentration gradients are neglected. The numerical procedure and numerical results are presented in the next two sections. Concluding remarks are made in the final section.

## CALCULATION PROCEDURE

The nonsingular boundary integral formulation developed by Loewenberg & Hinch (1996) was used to compute the interactions and trajectories of deformable drops ( $Ca > 0$ ) in shear-flow. For the limiting case  $Ca \rightarrow 0$ , spherical drop trajectories were obtained from Zinchenko (1983, 1984).

Figure 1: Schematic of relative trajectory between pair of deformable interacting drops in shear flow.



Self-diffusivities— The self-diffusion tensor is defined as half the rate-of-change of the random walk variance:

$$\mathbf{D} = \lim_{t \rightarrow \infty} \frac{1}{2} \frac{d}{dt} \langle \Delta \Delta \rangle, \quad (1)$$

where the cross-flow random walk displacement,  $\Delta$  has zero mean. The cross-flow displacement,  $\Delta = (\Delta_2, \Delta_3)$ , is defined in fig. 1. For given values of  $Ca$  and  $\lambda$ , the cross-flow displacement of a drop resulting from its pairwise interaction with another identical drop depends on the initial offset of the drop trajectories,  $(x_2^0, x_3^0)$ , at large separations in the flow direction,  $x_1$ . Only pairwise interactions between identical drops are considered on the assumption that the emulsion is dilute and monodisperse.

The rate of interactions that result in a particular cross-flow displacement,  $\Delta(x_2^0, x_3^0; Ca, \lambda)$ , is  $n \dot{\gamma} |x_2^0| dx_2^0 dx_3^0$ , where  $n$  is the number density of drops:  $\phi = \frac{4\pi}{3} a^3 n$ . By definition (1), the dimensionless self-diffusion coefficient for drops in a dilute emulsion is (da Cunha & Hinch 1996):

$$f_\alpha(Ca, \lambda) = \frac{D_\alpha}{\phi \dot{\gamma} a^2} = \frac{3}{2\pi} \int_0^\infty \int_0^\infty \Delta_\alpha^2 x_2^0 dx_2^0 dx_3^0, \quad (2)$$

where  $\alpha = 2$  or  $3$  for cross-flow self-diffusion in the velocity gradient or the vorticity direction (*cf.* fig. 1). The result exploits the four-fold symmetry of integration in the  $x_2^0 - x_3^0$  plane.

For deformable drops, the double integral of formula (2) was evaluated with about 1% error using 32 integrand evaluations (trajectory calculations) on a truncated square domain and extrapolating the result to infinity using the far-field form of the pair interaction (Kim & Karrila 1991). The calculations presented herein were obtained with a  $4 \times 4$  domain. A comparison to the values obtained with an  $8 \times 8$  domain indicated that the truncation error is 1-2%.

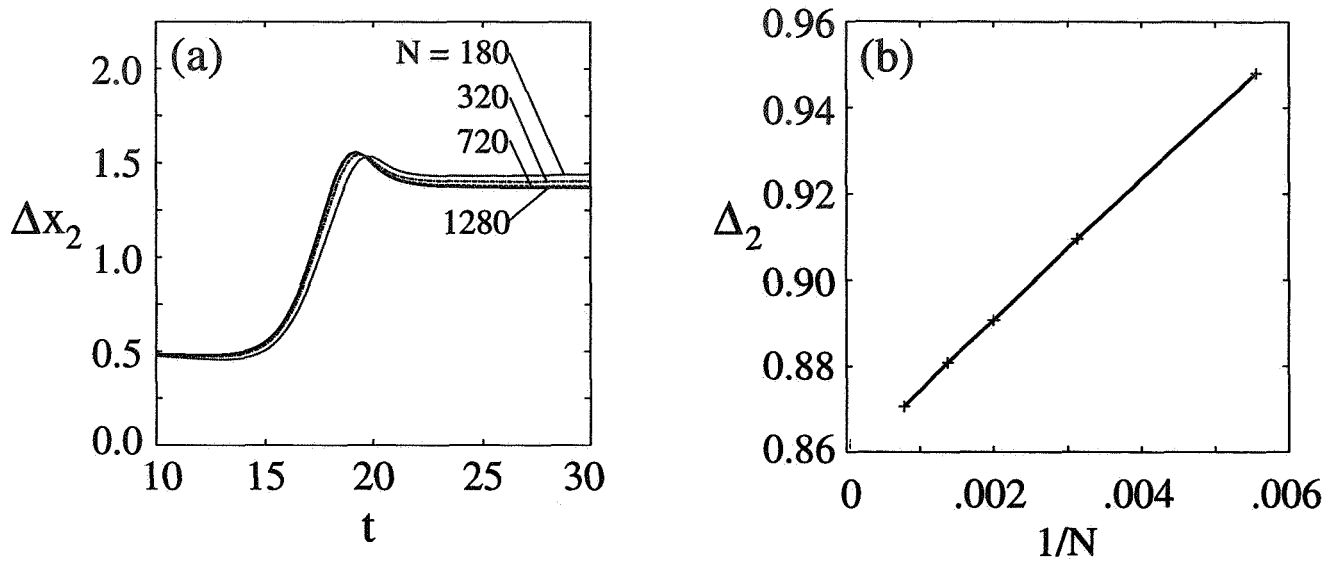


Figure 2: Relative trajectory of two interacting drops for  $Ca = 0.3$ ,  $\lambda = 1$ ; initially, one drop centered at origin and other drop at  $(-10, 0.5, 0)$ . a) Cross-flow separation (velocity gradient direction) versus time; results obtained using  $N = 180$  (dotted curve), 320 (dashed-dotted curve), 720 (dashed curve), and 1280 (solid curve) boundary elements. b) Cross-flow displacement versus reciprocal number of boundary elements,  $1/N$ .

Unstabilized hydrodynamically interacting spherical drops will coalesce for  $R \leq 2E_{12}^{1/3}$ , where  $R = \sqrt{(x_2^0)^2 + (x_3^0)^2}$  is the magnitude of the initial trajectory offset and  $E_{12}$  is the “collision efficiency” (Wang *et al.* 1994). Herein, spherical drops were stabilized against coalescence by supplementing the hydrodynamic interaction with a singular, infinitesimally short-range repulsion (Zinchenko 1984). For spherical drops with short-range repulsion,  $\Delta(x_2^0, x_3^0)$  is nonzero only within the circular domain  $R \leq 2E_{12}^{1/3}$ . The mobility functions were tabulated for improved computational speed. For spherical drops formula (2) was evaluated with about 0.1% error using 1225 trajectory calculations.

Deformable drops can also be stabilized with a short-range repulsive interaction (Loewenberg & Hinch 1996) however, this was implemented only for  $2 \leq \lambda \leq 5$  and for  $\lambda < 0.1$  on the most closely-spaced trajectories ( $R < 1$ ). Very small surface separations occur under these conditions. For  $\lambda = 1$ , we confirmed that the short-range repulsion had a negligible effect on the trajectories of deformable drops.

Cross-flow trajectory offsets were obtained with one drop initially centered at the origin and the second at a downstream location,  $(-X_1, x_2^0, x_3^0)$ . Trajectory integration was continued until the second drop passed the plane  $x_1 = +X_1$ . For deformable drops, the initial drop shapes corresponded to the stationary shapes of isolated drops under the same flow conditions. The error induced by trajectory truncation is  $O(X_1^{-3})$  (Kim & Karrila 1991). We used  $X_1 = 8$  for deformable drops and  $X_1 = 20$  for spherical drops. Based on a limited number of calculations with larger values of  $X_1$ , we estimate that trajectory truncation error is about 1% for deformable drops and about 0.1% for spherical drops.

**Computation Time and Numerical Convergence**— For deformable drops with  $Ca = 0.3$  and  $\lambda = 1$ , self-diffusivities were obtained in 2 hours on a workstation using  $N = 720$  boundary elements. The calculations are 3–4 times slower for  $\lambda \neq 1$  because an iterative solution of the integral equation is required.

The results depicted in fig. 2 demonstrate numerical convergence of the boundary integral calculations for trajectories of deformable drops. Fig. 2b demonstrates that the total discretization error resulting from

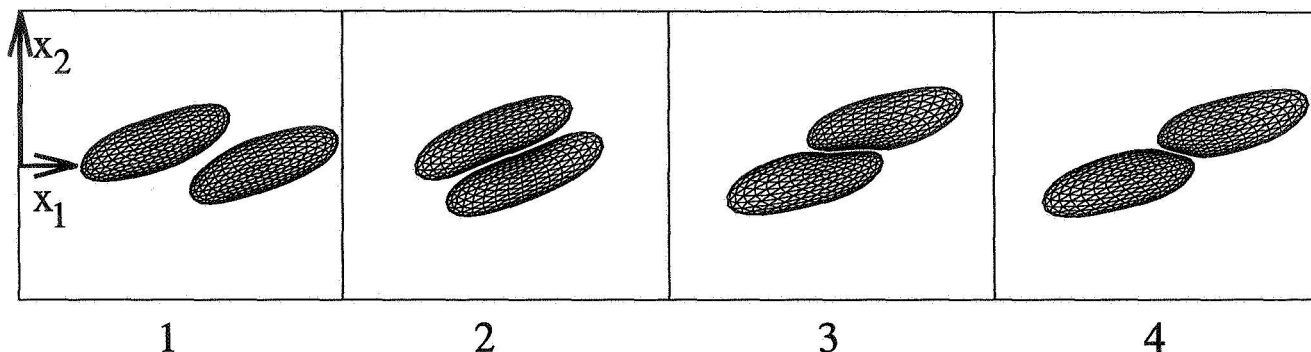


Figure 3: Sequences (1-4) showing the interaction between two drops in shear flow with  $Ca = 0.4$ ,  $\lambda = 1$ . Initially, one drop centered at origin and other drop at  $(-10, 0.5, 0)$ .

the curvature calculation, surface integration, and trajectory integration is  $O(N^{-1})$ . Herein, self-diffusivities were computed with  $N = 720$  thus, discretization errors are about 2% which is comparable to the remaining sources of error discussed above.

Self-diffusivities for spherical drops require less than a minute of CPU time and are accurate to about 0.1%.

## NUMERICAL RESULTS

**Drop Breakup**—An example of a pair interaction between deformable drops in shear-flow is depicted in fig. 3. The critical capillary number for breakup of an isolated drop in shear flow is lowest for  $\lambda \approx 1$ ; for  $\lambda = 1$ ,  $Ca \simeq 0.41$  is critical (Rallison 1981). The trajectory depicted in fig. 3 demonstrates that even for capillary numbers very close to critical, strong pairwise interactions do not result in drop breakup. Other calculations with  $\lambda \neq 1$  also showed no tendency for interaction-enhanced breakup. Apparently pairwise drop interactions do not induce significantly subcritical capillary number breakup. Thus, the critical capillary number is a weak function of volume fraction at least in dilute emulsions.

In part, breakup is averted because of the reduced cross-section for interaction between highly deformed drops. Breakup requires enhanced drop elongation but a detailed inspection of the numerical results revealed that the extra deformation induced by a pairwise interaction tends to deform drops in the  $x_3$ -direction. Deformable drops can easily squeeze past each other which tends to prevent breakup.

**Self-diffusivities**— Figs. 4 and 5 depict self-diffusivities as functions of shear-rate (capillary number) and viscosity ratio. Self-diffusion is only a moderate function of capillary number; figs. 4 and 5 show that self-diffusivities vary by a factor of about 2 as the capillary number is varied over a wide range. By contrast, self-diffusivities are a strong function of viscosity ratio.

Anisotropic self-diffusion results from the bias of trajectory displacements in the velocity gradient direction. Self-diffusion in the velocity gradient direction,  $f_2$  is much larger than self-diffusion in the vorticity direction,  $f_3$ . For stabilized spherical bubbles ( $\lambda = 0$ ), it can be shown that the ratio  $f_2/f_3$  is exactly 2. For deformable bubbles with  $Ca = 0.3$ ,  $f_2/f_3 \simeq 6$ . Fig. 5 indicates that anisotropy increases with viscosity ratio;  $f_2/f_3 > 20$  for  $\lambda \geq 10$ .

For  $\lambda = 10$ ,  $f_2$  and  $f_3$  are approximately equal to the self-diffusivities predicted for spherical particles with 3% roughness (da Cunha & Hinch 1996). For  $\lambda < 10$ , drop diffusivities are considerably larger than the values for rough spherical particles.

As expected, self-diffusivities vanish for large  $\lambda$  because  $D = O(\phi^2)$  for smooth spheres (Wang *et al.* 1996). The results depicted in fig. 5 indicate that self-diffusion becomes insensitive to capillary number

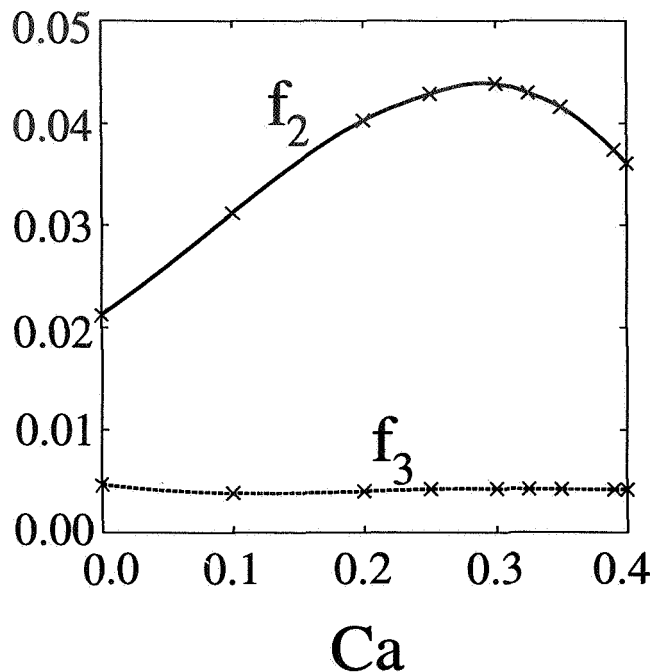


Figure 4: Self-diffusion coefficients as a function of capillary number for  $\lambda = 1$ ; solid curve: diffusion parallel to velocity gradient,  $f_2$ ; dashed curve: diffusion parallel to vorticity,  $f_3$ .

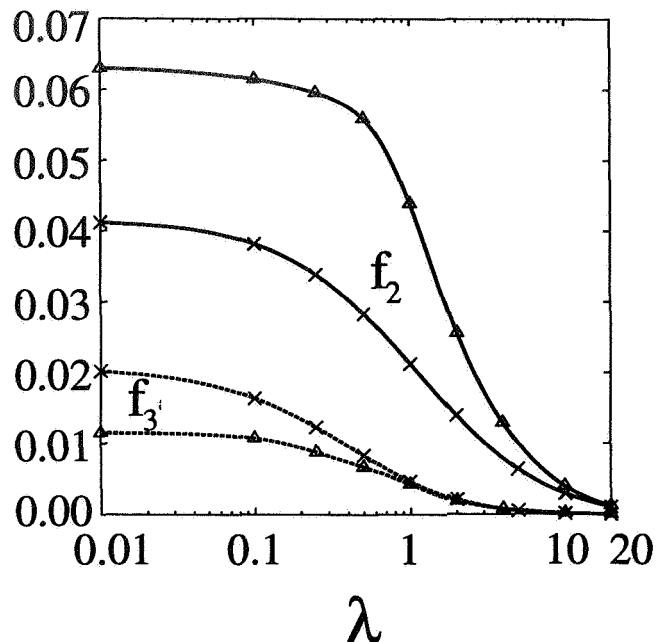


Figure 5: Self-diffusion coefficients as a function of viscosity ratio for  $Ca = 0.3$  ( $\Delta$ ) and  $Ca = 0$  ( $\times$ ); solid curves: diffusion parallel to velocity gradient,  $f_2$ ; dashed curves: diffusion parallel to vorticity,  $f_3$ .

for large viscosity ratios. Closer inspection of the numerical results indicates that self-diffusivities vanish exponentially for  $\lambda \gg 1$ .

Fig. 4 shows that  $f_2$  exhibits a maximum which may result from a balance between the increase of far-field ( $R > 2$ ) trajectory displacements with drop deformation and the decrease of near-field trajectory displacements with reduced drop cross-section. Under the same conditions,  $f_3$  is essentially independent of  $Ca$ . Fig. 4 shows a smooth transition from results for  $Ca \geq 0.1$  to the results for  $Ca = 0$  that were obtained using spherical drops stabilized against coalescence by a short-range singular repulsion.

## CONCLUSIONS

Cross-flow self-diffusivities have been computed for drops in a dilute emulsion. The results show that self-diffusivities depend strongly on the viscosity ratio and moderately on the capillary number. Self-diffusivities are much larger in the velocity gradient direction than in the vorticity direction. Drops have large self-diffusivities compared to rigid spherical particles.

The interactions between deformable drops were described with boundary integral calculations;  $O(1/N)$  numerical convergence was obtained, where  $N$  is the number of boundary elements. Mobility functions for spherical drops were used to describe the interactions between drops in the zero deformation limit.

The calculations also indicate that drop interactions do not induce significantly subcritical capillary number breakup. In dilute emulsions, the critical capillary number is a weak function of volume fraction because deformable drops can easily squeeze past each other.

## ACKNOWLEDGEMENTS

The authors thank Dr. Alexander Zinchenko for the use of his FORTRAN subroutines for computing the mobility functions of spherical drops. This work was supported by a grant from NASA Microgravity Science and Applications Division, Lewis Research Center.

## REFERENCES

- Brady, J.F. & Bossis, G. 1987 Self-diffusion of particles in concentrated suspensions under shear. *J. Chem. Phys.* **87**, 5437-5448.
- da Cunha, F.R. & Hinch, E.J. 1996 Shear-induced dispersion in a dilute suspension of rough spheres. *J. Fluid Mech.* **309**, 211-223.
- Eckstein, E.C., Bailey, D.G. & Shapiro, A.H. 1977 Self-diffusion of particles in shear flow of a suspension. *J. Fluid Mech.* **79**, 191-208.
- Grace, H.P. 1971 Dispersion phenomena in high viscosity immiscible fluid systems and application of static mixers as dispersion devices in such systems. *Eng. Found., Res. Conf. Mixing, 3rd, Andover, N.H.* republished 1982 in *Chem. Eng. Commun.* **14**, 225-277.
- Hinch, E.J. & Acrivos, A. 1980 Long slender drops in a simple shear flow. *J. Fluid Mech.* **98**, 305-328.
- Kim, S. & Karrila, S.J. 1991 *Microhydrodynamics: Principles and Selected Applications*, Butterworth-Heinemann.
- Leighton, D.T. & Acrivos, A. 1987 Measurement of shear-induced self-diffusion in a concentrated suspension of spheres. *J. Fluid Mech.* **177**, 109-131.
- Loewenberg, M. & Hinch, E.J. 1996 Numerical simulation of a concentrated emulsion in shear flow. *J. Fluid Mech.* In press.
- Rallison, J.M. 1981 A numerical study of the deformation and burst of a drop in general shear flows. *J. Fluid Mech.* **109**, 465-482.
- Wang, H., Zinchenko, A.Z. & Davis, R.H. 1994 The collision rate of small drops in linear flow fields. *J. Fluid Mech.* **265**, 161-188.
- Wang, Y., Mauri, R. & Acrivos, A. 1995 Transverse shear-induced diffusion of spheres in a dilute suspension. *J. Fluid Mech.* In review.
- Zinchenko, A.Z. 1983 Hydrodynamic interaction of two identical liquid spheres in a linear flow field. *Prikl. Mat. Mech.* **47**, 56-63.
- Zinchenko, A.Z. 1984 Effect of hydrodynamic interactions between the particles on the rheological properties of dilute emulsions. *Prikl. Mat. Mech.* **48**, 198-206.

## DROPS IN SPACE: SUPER OSCILLATIONS AND SURFACTANT STUDIES

Robert E. Apfel\*, Yuren Tian\*, Joseph Jankovsky\*, Tao Shi†, X. Chen\*, R. Glynn Holt\*\*,\*\*\*, Eugene Trinh\*\*, Arvid Croonquist\*\*, Kathryn C. Thornton\*\*\*, Albert Sacco, Jr.\*\*\*, Catherine Coleman\*\*\*, Fred W. Leslie\*\*\*, and David H. Matthiesen\*\*\*

\* Yale University, Department of Mechanical Engineering, New Haven, CT 06520-8286

\*\*Jet Propulsion Laboratory, California Institute of Technology, Pasadena, CA 91109

\*\*\*STS 73 Payload Crew; Mail Code CB, Johnson Space Center, Houston, TX 77058

† Emory University, Department of Physics, Atlanta, GA 30322

An unprecedented microgravity observation of maximal shape oscillations of a surfactant-bearing water drop the size of a ping pong ball was observed during a mission of Space Shuttle Columbia as part of the second United States Microgravity Laboratory-USML-2 (STS-73, October 20-November 5, 1995). The observation was precipitated by the action of an intense sound field which produced a deforming force on the drop. When this deforming force was suddenly reduced, the drop executed nearly free and axisymmetric oscillations for several cycles, demonstrating a remarkable amplitude of nonlinear motion. Whether arising from the discussion of modes of oscillation of the atomic nucleus, or the explosion of stars, or how rain forms, the complex processes influencing the motion, fission, and coalescence of drops have fascinated scientists for centuries. Therefore, the axisymmetric oscillations of a maximally deformed liquid drop are noteworthy, not only for their scientific value but also for their aesthetic character.

Scientists from Yale University, the Jet Propulsion Laboratory (JPL) and Vanderbilt University conducted liquid drop experiments in microgravity using the acoustic positioning/manipulation environment of the Drop Physics Module (DPM). The Yale/JPL group's objectives were to study the rheological properties of liquid drop surfaces on which are adsorbed surfactant molecules, and to infer surface properties such as surface tension, Gibb's elasticity, and surface dilatational viscosity by using a theory which relies on spherical symmetry to solve the momentum and mass transport equations [1]. The technique involves the acoustic squeezing and releasing of the liquid drop, and the measurement of the subsequent free decay frequency and damping constant [2]. For small amplitude motion, it is desirable to excite only the lowest-order (energy) normal mode of the drop, the axisymmetric quadrupole mode, in

which the drop oscillates between an oblate and prolate shape. In our chamber this oblate-prolate alternation is seen in the X-view of the DPM, while in the Z view one observes a simple circular shape.

The Drop Physics Module (DPM) facility was designed by the Jet Propulsion Laboratory and built by Loral Corporation's Electro-Optical Sensors Division. This module is essentially an air-filled box at one atmosphere pressure with inner dimensions (X, Y, and Z) of 12.4 cm, 12.4 cm, and 15.2 cm, respectively. Four custom high-amplitude, titanium-dome acoustic loudspeakers were placed in the box along the intersections of the bottom and side panels. A pair of stepper-motor-controlled injectors are used to inject and retrieve drops, ranging from 1-14 cc in our experiments. A common configuration for drop manipulation consists of opposing driving speakers 1 and 3 in the (100) X mode, speakers 2 and 4 in the degenerate (010) Y mode, and all four speakers in the (001) Z mode, typically 1350, 1350, and 1130 Hz, respectively.

The payload crew scientists on board Columbia operated the DPM via an interactive software interface, allowing the alteration of the acoustical environment by changing speaker drive voltages, frequencies and phases. They were supported on the ground by the payload operations team of the Marshall Space Flight Center (Huntsville, Al.) and the DPM Science Team, which included the scientific investigators, development engineers and support personnel. Almost continuous real-time communication between the Spacelab team and the ground team via voice, telemetry, and video was available. These links enabled results to be immediately evaluated, allowing for parameter adjustments over the course of the experiments which could not be defined before the mission, and which were absolutely essential for the carefully timed sequences that led to our observations.

From that oscillation data both the frequency of oscillation and the decay constant can be retrieved. The oscillation is considered a "good one" if the Z view of the oscillation displays a circular outline for the drop which changes in size during the oscillation. This confirms the axisymmetric character of the oscillation. This aspect of the motion, along with the idealized spherical shape made possible by microgravity, makes data analysis straightforward.

The drop oscillation sequence reviewed here involved the oscillation of a 6.6 cc drop (2.33 cm diameter) water drop containing the non-ionic surfactant Triton-X-100, which is commonly used in detergents and mixing agents. The chemical formula is  $\text{CH}_3\text{C}(\text{CH}_3)_2\text{CH}_2\text{C}(\text{CH}_3)_2\text{C}_6\text{H}_4\text{E}_{(n)}\text{OH}$ , where  $\text{E}=\text{OCH}_2\text{CH}_2$ , and ranges from 9 to 10. It was saturated in the water at the critical micelle concentration



(CMC) — that is, the concentration beyond which small aggregates of the material will form in the bulk of the liquid and negligible lowering of the surface tension will occur. The CMC for Triton is a minuscule  $1.4 \times 10^{-4}$  g/ml, at which the approximate static surface tension of this aqueous solution is 0.03 Newtons/m (less than half that of pure water). It is thus readily apparent why these types of materials are of interest to scientists and engineers -- tiny concentrations leave bulk properties unchanged, but result in marked surface viscoelastic properties, and thus alter the surface and bulk motion dramatically.

The microgravity sequence (black background) shown in Figure 1 involved a drop that was slowly squeezed so that in the Z-view the circular outline grew and the X-view appeared initially as a narrow ellipse of aspect ratio of 4.5. One complete cycle is shown here, both in X and Z views, although the complete video shows about 20 cycles (in about 17 seconds) before the oscillation reverts to the lowest energy quadrupole mode. A World Wide Web animated video sequence can be found at <http://www.yale.edu/engineering/fac-info/apfel-data/drop.mpg>. The cigar-shaped image of 6th frame has an aspect ratio approaching 3, which, in the parlance of nuclear modeling is called "hyperdeformed" [3]. A second remarkable feature is that the drop did not fission. The lower surface tension that allowed for the large deformations also probably prevented the elongated sections from pinching off.

These observations are borne out by numerical computations of the evolution of the shape of greatly deformed drops using the boundary integral method as adapted by Tao et al. to the case of drop motion in the presence of an intense acoustic field which can be used to cause both static and dynamic shape changes.<sup>4,5</sup> This method permits the study of large free or forced shape oscillations of axisymmetric drops, including the effects of viscosity, but not including the presence of surfactants or surface damping. We wondered whether such an analysis would produce drop shapes comparable to our observations. If so, they would permit us to extract data such as the dynamic surface tension, which can differ from the statically measured value. Such differences can provide important information on the rate of processes occurring as surfactant transfers back and forth between the surface and its sublayer.

Figure 1 also shows the predictions of the shape oscillations using the boundary integral method (X-view). These frames are displayed above the corresponding observations. The numbers indicated in each frame show the nondimensional time given by the ratio of the real time to the factor  $T = a_0/v_0$ , where  $v_0 = (2\sigma/\rho a_0)^{1/2}$ , which is the capillary wave speed. Here  $\sigma$  is the surface tension,  $\rho$  is the liquid density, and  $a_0$  is the drop radius. The computation was carried out for a Reynolds number ( $\rho v_0 a_0/\mu$ ) of 600,

where  $\mu$  is the shear viscosity, taken to be about 1.5 times that of water to account for the presence of the surfactant which increases the surface layer damping. The capillary wave speed is taken to be about 7.5 cm/s, which is estimated from the surface tension of Triton X-100 at this concentration. Note that when we also carried out the same calculation for zero viscosity, the predictions indicated that the drop would bifurcate, whereas in the case shown, the image tracks closely the experimental observations.

Analysis of the real time measurements from USML-2 and the non-dimensional time from the predictions of the boundary integral method allows one to compute a dynamic surface tension of approximately  $33.5 \pm 1.0$  dyne/cm ( $0.0335$  N/m), which is slightly higher than the statically measured value for a 1 CMC solution of Triton X-100 of 31 dyne/cm. A higher dynamic surface tension might be expected, because surfactant transport to the surface is a rate-limited process, and the equilibrium concentration of surfactant is not fully achieved during the period of oscillation. While surfactant molecules in a thin boundary layer near the surface can reach the surface as it rapidly expands, diffusion from the bulk will be too slow to fully replenish the boundary layer. Yet, in the present case the drop begins in the statically deformed shape (maximum surface area), and therefore the surfactant does not have to diffuse to the surface, but only redistribute itself on the surface, which evidently happens on a time scale that is short compared to the drop motion.

It is truly remarkable that the shapes predicted correspond closely to the data. Such a correspondence through a complete cycle not only validates for the first time the use of the theoretical methodology of the boundary integral method for this special and unprecedented maximum oscillation observation, but also enables the prediction of dynamic surface tension. Future work will concentrate on the analysis of the decaying oscillation for this and one other surfactant material, which should permit the deduction of the surface viscosity coefficient and Gibbs elasticity, in addition to the dynamic surface tension.

## REFERENCES

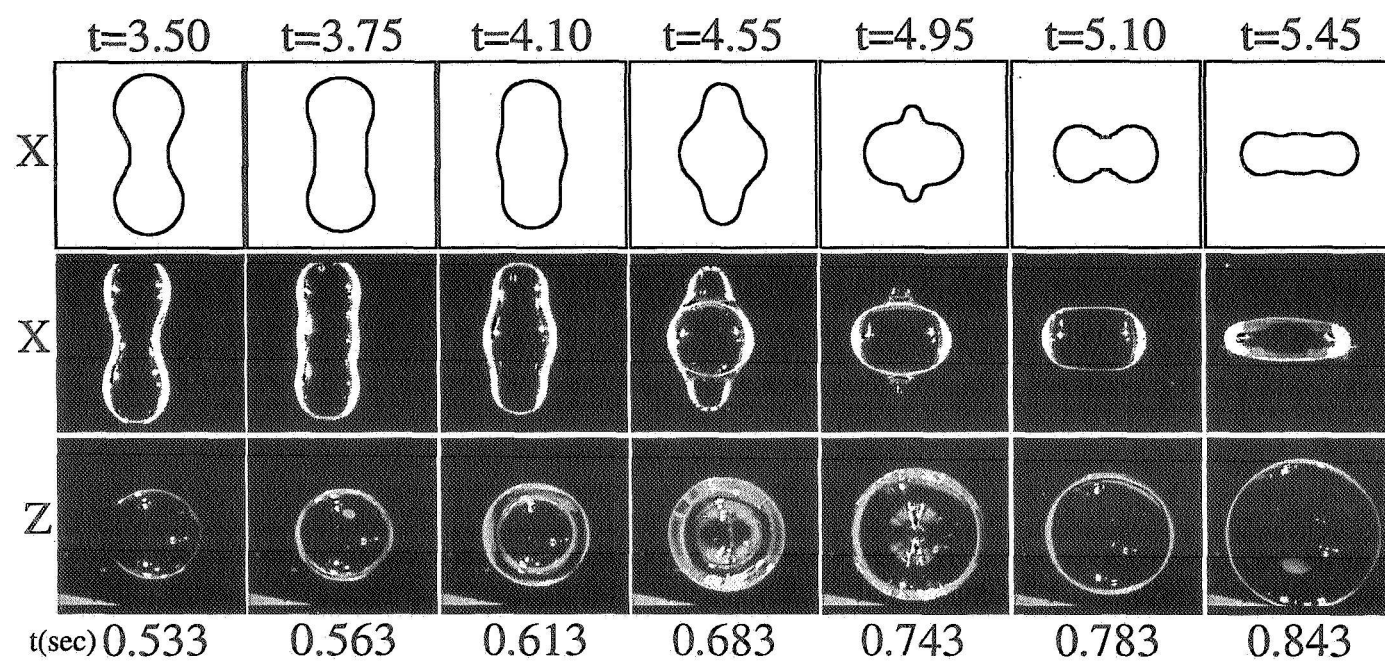
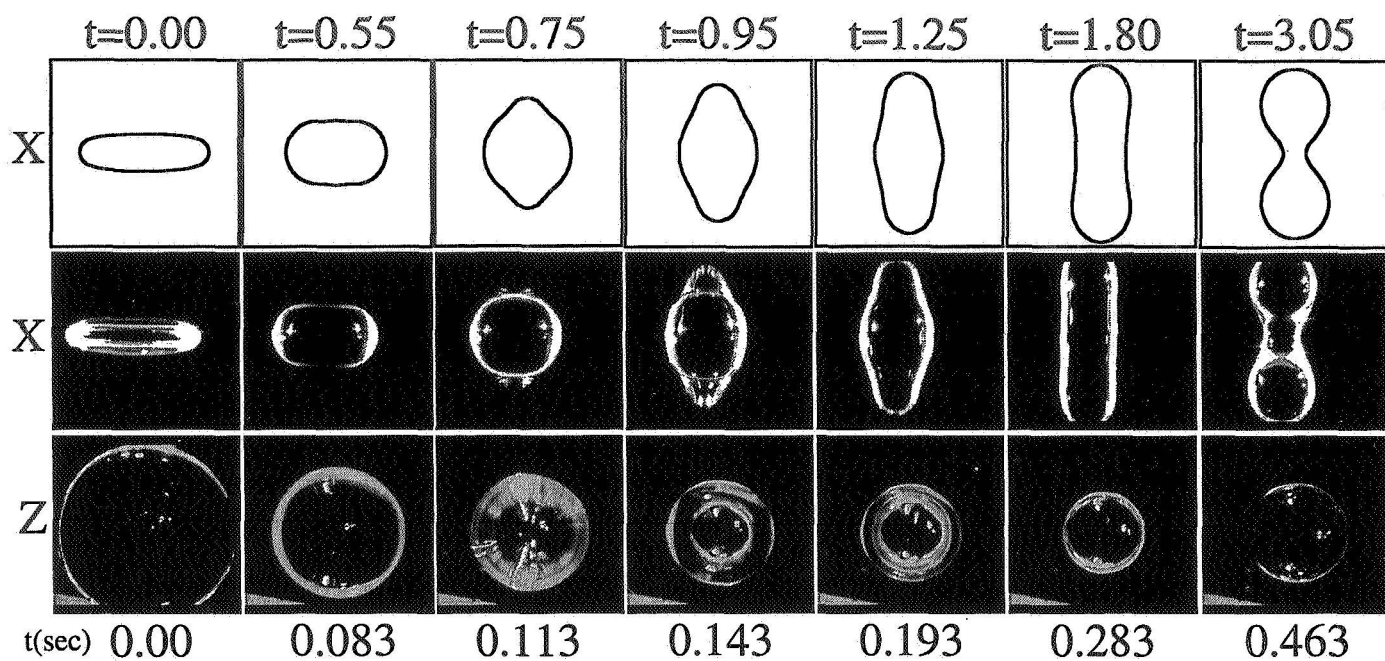
1. Tian, Y., Holt, R. G., and Apfel, R. E., Phys. of Fluids **7**, 2938 (1995).
2. Lu, H. L. and Apfel, R. E., J. Fluid Mech. **222**, 351 (1991)
3. Schwarzschild, B., in "Search and Discovery" section of Physics Today, Nov. 1995, pp. 17-19.
4. Shi, W. T. and Apfel, R. E., Phys. Fluid **7**, 1545 (1995).
5. Shi, W. T., Apfel, R. E., and Holt, R. G., Phys. Fluid **7**, 2601, 1995

## ACKNOWLEDGMENT

This work has been supported by NASA through a grant administered by the Jet Propulsion Laboratory, Contract 958722.

## FIGURE CAPTION

Figure 1: Sequence of 14 frames showing single complete oscillation of a 6.6 cc drop that begins in a highly deformed (oblate) shape owing to a high intensity acoustic field, and which then oscillates after the acoustic field intensity is suddenly reduced. The top images in each row are the X (side) view, and the bottom images are the Z (top) view demonstrating the axisymmetric nature of the oscillation. The time of each frame is marked. Shown above the X view observations are a sequence of frames computed using the boundary integral method, assuming a Reynolds number of 600. The non-dimensional time,  $T$ , shown with each frame is defined in the text. Note that the last two frames of the predictions differ from the observations, because the prediction are showing the center plane of the drop (which is dimpled in), whereas the observations are showing the front view image which cannot show the inward dimpling effect.



# THE ONSET OF RESONANCE-CONTROLLED INSTABILITY IN SPHERICAL BUBBLE OSCILLATIONS

R. Glynn Holt, D. Felipe Gaitan  
Jet Propulsion Laboratory, California Institute of Technology  
Pasadena, CA 91109

## ABSTRACT

Single bubble dynamics are investigated using acoustic techniques for isolation and manipulation. The goal of the investigations is to understand the dynamic origin of the various phenomena that bubbles exhibit: light emission, enhanced mass transport, chaotic and quasiperiodic oscillations and translations. Once understood, acoustically manipulated bubbles can serve as platforms for materials effects on free surfaces, using surfactants to alter surface rheology and observing how that affects both dynamics and also mass transport. The effects of gravity on the problem will be shown to be significant. The first set of observations from 1g experimentation are presented. These observations are of the onset conditions for instability of the spherical shape of the bubble. For the size range 55 - 90 microns in diameter we observe instability governed by resonant mode coupling, which is significantly affected by the buoyant force and its effects.

## INTRODUCTION

A bubble is a laboratory for the study of a surprising variety of physics problems. Heat transport [1], mass transport [2], surfactant effects [3], shock waves [4], chaos [5], free surface instability [6], and even electromagnetic radiation [7] are all phenomena associated with the highly nonlinear oscillations of air bubbles in water. It is impossible, however, to separate the study of any of these phenomena from the fundamental mechanics of the bubble wall's oscillation, coupled to the thermodynamics of the interior. Thus it is crucial to make detailed observations of bubble mechanics in concert with other investigations of material or transport properties.

Many areas of science and technology depend on bubble dynamics. In the field of biomedical ultrasound, many of the effects studied in the ultrasound community (such as enhanced cell lysis, sonochemical reactions, ultrasonic cleaning, etc.) depend on the mechanical response of a bubble to a sound field. In the field of surface rheology, knowing the mechanical response of bubbles lets us use them as tools to probe the effects of surface active agents, much as drops are currently being used [8]. In addition to being a closed, isolated interface, one of the major reasons a bubble is used in these contexts is that a bubble can produce both pure dilatational, shear, and a combination of dilatational and shear interfacial motions. Mass transport research on the effect of surfactants on the diffusion of gas across the air water interface [Fyrillas and Szeri in 3] also relies on detailed bubble mechanics, and will eventually lead to understanding the fundamentals of air-sea mass transfer. Ambient noise in the ocean (which has been shown to be largely due to volume oscillations of bubbles near the sea surface [9]) has been conjectured to depend on precisely the nonlinear shape/volume mode energy transfer for which we present results in this paper [10].

In the microgravity environment, bubbles are important for two reasons. The first is that bubbles experience a buoyant force due to gravity, and the justification for microgravity experimentation is simply the removal of the buoyant force and its effects. Static deformation of the equilibrium shape changes the *very nature* of the coupling between volume and shape mode(s), which we will show is the primary instability for a bubble [11]. As well, translatory oscillations of the bubble guarantee that the onset of shape oscillations in 1g will occur at relatively low pressure values, making *impossible* the observation of the predicted volume-oscillation bifurcation superstructure [12].

Bubbles are best studied in isolation, without contact and contamination from containers, and then non-invasively manipulated. Perhaps the most effective scheme is that of acoustic levitation, where the nonlinear acoustic radiation force balances the buoyant force in 1g, and merely positions at

pressure maximum in 0g. On the practical side, however, measurements on bubbles in 1g are compromised because positioning is coupled to driving force, and nonlinear effects such as self-oscillation and streaming occur due to the coupling (via the necessarily high-amplitude acoustic field) of the volume and translational modes. Decoupling driving from positioning is *impossible* in 1g.

Secondly, apart from bubbles being the subjects of microgravity research themselves, *bubbles occur in fluids in space*, and their appearance is fraught with problems, not least of which is how to get rid of them! Fluids experiments (Drop Physics Module, Zeolite Crystal Growth, Oscillatory Thermocapillary Flow, Generic Bioprocessing Apparatus) on both the STS-50 and STS-73 missions have often developed bubbles whose presence and dynamics affected what was being measured. Most proposed schemes for elimination of unwanted bubbles (acoustic, thermocapillary, electrophoretic) depend on dynamics of bubbles for their efficacy. Once again understanding bubble mechanics is seen as fundamental to a host of practical problems.

We present here the results from the first phase of our planned experimentation: the investigation of the onset of non-spherical oscillations of the shape of the bubble. These Faraday shape oscillations form a natural boundary in the parameter space of bubble dynamics, since experimentation on spherical bubbles can occur only at pressures and radii below the critical values. Above the threshold, the amplitude of these shape oscillations can rapidly grow, and lead to breakup of the bubble. We will limit ourselves to a brief descriptive background of the problem, followed by an experiment description and results.

## BACKGROUND: THE SHAPE OSCILLATION PROBLEM

A gas/vapor bubble in water is a highly nonlinear system. This is most readily seen when the bubble is subject to an external forcing, such as is the case when a time-varying acoustic field is imposed. Suppose that the acoustic wavelength is much larger than the bubble radius  $R_0$  ( $k_a R_0$  small, where  $k_a$  is the acoustic wavenumber in water). During a compression phase of the field, the bubble, since it is highly compressible, will contract, accelerating inward. The pressure and temperature will increase. Eventually, the contraction halts, reverses, and the bubble begins expanding. During the expansion phase of the external field, the bubble expands, cooling and reducing the pressure in its interior.

This oversimplified picture gives us at least a qualitative insight into the motion. The nonlinear restoring force is largely thermodynamic during collapse (due to the increased interior pressure) and expansion, since equilibrium implies a static pressure stress balance across the bubble wall. The nonlinear damping is due to thermal, bulk viscous and sound radiation mechanisms in the case of a pure liquid, and additionally due to surface viscosity for liquids with surfactants. For a fixed equilibrium radius  $R_0$ , the bubble will exhibit a fundamental linear resonance frequency  $f_0$ . For an air bubble in water of radius  $R_0 = 64$  microns,  $f_0 \sim 50$  kHz at atmospheric pressure.

Consideration of the spherically symmetric problem yields predictions of highly nonlinear dynamics as the acoustic pressure  $P_a$  is increased. Numerical integration of the equation of motion for a driven, *spherical* bubble predicts the resonant creation of *periodic* (and via standard period-doubling bifurcations *chaotic*) families of solutions via resonant *saddle-node* bifurcations. The Farey ordering [12] of the resonant saddle-node bifurcations imposes a recurrent superstructure which controls the appearance of period-doubling bifurcations to chaos. One of the goals of this research is to observe this behavior, or determine why it is not observed.

Under what conditions will spherical symmetry become unstable, and further under what conditions will this instability lead to observable distortions of the shape and eventual breakup of the bubble? There are two candidate instabilities: Rayleigh-Taylor (RT, [13]), and parametric or Faraday (F, [14]). It can be shown that, during at least some part of its motion, a bubble is RT unstable. RT instability occurs for accelerated interfaces when density and pressure gradients across the interface are opposed. RT occurs on a fast time scale, and is thus likely to be violent in its effects on the bubble surface if conditions allow it to develop. At first glance, RT appears very likely to destroy a bubble at its first collapse.

F, in contrast, requires a *resonant interaction* for the necessary energy exchange. A free liquid surface, when vibrated periodically and normal to its surface plane, will exhibit Faraday waves with *half* the driving frequency when the excitation overcomes the damping [15]. In addition to requiring a finite threshold excitation, sufficient time is required for the coupling to occur, typically 2 or more cycles of the periodic excitation. Finally, since a bubble is a closed surface whose circumference is of the same order as the capillary wavelength, the energy must excite a normal mode of the bubble, constrained by a resonance condition similar to the classic  $f_{\text{shape}} / f_{\text{volume}} = 1/2$ , and consideration must be given to the damping of the normal modes. Theoretical treatments of this problem [Strube, Eller and Crum in 6] predict that such instabilities will occur near the  $(P_a R_0)$  values where the interesting spherical dynamics occurs. Thus, we want to resolve the issue of the dynamical behavior of bubbles over a wide range of parameter space  $(P_a R_0)$ : what behaviors obtain, and why?

## EXPERIMENT

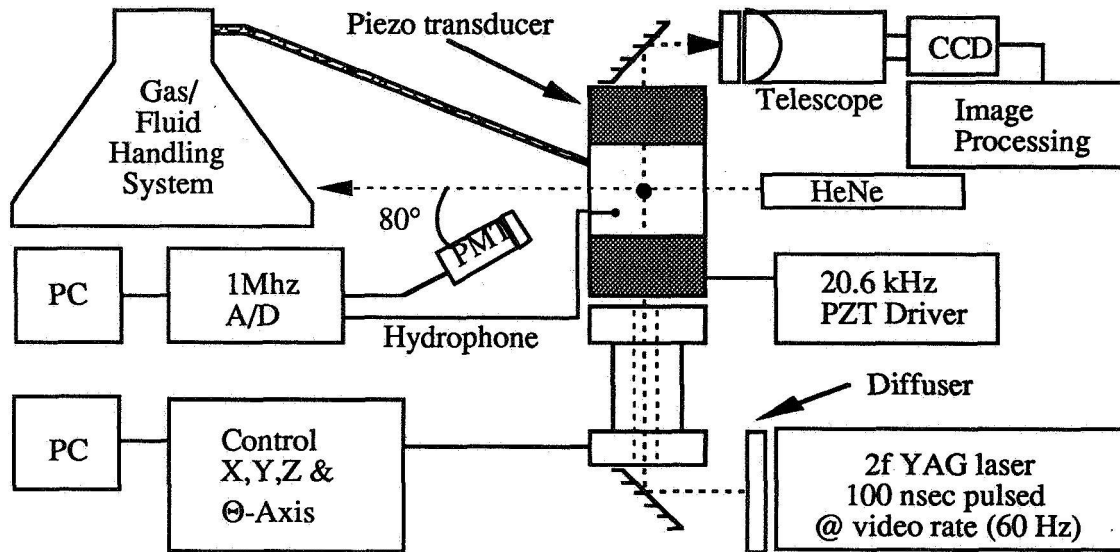


Figure 1: Schematic of setup for acoustically levitating and imaging bubbles in water

Air bubbles initiated via electrolysis are acoustically levitated in water in the  $f_a = 20.6$  kHz standing wave field of a cylindrical resonance cell as illustrated in Fig. 1 [16]. The acoustic pressure  $P_a$  at the antinode is obtained from a custom hydrophone mounted near the  $z$  antinode and 1cm away from the side wall inside the cell. The hydrophone is calibrated by balancing the buoyant force with the acoustic force for a variety of bubble sizes and positions along the  $z$  axis pressure gradient, always using small amplitude oscillations. For calibration purposes,  $R_{ave}$  ( $= R_0$  for a linearly oscillating bubble) is measured directly by measuring the locations of the peaks encountered by sweeping a detector from  $20^\circ$  to  $90^\circ$  in the polarization-plane forward scattering of an incident linearly polarized He-Ne beam using Mie theory [17].  $R_0$ ,  $R_{max}$  and  $R_{min}$  are obtained from single frame video images illuminated at 1 pulse per frame (maximum 1 ms pulse width);  $R_0$  in particular is obtained by turning the sound field off instantaneously when the bubble is in the focal plane of the imaging system.  $R(t)$  is obtained from a PMT located at  $80^\circ$  from the forward [18]. Corroborating  $R(t)$  information is obtained from a fast photodiode directly in the forward diffraction lobe of the bubble. Distilled, de-ionized, carbon and particulate filtered water was used for all measurements. Dissolved gas concentrations less than saturation were obtained by allowing the water to equilibrate at a reduced pressure.

The practical key to performing the measurements we report here is the slowing of the mass transport time scale within two pressure constraints: our lowest obtainable pressures are bounded by the minimum trapping pressure, while the highest obtainable pressures (for a given  $R_0$ ) are bounded by the threshold for Faraday shape oscillations and breakup of the bubble. Within these bounds, for a fixed  $P_a$  and dissolved gas concentration, the system will self-select one (or very few) bubble size  $R^*$  which will be in dynamic mass equilibrium. By varying the dissolved gas concentration we can cause that size range to span the entire space from 1 to 100 microns. We can vary  $P_a$  near  $R^*$  where  $dR_0/dt$  is small, and observe the onset of shape oscillations quasistatically.

## RESULTS

At low  $P_a$ , the bubble remains spherical, and exhibits the weak nonlinear trait of harmonic generation [16], with the response remaining periodic with the same period  $T_a$  as the acoustic field. Figure 2a shows the measured  $P_a$  and  $R$  as functions of time; note the strong 2nd harmonic component. The bubble in Figure 2 had an equilibrium size of 66 microns, and a linear resonance frequency of 48 kHz, very nearly twice the acoustic frequency  $f_a$ . The pattern repeats itself for smaller bubbles as their linear resonance frequency nears an integer multiple of  $f_a$ . Thus, we observe the pre-saddle-node harmonic resonance predicted by theory. However, all the spherically symmetric oscillations we have observed have been strictly periodic with period  $T_a$ , and remain below the amplitudes required for the saddle-node bifurcation predicted. What prevents this bifurcation?

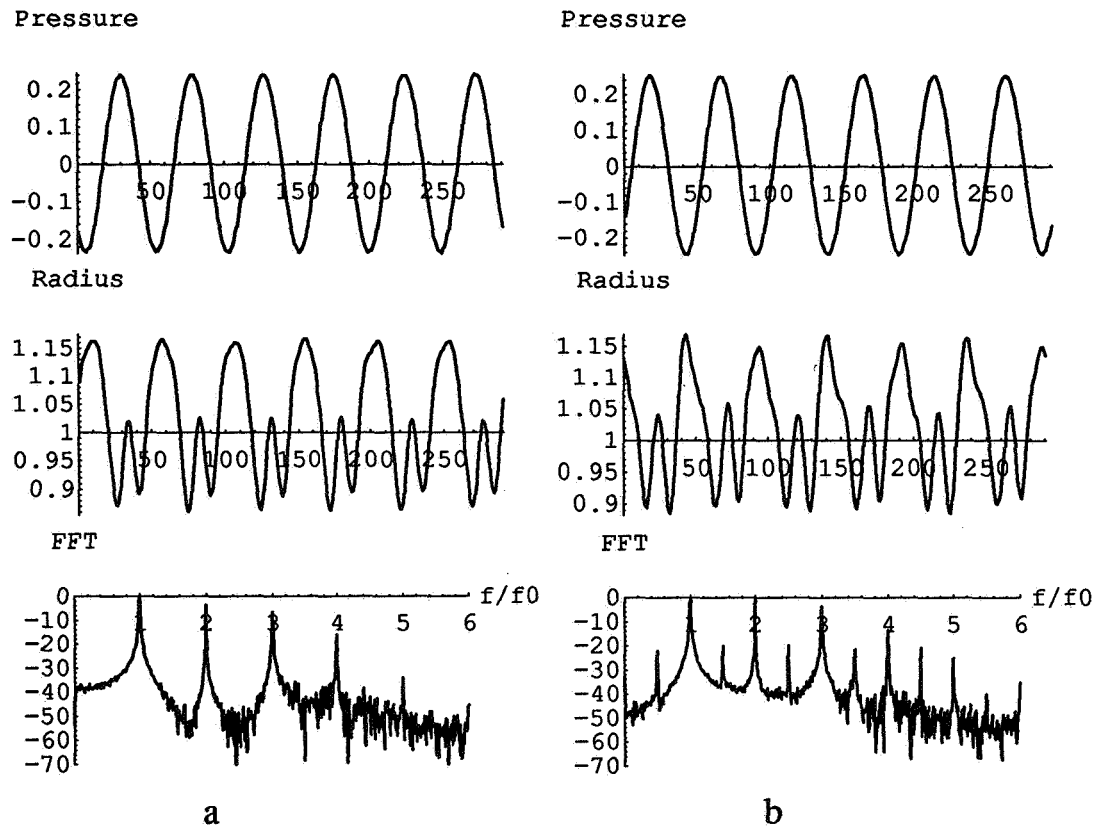


Figure 2: Response of a 66 micron radius bubble to an acoustic pressure of 0.24 bar at 20.6 kHz. a) from top to bottom: the pressure vs time (arbitrary units) from the hydrophone; normalized radius vs time from the 80° PMT scattered light; and FFT of the radius. b) The same data at 0.25 bar, just after the onset of a mode 5 shape oscillation. The signature of the shape oscillation is the peak at  $f/f_0 = 1/2$ .



Our observations show that, for all acoustic pressures  $P_a$  below 1.3 bar for air bubbles in water, the instability which develops first is the Faraday instability. The signature of this instability is often a period-doubling of the scattered laser signal, as shown in Fig. 2b for a 66 micron bubble driven just past the onset of the 5-lobed mode, identified by video image analysis. Figure 3 shows a subset of the measured ( $P_a R_0$ ) values for onset of an oscillation of the shape of the bubble, and thus the loss of spherical stability. The observed modes are indicated by the symbol type. Notice also the set of theoretical curves for onset of the different modal oscillations: we will discuss these in the next section. We concentrate on understanding the experimental data in simple terms in this section.

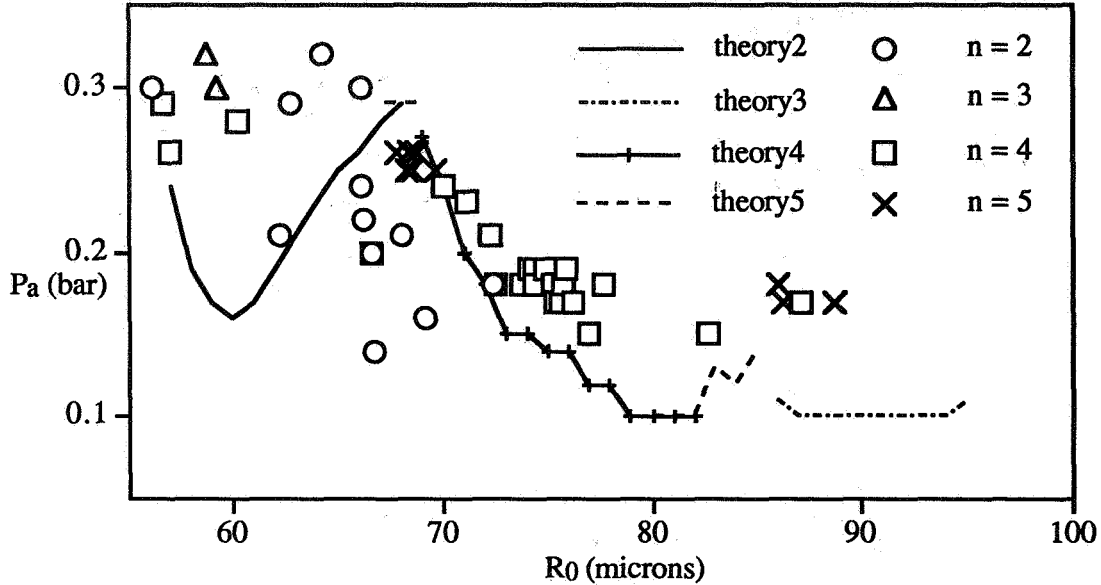


Figure 3: Measured threshold acoustic pressure  $P_a$  and equilibrium radius  $R_0$  for onset of shape oscillations (Faraday instability: mode observed given by symbol). All data presented are for air bubbles levitated in pure water driven at 20.6 kHz at 22° C at ambient pressure of 1 bar. The theoretical thresholds and modes presented for comparison are courtesy of M. Brenner, calculated using the algorithm presented in [6].

The general trend of higher threshold at smaller bubble size (averaged over different modes) is just the stabilizing effect of the curvature  $1/R$ . Most of the dips and peaks, and the presence and location of specific normal modes can be understood in terms of resonances. A particular shape mode  $n$  is in *external resonance* to the driving field (via the forced non-resonant response of the volume mode) when  $f_n / f_a \sim i / 2$ ,  $i = 1, 2, 3, \dots$ , and we speak of  $i:2$  external resonance. A shape mode  $n$  is in *internal resonance* with the resonating volume mode when  $f_n / f_0 \sim j / 2$ ,  $j = 1, 2, 3, \dots$ , hence  $j:2$  internal resonance. Understanding that the energy transfer mechanism is the Faraday instability is the reason for the factor of 2 in the denominator. The locations in ( $P_a, R_0$ ) space where  $i$  and  $j$  are integers are not in general coincident. For bubbles in the range presented here, either resonance is equally likely; for very small bubbles, only internal resonance is possible at kHz frequencies. Note that, though we use the classification 'shape modes in external resonance with the driving field', the field does not directly force the modal oscillation.

Figure 4 plots the ratio of mode (shape or volume) frequency to acoustic driving frequency  $f_a$  using the measured  $R_0$  and the observed mode number (assumed axisymmetric) at the onset of shape oscillation. Analytical curves for the Lamb frequency [19] for the shape modes 2 - 5 are plotted, as is an analytical expression for the fundamental linear resonance frequency for the volume mode [20] at ambient pressure. Thus, points where the halved volume frequency curve intersects any shape modal frequency curve (e.g., the  $n = 4$  curve near 60 microns) represent the condition for 1:2 internal resonance, or  $j = 1$  [a slightly different definition from that of Feng et al. in 21]. Points where a shape frequency curve intersects a line  $i = 1, 2, 3$  represent  $i:2$  external resonance: e.g.,  $i = 1$  for the  $n = 2$  curve near 60 microns.

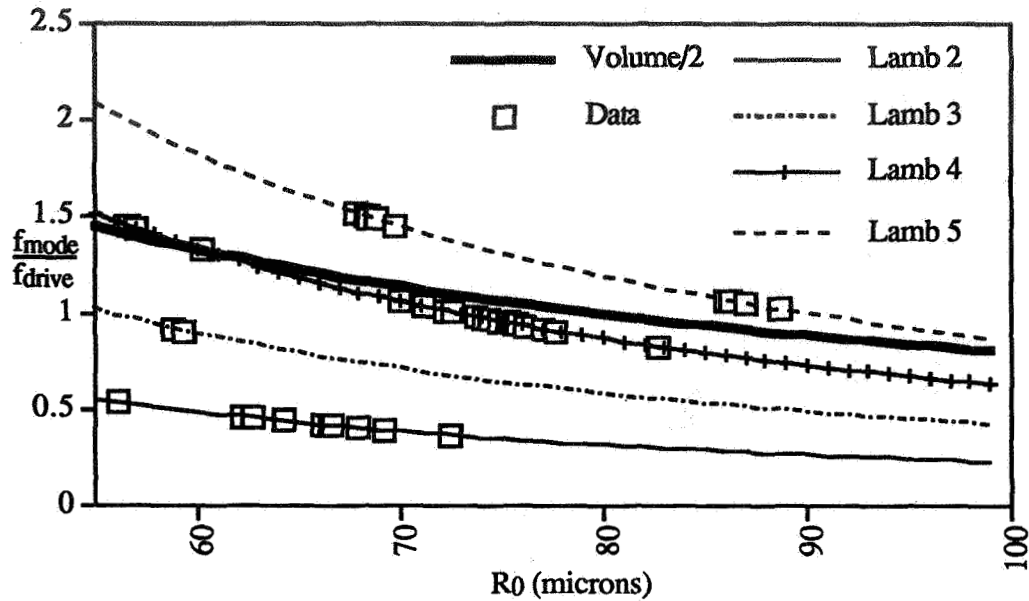


Figure 4: Shape and volume modal frequencies vs  $R_0$ . The points labeled Data are the theoretical shape frequencies calculated for the observed mode and  $R_0$ . Curves labeled 'Lamb  $n$ ' were generated using the analytical expression of Lamb [19] for capillary waves. The curve 'Volume/2' is the analytical approximation to the linear resonance frequency of the volume mode due to Minneart [20].

Figure 4 clearly shows the organizing principle of resonance: the data fall in bunches near points of internal or external resonance. The origin of the peak and valley in the measured threshold between 60 and 70 microns is clear: it is due to an approximate 2:1 external resonance of the  $n = 2$  mode. The observation of the  $n = 4$  mode at onset between 70 and 80 microns is due to a *double resonance*:  $j \sim 1$  and  $i \sim 2$  simultaneously (this region is usually called the '2nd harmonic' resonance, since the bubble's linear volume frequency is twice the driving frequency, and the bubble oscillates nonlinearly with a strong  $2f_a$  component near this size).

#### DEVIATIONS FROM THEORY: THE EFFECT OF GRAVITY

The theoretical threshold curves in Figure 3 were generated using a technique presented in Brenner et al. [6]. The radius variable in the nonlinear 2nd order ODE describing spherical bubble dynamics [the 'Rayleigh-Plesset equation', 22] is replaced by an expansion in normal shape modes described by Legendre polynomials. A linear-form 2nd order ODE for the amplitudes  $a_n$  of the shape modes  $n$  is derived, possessing nonlinearly time-varying coefficients (a generalization of Hill's equation). This approach can account for both internal and external resonances of all orders, but does not account for the effect of the buoyant force.

In Fig. 3 we see good agreement for the location of the threshold for the 4 mode, and fair agreement for the 5 mode. The 3 mode appears to be in disagreement, but this is partially due to the fact that it becomes more important in the ranges 15 - 40 microns, and for 90-110 microns; we see the 3 mode often in these regimes, but the data is not yet fully reduced.

The effect of gravity can be seen in the striking disagreement between theory and experiment for the 2 mode between 60 and 70 microns in Figure 3. Experiment shows the 2 appears initially at larger pressures than the theory predicts, and then a strong resonance dip to onset at anomalously low pressures occurs. Figure 4 reveals that these data are all in 1:2 external resonance with the acoustic field via the nonresonant (entrained) response of the spherical volume pulsations. How can the presence of gravity explain this?

The key is the slight deformation of the bubble due to the balance of the time-averaged acoustic force and the buoyant force. Marston [23] showed theoretically that the primary spatial component of the acoustic force was the quadrupole ( $n = 2$ ) term. Holt et al. [24] among others have

verified this for larger bubbles. Yang, Feng and Leal [21] investigated the influence of an external pressure or flow field with quadrupole spatial characteristics on the resonant coupling. In particular, they found that not only were energy-exchange and stability different from the free-field cases previously studied, a different coupling mechanism was discovered, of  $O(3/2)$ . One general conclusion was that mode-mode coupling was significantly enhanced over the free-field case, and more likely to occur at lower amplitudes (and hence lower driving pressures).

Thus, the resonance dip between 65 and 70 microns is explained: the quadrupole deformation due to the buoyant force lowers the necessary threshold for onset of shape oscillations. Things are not as clear in attempting to explain the appearance of the 4 mode near 60 microns, but enhancement of the 2 - 4 mode coupling is possible, since the theory predicts the 2 should be excited. However, at 60 microns the 4 mode is in 1:2 resonance with the volume mode, providing an alternative explanation.

## CONCLUSION

Understanding the nonlinear dynamics of driven bubble oscillations is important as a basic problem in fluid physics and nonlinear dynamics. There exists a complex set of behavior(s) whose observation depends on nonlinear resonant coupling, internal resonances and their structures, initial conditions and external parameters and fields. The implications this understanding will have for other fields in which bubble phenomena play a role will be far-reaching. The research presented here represents a first step towards a global understanding of bubble behavior. The future directions of this research as outlined above all depend on an accurate and quantitative understanding of the nonlinear mechanics of bubble oscillations. Gravity has significant and subtle effects on the problem, and it is clear that *microgravity* experimentation would provide both qualitative and quantitative improvements. The dominance of surface tension forces and the lack of a buoyant force would not only enable direct comparison with theories, but would allow access to parameter space forbidden in 1g due to the need for levitation.

## REFERENCES

1. Yasui, K., J. Acoust. Soc. Am. **98**, 2772 (1995).
2. Löfstedt, R. et al., Phys. Rev. E **51**, 4400 (1995).
3. Crum, L.A., J. Acoust. Soc. Am. **68**, 203 (1980); Johnson, D.O. and K.J. Stebe, J. Colloid Interface Sci. **168**, 21 (1994); Fyrrillas, M.M. and A.J. Szeri, J. Fluid. Mech. **289**, 295 (1995).
4. Hickling, R. and M.S. Plesset, Phys. Fluids **7**, 7 (1964); Wu, C.C. and P.H. Roberts, Phys. Rev. Lett. **70**, 3424 (1993).
5. Holt, R.G., D.F. Gaitan, A.A. Atchley and J. Holzfuss, Phys. Rev. Lett. **72**, 1376 (1994).
6. Birkhoff, G., Q. Appl. Mech. **12**, 306 (1954); **13**, 451 (1956); Strube, H.W., Acustica **25**, 289 (1971); Hullin, C., Acustica **37**, 64 (1977); Brenner, M.P. et al., Phys. Rev. Lett. **75**, 954 (1995).
7. Marinesco, N. and J.J. Trillat, Proc. R. Acad. Sci. **196**, 858 (1933); Gaitan, D.F. et al., J. Acoust. Soc. Am. **91**, 3166 (1992); Barber, B.P. and S.J. Putterman, Nature **352**, 318 (1991).
8. Tian, Y., R.G. Holt and R.E. Apfel, Phys. Fluids **7**, 2938 (1995).
9. Prosperetti, A., H.C. Pumphrey and L.A. Crum, J. Geophys. Res. **94**, 3255 (1989).
10. Longuet-Higgins, M.S., J. Fluid Mech. **201**, 525 (1989a); **543** (1989b); **224**, 531 (1991).
11. Holt, R.G. and D.F. Gaitan, APS Bulletin **40**, 1960 (1995).
12. Parlitz, U., V. Englisch, C. Scheffczyk, and W. Lauterborn, J. Acoust. Soc. Am. **88**, 1061 (1990).
13. Taylor, G.I., Proc. Royal Soc. A **201**, 192 (1950).
14. Faraday, M. Phil. Trans. Royal Soc. London **121**, 299 (1831).
15. Miles, J., J. Fluid Mech. **248**, 671 (1993).
16. Holt, R. Glynn and Lawrence A. Crum, J. Acoust. Soc. Am. **91**, 1924 (1992).
17. Lentz, W.J. et al., Appl. Opt. **34**, 2648 (1995).
18. Holt, R. G. and L. A. Crum, Appl. Opt. **29**, 4182 (1990).
19. Lamb, H., *Hydrodynamics* (Dover, New York, 1945).
20. Minnaert, M. Phil. Mag. **16**, 235 (1933).
21. Mei, C.C. and X. Zhou, J. Fluid Mech. **229**, 29 (1992); Feng, Z.C. and L.G. Leal, Phys. Fluids **5A**, 826 (1993); Yang, S.M., Feng, Z.C. and L.G. Leal, J. Fluid Mech. **247**, 417 (1993).
22. Rayleigh, Phil. Mag. **34**, 94 (1917); Plesset, M.S., J. Appl. Mech. **16**, 277 (1949).
23. Marston, P.L., J. Acoust. Soc. Am. **67**, 15 (1980).
24. Holt, R.G. and E.H. Trinh, J. Acoust. Soc. Am. **95**, 2938 (1994).



# SHAPE OSCILLATIONS OF GAS BUBBLES WITH NEWTONIAN INTERFACIAL RHEOLOGICAL PROPERTIES

Ali Nadim

Department of Aerospace and Mechanical Engineering  
Boston University, 110 Cummington Street, Boston, MA 02215

## ABSTRACT

The oscillation frequency and damping rate for small-amplitude axisymmetric shape modes of a gas bubble in an ideal liquid are obtained, in the limit when the bubble interface possesses Newtonian interfacial rheology with constant surface shear and dilatational viscosities. Such results permit the latter surface properties to be measured by analyzing experimental data on frequency shift and damping rate of specific shape modes of suspended bubbles in the presence of surfactants.

## INTRODUCTION

Shape oscillations of bubbles and drops, freely-suspended in microgravity or acoustically-levitated on earth, have been suggested as a technique for measuring such surface rheological properties as dynamic surface tension and shear and dilatational interfacial viscosities. As a prerequisite to such non-contact surface rheometry, one needs to have expressions for both the oscillation frequency and the damping parameter of the particular shape modes excited in the experiments (typically the quadrupole mode), when surface rheological effects are present and significant. The shape modes of an acoustically levitated drop or bubble can be excited by modulating the frequency of the ultrasound which is being used for levitation, at a frequency which is close to the natural frequency of the desired shape mode [10, 11, 12]. Since the natural frequency of each shape mode is dependent upon properties of the interface [9, 13] (e.g., surface tension and surface rheological constants), such an experiment can be used to measure the interfacial properties [1, 2, 4, 5, 8, 15, 16]. In particular, when the drop or bubble oscillations take place in the presence of surfactants, the contaminated interface exhibits a viscous behavior, with surface shear and dilatational viscosities which are often difficult to measure accurately by other means [3]. Thus, observation of the forced and free oscillations of drops or bubbles can be quite useful as a technique for a non-contact measurement of the surface viscosities, provided that explicit expressions are available relating the oscillation frequency and damping constants of the shape modes to the interfacial properties. Some expressions of this type have already been found [9, 13], although under certain restrictive assumptions. The present contribution derives analytical expressions for the frequency and damping rates of axisymmetric shape modes of gas bubbles in ideal liquids, when the interface possesses constant Newtonian rheological properties.

Surface rheological effects arise in the presence of surfactants, which are long molecules with separated hydrophilic and hydrophobic segments [3, 7]. In the presence of an interface

between an aqueous and a non-aqueous phase, surfactants preferentially adsorb at that surface. In addition to modifying the surface tension at the interface, an adsorbed layer of surfactants at a fluid-fluid interface may possess its own rheological properties (e.g., viscosity or elasticity), distinct from those of the bulk phases on either side. Scriven [14] provided the tensorial form of the constitutive equation for a “Newtonian” surface fluid, although the concept of surface viscosity originated with Plateau and Boussinesq [3].

## INTERFACIAL RHEOLOGY

The rheological behavior of a surfactant-laden interface can be characterized by specifying the surface stress tensor  $\Pi_s$ , which for a Boussinesq-Scriven Newtonian surface layer [14] has the invariant form

$$\Pi_s = \sigma \mathbf{I}_s + 2\mu_s[\mathbf{E}_s - \frac{1}{2}\mathbf{I}_s(\mathbf{I}_s : \mathbf{E}_s)] + \kappa_s \mathbf{I}_s(\mathbf{I}_s : \mathbf{E}_s), \quad (1)$$

in which

$$\mathbf{E}_s \equiv \frac{1}{2}[(\nabla_s \mathbf{u}) \cdot \mathbf{I}_s + \mathbf{I}_s \cdot (\nabla_s \mathbf{u})^\dagger], \quad (2)$$

is the surface rate-of-strain tensor. Here,  $\mu_s$  and  $\kappa_s$  are the shear and dilatational surface viscosities,  $\sigma$  is the surface tension,  $\nabla_s \equiv \mathbf{I}_s \cdot \nabla$  is the surface gradient operator,  $\mathbf{I}_s$  is the surface unit tensor which is related to the three-dimensional unit tensor  $\mathbf{I}$  via  $\mathbf{I}_s = \mathbf{I} - \hat{\mathbf{n}}\hat{\mathbf{n}}$  and  $\mathbf{u}$  is the velocity vector at the interface. In addition, the superscript  $^\dagger$  designates the transpose of the tensor to which it is attached and  $\hat{\mathbf{n}}$  is the normal unit vector at the surface. The surface stress tensor appears in the dynamic boundary condition at a fluid/fluid interface in the form

$$\hat{\mathbf{n}} \cdot (\Pi_l - \Pi_g) + \nabla_s \cdot \Pi_s = \mathbf{0}, \quad (3)$$

in which  $\Pi_l$  and  $\Pi_g$  are the respective stress tensors in the liquid and gas phases, and with the unit normal  $\hat{\mathbf{n}}$  taken to point from the gas to the liquid phase. Equation (3) represents an instantaneous balance of all forces acting on the interface, valid if the inertia of the interface is negligible. The dot products of (3) with  $\hat{\mathbf{n}}$  and with  $\mathbf{I}_s$  result in the normal and tangential stress balance at the interface, respectively. In general, surface properties  $\sigma$ ,  $\mu_s$  and  $\kappa_s$  all depend on the local concentration of surfactants on the interface, which needs to be found by solving a surface transport equation. In this brief contribution, however, we focus on highly contaminated bubbles whose interfacial material properties have constant values, independent of surfactant concentration.

## RESULTS FOR A NEARLY-SPHERICAL BUBBLE

As an illustrative example, consider the idealized problem of slight perturbations of an initially spherical bubble with equilibrium radius  $a_o$  and surface tension  $\sigma_o$ . Gravitational effects are neglected on the assumption that the Bond number,  $\rho_l a_o^2 g / \sigma_o$ , (with  $\rho_l$  the density of the external liquid and  $g$  the gravitational constant) is small. Thus, the equilibrium

pressures outside and inside the bubble are respectively given by  $p_o$  and  $\hat{p}_o = p_o + 2\sigma_o/a_o$ . The bubble is assumed to contain an ideal gas which has a uniform pressure determined by its instantaneous volume. The surrounding liquid of infinite expanse is treated as an incompressible *ideal* fluid with its velocity field deriving from a scalar potential. For this problem, it is convenient to work in a spherical coordinate system  $(r, \theta, z)$ , in which  $r$  and  $\theta$  are the radial distance from the origin and the polar angle measured from the  $z$ -axis. Let  $\epsilon$  be a small parameter measuring the magnitude of deformation. For axisymmetric surface deformations, the instantaneous shape of the bubble can be written in the form  $r = a_o[1 + \epsilon f(\theta, t)]$ , where  $f(\theta, t)$  is the shape correction function.

For such slight perturbations from equilibrium shape, all quantities can be expanded in powers of the small parameter  $\epsilon$ , as given in the following list:

Coordinate $r$ of a surface point	$a_o + \epsilon a_o f(\theta, t)$
Exterior velocity potential	$\epsilon \Phi(r, \theta, t)$
Normal interface velocity	$\epsilon U(\theta, t)$
Tangential interface velocity	$\epsilon V(\theta, t)$
Exterior pressure at the surface	$p_o + \epsilon p(\theta, t)$
Interior pressure	$\hat{p}_o + \epsilon \hat{p}(t)$
Surface rate-of-strain	$\epsilon N(\theta, t)$
Surface rate-of-dilatation	$\epsilon M(\theta, t)$ .

Here, the surface rates of dilatation and strain—corresponding to the trace of (2) and its remaining traceless part—can be related to the surface velocities given in the same table by

$$M(\theta, t) = \frac{1}{a_o} \left[ \frac{1}{\sin(\theta)} \frac{\partial}{\partial \theta} [\sin(\theta) V] + 2U \right], \quad (4)$$

$$N(\theta, t) = \frac{1}{a_o} \left[ \frac{\partial V}{\partial \theta} - \cot(\theta) V \right]. \quad (5)$$

The complete set of equations which describe the linearized dynamics of the bubble at  $\mathcal{O}(\epsilon)$  can now be formulated as follows. Since the perturbation from the equilibrium spherical shape is assumed to be small, all surface boundary conditions can, to leading order, be imposed at the undisturbed position of the bubble surface,  $r = a_o$ . The velocity potential of the exterior liquid phase is a solution to

$$\nabla^2 \Phi = 0 \quad (r > a_o) \quad (6)$$

subject to boundary conditions

$$\Phi \rightarrow 0 \quad \text{as } r \rightarrow \infty, \quad (7)$$

$$\partial \Phi / \partial r = a_o \partial f / \partial t = U(\theta, t) \quad \text{at } r = a_o, \quad (8)$$

where (8) results from the kinematic condition at the surface. The normal stress condition, obtained by taking the dot product of (3) with  $\hat{n}$ , presently takes the form

$$\hat{p} - p = \frac{2}{a_o} (\kappa_{so} M) - \frac{\sigma_o}{a_o} \left[ \frac{\partial^2 f}{\partial \theta^2} + \cot(\theta) \frac{\partial f}{\partial \theta} + 2f \right], \quad (9)$$

while the tangential stress condition, obtained by taking the dot product of (3) with  $(\mathbf{I} - \hat{\mathbf{n}}\hat{\mathbf{n}})$ , reduces to

$$0 = -\frac{\partial}{\partial\theta}(\kappa_{so}M + \mu_{so}N) - 2\mu_{so}\cot(\theta)N. \quad (10)$$

Here, the surface viscosities  $\kappa_{so}$  and  $\mu_{so}$  are constants. The perturbation to the exterior pressure at the bubble surface is determined from the velocity potential by means of Bernoulli's equation for potential flow

$$p = -\rho_l \left. \frac{\partial\Phi}{\partial t} \right|_{r=a_o}, \quad (11)$$

with the higher order terms in  $\epsilon$  omitted.

The set of equations given above, together with an equation-of-state which relates the uniform pressure inside the bubble to its instantaneous volume, fully characterize the linearized dynamics of the slightly perturbed surfactant-laden bubble. The solution to this set of equations can be obtained by modal expansion. Let the surface deformation  $f(\theta, t)$  and the surface tangential velocity  $V(\theta, t)$  have decompositions of the form

$$f(\theta, t) = \sum_{n=0}^{\infty} f_n(t) P_n(\cos\theta), \quad (12)$$

$$V(\theta, t) = \sum_{n=1}^{\infty} V_n(t) \frac{dP_n(\cos\theta)}{d\theta}, \quad (13)$$

where,  $P_n(\cos\theta)$  represents the Legendre function of order  $n$ . The kinematic condition (8) allows a similar modal expansion to be obtained for the normal velocity  $U(\theta, t)$  with coefficients given by  $\dot{f}_n(t)$ , and the solution to the exterior velocity potential, satisfying (6)–(8), can also be found easily, resulting in an expression for the exterior pressure at the surface, based on Bernoulli's relation. The pressure in the bubble interior is found to depend only upon the  $n = 0$  term in the shape expansion to this order in  $\epsilon$ . The so-called breathing (i.e.  $n = 0$ ) mode of the bubble is thus the only mode that is affected by the pressure within the bubble, which provides the primary “restoring force” for bringing the bubble back to its equilibrium volume. Here we will concentrate on the shape modes ( $n > 1$ ) for which the characteristic time is determined by surface tension. Hence, we adopt the equilibrium radius  $a_o$  as the length scale and define the time scale  $\tau$  by

$$\tau \equiv (\rho_l a_o^3 / \sigma_o)^{1/2}. \quad (14)$$

Variables  $t$ , and  $(U, V)$  are then rendered dimensionless using respective scales  $\tau$  and  $a_o/\tau$  and dimensionless surface viscosities are defined by

$$\kappa^* = \frac{\kappa_{so}}{\sigma_o \tau}, \quad \mu^* = \frac{\mu_{so}}{\sigma_o \tau}. \quad (15)$$

Substitution of the modal expansion into the the normal and tangential stress conditions (9) and (10) produces the following coupled equations for the evolution of the  $n$ -th mode:

$$\frac{1}{n+1} \ddot{f}_n + 4\kappa^* \dot{f}_n + (n-1)(n+2)f_n = 2\kappa^* n(n+1) V_n, \quad (16)$$



$$2\kappa^* \dot{f}_n = [\kappa^* n(n+1) + \mu^* (n-1)(n+2)] V_n. \quad (17)$$

Here, overdot represents differentiation with respect to dimensionless time and  $f_n$  and  $V_n$  are also dimensionless. If exponential behavior of the form  $e^{\lambda_n t}$  is assumed in each of the modal coefficients, the linear system (16)–(17) produces an eigenvalue problem for  $\lambda_n$  which determines the frequency and damping rate of the  $n$ -th shape mode.

Interestingly, for any mode of the bubble, if the surface shear viscosity  $\mu^*$  is set to zero, the equation for the  $n$ -th shape mode reduces to

$$\ddot{f}_n + (n-1)(n+1)(n+2) f_n = 0. \quad (18)$$

Thus, in the absence of surface shear viscosity, the linearized shape oscillations are the same as those for a clean bubble. In that case, the dimensionless frequency of oscillations is found from (18) to be

$$(\omega_n^*)^2 = (n-1)(n+1)(n+2), \quad (19)$$

in agreement with known results [6]. For the quadrupole ( $n=2$ ) mode, the eigenvalues  $\lambda_2$  are easily found to be

$$\lambda_2^\pm = -\frac{12\kappa^* \mu^*}{3\kappa^* + 2\mu^*} \pm i \sqrt{12 - \left(\frac{12\kappa^* \mu^*}{3\kappa^* + 2\mu^*}\right)^2}. \quad (20)$$

The complex conjugate pair of eigenvalues (20) characterize the damped oscillation of the quadrupole shape mode, as modified by constant surface shear and dilatational viscosities. If either of these vanishes, the oscillation reduces to that dictated by the Lamb formula (19). In the limit when one of the surface viscosity coefficients is much smaller than the other, (20) shows that it is the *smaller* of the two viscosities which contributes the most to damping and frequency modification.

## OUTLOOK

Although idealized, the above calculation can be used, in conjunction with existing estimates of surface viscosity coefficients, to show that surface rheological effects can exert a strong influence on the frequency-shift and damping of the oscillations. To make quantitative comparisons against experimental results (e.g., see [2]), however, one must also include in the analysis the effects of viscous boundary layers in the bulk fluids [11], as well as the influence of surface and bulk transport of surfactants and their sorptive exchange, the role of Marangoni stresses, and possible nonlinear modal interactions when the amplitude of oscillations is large. Such issues are currently under investigation and will be addressed in forthcoming contributions.

## References

- [1] ASAKI, T. J., MARSTON, P. L. & TRINH, E. H. 1993 Shape oscillations of bubbles in water driven by modulated ultrasonic radiation pressure: Observations and detection with scattered laser light. *J. Acoust. Soc. Am.* **93**, 706–713.

- [2] ASAKI, T. J., MARSTON, P. L. 1995 Free decay of shape oscillations of bubbles acoustically trapped in water and sea water. *J. Fluid Mech.* **300**, 149–167.
- [3] EDWARDS, D. A., BRENNER, H. & WASAN, D. T. 1991 *Interfacial Transport Processes and Rheology*. Butterworth-Heinemann.
- [4] HSU, C. J. & APFEL, R. E. 1985 A technique for measuring interfacial tension by quadrupole oscillation of drops. *J. Colloid Interface Sci.* **107**, 467–476.
- [5] HSU, C. & APFEL, R. E. 1987 Model for the quadrupole oscillations of drops for determining interfacial tension. *J. Acoust. Soc. Am.* **82**, 2135–2144.
- [6] LAMB, H. 1945 *Hydrodynamics*. Dover.
- [7] LEVICH, V. G. 1962 *Physicochemical Hydrodynamics*. Prentice-Hall.
- [8] LU, H.-L. & APFEL, R. E. 1990 Quadrupole oscillations of drops for studying interfacial properties. *J. Colloid Interface Sci.* **134**, 245–255.
- [9] LU, H.-L. & APFEL, R. E. 1991 Shape oscillations of drops in the presence of surfactants. *J. Fluid Mech.* **222**, 351–368.
- [10] MARSTON, P. L. & APFEL, R. E. 1979 Acoustically forced shape oscillations of hydrocarbon drops levitated in water. *J. Colloid Interface Sci.* **68**, 280–286.
- [11] MARSTON, P. L. 1980 Shape oscillation and static deformation of drops and bubbles driven by modulated radiation stresses—theory. *J. Acoust. Soc. Am.* **67**, 15–26; Erratum **71**, 511 (1982).
- [12] MARSTON, P. L. & APFEL, R. E. 1980 Quadrupole resonance of drops driven by modulated acoustic radiation pressure—experimental properties. *J. Acoust. Soc. Am.* **67**, 27–37.
- [13] MILLER, C. A. & SCRIVEN, L. E. 1968 The oscillations of a fluid droplet immersed in another fluid. *J. Fluid Mech.* **32**, 417–435.
- [14] SCRIVEN, L. E. 1960 Dynamics of a fluid interface. *Chem. Eng. Sci.* **12**, 98–108.
- [15] TRINH, E., ZWERN, A. & WANG, T. G. 1982 An experimental study of small amplitude drop oscillations in immiscible liquid systems. *J. Fluid Mech.* **115**, 453–474.
- [16] TRINH, E., MARSTON, P. L. & ROBEY, J. L. 1988 Acoustic measurement of the surface tension of levitated drops. *J. Colloid Interface Sci.* **124**, 95–103.

# **Interfacial Phenomena**



**Microscale hydrodynamics in near moving contact line**

Stephen Garoff, Carnegie Mellon University

**Paper not available**



# FREE-SURFACE AND CONTACT LINE MOTION OF LIQUID IN MICROGRAVITY

Leonard W. Schwartz

Departments of Mechanical Engineering and Mathematical Sciences

The University of Delaware

Newark, DE 19716

## ABSTRACT

This project involves fundamental studies of the role of nonlinearity in determining the motion of liquid masses under the principal influences of surface tension, viscosity and inertia. Issues to be explored are relevant to aspects of terrestrial processes, as well as being immediately applicable to fluid management in a low-gravity environment. Specific issues include (i) the mechanics of liquid masses in large-amplitude motions, (ii) the influence of bounding surfaces on the motion and (iii) the ability of such surfaces to control liquid motion by wetting forces, especially when they are augmented by various surface treatments. Mathematical techniques include asymptotic analysis of the governing equations, for problem simplification, and numerical simulation, using both boundary-element and finite-difference methods. The flow problem is divided into an 'outer' or inviscid potential-flow region and one or more inner, or viscous dominated, regions. Relevant to one inner region, the vicinity of the contact line, we discuss time-dependent simulation of slow droplet motion, on a surface of variable wettability, using the lubrication approximation. The simulation uses a disjoining pressure model and reproduces realistic wetting-dewetting behavior.

## INTRODUCTION

From an engineering viewpoint, it is often necessary to maintain the location of a quantity of liquid in an enclosed vessel. This task is made simple in terrestrial gravity where the liquid in a partially-filled container can naturally be assumed to locate itself near the 'bottom' of the vessel. In the absence of gravity, however, it is possible for a liquid mass to become disconnected and become intermixed with its own vapor in an a priori unpredictable manner. Similarly, when the stabilizing gravitational potential is not present, the center of mass of a liquid region may move a large distance when disturbed by relatively small applied forces, with influence on the overall dynamics of a space vehicle.

Liquid motion in microgravity allows a more complete examination of surface tension and wetting forces. In normal gravity, capillary forces are restricted to short length scales and their influence, while important, is often obscured by the concurrent high level of viscous damping. When terrestrial gravity is removed, the spatial extent of capillary-dominated regions is greatly magnified and more detailed measurement is possible.

A strategy for control of liquid motion involves the location and surface treatment of container walls. The motion of a liquid front on a solid surface is governed in part by the energetics of the three interfaces that meet at the so-called contact line. A local force balance specifies the static contact angle between the phases there. Terrestrial experiments have indicated surprisingly high rates of damping of liquid motions which has been attributed to energy dissipation at moving contact lines [1]. For a surface whose energies vary with position, e.g. if the surface is 'contaminated,' it is possible for the contact line to be trapped in various local energy minima leading to a significant difference, or hysteresis, between advancing and receding contact angles [2]. Forced motion of the contact line on these surfaces will require a succession of small energy barriers to be overcome and may provide sufficient dissipation to prevent large motions. Quasi-static analyses by Schwartz & Garoff [3,4] considered various patterns of surface wettability. Some of their predictions were confirmed experimentally. Those results are only appropriate to very slow imposed motions. One goal of the present project is the extension to finite speed, where viscous forces must also be considered. Small scale roughness is believed to play a role similar to surface contamination [5].

## THE LARGE-SCALE INVISCID PROBLEM

Large-scale oscillations of liquid masses involve, principally, interchange between the kinetic energy of motion and potential energy stored as elongation of the bounding surface. Solutions for wave motions of infinitesimal amplitude are well known. For example, the small-amplitude oscillation of a liquid droplet was predicted by Rayleigh in 1877 [6]. Large amplitude motions, on the other hand, are highly nonlinear and will, in general, require numerical solution. Sloshing motions of low viscosity liquids in tanks of moderate or large size may, away from the walls and contact lines, be considered to be irrotational potential flows. The potential  $\phi$  is found as the solution of Laplace's equation

$$\nabla^2 \phi = 0, \quad (2.1)$$

subject to the kinematic boundary condition

$$DF/Dt = 0 \quad (2.2)$$

on the free interface  $F(x, y, z, t) = 0$ . Here  $D/Dt$  is the substantial derivative. The solution must also satisfy the condition of no normal relative velocity at stationary or moving impermeable boundaries. Additionally, on the free surface, whose shape evolution needs to be found as part of the solution, we have the dynamic condition

$$\phi_t + (1/2)(\phi_x^2 + \phi_y^2 + \phi_z^2) + \frac{p^{(s)}}{\rho} + \sigma \left( \frac{1}{R_1} + \frac{1}{R_2} \right) = C(t). \quad (2.3)$$

Here  $\rho$  is the constant liquid density,  $\sigma$  is surface tension, and  $C(t)$  is a function of time only.  $R_1$  and  $R_2$  are principal radii of curvature. The applied surface pressure  $p^{(s)}$  is ordinarily taken equal to zero without loss of generality; here, however, it may be used to represent the far-field influence of the 'inner' moving contact-line problem. Time-dependent solutions of (2.1) - (2.3) can be achieved using boundary-integral methods for two-dimensional or axisymmetric problems. These techniques find generalization in the so-called panel methods for three-dimensional problems. An example of a boundary-integral solution to a two-dimensional problem is shown in Fig. 1 where a limiting wave form traps a vapor bubble [7].

## DROPLET MOTION ON SUBSTRATES OF MIXED WETTABILITY

We treat the low-Reynolds-number motion of a thin Newtonian liquid layer onto a previously-dry surface. The mathematical model employs the long-wave or "lubrication" approximation. To leading order in the free-surface inclination, only a one-dimensional, unidirectional flow problem needs to be solved. Performing this integration across the thin dimension first results in a reduction of the dimensionality of the problem. Consistent with the lubrication hypothesis, many physical effects of interest can be modeled much more simply. Asymptotic derivations of the lubrication model, for two-dimensional problems with a free surface, are given by Benney [8] and Atherton & Homsy [9].

Within this approximation, integral mass conservation and the creeping-motion force balance are combined to yield

$$h_t = -\nabla \cdot \mathbf{Q} = \frac{1}{3\mu} \nabla \cdot (h^3 \nabla p) \quad (3.1)$$

where

$$p = -\sigma \nabla^2 h - \Pi = -\sigma \nabla^2 h - B \left( \frac{1}{4h^4} - \frac{1}{3h^* h^3} \right) \quad (3.2)$$

Here  $h$  is the coating thickness,  $p$  is pressure and  $\mu$  is viscosity. The  $\nabla$  - operator is two-dimensional, and is written using the substrate coordinates, and  $t$  is time. The first term in (3.2) incorporates the thin-layer approximation to the surface curvature while the second is a two-term model of disjoining pressure that allows contact-line motion, as described below.  $B$  and  $h^*$  are positive constants. The form of the disjoining term depends on the material system. Teletzke et al give various choices including the one used here [10]. Several flow simulations, using a form of disjoining pressure, have appeared [10,11].

When a liquid advances onto a previously-dry substrate, the usual mathematical description of the motion fails in the immediate vicinity of the three-phase line, i.e. the line where the liquid, solid, and



the vapor meet. The standard boundary condition, when a viscous liquid is in contact with a solid, is no relative motion between the liquid and the solid, the so-called 'no-slip' condition. It has been shown that solutions incorporating the no-slip condition lead to paradoxical results; the work required to move a liquid onto a dry surface is infinite [12,13]. Clearly the no-slip condition must be abandoned very near the moving contact point or line. Several slip models, involving a free parameter, have been proposed [14,15,16]. Other possibilities are a uniform precursor layer [17], a grid-slip model that allows motion onto dry regions, with the rate of advance dependent on the numerical mesh spacing [18], and shear-thinning rheology near the contact line [19]. Figures (2a) and (2b) show calculations for liquids advancing onto nominally-dry substrates. Figure (2a) shows the development of fingers or drip marks for gravity-driven flow on a vertical substrate [18]. Figure (2b), using a uniform precursor layer, simulates finger development on a spherical body.

The inclusion of the the disjoining terms in (3.2) is another technique that will allow contact-line motion using a thin wetting layer. Consider the spreading of an initially axisymmetric droplet onto a nominally-dry substrate. The evolution equation is nondimensionalized by measuring  $h$  in units of  $h_0$ , a typical film thickness. The substrate coordinates  $(x, y)$  are measured in units of  $L$  and the unit of time is  $T^* = 3\mu L^4/(\sigma h_0^3)$ . In dimensionless form, the evolution equation is

$$h_t = -\nabla \cdot (h^3 \nabla \nabla^2 h) + C \nabla \cdot \left[ \left( 1 - \frac{h}{h^*} \right) \frac{\nabla h}{h^2} \right] \quad (3.3)$$

where

$$C = \frac{BL^2}{\sigma h_0^5}. \quad (3.4)$$

The now-dimensionless parameter  $h^* \ll 1$  and, for droplet spreading, when combined with the value of  $C$ , prescribes the value of the equilibrium contact angle on a given substrate material. The energy per unit area of the substrate is composed of two parts. Within the lubrication approximation, the surface tension energy density is

$$e^{(\sigma)} = \frac{1}{2} \sigma \nabla h \cdot \nabla h \quad (3.5a)$$

and the disjoining energy density is

$$e^{(d)} = - \int_{\frac{3}{4}h^*}^h \Pi(h') dh' = \frac{B}{6h^{*3}} \left[ \frac{16}{27} - \frac{h^{*2}}{h^2} \left( 1 - \frac{h^*}{2h} \right) \right] \quad (3.5b)$$

both in dimensional units.  $e^{(d)}$  has a minimum at  $h = (3/4)h^*$  and (3.5b) is normalized so that  $e^{(d)}$  is zero there. It is possible to identify the value of  $B/h^{*3}$  with the equilibrium contact angle. For a static situation,  $e_{SV}^{(d)} = e^{(d)}(3h^*/4) = 0$  and  $e_{SL}^{(d)} = e^{(d)}(h \rightarrow \infty)$  when  $h^*$  is very small. A local force balance at the contact point gives

$$\sigma \cos \theta_c = \gamma_{SV} - \gamma_{SL} = \sigma - \frac{8}{81} \left( \frac{B}{h^{*3}} \right) \quad (3.6)$$

which, consistent with the small-slope approximation, yields

$$\theta_c \approx \frac{4}{9} \left( \frac{B}{\sigma h^{*3}} \right)^{1/2}. \quad (3.7)$$

Here the subscripts S, L, and V have their usual meaning of solid, liquid, and vapor respectively. Since  $\theta_c$  is the material property to be reproduced, constancy of the quantity  $C/h^{*3}$  is to be maintained as  $h^*$  becomes small. Provided  $h^*$  is taken sufficiently small, simulation results become independent of its actual value. Numerical tests reveal that a droplet will stabilize with a maximum inclination approximately given by (3.7), smaller values of  $h^*$  producing closer agreement. In this sense the actual value of  $h^*$  is not needed; the only material property required is the apparent static contact angle.

Few surfaces are ever ideally clean. Moreover, one may wish to purposely place patterns of contamination on a substrate in order to arrest liquid motion. Equation (3.3) is capable of simulating such a situation by

prescribing different values of  $C$  in particular substrate locations. Figure 3 shows the result of a time-dependent simulation where a drop of non-equilibrium shape is placed approximately at the center of a "cross" of poor-wetting material. The contact angle, using (3.7) is twice as large on the cross, compared to the surrounding field. Reflection symmetry conditions are used at the boundaries of the computational domain. Figure 4 contains contour plots of the same simulation with the wettability boundaries superimposed. Rather realistic features are exhibited by the simulation; apparent advancing and receding contact angles are speed-dependent and the motion proceeds by alternating slow and rapid events. This is readily seen in Figure 5 where the variation of the integrated energy components, using (3.5), is shown. This is similar to the result of the quasi-static analyses of Schwartz & Garoff [3,4] who termed the process "sticking, stretching, and jumping" in their model of contact-angle hysteresis. The simulation ends with the droplet finding a stable energy minimum by merging with its neighbors in one corner. The rate of decrease of the total energy in Figure 5 can be shown to be equal to the rate of viscous dissipation. Notice that when the motion has ceased, the energy is approximately equally-partitioned between its two components.

These computations use an alternating-direction-implicit (ADI) algorithm based on the scheme of Peaceman & Rachford [20], generalized to the present higher-order diffusive system. Nonlinearity is treated simply by evaluating prefactors at the old time level. The algorithm is quite stable and time stepping is adaptive, with larger steps being used when the surface shape is changing slowly. Steps can be as large as a factor of  $10^7$  bigger than the limiting step size for an explicit method. Basic features of the simulation have been verified to be invariant under temporal and spatial refinement and the choice of values for  $h^*$ . Additional tests of convergence are currently in progress. The run shown here, using a  $100 \times 100$  finite-difference grid, took about 30 minutes on a Pentium 100 PC configured as a UNIX workstation.

We intend to consider other disjoining pressure models to assess the sensitivity of flow behavior to this choice. Physical experiments on surfaces of controlled wettability can be compared with numerical predictions. For relatively large drops, in the laboratory, gravity effects will need to be considered. These can be inserted in the model without difficulty.

## REFERENCES

1. Keulegan, G. H. (1959), *J. Fluid Mech* 6, 33-50.
2. Johnson, R. E. & Dettre, R. H. (1969), *Surf. Colloid Sci.* 2, 85.
3. Schwartz, L. W. & S. Garoff (1985a), *J. Colloid Interf. Sci.* 106, 422 - 437.
4. Schwartz, L. W. & S. Garoff (1985b), *Langmuir* 1, 219 - 230.
5. Dussan V., E. B., *Ann. Rev. Fluid Mech.* 11, 371-400.
6. Rayleigh, Lord, (1877) "Theory of Sound," Dover Books, New York, 1945.
7. Schwartz, L. W. & Vanden-Broeck, J.-M. (1979) *J. Fluid Mech.* 95, 119-139.
8. Benney, D. J. (1966) , *J. Math. & Phys.* 45, 150-155.
9. Atherton, R. W. & Homsy, G. M. (1976), *Chem. Eng. Comm.* 2, 57-77.
10. Teletzke, G., Davis, H. T. & Scriven, L. E. (1987) *Chem. Eng. Comm.* 55, 41-81.
11. Williams, M. B. & Davis, S. H. (1982), *J. Colloid Interf. Sci.* 90, 220-228.
12. Moffatt, H. K. (1964), *J. Fluid Mechanics* 18, 1-17.
13. Huh, C. & Scriven, L. E. (1971), *J. Coll. Interf. Sci.* 35, 85-101, 1971.
14. Greenspan, H. P. & McCay, B. M. (1981), *Studies in Applied Mathematics* 64, 95-112.
15. Hocking, L. M. (1983), *Quart. J. of Mechanics & Appl. Maths* 36, 55-69, 1983.
16. Durbin, P. A. (1988), *J. Fluid Mech.* 197, 157-169.
17. Tuck, E. O. & Schwartz, L. W. (1990), *S.I.A.M. Review* 32, 453-469.
18. Schwartz, L. W. (1989), *Phys. Fluids A* 1, 443-445.
19. Weidner, D. E. & Schwartz, L. W. (1994) *Physics of Fluids* 6, 3535-3538.
20. Peaceman, D. W. & Rachford, H. H. (1955), *SIAM Journal* 3, 28-41.

## FIGURES

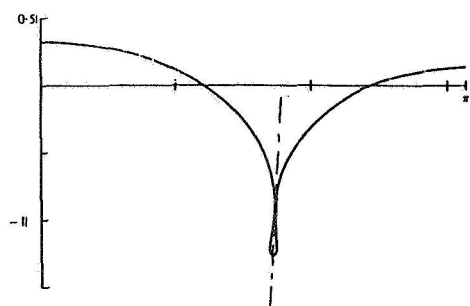


Fig. 1: A capillary-dominant progressive free-surface wave calculated by a boundary-integral method. A bubble is trapped [7].

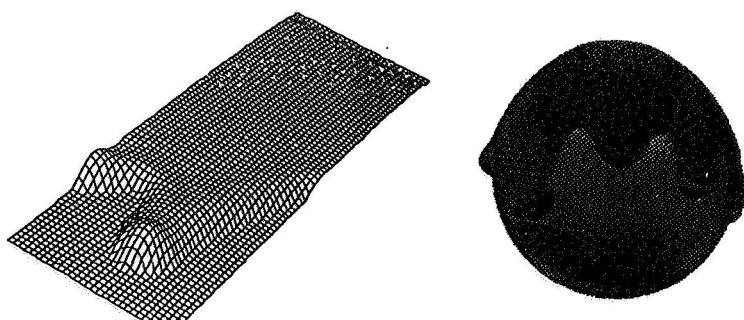


Fig 2: Flow simulations using two different wetting models. (a) A liquid mound on a vertical wall shows characteristic fingering patterns [18]. (b) Drainage on a sphere, using a uniform precursor layer.

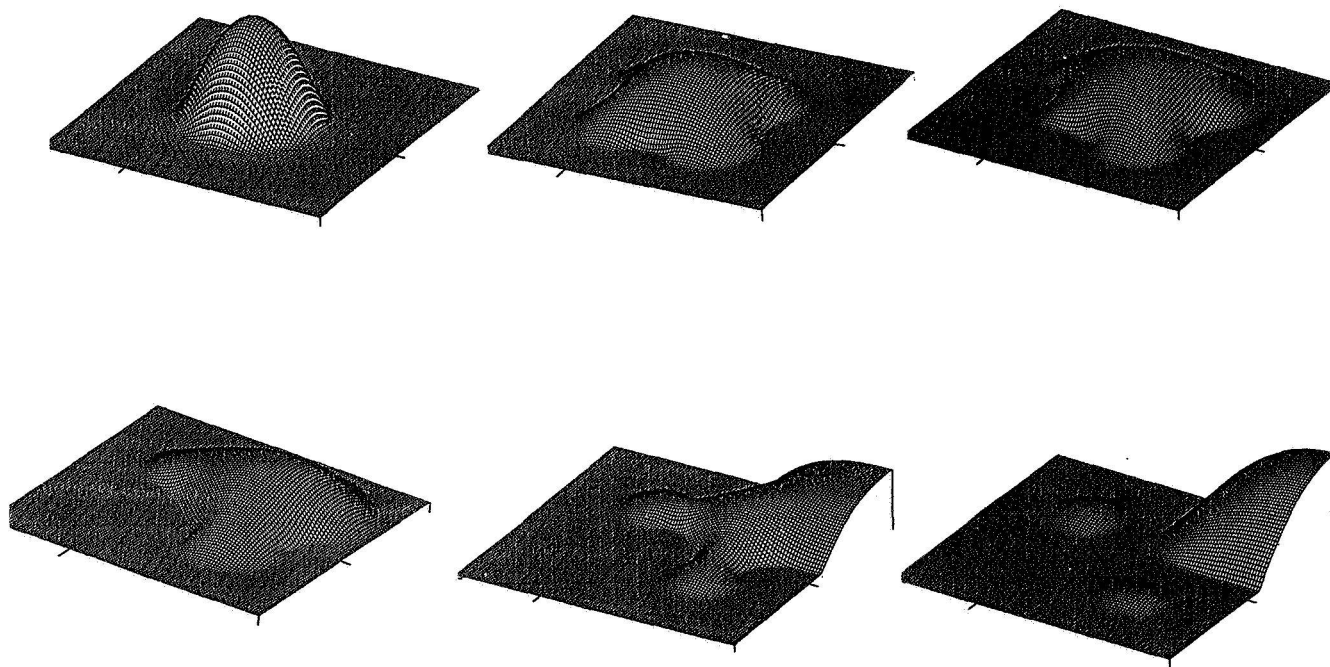


Fig 3: Simulation of droplet motion on a mixed-wettable surface. Parameter values are  $C_1 = 0.0002$ ,  $C_2 = (1/4) C_1$ ,  $h^* = 0.02$ . The grid size is  $0.01 L$  where  $L$  is the width of the window. Times are  $t/T^* = .001, .5, 4., 5.6., 7$ . The initial profile was  $h = (3/4)[h^* + \exp(-64 r^2)]$ .

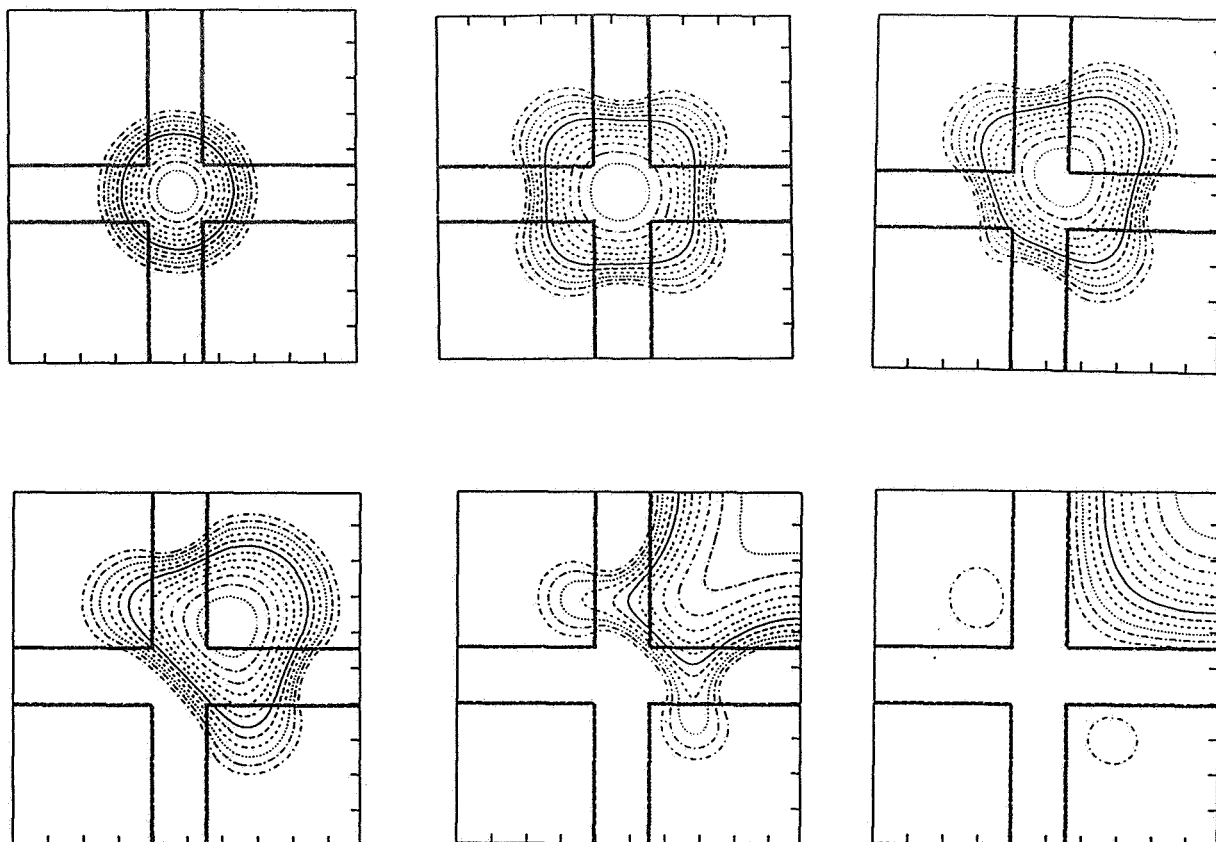


Fig 4: Contour plots for the profiles in Fig. 3 . The wettability boundaries are also shown.

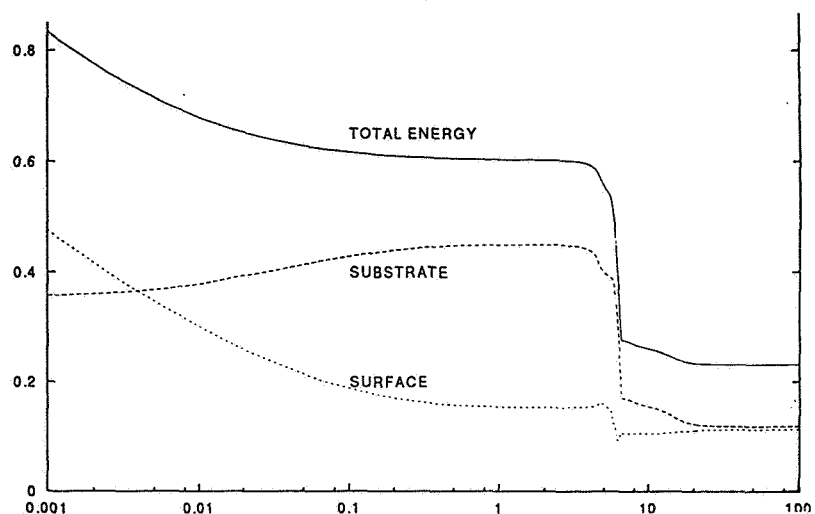


Fig. 5: Variation in integrated energies with  $t/T^*$ . The motion proceeds by alternating fast and slow events. Energies are measured in units of  $\sigma h_0^2$ .

# ON THE BOUNDARY CONDITIONS AT AN OSCILLATING CONTACT LINE: A PHYSICAL/NUMERICAL EXPERIMENTAL PROGRAM

Marc Perlin and William W. Schultz  
University of Michigan

## ABSTRACT

We will pursue an improved physical understanding and mathematical model for the boundary condition at an oscillating contact line at high Reynolds number begun by Ting & Perlin (1). We expect that the body force is locally unimportant for earth-based systems, and that the local behavior may dominate the mechanics of partially-filled reservoirs in the microgravity environment (Weislogel & Lichter 2).

One important space-based application for this contact-line study is for Faraday-waves. Oscillations in the direction of gravity (or acceleration) can dominate the fluid motion during take-off and reentry with large steady-state accelerations and in orbit, where fluctuations on the order of  $10^{-4}g$  occur about a zero mean. Our experience with Faraday waves has shown them to be “cleaner” than those produced by vertical or horizontal oscillation of walls. They are easier to model analytically or computationally, and they do not have strong vortex formation at the bottom of the plate. Hence many, if not most, of the experiments will be performed in this manner. The importance of contact lines in the microgravity environment is well established (Concus, et al. 3; Siggner & Weislogel 4; Capodanno 5; Kim, et al. 6; Lucassen, et al. 7; Merte, et al. 8).

We will compare high resolution measurements of the velocity field ( $10\mu m$  resolution) using particle-tracking and particle-image velocimetry as the fluid/fluid interface is approached from the lower fluid. The spatial gradients in the deviation provide additional means to determine an improved boundary condition and a measure of the slip region, unavailable from the work by Ting & Perlin. Dissipation, the size of the eddy near the contact line, and hysteresis will be measured and compared to linear and nonlinear models of viscous and irrotational but dissipative models.

## 1 INTRODUCTION AND THE STATE-OF-THE-ART

The contact line is the intersection between two distinct fluids and a solid: here, the fluids are water and air, the solid is glass. The contact angle  $\theta_c$  is defined as the angle between the tangent to the fluid interface at the contact line and the water-glass interface (see figure 1). Contact-line behavior may be couched as a relationship between the contact angle and the relative (liquid-to-solid) motion of the contact line. “Contact angle” is used in place of “apparent contact angle.” (the macroscopic contact angle, Dussan V. 9) To determine and quantify the contact-line behavior, precise measurements of the contact-line position (and thus velocity and acceleration) and dynamic contact angle (*i.e.* contact angle with a moving contact line) must be conducted.

Information regarding the contact line and contact angle in uni-directional viscous flows abounds in the literature. A complete and thorough discussion of static contact angle and dynamic contact angle for uni-directional relative velocities is given by Dussan V. (9). These results are representative for experiments with small Reynolds number, small Weber number, and small Froude number. For these cases, there is no inertial effect from contact-line movement. The relationship shows that the contact angle is a function of the contact-line velocity only, *i.e.*  $\theta_c = f(V_r)$ . In figure 2,  $\alpha_r$  represents the receding angle defined when  $V_r \rightarrow 0^-$  (the contact point moves toward the liquid),  $\alpha_a$  represents the advancing angle defined as  $V_r \rightarrow 0^+$  (the contact point moves away from the liquid). Because of the hysteresis, the contact-line boundary condition is nonlinear, even for low Reynolds number uni-directional, steady motion.

A difficulty arises in the solution of the viscous flow field — even with a (uni-directionally) moving contact line. Dussan V. & Davis (10) showed that a non-integrable-stress singularity occurs at the contact line if a moving contact line is forced to obey the no-slip boundary condition. A popular model to avoid the singularity that allows the contact point to move along the solid surface was originated by Navier. He postulated that the resistant stress at a fixed solid surface is proportional to the relative velocity or  $\beta u = \mu \partial u / \partial n$ . Here,  $\beta$  is a constant,  $u$  is the velocity parallel to the fixed solid surface,  $n$  is the distance normal to the solid surface, and  $\mu$  is the liquid dynamic viscosity. A terse description of this slip boundary condition is given by Goldstein (11).

As opposed to their uni-directional counterparts, oscillatory contact-line boundaries have not been studied experimentally in a significant way until very recently (1). Oscillatory contact-line boundaries are important in wave and other flow interactions with a solid boundary. Benjamin & Scott (12) and Graham-Eagle (13, 14) investigated waves propagating in a narrow open-channel with pinned-end (fixed contact-line position) edge conditions. Hocking (15)

demonstrated the importance of surface tension effects at a contact line and showed that the damping of gravity-capillary waves at a rigid boundary is mostly due to capillary effects. Several other publications that demonstrate the importance of capillary effects in wave motion and damping include Miles (16, 17, 18); Hocking & Mahdmina (19); Joo, Schultz & Messiter (20); Cocciaro, Faetti & Nobili (21); and Cocciaro, Faetti & Festa (22).

Quantitative information is sparse regarding oscillating contact lines. Based on the relationship given by Dussan V. (9) for uni-directional contact lines, Young & Davis (23) proposed four possible relationships between contact angle and contact-line velocity for an oscillating contact-line boundary: (a) with contact-angle hysteresis; (b) fixed contact line; (c) fixed contact angle; and (d) smooth contact-angle variation (no contact-angle hysteresis). Using these relationships and a force balance at the contact line, they presented a solution to the oscillatory contact-line motion in the creeping-flow limit. They considered small motion of the plate so that the inertial effect is small; therefore, the contact-line behavior is governed by a relationship similar to that of Dussan V. (9). They found that contact-angle hysteresis and steepening of the contact angle with increasing contact-line speed are dissipative effects. Also, they stated that the contact-line motion tends to lag behind the plate motion due to inertia.

Hocking (24) used an oscillatory contact-line boundary condition to calculate the waves generated by a vertically oscillating, vertical plate. Capillary effects were included in his analysis at the contact line. Two approximations originally proposed by Young & Davis (23) to the uni-directional model of Dussan V. (9) were used. Miles (17), addressing the same problem as Hocking, also used a Navier-slip boundary condition along the plate associated with a boundary condition at the contact line. In his analyses, viscosity was included and a non-zero initial free-surface meniscus was also considered in one case. A slip length,  $l_s$  (defined as slip velocity divided by shear at the wall), was adopted to replace the no-slip boundary condition along the entire plate. By a phenomenological hypothesis, he posed the slip boundary condition (equivalent to Navier's slip model with  $l_s = \mu/\beta$ )

$$V - V_{solid} = l_s \frac{\partial V}{\partial n},$$

where  $V$  is the vertical velocity along the plate ( $\frac{\partial \eta}{\partial t}$  at the contact line). He stated that  $l_s$  is a function of position along the plate surface and vanishes at a distance,  $l_v = \sqrt{2\nu/\omega}$  (the viscous length scale), away from the contact line. That is, the flow obeys the no-slip boundary condition at some distance  $l_n$  away from the contact line. For simplicity, he assumed that  $l_s$  is constant, but experimental results show this is unrealistic as mentioned by Miles (17).

From the discussion and conclusions of Ting & Perlin, the edge condition at an oscillatory solid boundary (i.e. a trijunction) is shown to be very important, but it is neither fully understood, nor predictable for large contact-line motion. Many theoreticians have adopted some form of the uni-directional model and a slip boundary condition along the solid surface, however, according to measurements by Ting & Perlin, this model is incorrect for large oscillatory (sinusoidal) plate motion. The qualitative behavior of the contact-line movement changes as the amplitude of the plate oscillation changes (figure 3, 4). The mean slip coefficient changes dramatically with oscillation amplitude as shown in figure 5.

Dissipation due to viscosity (and the vortex imaged by Ting & Perlin) and hysteresis are very important, ubiquitous phenomena. We will accurately measure this flow field and compare it directly to numerical results. As an example of the lack of understanding of dissipation in oscillatory flows, many published results present a discussion stating that a one to three order-of-magnitude increase in the viscosity is required to match numerical results with measured dissipation (e.g. Hocking 15 and Henderson & Miles 25). We believe this so-called effective viscosity is the result of contact-line-generated dissipation.

## 2 OBJECTIVES

The main goal of this research is to provide a physical explanation of oscillatory contact-line behavior, a more accurate boundary model for large-amplitude oscillations, and an attempt to model dissipation in the vicinity of the contact line. The proposed problem clearly requires an energetic, multi-disciplinary approach.

Specific objectives are: (1) to conduct precise measurements of the flow field in the immediate vicinity of the contact line and as a function of position along a vertically oscillating reservoir or upright plate using particle-image-velocimetry techniques; (2) to compare the measured velocity fields with those predicted by the exact analytic solution of Stokes, thus defining the slip region as well as elucidating the effect of the contact line, meniscus, and the interface on the local fluid physics, this by investigating the deviation from the exact solution; (3) to develop a proper boundary condition for the stick-slip motion of the contact-line region (Note that the Ting & Perlin model did not include the effects of acceleration directly.); (4) to develop a numerical code to simulate the flow field using the boundary condition

developed and the viscous equations of motion; and (5) to verify and quantify the accuracy of the boundary conditions developed by comparing the interfacial elevations and flow fields of the measurements with those of the numerics. In the following, we discuss the laboratory facility, experimental techniques, and the experiments; the numerical methods and simulation; the contact-line effects on Faraday waves; and the comparisons to be conducted.

### 3 LABORATORY FACILITY, EXPERIMENTAL TECHNIQUES, AND EXPERIMENTS

The study will include a synergistic set of physical and numerical experiments as follows: a contact-line model will be developed based upon physical experiments and the deviation of the experiments from the Stokes second problem solution; the newly determined boundary condition used in conjunction with the viscous equations and other boundary conditions will be solved numerically; and a comparison of the physical and numerical wave fields generated will quantify the effectiveness and applicability of the contact-line boundary condition. In addition, the energy dissipation at the contact-line region will be studied, especially with regard to the relatively large vortex discovered by Ting & Perlin.

Using a time series recorded by a high-speed camera of the contact-line region as illuminated by a laser sheet in the presence of dye-laden water, one obtains the position of the plate, the position of the contact line, and the apparent contact angle. Sufficient magnification is achieved with a proper choice of lenses and extension tubes; however, to obtain a detailed velocity field with a large number of velocity vectors still requires resolution available only on film. The relatively poor resolution of the video system was one of the limiting factors on the data of Ting & Perlin (1). These data had insufficient resolution to obtain meaningful accelerations through two differentiations of the plate/contact-line position. Our experience shows that 4"x5" Kodak Tmax 400 film works well for velocimetry with a film resolution on the order of 5 microns. Using the computer to generate the timing sequence, any desired phase of the oscillation can be captured on the film. In addition, a technique developed by Lin & Perlin removes light reflections present in the fluid-fluid interface, thus removing the ambiguity of the interfacial location and recording only those particles actually located in the lower fluid. The region of high shear (as seen by Ting & Perlin) immediately adjacent to the contact-line region will be studied also. From these data, we believe a reasonable boundary condition is achievable. We will have inferred the region (length) of slip through the comparison with the solution of the oscillating plate in a semi-infinite fluid. An improved boundary condition from that used by Ting & Perlin (1) will be formulated, since the acceleration information will now be available.

Experiments to verify the boundary condition will be conducted to determine the interfacial elevation and the particle velocities some distance away from the plate. These data will be used for comparison to the numerical solution of the flow field obtained with the boundary condition developed herein. Thus, the validity and accuracy of the model will be determined. We also intend to evaluate and compare other independent measures of contact angle (Concus, et al. 3; Seebergh & Berg 26; Li, et al. 27; van der Zanden & Chesters 28). Many of these are adapted to the microgravity environment, but may not be applicable for oscillatory flows.

### 4 NUMERICAL METHODS AND SIMULATION

We will model the flow near the contact line in a  $2 \times 2$  matrix of linear and nonlinear and inviscid and viscous flows. The inviscid model has been developed by Hocking (6), but only for linearized boundary conditions and with a simple contact-angle model that bears no resemblance to figure 2. On the other hand, there have been fully-viscous analyses by several groups (Kafka, et al. 29; Dussan, et al. 30), but for steady, creeping flow.

The flow we wish to model is high Reynolds number. Hocking (15, 24) showed that many of the major features (such as damping) can be retrieved from an inviscid, even irrotational model. This is important as modeling very high Reynolds number flows with a fully-viscous computation is quite daunting. Features such as slip length and the eddy near the contact line must of course be discarded.

We will extend Hocking's analysis to include a more general model for contact-line behavior, namely

$$\theta_c = \theta_c(V_r, \frac{dV_r}{dt}).$$

This model can be made sufficiently general to accommodate the experimental data of figure 3. This data shows that the contact angle versus relative speed has hysteresis itself, as opposed to the "usual" contact angle hysteresis represented by the vertical line in figure 3. A simplification when no contact angle hysteresis exists is possible for periodic motion with a complex  $\lambda$  (Miles 17),

$$V_r = \lambda \frac{\partial \eta}{\partial x},$$

at the expense of fitting the data of figure 3 only crudely.

When we model the viscous flow, we again resort first to linearized flow to simplify the problem and make it more amenable to analysis. Now a slip model is required. One important aspect that is not usually studied is that the slip coefficient in the unsteady case must be compatible with the contact angle model to avoid reintroducing a singularity at the origin. Specifically, at the contact line, we have two conditions on slip — a contact-angle condition and a slip condition. For the simplest contact angle relationship we get

$$V_r = \lambda \frac{\partial \eta}{\partial x} = l_s \frac{\partial V_{CL}}{\partial x}.$$

Since  $V_{CL} = \partial \eta / \partial t$ , this requires that  $\lambda = l_s \partial / \partial t$ . More complicated compatibility constraints are required for more general contact angle relationships.

In the last year or two of the contract period, we expect to run spectral element computations of modestly high Reynolds numbers. Then the linearized free surface boundary conditions can be relaxed and comparisons of eddy size and strength can be compared with the experiments.

## 5 CONTACT-LINE EFFECTS ON FARADAY WAVES

We review and discuss some pertinent results from Jiang, et al. (31) as regards contact-line effects on Faraday waves. Specifically, we discuss the competition between viscous effects (tend to decrease frequency) and contact-line effects (tend to increase frequency). The threshold forcing amplitude for the fundamental mode (wavenumber  $k_i=1$ ) was measured and a stability diagram is presented in figure 6 for three slightly-different fluids and two tank-aspect ratios (AR). Figure 6(a) presents the measurements of water (hollow triangle, AR=10 and hollow diamond, AR=2.61) and mixed water with fluorescein dye (hollow square, AR=10). Also shown is the subharmonic Faraday wave with two wavelengths in the tank (solid triangle,  $k_i=2$ , AR=10). Figure 6(b) shows the results for water mixed with Photo Flo 200, volume ratio 100:1 (solid square, AR=2.61 and solid diamond, AR=10). Dimensionless frequency  $p$  ( $\equiv 4\omega_i^2/\omega_f^2$  where  $\omega_i$  is the frequency of the excited mode and  $\omega_f$  is the forcing frequency) and dimensionless forcing amplitude  $q$  ( $\equiv 2fk_i \tanh k_i h$  where  $f$  is the forcing amplitude and  $h$  is the water depth) are evaluated based on the inviscid natural frequency  $\omega_i$ . If  $p$  and  $q$  lie within the upper and lower solid diagonal lines (unstable region), then subharmonic resonance will occur according to linear theory (Benjamin & Ursell 32); otherwise, the liquid surface is not excited (stable region). The dashed curves represent weakly-nonlinear predictions of Henderson & Miles (24), now denoted by H&M. The hollow circles represent their experiments (with Photo Flo present), shown in figure 6(b).

According to H&M, the viscous natural frequency  $\omega_v$  should be less than the inviscid natural frequency  $\omega_i$ , i.e.  $p_{min}$ , the  $p$  value associated with the minimum of  $q$  ( $q_{min}$ ), should be larger than one. However, our experimental results show an increase in  $\omega_v$ , not a decrease. As shown in figure 6(a), the  $p_{min}$  associated with each set of symbols is less than one, implying that  $\omega_v (\equiv \frac{1}{2}\omega_f |_{q_{min}}) > \omega_i$ . Benjamin & Scott (13) measured waves propagating in a brimful channel and concluded that the contact-line effect increases the wave celerity (phase speed). By reducing the tank aspect ratio and lessening the relative effect of the contact line by the addition of Photo Flo, we demonstrate this same phenomenon is responsible for our increased  $\omega_v$  for fixed wavenumber.

The aspect-ratio effect on the frequency is seen in figure 6(a) by comparing measurements in the wider tank (AR=2.61) and those in the narrow tank (AR=10). Due to weaker contact-line effect in the wider tank,  $\omega_v$  should be and is smaller, corresponding to an increase in  $p_{min}$ . Also, since the contact line and wall-boundary layers contribute the most to the dissipation, the effective damping in the wider tank is less owing to the smaller surface-area-to-volume ratio. Therefore  $q_{min}$  in the wider tank is smaller.

Figure 6(b) represents our measurements with the mixture of water and Photo Flo. Since the addition of Photo Flo reduces the contact-line effect,  $p_{min}$  and  $q_{min}$  are relatively more affected by viscous damping and the neutral-stability curve shifts towards H&M's prediction. H&M's theory still overpredicts  $q$  on the lower side of the neutral-stability curve and underpredicts  $\omega_v$ . Their experiments with a water-Photo Flo mixture (hollow symbols) agree with their theory quite well.

## 6 COMPARISONS

Measurements and numerics will be compared in detail. We will have a “closed-loop” prediction in the sense that our experiments will determine boundary condition along the plate. We will generate numerical solutions with these boundary conditions and finally compare them to the flow field adjacent to the plate to quantify and verify the applicability of our boundary condition.



## REFERENCES

1. Ting, C.-L. & Perlin, M. 1995 Boundary conditions in the vicinity of the contact line at a vertically oscillating plate: An experimental investigation. **J. Fluid Mech.** **295**, 263-300.
2. Weislogel, M.M. & Lichter, S. 1994 Low gravity capillary flow in a corner. **APS Bulletin** **39**, 1871.
3. Concus, P., Finn, R & Zablhi, F. 1992 On canonical cylinder sections for accurate determination of contact angle in microgravity. **Fluid Mechanics Phenomena in Microgravity**, ASME AMD 154.
4. Siginer, D.A. & Weislogel, M.M. (Eds.) 1994 Fluid Mechanics Phenomena in Microgravity. Winter Annual Meeting of ASME. Anaheim, CA, USA.
5. Capodanno, P. 1992 Small oscillations of a liquid in a container of revolution under zero gravity. **Eur J Mech B Fluids** **11**, 291-308.
6. Kim, I., Kamotani, Y. & Ostrach, S. 1994 Modeling bubble and drop formation in flowing liquids in microgravity. **AIChE J.** **40**, 19-28.
7. Lucassen, J., Lucassen-Reynders, E.H., Prins, A. & Sams, P.J. 1992 Capillary engineering for zero gravity. Critical wetting on axisymmetric solid surfaces. **Langmuir** **8**, 3093-3098.
8. Merte, H., Lee, H.S. & Keller, R.B. 1994 Report on Pool Boiling Experiment. Prototype Model Flown on STS-47, Rept. no. UM-MEAM-94-09.
9. Dussan V., E.B. 1979 On the spreading of liquids on solid surfaces: static and dynamic contact lines. **Ann. Rev. Fluid Mech.** **11**, 371-400.
10. Dussan V., E.B. & Davis, S.H. 1974 On the motion of a fluid-fluid interface along a solid surface. **J. Fluid Mech.** **77**, 71-95.
11. Goldstein, S. 1938 **Modern developments in fluid dynamics**. Vol. 2, Oxford University Press, London, 676.
12. Benjamin, T.B. & Scott, J.C. 1979 Gravity-capillary waves with edge constraints. **J. Fluid Mech.** **92**, 241-267.
13. Graham-Eagle, J. 1983 A new method for calculating eigenvalues with application to gravity-capillary waves with edge constraints. **Math. Proc. Camb. Phil. Soc.** **94**, 553-564.
14. Graham-Eagle, J. 1984 Gravity-capillary waves with edge constraints. D. Phil. thesis. University of Oxford.
15. Hocking, L.M. 1987 The damping of capillary-gravity waves at a rigid boundary. **J. Fluid Mech.** **179**, 253-266.
16. Miles, J.W. 1967 Surface-wave damping in closed basins. **Proc. R. Soc. Lond. A** **297**, 459-475.
17. Miles, J.W. 1990 Capillary-viscous forcing of surface waves. **J. Fluid Mech.** **219**, 635-646.
18. Miles, J. 1991 Wave motion in a viscous fluid of variable depth: Moving contact line. **J. Fluid Mech.** **223**, 47-55.
19. Hocking, L.M. & Mahdmina, D. 1991 Capillary-gravity waves produced by a wavemaker. **J. Fluid Mech.** **224**, 217-226.
20. Joo, S.W., Schultz, W.W. & Messiter, A.F. 1990 An analysis of the initial wavemaker problem. **J. Fluid Mech.** **214**, 161-183.
21. Cocciaro, B., Faetti, S. & Nobili, M. 1991 Capillary effects on surface gravity waves in a cylindrical container: wetting boundary conditions. **J. Fluid Mech.** **231**, 325-343.
22. Cocciaro, B., Faetti, S. & Festa, C. 1993 Experimental investigation of capillary effects on surface gravity waves: non-wetting boundary conditions. **J. Fluid Mech.** **246**, 43-66.
23. Young, G.W. & Davis, S.H. 1987 A plate oscillating across a liquid interface: effect of contact angle hysteresis. **J. Fluid Mech.** **174**, 327-356.
24. Hocking, L.M. 1987 Waves produced by a vertically oscillating plate. **J. Fluid Mech.** **179**, 267-281.
25. Henderson, D.M. & Miles, J. 1990 Single-mode Faraday waves in small cylinders. **J. Fluid Mech.** **213**, 95-109.
26. Seebergh, J.E. & Berg, J.C. 1992 Comparison of force and optical techniques for the measurement of dynamic contact angles. **Chem Eng Sci.** **47**, 4468-4470.
27. Li, D., Cheng, P. & Neumann, A.W. 1992 Contact angle measurement by axisymmetric drop shape analysis. **Adv. in Colloid and Interface Sci.** **39**, 347-382.
28. van Der Zanden, A.J.J. & Chesters, A.K. 1994 Experimental study of the meniscus shape associated with moving liquid-fluid contact lines. **Int. J. Multiphase Flow** **20**, 775-787.
29. Kafka, F. & Dussan V. 1979 On the interpretation of dynamic contact lines in capillaries. **J. Fluid Mech.** **95**, 539.
30. Dussan V., E.B., Rame, E. & Garoff, S. 1991 On identifying the appropriate boundary conditions at a moving contact line. An experimental investigation. **J. Fluid Mech.** **230**, 97-116.
31. Jiang, L., Ting, C.-L., Perlin, M. & Schultz W.W. 1995 Moderate and steep Faraday waves: Instabilities, modulation and temporal asymmetries", submitted to **J. Fluid Mech.**
32. Benjamin, T.B. & Ursell, F. 1954 The stability of the plane free surface of a liquid in vertical periodic motion. **Proc. R. Soc. Lond. A** **225**, 505-515.

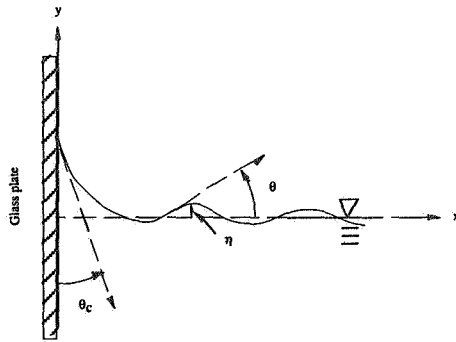


Figure 1. Sketch of contact-line region.

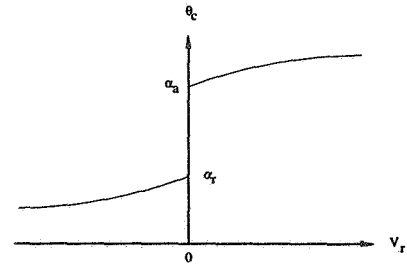


Figure 2. Contact angle vs. relative velocity.

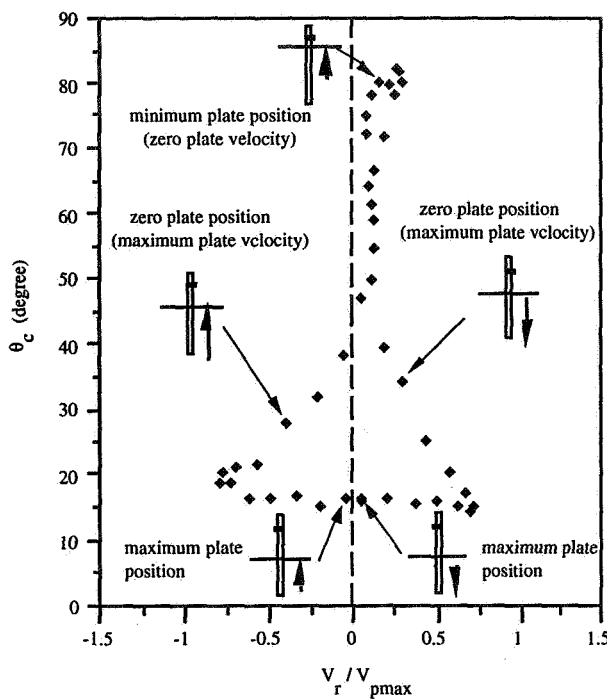


Figure 3. Typical graph of the contact angle vs. nondimensional relative velocity.

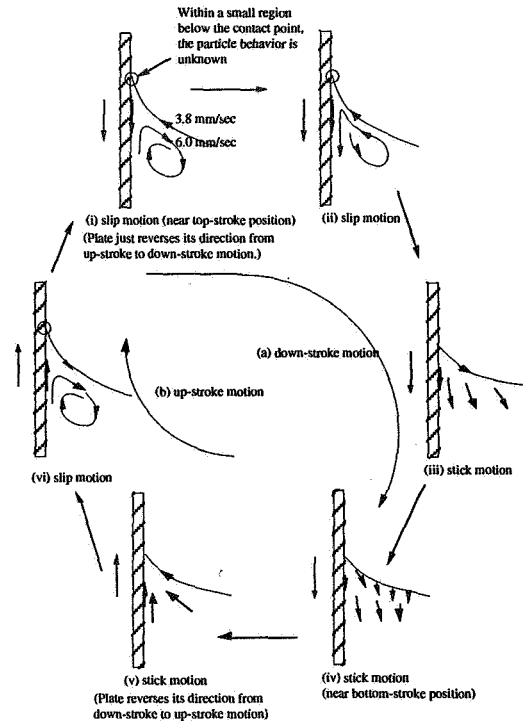


Figure 4. A pictorial sketch of particle trajectories near the contact line.

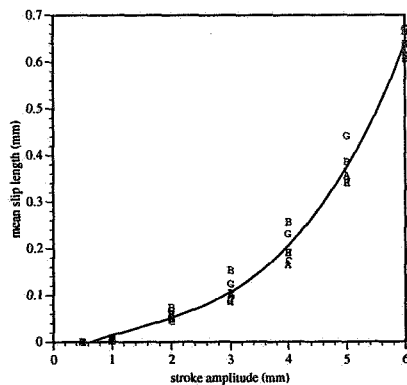


Figure 5. Mean slip length versus stroke amplitude.

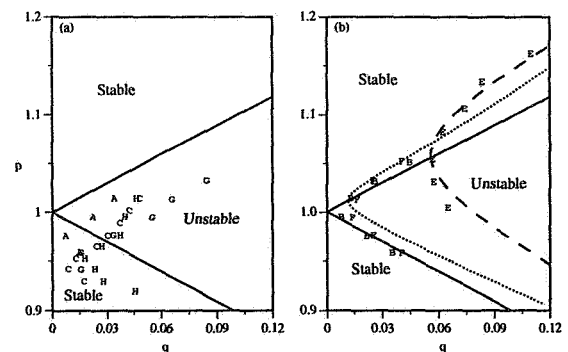


Figure 6. Subharmonic instability limit curves of Faraday waves for several experiments.

# THE MICROMECHANICS OF THE MOVING CONTACT LINE

Minsub Han, Seth Lichter, Chih-Yu Lin, and Yeong-Yan Perng  
Department of Mechanical Engineering  
Northwestern University  
Evanston, IL 60208-3111  
email: s-lichter@nwu.edu

## ABSTRACT

The proposed research is divided into three components concerned with molecular structure, molecular orientation, and continuum averages of discrete systems. In the experimental program, we propose exploring how changes in interfacial molecular structure generate contact line motion. Rather than rely on the electrostatic and electrokinetic fields arising from the molecules themselves, we augment their interactions by an imposed field at the solid/liquid interface. By controlling the field, we can manipulate the molecular structure at the solid/liquid interface. In response to controlled changes in molecular structure, we observe the resultant contact line motion. In the analytical portion of the proposed research we seek to formulate a system of equations governing fluid motion which accounts for the orientation of fluid molecules. In preliminary work, we have focused on describing how molecular orientation affects the forces generated at the moving contact line. Ideally, as assumed above, the discrete behavior of molecules can be averaged into a continuum theory. In the numerical portion of the proposed research, we inquire whether the contact line region is, in fact, large enough to possess a well-defined average. Additionally, we ask what types of behavior distinguish discrete systems from continuum systems. Might the smallness of the contact line region, in itself, lead to behavior different from that in the bulk? Taken together, our proposed research seeks to identify and accurately account for some of the molecular dynamics of the moving contact line, and attempts to formulate a description from which one can compute the forces at the moving contact line.

## INTRODUCTION

That fluid in the neighborhood of the contact line does not behave as fluid within the bulk is now supported by direct observation. In general, fluid near the interface with a solid or another liquid is found to possess different material properties from bulk fluid. Liquids in channels of molecular width were shown to possess a layered structure proximal to a solid surface. Liquid molecules are also found to possess a particular orientation at solid interfaces. Numerous other studies established the concept of *vicinal liquid*, in the vicinity of an interface, which has properties different from those within the bulk. Distinctive properties of these interfaces could in some cases be modeled numerically [1, 2].

Note that the experimental evidence cited above was not made on the moving contact line geometry. Most of the observations have been made at the solid/liquid interface which is the most accessible to available experimental techniques. These techniques also require that there is no

fluid motion. It is from these observations that one may infer that the same effects of molecular orientation and structure are present at the contact line.

## PROPOSED WORK

The proposed work is divided into three problems: Surface energy of the solid/liquid interface; Continuum model of the contact line region; and, Averaging and energy transport. The first problem addresses molecular structure at the solid/liquid interface. The second problem deals with molecular orientation. The third is concerned with questions arising when discrete (molecular) systems are modeled as continua.

### Surface Energy of the Solid/Liquid Interface

Introduction– This part of the proposed work is a look at the factors that give the solid/liquid interface its particular properties and how these factors affect the forces at a moving contact line. In the experiments an electric field is applied at the solid/liquid interface. In response to the field, the solid/liquid surface tension is altered and the contact line moves. Measurements of the position of the contact line<sup>1</sup> then allow us to compute the dynamic contribution of molecular structure to the force on the moving contact line.

Experiment-Concept– Adjacent to a conducting solid, then there will be a organized layer of vicinal liquid. The energy required to organize this layer contributes to the surface tension

$$\gamma_{SL} = \gamma_{SL}^{\circ} - E \quad (1)$$

where  $\gamma_{SL}^{\circ}$  is the surface tension in the absence of the organized layer and  $E$  is the energy per unit area contributed by the organized layer. Equation (1) is often referred to as Lippman's equation. In the case of simple point ions the contribution  $E$  to the surface tension can be calculated from double-layer theory

$$E = \frac{C}{2}(V_M - V_S)^2 \quad (2)$$

where  $V_S$  is the potential of the bulk liquid and the differential capacity of the double layer  $C$  depends on the parameters of the situation including the ionic content of the fluid. Note that by varying the applied potential  $V_M$  at the solid/liquid interface the ions in the double layer are reorganized resulting in a change in the energy stored in the double layer and a resultant change in the surface tension Eq. (1). This imbalance in force can be calculated by a form of Young's equation, the static form of which is given by

$$\gamma_{SV} - \gamma_{SL} = \gamma_{LV} \cos \theta \quad (3)$$

where  $\theta$  is the contact angle, and the subscripts indicate the surface tension at the solid/vapor (SV) and liquid/vapor (LV) interfaces. The imbalance of force thus created at the contact line will cause it to move. By measuring the motion of the contact line, the contribution to the surface

---

<sup>1</sup>For convenience, we often refer to the contact *line*, it being understood that there is actually a small finite *volume* of anomolous behavior.

tension from the organization in the solid/liquid interface  $E$  can be parsed out from the total surface tension  $\gamma_{SL}$ .

Experiment-Technique— A CCD camera observes changes in the rise height  $h(t)$  and contact angle  $\theta(t)$  at the moving contact line. A potentiostat applies and maintains a fixed potential at the surface of a conducting solid which is in contact with the liquid. The surface potential is changed by an step change of potential and the resultant change in contact line position  $h(t)$  and  $\theta(t)$  are recorded.

Proposed Work— We propose a series of experiments using water as the working fluid. The experimental protocol can be represented as

$$\text{Molecular Structure} \xrightarrow{\text{Eq. (2)}} E(t) \xrightarrow{\text{Eq. (1)}} \gamma_{SL}(t) \xrightarrow{\text{Eq. (3)}} F(t) \xrightarrow{\text{data}} \begin{cases} h(t) \\ \theta(t) \end{cases} \quad (4)$$

which yields a calculation of the force on the moving contact line which can be compared to measurements of its position and geometry. Starting on the left hand side of Eq. (4), double layer theory provides a description of the molecular structure of adsorbed ions in the neighborhood of a solid surface. From the theory one can calculate the energy  $E(t)$  stored in the organized ions at the solid/liquid interface. This energy contributes to the total surface tension at the solid/liquid interface  $\gamma_{SL}$ . The force  $F(t)$  on the contact line can then be computed by Young's equation. This time varying force can be correlated to the data  $h(t)$ ,  $\theta(t)$  measured from the contact line motion. In this manner, contact line position and geometry is measured coincident with the force generated at the moving contact line by the molecular double layer structure.

### Continuum Model of the Contact Line Region

Background— As discussed in the Introduction, there is experimental evidence that molecules at interfaces have preferred orientations. There is also experimental measurements supporting the supposition that accounting for the change of orientation of the liquid molecules at solid surfaces and the point couples induced by them is necessary in order to accurately predict the forces and loads in squeeze films and other flows restricted to thin domains. While the relevance of these measurements to the contact line geometry is not obvious, we consider that due to the large stresses expected near the moving contact line, as well as its restricted geometry, consideration of the scaling suggests that the forces at the contact line may be similarly affected by molecular orientation.

Concept— In this part of the work, effects of molecular orientation, and other molecular properties, will be formulated into a continuum model of the contact line. Preliminary work, described in a Master's Thesis [3], has shown that incorporating finite molecule size and molecular orientation may account for some of the anomalous features of the contact line region. Consider that molecules not only translate but also rotate and change their orientation. The molecular rotation in a Newtonian fluid would occur randomly with a short relaxation time. For example, the characteristic rotational period for a water molecule at room temperature is about  $10^{-11}$  second and is therefore negligible. If, however, the molecule is in a field that does not fluctuate randomly but controls the long-time behavior of the molecule, the contribution of the molecular rotation could be considerable. A polarized or polarizable molecule, for example, would orient itself to an

applied electric field, a field induced at a conducting wall, or due to configurational changes as it leaves one type of interfacial orientation and becomes incorporated into another. While reorienting itself, the fluid molecule would interact with the surrounding molecules. If its action on neighboring molecules is modeled as a couple applied on the fluid, the equation of motion would be

$$\rho \frac{D\vec{u}}{Dt} = -\nabla p + \rho \vec{f} + \mu \nabla^2 \vec{u} + \mu' \nabla \times \vec{L} \quad (5)$$

where  $\rho$  is the density,  $\vec{u}$  is the velocity,  $t$  is time,  $p$  is pressure,  $\mu$  is the viscosity,  $\mu'$  is a constant, and  $\vec{L}$  is the couple, respectively. Here, we have assumed that only a dilute population of atoms are strongly oriented; the remaining volume has no particular orientation. So, each oriented molecule influences its immediate neighborhood with no mutual interaction with other oriented molecules.

Proposed Work— The orientation of a molecule (or a cluster of molecules) can be indicated by a *director*. The director can be of dipole kind, or quadrupole kind, etc. For example, a quadrupole-kind director can be defined such that

$$m_{ij} \equiv \delta_{ij} - \cos \theta_i \cos \theta_j \quad (6)$$

where  $m_{ij}$  is the director,  $\delta_{ij}$  is the Kronecker delta, and  $\theta_i$  is the angle between the axis of a specified direction of the molecule and the  $i$ -th axis, respectively. The  $m_{ij}$  gives the degree of alignment of the molecule in the specified directions  $i, j$ . The quadrupole-type director can be related to the molecular rotation  $\omega_o$  [4]

$$\frac{Dm_{ij}}{Dt} = \omega_o \times m_{ij} - m_{ij} \times \omega_o \quad (7)$$

As an example, if a two-dimensional case ( $x, y$ )-domain is considered and  $\theta_o$  is the angle between the direction of the molecular orientation and the  $x$ -axis, then equation Eq. (7) reduces to

$$\frac{D\theta_o}{Dt} = \frac{\partial \theta_o}{\partial t} + u \frac{\partial \theta_o}{\partial x} + v \frac{\partial \theta_o}{\partial y} = -\omega_{oz} \quad (8)$$

If now Eq. (5) is also restricted to a two-dimensional domain, the streamfunction  $\psi$  can be introduced. If the equation is now nondimensionalized and considered in the limit of low Reynolds number, it can be written as

$$-C_O \nabla^2 \omega_{oz} + \nabla^4 \psi = 0 \quad (9)$$

where  $C_O$  is a known constant, and  $\omega_{oz}$  is the molecular rotation in the  $z$ -direction. Equations (8) & (9) should be solved simultaneously. The most difficult part of this work is seen to be that the couple field  $\vec{L}$  and the flow field are dependent. If successful, the slip condition could then be specified as a known function of the properties of the liquid, the solid, and the flow parameters.

## Averaging and Energy Transport

Concept— In formulating a continuum model from a description of molecular interaction, as outlined above, it is necessary to average over a collection of molecules. Within the bulk this averaging is a standard procedure which relies on the large number of molecules within the volume being averaged. Within the contact line region, however, the volume may not be sufficiently large to justify the use of the averaging procedures which work so well within the bulk. In this part of

the proposed research, we seek to determine 1) the minimum size for which bulk-type averaging is accurate, 2) how to average over small groups of molecules, as in the contact region, which may be smaller than this minimum size, and 3) how energy is transported in small systems.

Preliminary work– In preliminary work the interaction of molecules along an interface has been modeled as a one-dimensional chain of point masses interacting through a power-law potential. It can be shown that such a potential models the nearest-neighbor interactions between polarized molecules [5]. Much is known about systems of this type. However, almost all prior work was concerned with large systems or with the thermodynamic limit of broad-band forcing [6]. However, we have found that small systems do not show the same type of behavior as large systems [7]. The normalized entropy is defined as

$$\eta(t) \equiv \frac{S_{max} - S(t)}{S_{max} - S(0)} \quad (10)$$

where  $S(t)$  is the entropy of the system at time  $t$  whose maximum value is given by

$$S_{max} = \ln(N/2) \quad (11)$$

so that  $\eta = 1$  implies that all of the energy is in one mode, and  $\eta = 0$  is that the energy is equally shared by all modes. For large systems  $\eta$  decreases to zero or a small value (there are some exceptional cases given by Fermi-Pasta-Ulam recurrence). However, for small systems the entropy shows a cascade of peaks. These peaks appear even at extremely long times. The peaks in normalized entropy indicate organized motion among the masses. From further measurements of the dispersion of waves propagating along the chain we speculate that this organized motion may indicate the presence of solitary waves. In small systems this type of energy transfer appears to be intermittent, and the organized wave motion is disturbed by long intervals of thermal motion. In other preliminary work, contained in a Master's thesis [8], we have identified the frequency content of the organized motion. We have found that the evolution of the normalized entropy is self-similar as the number of masses  $N$  increases, at least over a limited range  $3 < N < 256$ . Within this range the time of occurrence of any particular peak  $t_{peak}$  scales with number of masses as  $t_{peak} \sim N^2$

Proposed work– In the proposed work, we address the following questions: 1) What is the minimum size such that a chain of masses (molecules) can be treated by the usual types of statistical averages [9]? However, these types of averages may not be valid when applied to the small numbers of atoms which make up the contact line region or the neighborhood of an interface. 2) What are the parameters which determine the continuum limit? The limit is not quite so simple as simply increasing the number of masses  $N$ . For example, if excited by a single spatial mode, the energy density—the energy per mass—has to decrease as  $N$  increases in order to reach the continuum limit. We here try to delineate how a discrete system approaches the continuum limit. In addition, we try to determine the proper manner to take the limit. 3) What types of behavior are found for small systems? In particular, what types of energy transport are found in small systems? We have already pointed out that in our preliminary work we have found that small systems seem to support intermittent solitary waves. We would like to determine the extent to which energy is transported along the interface (chain) by these types of waves.

## SUMMARY

Our overall goal is to accurately describe microgravity fluid motion in the presence of a moving contact line. We seek to identify the molecular dynamics which make the moving contact line a unique region and to then incorporate these dynamics into a continuum model. Part of our proposed research is experimental in which we measure how a vicinal layer affects contact line motion. These measurements relate contact line motion with changes in solid/liquid interfacial structure. Initially we are trying to use double layer theory to relate changes in double layer structure to contact line motion. Other analytical work seeks to formulate the effects of molecular orientation on contact line motion. Implicit in our continuum theory is a means of averaging discrete molecular behavior into continuum equation. We investigate the proper manner of averaging small collections of molecules by simulating the interface numerically and observing the behavior as a function of the parameters of the system including system size. We consider the proper limiting procedure needed in order to extract the continuum limit. However, we recognize also that small systems have behavior which is distinctively different from continuum behavior. We seek to identify the mechanisms of energy transport along the interface and how these mechanisms scale with system size.

## References

- [1] J. Koplik, J. R. Banavan, and J. F. Willemsen. Molecular dynamics of fluid flow at solid surfaces. *Phys. Fluids A*, 1:781–794, 1989.
- [2] P. A. Thomson and M. O. Robbins. Shear flow near solids: epitaxial order and flow boundary conditions. *Phys. Rev. A*, 41:6830–6837, 1990.
- [3] M. Han. Contact line dynamics: A non-Newtonian model. Master's thesis, Northwestern University, 1993.
- [4] J. S. Dahler and L. E. Scriven. Theory of structured continua i. general consideration of angular momentum and polarization. *Proc. Roy. Soc. Lond. A*, 274:504–517, 1963.
- [5] A. S. Davydov. The role of solitons in the energy and electron transfer in one-dimensional molecular systems. *Physica 3D*, 1 & 2:1–22, 1981.
- [6] R. Livi, M. Pettini, S. Ruffo, M. Sparpaglione, and A. Vulpiani. Equipartition threshold in nonlinear large Hamiltonian systems: The Fermi-Pasta-Ulam model. *Phys. Rev. A*, 31:1039–1045, 1985.
- [7] C. Y. Lin, S. Lichter, and C. Goedde. Continuum behavior of small discrete systems. In *Proceedings of the SIAM Annual Meeting*. Society for Industrial and Applied Mathematics, 1994. San Diego, CA, session CP25.
- [8] C. Y. Lin. Discrete to continuum behavior: Scaling rules for the one-dimensional Fermi-Pasta-Ulam model. Master's thesis, Northwestern University, 1995.
- [9] N. Davidson. *Statistical Mechanics*. McGraw-Hill Co., New York, NY, 1962.



## Dynamics of the Molten Contact Line

Ain A. Sonin and Stefano Schiaffino

Department of Mechanical Engineering  
Massachusetts Institute of Technology  
Cambridge, MA 02139

A great deal of work has been published on the capillarity-driven motion of an ordinary liquid over a solid surface (the *isothermal* dynamic contact line problem). The solution to this problem may be stated in terms of a functional relationship between the contact line speed  $U$ , the dynamic contact angle  $\theta$ , and the relevant properties of the system's three phases and their interfaces. One such relationship is the much-quoted empirical correlation of Hoffman (1975), who showed that for  $Ca = \mu U / \sigma < 1$ , where  $\mu$  is the liquid viscosity and  $\sigma$  the surface tension, a large amount of data spanning many orders of magnitude in  $Ca$  could be correlated approximately by the formula  $Ca \approx k(\theta^3 - \theta_e^3)$ , where  $\theta_e$  is the equilibrium contact angle and  $k \approx 0.013$ . On the theoretical side, the continuum theory of the moving contact line contains the well-known non-integrable shear stress singularity at the contact line [e.g. Tanner (1979), de Gennes (1985, 1990), Cox (1986), Leger (1992)]. The singularity can be removed by specifying a velocity slip model or cut-off very close to the contact line [e.g. Huh (1971, 1977), Dussan V. (1974, 1976, 1979, 1991), Durbin (1988), Haley (1991), Hocking (1992)], and the parameters can be chosen so as to yield agreement with experiment [Fermigier (1991), Chen (1992), Leger (1992)]. An entirely different theory for the dynamic contact line has been put forward by Blake (1969) based on Eyring's reaction rate theory for liquids. With an appropriate selection of physical parameters, this molecular-kinetic theory can also be brought into agreement with experimental data [Blake (1969, 1979, 1994), Gribanova (1992)]. Some progress has also been made recently in applying molecular-dynamic computations to the contact line (Thompson et al, 1993; Koplic & Banavar, 1995), but these are limited to mesoscale systems. Clearly, despite the large amount of work, this problem is not yet conclusively resolved.

In contrast to the ordinary contact line problem, virtually no information is available on the similar problem associated with a *molten* material spreading on a solid which is below the melt's fusion point. The latter is a more complex problem in which heat transfer and solidification take place simultaneously with spreading, and requires answers not only for the hot melt's advance speed over the cold solid as a function of contact angle, but also for how one is to predict the point of the molten contact line's arrest by freezing. These issues are of importance in evolving methods of materials

processing. For example, finely featured components can be fabricated under computer control by precise deposition of individual molten microdrops, each droplet solidifying by heat loss after it lands (Gao & Sonin, 1994). In this case, the point of a droplet's contact line arrest will control its post-deposition solid shape, that is, the shape of the basic microscale "building block" of the process.

The purpose of our work is to develop, based on both experiments and theory, an understanding of the dynamic processes that occur when a molten droplet touches a subcooled solid, spreads partly over it by capillary action, and freezes. We seek answers to the following basic questions. First, what is the relationship between the melt's contact line speed and the apparent (dynamic) contact angle? Secondly, at what point will the contact line motion be arrested by freezing?

A simple well-defined example is the deposition of a molten droplet at temperature  $T_0$  onto a semi-infinite, solid target at a temperature  $T_f$  below the melt's freezing point  $T_f$  (Fig. 1). If the scale is so small, or gravity so weak, that gravitational effects are negligible (small Bond number), and the deposition so gentle that the molten droplet does not break up upon impact (small or moderate Weber number), the droplet will typically spread in liquid form until the contact line is arrested by freezing, after which point the droplet's footprint will remain fixed, though the liquid above it may still undergo dynamic oscillations until solidification is complete. Since the subcooled target has an infinite thermal capacity, the final state will always be one where the deposited material is solid and at the target temperature.

The talk will describe three components of our work: (i) deposition experiments with small molten droplets, (ii) investigation of the dynamics of the molten contact line by means of a novel forced spreading method, and (iii) an attempt to provide a theoretical framework for answering the basic questions posed above.

(i) Deposition experiments were performed with molten droplets of waxes, water, and mercury. The thermal-dynamic scaling parameters for deposition are listed in Fig. 2, simplified to the case where the Weber number is small and the molten droplet and solid target are of the same material. Fig. 3 gives material properties and parameter values. The droplet radii ranged from 25  $\mu\text{m}$  for the wax to about 300  $\mu\text{m}$  for mercury and up to 1000  $\mu\text{m}$  for water. Mercury was included because it possesses typical metal properties but, owing to its low melting point, is relatively free of interfacial oxidation problems. A high speed camera provided information on the global droplet dynamics during impact and spreading, including time scales and the final drop shape (Fig. 4 gives the ratio of the arrested footprint radius  $R^*$  and  $a$ , from which contact angle can be derived), but did not

give enough resolution to accurately determine dynamic contact angles during the spreading process.

(ii) To better investigate the contact line dynamics, we devised the forced spreading experiment shown schematically in Fig. 5. Using an apparatus similar to Gao & Sonin's (1994), a continuous stream of molten microdrops (radius  $25\text{ }\mu\text{m}$ ) is ejected at frequency  $f$  and ballistically delivered to a point on the target surface. The droplets coalesce as they arrive to form a sessile liquid macrodrop which grows and spreads laterally over the target. This simulates the spreading of a single, impacting droplet. The delivery frequency provides control over the contact line velocity  $U=dR/dt$ , where  $R$  is the macrodrop's contact line radius. The contact line motion can be filmed with a standard CCD camera through a microscope objective.

The video sequence of Fig. 6 shows a forced spreading experiment with molten wax on solid wax (only waxes have been studied with this technique so far). In the early stages the contact line moves much as it would for an ordinary liquid, and the relationship between  $\theta$  and  $U$  is well represented by Hoffman's law with  $\theta_e=0$ . The contact line speed decreases as the macrodrop's base radius grows and, after the advance velocity slows to a critical value  $U^*$ , the contact line arrests rather abruptly at a radius  $R^*$  (Fig. 7). Our experiments show that  $U^*$  depends on target subcooling (Fig. 8), but is essentially independent of melt superheat  $(T_o-T_f)/(T_f-T_i)$  and independent also of the macrodrop's spreading history (Fig. 8), which in this experiment is controlled via the delivery rate  $f$  and time. The primary parameter which determines  $U^*$  appears to be the Stefan number  $S=c(T_f-T_i)/L$  based on target subcooling,  $c$  being the specific heat and  $L$  the latent heat. Contact line arrest is thus controlled mainly by processes near the contact line.

(iii) A freezing mechanism may be postulated based on the angle  $\theta_s$  of the solidification front at the contact line (Fig. 9). A melt droplet will spread until the apparent liquid contact angle  $\theta$  approaches  $\theta_s$ , at which point the supply of melt to the contact line cannot be maintained and the spreading must stop. If this is correct, the melt's apparent contact angle  $\theta$  will be given approximately by Hoffman's law with  $\theta_e=0$  as long as  $\theta_s \ll \theta$ , and contact line freezing will occur when  $\theta_s$  approaches  $\theta$ . The arrest condition would therefore be obtained by calculating  $\theta_s$ .

There is one problem with this: if we use the conventional continuum equations and boundary conditions (Fig. 10), the heat flux which controls the angle of the fusion interface is singular at the contact line (it has the same power-law form near the CL as Anderson & Davis's (1994) analysis for the purely conductive case). The angle  $\theta_s$  cannot therefore be computed unless the continuum equations and/or boundary conditions are modified with a physically correct mechanism that removes the mathematical singularity.

The mechanism is at this time open to some speculation. Our first approach has been to ask whether a material can be characterized with a given cutoff length  $\lambda$ . We ask, at what distance from the contact line should the heat flux of the continuum solution be terminated to give a  $\theta_s$  value in agreement with the experimental data for the arrest condition? Computations (Figs 10 and 11) show that the data for each of the three materials we have studied can indeed be adequately matched with a cut-off length  $\lambda$ , the value of which ranges from 0.08 to 0.3  $\mu\text{m}$  depending on material (Fig. 12). These lengths are large compared with molecular scale, but smaller than the typical velocity slip lengths that have been used to fit continuum theories of the ordinary dynamic contact line to experimental data.

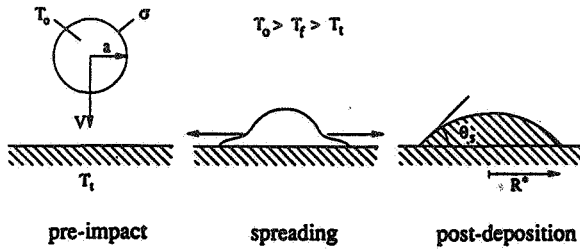
This research is at an early stage, and further work is required on both the experimental and theoretical sides to resolve the heat flux singularity and lay the basis for a complete theory of the molten contact line.

**Acknowledgement:** This work was supported by the National Science Foundation under Grants CTS-9122123 and CTS-9413026.

### References

- D. M. Anderson and S. H. Davis, *JFM* **268** (1994) 231-265
- T. D. Blake and J. M. Haynes, *J. Colloid and Interface Sci.* **30** (1969) 421-423
- T. D. Blake and K. J. Ruschak, *Nature* **282** (1979) 489-491
- T. D. Blake, "Dynamic contact angles and wetting kinetics", in *Liquid Film Coating: Scientific Principles and their Technological Implications*, P. Schweitzer and S. Kistler, eds. Chapman, 1994.
- J. D. Chen and N. W. Wada, *J. Colloid and Interface Sci.* **148** (1992) 207-222
- R. G. Cox, *JFM* **168** (1986) 169-194
- P. G. de Gennes, *Rev. Mod. Phys.* **57** (1985) 827-863
- P. G. de Gennes, X. Hua and P. Levinson, *JFM* **212** (1990) 55-63
- P. A. Durbin, *JFM* **197** (1988) 157-169
- E. B. Dussan V. and S. H. Davis, *JFM* **65** (1974) 71-95
- E. B. Dussan V., *JFM* **77** (1976) 665-684
- E. B. Dussan V., *Ann. Rev. Fluid Mechanics*, Vol. 11 (1979) 371-400
- E. B. Dussan V., E. Ramé and S. Garoff, *JFM* **230** (1991) 97-116
- M. Fermigier and P. Jenffer, *J. Colloid and Interface Sci.* **146** (1991) 226-241
- F. Gao and A. A. Sonin, *Proc. Royal Soc. London A* **444** (1994) 533-554
- E. V. Gribanova, *Advances in Colloid and Interface Science* **39** (1992) 235-255
- P. J. Haley and M. J. Miksis, *JFM* **223** (1991) 57-81
- L. M. Hocking, *JFM* **239** (1992) 671-681
- R. L. Hoffman, *J. Colloid and Interface Sci.* **50** (1975) 228-241
- C. Huh and L. E. Scriven, *J. Colloid and Interface Sci.* **35** (1971) 85-101
- J. Koplik and J. R. Banavar, *Ann. Rev. Fluid Mech.*, Vol 27 (1995) 257-292
- L. Leger and J. F. Joanny, *Reports on Progress in Physics* **55** (1992) 431-486
- C. G. Ngan and E. B. Dussan V. *JFM* **118** (1982) 27-40
- L. H. Tanner, *J. Phys. D.* **12** (1979) 1473-1484
- P. A. Thompson, W. B. Brinckerhoff & M. O. Robbins, *J. Adhesion Sci. Technol.* **7** (1993) 533-554

Fig. 1: Molten droplet deposition on subcooled solid of its own kind



$$Bo = \frac{\rho g a^2}{\sigma} \ll 1; \quad We = \frac{\rho V^2 a}{\sigma} \cong 0-10$$

#### Post-deposition droplet shape

- is not an equilibrium property (no equilibrium contact angle!)
- depends on thermal conditions and material properties

Fig. 3: Properties of Selected Materials

	$\alpha$ (m <sup>2</sup> /s)	$T_f$ (°C)	$S$ @ $T_f - T_t = 10^\circ\text{C}$	$Pr$	$Z$ @ $a = 100 \mu\text{m}$
Tin (Sn)	$4.0 \times 10^{-5}$	232	0.039	0.0065	$3.2 \times 10^{-3}$
Tin 60-Lead 40 eutectic	$3.3 \times 10^{-5}$	183	0.038	0.0077	$3.1 \times 10^{-3}$
Mercury (Hg)	$4.4 \times 10^{-6}$	-39	0.12	0.027	$2.0 \times 10^{-3}$
Water (H <sub>2</sub> O)	$1.4 \times 10^{-7}$	0	0.13	7.0	$1.2 \times 10^{-2}$
Microcrystalline wax	$6.1 \times 10^{-8}$	91	0.11	300	$3.6 \times 10^{-1}$

$\alpha$  = thermal diffusivity (m<sup>2</sup>/s)

$T_f$  = fusion temperature (°C)

Fig.2: Global scaling parameters for capillarity-driven droplet deposition

( $We < 1$ )

$$Z = \frac{\mu}{\sqrt{\rho \sigma a}} = \text{Ohnesorge number}$$

$$\tau = \frac{t}{\sqrt{\frac{\rho a^3}{\sigma}}} = \text{inertial/capillarity timescale}$$

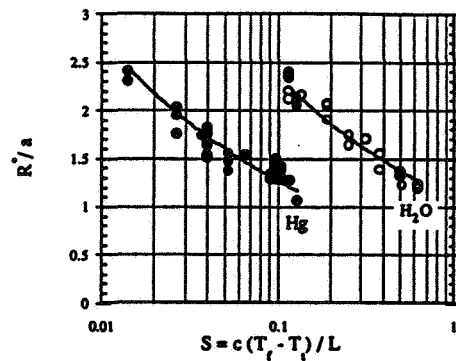
$$S = \frac{c(T_f - T_t)}{L} = \text{Stefan number}$$

$$\beta = \frac{T_o - T_f}{T_f - T_t} = \frac{\text{melt superheat}}{\text{target subcooling}}$$

$$Pr = \frac{V}{\alpha} = \text{Prandtl number}$$

$\Pi_i$  = additional parameters from quantities which characterize conditions at contact line

Fig. 4: Effects of thermal conditions on final droplet shape



#### Final base radius $R^*$

- decreases with increasing target subcooling  
 $S = c(T_f - T_t) / L$
- is insensitive to melt superheat  $\beta = (T_o - T_f) / (T_f - T_t)$

Fig. 5: The forced spreading experiment

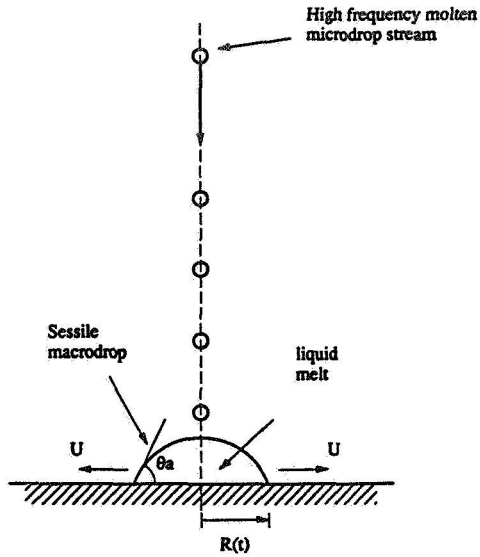


Fig. 6: Video sequence of forced spreading experiment. Microcrystalline wax,  $T_0=117^\circ\text{C}$ ,  $T_t=80^\circ\text{C}$ ,  $T_f=91^\circ\text{C}$ ,  $f=1\text{kHz}$ , the rectangle's width is  $100\text{ }\mu\text{m}$

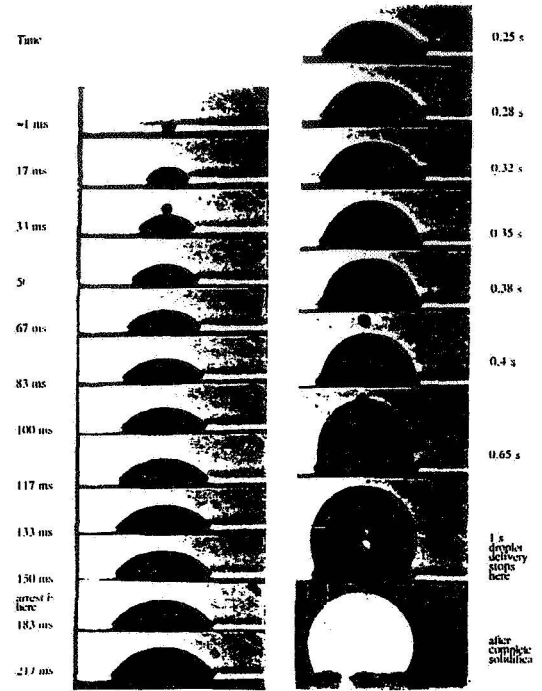


Fig. 7: Results from forced spreading experiments

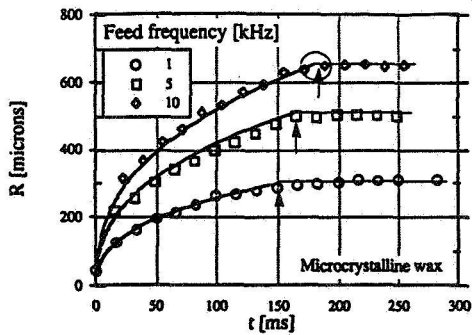
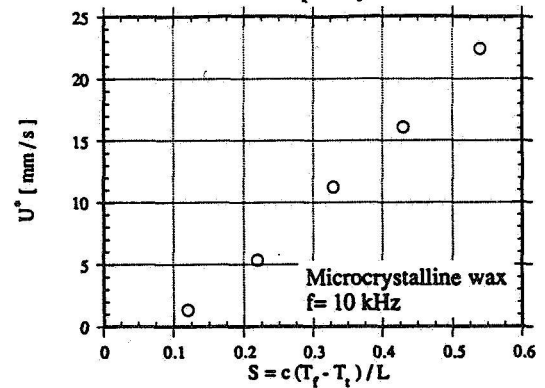


Fig. 8: CL speed just prior to arrest increases with target subcooling  $S$  and is independent of feed frequency  $f$



Contact line arrest conditions (apparent contact angle  $\theta_a$  and speed  $U^*$  just prior to arrest) are:

- (i) independent of macrodrop spreading history (i.e. no dependence on frequency of deposition)
- (ii) dependent on target subcooling

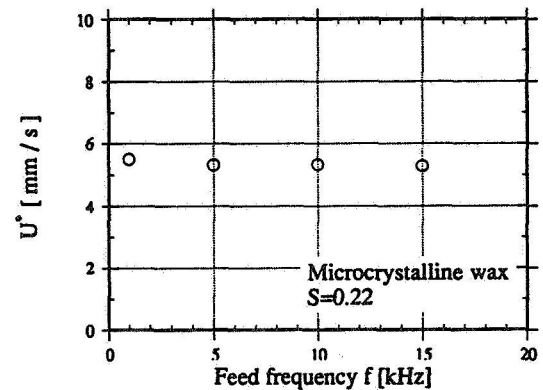


Fig. 9: The solidification front at the contact line

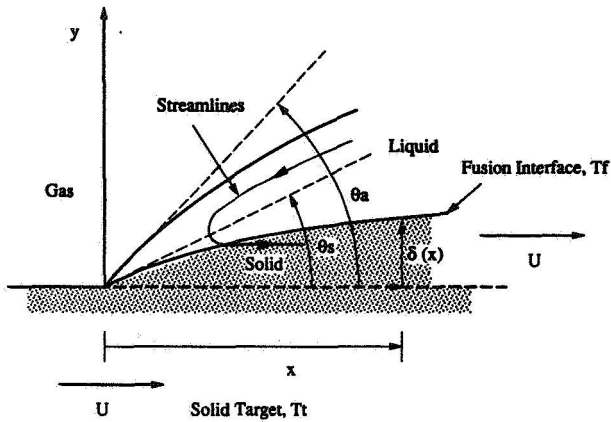


Fig. 10: Calculation of heat flux near the CL

Stefan condition:  $\rho UL \sin \theta_s = q_s - q_l \equiv q_s$

$$\phi = \frac{T - T_f}{T_f - T_i}; \quad X = \frac{Ux}{\alpha}, \quad Y = \frac{Uy}{\alpha}$$

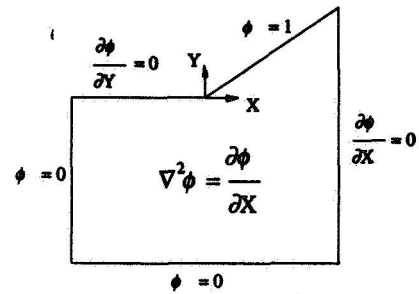


Fig. 11: Finite element calculation of temperature field for a wedge domain with  $\theta = \pi/6$

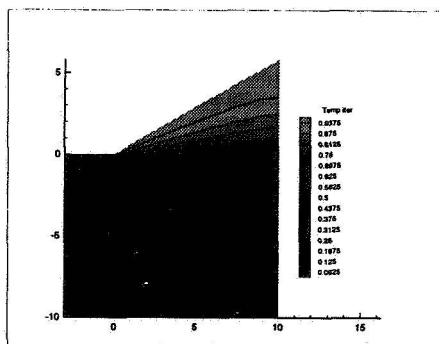
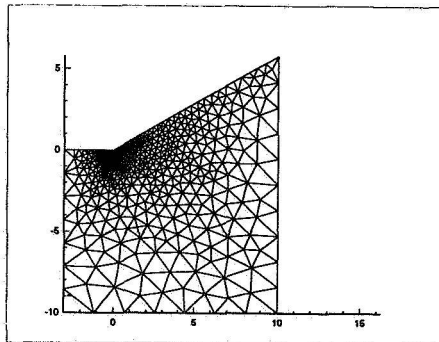
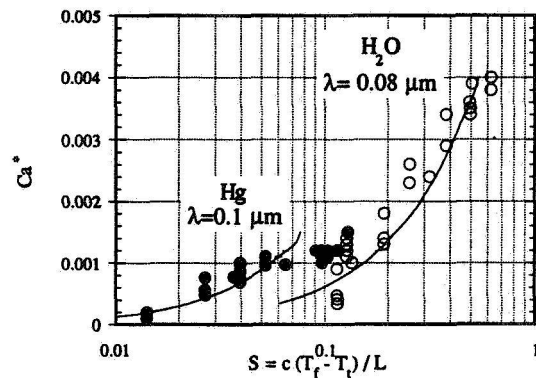
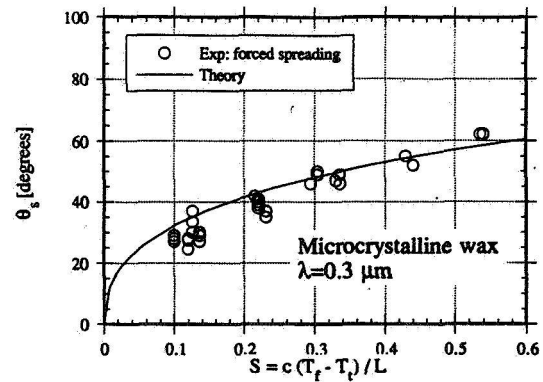


Fig. 12: Comparison of experiments and theory on molten contact line arrest







# WETTING HYSTERESIS AT THE MOLECULAR SCALE

Wei Jin<sup>1</sup>, Joel Koplik<sup>1</sup> and Jayanth R. Banavar<sup>2</sup>

<sup>1</sup>Benjamin Levich Institute and Department of Physics, City College of the City University of New York, New York, NY 10031

<sup>2</sup>Department of Physics and Materials Research Laboratory, Pennsylvania State University, University Park, PA 16802

## ABSTRACT

The motion of a fluid-fluid-solid contact line on a rough surface is well known to display hysteresis in the contact angle *vs.* velocity relationship. In order to understand the phenomenon at a fundamental microscopic level, we have conducted molecular dynamics computer simulations of a Wilhelmy plate experiment in which a solid surface is dipped into a liquid bath, and the force-velocity characteristics are measured. We directly observe a systematic variation of force and contact angle with velocity, which is single-valued for the case of an atomically smooth solid surface. In the microscopically rough case, however, we find (as intuitively expected) an open hysteresis loop. Further characterization of the interface dynamics is in progress.

## INTRODUCTION

The contact angle at which a meniscus separating two fluids meets a solid surface is an important quantity for both static and moving fluid interfaces. The static angle determines the shape of partially wetting drops and, when zero, implies that a drop will wet a surface completely. The dynamic contact angle of a moving interface is an important ingredient in its time evolution, and enters as a boundary condition in the free surface problem. In either case, a number of interesting issues arise, which are generically referred to as contact angle hysteresis [1,2].

Firstly, Young's equation relates the contact angle to the various interfacial free energies in the problem, and ostensibly implies a unique angle for a given solid-liquid-liquid system. In fact, one observes that a *range* of static angles is possible. The origin of this phenomenon is believed to be surface heterogeneity, which can be of two varieties. If the surface is structurally rough, having a non-planar shape at mesoscopic lengths between the atomic size and the resolution of the observations, then even a unique microscopic or intrinsic angle on a fluctuating surface may give a range of apparent macroscopic angles. If instead, the surface has chemical heterogeneities, then the microscopic angle may fluctuate from point to point and cause the apparent angle to vary with the location of the interface. In the dynamic case, a second phenomenon arises – the observed contact angle varies with the velocity of the meniscus. Here, in addition to surface effects, the viscous stress resulting from fluid motion will certainly affect the interfacial shape away from the surface, and perhaps cause further changes in the apparent angle.

Although contact angle hysteresis has been well documented in the laboratory, and is a common ingredient in recent hydrodynamic calculations, its origins involve the interplay of fluid dynamics and microscopic surface effects and the difficulties of the problem have discouraged computational or theoretical studies of its origins. In terms of quantitative calculations, several authors have considered the possible static interfacial configurations resulting from model surface heterogeneities. The latter have ranged from a 2-d sinusoidal variation in the position of a solid surface [3] to a more realistic periodic pattern of wettability variation on a solid plate [4]. In the latter case, Schwartz and Garoff consider the effects of dipping the plate into a fluid bath, and find multiple minima in the free energy, deducing that the meniscus motion consists of alternating stick and jump

events. Analytic time-dependent calculations of the origin of hysteresis have considered only the effects of a single defect – a localized region of different wettability [5], while molecular dynamics (MD) simulations aimed at the moving contact line singularity question [6] observed a systematic variation of contact angle with interface velocity.

In this paper we report on MD simulations of a Wilhelmy plate experiment, in which hysteresis is the focus. The Wilhelmy configuration of a plate dipped into a bath at fixed velocity directly gives the force as a function of plate velocity. Hysteresis appears as an open loop in the force-velocity plane as the plate velocity varies from positive to negative values. In this procedure, a direct measurement of angle is not needed, although the force is easily converted to an apparent angle, which can be approximately correlated with observation. The advantage is that angles are difficult to observe directly in the laboratory at short distances from the solid, and difficult to quantify in molecular simulations due to small-system fluctuations. We consider structural heterogeneity only, and solid surfaces which are either atomically smooth, periodically rough, or randomly rough. We find that roughness is necessary to obtain hysteresis.

## SIMULATION METHOD

Molecular calculations of fluid flow have become common [7], and the details of the present simulation are quite similar to that used previously in molecular studies of wetting processes [6,8,9]. In an MD calculation, one computes the (classical) motion of the individual atoms comprising the fluid by giving initial positions and velocities, and integrating Newton's equations of motion with a specified intermolecular potential. Since we are interested in fluid behavior near a solid wall, whose atomic size may be comparable to that of the fluid atoms, it is appropriate to treat the wall as a collection of atoms as well. A further consideration is that we wish the atoms to be as simple as possible so that typical correlation lengths are small compared to the size of the whole system, and continuum behavior may be expected. A soft-sphere atomic fluid with Lennard-Jones potentials is then optimal, but unfortunately leads to a rather diffuse interface [7], whose contact angle is difficult to establish. The interface may be sharpened up while retaining a monatomic fluid by considering the relative displacement of two immiscible viscous fluids, as in [6,8], although chain molecules in contact with near-vacuum [9] would have the same effect.

The interaction between atoms is a two-body potential of generalized Lennard-Jones form,

$$V_{ij}(r) = 4\epsilon \left[ \left( \frac{r}{\sigma} \right)^{-12} - c_{ij} \left( \frac{r}{\sigma} \right)^{-6} \right]$$

where  $\epsilon$  and  $\sigma$  are energy and length scales, respectively, and if  $m$  is the (common) atomic mass of the fluids, the appropriate time scale is  $\tau = \sigma\sqrt{m/\epsilon}$ . All quantities discussed below are non-dimensionalized using  $\{\sigma, \tau, \epsilon\}$ . The indices  $i, j$  label the atomic species, fluid-1, fluid-2, confining walls (W), and plate (P), and the coefficient matrix ( $c_{ij}$ ) is chosen as follows. Between any two atoms of the same species, we use the standard interaction strength,  $c_{ii} = 1$  for all  $i$ . Atoms of different immiscible fluids should have a weaker attraction, and we choose  $c_{12} = 0$ . The precise value controls the interfacial width, but we have not explored other choices. The fluid-plate interaction controls the wetting properties, and we choose the lower fluid to preferentially wet the plate,  $c_{1P} = 0.75$  and  $c_{2P} = 0.5$ . The interaction of the fluids and the plate with the top and bottom walls is of little consequence, and we take  $c_{1W} = c_{2W} = c_{PW} = 0$ . The remaining coefficients are determined by symmetry (Newton's third law). The  $r^{-12}$  term provides a strong short-distance repulsion to prevent overlap of the atoms, and we simply use the standard (unit) coefficient.

A snapshot of a typical simulated system is shown in Fig. 1, and is meant to mimic a laboratory Wilhelmy plate experiment. The system is fully three-dimensional but shown in a projected view for clarity. The two fluids have 11760 atoms each and are placed in a rectangular region of space with periodic boundary conditions in both horizontal directions. The fluids are confined in the vertical direction by solid walls and a solid plate straddles the fluid-fluid interface. The plate is periodic in

the vertical direction as well as the direction normal to the figure, so as to allow a steady state to be established when it moves. Initially, the fluid atoms are placed on lattice sites with density 0.8 and given a random initial velocity chosen from a Boltzmann distribution at temperature  $T = 0.8$ . After some time the atomic positions become disordered due to mutual interactions, although one sees some layering near the walls. The wall atoms are localized for all times on an approximate crystal structure by tethering them to the sites of a regular lattice by linear springs. In this way, one has a realistic solid structure while at the same time allowing heat generated by viscous friction to escape through the solid [8].

Motion is produced by translating the lattice of tether sites at a fixed velocity. The tethers then drag the wall atoms, and the wall atoms drag the fluid with them. During the simulation we record the atomic positions, from which the contact angle may be estimated, and the force on the plate – more precisely, the net force exerted by the fluid atoms on the plate atoms. In principle, the angle  $\theta$  and the force  $F$  are related by  $F = 2W\gamma \cos \theta$ , where  $W$  is the plate width and  $\gamma = 2.8$  is the surface tension (and 2 comes from the two sides of the plate), but in practice the force measurement is the most reliable in that it is less susceptible to statistical fluctuations. We have also measured the local velocity and stress fields, but at the translation velocities considered here, thermal noise dominates and little information is present. One does however observe fluid slip at the contact line, as in [6,8]. To study the force or contact angle as a function of velocity, the system is first equilibrated, then a small positive plate velocity is applied and the system proceeds at this velocity until the force reaches a steady state. The velocity is then increased until a new steady state is reached. As the plate velocity increases, the fluid-fluid interface becomes increasingly distorted and eventually hits the top wall. This value is discarded, and the velocity is now *decreased* systematically until at large negative values the interface hits the bottom wall. This value is again discarded, and the velocity is increased back to zero. The force (or contact angle) *vs.* velocity plot is then examined.

## RESULTS

First we consider an atomically smooth plate, where no hysteresis is anticipated. Indeed, the  $f - v$  plot Fig. 2 is, within statistical fluctuations, a single curve, with a single value of force depending only on the current velocity and not on the system's history. The change in the contact angle itself at least qualitatively follows the same trend: Fig. 3 gives snapshots of the three-phase region for various velocities. It is non-trivial to assign a specific value to the contact angle because of the fluctuations in the interface position itself at a given speed, as well as the change in shape of the interface with distance from the contact line. Previous work [10] has addressed the latter issue, at least, and further work on analysis of the angle *vs.* velocity relationship and the interfacial shape is in progress. In this simulation, the Reynolds number based on the plate velocity and half-width of the cell is at maximum speed 1.2, while the capillary number extends up to 2.1.

Next we have considered two types of *rough* plate, obtained by displacing groups of solid atoms outward from their ideal-lattice positions. We either displace a periodic array of square regions as in [4] or, more realistically, groups of atoms chosen at random are displaced. In either case we find an open hysteresis loop; the result for the random case is shown in Fig.4, while the periodic case falls somewhat between the latter and the smooth case but is clearly multivalued. The qualitative features of the contact line shape are somewhat similar to the smooth-plate case, except that it appears more diffuse in a projected view because of a stronger variation along the direction of the contact line, as the latter attempts to follow the heterogeneity. Once again, further analysis is in progress.

## CONCLUSIONS

Although these simulations have for the first time directly demonstrated the role of surface heterogeneity in producing hysteresis in a *dynamic* wetting process, they have only begun to explore the problem. We conclude by listing several further significant issues which are now under study, or which we will consider presently.

1. We have considered only the steady wetting characteristics – the force or angle observed after a long displacement at a particular velocity. The pre-asymptotic behavior, *i.e.*, the dynamic response to a change in wetting speed, is equally relevant. This topic amounts to exploring the *interior* of the hysteresis loop. Wetting behavior under cyclic operating conditions and its relation to dissipation have been considered theoretically [11], but only with simplified assumptions for the velocity dependence of the angle. Furthermore, the degree to which the phenomena studied here parallel the details of hysteresis in magnetic systems [12] is unclear.
2. We have simulated structural roughness alone, and only the simplest liquids. Various segregation phenomena may occur if the liquids are mixtures or if the molecules have specific end groups, or more generally if the chemistry of the system is non-trivial. The wetting of polymeric liquids is expected to be unusually interesting [13], even beyond the previously studied case of terraced wetting [9].
3. Analytic calculations for the motion of an interface near a single defect have shown a precursor of hysteretic behavior – a difference between the velocity seen at fixed force and the force measured at fixed velocity [5]. The calculations have been limited to the small-slope and lubrication approximations, however, and do not address multiple defects or systematic wettability variation at all. Since we can modify the solid surface at will, it is possible to explore the transition between isolated defects and various types of systematic heterogeneity.

## REFERENCES

1. J. F. Padday, ed., *Wetting, Spreading and Adhesion* (Academic, 1978).
2. E. B. Dussan V., *Annu. Rev. Fluid Mech.* **11**, 371 (1979); P. G. de Gennes, *Rev. Mod. Phys.* **57**, 827 (1985); L. Leger and J. F. Joanny, *Rep. Prog. Phys.* **55**, 431 (1992).
3. R. E. Johnson Jr. and R. H. Dettre, in *Surface and Colloid Science*, ed. E. Matejevic, **2**, 85 (1967).
4. L. W. Schwartz and S. Garoff, *Langmuir* **1**, 219 (1985).
5. J. F. Joanny and P. G. de Gennes, *J. Chem. Phys.* **81**, 552 (1984); E. Raphael and P. G. de Gennes, *J. Chem. Phys.* **90**, 7577 (1989); J. F. Joanny and M. O. Robbins, *J. Chem. Phys.* **92**, 3206 (1990); A. Paterson, M. Fermigier, P. Jennfer and L. Limat, *Phys. Rev. E* **51**, 1291 (1995).
6. J. Koplik, J. R. Banavar and J. F. Willemsen, *Phys. Fluids A* **1**, 781 (1989).
7. J. Koplik and J. R. Banavar, *Annu. Rev. Fluid Mech.* **27**, 257 (1995).
8. P. A. Thompson and M. O. Robbins, *Phys. Rev. Lett.* **63**, 766 (1989).
9. J.-x. Yang, J. Koplik and J. R. Banavar, *Phys. Rev. A* **46**, 7738 (1992); J. A. Nieminen and T. Ala-Nissila, *Phys. Rev. E* **49**, 4228 (1994); U. d'Ortona, J. De Coninck, J. Koplik and J. R. Banavar, *Phys. Rev. E* **53**, 562 (1996).
10. R. G. Cox, *J. Fluid Mech.* **168**, 169 (1986); J. A. Marsh, S. Garoff and E. B. Dussan V., *Phys. Rev. Lett.* **70**, 2778 (1993).
11. G. W. Young and S. H. Davis, *J. Fluid Mech.* **174**, 327 (1987).
12. K. Dahmen, *et al.*, *J. Appl. Phys.* **75**, 5946 (1994), and references therein.
13. K. R. Willson and S. Garoff, *Colloids and Surfaces* **89**, 263 (1994).

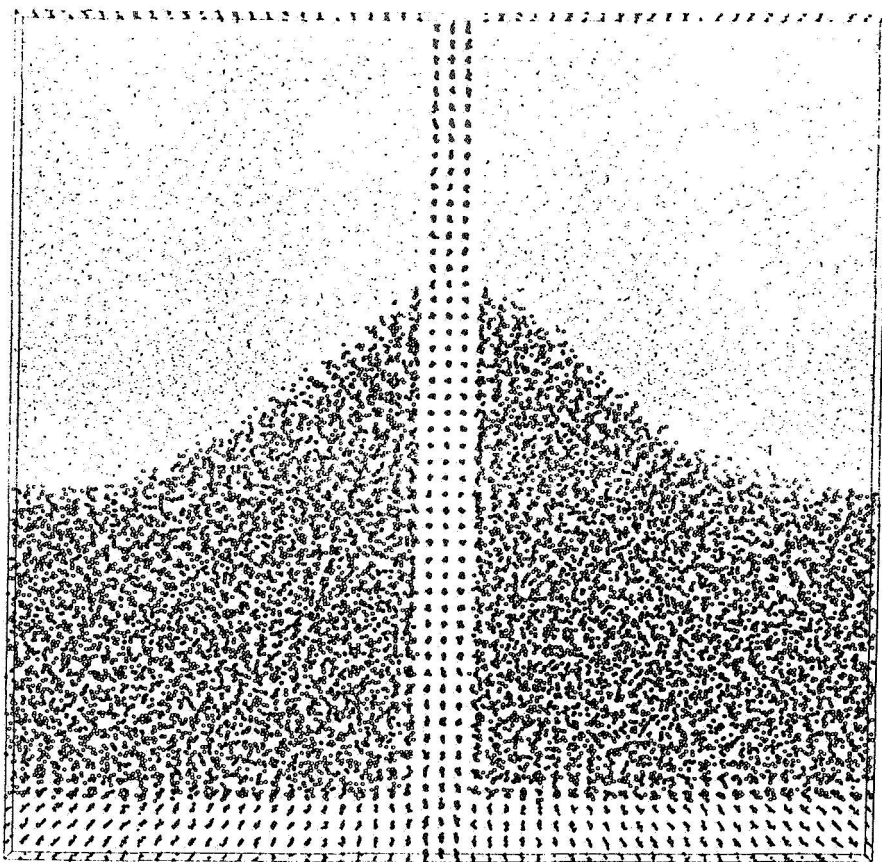


Fig. 1. Snapshot of a typical simulation run. Positions of all 27,040 atoms after time  $1800\tau$  at  $v = 0.07\sigma/\tau$ .

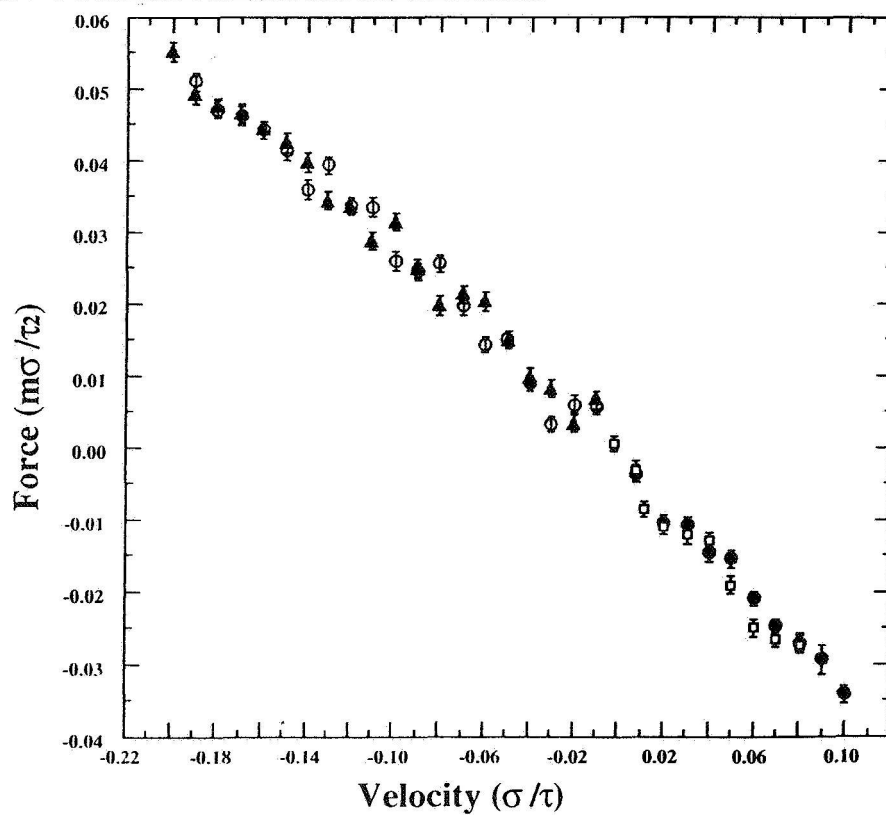


Fig. 2. Force - velocity plot for an atomically smooth plate.

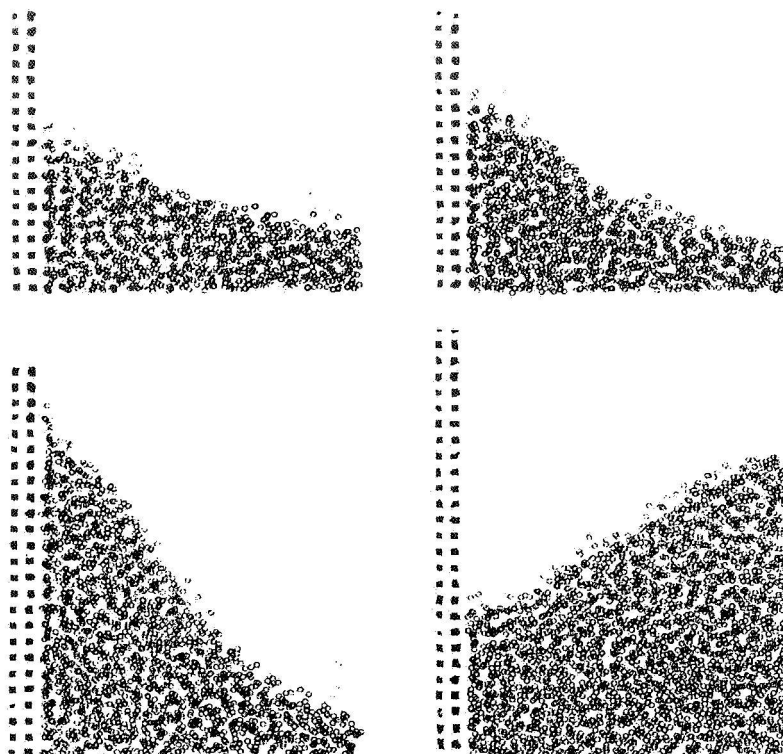
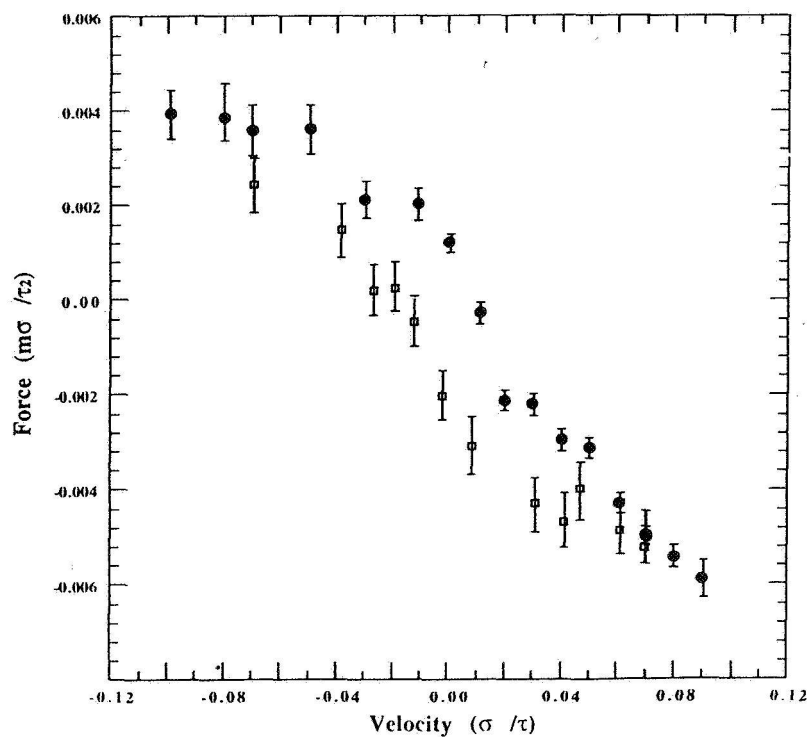


Fig. 3. Variation of instantaneous interface shape with velocity:  $v = 0.03$  (a),  $0.06$  (b),  $0.09$  (c),  $-0.20\sigma/\tau$  (d).

Fig. 4. Force - velocity plot for a randomly rough plate.



## Fluid creep effects on near-wall solute transport for non-isothermal ampoules\*

Dimitrios Papadopoulos<sup>†</sup> and Daniel E. Rosner<sup>‡</sup>

Department of Chemical Engineering, Yale University, New Haven  
CT 06520-8286, U.S.A.

There is growing practical and theoretical interest in developing accurate macroscopic modelling for flows arising in chemical or physical vapor transport (VT) crystal growth experiments, including those conducted in reduced gravity environments. An example has been given by Debe *et al.*,<sup>1</sup> who reported on experiments performed aboard the Space Shuttle flight in 1985. The authors used physical vapor transport to grow oriented metal-organic thin films of copper phthalocyanine (CuPc) on epitaxially active substrates sealed within non-isothermal ampoules. This particular process is characterized by a fairly low operating pressure (in the Torr range) and very steep gradients of temperature and concentration predominantly in the axial direction (normal to the surfaces of evaporation and deposition). Typical operating conditions and preliminary theoretical investigations regarding the CuPc system have been presented by Rosner and Keyes.<sup>2</sup> It is noteworthy that, according to the measurements of Debe *et al.*,<sup>1</sup> temperature gradients can reach values as high as 75 K/cm (corresponding to an  $O(10^{-3})$  fractional temperature difference over one mean-free-path) in the vicinity of the substrate. Rosner<sup>3</sup> first pointed out that, whereas Stefan and buoyancy-driven flows were negligible under the conditions employed, previously neglected rarefied gas dynamics phenomena become rather important sources of convection. In particular, the combination of rarefaction and strong gradients of temperature (and/or concentration) tangential to the side-walls of the ampoule induces convective flows known as thermal (and concentration) "creep" respectively. His order-of-magnitude estimates revealed that thermal creep effects can be non-negligible even at normal gravitational levels.

On the macroscopic level and under the conditions mentioned above, the bulk fluid mechanics can be adequately described by the familiar macroscopic equations as long as the *boundary conditions* are modified to account for the integrated effect of kinetic (Knudsen<sup>9</sup>) boundary layers adjacent to solid boundaries. For example, the most general boundary condition for velocity at a simple gas/solid interface reads<sup>4</sup>:

$$\mathbf{v} = \mathbf{v}_w + \zeta \frac{\partial \mathbf{v}_t}{\partial n} + \omega \left( \frac{2kT}{m} \right)^{1/2} \frac{1}{T} \cdot \left( \frac{\partial T}{\partial \mathbf{x}} - \mathbf{n} \frac{\partial T}{\partial n} \right) \quad (1)$$

\*Presented at 3rd Microgravity Fluid Physics Conference, 13-15 June, 1996, Cleveland, Ohio; supported, in part, by NASA Grant NAG-3-1654

<sup>†</sup>Graduate Research Fellow, HTCRE Laboratory, Yale University

<sup>‡</sup>Prof./Chair, Ch.E. Department, Yale University

where  $\mathbf{v}$ ,  $\mathbf{v}_w$  refer to the fluid and wall velocity respectively, subscript  $t$  denotes the component in the *tangent* plane,  $\mathbf{n}$  is the unit vector in the direction locally normal to the surface and  $\mathbf{x}$  is a general position vector. The indicated coefficients  $\zeta, \omega$  are *lengths* of the order of magnitude of the gas molecule mean-free-path and depend on the details of the intermolecular and the molecule/surface collision processes. Their values are obtained by solution of the Boltzmann equation or models thereof for idealized geometries. Equation (1) simply states that a velocity slip  $\mathbf{v} - \mathbf{v}_w$  is associated with a gradient of tangential velocity in the normal direction and a gradient of temperature *parallel* to the boundary, the latter contribution referred to as *thermal creep*. Similarly, for an isothermal gas mixture :

$$\mathbf{v} - \mathbf{v}_w = \zeta \frac{\partial \mathbf{v}_t}{\partial n} + \sigma D_{12} \left( \frac{\partial x_1}{\partial \mathbf{x}} - \mathbf{n} \frac{\partial x_1}{\partial n} \right). \quad (2)$$

Here,  $D_{12}$  is the binary diffusion coefficient and  $x_1$  is the species 1 mole fraction, while the coefficient  $\sigma$  is dimensionless. In analogy to eq. (1), the second contribution is called *concentration creep*.

Motivated by the growing importance of these phenomena, we have embarked on a series of computational studies to elucidate these fundamental creep-induced effects for a rarefied gas in simple, two-dimensional confined geometries. However, unlike previous related studies,<sup>5,6</sup> we resort to a *microscopic* description of the gas, mathematically expressed by the Boltzmann integro-differential equation. We employ the direct simulation Monte Carlo (DSMC) method of Bird,<sup>7</sup> the theoretical foundations and several practical applications of which can be found in reference 7. In the case of thermally induced flows, the no-time counter method of Bird<sup>7</sup> is used, as implemented for a hard-sphere gas. The scheme has been also extended to account for realistic molecular interaction models, an extension necessary if the diffusion physics underlying concentration creep are to be captured.

The results reported herein (see Ref. 4,8,10 for details) pertain to a two-dimensional cartesian cavity, with length  $L$  in the  $x$ -direction, height  $H$  in the  $y$ -direction and an aspect ratio  $\alpha \equiv L/H$ , here taken to be unity. The systems studied consist approximately of a total of  $10^5$  computational particles, corresponding to an average of several tens of particles in each cell since the average number of computational particles per cell  $N_c$  is a simulation parameter which can seriously affect the solution accuracy and associated cost. In addition, an increased value of  $N_c$  tends to alleviate possible disparities due to slightly different nonequilibrium collision rate expressions reported in the literature<sup>7</sup> and obviously represents the flow physics more closely. It is emphasized that axial gradients of temperature and concentration are imposed *via* appropriate microscopic boundary conditions but no creep velocity is specified along the side-walls as done in macroscopic formulations. Therefore, *creep velocities emerge as the problem solution without specifying them a priori*. Symmetry of the computational domain and the imposed boundary conditions allow for a reduction



of computational cost by a factor of two by simply imposing a symmetry boundary condition at the plane  $y = H/2$ . This is satisfied by requiring specular reflection for molecules ‘impinging’ upon this plane. Further details about the implementation can be found in Papadopoulos.<sup>8</sup>

Figure 1 depicts the velocity vector field together with the accompanying stream-tracer paths computed by our DSMC code for the specific choice of parameters  $\Delta T/T_o = 0.66$ ,  $T_o = 600\text{ K}$  and  $Kn_T = 5 \cdot 10^{-2}$ . The reference velocity  $u_{ref}$  chosen is computed by means of one-dimensional, linearized theory for a hard-sphere gas, based on the imposed tangential temperature gradient and other conditions. In figure 2 we show the computed flow field as induced by *concentration creep* for an Ar/He binary mixture. Spatial discretization is  $\Delta x = 0.3$  in mean-free-path units. Other relevant parameters take the values  $Kn = 2.3 \cdot 10^{-2}$ ,  $Kn_c = 4.8 \cdot 10^{-2}$ . Sufficiently far from the end-walls, concentration creep velocity scales increase with decreasing heavy species mole fraction  $x_1$ , in agreement with predictions of one-dimensional theory.

Straightforward order-of-magnitude estimates show that, for comparable gradients and fixed Prandtl number ( $Pr \simeq 2/3$ ), the ratio of thermal to concentration creep scales with the mixture Schmidt number  $Sc \equiv \nu/D_{12}$ . For typical operating conditions in CuPc/rare gas mixture systems, Rosner & Keyes<sup>2</sup> estimated  $Sc \simeq 3.7$ ; thus, concentration creep is expected to be less important in these systems. Since thermal creep and isothermal concentration creep flows have been investigated previously on an individual basis, it seems reasonable to follow up with an investigation on their combined effect as a further step towards actual complex systems. Other future plans include the development of a novel computational scheme that will enable calculating fine details of kinetic boundary layer structure. In addition, we are currently assessing the feasibility of various schemes to study these interesting effects in higher density systems. Our long-term goal is to contribute a fairly comprehensive study of creep phenomena in enclosures used in actual crystal growth experiments. We believe we have demonstrated the value of a microscopic approach in revealing the complex nature of microgravity flows within PVT ampoules. One of our main objectives is to guide the implementation of computationally efficient, yet physically realistic, *macroscopic* descriptions of such flows, to anticipate their consequences in crystal growth ampoule experiments. Indeed, microgravity offers a unique environment to study the fundamental and practical aspects of these phenomena without the obscuring effects of gravity.

## Acknowledgements

It is a pleasure to acknowledge valuable correspondence and discussions with I.B. Bernstein, M. Loewenberg, P. Garcia-Ybarra and D.W. Mackowski. This work has been supported by National Aeronautics and Space Administration under Grant No. NAG-3-1654.

## References

- <sup>1</sup> M.K. Debe, R.J. Poirier, E.L. Cook, L.R. Miller, M.S. Spiering and S.P. Floeder, "Gas-phase evolution and convective heat transfer in closed-cell vapor transport of organic thin films in microgravity and unit gravity," *J. Vac. Sci. Technol. A* **8**, 49 (1990).
- <sup>2</sup> D.E. Rosner and D.E. Keyes, "Theoretical studies in support of the 3M-vapor transport experiments", NASA Contractor Report 185122, Depts of Chemical and Mechanical Engineering, Yale University (1989).
- <sup>3</sup> D.E. Rosner, "Side-wall gas "creep" and "thermal stress convection" in microgravity experiments on film growth by vapor transport," *Phys. Fluids A* **1**, 1761 (1989).
- <sup>4</sup> D.H. Papadopoulos and D.E. Rosner, "Enclosure flows driven by non-isothermal walls," *Phys. Fluids* **7**, 2535 (1995).
- <sup>5</sup> A. Viviani and R. Savino, "Recent developments in vapour crystal growth fluid dynamics", *J. Crystal Growth* **133**, 217 (1993).
- <sup>6</sup> D.W. Mackowski, R.W. Knight, V.R. Rao and D.G. Walker, "Numerical investigation of thermal creep and thermal stress effects on microgravity physical vapor deposition," NASA-MSAD Microgravity Materials Science Workshop, May 1994, Huntsville, AL; D.W. Mackowski, V.R. Rao, D.G. Walker and R.W. Knight, "Numerical investigation of the effects of thermal creep in physical vapor transport," submitted to *J. Cryst. Growth* (1996).
- <sup>7</sup> G.A. Bird, *Molecular Gas Dynamics and the Direct Simulation of Gas Flows* (Oxford: Clarendon Press, 1994).
- <sup>8</sup> D.H. Papadopoulos, *Internal Flows Induced by Kinetic Boundary Layer Phenomena*, Ph.D. Dissertation, Yale University, November 1996.
- <sup>9</sup> D.E. Rosner and D.H. Papadopoulos, "Jump, slip and creep boundary conditions at non-equilibrium gas/solid interfaces," invited paper for *I/EC-Research E. Ruckenstein* birthday issue, to appear (September 1996).
- <sup>10</sup> D.H. Papadopoulos and D.E. Rosner, "Direct simulation of concentration creep in a binary gas-filled enclosure," submitted to *Phys. Fluids*, April 1996.
- <sup>11</sup> P. Garcia-Ybarra, J. Castillo and D.E. Rosner, "Morphological instability of a thermophoretically growing deposit," *J. Cryst. Growth* **116**, 105 (1991).

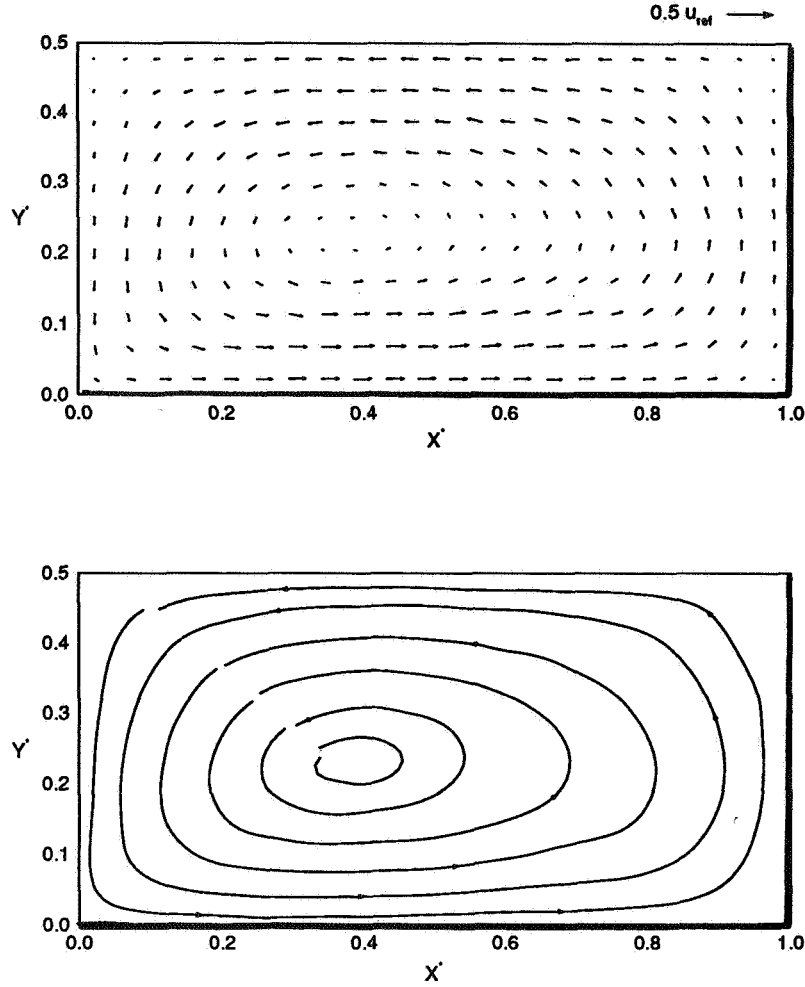


Figure 1: DSMC-calculated gas flow field due to *thermal creep* in a non-isothermal enclosure with  $Kn_T = 5 \cdot 10^{-2}$ ,  $T_0 = 600 \text{ K}$  and  $\Delta T/T_0 = 0.66$ . A linear variation of wall temperature is imposed along the  $y^* = 0$  plane whereas  $x^* = 0$ ,  $x^* = 1$  represent isothermal walls kept at temperatures  $T_1$ ,  $T_2$  respectively. The  $y^* = 1/2$  plane is a symmetry plane (see text for details). The thermal creep velocity predicted by one-dimensional, linearized theory for this specific set of parameters has been used as a reference velocity ( $u_{ref}$ ). Lower plot shows corresponding streamtraces.

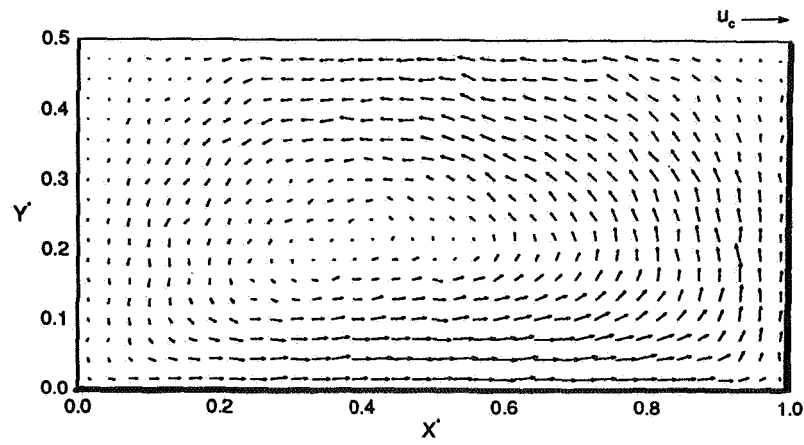


Figure 2: DSMC-calculated flow field induced by *concentration creep* for an Ar/He binary mixture. Relevant parameters take the values  $\Delta x = 0.3$ ,  $Kn = 2.3 \cdot 10^{-2}$ ,  $Kn_c = 4.8 \cdot 10^{-2}$ . Sufficiently far from the end-walls, concentration creep velocity scales increase with decreasing heavy species mole fraction  $x_1$ , as predicted by existing one-dimensional, linearized theories.

**The dissolution of an interface between miscible liquids**

James Maher, University of Pittsburgh

**Paper not available**



# EQUILIBRIUM FLUID INTERFACE BEHAVIOR UNDER LOW- AND ZERO-GRAVITY CONDITIONS. II

Paul Concus

Lawrence Berkeley Laboratory and Department of Mathematics  
University of California  
Berkeley, CA 94720

Robert Finn

Department of Mathematics  
Stanford University  
Stanford, CA 94305

## ABSTRACT

The mathematical basis for the forthcoming Angular Liquid Bridge investigation on board *Mir* is described. The anticipated liquid behavior used in the apparatus design is illustrated.

## INTRODUCTION

We describe here recent mathematical results that form the basis of our forthcoming space experiment, developed jointly with Mark Weislogel of NASA Lewis Research Center, which is scheduled for the Glovebox on the *Mir* 23/NASA 4 Mission in December, 1996. Our mathematical work is based on the classical Young-Laplace-Gauss formulation for an equilibrium free surface of liquid partly filling a container or otherwise in contact with solid support surfaces. In this formulation, when gravity is absent or can be neglected, which is the situation we consider here, the mechanical energy  $E$  of the system is given by

$$E = \sigma(S - S^* \cos \gamma). \quad (1)$$

The interfacial liquid-vapor surface tension parameter  $\sigma$  and the relative adhesion coefficient  $\cos \gamma$  of the liquid with the container walls are assumed to depend only on the material properties, which are taken here to be homogeneous (the same value of  $\cos \gamma$  on all parts of the container, as will be the case for the experiment).  $S$  and  $S^*$  are, respectively, the areas of the liquid-vapor free surface and of the solid-liquid interface.

Equilibrium configurations are those providing stationary values of the energy functional  $E$  subject to the condition of fixed liquid volume [1]. The equilibrium liquid-vapor free surfaces so determined are surfaces of constant mean curvature meeting the bounding walls with contact angle  $\gamma$ . We consider here values of the contact angle  $0 < \gamma < \pi$ . Of particular interest in our mathematical studies are situations in which small changes in contact angle or geometry can result in large changes, possibly discontinuous, of the equilibrium fluid configuration. Impetus for the present experiment arises largely from recent doctoral dissertations of two students associated with our study, John McCuan [2] and Lianmin Zhou [3], from whose contrasting results striking inferences can be drawn.

## ANGULAR LIQUID BRIDGE

In his work, McCuan found conditions under which an equilibrium tubular bridge in a wedge domain (Fig. 1) would be possible in zero gravity, and he gave the shape such a bridge might take. This work is a completely rigorous mathematical study, based on the classical formulation.

Consider a wedge domain with opening angle  $2\alpha$ ,  $0 < 2\alpha < \pi$ . The results McCuan proved contain the following (if the contact angles on the two sides of the wedge are different, the following results hold if  $\gamma$  on the left of the inequalities is their average):

*If  $\gamma > \pi/2 + \alpha$ , a bridge in the shape of a portion of a sphere making contact angle  $\gamma$  with the walls exists.*

*If  $\gamma \leq \pi/2 + \alpha$ , no physically realizable bridge is possible.*

It has not yet been proved whether or not other shape bridges may be possible when  $\gamma > \pi/2 + \alpha$ , or whether the spherical bridges are stable (provide a local minimum for the energy). However, our numerical results and those of H. Mittelman (private communication), obtained using the Surface Evolver software package [4], indicate that the spherical bridges are stable, at least for the representative cases we considered. Also, no bridge shapes other than the sphere have been found numerically. Note that McCuan's results imply that a bridge is possible only for  $\gamma > \pi/2$ . A spherical liquid bridge is shown in Fig. 4 for the case  $\alpha = 25^\circ$ ,  $\gamma = 130^\circ$ .

## BRIDGE BETWEEN PARALLEL PLATES – DISCONTINUOUS BEHAVIOR

The above results for liquid bridges in a wedge compare in a remarkable way with those for bridges between parallel plates (Fig. 2). This latter problem was studied initially from a rigorous mathematical point of view by Athanassenas [5] and by Vogel [6], and later using a more physical approach by Langbein [7]. (Note that in these papers, as is the case in [3] and here, the boundary conditions at the plates are prescribed contact angle, which arises from the variational condition for (1). For fixed end conditions, as considered in much of the materials science literature, the behavior of solutions is different.) In her doctoral dissertation, Zhou obtained definitive mathematical results that imply the following:

*For any value of the contact angle  $\gamma$  and for any liquid volume  $V$  greater than or equal to a critical value  $V_0(\gamma)$ , a unique stable liquid bridge exists between two parallel plates of given separation.*

It is known that any equilibrium bridge must be rotationally symmetric [6], [8] and that its free surface is a Delaunay surface [3], [9], [10]. For  $\gamma > \pi/2$  and for a specific liquid volume  $V_s(h)$  depending on the plate spacing  $h$ , the free surface is simply a portion of the surface of a sphere. For other values of the volume the Delaunay surface is different from a sphere.

These results, when combined with the results for the wedge, imply that a bridge between parallel plates may change its configuration and position markedly when one of the plates is tilted, even by a small amount, or it even may cease to exist as a bridge altogether; *a liquid bridge between parallel plates can behave discontinuously with respect to tilting of the plates*. In stability studies such as [3], [6], and [7], limited to the parallel plate geometry, this liquid bridge instability with respect to plate tilt is not observed.

As a specific example to illustrate the possibilities, consider the case  $\gamma > \pi/2$  and a bridge with volume  $V_s$  between parallel plates of spacing  $h$ , so that the bridge is spherical. Suppose the top plate is tilted clockwise by an angle  $2\alpha < 2\gamma - \pi$  about a pivot line in the plate that is a distance  $\frac{1}{2}h \tan \alpha$  from the symmetry axis of the bridge. Then this particular bridge remains an equilibrium one for the new tilted plate configuration, without any change in the radius of the sphere or in the



bridge's position on the lower plate. However, a bridge with any volume  $V$  different from  $V_s$  (and with the same contact angle) would change both position and shape discontinuously in altering to a spherical bridge in conjunction with the tilt, shifting to the right for  $V < V_s$  or to the left for  $V > V_s$ .

For  $\gamma \leq \pi/2$  an initial bridge would always behave discontinuously with respect to the tilt, regardless of volume, as it cannot persist as a bridge. It has to be expected that the liquid will jump to the edge of the plates in this case. If the tilted plates touch forming a wedge, then configurations described in the following section may form. The above phenomena are ones we wish to study in our forthcoming experiment.

## OTHER CONFIGURATIONS

When the conditions for a bridge in a wedge are not satisfied, liquid may assume a position as a blob in the shape of a portion of a sphere in contact with the edge, see Fig. 3. The condition for such a configuration to be possible is that  $|\gamma - \pi/2| \leq \alpha$ . (Recall we consider here only the case  $0 < 2\alpha < \pi$ .) Although the edge blobs have not been studied with the same mathematical completeness as have the bridges, they have been noted in [11] and [12] and for some examples studied numerically. Our numerical computations indicate that, as for the angular bridges, the spherical edge blobs are stable, and as yet we have found no other edge blob shapes numerically.

In our earlier work, which considers fluid behavior in the neighborhood of the vertex of a wedge, we have shown that if  $\alpha + \gamma < \pi/2$ , then fluid cannot remain as a blob in the edge but must spread arbitrarily far along the edge [1], [10]. See also [12] and the references there for a discussion of stability of liquid columns in a wedge.

## ANTICIPATED EXPERIMENT BEHAVIOR

The liquid behavior one might expect in a physical experiment in space, based on the Laplace-Young-Gauss formulation, is summarized in Fig 4. This figure illustrates the information discussed above, based in part on mathematically rigorous results and, where these are not available, on computational evidence for particular cases. The numerical solutions depicted in Fig. 4 were obtained using the Surface Evolver software package. The computations were carried out with initial approximations and transitions between configurations similar to those in which the experiment is designed to proceed, thereby enhancing appropriateness of the numerically based predictions on uniqueness and stability.

The upper two rows of Fig. 4 depict the nonwetting case  $\gamma > \pi/2$ : A liquid bridge between parallel plates is convex (part of a sphere for a specific fluid volume). Spherical tubular bridges and edge blobs exist for tilted plates, for the range of values indicated. Edge spread is not possible. For fixed  $\gamma > \pi/2$ , transition from tubular bridges to edge blobs occurs as  $\alpha$  increases through the value  $\gamma - \pi/2$ .

For the wetting case  $\gamma < \pi/2$ , a liquid bridge between parallel plates is concave. A tubular bridge between tilted plates is not possible, but the (spherical) edge blob and edge spread are. For fixed  $\gamma < \pi/2$ , the transition from edge blob to unbounded edge spread occurs as  $\alpha$  decreases through the value  $\pi/2 - \gamma$ . Computed edge blobs are shown (from different viewing perspectives) for the case  $\alpha = 25^\circ$ ,  $\gamma = 100^\circ$  in the second row and for  $\alpha = 20^\circ$ ,  $\gamma = 75^\circ$  in the bottom row.

The planned experiment will explore the transition between the configurations for a nonwetting and for a wetting fluid. As discussed above, when initially parallel plates are tilted, the fluid is predicted to behave discontinuously in general, the exception being the special case of a spherical

bridge and a particular pivot line. The other transitions, horizontally across the second and fourth rows of Fig. 4 as  $\alpha$  changes value, are gradual, as can be demonstrated by the explicit spherical solutions.

## CONCLUDING REMARKS

We have described fluid behavior predicted mathematically and computationally for the forthcoming Angular Liquid Bridge investigation on board the *Mir 23*/NASA 4 Mission. The predictions, which include discontinuous behavior, are based on the classical Young-Laplace-Gauss formulation. In the experiment there will be an opportunity to check the predictions against physical behavior and to observe the effects of hysteresis and other phenomena not included in the classical formulation.

## ACKNOWLEDGMENTS

We wish to thank Victor Brady for carrying out the numerical computations and for preparing the graphical output shown in Fig. 4. We wish also to thank John McCuan for helpful conversations and to thank Hans Mittelmann for providing us with some of the results of his numerical experiments. This work was supported in part by the National Aeronautics and Space Administration under Grant NCC3-329, by the National Science Foundation under Grants DMS-9400778 and DMS-9401167, and by the Applied Mathematical Sciences Subprogram of the Office of Energy Research, Department of Energy, under Contract Number DE-AC03-76SF00098.

## REFERENCES

1. Finn, R.: Equilibrium Capillary Surfaces, Springer-Verlag, New York, 1986. Russian translation (with Appendix by H.C. Wente), Mir Publishers, 1988.
2. McCuan, J.: Symmetry via Spherical Reflection and Spanning Drops in a Wedge, doctoral dissertation, Dept. of Mathematics, Stanford Univ., Stanford, CA, 1995.
3. Zhou, L.: The Stability Criterion for Liquid Bridges, doctoral dissertation, Dept. of Mathematics, Stanford Univ., Stanford, CA, 1995.
4. Brakke, K.: Surface Evolver, software package and manual available via the Internet from <http://www.geom.umn.edu/software/download/evolver.html>.
5. Athanassenas, M.: A variational problem for constant mean curvature surfaces with free boundary, *J. reine angew. Math.*, 377 (1987), 97–107.
6. Vogel, T. I.: Stability of a liquid drop trapped between two parallel planes, *SIAM J. Appl. Math.*, 49 (1987), 516–525.
7. Langbein, D.: Stability of liquid bridges between parallel plates, *Microgravity Sci. Technol.*, 5 (1992), 2–11.
8. Wente, H. C.: The symmetry of sessile and pendant drops, *Pacific J. Math.*, 88 (1980), 387–397.
9. Delaunay, C. E.: Sur la surface de révolution dont la courbure moyenne est constante, *J. Math. Pures Appl.*, 6 (1841), 309–315.
10. Concus, P. and Finn, R.: On capillary free surfaces in the absence of gravity, *Acta Math.*, 132 (1974), 177–198.

11. Mittelman, H. D. and Hornung U.: Symmetric capillary surfaces in a cube, Report LBL-31850, Lawrence Berkeley Lab., Univ. of Calif., Berkeley, CA, 1992.
12. Langbein, D.: Liquid surfaces in polyhedral containers, Microgravity Sci. Technol., 8 (1995), 148–154.

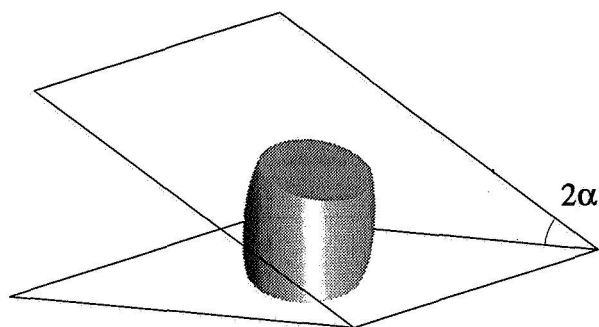


Figure 1. Tubular bridge in a wedge.

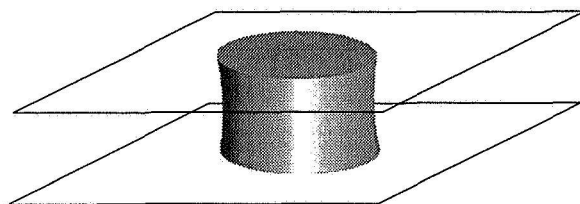


Figure 2. Bridge between parallel plates.

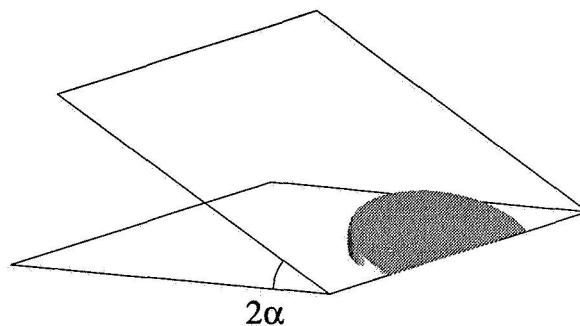
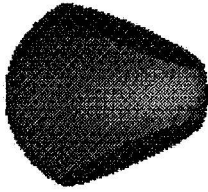


Figure 3. Edge blob.

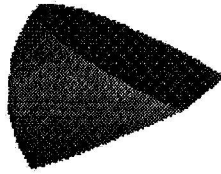
# NONWETTING LIQUIDS ( $\gamma > \pi / 2$ )



Bridge between parallel plates



Spherical bridge  
 $\gamma - \alpha > \pi / 2$



Edge blob  
 $\gamma - \alpha \leq \pi / 2$

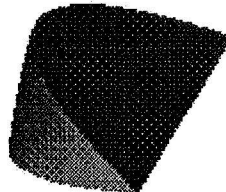
Edge spread  
not possible

# WETTING LIQUIDS ( $\gamma < \pi / 2$ )

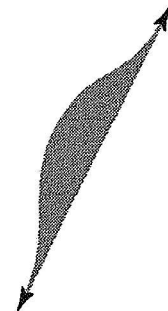


Bridge between parallel plates

Wedge bridge  
not possible



Edge blob  
 $\gamma + \alpha > \pi / 2$



Edge spread  
 $\gamma + \alpha \leq \pi / 2$

Figure 4. Fluid configurations. Upper two rows: nonwetting liquids; lower two rows: wetting liquids.

# CRITICAL VELOCITIES IN OPEN CAPILLARY FLOW

Michael Dreyer, Dieter Langbein, Hans J. Rath  
Center of Applied Space Technology and Microgravity  
University of Bremen, D-28359 Bremen, Germany

## INTRODUCTION

This paper describes the proposed research program on open capillary flow and the preliminary work performed theoretically and in drop tower experiments. The work focuses on the fundamental physical understanding of the flow through capillary bound geometries, where the circumference of the cross section of the flow path contains free surfaces. Examples for such a flow configuration are capillary vanes in surface tension tanks, flow along edges and corners and flow through liquid bridges. The geometries may be classified by their cross section areas, wetted circumferences and the radii of curvature of the free surfaces. Some possible geometries are depicted in Fig. 1. In the streaming float zone the flow path is bound by a free surface only. The ribbon vane is a model for vane types used in surface tension tanks, where a structure in proximity to the tank wall forms a capillary gap. A groove is used in heatpipes for the transportation of the condensed working fluid to the heat source and a wedge may occur in a spaceborne experiment where fluid has to be transported by the means of surface tension.

The research objectives are the determination of the maximum volume flux, the observation of the free surfaces and the liquid flow inside the flow path as well as the evaluation of the limiting capillary wave speed. The restriction of the maximum volume flux is due to convective forces (flow velocity exceeding the capillary wave speed) and/or viscous forces, i.e. the viscous head loss along the flow path must be compensated by the capillary pressure due to the curved free surface. Exceeding the maximum volume flux leads to the choking of the flow path, thus the free surface collapses and gas ingestion occurs at the outlet.

The means are ground-based experimental work with plateau tanks and in a drop tower, a sounding rocket flight and theoretical analysis with integral balances as well as full three dimensional CFD solutions for flow with free surfaces. Due to the hydrostatic pressure on earth the open capillary flow path dimension (perpendicular to the flow direction) cannot exceed the capillary constant  $l_c = \sqrt{\rho g / \sigma}$  and experiments with larger dimensions require a low gravity environment. The efforts will culminate in a definitive flight experiment with well chosen geometries for fundamental and reliable results.

## FLOW BETWEEN PARALLEL PLATES

### Motivation from surface tension tank technology

The capillary rise in open cross sections is used in surface tension tanks to transport and position the propellant under the condition of microgravity. Usual designs of surface tension tanks have a refillable reservoir from which the propellant is supplied to the engines. The purpose of the capillary vanes is to fill the reservoir. The filling of vanes in a compensated gravity environment

has been investigated by DREYER et al. [1]. For a new generation of surface tension tanks a design without a refillable reservoir is developed. The propellant is withdrawn directly from the capillary vanes and not from the reservoir. This yields higher volume fluxes through the vanes. Data on the flow through open capillary vanes are rare and not verified by experiments. The limits of the flow rate due to choking and the stability limits of the free surface are not known for different types of flow geometries with open cross section.

In a paper by JAEKLE [2] the design and the analysis of vanes in surface tension tanks are considered. The performance verification of capillary vanes relies completely on analysis. Testing on ground is not possible due to the hydrostatic pressure which prevents the establishment of the liquid volume in the gap by surface tension only. In the analysis section JAEKLE mentioned the similarities of the flow through vanes with flow in flexible tubes, open channels and compressible duct flow. Each of these flows is governed by similar equations and has a limiting or choking velocity.

For the use of capillary vanes in surface tension tank designs the critical velocity must be known. Exceeding this critical velocity leads to the ingestion of gas and thus to a malfunction of the thruster. Experimental verifications of the work of JAEKLE are not available. To achieve a better knowledge of the critical flow velocities in capillary vanes, experiments under reduced gravity conditions are performed funded by the European Space Agency (ESA) and the German Space Agency (DARA).

## Theoretical approach

Figure 2 shows a schematic drawing of the flow between two parallel plates with free surfaces at the sides. If a constant volume flux  $Q$  is applied, the radius of curvature  $R$  of the free surface changes in flow direction. The cross section area  $A$  is a function of  $R$  and changes in flow direction  $s$ .

The assumptions are the following: the problem is stationary, the flow is incompressible and isotherm, the properties density  $\rho$ , viscosity  $\mu$  and surface tension  $\sigma$  are constant at the given temperature  $T$ . The free surface at the sides of the capillary vane has one radius of curvature  $R$  in the plane perpendicular to the flow path. The second radius of curvature is neglected. The flow is one-dimensional in the direction of the vane axis, we apply a momentum balance in one direction. We consider an average value of the flow velocity in the direction of the vane axis  $s$  over the cross section area  $A$ . The cross section area  $A$ , the average velocity  $v$  and the pressure  $p$  change only gradually along the flow path.

Differentiating the mass balance we have

$$dv = -\frac{Q}{A^2} dA, \quad (1)$$

with the average flow velocity  $v$  in  $s$ -direction. We apply a Bernoulli equation in the direction of the vane axis with an additional friction term:

$$-\tau_w W ds - Adp - \rho g Adz = \rho A v dv. \quad (2)$$

The terms of the LHS of Eq. (2) are the friction force, the pressure force and the weight due to the gravitational acceleration ( $g$  is the gravity acceleration), respectively. The RHS of Eq. (2) is due to the convective acceleration occurring with the change of the cross section  $A$ . The friction term arises from the wall shear stress  $\tau_w$  multiplied by the wetted perimeter  $W$  and the differential path length  $ds$ . The effect of an additional friction drop due to the change of the velocity profile within the entrance length is neglected in the following calculations. The pressure force arises

from the surface tension times the radius of curvature of the free surface. The area  $A(R)$  and the derivative of the area with respect to the radius of curvature  $dA/dR$  can be calculated from the system geometry. Finally the differential equation for the change of the radius of curvature with respect to the path length  $dR/ds$  reads

$$\frac{dR}{ds} = \frac{\frac{k_f \nu}{32} \frac{W^2}{Q} + \frac{A^3 g}{Q^2} \frac{dz}{ds}}{\frac{dA}{dR} - \frac{\sigma}{\rho} \frac{A^3}{Q^2 R^2}}, \quad (3)$$

with a friction factor  $k_f$ . The change of the radius of curvature with the flow length setting  $g = 0$  is shown in Fig. 4 for the parameter:  $Q = 10.5$  ml/s, plate distance  $a = 5$  mm, plate breadth  $b = 30$  mm, Silicon Fluid 1.0 cSt. The minimal radius of curvature for the parallel plates equals  $a/2$ . For given parameters such as flow rate, geometry, etc. the maximum possible path length can be calculated from Eq. (3). Setting the denominator to zero one gets a velocity for the capillary wave speed.

Using proper scales such as lengths  $a$  and  $b$ , velocity  $\sqrt{2\sigma/\rho a}$  and gravity acceleration on earth  $g_0$  one gets the dimensionless equation

$$\frac{d\bar{R}}{d\bar{s}} = \frac{\frac{k_f}{32} \text{Oh} \frac{\bar{W}^2}{\bar{Q}} + \text{Bo} \frac{\bar{A}^3 \bar{g}}{2\bar{Q}^2} \frac{d\bar{z}}{d\bar{s}}}{\frac{d\bar{A}}{d\bar{R}} - \frac{\bar{A}^3}{\bar{Q}^2 \bar{R}^2}}, \quad (4)$$

with the OHNESORGE number  $\text{Oh} = \frac{\mu}{\sqrt{2\rho a \sigma}}$  and the BOND number  $\text{Bo} = \frac{\rho a^2 g_0}{\sigma}$ . The non-dimensional area  $\bar{A}$  contains the ratio  $\Lambda = a/b$ . The parameter range of the experiments is  $\Lambda = 0.1 \dots 0.3$ ,  $\text{Oh} = 0.0015 \dots 0.005$  and  $\text{Bo} = 0$  with respect to the application in surface tension tanks and the drop tower limitations.

## Results of drop tower experiments

The aim of the experiments is to verify the Eq. (3) for a parameter range which is comparable to the application of this equation in surface tension satellite tanks. Experiments have been performed in the drop tower Bremen. A test vane (flow length 100 mm) is positioned in the experiment container perpendicular to the free liquid surface under normal gravity conditions. During the free fall of the experiment the vanes fills itself due to the capillary force up to the top. At the top of the vane a constant volume flux is withdrawn. The maximum volume flux at a given length of the vane and the shape of the free surface at the sides will be evaluated and compared to the solutions of Eq. (3). Figures 5 and 6 show two videoprints of the drop tower experiment with the same parameter as Fig. 4. Figure 5 shows the parallel plates with the optical axis perpendicular to the plate plane. The flow is from the bottom to the top. A subcritical volume flux is applied to the withdrawal device at the top. The radius of curvature decreases in flow direction. No gas ingestion at the outlet occurs as expected for the supercritical case. The curves of the innermost point in Fig. 3 can be compared with the contour of the free surface in Fig. 5. Theory is limited up to the minimal contour, for the upper part of the vane (see Fig. 6) the second radius of curvature (which was neglected) plays an important role. Figure 6 shows the free surface at the sides in vicinity of the outlet. The contour of the free surface is clearly visible. The radii of curvature (in the direction of the vane and perpendicular to it) are evaluated with digital image processing. The corresponding experiments for supercritical conditions are in preparation.

## Conclusions

Eq. (3) gives a good estimate to adjust the volume flux to sub- and supercritical values. Within a drop tower experiment one certain volume flux can be adjusted. The resultant flow is either sub- or supercritical. Thus, only an upper and a lower bound for the maximum volume flux can be evaluated. A continuous increase and decrease of the volume flux would be desirable.

Stationary conditions cannot be achieved. Due to the start of the withdrawal after the filling of the capillary, the adjustment of free surface at the side to its final position needs more time than available during the free fall (4.74 s). But the drop tower is a unique tool to optimize the experimental setup and to get preliminary results for long-term microgravity facilities. As a next step a sounding rocket mission funded by ESA is scheduled for 1997. The calculation of the flow field and the resulting pressure with a finite element CFD code (FIDAP) is underway. The additional pressure drop due to the development of the flow field behind the entrance of the vane is taken into account. Furthermore, a complete analysis of the flow between parallel plates with free deformable surfaces at the sides is in preparation.

## STREAMING FLOAT ZONE

Since the advent of research under microgravity conditions, strong interest has been in investigations on liquid columns. Microgravity renders possible the establishment of large liquid columns. They are most convenient for studying static and dynamic effects of liquid surfaces under microgravity conditions. Axisymmetry considerably simplifies treatment by theory (LANGBEIN [3], [4]).

The scientific questions, which have to be solved by means of large liquid columns under microgravity conditions, are (i) the stability of liquid columns in rest and under the influence of rotation, (ii) the behavior of liquid columns under the influence of constant volume flows, (iii) the dynamics of breakage with particular regard to the volume distribution to the various fragments, inclusive of satellite drops, (iv) the resonance frequencies of liquid columns with respect to axisymmetric and non-axisymmetric surface deformations, (v) the onset of non-axisymmetric flows, (vi) the sensitivity of liquid volumes to random, periodic or pulse-type accelerations, (vii) stationary Marangoni convection in liquid columns, which either are heated to different temperatures at the bottom and the top or else are heated along the periphery by means of a ring heater, (viii) the onset of oscillatory Marangoni convection, i.e. the critical Marangoni number, when heating is intensified, and its hysteresis, when heating is reduced and the onset of turbulence

Within the scope of the present proposal we are interested in particular in the behavior of liquid columns under the influence of constant volume flows. If the column is established between two coaxial circular tubes, one finds a quadratic velocity profile (Hagen-Poiseuille flow) inside the tubes, whereas in the region of the floating zone one has the free-slip condition along the surface. There the flow is going to speed up. Distant from the orifices one can assume a uniform flow velocity. The length of the float zone on the other hand is limited by the Rayleigh instability. This relates the investigations to floating zone stability.

An increase in flow velocity acts like a decrease in pressure, such that the diameter of the column will shrink at the inlet and will widen at the outlet. Therefore, under 1g conditions one may expect a stabilizing effect of an upward flow and a destabilizing effect of a downward flow. Further objectives of interest are the beginning of oscillatory flows (critical numbers), and their relations to resonant modes. Do stationary non-axisymmetric flows arise or do they revolve around the axis?



# FLOW THROUGH LIQUID FILLED WEDGES

The dynamics of penetration of liquids into solid wedges under microgravity conditions has been and will be treated experimentally and theoretically. The case of good wetting between the liquid and the wedge, which entails fast wetting, is being investigated in drop tower experiments. The limit of slow penetration (bad wetting) has been studied in the IML-2 experiment DYLCO. The theory of liquid penetration into a wedge has been developed. It is based on the principle that the local flow in wedge direction is determined by the local gradient of capillary pressure. The limit of long times, when the curvature in wedge direction becomes negligible in comparison to the curvature perpendicular to it, allows for a similarity solution in position over the square root of time, such that the tip of the liquid meniscus proceeds proportional to  $\sqrt{t}$  also. The numerical solution of the full fourth order differential equation confirms this asymptotic result and the experimental findings as well.

The theory of liquid penetration is based on the assumption that in the planes perpendicular to the wedge the liquid surface is given by a circular section with radius  $R(z)$ ,  $z$  being the coordinate in the wedge direction. This principle recently has been successfully applied to the calculation of static liquid surfaces in polyhedral containers (LANGBEIN [5]). It has been shown that the liquid surface evolves exponentially from the cylindrical shape along the wedges to the spherical shape of the meniscus near the corners. The differential equation of liquid penetration into the wedge is obtained by requiring that the change in liquid volume on the side to be filled must equal the flow through the cross-section at  $z$ . This volume flow is generally proportional to the squared area of the cross section times the pressure gradient. The yielding equation is a fourth order partial differential equation for  $R(z, t)$ , which in general has to be solved numerically. On the other hand, it is similar in character to a diffusion equation with the modification that different powers of  $R(z, t)$  appear on its two sides.

The work on the liquid penetration into a wedge is necessary for the investigation of the flow through such a configuration. The theory will be expanded on that case and appropriate experiments will be carried out.

## ACKNOWLEDGMENTS

The funding of the drop tower flights by the German Space Agency (DARA) and the European Space Agency (ESA) is gratefully acknowledged. The work on the dynamics of liquid in edges and corners has been supported by the DARA under contract number 50 WM 9432.

## References

- [1] Dreyer, M., Delgado, A., Rath, H.-J., J. Colloid Interf. Sci. 163, 158-168 (1994).
- [2] Jaekle, D.E., AIAA-91-2172. 27th Joint Propulsion Conference, June 1991, Sacramento, CA.
- [3] Langbein, D., J. Fluid Mech. 213 (1990) 251-265
- [4] Langbein, D., Adv. Space Res. 13 (1993) (7)123-(7)132
- [5] Langbein, D., Microgravity sci. technol. VIII (1995) 148-154

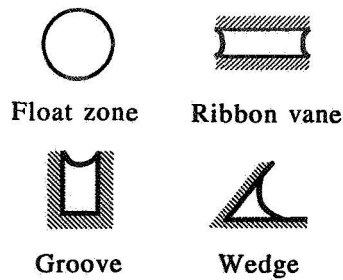


Figure 1: Different types of open capillary flow geometries. The flows is perpendicular to the paper plane.

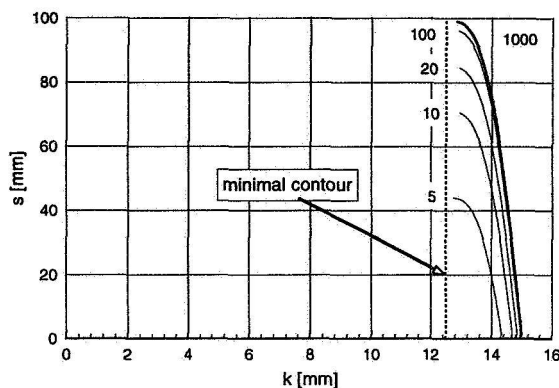


Figure 3: Plot of the innermost point of the free surface versus path length for the comparison with Fig. 5 ( $a = 5$  mm,  $b = 30$  mm).

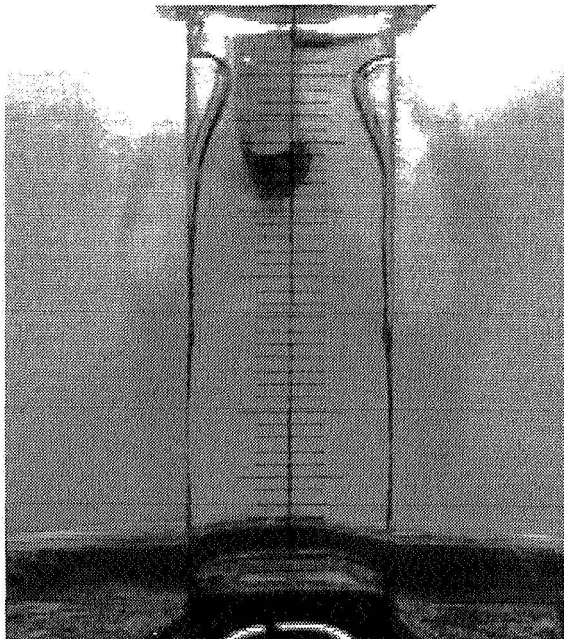


Figure 5: Videoprint of a subcritical flow between two parallel plates. The optical axis is perpendicular to the plates, the flow is from the bottom to the top (same parameter as Fig. 4).

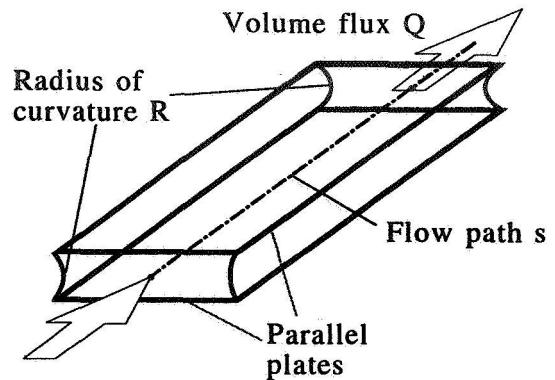


Figure 2: Schematic drawing of the flow between two parallel plates with a free surface at the sides. A constant volume flux is applied, the radius of curvature changes in flow direction.

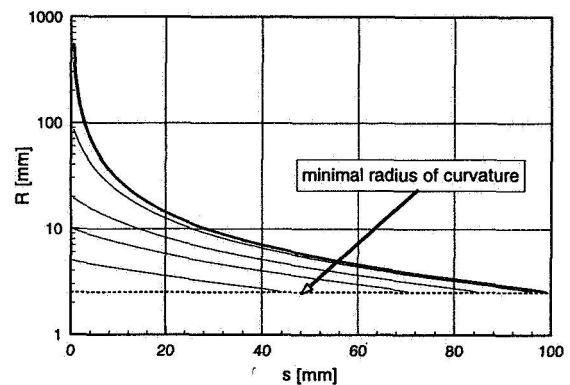


Figure 4: Plot of the radius of curvature versus the path length for different initial radii with  $Q = 10.5$  ml/s. The dashed line marks the minimal radius of curvature. The liquid is Silicon Fluid 1.0 cSt, plate distance 5 mm, plate breadth 30 mm.

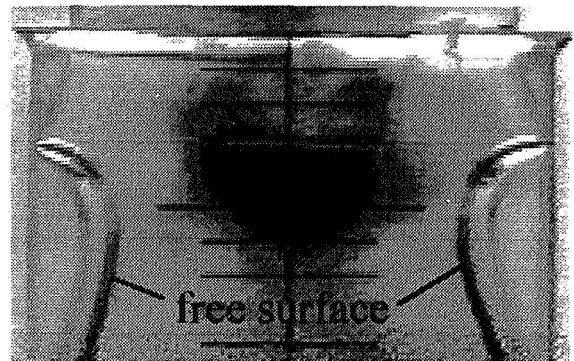


Figure 6: Detail from the top of the vane below the inlet. The meniscus is stable, no gas ingestion occurs. The free surface is clear visible.

# Thermoacoustic Effects at a Solid-Fluid Boundary: the Role of a Second-Order Thermal Expansion Coefficient

Ashok Gopinath  
Department of Mechanical Engineering  
Naval Postgraduate School, Code ME/Gk  
Monterey, CA 93943-5146, USA  
(E-mail: gopinath@nps.navy.mil)

## Abstract

Analytical and numerical studies are to be carried out to examine time-averaged thermal effects which are induced by the interaction of strong acoustic fields with a rigid boundary (thermoacoustic streaming). Also of interest is the significance of a second-order thermal expansion coefficient that emerges from this analysis. The model problem to be considered is that of a sphere that is acoustically levitated such that it is effectively isolated in a high-intensity standing acoustic field. The solution technique involves matched asymptotic analysis along with numerical solution of the boundary layer equations. The objective of this study is to predict the thermoacoustic streaming behavior and fully understand the role of the associated second-order thermodynamic modulus.

## 1 Introduction

Much interest has arisen in the past decade or so, in the study of fluid transport phenomena in the presence of an acoustic field (for instance, see review by Trinh [17]). In particular there has been a desire to understand the fluid mechanics and heat transfer processes in a microgravity environment where the acoustic field is the dominant force field in the system. The work has been motivated by the need to understand the behavior and influence of these transport phenomena for a series of microgravity experiments that have been conducted and planned. These experiments have been devised to serve a variety of purposes ranging from basic science studies, to investigations of containerless materials processing in a microgravity environment. These experiments involve the use of acoustic levitation (as one of the many different levitation techniques) to carefully isolate and study the phenomena in question in an effectively containerless manner. Of equal interest and importance has been the study of these fluid dynamical phenomena from the viewpoint of measurement of properties of the materials used in these levitation experiments. It is a combination of the above features, i. e. the study of novel transport phenomena coupled with the possible measurement of a second order thermodynamic modulus, which will form the focus of this study.

## 2 Background

This study centers around acoustic streaming and thermoacoustic transport effects induced by a strong acoustic field, and the significance of a material property (a thermodynamic modulus) of

the host fluid supporting the acoustic field. Such effects are typically encountered in primarily two fields of application requiring the interaction of high-intensity acoustics with rigid boundaries, namely, acoustic levitation, and thermoacoustics.

There exists a large body of literature on the applications of acoustic levitation and no attempt will be made to provide a review at this stage. However it is noted that the intense acoustic fields used for levitation give rise to steady streaming flows in the host fluid due to nonlinear effects related to the presence of rigid boundaries such as those of the sample and the container walls. Such flows have also been studied with an interest in predicting the heat transfer rates they induce. Based on the original work of Riley [10], Davidson [2], and Lee & Wang [8], Gopinath & Mills [6, 7] have made some predictions on the resulting heat transfer behavior in the context of containerless materials processing in a microgravity environment.

In contrast, the associated thermoacoustic transport effects have received little or no attention in this context. In particular there is a need to understand the second-order time-averaged thermal effects that may be induced by the interaction of the strong sound fields with rigid boundaries, *even in the absence of any externally imposed driving temperature potential*. This time-averaged thermal phenomenon has been aptly named *thermoacoustic streaming* in a review by Rott [12], using a direct analogy with *acoustic streaming*. Notable early work in this field includes that of Rott [11] and Merkli & Thomann [9], although all for internal duct geometries. Swift [15] also provides a fine review in a tutorial article, although again in a different context, i. e. for so-called thermoacoustic engines. However the role of this phenomenon in the context of acoustic levitation, and its impact on heat transport is still unclear.

### 3 Research Plan

The research plan involves the analytical/numerical examination of a model problem in which high-intensity acoustic fields are used for levitation in a microgravity environment so as to isolate and study thermoacoustic streaming effects, and thereby also, investigate the surprising role of an associated second-order thermodynamic modulus which emerges in these effects. Equally important in this study would be the role of the acoustic streaming motion itself, in its capacity to convect the heat generated by these second-order thermoacoustic effects. Based on the findings from this theory, suggestions will be made for possible future experiments for a more detailed study of these phenomena and for measurement of this thermodynamic modulus. It is emphasized for clarity that the above material property which arises is that of the host liquid, and not of the levitated sample (which merely serves as a suitable rigid boundary to induce these effects). A very preliminary analysis of but a portion of this problem has been attempted by Gopinath [5], which however is incomplete and needs to be treated in far greater detail.

#### 3.1 Analytical Formulation

The model problem to be studied will comprise of a sphere levitated so as to be effectively isolated in a high intensity plane standing acoustic field. The sphere will be initially treated as rigid with a large thermal inertia so as to decouple the fluid mechanics aspects from the thermal energy aspects. Starting with the governing Navier-Stokes equations formulated in axisymmetric spherical coordinates, a scale analysis will first be conducted to identify the dimensionless parameters of importance since this problem exhibits numerous parameter scales.

Thus far, most studies of this problem have relied on the incompressible flow assumption to render tractable the governing equations based on the solenoidality of the vector velocity field. Here too, this simplifying assumption will be made (at first) to allow complete attention on the

thermoacoustic effects which are the key effects being studied. In other words, on the basis of the different length scales of the problem, this assumption requires that the radian wavelength be much larger than the sphere radius, which is in turn taken to be much larger than the oscillatory amplitude of the fluid particle in the acoustic field. The latter condition further allows the flow to be considered attached to circumvent the complex situations arising from separated flow behavior. With these simplifying conditions there is now the added advantage of being able to incorporate the influence of the axial location of the rigid sphere in the standing sound field. All studies on acoustic streaming in such a situation have understandably focused on the sphere located at the velocity antinode in the standing field where these streaming effects are maximized (and not at the velocity node where they are essentially nonexistent). However the thermoacoustic streaming effects to be considered in this study are perfectly capable of being significant at both locations and the variation over this range is one of the aspects that will be investigated.

Once the basic behavior is established, later studies will include cases of larger sample diameters and/or ultrasonic levitating frequencies for which the sample size is comparable to the radian wavelength. The flow may no longer be considered incompressible and the strategy under these conditions is also briefly noted below.

### 3.2 Solution Methodology

For the effectively incompressible flow conditions, the vector velocity field can be conveniently expressed as the curl of a vectorized stream function,  $\vec{\psi}$ . In this manner the vector equations of fluid motion can be converted into a higher order scalar equation for the stream function in standard fashion. The energy equation, in its most general form, is also suitably non-dimensionalized using the appropriate scales determined earlier. For the more general compressible flow situation, the vector velocity field is expressed in addition as the gradient of a scalar potential,  $\phi$ , as

$$\vec{u} = \nabla \phi + \nabla \times \vec{\psi}$$

and this is incorporated into developing the governing equations in terms of  $\phi$  and  $\vec{\psi}$ .

It is identified that for the high frequencies being treated, a matched asymptotic expansion technique can be successfully used. The fluid domain being studied can be decomposed into a thin inner Stokes layer region adjacent to the wall of the sphere, with the remainder of the domain making up the outer region. For the inner region, the primary oscillatory flow behavior can be readily determined from a leading order solution of the governing equations. This can then be used with the vector equation of motion in its primitive form, to determine the leading order pressure field in the inner region. This procedure can be extended to the next higher order correction which would then yield a description of the acoustic streaming motion originating in the inner region, due to the nonlinear interactions of the first harmonic contributions from *both*  $\phi$  and  $\vec{\psi}$ .

The solution of the energy equation would also add new and interesting results in the study of such streaming phenomena. Just as the time-averaged fluid motion formed the focus in studies on acoustic streaming, it is the time-averaged thermal effects which will form the focus in this study of thermoacoustic streaming. It may be recalled that in the small sphere limit, the density fluctuations in the fluid are negligible in the continuity equation and hence allow the incompressible flow assumption. However preliminary analysis confirms that these density fluctuations are not negligible in the energy equation and are fully capable of making a significant contribution to the time-averaged thermal energy exchange mechanisms in the fluid. Such a deduction which could be easily overlooked is only possible because of the non-dimensionalized form of the governing equations which clearly shows the scales and magnitudes of the different contributions. It is emphasized that the sphere is not subject to any externally imposed heating/cooling mechanism. All the

time-averaged heat transfer effects to be studied are purely a manifestation of the thermoacoustic streaming effect arising from the interaction of the strong acoustic fields with the sphere boundary.

A detailed analysis of the energy equation to determine all the time-averaged contributions to the thermoacoustic streaming effect requires that the density fluctuations in the fluid be first determined. This is possible from a suitable equation of state of the fluid which additionally requires a knowledge of the pressure field in the fluid. The (isobaric) thermal expansion coefficient of the host fluid,  $\beta$ , (defined in the usual manner such that  $\beta T \equiv 1$  for an ideal gas) is

$$\beta = -\frac{1}{\rho} \left( \frac{\partial \rho}{\partial T} \right)_p,$$

and is found to have an important role in the time-averaged heat exchange to be investigated. In addition, analysis of these contributions shows that a heretofore ignored second-order thermal expansion coefficient also plays a key role in this time-averaged thermal energy exchange. This property arises in time-averaged contributions from pressure fluctuations and is in fact a thermodynamic modulus defined as

$$\xi = \frac{T}{\rho \beta} \left( \frac{\partial^2 \rho}{\partial T^2} \right)_p - 1$$

so that for an ideal gas,  $\xi \equiv 1$ . The significance of a related thermodynamic property was alluded to by Allen et al. [1, Eq. 4] and used by Swift [16] in their exploration of liquids as working substances in Stirling/Malone type engines. However no detailed work has been done in this area and possible interest in the use of liquids as working substances in thermoacoustic engines would warrant a more careful look into this property. It may be pointed out at this stage that similar higher order thermoacoustic properties of fluids have been investigated before, although in an entirely different setting; the recent papers by Sharma [13, 14] and the references therein provide a good indication of the interest in this type of fundamental work.

As for the boundary conditions in the present problem, as stated earlier the simplifying assumption of large sphere thermal inertia will be initially used to obtain a proper handle on the problem. This will be subsequently relaxed to allow a thermal interaction between the sphere and the fluid. This step would simulate the actual physics more realistically and allow for finite heat capacity effects of the sphere to be incorporated. As for the solution procedure, this change requires that the governing equations of motion in the fluid now also be coupled to the energy equations in both the fluid and the sphere. The primary temperature oscillations in the fluid need to be first determined from a leading order solution of the energy equation. In addition, the complete unsteady form of the heat conduction equation has to be solved to determine the temperature distribution in the sphere, and has to be also properly matched to the temperature distribution in the fluid to maintain interfacial continuity of temperature and heat flux.

The above discussion dealt with the solution methodology and the streaming effects only in the inner Stokes layer region. Although this region is very narrow, the mechanics therein are very crucial since the large velocity gradients in these Stokes layers are responsible for the origin of the thermoacoustic streaming effects. These effects result in a time-averaged temperature distribution being induced which in turn determines the steady temperature distribution in the rest of the fluid domain external to this narrow region. This behavior occurs in much the same way as the generation of the time-averaged acoustic streaming velocity distribution which in turn functions as a slip velocity in driving the steady flow in the outer region.

The mechanics of the inner region has to be appropriately coupled to that of the outer region. For the flow behavior, it would be necessary to ensure a proper matching of the stream function and the velocity potential between the inner and outer regions. In the absence of the thermoacoustic

streaming effect, the temperature could have been treated as a passive scalar field and could have also been coupled in a similar manner. In the present case however, the pressure and fluid density variations are also important and have to be carefully matched in a consistent manner. For the large streaming Reynolds being studied, the outer region is expected to have a boundary layer structure which will be numerically determined subject to the matching conditions from the inner region. This procedure is fairly well established for such flows as reported earlier by Gopinath & Mills [6] and Gopinath [3, 4]. Of particular interest in the outer region will be the influence of the steady acoustic streaming fluid motion on the steady thermoacoustic streaming temperature distribution. This feature will determine the steady convective heat transfer rate in the outer region and needs to be computed numerically from a boundary layer form of the governing equations. This behavior of the influence of the time-averaged flow on the time-averaged heat transport will describe the overall transport effect due to these combined streaming phenomena.

### 3.3 The Case of Drops/Bubbles

The case of the levitated sample being a compressible medium, such as a drop/bubble, would represent a more generalized version of this problem. For simplicity, the sample will be assumed to be spherical (for sufficiently small diameters and high surface tension), with the acoustic field sufficiently well controlled so as to not induce any shape oscillatory modes in the drop/bubble. For such cases, careful matching of the fluid velocities and stresses across the spherical interface is required, along with maintaining the continuity of temperature and heat flux. Based on progress with the case of the rigid sphere, this is the final problem that will be dealt with to establish more general results for these thermoacoustic effects.

## 4 Conclusions

This study provides a controlled setting to explore some fundamental thermoacoustic streaming transport behavior in conjunction with a study of the significance of a second-order thermodynamic modulus. It is hoped that with such a controlled study, it would be possible to obtain a good grasp of the nature of the thermoacoustic streaming phenomenon and identify the precise role of the above mentioned thermodynamic modulus. It is projected that the current theoretical analysis would also yield ideas for possible future experiments to explore these transport phenomena and measure this thermodynamic modulus. It is possible to envisage experiments which would involve the use of heat sensing instrumentation inside the levitated sphere to detect the temperature and heat transfer exchange rate with the sphere. This experimental data could then be correlated with the theoretical results which would serve as reference, to make inferences about the roles of the different heat exchange mechanisms.

## References

- [1] P. C. Allen, W. R. Knight, D. N. Paulson, and J. C. Wheatley. Principles of liquids working in heat engines. *Proc. Natl. Acad. Sci. USA*, 77(1):39–43, Jan. 1980.
- [2] B. J. Davidson. Heat transfer from a vibrating circular cylinder. *Int. J. Heat Mass Transfer*, 16:1703–1727, 1973.
- [3] A. Gopinath. Steady streaming due to small amplitude torsional oscillations of a sphere in a viscous fluid. *Quart. J. Mech. Appl. Math.*, 46(3):501–520, Aug. 1993.
- [4] A. Gopinath. Steady streaming due to small amplitude superposed oscillations of a sphere in a viscous fluid. *Quart. J. Mech. Appl. Math.*, 47(3):461–480, Aug. 1994.
- [5] A. Gopinath. Convective heat transfer from a sphere due to acoustic streaming : Effects of viscous dissipation and compressibility work. In *29th National Heat Transfer Conference, ASME-HTD vol. 248*, pages 9–21, Atlanta, Georgia, Aug. 1993.
- [6] A. Gopinath and A. F. Mills. Convective heat transfer from a sphere due to acoustic streaming. *ASME J. Heat Transfer*, 115:332–341, May 1993.
- [7] A. Gopinath and A. F. Mills. Convective heat transfer due to acoustic streaming across the ends of a Kundt tube. *ASME J. Heat Transfer*, 116:47–53, Feb. 1994.
- [8] C. P. Lee and T. G. Wang. Acoustic radiation force on a heated sphere including effects of heat transfer and acoustic streaming. *J. Acoust. Soc. Am.*, 83(4):1324–1331, April 1988.
- [9] P. Merkli and H. Thomann. Thermoacoustic effects in a resonance tube. *J. Fluid Mech.*, 70:161–177, 1975.
- [10] N. Riley. On a sphere oscillating in a viscous fluid. *Quart. J. Mech. Appl. Math.*, 19(4):461–472, 1966.
- [11] N. Rott. The heating effect connected with non-linear oscillations in a resonance tube. *J. Appl. Math. Phys. (ZAMP)*, 25:619–634, 1974.
- [12] N. Rott. Thermoacoustics. *Adv. Appl. Mech.*, 20:135–175, 1980.
- [13] B. K. Sharma. Isothermal volume derivative of thermodynamic Gruneisen parameter, nonlinearity parameter and intermolecular heat capacity of liquids. *J. de Physique*, 4(5):709–712, May 1994.
- [14] B. K. Sharma. Relationship between the Gruneisen parameter, Flory-Huggins interaction parameter and other thermoacoustic parameters in dilute polymer solutions. *J. de Physique*, 4(5):713–716, May 1994.
- [15] G. W. Swift. Thermoacoustic engines. *J. Acoust. Soc. Am.*, 84(4):1145–1180, Oct. 1988.
- [16] G. W. Swift. A Stirling engine with a liquid working substance. *J. Appl. Phys.*, 65(11):4157–4172, June 1989.
- [17] E. H. Trinh. Fluid dynamics and solidification of levitated drops and shells. In J. N. Koster and R. L. Sani, editors, *Low-Gravity Fluid Dynamics and Transport Phenomena*, pages 515–536. AIAA Series in Progress in Aeronautics and Astronautics, 1990. v.130.



# A FLUORESCENCE RECOVERY AFTER PHOTOBLEACHING (FRAP) TECHNIQUE FOR THE MEASUREMENT OF SOLUTE TRANSPORT ACROSS SURFACTANT-LADEN INTERFACES

Edward P. Browne and T. Alan Hatton  
Department of Chemical Engineering  
Massachusetts Institute of Technology  
Cambridge, MA 02139

## ABSTRACT

The technique of Fluorescence Recovery After Photobleaching (FRAP) has been applied to the measurement of interfacial transport in two-phase systems. FRAP exploits the loss of fluorescence exhibited by certain fluorophores when over-stimulated (photobleached), so that a two-phase system, originally at equilibrium, can be perturbed *without disturbing the interface* by strong light from an argon-ion laser and its recovery monitored by a microscope-mounted CCD camera as it relaxes to a new equilibrium. During this relaxation, the concentration profiles of the probe solute are measured on both sides of the interface as a function of time, yielding information about the transport characteristics of the system. To minimize the size of the meniscus between the two phases, a photolithography technique is used to selectively treat the glass walls of the cell in which the phases are contained. This allows concentration measurements to be made very close to the interface and increases the sensitivity of the FRAP technique.

## INTRODUCTION

Solute transport across surfactant-laden liquid-liquid interfaces is important in areas as diverse as industrial and analytical separations, tertiary oil recovery, controlled and targeted release drug delivery, and cell membrane transport. However, the mechanism by which this transport takes place is still poorly understood. The process is a complex one, in which electrostatics, steric effects and fluid dynamics all play a role. The disentanglement of these competing influences requires an ability measure unambiguously the resistance to solute transport offered by an interface under a variety of system conditions. Existing techniques, however, suffer from a number of serious limitations. Most of the methods currently employed, such as the stirred cell[1][2] or the rotating diffusion cell[3] involve convection of the fluids adjoining the interface. This requires a detailed knowledge of the hydrodynamic conditions near the interface, which is rarely available. Moreover, convection results in non-uniformities in the interfacial surfactant layer, leading to ambiguity in the interpretation of the results. Limitations of this type can be overcome through the use of purely diffusive systems, in which concentration profiles are recorded as a function of time as the solute moves from one phase to another in response to a perturbation from equilibrium. However, the methods used to detect concentration fields, such as interferometry, frequently require solute concentrations of a magnitude sufficient to perturb the interface itself. In addition, inherent in this kind of technique is the need to observe concentrations very close to the interface, but this is made difficult owing to the presence of the meniscus between the phases which may be up to 200  $\mu\text{m}$  thick. Therefore, what is required in order to measure unambiguously interfacial transport coefficients is a purely diffusive technique with a minimal interphase meniscus and a highly sensitive detection technique.

The technique of Fluorescence Recovery After Photobleaching (FRAP) has been adapted to meet these requirements. FRAP uses a fluorescent solute in a system originally at equilibrium, and perturbs the system using an intense beam of light. This overstimulates the fluorophore and causes it to cease fluorescent emission, a phenomenon known as photobleaching. Over time, the photobleached solute molecules diffuse out of the bleached zone, and the still-fluorescent molecules that were outside the bleached zone diffuse inwards as the system recovers towards equilibrium. This recovery is monitored over a period of time, and from this an interfacial transport coefficient is calculated. For example, if photobleaching takes place close to the interface in the upper phase, transport of *visible* fluorophore will take place from the lower phase to the upper phase as the system recovers. If in this case the system comprised of a lower aqueous phase and upper reversed-micellar phase, such a bleaching pattern would provide information about forward transport from the aqueous phase into the reversed-micellar phase. To reduce the thickness of the meniscus, a photolithography technique[4] is used which results in a meniscus 40  $\mu\text{m}$  deep.

## EXPERIMENTAL

The FRAP apparatus is shown in Figure 1. The two phases between which we wish to measure transport are contained in a glass-walled cell (*k*). The system is allowed to come to equilibrium, with the solute of interest (chiefly derivatives of fluorescein, which have excitation and emission wavelengths of 488 nm and 512 nm respectively) distributed between the upper and lower phase.

To perturb the system, a high intensity beam of light at 488 nm from the argon ion laser (*a*) is used to photobleach a given area of the cell. For example, if photobleaching takes place close to the interface in the upper phase, transport of *visible* fluorophore will take place from the lower phase to the upper phase as the system recovers. The light from the laser reflects off mirror (*b*), and falls on a half silvered mirror (*c*), splitting the beam into the bleaching beam, *cdghi*, and the observation beam, *clmi*. When bleaching is required, the shutter (*e*) is opened, allowing the full power of the bleaching beam to fall on the cell. A computer controlled translation stage (*g*) is included in the path to scan the beam rapidly back and forth across the cell parallel to the interface. This eliminates the complicating factor of concentration gradients *along* the interface, provided that the scanning is rapid relative to diffusional timescales in the system. A long focal length converging lens (*r*) controls the width of the beam. When the 488 nm beam reaches the dichroic mirror (*j*), the properties of the mirror are such that the light is reflected into the cell and photobleaching occurs.

The task of the observation beam, *clmi*, is to illuminate the cell when a concentration measurement is required. When the observation beam falls on the dichroic mirror, it is reflected towards the cell where it stimulates fluorescence emission. The emitted light at 512 nm can pass through the dichroic mirror and enter the microscope (*u*), where the image falls on a CCD camera (*v*) and is captured by a frame-grabber board (Data Translation, Inc.) installed in an IBM PC. The width of the cell along the beam is sufficiently small (2 mm) that it lies within the depth of field of the microscope. The image produced by the CCD camera is therefore a two dimensional projection of the contents of the cell. A rotating filter wheel (*n*) controls the level of illumination, and allows two different illumination levels to be used in systems where the solute partition coefficient differs significantly from unity. To prevent photobleaching by the observation beam due to long exposure times, a shutter (*p*) ensures that the observation beam falls on the cell only when an image is required. A beam expander (*w*) ensures a more uniform illumination field, and an optical flat (*o*) bleeds off a small fraction of the beam towards a second CCD camera (*t*) to allow monitoring of any variation in the laser beam power with time.

The operation and timing of the shutters, the translation stage, the filter wheel and the image acquisition from both cameras is controlled by the PC-based virtual instrumentation package Labview (National Instruments, Inc., TX).

The presence of a meniscus between the phases would ordinarily prevent sensitive measurement of interfacial resistance by optical techniques because the meniscus produces a blind zone up to 300  $\mu\text{m}$  thick around the interface. To minimize the meniscus between the two phases so that sensitive measurements can be made, the surface of the glass cell walls is treated by a photolithography technique so that the upper part of the cell, corresponding to the organic phase, is hydrophobic, and the lower part, corresponding to the aqueous phase, is hydrophilic. The edge of the meniscus adheres with a 90° contact angle to the line where the surface properties change, and judicious filling of the cell results in a meniscus that is as little as 40  $\mu\text{m}$  deep.

Early results indicated that natural convection was a major problem when conducting ground-based FRAP experiments. The local heating that occurred on bleaching resulted in gross movements of fluid, as shown in Figure 2. Refinements to the imaging and control apparatus has enabled the use of fluorophore concentrations as low as 50 nM, at which level the bleaching-induced heating is insufficient to cause the onset of convection.

## DATA ANALYSIS

The emission intensity at any point in the cell is proportional both to the observation beam intensity and to the concentration of the fluorophore at that point. In order to obtain the two-dimensional concentration field in the cell, it is necessary to take a pre-bleach image (when the system is at equilibrium and all

concentrations are known) so that all subsequent, post-bleach images may be calibrated and the dependency on observation beam profile removed.

If (i) the time required for the bleaching beam to scan across the cell is very small relative to the diffusional timescales of the system, and (ii) the width of the scan is very large compared to the observation area, the diffusional recovery is essentially one-dimensional. This allows us to use an average concentration across the observation area (parallel to the interface), and produce a one-dimensional concentration profile. The interfacial resistance in the system is taken as that value which provides the best fit of the one-dimensional unsteady state diffusion equation to all the concentration profiles *simultaneously*. (The diffusion coefficient in either phase can be measured independently through a FRAP experiment in which only one phase is present.)

## RESULTS

Figure 3 shows one-dimensional concentration profiles obtained for a single phase fluorescein/PEG/dextran/water system. Fluorescein concentration is 100 nM. An 800  $\mu\text{m}$  bleaching beam has been scanned across the middle of the image. The recovery from the bleaching with time is clearly visible. The curves in Figure 3 give the best fit of the one-dimensional unsteady state diffusion equation to these data, using a diffusion coefficient of  $0.4 \times 10^{-5} \text{ cm}^2\text{s}^{-1}$  (this is for a single-phase system, with no interface present). The initial condition used in solving the diffusion equation is derived from the experimental concentration profile obtained immediately after bleaching. In this way, diffusion coefficients for our chosen fluorophores can be measured directly, leaving the interfacial resistance as the only unknown parameter in two-phase systems.

Figure 4 shows results obtained from an experiment with a fluorescein-containing water-NaCl / AOT-heptane reversed micellar system. These results were obtained before the addition of the rotating filter wheel to the FRAP system. The aqueous phase has been bleached, resulting in 'back' transport of unbleached fluorophore preferentially from the reversed-micellar phase to the aqueous phase. The fit of the diffusion equation given by the curves in Figure 4 is for an interfacial resistance of  $5000 \text{ s cm}^{-1}$ . The solute partition coefficient is taken into account by the image processing algorithm used to extract the concentration data from the intensity images in such a way that a discontinuity of concentration across the interface, as seen in Figure 4, is attributable to interfacial resistance and not to the effect of a non-unity partition coefficient. Although the fit is not as good as in the single-phase (Figure 3) or two-phase aqueous polymer systems (not shown), and the data for the organic phase is very noisy, an interfacial effect is clearly visible in these preliminary experiments. Further refinement of the technique is necessary to reduce the noise present in the concentration profiles and increase the sensitivity of the technique. Preliminary results obtained on addition of the rotating filter wheel (which allows the use of two different levels of illumination by the observation beam) have been encouraging. In particular, detailed, low-noise images are available in the reversed-micellar phase for the first time (Figure 5). Previously, it had not been possible to observe any bleaching effects in the reversed-micellar phase, which would be necessary for observing 'forward' transport from the aqueous phase into the reversed-micellar phase.

## CONCLUSIONS

Results to date show that interfacial transport effects can be observed using the FRAP technique in a variety of systems, and that it will provide a sensitive means to determine interfacial resistance free from the ambiguity inherent in convective methods of measurement.

## REFERENCES

1. Dungan, S.R., Bausch, T., Hatton, T.A., Plucinski, P., and Nitsch, W., "Interfacial Transport Processes in the Reversed Micellar Extraction of Proteins". *Journal of Colloid and Interface Science*, v.145 (1991), pp. 33-49.
2. Plucinski, P. and Nitsch, W., "Mechanism of Mass Transfer between Aqueous Phase and Water-in-Oil Microemulsion". *Langmuir*, v.10 (1994), pp. 371-376.
3. Albery, W.J., Choudhery, R.A., Atay, N.Z., and Robinson, B.H., "Rotating Diffusion Cell Studies of Microemulsion Kinetics". *Journal of the Chemical Society, Faraday Transactions I*, v. 83 (1987), pp. 2407-2419.
4. Aunins, A.H., *Solute Transport Across Surfactant Laden Interfaces: Developement of a Novel Interferometric Technique for Measuring Interfacial Resistance*, Ph.D. Thesis, Massachusetts Institute of Technology, Cambridge MA, 1991

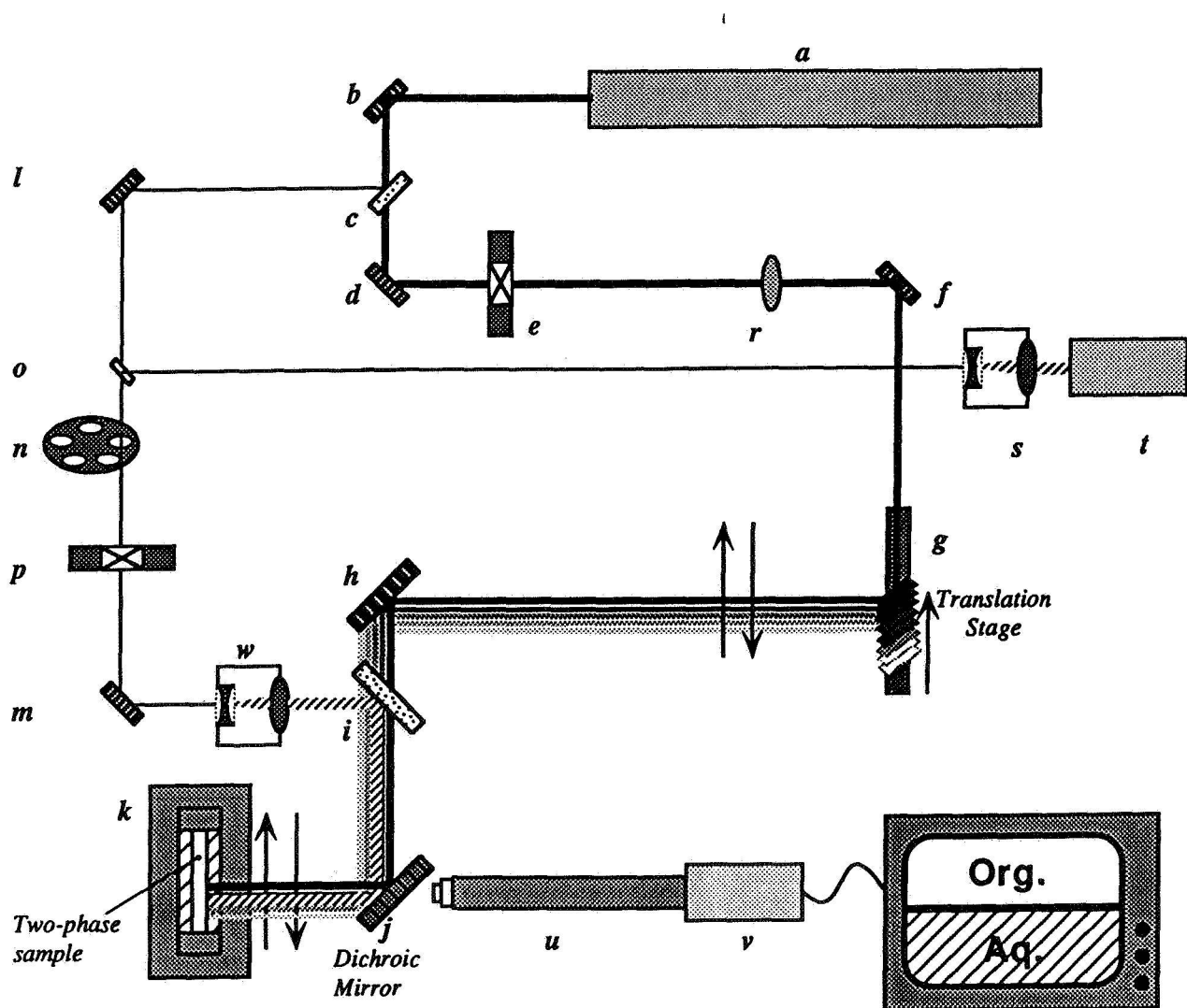


Figure 1. FRAP System

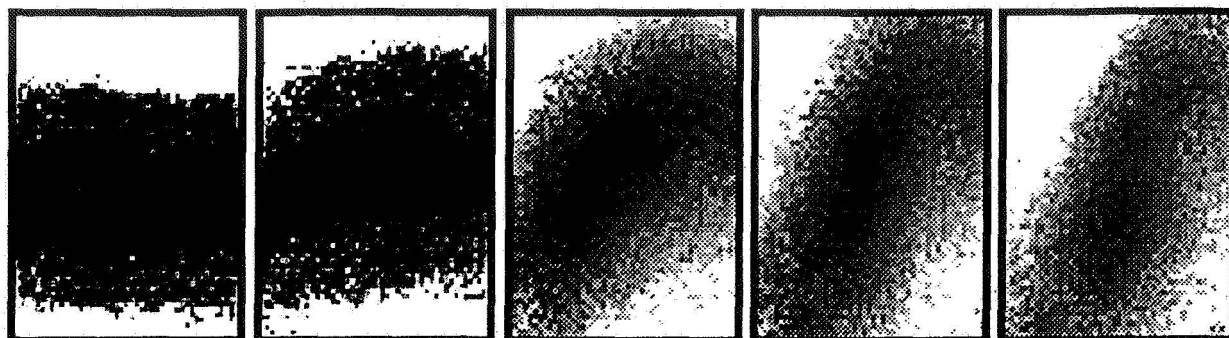


Figure 2. Photobleaching-induced Convection

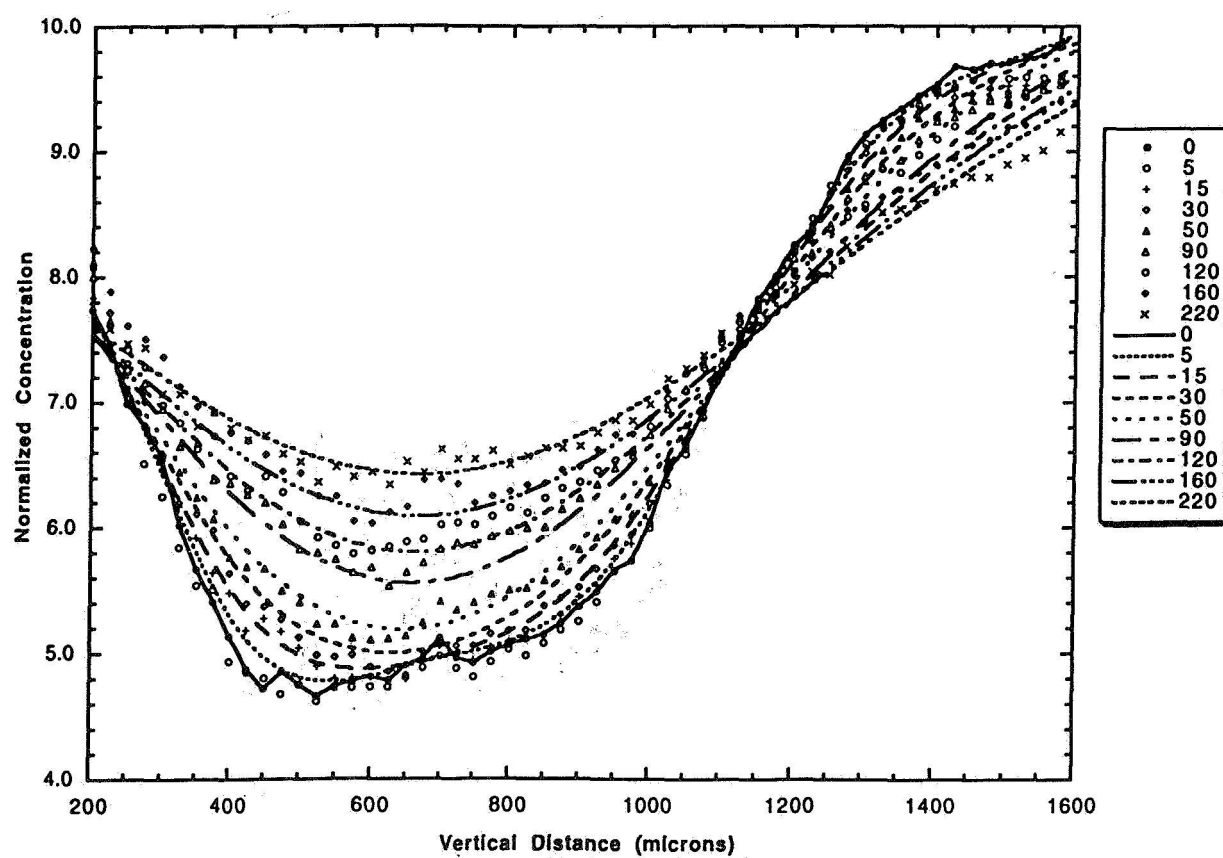


Figure 3. Fluorescein in PEG/Dextran/Water System

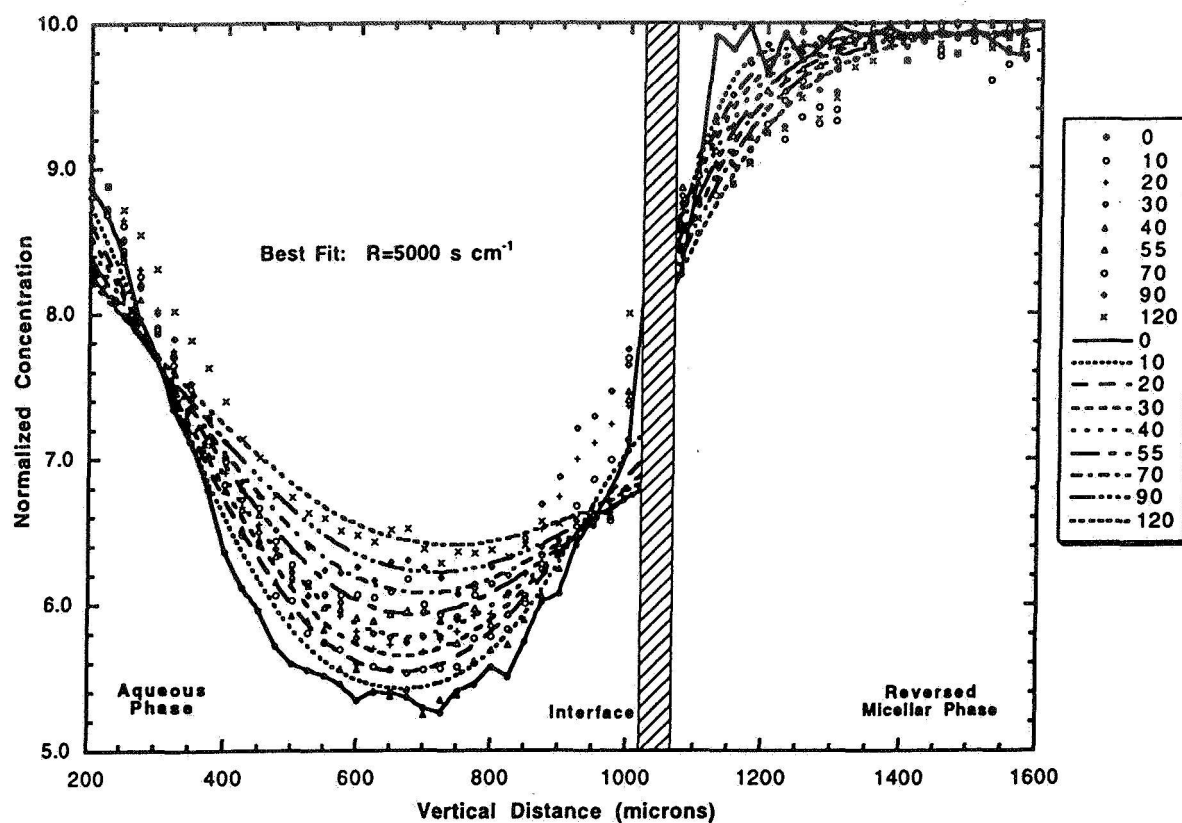


Figure 4. Water/AOT Reversed Micellar System

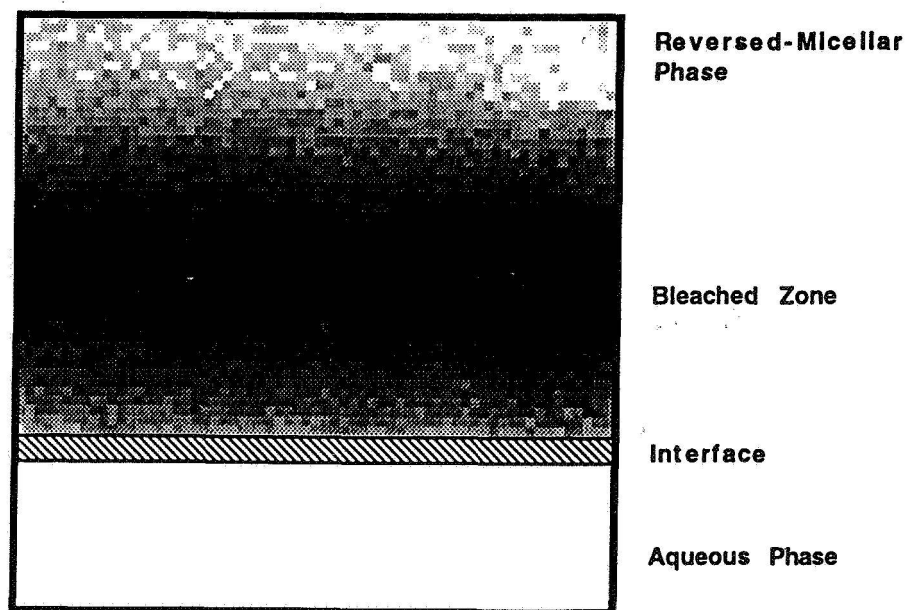


Figure 5. Reversed-Micellar Phase Photobleaching

# INVESTIGATION OF THERMAL STRESS CONVECTION IN NONISOTHERMAL GASES UNDER MICROGRAVITY CONDITIONS

Daniel W. Mackowski and Roy W. Knight  
Mechanical Engineering Department, Auburn University, AL 36849

## ABSTRACT

Microgravity conditions offer an environment in which convection in a nonisothermal gas could be driven primarily by thermal stress. A direct examination of thermal stress flows would be invaluable in assessing the accuracy of the Burnett terms in the fluid stress tensor. We present a preliminary numerical investigation of the competing effects of thermal stress, thermal creep at the side walls, and buoyancy on gas convection in nonuniformly heated containers under normal and reduced gravity levels. Conditions in which thermal stress convection becomes dominant are identified, and issues regarding the experimental measurement of the flows are discussed.

## INTRODUCTION

Kinetic theory of gases predicts that temperature gradients can be constitutively related to fluid stresses. These effects, referred to as thermal stress, are described by the Burnett contributions to the fluid stress tensor, which in turn constitutes the second-order approximation in Knudsen number  $Kn (= l/L$ , where  $l$  is the gas mean-free path and  $L$  is the characteristic system length) to the Boltzmann equation – the Navier–Stokes equations representing the first-order approximation.<sup>1</sup> To date, the main application of the Burnett terms in fluid mechanics modeling has been to extend the range of validity of continuum-based formulations to transitional Knudsen regimes ( $0 < Kn < O(1)$ ) and highly nonequilibrium conditions (i.e., large temperature gradients). For example, inclusion of the Burnett terms have been shown to improve the accuracy of calculated velocity and temperature fields for hypersonic flow as compared to conventional Navier–Stokes formulations.<sup>2</sup> Even in such situations, however, the contributions of the Burnett terms to fluid stress are relatively small compared to those arising from velocity gradients. Likewise, the effect of thermal stress in non-isothermal, slow-moving gases under normal gravity conditions will typically be negligible compared to buoyant forces.

One situation where thermal stress can become a primary convection mechanism in a nonisothermal gas is the microgravity environment. Beginning with Rosner in 1989, several investigations have been performed to determine the effects of thermal stress (and the often-more-important mechanism of thermal creep at the container side walls) on vapor transport in  $\mu\text{g}$  crystal growth processes.<sup>3–5</sup> However, a direct observation of convection that results from thermal stress, which would be possible in a buoyancy-free environment, would be of key interest in itself – in that it would provide highly useful information towards assessing the validity of the Burnett terms.

The objective of our work is to assess the feasibility of such an approach. Specifically, we intend to conduct detailed numerical investigations of gas convection in closed, nonuniformly heated containers, with the goal of identifying optimum conditions for the generation and measurement of thermal stress flows. This paper presents some preliminary results from our investigation.

## MODEL AND FORMULATION

As a starting point, we consider the simple system in which a gas is contained within a cylindrical enclosure with controlled temperature and/or heat flux conditions on all surfaces. The system is taken to be axisymmetric (corresponding to axial-directed gravity and symmetric

boundary conditions) and in steady state. The governing continuity, momentum, and energy equations are

$$\frac{1}{r} \frac{\partial \rho r v}{\partial r} + \frac{\partial \rho u}{\partial z} = 0 \quad (1)$$

$$\frac{1}{r} \frac{\partial \rho r v^2}{\partial r} + \frac{\partial \rho u v}{\partial z} = -\frac{\partial P}{\partial r} + \frac{1}{r} \frac{\partial r \tau_{rr}}{\partial r} + \frac{\partial \tau_{rz}}{\partial z} - \frac{\tau_{\phi\phi}}{r} \quad (2)$$

$$\frac{1}{r} \frac{\partial \rho r u v}{\partial r} + \frac{\partial \rho u^2}{\partial z} = -\frac{\partial P}{\partial z} + \frac{1}{r} \frac{\partial r \tau_{rz}}{\partial r} + \frac{\partial \tau_{zz}}{\partial z} - \rho g \quad (3)$$

$$\frac{1}{r} \frac{\partial \rho c_p r v T}{\partial r} + \frac{\partial \rho c_p u T}{\partial z} = \frac{1}{r} \frac{\partial}{\partial r} r k \frac{\partial T}{\partial r} + \frac{\partial}{\partial z} k \frac{\partial T}{\partial z} \quad (4)$$

in which  $u$  and  $v$  are the axial and radial components of velocity.

The effect of thermal stress will appear in the fluid stress tensor  $\tau$ , which will be comprised of the 'classical' Newton-Stokes relations and the higher-order Burnett terms. Since the flows will be relatively slow-moving, the only significant Burnett terms will be those corresponding to temperature gradients. With this approximation, the thermal stress contribution to the stress tensor appears<sup>5,6</sup>

$$\tau_T = -\frac{\mu^2 \mathcal{R}}{P} \left[ \omega_3 \left( \nabla \nabla T - \frac{1}{3} (\nabla^2 T) \mathbf{I} \right) + \frac{\omega_5}{2T} \left( (\nabla T)(\nabla T) - \frac{1}{3} (\nabla T \cdot \nabla T) \mathbf{I} \right) \right] \quad (5)$$

In the above,  $\mu$  is the dynamic viscosity,  $\mathcal{R}$  is the specific gas constant, and  $\omega_3$  and  $\omega_5$  are Burnett coefficients, which depend on the force interactions between the gas molecules. We assume here the case of Maxwellian molecules, for which  $\omega_3 = \omega_5 = 3$ .<sup>2</sup>

The velocity boundary conditions on the side and end walls are

$$u(r = R, z) = \frac{C_s \nu}{T} \frac{\partial T}{\partial z} \bigg|_{r=R}, \quad v(r = R, z) = 0 \quad (6)$$

$$u(r, z = 0, L) = 0, \quad v(r, z = 0, L) = \frac{C_s \nu}{T} \frac{\partial T}{\partial r} \bigg|_{z=0,L} \quad (7)$$

in which  $C_s$  is a dimensionless coefficient that has the value of 3/4 for Maxwellian molecules with complete accommodation. The velocity slip conditions in the above are typically referred to as 'thermal creep'. In the results presented herein, we neglect the effects of temperature jump and viscous slip at the wall – which will be appropriate for near-continuum (i.e.,  $Kn \ll 1$ ) conditions.

The gas is taken to be monatomic (with  $Pr = 2/3$ ), and we assume that the dynamic viscosity varies with temperature according to  $\mu \propto T^{0.72}$ .<sup>2</sup> In all presented results we have used Burnett and creep coefficients for Maxwellian molecules.

Numerical solution of Eqs. (1–4) was accomplished using the SIMPLE algorithm.<sup>7</sup> A non-uniform mesh, typically of 21 and 41 nodes in the radial and axial directions, respectively, was employed. Discretization of the thermal stress source terms in the momentum equations followed the control volume procedure as outlined in Ref. 7. Inclusion of the third-order temperature derivatives in the thermal stress terms would, in principle, require the specification of additional thermal boundary conditions at the surfaces. However, energy transport is dominated by conduction for the slow-moving conditions of the system. The energy equation thus becomes effectively decoupled from the momentum equations, which results in a second-order system for the temperature field.



In all cases, the presented results for temperature and velocity are within 0.5% of the values obtained when the grid spacing was halved. Results from the code for free convection heat transfer in cylindrical enclosures were found to be in acceptable agreement with previously published values. We are unaware of previously published numerical calculations for thermal stress convection for similar conditions to those examined here.

### Calculation Results

Calculations were performed on a system corresponding to helium at 1 atm pressure in a  $L = 2$  cm,  $R = 1$  cm container. The end walls at  $z = 0$  and  $z = L$  were isothermal at 300 and 600 K, respectively. The side wall was maintained at 300 K, except for a 1 mm adiabatic strip adjacent to the hot end of the container. The rationale for the thermal conditions is to devise a system which minimizes temperature gradients along the surfaces (which drive creep flows along the surfaces) while maintaining relatively large temperature gradients in the bulk gas (the source of thermal stress). In this regard, an 'ideal' situation would have the top and side walls of the container at uniform yet different temperatures.<sup>6</sup> Such a condition, however, is both physically unrealistic and numerically troublesome – and we therefore include the 1 mm adiabatic length between the cold and hot surfaces.

Figure 1 shows calculated isotherms and dimensionless velocity vectors for a system at unit gravity (directed towards the cold end). The origin of the container in the velocity vector plot is in the lower left corner, and the legend refers to the scale of the velocity arrow in units of  $\nu_C/L$ , where  $\nu_C$  is the kinematic viscosity of the gas at the cold temperature ( $\approx 2 \text{ cm}^2/\text{s}$  for helium at STP). Thermal creep is seen to result in a strong recirculation of the gas along the adiabatic section of the side wall, whereas buoyancy leads to a counter-rotating vortex within the main section of the container. Reduction of  $g$  to  $10^{-3}$  results in the apparent disappearance of the buoyant recirculation, as seen in Fig. 2. However, magnification of the velocity scale by a factor of 20 reveals the convection pattern created by thermal stress, which is shown in the right-hand plot. The vectors directly within the thermal creep recirculation zone have been removed here, to avoid 'spilling' into the rest of the plot. The magnitude of the predicted velocities generated from thermal stress for the given conditions, at around  $0.1\nu_C/L \approx 1 \text{ mm/s}$ , are consistent with order-of-magnitude estimations by Viviani et al..<sup>5</sup> Results for zero gravity are essentially unchanged from those appearing in Fig. 2.

To distinguish between the flows resulting from thermal creep and thermal stress, we present in Fig. 3 vector plots of the flows calculated with thermal stress and without thermal creep (a, left), and with creep and without stress (b, right). The values of  $g$  is the same as in the previous plot. By comparison of Figs. 3b and 2, one sees that thermal stress is the primary source of convection in all but the adiabatic corner of the enclosure. It is difficult to draw any general conclusions regarding the recirculation generated by thermal stress – except that it is considerably more complicated than that generated by buoyancy. In Fig. 3a the largest velocities generated by stress act somewhat similar to those produced by creep at the side wall, in that the flow is pushed along the adiabatic section of the wall towards the hot end of the enclosure. However, a second recirculation pattern results in a flow of gas along the wall towards the cold end. Additional calculations (not shown here) have indicated that the nature of the thermal stress recirculation is strongly dependent on the value of the hot/cold temperature ratio, the length of the adiabatic zone, and the variation of viscosity with temperature.

## Flow Measurement Issues

A concurrent task in our work will be to identify feasible means of measuring gas velocities that result from thermal stress convection in  $\mu g$  conditions. Methods based on the tracking of small seed particles in the gas, such as LDV, would generally be biased by thermophoretic motion of the particles – which would be significant in the highly nonisothermal conditions of an experiment. However, since particle sedimentation is not as critical an issue in the  $\mu g$  environment as it is on earth, relatively large particles – with correspondingly lower thermophoretic diffusivities – could be used to track the flow.

To further examine this concept, we calculated the trajectories of ‘test’ particles that were released into flowfields calculated under various thermal and gravitational conditions. Assuming that the particles have zero inertia and zero Brownian motion, the positions of the particles are obtained by integration of the motion equations:

$$\frac{dr_p}{dt} = v - \frac{f_T \nu}{T} \frac{\partial T}{\partial r} \quad (8)$$

$$\frac{dz_p}{dt} = u - \frac{f_T \nu}{T} \frac{\partial T}{\partial z} - B m_p g \quad (9)$$

where  $f_T$  is a thermophoretic diffusion factor for the particle,  $B$  is the particle mobility, and  $m_p$  is the particle mass. For spherical particles of radius  $a_p$ , the mobility and thermophoretic factors are approximated as<sup>8</sup>

$$B = \frac{f_c}{6\pi\mu a_p} \quad (10)$$

$$f_T = \frac{2f_c C_S(\phi + C_t K n_p)}{(1 + 3C_m K n_p)(1 + 2\phi + 2C_t K n_p)} \quad (11)$$

where  $K n_p = l/a_p$  is the particle Knudsen number,  $\phi = k_g/k_p$  is the ratio of gas and particle thermal conductivities,  $C_m$  and  $C_t$  ( $\approx 1.14$  and  $2.2$ ) are the momentum exchange and temperature jump coefficients, and  $f_c$  is the Millikan correction factor,

$$f_c = 1 + K n_p (1.2 + 0.41 \exp(-0.88/K n_p)) \quad (12)$$

An increasing correspondence between the particle trajectory and the flow streamlines is obtained by reducing both  $f_T$  and  $m_p g$ . Equation (11) shows that former can be reduced by increasing both particle size and particle thermal conductivity. Using, for example, a  $10 \mu m$  aluminum particle ( $\phi \approx 0.001$ ,  $K n_p \approx 0.03$  for helium at 450 K, 1 atm) gives a thermophoretic factor  $f_T \sim 0.07$  – which results in roughly comparable magnitudes of particle thermophoretic and thermal stress convective velocities for the conditions modelled in the previous section. Calculated trajectories for the particle, which is released at the point  $r_{p,0}^* = 0.1$  and  $z_{p,0}^* = 1$ , are shown in Fig. 4a. The flow conditions correspond to those presented in Fig. 2, except with unit,  $10^{-2}$ ,  $10^{-3}$ , and zero gravity levels. Shown in Fig. 4b are results calculated under identical conditions, except with the absence of thermal stress convection in the flow field.

In unit gravity, the trajectory of the particle is controlled mainly by gravitational forces, and to a lesser extent buoyant recirculation of the gas. However, at lower gravity levels both thermophoresis and thermal stress convection are shown to have a significant effect on the particle trajectory. Since the temperature fields calculated with and without thermal stress are essentially

identical, differences in the trajectories shown in Figs. 4a and b therefore result entirely from the action of thermal stress convection.

### SUMMARY

Our preliminary calculations indicate that thermal stress convection in gases could be isolated and examined in the microgravity environment. Of course, much remains to be performed to completely assess the feasibility of an experiment towards this end. Our future work will examine various strategies of heating an enclosed gas – with the objective of identifying methods which maximize the predicted convection from thermal stress while minimizing thermal creep at the walls. For example, it may be desirable to heat a gas via localized absorption of radiation – as opposed to maintaining different temperatures on the walls of the container. We will also further explore particle tracking methods for measurement of the gas convective velocities. Finally, the ‘inverse’ problem needs to be examined, i.e., given measurements of convective flows in nonisothermal,  $\mu g$  conditions, what can be said about the veracity of the Burnett contributions to the fluid stress tensor?

### REFERENCES

1. S. Chapman, and T. G. Cowling, *The Mathematical Theory of Non-Uniform Gases*, Cambridge University Press, London, 1970.
2. X. Zhong, R. W. MacCormack, and D. R. Chapman, “Stabilization of the Burnett Equations and Application to Hypersonic Flows,” *AIAA J.*, **31**, 1036–1043, 1993.
3. D. E. Rosner, “Side wall gas ‘creep’ and ‘thermal stress convection in microgravity experiments on film growth by vapor transport,” *Phys. Fluids A1*, 1761, (1989).
4. L. G. Napolitano, A. Viviani, and R. Savino, “Fluid dynamic modelling of crystal growth from vapour,” *Acta Astronautica* **28**, 197, (1992).
5. A. Viviani, and R. Savino, “Recent developments in vapour crystal growth fluid dynamics,” *J. Crystal Growth* **133**, 217, (1993).
6. M. N. Kogan, “Molecular Gas Dynamics,” in *Annual Review of Fluid Mechanics*, M. Van Dyke and W. G. Vincenti, Eds., Annual Review, Palo Alto, 1973, Vol. 5, pp. 383.
7. S. V. Patankar, *Numerical Heat Transfer and Fluid Flow*, McGraw-Hill, N.Y., 1980.
8. L. Talbot, R. K. Cheng, R. W. Schefer, and D. R. Willis, “Thermophoresis of particles in a heated boundary layer,” *J. Fluid Mech.* **101**, 737, (1980).

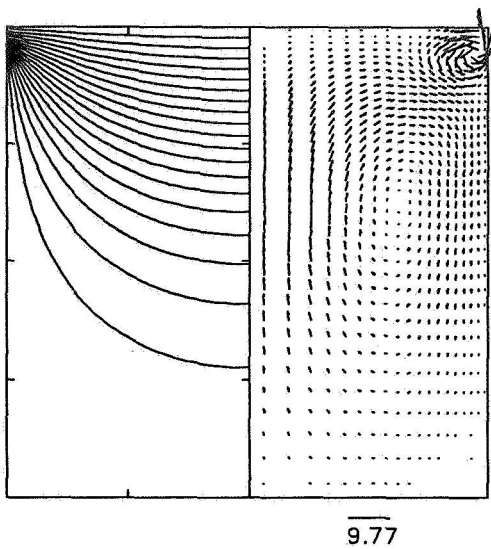


Fig. 1. Isotherms and velocity vectors, unit gravity.

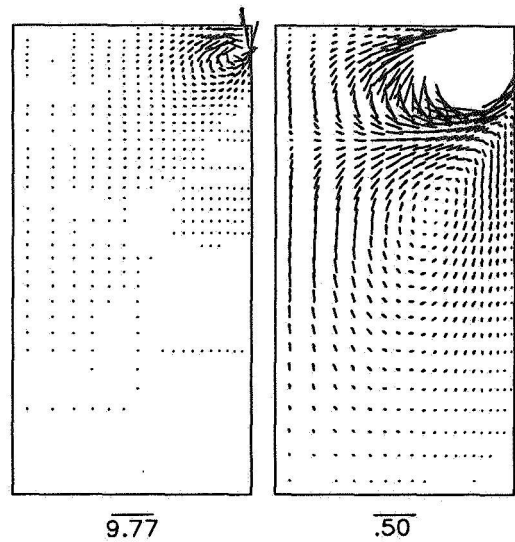


Fig. 2. Velocity vectors, reduced gravity

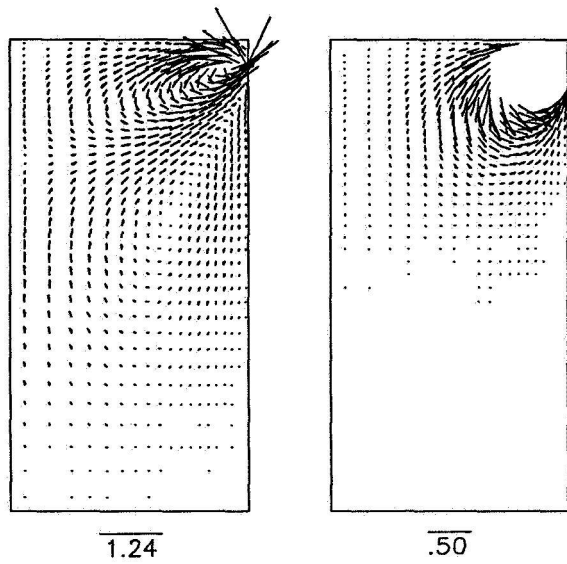


Fig. 3. Separate effects of thermal stress (left) and creep (right)

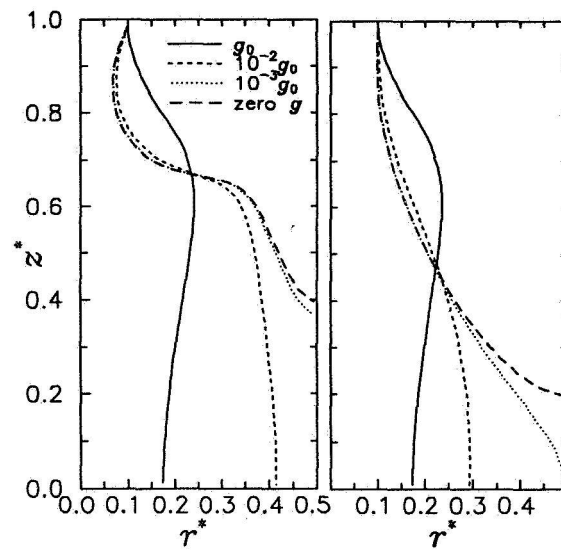


Fig. 4. Particle tracks with (left) and without (right) thermal stress

# PHORETIC AND RADIOMETRIC FORCE MEASUREMENTS ON MICROPARTICLES IN MICROGRAVITY CONDITIONS

by

E. James Davis

Department of Chemical Engineering, Box 351750

University of Washington

Seattle, WA 98195

## ABSTRACT

Thermophoretic, diffusiophoretic and radiometric forces on microparticles are being measured over a wide range of gas phase and particle conditions using electrodynamic levitation of single particles to simulate microgravity conditions. The thermophoretic force, which arises when a particle exists in a gas having a temperature gradient, is measured by levitating an electrically-charged particle between heated and cooled plates mounted in a vacuum chamber. The diffusiophoretic force arising from a concentration gradient in the gas phase is measured in a similar manner except that the heat exchangers are coated with liquids to establish a vapor concentration gradient. These phoretic forces and the radiation pressure force acting on a particle are measured directly in terms of the change in the dc field required to levitate the particle with and without the force applied. The apparatus developed for the research and the experimental techniques are discussed, and results obtained by thermophoresis experiments are presented. The determination of the momentum and energy accommodation coefficients associated with molecular collisions between gases molecules and particles and the measurement of the interaction between electromagnetic radiation and small particles are of particular interest.

## INTRODUCTION

In the absence of gravity, a number of forces on small particles can be the dominant force leading to particle movement and deposition on surfaces. Such forces may be undesirable for containerless processing and other applications. A small particle exposed to an external temperature gradient will experience a thermophoretic force as a result of differences in momentum transferred to the particle by the gas molecules colliding with the particle from the hot and cold sides. This principle is the basis of the thermopositor, which is used to deposit aerosol particles from a gas stream onto a cold surface, and is used in the modified chemical vapor deposition (CVD) process for optical fiber production (Morse *et al.*, 1985). The deposition of soot and carbonaceous particles on colder surfaces in contact with a hot gas can be an undesired result of thermophoresis. The thermophoretic force has been used to prevent particles from depositing on wafer surfaces in the micro-electronics industry (Ye *et al.*, 1991; Bae *et al.*, 1994; Lee *et al.*, 1996). As indicated in the extensive surveys of thermophoresis and diffusiophoresis by Waldmann and Schmitt (1966) and by Derjaguin and Yalamov (1972), there exists a large literature on the theories of phoretic phenomena, but there remains a paucity of high-quality data.

The need for experimental data is absolute, for existing theories require knowledge of accommodation coefficients and other coefficients to predict the relevant force. Maxwell (1879) recognized and addressed this problem early in his development of the kinetic theory of gases, and he introduced the concept of partial accommodation of gas molecules with a surface. Momentum and energy are exchanged by molecular collisions, and the possible extent of the interaction ranges

from reflection (specular emission) to complete accommodation (diffuse emission) with the surface. Accommodation coefficients for momentum and energy may be defined by

$$\alpha_m = (M_i - M_e)/(M_i - M_s) \text{ and } \alpha_t = (E_i - E_e)/(E_i - E_s) \quad [1]$$

Here  $M$  represents the average tangential components of the momentum of molecules, and  $E$  is the average energy flux. Subscripts  $e$ ,  $i$  and  $s$  refer, respectively, to molecules emerging from the surface, incident molecules, and molecules leaving in Maxwellian equilibrium with the surface.

Application of kinetic theory represents one of three approaches to the theories of thermophoresis and diffusiophoresis which have been taken: (i) continuum theory and deviations from continuum theory due to slip, (ii) solutions based on linearization of the Boltzmann equation, and (iii) semi-theoretical models. When the mean free path,  $\ell$ , of the gas molecules is small compared with the radius,  $a$ , of a spherical aerosol particle, that is, when the Knudsen number,  $Kn$ , is small ( $Kn = \ell/a \ll 1$ ), continuum theory applies. As the Knudsen number increases, discontinuities in the temperature and gas velocity occur near the surface, and slip models have been used to account for the deviations from continuum theory. When  $Kn \gg 1$ , gas molecules colliding with the surface can be in the free-molecule regime and have a Maxwell-Boltzmann distribution of molecular velocities.

Rigorous analysis of the thermophoretic force for arbitrary Knudsen number is fraught with difficulty. Determination of the molecular velocity distribution function requires solution of the Boltzmann equation with appropriate boundary conditions. One solution that looks promising is that of Loyalka (1992), who developed a scheme for the solution of the linearized form of the Boltzmann equation, which he used to perform computations of the thermophoretic force for hard spheres. Little is known about the phoretic forces on nonspherical particles.

The interaction between small particles and electromagnetic radiation is well-understood for small spheres, for Mie theory can be applied to microspheres illuminated by a monochromatic planar wave, provided that the optical properties (size and complex refractive index) of the particle is known. For crystalline particles and other small masses having an irregular shape, electromagnetic scattering theory is not yet adequate to predict the radiation pressure force, and yet crystalline particles and amorphous particles are more likely to be encountered in applications than spherical particles.

## OBJECTIVES

The primary objective of this research is to make precise measurements of phoretic and radiometric forces on microparticles. The phoretic force data on microspheres will be analyzed to determine accommodation coefficients and slip coefficients needed to predict phoretic phenomena. Radiometric force data will be used to determine the optical properties of carbonaceous particles such as soot and other contaminants. Measurements of phoretic forces on particles of irregular shape will be used to determine the effects of particle morphology and rotational motion on gas/particle interactions.

## THEORETICAL BACKGROUND

In analyses of the free molecule regime ( $Kn \gg 1$ ) it is usually assumed that the velocity distribution function of molecules colliding with the particle is not disturbed by the particle. Based on the Chapman-Enskog distribution function for a non-uniform gas, Waldmann (1959) developed the following equation for the thermophoretic force on a sphere

$$F_{fm} = -\frac{32}{15} a^2 \frac{k_{tr}}{\bar{c}} \nabla T_{\infty}, \quad [2]$$

in which  $k_{tr}$  is the translational part of the thermal conductivity of the gas,  $\nabla T_{\infty}$  is the external temperature gradient in the region unperturbed by the particle, and  $\bar{c}$  the mean molecular speed given by

$$\bar{c} = \sqrt{8kT/\pi m}. \quad [3]$$

Here  $k$  is Boltzmann's constant, and  $m$  is the molecular mass.

An analogous theory in terms of the vapor concentration gradient applies to diffusiophoresis.

The near-continuum regime or slip flow regime ( $Kn < 0.1$ ) was first analyzed by a slip flow model by Epstein (1929), who solved the Navier-Stokes equations and Laplace's equation for the temperature field, taking into account thermal slip at the gas/particle boundary. Recognizing that experimental evidence did not support Epstein's theory, Brock (1962) extended the analysis to include the velocity slip and temperature jump boundary conditions. His result may be written in the form

$$F_{th} = -6\pi a^2 (0.499) \rho \bar{c} \sigma \frac{k_2}{p} Kn \gamma(c_m Kn) \delta(k_1, k_2, c_t Kn) \nabla T_{\infty}. \quad [4]$$

Here  $\gamma$  is a function of the product  $c_m Kn$ , where  $c_m$  is a velocity slip constant, and  $\delta$  is a function of  $c_t Kn$  and the thermal conductivities of the sphere and gas,  $k_1$  and  $k_2$ , respectively. Here  $c_t$  a temperature jump constant, and the phenomenological coefficient  $\sigma$  accounts for tangential thermal slip. The constants  $c_m$  and  $c_t$  are related to the momentum and thermal accommodation coefficients.

The intermediate or Knudsen regime ( $Kn \sim 1$ ) is much more difficult to analyze than the continuum and free-molecule regimes. An example of a theoretical analysis is Dwyer's (1967) application of the 13-moment method of Grad to obtain an equation to third order in  $Kn$  of the form

$$F_{th} = -\frac{16}{15} \pi a^2 \frac{k_2}{\bar{c}} \left\{ c_t Kn^2 + \left[ \frac{1 + 2k_2/k_1}{c_m (12 Kn + \alpha_t)} + \frac{k_2}{k_1} \right] Kn + \frac{2c_t Kn}{(12c_m Kn + 1) \left[ \frac{6c_t}{15} Kn^3 + \left( \frac{1}{5} - \frac{3R\mu}{2k_1} \right) Kn^2 + \frac{1}{3} \left( 1 + \frac{2k_2}{k_1} + 2Kn\pi c_t \right) \left( \frac{3c_m Kn + 1}{12c_m Kn + 1} \right) \right]} \right\} \nabla T_{\infty}. \quad [5]$$

Note that coefficients  $c_m$ ,  $c_t$ ,  $\alpha_m$  and  $\alpha_m$  all appear in the equation.

The more recent analysis of Loyalka (1992) based on solution of the Boltzmann equation does not result in a closed form solution.

## APPARATUS & TECHNIQUES

Direct measurements of phoretic forces are being measured by stably levitating single droplets and particles electrostatically. Davis (1992) reviewed the principles and applications of electrodynamic trapping. As shown in Figure 1, a double-ring EDB of the type analyzed by Davis

*et al.* (1990) is mounted in a stainless steel vacuum chamber for thermophoresis studies. Parallel stainless steel rings are mounted above and below the midplane of the balance. When the levitated particle is positively charged, the potentials applied to the top and bottom electrodes are, respectively

$$V_t = -V_{dc} + V_{ac}\cos\omega t, \text{ and } V_b = +V_{dc} + V_{ac}\cos\omega t, \quad [6]$$

in which  $\omega = 2\pi f$  is the circular frequency of the ac source having frequency  $f$ ,  $2V_{dc}$  is the levitation voltage, and  $V_{ac}$  is the amplitude of the ac potential.

The ac field exerts no time-average force on the particle, so the dc field balances the gravitational force and any other vertical force  $F_z$ , according to the equations

$$qC_o \frac{V_{dc,o}}{z_o} = -mg, \text{ and } qC_o \frac{V_{dc}}{z_o} = -mg + F_z \quad [7]$$

where  $q$  is the coulombic charge on the particle,  $C_o$  and  $z_o$  are geometrical constants,  $m$  is the particle mass, and  $g$  is the acceleration of gravity.

Solving for  $F_z$  using Eq. [7], we obtain

$$\frac{F_z}{mg} = 1 - \frac{V_{dc}}{V_{dc,o}} = -\frac{\Delta V}{V_{dc,o}} = \frac{V_{dc} - V_{dc,o}}{V_{dc,o}}. \quad [8]$$

Thus, the ratio of the thermophoretic force to the particle weight is obtained by making two voltage measurements. First, the levitation voltage is recorded in the absence of the force of interest, and then after the force is applied. By varying the pressure in the vacuum chamber and repeating the voltage measurements, the phoretic force can be determined as a function of the Knudsen number.

Identical hollow copper chambers (pillboxes) are mounted above and below the electrodes to generate a temperature gradient. Each chamber is connected to a constant temperature bath. The upper cell can be operated in the range  $0^\circ$  to  $120^\circ\text{C}$ , and the lower cell range is  $-40^\circ$  to  $120^\circ\text{C}$ . In experiments the upper cell is maintained at a higher temperature than the lower cell to minimize or eliminate natural convection. Natural convection can only be totally eliminated by operating the entire apparatus in a microgravity environment.

A laser beam enters horizontally through a window in one of the access ports, and a 512 pixel photodiode array is mounted at the exit of a second port to measure the phase function (scattered intensity as a function of angle) of a levitated sphere.

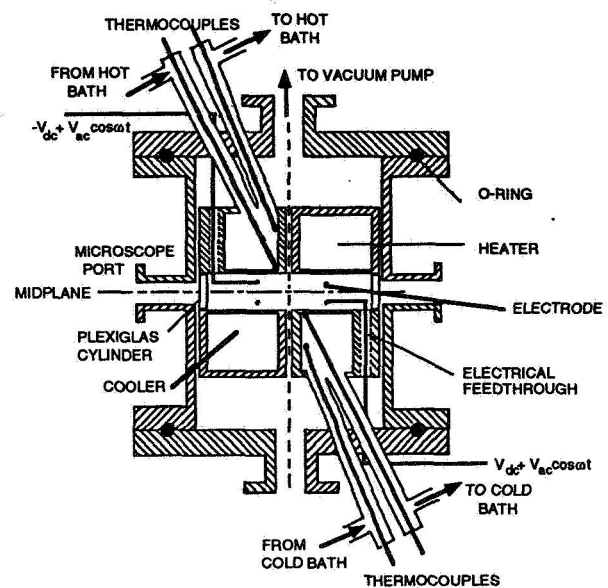


Figure 1. The apparatus used for thermophoresis studies.



## EXPERIMENTAL RESULTS

For all of the experiments for which  $Kn$  exceeded 3 a decrease in the thermophoretic force was observed. The apparent decrease in the thermophoretic force arises because the temperature gradient used in the computation of the ordinate is not the effective temperature gradient for large values of  $Kn$ . As the mean free path of the gas approaches the distance between the heated and cooled plates, the temperature gradient at the center of the chamber deviates from the assumed continuum value, for there are temperature jumps at the solid surfaces. There is a second Knudsen number,  $Kn_2 = \ell/H$ , which must be taken into account in the interpretation of the data. Devienne (1965) proposed the following correction to  $\nabla T_\infty$  for heat transfer between flat plates in the Knudsen regime

$$\nabla T_{Kn} = \frac{\nabla T_\infty}{(1+2c_t Kn_2)} = \frac{\nabla T_\infty}{(1+2c_t aKn/H)} \quad [9]$$

Based on this correction, we use the adjusted force,  $(1+2c_t Kn_2)F_{th}/(a^2 \nabla T_\infty)$ , in the presentation of data for  $Kn > 3$ .

A small sample of the data published by Li and Davis (1995a,b) are presented herein. Figure 2 shows the effect of the carrier gas on the thermophoretic force for dioctyl phthalate (DOP) droplets. The free-molecule solution of Waldmann is seen to be approached in the limit of large  $Kn$ . Figure 3 shows the same asymptotic behavior for glass and polystyrene latex (PSL) spheres and DOP. The properties of the particle are seen to have much smaller effect on the thermophoretic force than the gas properties.

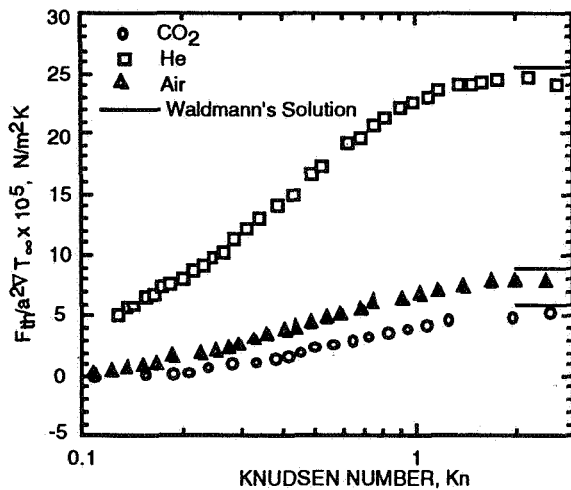


Figure 2. The effect of carrier gas on the thermophoretic force.

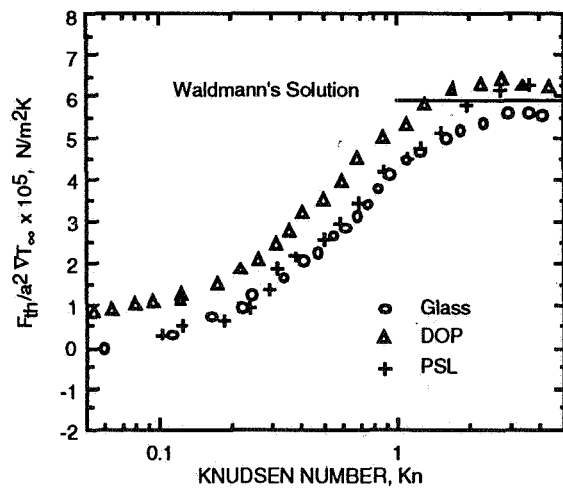


Figure 3. The effect of particle properties on the thermophoretic force.

Figures 4 and 5 compare theoretical and experimental results in air for the four types of particles studied. Loyalka's theory appears to be in reasonable agreement with the data in the Knudsen regime.

Additional work on the measurement of the radiation pressure force is being carried out, and the existing equipment will be modified for diffusiophoresis experiments.

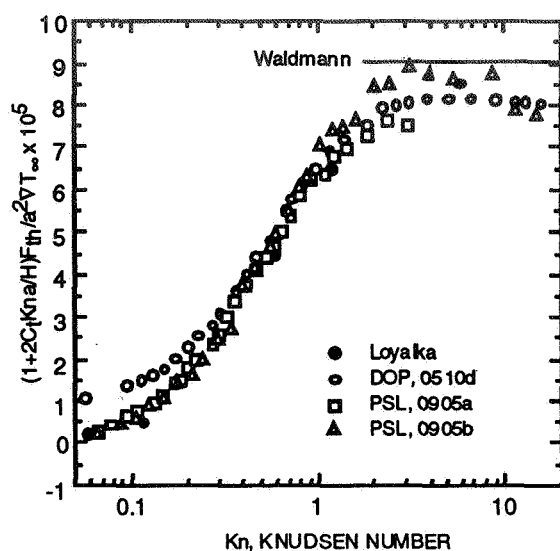


Figure 4. A comparison among the data for DOP and PSL particles and the theories of Waldmann (1959) and Loyalka (1992).

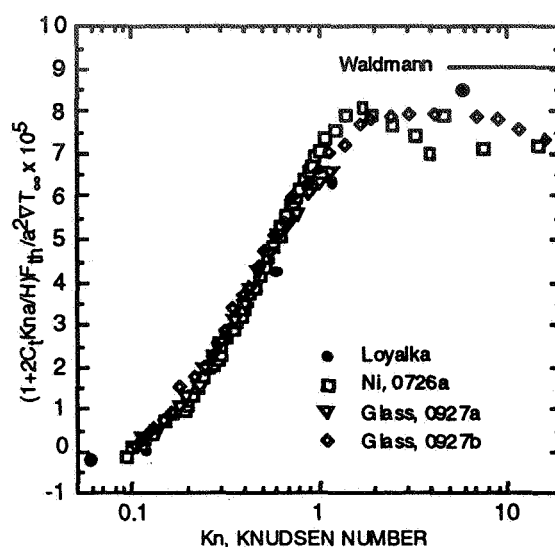


Figure 5. A comparison among the data for nickel and glass spheres and the theories of Waldmann (1959) and Loyalka (1992).

#### LITERATURE CITED

- Bae, G.N., Lee, C.S. and Park, S.O. (1994) *Aerosol Sci. Technol.* **21**, 72-82.
- Brock, J.R. (1962) *J. Colloid Sci.* **17**, 768-780.
- Davis, E.J., Buehler, M.F. and Ward, T.L. (1990) *Rev. Sci. Instrum.* **61**, 1281-1287.
- Davis, E.J. (1992) in *Advances in Chemical Engineering*, Vol. 18, Academic Press, New York, pp. 1-94.
- Derjaguin, B.V. and Yalamov, Yu.I. (1972) in *Topics in Current Aerosol Research*, Pergamon Press, Oxford, pp. 1-200.
- Devienne, F.M. (1965) in *Advances in Heat Transfer*, Vol. 2, Academic Press, New York, pp. 272-352.
- Dwyer, H.A. (1967) *Phys. Fluids* **10**, 976-984.
- Epstein, P.S. (1929) *Z. Physik* **54**, 537-563.
- Lee, J.H., Moon, W.S. and Park, S.B. (1996) *Korean J. Chem. Eng.* **13**, 7-14.
- Li, W. and Davis, E.J. (1995a) *J. Aerosol Sci.* **26**, 1063-1083.
- Li, W. and Davis, E.J. (1995b) *J. Aerosol Sci.* **26**, 1085-1099.
- Loyalka, S.K. (1992) *J. Aerosol Sci.* **23**, 291-300.
- Maxwell, J.C. (1879) *Phil. Trans. Roy. Soc.*, (see *The Scientific Papers of James Clerk Maxwell*, Vol. 2, Cambridge University Press, pp. 681-712, 1890).
- Morse, T.F., Wang, C.Y. and Cipolla, J.W., Jr. (1985) *J. Heat Transfer* **107**, 155-160.
- Waldmann, L. (1959) *Z. Naturforsch* **14a**, 589-599.
- Waldmann, L. and Schmitt, K.H. (1966) in *Aerosol Science*, C.N. Davies, ed., Academic Press, London, pp. 137-162.
- Ye, Y., Pui, D.Y.H., Liu, B.Y.H., Opiolka, S., Blumhorst, S. and Fissan, H. (1991) *J. Aerosol Sci.* **22**, 63-72.

# CROSS-EFFECTS IN MICROGRAVITY FLOWS

S. K. Loyalka, R. V. Tompson, I. N. Ivchenko, T. K. Ghosh, S. A. Hamoodi,  
K. A. Hickey, C. M. Huang, P. A. Tebbe, D. H. Gabis, P. Tekasakul, J. A. Bentz

Particulate Systems Research Center  
Departments of Nuclear, Chemical, and Mechanical and Aerospace Engineering  
College of Engineering  
University of Missouri-Columbia  
Columbia, MO 65211

## ABSTRACT

Film growth by chemical/physical vapor deposition is a process of considerable interest in micro-gravity experiments. The absence of natural convection should allow better control of film growth processes but, in highly non-isothermal ampoules, thermal slip (creep) can become a matter of significant concern. The reported research is a theoretical and experimental investigation of the flow of gas/vapor mixtures under non-continuum conditions. The Boltzmann equation has been solved for a monatomic gas under non-condensing conditions and the various phenomenological coefficients have been computed. Computations for realistic potentials as well as for velocity and creep slip have been completed and the creep slip has been found to be dependent on the type of gas confirming the accuracy of previous variational results. The variational technique has been extended and planar flows calculated via the Burnett solutions. Velocity, diffusion and creep slips have been computed for gas mixtures and previously unknown dependencies of the creep slip on the mixture properties have been observed. Also for gas mixtures, an integral representation of the linearized Boltzmann operator has been developed for use in numerical and variational calculations for all intermolecular force laws. Two, two-bulb capillary systems have been designed, built and tested for the measurements of cross-flows; one of glass for isothermal measurements and one of stainless steel for non-isothermal measurements. Extensive data have been collected for Ar-He and N<sub>2</sub>-He mixtures at a variety of pressures and mole ratios. Viscosity, velocity slip coefficients and tangential momentum accommodation coefficients have been obtained from measurements with a spinning rotor gauge via a new theory that has been formulated for the spinning rotor gauge in the slip regime. The FIDAP fluid dynamics code has been applied to condensing flows in ampoules in the continuum regime and agreement obtained with the earlier work of Duval.

## I. INTRODUCTION

Film growth by chemical/physical vapor deposition is a process of considerable interest in micro-gravity experiments. The absence of natural convection should allow better control of growth processes but, in highly non-isothermal ampoules, thermal slip (creep) can become a matter of significant concern even for Knudsen numbers as small as  $10^{-3}$ . Thus, it is important to understand and control the flows that arise from the molecular rather than the mere continuum nature of the gases and vapors. Molecular flows have been extensively studied in the past; both experimentally and theoretically. The theoretical investigations, excepting rare circumstances, have been confined to models of the Boltzmann equation which are not adequate for the description of flows of gas mixtures. Also, the experimental investigations did not address the non-continuum aspects of non-isothermal flows of the mixtures. Thus, there exists a strong need for new theoretical investigations with experimental confirmation of the results and practical application of the new findings.

To describe molecular flows, we consider the diffusion of one or more species (molecular mass  $m_i$ , number density  $n_i$ ) in an arbitrary gas mixture. Mathematically, for the distribution,  $f_i(\mathbf{r}, \mathbf{c})$ , the problem consists of solving the boundary value problem:

$$\begin{aligned} \mathbf{c}_i \cdot \frac{\partial f_i}{\partial \mathbf{r}} &= \sum_{j=1}^n J(f_i, f_j), \\ f_i^+(\mathbf{r}, \mathbf{c}_i) &= A f_i^-(\mathbf{r}, \mathbf{c}_i), \quad \mathbf{c}_i \cdot \mathbf{n}_r > 0, \quad \mathbf{r} \in \partial S, \end{aligned} \quad (1)$$

where  $\mathbf{c}_i$  is the molecular velocity (of species  $i$ ),  $\mathbf{r}$  is the position coordinate,  $J$  is the nonlinear collision operator,  $\mathbf{n}_r$  is a unit vector normal to the surface and directed into the gas-vapor mixture,  $f_i^-$  is the incident distribution,  $f_i^+$  is the emergent distribution, and  $A$  is a general gas-surface scattering operator (which includes reactions, condensation, accommodation coefficients, etc.).

The driving terms in the problem are the partial pressure gradients  $\nabla P_{i,asy}(\mathbf{r})$  and the temperature gradient  $\nabla T_{asy}(\mathbf{r})$  and, hence, the overall partial pressure differences and the temperature difference.

The quantities of major interest in this problem are the mass fluxes,  $\mathbf{J}_i$ , and the total heat flux,  $\mathbf{J}_Q$ , which are expressed as:

$$\begin{aligned} \mathbf{J}_i &= \int m_i \mathbf{c}_i f_i(\mathbf{r}, \mathbf{c}_i) d\mathbf{c}_i, \\ \mathbf{J}_Q &= \int \frac{1}{2} m_i \mathbf{c}_i^2 \mathbf{c}_i f_i(\mathbf{r}, \mathbf{c}_i) d\mathbf{c}_i. \end{aligned} \quad (2)$$

It is useful, however, to consider only the diffusive and conductive components (both with respect to the mean mass velocity,  $\mathbf{V}$ ) which are expressed as:

$$\begin{aligned} \mathbf{J}_{i,d} &= \int m_i (\mathbf{c}_i - \mathbf{V}) f_i(\mathbf{r}, \mathbf{c}_i) d\mathbf{c}_i = \mathbf{J}_i - \rho_i \mathbf{V}_i, \\ \mathbf{J}_h &= \sum \int \frac{1}{2} m_i (\mathbf{c}_i - \mathbf{V})^2 (\mathbf{c}_i - \mathbf{V}) f_i(\mathbf{r}, \mathbf{c}_i) d\mathbf{c}_i. \end{aligned} \quad (3)$$

For small gradients, one can write:

$$\begin{aligned} \mathbf{J}_{i,d} &= \sum L_{j,dd} \mathbf{X}_j + L_{i,dh} \mathbf{X}_h, \\ \mathbf{J}_h &= \sum \frac{P_0}{\rho_i} L_{i,hd} \mathbf{X}_i + L_{hh} \mathbf{X}_h, \end{aligned} \quad (4)$$

where:

$$\begin{aligned} \mathbf{X}_i &= \nabla (P_{i,asy}(\mathbf{r}) - P_{i,0}) / P_{asy}, \\ \mathbf{X}_h &= \nabla (T_{i,asy}(\mathbf{r}) - T) / T_0. \end{aligned} \quad (5)$$

Here,  $L_{i,dd}$  and  $L_{hh}$  are the phenomenological coefficients due to the direct effects, and  $L_{i,dh}$  and  $L_{i,hd}$  are the coefficients related to the cross-effects. These coefficients are known for continuum conditions but what we require is information for the entire range of Knudsen numbers.

## II. RESEARCH OBJECTIVES

Our main objective has been to obtain greater understanding of the heat and mass transfer for a gas-vapor mixture with an emphasis on the cross-effects and their role in micro-gravity experiments. Towards this goal we have sought to :

1. Solve the Boltzmann and the Wang-Chang and Uhlenbeck equations to determine the flow (mass or heat) rates and the matrix of the phenomenological coefficients,  $L$ , for arbitrary Knudsen number (ratio of mean free path to characteristic flow dimension), arbitrary gas mixtures, realistic intermolecular and gas-surface interaction potentials, and for both small gradients (linear problems) as well as large gradients (non-linear problems);
2. Verify our results by acquiring experimental data;
- 3 And, explore applications of our results to simulations of flows in ampoules.

## III. PROGRESS

We have made progress on all aspects of the project. Concerning the first objective, we have:

- Solved numerically the Boltzmann equation for a monatomic gas under non-condensing conditions assuming rigid sphere molecules and a cylindrical geometry. All of the phenomenological coefficients have been computed.
- Computations for realistic potentials (monatomic gas) as well as the velocity and the creep slip have been completed. The creep slip is found to be dependent on the type of gas and our results confirm the accuracy of recently reported variational results.
- The variational technique also has been extended and it has been shown that planar flows can be computed very efficiently, for all Knudsen numbers, by use of the Burnett solutions.
- The velocity, diffusion and creep slips also have been computed for gas mixtures. The creep slip has been found to have previously unknown dependencies on mixture properties. Jump coefficients appropriate to condensing as well non-condensing environments have been computed.
- For gas mixtures, an integral representation of the linearized Boltzmann operator, convenient for numerical and variational computations for all intermolecular force laws, has been obtained. The kernels are currently being used for computation of the flows.

For the measurement of the cross-flows:

- A glass, two-bulb, capillary apparatus for isothermal experiments was designed, built, and tested. Experimental data on two gas mixtures (Ar-He, N<sub>2</sub>-He) at several pressures (0.1 torr to 40 torr total pressure) and mole ratios have been obtained and are found to be in good agreement with the theoretical predictions for the diffusion slip.
- A stainless steel two-bulb capillary apparatus for non-isothermal experiments was designed, built, and tested. For isothermal conditions, data on two gas mixtures (Ar-He, N<sub>2</sub>-He) at several pressures (0.5 torr to 20 torr total pressure) and mole ratios previously examined with the glass apparatus have been reproduced. For non-isothermal conditions, extensive data acquisition for single gases as well as for several gas mixtures has been performed and is continuing.
- Measurements of tangential momentum accommodation coefficients for several gases and gas mixtures in the transition regime have been completed by observing the torque on a levitated rotating sphere (aka. the spinning rotor or the molecular drag pressure gauge) in controlled environments.
- We have also formulated a theory for the spinning rotor gauge in the slip regime. This has allowed new measurements of viscosities and tangential momentum accommodation

coefficients in several monatomic and polyatomic gases. Measurements are now being extended to gas mixtures.

Regarding the application of our new results:

- We have completed application of the FIDAP code for calculation of condensing flows in ampoules in the continuum regime. The results agree well with those of Duval who had used different numerical approaches. These calculations, in collaboration with Dr. Duval, are now being extended to include slips and jumps.

Our stainless steel two-bulb experimental apparatus is shown in Fig. 1. A comparison of the experimental data for the thermal transpiration ratio with the calculated results (based on the Boltzmann equation and rigid sphere molecules) is shown in Fig. 2. Some typical experimental data corresponding to flows of rarefied gas mixtures under temperature gradients are shown in Fig. 3. A cross-sectional view of the spinning rotor gauge is shown in Fig. 4 and some typical data and results obtained with it are shown in Fig. 5 and listed in Table 1.

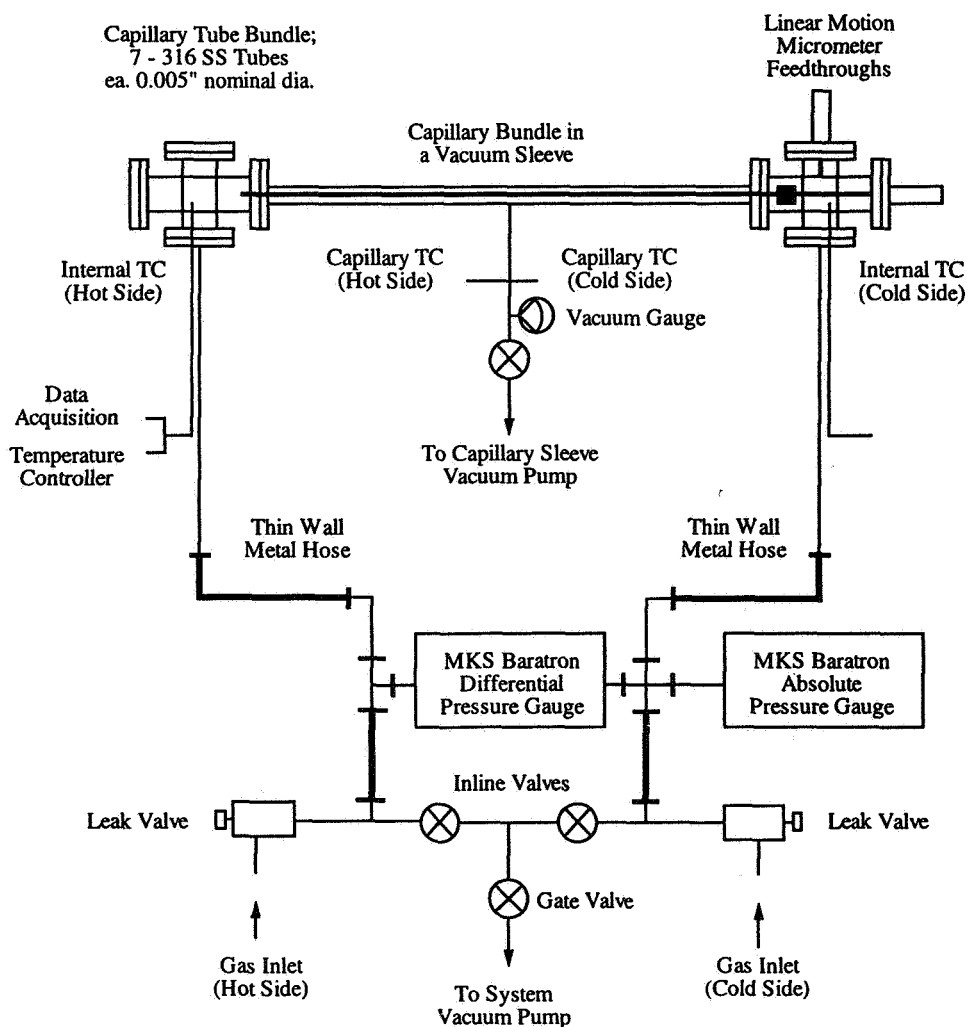


Fig. 1: Stainless steel two-bulb capillary apparatus. The hot side is heated by an electric heater tape and is heavily insulated. The cold side is regulated by circulating coolant from a refrigerated circulator bath and is also insulated.

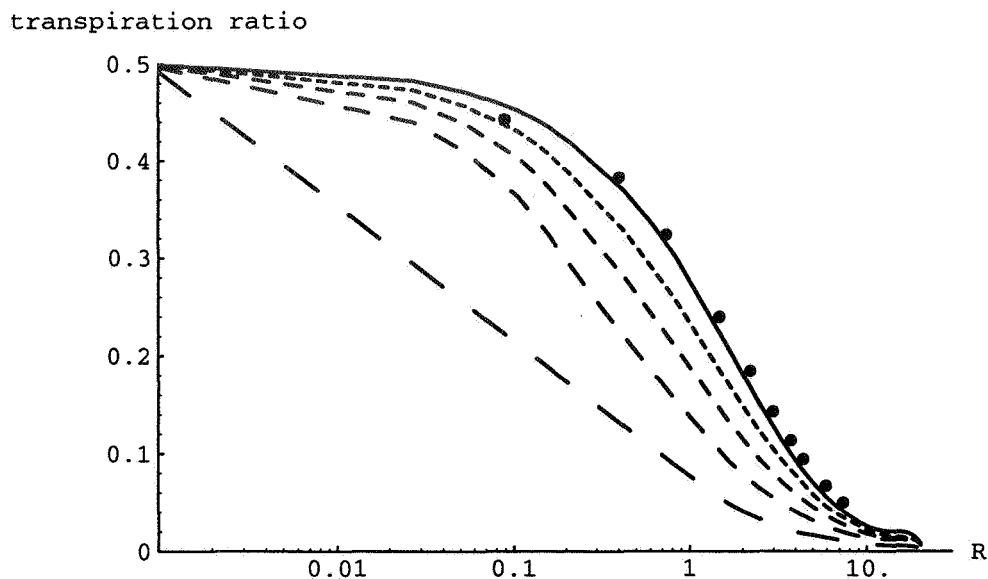


Fig. 2: Thermal transpiration ratio,  $(\Delta p/p)/(\Delta T/T)$ , for a rigid sphere gas as a function of the inverse Knudsen number,  $R$  (capillary radius/mean free path), and the coefficient of diffuse specular reflection,  $\alpha$ . The solid line corresponds to  $\alpha = 1$ . The lowest dashed line corresponds to  $\alpha = 0.2$ . The dots indicate our experimental data for helium.

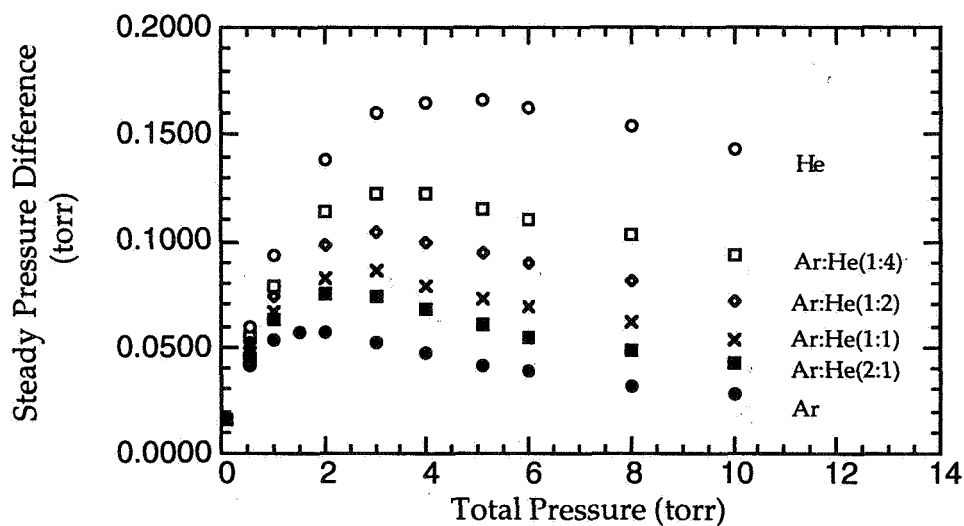


Fig. 3: The steady pressure difference of Ar-He gas mixtures as a function of the total system pressure for different mole fractions in the stainless steel two-bulb capillary apparatus.

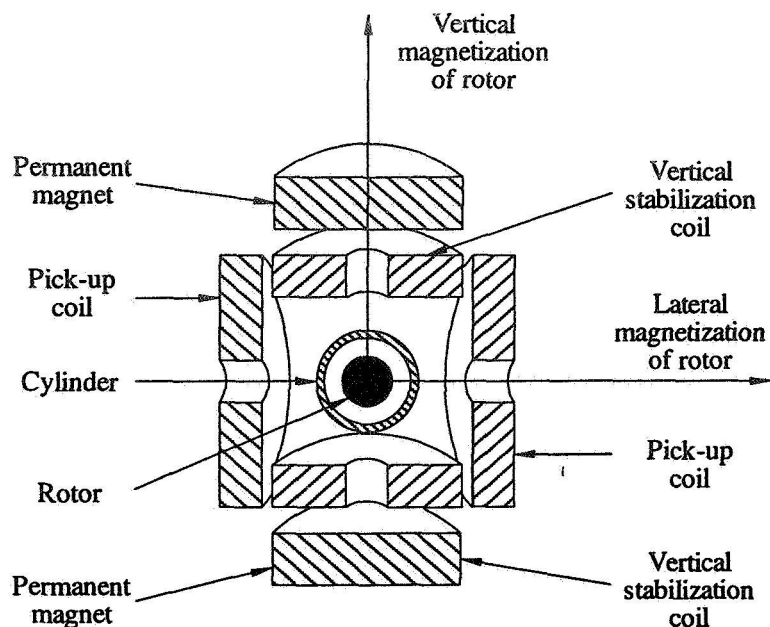


Fig. 4: A Cross-sectional view of the spinning rotor gauge.

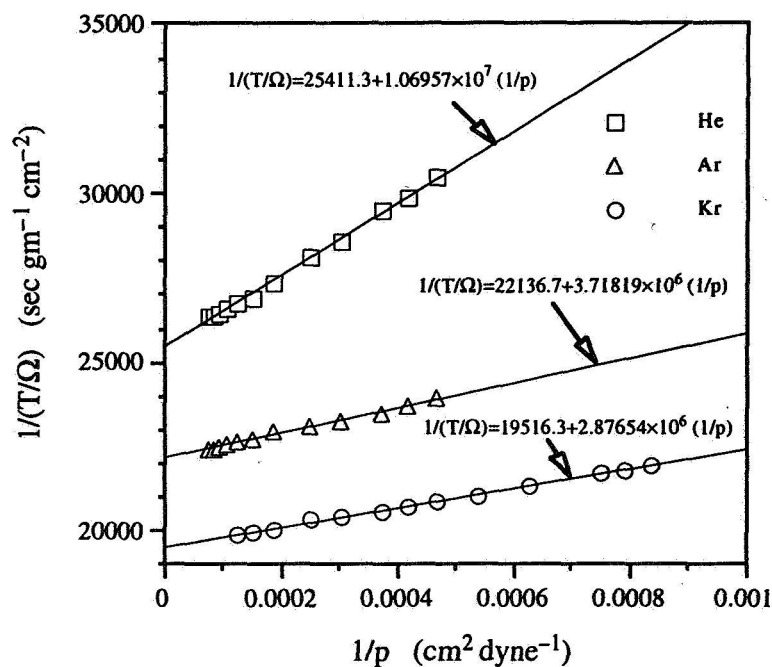


Fig. 5: The reciprocal of the torque plotted as a function of the reciprocal pressure for He, Ar and Kr in the slip regime. Values of the torque were determined from angular retardation rates measured with a spinning rotor gauge employing a 3.85 mm diameter steel rotor. The inner diameter of the surrounding cylinder was 7.00 mm. Linear least-squares fits to each set of data are also shown.



TABLE 1. Viscosities, velocity slip coefficients, and tangential momentum accommodation coefficients obtained with the spinning rotor gauge. The quantities shown are averaged over three sets of data for the 3.85 mm and 4.50 mm spheres, and over four sets of data for the 4.00 mm sphere. The reciprocal of the torque on a spinning rotor is first plotted against the reciprocal of the pressure. A linear, least-squares fit is then made to the data in the slip regime. The slope of this line is then proportional to the velocity slip coefficient while the intercept is inversely proportional to the viscosity. The tangential momentum accommodation coefficient is calculated directly from the velocity slip coefficient.

Gas	Rotor diameter (mm)	Dynamic viscosity ( $\times 10^7$ ) (gm cm <sup>-1</sup> sec <sup>-1</sup> )	Velocity slip coefficient	Tangential momentum accommodation coefficient
He	3.85	1973	1.0657	0.9599
	4.00	1973	1.1041	0.9542
	4.50	1973	1.1848	0.9043
Ar	3.85	2257	1.1661	0.9128
	4.00	2254	1.1742	0.9105
	4.50	2228	1.2837	0.8626
Kr	3.85	2557	1.3546	0.8356
	4.00	2539	1.1222	0.9330
	4.50	2525	1.3896	0.8223

## BIBLIOGRAPHY

1. Ivchenko, I. N., Loyalka, S. K. and Tompson, R. V., "On the Use of Conservation Laws in Planar Slip Flow Problems," *High Temperature* **33**(1), 66-72 (1995).
2. Ivchenko, I. N., Loyalka, S. K. and Tompson, R. V., "On the Collision Kernels for Gas Mixtures," *Ann. Nuc. Energy* (Accepted, to appear in 1996).
3. Gabis, D. H., Loyalka, S. K. and Storvick, T. S., "Measurements of the Tangential Momentum Accommodation Coefficient in the Transition Flow Regime with a Spinning Rotor Gauge," *JVST A* (Accepted, to appear in August 1996).
4. Loyalka, S. K., "Theory of the Spinning Rotor Gauge in the Slip Regime," *JVST A* (Accepted, to appear in September 1996).
5. Tekasakul, P., Bentz, J. A., Tompson, R. V. and Loyalka, S. K., "The Spinning Rotor Gauge: Measurements of Viscosity, Velocity Slip Coefficients, and Tangential Momentum Accommodation Coefficients," *JVST A* (Accepted, to appear in September 1996).
6. Ivchenko, I. N., Loyalka, S. K. and Tompson, R. V., "Slip Coefficients for a Binary Gas Mixture I," (submitted).



# DYNAMICAL MODELING OF SURFACE TENSION

J. U. Brackbill and D. B. Kothe

Theoretical Division, Los Alamos National Laboratory  
Los Alamos, NM 87545

In a recent review it is said that free-surface flows “represent some of the difficult remaining challenges in computational fluid dynamics” [Tsai and Yue, 1996]. There has been progress with the development of new approaches to treating interfaces, such as the level-set method and the improvement of older methods such as the VOF method [Kothe *et al.*, 1996].

A common theme of many of the new developments has been the regularization of discontinuities at the interface. One example of this approach is the continuum surface force (CSF) formulation for surface tension, which replaces the surface stress given by Laplace’s equation by an equivalent volume force [Brackbill *et al.*, 1992].

Here, we describe how CSF formulation might be made more useful. Specifically, we consider a derivation of the CSF equations from a minimization of surface energy as outlined by Jacqmin [1996]. This reformulation suggests that if one eliminates the computation of curvature in terms of a unit normal vector, parasitic currents may be eliminated. For this reformulation to work, it is necessary that transition region thickness be controlled. Various means for this, in addition to the one discussed by Jacqmin [1996], are discussed.

## Derivation of the CSF Equations from an Energy Functional

Beginning with the energy attributed by Jacqmin [1996] to van der Waals, we show that minimization of the surface energy is equivalent to Plateau’s problem [Logan], in which surface area is minimized. Further, following Jacqmin’s virtual work argument, we derive a CSF-like formulation. The difference between this and the standard CSF formulation illuminates the origin of parasitic currents and suggests that these are best eliminated by controlling the interface thickness.

Consider an incompressible fluid with density  $\rho_1$  in region  $\Omega$  separated by a closed surface  $\partial\Omega$  from a second incompressible fluid with density  $\rho_2$ ;

$$\rho = \begin{cases} \rho_1, & \mathbf{x} \in \Omega \\ \rho_2, & \mathbf{x} \notin \Omega. \end{cases} \quad (1)$$

On  $\partial\Omega$ , in the usual surface tension formulation given by Laplace’s equation, a surface stress boundary condition is imposed,

$$(p_1 - p_2 + \sigma\kappa)\hat{\mathbf{n}} = 0, \quad (2)$$

where  $p_{1,2}$  is the pressure in fluids 1 and 2,  $\sigma$  is the surface tension coefficient, and  $\kappa$  is the local surface curvature.

In the CSF model, the density,  $\rho$ , is replaced by a regularized density that is calculated by convolving  $\rho(\mathbf{x})$  with an interpolation function,  $S(\mathbf{x}' - \mathbf{x}; h)$ .  $S$  has bounded support

$h$ , is normalized, and decreases monotonically with increasing  $|\mathbf{x} - \mathbf{x}'|$ . The regularized density,

$$\tilde{\rho}(\mathbf{x}) = \frac{1}{h^3} \int_v \rho(\mathbf{x}') S(\mathbf{x} - \mathbf{x}') d^3 x' , \quad (3)$$

is differentiable,

$$\nabla \tilde{\rho}(\mathbf{x}) = \frac{1}{h^3} \int \rho(\mathbf{x}') \nabla S(\mathbf{x} - \mathbf{x}') d^3 x' . \quad (4)$$

Consider the term in the surface-energy integral, given by Jacqmin [1996].

$$e = \int d^3 x \left[ \frac{1}{2} \alpha \nabla \tilde{\rho}(\mathbf{x}) \cdot \nabla \tilde{\rho}(\mathbf{x}) + \beta f(p) \right] , \quad (5)$$

in which the first term is proportional to composition gradients. As in Brackbill *et al.* [1992],  $\nabla \tilde{\rho}$  is given by an integral over the interface,

$$\nabla \tilde{\rho}(\mathbf{x}) = \frac{[\rho]}{h^3} \int_{\partial\Omega} \hat{\mathbf{n}}(\mathbf{x}_s) S(\mathbf{x} - \mathbf{x}_s) dA , \quad (6)$$

where  $[\rho] = \rho_1 - \rho_2$ . Substituting this expression into Eq. (5) and setting  $\beta = 0$  gives

$$I = \frac{[\rho]^2}{h^2} \int_{\partial\Omega} \int_{\partial\Omega'} \hat{\mathbf{n}}(\mathbf{x}_s) \cdot \hat{\mathbf{n}}(\mathbf{x}'_s) T(\mathbf{x}_s, \mathbf{x}'_s; h) dA dA' , \quad (7)$$

where  $T$  is a “mass-matrix” defined by

$$T(\mathbf{x}_s, \mathbf{x}'_s; h) = \frac{1}{h^4} \int d^3 x S(\mathbf{x} - \mathbf{x}'_s) S(\mathbf{x} - \mathbf{x}_s) . \quad (8)$$

Clearly, when  $h$  is small compared with the local radius of curvature,  $T = \delta(\mathbf{x}_s - \mathbf{x}'_s)$ , and the ratio of  $e$  to the area of the interface is a constant,

$$A = e/[\rho]^2/h^2 . \quad (9)$$

Thus, minimizing the energy integral (with  $\beta = 0$ ) is equivalent to minimizing the surface area, a classic variational problem called Plateau’s problem [Logan, 1987].

Following Jacqmin, we include the surface energy contribution in the total energy of the fluid,

$$E = \int \frac{1}{2} \rho \mathbf{u}^2 + \frac{1}{2} \alpha (\nabla \rho)^2 dV . \quad (10)$$

For simplicity, we neglect the wall-surface energy. Energy is a constant of the motion, so that

$$0 = \int \left[ \frac{\partial}{\partial t} \frac{1}{2} \rho \mathbf{u}^2 + \alpha \nabla \rho \cdot \frac{\partial}{\partial t} \nabla \rho \right] dV . \quad (11)$$

The first term is the work done by forces acting on the fluid,

$$\frac{\partial}{\partial t} \frac{1}{2} \rho \mathbf{u}^2 = \mathbf{u} \cdot \mathbf{F} . \quad (12)$$

The second term can be integrated by parts to yield

$$0 = \int \mathbf{u} \cdot [\mathbf{F} + \alpha (\nabla^2 \rho) \nabla \rho] dV , \quad (13)$$

where we have substituted the continuity condition for an incompressible fluid,

$$\frac{\partial \rho}{\partial t} = -\mathbf{u} \cdot \nabla \rho . \quad (14)$$

Conservation of energy must hold whatever the velocity. Thus the surface tension force is given by

$$\mathbf{F} = -\alpha (\nabla^2 \rho) \nabla \rho \quad (15)$$

or substituting  $\mathbf{n} = \nabla \rho$ ,

$$\mathbf{F} = -\alpha (\nabla \cdot \mathbf{n}) \mathbf{n} .$$

By comparison, the CSF force is

$$\mathbf{F}_{\text{CSF}} = \sigma \kappa(\mathbf{x}) \frac{\nabla \tilde{\rho}(\mathbf{x})}{[\rho]} , \quad (16)$$

where the curvature is given by

$$\kappa = -\nabla \cdot \hat{\mathbf{n}} . \quad (17)$$

Since  $\mathbf{n} \cong \frac{[\rho]}{h} \hat{\mathbf{n}}$ , then

$$\nabla \cdot \mathbf{n} = \frac{[\rho]}{h} \nabla \cdot \hat{\mathbf{n}} + 0 \left( \frac{h}{R} \right)^2 \quad (18)$$

and  $F_{\text{CSF}}$  and the variational force are equal when

$$\alpha = \frac{h}{[\rho]^2} \sigma . \quad (19)$$

(Jacqmin, using the incompressible flow condition,

$$\nabla \cdot \mathbf{u} = 0 , \quad (20)$$

integrates by parts the second term in Eq. (13) to derive the potential form of the surface tension,

$$\mathbf{F} = -\rho \nabla \mu , \quad (21)$$

where  $\mu = -\alpha \nabla^2 \tilde{\rho}$  is the chemical potential.)

### Parasitic Currents

Parasitic currents are a troubling artifact of the CSF formulation. These slowly growing vortical flows in the transition region are driven by a vorticity source term equal

to  $\nabla \times \mathbf{F}/\rho$ . Jacqmin's form, Eq. (21), gives no contribution to this term. Equation (15) does give a contribution,

$$\nabla \times \mathbf{F}/\rho = -\frac{\alpha}{\rho} \nabla(\nabla^2 \rho) \times \nabla \rho. \quad (22)$$

This contribution will be nonzero until the "curvature,"  $\nabla^2 \rho$ , of the interface is equal to a constant. Since this minimizes the surface energy, it would seem to be the correct physical result. The CSF formulation gives a similar contribution,

$$\nabla \times \mathbf{F}/\rho = \frac{\sigma}{[\rho]} \nabla \kappa \times \nabla \tilde{\rho}. \quad (23)$$

However, the calculation of the unit normal from the gradient of the density requires some care to avoid singularity, which appears to cause relatively large alterations of the curvature with small displacements of the interface. These, we believe, are the most probable source of the parasitic currents.

### Comments on Controlling Transition Region Thickness

The essential difference between the CSF formulation, which was derived by the construction of a surface delta function that reproduces Laplace's equation in the limit of vanishing  $h$ , and the variational form is in the expression for the curvature. In the variational form,  $\nabla \cdot \mathbf{n}$  replaces  $\kappa = -\nabla \cdot \hat{\mathbf{n}}$ . This substitution is valid if the transition region remains narrow.

Particle-in-cell methods and front-tracking methods in general provide solutions which preserve narrow transition regions. Further, as Kothe *et al.* note [2], the VOF technique eliminates numerical diffusion normal to the interface. (An example of a VOF calculation in three dimensions is shown in Fig. 1.) Thus, it is reasonable to expect that a reformulation of the CSF model which eliminates the calculation of the unit normal can be successfully implemented in a numerical code.

One can also consider techniques that actively control interface thickness. For example, in Jacqmin's formulation, the second term in the surface energy integral, Eq. (5), controls the thickness of the interface. Jacqmin notes that its effect is to segregate two immiscible fluids. By appropriate choices of  $f(\rho)$ , this term introduces a nonlinear diffusion that tends to narrow the transition region.

The use of this term in the energy integral to steepen the interface appeals to a physical cause. However, interface steepening can be introduced in a formulation that is purely numerical. Yabe [Yabe and Xiao, 1995], for example, discusses the convection of the density, Eq. (1), described in one dimension by

$$\frac{\partial \rho}{\partial t} + u_i \frac{\partial \rho}{\partial x_i} = 0. \quad (24)$$

The same equation describes the advection of any function of  $\rho$ ,

$$\frac{\partial F(\rho)}{\partial t} + u_i \frac{\partial F(\rho)}{\partial x_i} = 0. \quad (25)$$

Specifically, Yabe and Xiao consider the tangent function,

$$F(\rho) = \tan [0.99\pi (\rho/\langle\rho\rangle - 0.5)] , \quad (26)$$

where  $\langle\rho\rangle = 1/2(\rho_1 + \rho_2)$ . The factor 0.99 avoids infinite values when  $\rho = \rho_1$  or  $\rho_2$ . It is necessary, of course, that  $\rho_1 \leq \rho \leq \rho_2$ .

The technique maintains the sharpness of the transition region in the following way. The numerical solution of Eq. (25) will result in some numerical diffusion with diffusivity,  $\sigma = \sigma(\Delta x^n, \Delta t^m)$ . Thus, the associated equation can be written (in one dimension)

$$\frac{\partial F}{\partial t} + u_i \frac{\partial F}{\partial x_i} = \sigma \frac{\partial^2 F}{\partial x_i^2} . \quad (27)$$

Substituting this equation into the original advection equation (24), with the transformation given by Eq. (26), one finds that solutions of the ordinary differential equation,

$$\frac{d^2\rho}{dx^2} + \pi F(\rho) \left( \frac{d\rho}{dx} \right)^2 = 0 , \quad (28)$$

are stationary solutions of Eq. (24). The solution to this equation,

$$\rho = \frac{2}{\pi} \tan^{-1} (e^{\pi x}) , \quad (29)$$

is a continuous function with a steep transition between two nearly constant states.

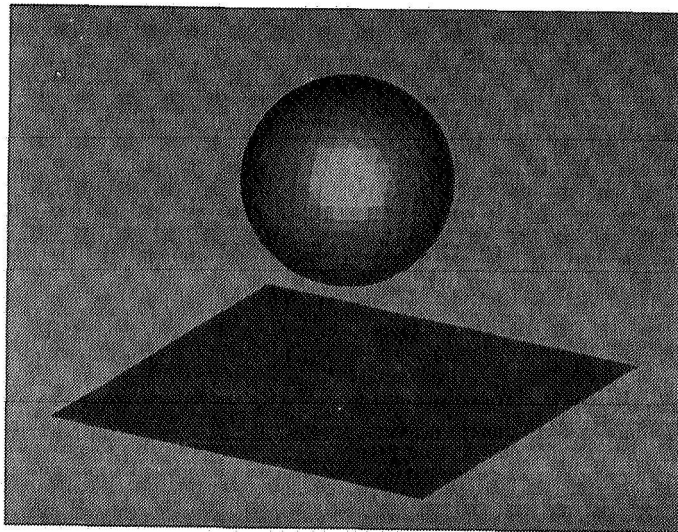
## References

1. W. T. Tsai and D. K. P. Yue, "Computation of Nonlinear Free-Surface Flows," *Ann. Rev. Fl. Mech.* **28**, 249–278, 1996.
2. D. B. Kothe, W. C. Rider, S. J. Mosso, J. S. Brock, and J. L. Hochstein, "Volume Tracking of Interfaces Having Surface Tension in Two and Three Dimensions," 34th Aerospace Science Meeting, Reno, January 1996, paper AIAA 96-0859.
3. J. U. Brackbill, D. B. Kothe, and C. Zemach, "A Continuum Method for Modeling Surface Tension," *J. Comput. Phys.* **100**, 335, 1992.
4. D. Jacqmin, "An Energy Approach to the Continuum Surface Tension Method," 34th Aerospace Sciences Meeting, Reno, January 1996, paper AIAA 96-0858.
5. J. David Logan, *Applied Mathematics*, John Wiley, New York, 1996.
6. T. Yabe and F. Xiao, "Description of Complex and Sharp Interface with Fired Grids in Incompressible and Compressible Fluids," *Computers Math. Applic.* **29**, 15–25, 1995.

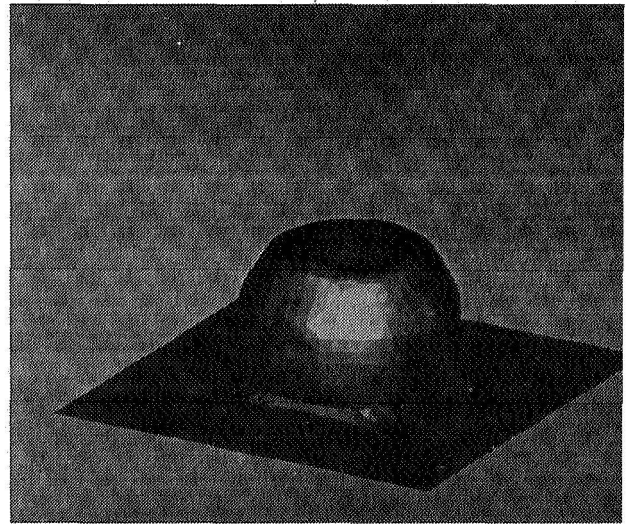
### Figure Captions

A shallow-pool drop splash calculation is shown in Figs. 1–4. The mesh spans  $[0.0, 8.0]$  (cm) in the  $x$  and  $y$  directions and  $[-8.0, 8.0]$  (cm) in the  $z$  direction with  $16 \times 16 \times 32$  cells. A spherical drop with a 4.0 cm radius is centered at  $(0.0, 0.0, 3.0)$  above a shallow pool in the  $xy$  plane that occupies  $z = [-8.0, -5.5]$ . The drop and pool are the same fluid, with 10 times the density of the background fluid density. Surface tension is neglected and the fluids are assumed to be inviscid. Gravity is  $(0.0, 0.0, -980.6)$  cm/s<sup>2</sup>. Interfaces are tracked with our new 3-D piecewise planar volume tracking algorithm, and the incompressible flow is modeled with an approximate projection technique.

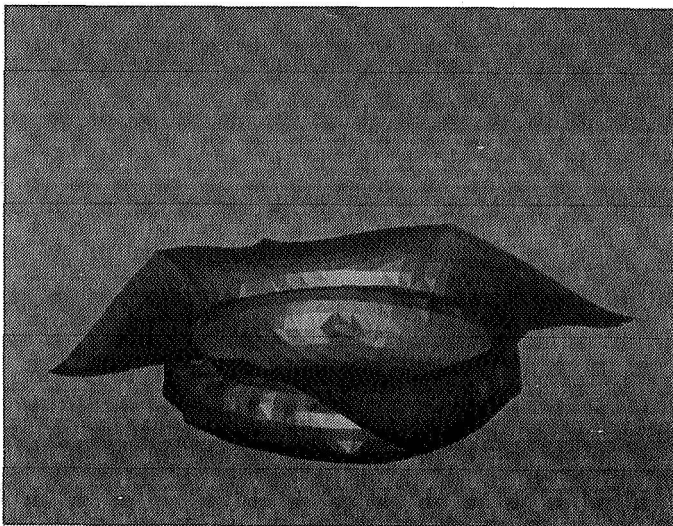
The drop size is large compared to the shallow pool (having a volume 25% of the pool volume), so the drop impact on the pool generates a sizable splash and rebound jet, as seen in Figs. 3 and 4. Plotted are isosurfaces of the  $1/2$  volume fraction level at  $t = 0$  (1),  $t = 0.12$  (2),  $t = 0.20$  (3), and  $t = 0.40$  (4).



(1)



(2)



(3)



(4)



# **Electric and Magnetic Effects**



# CONTROL OF FLOWING LIQUID FILMS BY ELECTROSTATIC FIELDS IN SPACE

S. George Bankoff, Michael J. Miksis, and Hyo Kim<sup>1</sup>  
Northwestern University  
Evanston, Ill. 60208 USA

## ABSTRACT

A novel type of lightweight space radiator has been proposed which employs internal electrostatic fields to stop coolant leaks from punctures caused by micrometeorites or space debris. Extensive calculations have indicated the feasibility of leak stoppage without film destabilization for both stationary and rotating designs. Solutions of the evolution equation for a liquid-metal film on an inclined plate, using lubrication theory for low Reynolds numbers, Karman-Pohlhausen quadratic velocity profiles for higher Reynolds numbers, and a direct numerical solution are shown. For verification an earth-based falling-film experiment on a precisely-vertical wall with controllable vacuum on either side of a small puncture is proposed. The pressure difference required to start and to stop the leak, in the presence and absence of a strong electric field, will be measured and compared with calculations. Various parameters, such as field strength, film Reynolds number, contact angle, and hole diameter will be examined. A theoretical analysis will be made of the case where the electrode is close enough to the film surface that the electric field equation and the surface dynamics equations are coupled. Preflight design calculations will be made in order to transfer the modified equipment to a flight experiment.

## INTRODUCTION

Electrostatic forces are inherently weak relative to gravitational forces, and hence have been of limited use in controlling liquid jets, films, etc. In microgravity environments, however, the situation is quite different, and some interesting new applications arise. The usages of electric fields for effecting and improving phasic separations, ionic separations, and molecular separations are well-known. However, the effect of strong electrostatic fields on free-surface flows, and in particular, the flow of thin films on a solid substrate is quite new, and potentially of considerable practical importance in microgravity.

Electric fields tend to pull a conductive (or dielectric) material into a non-conductive (or near vacuum) adjacent region. When applied to a free-flowing film, the electric field produces a surface wave, which may become unstable and contact the electrode above the film which produces the electric field. With proper design, however, the surface wave amplitude is limited to a safe value, and the wave is washed harmlessly away downstream. The tensile stress exerted by the field opposes the hydrostatic and vapor pressure tending to drive the liquid through a puncture caused by a collision with a micrometeorite or space debris. Hence this promises to be an effective device for stopping leaks from relatively large micrometeorite collisions, which

<sup>1</sup> Now with Korea Gas Co., Anson City, S. Korea

would make membrane-type pumped-loop space radiators practical. This should result in a considerable weight saving over heat pipe radiators.

The theory and possible designs have been extensively investigated by Kim, et al. (Refs. 1-5). These detailed analytical and design calculations have pointed to the feasibility and stability of several variants, both rotating and non-rotating, of the electrostatic liquid-film radiator concept. To test it experimentally would seem to require a microgravity environment. This is because on earth gravitational forces are many thousands of times greater than electrostatic forces. However, a relatively inexpensive, but sophisticated experiment has been devised which will allow preliminary testing of the leak-stopping concept on earth in our laboratory. Extensive tests will be performed over a three year period, after which a design study will be conducted for flight experiments for further tests under microgravity conditions.

In addition, we wish to examine a theoretical problem which extends the previous analytical work. Basic to the previous work was the assumption that the electric field (Laplace) equation is uncoupled from the evolution equation for the surface waves, since the distance from the electrode to the film is at least an order of magnitude greater than the thickness of the base film. When this is no longer true, the coupled equation system must be solved numerically, presenting a challenging problem for boundary integral methods.

#### THIN FILM FLOW ON AN INCLINED FLAT MEMBRANE

The simplest problem is flow of a thin film on an inclined flat plate, where the film is both stabilized and driven by gravity. In space gravity would be replaced by centrifugal force, produced by rotation and/or azimuthal flow along a curved surface, such as a cylinder. Figure 1 shows a flat membrane inclined at an angle  $\beta$  to the direction of gravity, above which a liquid film flows. Above the film is suspended a charged foil (electrode), whose field causes a standing trough, followed by a crest, in the film surface. The equations are the Laplace equation in the vacuum, and scaled continuity and momentum equations in the liquid. At the free liquid surface the boundary conditions are that the tangential electric field, the normal displacement field, the tangential stress and the normal stress are continuous, together with a kinematic condition on the fluid particles. The electric field appears only in the normal stress boundary condition. There are four dimensionless constants (Reynolds (Re), Froude (Fr), capillary (Ca) and electrostatic field numbers (K)) which need to be specified to solve the problem.

Here the capillary number is

$$Ca = \frac{2\mu U_0}{\sigma} \quad (1)$$

where  $\mu$  is the liquid viscosity,  $\sigma$  is surface tension and  $U_0$  is the average liquid velocity. The electrostatic field number is given by

$$K = \frac{\epsilon_0 d F^2}{16 \pi \mu U_0}, \quad (2)$$

where  $\epsilon_0$  is the vacuum dielectric constant,  $F$  is the electric field strength and  $d$  is the mean film thickness.

Since the length of the electrode in the direction of flow is effectively infinite, or at least large compared to the mean film thickness, a thin-film analysis is appropriate. This was performed for Reynolds numbers of  $O(1)$  (proposed experiment) and of  $O(1/\xi)$  (proposed radiator), where  $\xi \ll 1$  is the ratio of the film thickness to a characteristic length in the flow direction. In the former case lubrication theory can be employed, and a nonlinear evolution equation can be derived, in a similar fashion as many other investigators (Ref. 6), except that an electrostatic term has been added on the right-hand side.

The electric field is determined by solving the Laplace equation for the electric potential  $\phi(x, y)$  in the fluid  $\phi_f$ , and the electric potential,  $\phi_v$ , in the vacuum region above the fluid but below the charged plate (Figure 1). The fluid region,  $V_f$ , is defined by  $0 \leq y \leq h(x, t)$  and  $-\infty < x < \infty$ , where  $y = h(x, t)$  is the height of the film above the inclined plane, and the vacuum region,  $V_v$ , is defined by the strip  $-\infty < x < \infty$  and  $h(x, t) \leq y \leq \hat{H}$ . The boundary conditions are that

$$\phi(x, \hat{H}) = F \hat{H} \phi(x), \quad \text{for } y = \hat{H}, \quad (3a)$$

$$\phi = 0, \quad \text{for } y = 0. \quad (3b)$$

The function  $\phi(x)$  is a given dimensionless function of  $x$ , and the product  $F \hat{H}$  is a constant with units of electric potential. Along  $y = h(x, t)$  we have the boundary conditions that the tangential electric field and the normal displacement field are continuous (Landau, et al., 1984)

$$\phi^f(x, h, t) = \phi^v(x, h, t), \quad \epsilon_f \frac{\partial \phi^f}{\partial n} = \epsilon_0 \frac{\partial \phi^v}{\partial n}. \quad (4a, b)$$

Here  $\epsilon_f$  is the dielectric constant of the fluid and the partial derivative is in the direction of the outward unit normal,  $n$ , to the interface.

Following the now-standard procedures of Benney (Ref. 6) and Gjevik (Ref. 7) one can derive the nonlinear long-wave evolution equation for the film thickness as a function of time and space.

$$\frac{\partial h}{\partial t} + 3h^2 \frac{\partial h}{\partial x} + \xi \frac{\partial}{\partial x} \left[ \frac{6}{5} Re h^6 \frac{\partial h}{\partial x} - \cot(\beta) h^3 \frac{\partial h}{\partial x} + \frac{2}{3} \frac{\xi^2}{Ca} h^2 \frac{\partial^3 h}{\partial x^3} \right]$$

$$+ \frac{2}{3} \xi K \left( 1 - \frac{1}{\epsilon_f} \right) \frac{\partial}{\partial x} \left( h^3 \frac{\partial}{\partial x} [E_{on}^v]^2 \right) = 0 \quad (5)$$

Upon linearization, one can perform an Orr-Sommerfeld stability analysis, leading for long waves to the critical Reynolds number:

$$Re < \frac{5}{6} \cot(\beta) - \frac{10K}{9} H^2 \frac{\left( 1 - \frac{1}{\epsilon_f} \right)^2}{\left( \frac{1}{\epsilon_f} + H - 1 \right)^3} \quad (6)$$

where  $H$  is the height of the electrode above the mean film surface. If  $K = 0$ , the Yih-Benjamin (Refs. 9,10) expression for the critical Reynolds number is obtained.

It is found that shocks can form, after which the lubrication equation is no longer valid. Nevertheless, with a finite length electrode these disturbances can wash harmlessly out from under the electrode and be carried away downstream. For large Reynolds numbers, Karman-Pohlhausen-type equations are derived:

$$\frac{\partial h}{\partial t} = - \frac{\partial q}{\partial x} \quad (7)$$

$$\frac{\partial q}{\partial t} + \frac{\partial}{\partial x} \left( \frac{6}{5} \frac{q^2}{h} \right) = \frac{2\bar{K}h}{R} \frac{\partial}{\partial x} (E_n^v)^2 - \frac{3}{R} \frac{q}{h^2} + \frac{\cos(\beta)}{Fr^2} \left( \frac{h}{B} - h \frac{\partial h}{\partial x} \right). \quad (8)$$

where  $q$  is the volumetric flow rate per unit width.

From these equations a dispersion equation and steady-state solutions can be developed. Finally, numerical solutions, using the SOLA code, and a realistic electrostatic field, based on a single finite-length electrode rather than an infinite-length electrode, are obtained.

## RESULTS

The linear eigenvalue problem was solved numerically by a shooting method. Figure 2 shows the neutral stability curves (i.e.  $c_i = 0$ ) in the  $\alpha$  -  $Re$  plane for the case of  $Ca = \infty$ , i.e., no surface tension, and for  $Ca = 2 \times 10^{-4}$ , and for both  $K = 0$ , (no electric field) and  $K = 253.1$ . It is seen that small Reynolds number flows are stable, while increasing  $Re$  for fixed wavelength will cause the flow to become unstable. Note that the effect of the electric field is to lower the value of the critical Reynolds number at which the flow becomes unstable. Also note that the surface tension increases the critical Reynolds number for both  $K = 0$  and  $K$  not equal to zero.

We plot the steady solution of both the lubrication model with  $Ca = \infty$  in Figure 3 and the steady-state Karman-Pohlhausen approximation in Figure 4. In order to simulate a slowly-varying potential we set  $\Phi =$

$\exp(-100x^2)$ . This potential has the slowly varying form of the assumptions for  $\xi$  small. The steady lubrication model is a second-order ordinary differential equation, which can be integrated once to reduce it to a first order equation. With the higher Reynolds numbers, the tendency to form a shock is greatly reduced and the wave shapes and amplitudes are in fair agreement, despite the small Reynolds number implicit in the lubrication model. Figure 5 shows the development of the surface wave at  $Re = 189$ , as determined by numerical solution of the full equations. It is seen that a peak height is reached with time at an amplitude of about 30% of the mean layer thickness. However, since the electrode is far from the film, the wave will be washed harmlessly downstream out of the influence of the electrode. Figure 6 shows the pressure at the bottom of the liquid layer directly over the puncture, where  $p = 0$  in the vacuum. The combined dimensionless vapor pressure and hydrostatic head tending to drive the liquid out of the hole is more than balanced by tension (negative pressure) due to the electric field with a margin of about two. The tension can be made larger by increasing the field strength and/or the Reynolds number. Figures 7 and 8 show that the Karman-Pohlhausen method gives quite similar results to the direct numerical solution.

### CONCLUSIONS

Calculations by three methods show that leaks from a liquid-film radiator with internal electrodes and surface puncture detection can be stopped with a safety factor of at least two. An experiment on earth is being undertaken to test some of these predictions and to determine feasible operating conditions.

### ACKNOWLEDGMENT

The theoretical work was supported by a grant from the Nuclear Energy Division of the Department of Energy. The experimental work is being supported by a grant from NASA.

### REFERENCES

11. Kim, H.; Bankoff, S.G.; and Miksis, M.J.: Lightweight Space Radiator with Leakage Control by Internal Electrostatic Fields, Proc. Eighth Symp. on Space Nuclear Power Systems, Albuquerque, NM, CONF-910116, 1991, pp. 1280 1285.
2. Kim, H.; Bankoff, S.G.; and Miksis, M.J.: The Effect of an Electrostatic Field on Film Flow Down an Inclined Plane, Phys. Fluids, Vol. 4, 1992a, pp. 2117 2130.
3. Kim, H.; Bankoff, S.G.; and Miksis, M.J.: The Electrostatic Liquid-Film Radiator for Heat Rejection in Space. ASME/AIChE National Heat Transfer Conference, 1992, Anaheim, CA.
4. Kim, H.; Bankoff, S.G.; and Miksis, M.J.: Interaction of an Electrostatic Field with a Liquid Film Flow Within a Rotating Conical Space Radiator. AIAA J. Propulsion and Power, Vol. 9, 1993, pp. 245 254.
5. Kim, H.; Bankoff, S.G.; and Miksis, M.J.: The Cylindrical Electrostatic Liquid Film Radiator for Heat Rejection in Space, J. Heat Transfer, Vol. 116, 1994, pp. 986 992.
6. Bankoff, S.G.; Miksis, M.J.; Kim, H.; and Gwinner, R.: Design Considerations for the Rotating Electrostatic Liquid-Film Radiator: Proc. of the 6th Int. Topical Meeting on Nuclear Reactor Thermalhydraulics, Grenoble, France, Oct. 5-8; also in Nucl. Eng. and Design, Vol. 149, 1994, pp. 441 447.

7. Benney, D.J.; Long Waves on Liquid Films: J. Math. and Phys. 1966, Vol. 45, 150.
8. Gjevik, B.: Occurrence of Finite-Amplitude Surface Waves on Falling Liquid Films: Phys. Fluids, Vol. 13, 1970, 1918.
9. Benjamin, T.B.: Wave Formation in Laminar Flow Down an Inclined Plane: J. Fluid Mech. Vol. 2, 1957, p. 554.
10. Yih, C.S.: Stability of Liquid Flow Down an Inclined Plane: Phys. Fluids, Vol. 5, 1963, p. 321.



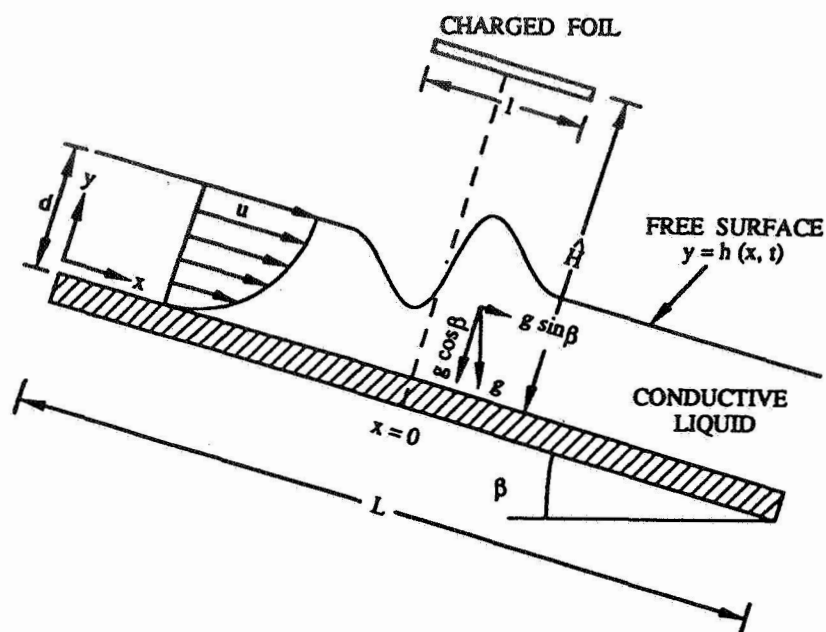


Fig. 1. The coordinate scheme of the plane flow with  $x = 0$  as puncture location.

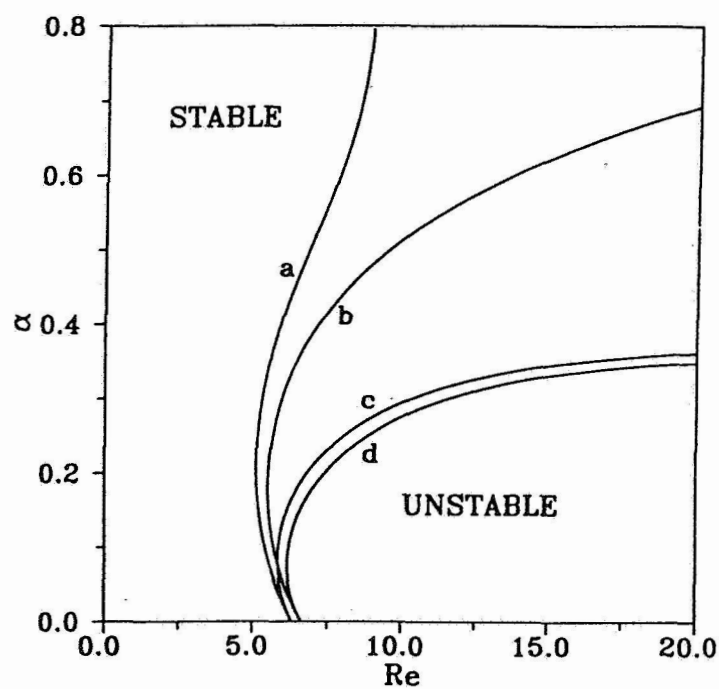


Fig. 2. Neutral stability curves in the  $\alpha$  -  $Re$  plane for  $\beta = 0.1$  radians,  $H = 13 \frac{1}{3}$  (a:  $K = 253.1$  and  $Ca = \infty$ , b:  $K = 0$  and  $Ca = \infty$ , c:  $K = 253.1$  and  $Ca = 2 \times 10^{-4}$  and d:  $K = 0$  and  $Ca = 2 \times 10^{-4}$ ).

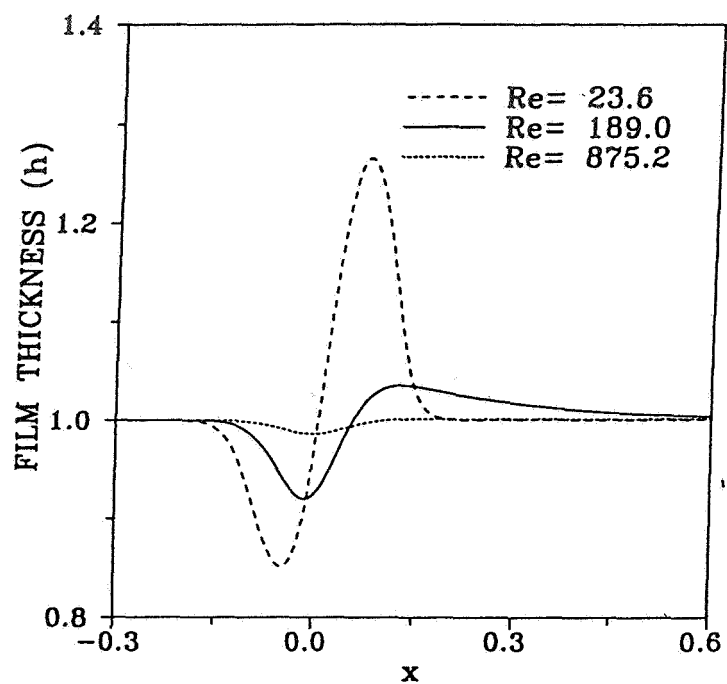


Fig. 3. Steady state solutions in the lubrication model with zero surface tension,  $F = 20\text{KV/cm}$  and  $\beta = 0.1$  rad ( $Re = 23.6, 189.0, 875.2$ ).

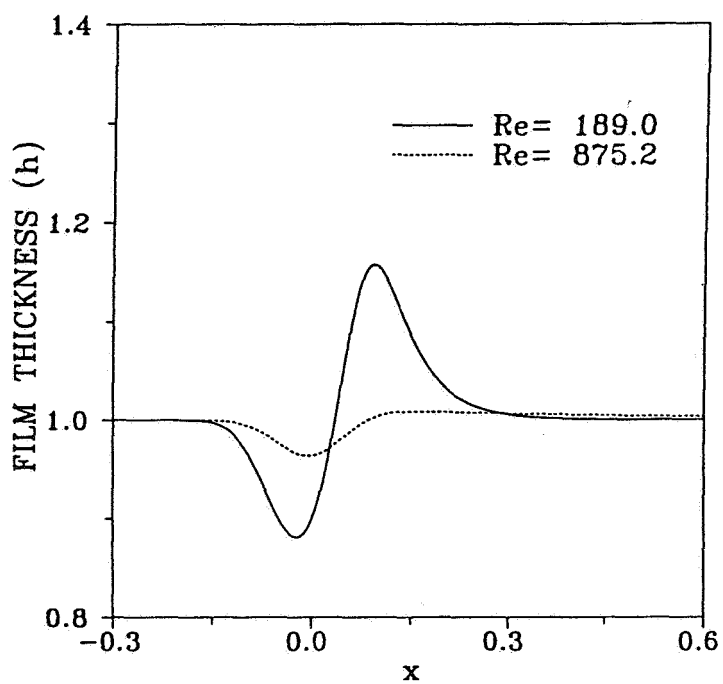


Fig. 4. Steady state solutions in the Karman-Pohlhausen model with zero surface tension,  $F = \text{KV/cm}$  and  $\beta = 0.1$  rad ( $Re = 189.0, 875.2$ ).

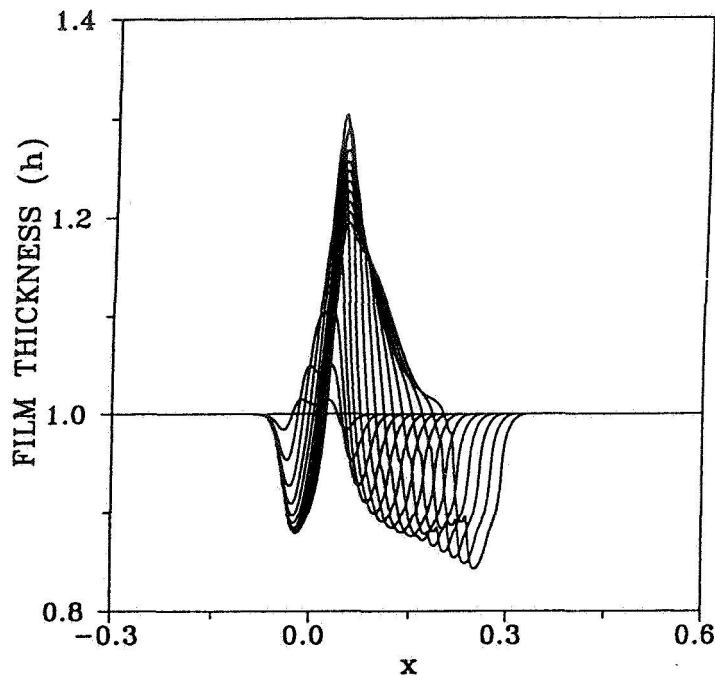


Fig. 5. Free surface  $h$  vs.  $x$  as determined by (2-5) - (2-13) for  $t = n(0.01)$ ,  $n = 1, \dots, 15$  with  $F = 20.0$  KV/cm,  $\beta = 0.1$  rad,  $d = 0.15$  cm,  $g = 100$  cm/s<sup>2</sup>,  $\sigma = 0$ ,  $Re = 189.0$ ,  $K = 28.87$ ,  $H = 13 \frac{1}{3}$  and the other parameter for lithium at 700°K.

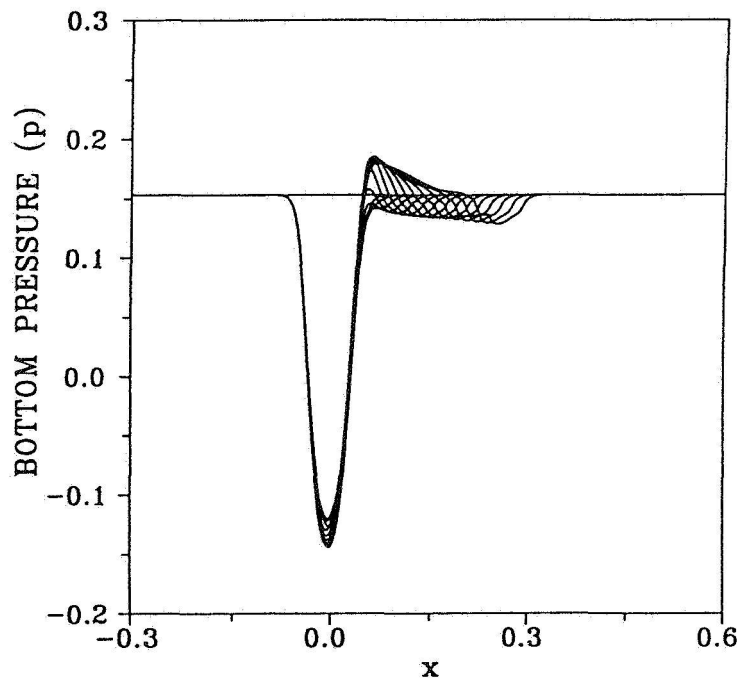


Fig. 6. Bottom pressure  $p$  vs.  $x$  as determined by (2.5) - (2-13) for  $t = n(0.01)$ ,  $n = 1, \dots, 15$  with  $F = 20.0$  KV/cm,  $\beta = 0.1$  rad,  $d = 0.15$  cm,  $g = 100$  cm/s<sup>2</sup>,  $\theta = 0$ ,  $Re = 189.0$ ,  $K = 28.87$ ,  $H = 13 \frac{1}{3}$  and the other parameter for lithium at 700° K.

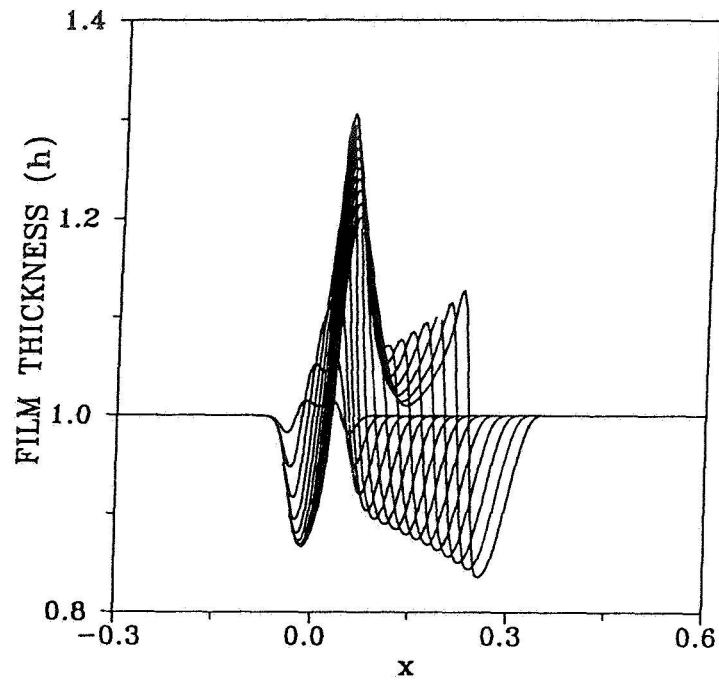


Fig. 7. Free surface  $h$  vs.  $x$  as determined by the Karman-Pohlhausen model (2.46) - (2-47) for  $t = n(0.01)$ ,  $n = 1, \dots, 15$  with  $F = 20.0$  KV/cm,  $\beta = 0.1$  rad,  $d = 0.15$  cm,  $g = 100$  cm/s<sup>2</sup>,  $\theta = 0$ ,  $Re = 189.0$ ,  $K = 28.87$ ,  $H = 13 \frac{1}{3}$  and the other parameter for lithium at  $700^\circ$  K

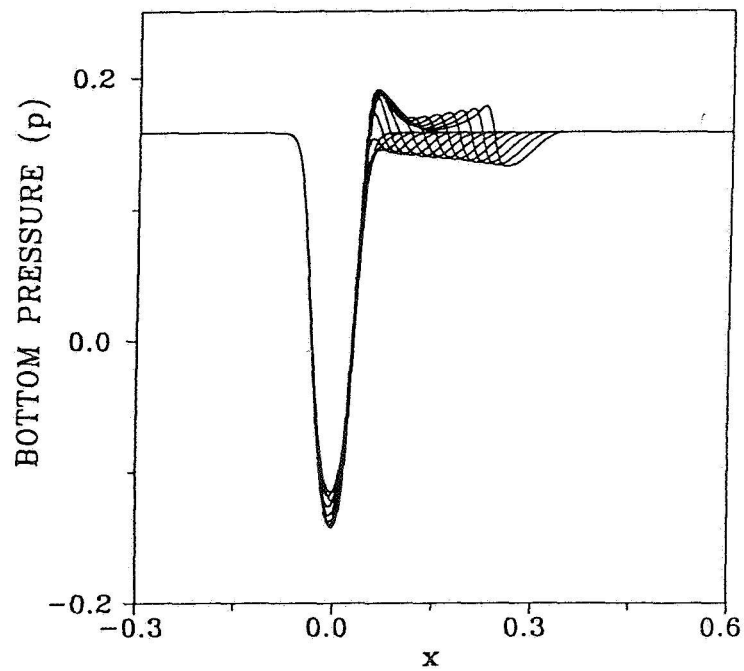


Fig. 8. Bottom pressure  $p$  vs.  $x$  as determined by the Karman-Pohlhausen model (2.46) - (2-47) for  $t = n(0.01)$ ,  $n = 1, \dots, 15$  with  $F = 20.0$  KV/cm,  $\beta = 0.1$  rad,  $d = 0.15$  cm,  $g = 100$  cm/s<sup>2</sup>,  $\theta = 0$ ,  $Re = 189.0$ ,  $K = 28.87$ ,  $H = 13 \frac{1}{3}$  and the other parameter for lithium at  $700^\circ$  K.

# MAGNETOTHERMAL CONVECTION IN NONCONDUCTING DIAMAGNETIC AND PARAMAGNETIC FLUIDS

Boyd F. Edwards, Department of Physics,  
Donald D. Gray, Department of Civil and Environmental Engineering, and  
Jie Huang, Department of Physics  
West Virginia University  
Morgantown, WV 26506

## ABSTRACT

Nonuniform magnetic fields exert a magnetic body force on electrically nonconducting classical fluids. These include paramagnetic fluids such as gaseous and liquid oxygen and diamagnetic fluids such as helium. Recent experiments show that this force can overwhelm the force of gravity even at the surface of the earth; it can levitate liquids and gases, quench candle flames, block gas flows, and suppress heat transport. Thermal gradients render the magnetic force nonuniform through the temperature-dependent magnetic susceptibility. These thermal gradients can therefore drive magnetic convection analogous to buoyancy-driven convection. This magnetothermal convection can overwhelm convection driven by gravitational buoyancy in terrestrial experiments.

The objectives of the proposed ground-based theoretical study are (a) to supply the magnetohydrodynamic theory necessary to understand these recent experiments and (b) to explore the consequences of nonuniform magnetic fields in microgravity. Even the linear theory for the onset of magnetothermal convection is lacking in the literature. We intend to supply the linear and nonlinear theory based on the thermohydrodynamic equations supplemented by the magnetic body force. We intend to investigate the effect of magnetic fields on gas blockage and heat transport in microgravity. Since magnetic fields provide a means of creating arbitrary, controllable body force distributions, we intend to investigate the possibility of using magnetic fields to position and control fluids in microgravity. We also intend to investigate the possibility of creating stationary terrestrial microgravity environments by using the magnetic force to effectively cancel gravity. These investigations may aid in the design of space-based heat-transfer, combustion, and human-life-support equipment.

## INTRODUCTION

Elementary electromagnetism shows that a nonuniform magnetic field exerts a body force on permeable materials. The familiar potential energy  $U = -\mathbf{m} \cdot \mathbf{B}$  favors alignment of a magnetic dipole  $\mathbf{m}$  with a static external magnetic induction  $\mathbf{B} = \mu\mathbf{H}$  (in SI units). When  $\mathbf{B}$  is nonuniform, this potential produces a force  $\mathbf{F}_m = -\nabla U = \nabla(\mathbf{m} \cdot \mathbf{B}) = (\mathbf{m} \cdot \nabla)\mathbf{B}$  on the dipole. The corresponding force per unit volume on a permeable magnetic material of magnetization (magnetic moment per unit volume)  $\mathbf{M} = \chi\mathbf{H}$  is

$$f_m = (\mathbf{M} \cdot \nabla)\mathbf{B} = \frac{1}{2}\chi\mu_0\nabla H^2, \quad (1)$$

where the small typical volumetric susceptibilities  $-10^{-5} < \chi < 10^{-3}$  have allowed us to set  $\mu = \mu_0(1+\chi) \approx \mu_0$ . This magnetic body force is not the ponderomotive force of magnetohydrodynamics, which requires a conducting fluid, but arises simply from the force of a nonuniform magnetic field on the molecular dipoles. More detailed treatments (ref. 1) confirm the presence of this magnetic body force.

Apart from exotic ferrofluids (colloidal suspensions of monodomain ferromagnetic particles which do not occur naturally), all electrically insulating fluids are either diamagnetic ( $\chi < 0$ ;  $\chi \approx -10^{-5}$ ) or paramagnetic ( $\chi > 0$ ;  $\chi \approx 10^{-3}$ ). Magnetic properties result from the orbital angular

momentum and spin of electrons, which combine to yield a net intrinsic magnetic moment of the molecule. In addition, an applied magnetic field leads to a small induced magnetic moment whose magnetic flux opposes the applied magnetic flux. In paramagnetic materials such as oxygen, unfilled electronic shells produce a net intrinsic magnetic moment which overwhelms the induced moment. In these materials, the magnetic moments tend to align in the direction of the field so that  $\chi > 0$ , thereby enhancing the field. Diamagnetic materials such as helium, argon, and water have ground-state electronic shells that are completely filled, yielding no net intrinsic magnetic moment. In contrast with the mislabel “nonmagnetic” often given to these materials, their small induced magnetic moments tend to align in a direction opposite the field, yielding small negative values of  $\chi$  and thereby reducing the magnetic field. Consequently, the magnetic body force, Eq. (1), tends to move diamagnetic materials into regions of lower field, whereas it tends to move paramagnetic materials into regions of higher field. This force can balance gravity in both diamagnetic and paramagnetic materials. All ferromagnetic materials are paramagnetic in the molten state.

Paramagnetic fluids have volumetric susceptibilities that are typically proportional to the ratio of mass density  $\rho$  to temperature  $T$  according to Curie’s law (refs. 2, 3);

$$\chi = C \frac{\rho}{T} , \quad (2)$$

where  $C$  is a constant characteristic of the fluid.

The proposed study will utilize the equations governing magnetothermal convection in electrically nonconducting incompressible fluids,

$$\rho \left[ \frac{\partial \mathbf{v}}{\partial t} + (\mathbf{v} \cdot \nabla) \mathbf{v} \right] = -\nabla P + \rho \mathbf{g} + \eta \nabla^2 \mathbf{v} + \mathbf{f}_m \quad (3a)$$

$$\frac{\partial T}{\partial t} + \mathbf{v} \cdot \nabla T = D \nabla^2 T \quad (3b)$$

$$\nabla \cdot \mathbf{v} = 0 . \quad (3c)$$

Here,  $\mathbf{f}_m$  is the magnetic body force discussed above,  $\eta$  is the viscosity,  $\mathbf{v}$  is the fluid velocity,  $D$  is the thermal diffusivity, and  $\mathbf{g}$  is the acceleration of gravity. General flows require an additional term in this force proportional to the gradient of a scalar (ref. 1). This additional term has been subsumed into the pressure term above, so that the pressure  $P$  contains both thermal and magnetic contributions. The magnetic contribution vanishes identically when the susceptibility is directly proportional to the density, such as for Eq. (2).

An upward magnetic body force  $\mathbf{f}_m$  can easily balance the downward gravitational body force  $\mathbf{f}_g = \rho \mathbf{g}$ , thereby levitating liquids and gases on earth. This balance requires a magnetic induction gradient  $G = |B \nabla B| = \mu_0 g / |\chi_m|$ , where  $\chi_m = \chi / \rho$  is the specific susceptibility. A number of ordinary diamagnetic fluids including water, ethanol, and hydrogen have recently been levitated with gradients up to  $G = 3000 \text{ T}^2/\text{m}$  and fields up to 30 T (refs. 4, 5). Field gradients necessary to balance earth’s gravity for paramagnetic fluids are reduced by a factor  $10^{-2} - 10^{-3}$  owing to their larger susceptibilities. In space, the necessary field gradients are reduced by a factor  $10^{-4} - 10^{-6}$  owing to the reduction in the gravitational acceleration, making levitation possible using small, even hand-held, permanent magnets or electromagnets. Thus, it is feasible to control and position classical fluids in space using the magnetic body force.

## MAGNETOTHERMAL CONVECTION

Buoyancy-driven convection in a stationary closed container requires gradients in the gravitational body force, often achieved by temperature-induced density gradients. Correspondingly,

gradients in the magnetic body force can also drive convection analogous to buoyancy-driven convection. For paramagnetic fluids, gradients in the temperature and the density can supply such gradients through Eq. (2).

The first clear observation of such convection, called the Glenda effect, was reported by Carruthers and Wolfe in 1968 (ref. 3), who experimented with the effect of a 1.55 T electromagnet on gaseous oxygen near room temperature and pressure. They used a rectangular convection chamber in which one wall was heated, the opposite wall was cooled, and the remaining walls were insulated. In the absence of applied magnetic fields, gravitational buoyancy formed a circulation with upflow along the heated vertical wall and downflow along the cooled vertical wall. Placing the chamber in a horizontal field with a vertical gradient (due to fringing of field lines) produced a temperature-dependent magnetic body force opposite to gravity, which reversed the direction of circulation compared to the nonmagnetic case. Thus Carruthers and Wolfe demonstrated that a nonuniform magnetic field can reverse gravitational convection in oxygen.

With the heated wall at the floor of the chamber, the horizontal magnetic field augmented or reduced the Rayleigh-Benard convection observed with no field, depending on the direction of the field gradient. Most startling of all was the observation of vigorous magnetically-driven convection when heating from above, a situation which is stable in the absence of a magnetic field.

The same phenomena were seen in oxygen at reduced pressures and in air, although the magnitudes were smaller. In nitrogen, which is diamagnetic, there were no observable magnetic effects. Carruthers and Wolfe attributed their observations to the fact that oxygen is paramagnetic and that its susceptibility depends on temperature. Although this explanation is likely to be correct, Carruthers and Wolfe did not derive the equations of motion or present any solutions.

In 1977, Clark and Honeywell (ref. 6) rediscovered the Glenda effect the hard way. Beginning about 1970, Honeywell's group began a series of tests to measure the Senftleben-Beenakker effect, a reduction in the thermal conductivity of oxygen gas at low temperatures and pressures caused by a uniform magnetic field. They performed tests using an annular convection chamber in which the inner cylinder was heated. The axis of the chamber was vertical and the magnetic field was horizontal. Because the expected reduction in thermal conductivity was only about 1%, the experiment was conducted with great precision.

The investigators were shocked when the data indicated a 20 to 50% increase in thermal conductivity. After years of rechecking the experiments and the analysis, they finally traced this increase to the small (0.2%) inhomogeneities in their magnetic field. Thus, the Glenda effect can appear where it is unexpected, and can be surprisingly large. It is likely that other experimentalists have seen the Glenda effect without realising it. Indeed, Carruthers and Wolfe had earlier pointed out the potential of the Glenda effect to distort precision electrical measurements.

Clark and Honeywell (ref. 6) presented a rather cursory derivation of the governing equations and obtained a solution for fully developed natural convection of an ideal gas between infinite, parallel vertical plates, including both gravitational and Glenda forces. Although the solution was two dimensional and the experiment axisymmetric, the theoretical predictions were close enough to the data to convince the authors that the Glenda effect dominated the flow. Their analysis ignores horizontal magnetic gradients, which may play an important role.

A series of recent experiments (refs 7, 8) reveals convection in a paramagnetic solution of gadolinium nitrate. These experiments identify precise convective thresholds for vertical thermal and magnetic-field gradients. For example, they found that stabilizing vertical magnetic-field gradients exceeding  $G = 15 \text{ T}^2/\text{m}$  completely suppress convection when the layer is heated from below, and that destabilizing magnetic-field gradients exceeding  $G = 5 \text{ T}^2/\text{m}$  produce convection when the layer is heated from above. These thresholds, and the accompanying convection, are of prime interest in the proposed study.

Finlayson (ref. 9) considered the theoretical convective instability of ferrofluids under vertical magnetic fields which are *spatially uniform* in the absence of a thermal gradient. Further experimental and theoretical work on such ferrofluids is summarized in Stiles and Kagan (ref. 10).

Theoretical analysis of the experiments of Carruthers and Wolfe (ref. 3) and of Braithwaite *et al.* (ref. 7) can be carried out generally. Both experiments involve a temperature gradient in the fluid imposed by two parallel bounding conducting plates at temperatures  $T = T_0 \pm \Delta T/2$ . These plates are horizontal for Braithwaite *et al.* and are both horizontal and vertical for Carruthers and Wolfe. To understand the various convection patterns seen in these experiments, it is convenient to write the equations of motion in terms of the deviations from a static thermal conduction state with a uniform thermal gradient  $\nabla T = (\Delta T/d)\hat{n}$ , where  $\hat{n}$  is the unit vector normal to this gradient, and  $d$  is the separation between these plates. Dimensionless deviations about this state satisfy

$$\mathcal{P}^{-1} \left[ \frac{\partial \mathbf{u}}{\partial t} + (\mathbf{u} \cdot \nabla) \mathbf{u} \right] = -\nabla p + \mathbf{R}\theta + \nabla^2 \mathbf{u} ,$$

$$\frac{\partial \theta}{\partial t} + \mathbf{u} \cdot \nabla \theta + \hat{n} \cdot \mathbf{u} = \nabla^2 \theta$$

$$\nabla \cdot \mathbf{u} = 0 .$$

Here,  $\mathbf{u}$ ,  $p$ , and  $\theta$  are respectively the dimensionless velocity, pressure, and temperature; length, time, temperature, and pressure are measured respectively in units of  $d$ ,  $d^2/D$ ,  $\Delta T$ , and  $D\eta/d^2$ . Dimensionless parameters include the Prandtl number  $\mathcal{P} = \nu/D$  and a vector Rayleigh number

$$\mathbf{R} = \frac{g\alpha\Delta T d^3}{\nu D} \left( -\hat{g} + \frac{\mu_0}{2\alpha g \rho_0 d} \frac{d\chi}{dT}|_{T_0} \nabla H^2 \right) \quad (4)$$

which includes magnetic effects. The applied magnetic field  $\mathbf{H}$  is measured in amperes per meter, but is considered here as a function of dimensionless position  $\mathbf{x}$ . In arriving at these equations, we have made use of first-order Taylor expansions about  $T_0$  in the temperature-dependent density and susceptibility. We have also employed the usual Boussinesq approximation, that is, we have retained density changes only in the large gravity term. An important task in the project is to justify this approximation rigorously.

The vector Rayleigh number involves the thermal expansion coefficient  $\alpha$ , the density  $\rho_0$  at temperature  $T_0$ , the kinematic viscosity  $\nu = \eta/\rho_0$ , and the unit vector  $\hat{g}$  in the direction of gravity. The prefactor in the Rayleigh number applies to Rayleigh-Bénard convection for a fluid layer heated from below in the absence of any magnetic fields. For a Curie's law paramagnetic material [Eq. (2)], the magnetic term involves

$$\frac{d\chi}{dT}|_{T_0} = -\chi_0 \alpha \left( 1 + \frac{1}{\alpha T} \right) .$$

The first and second terms in this expression follow respectively from the implicit temperature dependence through  $\rho$  and from the explicit temperature dependence in Eq. (2). Setting  $\hat{z} = \hat{g}$  and  $\mathbf{H} = H(z)\hat{z}$  yields  $\mathbf{R} = -R_m \hat{z}$ , with a scalar 'magnetic' Rayleigh number  $R_m$  agreeing with Braithwaite *et al.* The form  $\mathbf{H} = H(z)\hat{z}$  gives an unphysical nonzero divergence  $\nabla \cdot \mathbf{B}$  of the magnetic induction  $\mathbf{B} = \mu \mathbf{H}$ . In contrast, our vector Rayleigh number is completely general, allowing for both horizontal and vertical components of  $\mathbf{H}$  satisfying both  $\nabla \cdot \mathbf{B} = 0$  and  $\nabla \times \mathbf{H} = 0$ . Thus, the appropriate Rayleigh number for the problem is a vector which is generally nonuniform in both magnitude and direction owing to nonuniformities in  $\nabla H^2$ . One of the objectives of the project is to study the effects of these nonuniformities to determine when magnetic effects [the second term in Eq. (4)] can be used to cancel buoyancy effects [the first term]. Such studies will be carried out both analytically and numerically.



## POTENTIAL SIGNIFICANCE

The Glenda effect allows the creation of a virtually arbitrary, controllable body force distribution in paramagnetic fluids such as oxygen, nitric oxide, aqueous ferric perchlorate, and numerous transition metal molten salts. Similar, although weaker, forces can be produced in diamagnetic fluids. The potential applications of this unique and largely unexplored phenomenon are likely far broader than we can presently envision, but several attractive possibilities have been suggested.

In considering potential uses, it is important to recognize that the magnetic body force is independent of gravity. While strong enough to be important in normal Earth gravity for fluids such as oxygen and air, its greatest utility will surely be in microgravity environments where it may be the only significant body force.

Magnetothermal forces should occur whenever a wire carrying electricity heats the surrounding air. Undoubtably the effect is usually negligible, but there may be some anomalies for which it is the unrecognized cause. It would be particularly important to account for or eliminate the Glenda effect in very precise measurements of fluid properties.

In principle, one could inhibit or enhance the effects of gravitational convection on Earth or create artificial "natural" convection in an orbiting spacecraft, thus enhancing or suppressing mixing and heat transfer as may be opportune. These abilities may be of interest for both engineering and scientific applications.

A remarkable apparatus called the Geophysical Fluid Flow Cell has used electrical permittivity gradient forces to simulate a radial gravity field in the gap between rotating concentric hemispherical shells for planetary and stellar atmospheric circulation experiments. The working fluid in these tests was a liquid with a Prandtl number of 8.4 (ref. 11), which is at least an order of magnitude higher than the prototype value in most cases. If an experiment of this type could be designed using the Glenda effect, oxygen, with its Prandtl number of 0.7, could be used to achieve closer similarity with the prototype. The simulated gravity field in the Geophysical Fluid Flow Cell varied with the inverse fifth power of the radius, rather than the inverse square dependence of true gravity. It might be possible to approach the correct dependence more closely using Glenda forces.

Measurements have confirmed that the gravitational environment on an orbiting spacecraft is characterized by an effective gravitational acceleration which varies randomly in direction and in time with a frequency range of 0.1 to 10 Hz. The amplitude of this g-jitter is on the order of 0.01% of the earth normal value (ref. 12). Given a suitable control system, it might be possible to cancel much of the g-jitter by using the Glenda effect. It would very likely be possible to generate controlled g-jitter without using a shake table, either in orbit or on the Earth.

The Glenda effect could be used to pump paramagnetic fluids such as liquid oxygen or to deflect fluid currents without using any moving parts, if that should be desirable.

Many potential applications lie in the field of materials processing, particularly in the microgravity environment. In some instances it is important to prevent contact between a melt and the walls of the container. Electromagnetic forces, acoustic standing waves, and gas streams have been used to achieve this goal (ref. 12). The Glenda effect may have advantages for insulating paramagnetic fluids. The possible importance of the Glenda effect in crystal growth was pointed out by Carruthers and Wolfe (ref. 3) who used it to explain observations on the growth of ferrous ammonium sulfate crystals in a magnetic field. The Glenda effect might be particularly useful in connection with the growth of crystals from insulating paramagnetic melts.

## REFERENCES

1. R. E. Rosensweig, 1985. *Ferrohydrodynamics*, Cambridge University Press, New York, Chaps. 4, 5.
2. N. W. Ashcroft and N. D. Mermin, 1976. *Solid State Physics*, Saunders College, Philadelphia, Chap. 31
3. J. R. Carruthers and R. Wolfe, 1968. Magnetothermal Convection in Insulating Paramagnetic Fluids, *Journal of Applied Physics*, 39, 5718-5722.
4. E. Beaunon and R. Tournier, 1991. Levitation of organic materials, *Nature* 349, 470.
5. C. G. Paine and G. M. Seidel, 1991. Magnetic levitation of condensed hydrogen, *Rev. Sci. Instrum.* 62, 3022.
6. D. C. Clark and W. I. Honeywell, 1977. Magnetothermal Convection of Oxygen Gas in Nonuniform Magnetic Fields, *American Institute of Chemical Engineers Journal*, 23, 553-558.
7. D. Braithwaite, E. Beaunon, and R. Tournier, 1991. Magnetically controlled convection in a paramagnetic fluid, *Nature* 354, 134.
8. E. Beaunon, D. Bourgault, D. Braithwaite, P. de Rango, R. Perrier de la Bathie, A. Sulpice, and R. Tournier, 1993. *J. Phys. I France* 3, 399.
9. B. A. Finlayson, 1970. Convective instability of ferromagnetic fluids, *J. Fluid Mech.* 40, 753.
10. P. J. Stiles and M. Kagan, 1990. Thermoconvective instability of a horizontal layer of ferrofluid in a strong vertical magnetic field, *J. Magn. Magn. Mat.* 85, 196.
11. J. E. Hart, G. A. Glatzmaier, and J. Toomre, 1986. Space-laboratory and Numerical Simulations of Thermal Convection in a Rotating Hemispherical Shell with Radial Gravity, *Journal of Fluid Mechanics*, 173, 519-544.
12. S. Ostrach, 1982. Low-Gravity Fluid Flows, *Annual Review of Fluid Mechanics*, 14, 313-345.

# WAVES IN RADIAL GRAVITY USING MAGNETIC FLUID

Daniel R. Ohlsen, John E. Hart,  
Program In Atmospheric and Oceanic Sciences  
University of Colorado  
Boulder, CO 80309-0311

and Patrick D. Weidman  
Department of Mechanical Engineering  
University of Colorado  
Boulder, CO 80309-0427

## ABSTRACT

We are beginning laboratory experiments using magnetically active ferrofluids to study surface waves in novel geometries. Terrestrial gravity is eliminated from the dynamics, and the magnetic body force felt by ferrofluid in the presence of a magnetic field gradient is used to create a geopotential field which is a section of or an entire sphere or cylinder. New optical, electromagnetic and ultrasonic diagnostic techniques are under development to initially study capillary-gravity wave propagation and interaction in such geometries.

## INTRODUCTION

Terrestrial laboratory experiments studying various fluid dynamical processes are constrained, by being in an Earth laboratory, to have a gravitational body force which is uniform and unidirectional. Therefore fluid free-surfaces are horizontal and flat. Such free surfaces must have a vertical solid boundary to keep the fluid from spreading horizontally along a gravitational potential surface. In the absence of terrestrial gravity, surface tension forms fluid masses into spherical balls without solid boundaries, as demonstrated on the Space Shuttle in the Drop Physics Module [ref. 1, for example]. A fundamentally different problem is the behavior of fluids with a *body* force rather than a surface force that generates the spherical geometry. We are beginning a suite of experiments on a wide range of phenomena that use magnetic body forces in so-called "ferrofluids" to generate unique configurations for physical modeling.

The linear and nonlinear characteristics of traveling or standing waves on a liquid surface are a classic problem in fluid dynamics. Capillary-gravity waves represent an interaction of fluid inertia with the local gravitational *body* restoring force *and* free-surface boundary curvature *surface* tension [2]. It is of great theoretical interest to contrast wave behavior with and without lateral boundaries. Lateral boundaries have a strong effect on the spatial structures (fronts, pulses, solitons, etc.) observed in nonlinear propagating wave systems [3, for an extensive review]. With a spherical magnetic body force a straight circumferential channel formed by boundaries at  $\pm$  latitudes is an experimental system for free-surface capillary-gravity waves which has periodic boundary condition in one direction. Similarly, an entire spherical surface is boundary-less and periodic in two-dimensions. For an overfull channel, the sidewall boundary contact line becomes pinned and the additional cross channel curvature increases the wave speed [4]. In an equatorial channel geometry, the contact lines are of the same length (as opposed to in an annular geometry) and this symmetry makes comparison to theory easier. The additional longitudinal curvature further increases the wave speeds.

If the gravitational force oscillates in time, then standing capillary gravity waves are excited. This is normally accomplished by vibrating a fluid container vertically. These "Faraday waves" have become, along with Rayleigh-Benard convection, a canonical system for studies of non-equilibrium pattern formation,

spatio-temporal evolution, and chaos [3]. The spherical geometry, with parametric oscillation obtained by oscillating our magnetic field, is a very clean system for investigating such parametrically excited waves, without complications of boundary shapes and contact angles which can determine patterns and mode competition dynamics even very far from the boundaries [5].

## BACKGROUND

Ferrofluids are dilute suspensions of magnetic dipoles, for example magnetite particles of order 10 nm diameter, suspended in a carrier fluid. A surfactant coating keeps the particles separate enough that thermal Brownian motions in the fluid are sufficient to overcome both gravity and particle-particle attraction to keep the dipoles in suspension. For flows in which external magnetic field variations and the bulk fluid motions are slow compared to the time for the magnetic fluid particles to rotate ( $\sim 10^{-6}$  s), the fluid magnetization,  $\vec{M}$ , is parallel to the applied magnetic field,  $\vec{H}$ . If there is a gradient in  $H \equiv |\vec{H}|$ , then there will be a systematic body force owing to the slight but persistent correlation of field strength and pole sense. The body force terms in the Navier-Stokes equations become:

$$\rho \frac{d\vec{u}}{dt} + \dots = \dots + \rho \nabla \Phi + M \nabla H.$$

where  $\nabla \Phi = \vec{g}$  as usual. The superparamagnetic ferrofluid response is complicated by the fact that  $M$  is a function of the applied field unlike  $\rho$  for the gravitational case. ( $M$  increases linearly with  $H$  for small  $H$  and saturates at constant  $M$  for large  $H$ .) Ferrofluids became commercially available in the 1960's and have been used in several engineering applications [6].

One of the first scientific applications of the ferrofluid magnetic body force in an experiment large enough for inertial forces to be important was initiated by one of the investigators (DRO). Equatorially trapped Kelvin and Rossby waves, which are important in large-scale atmospheric and oceanic fluid dynamics, were studied in the laboratory for the first time. This laboratory experiment demonstrates the basic technique to be used in the present study. A sketch and photograph from this study are shown in Figure 1. The apparatus was cylindrically axisymmetric, and the body force on the water-based ferrofluid depends only on the field strength and gradient from an interior magnet. A cylindrical magnet was embedded in a smooth, solid, plaster/plastic spherical core. The geopotential field and its gradient, the body force, were made nearly spherical by careful choice of magnet shape and size in relation to the solid core, and by immersing the "planet" and its ferrofluid ocean in immiscible silicone oil of the same density. Thus the earth gravity was removed from the dynamics of the ferrofluid/oil interface and the only dynamically active force was the radial magnetic gravity. The entire apparatus rotated, and waves were forced by exterior magnets. In the photograph in Figure 1b, an example very large height perturbation is forced by an additional, stationary, hand-held magnet at left. Upon release such a bulge propagated in the co-rotating or eastward direction (as a Kelvin wave) or in the counter-rotating or westward direction (as a Rossby wave) along the equator, trapped there by the overall rotation and spherical geometry.

The fluid height on the equator as a function of longitude was observed in profile by viewing the limb of the black ferrofluid spheroid against a white background. Video frames of the waves were grabbed and then contoured and converted to polar coordinates. The radial displacement amplitude,  $r - r_0$ , at each longitude,  $\phi$ , where  $r_0(\phi)$  is the undisturbed radius, is contoured in Figure 2. A side view of the waves showed that the amplitude was trapped to near-equator latitudes, as expected, for both the eastward Kelvin waves and westward Rossby waves in this rapidly rotating experiment. The time/longitude contour plot of equator height in Figure 2a shows a Kelvin wave propagating eastward at constant speed more than twice around the spheroid. In Figure 2b a westward Rossby wave propagates much slower. The theoretical linear Rossby wave speeds are 1/3, 1/5, 1/7, etc. of the Kelvin wave speed and those slopes are shown in Figure 2b

for reference. These experiments were the first laboratory study of this class of waves which have been recently observed with satellite altimetry in the Pacific ocean [7] and appear to be an integral component of the equatorial climate system, especially the El Niño - Southern Oscillation [8]. Because of the high cost of ferrofluids, these are some of the first experiments in which inertial effects are important. These large experiments (~ a few liters) were possible by using new inexpensive ferrofluid at large dilution.

## FUTURE WORK

A larger version of the spherical geometry experimental setup in Figure 1 is being constructed. The size increase and use of fluids with smaller viscosity will give more than an order of magnitude reduction in viscous damping. With this apparatus we will first investigate capillary gravity waves at the interface of a neutral two-fluid system in a zonal channel. In particular we will study the effects of pinned contact lines on nonlinear waves and the dynamics of nonlinear waves leading to contact line rupture. Pinned contact lines used for stabilizing stationary and rotating liquid columns in float-zone crystal growth experiments are sensitive to residual accelerations in the microgravity environment of a spacecraft [9]. Although many studies have been made of the effect of g-jitter on the stability of cylindrical fluid columns [10, 11], few studies directly concerned with the problem of pinned contact line rupture are available. Weidman, *et al.*, [12] have investigated the *static* rupture of pinned rotating menisci formed by overfilling annular grooves in a rotating disk. We will investigate the *dynamic* rupture of contact lines pinned to the boundary of a circular basin at the North pole or pinned to the continuous edges of an equatorial cylindrical zone (Figure 3a) using both sinusoidal variation of the magnetic radial gravity (using an interior electromagnet) or large amplitude traveling waves, in both stationary and rotating experiments. Pinned contact lines which are stable at the onset of infinitesimal hydrodynamic instability, will rupture at sufficiently large g-jitter amplitude, or during interference of two colliding or over-taking large-amplitude waves in the periodic geometry. Experimentally, these waves can be cleanly generated by magnets external to the fluids.

Studies of standing capillary-gravity waves in laterally bounded containers, forced by parametric oscillation of gravity, have undergone a recent resurgence. We will initiate a new class of ferrofluid experiments on a sphere or in an equatorial channel to study pattern formation with periodic boundaries and no contact angle impurities. On the entire spherical surface or in a polar basin formed by a high-latitude circle boundary, symmetry-breaking effects of rotation on traveling and standing waves patterns will be studied. Our initial analysis indicates that we will have sufficient electromagnetic driving strength in the frequency range 0.01 to 10 Hz, to generate Faraday wave patterns by parametric excitation with up to a few tens of waves in a circumference on the sphere or somewhat fewer fitting around inside a polar basin. The spherical system has the periodic boundaries of the standard theoretical development [5] but which have not been previously possible experimentally.

Ferrofluid experiments offer the potential for conducting laboratory studies of thermally driven oceanic flows over a substantial part of a sphere. As opposed to Earth atmospheric motions, in which sphericity, or the so-called Beta effect, is generally **not** a dominant term in the vorticity budget, slow deep overturning oceanic motions are highly constrained by the dynamical influence of planetary vorticity advection. Such effects cannot be studied in the terrestrial laboratory, when the all important case of continuous thermal stratification is considered, because of the strong gravity induced cells that have no oceanic analogs. Previous GFFC-type [13] experiments are also ill-suited to oceanic flow modeling because they are too viscous (thin gaps). We will address the key **technical** issues in building a relatively simple but effective microgravity based experiment to enable laboratory study of continuously stratified spherical flows in complex basins spanning a latitude range of at least plus or minus 60 degrees (Figure 3b). We realize that such an experiment must be conducted in microgravity, and our terrestrial demonstration experiment will be

contaminated by terrestrial gravity induced flows. The main technical issues to explore are: 1) how to get a large enough magnetic buoyancy frequency in an apparatus of sufficient size, 2) how to stratify and force motion in the experiments, and 3) how to visualize the flows effectively.

## ACKNOWLEDGMENT

The previous work was supported by grants from the Office of Naval Research and National Science Foundation.

## REFERENCES

1. Wang, T.G., A.V. Anilkumar, C.P. Lee, and K.C. Lin: *J. Fluid Mech.*, **276**, 389-403, 1994.
2. Lighthill, J: *Waves in Fluids*. Cambridge University Press, 1978.
3. Cross, M.C. and P.C. Hohenberg: *Rev. Mod. Phys.* **65**, 851-1112, 1993.
4. Benjamin, T. B. and J.C. Scott: *J. Fluid Mech.*, **92**, 241-267, 1979.
5. Miles, J. and D. Henderson: *Annu. Rev. Fluid Mech.*, **22**, 143-165, 1990.
6. Rosensweig, R.E.: *Ferrohydrodynamics*. Cambridge University Press, 1985.
7. Delcroix, T., J. Picaut, and G. Eldin: *J. Geophys. Res.* **96** (Suppl.), 3249-3262, 1991.
8. Philander, S.G.: *El Niño, La Niña, and the Southern Oscillation*. Academic Press, 1990.
9. Martinez, I., J.M. Haynes, and D. Langbein: in *Fluid Sciences and Materials Science in Space, A European Perspective*, ed. Walter, H.U. Springer, Berlin, 1997.
10. Zhang, Y. and J. I. D. Alexander: *Phys. Fluids A*, **2**, 1966-1974, 1990.
11. Lyell, M. J.: *Phys. Fluids A*, **3**, 1828-1831, 1991.
12. Weidman, P. D., S. Krumdieck, and P. Rouse: *J. Fluid Mech.*, **219**, 25-50, 1990.
13. Hart, J.E., G.A. Glatzmaier, and J. Toomre: *J. Fluid Mech.*, **173**, 519-544, 1986.

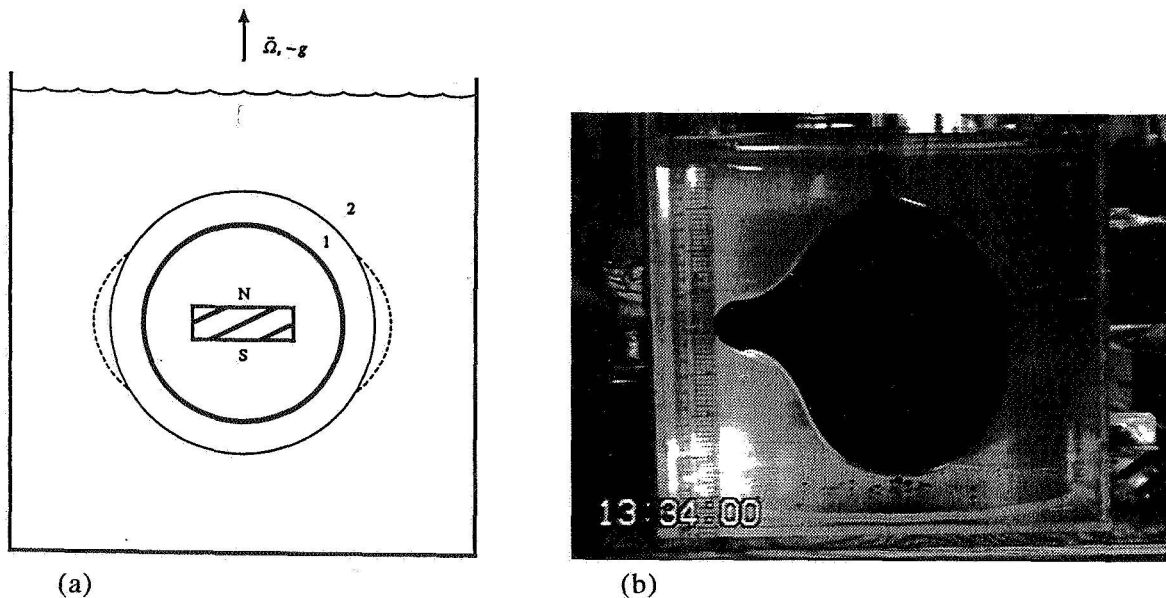


Figure 1. Side view schematic cross section (a) and photograph (b) of cylindrically symmetric experiment. A cylindrical tank holds a silicone oil-freon mixture (2) surrounding a water-based ferrofluid layer (1) on a plaster/plastic ball covering a strong permanent magnet.  $\rho_1 \cong \rho_2$ . The entire apparatus rotates at angular velocity,  $\Omega$ . In the photograph, an external magnet forces a large amplitude wave.

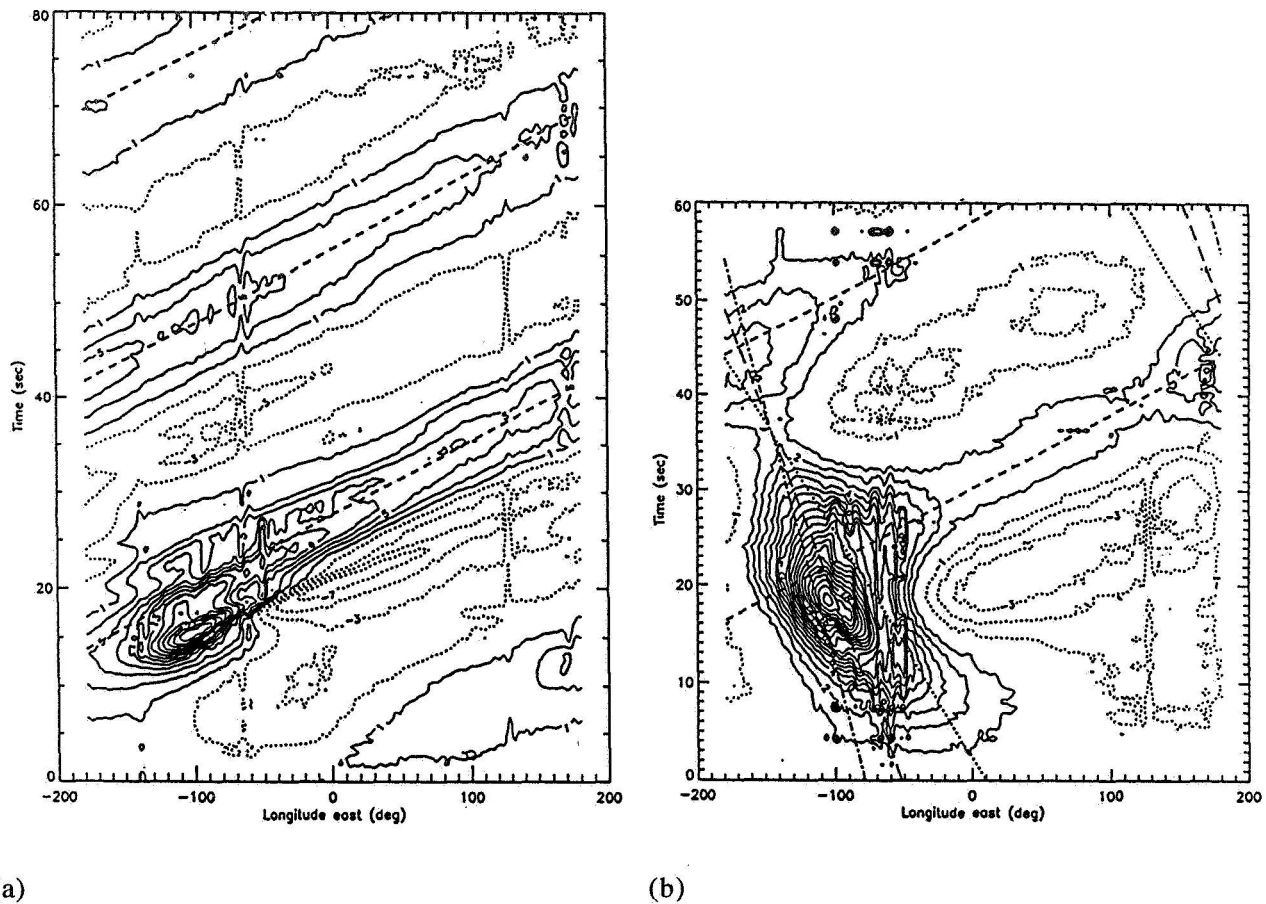


Figure 2. Contours of displacement height,  $r - r_0$ , near the equator as a function of longitude and time. a) Eastward forcing at about the Kelvin wave speed. b) Westward forcing at 0.44 times speed of a). The eastward line, ---, has constant speed,  $c$ . The lines  $\cdots$ , ---, and  $\cdots$  correspond to westward speeds which are  $1/3$ ,  $1/5$ , and  $1/7$  of  $c$ , respectively.

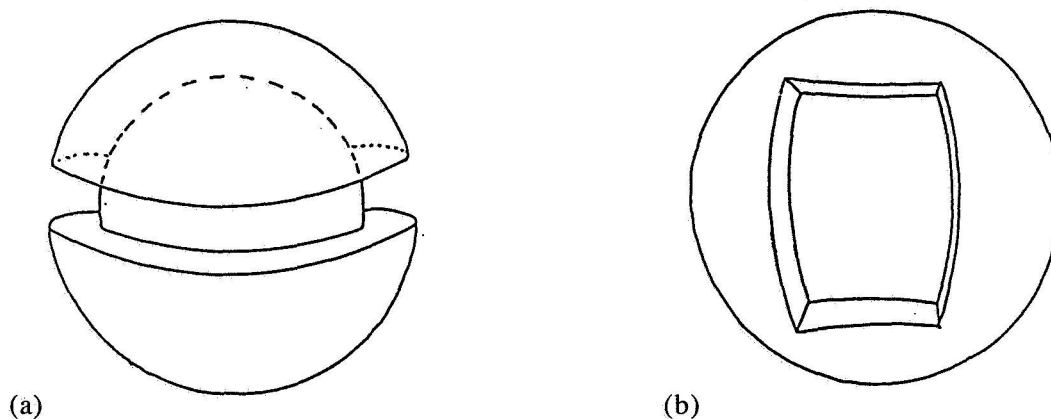


Figure 3. Schematic of (a) equatorial channel and (b) ocean basin experiments.





# Binary Oscillatory Crossflow Electrophoresis

Richard F. Molloy, Christopher T. Gallagher, and David T. Leighton, Jr.

Department of Chemical Engineering, University of Notre Dame

## Abstract.

We present preliminary results of our implementation of a novel electrophoresis separation technique: binary oscillatory cross flow electrophoresis (BOCE). The technique utilizes the interaction of two driving forces, an oscillatory electric field and an oscillatory shear flow, to create an active binary filter for the separation of charged species. Analytical and numerical studies have indicated that this technique is capable of separating proteins with electrophoretic mobilities differing by less than 10%. With an experimental device containing a separation chamber 20cm long, 5cm wide, and 1mm thick, an order of magnitude increase in throughput over commercially available electrophoresis devices is theoretically possible.

## Introduction.

Electrophoresis has long been shown as an effective process for the separation of particles and biological macromolecules based on small differences in electrophoretic mobility. Since Tiselius [1] discovered electrophoresis in 1937, the technique has become a cornerstone for biochemical analysis and has branched into several different subfields. Despite its attention, several key problems have prevented electrophoresis techniques from scaling up to commercial processes. Among these are Joule heating and crescent dispersion caused by electroosmosis, parabolic velocity profiles of the carrier electrolyte, and electrohydrodynamic effects [2], [3].

The present research project, binary oscillatory crossflow electrophoresis, has the potential for significant improvements in throughput and resolution over conventional CFFE techniques. This technique relies on the interaction of an oscillatory electric field and an oscillatory shear flow, shown in Figure 1.

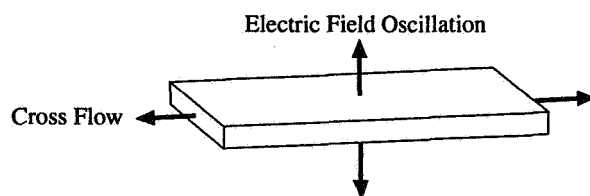


Figure 1: Direction of motions in a binary oscillatory crossflow electrophoresis cell.

By appropriate selection of frequency and phase of oscillation of the two interacting driving forces, an effective filter can, in principle, be created that will allow proteins either higher or lower than a chosen electrophoretic mobility to pass through the device. The technique could be used for both analytical and preparative work by programming the filter setpoint with time and collecting proteins that pass through the device at each setpoint. For continuous isolation of a particular fraction from a complex mixture feed, a network of four of these devices could be used.

## Analytical Model

The driving forces in the binary separator are an oscillatory convective flow and an oscillatory electric field. The solute molecules will have some net motion that is a complex function of the two driving forces, the electrophoretic mobility, and the diffusion of the species. The cross flow may be written as

$$u_x = 4u_{max} \frac{y}{b} \left( 1 - \frac{y}{b} \right) f(\omega t) \quad (1)$$

where  $u_x$  is the fluid velocity in the  $x$  direction,  $u_{max}$  is the velocity of the center line,  $y$  is position in the gap,  $b$  is the gap thickness,  $\omega$  is the frequency of oscillation,  $t$  is time, and  $f$  is some periodic function of  $\omega t$ . The motion of a particular solute molecule across the channel will depend on  $f(\omega t)$  and the position of the molecule in the gap. If we neglect diffusion, we may write the motion of the solute across the gap due to an oscillatory electric field as

$$\frac{dy}{dt} = \frac{\mu E_o}{\omega} \frac{d}{dt} g(\omega t) = \mu E_o h(\omega t) \quad (2)$$

where  $\mu$  is the electrophoretic mobility,  $E_o$  is the characteristic amplitude of the electric field,  $g(\omega t)$  is the oscillatory motion of the solute, and  $h(\omega t)$  is the oscillation of the electric field. Integrating this equation, we can solve for the position across the gap of the solute molecule.

$$\frac{y}{b} = \alpha g(\omega t) \quad (3)$$

where  $\alpha = \frac{\mu E_o}{\omega b}$  is the dimensionless electrophoretic mobility and  $g(\omega t)$  is bounded between 0 and 2. Substituting the position of the solute molecule into equation 1 and taking the time average, we will have an equation that describes the motion of a solute molecule in the absence of molecular diffusion:

$$\left\langle \frac{dx}{dt} \right\rangle = 4u_{max}\alpha \left( \langle g(\omega t)f(\omega t) \rangle - \alpha \langle g(\omega t)^2 f(\omega t) \rangle \right) \quad (4)$$

where  $\langle \cdot \rangle$  is the time average over one period. Equation (4) is limited to dimensionless mobilities  $\alpha \leq 0.5$ . The maximum value of  $\alpha$  corresponds to a solute molecule that just reaches the opposite wall during one period of oscillation. With equation (4) we may evaluate the solute velocity across the channel for combinations of arbitrary choices for  $f(\omega t)$  and  $g(\omega t)$ . Chandhok and Leighton [4] chose  $g(\omega t) = 1 - \cos(\omega t)$  and showed that the only Fourier modes of a general periodic function  $f(\omega t)$  that contributed to a migration velocity were a steady flow,  $\cos(\omega t)$ , and  $\cos(2\omega t)$ . While this analytic solution is very useful for qualitatively determining the performance of such a separations device, the solution is seriously limited by neglecting the effects of diffusion. This is particularly true since the interaction of diffusion with an oscillatory shear flow has been shown to increase the dispersion in the direction of motion by several orders of magnitude [5], [6]. Furthermore, bounding the maximum value of  $\alpha$  significantly limits the possible operating parameters of the system.

In order to better characterize the motion of the solute, we numerically simulated the solute motion in the channel including the effects of diffusion. To perform the numerical simulation, we used a molecular dynamics approach. At each time step, we added a random walk of length  $\sqrt{2\lambda\Delta t}$  to the electrophoretic motion of a solute molecule and used the resulting position to calculate the displacement in the direction of the fluid motion. The simulation was carried out for 1000 molecules and the average position and variance of the solute as a function of time were recorded. From the position data we determined the time averaged solute velocity and the effective diffusion coefficient in the direction of motion of the solute. We ran the simulation until the velocity reached a steady value, usually after only a few periods of oscillation.

For our simulation we have chosen the gap width  $b = 0.1$  cm, and by arbitrarily choosing the dimensional electrophoretic mobility of a particular species and the oscillation frequency  $\omega$ , we fix the electric field amplitude for a desired value of  $\alpha$ . Consequently, our choice of the above parameters fixes the dimensionless diffusivity. We simulated the solute motion for an electric field of amplitude  $h(t) = \sin(\omega t) - 0.05$  coupled with both  $f(\omega t) = \cos(\omega t)$  and  $f(\omega t) = \cos(2\omega t)$ . The small steady component to the electric field strength of 0.05 is important to refocus the solute at the lower wall during each period. The velocities for the solute as a function of  $\alpha$  for  $f(t)$  equal to  $\cos(\omega t)$ ,  $\cos(2\omega t)$ , and  $\cos(\omega t) - \cos(2\omega t)$  coupled with  $h(t) = \sin(\omega t) - 0.05$  were simulated and are shown in Figure 2.

Note that  $f(t)$  equal to  $\cos(\omega t)$  and  $\cos(2\omega t)$  both lead to negative velocities, with the maximum amplitude occurring at different mobilities. For a binary separation to be possible, the time averaged velocity for the solute molecules must change sign at some critical value of the electrophoretic mobility. Because the fluid motion does not directly influence the migration across the gap, the effect of each mode of the imposed solvent velocity on the time averaged solute velocity is linearly additive. As a result, we chose to subtract the two modes. The velocity resulting from  $f(\omega t) = \cos(\omega t) - \cos(2\omega t)$  coupled with  $h(t) = \sin(\omega t) - 0.05$  meets the constraints for a binary separation. In addition,  $\frac{d(v_A/u_{max})}{d\alpha}$  is large near the mobility with zero net velocity, a condition for sharp separation.

To determine the characteristic throughput and selectivity of the device, we consider a cell connecting two reservoirs of fluid. In one reservoir, we impose some concentration  $c_{A1}$ , in the other reservoir we impose a concentration of zero by flushing it with buffer. The cell is of length  $L$ , width  $W$ , and thickness  $b$  with operating parameters as listed above. The cross flow will oscillate with  $f(\omega t) = \cos(\omega t) - \cos(2\omega t)$  and  $u_{max} = \Delta x \omega$  where  $\Delta x$  is the characteristic amplitude of fluid oscillation.

To find the flux through a cell we start with the governing equation

$$k_{eff}^* \frac{\partial^2 c_A^*}{\partial x^{*2}} = v_A^* \frac{\partial c_A^*}{\partial x^*} \quad (5)$$

where  $k_{eff}$  is the dispersion coefficient determined numerically,  $x$  is the direction of flow,  $c_A$  is the concentration of species A, and  $v_A$  is the velocity of species A depicted in Figure 2. Equation (5) is the result of substituting the flux into the mass balance. By integrating twice and imposing the boundary conditions of  $c_A^*(x^* = 0) = 1$  and  $c_A^*(x^* = L/\Delta x) = 0$ , we can solve for the dimensionless concentration profile. Substituting the dimensionless concentration profile into the flux equation, we find the the dimensionless flux is

$$N_A^* = v_A^* \frac{1}{1 - \exp\left(\frac{-v_A^* L}{k_{eff}^* \Delta x}\right)} \quad (6)$$

Figure 3 shows a plot of  $N_{Ax}^*$  as a function of  $\alpha$  for a value of  $\frac{\Delta x}{L} = \frac{1}{5}$  where  $v_A^*$  is as shown in Figure 2 and  $k_{eff}^*$  is determined numerically. The curve labeled high pass represents the flux

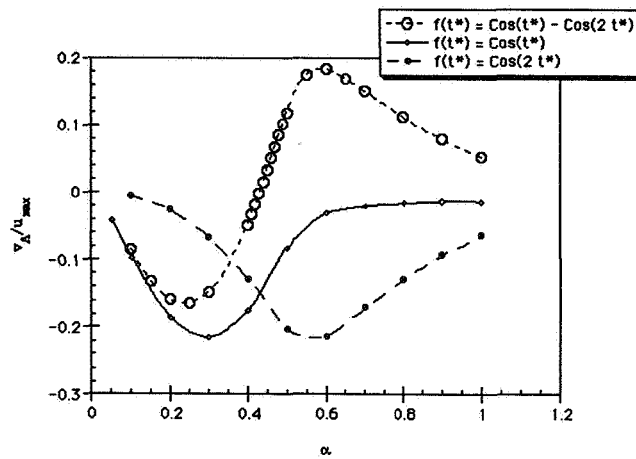


Figure 2: Plot of dimensionless velocity versus dimensionless electrophoretic mobility including the effects of cross-streamline diffusion.

when  $f(\omega t) = \cos(\omega t) - \cos(2\omega t)$ , and the curve labeled low pass represents the flux when  $f(\omega t) = \cos(2\omega t) - \cos(\omega t)$ .

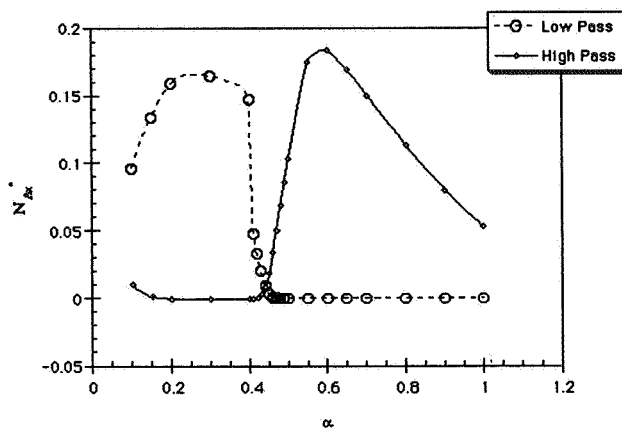


Figure 3: Plot of Dimensionless Flux versus dimensionless electrophoretic mobility.

Clearly the flux changes very dramatically near  $\alpha = 0.41$  for both high and low pass operation. For a 10% change in  $\alpha$  about this point, the flux increases two orders of magnitude.

### Experimental.

To verify the analytical and numerical results of the BOCE technique, an experimental system including a single binary separation cell, two reservoirs and an electrolyte bath was constructed. The cell is similar to that of Giddings [7], and allows continuous flow of solute in a buffer solution through a separation chamber 20.0 cm long, 5.0 cm wide, and 0.1 cm thick. Care was taken to address problems inherent in electrical flow cells of this type; mainly gas generation from electrode reaction, Joule Heat and membrane flexure.

The BOCE cell is approximately 24.0 cm long, 7.0 cm wide, and 2.0 cm thick. The central separation chamber of the cell is machined from a plastic sheet that is divided into two halves to accommodate feed and exit channels. Fluid is introduced at either end of the chamber by means of a stainless steel syringe connected to polypropylene fittings extending through the electrolyte bath and connecting to the reservoirs. The separation chamber is sandwiched between two cellulose membranes, supported by the electrode screens. The layers are clamped between two plexiglass blocks. In the center of each block a rectangular opening approximately the size of the separation chamber was machined. This design allows the central chamber to be sealed with the membranes and screen support using bolts to provide uniform pressure around the perimeter.

Giddings [7] found in experiments using a similar device that cellulose membranes are prone to flexing even upon small pressure fluctuations. The requirement of fixed volume in the separation chamber thus necessitates the use of a support. Aside from chemical compatibility with the buffer solution and mechanical strength, the electrical resistance was an important consideration. It was therefore decided that the electrode screens could be used as supports, thus serving dual purposes. This reduced the electrode separation to under 1.1 mm.

Gas bubbles and Joule heat are removed by submerging the entire cell in an electrolyte bath open to atmosphere. The bath accommodates up to 6 liters of electrolyte fluid and copper cooling coils. The cell is positioned in the bath with the 7.0 cm side forming the vertical axis, and gas bubbles generated from electrode reaction are removed from the electrodes through the machined

openings in the clamping block halves.

The two oscillatory driving forces were provided by a KEPCO BOP100-4M bipolar power supply capable of constant current operation and a specially designed syringe pump. The electric field was controlled using LabVIEW software and a 100 MHz Pentium personal computer. Bulk fluid conductivity data was acquired into LabVIEW using a Cole-Parmer conductivity meter and the amplitude of the current waveform was simultaneously adjusted to maintain the desired electric field. The flow waveforms were delivered to the syringe pump using a Galil DMC-1500 motion controller and software. Position data from the syringe pump was fed back into LabVIEW allowing phase locking of the two driving forces to within a few milliseconds. Temperature was monitored using the Cole-Parmer conductivity meter and protein concentration was analyzed using a Varian UV-VIS spectrometer.

## Results

The focus of preliminary experiments was to verify qualitatively that the interaction of a purely oscillatory shear flow with an oscillatory electric field could indeed lead to the net convection of a single charged protein species under conditions of uniform concentration throughout the system. Furthermore, we sought to demonstrate that by changing the dimensionless mobility,  $\alpha$ , by changing the amplitude of the electric field, we could change the sign and magnitude of the velocity of the protein. To this end preliminary experiments were conducted using Bovine Hemoglobin (BHb) dissolved in a sodium acetate/acetic acid buffer of pH 4.5 and conductivity of approximately  $375.0 \frac{\mu S}{cm}$ . Based on results from Douglas et. al. [8], the electrophoretic mobility of BHb was approximately  $17.4e^{-5} \frac{cm^2}{V_{sec}}$ . The choices of waveforms included  $h(wt) = \sin(wt) - 0.05$  for the electric field and  $f(wt) = 2\cos(2wt)$  for the crossflow. The concentration throughout the system was initially uniform using a 0.021 wt% solution of BHb. The syringe, which served as the inlet reservoir, was filled with a volume of 8mL of protein solution, while the outlet reservoir contained approximately 40mL of the same solution.

For each of the experiments, the frequency of oscillation was chosen to be  $0.068 \frac{1}{sec}$  and the stroke volume to be 1.5 mL. For  $\alpha = 0.25$ , an electric field amplitude of  $9.795 \frac{V}{cm}$  was required, and for  $\alpha = 0.5$ , the amplitude was doubled. In both experiments, the concentration of the outlet reservoir was monitored with time. The results of the experiment using  $\alpha = 0.5$  is shown in Figure 4. Note the concentration of the outlet reservoir increased by over 10% for 20 minutes of run time while the syringe concentration (not shown) was almost entirely depleted. The results of these experiments indicate that even with initially uniform concentrations, a net flux could be obtained for both choices of  $\alpha$ , and furthermore, the magnitude of the velocity qualitatively agreed with theory.

Experiments will continue with single protein species using various oscillatory shear flows and dimensionless mobilities under both transient and steady state conditions. From these experiments we hope to achieve quantitative comparisons of the net velocity and effective diffusivity of various protein species. Additionally, we will conduct multi-protein experiments in an attempt to verify that binary oscillatory crossflow electrophoresis as an effective binary separation technique.

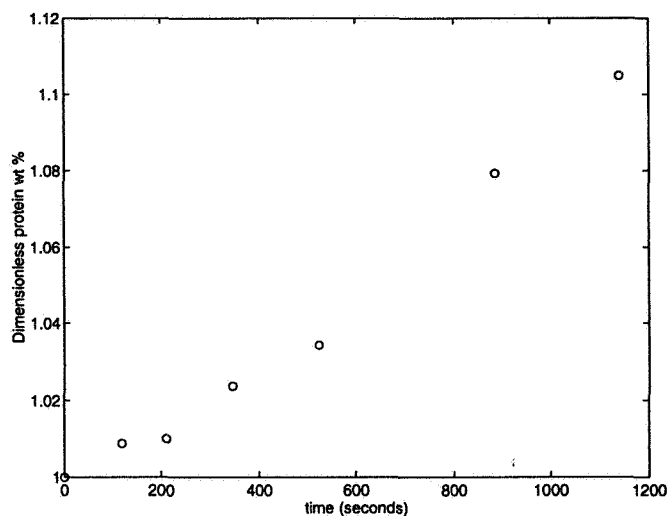


Figure 4: Plot of dimensionless weight percent of Bovine Hemoglobin in the outlet reservoir versus time for a dimensionless electrophoretic mobility of  $\alpha = 0.5$ .

## References

- [1] Tisilius, A., "A New Apparatus for Electrophoretic Analysis of Colloidal Mixtures," *Trans. Farad. Soc.*, **33**, 524 (1937)
- [2] Rhodes, P.H., R.S. Snyder, and G.O. Roberts, "Electrohydrodynamic Distortion of Sample Streams in Continuous Flow Electrophoresis" *J. Colloid and Interface Sci.* **Vol 129 No 1**, 78 (1988)
- [3] Sayville, D.A., "Electrohydrodynamic Deformation of a Particulate Stream by a Transverse Electric Field " *The American Physical Soc.* **Vol 71 No 18**, Nov 1, 2907 (1993)
- [4] Chandhok, A.K., and D.T. Leighton, Jr., "Oscillatory Cross-Flow Electrophoresis," *AIChE Journal*, **Vol 37 No 10**, 1537 (1991)
- [5] Aris, R., "On the Dispersion of a Solute by Diffusion Convection and Exchange Between Phases," *Proc. Roy. Soc. A*, **252**, 539 (1959)
- [6] Watson, E.J., "Diffusion in Oscillatory Pipe Flow," *Journal of Fluid Mechanics*, **Vol 133**, 233 (1983)
- [7] Giddings, J.C., M.N. Myers, K.D. Caldwell, and S.R. Fisher, "Analysis of Biological Macromolecules and Particles by Field-Flow Fractionation" *Methods of Biochemical Analysis*, **Vol 26** 79 (1976)
- [8] Douglas, N.G., A.A Humffray, H.R.C. Pratt, and G.W. Stevens, "Electrophoretic Mobilities of Proteins and Protein Mixtures," *Chem Eng Sci*, **Vol 50 No 5**, 743 (1995)

**Electrokinetic transport of heterogeneous particles in suspensions**

John Anderson, Carnegie Mellon University

**Paper not available**





# ELECTROHYDRODYNAMIC INTERACTION OF A PAIR OF SPHERICAL DROPS

J. A. Erker\* and J. C. Baygents<sup>†\*</sup>

Program in Applied Mathematics\*

Department of Chemical and Environmental Engineering<sup>†</sup>

The University of Arizona

Tucson, AZ 85721

## ABSTRACT

The axisymmetric electrohydrodynamic interaction between two spherical emulsion drops has been examined, using the leaky dielectric model to represent the constitutive behavior of the liquid phases. The results follow from the general solutions in bispherical coordinates to the Laplace equation for the electric potential and the Stokes equations for the velocity field. For drops of similar composition, the electrical interactions induced between the drops by the imposition of the electric field are always attractive, meaning they favor coalescence of the drop pair. The hydrodynamic interactions, however, are not always favorable and, indeed, are shown in certain circumstances to drive the drops apart.

## INTRODUCTION

The response of individual emulsion drops to the imposition of electric fields has been studied for a number of decades. The archetypal work on the subject is that due to Taylor (ref. 1), who first elucidated the role played by weak electrical conduction processes in the context of drop deformation caused by externally-imposed electric fields. Central to the drop deformation, Taylor showed, were steady fluid circulations driven in and about the drop. The circulations stem from interfacial electrical stresses that arise as a consequence of ohmic conduction processes in the liquids.

The circulations described by Taylor have since been recognized to be of technological significance as a tool to enhance heat and mass transfer in liquid-liquid dispersions. In the work that we summarize below, we show that the circulations are also significant with regard to the interactions that occur between neighboring drops in a space-filling dispersion. That is, we find the imposition of an electric field drives relative motion between a pair of drops that is a strong function of the hydrodynamics. The behavior of the emulsified drops thus contrasts with that of aerosols, where electrical interactions dominate the pairwise behavior.

## PROBLEM STATEMENT

Consider two spherical emulsion drops immersed in a fluid with which they are immiscible. In general, the drops need not be the same size, and may possess electromechanical properties (e.g. viscosity  $\mu$ , electrical conductivity  $\sigma$  and dielectric constant  $\epsilon$ ) distinct from one another as well as from those of the surrounding fluid (Fig. 1). Suppose now that a uniform electric field of strength  $E_\infty$  is externally applied along the line of centers of the drops. If the fluids are poor conductors, free charge will accumulate at the interfaces with the result that: one, the drops exert electrical forces on one another; and two, tangential

Maxwell stresses drive fluid circulation in and around the drops (ref. 1). Depending on the resultant of the electrical and hydrodynamic interactions, the relative motion between the drops may be such that they are either drawn together, or they move apart.

In the present analysis, we use the leaky dielectric model to represent the constitutive behavior of the fluids. Furthermore, we examine the case where surface tension is sufficiently high so as to hold the drops spherical. This fixed nature of the geometry facilitates an analytic solution of the electrohydrodynamic problem in the form of an expansion in bispherical harmonics.

Provided the charge relaxation time  $\epsilon_3\epsilon_0/\sigma_3$  is small compared to the characteristic time associated with that of fluid motion,  $\mu_3/\epsilon_3\epsilon_0 E_\infty^2$ , one can solve for the electric potential independently of the flow-field. The electrostatics are governed by the Laplace equation

$$\nabla^2 \Phi_i = 0 \quad \text{for} \quad i = 1, 2, 3, \quad (1)$$

where  $\Phi_i$  is the potential in each of the three regions (Fig. 1). The boundary conditions on the drop surfaces are those of continuity of both  $\Phi$  and the normal component of electric current density. Far from the drops,  $-\nabla\Phi$  goes over to the applied field.

The flow is slow and axisymmetric, so in cylindrical coordinates,

$$E^4 \psi = 0, \quad \text{with} \quad E^2 = r \frac{\partial}{\partial r} \left( \frac{1}{r} \frac{\partial}{\partial r} \right) + \frac{\partial^2}{\partial z^2}, \quad (2)$$

and  $\psi$  is the stream function. The velocity is continuous, and the tangential components of the stress balance on the drop surfaces. The normal stress balance is not considered explicitly; instead we apply a kinematic condition to the normal component of the velocity.

The solution to the Stokes equation gives us the forces on the drops due to the electrically-driven circulations, as well as the hydrodynamic resistance to the relative motion of the drops. The translational velocities  $V_1$  and  $V_2$  of the drops, both of which are in the  $z$  direction, follow from balancing the force due to the electrical interactions between the drops with the two hydrodynamic forces, viz. the hydrodynamic force that stems from the electrically-driven circulations and that due to the hydrodynamic resistance to the drops' relative motion.

For simplicity, all variables are made dimensionless through division by the following characteristic quantities: length,  $a_1$ ; electric potential,  $a_1 E_\infty$ ; stress,  $\epsilon_3\epsilon_0 E_\infty^2$ ; and velocity,  $a_1 \epsilon_3\epsilon_0 E_\infty^2 / \mu_3$ .

Owing to the geometry of the problem, it is convenient to introduce bispherical coordinates  $\xi$  and  $\eta$ , which are related to (dimensionless) cylindrical coordinates  $r$  and  $z$  in the following manner:

$$z = \frac{a \sinh \xi}{\cosh \xi - \cos \eta}; \quad r = \frac{a \sin \eta}{\cosh \xi - \cos \eta}. \quad (3)$$

$\xi > 0$  for  $z > 0$ ,  $\xi < 0$  for  $z < 0$ , with  $\xi = 0$  on the plane  $z = 0$  and for infinite distance from the drops.  $\eta$  represents the inverse tangent of the angle between two lines drawn to a point from the drop centers. The surfaces of drops 1 and 2 have constant values of  $\xi$ , denoted  $\xi_1$  and  $\xi_2$ . These values are related to the drop radii and distances  $d_i$  from the plane  $z = 0$  by  $a_i/a_1 = \pm a \operatorname{cosech} \xi_i$  and  $d_i/a_1 = \pm a \coth \xi_i$ , with the plus and minus signs for  $i = 1$  and  $2$ , respectively.

## RESULTS AND DISCUSSION

The solution to the electrostatics problem in the bispherical system is (ref. 2)

$$\Phi_1 = -z + (\cosh \xi - \mu)^{\frac{1}{2}} \sum_{n=0}^{\infty} C_n \exp \left[ - \left( n + \frac{1}{2} \right) \xi \right] P_n(\mu), \quad (4)$$

$$\Phi_2 = -z + (\cosh \xi - \mu)^{\frac{1}{2}} \sum_{n=0}^{\infty} D_n \exp \left[ \left( n + \frac{1}{2} \right) \xi \right] P_n(\mu), \quad (5)$$

$$\Phi_3 = -z + (\cosh \xi - \mu)^{\frac{1}{2}} \sum_{n=0}^{\infty} \left\{ A_n \exp \left[ -\left( n + \frac{1}{2} \right) \xi \right] + B_n \exp \left[ \left( n + \frac{1}{2} \right) \xi \right] \right\} P_n(\mu) \quad (6)$$

where  $\mu = \cosh \eta$ , and  $P_n(\mu)$  is the  $n$ th Legendre polynomial. The constants  $A_n, B_n, C_n$ , and  $D_n$  are determined via recursion relations obtained by applying the boundary conditions and using the orthogonality of the Legendre polynomials.

Knowing the potential enables us to get an explicit expression for the electric stress at the surface, which in turn gives us an expression for the total electric force on each drop, as we integrate the stress over each drop surface, viz.

$$F_i^{\text{elec}} = 2\pi \int_{-1}^1 \left\{ \frac{1}{2} \frac{1 - \mu \cosh \xi}{\cosh \xi - \mu} \left[ -\frac{\sigma_i}{\sigma_3} \left( \frac{\partial \Phi_i}{\partial \xi} \right)_{\xi_i}^2 + (1 - \mu^2) \left( \frac{\partial \Phi_i}{\partial \mu} \right)_{\xi_i}^2 \right] - \frac{\sigma_i}{\sigma_3} \sinh \xi \frac{1 - \mu^2}{\cosh \xi - \mu} \frac{\partial \Phi_i}{\partial \xi} \right|_{\xi_i} \frac{\partial \Phi_i}{\partial \mu} \right|_{\xi_i} \right\} d\mu, \quad i = 1, 2. \quad (7)$$

Note the tangential component of the electric stresses also contribute to the tangential stress balance condition for the drop surfaces and this drives the velocity field.

The general solution to the Stokes equation for the stream function  $\psi$  is

$$\psi_i = (\cosh \xi - \mu)^{-\frac{3}{2}} (1 - \mu^2) \sum_{n=1}^{\infty} U_{in}(\xi) P'_n(\mu), \quad i = 1, 2, 3, \quad (8)$$

where

$$U_{in}(\xi) = a_{in} \sinh \left[ -\left( n - \frac{1}{2} \right) \xi \right] + b_{in} \cosh \left[ \left( n - \frac{1}{2} \right) \xi \right] + c_{in} \sinh \left[ -\left( n + \frac{3}{2} \right) \xi \right] + d_{in} \cosh \left[ \left( n + \frac{3}{2} \right) \xi \right], \quad i = 1, 2, 3. \quad (9)$$

Thus the boundary conditions can be recast as equations in  $U_1(\xi_1)$  and  $U_2(\xi_2)$ , which comprise a linear system of equations for the stream function coefficients  $a_{in}, b_{in}, c_{in}$ , and  $d_{in}$  for each  $n$  from 1 to  $\infty$ .

Sozou (ref. 3) has implemented this scheme for the particular situation involving identical drops, subject to the restriction that there be no relative motion between the drops. Here we relax Sozou's constraints, allowing for relative motion and considering drops of different size and electromechanical properties. The principal results that come from our analysis, then, are the drop velocities  $V_1$  and  $V_2$ , and the conditions for which no relative motion obtains.

The coefficients for the external flow field are used to compute the net hydrodynamic force  $F_i^{\text{hyd}}$  exerted on the drops, through the well-known formulae (ref. 4)

$$F_i^{\text{hyd}} = F_i^{\text{rel}} + F_i^{\text{circ}} = -\frac{2\sqrt{2}\pi}{a} \sum_{n=1}^{\infty} n(n+1) (a_{3n} \pm b_{3n} + c_{3n} \pm d_{3n}), \quad (10)$$

with the plus and minus signs corresponding to  $i = 1$  and  $2$ , respectively. The coefficients  $a_{in}, b_{in}, c_{in}$ , and  $d_{in}$  are linear in  $V_1$  and  $V_2$ , and  $F_i^{\text{hyd}}$  involves a contribution from the relative motion  $F_i^{\text{rel}}$  and from the electrically-driven circulation  $F_i^{\text{circ}}$ . Since  $F_i^{\text{rel}}$  is a linear combination of  $V_1$  and  $V_2$ , one may write

$$F_1^{\text{rel}} = DC_{11}V_1 + DC_{12}V_2, \quad F_2^{\text{rel}} = DC_{21}V_1 + DC_{22}V_2, \quad (11)$$

where  $DC_{11}$ ,  $DC_{12}$ ,  $DC_{21}$ , and  $DC_{22}$  are the drag coefficients for the relative motion (refs. 5 and 6). Finally, balancing  $F_i^{\text{elec}}$ ,  $F_i^{\text{rel}}$ , and  $F_i^{\text{circ}}$  on each drop yields the drop velocities, viz.

$$V_1 = - \left[ DC_{22}(F_1^{\text{elec}} + F_1^{\text{circ}}) - DC_{12}(F_2^{\text{elec}} + F_2^{\text{circ}}) \right] / \Delta, \quad (12)$$

$$V_2 = \left[ DC_{12}(F_1^{\text{elec}} + F_1^{\text{circ}}) - DC_{22}(F_2^{\text{elec}} + F_2^{\text{circ}}) \right] / \Delta, \quad (13)$$

where

$$\Delta = DC_{11} DC_{22} - DC_{12} DC_{21}. \quad (14)$$

In Fig. 2, we give the translational velocity of drop 1 as a function of center-to-center separation for the special case that the drops are identical. For this circumstance, the electric forces on the drops are attractive. The electrically-driven circulations are attractive when  $\sigma_1/\sigma_3 < \epsilon_1/\epsilon_3$ , repulsive for  $\sigma_1/\sigma_3 > \epsilon_1/\epsilon_3$ , and vanish when  $\sigma_1/\sigma_3 = \epsilon_1/\epsilon_3$ . Plots are given for various conductivity ratios  $\sigma_1/\sigma_3$ , with viscosity ratio  $\mu_1/\mu_3$  fixed at 1.0 and dielectric constant ratio  $\epsilon_1/\epsilon_3$  fixed at 2.0. A negative velocity indicates that the drops are moving toward one another, so one can see that for certain values of  $\sigma_1/\sigma_3 > \epsilon_1/\epsilon_3$ , the drops may move apart. Physically, this means that the tangential electric stresses acting on the drop surfaces drive circulations that not only oppose drop motion, but are strong enough to overcome the attractive force due to electric interactions.

In Fig. 3 there are given plots of combinations of conductivity ratio  $\sigma_1/\sigma_3$  and dielectric constant ratio  $\epsilon_1/\epsilon_3$  for various drop separations at which the relative motion between the drops vanishes. Again, for simplicity, the results shown are for identical drops. Given a curve for a particular separation  $D = (d_1 + d_2)/a_1$ , the area underneath the curve represents combinations of  $\sigma_1/\sigma_3$  and  $\epsilon_1/\epsilon_3$  for which the drops are driven apart by the fluid flow when the separation is at least  $D$ . For values of  $\sigma_1/\sigma_3$  and  $\epsilon_1/\epsilon_3$  that lie above the curve, the drops translate toward each other when at separations less than  $D$ . Thus, we see in Fig. 3 that a smaller variety of electrical properties facilitate coalescence for larger separations. This is mainly because  $F_i^{\text{elec}}$ ,  $i = 1, 2$ , decays inversely with drop separation to the fourth power, whereas the interactions due to the circulations decay as one over the separation squared.

## CONCLUDING REMARKS

The results presented here are a useful leading-order analysis for electrohydrodynamic interactions involving drops that may deform modestly under the action of an electric field. In general, keeping track of drop shape must be done numerically. The analytic results offer the advantage of providing qualitative behavior, such as the direction of the drops' translation for different values of  $\sigma_i/\sigma_3$ ,  $\epsilon_i/\epsilon_3$ ,  $\mu_i/\mu_3$ , and drop separation. Such information is rather cumbersome to generate numerically, especially when the relative motion is weak. Denoting the interfacial tension as  $\gamma$ , we note that the capillary number  $Ca = a_1 \epsilon_3 \epsilon_0 E_\infty^2 / \gamma$  is small ( $\ll 1$ ) in our study, and thus one can add corrections to the solution presented, using  $Ca$  as a perturbation parameter.

The results are most useful for appreciable drop separations, i.e. when the gap between the drop surfaces is at least the radius of the smaller drop. Referring to Eqs. (6), (7), and (8), we note that for smaller separations, it takes more terms in the sums for  $\Phi$  and  $\psi$  to make these expressions accurate. Simple expressions for hydrodynamic resistance have been derived (refs. 7, 8) based on asymptotic analysis of the infinite sum that appears in Eq. (10) for the case of strictly spherical drops. In addition, it is at smaller separations where drop deformation becomes more significant. Indeed, it has been noted by Davis et al. (ref. 8) and others that, for small separations with the drops moving toward one another, the attendant

increase in pressure within the lubrication layer results in dimpling of the drop surfaces. A subject for subsequent investigation, therefore, would be the influence of the electrohydrodynamic circulations on such dimpling.

#### REFERENCES

1. Taylor, G.; The Circulation Produced in a Drop by an Electric Field, *Proc. Roy. Soc. A*, Vol. 291, 1966, pp. 159-167.
2. Stoy, R.D.; Solution Procedure for the Laplace Equation in Bispherical Coordinates for Two Spheres In a Uniform External Field: Parallel Orientation, *J. Appl. Phys.*, Vol 65, No. 7, April 1989, pp.2611-2615.
3. Sozou, C.; Electrohydrodynamics of a Pair of Liquid Drops, *J. Fluid Mech.*, Vol. 67, part 2, 1975, pp. 339-349.
4. Stimson, M.; and Jeffery, G.B.; The Motion of Two Spheres in a Viscous Fluid, *Proc. Roy. Soc. A*, Vol. 334, 1926, pp. 110-116.
5. Rushton, E.; and Davies, G.A.; The Slow Unsteady Settling of Two Fluid Spheres Along Their Line of Centres, *Appl. Sci. Res.*, Vol 28, July 1973, pp. 37-61.
6. Haber, S.; Hetsroni, G.; and Solan, A.; On the Low Reynolds Number Motion of Two Droplets, *Int. J. Multiphase Flow*, Vol 1, 1973, pp. 57-71.
7. Beshkov, V.N.; Radoev, B.P.; and Ivanov, I.B.; Slow Motion of Two Droplets and a Droplet Interface Towards a Fluid or Solid Interface, *Int. J. Multiphase Flow*, Vol. 4, pp. 563-570.
8. Davis, R.H.; Schonberg, J.A.; and Rallison, J.M.; The Lubrication Force Between Two Viscous Drops, *Phys. Fluids A*, Vol. 1, No. 1, Jan. 1989, pp. 77-81.

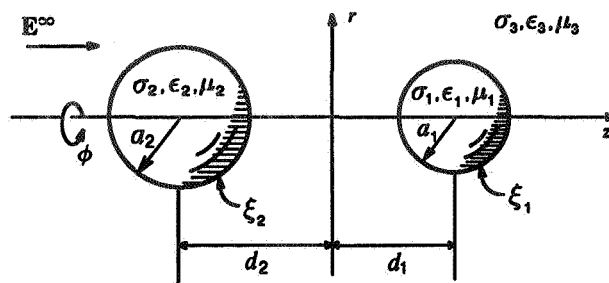


Figure 1: Definition sketch.

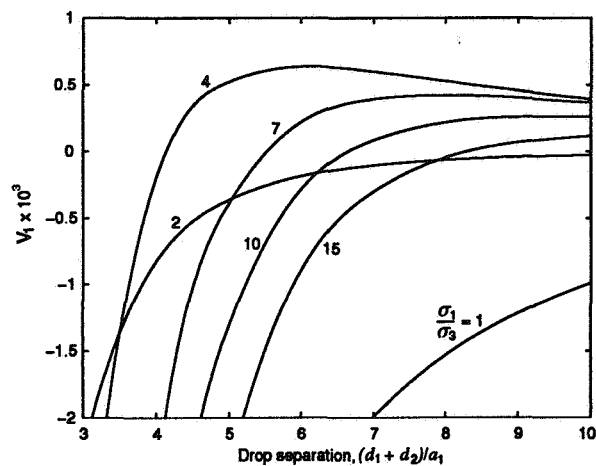


Figure 2: Velocity of drop 1 as a function of center-to-center separation, for various values of  $\sigma_1/\sigma_3 (= \sigma_2/\sigma_3)$ . The unit of length is the radius of drop 1.  $\mu_1/\mu_3 = \mu_2/\mu_3 = 1$ ;  $\epsilon_1/\epsilon_3 = \epsilon_2/\epsilon_3 = 2$ .

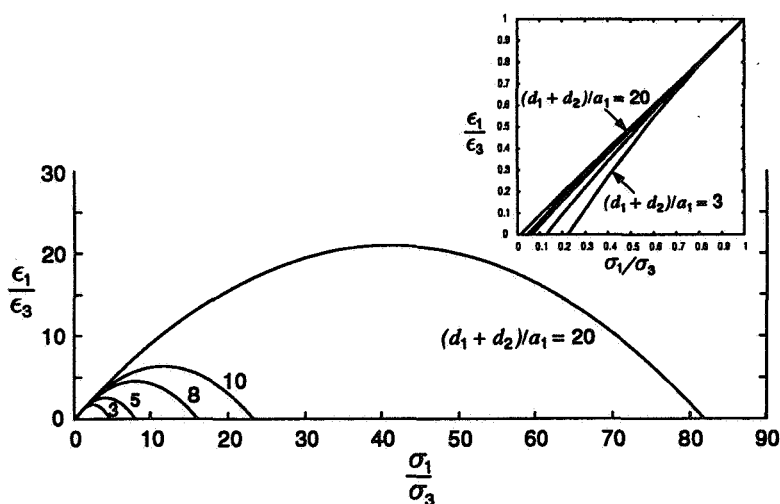


Figure 3: Combinations of conductivity and dielectric constant that hold two drops fixed in space, for various center-to center separations.  $\mu_1/\mu_3 = \mu_2/\mu_3 = 1$ ;  $a_1 = a_2$ ;  $\sigma_1/\sigma_3 = \sigma_2/\sigma_3$ ;  $\epsilon_1/\epsilon_3 = \epsilon_2/\epsilon_3$ .

# CELL AND PARTICLE INTERACTIONS AND AGGREGATION DURING ELECTROPHORETIC MOTION

Hua Wang<sup>1</sup>, Shulin Zeng, Michael Loewenberg<sup>2</sup>, Paul Todd, and Robert H. Davis

Department of Chemical Engineering

University of Colorado

Boulder, Colorado 80309-0424

## ABSTRACT

The stability and pairwise aggregation rates of small spherical particles under the collective effects of buoyancy-driven motion and electrophoretic migration are analyzed. The particles are assumed to be non-Brownian, with thin double-layers and different zeta potentials. The particle aggregation rates may be enhanced or reduced, respectively, by parallel and antiparallel alignments of the buoyancy-driven and electrophoretic velocities. For antiparallel alignments, with the buoyancy-driven relative velocity exceeding the electrophoretic relative velocity between two widely-separated particles, there is a "collision-forbidden region" in parameter space due to hydrodynamic interactions; thus, the suspension becomes stable against aggregation.

## INTRODUCTION

Colloidal suspensions play important roles in many engineering fields, including materials processing, environmental engineering, chemical engineering, and biotechnology. An important goal in many such processes is to predict the conditions for which a suspension is stable against aggregation, or the particle aggregation rate for an unstable suspension. In an unstirred suspension, buoyancy-driven relative particle motion may result in aggregation of particles with different sizes or density. In addition, most colloidal particles are charged and so migrate in an applied electric field. In a heterogeneous suspension, electrophoretic relative motion and aggregation of particles with different electric charges or  $\zeta$ -potentials may occur [1,2].

Gravity-induced particle aggregation has been studied by Melik and Fogler [3] and Davis [4], who employed trajectory analyses to predict pairwise particle collision rates. Recently, Nichols, Loewenberg and Davis [5] analyzed the stability criteria and pairwise aggregation rates for electrophoretic motion of colloidal spheres with differing zeta potentials and thin, unpolarized electric double layers. Their results indicate that hydrodynamic interactions generally have a weaker effect on the collision rate for electrophoretic motion than for gravity motion. As a result, the collision efficiencies for electrophoresis generally exceed those for buoyancy-driven motion by an order of magnitude. In these studies, the effects of gravity motion and electrophoretic migration were examined independently. However, gravity and electrophoresis may act simultaneously in some applications. One example is the separation of slowly sedimenting suspensions, for which an electric field may be employed to accelerate the initial formation of aggregates; once the aggregates become large enough, gravity will play a more important role.

Stability criteria and aggregation rates of charged particles in a dilute colloidal suspension under the collective action of gravity and an electric field are considered in this work. Of particular interest are the cases of parallel and antiparallel alignment of the undisturbed gravity and electrophoretic velocities, as these may lead to greatly increased or reduced aggregation rates, respectively.

## THEORETICAL DEVELOPMENT

A dilute colloidal suspension containing spherical particles dispersed in an isothermal fluid of Newtonian viscosity  $\mu$  and density  $\rho$  is considered. For dilute suspensions, the probability of a third particle influencing

<sup>1</sup>Present address: General Electric Company, Schenectady, NY 12301

<sup>2</sup>Present address: Department of Chemical Engineering, Yale University, New Haven, CT 06524-2159

the relative motion of two particles is small, and so the analysis is restricted to binary interaction of two spherical particles of radii  $a_1$  and  $a_2$ , densities  $\rho_1$  and  $\rho_2$ , and zeta potentials  $\zeta_1$  and  $\zeta_2$ , respectively. The particles are assumed to be small enough so that inertia may be neglected, but sufficiently large that Brownian motion is negligible. These assumptions are valid for sedimenting particles of approximately  $1\ \mu\text{m}$  -  $50\ \mu\text{m}$  in radii [4]. For electrophoretic motion, these assumptions are valid over a broader range of  $0.1\ \mu\text{m}$  -  $1\ \text{cm}$  in radius [2,5]. This study is also restricted to particles with moderate surface potentials and thin electric double layers.

The velocity of each particle is linearly dependent on gravity, the electric field, and the interparticle forces. Moreover, the relative velocity  $V_{12} = U_2 - U_1$  can be decomposed into motion along and normal to the line of centers:

$$V_{12} = V_{12}^{G,o} \cdot \left[ \frac{\mathbf{rr}}{r^2} L^G(s) + \left( I - \frac{\mathbf{rr}}{r^2} \right) M^G(s) \right] + V_{12}^{E,o} \cdot \left[ \frac{\mathbf{rr}}{r^2} L^E(s) + \left( I - \frac{\mathbf{rr}}{r^2} \right) M^E(s) \right] - \frac{a_1 a_2}{6\pi\mu a_1 a_2} \frac{\mathbf{rr}}{r^2} G(s) \cdot \nabla \Phi_{12} \quad , \quad (1)$$

where  $\mathbf{r}$  is the vector from the center of particle 1 to the center of particle 2,  $I$  is the unit second-order tensor,  $s = 2r/(a_1 + a_2)$  is the dimensionless separation between particle centers, and  $\Phi_{12}(r)$  is interparticle force potential.

The relative velocity for two widely separated particles due to gravity is given by the Stokes formula:

$$V_{12}^{G,o} = U_2^{G,o} - U_1^{G,o} = \frac{2(\rho_1 - \rho)a_1^2(1 - \lambda^2\gamma)}{9\mu} \mathbf{g} \quad , \quad (2)$$

where  $\lambda = a_2/a_1$  is the particle size ratio,  $\gamma = (\rho_2 - \rho)/(\rho_1 - \rho)$  is the buoyant density ratio, and  $\mathbf{g}$  is the gravitational acceleration vector. By contrast, the electrophoretic relative velocity of two widely separated particles is independent of their sizes, shapes, and densities [5]:

$$V_{12}^{E,o} = U_2^{E,o} - U_1^{E,o} = \frac{\epsilon\zeta_1(\beta - 1)}{\mu} \mathbf{E} \quad , \quad (3)$$

where  $\beta = \zeta_2/\zeta_1$  is the ratio of zeta potentials, and  $\mathbf{E}$  is the applied electric field.

The interparticle force acts only along the line of centers and is given by  $-\nabla\Phi_{12}$ , with the total interparticle potential assumed to be the sum of the individual attractive and repulsive contributions by DLVO theory. The attractive van der Waals potential for spheres close together is [5]:

$$\Phi_A = -\frac{Aa_1a_2}{6(a_1 + a_2)h} \left[ 1 - \frac{5.32h}{\lambda_L} \ln \left( 1 + \frac{\lambda_L}{5.32h} \right) \right] \quad , \quad (4)$$

where  $h$  is the separation between particles surfaces,  $\lambda_L$  is the London retardation wavelength, of approximately  $0.1\ \mu\text{m}$ , and  $A$  is the Hamaker constant, which is typically of order  $10^{-19}$  -  $10^{-21}$  J. The electrostatic repulsive potential due to thin overlapping double layers and modest surface potentials is [5]:

$$\Phi_R = \frac{\epsilon a_1 a_2 (\zeta_1^2 + \zeta_2^2)}{4(a_1 + a_2)} \left[ \frac{2\zeta_1 \zeta_2}{\zeta_1^2 + \zeta_2^2} \ln \left( \frac{1 + \exp(-\kappa h)}{1 - \exp(-\kappa h)} \right) + \ln(1 - \exp(-2\kappa h)) \right] \quad , \quad (5)$$

where  $\kappa$  is the reciprocal double-layer thickness, which increases with the ionic strength of the surrounding fluid. The above expression is valid for constant surface potentials  $\kappa a > 10$ , and  $\zeta < 60\ \text{mV}$ .

The relative mobility functions for motion along the line of centers ( $L^G$ ,  $L^E$ , and  $G$ ) and motion normal to the line of centers ( $M^G$  and  $M^E$ ) describe the effects of hydrodynamic interactions between two spherical particles in creeping flow.  $L^E$ ,  $M^E$  and  $G$  depend only on the size ratio,  $\lambda$ , and the dimensionless distance between centers,  $s$ ,



and are unchanged when  $\lambda$  is replaced by  $\lambda^{-1}$ .  $L^G$  and  $M^G$  also depend on the buoyant density ratio,  $\gamma$ , and are unchanged when  $\lambda$  and  $\gamma$  are replaced by  $\lambda^{-1}$  and  $\gamma^{-1}$ , respectively.

For the electrophoretic relative mobilities,  $L^E$  and  $M^E$ , a far-field reflection solution [6], a boundary collocation solution [7,8], and a near-field lubrication solution [2] are used in this study. The relative mobility  $G$  and the buoyancy-driven relative mobilities,  $L^G$  and  $M^G$ , are taken from [9]. The relative mobilities approach unity when the particles are far apart, indicating the absence of hydrodynamic interactions. As the two particles approach each other, the mobilities decrease due to hydrodynamic interactions. For widely separated particles, the relative mobility functions for particles in buoyancy-driven motion depart from unity as  $1/r$ . In contrast, electrophoretic motion of charged particles and their neutralizing double layers has a force-free nature, and the mobility functions have a weaker departure, as  $1/r^3$ . As the separation between two particles vanishes, the mobilities along the line of centers approach zero, whereas the mobilities normal to the line of centers tend to finite limits. For particles in close approach, the electrophoretic relative mobilities are much larger than the buoyancy-driven mobilities due to electrically-driven convection in the electrical double-layer, which facilitates the removal of fluid from the near-contact region that separates two approaching particles, a phenomenon called “electro-osmotic fluid withdrawal” [2].

Decomposing the relative velocity into components along and normal to the line of centers yields:

$$V_r = -[L^G(s) + V_{12}^{E,o} L^E(s) / V_{12}^{G,o}] \cos \theta - \frac{G(s)}{N_A} (f_A(s) - N_R f_R(s)) , \quad (6)$$

$$V_\theta = [M^G(s) + V_{12}^{E,o} M^E(s) / V_{12}^{G,o}] \sin \theta , \quad (7)$$

where  $\theta$  is the angle from  $V_{12}^{G,o}$  to  $r$ , and  $V_r$  and  $V_\theta$  are the components of the relative velocity along and perpendicular to the line of centers, respectively, made dimensionless by  $V_{12}^{G,o} = |V_{12}^{G,o}|$ , and  $V_{12}^{E,o} = V_{12}^{E,o} \cdot V_{12}^{G,o} / V_{12}^{G,o}$ . The parameter  $N_A = 6\pi V_{12}^{G,o} a^2 / A$  represents the ratio of gravitational and van der Waals forces, where  $a = (a_1 + a_2)/2$  is the average radius. The function  $f_A(s)$  is the dimensionless van der Waals force deduced from equation (4). The parameter  $N_R = \epsilon \zeta_1^2 a / A$  describes the characteristic strength of electrostatic repulsion relative to van der Waals attraction. The function  $f_R(s)$  is the dimensionless electrostatic repulsion from equation (5).

By restricting our attention to electric fields which are parallel or antiparallel to the gravity vector, the pairwise aggregation rate per unit volume of the dispersion may be expressed as a collision cross-section times the flux of particle pairs:

$$J_{12} = n_1 n_2 \pi (a_1 + a_2)^2 V_{12}^o E_{12} , \quad (8)$$

where  $n_1$  and  $n_2$  are the number of particles of types 1 and 2, respectively, per unit volume,  $V_{12}^o = |V_{12}^{G,o} + V_{12}^{E,o}|$  is the magnitude of the relative velocity of two isolated particles, and  $E_{12}$  is the collision efficiency. The collision efficiency is unity when the particles move in rectilinear motion without interactions; values differing from unity account for hydrodynamic and interparticle interactions. The collision efficiency is related to the critical parameter,  $E_{12} = \sigma_c^2 / (a_1 + a_2)^2$ , where  $\sigma_c$  is the critical impact parameter defined such that particle aggregation occurs if the initial horizontal offset is  $\sigma \leq \sigma_c$ , as shown in Figure 1.

Following earlier work for collisions induced individually by gravity [3,4] and electrophoresis [5], the relative trajectories of two particles are determined by integrating the relative trajectory equation, which results from dividing (6) by (7):

$$\frac{ds}{d\tau} = -s \frac{[L^G + V_{12}^{E,o} L^E / V_{12}^{G,o}] \cos \theta + [G(f_A - N_R f_R) / N_A]}{[M(s) + V_{12}^{E,o} M^E / V_{12}^{G,o}] \sin \theta} , \quad (9)$$

where  $\tau = 2V_{12}^0 t / (a_1 + a_2)$  is the dimensionless time. The critical impact parameter is determined by integrating equation (9) backwards from a critical point where  $\theta = \pi$  and  $V_r = 0$ , as described previously for gravity [4] and electrophoresis [5] acting independently.

## RESULTS AND DISCUSSION

When a colloidal suspension is said to be stable, it usually means that electrostatic or other repulsive forces prevent the particles from aggregating. When the electrophoretic and gravitational velocities of charged colloidal particles are in opposite directions, however, there may be a purely hydrodynamic stability against aggregation. Consider, for example, the dimensionless relative velocity along the line of centers for the case  $V_{12}^{G,0} / V_{12}^{E,0} = -2.5$ ,  $\lambda = 0.5$ , and  $\gamma = 1$ , illustrated in Figure 2. For this case, the relative motion due to gravity exceeds that due to electrophoresis when the two spheres are well separated, and so the faster-moving sphere approaches the slower-moving one. As the spheres become closer together, hydrodynamic interactions reduce the gravity-induced relative motion more than the electrophoretic relative motion. At a separation distance of about 1.5 average radii, then, the oppositely directed relative velocities balance, and the relative motion along the line of centers is arrested. Thus, the different behavior of pairwise hydrodynamic interactions for gravitational and electrophoretic motion prevents the two spheres from becoming sufficiently close to aggregate.

In the absence of interparticle attractive and repulsive forces, the stability condition of zero relative velocity along the line of centers is, from equation (6),

$$-V_{12}^{G,0} / V_{12}^{E,0} = L^E(s) / L^G(s) .$$

For widely separated spheres ( $s \rightarrow \infty$ ),  $L^E \rightarrow 1$  and  $L^G \rightarrow 1$ , and so  $-V_{12}^{G,0} / V_{12}^{E,0} = 1$  is the lower limit of the stable region of parameter space. As the separation distance  $s$  decreases,  $L^G$  decreases faster than does  $L^E$ , so that  $L^E/L^G$  increases, and the upper limit of the stable region occurs for very small critical separations at which the relative velocity is arrested. In this case,  $L^E/L^G$  approaches a constant provided by lubrication theory [2]. The results are shown in Figure 3 as a function of the size ratio,  $\lambda$ , for buoyant density ratios of  $\gamma = 0$  and  $\gamma = 1$ . A rather large range of relative magnitudes of gravitational and electrophoretic motion is encompassed by the stable or "collision-forbidden" zone, indicating that undesirable aggregation during sedimentation to separate particles by size or density may be eliminated by applying an electric field, if the particles also differ in surface charge or potential.

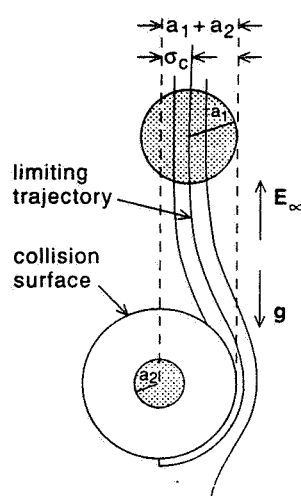


Fig. 1 - Schematic of relative trajectories of two spheres due to gravity and electrophoresis.

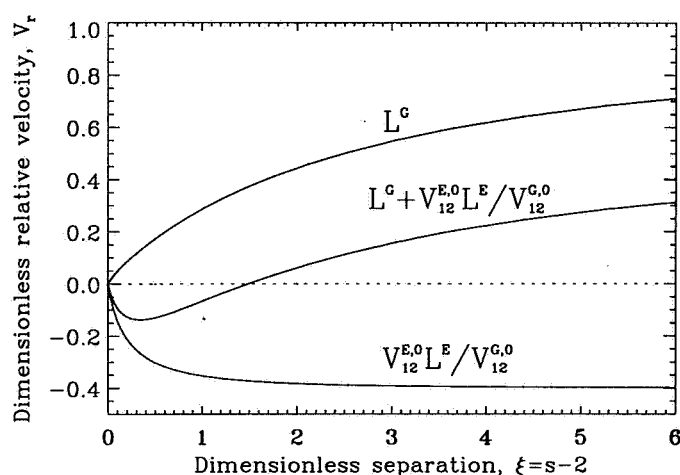
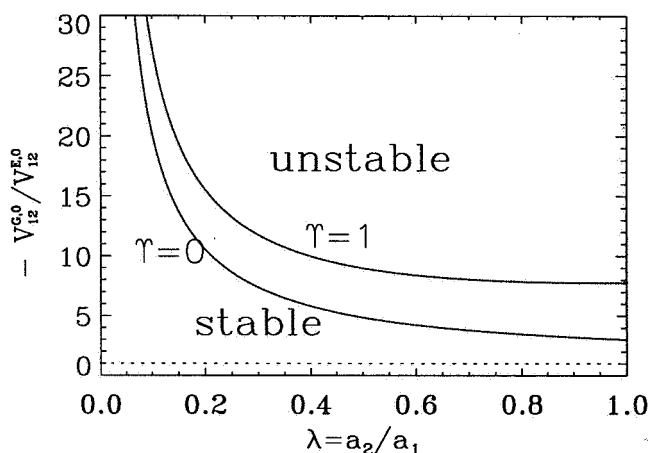


Fig. 2 - Dimensionless relative velocity along the line of centers due to gravity, electrophoresis, and combined effects.

A typical plot of the collision efficiency as a function of the relative velocity parameter  $V_{12}^{G,o}/V_{12}^{E,o}$  is shown in Figure 4 for  $\gamma = 2$ ,  $\beta = 0.5$ ,  $\lambda_L/a = 0.044$ ,  $\kappa a = 10^3$ ,  $N_A = 10^4$ , and  $N_R = 10^2$ . The collision rate per unit volume in the suspension is then given by equation (8). For  $|V_{12}^{G,o}/V_{12}^{E,o}| \gg 1$  and  $|V_{12}^{G,o}/V_{12}^{E,o}| \ll 1$ , the previous results for gravitational aggregation and electrophoretic aggregation, respectively, acting alone are recovered [4,5]. In general, the collision efficiencies for electrophoresis exceed those for sedimentation because of the weaker hydrodynamic interactions for electrophoresis. Also, the collision efficiencies are reduced for small size ratios, because the smaller particle then tends to follow the streamlines around the larger particle and not collide with it.

Varying the parameter  $V_{12}^{G,o}/V_{12}^{E,o}$ , which is the ratio of the relative velocity due to gravity to that due to the electric field for well-separated spheres, reveals some provocative phenomena. When this parameter is positive, electrophoresis and gravity aid each other. In this case, the collision efficiency decreases as  $V_{12}^{G,o}/V_{12}^{E,o}$  increases, due to the stronger hydrodynamic interactions (which inhibit approach and aggregation) for gravity. The downturn for  $V_{12}^{G,o}/V_{12}^{E,o} \rightarrow 0$  is a consequence of the attractive van der Waals forces becoming negligible in this limit with fixed  $N_A$ . When  $V_{12}^{G,o}/V_{12}^{E,o} < 0$ , electrophoresis and sedimentation are in opposite directions. For  $-1 < V_{12}^{G,o}/V_{12}^{E,o} < 0$ , the collision efficiency increases as  $V_{12}^{G,o}/V_{12}^{E,o}$  decreases, and may even exceed unity (implying that hydrodynamic interactions *increase* the collision rate!). In this case, the net relative velocity is dominated by electrophoresis but reduced by gravity; as one particle approaches the other, hydrodynamic interactions cause the gravitational relative velocity to decrease more than electrophoretic relative velocity, so that the net relative velocity *increases*, and the spheres are drawn together at an enhanced rate. In contrast, when  $V_{12}^{G,o}/V_{12}^{E,o} < -1$ , the net relative velocity is dominated by gravity and reduced by electrophoresis. Then as one particle approaches the other, the gravitational velocity is reduced by hydrodynamic interactions to a greater extent, so that the relative velocity decreases. This causes the collision efficiencies to be reduced, and the collision-forbidden zone described earlier is apparent.



**Fig. 3** - Stability diagram showing the collision-forbidden (stable) region of parameter space for antiparallel alignment of gravitational and electrophoretic motion of two different particle species.

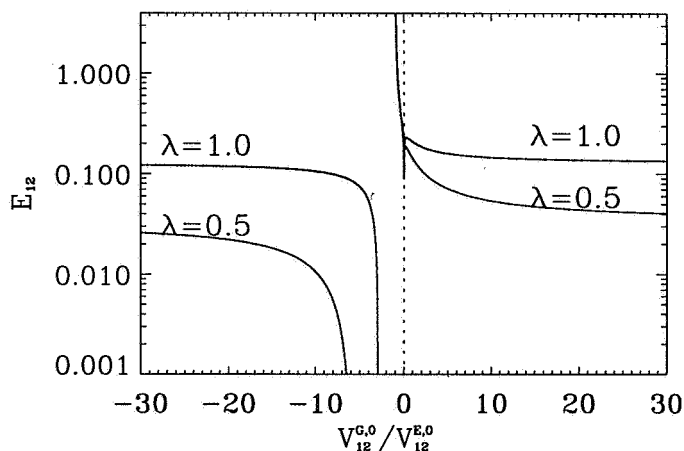


**Fig. 4** - Collision efficiency for combined gravitational and electrophoretic motion.

## CONCLUSIONS AND FUTURE WORK

A trajectory analysis employing hydrodynamic mobility functions has been employed to predict pairwise aggregation rates of small spherical particles in a heterogeneous suspension subject to both gravitational and electrophoretic particle motion. Depending on the relative orientation and magnitude of the gravity vector and the electric field, aggregation may be enhanced or retarded. Due to the stronger hydrodynamic interactions for

gravitational motion, a “collision-forbidden” region is predicted for antiparallel alignment of the gravitational and electrophoretic velocities over a broad range of the relative magnitude of these velocities.

Experiments are planned to test the theoretical predictions. Bidisperse mixtures of small particles with different surface charges will be allowed to sediment under normal gravity, with and without an electric field applied. Both parallel and antiparallel orientations of the electric field and gravity will be employed, including within the collision-forbidden region, to determine the conditions for which aggregation, and hence the sedimentation rate, is enhanced or suppressed. A shallow density gradient will be employed to suppress free convection in the suspending fluid.

Zone electrophoresis experiments, in which the motion and interaction of bands of particles are observed, will also be performed. It is hoped that these will allow direct observation of aggregates, as illustrated in Figure 5 and simulated in Figure 6, where a band of faster-moving particles pass through a band of slower-moving particles to generate a band of aggregates with intermediate mobility.

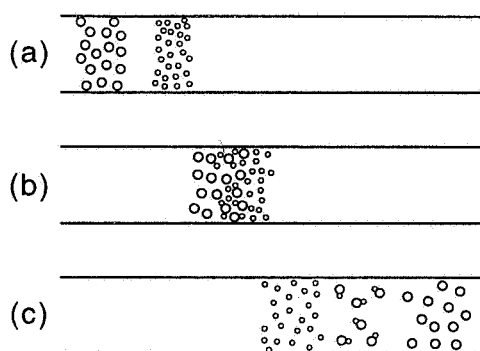


**Fig. 5** - Schematic of aggregation during zone electrophoresis of a high-mobility band passing through a low-mobility band.

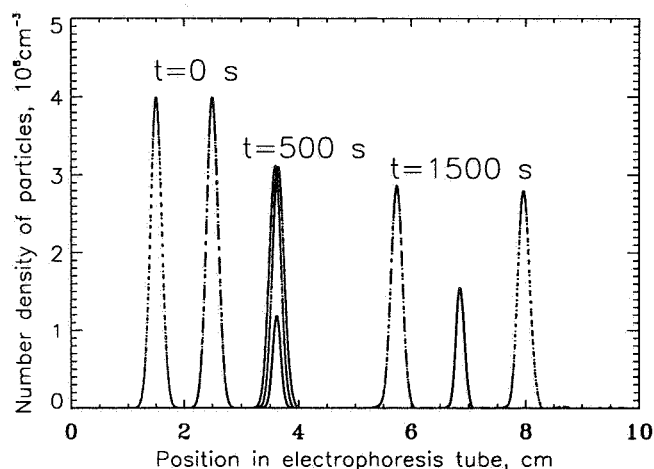


**Fig. 6** - Simulation of aggregation during zone electrophoresis of a high-mobility band passing through a low-mobility band.

## REFERENCES

1. Todd, P. and Hjertén, S., in *Cell Electrophoresis* (ed. Schutt, W. and Klinkmann, H.), Walter de Gruyter and Co., New York, 1985, p. 23.
2. Loewenberg, M. and Davis, R. H., *J. Fluid Mech.*, 1995, **288**, 103.
3. Melik, D. H. and Fogler, H. S., *J. Colloid Interface Sci.*, 1984, **101**, 72.
4. Davis, R. H., *J. Fluid Mech.*, 1984, **145**, 179.
5. Nichols, S. C., Loewenberg, M. and Davis, R. H., *J. Colloid Interface Sci.*, 1995, **176**, 342.
6. Chen, S. B. and Keh, H. J., *AIChE J.*, 1988, **34**, 1075.
7. Keh, H. J. and Yang, F. R., *J. Colloid Interface Sci.*, 1990, **139**, 105.
8. Keh, H. J. and Yang, F. R., *J. Colloid Interface Sci.*, 1991, **145**, 362.
9. Jeffery, D. J. and Onishi, Y. J., *J. Fluid Mech.*, 1984, **139**, 261.

# **Biofluid Mechanics**



# MICROGRAVITY EFFECTS ON TRANSENDOTHELIAL TRANSPORT

John M. Tarbell  
Physiological Transport Studies Laboratory  
Department of Chemical Engineering  
The Pennsylvania State University  
University Park, PA 16802-4400

## ABSTRACT

The endothelial cell (EC) layer which lines blood vessels from the aorta to the capillaries provides the principal barrier to transport of water and solutes between blood and underlying tissue. Endothelial cells are continuously exposed to the mechanical shearing force (shear stress) and normal force (pressure) imposed by flowing blood on their surface, and they are adapted to this mechanical environment. When the cardiovascular system is exposed to microgravity, the mechanical environment of endothelial cells is perturbed drastically and the transport properties of EC layers are altered in response. We have shown recently that step changes in shear stress have an acute effect on transport properties of EC layers in a cell culture model, and several recent studies in different vessels of live animals have confirmed the shear-dependent transport properties of the endothelium.

We hypothesize that alterations in mechanical forces induced by microgravity and their resultant influence on transendothelial transport of water and solutes are, in large measure, responsible for the characteristic cephalad fluid shift observed in humans experiencing microgravity. To study the effects of altered mechanical forces on transendothelial transport and to test pharmacologic agents as counter measures to microgravity induced fluid shifts we have proposed ground-based studies using well defined cell culture models.

In future experiments, we will determine how alterations in hemodynamic forces (pressure and shear stress) affect transendothelial water and protein fluxes using endothelial cells cultured on porous filters and exposed to controlled pressure and shear forces in a unique rotating disk device. The role of intracellular biochemical signalling pathways which are known to be sensitive to mechanical forces will be probed with chemical inhibitors, and pharmacologic agents, known to affect these biochemical pathways, will be tested to determine if they can counteract the effects of altered mechanical forces on transendothelial transport properties.

## INTRODUCTION

Blood vessel walls are lined by a monolayer of endothelial cells which, in addition to providing a blood contacting surface resistant to clotting, forms the principal barrier to transport of water and solutes across the wall. Regulation of water and solute transport is critical for controlling the chemical milieu of tissues serviced by individual vessels. Acute alteration of the endothelial transport barrier in response to the release of chemical agents (e.g., histamine, thrombin) produces local edema which is a central process in the inflammatory response (Ref. 1). Variations in endothelial resistance to transport of macromolecules such as low density lipoprotein are believed by many to play a role in the localization of atherosclerotic plaques in the arterial system (Ref. 2). Changes in transvascular pressure gradient associated with exposure to microgravity conditions in space travel lead to major fluid shifts between vascular and tissue compartments separated by endothelial barriers (Ref. 3). These fluid shifts affect physiological adaptation to space in profound ways (Ref. 4).

Redistribution of fluid volume and solutes between plasma and tissue spaces is dictated by complex physiological interactions among transport mechanisms operative at the level of the microvasculature. The basis for understanding fluid transport across the capillary wall is Starling's law

$$J_v = L_p A \left[ (P_p - P_t) - \sigma (\pi_p - \pi_t) \right] \quad (1)$$

where  $J_v$  is the volumetric flow rate of fluid across the capillary wall,  $A$  is the surface area of the capillary,  $L_p$  is the hydraulic conductivity,  $P$  is the hydrostatic pressure,  $\pi$  is the oncotic pressure, and the subscripts  $p$  and  $t$  denote plasma and tissue, respectively.  $L_p$  and  $\sigma$  are properties of the capillary wall (endothelial cell layer), and the differences in hydrostatic pressure and oncotic pressure across the wall provide the driving forces for fluid transport. The oncotic pressure depends on the concentration of protein whose transport is governed by the equation

$$J_s = P_e A (C_p - C_t) + (1 - \sigma) J_v \bar{C} \quad (2)$$

where  $J_s$  is the solute (protein) flow rate,  $C$  is the solute concentration,  $\bar{C}$  is the average concentration across the capillary wall, and  $P_e$  is the endothelial permeability, another transport property of the endothelial layer. Under normal conditions there is a slight imbalance between the hydrostatic and oncotic pressure driving forces in eqn. (1) leading to a net filtration from the plasma to the tissue at the arterial end of the microcirculation and a net resorption from the tissue to the plasma at the venous end. Any excess of filtration over resorption is normally compensated for by lymphatic flow which returns fluid to the venous system. It is conventional to think of membrane transport properties ( $L_p, \sigma, P_e$ ) as constants, with changes in pressure and concentration gradients driving changes in water and solute flux. However, a fascinating characteristic of endothelial membranes which has become increasingly evident in the last few years is that their transport properties depend on the chemical and mechanical environment in which they reside.

Microgravity Induced Perturbations to the Mechanical Environment – When the body is exposed to microgravity, the blood pressure is reduced below the heart and elevated above the heart due to removal of the gravitational pressure gradient. As a result, the transvascular pressure gradient ( $P_p - P_t$ ) and proportionate interstitial fluid flow (see eqn. 1) are reduced in the lower body (below the heart) and elevated in the upper body (above the heart). The net result is a resorption of fluid from the tissue space in the lower body and a filtration of fluid into the tissue space in the upper body. This leads to an overall shift of interstitial fluid from the lower to the upper body which manifests itself, for example, in the reduction in calf volume (resorption) and increase in facial volume (filtration) which are characteristically observed in astronauts exposed to microgravity (Ref. 4 and Ref. 5).

In addition to the significant changes in pressure forces on the endothelial cell lining of blood vessels which are induced by microgravity, there are changes in the tangential stress (shear stress) of flowing blood on the endothelial cell surface as well. The shear stress on the blood vessel wall (wall shear stress) is proportional to the blood flow rate, and it is well known that blood flow rate is perturbed in microgravity (Ref. 3). The flow perturbations associated with microgravity have been simulated by ground-based experiments involving elevation of limbs (Ref. 5) and whole-body tilt (Ref. 4 and Ref. 6). For example, forearm elevation, which reduces transmural pressure ( $(P_p - P_t)$  in eqn. 1), simulating exposure to microgravity in the lower body, leads to a reduction in blood flow (and associated wall shear stress) by a mechanism which is believed to involve post capillary vessel collapse producing increased flow resistance (Ref. 5). Similar trends in blood flow change have been observed in the lower extremities of human subjects exposed to  $-6^\circ$  head-down-tilt (Ref. 4). Aratow et al. (Ref. 6) have observed that forehead cutaneous flow increases after exposure to  $-6^\circ$  head-down-tilt.

In summary, the mechanical environment of endothelial cells exposed to microgravity can be characterized by: (1) a reduction in pressure and a reduction in shear stress for vessels in the lower extremities, and (2) an increase in pressure and an increase in shear stress for vessels in the head. These two types of mechanical perturbations will be imposed on our endothelial cell culture model and the responses of the membrane transport properties ( $L_p$  and  $P_e$ ) will be determined (see question #1 below).



Effect of Flow (Shear Stress) on Endothelial Transport – The first unambiguous demonstration of a direct effect of shear stress on endothelial transport was reported by our group (Ref. 7) using bovine aortic endothelial cells (BAECs) cultured on a porous substrate mounted on the wall of a parallel plate flow chamber. This work showed a 10-fold increase in albumin permeability ( $P_a$ ) within one hour after the onset of 10 dynes/cm<sup>2</sup> steady shear stress. The permeability returned to pre-shear baseline levels within two hours after the removal of shear stress. The absence of a boundary layer diffusion resistance was clearly demonstrated. More recent work by our group (Ref. 8) has shown a direct effect of shear stress on the hydraulic conductivity ( $L_p$ ) of BAEC monolayers in culture. A significant increase in  $L_p$  was observed after 1 hour of exposure to 20 dynes/cm<sup>2</sup> of shear stress which did not return to baseline within 2 hours after removal of shear. This suggests that shear stress affects water and albumin transport across the endothelium in different ways.

Recent ex vivo and in vivo studies (refs. 9-14) provide mounting evidence that endothelial permeability increases as flow (wall shear stress) increases, as we have demonstrated in our in vitro system. To the best of our knowledge, there have not been any studies of the effects of changes in transmural pressure ( $P_p - P_i$ ) on the transport properties ( $L_p$ ,  $P_a$ ) of endothelial layers. The experiments proposed under question #1 will be the first to examine this important question.

Cellular Control of Permeability – Macromolecular permeability of the endothelium is affected by many chemical mediators which activate second messenger systems within the cell. Histamine, bradykinin, and thrombin increase permeability of cultured endothelial monolayers by a mechanism of cell retraction involving cytoskeletal rearrangement of actin and myosin (Ref. 15). Cell retraction opens up the paracellular pathway between adjacent endothelial cells. Histamine, bradykinin, and thrombin receptors are coupled to guanine-binding proteins (G-proteins) which, when activated, increase the activity of phospholipase C (PLC) (Ref. 16). PLC cleaves phosphatidylinositol 4,5-bisphosphate ( $PIP_2$ ) to yield two products, sn-1,2-diacylglycerol (DAG) and inositol 1,4,5-triphosphate ( $IP_3$ ). Both of these products act as second messengers. The second messenger role of  $IP_3$  is to stimulate calcium release from its intracellular stores in the endoplasmic reticulum. On the other hand, DAG along with calcium and phosphatidylserine increase the activity of membrane bound protein kinase C (PKC). PKC phosphorylates specific serine and threonine residues in target proteins and causes an increase in endothelial permeability (Ref. 17). Intracellular calcium can also activate the calmodulin-dependent enzyme myosin light-chain kinase (MLCK), and the subsequent phosphorylation of myosin leads to cell retraction in endothelial cells (Ref. 15). These two pathways may interact since it is known that PKC can increase the sensitivity of contractile proteins to calcium (Ref. 18). Thus in cultured cells, an important mechanism for increased endothelial permeability is associated with a PLC mediated increase in intracellular calcium which via PKC and calcium-calmodulin induces contraction of cytoskeletal elements.

On the other hand, cellular relaxation associated with increased cell to cell contact has been proposed to decrease endothelial permeability (Ref. 19). Chronically elevated intracellular cAMP, maintained by a stable cAMP analogue, dibutyl cAMP (db cAMP), decreases endothelial monolayer permeability to small molecules ranging in size from water to polyethylene glycol (Ref. 20). A similar reduction of sucrose transport results from stimulation of adenylate cyclase which elevates cAMP (Ref. 17). Intracellular pulses of cAMP have been shown to increase cell-cell contact, cell surface area and cell relaxation (Ref. 21). It has also been suggested that cAMP may modulate the activity of enzymes within the calcium-calmodulin-regulated actin-myosin contractile apparatus (Ref. 22).

Oliver (Ref. 23) showed that the sucrose permeability of BAECs in culture is reduced by endothelium-derived relaxing factor (EDRF) through a mechanism involving cGMP and suggested that this occurs as a result of cell relaxation which narrows the width of interendothelial junctions. On the other hand, Meyer and Huxley (Ref. 24) observed an increase in venular and true capillary  $L_p$  in the rat mesentery after perfusion with the nitric oxide (NO) donor sodium nitroprusside (SNP) or atrial natriuretic peptide (ANP), which is believed to be a NO-independent activator of cGMP. They did not observe a response of  $L_p$  to SNP or ANP in arteriolar capillaries. Kubes (Ref. 25) also observed an increase in

microvascular permeability after administration of ANP in the feline small intestine but surprisingly found that ANP exposure did not lead to an increase in tissue cGMP. Yet they still observed a reduction in permeability when cGMP was increased by other agents. Thus, the effects of NO and cGMP on barrier properties of the endothelium are somewhat controversial and appear to depend on the specific vascular origin of the endothelium.

From the studies outlined above it appears plausible that endothelial permeability is controlled by two transduction systems which modulate the transport resistance of the paracellular pathway. First, there is a mechanism involving increased intracellular calcium and PKC which increases permeability. Second, there is a mechanism involving increases in the cyclic nucleotides, cAMP and possibly cGMP, which decreases permeability. The relative activity of each of these systems may be responsible for overall control of endothelial permeability.

**Biochemical Mechanisms of Shear Stress on EC Transport** – In recent studies (Ref. 8) we have shown that preincubation of endothelial monolayers with db cAMP or the general phosphodiesterase inhibitor, IBMX, at levels which did not alter baseline  $L_p$ , completely inhibited (IBMX) or highly attenuated (db cAMP) the long-time increase in  $L_p$  observed with 20 dynes/cm<sup>2</sup> shear stress. The short-time decrease in  $L_p$  was completely blocked by these chemical agents as well. This indicates that elevation of the intracellular second messenger, cAMP, can oppose shear induced changes in  $L_p$ . We have also shown (unpublished) that the long-time shear-induced increase in  $L_p$  can be almost completely inhibited by preincubating the monolayer with the general G-protein inhibitor, GDP- $\beta$ S. These results indicate that shear stress alters endothelial  $L_p$  by a cellular mechanism involving signal transduction.

### EXPERIMENTAL DESIGN

In the microgravity fluid physics grant recently funded by NASA we will use in vitro cell culture models to explore the effects of altered hemodynamic forces associated with microgravity on the transport properties of vascular endothelium. The three major research questions and an overview of the associated methods are described briefly below.

Question #1: How do alterations in hemodynamics (pressure and wall shear stress) simulating microgravity affect endothelial transport properties ( $L_p$  and  $P_e$ )?

**Overview:**  $L_p$  and  $P_e$  of monolayers of representative arterial endothelial cells (bovine aortic endothelial cells – BAECs) and microvascular endothelial cells (bovine retinal microvascular endothelial cells – RMECs) will be measured simultaneously in a unique shearing apparatus (Ref. 8). The dynamic response of  $L_p$  and  $P_e$  to changes in transmural pressure and wall shear stress simulating exposure to microgravity hemodynamics will be determined over a time period long enough to achieve a steady state response (up to 6 hours).

**Hemodynamic Conditions:** Experiments will be run under "normal gravity" conditions to establish baseline values of  $L_p$  and  $P_e$  initially. It is anticipated that 1-2 hours will be required to establish steady state baseline values after initiating an experiment. Then step changes in transmural pressure ( $\Delta P$ ) and wall shear stress ( $\tau_w$ ) to a microgravity condition will be imposed, and  $L_p$  and  $P_e$  will be determined continuously for up to 5 additional hours or until new steady state values are obtained. Simulations of microgravity will initially involve step changes in transmural pressure of 20 cmH<sub>2</sub>O and step changes in wall shear stress corresponding to 3-fold changes in flow rate. The magnitudes of these step changes can be varied. Alterations of the hemodynamics in 4 different circulatory regions will be simulated as indicated in Table I.

Questions #2: What biochemical pathways mediate the influence of pressure and shear stress on endothelial transport properties ( $L_p$  and  $P_e$ )?

**Overview:** The mechanism by which endothelial cells sense mechanical forces imposed by flowing fluids and transduce them to intracellular chemical signals are not clearly understood. Certain evidence (e.g., Ref. 26) indicates that it involves the activation of several classes of G-proteins while other evidence (e.g., Ref. 27) points to a role for surface integrin molecules as the transducing element.

Shear stress could activate G-proteins by transiently mimicking agonist binding or could mechanically perturb G-proteins directly. G-proteins, in turn, activate a myriad of signal transduction pathways to elicit physiological responses. Integrins can transmit surface shear forces to the cytoskeleton directly. There are at least two hypotheses to explain how endothelial cells control their transport properties. First, there is a mechanism involving increased intracellular calcium, MLCK, and PKC that leads to cytoskeletal rearrangements, resulting in cell retraction of endothelial cells to increase  $P_e$  and  $L_p$ . A second hypothesis suggests that cyclic nucleotides, cAMP and possibly cGMP increase endothelial barrier function by enhancing cell to cell contact, resulting in decreased endothelial transport properties. The objective of this part of the study is to elucidate the roles played by these signal transduction pathways in pressure and shear-induced alterations in  $P_e$  and  $L_p$ . By utilizing various inhibitors and modulators of the signal transduction components under defined hemodynamic conditions while simultaneously measuring  $L_p$  and  $P_e$ , we will test these two hypotheses.

Question #3: Can the transport properties of endothelial monolayers be manipulated by pharmacologic agents in the hemodynamic environment of microgravity?

To reduce net resorption of fluid from tissue space in the lower extremities under microgravity conditions it would be desirable to increase  $L_p$  on the arterial side to enhance filtration and to reduce  $L_p$  on the venous side to inhibit resorption. To reduce net filtration in regions above the heart it would be useful to reduce  $L_p$  on the arterial side and increase  $L_p$  on the venous side. In this phase of the proposed research we will test pharmacologic agents in order to identify those which are capable of significantly enhancing or inhibiting the transport properties of the endothelium under the hemodynamic conditions of microgravity. The search for effective drugs will be guided by our knowledge of the biochemical pathways which control endothelial transport as determined under question #2. We realize at the outset that there are potential problems associated with the use of drugs to provide counter measures to microgravity induced physiological changes. Successful drugs need to be as site specific as possible with minimal systemic side effects. It may, however, ultimately be possible to use modern drug delivery technologies to obtain local delivery with minimal systemic effects.

#### LITERATURE CITED

1. Michel, C.C. Capillary permeability and how it may change. *J. Physiol.* **404**, 1-29 (1988).
2. Barakat, A.I., Uthoff, P.A.F. and Colton, C.K. Topographical mapping of sites of enhanced HRP permeability in the normal rabbit aorta. *J. Biomech. Eng.* **114**, 283-292 (1992).
3. White, R.J., Leonard, J.I., Srinivasan, R.S. and Charles, J.B. Mathematical analysis of acute and chronic cardiovascular changes during extended duration orbiter flights. *Acta Astronautica* **23**, 41-51 (1991).
4. Montgomery, L.D., Parmet, A.J. and Booher, C.R. Body volume changes during simulated microgravity: auditory changes, segmental fluid redistribution, and regional hemodynamics. *Ann. Biomed. Eng.* **21**, 417-433 (1993).
5. Hildebrandt, W., Herrmann, J. and J. Stegemann. Fluid balance versus blood flow autoregulation in the elevated human limb: a role of venous collapse. *Eur. J. Appl. Physiol.* **69**, 127-131 (1994).
6. Aratow, M., Hargens, A.R., Meyer, J.U. and S.B. Arnaud. Postural responses of head and foot cutaneous microvascular flow and their sensitivity to bed rest. *Aviation, Space and Environmental Medicine* **62**, 246-251 (1991).
7. Jo, H., Dull, R.O., Hollis, T.M. and J.M. Tarbell. Endothelial albumin permeability is shear-dependent, time-dependent and reversible. *Am. J. Physiol.* **260**, H1992-H1996 (1991).
8. Sill, H.W., Chang, Y.S., Artman, J.R., Frangos, J.A., Hollis, T.M. and J.M. Tarbell. Shear stress increases hydraulic conductivity of cultured endothelial monolayers. *Am. J. Physiol.* **H535-H543** (1995).
9. Lever, M.J., Tarbell, J.M. and C.G. Caro. The effect of luminal flow in rabbit carotid artery on transmural fluid transport. *Exp. Physiol.* **77**, 553-563 (1992).

10. Crone, C. and D.G. Levitt. Capillary permeability to small solutes. In: Handbook of Physiology, Sect. 2, The Cardiovascular System, ed. Renkin, E.M. and Michel, C.C., Am. Physiol. Soc., Bethesda, MD, Vol. 4, pp. 411-466 (1984).
11. Shibata, M. and A. Kamiya. Blood flow dependence of local capillary permeability of Cr-EDTA in the rabbit skeletal muscle. Japanese J. Physiol. 42, 631-639 (1992).
12. Yuan, Y., Granger, H.J., Zawiega, D.C. and W.M. Chilian. Flow modulates coronary venular permeability by a nitric oxide-related mechanism. Am. J. Physiol. 263, H641-H646 (1992).
13. Williams, D.A., Thipakorn, B. and V.H. Huxley. In situ shear stress related to capillary function. ASEB J. 8, M183 (1994).
14. Caldwell, J.H., Martin, G.V., Raymond, G.M. and J.B. Bassingthwaite. Regional myocardial flow and capillary-surface area products are nearly proportional. Am. J. Physiol. 267, H654-H666 (1994).
15. Wysolmerski, R.B. and D. Lagunoff. Involvement of myosin light-chain kinase in endothelial cell retraction. Proc. Natl. Acad. Sci. 87, 16-20 (1990).
16. Xu, J. and D. Chuang. Serotonergic, adrenergic, and histaminergic receptors coupled to phospholipase C in cultured cerebellar granule cells of rats. Bioch. Pharmac. 36, 2353-2358 (1987).
17. Oliver, J.A. Adenylate cyclase and protein kinase C mediate opposite actions on endothelial junctions. J. Cell. Physiol. 145 536,548 (1990).
18. He, P. and F.E. Curry. Albumin modulation of capillary permeability: role of endothelial cell  $\text{Ca}^{2+}$ . Am. J. Physiol. 265, H74-H82 (1993a).
19. Morel, N.M.L., Dodge, A.B., Patton, W.F., Herman, I.M., Hechtman, H.B. and D. Shepro. Pulmonary microvascular endothelial cell contractility on silicone rubber substrate. J. Cell. Physiol. 141, 653-659 (1989).
20. Haselton, F.R., Mueller, S.N., Howel, R.E., Levine, E.M. and A.P. Fishman. Chromatographic demonstration of reversible changes in endothelial permeability. J. Appl. Physiol. 67(5), 2032-2048 (1989).
21. Patton, W.F., Alexander, J.S., Dodge, A.B., Patton, R.J., Hechtman, H.B. and D. Shepro. Mercury-arc photolysis: A method for examining second messenger regulation of endothelial cell monolayer integrity. Biochemistry 196, 31-38 (1991).
22. He, P. and F.E. Curry. Differential actions of cAMP on endothelial  $\text{Ca}^{+2}$  and permeability in microvessels exposed to ATP. Am. J. Physiol. 265, H1019-H1023 (1993b).
23. Oliver, J.A. Endothelium-derived relaxing factor contributes to regulation of endothelial permeability. J. Cell. Physiol. 151, 506-511 (1992).
24. Meyer Jr., D.J. and V. H. Huxley. Capillary hydraulic conductivity is elevated by cGMP-dependent vasodilators. Circ. Res. 70, 382-391 (1992).
25. Kubes, P. Nitric oxide-induced microvascular permeability alterations: a regulatory role for cGMP. Am. J. Physiol. 265, H1909-H1915 (1993).
26. Kuchan, M.J., Jo, H. and J.A. Frangos. Role of G proteins in shear stress-mediated nitric oxide production by endothelial cells. Am. J. Physiol. 267, C753-C758 (1994).
27. Wang, N., Butler, J.P. and D.E. Ingber. Mechanotransduction across the cell surface and through the cytoskeleton. Science 260, 1124-1127 (1993).

# THE PROPAGATION OF A LIQUID BOLUS THROUGH AN ELASTIC TUBE AND AIRWAY REOPENING

Peter D. Howell & James B. Grotberg  
Biomedical Engineering Department  
Northwestern University  
Evanston, IL 60208

## ABSTRACT

We use lubrication theory and matched asymptotic expansions to model the quasi-steady propagation of a liquid bridge through an elastic tube. In the limit of small capillary number, asymptotic expressions are found for the pressure drop across the bridge and the thickness of the liquid film left behind, as functions of the capillary number, the thickness of the liquid lining ahead of the bridge and the elastic characteristics of the tube wall. For a given precursor thickness, we find a critical propagation speed, and hence a critical imposed pressure drop, above which the bridge will eventually burst, and hence the tube will reopen.

## INTRODUCTION

An airway in a lung may crudely be described as an elastic tube with a viscous liquid lining. It is well-known that this lining is susceptible to an instability driven by capillarity at its free surface. If the initial lining thickness is sufficiently large, the instability culminates in the formation of a liquid bridge (known in the medical context as a bolus) which blocks the tube. This phenomenon, known as airway closure, can lead to respiratory difficulty. It is known to be exacerbated by increased liquid content in the lung and by increased airway wall flexibility (ref. 1). In normal gravity, airway closure is generally confined to the lower regions of the lung. However, in microgravity airway closure still occurs and appears to be more homogeneously distributed (ref. 2).

Once such a liquid bolus has been formed, it propagates along the airway under the pressure drops imposed across it during respiration. As it does so, it leaves behind a thin liquid film. If the thickness of the trailing film exceeds that of the liquid lining ahead of the bolus, then the bolus must decrease in volume as it propagates, leading ultimately to reopening of the airway. In this paper we model the propagation of a liquid bolus along an elastic tube and hence deduce minimum criteria for airway reopening. In particular, we find that a more compliant airway is easier to reopen.

## SYMBOLS

See figure 1 for a definition sketch.

$a$	tube radius
$U$	bolus propagation speed
$\sigma$	liquid surface tension
$\mu$	liquid viscosity
$h_1, h_2$	trailing film thickness, precursor film thickness
$P_1, P_2, P_b$	pressure behind bolus, ahead of bolus and in bolus respectively.
$w$	tube wall displacement
$Ed$	tube wall stiffness (Youngs modulus times thickness)

### Dimensionless parameters

Capillary number	$Ca = \mu U / \sigma$
Dimensionless pressure drop	$\Delta P = a (P_1 - P_2) / 2\sigma$
Dimensionless wall flexibility	$G = \frac{\sigma}{Ed} \left( \frac{a}{h_1} \right)^2 (3Ca)^{2/3}$

### ASYMPTOTIC ANALYSIS

Throughout this paper we assume that the flow is axisymmetric and that inertia may be neglected (*i.e.* that the Reynolds number is small); our governing equations are therefore the axisymmetric Stokes equations. At the free surface of the liquid, we have the classical balance between liquid stress and interfacial tension. We perform an asymptotic analysis of the problem, assuming that the capillary number is a small parameter. This approach has been adopted by many previous authors, and applied to such problems as the flow of bubbles in tubes (ref. 3, ref. 4), the dynamics of free surfaces in Hele-Shaw cells (ref. 5) and plate withdrawal (ref. 6). Our analysis represents a generalisation of these papers to allow for flexibility of the tube wall. In this paper we employ a very simple (essentially linear) relation between the inwards wall displacement  $w$  and the pressure drop across it, namely

$$P_1 - P_b - \frac{\sigma}{a} = \frac{Ed}{(a-w)} \frac{w}{a}. \quad (1)$$

The key observation is that at small capillary number, in most of the flow domain viscous dissipation is dominated by surface tension. Indeed in the leading-order problem, obtained by setting the capillary number to zero, there is no flow and the problem is simply one of capillary statics. Formally, nondimensionalising the Stokes equations (using  $U$ ,  $a$  and  $2\sigma/a$  as scales for velocity, length and pressure respectively) reveals that

$$P_b \sim \text{const.} + O(Ca), \quad (2)$$

and so the two free surfaces are, to leading order, surfaces of constant mean curvature, that curvature being the ratio between the constant pressure difference across each surface and the interfacial tension  $\sigma$ . Also imposing that the surfaces be axisymmetric and analytic, the only admissible constant-mean-curvature surfaces are hemispheres, with leading-order mean curvature  $2/a$ .

We can anticipate that the scalings employed above will break down where the liquid free surfaces become close to the tube wall, since the hemispheres described above cannot be joined analytically to the uniform films ahead of and behind the bolus. Instead, there are transition regions (see figure 1) between the uniform films and the hemispheres, in which the pressure ceases to be constant as viscous dissipation becomes important. However, asymptotic simplification can still be achieved since in the transition regions the liquid layer is thin, with a slowly-varying free surface, so that we can employ lubrication theory.

Consider first the rear meniscus. If the film thickness  $h$  and wall displacement  $w$  are nondimensionalised with  $h_1$  and axial distance  $z$  with  $h_1 (3Ca)^{-1/3}$ , then in a frame moving with the bolus  $h$

is found at leading order to satisfy a variant of the Landau-Levich equation:

$$w'''(z) + h'''(z) = \frac{h-1}{h^3}. \quad (3)$$

Coupled to this is the leading-order dimensionless wall law from (1), namely

$$w = G(w'' + h''), \quad (4)$$

where  $G$  is the dimensionless flexibility: as  $G \rightarrow 0$ , the tube becomes rigid and the classical Landau-Levich equation is recovered.

Equations (3) and (4) combine to a single ordinary differential equation for  $\eta := h + w$  (i.e. the free-surface profile):

$$\eta''' = \frac{\eta - G\eta'' - 1}{(\eta - G\eta'')^3}. \quad (5)$$

An initial condition for (5) is that the film become uniform far away from the bolus, and by linearising about  $\eta = 1$  it is apparent that this one initial condition specifies the problem completely. Moreover the unique solution satisfying this condition has the asymptotic behaviour

$$\eta \sim 1 + e^{lz} \text{ as } z \rightarrow -\infty, \quad (6)$$

where  $l$  is the unique real, positive root of the cubic

$$\lambda^3 + G\lambda^2 - 1 = 0; \quad (7)$$

equation (6) is used as an initial condition in integrating (5) numerically.

The solution of (5) with initial condition (6) is found to behave quadratically for large, positive  $z$ :

$$\eta \sim \frac{1}{2}Az^2 + Bz + C \text{ as } z \rightarrow \infty, \quad (8)$$

where  $A$ ,  $B$  and  $C$  are numerically-determined constants. Notice that these constants are not all uniquely determined because the origin for  $z$  may be chosen arbitrarily; however  $A$  and the combination  $F \equiv AC - B^2/2$  are independent of the origin chosen for  $z$  and so are determined uniquely for any fixed  $G$ .

The final step is to match the transition region with the outer, bolus solution. Formally, we apply Van Dyke's matching rule (ref. 7) to the three-term outer solution (in which the free surface is hemispherical up to  $O(Ca)$ ) and the one-term inner solution found above. Matching the curvature gives the well-known asymptotic relation for the trailing film thickness:

$$\frac{h_1}{a} \sim A(G) (3Ca)^{2/3}. \quad (9)$$

Moreover, the higher-order matching gives asymptotic expressions for the apparent contact radius and contact angle of the meniscus. From these, the first perturbation to the meniscus curvature can be found, and hence the pressure difference across the rear meniscus is given asymptotically by

$$\frac{a}{2\sigma} (P_1 - P_b) \sim 1 + F(G) (3Ca)^{2/3}. \quad (10)$$

Now we apply the same asymptotic arguments to the front meniscus. The same differential equation (5) is found for  $\eta$  (here nondimensionalised with the precursor film thickness  $h_2$ ), with  $G$  replaced by  $\tilde{G} := G h_1^2 / h_2^2$  and the initial condition of uniform  $\eta$  now imposed for large positive  $z$ . In contrast to the rear meniscus, this problem admits a one-parameter family of solutions, with asymptotic behaviour

$$\eta \sim 1 + \alpha e^{-z/2\tilde{l}^2} \cos(\sqrt{(4\tilde{l}^2 - 1)}z/2\tilde{l}^2) \quad \text{as } z \rightarrow \infty, \quad (11)$$

( $\tilde{l}$  is the real positive solution of (7) with  $G$  replaced by  $\tilde{G}$ ). Once again the transition film behaves quadratically as it approaches the meniscus:

$$\eta \sim \frac{1}{2} \tilde{A} z^2 + \tilde{B} z + \tilde{C} \quad \text{as } z \rightarrow -\infty. \quad (12)$$

Now, however, the translation-invariant constants  $\tilde{A}$  and  $\tilde{F} \equiv \tilde{A}\tilde{C} - \tilde{B}^2/2$  are both functions of the initial condition  $\alpha$ . Matching the parabola (12) with the front meniscus gives

$$\tilde{A} = \frac{h_2}{a(3Ca)^{2/3}}; \quad (13)$$

the shooting parameter  $\alpha$  must be adjusted until  $\tilde{A}$  satisfies this (recall that  $h_2$  is a physically specified quantity, while  $h_1$  is a quantity to be found). The pressure difference across the front meniscus is given by

$$\frac{a}{2\sigma} (P_2 - P_b) \sim 1 + \tilde{F} (3Ca)^{2/3}. \quad (14)$$

Here,  $\tilde{F}$  is in effect a function of  $\tilde{A}$ : for each fixed  $\tilde{G}$  they may be plotted against one another using  $\alpha$  as a parameter. Hence the total pressure drop driving the bolus is related to its propagation speed by

$$\frac{a}{2\sigma} (P_1 - P_2) \sim \left[ F(G) - \tilde{F} \left( \tilde{G}; \frac{h_2}{a(3Ca)^{2/3}} \right) \right] (3Ca)^{2/3}. \quad (15)$$

For a rigid tube, when  $G \equiv \tilde{G} \equiv 0$ , this means that, given the precursor layer thickness  $h_2$  and the imposed pressure drop  $P_1 - P_2$ , the propagation speed of the bolus is given by (15); then the trailing film thickness  $h_1$  can be found from (9). In general the situation is more complicated; (15) and (9) are



coupled since  $h_1$  appears in  $G$ .

### REOPENING CRITERION

The condition for the bolus eventually to rupture is that  $h_1$  be greater than  $h_2$ . From (9) we can deduce a critical capillary number above which this condition is satisfied:

$$\text{reopening} \leftrightarrow Ca > Ca_c = \frac{1}{3} \left( \frac{h_2}{a} \right)^{3/2} f \left( \frac{a}{h_2} \frac{\sigma}{Ed} \right), \quad (16)$$

where  $f$  is a numerically-determined function. Hence from (15) the minimum pressure difference  $\Delta P_c$  required to reopen the tube takes the form

$$\Delta P_c = \frac{2\sigma h_2}{a^2} g \left( \frac{a}{h_2} \frac{\sigma}{Ed} \right), \quad (17)$$

where  $g$  is a second numerically-determined function.

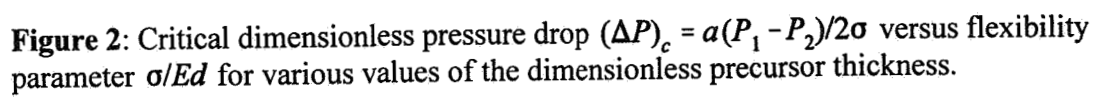
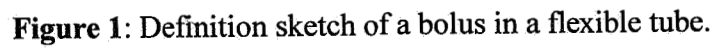
Typical critical pressure drops are plotted against the flexibility parameter  $\sigma/Ed$  in figure 2. It can be seen that increased wall flexibility decreases the critical pressure drop, *i.e.* makes the tube easier to reopen. The effect appears to be very slight compared to the increase in critical pressure drop caused by increasing precursor layer thickness; this is not surprising given that the present analysis is only valid for relatively stiff walls.

### ACKNOWLEDGMENTS

This work was supported by NASA through grant NAG3-1636.

### REFERENCES

1. Halpern, D.; and Grotberg, J.B.; Fluid-Elastic Instabilities of Liquid-lined Flexible Tubes, *J. Fluid Mech.*, Vol. 244, 1992, pp. 615-632.
2. Guy, H.J.B.; Prisk, G.K.; Elliott, A.R.; Deutschman III, R.A.; and West, J.B.; Inhomogeneity of Pulmonary Ventilation During Sustained Microgravity as Determined by Single-breath Washouts, *J. Appl. Physiol.*, Vol. 76, 1994, pp. 1719-1729.
3. Bretherton, F.P.; The Motion of Long Bubbles in Tubes, *J. Fluid Mech.*, Vol. 10, 1961, pp. 166-188.
4. Schwarz, L.W.; Princen, H.M.; and Kiss, A.D.; On the Motion of Bubbles in Capillary Tubes, *J. Fluid Mech.*, Vol. 172, 1986, pp. 259-275.
5. Park, C.-W.; and Homsy, G.M.; Two-phase Displacement in Hele Shaw Cells: Theory, *J. Fluid Mech.*, Vol. 139, 1984, pp. 291-308.
6. Wilson, S.D.R.; The Drag-out Problem in Film Coating Theory, *J. Engng Maths*, Vol. 16, 1982, pp. 209-216.
7. Van Dyke, M.; *Perturbation Methods in Fluid Mechanics*, Academic.



# **Convective Flows**



# GRAVITY-DEPENDENT TRANSPORT IN INDUSTRIAL PROCESSES

Simon Ostrach and Yasuhiro Kamotani  
Department of Mechanical and Aerospace Engineering  
Case Western Reserve University  
Cleveland, Ohio 44106

## ABSTRACT

Gravity dependent transport phenomena in various industrial processes are investigated in order to indicate new directions for micro-gravity research that enhance the commercial success of the space program. The present article describes the commercialization possibilities of such topics associated with physicochemical transport phenomena. The topics are: coating flow, rotating electrochemical system, and convection in low Prandtl number fluids. The present study is directed to understand these phenomena, and to develop a knowledge base for their applications with emphasis to a micro-gravity environment.

## INTRODUCTION

Ostrach (ref. 1) indicated new directions for micro-gravity research that could enhance the commercial success of the space program. In particular, it is pointed out that the research is dispersed over a number of disciplines but the underlying, and unifying basis for new and unusual aspects are gravitationally modified biophysicochemical transport phenomena. The important implications include the effects of fluid flow, heat and mass transfer on biology and chemical reactions. Inversely, the transport phenomena associated with such processes are different in a modified gravitational environment. Such phenomena are vital elements of the chemical, pharmaceutical, energy production, material processing, and biotech industries. The present results demonstrate a great potential for space applications.

Furthermore, ground-based research and the corresponding industrial applications in space have been identified. The present research effort has resulted in various topics. First, transport phenomena in zeolite growth were thoroughly investigated, and subsequently a method for increasing the crystal size by adding nutrient after crystallization was developed. Second, the effect of regular and random modes *g-jitter*, on liquid motion in an open container under microgravity environment was examined numerically and analytically. Third, a theoretical analysis of bubble formation in continuous liquid phase under both terrestrial and microgravity environments investigated though more experimental research is still under way. Fourth, an experimental study on double diffusive convection was completed. Fifth, a scaling and theoretical analysis were performed to understand transport phenomena in supercritical fluid extraction. To date, all these topics have been thoroughly investigated and a detail description can be found elsewhere (ref. 1 and 12). The current research topics are described individually in the following sections: rotating electrochemical systems, coating flows, and convection in low Prandtl number fluids.

## ROTATING ELECTROCHEMICAL SYSTEMS

The present study shows that there is a need to increase mass transport by a rotating system to achieve a high density power system in micro-gravity. Ostrach et al., (ref. 2) completed scaling and experimental studies on natural convection in a shallow rotating annulus subjected to axial stable temperature gradient. The present work, in essence, is an extension of that study.

The present research was motivated by the discovery of a rotating nickel-zinc (Ni-Zn) battery system. The main advantages of this system include the following: a high specific energy (~80 KWh/Kg), an excellent power performance (~100+ KW/Kg), a good performance in cold ambient temperatures, inexpensive, and low toxicity materials. These excellent performance characteristics make a rotating battery a leading candidate for energy generation and storage in micro-gravity. The development and commercialization of stationary Ni-Zn battery have been hindered for decades mainly due to the limited life cycles. Failure of this battery is typically associated with two phenomena: First, zinc dendrite formation and propagation that leads to the cell shorting. Second, zinc material redistribution (or shape change), which leads to gradual capacity loss. Conversely, by rotating the battery, the following performance enhancements are noticed: First, at rotations corresponding to 50 times the earth's gravitation the dendrite growth is nearly eliminated. This

leads to the stabilization of the electrode morphology and the battery life is prolonged to well over 1000 cycles, which is an industrially accepted standard. Second, the discharging electrical current density is increased by a factor of five.

Weng et al., (ref. 7) have experimentally and numerically studied the solutal convection inside shallow rotating electrochemical cell subject to concentration difference between two electrodes. A dilute binary electrolyte, cupric-sulfate system is the working fluid in both experimental and numerical simulations. The limiting current method is used to measure the mass transfer rate in cells. Numerical analysis is limited to cases when the flow is axisymmetric and laminar. The Boussinesq approximation is adopted for the centrifugal thermal buoyancy term in the numerical model. The basic equations with their appropriate boundary conditions are discretized and solved by SIMPLEC scheme to obtain velocity fields, concentration profiles, and local and average mass transfer rates at the electrodes.

The following non dimensional parameter characterize the rotating battery upper range: an Ekman number,  $Ek = \nu/(\Omega H)^2$  ( $\sim 1.07 \times 10^{-3}$ ), a solutal Rossby number,  $Ro_m = \beta_m \Delta C$  ( $\sim 2.24 \times 10^{-3}$ ),  $Ra_\Omega = \Omega^2 \beta_m \Delta C R^4 / \nu \alpha$  ( $\sim 2.63 \times 10^{11}$ ), a centrifugal Rayleigh number, a Schmidt number,  $Sc = \nu/D$  ( $\sim 2380$ ), an aspect ratio,  $Ar = H/R$  ( $\sim 1/15$ ), and a Froude number,  $Fr = R\Omega^2/g$  ( $Fr > 1$ ) (where  $\Omega$  is the speed in rad/s;  $\beta_m$  is the concentration expansion coefficient;  $D$  is diffusivity;  $H$  the height of the cell). In the present parametric ranges Ekman and centrifugal buoyancy-driven flows have been identified. Although centrifugal buoyancy and Coriolis force increased simultaneously with  $Ro_m$  the increase rate of the former was greater than that of the latter. *Figure 1* shows the dependency of the overall mass transfer rate on the centrifugal Rayleigh number. This figure shows that the present results agree well with the scaling law derived by Ostrach et al., (ref. 2) and the experimental results obtained by Hudson et al., (ref. 8). The combined uncertainty using the root sum square method in the determination of the  $Ra$  is  $\pm 10\%$ ,  $Fr$  is  $\pm 2\%$ , and the  $Sh$  is  $\pm 10\%$ .

The present work has classified into two categories the flow structure and the concentration distribution. First, at relatively low rotation speed, the core flow is mainly unicellular. *Figure 2a* shows unicellular flow sandwiched between two Ekman layers; one near the top wall, and the other at the bottom, also demonstrated by the steep concentration of iso-solute lines in *Figure 2b*. Second, when the rotation speed exceeds a critical value, or whenever the  $Ek$  is less than a certain value, a series of secondary flow cells appears in the core region as demonstrated in *Figure 2b*. The secondary flow is induced by Coriolis force, and its direction is opposite to the primary flow. Since the Coriolis force opposes the centrifugal buoyancy force, the centrifugal buoyancy is greatly weakened in the core region, causing the flow direction to change. The interaction between the core flow and the strong flow motion in the Ekman layer leads to the formation of the multiple cell flow structure. However, the multiple flow cells mainly occur in the core region, hence their influence on the mass transfer rate on electrodes is weak. This conclusion is portrayed in *Figure 3* which shows the numerical local Sherwood number  $Sh_H$  against the  $r/R$ . Farther increase in rotation speed causes the secondary cells to interact with the Ekman layer leading to unsteady, or turbulent flow. It is evident from *Figure 3* that the centrifugal buoyancy force enhances the mass transfer rate to the electrodes. This fact is used for the following conclusions: Since the local mass transfer to the electrode can be controlled, then shape-change effects are stabilized. This leads to increase the charging and discharging life cycle and gives a high specific power. The present results are beneficial to an optimal design of rotating batteries although more work is being pursued to obtain a better understanding of the stability and performance characteristics at higher gravitational levels.

## COATING FLOW

Industrial coating processes involve covering surfaces with one or more uniform liquid layers which are subsequently cured or dried to form films. A major problem faced in these processes is the stability of the coating film before the curing process occurs. Recently, a renewed interest in coating flow has emerged because of new economically significant technologies, for instance the use coating flow in semiconductor industry. Correspondingly, there is a need to improve productivity, economy, and uniformity in the traditional coating process (for example photography films, and paper, X-ray films, paper, welding, galvanized steel, and laminated composites).

In these processes, the final film thickness can be very thin and must be highly accurate. Productivity reasons strive for high speed applications, and several discrete film layers are at times applied simultaneously. As a result of such demands, attempts to use a specific coating process for a given application frequently fail. The liquid layer may not be continuous and, if it is, waves or streaks may occur. Also, numerical and experimental studies on coating flow, show that the final film thickness in micro-gravity can be made much larger with greater precision. The present experimental and

numerical data indicates that gravity significantly influences the stability of a coating film. The coating film exhibits interfacial instability beyond a certain Reynolds number. Ultimately, the coating film becomes wavy (ref. 4 and 5).

The present work explores coating flow at high parametric ranges (high capillary number,  $Ca = \mu U / \sigma$ , and high Reynolds number  $Re = Uh_o / \nu$ , property number  $Po = \mu(g/\rho\sigma^3)^{1/4} = \{(Ca/Re) * (h_o/h_\sigma)\}^{1/2}$ ), strongly motivated by practical considerations. (Where  $\nu$  is the kinematic viscosity;  $\sigma$  is the surface tension at the liquid-air interface;  $U$  is the substrate withdrawal rate;  $h_o$  is the final film thickness; and  $h_\sigma$  is the capillary rise height.) The following non dimensional parameters characterize the coating flow range for the aforementioned industrial applications:  $Ca \sim 1.0 \times 10^{-3}$  to 4.0;  $Re \sim 3.0 \times 10^{-3}$  to 2.0;  $Po \sim 8.0 \times 10^{-2}$  to 257.0.

The results presented in *Figure 4* are based on experimental work described in detail by Kizito et al. (ref. 5). The combined uncertainty using the root sum square method in the determination of the  $Ca$  is  $\pm 1.2\%$ , and the  $Re$  is  $\pm 1.23\%$ . *Figure 4* depicts the following trends: First, beyond a certain  $Ca$ , the non dimensional film thickness becomes constant independent of  $Ca$ . Second, there is a final film thickness dependency on the  $Re$  expressed by a fluid  $Po$ . For instance, at  $Ca=0.1$ , and  $P=5.6$  with a higher  $Re$  has the non-dimensional final film thickness  $T_o = (\rho g h_o^2 / \mu U_o)^{1/2} = 0.69$ . The same  $Ca=0.1$ , gives  $T_o=0.54$  for  $Po=53.0$ . *Figure 4* shows that beyond a certain  $Po=26$ , the non-dimensional final film thickness ceases to depend on the  $Re$ . Also, *Figure 4* compares the present work with the experiment of Lee et al., (ref. 9), and the theoretical relationship obtained by Levich. The figure shows that Levich's theoretical relationship ( $T_o = 0.93 Ca^{1/6}$ ) used extensively in the past, does not hold for the most part of the present work. The new aspects *Figure 4* presents are: beyond a certain  $Ca$ ,  $T_o$  becomes constant independent of  $Ca$ , and a dependency of  $T_o$  on the  $Re$ . In general, the figure reveals that when the  $Re_r$  ( $Re_r = \rho^2 g h_o^3 / 3 \mu^2$ ) exceeds unity, a dip coating film becomes unstable. The  $Re_r$  measures the magnitude of gravity induced shear in the final film region.

In most work to date the interface shape at liquid line has been assumed to be described by a static meniscus equation. However, a new aspect of importance to the stability and the understanding of coating flow is shown in *Figures 5, and 6*. These figures show the meniscus deformation at the liquid pool lines, identified as the apparent cusp formation. *Figure 5* shows an interfacial profile at:  $Po=5.6$ ,  $Ca = 0.4$ , and  $Re = 19.5$ , and the profile is obtained experimental by optically sectioning the coating flow field at the line. *Figure 6* shows the region occupied by the fluid, its meniscus, streamlines and velocity vectors when the parameters are:  $Ca=4.1$ , and  $Re=6.5$ , consequently simulating a fluid with  $Po=53.0$ . The numerical solution is obtained using a Fluent Nekton code. The cause of the apparent cusp on the interface is attributed to the inertia effect of the return flow. The results obtained in this study can be used to design an optimal coating device although more work is needed to confirm the cause of the wavy motion. The wavy motion in the final film region is mainly attributed to gravity induced shear, although gravity induced return flow causing the apparent cusp or a capillary gradient may have a role. In order to test these assertions, a microgravity environment will allow one to sort out the gravity induced shear instability from that caused by a capillary gradient.

## CONVECTION IN LOW PRANDTL NUMBER FLUIDS

Industrial crystal growth processes involve solidification of melt at significantly high temperature gradients. At these temperature gradients, natural convection can have a profound influence on the structure, and quality of the final solid phase. Specifically, oscillatory or time dependent convection in the liquid phase is undesirable because it results in periodic inhomogeneities in the final crystals. For example, compositional variations of a few percentages down to a sub-micron length scale affect the performance, the properties of the doped semi-conductors, and the structural integrity of alloy materials. Since semi-conductor crystals are a very important component of the electronic industry, it is worthwhile to seek a control strategy that will lead to the reduction of these periodic inhomogeneities. The control strategy requires a good understanding of the detailed physics of the transport phenomena in liquid metals which are used to simulate semi-conductor materials in their liquid phase. Natural convective flow of a low-Pr fluid develops fluctuations in the temperature outside the viscous boundary layer, which in many cases result in unsteady or oscillatory flows. These phenomena are inherently non-linear making analysis very difficult. Therefore, a combination of experimental and numerical approaches is used in the present study.

The present study is an extension of work by Kamotani et al., (ref. 6) who investigated natural convection of a liquid metal in cylinders whose wall ends are differentially heated. In particular, the present work is designed to investigate

convection in a simulated floating zone melting technique, which is one of the major configurations used in industrial crystal growth processes. The present experiments cover a wider range of  $Ar$  (aspect ratio) than those used in the crystal growth technique in order to study oscillatory convection under more general conditions. Thermocouples are placed in different azimuthal positions along the wall to detect the onset of oscillations, and to determine the oscillation flow structures and frequencies. The non-dimensional parameter range for the present study is:  $Ra \gg 1$ ,  $Ar > 1$ ,  $Pr < 1$ ,  $Hr < 1$ .  $Ra^*$  ( $Ra^* = g\beta\Delta T(L/2)^3/\nu\alpha$ ) is a Rayleigh number based on a half of the height, and  $Hr$  is a relative heating zone size. Figure 7 schematically shows the present experimental configuration; a detailed description is by Selver et al., (ref. 10). A data acquisition system by Keithley Instruments is used to convert the thermocouple outputs to digital values. Real time computer graphics generated by Labtech are used to determine the onset of oscillations. The critical temperature difference value for the onset of oscillation is reproducible within  $\pm 10\%$ .

The critical Rayleigh number values for the onset of oscillation are presented in Figure 8. The present data are compared with those measured by other investigators (ref. 6 and 11) whose configuration is heated-from-below. Good agreement is obtained although the basic flow changes below  $Ar^*=3$  in the present configuration. The change in the basic flow can be attributed to two flow structures before oscillations appear. The flow structures have been identified as unicellular and axisymmetric flow. To rule out non-uniformity as an influence on the critical values, the test section was tilted about 5 degrees, and no change in  $Ra_{cr}$  values was observed within experimental error. Temperature oscillation pattern and the corresponding frequency are presented in Figure 9. The figure shows the power spectrum versus the frequency and the temperature versus time for  $Ar^*=2$ . The frequency values are obtained using a Fast Fourier Transform to the thermocouple outputs. The study of the amplitude and phase of temperature traces at different azimuthal position reveals the aforementioned the convective flow structure. The oscillation modes also correspond to these two basic flow structures before oscillation. First, whenever  $Ar^*$  is large, the oscillations are due to the fact that the unicellular motion is rotating back and forth. Second, when  $Ar^*$  is below 3, the oscillation pattern is associated with a rotating non-axisymmetric toroidal pattern around the axis.

## REFERENCES

1. Ostrach, S., "Industrial Processes Influenced by Gravity," NASA CR-182140, C-21066-G. 1988
2. Ostrach, S., Golic, I., Kamotani, Y., and Jiang, H. D., "Thermal Convection in A Shallow Rotating Annulus," 18th International Congress of Theoretical and Applied Mechanics, Haifa, Israel, August. 1992
3. Ostrach, S. Kizito, J. P., and Kamotani, Y., "Free Coating Flow at High Capillary and "Free Coating flow at High Capillary and Reynolds numbers," AMD-Vol. 184, ASME, 1995, pp 1-11.
4. Kizito, J. P., Ostrach, S., and Kamotani, Y., "Coating Flows In Micro-gravity," M.S. Thesis, Case Western Reserve University, Cleveland. 1991
5. Kizito, J. P., Ostrach, S., and Kamotani, Y., "Free Coating Flow at High Capillary and Reynolds Numbers," Ph.D. Thesis, Case Western Reserve University, Cleveland. 1995
6. Kamotani, Y., Weng, F. B., Ostrach, S., and Platt, J., "Oscillatory Natural Convection of a Liquid Metal in Circular Cylinders," Journal of Heat Transfer, Vol. 116, 1994, pp. 627-632.
7. Weng, F. B., Ostrach, S., and Kamotani, Y., Ph.D. Thesis, "Rotating Electrochemical Systems," Case Western Reserve University, Cleveland. 1996
8. Hudson, J. L., Tang, D. and Abell, S., "Experiments on Centrifugally Driven Thermal Convection in a Rotating Cylinder," J. Fluid Mech., V.86, Part 1, 1978, pp. 147-159.
9. Lee, C. Y. and Tallmadge, J. A., "Dynamic Profile Data at Low Capillary Numbers," Ind. Eng. Ch. Fundamentals, Vol. 13, No. 4, pp 356-360., 1974.
10. Selver, R., Kamotani, Y., and Ostrach, S., "Convection In Low Prandtl Number Fluids," Ph.D. Thesis, Case Western Reserve University, Cleveland. 1996



11. Muller, G., Neumann, G., and Weber, W., "Natural Convection in Vertical Bridgman Configurations," Journal of Crystal Growth, Vol. 70, 1984, pp. 78-93.

12. Ostrach, S., and Kamotani, Y., "Gravity-dependent Transport in Industrial Processes," 2nd Microgravity Fluid Physics Conference, NASA Pub. 3276, 1994.

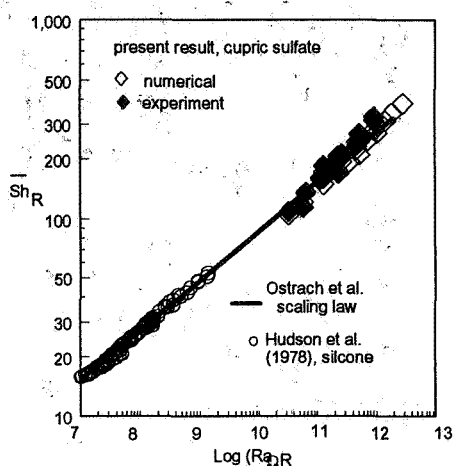


Figure 1 Cent. Rayleigh number vs. Sherwood number for present and published data

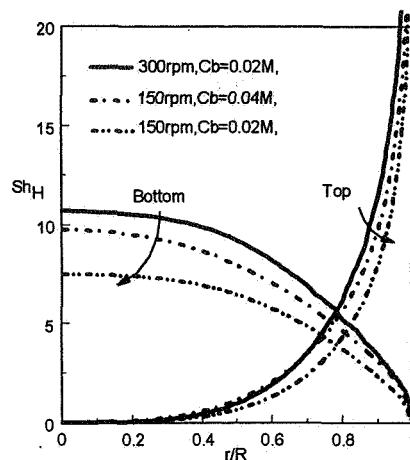


Fig. 3 Local Sherwood number distribution for  $Ar=0.0333$  (numerical calculation)

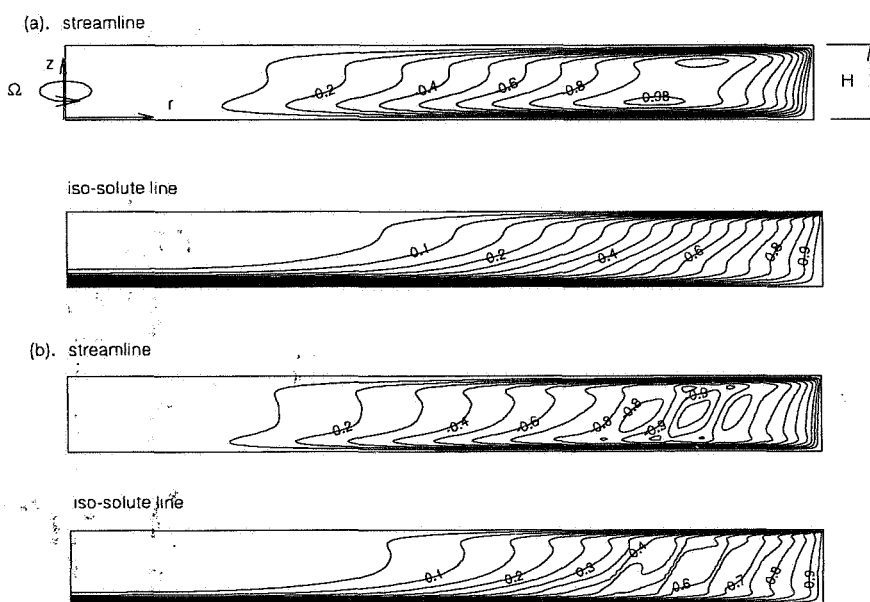


Figure 2 Contour plots of streamline, iso-solute line (vertical scale x3)

(a).  $\Omega=150$  rpm,  $\Delta C=0.04M$ ,  $Ra_{\Omega R}=6.58 \times 10^{10}$ ,  $Ek=0.0115$ ,  $ScRo_s=10.63$ ,  $Ar=0.033$   
 (b).  $\Omega=300$  rpm,  $\Delta C=0.04M$ ,  $Ra_{\Omega R}=2.63 \times 10^{11}$ ,  $Ek=0.0057$ ,  $ScRo_s=10.63$ ,  $Ar=0.033$

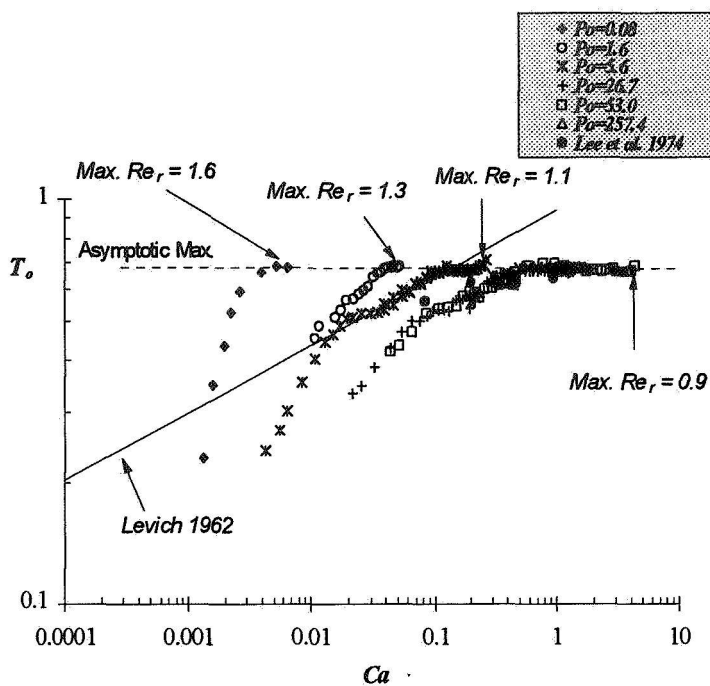


Figure 4: Non-dimensional final thickness as a function of  $Ca$



Figure 5: Interfacial profile at:  $Po=5.6$ ,  $Ca = 0.4$ , and  $Re = 19.5$

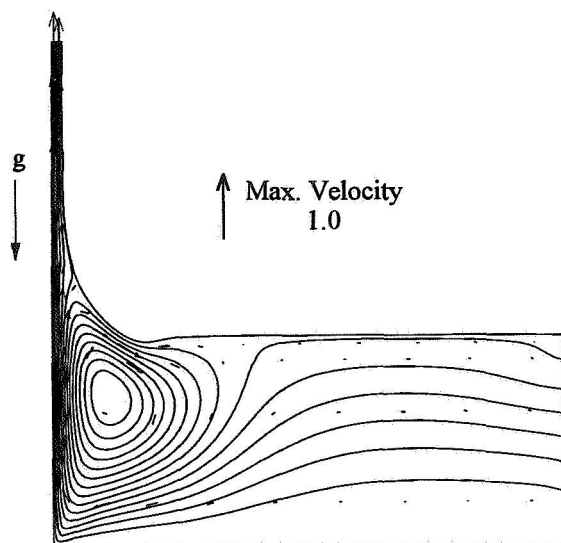


Figure 6: Numerical Interfacial profile at:  $Po=53.0$ ,  $Ca = 4.1$ , and  $Re = 6.5$

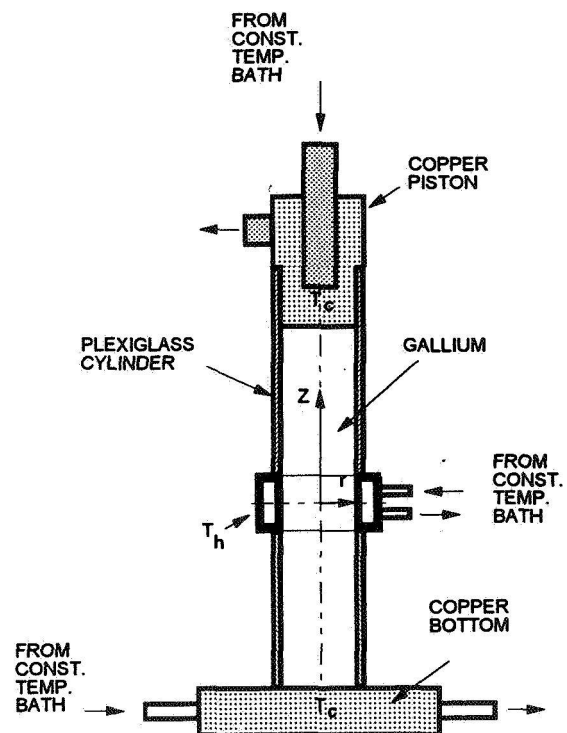
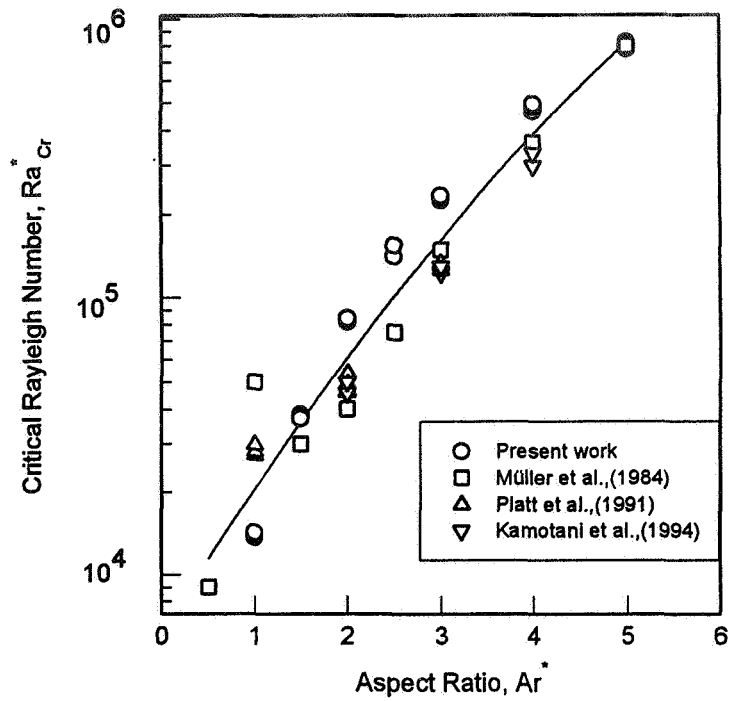


Figure 7: Experimental setup for convection in low  $Pr$  fluids



\*  $Ra$  and  $Ar$  are based on the half of the test section height.

Figure 8 Comparison of critical Rayleigh numbers for vertical case with those of other investigators.

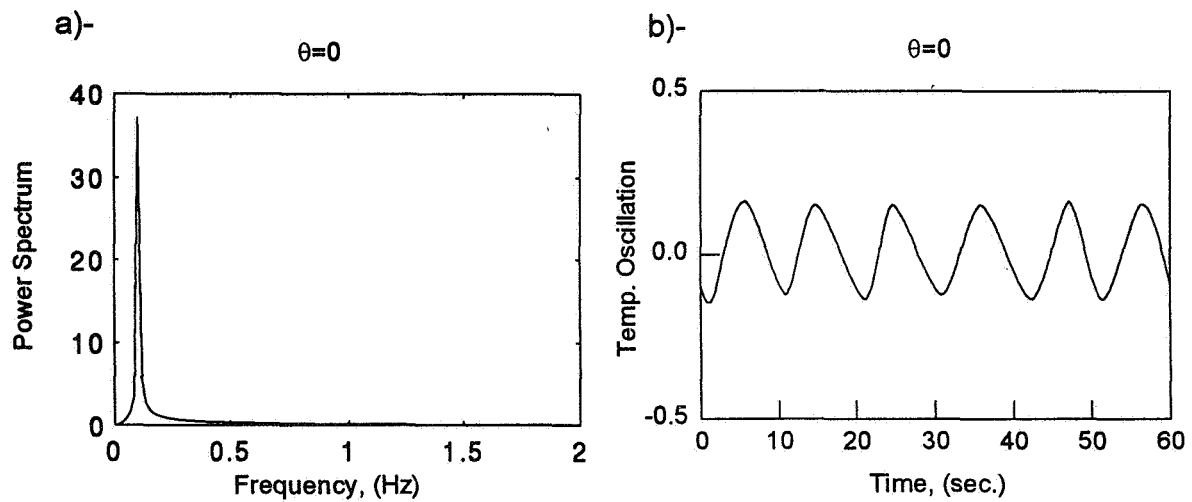


Figure 9 Temperature oscillations for  $Ar=2$   
a- Power Spectrums versus Frequency  
b- Temperature traces versus Time



# EXPERIMENTS ON THERMAL CONVECTION IN ROTATING SPHERICAL SHELLS WITH RADIAL GRAVITY: THE GEOPHYSICAL FLUID FLOW CELL

John E. Hart

Department of Astrophysical, Planetary and Atmospheric Sciences  
University of Colorado  
Boulder, CO 80309

## ABSTRACT

Experiments designed to study the fluid dynamics of buoyancy driven circulations in rotating spherical shells were conducted on the United States Microgravity Laboratory II spacelab mission. These experiments address several aspects of prototypical global convection relevant to large scale motions on the Sun, Earth, and on the giant planets. The key feature is the consistent modeling of radially directed gravity in spherical geometry by using dielectric polarization forces. Imagery of the planforms of thermally driven flows for rapidly-rotating regimes shows an initial separation and eventual merger of equatorial and polar convection as the heating (i.e. the Rayleigh number) is increased. At low rotation rates, multiple-states of motion for the same external parameters were observed.

## INTRODUCTION

The existence of extremely strong and axisymmetrically banded zonal winds on the giant planets represents one of the most outstanding problems in planetary science (Ingersoll, ref. 1). Several theories have been proposed (Busse, ref. 2, Dowling, ref. 3, Marcus and Lee, ref. 4), but recent data from the Galileo immersion probe, which showed strong winds increasing with depth in the Jovian atmosphere over many scale heights, seems to lend support to those theories (e.g. ref. 2) that couple the observed cloud top zonal winds with deep convection. It is postulated that such deep convection, under the influence of sphericity and strong basic rotation of the planetary atmosphere, can organize and generate substantial zonal winds through wave interactions. Indeed, high resolution three-dimensional numerical models (e.g. Sun et. al., ref. 5) have shown that banded zonal winds (albeit very weak ones) can be formed by such processes. Similar mechanisms have been proposed to explain the differential rotation of the Sun (e.g. Gilman, ref. 6). One important aspect of these models is the existence of columnar "banana cell" convection, aligned with the rotation axis. Nonlinear interactions of the convective columns generate zonal flows. One may ask why we don't see the tips of the banana cells in the cloud patterns of Jupiter, for example. Idealized, but extremely high Rayleigh number calculations of Brummel and Hart (ref. 7), show that it is possible for **weak** convective columns to generate **extremely fast** zonal jets. In this case the motion field is dominated by the jets and it becomes difficult to observe the underlying convection cells. Additionally, these computations showed that the whole zonal-flow / convective-column system can pulsate, leading to alternating bursts of convective turbulence, then enhanced zonal jets. Burps of convection on Saturn (e.g. Sanchez-Lavega, ref. 8) are similar in appearance. Because the Brummell-Hart model is two-dimensional (by the Taylor-Proudman constraint), it would be interesting, but very difficult, to extend 3-D models into the appropriate parameter range for strong jets and pulsations. Alternatively, laboratory experiments may be used to test some of the simulation results.

Laboratory models can play an important role in contributing to our understanding of geophysical flows. However, to be relevant for astrophysical and planetary application lab experiments must replicate the unifying features of planets and stars: they are spherical with centrally directed radial gravity, they rotate at various magnitudes, and motions are driven thermally in response to different types of heating. Of these criteria the first is the most difficult to satisfy, because in the terrestrial laboratory gravity is unidirectional, so in any

rotating experiment the rotation vector and the gravity vector maintain a fixed relative orientation. In order to overcome this obstacle we have developed a method for studying thermally driven convection within a rotating spherical shell of fluid, using electro-hydrodynamic polarization forces to generate the required **radial** buoyancy forces. However, the radial forces are relatively weak, about 0.1 g, and so are overwhelmed by terrestrial gravity. Thus the microgravity spacelab environment is uniquely suited for experiments of this type. The instrument, called the Geophysical Fluid Flow Cell (GFFC), initially flew on Spacelab-3 in 1985 and the results were reported in Hart, Glatzmaier and Toomre (ref. 9). A reflight on USML-2 in 1995 permitted observations over a wider range of parameters while using a different imaging procedure designed to facilitate the acquisition of data on the time-dependence of convective states. The fundamental principle of the experiment is briefly explained below, followed by a short summary of the preliminary results from USML-2.

## DESCRIPTION OF THE EXPERIMENT

Figure 1 shows a cross-section of the GFFC. The inner spherical shell is a nickel-plated mirror. The outer shell is a transparent sapphire hemispherical dome with an electrically conducting coating applied to the inner surface. The inner and outer radii are  $R_i = 3.3\text{ cm}$  and  $R_o = 2.4\text{ cm}$ , respectively. A 300 Hz. a.c. voltage  $V$  is applied across the dielectric 0.65 centistoke silicone fluid contained in the gap. The resulting radial electric field leads to a centrally directed polarization force which is nearly linear in the liquid density, with magnitude proportional to the square of the applied voltage. As shown in ref. 9, the equations of motion for the silicone oil in zero-g are isomorphic to those for a Boussinesq thermally convecting liquid in a spherically symmetric geopotential that goes like inverse radius to the fourth power, provided dissipative electrical heating (which is a small effect) is neglected. Studies of the linear instability problem in spherical shells with varying gravity distributions show that for the aspect ratio of the GFFC experiments,  $R_i/(R_o - R_i) = 2.65$ , the linear eigenfunctions with  $r^2$  vs.  $r^3$  gravity distributions are nearly identical.

Motions are driven by imposing various thermal distributions on the inner and outer shells. If the inner sphere is at a uniform temperature hotter than the constant temperature outer wall, then unstable convective motions in the radial electrostatic gravity field are excited by this spherically symmetric heating distribution. Such forcing boundary conditions are relevant for modeling the Sun and the Earth's mantle, where the driving is thought to be symmetric. However, latitudinal (as well as radial) gradients of applied heating can be imposed, modeling, perhaps, situations where rotating convective motions are driven by external latitudinally-dependent solar fluxes, as well as by a symmetric internal heat source (e.g. Jupiter). The degree of heating is measured by the standard Rayleigh number  $Ra = g\gamma\Delta T d^3/\kappa\nu$ , based on the applied temperature difference and the magnitude of the imposed electrostatic gravity  $g$  (proportional to  $V^2$ , with a maximum of about 0.1 g). Here  $\gamma$  is the variation of permittivity with temperature,  $\kappa$  is the thermal diffusivity, and  $\nu$  is the kinematic viscosity. In the GFFC  $Ra$  ranges from 0 to about  $2 \times 10^6$ . The relative degree of rotation is measured by the Taylor number  $Ta = (2\Omega d^2/\nu)^2$  based on the gap width, rotation rate, and fluid viscosity. Low rotation regimes have  $Ta < 1000$  or so, while the maximum attainable value in the GFFC is about  $10^6$ .

Flows are visualized by a back-focus Schlieren system giving information on the radially averaged temperature structures in the convecting liquid. Data were recorded on 16mm film for post-mission processing and analysis, and the images were also relayed to ground during the mission to enable near real-time changes in the experiment protocols (e.g. changes in  $Ra$ ,  $Ta$ , heating distribution, etc.). The video and 16mm data comprise the main data sources, with the former containing a limited and the latter having a more substantial imbedded record of the experiment parameters (e.g. high voltage, time, temperatures measured at various points by thermistors, etc.). For more extensive discussion of the instrument see ref. 9.

## RESULTS

Instrument performance. The Geophysical Fluid Flow Cell Experiment carried out 29 separate 6 hour runs using different parameters (cell rotation rate, heating distributions, etc.). Eighteen of the runs were nominal in terms of instrument performance, except for indications that suggested higher than expected temperatures along the outer sphere's equator. Because of this overtemperature problem, science activities were focused on situations with spherically symmetric heating (the so-called "solar model" cases). The last eleven runs were affected by the failure of the 16mm film transport, leaving the video as the primary data source. This was compensated for by running experiments towards the end of the mission with commanded boundary temperatures similar to those run earlier in the mission on which film data is available.

Scientific Results: The following are the preliminary results based on video downlink recorded during USML-2 (analysis of the 16mm film data has just commenced). The experiments fell into several classes depending on the rotation rate (rapid or slow: e.g. solar-like or mantle-like). In each case new states were observed and are summarized below.

1) Studies of rotating convection with spherically symmetric heating revealed possible multiple jets in latitude, with prograde (same sense as the basic rotation) motion of thermal waves at low and high latitudes and retrograde pattern rotation at mid-latitude (see figure 2). Such differential pattern propagation has not been previously seen in computational models, and these results may provide an alternative view on the mechanisms for "banded"-looking structures in planetary atmospheres like Jupiter. However, contrary to suggestions from our Taylor-column idealized models, no vacillatory (periodic global pulsation) states were observed.

2) An extensive study of slowly rotating convection was carried out, and two distinct convection patterns were observed in experiments with the same external parameters but with different initial conditions. This means that the long-time evolution of modestly convecting flows in slowly rotating spherical shells (like earth's mantle) is not unique, but depends on initial conditions. Equivalently the "climate" can be persistent, or locked, for long times as external conditions change slowly. In addition, information was obtained on how these persistent states evolve as parameters are increased across stability boundaries. Figures 3a and 3b illustrate the instability of "horseshoe convection", wherein the off-center ring of convection breaks down by north-south oriented stripe formation as the voltage is increased from 1.44kV to 1.56 kV.

3) A large data set (several different rotation rates, many different heating rates) was obtained on the transition between anisotropic north-south oriented "banana convection" and more isotropic non-aligned convection. These results, when quantified by digital analysis of the data films and tapes, will permit testing of simple scaling arguments for this transition. Once verified, these scalings can be used to classify the expected global convection regimes of planets and stars.

4) Experiments with latitudinal heating gradients showed evidence for baroclinic waves. This instability is interesting because it has combined attributes of both ordinary thermal convection and rotating slantwise convection. The latter instability is central to the circulation of the earth's atmosphere, but its occurrence as a combined instability supports recent computational modeling of such instabilities in rotating spherical shells.

5) Other experiments with latitudinal heating showed how spiral wave convection breaks down to turbulence by secondary branching.

## ACKNOWLEDGMENTS

The author thanks NASA for financial and technical support of this project through contract NAS-8-31958 to the University of Colorado. Many people have contributed to the development of the hardware and interpretation of the experimental results. I would especially like to thank Dr. Fred Leslie and the crew of

engineers at the Marshall Space Center for their untiring work getting a twenty year old instrument ready for its successful reflight on USML-2.

## REFERENCES

1. Ingersoll, A.P.: Atmospheric dynamics of the outer planets. *Science*, vol. 248, pp. 308 - 315, 1990.
2. Busse, F.H.: Convection driven zonal flows and vortices in the major planets. *Chaos*, Vol. 4, pp. 123 - 133, 1994.
3. Dowling, T.E.: Dynamics of Jovian Atmospheres. *Ann. Rev. Fluid Mech.*, vol. 27, pp. 293 - 334, 1995.
4. Marcus, P.S. and Lee, C.: Jupiter's Great Red Spot and zonal winds as a self-consistent, one layer, quasi-geostrophic flow. *Chaos*, vol. 4, pp. 269 - 286, 1994.
5. Sun, Z-P, Schubert, G., and Glatzmaier, G.A.: Banded surface flow maintained by convection in a model of the rapidly rotating giant planets. *Science*, vol. 260, pp. 661-664, 1993.
6. Gilman, P.A.: The solar dynamo: observations and theories of solar convection, global circulations and magnetic fields. *Physics of the Sun*, Ed. P.A. Sturrock, vol. 1, chap. 5, pp. 95 - 160, Riedel, 1986.
7. Brummell, N.H., and Hart, J.E.: High Rayleigh number  $\beta$ -convection. *Geophys. and Astrophys. Fluid Dyn.*, vol. 68, pp. 85 - 114, 1993.
8. Sanchez-Lavega, A.: Saturn's Great White Spots. *Chaos*, vol. 4, pp. 341 - 353, 1994.
9. Hart, J.E., Glatzmaier, G.A., and Toomre, J.: Space-laboratory and numerical simulations of thermal convection in a rotating hemispherical shell with radial gravity. *J. Fluid Mech.*, vol 173, pp. 519 - 544, 1986.

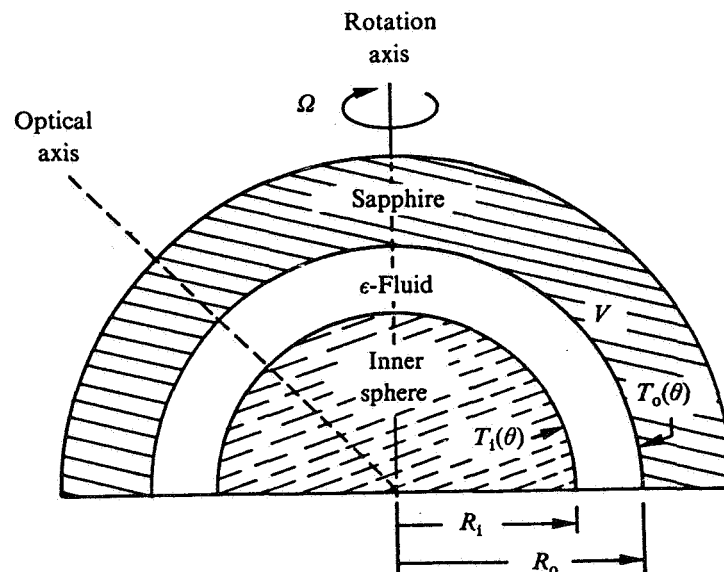


Figure 1. Cross-section of the test cell used to study global convection in a rotating hemispherical shell of fluid in the presence of an electrostatic radial gravity field. That gravity is achieved by imposing an alternating potential  $V$  (0 to 10 kilovolts) across the fluid shell.





Figure 2. Schlieren map of a turbulent “solar-model” case with rapid rotation and spherically symmetric heating. The equator is at the top of the picture and the pole is at the bottom. The features propagate prograde at the bottom and top of the frame, while moving retrograde at mid-latitude.

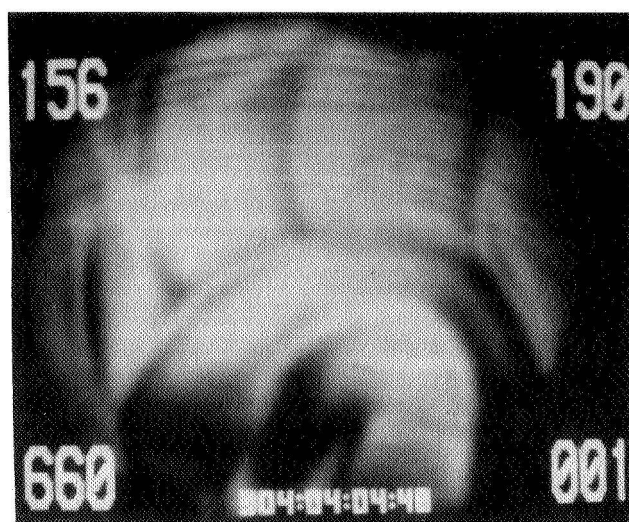
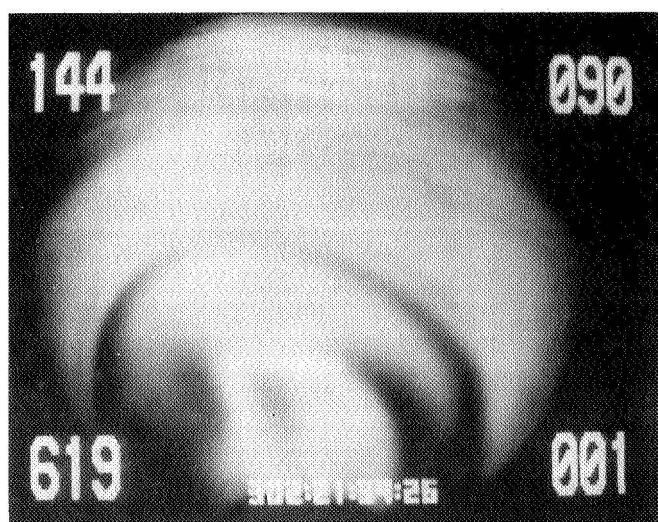


Figure 3 . A stable low rotation convection state consisting of an off-axis polar convecting ring (left). As the voltage (i.e. gravity) is increased this nearly axisymmetric state breaks down as columnar modes appear, extending from mid-latitude down into the tropics (right). The equator is at the top and the pole at the bottom.



# **A GEOPHYSICAL FLOW EXPERIMENT IN A COMPRESSIBLE CRITICAL FLUID**

John Hegseth and Laudelino Garcia  
Department of Physics  
University of New Orleans, New Orleans, Louisiana 70148

## **SCIENCE OBJECTIVES**

The first objective of this experiment is to build an experimental system in which, in analogy to a geophysical system, a compressible fluid in a spherical annulus becomes radially stratified in density through an A.C. electric field. When this density gradient is demonstrated, the system will be augmented so that the fluid can be driven by heating and rotation and tested in preparation for a microgravity experiment. This apparatus consists of a spherical capacitor filled with critical fluid in a temperature controlled environment. To make the fluid critical, the apparatus will be operated near the critical pressure, critical density, and critical temperature of the fluid. This will result in a highly compressible fluid because of the properties of the fluid near its critical point. A high voltage A.C. source applied across the capacitor will create a spherically symmetric central force because of the dielectric properties of the fluid in an electric field gradient. This central force will induce a spherically symmetric density gradient that is analogous to a geophysical fluid system. To generate such a density gradient the system must be small ( $\approx 1$  inch diameter). This small cell will also be capable of driving the critical fluid by heating and rotation. Since a spherically symmetric density gradient can only be made in microgravity, another small cell, of the same geometry, will be built that uses incompressible fluid. The driving of the fluid by rotation and heating in these small cells will be developed. The resulting instabilities from the driving in these two systems will then be studied.

The second objective is to study the pattern forming instabilities (bifurcations) resulting from the well controlled experimental conditions in the critical fluid cell. This experiment will come close to producing conditions that are geophysically similar and will be studied as the driving parameters are changed.

## **RELEVANCE OF THE SCIENCE AND POTENTIAL APPLICATIONS**

Some of the most urgent problems of social concern are related to geophysical flows. Examples of these problems are the climate change from the greenhouse effect, natural disasters from violent storms, and earthquakes resulting from mantle convection. Because of the disastrous effects that these and other geophysical phenomena have, considerable scientific resources have been devoted to these problems. Aside from their social consequences, geophysical flows are interesting in and of themselves and have been an inspiration for concepts such as deterministic chaos and two dimensional turbulence. Much of the information regarding geophysical flows has come from direct planetary observations and numerical models. The former is uncontrollable with many complicated factors influencing the flow. The latter is remarkable in that it comes close at all to mimicking the former. We are developing a prototype experimental system that will take full advantage of the microgravity environment to study these types of flows. The unique characteristic of this system - as compared to previous efforts - is that we will create a system where a spherically symmetric density gradient is established in a compressible fluid. This will mimic the single most striking and obvious property of any geophysical flow, the radial density gradient. The results from our prototype experimental system should establish facts and phenomenon for simulators and theoreticians to explain under simplified conditions.

To understand how our experimental system works, elements from the physics of critical phenomenon (of phase transitions), electrodynamics, and compressible fluid dynamics have to be considered. As is well known in critical phenomena, there exists in fluids a special point in the  $(p, T, \rho)$  phase diagram where the distinction between the gas phase and the liquid phase disappears ( $p$  is the pressure,  $T$  is the temperature, and  $\rho$  is the

density of the fluid). This point in the phase diagram is called the critical point ( $p_c$ ,  $T_c$ ,  $\rho_c$ ). Near the critical point many properties of a fluid, both thermodynamic and transport, diverge. The compressibility of a fluid is one of the most strongly divergent properties of a fluid[1]. Over the years many investigators in critical phenomenon have been frustrated by the difficulty that the earth's gravity makes in experiments with fluids near the critical point. In particular, the gravitational field induces a strong density gradient in the fluid that masks many interesting and exotic properties of critical fluids[1][2]. More recently, the microgravity environment now available has made more detailed investigations possible and has lead to some unexpected results[3][4].

An electric field influences a dielectric fluid near the critical point. These influences include the modification of the thermodynamics of a fluid and the mechanical body force exerted on a fluid in a non uniform field[5]. Thermodynamically, the electric field must be considered another state variable. Mechanically, the electric field produces a body force on a fluid. A uniform field will exert a force on any free charge in a fluid and polarize the molecules of a fluid (i.e., induce a dipole moment in the charge distribution of a molecule and exert a torque on a polar molecule tending to align the molecules with the electric field). A non uniform field, or an electric field *gradient*, will polarize the fluid and exert a force on the fluid[5]. In spherical geometry, such as concentric spheres with dielectric fluid between them (a spherical capacitor), as shown in Figure 1, the electric field gradient produces a central body force that is similar to gravity. This effect has been used effectively in space experiments to study geophysical instabilities driven by buoyancy and rotation[6][7] in incompressible dielectric fluids. These experiments have yielded many interesting flow patterns and have shown how a dielectrophoretic force also has a buoyancy associated with it. In our experiment we will induce a spherical density gradient in a compressible critical fluid using the concentric spheres geometry and drive the system far from equilibrium by heating and rotation. The resulting instabilities and flow patterns will be studied.

## RESEARCH APPROACH

It is a well established experimental fact that the gravitational field of the earth stratifies a critical fluid in density because of its high compressibility. In a compressible dielectric fluid, the central force present in a spherical capacitor will also lead to a density gradient[5] in a manner similar to a compressible fluid in a gravitational field[8][1][2]. The density stratification from the earth's gravity, however, makes it impossible to make a spherically symmetric density gradient on earth using an electric field. Doing this experiment in microgravity is necessary. In addition, near the critical point the properties of the fluid make it highly sensitive to buoyancy from gravity. The temperature difference needed to drive convection gets very small as the average temperature approaches  $T_c$ . The high pressure of a critical fluid cell also makes it more difficult to develop the mechanical and thermal forcing mechanisms. Simplifying the development of the cell by using an incompressible fluid at room temperature and pressure in a ground-based study is desirable. Because the central force on a fluid in a spherical capacitor decreases in radius  $r$  as  $r^{-6}$ , a small incompressible fluid cell can create a large effective gravity. This makes it possible to make a second cell in parallel to the critical cell to complement and enhance the study of the critical fluid cell. In addition it enhances and expedites the development of the critical fluid cell since it can be more easily tested. The simplified cell will also help to predict phenomena that will occur in a space experiment. We are in the process of preparing an incompressible fluid cell.

The novel combination of a dielectric fluid near its critical point with a rotating inner sphere and convection, put together here for geophysical similarity, is something that has, to our knowledge, never been studied before. Because the thermodynamics and transport processes in a critical fluid are so novel and interesting, most of the previous work in critical fluids has been concerned with these properties. Very few fluid dynamics experiments have been done in a critical fluid[9], and none, that we are aware of, in the presence of an electric field. We are presently attempting to test a critical fluid cell to see if appreciable density changes can be induced through electrostriction and dielectrophoresis in a critical fluid.

Several successful electroconvection experiments have provided interesting results of geophysical significance. These previous attempts to produce spherical electroconvection experiments in incompressible fluids have shown that it is often only possible to do them in space[6][7][10][11]. The need to do the experiments in space comes partly from designing a system that can obtain high Reynolds numbers. This constraint requires that a relatively large system be built. If the system is too large, however, getting an appreciable effective gravity using an electric field below the breakdown voltage of the fluid is difficult. In a smaller system, however, getting a large effective gravity should be possible. Unfortunately such a small system compromises the possible Reynolds numbers and makes the construction of a system with a small aspect ratio  $\Gamma$  ( $\Gamma$  = ratio of the gap between the spheres to the radius of the inner sphere), such as the atmosphere or ocean, difficult. There are, however, other interesting geophysical systems, such as the earth's core, that do have a large aspect ratio and smaller Reynolds numbers. Table 1 shows estimates of various geometries and dimensionless parameters for comparison of our system to other geophysical systems. It shows that the critical fluid cell and the incompressible fluid cell could make a good analog to a planetary core. Producing cells with small aspect ratios that approach the geometrical similarity of an ocean is also possible.

The experimental system, shown in Figure 1, will have many similarities to a geophysical system. The experimental system will consist of two concentric conducting spheres with a large A.C. potential difference applied between them. Between the two spheres a dielectric fluid will be placed. The temperature of the fluid will be controlled such that the fluid is close to its critical point and as such will be highly compressible. Electrostriction and dielectrophoresis will induce a spherically symmetric density gradient in microgravity. The central sphere rotates at a controllable constant rate by attaching it to a magnet in the cell that will be magnetically coupled to another dipole magnet outside the cell (see Figure 1). These two magnets will be driven by an external motor. Convection will be induced in the cell by controlled radiative heating. Several diagnostic techniques are used, including holographic interferometry and Particle Image Velocimetry.

## SCIENCE RESULTS

We have constructed a preliminary cell and begun testing of the density gradient by applying an electric field. This cell uses a piece of cylindrical copper 3 inches long and 3 inches in diameter. A 1.5 inch diameter cylindrical hole is milled through its center along the cylinder axis. Inside of this hole is placed a small spherical electrode, as can be seen in Figure 2. Two sapphire windows are placed at each end of the copper so that light may pass through the region near the spherical electrode and to seal the  $\text{SF}_6$  in the cell. The high potential is applied to this electrode and the surrounding copper is grounded. The cell is temperature controlled using a YSI thermistor and a National Instruments AT-MIO-16X DAQ board with Labview software. Figure 2 shows a holographic interferogram before the electric field has been applied. We have to date found the following preliminary results: on applying 3000 volts (RMS) to the cell when the fluid is  $\approx 20\text{mK}$  above the critical point (supercritical fluid), we have observed a fringe shift of  $\sim 1/2$  of a wavelength. This corresponds to  $\sim 0.005\%$  change in density near the electrode. This is less than we would expect in zero gravity. In  $1g$  the presence of convection caused by buoyancy should decrease the density change.

## RESEARCH PLANS

In its currently planned final form, the critical fluid cell will include two transparent sapphire domes coated with indium tin oxide that will form the outer sphere which will be concentric with a  $\approx 0.25$  inch diameter conducting sphere at the center, as shown in Figure 1. The above mentioned incompressible fluid cell will be tested and information and techniques gained from it will be used to build this critical fluid cell. Based on the results of our tests that are currently being conducted, we anticipate the approach shown in Figure 1 will be used.

When the final critical fluid cell is developed, the diagnostic techniques will be used in an NASA KC-135 or DC-9 aircraft to test for a spherically symmetric density gradient in low gravity and for expected flow

patterns. In preparation for this, the 1g case will be explored first so that some idea of reasonable parameter values will be known in advance.

## REFERENCES

- [1] M. R. Moldover, J. V. Sengers, R. W. Gammon, and R. J. Hocken, "Gravity effects in fluids near the gas-liquid critical point", *Rev. Mod. Phys.*, **51**, 79 (1979).
- [2] P. C. Hohenberg and M. Barmatz, "Gravity effects near the gas-liquid critical point", *Phys. Rev. A*, **6**, 289, (1972).
- [3] H. Boukari, J.N. Shumeyer, M.E. Briggs, and R. W. Gammon, "Critical speeding up in pure fluids", *Phys.Rev.A*, **41**, 2260 (1990).
- [4] B. Zappoli, D. Bailly, Y. Garrabos, B. LeNeindre, P. Guenoun, and D. Beysens, "Anomalous heat transport by the piston effect in supercritical fluids under zero gravity", *Phys. Rev. A* **41**, 2264 (1990).
- [5] L. D. Landau and E. M. Lifshitz, *Electrodynamics of Continuous Media*, (Addison- Wesley, Reading Mass., 1960).
- [6] J. E. Hart, J. Toomre, A.E. Deane, N. E. Hurlburt, G. E. Glatzmaier, G. H. Fichtl, F. Leslie, W. W. Fowles, P. A. Gilman, "Laboratory experiments on planetary and stellar convection performed on spacelab 3", *Science*, **234**, 61 (1986).
- [7] C. Egbers, A. Delgado, and H. J. Rath, "First experimental investigation of density driven large-scale ocean motions under microgravity, *ASME Forum Micro. Flows*, **111**, 41 (1991).
- [8] L. D. Landau and E. M. Lifshitz, *Statistical Physics Part 1*, 3rd ed. (Pergamon Press, New York, 1982).
- [9] M. Assenheimer and V. Steinberg, "Rayleigh-Bénard Convection near the Gas-Liquid Critical Point", *Phys.Rev.Lett.*, **70**, 3888 (1993).
- [10] J. E. Hart, G. A. Glatzmaier, and J. Toomre, "Space-laboratory and numerical simulations of thermal convection in a rotating hemispherical shell with radial gravity", *J. Fluid Mech.*, **173**, 519 (1986).
- [11] J. E. Hart, "Studies of Earth Simulation Experiments", *NASA-Contractor Report, NASA CR-2753*, (1976).

	compressible SF <sub>6</sub>	incompress. DC-200 .65cs	outer core	ocean	atmosphere
$\Gamma$	1.5	1.5	1.5	$6 \times 10^{-4}$	$5 \times 10^{-3}$
$R_o$	0-385	0-1500	$21-2 \times 10^{-14}$	1800	$1 \times 10^6$
S	$\infty-0.333$	N/A	$10^4$	0.16	$10^3$
$F_r$	0-0.002	0-0.002	$9 \times 10^{-4}$	$3 \times 10^{-3}$	$3 \times 10^{-3}$
$R_a$	0- $\infty$	0- $7 \times 10^6$	unknown	$10^{14}$	$10^{14}$
$P_r$	1- $\infty$	8	unknown	7-50	0.25

Table 1. The above table shows dimensionless parameters for comparison of the laboratory systems with other geophysical systems. These numbers are based on a flow cell with inner radius  $r_i=0.5\text{cm}$  and outer radius  $r_o=1.27\text{cm}$  using SF<sub>6</sub> in the compressible cell and Dow Corn DC-200 0.65 CS silicone oil in the incompressible flow cell. The height of the atmosphere is taken to be 30,000m which is where the average temperature begins to increase. The Reynolds Number,  $R_o$ , is  $R_o = \Omega r_i d / \nu$  where  $\nu$  is the kinematic viscosity and  $\Omega$  is the rotation of the inner sphere and  $d$  is the gap between the spheres. This parameter characterizes the mechanical driving of the system through the rotation of the sphere (note that we do not refer to the "rotating

frame" parameters, i.e., the Ekman and Rossby numbers). The thermal driving of the system though heating is characterized by the Rayleigh number  $R_a = \alpha T g d^3 / \kappa \nu$  or  $R_e = \gamma \Delta T g_e d^3 / \kappa \nu$  where  $\alpha$  is the thermal expansion coefficient,  $\gamma$  is the dielectric variability,  $\Delta T$  is the temperature difference across the gap of width  $d$ ,  $g$  or  $g_e$  is the acceleration that in our case can be due to gravity,  $g$ , or an equivalent electrostatic acceleration,  $g_e$ , and  $\kappa$  is the thermal diffusivity. We have used the turbulent eddy viscosity and not the kinematic viscosity in the Rayleigh and Reynolds numbers for the ocean and atmosphere. A material parameter important to convection in fluids is the Prandtl number  $P_r = \nu / \kappa$ . Because the properties of a critical fluid diverge,  $R_a$  also diverges for a given  $\Delta T$  near a fluids' critical point. In addition  $P_r$  also exhibits this behavior and can therefore be adjusted over many orders of magnitude by adjusting the average temperature. Another important parameter for our system is the Froude number  $F_r = \Omega^2 r / g$  or  $F = \Omega_e r / g_e$  that, in our case, compares the centrifugal acceleration with the central acceleration (electrostatic or gravitational). In order for the acceleration to be radial it is necessary for  $F_r$  to be small, i.e.,  $F_r \ll 1$ . One remaining important dimensionless parameter in a rotating flow with a density gradient is the stratification parameter  $S = g \Gamma \Delta \rho / 2 d \rho \Omega$ . If  $S$  is large, then density stratification is important.  $g_e$  is calculated using the formula for the dielectrophoretic force. The earth's core shows a large variation in  $R_a$  and an unknown  $R_e$  and  $P_r$ . This shows the lack of knowledge of the earth's core that exists today.

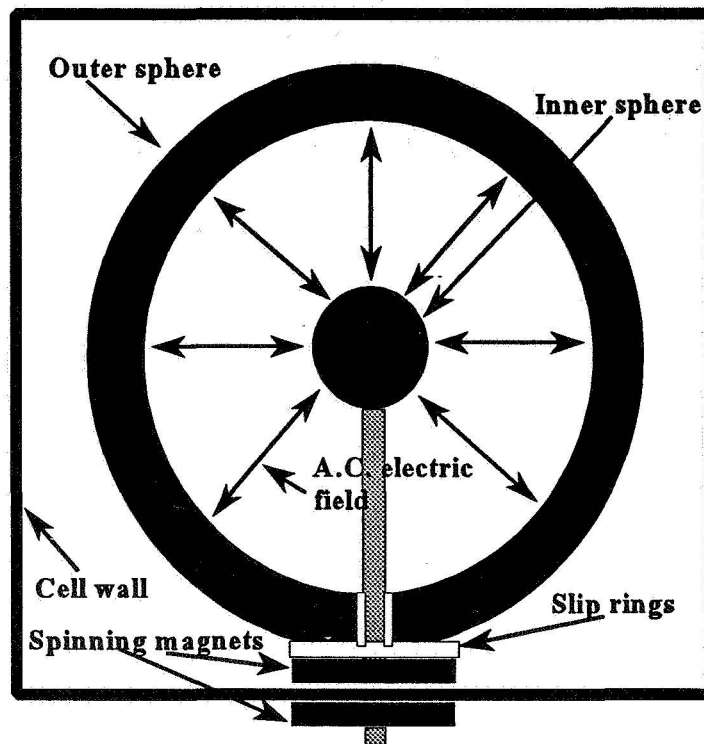


Figure 1. Above is a schematic of the compressible flow cell currently planned. Fluid near the critical point is contained inside a cell. A large A.C. potential difference applied across two conducting concentric spheres induces a spherical density gradient in the fluid between the spheres. Inside the cell will be a permanent dipole magnet attached to a conducting rod (which is attached to the inner sphere and insulated from the outer sphere). Slip rings will support the rotation of the inner sphere and allow electrical connections it. Outside the cell will be another dipole magnet connected to a step motor. The inner and outer dipole magnets will be coupled. Because the fluid in the critical fluid cell is under considerable pressure, these two magnets will allow a mechanical coupling to the outside of the cell for rotating the inner sphere. Sapphire windows in the cell will also allow infrared light from a well-calibrated source to heat the inner sphere. This heating method considerably simplifies

the cell design and maintains geophysical similarity. The density variations will be observed by using holographic interferometry where laser light is passed through the cell to produce an interference pattern

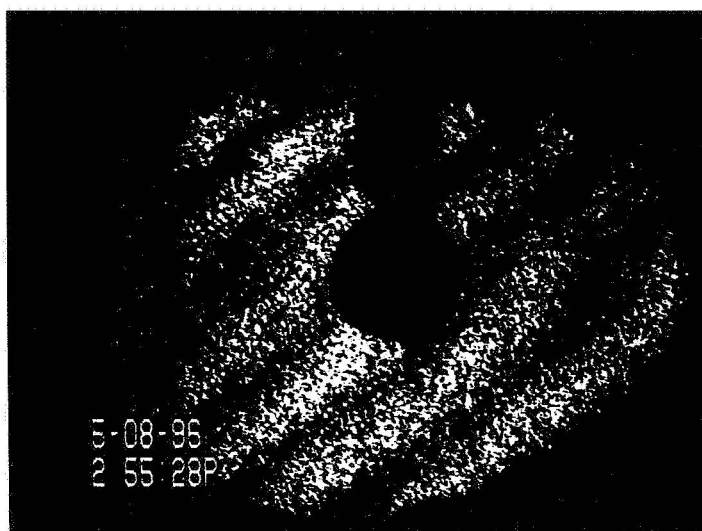


Figure 2. Shown above is a view through the preliminary cell filled with SF<sub>6</sub> near the critical point. The dark circle in the middle is the 1/4 inch diameter spherical electrode. The dark stripes are interference fringes made using holographic interferometry. These fringes are reference fringes made by tilting an object beam mirror between holographic exposures. We have observed a fringe shift of  $\sim 1/2$  of a wavelength on applying 3000 volts (RMS) to the cell when the fluid is  $\approx 20$ mK above the critical point (supercritical fluid).



# Experimental Study of Liquid Jet Impingement in Microgravity: The Hydraulic Jump

C.T. Avedisian and Z. Zhao

Sibley School of Mechanical and Aerospace Engineering

Cornell University

Ithaca, New York 14853-7501

## Abstract

A preliminary study of the circular hydraulic jump (CHJ) in microgravity is reported using water as the working fluid. The evolution of the CHJ radius was measured during a sudden transition from normal to microgravity in a drop tower. The downstream height of the CHJ was controlled by submerging the target plate in a tank filled with water to the desired depth, and the measurements are compared with an existing theory for the location of the CHJ.

Results showed that the CHJ diameter was larger in microgravity than normal gravity. The adjustment of the CHJ diameter to a sudden change in gravity occurred over a period of about 200ms for the conditions of the present study, and remained constant thereafter. For flow conditions that a CHJ was not first established at normal gravity but which later appeared during the transition to microgravity, the CHJ diameter was not constant during the period of microgravity but continually changed. Good agreement between the measured and predicted CHJ diameter was found for the normal gravity data, but comparatively poorer agreement was observed for the microgravity measurements.

## Introduction

Impingement of a circular liquid jet onto a surface is important in a variety of processes: impingement cooling of electronic devices, materials in manufacturing processes, laser mirrors, and aircraft generator coils; and vapor absorption refrigeration cycles. A feature of impinging liquid jets is their potential for dissipating high heat transfer rates and undergoing a hydraulic jump. Downstream of a CHJ liquid velocity is less than upstream of it and heat transfer is reduced. It is, therefore, important to predict the location of the CHJ and the parameters upon which it depends. Gravity figures prominently in both the location of the CHJ and the abruptness with which the fluid height increases across the jump. The CHJ occurs where the expanding liquid jet undergoes a transition from a 'supercritical' to a 'subcritical' flow, in the sense of a suitably defined Froude number being greater or less than unity, respectively.

This study is a preliminary effort to improve the understanding of the effect of gravity on a CHJ formed from a laminar circular jet. To isolate the influence of gravity, the fluid and target surface temperatures were the same. Specific objectives were to 1) measure the evolution of a CHJ upon a sudden transition from normal gravity (i.e.,  $G=g/g_0=1$  where  $g_0=9.8\text{m/s}^2$ ) to microgravity ( $G\ll 1$ ), and 2) compare the results with available analyses of jet impingement in microgravity. Existing analyses predict that a CHJ diameter is larger at  $G\ll 1$  than at  $G=1$ . The present experiment was designed to test this prediction. Measurements were made of the following: 1) evolution of the CHJ radius during the transition from  $G=1$  to  $G\ll 1$ ; 2) the steady state CHJ radius at  $G\ll 1$  (also data at  $G=1$  for comparison); and 3) the evolution of the liquid film thickness across the jump during the transition from  $G=1$  to  $G\ll 1$ . The parameters were the liquid flow rate, jet orifice opening, and the downstream liquid height. The decision to focus on the transition from  $G=1$  to  $G\ll 1$  was made because of the available experimental run time of just over 1s.

## Brief Review of Related Work

An extensive literature exists on jet impingement in general, and the hydraulic jump in particular. Standard fluid mechanic textbooks provide basic formulations for planar hydraulic jumps (e.g., Allen and Ditsworth 1972; Fox and McDonald 1992). On the CHJ, Nirapathdongporn (1968) reports an extensive search of literature prior to 1968 and reviews the various theories. A number of numerical studies have predicted the behavior of the CHJ in microgravity. At precisely  $G=0$ , no jump is predicted (e.g., Thomas et al. 1990). In the vicinity of a jump at  $G=1$ , back-flow, separation, and eddies are observed in experimental studies and predicted in early treatments of the problem (e.g., Craik et al. 1981; Tani 1949), but no experimental observations have been reported for  $G\ll 1$ .

A theoretical analysis by Watson (1964) results in a closed-form solution to the laminar momentum and continuity equations for the CHJ diameter where an inviscid approximation is made for the stagnation region and the flow downstream of the jump, and the flow is self-similar upstream of the CHJ. Some failures of the model are analyzed by Bowles and Smith (1992) who predict the film thickness shape near the jump, and Liu and Lienhard (1993)

who discuss the importance of viscous drag and surface tension. Numerical solutions by Chaudhry (1964) and Higuera (1994) account for the effect of turbulence and heat transfer and provide predictions of both the CHJ diameter and film thickness downstream of the jump.

One experimental study is known on the problem of jet impingement at  $G \ll 1$  (Labus 1976). The focus was on studying the shapes assumed by a free liquid surface rolling off of the edge of a plate on which the liquid impinges. A drop tower was used to create the microgravity environment. A hint of what to expect for the CHJ diameter at  $G \ll 1$  was noted by the observation that no CHJ occurred during any of the  $G \ll 1$  tests while they were a common occurrence at  $G=1$  for nominally the same flow conditions.

### Experimental Design

A microgravity environment for the present experiments was created by using a drop tower. Central to the success was the ability to observe all desired features of the flow within the available experimental run time. It was anticipated that the reaction time of the CHJ radius to sudden changes in  $G$  would be much less than the available experimental time (on the order of 1s for the facility used). While this was verified for most of the conditions analyzed, for some it was not as discussed in the next section.

The general design of the drop tower used here has been described in past (unrelated) studies (Avedisian et al. 1988; Jackson et al. 1994). It provides for a 7.6m free-fall of an instrumentation package which houses the experiment to give an experimental run time of about 1.25s and a capability for the package to be shielded from air drag. However, the drag shield was not used in this preliminary study for convenience and simplicity of operation. The  $G$  value of the unshielded package has a projected maximum after 1.25s of free-fall of about  $2.2 \times 10^{-2}$  (Avedisian et al. 1988); the shielded package has a maximum  $G$  about two orders of magnitude less (Jackson and Avedisian 1994).

A schematic diagram of the apparatus is shown in fig. 1. The components are the following: recirculating pump; plenum containing beads and a flow straightener (to dampen the inlet flow) and a removable orifice plate attached at one end; plexiglas chamber within which the target plate is mounted; flow control valve; and cameras and lighting. The height of the liquid level downstream of the jump is controlled by submerging the target plate to the desired depth by raising the water level above the plate. The experimental conditions examined were the following. The downstream fluid height,  $h_\infty$ , was 2.0 mm, 4.0 mm, 6.0 mm, 10.0 mm, or 15.0 mm. The liquid flow rates were 2.39ml/s, 6.32ml/s, 9.93ml/s, or 26.47ml/s. To create laminar jets, a sharp-edged orifice was used. Orifice diameters of 1.22mm, 2.56mm and 3.83mm were used. They were machined into a stainless steel plate that could be bolted to the bottom of the plenum. The plenum was mounted such that the orifice was 7.62cm above the target surface. The diameter of the liquid jet,  $D_j$ , at a reference  $2D_j$  above the target surface was measured directly.

The target plate was a 6.35 mm thick and 23 cm diameter pyrex glass disk painted black on its back to reduce light reflections. A mirror tilted to  $45^\circ$  under the plate allowed for observations of the underside of the jet. Additional viewing angles were along the plane to show the cross-sectional profile shape of the liquid film across the CHJ, and an angled top view for global features of the CHJ. The working fluid was water at room temperature in all the experiments.

To keep the design simple, the primary means of data acquisition was photographic. A 35mm Nikon F3 camera with MD-4 motor drive (operated at 5 frames/s) and attached 105 mm NIKKOR macro lens was used to record images at all three camera positions. Video images using a COHU CCD camera (30 images/s) with attached 28mm NIKKOR macro lens were used to record the evolution of the CHJ in the transition to microgravity. All cameras and lenses were securely mounted to prevent damage due to the shock of the impact. Lighting was provided by halogen lamps. The CHJ diameter was measured from video images of underneath views using a 'video caliper' electronically placed on the video image. A precision ruler (Schaedler Quinzel, Inc., USA) was added to the image to calibrate (to  $\pm 158 \mu\text{m}$ ) the voltage output from the caliper. Side views were used to obtain the cross-sectional shape of the liquid film across the CHJ. The side view images were fed into a MAC-based data acquisition system (AUTOMATIX Image Analysis Program) and an operator-selected gray scale was used to identify the various boundaries involved. A 19.05 mm diameter ball bearing image converted the side view pixel count to length with a precision of about  $\pm 66 \mu\text{m}$ .

### Discussion of Results

The response of the CHJ boundary to the transition from  $G=1$  to  $G \ll 1$  is shown in the representative series of photographs of fig. 2 for a flow rate of  $9.6 \times 10^{-6} \text{ m}^3/\text{s}$  and  $h_\infty = 4 \text{ mm}$  for the 2.54 mm diameter orifice opening. The time interval between the photos is about 200 ms and a CHJ initially exists at  $G=1$ . In the vicinity of the stagnation point the liquid spreads in a thin film with a smooth surface and then rises abruptly to form a surface roller

in the downstream flow at the CHJ. On the transition to  $G \ll 1$  (fig. 2b), the liquid boundary at the CHJ appears to be pushed outward; a similar effect occurs at the stagnation point as well where the vertical jet turns and flows horizontally. The mechanism for these effects may be the de-stabilizing effect that  $G \ll 1$  has on balancing the hydrostatic pressure in the downstream film with the surface tension force on the free surface of the CHJ boundary. At  $G \ll 1$ , the hydrostatic pressure is reduced in the downstream flow and the radius of curvature of the CHJ boundary increases to compensate. This change in curvature of the CHJ boundary creates surface waves at  $G \ll 1$  in the downstream flow as shown in fig. 2c. Concurrently, the CHJ diameter increases because of the increase in the upstream Froude number caused by the reduction of  $G$ .

The profile shape of the liquid across the CHJ during the transition to  $G \ll 1$  is shown in fig. 3 at five different times after release of the package (at  $t=0s$ ,  $G=1$ ) for one flow rate. The dotted line references the target plate. The CHJ boundary was assumed to correspond to the radial position at which the fluid film first increased (note the vertical dotted lines in figure 3) and surface waves first appeared (see fig. 2). The difficulty of identifying the CHJ boundary at  $G \ll 1$  is evidenced in figs 2 and 3 by the more gradual transition of the CHJ boundary at  $G \ll 1$  due to the reduction in hydrostatic pressure in the downstream film at  $G \ll 1$  as noted above.

Fig. 4 shows the evolution of the CHJ radius on the transition from  $G=1$  to  $G \ll 1$  at two different flow rates for the 2.56 mm diameter orifice and  $h_\infty=4$  mm when a jump initially existed at  $G=1$ . Fig. 5 shows the evolution when no jump initially existed at  $G=1$  for the 1.22mm orifice and  $h_\infty=15$ mm. The CHJ diameter was averaged over the time interval of 400ms to 600ms after release of the package. When no jump existed at  $G=1$  (fig. 5), the process of establishing a CHJ at  $G \ll 1$  was found to first require a brief period in which the liquid near the impingement spot thinned to eventually form the CHJ. Thereafter, the CHJ diameter continuously changed over the entire period of observation (1.25s) as shown in fig. 5, and taking the CHJ diameter in the interval of 400ms to 600ms is more approximate for this case.

Figs. 4 and 5 show that the CHJ diameter increases during the transition to  $G \ll 1$ . The fluid response time to re-establish a new CHJ position after  $G \ll 1$  is about 200 ms for  $Q=9.93$ ml/s and  $Q=26.47$ ml/s as shown in fig. 4. The CHJ diameter eventually reaches a constant value at  $G \ll 1$  within the observation period when a CHJ first existed at  $G=1$ , but continuously changes over the entire period of observation when no CHJ existed at  $G=1$ . The increase in the CHJ diameter for both cases is due to the increased upstream supercritical Froude number created by a reduction of gravity. In addition, though  $G$  continuously increases during the flight of the unshielded package due to air drag (Avedisian et al. 1988), the change was not enough to measurably effect the CHJ diameter after 200ms as shown in fig. 4.

A simplified viewpoint of the origin of a CHJ is that flow of a supercritical expanding film is slowed by friction at the wall and the increasing flow area (due to the radial geometry) until a point is reached at which the flow cannot adjust to the changing downstream conditions because  $Fr > 1$  without experiencing a 'jump' in film thickness to satisfy mass conservation. Quantitative developments of the CHJ assume it to be a transition from a flow in which small perturbations are unable to propagate upstream to one in which they are (Higuera 1994). The liquid jet expanding under the influence of an adverse gravitational pressure gradient eventually separates (Tani 1949) as a result of a nonlinear interaction between the wall shear stress, surface tension and the pressure gradient across the film (Bowles and Smith 1992; Gajjar and Smith 1983). This interaction leads to an upstream influence and the CHJ is the result that allows an adjustment of the flow to downstream conditions.

The radial location of the CHJ is most simply determined by assuming a frictionless fluid and applying a mass and momentum balance across a steady CHJ to relate the CHJ diameter,  $D_h$ , to the downstream fluid thickness  $h_\infty$ , the flow rate  $Q$ , and the upstream film thickness  $h$  as

$$[Q/(\pi D_h)]^2 (1/h - 1/h_\infty) = 1/2 g_0 (h_\infty^2 - h^2) G \quad 1$$

From eq. 1,  $D_h$  can only be determined if  $h_\infty$  is known - a motivation for the particular experimental design (fig. 1). As  $G \rightarrow 0$ ,  $D_h \rightarrow \infty$  and no jump occurs. Eq. 1 is predictive only in the limit of a high velocity flow. Watson (1964) accounts for viscous effects by using a boundary layer model to predict the velocity profile across the upstream film and finds that the flow becomes self-similar at some radial position away from the stagnation point. This theory has the essential features of more advanced treatments (e.g., Bowles and Smith 1992; Higuera 1994) and is applied to the present data. The modification of eq. 1 due to Watson (1964) for the case of a boundary layer that covers the entire film can be expressed in non-dimensional form as (Middelmann 1995)

$$Y = 26/(R^3 + 287) \quad 2$$

where  $Y \equiv RH/Fr_{\infty} + 1/(2RH)$ ,  $R \equiv D_h/D_j Re^{-1/3}$ ,  $Re \equiv 4Q/(\pi D_j \nu)$ ,  $H \equiv 2h_{\infty}/D_j Re^{1/3}$ ,  $Fr_{\infty} \equiv U_j^2/(G g_0 h_{\infty})$  and the approximation  $h_{\infty} \gg h$  has been made. The inviscid limit is  $R \rightarrow 0$  in eq. 2.  $Y$  and  $R$  are known from the experimental results:  $D_h$  as discussed previously, and  $h_{\infty}$  and  $Q$  as input parameters ( $U_j = Q/[\pi D_j^2/4]$ ). A reference location of  $2D_j$  above the target surface was used to measure  $D_j$ . For the water kinematic viscosity at 300°K,  $\nu \approx 8.95 \times 10^{-7} \text{ m}^2/\text{s}$  (Keenan et al. 1969). An average  $G$  of  $1.1 \times 10^{-2}$  is used over the free-fall distance.

Fig. 6 shows the variation of  $Y$  with  $R$ . The inviscid limit (dotted line) clearly does not predict any of our measurements (a not unexpected result (Watson 1964)). All of the  $G=1$  data are predicted reasonably well when viscosity effects are included (eq. 2). This agreement suggests that for the experimental parameters examined the conditions of Watson's analysis are reasonably well satisfied in the experiments, for example the neglect of viscous drag at the plate and the boundary layer being fully developed in the film. On the other hand all of the measurements of  $D_h$  for  $G \ll 1$  show poorer agreement with eq. 2. This result may indicate a number of possibilities, including that some process not included in the development of eq. 2 becomes important at  $G \ll 1$ . Candidates include flow separation downstream of the jump and the nonuniform downstream velocity, neglect of viscous drag at the surface of the plate, or surface tension, in addition to uncertainties in identifying the CHJ boundary at  $G \ll 1$  noted above.

## Conclusions

Experimental measurements of the CHJ in microgravity showed the following results for the particular experimental conditions examined: 1) a steady CHJ can be established in microgravity; 2) the CHJ in microgravity is larger than at normal gravity, other flow conditions being the same; 3) the fluid response time during the transition to microgravity is on the order of 200ms when a jump exists at normal gravity; 4) when flow conditions are such that a CHJ does not exist at normal gravity, the fluid response time appears to be greater than 1s after the transition to microgravity; 5) the film thickness across the CHJ boundary at  $G \ll 1$  is more gradual due to the reduction in hydrostatic pressure in the downstream film; and 6) the  $G=1$  measurements are well correlated by an existing formulation but the microgravity measurements show comparatively poorer agreement.

## Acknowledgments

The authors wish to thank the Microgravity Science and Application Division of NASA for supporting this preliminary study. Thanks go to Dr. David Chao of NASA for serving as technical monitor and for his encouragement throughout the course of this study, and to Mr. Jack Salzman of NASA for drawing to the authors' attention the reference to Labus (1976). The assistance of Messrs. Jun-Eu Tang and Hanwook J. Kim of Cornell in performing some of the experiments is appreciated.

## REFERENCES

- Allen, T. and Ditsworth, R.L. (1972) *Fluid Mechanics*, pp. 291-291, McGraw-Hill, New York.
- Avedisian, C.T., Yang, J.C and Wang, C.H. (1988) *Proc. R. Soc. Lond* **A420**, 183.
- Bowles, R.I. and Smith, F.T. (1992) *J. Fluid Mechanics*. **242**, 145.
- Chaudhury, Z.H. (1964) *J. Fluid Mechanics*. **20**, 501.
- Craik, A.D.D., Latham, R.C., Fawkes, M.J. and Gribbon, P.W.F. (1981) *J. Fluid Mechanics* **112**, 347.
- Fox, R.W. and McDonald, A.T. (1992) *Introduction to Fluid Mechanics*, 4th edition, pp. 525-530, John Wiley, New York.
- Gajjar, J.S.B. and Smith, F.T. (1983) *Mathematika* **30**, 77.
- Higuera, F.J. (1994) *J. Fluid Mechanics*. **274**, 69.
- Jackson, G.S. and Avedisian, C.T. (1994) *Proc. R. Soc. Lond.*, **A446**, 257-278.
- Keenan, J.H., Keys, F.G., Hill, P.G., and Moore, J.G. (1969) *Steam Tables*, p. 114, John Wiley, New York.
- Labus, T.L. (1976) "Liquid Jet Impingement Normal to a Disk in Zero Gravity," Ph.D. Thesis, University of Toledo.
- Liu, X. and Lienhard, J.H. (1993) *Exp. Fluids*, **15**, 108.
- Middelmann S. (1995) *Modeling Axisymmetric Flows*, Chapter 5, New York, Academic Press.
- Nirapathdongporn, S. (1968) "Circular Hydraulic Jump", M.Eng. Thesis, Asian Institute of Technology, Bangkok, Thailand.
- Thomas, S., Hankey, W.L., Faghri, A., and Rahman, M.M. (1990) *J. Heat Transf.* **112**, 728.
- Tani, I. (1949) *J. Phys. Soc. Japan* **4**, 212.
- Watson, E.J. (1964) *J. Fluid Mechanics* **20**, 481.

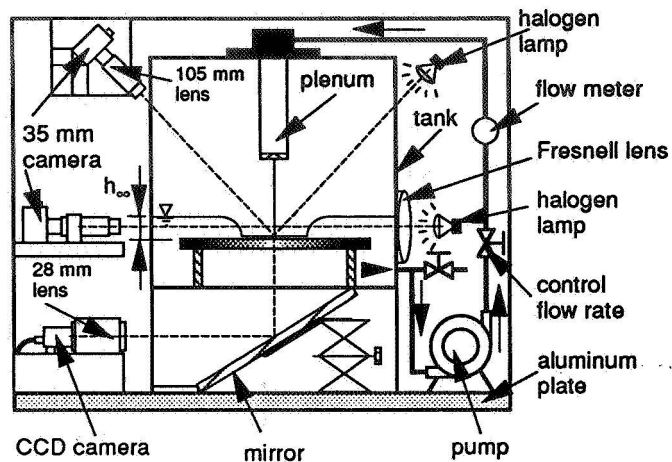
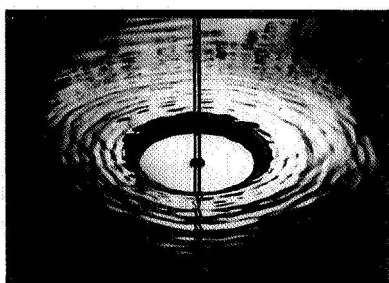
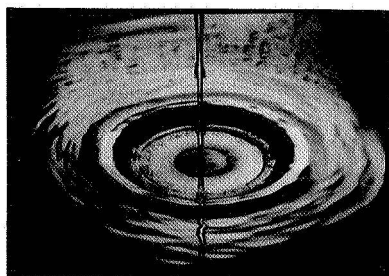


**Figure 1**



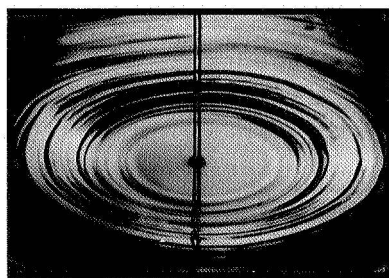
$t=0, G=1$

**Figure 2a**



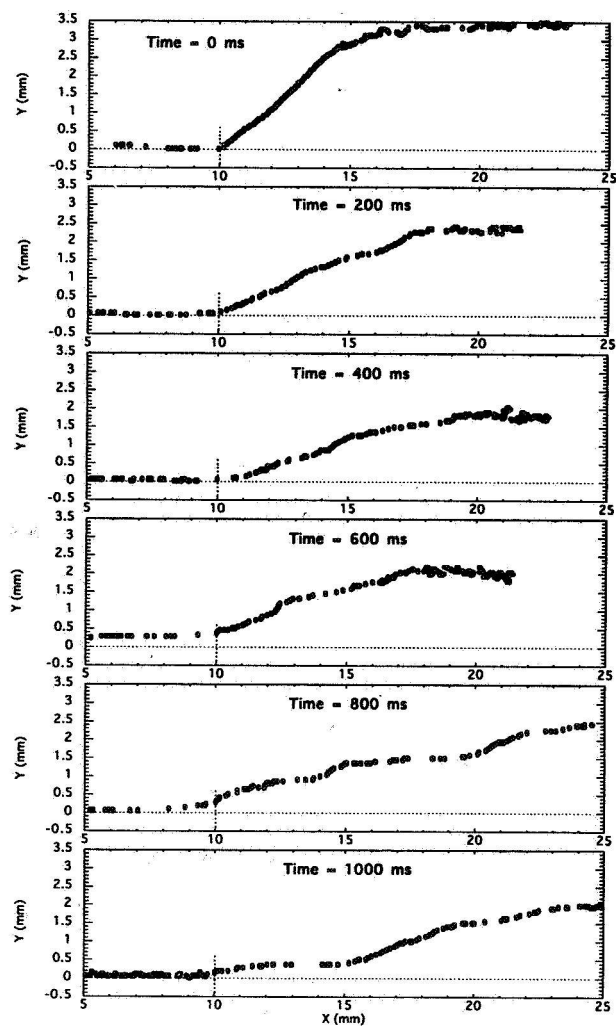
$t=200 \text{ ms}, G \ll 1$

**Figure 2b**



$t=400 \text{ ms}, G \ll 1$

**Figure 2c**



$t=0, G=1; t>0, G \ll 1$

**Figure 3**

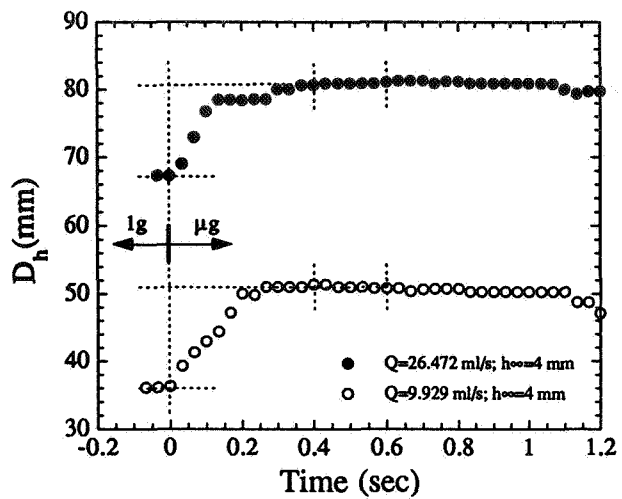


Figure 4

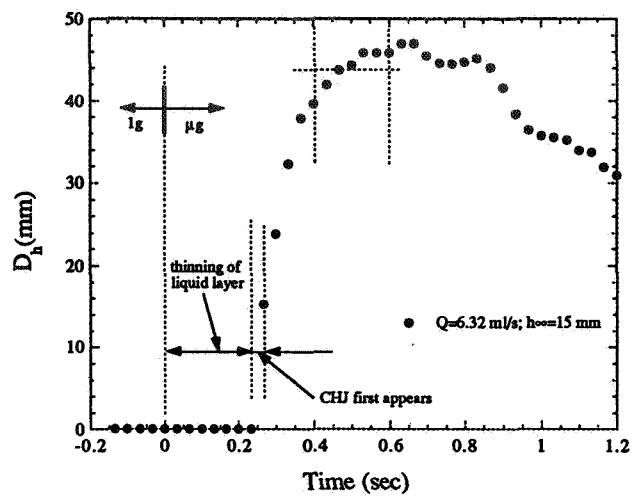


Figure 5

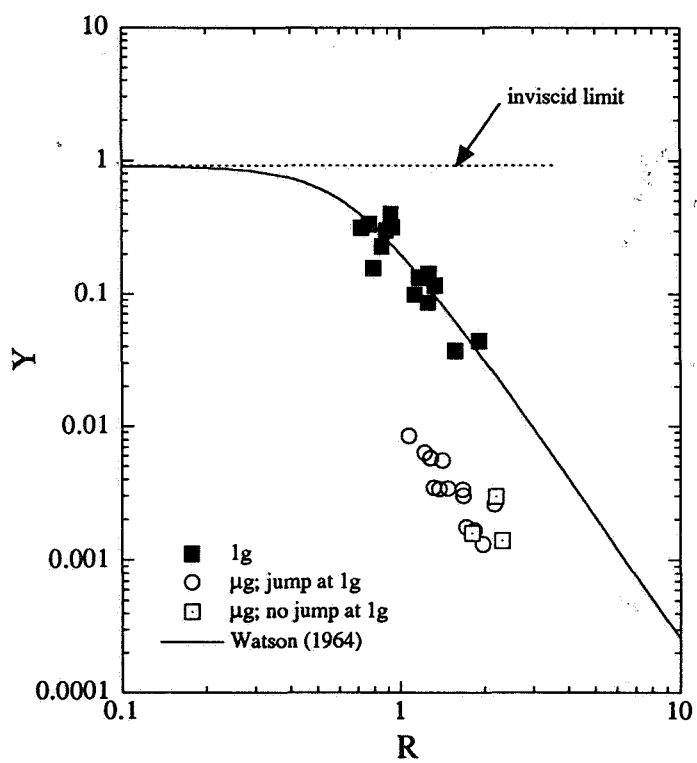


Figure 6

**STUDIES OF RADIATION-DRIVEN AND BUOYANCY-DRIVEN  
FLUID FLOWS AND TRANSPORT**  
(NASA Grant No. NAG3-1653)

Paul D. Ronney and Justin M. Fortmeyer  
Department of Mechanical Engineering  
University of Southern California, Los Angeles, CA 90089-1453

**ABSTRACT**

It is well known that radiative heat transport influences many types of buoyant flows due to its effect on the temperature and thus density field in the fluid medium. It is of interest to study gaseous flows driven solely by radiation in the absence of buoyancy, particularly because of its application to astrophysical flows that are well known from astronomical observations and numerical simulation. However, no laboratory-scale experiments of this phenomenon have ever been conducted. To study the possibility of obtaining such flows in the laboratory, an apparatus was built to produce large temperature differences ( $\Delta T$ ) up to 300K in a gas confined between flat parallel plates.  $\text{SF}_6$  was used as the radiatively-active gas because its Planck absorption length is much shorter than that of any other common non-reactive gas. The NASA-Lewis 2.2 second drop tower was used to obtain reduced gravity in order to suppress buoyancy effects. To image the resulting flows, a laser shearing interferometer was employed. Initial results indicate the presence of flow that does not appear to be attributable to the residual flow resulting from buoyancy influences before the drop. For  $\Delta T > 70\text{K}$ , slight deformations in the interferometer fringes seen at lower  $\Delta T$  became large unsteady swirls. Such behavior did not occur for radiatively-inactive gases, suggesting that a flow driven solely by radiation was obtained in  $\text{SF}_6$  and to a lesser extent in  $\text{CO}_2$ . This was more pronounced at higher pressures and plate spacings, consistent with our scaling predictions.

**INTRODUCTION**

Radiation-driven flows occur in many gases and liquids that are neither completely transparent nor completely opaque to electromagnetic radiation. This effect of importance to many practical problems including glass and semiconductor processing; oceanographic or atmospheric flows with application to global climatic change; astrophysical flows; plasma physics; combustion systems; solar energy collection; nuclear explosions and heat transfer in inhabited enclosures.

We have proposed that flow driven solely by radiative effects without imposed hydrodynamic or hydrostatic pressure gradients may be possible for the following reason. If a parcel of gas receives slightly more heating than the surrounding gas, its temperature increases. In gases with a strongly temperature-dependent Planck absorption length ( $l_p$ ) such as  $\text{SF}_6$ , this temperature increase results in a significant decrease in the absorptivity, which in turn causes an increase in the radiative conductivity. For  $\text{SF}_6$  the radiative conductivity is roughly proportional to  $T^5$ . The local increase in temperature would encourage further heat transfer throughout the gas and upon coupling with thermal expansion effects, may produce a flow. Evidence of this instability has been found in  $\mu\text{g}$  combustion experiments (ref. 1). In combustible  $\text{CH}_4\text{-O}_2$  and  $\text{H}_2\text{-O}_2$  mixtures diluted with  $\text{SF}_6$ , a flame structure characterized by the sudden fingering of an evolving front has been observed, particularly at high pressures. The fingering occurred in  $\text{SF}_6$ -diluted mixtures but not  $\text{N}_2$ -,  $\text{Ar}$ - or  $\text{CO}_2$ -diluted mixtures, which is to be expected if the proposed instability mechanism is present because  $\partial l_p / \partial T$  is much larger for  $\text{SF}_6$  and because at the conditions tested only  $\text{SF}_6$  is optically thick. For the current study, we examined radiative flow instability in a non-reacting gas at  $\mu\text{g}$  with an imposed heat source of known character, rather than a chemical reaction whose heat release characteristics are intimately coupled to the thermal field.

Many theoretical and computational studies of radiation-driven flows appear in the astrophysical literature (refs. 2 - 4) because of its relevance to solar flares, the formation of galaxies, etc., yet no experimental studies of analogous flows have been conducted in a laboratory setting. Scaling analyses indicate that at earth gravity, this flow would be overwhelmed by buoyant convection even in a highly radiatively-active gas such as  $\text{SF}_6$ . Depending on the orientation, buoyancy would either suppress the instability or would be overshadowed by Rayleigh-Benard convection. Consequently, microgravity conditions are needed for an experiment test for the existence of this type of flow. The intent of the current experimental study is to explore aspects of radiation-dominated fluid flows which cannot be studied at earth gravity.

## EXPERIMENTAL APPARATUS AND PROCEDURES

### Experimental Background

A modified Rayleigh-Benard type of apparatus was utilized for these experiments. It consisted of two parallel flat plates with a gap between them varying from 2 to 5 cm (see Fig. 1.) The upper hot plate was resistively heated and the lower cold plate was thermoelectrically or water cooled. 1-cm thick plates were used to ensure uniform temperature across the plate and to ensure that their thermal response time was very large compared to the low-gravity test duration. A large temperature difference (up to 300K) could be maintained between the two plates. Locating the hot plate on top of the cold plate minimized the buoyant flow in the test section before the drop, however, some buoyant flow within the test section was unavoidable because of the flow off of the top of the hot plate. This flow is undesirable because a finite amount of time is required for it to decay once buoyancy is removed, *i.e.*, when the drop begins. This makes it more difficult to determine whether flow observed during  $\mu\text{g}$  conditions is a result of radiative effects or decaying buoyant flow. A set of baffles and blocks of insulation was used to minimize this flow. Also, comparisons were made between tests conducted at similar earth-gravity Grashof numbers with radiative and non-radiative gases (see below). The plates and their supporting structure are housed in a well-insulated, sealed aluminum chamber. The NASA-Lewis 2.2 second drop tower facility was employed to obtain low-gravity conditions.

### Measurement Techniques

Two types of measurements were made: thermal properties and imaging. The thermal properties are used to verify the 1-d transport equations, to quantify spatial and temporal deviations from steady and/or 1-d profiles (*i.e.*, to identify instabilities) and to quantify the amplitude and spectrum of the disturbances. Thermal properties were measured by thermocouples and radiometers. Imaging provided qualitative information on the overall flow. Temperatures were measured with fine-wire thermocouples (50 $\mu\text{m}$ ) were placed at several locations within the gas. Since their size was much smaller than the scales under consideration, their influence on heat transport can be considered negligible. To measure fluctuations in radiant energy flux, two thermopile-type narrow-angle shielded radiometers were placed in the gap between the plates. They were oriented parallel to each other, but separated by a horizontal distance of 8 cm, in order to obtain a relative measurement of fluctuations in radiant energy present at any given time during the drop test.

A shearing interferometer (Fig. 2) was developed for flow imaging in the drop tower, since the gases tested are transparent at visible wavelengths. A great deal of attention was given to its sensitivity as well as its ruggedness so that in the future, quantitative measurements as well as qualitative information may be obtained.



## Radiative Media

The test gases were chosen based on their radiative properties.  $\text{SF}_6$  and  $\text{CO}_2$  were used in the bulk of the tests to represent strongly radiating gases. Although  $\text{SF}_6$  has the smallest  $I_p$  and the most rapid decrease in  $I_p$  as  $T$  increases, initial drop tests performed with  $\text{CO}_2$  also showed considerable radiatively-driven flow.  $\text{N}_2$ , a nonradiating medium, was utilized to determine if any flow would be encountered in the absence of radiative effects.

## RESULTS AND DISCUSSION

At higher pressures and temperatures, flows were observed in  $\text{SF}_6$  that did not appear to be a residual of the buoyancy-induced flow present prior to the drop tests. Drop tests performed with high pressure  $\text{CO}_2$  also produced significant flow. The tests with  $\text{N}_2$  did not produce any visual indication of the presence of fluid motion other than the decay of the buoyant flow present before the drop. Since  $\text{N}_2$  is not a radiating gas, this is in accordance with the proposal outlined above.

Figure 3 shows an interferometer image of the flow in  $\text{SF}_6$  at 2 atm taken near the end of the drop test. The large deformation of the fringes in the right half of the frame denote a sharp density gradient and the presence of flow. This is the most likely time frame for a radiatively-driven flow to materialize, since the estimated time scale for the onset of radiation at microgravity ranges from .5-5 seconds.

Although the  $\text{CO}_2$  did not exhibit as much flow as  $\text{SF}_6$ , tests conducted at pressures above 2 atm. revealed a significant amount of fluid motion. In fact,  $\text{CO}_2$  tests and  $\text{N}_2$  tests performed at the same Grashof number were noticeably different. Figures 4 and 5 show interferometer images from  $\text{CO}_2$  and  $\text{N}_2$  drop tests, respectively, taken near the end of the drop. The  $\text{CO}_2$  image shows several regions where fringe deformation is significant, while in the  $\text{N}_2$  test only minimal fringe deformation is observed. It is significant that even though the earth-gravity Grashof numbers are nearly the same for these two cases, in the  $\text{CO}_2$  case the flow persists throughout the drop whereas in  $\text{N}_2$  the flow is steadily decaying, indicating that in the  $\text{CO}_2$ , radiatively-induced flow dominates.

## CONCLUDING REMARKS

Additional drop tests are being performed at NASA-Lewis in order to further isolate and eventually quantify the flows. In particular, we intend to measure the spectra of the temperature and radiative flux fluctuations and compare these to theoretical predictions from the astrophysical literature. The NASA-Lewis drop tower only provides 2.2 seconds of microgravity, so the long-term behavior of these radiatively-driven flows is unknown. The short time duration also prohibits the complete decay of the residual effects of buoyant flow at one-g. The interferometer images indicate that more microgravity time is needed to fully characterize and understand the phenomena of radiation-driven flows.

## ACKNOWLEDGMENTS

We gratefully acknowledge the support of the staff at the 2.2 second drop tower at NASA-Lewis Research Center.

## REFERENCES

1. Lozinski, D., Buckmaster, J. D., Ronney, P. D.: Absolute flammability limits and flame balls in optically thick mixtures. *Combustion and Flame* 97, 301 (1994).
2. Field, G. B.: Thermal instability. *Astrophys. J.* 142, 531 (1965).
3. Balbus, S. A.: Local dynamic thermal instability. *Astrophys. J.* 303, L79 (1986).
4. Karpen, J. T., Picone, J. M., Dahlberg, R. B.: Nonlinear thermal instability in the solar transition region. *Astrophys. J.* 324, 590 (1988).

## PUBLICATIONS/PRESENTATIONS:

- Liu, J. B., Ronney, P. D., "Robust Interferometer System for Drop Tower Experiments," SPIE International Symposium on Optical Science, Engineering, and Instrumentation, July 9-14, 1995, San Diego, CA.
- Fortmeyer, J. M. and Ronney, P. D., "Radiatively-Driven Flow in Gases," 48th Annual Meeting, Division of Fluid Dynamics, American Physical Society, Irvine, CA, November 19-21, 1995.

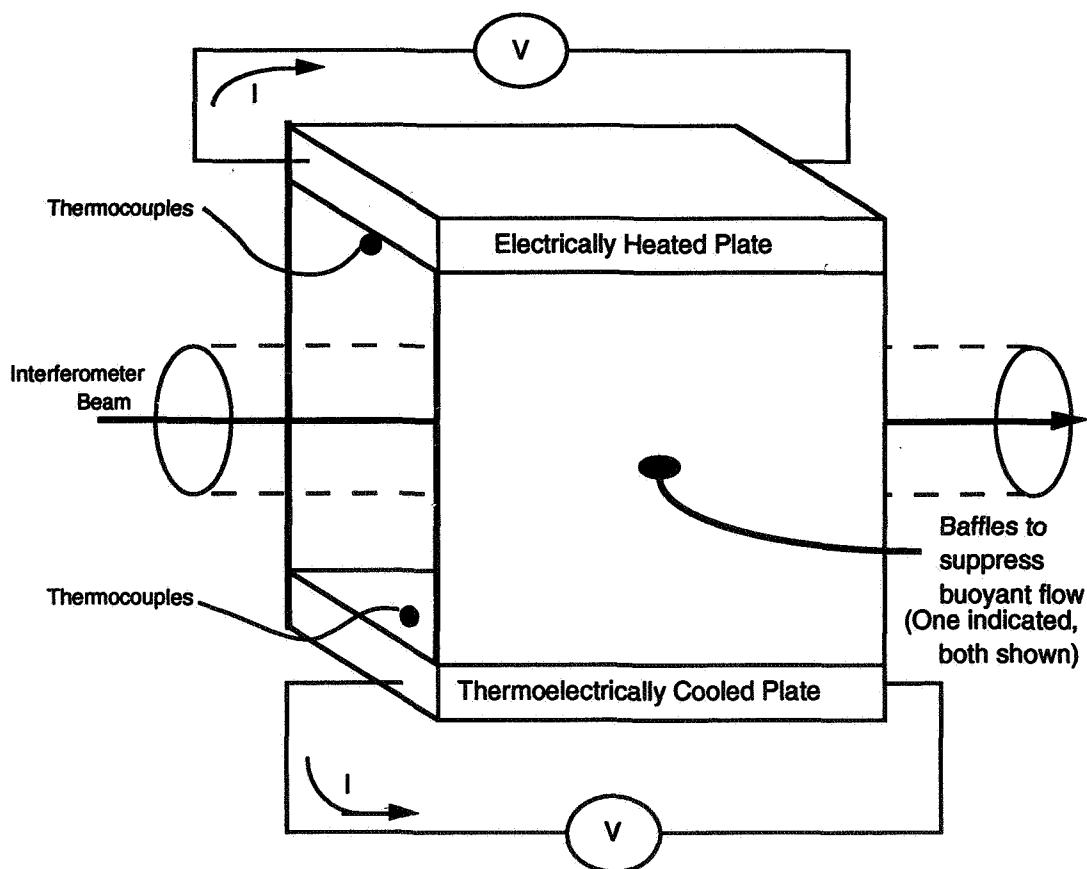


Figure 1. Test apparatus block diagram (expanded in vertical direction for clarity).

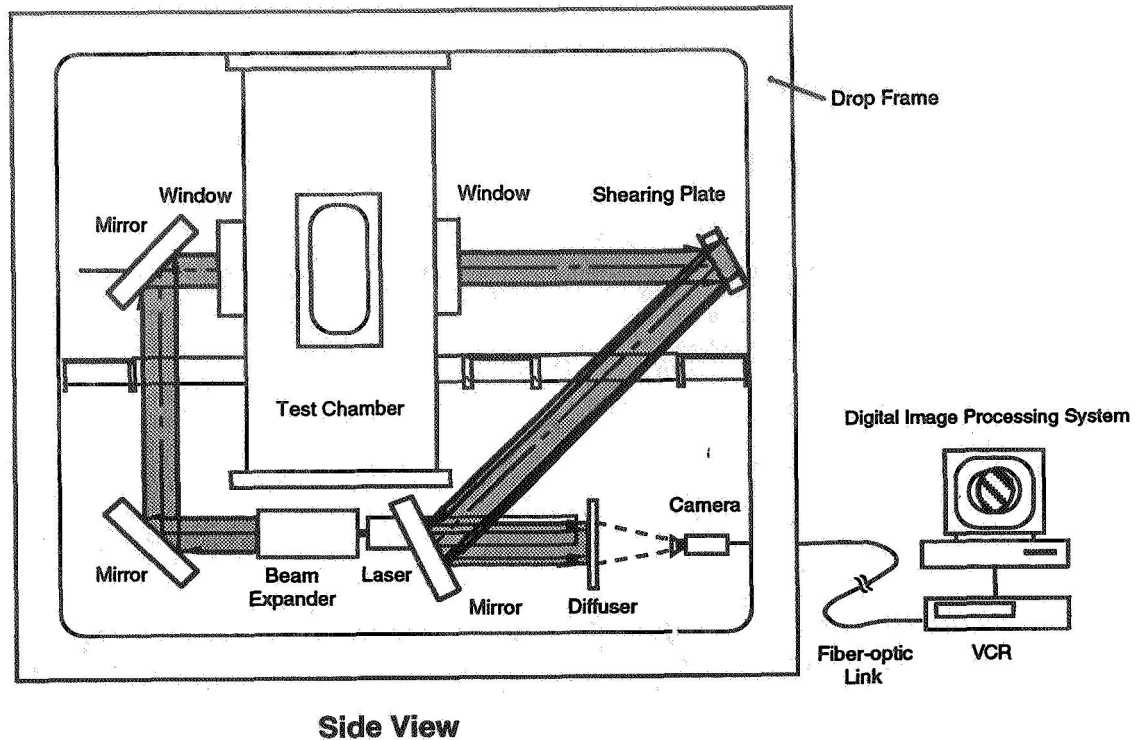


Figure 2. Interferometer and drop frame block diagram.

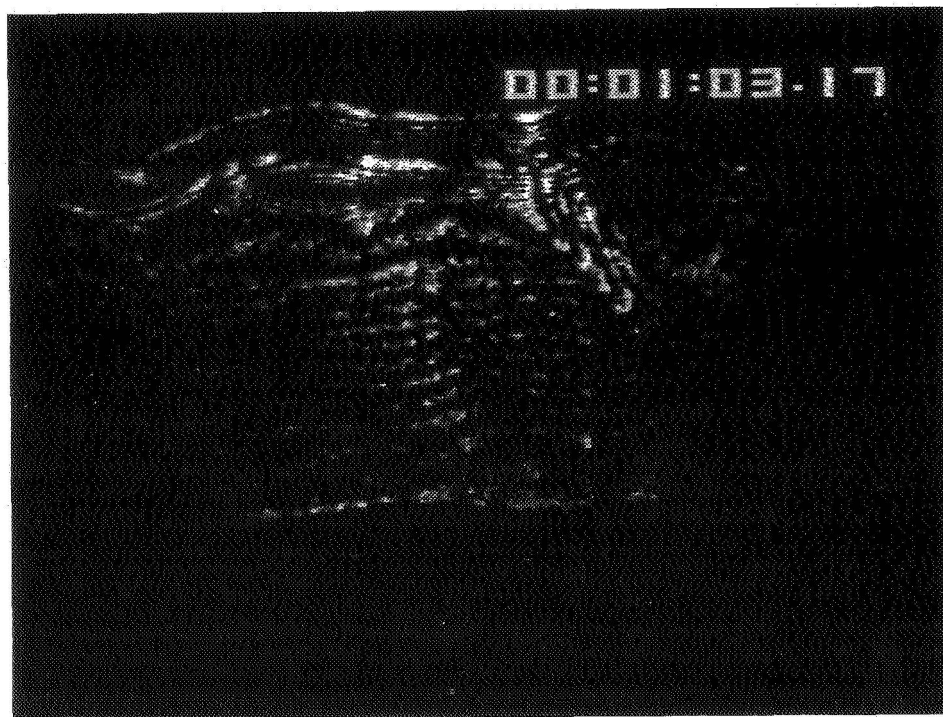


Figure 3. Interferometer image of radiation-driven flow at  $\mu\text{g}$  taken near end of drop period. Gas:  $\text{SF}_6$ ; pressure: 2 atm; plate spacing: 2 cm;  $\Delta T=105\text{K}$ . Note strong fringe deformation in fringes in upper right of image indicating density gradient. Fringes are parallel lines when no flow is present.

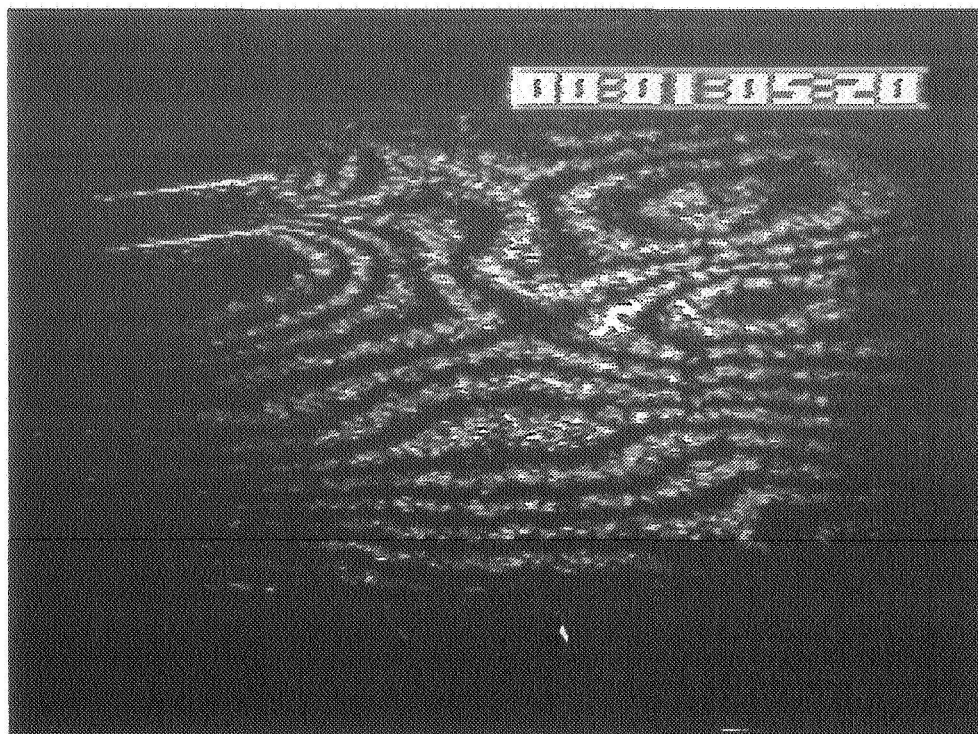


Figure 4. Interferometer image of radiation-driven flow at  $\mu\text{g}$  taken near end of drop period. Gas:  $\text{CO}_2$ ; pressure: 3.2 atm; plate spacing: 2 cm; Grashof number at earth gravity:  $1.4 \times 10^6$ .

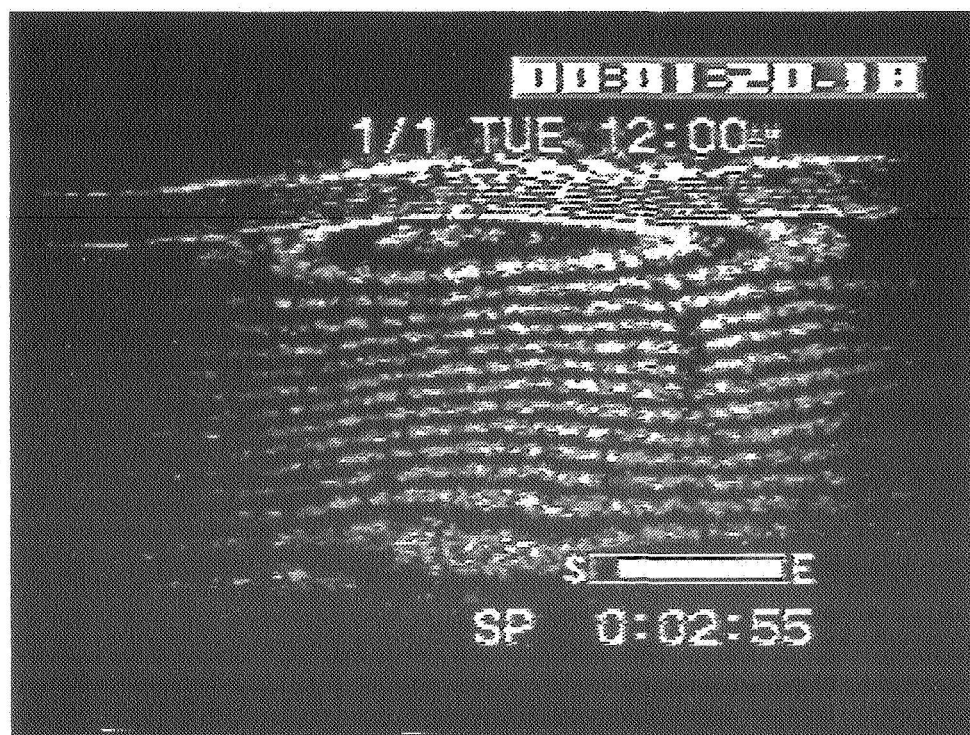


Figure 5. Interferometer image of decaying buoyant flow at  $\mu\text{g}$  taken near end of drop period. Gas:  $\text{N}_2$ ; pressure: 4.6 atm; plate spacing: 2 cm. Grashof number at earth gravity:  $9.2 \times 10^5$ .

## ACOUSTIC STREAMING AND HEAT AND MASS TRANSFER ENHANCEMENT

E.H. Trinh<sup>1</sup> and A. Gopinath<sup>2</sup>

<sup>1</sup>Jet Propulsion Laboratory  
California Institute of Technology  
and

<sup>2</sup>Naval Post-Graduate School

### ABSTRACT

A second order effect associated with high intensity sound field, acoustic streaming has been historically investigated to gain a fundamental understanding of its controlling mechanisms and to apply it to practical aspects of heat and mass transfer enhancement. The objectives of this new research project are to utilize a unique experimental technique implementing ultrasonic standing waves in closed cavities to study the details of the generation of the steady-state convective streaming flows and of their interaction with the boundary of ultrasonically levitated near-spherical solid objects. The goals are to further extend the existing theoretical studies of streaming flows and sample interactions to higher streaming Reynolds number values, for larger sample size relative to the wavelength, and for a Prandtl and Nusselt numbers parameter range characteristic of both gaseous and liquid host media. Experimental studies will be conducted in support to the theoretical developments, and the crucial impact of microgravity will be to allow the neglect of natural thermal buoyancy. The direct application to heat and mass transfer in the absence of gravity will be emphasized in order to investigate a space-based experiment, but both existing and novel ground-based scientific and technological relevance will also be pursued.

### I. INTRODUCTION

The active control of the rates of heat and mass transfer in non-isothermal systems is often a desired capability associated with many industrial and technological practices. In general, this is accomplished by varying the interfacial area and by inducing appropriate flow fields in the medium through which transport takes place. For example, the control of gas and melt flow rates, atomizing gas pressure, initial melt temperature, and host medium conductivity are used to change the quenching rate in gas atomization processes of powder metallurgy. In the case of multi-component or multi-phase disperse systems dealing with direct contact heat transfer, distillation, or liquid extraction, some enhancement of transport or reaction rates has been obtained through the use of electric fields which induce drop oscillations as well as internal flow within the fluid particle. Thus, even for Earth-bound activities for which natural convection is often important, the control of *flow fields* in the vicinity of the contact interfaces is of significant practical value.

In a low gravity environment, the drastic reduction of natural buoyancy will make the contribution from any externally imposed flow field even more important. For example, heat transfer processes involving change of phase (such as boiling) are drastically affected by the elimination of buoyancy-driven removal of vapor bubbles. In the *absence* of artificially induced flows, heat or mass transfer in microgravity is expected to be dominated by radiation, conduction, or diffusion processes. A minor contribution may also come from thermocapillary flows (Marangoni convection) in the case of free liquid-gas interfaces. In currently utilized manned spacecraft, however, another source of *steady-state or time-varying convective flows* arises from the residual fluctuating acceleration background (the so-called "g-jitters"). The appearance of *steady-state* flows have been predicted, and under certain conditions involving a range of values for the Prandtl number, the vibration frequency, and for a large enough Rayleigh number, these flows could significantly impact heat transport processes (Kamotani, Prasad, and Ostrach (1981)<sup>1</sup> and Farooq and Homsy (1994)<sup>2</sup>).

Although the frequencies associated with the microgravity g-jitters are centered around relatively low values (0.1 to 10 Hz), the physical mechanism responsible for the creation of the steady convective flows is very similar to the case of higher frequency *acoustic streaming*. In both situations, time-varying Reynolds stresses generate vorticity in a thin Stokes boundary layer at the interface between the fluid and an object. As a result, a thicker steady-state flow boundary layer is generated. In both situations, the resulting convective velocity at the edge of this steady-state flow layer induces steady fluid motion which is

propagated into the *bulk* of the fluid medium. There is a difference, however, in the characteristics of the steady-state flow outside the Stokes boundary layer in the two cases: for acoustic streaming this flow remains irrotational, while it is rotational in the case of a fluctuating gravitational field (g-jitter driven). In the latter situation, the time-varying body force (buoyancy) responsible for the flow is not conservative but is rotational, and the steady-state convective flow *outside* the Stokes layer is *directly* driven by the Reynolds stresses (Amin (1988)<sup>3</sup>). This difference, however, does not affect the impact of the steady-state convective flows on the heat and mass transport properties, and to a large extent, information gathered by studying acoustic streaming will be relevant to the case of a time-varying gravitational acceleration.

Acoustic streaming-induced convective flows have also been shown to substantially enhance heat and mass transfer, even under the full action of the Earth gravitational field. A detailed understanding of this effect is not yet available, however, because *natural convection* interferes with accurate heat and mass transport measurements under most experimental conditions found in Earth-based laboratories. The exception might be found at very high acoustic pressure at which stage the second order streaming flow becomes turbulent and theoretical analysis is even more complicated. We plan to carry out a ground-based research program to experimentally and theoretically examine both the configuration and stability of acoustically induced streaming flows in order to advance the understanding of the physical mechanisms responsible for their generation, and to develop a predictive model for the observed enhancement in the rates of heat and mass exchange. The capability to virtually eliminate steady natural convection in microgravity will be examined to assess the possibility of performing experimental measurements that are not possible on Earth, but that could impact the understanding of both Earth-based and microgravity problems. We thus believe that the problem of controlling heat and mass transfer through induced external flow is important to technological applications both on Earth and in microgravity, that acoustic streaming-modulated transport processes are of current scientific interest, and that this phenomenon could be better understood by carrying out microgravity studies. Further, we think that the similarity between acoustically and g-jitters-induced streaming is significant enough to be useful in the investigation of the microgravity streaming problem. The specific objectives are:

- (1) To quantitatively characterize the acoustically-induced flows and thermal fields in fluid-filled enclosures and around freely suspended (levitated) spherical particles which are at the same as well as at higher temperature than the surroundings. Of particular interest are the causes and conditions for the onset of instability of these flow fields in 1 G and in low gravity.
- (2) To measure the effects of these flows on the *rate of heat transfer* in 1 G as well as in reduced gravity using *finite-size* enclosures.
- (3) To compare the experimental results with an *analytical and numerical model* developed for the case of zero gravity.
- (4) To assess the validity and desirability of potential *long duration* microgravity investigations to gain new information in a parameter range not accessible to Earth-based experiments.

These studies will be carried out for finite Prandtl numbers ( $0.1 < \text{Pr} < 10$ ) to cover the cases of gaseous and liquid host media, for a range of streaming Reynolds number,  $R_s$ , typical of currently relevant systems ( $1 < R_s < 10,000$ ), and for Grashof numbers ranging between 0 (zero G or isothermal system) and values reflecting temperature differences up to  $500^\circ \text{C}$  in gas and liquid media in 1 G. The range of the Peclet ( $\text{Pe} = R_s \text{Pr}$ ) and of the Rayleigh ( $\text{Ra} = \text{Pr} \cdot \text{Gr}$ ) will be determined by the other non-dimensional numbers listed above. Radiative effects will be experimentally assessed, but not theoretically modeled as the temperature will be restricted to moderate values ( $T < 500^\circ \text{C}$ ). The heat transfer measurement approach will involve the usual correlation between the Nusselt ( $\text{Nu}$ ) and Reynolds and Prandtl numbers, i.e.  $\text{Nu} = F(R_s) \cdot G(\text{Pr})$ , where  $F$  and  $G$  are functions to be determined.

## II. SPECIFIC OBJECTIVES AND IMPLEMENTATION

In general, for the problem of streaming and heat transfer from an *isolated spherical or cylindrical object immersed in an infinite fluid medium*, the analytical solution of the complete set of equations for a wide range of the relevant non dimensional numbers is not possible. Even if it was



available, a single solution would not be valid over the entire space because of the existence of viscous and thermal boundary layers. Matched asymptotic expansion methods using the non-dimensionalized amplitude( $\epsilon$ ) of the acoustic wave as expansion parameter have been used, and solutions have been obtained for the problem of the heat transfer from spherical and cylindrical objects in limited ranges and under certain limiting values of the characteristic Reynolds ( $Re_s = U_s^2 / \omega \nu$ , where  $U_s$  is the characteristic streaming velocity,  $\omega$  is the acoustic angular frequency, and  $\nu$  is the fluid medium kinematic viscosity), Prandtl (Pr), Grashof (Gr), and Strouhal ( $S=1/\epsilon$ ) numbers. This expansion approach allows the general equations of motion to be decomposed into a set of independent linear and nonlinear equations of increasing order in the parameter  $\epsilon$  (Riley (1965)<sup>4</sup>, Davidson (1973)<sup>6</sup>, Amin (1988)<sup>3</sup>).

The fundamental assumption at the basis of all the approaches based on series expansions of the stream function and temperature field around a heated sample in a streaming flow field is invalid in the case of higher amplitude time-varying fluctuations found in high intensity sound fields. Such high levels are encountered in ground-based ultrasonic levitation of liquid and solid samples at ambient and high temperature. The steady streaming velocity reaches very high values, and neither the flow or thermal fields can be described by available theories. Experimental evidence (Trinh and Robey (1995)<sup>5</sup>) shows the appearance of new configurations and instabilities in the flow fields which are not theoretically predicted. In addition, real physical systems are characterized by *finite dimensions and large temperature differences* which cannot yet be simulated by theories that assume a fluid medium of infinite extent, no attenuation, and small differences in temperature in order to preserve the Boussinesq approximation, and to avoid the complications of a high temperature theory.

Time-independent streaming is one of the nonlinear effects associated with the propagation of high intensity acoustic waves in a fluid medium. This *steady* flow generated by a sound field has been extensively analyzed by Nyborg and other modern researchers (Nyborg (1965)<sup>7</sup>, Zarembo (1971)<sup>8</sup>, Lighthill (1978)<sup>9</sup>), but Rayleigh was once again an early investigator of this phenomenon (Rayleigh (1896)<sup>10</sup>). As a result, the principal physical mechanisms responsible for the generation of the flows have been identified, and a fairly good general understanding has been obtained. Streaming flows are generally divided into two separate classes: in the first category they are generated in a free acoustic plane wave propagating into the bulk of a fluid medium, sometimes called volume streaming or "Quartz wind" (Eckardt (1948)<sup>11</sup>), and in the other category they arise because of the interaction of the sound wave with boundary walls or objects in its path. In this research project we are mostly concerned with the streaming flows in the second category, and we concentrate on the streaming fields due to standing acoustic waves inside *enclosures of finite dimensions*, and on the flows induced around single spherical samples suspended at the velocity antinodes.

## 1. EXPERIMENTAL OBJECTIVES

(1) Isothermal streaming around a freely suspended solid sphere. Quantitative and qualitative flow field measurement will be carried out in order to establish a baseline condition. The orientation of the cell will be changed from parallel, to perpendicular, and to anti-parallel to the gravity vector in order to filter out any gravitational bias. Quantitative velocity measurements will be performed using PIV for low sound pressure levels. The flow fields should be very similar to those shown in figure 1. The position of the attached eddies will be above or below the sample equator depending upon the velocity direction of the outer primary streaming. The measurements will be carried out for increasing sound pressure level (or Reynolds number  $Re_s$ ) in order to record the evolution of the attached eddies. The uniform temperature condition will be established by enclosing the test chamber in a temperature controlled environment. Air (Pr=0.7), water (Pr=7), and silicone oil (Pr=5) will be initially selected because they have been well characterized in the past and they will also allow a range in the streaming Reynolds number  $Re_s$ . The size of the sample will range between 0.1 and 0.5 cm in radius. This is translated into  $k_{ac} \cdot R$  parameter between 0.4 to 0.9 (where  $k_{ac}$  is the acoustic wave number).

(2) Streaming around a heated spherical sample. Flow field mapping will first be carried out for varying Grashof number ( $Gr = g D^3 \beta (\Delta T) / \nu^2$ , where  $g$  is the gravitational acceleration,  $\beta$  is the thermal expansion coefficient,  $\nu$  the fluid kinematic viscosity, and  $D$  is the sphere diameter), or Rayleigh number since  $Ra = Gr \cdot Pr$ . The mapping of the stability regions of the various flow configurations will be done in the parameter space involving the streaming Reynolds number, the Rayleigh number, and to a limited extent

the Prandtl number. This will cover the three cases of sound field orientation with respect to the Earth-based gravitation acceleration vector: parallel, normal, and anti-parallel.

Short duration low-gravity tests will also be performed aboard NASA airplanes flying parabolic trajectories. This will provide 15 to 20 seconds of 0.01 to 0.05 G steady background acceleration with varying amount of transient acceleration superposed. This noisy acceleration background does not allow extensive quantitative measurements, but it provides both qualitative results as well as a test bed for low-gravity experimental techniques development.

Heat transfer measurements will be carried out for spot-heated, stably held samples in different locations in the ultrasonic standing wave in air. Once again, the measurements will be carried out as a function of the streaming Reynolds number (which carries information on the sound pressure level), and of the Grashof number (which involves  $\Delta T$ ). The Nusselt number ( $Nu = Q / kD\Delta T$ , where  $Q$  is the total energy transferred, and  $k$  is the thermal conductivity of the fluid) will be measured, and a correlation in the form  $Nu = F(Pr) \cdot (R_s)^{1/2}$  (where  $F(Pr)$  is a function of the Prandtl number) will be sought. Earth-based measurements will be carried out in detail, and short-duration low-gravity measurements will be attempted. Another, more standard correlation between the Nusselt and Grashof number  $Nu = G(Gr)$  will be investigated for fixed streaming Reynolds numbers.

(3) Steady and oscillatory streaming flows in closed cavities. The stability of streaming flow fields in empty chambers will also be investigated by flow visualization methods in isothermal and non-isothermal systems. Earth-based experiments will investigate the coupling between the natural buoyancy-driven motion with the acoustically driven flows in *air* and in the  $Ra-R_s$  parameter space, and low gravity tests will reveal the most glaring flow field differences. Amplitude modulation of the ultrasonic field can be precisely controlled, and the investigation of the frequency response of such a system to singly and multiply periodic excitation will be initiated. Once again, the construction of a bifurcation diagram to represent the various stability regions and transition points will be attempted. Similar experiments will be also initiated for liquid-filled cavities similarly driven through ultrasonic standing waves.

## 2. THEORETICAL OBJECTIVES

(1) Superposition of an axisymmetric steady convection on the streaming flow around an isolated spherical sample in a uniform temperature cavity.

Earlier analyses using higher order boundary-layer theory was used by Riley (1975)<sup>12</sup> to study the streaming problem around a cylinder, and later extended to the case of a sphere in a non homogeneous pulsating sound field (1980)<sup>13</sup> will be further modified by including a superposed uniform convective flow field of the type observed at ultrasonic frequency and in a closed cavity (see figure 1). Axisymmetric configuration and isothermal conditions will be used, and this additional imposed flow field will be modeled as a large scale vortex flow with appropriate boundary conditions away from the sample. In the vicinity of the sample, the flow is nearly one-dimensional with a weak shear component due to the gradient along the radial direction. Under these circumstances standard techniques used in sound propagation in moving media can be applied.

(2) Superposition of streaming flow solution to the free convection problem.

A numerical treatment of the free convection boundary-layer problem around a heated sphere for large Grashof number was authored by Pötter and Riley (1980)<sup>14</sup>. Essential characteristics of the plume around the sphere were reproduced, and a reasonable agreement with experimental results was observed. Two simple extension to this analysis can be envisioned: a steady convective circulation opposite to, or in the same sense as the natural buoyancy flow can be added as a background, or the case of an oscillating heated sphere can be treated. In both cases, major characteristics of the realistic streaming problem can be simulated and flow fields predicted, at least within the boundary layer approximation.

(3) Extension of the theory for the heat transfer from heated sphere due to acoustic streaming.

Gopinath and Mills (1993)<sup>15</sup> have presented an analytical and numerical treatment of the problem of acoustic streaming and heat transfer from a free sphere under the assumption of small and large Reynolds numbers and for small values of the  $k_{ac} \cdot R$  parameter. Additional restrictions were small  $\Delta T$  and the absence



of free convection. Under these circumstances, the experimental validation of the theoretical predictions remains problematic, but it could be attempted by performing initial short-duration low-gravity measurements with very small levitated samples. In order to extend the applicability of this work, however, a simplistic approach will be to try to extend this approach by relaxing the constraint  $R_s \gg 1$  and by extending the approximation to larger values for  $k_{ac}R$ .

### 3. EXPERIMENTAL APPROACH

A previously used ultrasonic standing-wave experimental apparatus used between 20 and 40 kHz and with air as a host fluid<sup>21</sup> will be adapted to this proposed research. Standard flow visualization methods using smoke tracers and laser sheet illumination has been shown to be very effective for this specific frequency range and for spherical samples between 0.1 and 1 cm in diameter. For streaming Reynolds number in the lower range ( $R_s < 50$ ) full field Particle Image Velocimetry techniques<sup>16,17</sup> can provide quantitative measurements of the particles velocities. A correction factor will be empirically derived to account for the inertia of the smoke particles. This correction will be very small because of the small size of the smoke particles used in air, but could become non-negligible for other tracer particles used in a liquid host. A schematic description is given in figure 2

The test chamber will be thermally controlled and the tracer particles will not react with the host liquid. The injected smoke for flow visualization in air will be cooled to ambient cell temperature prior to injection into the standing wave region. The temperature of the suspended sample will be measured using an IR thermal imaging camera with reference calibration. The crucial thermal measurements are really concerned with temperature changes due to the effects of streaming, and are less sensitive to absolute temperature measurement accuracy. A resolution of 0.01 °C in temperature is judged adequate for the heat transfer measurement considered. For a levitated sample, the heat transfer is strictly through the fluid phase, while in the case of mechanically suspended samples, we must consider conduction heat loss through the suspending thin wires. Radiation heat transfer will be evaluated for the higher temperature range measurements by using samples with well characterized emittance as a function of temperature.

Levitated samples will be heated by a focused laser source which must be calibrated. The energy absorbed by the sample will be calculated by using temperature dependent optical absorptance values at the relevant incident wavelength. Holographic interferometry methods previously developed and used at lower acoustic frequencies<sup>18</sup> will also be implemented to map the thermal field around the free samples. Both ultrasonic and electrostatic levitation of spherical samples will be used to allow the free suspension of heated as well as unheated spheres. The addition of electrostatic levitation requires the presence of free charges and an electric field, but it allows the investigation of streaming flow fields around a free sample at very low streaming Reynolds numbers. The levitation of the sample through ultrasonic means alone would require a minimum sound intensity which would already lead to a very high Reynolds number.

### REFERENCES

1. Y. Kamotani, A. Prasad, and S. Ostrach, "Thermal convection in an enclosure due to vibration aboard spacecrafts", *AIAA Journal* **19**, 511 (1981)
2. A. Farooq and G.M. Homsy, "Streaming flows during g-jitter-induced convection", *J. Fluid Mech.* **271**, 351 (1994)
3. N. Amin, "The effect of g-jitter on heat transfer", *Proc. Roy. Soc. Lond. A* **419**, 151 (1988)
4. N. Riley, "Oscillating viscous flows", *Mathematika* **12**, 161 (1965) and N. Riley, "Oscillating viscous flows. Review and extension", *J. Inst. Maths. & Applys.* **3**, 419 (1967)
5. E.H. Trinh and J.L. Robey, "Experimental study of streaming flows associated with ultrasonic levitators", *Phys. Fluids* **6**, 3567 (1994)
6. B.J. Davidson, "Heat transfer from a vibrating circular cylinder". *Int. J. Heat Mass transfer*, **16**, 1703 (1973)
7. W.L.M. Nyborg, "Acoustic Streaming", in *Physical Acoustics*, W. P. Mason Editor, vol. II part B, 265 (1965)
8. L.K. Zarembo, "Acoustic Streaming" in *High Intensity Ultrasonic Fields*, L.D. Rozenberg Editor, Pt. III, 137-199 (1971)
9. J. Lighthill, "Acoustic Streaming", *J. Sound Vib.* **61**, 391 (1978)

10. Lord Raleigh, *Theory of Sound*, Vol. 2, Dover Publications (1945)
11. C. Eckardt, "Vortices and streams caused by sound waves", *Phys. Rev.* 73, 68 (1948)
12. N. Riley, "The steady streaming induced by a vibrating cylinder", *J. Fluid Mech.* 68, 801 (1975)
13. N. Amin and N. Riley, "Streaming from a sphere due to a pulsating source", *J. Fluid Mech.* 210, 459, (1990)
14. J. Potter and N. Riley, "Free convection from a heated sphere at large Grashof number", *J. Fluid Mech.* 100, 769 (1980)
15. A. Gopinath and A.F. Mills, "Convective heat transfer from a sphere due to acoustic streaming", *J. Heat Transfer*, 115, 332 (1993)
16. C.E. Willert and M. Gharib, "Three-dimensional particle imaging with a single camera", *Expt. Fluids* 12, 353 (1992)
17. D. Dabiri and M. Gharib, "Digital particle image thermometry: The method and implementation", *Expt. Fluids* 11, 77 (1991)
18. E. Leung, E. Baroth, C. K. Chan, and T.G. Wang "Thermal Acoustic interaction and flow phenomena", *AIP Conference Proceedings* 197, T.G. Wang Editor, Am. Institute of Physics (NY) (1988)

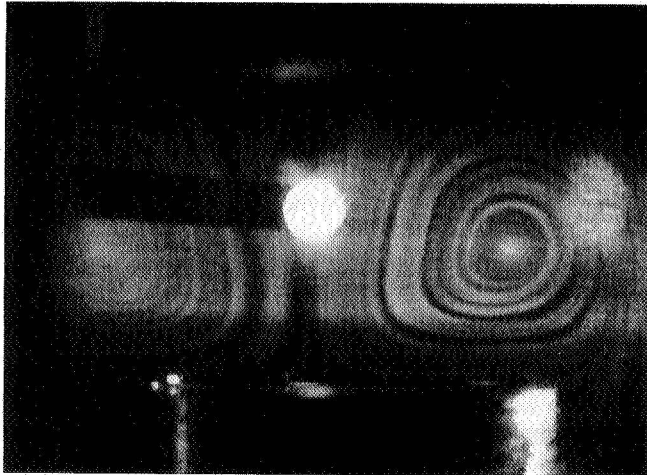


Figure 1

Photograph of streaming flow field in a closed cavity around a levitated sample

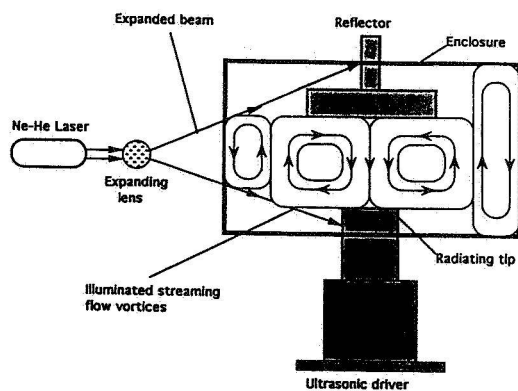


Figure 2

Schematic description of a basic experimental apparatus

# CURRENT RESULTS AND PROPOSED ACTIVITIES IN MICROGRAVITY FLUID DYNAMICS

V.I. Polezhaev  
Russian Academy of Sci.  
Institute for Problems in Mechanics,  
Prospect Vernadskogo 101, Moscow, 117526, Russia

## ABSTRACT

Overview of the results in microgravity fluid dynamics during last two years with a goal to discuss the problems, which may be of interest for the International cooperation is done.

## INTRODUCTION

The Institute for Problems in Mechanics RAS is the main Institute in Mechanics in Russian Academy of Sci. It includes departments of classical mechanics (analytical mechanics, gyroscopes, navigation, optimal control and robots) as well as solid state mechanics (elasticity and deformation, shell's oscillations, lubrication etc.) and fluid mechanics, including combustion, plasma and laser gasdynamics.

Laboratory of the mathematical and physical modelling in fluid mechanics of this Institute develops models, methods and software for analysis of fluid flow, instability analysis, direct numerical modelling and semi empirical models of turbulence as well as experimental research and verification of the models and applications in technological fluid dynamics, microgravity fluid mechanics, geophysics and a number of engineering problems.

This paper presents overview of the results in microgravity fluid dynamics during last two years since 2nd Microgravity Fluid Physics Conference (June, 1994, Cleveland) and 1st International Aerospace Congress (August, 1994, Moscow), which enhanced International cooperation in Microgravity in Russia. Nonlinear problems of weakly compressible and compressible fluid flows are discussed. Scientific basis of this research is contained in the books [1,2].

## THERMAL/DYNAMICAL ACTIONS FOR CONTROL OF CONVECTION DURING CRYSTAL GROWTH

General idea of this work is investigation alternative microgravity possibilities to reduce inhomogeneities in semiconductors that are induced by gravitational or nongravitational types of convection in terrestrial environments [3,4]. Low energetic thermal/dynamical actions for the growth of semiisolating GaAs monocrystals with low density dislocations (thermal waves, steady state and unsteady rotation and/or vibration) are used in modified ground-based Czochralsky techniques with diagnostic of the GaAs monocrystals. Developing of the methods for experimental and theoretical research and comparison the results are presented below.

For measurements of temperature distribution during single crystal growth modification of the system for the temperature field diagnostic was carried out in the Branch of the Institute of Crystallography, Kaluga [5] (Fig.1). The pilot crystal's models manufactured of special ceramics having thermophysical properties similar to those of GaAs were used to make preliminary measurements of temperature distribution in a system investigated. Thermocouples were installed into these pilot models which provided a safe contact between the thermocouples and the object measured. The amplitude-frequency characteristics of thermocouples were determined before-hand which then made it possible to estimate the frequency spectrum of temperature fluctuations in the melt and across the crystal. GaAs single crystals with the diameter of about 80 mm were grown under the same thermal conditions. The growth direction was (001) and the change of the diameter did not exceed 2 mm at pulling rate 2-3 mm/h. Single crystals were grown at constant temperature of the heater.

The experimental investigation was also made concerning the temperature change in subcrystalline region and across the crystal at iso- and counterrotation of the crystal and the crucible with the melt and rotation of the crucible with the melt under acceleration. These actions caused considerable change in the spectrum of temperature fluctuations and were much more sensitive in comparison with the heating control. The described actions and some other ones similar in influencing the process of single crystal growth are classified by as "low energetic" actions because of in that case change in power supplied to the heater was small (not more than 1%) as compared to fixed power.

Mathematical modelling was made, using model of Czochralsky crystal growth which includes hydrodynamics and heat transfer in the crucible on the basis of unsteady Navier-Stokes equations (Boussinesque approach) and a model of a crystal as rotating disc on the melt surface (Fig.2). Special version of PC - based system which is extension of the system "COMGA" was used for this approach. It includes now as a part of Computer laboratory on the basis of this system [6]. Cylindrical crucible radius  $R_c = 7$  cm which filled by GaAs melt to height  $H = 4$  cm and crystal radius  $R_s = 3.8$  cm was considered. The crucible wall temperature was uniform and in general case can be dependent on time. Temperature on the solid/liquid interface was supply as 1511 K and interface between melt and encapsulant is adiabatic. No-slip conditions for radial velocity and free condition for angular velocity are assumed on the LEC interface. The crucible and crystal rotate with constant angular velocities  $w_c = 16$  rpm and  $w_s = -6$  rpm. Prandtl number was assumed as  $Pr = 0.07$ . Using the scale of length for this problem is the crucible radius  $R_c$ , one can obtain nondimensional parameters are Grashof number  $Gr = 7.8 \cdot 10^7$ , crucible Reynolds number  $Re_c = 1.6 \cdot 10^4$  and crystal Reynolds number  $Re_s = 6 \cdot 10^3$ . The calculations were made on nonuniform grid  $75 \times 51$  nodes, stretching to crucible walls and solid/liquid interface (minimum space step was equal to 0.2 mm). The computer code was tested for the problem on thermal convection with low Prandtl number fluid (0.015) for Grashof number -  $1.6 \cdot 10^5$ . Maximum value of stream function was in a good agreement with the results [7] as well as our previous results [1]. The calculation of unsteady problem for constant crucible temperature  $T_c = 1541$  K including thermal convection and rotations of the crucible and the crystal was made. As it was obtained for such values of parameters in previous works (see [1, 5]) the nonregular undamped oscillations of temperature field and motion structure induced by convective instability are observed. Fig 2 illustrates the complex interaction between thermal and force convections (the instantaneous patterns of temperature, rotation moment and stream function are shown). The dependence of the measured (a) and calculated (b) melt temperature in the point near the axis (2 mm below the liquid/solid interface) is given in Fig.3. The oscillations with maximum temperature amplitude till to one degree are good visible. Using described technique the influence of harmonic crucible temperature changing on the amplitude of these oscillations near solid/liquid interface was investigated [5] and analysis of the dynamical actions is in progress.

## ANALYSIS OF NEAR CRITICAL PROCESSES ON THE BASIS OF COMPRESSIBLE FLUID MODEL

The goal of this work is study compressible fluid flow and heat transfer near critical point for quantitative analysis of the microgravity experiments and analysis of gravitation sensitivity for certification of the orbital complexes for near critical experiments in microgravity. Special numerical schemes and computer codes for 1D and 2D approaches are developed on the basis of Navier-Stokes equations for compressible fluid with Van der Waals thermodynamics state equation [8]. The results one-dimensional analysis for the problem with rigid wall heating in zero gravity is in well agreement with previous results of B.Zappoli and co-workers, where "piston effect" was calculated on the basis of direct numerical simulation (see [9,10] and cited references).

Fig.4 shows new results for two-dimensional thermoacoustic - dominated regime processes in the earlier stage of "switch on" the heat pulse in zero gravity. Two-dimensional density isolines which will be of interest to registrate in the earlier stage of "switch on" the heat pulse in microgravity in a model of near critical point instrument (see [10] and cited references) with the goal of benchmark mathematical models and analysis of gravitational sensitivity near-critical fluid processes.

The Institute for Problems in Mechanics have presented a proposal and scientific plan for the use of the French instrument "Alice-1" for cooperative investigation in a framework of the plan for analysis of gravitational sensitivity in liquid/gas systems and convective sensor with the Perm University. Instrument "Alice-1" is exist now in the working state aboard "Mir" station and it is property of RKK "Energia", but "know-how" of this instrument is a property of CNES. Program realization of the orbital experiment for near critical  $\text{CO}_2$  and  $\text{SF}_6$  was presented by CNES using ordinary procedure [10]. Experiment was realized 30.09-4.10, 1995 by Russian kosmonavt S.V. Avdeev. Preparation and analysis of the results are in progress. For the use of "Alice-1" instrument as a tool for measurement gravitational sensitivity of compressible liquid/gas systems evolution of the optical pictures to density fields in quantitative form should be done.

### CONVECTIVE INSTABILITY AND SPATIAL STRUCTURE OF CONVECTION IN PARALLELEPIPED

A problem of convective instability and convection structure in boat-type configuration related to macro- and microinhomogeneities of crystals grown from the melts has a long-term history [1-4, 11]. A focus of this part of the work is concentrated on the analysis of spatial structure of thermal gravitational convection in a long parallelepiped with differently heated side boundaries, using both stability analysis technique and direct numerical calculation on the basis of three-dimensional Navier-Stokes equations.

Three dimensional unsteady Navier-Stokes equations (Boussinesque approach) are solved in the form of velocity-pressure variables with governing parameters Grashof, Prandtl numbers and two aspect ratios  $W/H$  and  $L/H$ . An equation for two dimensional basic flow was found, using definition of basic flow in the case of infinite length for a closed flow in rectangle and boundary conditions [12]. It's solution contains Birikh-type basic flow [13] in the limiting case of  $W \gg H$ . Spatial structure of convection in a parallelepiped including basic flow are shown in Fig 5. Dependency of the critical Grashof number on the  $W/H$  using linear stability analysis of the basic flow is correlated with results of direct numerical solution of 3D Navier-Stokes equations for the case of  $Pr=0$ ,  $L/H=20$ ,  $Gr=200000$  (Fig.5B). Velocity field structure in supercritical domain near critical line is shown on the Fig.5C. Strong dependency of the critical Grashof number with reduce of the  $W/H$  shows "geometric" possibility for control of gravitational convection.

### COMPUTER LABORATORY FOR CONVECTION AND HEAT/MASS TRANSFER IN MICROGRAVITY

Computer laboratory is intellectual shell of the system "COMGA", including help in the statement of the problem, benchmark of computer results and multiparametrical analysis of fundamental and applied problems. was recently developed and described in [6]. Pc-based system as a core of computer laboratory contains all tools which need for modelling hydrodynamics, heat/mass transfer processes and collected in personal computer. Each of separate version of the this system occupies memory on one disk and presents a flexible and convenient software tool for modelling of forced, gravity-driven and surface tension-driven thermoconcentrational convection on the basis of Navier-Stokes equations in Boussinesque and Boussinesque-Darcy approach (see detailed references in [6]). This version of the system is based on the two-dimensional (plane or axisymmetrical - with three velocity components) unsteady Navier-Stokes equations. Temporal behavior (rotation, vibration) of body force is taken in account.

Contents of computer laboratory includes forced flows of isothermal liquid, natural gravitational convection, surface tension-driven convection, interaction between different types of convection and applications. Each task can supports of text books on viscous flows and heat transfer or monographs on buoyancy-induced flows and transport or convective stability and applied problems in microgravity and supplied by additional references on experimental and theoretical researches (see references in [6]). Special sign (\*) in the contents of computer laboratory marks problem, solved in previous works, using different kind of methods and software. Other sign

(\*\*) marks problem solved in previous works or renewed using "COMGA" system and sign (\*\*\*) - new problems solved with a help of this system.

Fig.6A-C shows some results of steady-state and unsteady problems of thermal gravitational and thermocapillary convection (vertical layers with side heating for ordinary and porous media and onset of thermal gravitational convection after suddenly bottom heating and thermocapillar convection and instability in floating zone). Fig.6C shows new result of this computer laboratory-benchmark of the flow/temperature structure and oscillations due to convective instability in dependency on Marangoni number and aspect ratio using HP 735 workstation [14]. It is shown that axisymmetrical mode exists for high Pr number and results correlate with experimental data [15] (see references and discussion in [14]).

Special part of the system uses real microaccelerations data measured by means of an accelerometer or calculated in space flight [16].

Computer laboratory should be used also as a tool for education from initial courses of physics (hydrostatics, hydrodynamics and elementary transport processes) for definition and demonstration buoyancy phenomena (stability of hydrostatic equilibrium), laminar flows, boundary layer etc. (see, mini-plan of Computer Laboratory [17]). For special courses in fluid mechanics and heat transfer computer support of elements boundary layer theory, stability and turbulence can be done. For engineering courses on fundamentals of heat transfer theory of heat conductivity can be demonstrated as well as convective heat transfer across layers with demonstration of structure and heat/mass transfer characteristics. A number of mentioned problems of Computer laboratory may be recommended to use for graduated education in microgravity fluid mechanics [6,17].

## CONCLUDING REMARKS

Above mentioned problems as study temperature oscillations in the melts and thermal/dynamical control of crystal growth, analysis of near critical fluid processes, stability and spatial structure of convection in the melts may be potential directions for future projects. Three topics in cooperation of IPMech with other organizations may be add :

1. Microacceleration and gravitational sensitivity analysis on the orbital complexes (with Keldysh Inst. of Applied Math., RKK "Energia", Inst. for Problems in Mech.) [6, 18]
2. Theoretical and experimental study and flight experiment on Microgravity Sensor, proposed on MIR (ISS). (RKK "Energia", Inst. for Problems in Mech. and Perm State University) [6, 19]
3. Education on Microgravity Fluid Mechanics using computer laboratory (Inst. for Problems in Mech. and Perm State University) [6, 17].

## ACKNOWLEDGMENTS

These works were supported partly by NASA (NAS-15-10110), Russian Fond of Fundamental Research (94-01-01551), International Science Foundation (NJE9100), RKK "Energia" and CNES.

## REFERENCES

1. Polezhaev V.I., Bune A.V., Veresub N.A. et al. Mathematical Modelling of convective heat and mass transfer on the basis of Navier-Stokes equations, M., Nauka, 1987, (in Russian).
2. Polezhaev V.I. Bello M.S., Veresub N.A. et al Convective processes in microgravity, M., Nauka, 1991, 240p. (in Russian).

3. Matthiesen D.H., Wargo M.J., Witt A.F. Opportunities for Academic Research in a Low- Gravity Environment : Crystal Growth In : Opportunities for Academic Research in a Low- Gravity Environment : Crystal Growth (Eds. G.A. Hazenrigg, J.M. Reynolds), Progress in Astronautics and Aeronautics, V.108, pp.125-141, AIAA, N.Y.,1986
4. Müller G. Convection and inhomogeneities in crystal growth from the melt. In: Crystals: Growth, Properties and Applications. Berlin, Springer 1988, V.12, 1-133.
5. Kosushkin V.G., Polezhaev V.I., Zakharov B.G. Ground-based experiments and alternatives in GaAs crystal growth. In : Proceedings of the Microgravity Science and Applications Session. International Aerospace Congress, Moscow, (Eds.) R.K.Crouch, V.I. Polezhaev, 1995, p.141-146.
6. Polezhaev V.I., Ermakov M.K., Griaznov V.I. et. al Computer Laboratory on Convective Processes in Microgravity: Concepts, Current Results and Perspective. 46 International Astronautical Congress, IAF-95 J.3.11, October 2-6, 1995, Oslo, Norway.
7. Bottaro A. and Zebib A./Physics of fluids A, 1988, V.31, p.495.
8. Gorbunov A.A. Numerical modelling of the hydrodynamics of a self-gravitating volume of relativic gas, Seminar on numerical methods in heat and mass transfer problems led by V.I.Polezhaev, L.A. Chudov and G.G. Ghushko, Fluid Dynamics Vol.29 No5, 1994, 734.
9. Beysens D. New Critical Phenomena Observed Under Weightlessness In: Materials and Fluids under low gravity, L.Ratke, H.Walter, B. Feurbacher, (Eds.), Proceedings of the IXth European Symposium on Gravity -Dependent Phenomena in Physical Sciences ,Berlin, Germany, 2-5 May, 1995, Lecture Notes in Physics, V.464, Springer-Verlag, 1996, P. 3-25.
10. Zappoli B., Durand-Daub in A. Heat and mass transport in a near super critical fluid// Physics of Fluids. 1994, May.V.6. N 5. P.1929-1936.(American Institute of Physics)
11. Roux B, (Ed.) Numerical simulation of oscillatory convection in low - Pr fluids. Notes on Numerical Fluid Mechanics, 27, Vieweg, 1990, 365 p.
12. Nikitin S.A., Pavlovsky D.S., Polezhaev V.I. Stability and spatial convection structure in a long horisontal layers with side heating, Izv. AN, MZG, 1996, N4, 28-37 (in Russian)
13. Birikh R.V., Termocapillary convection in a horizontal liquid layer, PMM, 1966, 30, 356-361.
14. Griaznov V.I. CFD Simulation of the Oscillatory Floating-Zone convection for high Prandtl numbers. Proceedings of the Microgravity Science and Applications session International Aerospace Congress, Moscow, August 16-17, 1994, NASA/IPMech., Moscow, 1995, pp. 113-117
15. Velten R., Schwabe D and Scharmann A. The periodic instability of thermocapillary convection in cylindrical liquid bridges Phys. Fluids A, v.3, n2, 1991, 267-279

16. Polezhaev V.I. Toward the quantitative analysis and control of convective processes in microgravity. In: Microgravity Quarterly, 1994, vol. 4, N 4, "Highlights of the International Workshop on Non-Gravitational Mechanisms of Convection and Heat/Mass Transfer", p.241-246.
17. M.K. Ermakov, S.A. Nikitin, V.I. Polezhaev. New computer technology using PC-Based system in education of fluid dynamics, heat- and mass transfer. International Conference on Eng. Education, Moscow, May 21-23, 1995
18. Sazonov V.V., Komarov M.M., Belyaev M.Ya. et. al. Evaluation of quasi-state component in acceleration on board the earth artificial satellite. Inst. of Appl. Math., preprint N 45, 1995, pp. 30. (in Russian).
19. G.P. Bogatyryov, G.F. Putin, M.K. Ermakov, S.A. Nikitin et al. A System for Analysis and Measurement of Convection aboard Space Station: Objectives, Mathematical and Ground-Based Modelling, AIAA 95-0890, 33rd Aerospace Sciences Meeting and Exhibit, Jan. 9-12, 1995, Reno, NV.



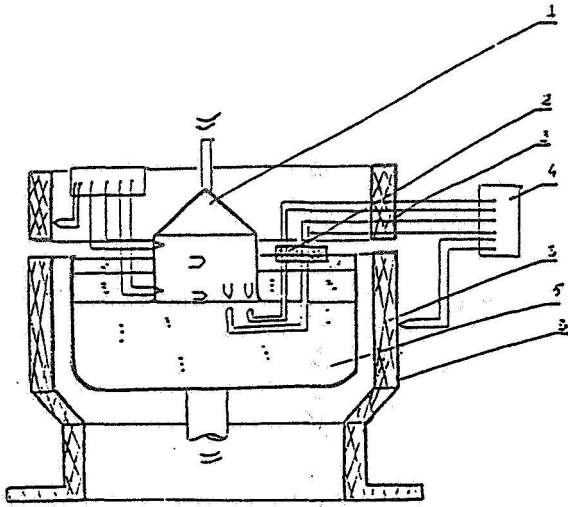


Fig.1 Scheme of the temperature measurements system in a melt and along the crystal  
1 - seed, 2 - float with thermocouples, 3 - heater, 4 - system for temperature measurements and registration, 5 - crucible with a melt

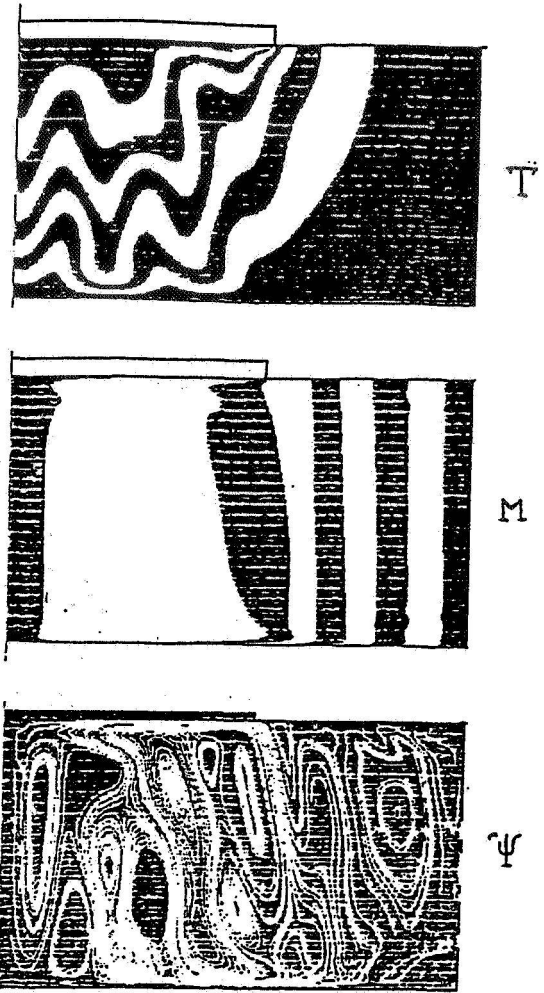


Fig.2 Instantaneous fields of temperature, rotation moment and stream function for thermal convection ( $\Delta T = 30^\circ \text{K}$ ) and rotation of crucible ( $\omega_c = 16 \text{ rpm}$ ) and crystal ( $\omega_s = -6 \text{ rpm}$ )

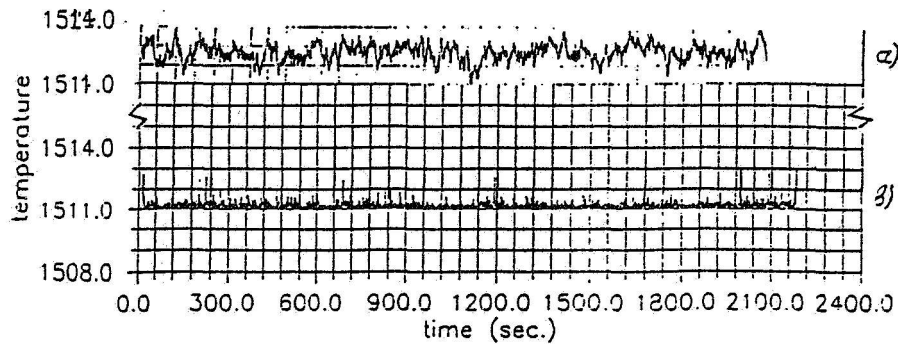
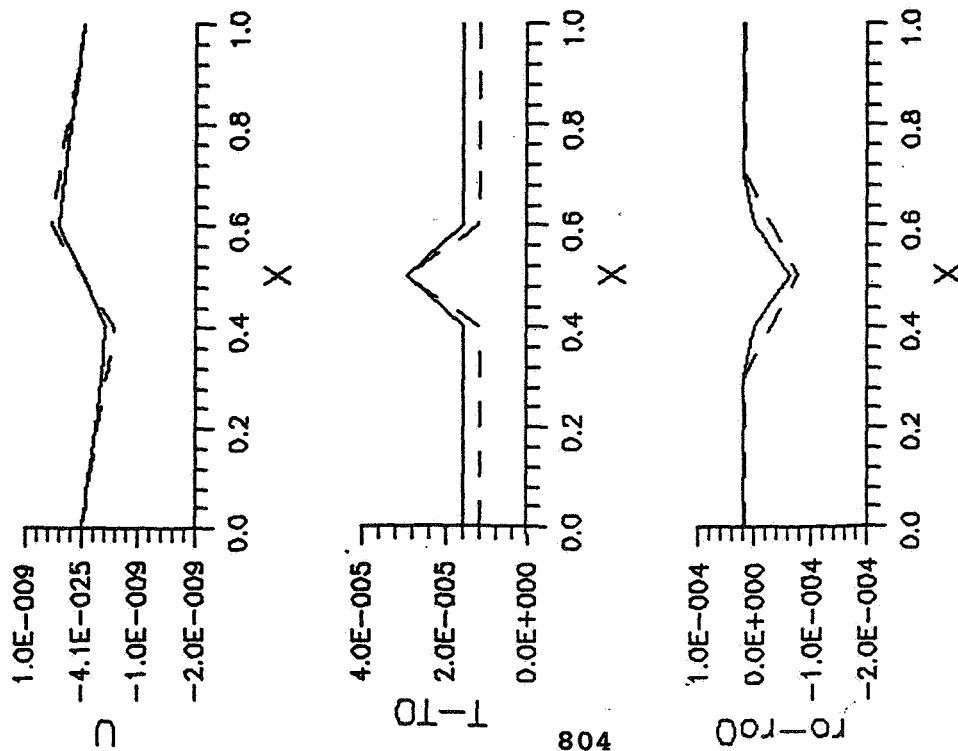
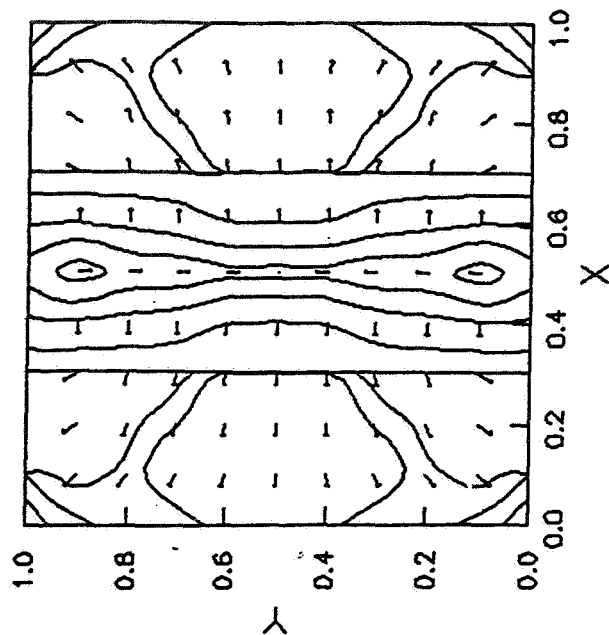


Fig.3 Measurements (a) and calculations (b) of the temperature fluctuations in the melt near axis under constant crucible temperature for a case of thermal convection and rotation of crucible (16 rpm) and crystal (-6 rpm)



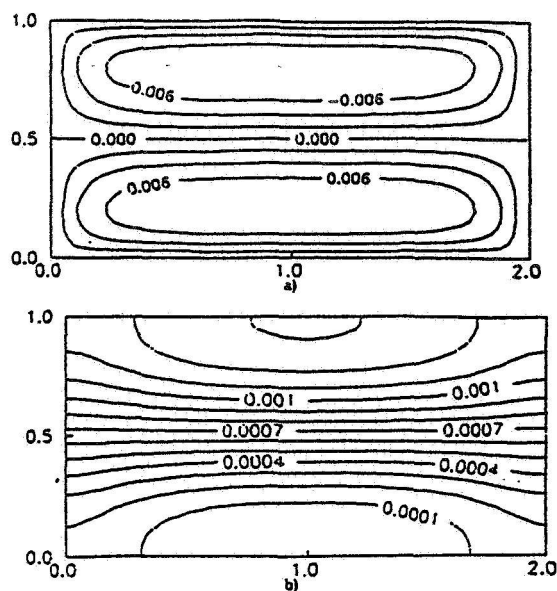
a) Velocity, temperature and density difference profiles in  $y=0.5$  section: - - - - 1D, ——— 2D



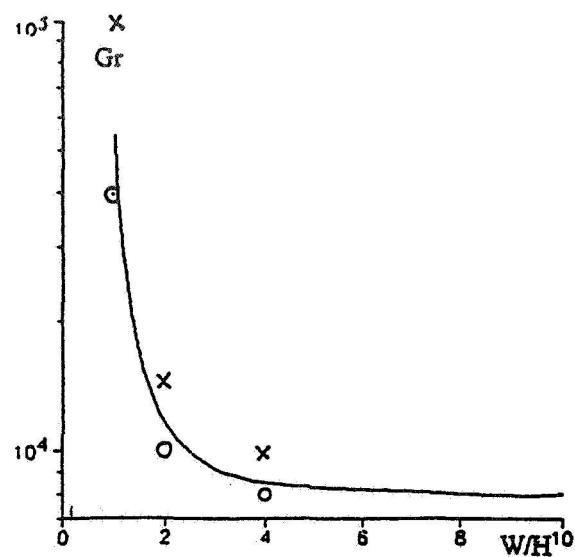
b) Density difference isolines and velocity vector field, 2D model

Fig.4 Thermoacoustic process near critical point after "knife" pulse heating in  $x = 0.5$  crosssection, ( $10^{-5}$  °K during 0.004sec.),  $L=1$  cm,  $t = 1.26$  sec, simulation on the basis of compressible Navier-Stokes equations, Van-der-Waals state equation.

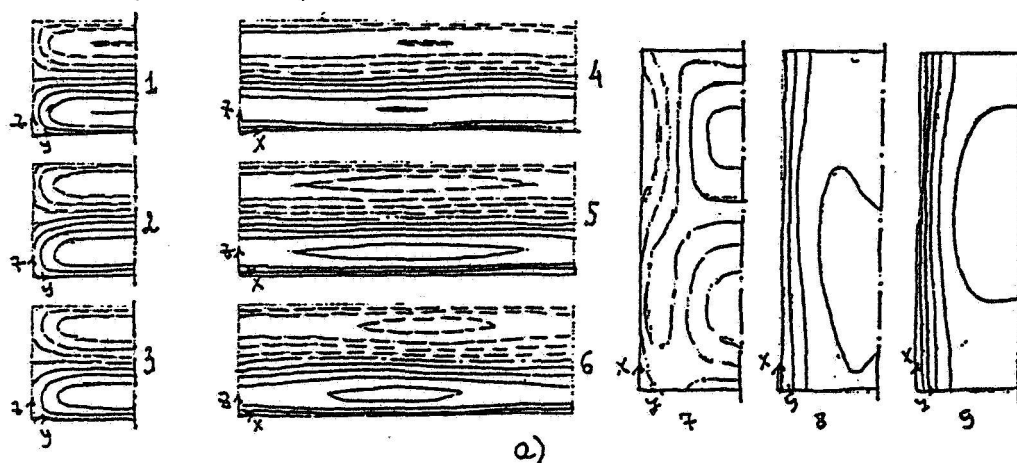
$$\left( \mu = \frac{T - T_c}{T_c} = 10^{-3} \right), \text{CO}_2$$



A. Basic flow for  $W/H=2$ :  
isolines of velocity (a) and temperature (b)



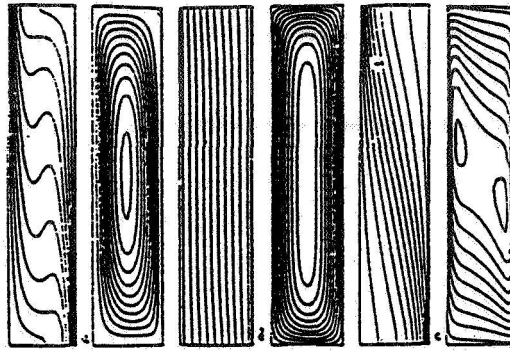
B. Dependency of the critical grashof number on the width  
stability analysis: \_\_\_\_\_  
finite difference calculation: o - basic flow,  
x - secondary structure



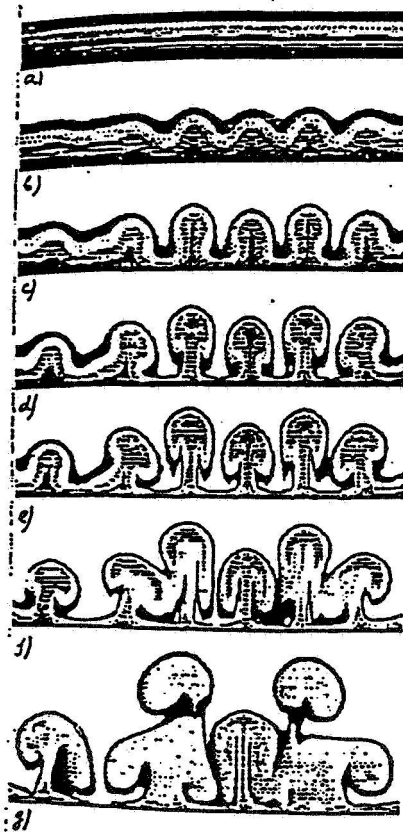
C. Isolines of the velocity component  $u$  in the  
central cell of the layer.

1 -  $x=10$ , 2 -  $x=10,7$ , 3 -  $x=11,35$  (vertical crosssection)  
4 -  $y=0,125$ , 5 -  $y=0,5$ , 6 -  $y=0,875$  (vertical crosssection)  
7 -  $z=0,125$ , 8 -  $z=0,25$ , 9 -  $z=0,5$  (horizontal crosssection)

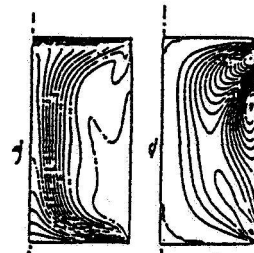
Fig.5 Stability and spatial structure of convection in  
parallelepiped



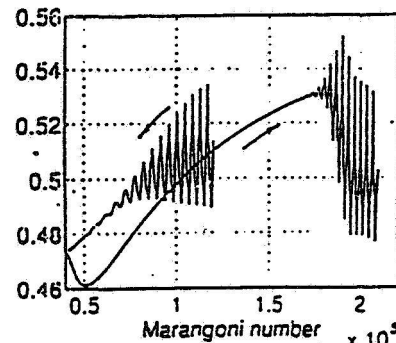
A. Thermal gravity-driven convection in permeable isotropic and anisotropic porous vertical layer with side heating: air,  $Gr = 10^5$  (a), isotropic (b) and anisotropic (c) porous media



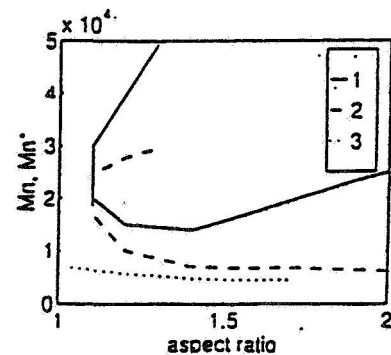
B. Isotherms in the problem of unsteady thermal behavior  $\alpha/t^2 = 0.0135$  (a),  $0.0138$  (b) ...  $0.0145$  (g).



C. Temperature (a) and stream function (b) for floating zone ( $H/R=2$ ,  $Mn=10^5$ ,  $Pr=32$ ). Oscillation regime



D. Temperature oscillation at  $x=0.25$ ,  $y=0.5$  for decreasing and increasing  $Mn$  numbers.



E. Critical Marangoni numbers for  $Pr=7$   
1 - plane A-Mn, 2 - plane A-Mn\*, calculations  
3 - plane A-Mn\*, experiment [15]

Fig.6 Results of calculation on the basis of Computer laboratory.

# EFFECT OF SPACECRAFT ROTATION ON FLUID CONVECTION UNDER MICROGRAVITY

Valentin S. Yuferev, Elvira N. Kolesnikova, Yuri A. Polovko, and Alexander I. Zhmakin  
Ioffe Physical-Technical Institute, St. Petersburg, 194021, Russia

## ABSTRACT

The influence of the rotational effects on two-dimensional fluid convection in a rectangular enclosure with rigid walls during the orbital flight is considered. It is shown that the Coriolis force influence both on steady and oscillatory convection becomes significant at Ekman numbers which are quite attainable in the space orbital conditions. In the case of harmonic oscillations of the gravity force appearance of the resonance phenomena is demonstrated. Dependence of the height and shape of the resonance peak on aspect ratio of a rectangular domain and orientation of vectors of the gravity force and the angular rotation velocity is studied. Special attention is given to non-linear effects caused by convective terms of Navier-Stokes equations. The convection produced by variations of the angular rotation velocity of a spacecraft is also discussed. It is shown that in some cases the latter convection can be comparable with another kinds of convection.

## INTRODUCTION

It is well-known that rotation of fluids can result in appearance of quite unusual flow patterns (ref. 1). It is natural therefore that rotational effects are to be considered when studying convection of fluids in the orbital flight conditions. Here first of all it is necessary to take into account the Coriolis force which is arisen when convective motion is considered in the coordinate system attached to the container with fluid. Strange as it may be seen but a very small attention has been paid so far to the Coriolis force effect on fluid convection in a microgravity environment (ref. 2). The most of researchers have restricted themselves to using the model of effective acceleration (ref. 3) that is equivalent to consideration of the case of harmonic gravity oscillation without any Coriolis force action. It is obvious that in such approach the peculiarities inherent to flow patterns in rotating fluids are lost.

The effect of the Coriolis force is determined by Ekman number  $Ek = \nu / (\Omega L^2)$ , where  $L$  is the characteristic length,  $\nu$  is the kinematic viscosity and  $\Omega$  is the angular rotation velocity. In table 1 the basic characteristic of the fluid convection in the orbital experiments are compared with parameters of the atmosphere flows in the terrestrial conditions. One can see that Ekman numbers on a spacecraft board can be in principle as small as in the Earth atmosphere, where the influence of the Coriolis force is recognized. Another specific features of the convection during the orbital flight are manifested when angular rotation velocity of the spacecraft is varied. In particularly, in this case acceleration  $\mathbf{r} \times d\Omega/dt$  where  $\mathbf{r}$  is the radius-vector originating from some fixed point within the rotating container is appeared. Since this acceleration field is vortex it can not be included into the pressure gradient term and will result in convection motion even if the fluid is isothermal. It is just these rotational effects and their interaction with g-jitter that are studied in the present paper.

## FORMULATION OF THE PROBLEM

Boussinesque approximation for the thermal convection of incompressible fluid is used. As the Ekman numbers are assumed to be moderate we use scaling adopted in the natural convection problems and take the enclosure height  $h$ ,  $\Delta T$ ,  $\rho g_0 \beta h \Delta T$ ,  $g_0$  and  $\Omega_0$  as the scales for the length, temperature, pressure, microacceleration and angular velocity, respectively. At the same time the choice of the velocity and time scales were taken dependent on the convection intensity  $[u] = \nu/h Gr^{1-\frac{\alpha}{2}}$ ,  $[t] = h^2/\nu Gr^{\frac{\alpha}{2}}$

where  $Gr = g_0 \beta \Delta T h^3 \nu^{-2}$  is the Grashof number and coefficient  $\alpha$  is equal to zero in the case of weak convection (Stokes approximation) and unity when convection is intensive and described by the full Navier-Stokes equation. The enclosure is assumed to be infinite in OY direction. The latter means that the present problem formulation describes the fluid flow in the middle part of the three-dimensional enclosure when its dimension in OY direction considerably greater than dimensions along OX and OZ axes. The microacceleration vector was written in the form  $\mathbf{g}(t) = \tilde{\mathbf{g}}(t) + \mathbf{r} \times d\tilde{\boldsymbol{\Omega}}/dt$  where the first term results in generation of Archimedian force while the second one describes the isothermal vortex acceleration field in the fluid. No restrictions are imposed on the directions of the vectors  $\mathbf{g}$  and  $\tilde{\boldsymbol{\Omega}}$ . In solving the thermal equation the upper and lower walls were assumed to be isothermal while the side walls - to be adiabatic. The presented formulation generalizes the problem commonly used when considering flow in a rotating annulus heated from below or due to a horizontally applied temperature gradient (see, for example, ref. 4).

## CALCULATION RESULTS

The effect of the Coriolis force on steady convection.— For constant gravity force this problem was studied by many authors and our only aim is to demonstrate shortly the Coriolis force influence on the magnitude of convection. For definiteness it is assumed that  $g_{1x} = 1$ ;  $g_{1y} = g_{1z} = 0$ ;  $\Omega_x = 0$ ,  $\Omega_z = 1$ ,  $T = z$  and aspect ratio  $d = 2$ . Fig. 1 shows dependence of the maximal velocity components on the Ekman number. With decrease of Ekman number the  $x$ - and  $z$ -components of the velocity diminishes while the  $y$ -component (thermal wind) at first increases quite quickly but then begins to decrease too. The Coriolis force influence on the structure of stationary flow is illustrated by fig. 2. One can see that the presence of the Coriolis force results in formation of the flow core with very low velocity and qualitative changes in the temperature field.

Weak convection under harmonic gravity oscillations.— It is known that if  $Gr < 100$  or  $\omega \gg 1$  or Rossby number  $Ro = Ek \sqrt{Gr} \ll 1$  then one can use the Stokes approximation. The bulk of attention in this section is given to the resonance phenomenon which arises when  $Ek \ll 1$  and  $\omega \gg 1$ . Here first of all it is necessary to note that point  $\omega = 2 Ek^{-1}$  is singular. In this case near the walls of the enclosure the specific boundary layers with thickness proportional to  $\omega^{1/2}$  can be developed while in the central part of a cavity velocity distribution remains weakly dependent on the frequency. Besides, at  $\omega < 2 Ek^{-1}$  differential operator of an inviscid equation changes its type transforming into hyperbolic operator. It is just of this change of the operator type that is the reason of the resonance appearance. As a characteristic of the intensity of oscillatory convection we used the root-mean-square (rms) velocity of the fluid (over a period of oscillation). Fig. 3 demonstrates the dependence of the maximum rms velocity on Ekman number and frequency  $\omega$  in cross-section  $x=0$ . One can see, that starting with some value of frequency this dependence has a distinct resonant character. The resonance appears when near the walls the Ekman boundary layers are developed while inside the enclosure an inviscid core is formed. The height and shape of the resonance peak strongly depends on aspect ratio of the enclosure and on orientation of the vectors of the microacceleration and angular rotation velocity. In real conditions of the orbital flight the resonance phenomenon will arise only under action of the extremely low frequency microaccelerations and can be observed provided that convection caused by these microaccelerations will be compared with the convection produced by the stronger high-frequency vibrations.

Nonlinear effects.— In the Stokes approximation the velocity field remains “monochromatic” under harmonically modulated gravity and contains only a single harmonic with the frequency  $\omega$  while the temperature is not changed in time at all. If we consider the full Navier-Stokes equations then additional harmonics of the flow field (including time-averaged component) are excited and time variation of the temperature nonuniform across a fluid region appears. The structure of the time-averaged flow in XOZ plane is shown in fig. 6 for three values of Ekman numbers, the middle of them being the value

corresponding to the resonance peak of the maximum of rms velocity. A rather complex pattern of the time-averaged flow is a result of non-linear effects. It is necessary to emphasize, that in the case under consideration the time-averaged flow is small relative to the basic pulsatile motion and therefore its study is of only theoretical interest. However, if fluid has a free boundary then intensity of the time-averaged flow can be quite significant and compared with that of the pulsatile one. Fig. 7 shows that in the case of the intensive convection ( $Gr = 10^4$ ) the resonance phenomena arises too, although Rossby number is of order of unity. It is seen that the consideration of the convective terms in governing equations results in decreasing the height of resonance peak and manifests itself mainly in vicinity of this peak.

The influence of variation of the angular rotation velocity.—Isothermal convection under harmonic oscillations of the angular rotation velocity  $\Omega = \Omega_0 \exp(j\omega t)$  is considered. Vector  $\vec{\Omega}$  is directed along OY axis and convection velocity is normalized to  $\Omega_0 h$ . Fig. 8 shows that with increase of  $\omega$  maximal rms velocity quickly approaches to its maximal value. Thus, for example, if  $\omega, \Omega_0 \approx 0.001 \text{ s}^{-1}$  (free flight),  $v \approx 0.001 \text{ cm}^2 / \text{s}$  and  $h$  is of order 1-5 cm then convective velocity will be of order of  $10^{-5} \div 10^{-3} \text{ cm} / \text{s}$  that is compared with convection produced by Archimedian force at low level of g-jitter ( $\sim 1\text{-}10 \mu g$ ). Moreover, co-action of variation of the angular velocity and j-gitter can in principle lead to appearance of the new quite unusual resonance depending on the phase difference between oscillations of gravity and angular velocity (ref. 5).

## CONCLUDING REMARKS

1. The Coriolis force is an essential element of the microgravity environment. The influence of the Coriolis force can become significant when  $Ek < 0.1$ . These values of Ekman numbers are quite attainable in the space orbital conditions if, for example, the size of container with fluid is of order 10 cm for the water, 3-4 cm for the semiconductor melts and 1 cm for the liquid helium.

2. In design of a space fluid convection experiment it is necessary to control level of both microaccelerations and variations of angular rotation velocity.

The research was carried out under a contract between NASA and Russian Space Agency, grant N 920-5208/95.

## REFERENCES

1. Greenspan, H.P.: The theory of rotating fluids. 1968, Cambridge University Press.
2. Yuferev, V.S.; and Kolesnikova, E.N.: Combined action of microgravitation and the Coriolis force on the motion of a liquid in the middle part of a three-dimensional thin rectangular region. Tech. Phys. Lett., Vol. 21, 1995, pp. 178 179.
3. Polezhaev, V.I.: Microacceleration regimes, gravitational sensitivity and methods for analysis of the technological experiments in microgravity, *Mechanika zhidkosti i gasa*, No. 5, 1994, pp. 22 36 (in Russian).
4. Hunter, C.: The axisymmetric flow in a rotating annulus due to a horizontally applied temperature gradient. *J. Fluid Mech.*, Vol. 27, 1967, pp. 753 778.
5. Yuferev, V.S.; and Kolesnikova, E.N.: The effect of the Coriolis force on the convection of a liquid under weightless conditions in the presence of angular and linear oscillations of an orbital station about its center of mass. Tech. Phys. Lett., Vol. 21, 1995, pp. 500 502.

**Table 1**

	<u>Atmosphere flows</u>	<u>Convective motion in the orbital flight conditions</u>
Kinematic viscosity	$\sim 1 \text{ cm}^2/\text{s}$	$10^{-2} - 10^{-4} \text{ cm}^2/\text{s}$
Length scale	$10^4 - 10^5 \text{ cm}$	$1 - 100 \text{ cm}$
Angular rotation velocity	the Earth $\sim 5 \cdot 10^{-5} \text{ s}^{-1}$	spacecraft $\sim 10^{-3} \text{ s}^{-1}$
Ekman number	$10^{-4} - 10^{-5}$	$10 - 10^{-5}$

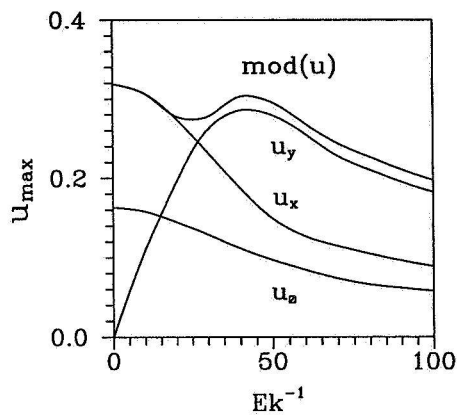


Fig. 1. The dependence of the maximal values of the velocity components and velocity module over cross-section XOZ on Ekman number.  $Pr=1.0$ ;  $Gr=10^4$ .

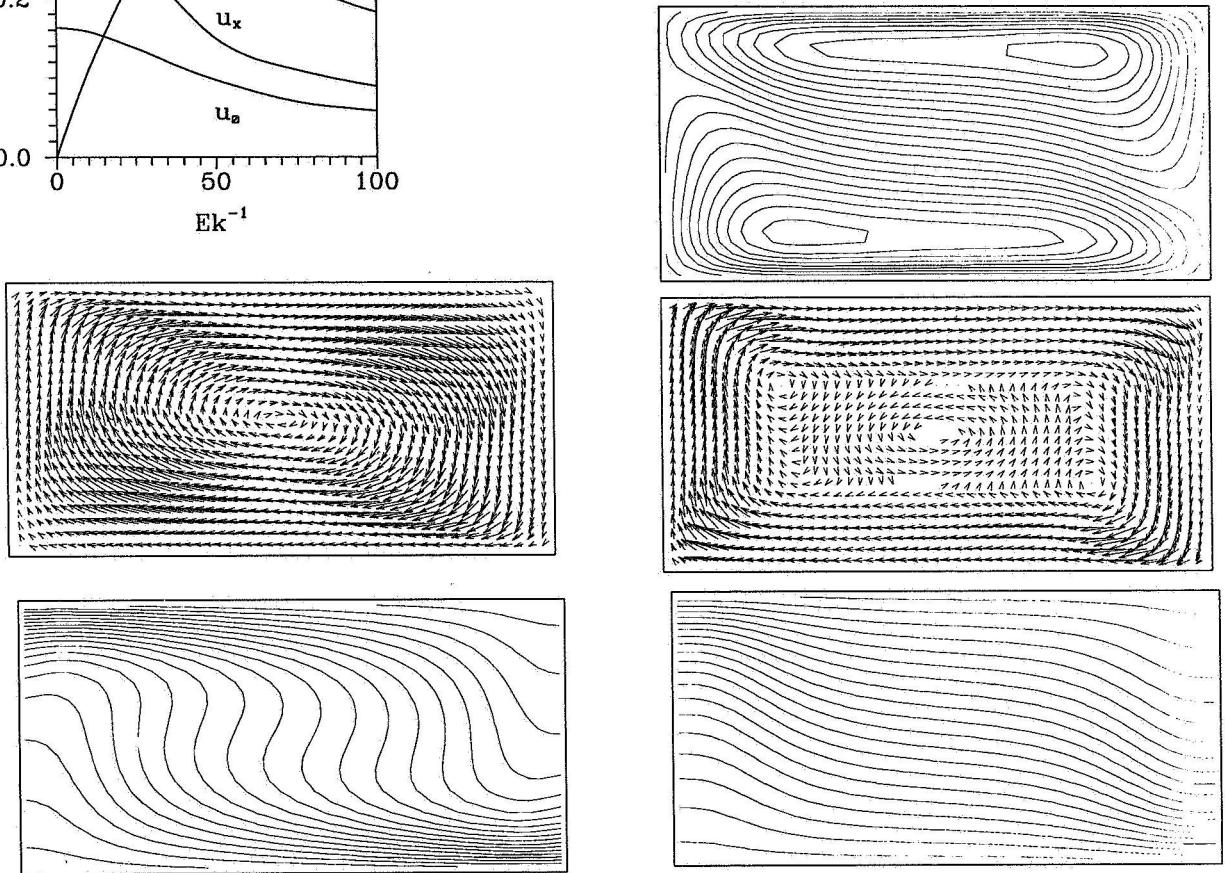


Fig.2 The effect of the Coriolis force on the structure of the stationary flow.  $Gr = 10^3$ ;  $Pr = 1.0$ . right -  $Ek^{-1} = 100$ ; left -  $Ek^{-1} = 0$ .



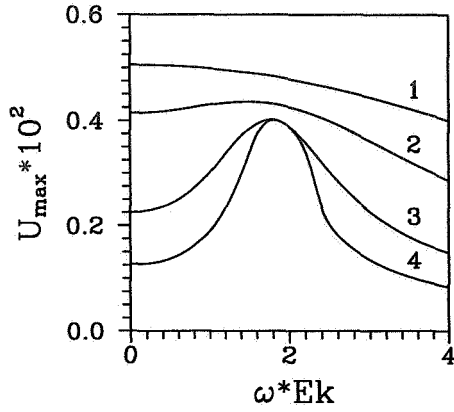


Fig. 3. The dependence of the maximal rms velocity on Ekman number and modulation frequency. Curves: 1 -  $Ek^{-1}=10$ ; 2 - 20; 3 - 50; 4 - 100. Aspect ratio and orientation is the same as in Fig. 1.

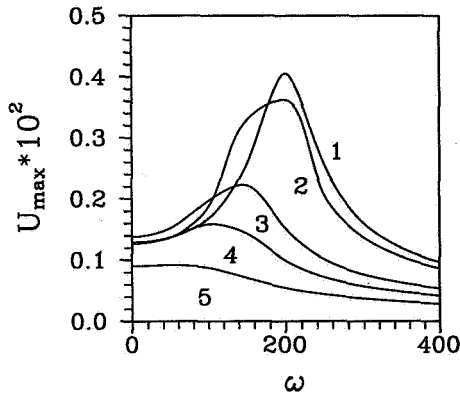


Fig. 4. Effect of the aspect ratio on the maximal rms velocity.  $Ek = 0.01$ , curves: Aspect ratio: 1 - 6.0; 2 - 2.0; 3 - 1.0; 4 - 0.8; 5 - 0.6. Orientation is the same as in Fig. 1.

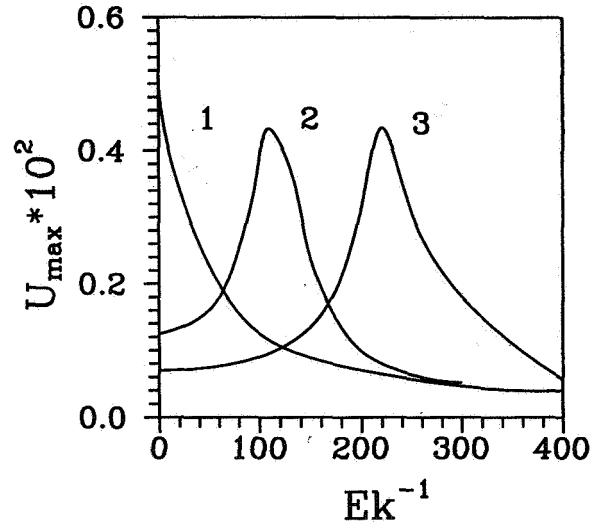
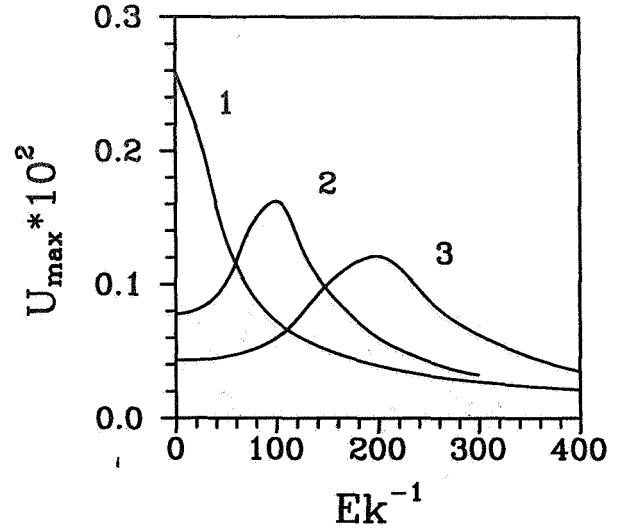


Fig. 5. The effect of the mutual orientation of the microacceleration and angular rotation vectors on the maximal rms velocity at the cross-section  $x = 0$ .

a)  $\Omega_x = \Omega_z = 1$ ;  $g_x = 1$ ;  $g_y = g_z = 0$ ;  $d = 1.0$ ;

b)  $\Omega_x = 1$ ;  $\Omega_z = 0$ ;  $g_y = 1$ ;  $g_x = g_z = 0$ ;  $d = 2.0$ .

Curves: 1 -  $\omega = 20$ ; 2 - 200; 3 - 400.

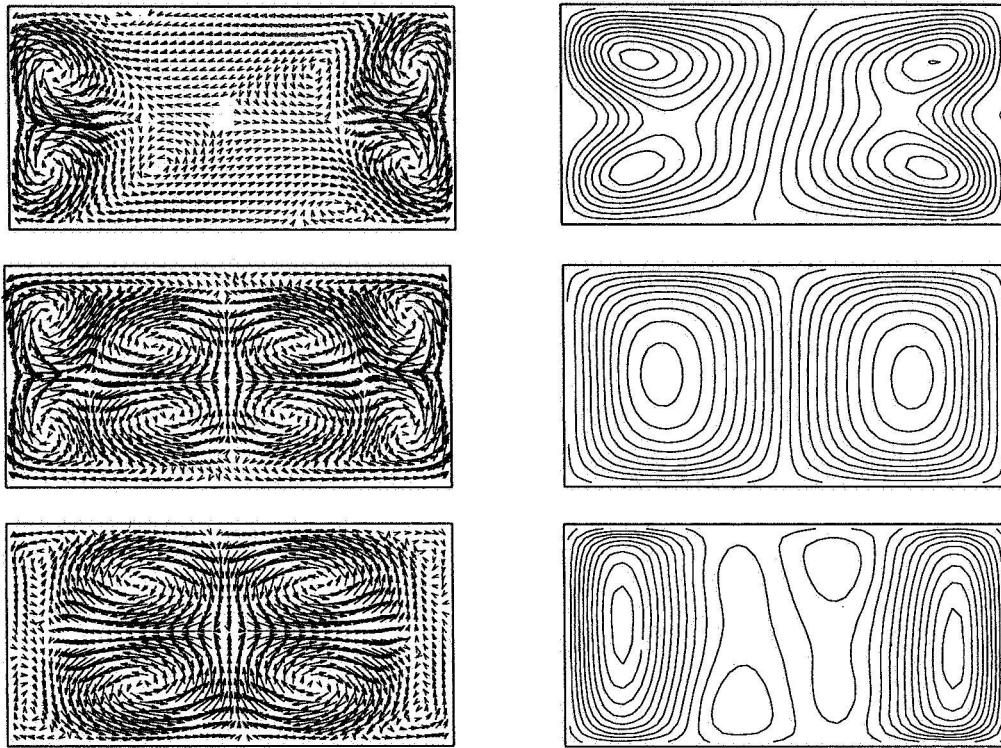


Fig. 6. Contour lines of the time-averaged flow:  $y$  – component of the velocity (right), velocity vectors in XOZ plane (left) at  $Gr=10^3$ ;  $Pr=1$ .  $Ek^{-1}=50$  (upper); 110 (middle) and 200 (lower).

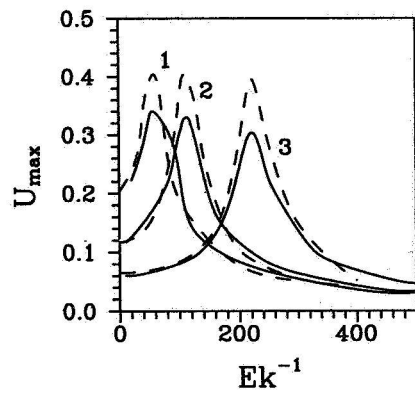


Fig. 7. The effect of the convection intensity on the maximal rms velocity.  $Gr=10^4$ , solid lines corresponds to solution of the full Navier-Stokes equations; dashed lines - Stokes approximation. Curves: 1 -  $\omega = 1$ ; 2 - 2; 3 - 4.

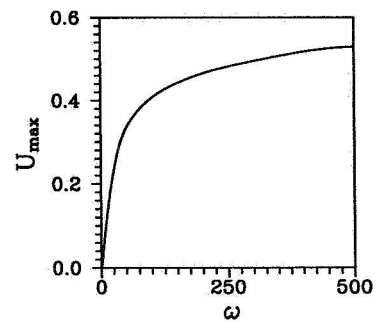


Fig. 8. The dependence of the maximal rms velocity on frequency of the angular velocity variation (Stokes approximation).

# A SYSTEM FOR MEASUREMENT OF CONVECTION ABOARD SPACE STATION

Gennady P. Bogatyrev, Aleksei V. Gorbunov and Gennady F. Putin

Department of General Physics  
Perm State University  
15, Bukirev Str., Perm, 614600, Russia

Alexander I. Ivanov  
Scientific Technical Center  
RSC "Energia"  
Kaliningrad, 141070, Russia

Sergei A. Nikitin and Vadim I. Polezhaev  
Laboratory of Physical and Numerical Modeling in Hydrodynamics  
Institute for Problems in Mechanics, RAS  
101, Vernadskyi Str., Moscow, 117526, Russia

## ABSTRACT

A simple device for direct measurement of buoyancy driven fluid flows in a low-gravity environment is proposed. A system connecting spacecraft accelerometers data and results of thermal convection in enclosure measurements and numerical simulations is developed. This system will permit also to evaluate the low frequency microacceleration component. The goal of the paper is to present objectives and current results of ground-based experimental and numerical modeling of this convection detector.

## INTRODUCTION

Estimations based on theoretical studies and terrestrial experiments show that the spacecraft acceleration level is sufficiently high in order to induce the buoyancy-driven convection and to influence the heat- and mass transfer processes ( refs. 1 and 2 ). At present the existence of buoyancy-driven motions in low-gravity environment can be judged only from indirect indications because there have been few space flight experiments with the objective of directly and quantitatively measuring the effect of this convection and conclusions of the experiments contradict one another. Accordingly, it is desirable to conduct a simple experiment to detect and investigate the buoyant convection phenomenon directly in orbit.

On the other hand, the gravitational and inertial sensitivity of flows in nonisothermal liquid and gaseous mediums makes it possible to propose a method of measuring the microaccelerations aboard a spacecraft based on recording the temperature stratification due to buoyant convection (refs. 1 and 2 ). Especially promising is the utilization of a convection detector to measure the magnitude and direction of the low-frequency components of a force field inaccessible to most other instruments currently in use.

A possibility of detecting weak convection based on observing the propagation of a thermal front between coaxial cylinders was considered in ( refs. 3 and 4 ). The justification of the method and preliminary results of a laboratory and numerical simulation of the motions in a cubic enclosure were presented in ( refs. 5 and 6 ). The modern opinion at the concept, design and testing of the convective sensor is described below.

## EXPERIMENTAL APPARATUS AND PROCEDURES

Figure 1 shows a sketch of the cell module. In order to reduce the influence of the cavity corners and to simplify a structure of the motion, especially in the case of pendulum swinging of the sensor, it was solved to use the convective chamber in the form of a circular cylinder instead of cubic one. The 45.4 mm diameter  $\times$  45.0 mm height

test container consisted of two parallel flat aluminium plates separated by an annular plastic wall. An air was used as the working fluid. The left hot plate was resistively heated and the right cold plate was fan air cooled. Sealing and thermal insulation were used to minimize the influence of surrounding atmosphere pressure, composition and temperature changes. The temperature difference  $\Delta T$  between hot and cold enclosure bounds was measured by thermocouple junctions embedded into the heat exchangers. The junctions of a second differential thermocouple placed within the cavity at a 10 mm distance from the heater and side wall measured the temperature deviations  $\Delta t$  from thermal diffusion profiles, i. e. , identified convection.

Figure 2 shows the nondimensional intensity of convection  $\Theta = \Delta t / \Delta T$  as a function of Rayleigh number  $Ra = g\beta\Delta TH^3 / \nu\chi$ . Here ,  $\beta$ ,  $\nu$  and  $\chi$  are the coefficients of thermal expansion, kinematic viscosity and thermal diffusivity,  $H$  is the cell diameter and  $g$  is the gravity acceleration. For small values of  $Ra$  a linear relationship  $\Theta = a Ra + b$  may be obtained, where  $a = (1.2 \pm 0.2) \times 10^{-4}$  and  $b = (5.8 \pm 0.4) \times 10^{-4}$ . This formula permits to estimate the threshold of sensitivity of testing sensor in weightlessness. For temperature difference  $\Delta T = 50^\circ\text{C}$  the minimum measured acceleration can be equal to  $(3.5 \pm 0.4) \times 10^{-6} g_0$ , where  $g_0$  is terrestrial gravity.

## THEORETICAL ANALYSIS AND MODELING

Last time the computer laboratory COMGA for analysis of convectional processes in a weightlessness environment is developed including widespread class of gravity and non-gravity motive forces in one- and two component mediums and taking into consideration the complicated spatial-temporal changes of microaccelerations ( ref. 7 ). This laboratory contains the specially worked out interface for analysis both the real tape-records of spacecraft microaccelerometers and the results of numerical simulations taking into account the space station characteristics and the dynamics of its flight ( ref. 8 ).

Figure 3 shows an example of time evolution of a low-frequency part of microaccelerations along one of the coordinate axes ( $x$ ) calculated from the initial acceleration data of the Orbital Complex " Mir " with the method described in ( ref. 8 ).

Figure 4 illustrates the behavior of the liquid temperature found on the base of two dimensional COMGA model for the quasi-static microgravity environment represented in figure 3. The case of 10 cm characteristic size,  $50^\circ\text{C}$  temperature difference applied and ethanol as a testing fluid is considered. The amplitude of fluid temperature oscillations in this realization reaches  $8^\circ\text{C}$ . This result demonstrates the gravitational sensitivity of the described system and the possibility of determination of low- frequency accelerations through the fluid motion response (ref. 2 ).

Figure 5 shows the instantaneous pictures of flow and temperature fields obtained with the help of discussed computer laboratory. At the same time the momentary direction and value of microacceleration vector and the magnitudes of velocity and temperature for one of the cavity points are shown at the interface screen. This results are corresponding also to the parameters refereed in figures 4 and 5. An example of computation of thermal convection in melting semiconductor using the accelerations data obtained by setup SAMS onboard Space Shuttle is given in ( ref. 8 ).

For modeling described experiments we used the Navier-Stokes equations in the Boussinesq approximation in the right-handed coordinate system  $xyz$  related to the enclosure, which moves with angular velocity  $\Omega(\tau)$  about the fixed axis. In this coordinate system the axis of rotation is parallel to the  $z$  axis and is given by the equations  $x=x_0$  and  $y=y_0$ :

$$\rho \left( \frac{\partial \mathbf{V}}{\partial \tau} + (\mathbf{V} \nabla) \mathbf{V} - 2(\mathbf{V} \times \boldsymbol{\Omega}) \right) = -\nabla p + \mu \Delta \mathbf{V} + \rho(g(\tau) - \boldsymbol{\Omega} \times (\boldsymbol{\Omega} \times \mathbf{r}') - \dot{\boldsymbol{\Omega}} \times \mathbf{r}')$$

$$\frac{\partial T}{\partial \tau} + (\mathbf{V} \nabla) T = \chi \Delta T$$

$$\text{div} V = 0$$

where  $\rho$  is the density,  $V$  is the velocity,  $p$  is the pressure,  $r'$  is the radius vector connecting the axis of rotation with a certain point inside the enclosure,  $r'=(x', y')=r-r_0$ ,  $r=(x, y)$ ,  $r_0=(x_0, y_0)$ ,  $\dot{\Omega}$  is the angular acceleration, and  $g(\tau)$  is the acceleration of gravity vector.

On all-the walls boundary conditions for the velocity are the no-slip ones. The temperature on the cold boundary of the enclosure was assumed to be equal to 20°C, and the temperature on the heated boundary was made constant on the interval 24-80°C. On the side faces of the enclosure for the temperature we consider either adiabatic conditions or a linear profile.

The results presented here were obtained by the finite-difference method using 17×17 and 33×33 grids. Some control calculations were also made by the finite-difference method in the two-dimensional and three-dimensional cases for a constant angle of inclination of the chamber using 33×33 and 15×15 grids. Test calculations on various grids using different methods showed that acceptable accuracy (within 5% with respect to temperature and 10% with respect to velocity) can be achieved using a 17×17 grid, and this grid was adopted for main calculations.

## REFERENCES

1. Barmin, I.V.; Polezhaev, V.I.; Putin, G.F. et al.: The Program of Investigations of Hydrodynamics Phenomena in Weightlessness. Proceedings RAS [in Russian ], Phys. Series, 1985, Vol. 49, No.4, pp. 643-648.
2. Polezhaev, V.L.; Bello, M.S.; Verezub, N.A. et al.: Convective Processes in Microgravity [ in Russian ], Moscow, 1991, p.240.
3. Kosvintsev, S.R.; Putin, G.F. et al.: Ground Simulation of Thermal Convection under Conditions Approximating Weightlessness, Numerical and Experimental Modeling of Hydrodynamic Phenomena in Microgravity [ in Russian ], Ural Branch of the USSR Academy of Sciences, Sverdlovsk, 1988, p.56.
4. Bogatyrev, G.P.; Kostarev, K.G. et al.: Propagation of a Thermal Front between Coaxial Cylinders, Numerical and Experimental Modeling of Hydrodynamic Phenomena in Microgravity [ in Russian ], Ural Branch of the USSR Academy of Science, Sverdlovsk, 1988, p.63.
5. Bogatyrev, G.P.; Ivanov, A.I.; S.A.; Polezhaev, V.I.; Putin, G.F. et al.: Experimental and Theoretical Investigation of Thermal Convection in a Terrestrial Model of a Convection Detector, Fluid Dynamics, Vol. 29, No.5, 1994, pp.645-652.
6. Bogatyrev, G.P.; Putin, G.F.; Polezhaev, V.I.; Ivanov, A.I. et al.: A System for Analysis and Measurement of Convection aboard Space Station: Objectives, Mathematical and Ground-Based Modeling, AIAA Paper 95-0890, Jan. 1995.
7. Polezhaev, V.; Ermakov, M.; Griaznov, V. et al.: Computer Laboratory on Convective Processes in Microgravity: Conception, Current Results and Perspective, IAF-95-9.3.11., 46th Intern. Astronaut. Congress, Oct. 1995, Norway.
8. Sazonov, V.V.; Belyaev, M.Ya. et al.: Evaluation of Quasi-Static Component in Acceleration on board Earth Artificial Satellite [ in Russian ], Inst. of App. Math., Paper No.45, 1995, p. 630.

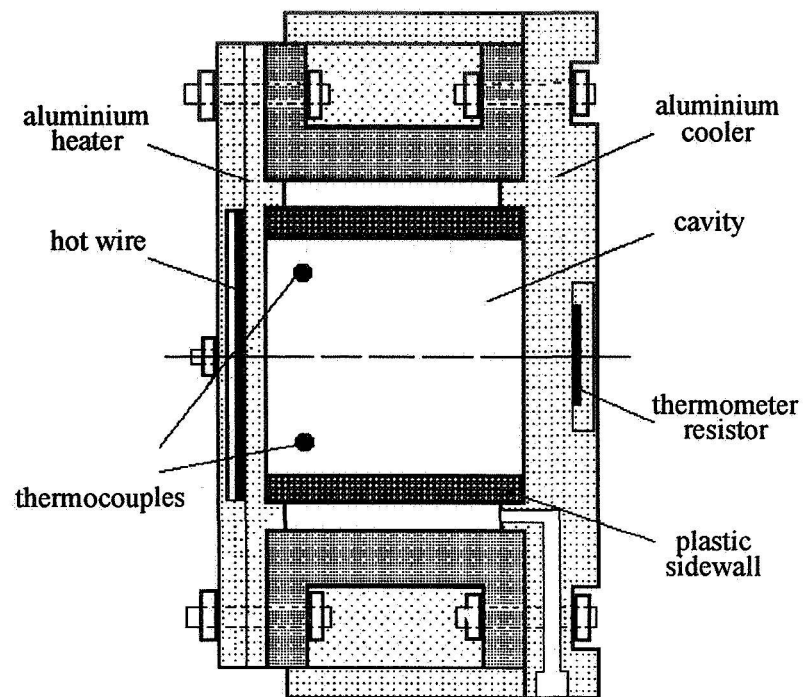


Figure 1.- Schematic of the test enclosure.

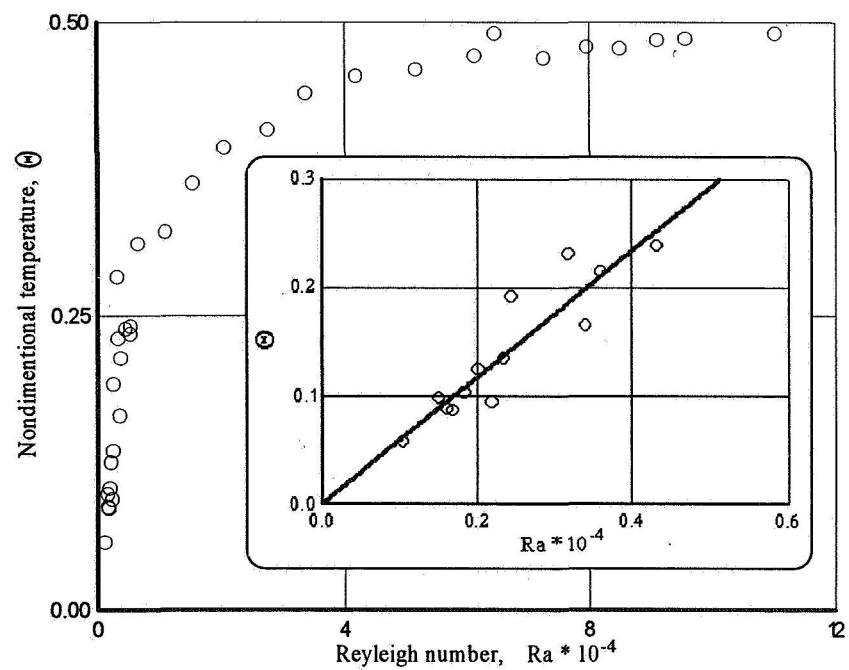


Figure 2.- Plot of the intensity of convection of air versus Rayleigh number.

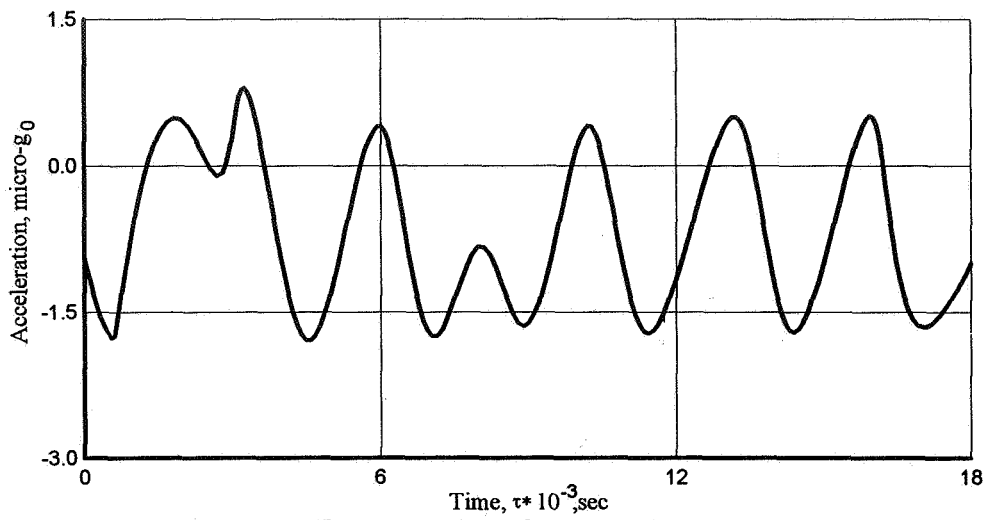


Figure 3.- Time variation of computed quasi-static microacceleration component.

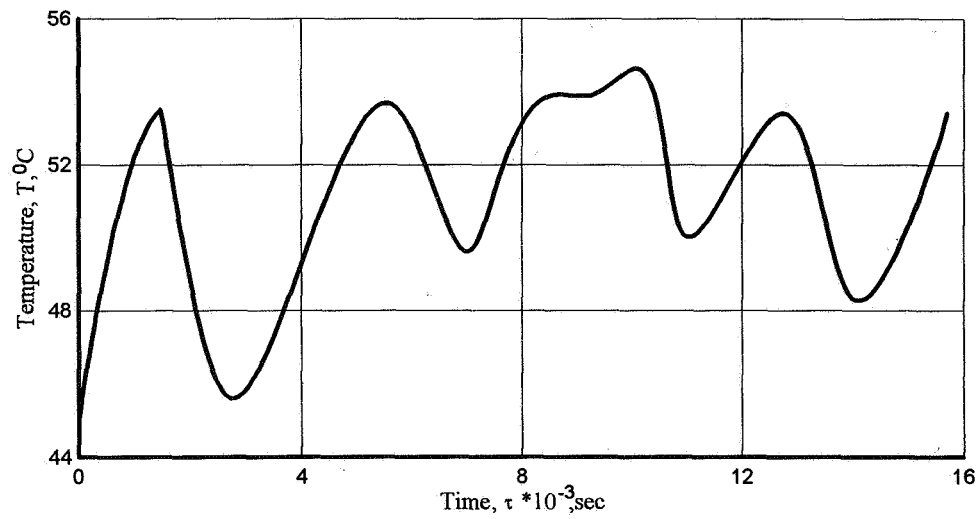


Figure 4.- Computed temperature time variation in the cell.

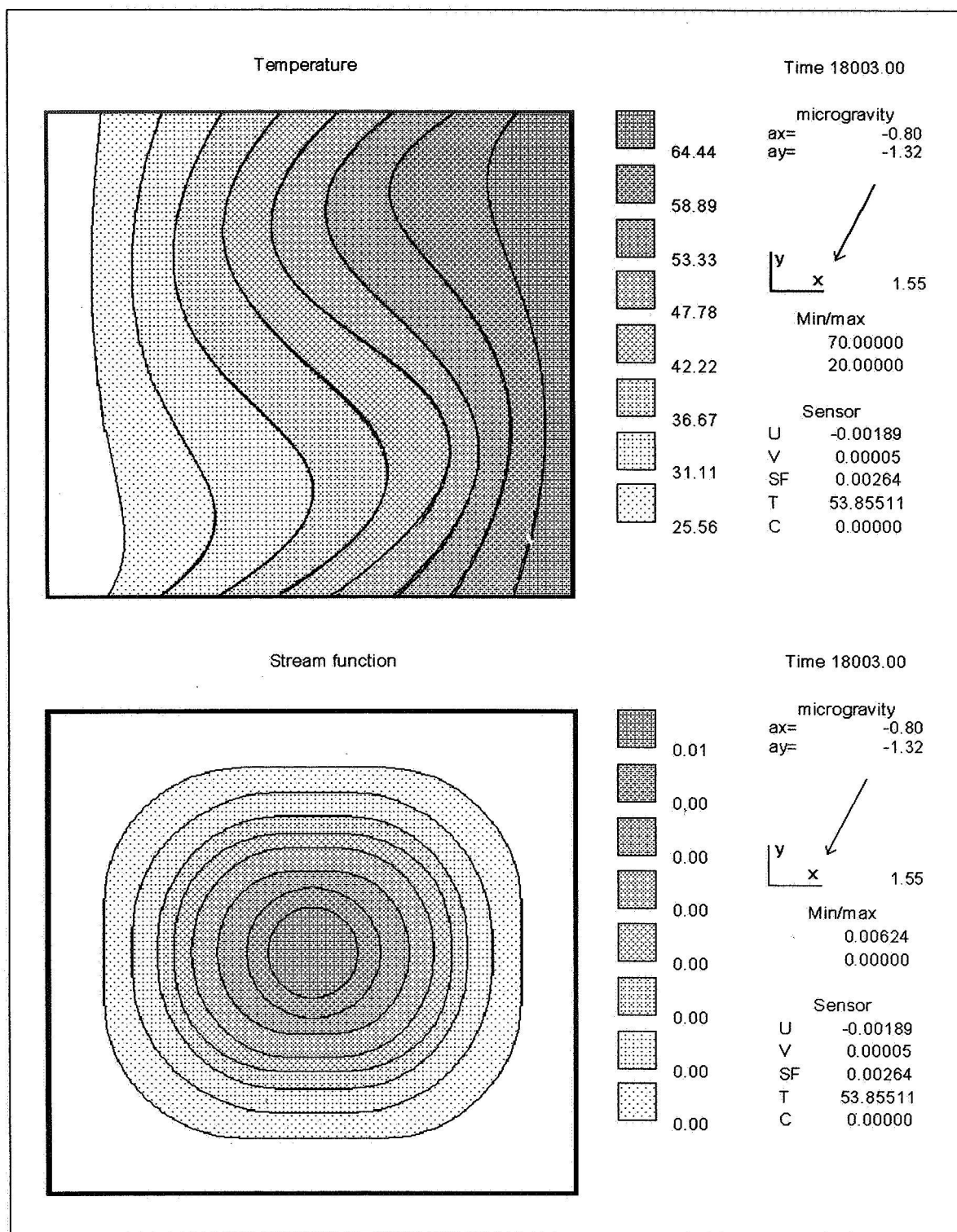


Figure 5.- Temperature and flow fields in a cell heated from the right side.



# **Experimental Techniques**



# A NEW GENERATION FIBER OPTIC PROBE : CHARACTERIZATION OF BIOLOGICAL FLUIDS, PROTEIN CRYSTALS, AND OPHTHALMIC DISEASES

Rafat R. Ansari and Kwang I. Suh

NASA Lewis Research Center / CWRU

Mail Stop 333-1, 21000 Brookpark Road, Cleveland, Ohio 44135

Phone: (216) 433-5008, Fax: (216) 977-7138, e-mail: ransari@lerc.nasa.gov

## ABSTRACT

A new fiber optic probe developed for determining transport properties of sub-micron particles in fluids experiments in a microgravity environment has been applied to characterize particulate dispersions/suspensions in various challenging environments which have been hitherto impossible. The probe positioned in front of a sample delivers a low power light (few nW - 3mW) from a laser and guides the light which is back scattered by the suspended particles through a receiving optical fiber to a photo detector and to a digital correlator. The probe provides rapid determination of macromolecular diffusivities and their respective size distributions. It has been applied to characterize various biological fluids, protein crystals, and ophthalmic diseases.

## INTRODUCTION

In the past few years dynamic light scattering (DLS) instrumentation has embraced several new and innovative technological advances. The immediate impact of these have resulted in the miniaturization of DLS instrumentation<sup>1</sup>. One of those advances is the use of fiber optics in DLS. Especially, the use of monomode optical fibers in designing and fabricating a DLS system was first initiated by Brown<sup>2</sup> in his 90° scattering system. Later, a lensless single fiber probe was used by Weiss and Horn<sup>3</sup> to study highly concentrated systems (1-40% w/v) without the adverse effect of multiple light scattering. However, since the scattering volume has to be positioned right at the tip of the fiber, the probe had to be immersed in the sample, making it no longer a non-invasive measurement. Also, the heterodyning effect caused by the internal reflection at the tip of the fiber necessitated a great deal of care in fabrication, and it could not be used for dilute samples with concentrations below 1% w/v or particles smaller than 30 nm because the reflected signal dominated the scattered signal. A lensless back-scatter fiber optic probe was developed to study concentrated particulate dispersions by Dhadwal et al.<sup>4</sup> Subsequently, Ansari et al.<sup>5</sup> and Dhadwal et al.<sup>6</sup> have shown the utility of their probe to the studies of cataractogenesis in excised bovine and cadaver eye lenses, and in live animals<sup>7</sup>. Unfortunately this probe has certain limitations and posed severe constraints in probing different parts of the eye, mainly due to a large scattering volume and a short penetration depth. Ansari and Suh<sup>8</sup> recently developed a new DLS probe to study nucleation and aggregation phenomena during protein crystal growth in space (microgravity) experiments. The new probe is compact, rugged, and provides accurate particle size determination of variety of colloidal dispersions in 5 seconds at extremely low laser power levels. Furthermore, it does not require any vibration isolation, index matching, or optical alignment, and it can be used with many different shapes and sizes of sample containers. These include regular spectroscopic cuvettes, capillary tubes, common laboratory utensils (beakers, graduated cylinders, conical flasks, glass/clear plastic container vessels), concentric cells containing two different solutions, and hanging fluid droplets of colloidal particles. The new probe is applied to several different applications which require characterization of various suspensions/dispersions in a wide range of particle sizes and concentrations from very dilute (water-like) dispersions to highly concentrated (milk-like) suspensions in a variety of challenging situations. These applications include monitoring protein crystallization in different hanging drop configurations suitable for microgravity experiments<sup>9</sup>, complete eye diagnostics<sup>10-12</sup>, zeolite crystal growth<sup>13</sup>, study of clay-polymer interactions, particle sizing in a rotating cell to avoid sedimentation due to gravity, characterization of food colloids, microemulsion and micellar systems, and tissue and skin analysis.

Protein crystals have been experimentally grown in 28 US Space Shuttle flights. One preferred method is to grow these crystals in hanging drops (~30μL) in a reduced gravity environment offered by the Space Shuttle orbiter or space station. In laboratory settings, DLS has been used to study protein solutions and crystal growth processes by Casay and Wilson<sup>14</sup>, Malkin and McPherson<sup>15</sup>, and references therein. However, in hanging droplets and in microgravity experiments, elaborate instrumentation and optical alignment problems have made in-situ and on-line applications difficult. Ansari et al.<sup>8,9</sup> have demonstrated that such experiments are now feasible. The new probe has

been successfully used in various earth and space-bound (microgravity) protein crystallization system configurations<sup>9</sup>.

Cataracts remain the major cause of blindness affecting about 50 million people each year worldwide. It is estimated that over \$5 billion will be spent this year in treating cataract patients in the United States alone<sup>16</sup>. There is no medical treatment to prevent or halt the progression of a cataract; nor is there any way to reverse a cataract once it is formed. The only known treatment is surgical. However, a medical treatment could be possible if we understand how a cataract forms and what makes it grow<sup>16</sup>. In order to find a medical treatment for cataracts, first, we must be able to detect a growing cataract in early stages of formation. The ability of such a detection will be useful in patient monitoring and in the development and testing of possible "anticataract" drugs. The technique of dynamic light scattering (DLS) or quasi-elastic light scattering (QELS) was first applied to the study of cataractogenesis in the pioneering work of Tanaka and Benedek<sup>17</sup>. An extensive review of using QELS to study cataracts has been given by Bursell et al<sup>18</sup>. DLS/QELS being a non-invasive and quantitative technique seems to hold promising potential in its use as a routine ophthalmic device. But its commercial scope as an ophthalmic diagnostic tool in clinical settings hitherto has not been materialized. Since the original application of QELS, some twenty years ago by Tanaka and Benedek<sup>16</sup>, every subsequent study focused on rather easily accessible part of the eye i.e. the aqueous humor and the lens. Most recently Ansari et al<sup>12</sup>, in the USA and Rovati et al<sup>19</sup>, in Switzerland reported the first experiments directed to the studies of the vitreous humor. Ansari et al<sup>10,11</sup>, have also shown recently that the new probe alleviates many major concerns discussed earlier when used as an ophthalmic diagnostics device and is much superior in performance when compared with the earlier reported work<sup>5-7</sup>. Furthermore, the major problem of probing different parts of the eye has been solved. In this paper we report the characterization of several solutions at different particle sizes (7-800nm in diameter) and concentrations (0.0001-10.0% w/v), and the characterization of bovine lenses and the eyes of live animals (rabbits and mice).

## EXPERIMENTAL PROCEDURE AND SETUP

A fiber optic probe comprising two monomode optical fibers and two GRIN micro lenses, as illustrated in

Figure 1, provides a compact and remote means of studying the dynamical characteristics of the macromolecules in a sample. A 13 mm diameter fiber optic probe contains the necessary optics to perform DLS measurements at a scattering angle of 161.5°. Two monomode optical fibers, each housed in a stainless steel ferrule, are mounted into a separate stainless steel housing. An air gap (0-0.5 mm) is intentionally left between the fiber housing and the lens housing in order to produce a tightly focused spot in the scattering volume. The two optical fibers in their housings are aligned and fixed into position off-axis with the GRIN lens. The two housings are placed inside

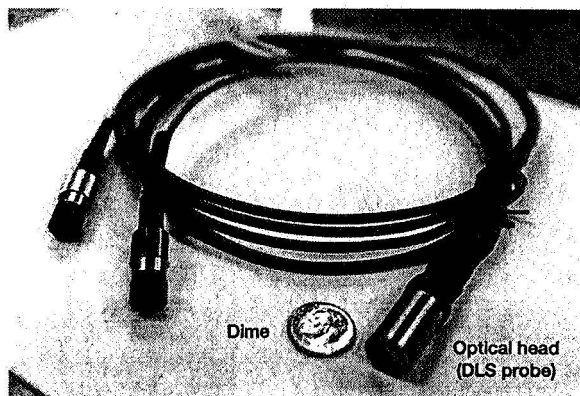
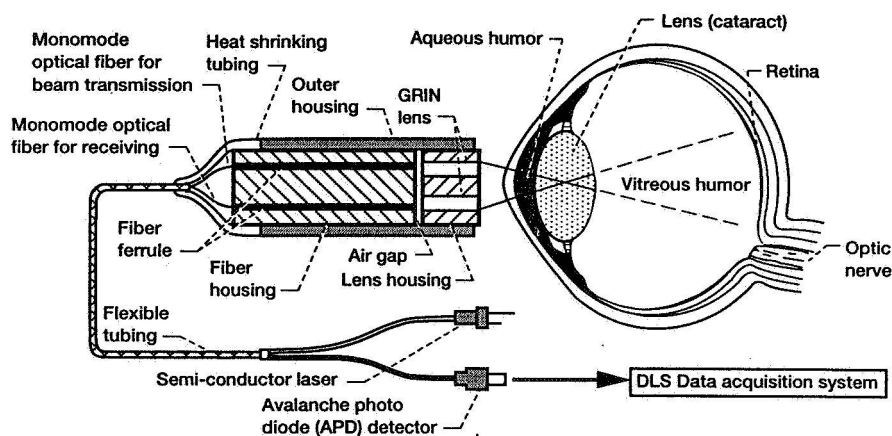


Figure 1. A new fiber optic DLS probe.

a third (outer) housing made of stainless steel, and the back end of the housing is covered with a heat-shrink tubing. The two free ends of the optical fibers were terminated with FC/PC-type male connectors for easy mating with the laser and an avalanche photodiode detector (APD). The DLS data was analyzed using the commercial software provided by the Brookhaven Instruments Company of New York.

## RESULTS

First, we report a series of DLS experiments on polystyrene solutions at several different concentrations (0.0001 - 10.0% w/v) and particle sizes (32 - 800nm in diameter), and bovine serum albumin (BSA) solutions at five different concentrations (2 - 10 %), all with 30 second experiment duration. The resulting average particle sizes are shown in figure 2. The new probe accurately and reliably measures the particle size from 7nm to 800nm in diameter with concentrations ranging from 0.0001 to 10.0% w/v. Figure 3 shows DLS experiments at two different experiment durations (5 seconds and 30 seconds) using 1% BSA solution. The resulting time correlation functions (TCF) and particle size distributions (see inset) display the excellent quality of data collected even with experiment duration as short as 5 seconds.

Figure 4 shows a 3-D DLS scan of an intact bovine eye lens, which shows detailed structure of the lens in terms of  $\alpha$  crystalline size and its distribution in the lens tissue. In a normal eye lens,  $\alpha$ ,  $\beta$ , and  $\gamma$  crystallines (proteins) concentration is ~35 wt.%. Since  $\alpha$  crystallines are the largest (molecular weight  $\sim 1 \times 10^6$  daltons) in size they scatter most of the incident laser light. In the resulting average particle sizes, we find a specific trend as we move inside the lens and away from the anterior cortex. We see gradual increase in the particle size as we move from the anterior cortex to the nucleus of the lens. The same trend can also be observed as we move from the peripheral region to the nucleus. The size gradually decreases as we move out of the nucleus region and into the posterior cortex.

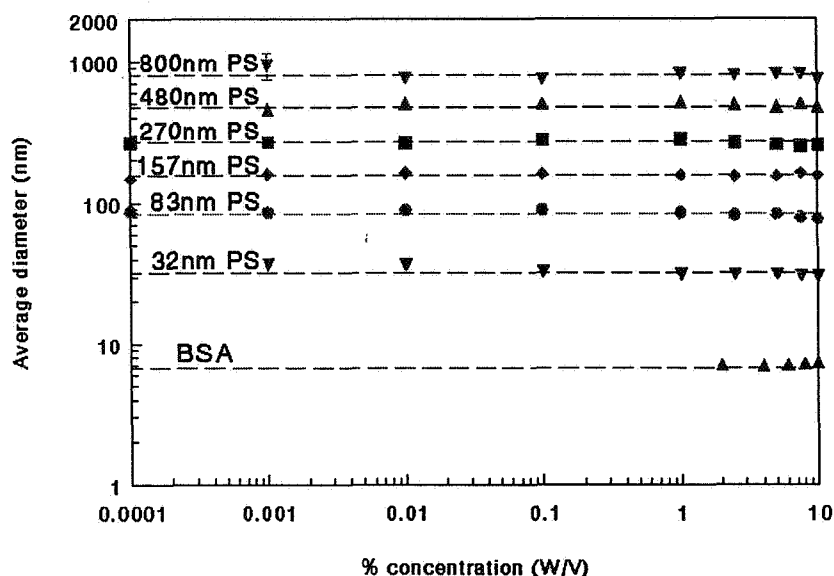


Figure 2. Calibration result with suspensions/dispersions of polystyrene and bovine serum albumin (BSA).

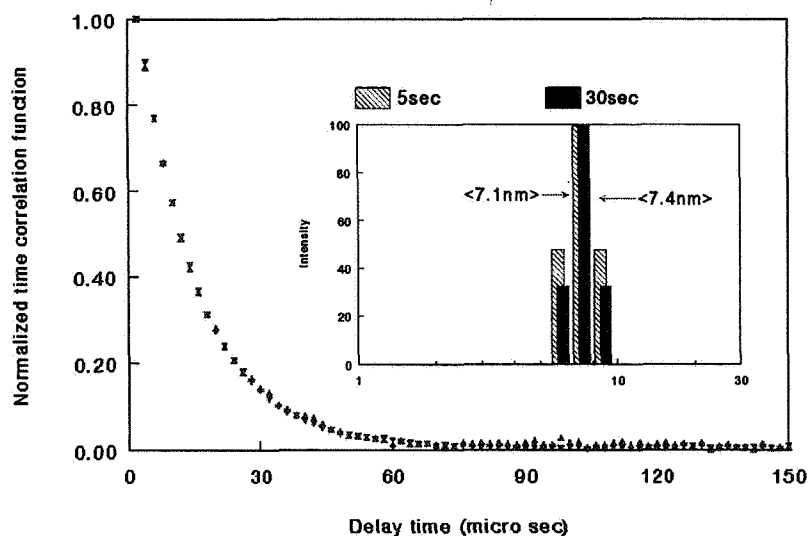


Figure 3. Normalized time correlation function (TCF) and particle size distribution for a 2% BSA solution using a laser power of 1.0mW at 5 and 30 second experiment duration.

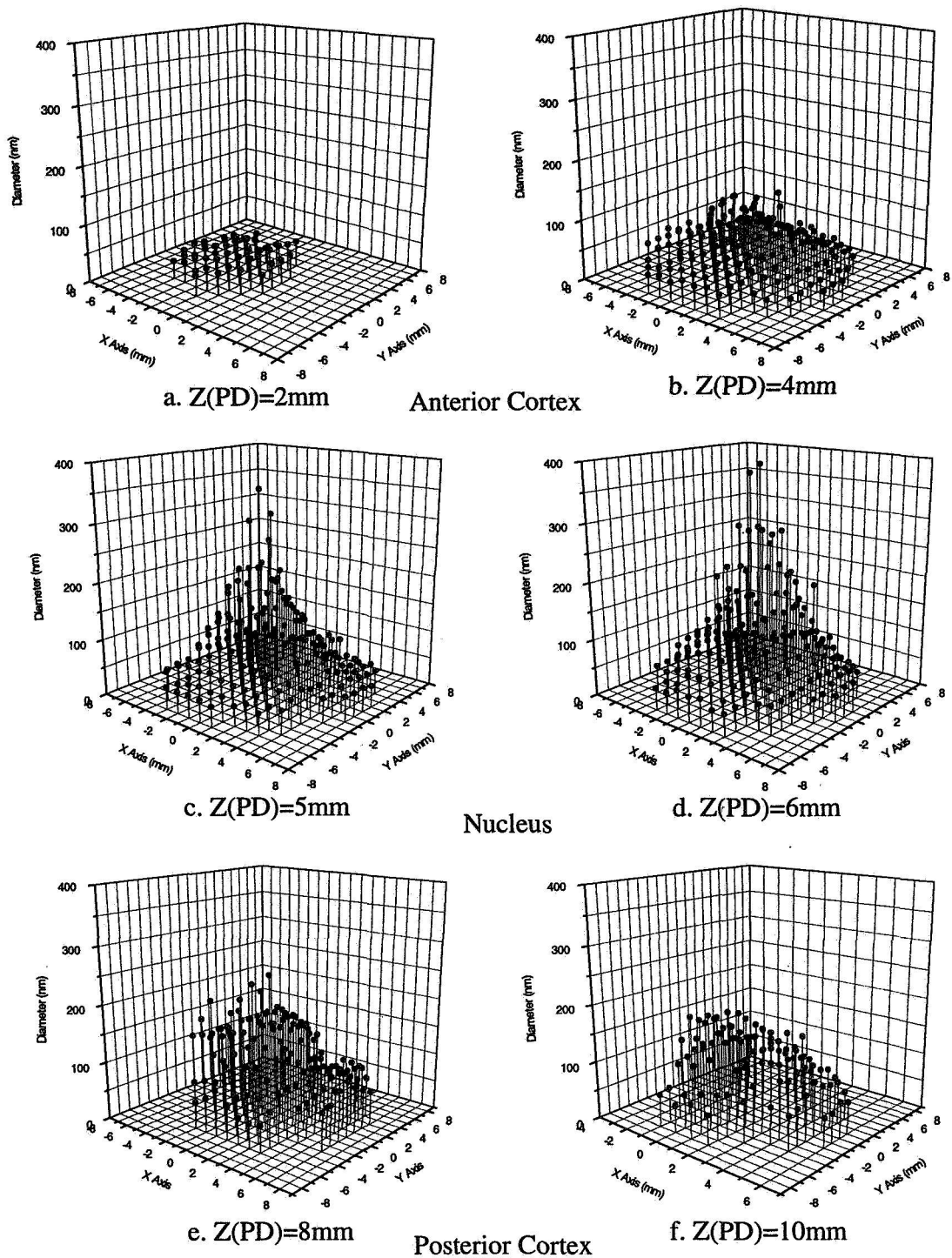


Figure 4. 3-D scanning of a bovine eye lens. The Z(PD)-axis represents the distance (penetration depth) from the front surface of the lens to the measurement point inside the lens.

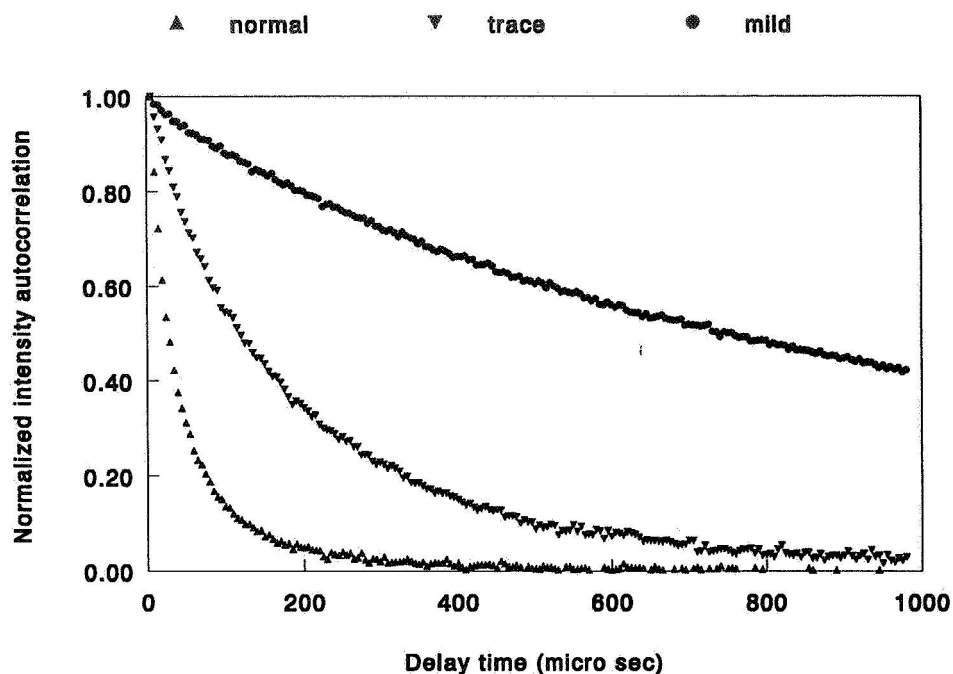


Figure 5. In-vivo cataractogenesis (DLS) measurements in Philly mice.

The Philly mouse is a good animal model of hereditary cataract<sup>20</sup>. Philly mice develop cataracts spontaneously between day 26 and 33 after their birth. This mouse model can be useful in the screening of anti-cataract drugs. We report a series of DLS experiments performed in Philly mice in collaboration with National Eye Institute (NEI) of National Institutes of Health (NIH). We applied our DLS probe to study the progression of cataractogenesis in this mouse model and to show the feasibility and safe use of our device in laboratory animals. Figure 5 shows DLS time correlation data on three Philly mice. It is quite challenging to perform DLS measurements in these animals because these animals have very small eyes. The lens in these animals has a diameter of less than 2 mm. The data includes a 45 day old normal mouse of the control FVB/N strain and two Philly mice roughly 26-29 days old. The eye examinations of these mice conducted with a slit-lamp apparatus concluded a normal (transparent) and two other eyes having trace and mild cataracts. These examinations were conducted within few minutes of the DLS measurements. Each measurement only took 5 seconds at a laser power of 50  $\mu$ W. The changing slope of the time correlation functions is an indication of cataractogenesis. We can quantitatively monitor

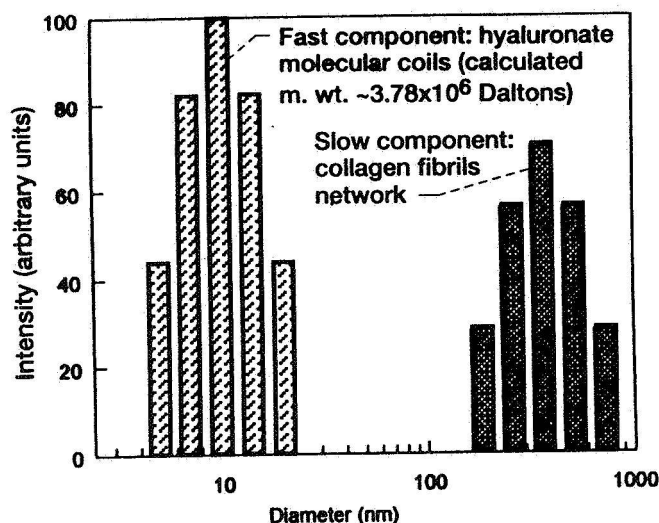


Figure 6. Size distribution for a 6 month old rabbit vitreous humor. Penetration depth from the corneal surface is 11mm.

cataractogenesis with reasonable reliability and reproducibility (5%-10%)<sup>21</sup>.

The vitreous humor of the eye described by Sebag<sup>22</sup> is the least understood part of an eye. We present preliminary DLS measurements made in vivo on a six month old live rabbit. The vitreous body shows strongly two-exponential behavior, i.e. a fast and a slowly diffusing component, consistent with its gel-like properties. We see almost constant value for the fast component in this region. We ascribe this fast component due to the diffusion of hyaluronate molecular coils in water and the slow diffusion component due to the collagen-fibril network. A size distribution of the vitreous is presented in Figure 6. We calculated the molecular weight for the fast component to be  $3.78 \times 10^6$  daltons. This is consistent with the range ( $2-4.5 \times 10^6$ ) of values given by Balazs and Delinger<sup>23</sup>. More in-vivo experimental work is being performed at this time in our laboratory to fully understand the structure of the vitreous humor. We have recently concluded three dimensional (3-D) scans of the bovine vitreous which is reported elsewhere<sup>12</sup>.

## CONCLUSION

In this report we have briefly described a new DLS probe to characterize various biological fluids, protein crystals, and ophthalmic diseases. The new probe is compact, rugged, non-invasive, and is free of optical alignment. Furthermore, it uses very low laser power, produces data with high spatial coherence, and exhibits no adverse effect of multiple light scattering even with highly concentrated systems (up to 10% w/v with particle size of 800nm in diameter). The probe has been and is being successfully used for several different applications in various challenging environments including monitoring protein nucleation, aggregation, and crystallization in various space-bound (microgravity) hanging drop apparatus<sup>9</sup>, eye diagnostics experiment on live animals as well as excised eyes<sup>10-12</sup>, a zeolite crystal growth experiment<sup>13</sup>, experiments in a rotating cell to minimize the sedimentation due to the gravitational effect, and clay-polymer interaction in a graduated cylinder.

## ACKNOWLEDGMENTS

The authors are grateful to the Microgravity Science and Applications Division (MSAD), code UG of the NASA headquarters for supporting this research. This work was completed under a NASA grant NCC 166-3/CWRU. The Philly mice were made available by S. Zigler and P. Russell of the National Eye Institute, Bethesda, MD. Kwang Suh would like to thank NASA Lewis Research Center and the National Research Council for the award of a postdoctoral research fellowship.

## REFERENCES

1. R. G. W. Brown, J.G. Burnett, J. Mansbridge, and C. I. Moir, "Miniature Laser Light Scattering Instrumentation for Particle Size Analysis," *Appl. Opt.* **29**, 4159-4169, 1990.
2. R. G. W. Brown, "Optical fibre sensing using light scattering techniques," *J. Phys. E: Sci. Instrum.*, **20**, 1312-1320 (1987).
3. Weiss and D. Horn, "Single-mode fibers in fiber-optic quasielastic light scattering: A study of the dynamics of concentrated latex dispersions," *J. Chem. Phys.*, **94**, 6429-6443 (1991).
4. Dhadwal, H.S., Ansari, R.R., Meyer, W.V., "A fiber Optic Probe for Particle Sizing in Concentrated Suspensions", *Rev. Sci. Instrum.* **62** (12), December 1991.
5. Ansari, R.R., Dhadwal, H.S., Campbell, M.C.W., and DellaVecchia, M.A., "A Fiber Optic Sensor for Ophthalmic Refractive Diagnostics", *Proc. of Fiber Optic Medical and Fluorescent Sensors and Applications*, January 23-24, 1992, Los Angeles, CA., SPIE Vol. 1648.
6. Dhadwal, H.S., Ansari, R.R., DellaVecchia, M.A., "Coherent Fiber Optic Sensor for Early Detection of Cataractogenesis in a Human Eye Lens", *J. Opt. Engineering*, Vol. 32, No. 2, February 1993.
7. H.S. Dhadwal, R.R. Ansari, M.A. DellaVecchia, S. Dubin, "Fiber optic system for in vivo sizing of proteins in animal eye lenses", *proc. Ophthalmic Technologies V*, SPIE, vol. 2393, pp. 227-236, 4-5 February 1995, San Jose, CA.
8. R. R. Ansari and K. I. Suh, "Sizing of colloidal particles and protein molecules in a hanging fluid drop," *Proc. Biomedical Optoelectronics in Clinical Chemistry and Biotechnology*, SPIE, Bios Europe '95, September 12-16, 1995, **2629** (23), Barcelona, Spain.
9. R. R. Ansari, K. I. Suh, A. Arabshahi, W. W. Wilson, T. L. Bray, and L. J. DeLucas, "A fiber optic probe for monitoring protein aggregation, nucleation, and crystallization," accepted for publication, *J. Crystal Growth*, 1996.



10. R. R. Ansari, K. I. Suh, M. A. DellaVecchia, and S. Dubin, "Early diagnosis of cataracts using a fiber optic system," in audio/video Proc. Cataract and Refractive Surgery: Current Issues, Session 2-B, ASCRS Symposium on Cataract, IOL and refractive surgery, April 1-5, 1995, San Diego, CA.
11. R. R. Ansari, K. I. Suh, M. A. DellaVecchia, and S. Dubin, "Ophthalmic diagnostics using a new dynamic light scattering fiber optic probe," Proc. Medical Application, Conference on laser in Ophthalmology III, SPIE, Bios Europe '95, September 12-16, 1995, **2632** (18), Barcelona, Spain.
12. R. R. Ansari and K. I. Suh, "Three-dimensional scanning of eye (lens and vitreous) using a newly developed dynamic light scattering probe," Proc. Ophthalmic Technologies VI, SPIE, Bios '96, January 27 - February 2, 1996, **2673**, San Jose, CA.
13. K. S. N. Reddy, L. M. Salvati, P. K. Dutta, P. Abel, K. Suh, and R. R. Ansari, "Reverse micelle based growth of zincophosphate sodalite : examination of crystal growth," accepted for publication, J. Phys. Chem., 1996.
14. G. A. Casay and W. W. Wilson, "Laser scattering in a hanging drop vapor diffusion apparatus for protein crystal growth in a microgravity environment," J. Crystal Growth, **122**, 95-101, 1992.
15. A. J. Malkin and A. McPherson, "Light-scattering investigations of nucleation processes and kinetics of crystallization in macromolecular systems," Acta Cryst. **D50**, 385-395, 1994.
16. J. Shulman, "Cataracts : The complete guide from diagnostics to recovery for patients and families," St. Martins Press, New York, 1993.
17. T. Tanaka and G. B. Benedek, "Observation of protein diffusivity in intact human and bovine lenses with application to cataract," Investigative ophthalmology, **14**(6), 449-456 (1976)
18. S. E. Bursell, P. C. Magnante and L. T. Chylack Jr., "In vivo uses of quasielastic light scattering spectroscopy as a molecular probe in the anterior segment of the eye," in Noninvasive Diagnostic Techniques in Ophthalmology, editor Barry R. Masters, Springer-Verlag, New York (1990)
19. L. Rovati, F. Frankhauser II, and J. Ricka, "Dynamic light scattering spectroscopy of in-vivo human vitreous," Proc. Medical Application, Conference on laser in Ophthalmology III, SPIE, Bios Europe '95, September 12-16, 1995, **2632** (18), Barcelona, Spain.
20. F. Kador, H. N. Fukui, S. Fukushi, H. M. Jernigan Jr., and J. H. Kinoshita, "Philly Mouse: A New Model of Hereditary Cataract", Exp. Eye Res. **30**, 59-68, 1980.
21. R. Ansari and K. I. Suh, "In situ and in vivo diagnostics of biological fluids," Proc. Optical Diagnostics of Biological Fluids, SPIE, Bios '96, January 27 - February 2, 1996, **2678C**, San Jose, CA.
22. J. Sebag, "The Vitreous; structure, function, and pathobiology", Springer-Verlag, 1989.
23. Balazs, J.L. Denlinger, "The Vitreous", in: The Eye, vol. IA, editor, H. Davson, Academic Press, pp. 533-589, 1984.



# APPLICATION OF PHASE SHIFTED, LASER FEEDBACK INTERFEROMETRY TO FLUID PHYSICS

Ben Ovryn<sup>1</sup>, Steven J. Eppell<sup>2</sup>, James H. Andrews<sup>3</sup> and John Khaydarov<sup>4</sup>

<sup>1</sup>NYMA Inc. NASA Lewis Group  
NASA Lewis Research Center, MS 110-3  
21000 Brookpark Road  
Cleveland, Ohio 44135  
ovryn@wave.lerc.nasa.gov

<sup>2</sup>Department of Biomedical Engineering  
Case Western Reserve University  
Cleveland, Ohio 44106  
<sup>3,4</sup>Ohio Aerospace Institute  
<sup>3</sup>Currently with: Department of Physics  
Youngstown State University

## ABSTRACT

We have combined the principles of phase-shifting interferometry (PSI) and laser-feedback interferometry (LFI) to produce a new instrument that can measure both optical path length (OPL) changes and discern sample reflectivity variations. In LFI, coherent feedback of the incident light either reflected directly from a surface or reflected after transmission through a region of interest will modulate the output intensity of the laser. LFI can yield a high signal-to-noise ratio even for low reflectivity samples.

By combining PSI and LFI, we have produced a robust instrument, based upon a HeNe laser, with high dynamic range that can be used to measure either static (dc) or oscillatory changes along the optical path. As with other forms of interferometry, large changes in OPL require phase unwrapping. Conversely, small phase changes are limited by the fraction of a fringe that can be measured. We introduce the phase shifts with an electro-optic modulator (EOM) and use either the Carre or Hariharan algorithms to determine the phase and visibility.

We have determined the accuracy and precision of our technique by measuring both the bending of a cantilevered piezoelectric bimorph and linear ramps to the EOM. Using PSI, sub-nanometer displacements can be measured. We have combined our interferometer with a commercial microscope and scanning piezoelectric stage and have measured the variation in OPL and visibility for drops of PDMS (silicone oil) on coated single crystal silicon. Our measurement of the static contact angle agrees with the value of 68° stated in the literature.

## INTRODUCTION

### Optical response of the laser feedback interferometer

The optical response of the laser with external feedback is in general a nonlinear function of the reflectivity of the object and the variation in the optical path length. The governing model (Figure 1) considers the reflection from the sample ( $M_3$ ) as forming a Fabry-Perot interferometer with the output mirror of the laser ( $M_2$ ). Our model for the modulation of the irradiance of the cavity neglects the finite response time of the laser cavity (an assumption which is valid in our experiments), assumes that the reflectivity,  $R_2$ , of the laser mirror ( $M_2$ ) is close to unity and includes the possibility of multiple reflections from the sample. The irradiance in the interferometer, which is a function of the reflectivity of the sample and the optical path length,  $\delta(t)$ , is given as (for details of the derivation see Ovryn et. al.)<sup>1</sup>:

$$I(m, \delta(t)) = I_o \left( 1 + m \sum_{i=1}^{\infty} (R_2 R_3)^{\frac{i-1}{2}} \cos \left( \frac{i4\pi}{\lambda} \delta(t) + \Psi \right) \right) \quad (1)$$

where  $\delta(t)$  is the change in the optical path length (OPL),  $\Psi$  represents an arbitrary overall phase factor,  $I_o$  is the average laser irradiance, and  $m$  is the modulation parameter (fringe visibility) which is given as:

$$m = \gamma \sqrt{R_3} \quad (2)$$

where  $\gamma$  is a function of the reflectivities of the laser mirrors and intrinsic laser parameters. Significantly, it can be

observed that the fringe modulation is directly proportional to the amplitude reflectivity of the object. When multiple reflections from the object can be ignored only the first term in the summation is significant and the response of the interferometer, Eq. 1, simplifies to:

$$I(m, \delta(t)) = I_o (1 + m \cos(\frac{4\pi}{\lambda} \delta(t) + \Psi)) \quad (3)$$

For a d.c. and oscillatory change in OPL,  $\delta(t) = n(a + b \sin \omega t)$ , Eq. 1 yields, ( $\Psi = 0$ ):

$$I(\omega, t) = I_o (1 + m (\cos(2kna)J_0(2knb)) - 2 \sin(2kna)J_1(2knb) \sin(\omega t) + 2 \cos(2kna)J_2(2knb) \sin(2\omega t) - \dots) \quad (4)$$

### Phase shifting interferometry

When multiple reflections are negligible, the interferometer response of Eq. 3 is the standard form for a two beam interferometer. In this case, phase shift methods can be applied to determine the OPL and the fringe visibility. In phase shifting interferometry (PSI) a series of experimentally controlled optical path length changes are introduced in order to solve for the sample's phase,  $\phi(t)$ , and visibility,  $m(t)$  from a least squares solution to an over determined set of measurements.<sup>1,2</sup> There are several algorithms which can be employed; in our work, we have used either the Carre or the Hariharan algorithm to solve for the phase and the visibility.<sup>1,2</sup> The strength of using an over determined set of measurements is that a solution for the phase,  $\phi(t)$ , can be found which is independent of the other unknowns ( $I_o$  and  $m$ ); similarly, a solution can be found for  $m(t)$  which is independent of  $\phi(t)$  and  $I_o$ . Since the phase is determined modulo  $2\pi$ , the phase must be unwrapped in order to determine large changes in the OPL. Additionally, there is no ambiguity in the sign of the change in the OPL. As an illustration of this approach, consider the case where four phase shifts are used:  $\Psi_1=0$ ,  $\Psi_2=\pi/2$ ,  $\Psi_3=\pi$ ,  $\Psi_4=3\pi/2$ . Substituting these phase steps into Eq. 3, produces a set of four equations:

$$\begin{aligned} I_1(t) &= I_o (1 + m(t) \cos \phi(t)) & I_3(t) &= I_o (1 + m(t) \cos(\phi(t) + \pi)) \\ I_2(t) &= I_o (1 + m(t) \cos(\phi(t) + \frac{\pi}{2})) & I_4(t) &= I_o (1 + m(t) \cos(\phi(t) + \frac{3\pi}{2})) \end{aligned}$$

Therefore:

$$\begin{aligned} \tan \phi(t) &= \frac{I_2(t) - I_4(t)}{I_3(t) - I_1(t)} & I_o &= \frac{(I_1(t) + I_2(t) + I_3(t) + I_4(t))}{4} \\ m(t) &= \frac{\sqrt{(I_2(t) - I_4(t))^2 + (I_3(t) - I_1(t))^2}}{2I_o} \end{aligned}$$

### METHODS

There are several configurations that can be used to observe laser feedback effects. The laser power can be monitored by dividing the beam (using a beam splitter) from the front mirror of the laser or, as in our experiments, by monitoring the power of the beam which leaves the back mirror. In this simple configuration, the interferometer can be used for fringe counting. To achieve higher accuracy, we use an electro-optic modulator situated in the beam path between the front mirror of the laser and the object and employ PSI techniques.

### Measurement of the harmonic response of the laser feedback interferometer

To verify the harmonic response of LFI, Eq. 4, we performed the following experiments. The light from a HeNe laser (Uniphase, 1107P), was modulated with an electro-optic modulator (New Focus, 4002 and New Focus, high voltage amplifier 3211) before passing through a pair of linear polarizers and illuminating a mirror mounted on a piezoelectric translator (Burleigh, PZ 81 with RC-44 driver). After reaching the mirror, the light was retro-reflected and re-entered the laser cavity. The power of the beam from the rear mirror of the laser was measured using a photodetector (New Focus, 1201 or 1801). The frequency and amplitude of the sinusoidal voltage to both the mirror and EOM were controlled independently by using a function generator (Stanford Research Systems, DS 340) and the source out on a spectrum analyzer (Stanford Research Systems, 770), respectively. The signal from the photodetector was sent directly to the spectrum analyzer and saved as a digitized waveform. In this configuration, changes in the optical path length could be achieved by changing the d.c. offset on the high voltage EOM amplifier.

### Calibration of the phase shifting method using a piezoelectric bimorph

In order to prove the utility of the phase shift method as applied to LFI, we measured the cantilever bending of a piezoelectric bimorph; the bending of the bimorph is directly proportional to the applied voltage and is a quadratic function of the cantilever length.<sup>1</sup> Figure 2 presents a schematic of the apparatus used for this measurement. The bimorph was mounted in a clamp so that it formed a cantilever 20 mm in length. The clamp was attached to a uniaxial translation stage (UT 100, Klinger Inc.) which operated under closed loop control. A long working distance 50 x 0.42 NA objective (G Plan NIR, Mitutoyo, Inc.) was used to focus the laser spot on the surface of the bimorph.<sup>2</sup>

The phase was measured using the Carre algorithm with the four phase shifts introduced by applying discrete voltages to the electro-optic modulator. The phase shifts were controlled by a board inside a PC (DAS 1800HR, Keithley Inc.) which also acquired the voltage either directly from the photodetector; samples were digitized at 16 bits at up to 100 kHz. After acquiring the four phase shifts, the PC determined the phase, the visibility and  $I_0$  on line. Our program also allows the user to average repeated phase measurements and provides the option of collecting many samples of the signal voltage from the photodetector at each phase shift and averaging. To determine the bending, the difference in phase before and after applying a voltage to the bimorph was obtained at various positions on the surface. The entire apparatus was mounted on a vibration isolation table and enclosed in a double Plexiglass box which reduced thermal drift and acoustical excitation; before data collection, the laser was at thermal equilibrium.

### Measurement of random and systematic errors associated with the PSI-LFI method

To determine the random and systematic errors associated with the phase shift method, the bimorph was replaced with a small piece of single crystal silicon which was held fixed at the focus of the microscope objective. The change in phase due to a slowly varying (0.1 Hz) triangular wave applied to the EOM was measured for varying amounts of incident power on the sample; the magnitude of the ramp was set to provide a change in the optical path length of approximately 316 nm. To vary the power in the object beam, two polarizers were placed between the EOM and the back aperture of the microscope objective. A fixed linear polarizer was situated directly behind the EOM with orientation parallel to the polarization of the laser and a linear polarizer on a rotation stage (New Focus, 5524 and 8401) was placed between the first polarizer and the objective lens. The phase and visibility were measured using the Hariharan algorithm at several fixed settings of the rotatable polarizer as the power on the sample varied.

### Measurement of the static contact angle of PDMS on coated silicon wafer

To produce high spatial resolution measurements over a whole field, we have combined our phase-shifted LFI with a piezoelectric stage which translated the sample along two axes under closed-loop control (S221, Queensgate, Inc.) and incorporated the instrument into a commercial microscope (Jenavert, Carl Zeiss).<sup>2</sup> We produced images of small drops of 60,000 cS PDMS (silicone oil) which were placed on a fluorinated (FC-723, 3M, Inc.) coated single crystal silicon wafer; the surface of the wafer was wiped with toluene and dipped into the barrier coat. Images were obtained by measuring the phase and visibility at discrete points on the drop and substrate with a 50 x 0.8 NA objective.

## RESULTS

### Harmonic response of the laser feedback interferometer

Figure 3 (left) shows the maximized first and second harmonics (top and bottom, respectively) when the EOM was modulated with a sinusoidal voltage at 2 kHz while the piezoelectric mirror remained stationary. The amplitude of the harmonic terms were controlled by varying the d.c. voltage ( $a$  in Eq. 4) to the EOM. These results illustrate that the even and odd harmonics are in phase quadrature.

Figure 3 (right) shows the LFI response when the EOM was modulated at 30 kHz and the mirror was oscillated at 3 kHz. Figure 3 (top, right) shows the effect of maximizing the LFI response at the fundamental frequency. In this case, both the 30 kHz EOM signal and the weaker 3 kHz signal from the mirror can be observed. An interesting effect is observed when the second harmonic response is maximized (Fig. 3, bottom, right); not only is the second harmonic of the EOM maximized at 60 kHz, but a response is observed at 33 and 27 kHz; this beating between the two frequencies can also be viewed as sum and difference frequency LFI, respectively.

### Calibration of the phase shifting method using a piezoelectric bimorph

Figure 4 illustrates the measured bending of the piezoelectric bimorph for two separate voltages, 4.0 volts (insert) and -0.5 V. The data were acquired using four discrete phase shifts (with the Carre algorithm) and by obtaining the change in the optical path length cause by the applied voltage. Superimposed on each curve is a quadratic fit, which represents the predicted shape. The method unambiguously predicts the direction of the bending.<sup>1</sup>

### Measurement of random and systematic errors associated with the phase shift method

Figure 5 shows the variation in OPL and visibility due to phase drift during a 90 second period; the visibility was essentially constant during this time period. Systematic drift has also been observed.<sup>1,2</sup> Figures 6 and 7 show the change in the optical path length (top) and fringe modulation (middle) due to a ramp applied to the EOM. In Figure 6, the average modulation was 0.0488; while in Figure 7, the maximum amount of light was allowed to pass through to the object. Also shown in Figures 6 and 7 is the difference in OPL between a half-period of the ramp and a least squares fit to the ramp (bottom curves). Periodic variations in the OPL (Fig. 7 bottom) and in visibility (Fig. 7, middle) can be observed for the higher visibility case. For the lower visibility case, the systematic errors no longer dominate and the rms phase error was 0.3 nm. The rms error in OPL calculated for a range of fringe visibilities indicates that the minimum error in the OPL (0.3 nm) was achieved for a visibility of 0.05.<sup>1</sup>

### Measurement of the static contact angle of PDMS on coated silicon wafer

Figure 8 show the variation in the optical path length (left) and the visibility (right), respectively, for a 26  $\mu\text{m}$  diameter drop of silicone oil ( $n=1.447$ ). It can be observed that the visibility falls off very rapidly at the periphery of the drop. The static contact angle for this drop was calculated from twice the inverse tangent of the ratio of the height to the radius of the drop. The apex of the drop was determined to be 8.8  $\mu\text{m}$  above the substrate and the diameter of drop was determined to be 26  $\mu\text{m}$ . The contact angle of 68° agrees with the literature.<sup>3</sup>

The measurement of the OPL requires not only a measurement of the phase, but also knowledge of the index of refraction of the fluid and a determination of the correction factor for the microscope objective. The correction factor for the objective was determined from the literature to be 1.26.<sup>4</sup> We have not yet measured the accuracy of the correction factor for our microscope objective. Additionally, we have not yet determined the accuracy of the scanning stage; the closed loop stage has a stated precision of 5 nm.

## DISCUSSION and CONCLUSIONS

We have designed a laser feedback interferometer which can be used to measure oscillatory and d.c. changes in the OPL. We have successfully combined the principles of PSI with LFI. We have measured the bending curve for a piezoelectric bimorph to verify the accuracy and precision (Fig 4).<sup>1,2</sup> Figures 6 and 7 verify that sub-nanometer d.c.

(and slowly time varying) displacements can be measured with this method. While we have found that the combination of PSI and LFI has produced a robust measuring technique, we have also observed several nuances of its behavior. We have observed systematic oscillations in the determination of the fringe visibility and the optical path length caused by the breakdown of the assumption that multiple reflections can be ignored; we have developed a model to describe this error.<sup>1,2</sup>

Our preliminary measurement of the static contact angle of PDMS on fluorinated silicon agree with the literature, however, we have not yet determined the precision of this measurement. Since the phase changes rapidly at the edge of the drop, high spatial resolution is required to adequately sample the phase. As further calibration of the technique, we intend to measure a range of contact angles.

## ACKNOWLEDGEMENTS

This work is funded under a MSAD Advanced Technology Development Grant to NASA Lewis. We thank Jeff Mackey (NYMA, Inc.) for providing the index of refraction of PDMS.

## REFERENCES

1. Ovrn, B; Andrews, J.H., Eppell, S. and Khaydarov, J.: Phase-shifted, real-time laser feedback interferometry, SPIE Vol. 2860, 1996, pp 263-275.
2. Ovrn, B; Andrews, J.H., and Eppell, S: Phase-measuring laser feedback interferometry: applications to microscopy, SPIE Vol. 2655, 1996, pp 153-163.
3. Extrand, C.W: Spontaneous spreading of viscous liquid drops, J. Colloid and Interface Sci, 157, 1993, 72-76.
4. Schulz, G. and Elssner, K. E.: Errors in phase-measurement interferometry with high numerical apertures, Appl. Opt. 30, 1991, 4500- 4506.

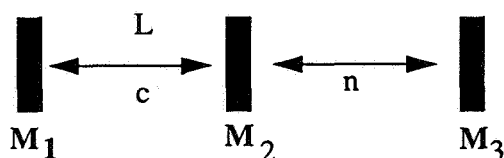


Figure 1. Model for the effect of feedback from the sample, represented by M<sub>3</sub>.

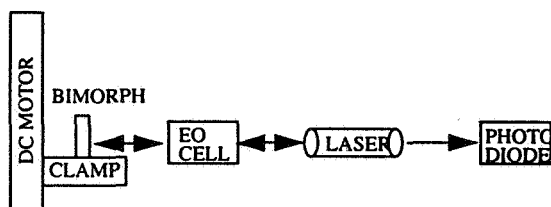


Figure 2. Schematic diagram of the LFI used to measure cantilever bending of the bimorph.

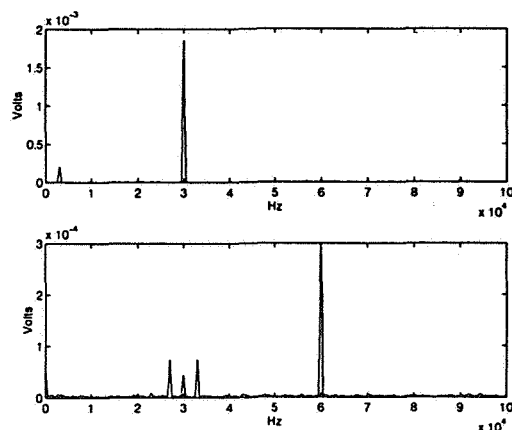
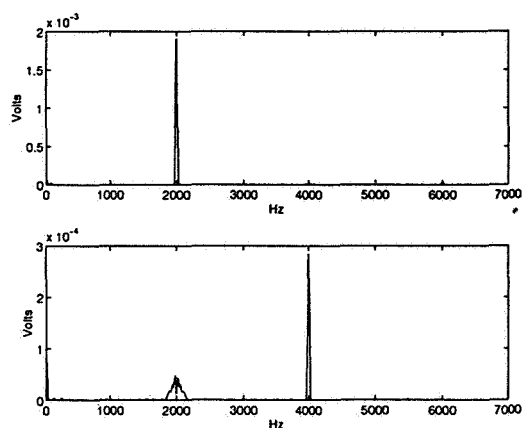


Figure 3. The harmonic response of the interferometer when the EOM was modulated at 2 kHz with the sample (mirror) held stationary (left) and with the EOM oscillating at 30 kHz and the mirror at 2 kHz (right). Changing the dc offset to the EOM was used to maximize either the fundamental (top) or second harmonic (bottom).

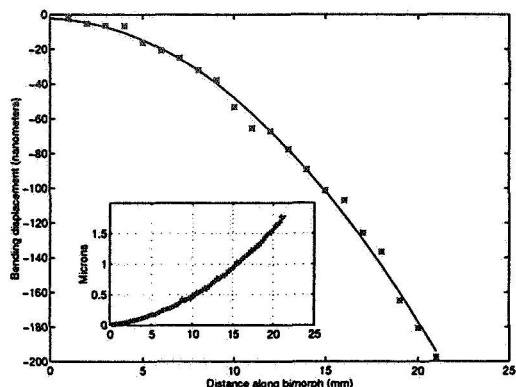


Figure 4. Bending curves for the bimorph for when two separate voltages were applied: 4.0 V (inset) and -500 mV.

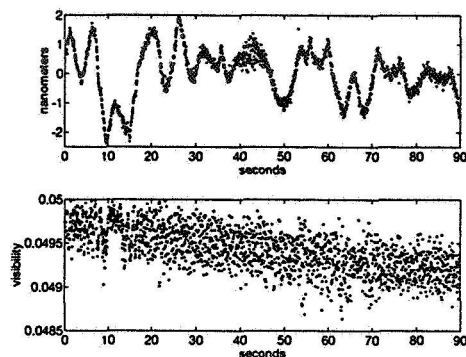


Figure 5. Drift in the optical path and visibility during a 90 second period. The visibility was essentially constant during this period.

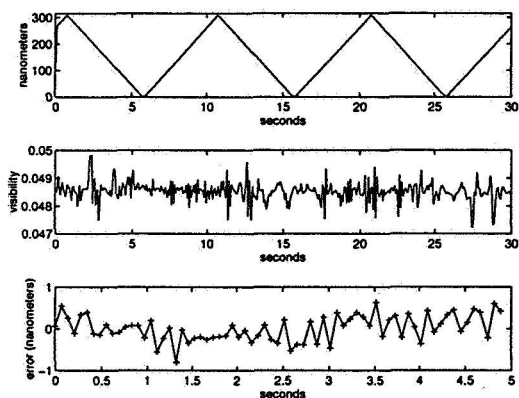


Figure 6. OPL variation caused by a 0.1 Hz ramp applied to the EOM (top). Also shown is the fringe visibility (middle) and the phase error (bottom). The phase error was calculated from the difference between a data and a least squares line.

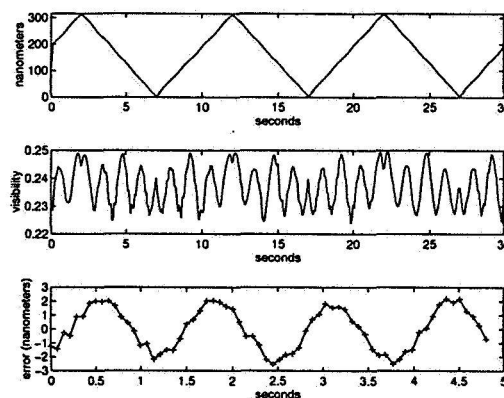


Figure 7. OPL variation caused by a 0.1 Hz ramp applied to the EOM (top) when the visibility was set to the maximum value. Also shown is the fringe visibility (middle) and the phase error (bottom).

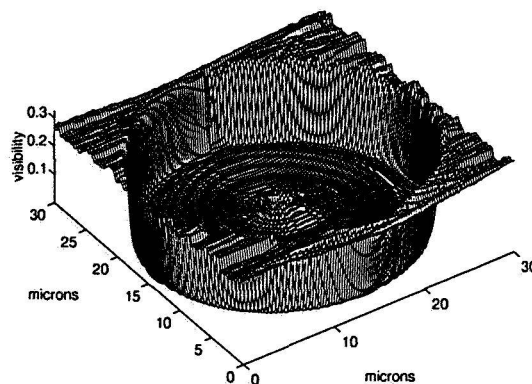
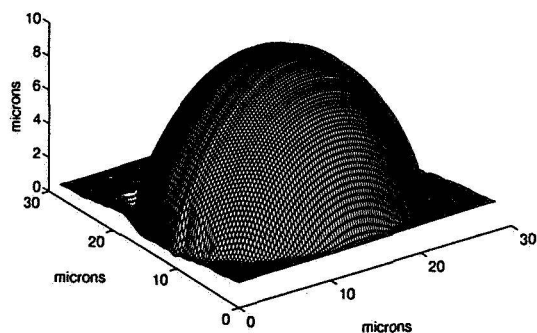


Figure 8. OPL (left) and visibility (right) variation across a static PDMS drop on fluorinated silicon wafer. The image was produced using a 50 x 0.8 NA objective. Scanning time was about 50 msec/data pixel; the images are 240 x 240 pixels.



**Laser light scattering—expanding the boundaries**

William Meyer, Ohio Aerospace Institute/NASA Lewis

**Paper not available**



# NASA's Third Microgravity Fluid Physics Conference Cleveland, Ohio

## *Wednesday, June 12, 1996*

- 2-5 P.M. Tour of NASA Lewis (advance reservation required); leaving from Sheraton  
5-8 P.M. Registration and cash bar: Sheraton City Centre Hotel (Grand Ballroom Lobby)

## *Thursday, June 13*

- 7:30 A.M. Registration (Grand Ballroom Lobby): Sheraton City Centre Hotel  
9:00 Opening plenary (Grand Ballroom); Chair: Jack Salzman, NASA Lewis  
Welcome—Martin Kress, NASA Lewis  
9:15 Conference objectives—Brad Carpenter, NASA Headquarters  
9:35 Conference organization—Richard Ziegfeld, NYMA  
9:45 Keynote: History and future development of the moon: opportunities for fluid physicists—Michael Duke, Lunar and Planetary Institute  
10:30 Break  
11:00 Microgravity research opportunities—Stephen Davis, Northwestern University  
11:20 Space flight experiment in the Space Station era—Edward Winsa, NASA Lewis  
11:40 Process for selecting investigators for space flight experiments—Jack Salzman, NASA Lewis  
12:00 Lunch  
1:30 P.M. Parallel Session 1 (5 papers/breakout): 3 parallel breakouts  
3:10 Break  
3:40 Parallel Session 2 (6 papers/breakout): 3 breakouts  
5:40 Free time  
6:30 Reception (Grand Ballroom)  
7:30 Dinner (Grand Ballroom)  
8:30 After Dinner Session (Grand Ballroom): Jack Salzman, NASA Lewis, presiding  
Experiences with critical point experiments in microgravity—Michael Moldover, NIST

## *Friday, June 14*

- 8:00 A.M. Friday Plenary (Grand Ballroom) Chair: S. George Bankoff, Northwestern  
Keynote: Multiphase flow: the gravity of the situation—Geoff Hewitt, Imperial College, London  
8:40 Break  
9:00 Parallel Session 3 (4 papers/breakout): 3 breakouts  
10:20 Break  
10:40 Parallel Session 4 (4 papers/breakout): 3 breakouts  
12:00 Lunch  
1:30 P.M. Parallel Session 5 (5 papers/breakout): 3 breakouts  
3:10 Break  
3:30 Parallel Session 6 (6 papers/breakout): 3 breakouts  
5:30 Break  
7:30 International Forum (Dolder-Hassler) Chair: Brad Carpenter, NASA Headquarters

## *Saturday, June 15*

- 8:00 A.M. Saturday plenary (Grand Ballroom) Chair: Paul Chaikin, Princeton University  
Keynote: Complex fluids: science, technology and microgravity—David Weitz, University of Pennsylvania  
8:40 Break  
9:00 Parallel Session 7 (4 papers/breakout): 3 breakouts  
10:20 Break  
10:40 Parallel Session 8 (4 papers/breakout): 3 breakouts  
12:00 Lunch in hotel (Dorothy Fuldheim Room); forum: NRA plans, questions/answers; Brad Carpenter, NASA Headquarters, presiding  
1:30 P.M. Parallel session 9 (5 papers/breakout): 3 breakouts  
3:10 Adjourn

## **Wednesday, June 12, 1996**

2:00 - 5:00 p.m. Tour of NASA Lewis Research Center

5:00 - 8:00 p.m. Registration and Cash Bar

Sheraton City Centre Hotel

(Grand Ballroom Lobby)

---

## **Thursday, June 13, 1996**

### **Morning**

7:30 a.m.	Registration (Grand Ballroom Lobby)
9:00 a.m. - 12:00 noon	Opening Plenary Jack Salzman, Chair, NASA Lewis (Grand Ballroom)
9:00 a.m.	Welcome Martin Kress, NASA Lewis
9:15 a.m.	Conference Objectives Brad Carpenter, NASA Headquarters
9:35 a.m.	Conference Organization Richard Ziegfeld, NYMA
9:45 a.m.	Keynote: History and future development of the moon: opportunities for fluid physicists Michael Duke, Lunar and Planetary Institute
10:30 a.m.	Break
11:00 a.m.	Microgravity research opportunities Stephen Davis, Northwestern Univ.
11:20 a.m.	Space flight experiment in the Space Station era Edward Winsa, NASA Lewis
11:40 a.m.	Process for selecting investigators for space flight experiments Jack Salzman, NASA Lewis
12:00 - 1:30 p.m.	Lunch

**Thursday Afternoon**  
**Parallel Session 1**  
**1:30 - 3:10 p.m.**

**Multiphase Flow I**

**Session Chair: Hasan Oguz, Johns Hopkins Univ.  
 Grand Ballroom)**

**1:30 paper #86**

**Clark McCready, Univ. of Notre Dame:**  
 Fundamental processes of atomization in  
 liquid-fluid flows

**1:50 paper #88**

**John McQuillen, NASA Lewis:** Study of  
 two-phase gas-liquid flow behavior at  
 reduced gravity conditions

**2:10 paper #10**

**Emuri Balakotaiah, Univ. of Houston:**  
 Stability of wavy films in gas-liquid two-  
 phase flows at normal and microgravity  
 conditions

**2:30 paper #1**

**Yavood Abdollahian, S. Levy, Inc.:**  
 Experimental and analytical study of two-  
 phase flow parameters in microgravity

**2:50 paper #68**

**Edward Keshock, Cleveland State Univ.:**  
 Two-phase annular flow in helical coil  
 flow channels in a reduced gravity  
 environment

**Granular Media**

**Session Chair: Ashok Sangani,  
 Syracuse Univ.  
 (Ritz)**

**paper #63**

**James Jenkins, Cornell Univ.:**  
 Microgravity segregation in binary  
 mixtures of inelastic spheres driven by  
 velocity fluctuation gradients

**paper #46**

**Joe Goddard, Univ. of California-San  
 Diego:** Material instabilities in  
 particulate systems

**paper #16**

**Robert Behringer, Duke Univ.:** Dynamics  
 of granular materials

**paper #92**

**Masami Nakagawa, The Lovelace Inst.:**  
 NMRI measurements of flow of granular  
 mixtures

**paper #12**

**Rafat Ansari, Case Western Reserve  
 Univ./NASA Lewis:** A new generation  
 fiber optic probe for the characterization  
 of biological fluids, protein crystals and  
 ophthalmic diseases

**Thermocapillary Flows I**

**Session Chair: David Andereck, Ohio  
 State Univ.  
 (Dolder-Hassler)**

**paper #58**

**George Homsy, Stanford Univ.:**  
 Problems in microgravity fluid  
 mechanics: thermocapillary instabilities  
 and G-jitter convection

**paper #50**

**Hossein Haj-Hariri, Univ. of Virginia:**  
 Instability mechanisms in thermally-  
 driven interfacial flows in liquid-  
 encapsulated crystal growth

**paper #67**

**Robert Kelly, UCLA:** Studies in  
 thermocapillary convection of the  
 Marangoni-Benard type

**paper #71**

**Sindo Kou, Univ. of Wisconsin:**  
 Thermocapillary convection in low Pr  
 materials under simulated reduced-g  
 conditions

**paper #142**

**Abdelfattah Zebib, Rutgers Univ.:**  
 Oscillatory thermocapillary convection

3:10 - 3:40 p.m. Break

# **Thursday Afternoon**

## **Parallel Session 2**

### **3:40 - 5:40 p.m.**

#### **Solidification**

**Session Chair:** Ain Sonin, MIT  
(Grand Ballroom)

#### **3:40 paper #30**

Sam Coriell, NIST: Interface morphology during crystal growth: effects of anisotropy and fluid flow

#### **4:00 paper #33**

Stephen Davis, Northwestern Univ.: Shear stabilization of a solidifying front

#### **4:20 paper #102**

Dimos Poulikakos, Univ. of Illinois-Chicago: Fluid dynamics and solidification of molten solder droplets impacting on a substrate in microgravity

#### **4:40 paper #127**

Saleh Tanveer, Ohio State Univ.: Crystal growth and fluid mechanics problems in directional solidification

#### **5:00 paper #139**

Grae Worster, Cambridge Univ.: Interactions between solidification and compositional convection in alloys

**5:20**

#### **Colloids**

**Session Chair:** Ashok Sangani,  
Syracuse Univ.  
(Ritz)

#### **paper #37**

Douglas Durian, UCLA: The melting of aqueous foams

#### **paper #79**

Jing Liu, California State Univ.-Long Beach: Chain dynamics in a dilute magnetorheological fluid

#### **paper #2**

Bruce Ackerson, Oklahoma State Univ.: Growth and morphology of crystals made of hard spheres

#### **paper #28**

Noel Clark, Univ. of Colorado: Structure, hydrodynamics, and phase transition of freely suspended liquid crystals

#### **paper #22**

Paul Chaikin, Princeton Univ.: The dynamics of hard sphere colloidal dispersions

#### **paper #134**

David Weitz, Univ. of Pennsylvania: Colloid physics in microgravity

#### **G-jitter and Stochastic Flow**

**Session Chair:** George Homsy, St. Univ.  
(Dolder-Hassler)

#### **paper #132**

Jorge Viñals, Florida State Univ.: Fl physics in a fluctuating acceleration environment

#### **paper #105**

Seth Putterman, UCLA: Containerk ripple turbulence

#### **paper #59**

Norman Chigier, Carnegie Mellon U: Transport phenomena in stratified m fluid flow in the presence and absen gravity

#### **paper #3**

Iwan Alexander, Univ. of Alabama-Huntsville: Analysis of residual acceleration effects on transport and segregation during directional solidification of tin-bismuth in the MEPHISTO furnace facility

Peter Vrotsos, NASA Lewis: Space acceleration measurement and analy services available to the PI's

#### **paper #146**

Kamiel Rezkallah, Univ. of Saskatch Analysis of the hydrodynamics and t transfer aspects of microgravity two-flows

**5:40 p.m. Free time**

**6:30 p.m. Reception**  
(Grand Ballroom)

**7:30 p.m. Dinner**  
(Grand Ballroom)

**8:30 p.m.**

**After Dinner Session**

(Grand Ballroom) Jack Salzman, NASA Lewis, presiding  
Experiences with critical point experiments in microgravity  
Michael Moldover, NIST, speaker

**Friday, June 14, 1996**  
**Morning**

8:00 a.m. Friday Plenary  
S. George Bankoff, Chair, Northwestern  
(Grand Ballroom)

**Keynote:**  
Multiphase flow: the gravity of the situation  
Geoff Hewitt, Imperial College, London

8:40 a.m. Break

***Parallel Session 3***  
***9:00 - 10:20 a.m.***

**Multiphase Flow II**

**Session Chair:** Mark McCready, Univ. of Notre Dame  
(Grand Ballroom)

**9:00 paper #65**

Yasuhiro Kamotani, Case Western Reserve Univ.: Bubble generation in a flowing liquid medium and resulting two-phase flow in microgravity

**9:20 paper #94**

Hasan Oguz, Johns Hopkins Univ.: Production of gas bubbles in reduced gravity environment

**9:40 paper #73**

Richard Lahey, Rensselaer Polytechnic Inst.: Phase distribution phenomena for simulated microgravity conditions: experimental work

**10:00 paper #26**

Jacob Chung, Washington State Univ.: Bubble dynamics, two-phase flow, and boiling heat transfer in microgravity

**Liquid Bridges**

**Session Chair:** Paul Concus, Univ. of California-Berkeley  
(Ritz)

**paper #138**

Iwan Alexander, Univ. of Alabama-Huntsville: Dynamics and statics of nonaxisymmetric liquid bridges

**paper #85**

Philip Marston, Washington State Univ.: Stabilization and low-frequency oscillation of capillary bridges with modulated acoustic radiation pressure

**paper #116**

Michael Schatz, Univ. of Texas: Experimental control of thermocapillary convection in a liquid bridge

**paper #144**

William Meyer, OAI/Lewis: Laser light scattering—expanding the boundaries

**Convective Instability**

**Session Chair:** Hossein Haj-Hariri, Univ. of Virginia  
(Dolder-Hassler)

**paper #126**

Harry Swinney, Univ. of Texas: Long-wavelength instability in Marangoni convection

**paper #61**

Jeffrey Jacobs, Univ. of Arizona: An experimental study of Richtmyer-Meshokov instability

**paper #78**

Sung Lin, Clarkson Univ.: Absolute and convective instability of a liquid jet in microgravity

**paper #93**

Paul Neitzel, Georgia Inst. of Technology: Non-coalescence effects in microgravity

10:20 a.m. Break

**Friday Morning**  
**Parallel Session 4**  
**10:40 - 12:00 noon**

**Thermocapillary Flows II**  
**Session Chair: Abdelfattah Zebib,**  
**Rutgers Univ.**  
**(Grand Ballroom)**

**10:40 paper #4**

David Andereck, Ohio State Univ.:  
 Observations of time-dependent behavior  
 in the two-layer Rayleigh-Benard system

**11:00 paper #25**

Chuan Chen, Univ. of Arizona: Salt-  
 finger convection in a stratified fluid layer  
 induced by thermal and solutal capillary  
 motion

**11:20 paper #76**

A. Liakopoulos, Lehigh Univ.: Low-  
 dimensional dynamical models of thermal  
 convection

**11:40 paper #96**

Simon Ostrach, Case Western Reserve  
 Univ.: Surface tension driven convection  
 experiment

**Suspensions**  
**Session Chair: Bruce Ackerson,**  
**Oklahoma State Univ.**  
**(Ritz)**

**paper #39**

S. E. Elghobashi, Univ. of California-  
 Irvine: Effects of gravity on sheared  
 turbulence laden with bubbles or  
 droplets

**paper #115**

Ashok Sangani, Syracuse Univ.:  
 Behavior of rapidly sheared bubbly  
 suspensions

**paper #129**

Penger Tong, Oklahoma State Univ.:  
 Polymer-induced depletion interaction  
 and its effect on colloidal sedimentation  
 in colloid-polymer mixtures

**paper #48**

John Goree, Univ. of Iowa: Plasma dust  
 crystallization

**Bubbles and Drops I**  
**Session Chair: Grétar Tryggvason,**  
**Univ. of Michigan**  
**(Dolder-Hassler)**

**paper #18**

Luis Bernal, Univ. of Michigan:  
 Investigation of drop formation by a  
 vortex ring in microgravity

**paper #124**

Kathleen Stebe, Johns Hopkins Univ.:  
 Marangoni effects on drop deformation  
 and break-up in an extensional flow: the  
 role of surfactant physical chemistry

**paper #113**

Satwindar Sadhal, Univ. of Southern  
 California: Ground based studies of  
 thermocapillary flows in levitated drops

12:00 - 1:30 p.m. Lunch



**Friday Afternoon**  
**Parallel Session 5**  
**1:30 - 3:10 p.m.**

**Bubbles and Drops II**

**Session Chair: R. Subramanian,**  
**Clarkson Univ.**  
**(Grand Ballroom)**

**1:30 paper #21**

An-Ti Chai, NASA Lewis: Marangoni instability induced convection in evaporating liquid droplets

**1:50 paper #66**

Mohammad Kassemi, Ohio Aerospace Inst.: Bubble dynamics on a heated surface

**2:10 paper #131**

Grétar Tryggvason, Univ. of Michigan: Computations of drop collision and coalescence

**2:30 paper #97**

Chang-Won Park, Univ. of Florida: Marangoni effects on the bubble dynamics in a pressure driven flow

**2:50 paper #14**

Osman Basaran, Purdue Univ.: Forced oscillations of supported drops

**Critical Point Phenomena I**

**Session Chair: Robert Gammon, Univ. of Maryland**  
**(Ritz)**

**paper #17**

Robert Berg, NIST: Internal waves in CVX

**paper #54**

John Hegseth, Univ. of New Orleans: Growth and morphology of phase separating supercritical fluids

**paper #64**

Eric Kaler, Univ. of Delaware: Isopycnic phases and structures in  $H_2O/CO_2$ /ethoxylated alcohol surfactant mixtures

**paper #72**

Robert Kusner, NASA Lewis: Electric field induced interfacial instabilities

**paper #42**

Richard Ferrell, Univ. of Maryland: A brief survey of the equilibrium and transport properties of critical fluids and the degree to which microgravity is required for their experimental investigation

**Interfacial Phenomena I**

**Session Chair: Joel Koplik, City College of the City of New York**  
**(Dolder-Hassler)**

**paper #45**

Stephen Garoff, Carnegie Mellon Univ.: Microscale hydrodynamics in near moving contact line

**paper #117**

Leonard Schwartz, Univ. of Delaware: Free-surface and contact-line motion of liquids in a microgravity

**paper #99**

Marc Perlin, Univ. of Michigan: On the boundary conditions at an oscillating contact line: A physical/numerical experimental program

**paper #77**

Seth Lichter, Northwestern Univ.: The micromechanics of the moving contact line

**paper #122**

Ain Sonin, MIT: Dynamics of the molten contact line

3:10 p.m. Break

**Friday Afternoon**  
**Parallel Session 6**  
**3:30 - 5:30 p.m.**

**Phase Change I—Boiling**  
**Session Chair: Herman Merte, Univ. of Michigan**  
**(Grand Ballroom)**

**3:30 paper #133**  
 Peter Wayner, Jr., Rennselaer Polytechnic Inst.: Non-isothermal experimental study of the constrained vapor bubble thermosyphon

**3:50 paper #35**  
 Vijay Dhir, UCLA: Investigations of mechanisms associated with nucleate boiling under microgravity conditions

**4:10**

**4:30 paper #69**  
 Jungho Kim, Univ. of Denver: Design of an improved heater array to measure microscale wall heat transfer

**4:50 paper #121**  
 Marc Smith, Georgia Inst. of Technology: The development of novel, high-flux, heat transfer cells for thermal control in microgravity

**5:10 paper #51**  
 Kevin Hallinan, Univ. of Dayton: The development of a full field three-dimensional microscale flow measurement technique for application to near contact line flows

**Critical Point Phenomena II**  
**Session Chair: Richard Ferrell, Univ. of Maryland**  
**(Ritz)**

**paper #60**  
 Donald Jacobs, College of Wooster: Turbidity of a binary fluid mixture: determining  $\eta$

**paper #98**  
 Alexander Patashinski, Northwestern Univ.: Nonlinear dynamics and nucleation kinetics in near-critical liquids

**paper #143**  
 Greg Zimmerli, NYMA: Electrostriction of a critical fluid in microgravity

**paper #120**  
 Gregory Smedley, California Inst. of Technology: Solute nucleation and growth in supercritical fluid mixtures

**paper #43**  
 Robert Gammon, Univ. of Maryland: Critical fluid light scattering experiment—Zeno

**paper #136**  
 R. Allen Wilkinson, NASA Lewis: Critical fluid thermal equilibrium dynamics

**Interfacial Phenomena II**  
**Session Chair: Stephen Garoff, Carnegie Mellon Univ.**  
**(Dolder-Hassler)**

**paper #70**  
 Joel Koplik, City College of the City of New York: Wetting hysteresis at the molecular scale

**paper #111**  
 Daniel Rosner, Yale Univ.: Fluid creep effects on near-wall solute transport for non-isothermal ampoules

**paper #29**  
 Paul Concus, Univ. of California—Berkeley: Equilibrium fluid interface behavior under low- and zero-gravity conditions

**paper #106**  
 Hans Rath, Bremen Univ.: Critical velocities in open capillary flows

**paper #47**  
 Ashok Gopinath, Naval Postgraduate School: Thermoacoustic effects at a solid fluid boundary: The role of a second-order thermal expansion coefficient

**paper #145**  
 Ben Ovryn, NYMA: Applications of phase-shifted laser feedback interferometry to fluid physics

5:30 p.m. Break

**Friday Evening**  
***International Forum***  
**7:30 - 9:30 p.m.**

Brad Carpenter, Chair, NASA Headquarters  
(Dolder-Hassler)

- |           |  |
|-----------|--|
| 7:30 p.m. | Welcome and Opening Remarks<br>Brad Carpenter, NASA Headquarters   |
| 7:40 p.m. | Alexandre Feonychev, Research Institute for Applied<br>Mechanics and Electrodynamics of Moscow Aviation<br>Institute: Deformation of fluid column by action of<br>axial vibrations <b>paper #147</b>                             |
| 7:55 p.m. | Vadim Polezhaev, Institute for Problems in Mechanics, Russian<br>Academy of Science: Current results and proposed activities<br>in microgravity fluid dynamics <b>paper #100</b>   |
| 8:10 p.m. | Valentin Yuferev, Ioffe Physical-Technical Institute: Effect of<br>spacecraft rotation on fluid convection under microgravity<br><b>paper #141</b>   |
| 8:25 p.m. | Vladislav Pukhnachev, Lavrentyev Institute of Hydrodynamics:<br>Thermocapillary motion in an emulsion <b>paper #101</b>  |
| 8:40 p.m. | Olga Rodicheva and Evgeny Rodichev, Institute of Mechanics<br>at Moscow State University: Reliability of numerical<br>solutions and two-dimensional turbulence in the problem of<br>Rayleigh-Benard convection <b>paper #107</b> |
| 8:55 p.m. | Gennadi Putin, Perm State University: System for<br>measurement of convection aboard Space Station <b>paper #104</b>   |
| 9:10 p.m. | Discussions  |
| 9:30 p.m. | Adjourn  |

## **Saturday, June 15, 1996**

### **Morning**

8:00 a.m. Saturday Plenary  
Paul Chaikin, Chair, Princeton Univ.  
(Grand Ballroom)

#### **Keynote:**

Complex fluids: Science, technology and microgravity  
David Weitz, Univ. of Pennsylvania

8:40 a.m. Break

### ***Parallel Session 7*** ***9:00 - 10:20 a.m.***

#### **Phase Change II**

Session Chair: Peter Wayner, Jr.,  
Rensselaer Polytechnic Inst.  
(Grand Ballroom)

##### **9:00 paper #89**

Herman Merte, Univ. of Michigan: A  
study of nucleate boiling with forced  
convection in microgravity

##### **9:20 paper #40**

Amir Faghri, Univ. of Connecticut:  
Evaporation on/in capillary structures of  
high heat flux two-phase devices

##### **9:40 paper #55**

Cila Herman, Johns Hopkins Univ.:  
Experimental investigation of pool  
boiling heat transfer enhancement in  
microgravity in the presence of electric  
fields

##### **10:00 paper #20**

Van Carey, Univ. of California-Berkeley:  
Marangoni effects in boiling of binary  
fluid mixtures

#### **Electric and Magnetic Effects**

Session Chair: Robert Davis, Univ. of  
Colorado  
(Ritz)

##### **paper #95**

Daniel Ohlsen, Univ. of Colorado:  
Waves in radial gravity using magnetic  
fluid

##### **paper #13**

George Bankoff, Northwestern Univ.:  
Control of flowing liquid films by  
electrostatic fields in space

##### **paper #38**

Boyd Edwards, West Virginia Univ.:  
Magnetothermal convection in  
nonconducting diamagnetic and  
paramagnetic fluids

##### **paper #119**

Benjamin Shaw, Univ. of California-  
Davis: Electrohydrodynamic pool  
boiling in reduced gravity

#### **Interfacial Phenomena III**

Session Chair: Daniel Rosner, Yale Un  
(Dolder-Hassler)

##### **paper #91**

Ali Nadim, Boston Univ.: Shape  
oscillations of gas bubbles with Newtonian  
interfacial rheological properties

##### **paper #82**

Daniel Mackowski, Auburn Univ.:  
Investigation of thermal stress convection  
in nonisothermal gases under microgravity  
conditions

##### **paper #31**

E. James Davis, Univ. of Washington-  
Seattle: Phoretic and radiometric force  
measurement on microparticles in  
microgravity conditions

##### **paper #83**

James Maher, Univ. of Pittsburgh: The  
dissolution of an interface between  
miscible liquids

10:20 a.m. Break

**Saturday Morning**  
**Parallel Session 8**  
**10:40 - 12:00 noon**

**Multiphase Flow and Phase Change III**  
**Session Chair: Jungho Kim, Univ. of Denver**  
**Grand Ballroom)**

**Electro and Bio Fluids I**  
**Session Chair: John Anderson, Carnegie Mellon Univ. (Ritz)**

**Special Topics II**  
**Session Chair: Cila Herman, Johns Hopkins Univ. (Dolder-Hassler)**

**10:40 paper #80**  
**Michael Loewenberg, Yale Univ.: Self-diffusion of drops in a dilute sheared emulsion**

**paper #52**  
**John Hart, Univ. of Colorado: Experiments on thermal convection in rotating spherical shells with radial gravity: the geophysical fluid flow cell**

**paper #130**  
**Eugene Trinh, Jet Propulsion Lab.: Acoustic streaming and heat and mass transfer enhancement**

**11:00 paper #24**  
**J. H. Chan, Univ. of Wisconsin-Milwaukee: Rewetting of monogroove heat pipe in space station radiators**

**paper #140**  
**Xiao-lun Wu, Univ. of Pittsburgh: Nucleation and chiral symmetry breaking under hydrodynamic flows**

**paper #123**  
**Stephen Spiegelberg, Harvard Univ.: Extensional rheology of non-Newtonian materials**

**11:20 paper #103**  
**Andrea Prosperetti, Johns Hopkins Univ.: Acoustic bubble removal from boiling surfaces**

**paper #54**  
**John Hegseth, Univ. of New Orleans: A geophysical flow experiment in compressible critical fluids**

**paper #74**  
**Simon Ostrach, Case Western Reserve Univ.: Gravity-dependent transport in industrial processes**

**11:40 paper #109**  
**Chris Rogers, Tufts Univ.: Decoupling the role of inertia and gravity on particle dispersion**

**paper #75**  
**David Leighton, Univ. of Notre Dame: Binary oscillatory crossflow electrophoresis**

**paper #57**  
**R. Glynn Holt, Jet Propulsion Lab.: The onset of resonance-controlled instability in spherical bubble oscillations**

12:00 noon Lunch in hotel  
 (Dorothy Fuldheim Room)

**Forum:**  
**NRA plans, questions/answers**  
**Brad Carpenter, presiding, NASA Headquarters**

**Saturday Afternoon**  
**Parallel Session 9**  
**1:30 - 3:10 p.m.**

**Bubbles and Drops III**

**Session Chair:** Kathleen Stebe, Johns Hopkins Univ.  
 (Grand Ballroom)

**1:30 paper #125**

R. Subramanian, Clarkson Univ.:  
 Thermocapillary migration and interactions of bubbles and drops

**1:50 paper #6**

A.V. Anilkumar: Studies of the stability and dynamics of levitated drops

**2:10 paper #8**

Nasser Ashgriz, State Univ. of New York-Buffalo: Nonlinear bubble interactions in acoustic pressure fields

**2:30 paper #84**

Charles Maldarelli, City Univ. of New York: Controlling the mobility of a fluid particle in space by using remobilizing surfactants

**2:50 paper #7**

Robert Apfel, Yale University: Drops in space: super oscillations and surfactant studies

**Electro and Bio Fluids II**

**Session Chair:** David Leighton, Univ. of Notre Dame  
 (Ritz)

**paper #128**

John Tarbell, Pennsylvania State Univ.:  
 Microgravity effects on transendothelial transport

**paper #49**

James Grothberg, Northwestern Univ.:  
 The propagation of a liquid bolus through an elastic tube and airway reopening

**paper #32**

Robert Davis, Univ. of Colorado: Cell and particle interactions and aggregation during electrophoretic motion

**paper #15**

James Baygents, Univ. of Arizona: Studies on the response of emulsions to externally-imposed electric and velocity fields: Electrohydrodynamic deformation and interaction of a pair of drops

**paper #53**

T.A. Hatton, MIT: Interfacial transport and miscellar solubilization processes

**Special Topics III**

**Session Chair:** Sung Lin, Clarkson Univ.  
 (Dolder-Hassler)

**paper #9**

C. Thomas Avedisian, Cornell Univ.:  
 Experimental study of liquid jet impingement in microgravity: The hydraulic jump

**paper #27**

Ivan Clark, NASA Langley: Microgravity particle dynamics

**paper #110**

Paul Ronney, Univ. of Southern California: Studies of radiation-driven and buoyancy driven fluid flows and transport

**paper #81**

Sudarshan Loyalka, Univ. of Missouri: Cross effects in microgravity flows

**paper #19**

Jeremiah Brackbill, Los Alamos National Lab: Dynamical modeling of surface tension

3:10 p.m. Adjourn

# Third Microgravity Fluid Physics Conference

Attendance List  
June 13-15, 1996  
Cleveland, Ohio

Davood Abdollahian  
S. Levy, Inc.  
3425 S. Bascom Ave.  
Campbell, CA 95008  
Phone: 408-369-3865  
Fax: 408-371-6804  
E-mail: davood@levy.com

Yoshiyuki Abe  
Energy Fundamental Div.  
Electrotechnical Lab., MITI Japan  
1-1-4 Umezono  
Tsukuba, Ibaraki, 305 Japan  
Phone: 81-298-58-5749  
Fax: 81-298-58-5754  
E-mail: y.abbe@qm.etl.go.jp

Alex Abri  
ADF, Inc.  
2001 Aerospace Pkwy.  
Brook Park, OH 44142  
Phone: 216-977-1096  
Fax: 216-977-1269

Bruce J. Ackerson  
Dept. of Physics  
Oklahoma State University  
Stillwater, OK 74074  
Phone: 405-744-5819  
Fax: 405-744-6811  
E-mail: bjack@osuunix.ucc.okstate.edu

Andreas Acrivos  
The Levich Institute  
City University of New York  
T-1M; 140th Street & Convent Avenue  
New York, NY 10031  
Phone: 212-650-8159  
Fax: 212-650-6835

Sirish Agarwal  
Universities Space Research Association  
300 D Street, SW; Suite 801  
Washington, DC 20024  
Phone: 202-488-5124  
Fax: 202-479-2613  
E-mail: sagarwal@usra.edu

Manmohan D. Aggarwal  
Dept. of Physics  
Alabama A&M University  
P.O. Box 428  
Normal, AL 35762  
Phone: 205-851-5308  
Fax: 205-851-5622  
E-mail: aammxa01@asnaam.aamu.edu

Iwan Alexander  
Center for Microgravity and Materials Research  
The University of Alabama in Huntsville  
M-65, R.I. Bldg., CMMR  
Huntsville, AL 35899  
Phone: 205-895-6887  
Fax: 205-895-6791  
E-mail: iwan@cmmr.uah.edu

David Andereck  
Dept. of Physics  
The Ohio State University  
174 W. 18th Ave  
Columbus, OH 43210  
Phone: 614-292-2360  
Fax: 614-292-7557  
E-mail: andereck@mps.ohio-state.edu

Daniel M. Anderson  
Applied and Computational Mathematics Div.  
NIST  
Building 820, Room 365  
Gaithersburg, MD 20899  
Phone: 301-975-4333  
Fax: 301-990-4127  
E-mail: dmanders@cam.nist.gov

A. V. Anilkumar  
Dept. of Applied and Engineering Science  
Vanderbilt University  
6079-B  
Nashville, TN 37240  
Phone: 615-343-7293  
Fax: 615-343-8730  
E-mail: anil@vuse.edu

Mikhail A. Anisimov  
Institute for Physical Science & Technology  
University of Maryland  
College Park, MD 20742  
Phone: 301-405-8049  
Fax: 301-314-9404  
E-mail: anisimov@glue.umd.edu

Rafat R. Ansari  
NASA Lewis Research Center  
MS 333-1; 21000 Brookpark Rd.  
Cleveland, OH 44135  
Phone: 216-433-5008  
Fax: 216-977-7138  
E-mail: ransari@lerc.nasa.gov

Robert Apfel  
Dept. of Mechanical Engineering  
Yale University  
P.O. Box 208286  
New Haven, CT 06520  
Phone: 203-432-4346  
Fax: 203-432-7654  
E-mail: robert.apfel@yale.edu

Hassan Aref  
Dept. of Theoretical & Applied Mechanics  
University of Illinois/Urbana-Champaign  
216 Talbot Lab, 104 S. Wright St.  
Urbana, IL 61801  
Phone: 217-333-2329  
Fax: 217-244-5707  
E-mail: h-aref@uiuc.edu

Nasser Ashgriz  
Dept. of Mechanical & Aerospace Engineering  
State University of New York/Buffalo  
Buffalo, NY 14260  
E-mail: ashgriz@eng.buffalo.edu

C. Thomas Avedisian  
Dept. of Mechanical & Aerospace Engineering  
Cornell University  
Ithaca, NY 14850  
Phone: 607-255-5105  
E-mail: cta2@cornell.edu

M. Yousef Bahadori  
Power and Information Systems Div.  
Science Applications International Corp.  
21151 Western Ave.  
Torrance, CA 90501  
Phone: 310-781-8723  
Fax: 310-781-8730  
E-mail: bahadori@gecko.saic.com

Vemuri Balakotaiah  
Dept. of Chemical Engineering  
University of Houston  
Houston, TX 77204-4792  
Phone: 713-743-4318  
Fax: 713-743-4323  
E-mail: bala@uh.edu

R. Balasubramaniam  
NASA Lewis Research Center  
MS 500-102; 21000 Brookpark Rd.  
Cleveland, OH 44135  
Phone: 216-433-2878  
Fax: 216-433-8660  
E-mail: bala@lerc.nasa.gov

Kimberly Bambakidis  
NYMA, Inc.  
2001 Aerospace Pkwy.  
Brook Park, OH 44142  
Phone: 216-977-1142  
Fax: 216-977-1269  
E-mail: rimkus@dinah.lerc.nasa.gov

S. George Bankoff  
Dept. of Chemical Engineering  
Northwestern University  
Evanston, IL 60208  
Phone: 847-491-5267  
Fax: 847-491-3728  
E-mail: gbankoff@casbah.acns.nwu.edu



Osman A. Basaran  
School of Chemical Engineering  
Purdue University  
1283 Chemical Engineering Building  
W. Lafayette, IN 47907-1283  
Phone: 317-494-4061  
Fax: 317-494-0805  
E-mail: obasaran@ecn.purdue.edu

James C. Baygents  
Dept. of Chemical Engineering  
The University of Arizona  
Tucson, AZ 85721  
Phone: 520-621-6043  
Fax: 520-621-6048  
E-mail: jcb@maxwell.che.arizona.edu

Eric Begg  
Dept. of Mechanical Engineering  
University of Connecticut  
191 Auditorium Rd.; U-139 ME  
Storrs, CT 06268  
Phone: 860-486-2239  
Fax: 860-486-5088  
E-mail: begge@eng2.uconn.edu

Robert P. Behringer  
Dept. of Physics  
Duke University  
Box 90305  
Durham, NC 27708  
Phone: 919-660-2550  
Fax: 919-660-2525  
E-mail: bob@phy.duke.edu

Barney Bellagh  
Dept. of Flight Experiment  
ADF, Inc.  
3003 Aerospace Pkwy.  
Brook Park, OH 44142  
Phone: 216-977-0375  
Fax: 216-977-0350

Steve W. Benintendi  
Dept. of Mechanical Engineering  
Georgia Institute of Technology  
SSTC #2 Bldg., Room 200; 282 Ferst Drive  
Atlanta, GA 30332-0405  
Phone: 404-894-2279  
Fax: 404-894-2291  
E-mail: gt6825d@prism.gatech.edu

Robert F. Berg  
Dept. of Physical & Chemical Properties  
NIST  
Bldg. 221, Room A111  
Gaithersburg, MD 20899  
Phone: 301-975-2466  
Fax: 301-869-4020  
E-mail: rfberg@tiber.nist.gov

Luis P. Bernal  
Dept. of Aerospace Engineering  
The University of Michigan  
1320 Beal Ave.  
Ann Arbor, MI 48109-2118  
Phone: 313-764-3396  
Fax: 313-763-0578  
E-mail: lpb@engin.umich.edu

Frederick R. Best  
Center for Space Power  
Texas A&M University  
Room 223 WERC  
College Station, TX 77843-3113  
Phone: 409-845-8768  
Fax: 409-847-8857  
E-mail: FRB449A@Zeus.tamu.edu

Avijit Bhunia  
Dept. of Mechanical & Aerospace Engineering  
Case Western Reserve University  
Glennan Bldg.; 10900 Euclid Ave.  
Cleveland, OH 44106  
Phone: 216-368-2945  
E-mail: axb17@po.cwru.edu

Irene Bibyk  
NASA Lewis Research Center  
MS 500-115; 21000 Brookpark Rd.  
Cleveland, OH 44135  
Phone: 216-433-2362  
Fax: 216-433-8660

Jerzy Bławdziewicz  
Dept. of Chemical Engineering  
Yale University  
Mason Laboratory; 9 Hillhouse Ave.  
New Haven, CT 06520-8286  
Phone: 203-432-4594  
Fax: 203-432-7232  
E-mail: jerzy@stokes.eng.yale.edu

Fabian J. Bonetto  
Dept. of Environment & Energy  
Rensselaer Polytechnic Institute  
JEC 5048; RPI  
Troy, NY 12180  
Phone: 518-276-8592  
Fax: 518-276-3055  
E-mail: bonetf@rpi.edu

John Borden  
Jackson and Tull  
7375 Executive Pl.; Suite 200  
Seabrook, MD 20706  
Phone: 301-805-4545  
Fax: 301-805-4538  
E-mail: john.bor@jnt.com

Jeremiah U. Brackbill  
Theory Division  
Los Alamos National Laboratory  
MS B216  
Los Alamos, NM 87545  
Phone: 505-667-8811  
Fax: 505-665-5926  
E-mail: jub@lanl.gov

Richard J. Braun  
Dept. of Mathematical Sciences  
University of Delaware  
501 Ewing Hall  
Newark, DE 19716  
Phone: 302-831-1869  
Fax: 302-831-4511  
E-mail: braun@math.udel.edu

Ralph E. Bucknam  
P.O. Box 2151  
Halesite, NY 11743-0874  
Phone: 516-427-9322

Kathryn M. Butler  
Building & Fire Research Lab.  
NIST  
Bldg. 224; MS B258  
Gaithersburg, MD 20899  
Phone: 301-975-6673  
Fax: 301-975-4052  
E-mail: kathryn.butler@nist.gov

James Cake  
NASA Lewis Research Center  
MS 500-205; 21000 Brookpark Rd.  
Cleveland, OH 44135  
Phone: 216-433-3565  
Fax: 216-433-8660

Van P. Carey  
Dept. of Mechanical Engineering  
University of California/Berkeley  
6123 Etcheverry Hall  
Berkeley, CA 94720  
Phone: 510-642-7177  
Fax: 510-642-6163  
E-mail: vcarey@me.berkeley.edu

Brad Carpenter  
Code UG  
NASA Headquarters  
Washington, DC 20546-0001  
Phone: 202-358-0826  
Fax: 202-358-3091  
E-mail: bcarpenter@hq.nasa.gov

An-Ti Chai  
NASA Lewis Research Center  
MS 500-102; 21000 Brookpark Rd.  
Cleveland, OH 44135  
Phone: 216-433-2073  
Fax: 216-433-8050

Paul Chaikin  
Dept. of Physics  
Princeton University  
P.O. Box 708  
Princeton, NJ 08544  
Phone: 609-258-4338  
Fax: 609-258-6360  
E-mail: chaikin@pupgg.princeton.edu

Arnon Chait  
NASA Lewis Research Center  
MS 105-1; 21000 Brookpark Rd.  
Cleveland, OH 44135  
Phone: 216-433-3558  
Fax: 216-433-5033  
E-mail: chait@sarah.lerc.nasa.gov

Cho Lik Chan  
Dept. of Aerospace & Mechanical Engineering  
The University of Arizona  
Aeronautical Bldg. #16  
Tuscon, AZ 85721  
Phone: 520-621-2503  
Fax: 520-621-8191  
E-mail: cholik@sherlock.ame.arizona.edu

S. H. Chan  
Dept. of Mechanical Engineering  
University of Wisconsin  
P.O. Box 784  
Milwaukee, WI 53201  
Phone: 414-229-5001  
Fax: 414-229-6958  
E-mail: shc@alpha2.csd.uwm.edu

David F. Chao  
NASA Lewis Research Center  
MS 500-102; 21000 Brookpark Rd.  
Cleveland, OH 44135  
Phone: 216-433-8320  
Fax: 216-433-8050  
E-mail: david.chao@lerc.nasa.gov

David J. Chato  
NASA Lewis Research Center  
MS 60-4; 21000 Brookpark Rd.  
Cleveland, OH 44135  
Phone: 216-977-7488  
Fax: 216-977-7545  
E-mail: david.chato@lerc.nasa.gov

Chuan F. Chen  
Dept. of Aerospace & Mechanical Engineering  
The University of Arizona  
Tuscon, AZ 85721  
Phone: 520-621-8199  
Fax: 520-621-8191  
E-mail: chen@ame.arizona.edu

Francis Chiaramonte  
NASA Lewis Research Center  
MS 500-102; 21000 Brookpark Rd.  
Cleveland, OH 44135  
Phone: 216-433-8040  
Fax: 216-433-8660  
E-mail: fchiara@lerc.nasa.gov

Jacob N. Chung  
Dept. of Mechanical & Materials Engineering  
Washington State University  
Pullman, WA 99164-2920  
Phone: 509-335-3222  
Fax: 509-335-4662  
E-mail: chung@mme.wsu.edu

Ivan O. Clark  
NASA Langley Research Center  
MS 473  
Hampton, VA 23681-0001  
Phone: 804-864-1500  
Fax: 804-864-7891  
E-mail: i.o.clark@larc.nasa.gov

Noel Clark  
Dept. of Physics/Condensed Matter Lab.  
University of Colorado  
Campus Box 390  
Boulder, CO 80309  
Phone: 303-492-6420  
Fax: 303-492-2998  
E-mail: clarkn@bly.colorado.edu

Rita L. Cognion  
ADF, Inc.  
2001 Aerospace Pkwy.  
Brook Park, OH 44142  
Phone: 216-977-1097  
Fax: 216-977-1269  
E-mail: cognion@dinah.lerc.nasa.gov

Catherine Coleman  
NASA Johnson Space Center  
Houston, TX 77058  
Phone: 713-244-8975  
E-mail: cgcolema@cal.jsc.nasa.gov

Lance R. Collins  
Dept. of Chemical Engineering  
The Pennsylvania State University  
118-B Fenske Laboratory  
University Park, PA 16802  
Phone: 814-863-7113  
Fax: 814-865-7846  
E-mail: lxc12@cac.psu.edu

Paul Concus  
Dept. of Mathematics  
University of California  
LBL-50A/2152  
Berkeley, CA 94720  
Phone: 510-486-5508  
Fax: 510-486-5401  
E-mail: concus@math.berkeley.edu

Robert Corban  
NASA Lewis Research Center  
MS 500-217; 21000 Brookpark Rd.  
Cleveland, OH 44135  
Phone: 216-433-6642  
Fax: 216-433-8660  
E-mail: rcorban@lerc.nasa.gov

Sam Coriell  
NIST  
Materials Bldg. 233, Room A-153  
Gaithersburg, MD 20899  
Phone: 301-975-6169  
Fax: 301-926-7975  
E-mail: corell@coral.nist.gov

Robert R. Czys  
Illinois State Water Survey  
University of Illinois  
2204 Griffith Drive  
Champaign, IL 61820  
Phone: 217-333-8496  
Fax: 217-244-0220  
E-mail: r-czys@uiuc.edu

Nihad Daidzic  
Ctr. for Microgravity Research & Applications  
Vanderbilt University  
P.O. Box 6079, Station B  
Nashville, TN 37235  
Phone: 615-343-6965  
Fax: 615-343-8730  
E-mail: daidzicn@vuse.vanderbilt.edu

Anita Danak  
5556 Broadview Rd., #3425  
Parma, OH 44134  
Phone: 216-749-5417

E. James Davis  
Dept. of Chemical Engineering  
University of Washington  
Box 351750  
Seattle, WA 98195-1750  
Phone: 206-543-2250  
Fax: 206-543-3778  
E-mail: davis@cheme.washington.edu

Robert H. Davis  
Dept. of Chemical Engineering  
University of Colorado  
Campus Box 424  
Boulder, CO 80309-0424  
Phone: 303-492-7314  
Fax: 303-492-4341  
E-mail: davisr@spot.colorado.edu

Stephen H. Davis  
Dept. of Engineering Sciences & Applied Mathematics  
Northwestern University  
2145 Sheridan Rd.  
Evanston, IL 60208  
Phone: 847-491-5397  
Fax: 847-491-2178  
E-mail: sdavis@nwu.edu

Robert De Bruijn  
VanderWaals-Zeeman Inst./Univ. van Amsterdam  
Valckenierstraat 65  
1018 XE Amsterdam, the Netherlands  
Phone: 31-0-20-5256382  
Fax: 31-0-20-5255788  
E-mail: debruijn@phys.uva.nl

Henry C. De Groh  
NASA Lewis Research Center  
MS 105-1; 21000 Brookpark Rd.  
Cleveland, OH 44135  
Phone: 216-433-5025  
Fax: 216-433-5033

Richard DeLombard  
NASA Lewis Research Center  
MS 500-216; 21000 Brookpark Rd.  
Cleveland, OH 44135  
Phone: 216-433-5285  
Fax: 216-433-8660

Eldon Decker  
Dept. of Physics  
Carnegie Mellon University  
5000 Forbes Ave.  
Pittsburgh, PA 15213  
Phone: 412-268-6283  
Fax: 412-268-0648  
E-mail: eldon@cmu.edu

Danny M. Deffenbaugh  
Div. of Mechanical & Fluids Engineering  
Southwest Research Institute  
6220 Culebra Rd.  
San Antonio, TX 78238  
Phone: 210-522-2384  
Fax: 210-681-9661  
E-mail: ddeffenbaugh@swri.edu

Michael M. Degen  
Dept. of Physics  
The Ohio State University  
174 W. 18th Ave.  
Columbus, OH 43210  
Phone: 614-292-0119  
Fax: 614-292-7557  
E-mail: degen@mps.ohio-state.edu

Vijay K. Dhir  
Dept. of Mechanical & Aerospace Engineering  
University of California/Los Angeles  
46-147 Engr. IV  
Los Angeles, CA 90095  
Phone: 310-825-8507  
Fax: 310-206-4830  
E-mail: vdhir@seas.ucla.edu

Jennifer Dockstader  
Microgravity Education Outreach  
Microgravity News  
1040-D Settlers Landing Rd.  
Hampton, VA 23669  
Phone: 804-723-2197  
Fax: 804-723-0241  
E-mail: j.l.dockstader@larc.nasa.gov

Franklin T. Dodge  
Div. of Mechanical & Fluids Engineering  
Southwest Research Institute  
6220 Culebra Rd.  
San Antonio, TX 78238  
Phone: 210-522-2306  
Fax: 210-681-9661  
E-mail: fdodge@swri.edu

Michael Dreyer  
Center of Applied Space Technology & Microgravity  
ZARM University of Bremen  
Am Fallturm  
D-28359 Bremen, Germany  
Phone: 49-421-218-4038  
Fax: 49-421-218-2521  
E-mail: dreyer@zarm.uni-bremen.de

Francois Drolet  
SCRI  
The Florida State University  
470 Science Center Library  
Tallahassee, FL 32308  
Phone: 904-644-2434  
Fax: 904-644-0098  
E-mail: drolet@scri.fsu.edu

J. C. Duh  
NASA Lewis Research Center  
MS 500-102; 21000 Brookpark Rd.  
Cleveland, OH 44135  
Phone: 216-433-2850  
Fax: 216-433-8050  
E-mail: fsmicro@ariel.lerc.nasa.gov

Michael Duke  
Lunar and Planetary Institute  
3600 Bay Area Blvd.  
Houston, TX 77058  
Phone: 713-244-2036  
Fax: 713-244-2006  
E-mail: duke@lpi.jsc.nasa.gov

Allen B. Duncan  
Dept. of Mechanical & Industrial Engineering  
Marquette University  
1515 Wisconsin Ave.  
Milwaukee, WI 53233  
Phone: 414-288-7849  
Fax: 414-288-7082  
E-mail: DuncanA@vms.csd.mu.edu

William W. Durgin  
Provost's Office  
Worcester Polytechnic Institute  
100 Institute Rd.  
Worcester, MA 01609  
Phone: 508-831-5065  
Fax: 508-831-5774

Douglas J. Durian  
Dept. of Physics  
University of California/Los Angeles  
405 Hilgard Avenue  
Los Angeles, CA 90095-1547  
Phone: 310-206-2645  
Fax: 310-825-5734  
E-mail: durian@physics.ucla.edu

Walter Duval  
NASA Lewis Research Center  
MS 105-1; 21000 Brookpark Rd.  
Cleveland, OH 44135  
Phone: 216-433-5023  
Fax: 216-433-5033  
E-mail: duval@sarah.lerc.nasa.gov

Donald L. Edberg  
McDonnell Douglas Aerospace  
5301 Bolsa Ave; A3-Y955-11-2  
Huntington Beach, CA 92647-2099  
Phone: 714-896-5210  
Fax: 714-896-6930  
E-mail: edberg@netsun.mdc.com

Boyd Edwards  
Dept. of Physics  
West Virginia University  
P.O. Box 6315  
Morgantown, WV 26506-6315  
Phone: 304-293-3422 Ext. 1433  
Fax: 304-293-5732  
E-mail: edwards@wvnmms.wvnet.edu

Said Elghobashi  
Dept. of Mechanical & Aerospace Engineering  
University of California/Irvine  
4220 Gateway Engineering Bldg.  
Irvine, CA 92717  
Phone: 714-824-6131  
Fax: 714-824-8585  
E-mail: selghoba@uci.edu

Amir Faghri  
Dept. of Mechanical Engineering  
University of Connecticut  
191 Auditorium Rd.; U-139  
Storrs, CT 06269  
Phone: 860-486-2090  
Fax: 860-486-5088  
E-mail: faghri@eng2.uconn.edu

Donald L. Feke  
Dept. of Chemical Engineering  
Case Western Reserve University  
10900 Euclid Ave.  
Cleveland, OH 44106-7217  
Phone: 216-368-2750  
Fax: 216-368-3017  
E-mail: dlf4@po.cwru.edu

Zaichun Feng  
Dept. of Mechanical Engineering  
Massachusetts Institute of Technology  
Bldg. 3-364; 77 Massachusetts Ave.  
Cambridge, MA 02139  
Phone: 617-253-6345  
Fax: 617-258-5802  
E-mail: zfeng@mit.edu

Alexander Feonychev  
Research Inst./Applied Mechanics & Electrodynamics  
Moscow Aviation Institute  
4 Volokolamskoe str. GSP-47  
Moscow, 125810 Russia  
Phone: 7-095-158-0020  
Fax: 7-095-158-0367  
E-mail: riame.mai@rex.iasnet.com

Richard A. Ferrell  
Dept. of Physics  
University of Maryland  
College Park, MD 20742  
Phone: 301-405-6148  
Fax: 301-314-9465

Brian Finley  
NYMA, Inc.  
2001 Aerospace Pkwy.  
Brook Park, OH 44142  
Phone: 216-977-1185  
Fax: 216-977-1269  
E-mail: finley@lerc.nasa.gov

Terry Fleener  
Cryogenics New Business  
Ball Aerospace and Technologies Corp  
P.O. Box 1062  
Boulder, CO 80306-1062  
Phone: 303-939-4413  
Fax: 303-939-6307  
E-mail: rreinker@ball.com

Greg Forest  
Dept. of Mathematics  
The Ohio State University  
231 W. 18th Ave.  
Columbus, OH 43210  
Phone: 614-292-9363  
Fax: 614-292-1479  
E-mail: forest@math.ohio-state.edu

Carl Franck  
Dept. of Physics  
Cornell University  
Clark Hall  
Ithaca, NY 14853  
Phone: 607-255-3562  
Fax: 607-255-6428  
E-mail: cpf1@cornell.edu

Thorsten Franke  
Dept. of Mechanical Engineering  
The Johns Hopkins University  
122 Latrobe; 3400 N. Charles St.  
Baltimore, MD 21218  
Phone: 410-516-7555  
Fax: 410-516-4316

Alexander Frenkel  
Dept. of Mathematics  
University of Alabama  
Tuscaloosa, AL 35487-0350  
Phone: 205-348-5434  
Fax: 205-348-7067  
E-mail: afrenkel@gp.as.ua.edu

Robert Friedman  
NASA Lewis Research Center  
MS 500-115; 21000 Brookpark Rd.  
Cleveland, OH 44135  
Phone: 216-433-5697  
Fax: 216-433-8660

Robert W. Gammon  
Inst. for Physical Science & Technology  
University of Maryland  
College Park, MD 20742  
Phone: 301-405-4791  
Fax: 301-314-9509  
E-mail: rg2@umail.umd.edu

Laudelino Garcia  
Dept. of Physics  
University of New Orleans/Lakefront  
New Orleans, LA 70148  
Phone: 504-286-6046

Stephen Garoff  
Dept. of Physics  
Carnegie Mellon University  
5000 Forbes Ave.  
Pittsburgh, PA 15213  
Phone: 412-268-6877  
Fax: 412-681-0648  
E-mail: sg2e@andrew.cmu.edu

Jorge E. Gatica  
Dept. of Chemical Engineering  
Cleveland State University  
1960 E. 24 St.; SH455  
Cleveland, OH 44115  
Phone: 216-523-7274  
Fax: 216-687-9220

Morris Girgis  
Dept. of Manufacturing Engineering  
Central State University  
1400 Brush Row Rd.  
Wilberforce, OH 45384  
Phone: 513-376-6309  
Fax: 513-376-6679  
E-mail: girgis@cesuxa.crs.edu

Thomas Glasgow  
NASA Lewis Research Center  
MS 105-1; 21000 Brookpark Rd.  
Cleveland, OH 44135  
Phone: 216-433-5013

Harland Glaz  
Dept. of Mathematics  
University of Maryland  
College Park, MD 20742  
Phone: 301-405-5470  
E-mail: hmg@math.umd.edu

Ari Glezer  
Dept. of Mechanical Engineering  
Georgia Institute of Technology  
281 Ferst Drive; SSTC#1, Room 202  
Atlanta, GA 30332-0405  
Phone: 404-894-3266  
Fax: 404-894-2291  
E-mail: ari.glezer@me.gatech.edu

Joe D. Goddard  
Dept. of Applied Mechanics & Engineering Sciences  
University of California/San Diego  
9500 Gilman Drive  
La Jolla, CA 92093-0411  
Phone: 619-534-4508  
Fax: 619-534-4543  
E-mail: jgoddard@ucsd.edu

Suleyman A. Gokoglu  
NASA Lewis Research Center  
MS 500-115; 21000 Brookpark Rd.  
Cleveland, OH 44135  
Phone: 216-433-5499  
Fax: 216-433-8660  
E-mail: suleyman.gokoglu@lerc.nasa.gov

Ashok Gopinath  
Dept. of Mechanical Engineering  
Naval Postgraduate School  
Code ME/GK; 700 Dyer Road  
Monterey, CA 93943-5146  
Phone: 408-656-3400  
Fax: 408-656-2238  
E-mail: gopinath@nps.navy.mil

John A. Goree  
Dept. of Physics & Astronomy  
University of Iowa  
Iowa City, IA 52242  
Phone: 319-335-1843  
Fax: 319-335-1753  
E-mail: john-goree@uiowa.edu

Donald D. Gray  
Dept. of Civil & Environmental Engineering  
West Virginia University  
P.O. Box 6103  
Morgantown, WV 26506-6103  
Phone: 304-293-4024 Ext. 642  
Fax: 304-293-7109  
E-mail: gray@cemr.wvu.edu

Gary Gray  
Ohio Aerospace Institute  
MS 333-1; 21000 Brookpark Rd.  
Cleveland, OH 44135  
Phone: 216-433-2447  
Fax: 216-977-7138

Gary D. Grayson  
Rocket Based Propulsion Integration  
McDonnell Douglas Aerospace  
5301 Basa Ave.  
Huntington Beach, CA 92647  
Phone: 714-896-3311  
Fax: 714-896-2103  
E-mail: grayson@kmz.mdc.com

Hossein Haj-Hariri  
Dept. of Mechanical and Aerospace Engineering  
University of Virginia  
Thornton Hall  
Charlottesville, VA 22903  
Phone: 804-924-6290  
Fax: 804-982-2037  
E-mail: hh2b@virginia.edu

Roshanak Hakimzadeh  
NASA Lewis Research Center  
MS 500-216; 21000 Brookpark Rd.  
Cleveland, OH 44135  
Phone: 216-433-8738  
Fax: 216-433-8660  
E-mail: roshanak@lerc.nasa.gov

David G. Hall  
NYMA, Inc.  
2001 Aerospace Pkwy.  
Brook Park, OH 44142  
Phone: 216-977-1289  
Fax: 216-977-1269  
E-mail: tohall@lerc.nasa.gov

Nancy R. Hall  
NASA Lewis Research Center  
MS 500-102; 21000 Brookpark Rd.  
Cleveland, OH 44135  
Phone: 216-433-5643  
Fax: 216-433-8050  
E-mail: nancy.hall@lerc.nasa.gov

Kevin P. Hallinan  
Dept. of Mechanical & Aerospace Engineering  
University of Dayton  
300 College Park  
Dayton, OH 45469-0210  
Phone: 513-229-2875  
Fax: 513-229-2756  
E-mail: khallina@engr.udayton.edu



D'Arcy Hart  
C-CORE (Space Systems & Applications)  
Memorial University of Newfoundland  
St. Johns, NF A1B 3X5 Canada  
Phone: 709-737-4014  
Fax: 709-737-4706  
E-mail: djhart@morgan.ucs.mun.ca

John E. Hart  
Astrophysical & Planetary & Atmospheric Sciences  
University of Colorado  
CB 391  
Boulder, CO 80309  
Phone: 303-492-4248  
Fax: 303-492-3822  
E-mail: hart@tack.colorado.edu

A. Rashid Hasan  
Dept. of Chemical Engineering  
University of North Dakota  
P.O. Box 7101  
Grand Forks, ND 58202  
Phone: 701-777-3798  
Fax: 701-777-4838  
E-mail: rashid\_hasan@mail.und.nodak.edu

Mohammad M. Hasan  
NASA Lewis Research Center  
MS 60-4; 21000 Brookpark Rd.  
Cleveland, OH 44135  
Phone: 216-977-7494  
Fax: 216-977-7545  
E-mail: mohammad.hasan@lerc.nasa.gov

T. A. Hatton  
Dept. of Chemical Engineering  
Massachusetts Institute of Technology  
77 Massachusetts Ave.  
Cambridge, MA 02139  
Phone: 617-253-4588  
Fax: 617-253-8723  
E-mail: tahatton@mit.edu

Qun He  
Dept. of Mechanical & Aerospace Engineering  
University of Dayton  
300 College Park  
Dayton, OH 45469-0210  
Phone: 513-229-3463  
Fax: 513-229-2756  
E-mail: qhe@engr.udayton.edu

Uday Hegde  
NYMA, Inc.  
2001 Aerospace Pkwy.  
Brook Park, OH 44142  
Phone: 216-433-8744  
Fax: 216-433-8660

John Hegseth  
Dept. of Physics  
University of New Orleans/Lakefront  
New Orleans, LA 70148  
Phone: 504-286-6706  
Fax: 504-286-6048  
E-mail: jjhph@uno.edu

Dawn Heineman  
College of Integrated Science & Technology  
James Madison University  
300 South Main St.  
Harrisburg, VA 22807  
Phone: 216-433-3963  
Fax: 216-433-8060  
E-mail: dawn@einstein.lerc.nasa.gov

Diane Henderson  
Dept. of Mathematics  
The Pennsylvania State University  
218 McAllister Bldg.  
University Park, PA 16802  
Phone: 814-865-7527  
Fax: 814-865-3735  
E-mail: dmh@math.psu.edu

Cila Herman  
Dept. of Mechanical Engineering  
The Johns Hopkins University  
122 Latrobe; 3400 N. Charles St.  
Baltimore, MD 21218  
Phone: 410-516-4467  
Fax: 410-516-4316  
E-mail: herman@titan.me.jhu.edu

Geoffrey F. Hewitt  
Dept. of Chemical Engineering  
Imperial College  
Prince Consort Rd.  
London, SW7 2BY United Kingdom  
Phone: 44-171-594-5562  
Fax: 44-171-5994-5564  
E-mail: g.hewitt@ic.ac.uk

Myron E. Hill  
NASA Lewis Research Center  
MS 500-102; 21000 Brookpark Rd.  
Cleveland, OH 44135  
Phone: 216-433-5279  
Fax: 216-433-8660  
E-mail: m.e.hill@lerc.nasa.gov

John I. Hochstein  
Dept. of Mechanical Engineering  
The University of Akron  
EN312  
Memphis, TN 38152  
Phone: 901-678-2257  
Fax: 901-678-5459  
E-mail: jih@eagle.memphis.edu

R. Glynn Holt  
Jet Propulsion Laboratory  
MS 183-401; 4800 Oak Grove Dr.  
Pasadena, CA 91109  
Phone: 818-393-2531  
Fax: 818-393-5039  
E-mail: rgholt@voyager.jpl.nasa.gov

George M. Homsy  
Dept. of Chemical Engineering  
Stanford University  
MC 5025  
Stanford, CA 94305-5025  
Phone: 415-723-2419  
Fax: 415-725-7294  
E-mail: bud@chemeng.stanford.edu

Peter Howell  
Dept. of Biomedical Engineering/Technological Inst.  
Northwestern University  
2145 Sheridan Rd.  
Evanston, IL 60208  
Phone: 847-491-4308  
Fax: 847-491-5635  
E-mail: howell@asterix.bme.nwu.edu

Kwang-Chung Hsieh  
NYMA, Inc.  
MS 500-102; 21000 Brookpark Rd.  
Cleveland, OH 44135  
Phone: 216-433-8106  
Fax: 216-433-8050  
E-mail: tshsieh@scivax.lerc.nasa.gov

Jie Huang  
Dept. of Physics  
West Virginia University  
401 Newton Ave, Apt. 103  
Morgantown, WV 26505  
Phone: 304-293-3422 Ext. 1430

Michael D. Hudman  
Dept. of Mechanical Engineering  
Clarkson University  
Clarkson University; Box 5725  
Potsdam, NY 13699  
Phone: 315-268-3845  
Fax: 315-268-6438  
E-mail: hudmanmd@craft.camp.clarkson.edu

William A. Humphrey  
Dept. of Mechanical Engineering  
Carnegie Mellon University  
5000 Forbes Ave.  
Pittsburgh, PA 15213  
Phone: 412-268-3599  
Fax: 412-268-3348  
E-mail: wh2a+@andrew.cmu.edu

Steven Hymel  
Dept. of Physics  
University of New Orleans/Lakefront  
New Orleans, LA 70148  
Phone: 504-286-6046  
Fax: 504-286-6048  
E-mail: schph@uno.edu

Izuru Ishikawa  
Dept. of Mechanical Engineering  
The University of Michigan  
2182 G.G. Brown Bldg.  
Ann Arbor, MI 48105  
Phone: 313-936-0343  
Fax: 313-669-0274  
E-mail: izuru@engin.umich.edu

Donald T. Jacobs  
Dept. of Physics  
The College of Wooster  
Wooster, OH 44691  
Phone: 330-263-2390  
Fax: 330-263-2516  
E-mail: djacobs@acs.wooster.edu

Jeffrey W. Jacobs  
Dept. of Aerospace & Mechanical Engineering  
The University of Arizona  
Bldg. 16; Room 301  
Tuscon, AZ 85721  
Phone: 520-621-8459  
Fax: 520-621-8191  
E-mail: jacobs@ame.arizona.edu

Subash S. Jayawardena  
Dept. of Chemical Engineering  
University of Houston  
4200 Calhoun  
Houston, TX 77204-4792  
Phone: 713-743-4338  
Fax: 713-743-4323  
E-mail: subash@uh.edu

James T. Jenkins  
Dept. of Theoretical and Applied Mechanics  
Cornell University  
Kimball Hall  
Ithaca, NY 14853  
Phone: 607-255-7785  
Fax: 607-255-2016  
E-mail: jtt2@cornell.edu

Michael R. Johanson  
NYMA, Inc.  
2001 Aerospace Pkwy.  
Brook Park, OH 44142  
Phone: 216-977-1066  
Fax: 216-977-1269  
E-mail: johanson@lerc.nasa.gov

Damir Juric  
Dept. of Mechanical Engineering  
The University of Michigan  
304 Lay Auto Lab  
Ann Arbor, MI 48109  
Phone: 313-763-6613  
Fax: 313-764-4256  
E-mail: djuric@engin.umich.edu

K. Kailasanath  
Lab. for Computational Physics & Fluid Dynamics  
Naval Research Laboratory  
Code 6410  
Washington, DC 20375  
Phone: 202-767-2402  
Fax: 202-767-4798  
E-mail: kailas@lcp.nvl.navy.mil

Yasuhiro Kamotani  
Dept. of Mechanical & Aerospace Engineering  
Case Western Reserve University  
Glenman Bldg. 412  
Cleveland, OH 44106  
Phone: 216-368-6455  
Fax: 216-368-6445

Sang-Yoon Kang  
Dept. of Chemical Engineering  
Syracuse University  
B 31-2 Slocum Hts.,  
Syracuse, NY 13210  
Phone: 315-442-7139  
E-mail: sykang@syrr.edu

Shu-Hsin Kao  
Dept. of Mechanical Engineering  
The University of Michigan  
2634 Traver Rd.  
Ann Arbor, MI 48105  
Phone: 313-668-8612  
Fax: 313-668-8612  
E-mail: kao@engin.umich.edu

Allen Karchmer  
NASA Lewis Research Center  
MS 500-216; 21000 Brookpark Rd.  
Cleveland, OH 44135  
Phone: 216-433-5180  
Fax: 216-433-8660  
E-mail: a.karchmer@lerc.nasa.gov

Mohammad Kassemi  
NASA Lewis Research Center  
MS 105-1; 21000 Brookpark Rd.  
Cleveland, OH 44135  
Phone: 216-433-5031  
Fax: 216-433-5033  
E-mail: mohammad.kassemi@lerc.nasa.gov

Kazunori Kawasaki  
Dept. of Space Systems/Aerospace Div.  
Nissan Motor Co., Ltd., Tokyo  
5-1, Momoi, 3-chome, Suginami-Ku  
Tokyo, 167 Japan  
Phone: 81-3-3301-6673  
Fax: 81-3-3301-6711  
E-mail: chint@nova.lab.nissan.co.jp

Robert E. Kelly  
Dept. of Mechanical & Aerospace Engineering  
University of California/Los Angeles  
420 Westwood Plaza  
Los Angeles, CA 90095-1597  
Phone: 310-825-5489  
Fax: 310-206-4830

Edward G. Keshock  
Dept. of Mechanical Engineering  
Cleveland State University  
1983 E. 24th St.  
Cleveland, OH 44115  
Phone: 216-687-2494  
Fax: 216-687-9280  
E-mail: e.keshock@csuohio.edu

Dmitry K. Khrustalev  
Dept. of Mechanical Engineering  
University of Connecticut  
191 Auditorium Rd., U-139  
Storrs, CT 06269  
Phone: 860-486-3689  
Fax: 860-486-5088  
E-mail: dkhrust@eng2.uconn.edu

Boris Khusid  
The Levich Institute  
City College of New York  
Steinman Hall, T-1M; 140th Street & Convent Ave.  
New York, NY 10031  
Phone: 212-650-8487  
Fax: 212-650-6835  
E-mail: boris@lisgil.engr.ccny.cuny.edu

Jungho Kim  
Dept. of Engineering  
University of Denver  
Denver, CO 80208  
Phone: 303-871-3816  
Fax: 303-871-4450  
E-mail: jlcim@du.edu

John Kizito  
2307 Forestdale  
Cleveland, OH 44109  
Phone: 216-749-0019  
Fax: 216-749-0019  
E-mail: jpk5@po.cwru.edu

Stanley J. Kleis  
Dept. of Mechanical Engineering  
University of Houston  
4800 Calhoun  
Houston, TX 77204-4792  
Phone: 713-743-4536  
Fax: 713-743-4503  
E-mail: kleis@uh.edu

Richard H. Knoll  
NASA Lewis Research Center  
MS 500-202; 21000 Brookpark Rd.  
Cleveland, OH 44135  
Phone: 216-433-2419  
Fax: 216-433-8660

Fred J. Kohl  
NASA Lewis Research Center  
MS 500-115; 21000 Brookpark Rd.  
Cleveland, OH 44135  
Phone: 216-433-2866  
Fax: 216-433-8660  
E-mail: fred.kohl@lerc.nasa.gov

Bogdan Konsur  
Dept. of Mechanical Engineering  
The University of Illinois/Chicago  
9142 Kilpatrick Ave.  
Skokie, IL 60076  
Phone: 847-568-1625  
Fax: 312-413-0447  
E-mail: konsur@sun.me.uic.edu

Joel Koplik  
The Levich Institute  
City College of New York  
T-1M; 140th St. & Convent Ave.  
New York, NY 10031  
Phone: 212-650-8162  
Fax: 212-650-6835  
E-mail: koplik@sci.ccny.cuny.edu

Douglas B. Kothe  
Theoretical Division, Group T-3  
Los Alamos National Laboratory  
MS B216  
Los Alamos, NM 87545  
Phone: 505-667-9089  
Fax: 505-665-5926  
E-mail: dbk@lanl.gov

Sindo Kou  
Dept. of Materials Science & Engineering  
University of Wisconsin  
1509 University Ave.  
Madison, WI 53706  
Phone: 608-262-0576  
Fax: 608-262-8353  
E-mail: kou@engr.wisc.edu

Adam Krigel  
NASA Lewis Research Center  
21000 Brookpark Rd.; 21000 Brookpark Rd.  
Cleveland, OH 44135  
Phone: 216-433-3963  
E-mail: kreeg@einstein.lerc.nasa.gov

Rainer Kuhl  
DARA  
Koenigswinterer Strasse 522-524  
Bonn, 53227 Germany  
Phone: 0049-228-447-387  
Fax: 0049-228-447-714

Mark D. Kunka  
Dept. of Mathematics  
The Ohio State University  
231 West 18  
Columbus, OH 43210  
Phone: 614-292-5431

Akiyoshi Kuroda  
Dept. of Mechanical Engineering  
Hokkaido University  
North 13, West 8  
Sapporo, 060 Japan  
Phone: 81-11-706-6377  
Fax: 81-11-706-7889

Robert E. Kusner  
NASA Lewis Research Center  
MS 110-2; 21000 Brookpark Rd.  
Cleveland, OH 44135  
Phone: 216-433-9413  
Fax: 216-433-3793  
E-mail: kusner@lerc.nasa.gov

Girard Labossiere  
MDS&DS-KSC  
100 McDonnell Douglas Way  
Titusville, FL 32780

Ravindra B. Lal  
Dept. of Physics  
Alabama A&M University  
P.O. Box 71  
Normal, AL 35762  
Phone: 205-851-5309  
Fax: 205-851-5622  
E-mail: lal@caos.aamu.edu

Chris Lant  
ADF, Inc.  
2001 Aerospace Pkwy.  
Brook Park, OH 44142  
Phone: 216-977-1068  
Fax: 216-977-1269  
E-mail: lant@chester.lerc.nasa.gov

Juan C. Lasheras  
Dept. of Aero. & Mech. Engineering Science  
University of California/San Diego  
9500 Gilman Dr.  
La Jolla, CA 92093-0411  
Phone: 619-534-5437  
Fax: 619-534-7599  
E-mail: lasheras@ames.ucsd.edu

Daniel Lathrop  
Dept. of Physics  
Emory University  
Atlanta, GA 30322  
Phone: 404-727-4088  
Fax: 404-727-0873  
E-mail: dpl@complex.physics.emory.edu

Richard W. Lauver  
NASA Lewis Research Center  
MS 500-115; 21000 Brookpark Rd.  
Cleveland, OH 44135  
Phone: 216-433-2860  
Fax: 216-433-8660  
E-mail: richard.lauver@lerc.nasa.gov

Chun Ping Lee  
Microgravity Research & Applications  
Vanderbilt University  
Box 6079, Station B; Vanderbilt University  
Nashville, TN 37235  
Phone: 615-342-6959  
Fax: 615-343-8730  
E-mail: leecp@vuse.vanderbilt.edu

David T. Leighton  
Dept. of Chemical Engineering  
University of Notre Dame  
Notre Dame, IN 46556  
Phone: 219-631-6698  
Fax: 219-631-8366  
E-mail: dtl@darwin.cc.nd.edu

Todd Leonhardt  
Dept. of Physics  
Carnegie Mellon University  
5000 Forbes Ave.  
Pittsburgh, PA 15213  
Phone: 412-268-6283  
Fax: 412-268-0648  
E-mail: tl2s@andrew.cmu.edu

Fred Leslie  
NASA Marshall Space Flight Center  
MC ES71  
Huntsville, AL 35812  
Phone: 205-544-1633  
Fax: 205-544-9243

Ben Q. Li  
Dept. of Mechanical Engineering  
Louisiana State University  
2513A CEBA  
Baton Rouge, LA 70803  
Phone: 504-388-6488  
Fax: 504-388-5924  
E-mail: meli@lsucax.sncc.lsu.edu

Anthony Liakopoulos  
Dept. of Mechanical Engineering & Mechanics  
Lehigh University  
19 Memorial Drive West  
Bethlehem, PA 18015  
Phone: 610-758-4929  
Fax: 610-758-6224  
E-mail: al03@lehigh.edu

Hsing-Sheng Liang  
Dept. of Mech. Engineering & Aero. Mechanics  
The University of Michigan  
2182 G.G. Brown Bldg.  
Ann Arbor, MI 48105  
Phone: 313-936-0343  
Fax: 313-747-3170  
E-mail: hsliang@engin.umich.edu

Seth H. Lichter  
Dept. of Mechanical Engineering  
Northwestern University  
Evanston, IL 60208-3111  
Phone: 847-467-1885  
Fax: 847-491-3915  
E-mail: s-lichter@nwu.edu

Min Y. Lin  
Reactor Div.  
NIST  
MS E151  
Gaithersburg, MD 20899  
Phone: 301-975-6589  
Fax: 301-921-9847  
E-mail: lin@enh.nist.gov

Sung P. Lin  
Dept. of Mechanical & Aeronautical Engineering  
Clarkson University  
Box 5725  
Potsdam, NY 13699-5725  
Phone: 315-268-6584  
Fax: 315-268-6438  
E-mail: gw02@splin2.mie.clarkson.edu

Jerri S. Ling  
NASA Lewis Research Center  
MS 500-102; 21000 Brookpark Rd.  
Cleveland, OH 44135  
Phone: 216-433-2841  
Fax: 216-433-8050  
E-mail: zippy@A1.lerc.nasa.gov

Andrea J. Liu  
Dept. of Chemistry  
University of California/Los Angeles  
405 Hilgard Ave.  
Los Angeles, CA 90095-1547  
Phone: 310-825-8266  
Fax: 310-206-4038  
E-mail: liu@chemistry.ucla.edu

Jing Liu  
Dept. of Physics and Astronomy  
California State University/Long Beach  
1250 Bellflower Blvd.  
Long Beach, CA 90840  
Phone: 310-985-4913  
Fax: 310-985-7924  
E-mail: jliu@csulb.edu

Michael Loewenberg  
Dept. of Chemical Engineering  
Yale University  
Mason Laboratory, 9 Hillhouse Ave.  
New Haven, CT 06520-8286  
Phone: 203-432-4334  
Fax: 203-432-7232  
E-mail: michael.loewenberg@yale.edu

John M. Lopez  
Dept. of Mathematics  
The Pennsylvania State University  
316 McAllister Bldg.  
University Park, PA 16802  
Phone: 814-865-2491  
Fax: 814-865-3735  
E-mail: lopez@math.psu.edu

Tibor Lorik  
ADF, Inc.  
2001 Aerospace Parkway  
Brook Park, OH 44142  
Phone: 216-977-1188  
E-mail: lorik@dinah.lerc.nasa.gov

Sudarshan Loyalka  
Particulate Sys. Research Ctr.  
University of Missouri/Columbia  
0039 Engineering Complex  
Columbia, MO 65211  
Phone: 314-882-3568  
Fax: 314-882-2490  
E-mail: loyalka@ecvax2.ecn.missouri.edu

Weili Luo  
Dept. of Physics  
University of Central Florida  
4000 Central Florida Blvd.  
Orlando, FL 32816  
Phone: 407-823-5855  
Fax: 407-823-5112  
E-mail: luo@phys.physics.ucf.edu

Barry Luukkala  
Dept. of Physics  
Carnegie Mellon University  
5000 Forbes Ave.  
Pittsburgh, PA 15213  
Phone: 412-268-2756  
Fax: 412-268-0648

Margaret J. Lyell  
Dept. of Mechanical & Aerospace Engineering  
West Virginia University  
Box 6106  
Morgantown, WV 26506-6106  
Phone: 304-293-3111 Ext. 345  
Fax: 304-293-6689  
E-mail: lyell@cemr.wvu.edu

Daniel W. Mackowski  
Dept. of Mechanical Engineering  
Auburn University  
201 Ross Hall  
Auburn, AL 36849  
Phone: 334-844-3334  
Fax: 334-844-3307  
E-mail: dmckwski@eng.auburn.edu

James V. Maher  
Provost's Office  
University of Pittsburgh  
801 Cathedral of Learning  
Pittsburgh, PA 15260  
Phone: 412-624-4223  
Fax: 412-383-9640  
E-mail: jvmaher@vms.cis.pitt.edu

Charles Maldarelli  
The Levich Institute/Dept. of Chemical Engineering  
City College of New York  
140th St. & Convent Ave.  
New York, NY 10031  
Phone: 212-650-8160  
Fax: 212-650-6835  
E-mail: lidsA0@engr.ccny.cuny.edu

Seethambal S. Mani  
Dept. of Crystal Growth  
Northrop Grumman Corporation  
401-3A55; 1310 Beulah Road  
Pittsburgh, PA 15235  
Phone: 412-256-1446  
Fax: 412-256-1331  
E-mail: mani@cis.pgh.wec.com

Mark Marr-Lyon  
Dept. of Physics  
Washington State University  
Pullman, WA 99164-2814  
Phone: 509-335-3466  
Fax: 509-335-7816

Philip L. Marston  
Dept. of Physics  
Washington State University  
Pullman, WA 99164-2814  
Phone: 509-335-5343  
Fax: 509-335-7816  
E-mail: marston@wsu.edu

William J. Masica  
NASA Lewis Research Center  
MS 500-205; 21000 Brookpark Rd.  
Cleveland, OH 44135  
Phone: 216-433-2864  
Fax: 216-433-8660  
E-mail: william.j.masica@lerc.nasa.gov

Larry Mason  
Payload Sensors and Instruments  
Lockheed Martin Astronautics  
P.O. Box 179 M/S B0560  
Denver, CO 80201-0179  
Phone: 303-971-9076  
Fax: 303-977-0829  
E-mail: larry.w.mason@den.mmc.com

Jehanzeb Masud  
Dept. of Mechanical & Aerospace Engineering  
Case Western Reserve University  
10900 Euclid Ave.  
Cleveland, OH 44106  
Phone: 216-368-2945  
Fax: 216-368-6445  
E-mail: jxm52@po.cwru.edu

Kathleen McCloud  
Dept. of Physics & Astronomy  
University of Pittsburgh  
100 Allen Hall  
Pittsburgh, PA 15260  
Phone: 412-624-9003  
Fax: 412-624-9163  
E-mail: kathym@phyast.pitt.edu

William D. McCormick  
Dept. of Nonlinear Dynamics/Physics  
The University of Texas at Austin  
Austin, TX 78712  
Phone: 512-471-7413  
Fax: 512-471-1558  
E-mail: wdm@chaos.ph.utexas.edu

Mark J. McCready  
Dept. of Chemical Engineering  
University of Notre Dame  
171 Fitzpatrick Hall  
Notre Dame, IN 46556  
Phone: 219-631-7146  
Fax: 219-631-8366  
E-mail: mccready.1@nd.edu

Jeff McFadden  
Computing & Applied Mathematics Laboratory  
NIST  
Room 365, Building 820  
Gaithersburg, MD 20899  
Phone: 301-975-2711  
Fax: 301-990-4127  
E-mail: mcfad@cam.nist.gov

Richard M. McLaughlin  
Dept. of Mathematics  
University of Utah  
233 JWB Building  
Salt Lake City, UT 84112  
Phone: 801-581-8341  
Fax: 801-581-4148  
E-mail: rmm@math.utah.edu

John B. McQuillen  
NASA Lewis Research Center  
MS 500-102; 21000 Brookpark Rd.  
Cleveland, OH 44135  
Phone: 216-433-2876  
Fax: 216-433-8660  
E-mail: jmcquil@popserve.lerc.nasa.gov

Constantine Megaridis  
Dept. of Mechanical Engineering  
University of Illinois at Chicago  
M/C 251; 842 W. Taylor St.  
Chicago, IL 60607  
Phone: 312-996-3436  
Fax: 312-413-0447  
E-mail: cmm@uic.edu

Eckart Meiburg  
Dept. of Aerospace Engineering  
University of Southern California  
Los Angeles, CA 90089  
Phone: 213-740-5376  
Fax: 213-740-7774  
E-mail: eckart@spock.usc.edu



Carl Meinhart  
Scientific Research Lab  
Ford Motor Co.  
M02629, SRL; P.O. Box 2053  
Dearborn, MI 48121-2053  
Phone: 313-845-3786  
E-mail: cmeinhar@ford.com

John Merry  
ADF, Inc.  
2001 Aerospace Pkwy.  
Brook Park, OH 44142  
Phone: 216-977-1135  
Fax: 216-977-1269  
E-mail: merry.@chester.lerc.nasa.gov

Herman Merte, Jr.  
Dept. of Mechanical Engineering/Applied Mechanics  
The University of Michigan  
2148 G.G. Brown  
Ann Arbor, MI 48109-2125  
Phone: 313-764-5240  
Fax: 313-647-3170  
E-mail: merte@engin.umich.edu

William Meyer  
NASA Lewis Research Center  
MS 105-1; 21000 Brookpark Rd.  
Cleveland, OH 44135  
Phone: 216-433-5011

K. Y. Min  
NASA Lewis Research Center  
MS 110-2; 21000 Brookpark Rd.  
Cleveland, OH 44135  
Phone: 216-433-3963  
Fax: 216-433-3793  
E-mail: min@lerc.nasa.gov

Hans D. Mittelman  
Dept. of Mathematics  
Arizona State University  
Box 871804  
Tempe, AZ 85287-1804  
Phone: 602-965-6595  
Fax: 602-965-0461  
E-mail: mittelman@math.la.asu.edu

Michael R. Moldover  
NIST  
Bldg. 221, Room A111  
Gaithersburg, MD 20899  
Phone: 301-975-2459  
Fax: 301-869-4020  
E-mail: michael.moldover@nist.gov

S. Morris  
Dept. of Mechanical Engineering  
University of California/Berkeley  
6115 Etcheverry Hall  
Berkeley, CA 94720-1740  
Phone: 510-642-5545  
Fax: 510-642-3161  
E-mail: morris@euler.me.berkeley.edu

Brian J. Motil  
NASA Lewis Research Center  
MS 500-102; 21000 Brookpark Rd.  
Cleveland, OH 44135  
Phone: 216-433-6617  
Fax: 216-433-8050  
E-mail: bjmotil@lerc.nasa.gov

Ali Nadim  
Dept. of Aerospace & Mechanical Engineering  
Boston University  
110 Cummington St.  
Boston, MA 02215  
Phone: 617-353-3951  
Fax: 617-353-5866  
E-mail: nadim@bu.edu

Henry K. Nahra  
NASA Lewis Research Center  
MS 500-102; 21000 Brookpark Rd.  
Cleveland, OH 44135  
Phone: 216-433-5385  
Fax: 216-433-8050  
E-mail: nahra@cedar1.lerc.nasa.gov

Masami Nakagawa  
Organization 6212  
Sandia National Laboratories  
MS 0709; P.O. Box 5800  
Albuquerque, NM 87185-0709  
Phone: 505-844-3360  
Fax: 505-845-9500  
E-mail: mnakaga@sandia.gov

Amitabh Narain  
Dept. of Mechanical Engineering  
Michigan Technological University  
1400 Townsend Drive  
Houghton, MI 49931  
Phone: 906-487-2555  
Fax: 906-487-2822  
E-mail: narain@mtu.edu

Vedha Nayagam  
NASA Lewis Research Center  
MS 500-115; 21000 Brookpark Rd.  
Cleveland, OH 44135  
Phone: 216-433-8702  
Fax: 216-433-8660  
E-mail: v.nayagam@lerc.nasa.gov

G. Paul Neitzel  
School of Mechanical Engineering  
Georgia Institute of Technology  
Atlanta, GA 30332-0405  
Phone: 404-894-3242  
Fax: 404-894-2291  
E-mail: paul.neitzel@me.gatech.edu

Christoph Nicolet  
Center for Micromolecular Crystallography  
University of Alabama/Birmingham  
1716 University Blvd.; HBP 416  
Birmingham, AL 35294  
Phone: 205-934-7611  
Fax: 205-975-2517  
E-mail: nicolet@orion.cmc.uab.edu

Jay M. Ochterbeck  
Dept. of Mechanical Engineering  
Clemson University  
102 Fluor Dawlez EIB  
Clemson, SC 29634  
Phone: 864-656-3292  
Fax: 864-656-4435  
E-mail: jochter@ces.clemson.edu

Hasan Oguz  
Dept. of Mechanical Engineering  
Johns Hopkins University  
122 Latrobe Hall  
Baltimore, MD 21218  
Phone: 410-516-4651  
Fax: 410-516-7254  
E-mail: oguz@titan.me.jhu.edu

Cyril Okhio  
MFE  
Central State University  
1400 Brush Row Rd.  
Wilberforce, OH 45384  
Phone: 513-376-6197

Arthur C. Or  
Dept. of Mechanical & Aerospace Engineering  
University of California/Los Angeles  
Los Angeles, CA 90024-1567  
Phone: 310-836-0268  
Fax: 310-836-5590  
E-mail: or@ucla.edu

Alexander Oron  
Dept. of Applied Mathematics  
Northwestern University  
Evanston, IL 60208-3125  
Phone: 847-491-3149  
Fax: 847-491-2178  
E-mail: oron@arnold.esam.nwu.edu

Simon Ostrach  
Dept. of Mechanical & Aerospace Engineering  
Case Western Reserve University  
418 Glennan Bldg.; 10900 Euclid Ave.  
Cleveland, OH 44106  
Phone: 216-368-2942  
Fax: 216-368-6445  
E-mail: sxo3@po.cwru.edu

Ben Ovryn  
NASA Lewis Research Center  
MS 110-3; 21000 Brookpark Road  
Cleveland, OH 44135  
Phone: 216-433-8335  
Fax: 216-433-3793  
E-mail: ovryn@wave.lerc.nasa.gov

Ayo Oyediran  
AYT Corporation  
2001 Aerospace Pkwy.  
Brook Park, OH 44142  
Phone: 216-977-1049  
Fax: 216-977-1269  
E-mail: drayo@mars.lerc.nasa.gov

Salvatore Pais  
NASA Lewis Research Center  
MS 500-102; 21000 Brookpark Rd.  
Cleveland, OH 44135  
Phone: 216-754-1181

Dimitrios H. Papadopoulos  
Dept. of Chemical Engineering  
Yale University  
Rm. 306; 9 Hillhouse Ave.  
New Haven, CT 06520  
Phone: 203-432-4380  
Fax: 203-432-7232  
E-mail: papad@htcre.eng.yale.edu

Masood Parang  
NASA Lewis Research Center  
MS 500-112; 21000 Brookpark Rd.  
Cleveland, OH 44135  
Phone: 216-433-2627  
Fax: 216-433-8050  
E-mail: mparang@utk.edu

Chang-Won Park  
Dept. of Chemical Engineering  
University of Florida  
P.O. Box 116005  
Gainesville, FL 32611  
Phone: 352-392-6205  
Fax: 352-392-9513  
E-mail: park@che.ufl.edu

Ramkumar N. Parthasarathy  
School of Aerospace & Mech. Engineering  
The University of Oklahoma  
212 Felgar Hall; 865 Asp Avenue  
Norman, OK 73019  
Phone: 405-325-5011  
Fax: 405-325-1088  
E-mail: kumar@europa.ecn.uoknor.edu

Alexander Z. Patashinski  
Materials Research Center/Dept. of Chemistry  
Northwestern University  
2145 Sheridan Rd.  
Evanston, IL 60208  
Phone: 847-467-2618  
Fax: 847-491-9982  
E-mail: patashin@casbah.acns.nwu.edu

Michael E. Paulaitis  
Dept. of Chemical Engineering  
Johns Hopkins University  
3400 N. Charles St.  
Baltimore, MD 21218  
Phone: 410-516-7170  
Fax: 410-516-5510  
E-mail: michaelp@jhu.edu

Arne J. Pearlstein  
Dept. of Mechanical & Industrial Engineering  
University of Illinois/Urbana-Champaign  
1206 West Green St.  
Urbana, IL 61801  
Phone: 217-333-3658  
Fax: 217-244-6534  
E-mail: arne@ajpiris.me.uiuc.edu

Priyantha Perera  
Dept. of Mathematics  
Carnegie Mellon University  
Pittsburgh, PA 15213  
Phone: 217-244-8388

Marc Perlin  
Dept. of Naval Architecture & Marine Engineering  
The University of Michigan  
208 NAME Building  
Ann Arbor, MI 48109  
Phone: 313-763-4754  
Fax: 313-936-8820  
E-mail: perlin@engin.umich.edu

Charles A. Petty  
Dept. of Chemical Engineering  
Michigan State University  
A112 Research Complex/Engineering  
East Lansing, MI 48824  
Phone: 517-353-5486  
Fax: 517-432-1634  
E-mail: petty@che.msu.edu

Joel L. Plawsky  
Dept. of Chemical Engineering  
Rensselaer Polytechnic Institute  
110 Eighth St.  
Troy, NY 12180  
Phone: 518-276-6049  
Fax: 518-276-4030  
E-mail: plawsky@rpi.edu

Alex D. Pline  
NASA Lewis Research Center  
MS 500-102; 21000 Brookpark Rd.  
Cleveland, OH 44135  
Phone: 216-433-6614  
Fax: 216-433-8050  
E-mail: [apline@lerc.nasa.gov](mailto:apline@lerc.nasa.gov)

Vadim I. Polezhaev  
Institute of Problems in Mechanics  
Russian Academy of Sciences  
Prospect Vernadskogo 101  
Moscow, 117526 Russia  
Phone: 7-095-434-32-83  
Fax: 7-095-938-20-48  
E-mail: [polezh@ipm.msk.su](mailto:polezh@ipm.msk.su)

Dimos Poulikakos  
Dept. of Mechanical Engineering  
University of Illinois/Chicago  
842 W. Taylor St.  
Chicago, IL 60607  
Phone: 312-996-5239  
Fax: 312-413-0447

Burkhard Prause  
Dept. of Physics  
University of Notre Dame  
Notre Dame, IN 46545  
Phone: 219-631-4088  
Fax: 219-631-5952  
E-mail: [bprouse@campad.phys.nd.edu](mailto:bprouse@campad.phys.nd.edu)

John F. Prince  
NYMA, Inc.  
2001 Aerospace Pkwy.  
Brook Park, OH 44142  
Phone: 216-977-1105  
Fax: 216-977-1269  
E-mail: [jprince@lerc.nasa.gov](mailto:jprince@lerc.nasa.gov)

Andrea Prosperetti  
Dept. of Mechanical Engineering  
Johns Hopkins University  
122 Latrobe Hall  
Baltimore, MD 21218  
Phone: 410-516-8534  
Fax: 410-516-7254  
E-mail: [prosper@titan.me.jhu.edu](mailto:prosper@titan.me.jhu.edu)

Vladislav V. Pukhnachov  
Dept. of Applied Hydrodynamics  
Lavrentyev Institute of Hydrodynamics  
Lavrentyev Prospect 15  
Novosibirsk, 630090 Russia  
Phone: 7-3832-357401  
Fax: 7-3832-354050  
E-mail: [pukh@hydro.nsk.su](mailto:pukh@hydro.nsk.su)

Gennady F. Putin  
Dept. of Physics  
Perm State University  
15 Bukirev St.  
Perm, 614600 Russia  
Phone: 7-3422-69-76-21  
Fax: 7-3422-33-39-83  
E-mail: [putin@psu.ac.ru](mailto:putin@psu.ac.ru)

Seth Putterman  
Dept. of Physics  
University of California/Los Angeles  
Los Angeles, CA 90095  
Phone: 310-825-2269  
Fax: 310-206-5668

Dan Qu  
Dept. of Physics  
Carnegie Mellon University  
5000 Forbes Ave.  
Pittsburgh, PA 15213  
Phone: 412-268-3375  
Fax: 412-268-0648  
E-mail: [dqu@andrew.cmu.edu](mailto:dqu@andrew.cmu.edu)

Narayanan Ramachandran  
USRA; ES-75  
NASA Marshall Space Flight Center  
Huntsville, AL 35812  
Phone: 205-544-8308  
Fax: 205-544-8891  
E-mail: [ramachandran@gsi.msfc.nasa.gov](mailto:ramachandran@gsi.msfc.nasa.gov)

Nasser Rashidnia  
NASA Lewis Research Center  
MS 500-102; 21000 Brookpark Rd.  
Cleveland, OH 44135  
Phone: 216-433-3622  
Fax: 216-433-8050  
E-mail: [nasser@lerc.nasa.gov](mailto:nasser@lerc.nasa.gov)

Kathy Rawson  
Microgravity Educational Outreach  
Microgravity News  
1040-D Settlers Landing Rd.  
Hampton, VA 23669  
Phone: 804-723-2197  
Fax: 804-723-0241  
E-mail: k.w.rawson@larc.nasa.gov

Lonnie Reid  
NYMA, Inc.  
2001 Aerospace Pkwy.  
Brook Park, OH 44142  
Phone: 216-977-1012  
Fax: 216-977-1269

Kamiel S. Rezkallah  
Dept. of Mechanical Engineering  
University of Saskatchewan  
57 Campus Drive  
Saskatoon, SK S7N-5A9 Canada  
Phone: 306-966-5453  
Fax: 306-966-5427  
E-mail: kamiel@engr.usask.ca

Robert C. Rhome  
Code UG  
NASA Headquarters  
Washington, DC 20546-0001  
Phone: 202-358-1490  
Fax: 202-358-3091  
E-mail: robert.rhyme@hq.nasa.gov

James R. Robertson  
ADF, Inc.  
2001 Aerospace Pkwy.  
Brook Park, OH 44142  
Phone: 216-977-1151  
Fax: 216-977-1269

Judith Robey  
Code UG  
NASA Headquarters  
Washington, DC 20546-0001  
Phone: 202-358-0823  
Fax: 202-358-3091  
E-mail: jrobey@hq.nasa.gov

Terri D. Rodgers  
NASA Lewis Research Center  
MS 500-102; 21000 Brookpark Rd.  
Cleveland, OH 44135  
Phone: 216-433-8740  
Fax: 216-433-8050  
E-mail: terri.rodgers@lerc.nasa.gov

Evgeny B. Rodichev  
Institute of Mechanics  
Moscow State University  
Michurinskiy prosp. 1  
Moscow, 119899 Russia  
Phone: 007-095-939-5287  
Fax: 007-095-932-8841  
E-mail: er@sai.msu.su

Olga V. Rodicheva  
Institute of Mechanics  
Moscow State University  
Michurinskiy prosp. 1  
Moscow, 119899 Russia  
Phone: 007-095-939-2383  
Fax: 007-095-932-8841  
E-mail: rool@sai.msu.su

Chris B. Rogers  
Dept. of Mechanical Engineering  
Tufts University  
Anderson Hall  
Medford, MA 02155  
Phone: 617-627-3239  
Fax: 617-627-3058  
E-mail: crogers@tufts.edu

Rick Rogers  
NASA Lewis Research Center  
MS 105-1; 21000 Brookpark Rd.  
Cleveland, OH 44135  
Phone: 216-433-6512  
Fax: 216-433-5033

Paul D. Ronney  
Dept. of Mechanical Engineering  
University of Southern California  
OHE 430  
Los Angeles, CA 90089-1453  
Phone: 213-740-0490  
Fax: 213-740-8071  
E-mail: roney@rcf.usc.edu

Daniel E. Rosner  
Dept. of Chemical Engineering  
Yale University  
Mason Laboratory, Rm. 319; 9 Hillhouse Ave.  
New Haven, CT 06520-8286  
Phone: 203-432-4391  
Fax: 203-432-7232  
E-mail: rosner@htcre.eng.yale.edu

Michael A. Rother  
Dept. Chemical Engineering  
University of Colorado  
Campus Box 424  
Boulder, CO 80309-0424  
Phone: 303-492-1240  
Fax: 303-492-4341  
E-mail: rother@ucsu.colorado.edu

Brian M. Rush  
Dept. of Aerospace & Mechanical Engineering  
Boston University  
110 Cummings St.  
Boston, MA 02215  
Phone: 617-353-2814  
Fax: 617-353-5866  
E-mail: redman@bu.edu

Satwindar Singh Sadhal  
Dept. of Mechanical Engineering  
University of Southern California  
Olin Hall 430; MC 1453  
Los Angeles, CA 90089-1453  
Phone: 213-740-0492  
Fax: 213-740-8071  
E-mail: sadhal@rcf.usc.edu

Jack A. Salzman  
NASA Lewis Research Center  
MS 500-205; 21000 Brookpark Rd.  
Cleveland, OH 44135  
Phone: 216-433-2868  
Fax: 216-433-8660  
E-mail: jack.a.salzman@lerc.nasa.gov

Ashok S. Sangani  
Dept. of Chemical Engineering & Materials Science.  
Syracuse University  
320 Hinds Hall  
Syracuse, NY 13244  
Phone: 315-443-4502  
Fax: 315-443-2556  
E-mail: asangani@mailbox.syr.edu

Michael F. Schatz  
Dept. of Physics & Center for Nonlinear Dynamics  
University of Texas  
Austin, TX 78712  
Phone: 512-471-5425  
Fax: 512-471-1558  
E-mail: schatz@chaos.ph.utexas.edu

Kathy Schubert  
NASA Lewis Research Center  
MS 500-217; 21000 Brookpark Rd.  
Cleveland, OH 44135  
Phone: 216-433-5331  
Fax: 216-433-8660

William W. Schultz  
Dept. of Mech. Engineering & Applied Mechanics  
The University of Michigan  
313 Lay Auto Lab.  
Ann Arbor, MI 48109  
Phone: 313-936-0351  
Fax: 313-764-4256  
E-mail: schultz@engin.umich.edu

Leonard Schwartz  
Dept. of Mechanical Engineering  
University of Delaware  
Spencer Laboratory  
Newark, DE 19716  
Phone: 302-831-6830  
Fax: 302-831-3619  
E-mail: scwartz@me.udel.edu

Vincent M. Sciascia  
Dept. of Mechanical Engineering  
University of Illinois at Chicago  
842 W. Taylor  
Chicago, IL 60607-7022  
Phone: 312-996-5520  
Fax: 312-413-0447  
E-mail: u60698@uic.edu

Earl Scime  
Dept. of Physics  
West Virginia University  
P.O. Box 6315  
Morgantown, WV 26506  
Phone: 304-293-3422 Ext. 1437  
Fax: 304-293-5732  
E-mail: scime@wvnmvs.wvnet.edu

Robert Sekerka  
Carnegie Mellon University  
5000 Forbes Ave.  
Pittsburgh, PA 15213-3890  
Phone: 412-268-2753

Surajit Sen  
Dept. of Physics  
State University of New York/Buffalo  
239 Fronczak Hall  
Buffalo, NY 14221  
Phone: 716-645-6314  
Fax: 716-645-2507  
E-mail: sen@ubvms.cc.buffalo.edu

M. Keith Sharp  
Dept. of Civil & Environmental Engineering  
University of Utah  
3220 MEB  
Salt Lake City, UT 84112  
Phone: 801-581-6955  
Fax: 801-585-5477  
E-mail: m.k.sharp@m.cc.utah.edu

Benjamin D. Shaw  
Dept. of Mechanical & Aeronautical Engineering  
University of California/Davis  
Davis, CA 95616  
Phone: 916-752-4130  
Fax: 916-752-4158  
E-mail: bdshaw@ucdavis.edu

Michael Shoemaker  
ADF, Inc.  
2001 Aerospace Pkwy.  
Brook Park, OH 44142  
Phone: 216-977-1137  
Fax: 216-977-1269  
E-mail: fsshoe@lerc.nasa.gov

Rainee Simons  
NYMA, Inc.  
2001 Aerospace Pkwy.  
Brook Park, OH 44142  
Phone: 216-433-3462  
Fax: 216-977-1269

Bhim S. Singh  
NASA Lewis Research Center  
MS 500-102; 21000 Brookpark Rd.  
Cleveland, OH 44135  
Phone: 216-433-5396  
Fax: 216-433-8660  
E-mail: bhim.s.singh@lerc.nasa.gov

Mrityunjay Singh  
NASA Lewis Research Center  
MS 106-5; 21000 Brookpark Rd.  
Cleveland, OH 44135  
Phone: 216-433-8883  
Fax: 216-433-5544  
E-mail: msingh@lerc.nasa.gov

Ray Skarda  
NASA Lewis Research Center  
MS 500-102; 21000 Brookpark Rd.  
Cleveland, OH 44135  
Phone: 216-433-8728

Gregory T. Smedley  
Dept. of Environmental Engineering Science  
California Institute of Technology  
210-41; 1201 E. California Blvd.  
Pasadena, CA 91125  
Phone: 818-395-4130  
Fax: 818-568-8743  
E-mail: gsmedley@cco.caltech.edu

Marc K. Smith  
School of Mechanical Engineering  
Georgia Institute of Technology  
Atlanta, GA 30332-0405  
Phone: 404-894-3826  
Fax: 404-894-8496  
E-mail: marc.smith@me.gatech.edu

Linda Smolka  
Dept. of Mathematics  
The Pennsylvania State University  
218 McAllister Bldg.  
University Park, PA 16802  
Phone: 814-865-7527  
Fax: 814-865-3735  
E-mail: smolka@math.psu.edu

Robert S. Snyder  
NASA Marshall Space Flight Center  
MC ES71  
Huntsville, AL 35812  
Phone: 205-544-7755  
Fax: 205-544-8762  
E-mail: robert.snyder@msfc.nasa.gov

Thomas H. Solomon  
Dept. of Physics  
Bucknell University  
Lewisburg, PA 17837  
Phone: 717-524-1348  
Fax: 717-524-3760  
E-mail: tsolomon@bucknell.edu

Ain A. Sonin  
Dept. of Mechanical Engineering  
MIT  
Room 3-256, MIT  
Cambridge, MA 02139  
Phone: 617-253-2247  
Fax: 617-258-8559  
E-mail: sonin@mit.edu

Stephen H. Spiegelberg  
Div. of Applied Sciences  
Harvard University  
29 Oxford St.  
Cambridge, MA 02138  
Phone: 617-496-4152  
Fax: 617-495-9837  
E-mail: spiegel@stokes.harvard.edu

Thomas H. St. Onge  
NASA Lewis Research Center  
MS 500-217; 21000 Brookpark Rd.  
Cleveland, OH 44135  
Phone: 216-433-3557  
Fax: 216-433-8660  
E-mail: TStOnge@lerc.nasa.gov

Bob Stack  
Dept. of Cryogenics  
Ball Aerospace and Technologies Corporation  
P.O. Box 1062  
Boulder, CO 80306-1062  
Phone: 303-939-5788  
Fax: 303-939-6307

H. Philip Stahl  
Stahl Optical Systems  
5 Hyvue Dr.  
Newtown, CT  
Phone: 203-797-6606

Stephen Stanec  
Dept. of Physics  
Carnegie Mellon University  
5000 Forbes Ave.  
Pittsburgh, PA 15213  
Phone: 412-268-6283  
Fax: 412-268-0648

Kathleen J. Stebe  
Chemical Engineering Dept.  
Johns Hopkins University  
3400 N. Charles St.  
Baltimore, MD 21211  
Phone: 410-516-7769  
Fax: 410-516-5510  
E-mail: kjs@jhuvms.hcf.jhu.edu

Kroum Stoev  
Physics Dept.  
Carnegie Mellon University  
5000 Forbes Ave.  
Pittsburgh, PA 15213  
Phone: 412-268-6283  
Fax: 412-268-0648  
E-mail: ks7k@andrew.cmu.edu

Don Strayer  
Jet Propulsion Laboratory  
MC 79-24; 4800 Oak Grove Dr.  
Pasadena, CA 91109  
Phone: 818-354-1698  
Fax: 818-393-4878  
E-mail: dons@squid.jpl.nasa.gov

Kevin L. Stultz  
Stahl Optical Systems Inc.  
10397 South Lake Blvd.; STE K-28  
Parma, OH 44130  
Phone: 216-888-6204  
E-mail: kstultz@en.com



R. Shankar Subramanian  
Dept. of Chemical Engineering  
Clarkson University  
Box 5705  
Potsdam, NY 13699-5705  
Phone: 315-268-6648  
Fax: 315-268-6654  
E-mail: subraman@sun.soc.clarkson.edu

Kwang Suh  
NASA Lewis Research Center  
MS 333-1; 21000 Brookpark Rd.  
Cleveland, OH 44135  
Phone: 216-433-2447  
Fax: 216-977-7138  
E-mail: kwang.suh@lerc.nasa.gov

Loren B. Sumner  
Dept. of Mechanical Engineering  
Georgia Institute of Technology  
282 Ferst Drive; SSTC #2 Bldg.; Rm. 200  
Atlanta, GA 30332-0405  
Phone: 404-894-3783  
Fax: 404-894-2291  
E-mail: lsumner@stability.me.gatech.edu

Thomas Sun  
NASA Lewis Research Center  
MS 105-1; 21000 Brookpark Rd.  
Cleveland, OH 44135  
Phone: 216-433-5014

Lipiin Sung  
NASA Lewis Research Center  
MS 105-1; 21000 Brookpark Rd.  
Cleveland, OH 44135  
Phone: 216-433-5014

Harry L. Swinney  
Dept. of Physics  
University of Texas  
Austin, TX 78712  
Phone: 512-471-4619  
Fax: 512-471-1558  
E-mail: swinney@chaos.ph.utexas.edu

Saleh Tanveer  
Dept. of Mathematics  
The Ohio State University  
231 West 18th Ave.  
Columbus, OH 43210-1174  
Phone: 614-292-5710  
Fax: 614-292-1479  
E-mail: tanveer@math.ohio-state.edu

Rongjia Tao  
Dept. of Physics  
Southern Illinois University at Carbondale  
Carbondale, IL 62901  
Phone: 618-536-2117  
Fax: 618-453-1056  
E-mail: ga3756@siucvmb.siu.edu

Yong X. Tao  
Dept. of Mechanical Engineering  
Tennessee State University  
3500 John A. Merritt Blvd.  
Nashville, TN 37209  
Phone: 615-963-5390  
Fax: 615-963-5496  
E-mail: taoy@harpo.tnstate.edu

John M. Tarbell  
Dept. of Chem. Engineering  
The Pennsylvania State University  
Physiological Transport Studies Lab.; 155 Fenske Lab.  
University Park, PA 16802-4400  
Phone: 814-863-4801  
Fax: 814-865-7846  
E-mail: jmt@psuvm.psu.edu

Simon J. Tavener  
Dept. of Mathematics  
The Pennsylvania State University  
416 McAllister Bldg.  
University Park, PA 16802  
Phone: 814-865-3873  
Fax: 814-865-3735  
E-mail: tavener@math.psu.edu

Thomas W. Taylor  
Dept. of Physics  
Cleveland State University  
Cleveland, OH 44115  
Phone: 216-687-2047  
Fax: 216-523-7268

Patrick Tebbe  
Dept. of Mechanical & Aerospace Engineering  
University of Missouri/Columbia  
E2411 EBE  
Columbia, MO 65211  
Phone: 573-882-2785  
Fax: 573-884-5090  
E-mail: i312026@risc1.ecn.missouri.edu

S. N. Tewari  
Dept. of Chemical Engineering  
Cleveland State University  
Cleveland, OH 44115  
Phone: 216-523-7342  
Fax: 216-687-9220  
E-mail: tewari@csvax.csuohio.edu

Todd Tharpe  
Dept. F504  
McDonnell Douglas  
100 McDonnell Douglas Way  
Titusville, FL 32780  
Phone: 407-383-2817  
Fax: 407-269-6202

David B. Thiessen  
Dept. of Physics  
Washington State University  
Pullman, WA 99164-2814  
Phone: 509-335-4908  
Fax: 509-335-7816  
E-mail: thiessen@wsu.edu

Brian Tillotson  
Missiles & Space Div.  
Boeing  
MS JN-04; P.O. Box 240002  
Huntsville, AL 35824  
Phone: 205-461-3487  
Fax: 205-461-2551  
E-mail: brian@hsvaiv.bv.boeing.com

Padetha Tin  
NASA Lewis Research Center  
MS 105-1; 21000 Brookpark Rd.  
Cleveland, OH 44135  
Phone: 216-433-8164  
Fax: 216-433-5033  
E-mail: padetha@sarah.lerc.nasa.gov

Penger Tong  
Dept. of Physics  
Oklahoma State University  
Room 145, PSII  
Stillwater, OK 74078  
Phone: 405-744-5800  
Fax: 405-744-6811  
E-mail: ptong@osuunx.ucc.okstate.edu

Eugene H. Trinh  
Dept. of Adv. Materials & Fluids Processes Technology  
California Institute of Technology  
MS 183-401/JPL; 4800 Oak Grove Drive  
Pasadena, CA 91109  
Phone: 818-354-7125  
Fax: 818-393-5039  
E-mail: eugene.h.trinh@jpl.nasa.gov

Gretar Tryggvason  
Dept. of Mechanical Engineering & Applied Mechanics  
The University of Michigan  
1231 Beal Avenue; 321 W.E. Lay Automotive Lab.  
Ann Arbor, MI 48109-2121  
Phone: 313-763-1049  
Fax: 313-764-4256  
E-mail: gretar@engin.umich.edu

Peter Tschen  
NASA Lewis Research Center  
MS 500-216; 21000 Brookpark Rd.  
Cleveland, OH 44135  
Phone: 216-433-6578  
Fax: 216-433-8660

Daniel T. Valentine  
Dept. of Mechanical & Aeronautical Engineering  
Clarkson University  
Box 5725  
Potsdam, NY 13699  
Phone: 315-268-2204  
Fax: 315-268-6438  
E-mail: clara@sun.soe.clarkson.edu

Ronald J. Van Diest  
Dept. of Physics  
University of Amsterdam  
VanderWaals-Zeeman Institute; Valckenierstraat 65  
Amsterdam, 1018 XE the Netherlands  
Phone: 31 20 5256382  
Fax: 31 20 5255788  
E-mail: diest@nucleus.phys.uva.nl

Stephen J. Van Hook  
Dept. of Physics  
University of Texas at Austin  
Center for Nonlinear Dynamics  
Austin, TX 78712  
Phone: 512-471-5425  
Fax: 512-471-1558  
E-mail: svanhook@chaos.ph.utexas.edu

S. P. Vanka  
Dept. of Mechanical Engineering  
University of Illinois/Urbana-Champaign  
1206 W. Green St.  
Urbana, IL 61801  
Phone: 217-244-8388  
Fax: 217-244-6534

Illari Vihinen  
Dept. of Mechanical & Aerospace Engineering  
Clarkson University  
50 Elm St., #4  
Potsdam, NY 13676  
Phone: 315-265-8465  
Fax: 315-268-6438  
E-mail: vihineni@craft.camp.clarkson.edu

Jorge Vinals  
SCRI  
The Florida State University  
Tallahassee, FL 32306  
Phone: 904-644-1010  
Fax: 904-644-0098  
E-mail: vinals@scri.fsu.edu

Vladimir A. Volpert  
Dept. of Engineering Sciences & Applied Mathematics  
Northwestern University  
2145 Sheridan Road  
Evanston, IL 60208  
Phone: 847-491-3345  
Fax: 847-491-2178  
E-mail: v-volpert@nwu.edu

Janelle Vorreiter  
Dept. of Mechanical Engineering  
The Johns Hopkins University  
3400 N. Charles St.; 122 Latrobe  
Baltimore, MD 21218  
Phone: 410-516-7555  
Fax: 410-516-4316  
E-mail: vorreite@titan.me.jhu.edu

Pete Vrotsos  
NASA Lewis Research Center  
MS 500-216; 21000 Brookpark Rd.  
Cleveland, OH 44135  
Phone: 216-433-3560  
Fax: 216-433-8660  
E-mail: pete.vrotsos@lerc.nasa.gov

Sondra Walker  
Microgravity Outreach Office  
Microgravity News  
1040-D Settlers Landing Rd.  
Hampton, VA 23669  
Phone: 804-723-2197  
Fax: 804-723-0241  
E-mail: s.l.walker@larc.nasa.gov

C. H. Wang  
Dept. of Chemistry  
University of Nebraska/Lincoln  
632 Hamilton Hall; P.O. Box 880304  
Lincoln, NE 68588  
Phone: 402-472-5346  
Fax: 402-472-9402  
E-mail: chwang@unlinfo.unl.edu

Yanping Wang  
Dept. of Mathematics  
NJIT  
16 E. Midland Ave., 2nd floor  
Kearny, NJ 07032  
Phone: 201-997-6489

Michael J. Wargo  
Code UGS  
NASA Headquarters  
Washington, DC 20546-0001  
Phone: 202-358-0822  
E-mail: michael@microgravity.msad.hq.nasa.gov

Peter C. Wayner, Jr.  
Dept. of Chemical Engineering  
Rensselaer Polytechnic Institute  
Ri. 125  
Troy, NY 12180-3590  
Phone: 518-276-6199  
Fax: 518-276-4030  
E-mail: wayner@rpi.edu

Richard Webber  
Lubrizol Corp.  
29400 Lakeland Blvd.  
Wickliffe, OH 44092  
Phone: 216-943-1200 Ext. 2093  
Fax: 216-943-9020

Mark Weislogel  
NASA Lewis Research Center  
MS 500-102; 21000 Brookpark Rd.  
Cleveland, OH 44135

Phone: 216-433-2877  
Fax: 216-433-8660

David Weitz  
Dept. of Physics & Astronomy  
University of Pennsylvania  
209 S. 33rd St.  
Philadelphia, PA 19104  
Phone: 215-898-7522  
Fax: 215-898-2010  
E-mail: weitz@dept.physics.upenn.edu

Gerald Wilemski  
Lawrence Livermore National Laboratory  
L-482; P.O. Box 808  
Livermore, CA 94551-9900  
Phone: 510-422-7919  
Fax: 510-422-4982  
E-mail: wilemski1@LLNL.GOV

Allen Wilkinson  
NASA Lewis Research Center  
MS 500-102; 21000 Brookpark Rd.  
Cleveland, OH 44135  
Phone: 216-433-2075  
Fax: 216-433-8050  
E-mail: aw@lerc.nasa.gov

Bruce W. Wilson  
Dept. of Payloads and Flight Experiments  
McDonnell Douglas Aerospace  
5301 Bolsa Ave.; Mail Code A3-Y957-11-3  
Huntington Beach, CA 92647-2099  
Phone: 714-896-3311 Ext. 70002  
Fax: 714-896-2305  
E-mail: wilson#d#bruce@ssdgwy.mdc.com

Harris Wong  
Dept. of Eng. Sci. & Applied Mathematics  
Northwestern University  
2145 Sheridan Rd.  
Evanston, IL 60208  
Phone: 847-491-3149  
Fax: 847-491-2178  
E-mail: hwong@nwu.edu

Xiao-Lun Wu  
Dept. of Physics  
University of Pittsburgh  
Pittsburgh, PA 15260  
Phone: 412-624-0873  
Fax: 412-624-9163  
E-mail: xlwu@vms.cis.pitt.edu

Bin Xiong  
Dept. of Mechanical Engineering  
University of Illinois/Chicago  
842 West Taylor Street  
Chicago, IL 60607  
Phone: 312-996-4363  
Fax: 312-413-0447  
E-mail: xiong@dimos.me.uic.edu

Minwu Yao  
Ohio Aerospace Institute  
22800 Cedar Point Rd.  
Brook Park, OH 44142  
Phone: 216-962-3094  
Fax: 216-962-3120  
E-mail: yao@sarah.lerc.nasa.gov

Shinichi Yoda  
Space Experiment Dept.  
NASDA  
Sengen Z-1-1  
Tsukuba-shi, 305 Japan  
Phone: 81-298-52-2439  
Fax: 81-298-50-2233  
E-mail: syoda@nd.tksc.nasda.go.jp

Valentin S. Yuferev  
Ioffe Physical Technical Institute  
26 Polytekhnicheskaya  
St. Petersburg, 194021 Russia  
Phone: 812-247-9175  
Fax: 812-247-1017  
E-mail: valyuf@ammp3.ioffe.rssi.ru

Bernard Zappoli  
Dept. of Microgravity  
CNES  
18 Av. E Belin  
31055 Toulouse Cedex, France  
Phone: 33-61-27-4468  
Fax: 33-61-27-4013  
E-mail: zappoli@cst.cnes.fr

Abdelfattah Zebib  
Dept. of Mechanical & Aerospace Engineering  
Rutgers University  
Brett and Bowser Roads  
Piscataway, NJ 08855-0909  
Phone: 908-445-2248  
Fax: 908-445-3124  
E-mail: zebib@jove.rutgers.edu

Martin Zell  
Dornier Microgravity  
Daimler-Benz Aerospace  
Av der Bundesstrasse 3  
Immenstaad, 88039 Germany  
Phone: 49-7545-82963  
Fax: 49-7545-84429

Xianghuai Zhang  
Dept. of Mechanical Engineering  
Cleveland State University  
1797 E. 31st St.  
Cleveland, OH 44114  
Phone: 216-696-4346  
E-mail: zha2266@csuohio.edu

Xiaoguang Zhang  
Chemical Technology Div.  
Oak Ridge National Laboratory  
P.O. Box 2008; MS 6224  
Oak Ridge, TN 37831-6224  
Phone: 423-574-6797  
Fax: 423-241-4829  
E-mail: z48@ornl.gov

Greg Zimmerli  
NASA Lewis Research Center  
MS 500-102; 21000 Brookpark Rd.  
Cleveland, OH 44135  
Phone: 216-433-6577  
Fax: 216-433-8050  
E-mail: zimmerl@mars.lerc.nasa.gov

Jie Zou  
NASA Lewis Research Center  
MS 105-1; 21000 Brookpark Rd.  
Cleveland, OH 44135  
Phone: 216-433-5010  
Fax: 216-433-5033  
E-mail: jiezhou@sarah.lerc.nasa.gov



## AUTHOR INDEX

- Abdollahian, Davood, 109  
 Ackerson, Bruce, 395  
 Ahmed, Sayeed, 201  
 Alexander, J. Iwan, 461, 469  
 Andereck, C. David, 313  
 Anderson, D. M., 369  
 Anderson, John, 729  
 Andrews, James, 829  
 Anilkumar, A. V., 559  
 Ansari, Rafat, 821  
 Apfel, Robert, 585  
 Ashgriz, Nasser, 565  
 Avedisian, C. T., 779  
 Baker, G. R., 363  
 Balakotaiah, V., 103  
 Balasubramaniam, R., 553  
 Banavar, Jayanth, 635  
 Bankoff, S. George, 701  
 Barbat, Tiberiu, 565  
 Basaran, Osman, 547  
 Baygents, J. C., 731  
 Behringer, R. P., 245  
 Bentz, J. A., 685  
 Berg, Robert, 29  
 Bernal, Luis, 501  
 Beysens, Daniel, 35  
 Blake, John, 207  
 Bogatyrev, Gennady, 813  
 Bonetto, Fabian, 133  
 Borhan, A., 289  
 Boukari, Hacène, 67  
 Brackbill, J. U., 693  
 Braunsfurth, Manfred, 259  
 Briggs, Matthew, 67  
 Browne, Edward, 667  
 Budakian, R., 435  
 Carey, Van, 201  
 Chai, An-Ti, 521  
 Chaikin, P. M., 397  
 Chan, Cho, 319  
 Chan, S. H., 207  
 Chang, Hsueh-Chia, 89  
 Chen, C. F., 319  
 Chen, Yi-Ju, 481  
 Chen, X., 585  
 Chernov, A. A., 345  
 Chigier, Norman, 449  
 Ch'ng, Choon, 165  
 Chung, Jacob, 141  
 Clark, Ivan, 227  
 Clark, Noel, 409  
 Coleman, Catherine, 585  
 Colovas, Peter, 313  
 Concus, Paul, 649  
 Coriell, S. R., 345  
 Croonquist, Arvid, 585  
 Davis, E. James, 679  
 Davis, Robert, 737  
 Davis, Stephen, 351  
 Degen, Michael, 313  
 Dhir, V. K., 153  
 Dreyer, Michael, 655  
 Drolet, François, 429  
 Durgin, William, 61  
 Durian, Douglas, 383  
 Edwards, Boyd, 711  
 Elghobashi, Said, 443  
 Eppell, Steven, 829  
 Erker, J. A., 731  
 Faghri, Amir, 189  
 Favier, J.-J., 461  
 Feonychev, Alexander, 493  
 Ferrell, Richard, 53  
 Finn, Robert, 649  
 Fortmeyer, Justin, 785  
 Foster, M. R., 363  
 Fukushima, Eiichi, 251  
 Gabis, D. H., 685  
 Gaitan, D. Felipe, 591  
 Gallagher, Christopher, 89, 723  
 Gammon, Robert, 67  
 Garandet, J.-P., 461  
 Garcia, Laudelino, 773  
 Garoff, Stephen, 607  
 Garrabos, Yves, 35  
 Gent, David, 67  
 Ghosh, T. K., 685  
 Glezer, Ari, 171  
 Goddard, J. D., 241  
 Gopal, Anthony, 383  
 Gopinath, Ashok, 661, 791  
 Gorbunov, Aleksei, 813  
 Goree, John, 425  
 Gray, Donald, 711  
 Grothberg, James, 751  
 Hagenbuchle, Martin, 389  
 Haj-Hariri, H., 289  
 Hallinan, Kevin, 177  
 Hamoodi, S. A., 685  
 Han, Minsub, 621  
 Hart, John, 717, 767  
 Hatton, T. Alan, 667  
 He, Qun, 177  
 Hegseth, John, 35, 773  
 Herman, Cila, 195  
 Hewitt, Geoffrey, 3  
 Hickey, K. A., 685  
 Hinch, E. J., 579  
 Holt, R. Glynn, 585, 591  
 Homsy, George, 259  
 Honohan, A., 277  
 Howell, Peter, 751  
 Huang, C. M., 685  
 Huang, Jianming, 147  
 Huang, Jie, 711  
 Hudman, M., 277  
 Humphrey, William, 449  
 Ivanov, Alexander, 813  
 Ivchenko, I. N., 685  
 Jacobs, Donald, 75  
 Jacobs, Jeffrey, 271  
 Jankovsky, Joseph, 585  
 Jayawardena, S. S., 103  
 Jenkins, James, 235  
 Jin, Wei, 635  
 Johnson, Edward, 227  
 Joshi, Prakash, 61  
 Juric, Damir, 535  
 Kalachinskaya, Irina, 493  
 Kaler, Eric W., 41  
 Kalkur, T. S., 165  
 Kamotani, Yasuhiro, 121, 331, 759  
 Karthikeyan, Muthu, 147  
 Kassemi, M., 527  
 Kelly, R. E., 295  
 Keshock, Edward, 115  
 Khaydarov, John, 829  
 Khrustalev, Dmitry, 189  
 Kim, Hyo, 701  
 Kim, Jungho, 165  
 Knight, Roy, 673  
 Kolesenikova, Elvira, 807  
 Koplik, Joel, 635  
 Kothe, D. B., 693  
 Kou, S., 301  
 Krall, A. H., 403  
 Kusner, Robert, 47  
 Lacy, Claud, 553  
 Lahey, Richard, 133  
 Langbein, Dieter, 655  
 Langer, Stephen, 383  
 Lasheras, Juan, 443  
 Lee, C. P., 559  
 Leighton, David, 89, 723  
 Leslie, Fred, 585  
 Li, M., 397  
 Liakopoulos, A., 325  
 Lichter, Seth, 621  
 Lin, Chih-Yu, 621  
 Lin, Chün, 115  
 Lin, S. P., 277  
 Liu, Ching-Shi, 565  
 Liu, Jing, 389  
 Lizée, Arnaud, 461  
 Loewenberg, Michael, 579, 737  
 Louge, Michel, 235  
 Loyalka, S. K., 685  
 McCormick, W. D., 265, 487  
 McCready, Mark, 89  
 McFadden, G. B., 345  
 McKinley, Gareth, 377  
 Mackowski, Daniel, 673  
 McQuillen, John, 95, 109  
 Maher, James, 647  
 Maksimovic, Pepi, 501  
 Maldarelli, Charles, 571  
 Marr-Lyon, M. J., 475  
 Marston, P. L., 475  
 Martin, B., 419  
 Maruvada, S. R. K., 541  
 Matthiesen, David, 585  
 Megaridis, Constantine, 357  
 Merte, Herman, 183  
 Meyer, William, 397, 829  
 Miksis, Michael, 701  
 Min, Kyung, 47

Misawa, Masaki, 127  
 Molloy, Richard, 723  
 Morse, S. F., 475  
 Mortazavi, Saeed, 535  
 Motil, Brian, 201  
 Muehlner, Kurt, 487  
 Murray, B. T., 345  
 Nadim, Ali, 599  
 Nakagawa, Masami, 251  
 Nas, Selman, 535  
 Neitzel, G. Paul, 283  
 Niederhaus, Charles, 271  
 Nikitin, Sergei, 813  
 Nikolayev, Vadim, 35  
 Oakes, David, 61  
 Oğuz, Hasan, 127, 159  
 Ohlsen, Daniel, 717  
 Onuki, Akira, 47  
 Or, A. C., 295  
 Ostrach, Simon, 331, 759  
 Ovryn, Ben, 829  
 Papadopoulos, Dimitrios, 641  
 Park, Chang-Won, 541  
 Patashinski, Alexander, 81  
 Paulaitis, Michael, 41  
 Perlin, Marc, 615  
 Perng, Yeong-Yan, 621  
 Perrot, François, 35  
 Petrov, Valery, 487  
 Phan, S. E., 397  
 Pines, Vladimir, 81  
 Plawsky, Joel, 147  
 Pokhilko, Victor, 493  
 Polezhaev, V. I., 797, 813  
 Polovko, Yuri, 807  
 Poulikakos, Dimos, 357  
 Prosperetti, A., 159  
 Pukhnachov, Vladislav, 337  
 Putin, Gennady, 813  
 Putterman, S. J., 435  
 Quintel, J., 109  
 Rashidnia, N., 527  
 Rath, Hans, 655  
 Ratner, Mark, 81  
 Rawlins, W. Terry, 61  
 Resnick, Andrew, 469  
 Rezkallah, Kamel, 219  
 Rodichev, Evgeny, 465  
 Rodicheva, Olga, 465  
 Rogers, Chris, 455  
 Rogers, R., 397  
 Ronney, Paul, 785  
 Rosner, Daniel, 641  
 Russel, W. B., 397  
 Sacco, Albert, 585  
 Sadhal, Satwindar, 515  
 Sangani, Ashok, 411  
 Schatz, Michael, 265, 487  
 Schiaffino, Stefano, 627  
 Schultz, William, 615  
 Schulze, Timothy, 351, 369  
 Schwartz, Leonard, 609  
 Shaumeyer, J. N., 67  
 Shaw, B. D., 213  
 Shen, Ting, 207  
 Shi, Tao, 585  
 Singhal, Maneesh, 133  
 Slobozhanin, L. A., 469  
 Smedley, Gregory, 61  
 Smith, Marc, 171  
 Sonin, Ain, 627  
 Spiegelberg, Stephen, 377  
 Squires, Kyle, 455  
 Stahl, S. L., 213  
 Stebe, Kathleen, 509  
 Steen, Paul, 481  
 Subramanian, R. Shankar, 553  
 Suh, Kwang, 821  
 Swift, Jack, 265, 487  
 Swinney, Harry, 265, 487  
 Takagi, Shu, 127  
 Tanveer, S., 363  
 Tao, Y., 301  
 Tarbell, John, 745  
 Tebbe, P. A., 685  
 Tekasakul, P., 685  
 Tharrington, A., 419  
 Thiessen, D. B., 475  
 Thomson, J. Ross, 429  
 Thornton, Kathryn, 585  
 Tian, Yuren, 585  
 Todd, Paul, 737  
 Tompson, R. V., 685  
 Tong, Penger, 413  
 Trinh, Eugene, 515, 585, 791  
 Tryggvason, Grétar, 535  
 Van Hook, Stephen, 265, 487  
 Vedha-Nayagam, M., 357  
 Vera, Moin, 383  
 Vihinen, I., 277  
 Viñals, Jorge, 429  
 Voinov, Oleg, 337  
 Waggoner, R. Allen, 251  
 Wang, Hua, 737  
 Wang, T. G., 559  
 Wang, Yanping, 571  
 Wayner, Peter, 147  
 Weidman, Patrick, 717  
 Weitz, D. A., 25, 403  
 Wilemski, Gerald, 61  
 Wilkes, Edward, 547  
 Wilkinson, R. Allen, 67, 73  
 Worster, M. Grae, 369  
 Wozniak, Günter, 553  
 Wright, W., 435  
 Wu, Xiao-lun, 47, 419  
 Xu, Jieyong, 307  
 Yuferev, Valetin, 807  
 Zahm, J., 109  
 Zebib, Abdelfattah, 307  
 Zeng, Shulin, 737  
 Zhang, Nengli, 521  
 Zhao, Z., 779  
 Zhmakin, Alexander, 807  
 Zhu, J. X., 397  
 Zielinski, Richard, 41  
 Zimmerli, Greg, 59



REPORT DOCUMENTATION PAGE			Form Approved OMB No. 0704-0188	
Public reporting burden for this collection of information is estimated to average 1 hour per response, including the time for reviewing instructions, searching existing data sources, gathering and maintaining the data needed, and completing and reviewing the collection of information. Send comments regarding this burden estimate or any other aspect of this collection of information, including suggestions for reducing this burden, to Washington Headquarters Services, Directorate for Information Operations and Reports, 1215 Jefferson Davis Highway, Suite 1204, Arlington, VA 22202-4302, and to the Office of Management and Budget, Paperwork Reduction Project (0704-0188), Washington, DC 20503.				
1. AGENCY USE ONLY (Leave blank)	2. REPORT DATE September 1996	3. REPORT TYPE AND DATES COVERED Conference Publication		
4. TITLE AND SUBTITLE  Third Microgravity Fluid Physics Conference		5. FUNDING NUMBERS  WU-962-24-00		
6. AUTHOR(S)				
7. PERFORMING ORGANIZATION NAME(S) AND ADDRESS(ES)  National Aeronautics and Space Administration Lewis Research Center Cleveland, Ohio 44135-3191		8. PERFORMING ORGANIZATION REPORT NUMBER  E-10387		
9. SPONSORING/MONITORING AGENCY NAME(S) AND ADDRESS(ES)  National Aeronautics and Space Administration Washington, D.C. 20546-0001		10. SPONSORING/MONITORING AGENCY REPORT NUMBER  NASA CP-3338		
11. SUPPLEMENTARY NOTES  Responsible person, Bhim S. Singh, organization code 6712, (216) 433-5396.				
12a. DISTRIBUTION/AVAILABILITY STATEMENT  Unclassified - Unlimited Subject Category 34  This publication is available from the NASA Center for AeroSpace Information, (301) 621-0390.		12b. DISTRIBUTION CODE		
13. ABSTRACT (Maximum 200 words)  The conference's purpose was to inform the fluid physics community of research opportunities in reduced-gravity fluid physics, present the status of the existing and planned reduced gravity fluid physics research programs, and inform participants of the upcoming NASA Research Announcement in this area. The plenary sessions provided an overview of the Microgravity Fluid Physics Program, present and future areas of emphasis, information on NASA's ground-based and space-based flight research facilities—especially use of the International Space Station, and the process by which future investigators enter the program. An international forum offered participants an opportunity to hear from Russian speakers about their microgravity research programs. Three keynote speakers provided broad technical overviews on the history and future development of the moon and on multiphase flow and complex fluids research. One keynote paper and an extended abstract are included in the proceedings. One hundred and thirty-two technical papers were presented in 28 sessions. Presenters briefed their peers on the scientific results of their ground-based and flight research. One hundred and twenty-two papers are included here.				
14. SUBJECT TERMS  Fluid dynamics; Fluid mechanics; Microgravity; Reduced gravity; Heat transfer; Multiphase flow; Complex fluids			15. NUMBER OF PAGES 900	
			16. PRICE CODE A99	
17. SECURITY CLASSIFICATION OF REPORT Unclassified	18. SECURITY CLASSIFICATION OF THIS PAGE Unclassified	19. SECURITY CLASSIFICATION OF ABSTRACT Unclassified	20. LIMITATION OF ABSTRACT	